Vol. 70, No. 2 / 2023

e: ISSN 2068 – 2239
p: ISSN 2068 – 4215

INMATEH – AGRICULTURAL ENGINEERING

MAY - AUGUST

Managing Editorial Board - INMA Bucharest

INMATEH - Agricultural Engineering **journal is indexed in the next international databases:**
ELSEVIER /SciVerse SCOPUS, CLARIVATE - WEB of SCIENCE- Emerging Sources Citation Index (ESCI), ULRICHS Web: Global Serials Directory, CABI, SCIPIO, Index COPERNICUS International, EBSCO Publishing, Elektronische Zeitschriftenbibliothek

INMATEH - Agricultural Engineering
vol. 70, no.2 / 20213
e-ISSN: 2068–2239; p: ISSN: 2068–4215

https://inmateh.eu/ *E-mail: inmatehjournal@gmail.com*

Edited by: INMA Bucharest

National Institute for Research-Development of Machines and Installations
Designed for Agriculture and Food Industry - INMA Bucharest
6, Ion Ionescu de la Brad Bvd., sector 1, Bucharest, ROMANIA

CONTENT

DEVELOPMENT OF A TRICOPTER-HEXAROTOR AGRICULTURAL UAV DESTINED FOR THE REALIZATION OF PRECISION SPRAYING WORKS
/
DEZVOLTAREA UNUI UAV TRICOPTER-HEXAROTOR DESTINAT REALIZĂRII LUCRĂRILOR DE STROPIRE DE PRECIZIE

Mihai Gabriel MATACHE *, Iuliana GĂGEANU, Gabriel Valentin GHEORGHE*), Cătălin PERSU[1)], Marian CHIRIȚESCU, Mihaela NITU [1)]
INMA Bucharest / Romania;
Tel: 0727957693; E-mail: gabimatache@yahoo.com
DOI: https://doi.org/10.35633/inmateh-70-01

Keywords: *agricultural UAV, precision spraying, tricopter-hexarotor, autonomous*

ABSTRACT
The utilization of unmanned aerial vehicles (UAVs) for chemical application has become a topic of great interest to both researchers and the market in recent times. Producers have proposed the use of drones for joint spraying as a means of enhancing precision agriculture and productivity. However, chemical spraying is a highly specialized field where the quality of the spray is critical so the used UAV have to be precise and reliable. Within this paper will be presented the process of developing a tricopter-hexarotor chassis type UAV, electrically driven, fitted with a 66 litres tank and 6 anti-drift nozzles which will be used for precision spraying of agricultural crops based on preprogrammed flying missions.

ABSTRACT
Utilizarea vehiculelor aeriene fără pilot (UAV-uri) pentru aplicarea chimicalelor a devenit un subiect de interes în ultimul timp atât pentru cercetători cât și pentru piață. Producătorii au propus folosirea dronelor pentru stropirea integrată ca o modalitate de a îmbunătății productivitatea și agricultura de precizie. Totuși, stropirea cu substanțe chimice reprezintă un domeniu specializat în care calitatea stropirii este esențială astfel încât UAV-ul folosit trebuie să fie precis și fiabil. În cadrul acestei lucrări va fi prezentat procesul de dezvoltare al unui UAV având șasiul de tip tricopter-hexarotor, acționat electric, dotat cu un rezervor de 66 litri și 6 duze antidrift care va fi folosit pentru stropirea de precizie a culturilor agricole pe baza unor misiuni de zbor preprogramate.

INTRODUCTION

Main applications areas in the use of UAV are filming and photography, inspection and maintenance, mapping and surveying, surveillance and monitoring and precision agriculture, in addition to other miscellaneous applications (*del Cerro et al., 2021*).

One important component of Agriculture-4.0 is represented by drones and other mechatronic systems available to increase the Return on Investment, ensure the sustainability of the farming process and reduce environmental pollution near to "zero pollution". So, the role of UAV platforms is crucial in precision farming for sustainable agriculture. Aerial monitoring of crop vegetation status is a major factor in precision agricultural management. The health status of crops is analysed based on vegetation indices determined by reliable measurements performed with optical sensors installed onboard drones or through sampling devices mounted on UAV (*Zhang et al., 2022*). The monitoring of the resources and the state of the vegetation is performed aerially with non-contact sensors, the automatic data acquisition being correlated with the GPS coordinates and their processing in the GIS system for making spectral maps, all necessary in spatial and precision management (*de Castro et al.*, *2021; del Cerro et al., 2021; Wang et al., 2023*). Detection, identification, and quantification of crop diseases are therefore done by monitoring, the best results are obtained by thermography, chlorophyll-fluorescence, or with multi- and hyperspectral sensors.

[1] *Mihai Gabriel Matache, Ph.D. Eng., Iuliana Găgeanu, Ph.D. Eng., Gabriel Valentin Gheorghe, Eng., Cătălin Persu, Eng., Marian Chiriţescu, Tech.*

Basically, by aerial mapping of the arable area concerned, the following technological aspects of agricultural crops can be managed much better:

- Control of applied fertilizers, implicitly can be observed areas where increased attention is needed in terms of pollution or reducing the amount of waste that could have a detrimental effect on the environment;
- Neutralization of harmful plants that can infiltrate crops, consequently measures can be taken quickly to act in order to eliminate weeds and solve the harmful situation;
- Early detection of diseases and pests of agricultural crops leaves farmers the opportunity to adopt the best solutions to reduce them promptly.

After the online aerial monitoring of agricultural crops, the next stage is the offline processing of recording data to produce spectral maps. These maps are made by processing images using a dedicated programming medium. The spectral maps obtained from the processing of images recorded by the multispectral camera onboard the drone contain information on the state of crop vegetation. Afterwards, the use of specialized UAV platforms to precisely apply the phytosanitary treatments based on the obtained maps ensure sustainable development in agriculture. There were performed researches regarding the quality of the spraying process of different types of drones, taking into consideration aspects as pesticide load, downwash of multi-rotor UAV, droplet deposition, flight speed and height, number of drones etc (*Qi et al., 2023; Chen et al., 2022; Yang et al., 2022*), all these results contributing to the optimization of drone development in order to be used during spraying works.

In order to build an agridrone minimal knowledge of mechanics, electronics and IT or in a word mechatronics is required. The first step in designing a drone is to know the components of the drones and the materials they will be made of. Generally, an aerial drone is made up of hardware and software components. Most systems and components can be purchased, other simple parts can be made on a 3D printer with high manufacturing volume. A preliminary design flow for high payload aerial drones is recommended in the literature (*Ong et al., 2019*). The flowchart of the design flow for these UAS platforms is shown in Figure 1.

The design methodology is relatively new, it includes coaxial rotor propulsion systems that have the best pressure-to-volume ratio.

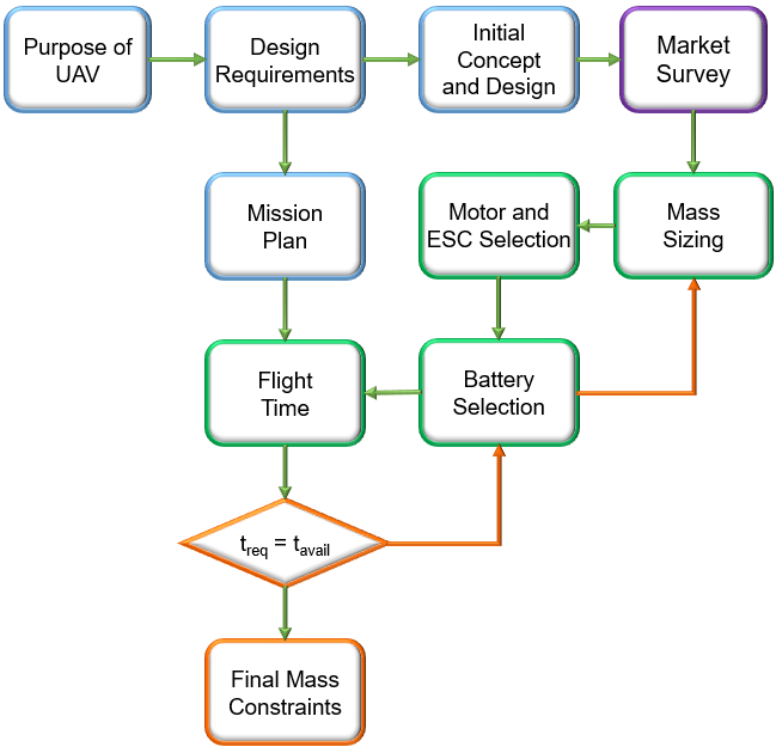

Fig. 1 - UAV system preliminary design flow chart (adapted from *Ong et al., 2019*)

Recently, UAVs for utility applications have the limits of the available flight time, considerable as operating autonomy values for various industrial applications of inspection, agriculture, surveillance and transportation.

Heavy UAS platforms are dominant in the logistics sector because their capabilities facilitate the autonomous transport of goods and reduce time in dangerous work missions. Payload mass is unpredictable in such applications. Therefore, to ensure that these drones are suitable for a wide range of actions, it is essential that the aerial vehicle has heavy lifting capabilities.

The process adapted to heavy drones can be applied to the design of conventional multi-functional tricopter-hexarotor configurations and then it is compared with other sizing methods proposed in this paper.
It is important to note that both the flight mission plan and the design requirements must be met individually and will be addressed in parallel. From the mission profile the required flight time (t_{req}) can be calculated and compared to the available flight time (t_{avail}) given the capacity of the selected battery pack. The approach is iterative. Instead of the empty drone weight (available/required) used in the conventional fixed-wing drone mass sizing methodology, the multirotor UAV design methodology was modified by comparing the flight time (available/required) on mass sizing by battery pack selection (*Ong et al., 2019*).

Agridrones intended for spraying agricultural crops generally have a frame structure, with 3 or more arms arranged radially and equidistantly for the installation of each propulsion system (motor + propeller) as well as a landing gear and other elements for fixing the equipment necessary for the flight mission on the structure.

The payload of the drone is ensured by the power of the propulsion system and the number of drone motors determines the shape of the frame for the UAV platform. The classification according to the number of motors of the structures of the most common multicopters used in precision agriculture is presented in Figure 2.

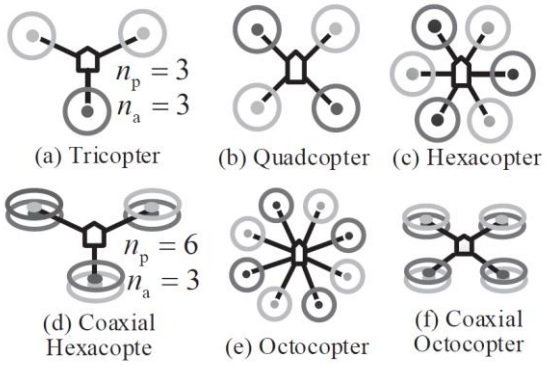

Fig. 2 - Schematic representation of current UAV multicopter structures (*Xunhua et al., 2019***)**
n_p – number of motors; n_a- number of arms

Coaxial drones have several advantages over traditional multi-rotors drones, as stated by *Karman Drones, (2023)*, as:

- enhanced stability due to their opposing rotor system, which cancels out rotation momentum, fact which allows for easier control of the UAV and to maintain a steady hover;

- increased lift capacity: a coaxial multi-rotor drone generates more thrust than a traditional one similar in size, due to its coaxial rotors spinning in opposite directions but having added thrust vectors. Thus, heavier payloads could be lifted, like bigger fluid tanks, without sacrificing flight performance;

- redundancy and reliability: coaxial drones offer a high level of redundancy in the event of a rotor failure. With rotors spinning in opposite directions, the drone can maintain stability and control even if one rotor fails.

- low noise: the opposing rotation of the rotors in a coaxial system produces less noise than a traditional one, making it a quieter option for applications that require low noise emissions, such as wildlife monitoring or urban surveillance.

Regarding development of tricopter – hexarotors, also called co-axial Y6 or coaxial hexacopters, there are results in the relevant literature which present the stages of development and testing of such UAVs, relevant for the state of the art from which present paper was inspired (*Czyba et al., 2015; Ong et al., 2019; Hamandi et al., 2020*)

Within this paper are presented the development and initial tests performed for a high capacity agricultural coaxial tricopter UAV, called 4.0-MHRT.66L, which was designed after point d) architecture from figure 2, for a payload of 66 litres of phytosanitary fluid, with 6 anti-drift nozzles and an electric double-pump for creating hydraulic pressure in the boom ramp. The initial test consisted in maximum thrust measurement, spraying system characterization and coverage degree assessment in different flying conditions.

MATERIALS AND METHODS

3D design

The 3D CAD design for the 4.0-MHRT.66L variant is presented in Figure 3. The mechanical structure is the novelty element for the 4.0-MHRT.66L agridrone, the structure chosen for the drone being outlined around the Y6 tricopter hexarotor concept. The arms of the drone were designed in the form of parallel aluminium tubes stiffened by means of a support, at the end of each tube being mounted the electric motor with a double propeller. The liquid substance tank was designed as a body composed of a truncated cone and a cylinder with rounded edges, constructed of fiberglass and mounted on top of the drone's main structure. Under the tank, the battery housing and flight equipment supports were designed. The spraying ramp together with the spraying nozzles were designed in a circular shape and mounted on supports, below the level of the lower motors.

a) Isometric view b) Top view

Fig. 3 – Functional model 3D design, 4.0-MHRT.66L

CAE analysis of 4.0 MHRT.66L functional model

Static FEM analysis was performed on the 3D model of the 4.0-MHRT.66 L functional model to verify the mechanical strength of the drone frame.

A structural analysis was performed in static mode, using the solid meshing type. The meshed structure totalled a number of 150199 nodes, with 71375 standard elements. The minimum size of the elements was 0.982496 mm and the maximum size was 16.9811 mm. The finite element analysis was made in the SolidWorks program. Figure 4 shows the meshed structure.

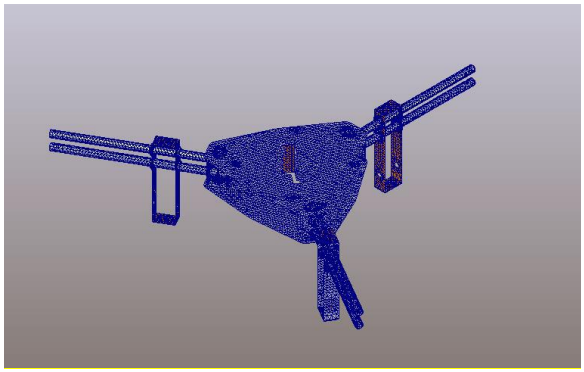

Fig. 4 - Structural model of functional model 4.0-MHRT.66L: discretization

The loading forces were applied to the motor mounts. The loading force had a value of 300 N. Thus, the total reaction force from the fixing points had a value of 1800 N. The minimum and maximum values of the equivalent stress state (Figure 5, a)) in the structural model of the drone were determined after performing the static analysis according to the fixings and loads presented previously. The maximum value of the equivalent stress was 313.8 MPa and was located at the point of contact between the drone arm and the landing gear leg, node 145839, which is located in the cylindrical joint of the drone arms through which they are connected to the drone body.

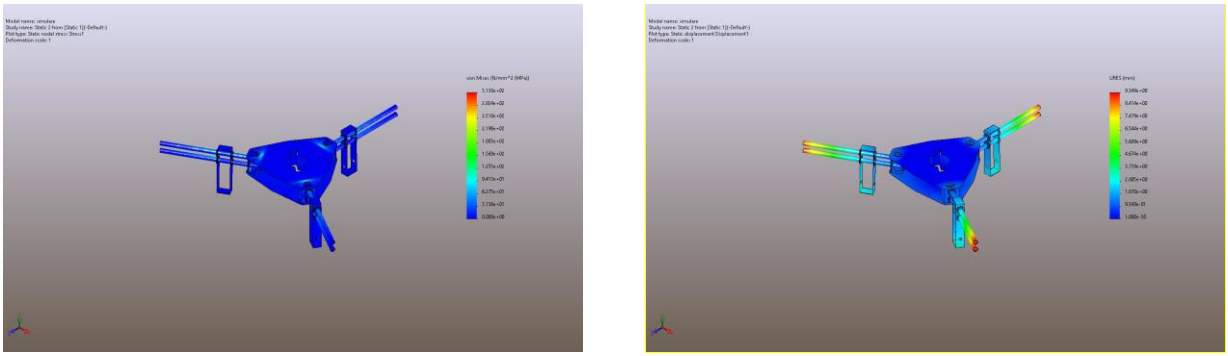

a) Von Misses equivalent stress b) Equivalent displacing

Fig. 5 – Static study results

The distribution of the resultant relative displacement field values in the structural model of the functional model MHRT.66L is graphically represented in Figure 5, b). The representation is made on the deformed shape of the structure. The maximum displacement related to the simulation was 9,349 mm at the tip of the drone arms, which can be taken up by the flexible nature of the frame. Following the study, the structural integrity of the drone's frame was validated up to loads of 1800 N, loads that exceed by 80% the maximum load for which the drone was designed.

Execution of the functional model 4.0-MHRT.66L

The agridrone functional model for applying phytosanitary treatments in field crops, MHRT.66L, is a Y hexarotor type drone powered by two AB2-17500mAh-51.8V, 14S Lithium batteries, it is equipped with 6 8700 W motors, type X9 Series Power System for Heavy Lift Drones X9PLus 36inch, whose rotation speed is controlled by 6 electronic speed controllers (ESC) of 120 A nominal (150 A maximum), three motors having two CCW blade propellers (rotating counterclockwise) and the other three motors having two CW blade propellers (rotating clockwise), all propellers having dimensions of 36'', has a 66-liter tank from which a 12 V DC electric pump, powered by 2 separate 12 V DC batteries, pumps with a pressure of up to 7.5 bar phytosanitary substances to a circular spray ramp on which 6 nozzle holders equipped with calibrated spray nozzles are mounted. The drone is equipped with a Pixhawk 4 Orange cube autopilot with Here 3 GNSS GPS module for precise positioning in the field and can be programmed to operate the electric pump to spray agricultural crops only on predefined areas based on the mission profile entered by the operator. Flight system settings were made using Mission Planner software.

Figure 6 shows the connection diagram of the control elements of the drone, based on which the wiring was done during the execution stage.

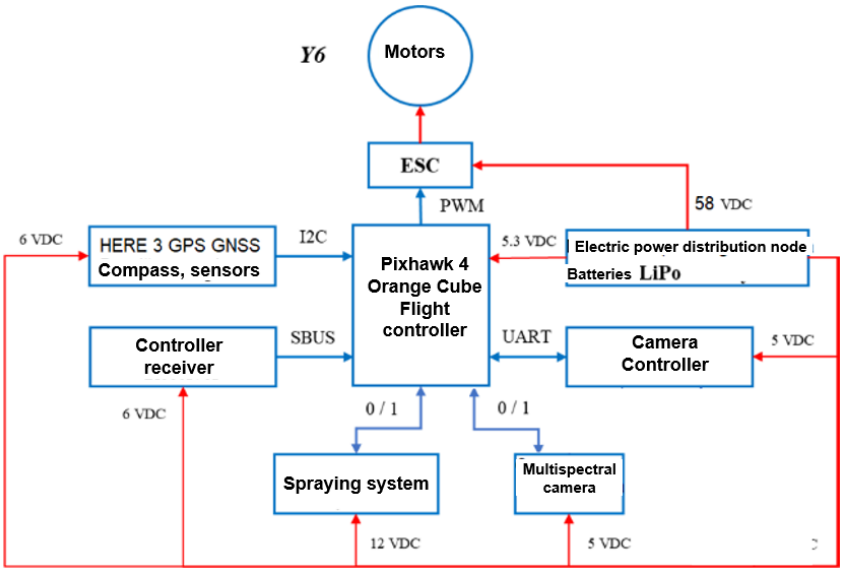

Fig. 6 – Wiring diagram of avionics elements 4.0-MHRT.66L

Figure 7 shows the central frame and the battery holder and how the drone arms are attached to the central frame.

Fig. 7 –MHRT.66L elements– main frame, arm - central frame assembly

Figure 8 shows aspects during the manufacturing process of the 66 litres tank made of composite material consisting of glass fibre and carbon fibre laminated with epoxy resin. The tank cap is equipped with a vent valve and inside it wave breakers have been created to reduce liquid movements and ensure stability during flight.

a) Mold lamination of the tank upper body

b) Tank bottom

c) Wave breaker building

d) Tank upper body

e) Assembled tank

Fig. 8 – 4.0-MHRT.66L components – tank

Figure 9 shows the functional model 4.0-MHRT, fully assembled, in the folded transport position and in the working position.

a) Functional model - folded for transport

b) Functional model - operating position

Fig. 9 – 4.0-MHRT.66L Functional model

In order to determine the main characteristics and operational parameters of the functional model, a series of tests were conducted. The experiments were carried out in the laboratory to determine the dimensions of the drone, the maximum take-off mass and the characteristics of the spraying system.

The **dimensions** of the 4.0 MHRT.66L drone functional model were determined by measuring using calibrated laboratory tape measures and scales.

The maximum take-off mass was determined by measuring the maximum takeoff force between the drone and a fixed point on the ground by means of a 5 KN load cell placed between the drone and the ground.

The flow rate through the nozzles of 4.0 MHRT agridrone functional model was determined by direct method, using a digital flowmeter and by volumetric method, measuring the liquid flowed for each nozzle in a 1-minute interval, at the working pressure. The pressure drop across the ramp on which the six nozzle holders are located was measured by means of a pressure transducer mounted in the place of a nozzle, on the nozzle holder.

In-situ experiments to determine spray uniformity and degree of coverage were conducted to demonstrate the functionality of the functional model. To carry out the tests, the following test methodology was applied:

- the tank of the drone was loaded with water solution and methylene blue;
- blue 0.3 type nozzles were installed on the drone's spraying ramp;
- water-soluble paper was applied to the ground to capture water droplets from the drone's nozzles;
- altitude and working speed were set, from the base station software, Mission Planner;
- transitions to 2 working speeds (3 and 5 m/s) and 3 working heights (3, 6, respectively 9 m) were made.

After these steps, high-definition images of the water-sensitive paper - 4962x7019 pixels (Figure 10) were taken using an EPSON L220 scanner for each test. Images were processed using software to obtain the coverage degree. For image processing, first the contrast between the colour of the droplets (blue) and the background colour (white) was increased. The blue pixels were then extracted as a percentage of the total pixels and thus the percentage coverage was measured.

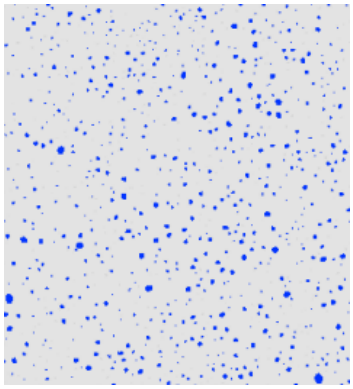

Fig. 10 – Scanned image of water-sensitive paper for determining the degree of coverage

Thus, with the drone set in automatic flight mode - ALTHOLD (automatic flight altitude maintenance) and commanded from the remote control, test flights were carried out with the tank loaded, with different flight speeds and working heights, the results obtained being presented in the following table.

The nozzle holders of the drone were equipped with blue 03 type nozzles and it worked at a pressure of 1.5 bar.

RESULTS

Dimensions of the 4.0 MHRT.66L drone functional model

After conducting the tests to determine the dimensions of the 4.0 MHRT.66L drone functional model, the following results were obtained:

- Diameter at the centre of the motors: 2.76 m
- Distance between motor centres: 2.30 m
- Height: 0.94 m
- Own mass without battery: 50 kg
- Weight of batteries: 12 kg
- Maximum mass with full liquid tank: 128 kg

Maximum thrust force

Table 1 shows the average values obtained regarding the maximum thrust force.

Table 1

Maximum thrust force

Acceleration (%)	ESC power (A)	Drone thrust force (N)
25%	37.5	389
50%	75	765
75%	112.5	1125
100%	150	1505

The maximum thrust force corresponds to a maximum ESC current level of 150 A at a battery charge level of 58 V and a maximum electric power of 8700 W/motor.

Characteristics of the spraying system

Figure 9 shows aspects of laboratory experiments to determine nozzle flow, total flow and working pressure. The following figure shows aspects of laboratory experiments to determine nozzle flow, total flow and working pressure.

Fig. 9 – Determination of flow rate and working pressure achieved by the 4.0-MHRT.66L drone functional model

The following table presents the average experimental results obtained for the work flow achieved by the 4.0 MHRT agridrone according to the size of the nozzle used. 4 types of nozzles with the following characteristics were used for experiments: spray angle: 120°, made of plastic material, working pressure range 1-6 bar. The type of nozzles was coded by colour and number, depending on the diameter of the respective nozzle.

Table 2

Spraying system characteristics

Working pressure (bar)	1.5			
Nozzle type	orange – 01	yellow-02	blue-03	red – 04
Flow rate per nozzle (l/min)	0.27	0.49	0.66	0.87
Total flow rate (l/min)	1.62	2.94	3.96	5.22

Determination of spray uniformity

Table 3 presents the experimental results obtained for the distribution uniformity.

Table 3

Uniformity of distribution under different working conditions

Crt. No.	Working speed - set (m/s)	Working altitude (m)	Working width (m)	Degree of coverage (%)
1.	3	3	4	48.2
2.	3	6	8	40.1
3.	3	9	10	38.2
4.	5	3	4	44.6
5.	5	6	8	39.2
6.	5	9	10	36.1

From the results obtained, it was found that the best uniformity of distribution was obtained for a 4 m working width and a 3 m altitude for both operating speeds.

CONCLUSIONS

In this paper, the stages of development of an agricultural UAV for carrying out phytosanitary treatments were presented. The agricultural drone made has the following advantages:

- constructive simplicity and the possibility of folding the arms for transport;
- operational safety (allows safe landing, even with a major failure of one of the motors);
- ease of use and performance;
- due to the use of CCW-type propellers above and CW-type propellers below, the Y-type hexarotor drone is much more stable and manoeuvrable;
- due to the special arrangement of the drone's supports in Y at 120º and the arrangement of the spray nozzles between the supports, the angle of the jet of the nozzles is directed directly downwards by the air currents related to the drone's motors, so that a uniform spraying of the crop plants is achieved;
- the precise application of phytosanitary treatments by means of the drone leads to a reduced consumption of phytosanitary substances and implicitly reduced costs;
- the possibility for farmers to treat agricultural crops targeted with phytosanitary substances only in the areas previously identified as needing phytosanitary treatment, without using machines on the ground, which compact the land and destroy part of the crop plants.

ACKNOWLEDGEMENT

This work was supported by a grant of the Romanian Ministry of Education and Research, through the project "Intelligent technology for high precision application of plant protection products, fertilizers and for seeding in hard-to-reach areas" – PN 23 04 01 01– Ctr. 9N/01.01.2023, within PNCDI III and of the Ministry of Research, Innovation and Digitalization through Program 1 - Development of the national research-development system, Subprogram 1.2 - Institutional performance - Projects for financing excellence in RDI, Contract no. 1PFE/30.12.2021.

REFERENCES

[1] de Castro, A.I.; Shi, Y.; Maja, J.M.; Peña, J.M. (2021). UAVs for Vegetation Monitoring: Overview and Recent Scientific Contributions. *Remote Sens. 13*, 2139. https://doi.org/10.3390/rs13112139

[2] del Cerro, J.; Cruz Ulloa, C.; Barrientos, A.; de León Rivas, J. (2021). Unmanned Aerial Vehicles in Agriculture: A Survey. *Agronomy, 11*, 203. https://doi.org/10.3390/agronomy11020203

[3] Chen, P.; Ouyang, F.; Zhang, Y.; Lan, Y. (2022). Preliminary Evaluation of Spraying Quality of Multi-Unmanned Aerial Vehicle (UAV) Close Formation Spraying. *Agriculture, 12*, 1149. https://doi.org/10.3390/agriculture12081149

[4] Czyba, R.; Szafranski, G.; Janik, M.; Pampuch, K.; Hecel, M. (2015). Development of co-axial Y6-Rotor UAV - design, mathematical modeling, rapid prototyping and experimental validation. *International Conference on Unmanned Aircraft Systems (ICUAS).* doi:10.1109/icuas.2015.7152402

[5] Hamandi, M.; Usai, F.Ș Sablé, Q.; Staub, N.; Tognon, M.; Franchi, A.; (2021). Survey on Aerial Multirotor Design: a Taxonomy Based on Input Allocation. *Int. Journal of Robotics Research, 40 (8-9),* 1015-1044, .1177/02783649211025998. hal-02433405v2

[6] Ong, W.; Srigrarom, S.; Hesse, H. (2019). Design Methodology for Heavy-Lift Unmanned Aerial Vehicles with Coaxial Rotors. *AIAA SciTech Forum*, San Diego, CA, USA, ISBN 9781624105784, doi:10.2514/6.2019-2095)

[7] Qi, P.; Zhang, L.;Wang, Z.; Han, H.; Müller, J.; Li, T.;Wang, C.; Huang, Z.; He, M.; Liu, Y.; He, X. (2023) Effect of Operational Parameters of Unmanned Aerial Vehicle (UAV) on Droplet Deposition in Trellised Pear Orchard. *Drones 2023, 7*, 57. https://doi.org/10.3390/drones7010057

[8] Xunhua, D.; Quan, Q.; Kai-Yuan C. (2019). Design Automation and Optimization Methodology for Electric Multicopter UAVs, School of Automation Science and Electrical Engineering, Beihang University, Beijing, 100191, China, Preprint to Elsevier August 20, 2019

[9] Yang, F.; Zhou, H.; Ru, Y.; Chen, Q.; Zhou, L. (2022). A Method to Study the Influence of the Pesticide Load on the Detailed Distribution Law of Downwash for Multi-Rotor UAV. *Agriculture, 12,* 2061. https://doi.org/10.3390/agriculture12122061

[10] Zhang, J.; Zhou, M.; He, K.; Guo, M.; Li, G.; Li, R. (2022). Research on plant sampling system in complex geographical environment using UAV, *INMATEH - Agricultural Engineering, Vol. 67, No. 2*, 166-175, https://doi.org/10.35633/inmateh-67-16

[11] Wang, R.; Zhang, Y.; Du, J.; Bi, Y. (2023). Hyperspectral image classification in desert grassland based on three-dimensional deep learning model, *INMATEH - Agricultural Engineering, Vol. 69, No. 1*, 492-500, https://doi.org/10.35633/inmateh-69-46

[12] ***Karman Drones. (2023). *How Co-axial Drones are Redefining Aerial Capabilities (2023)* https://www.linkedin.com/pulse/how-co-axial-drones-redefining-aerial-capabilities-karmandrones/

DESIGN AND DRAG REDUCTION PERFORMANCE ANALYSIS OF A POTATO HARVEST SHOVEL BASED ON THE SURFACE TEXTURE CHARACTERISTICS OF PANGOLIN SCALE
/
基于穿山甲鳞片表面纹理特征的马铃薯挖掘铲设计及减阻性能分析

Ping ZHAO*), Tiankuo YU, Guofa XU, Ruijin GUO, He LI, Hongfei XU, Tianci JIN, Dong JI
College of Engineering, Shenyang Agricultural University, Shenyang 110866 / China
Tel: +86-13591675814.; E-mail: zhaopingxdg@163.com
DOI: https://doi.org/10.35633/inmateh-70-02

Keywords: *Discrete element, Bionic, Surface texture, Simulation analysis, Soil adhesion*

ABSTRACT
Taking into account the physicochemical properties of soil and the complexity of adhesion interface, how to improve the soil adhesion on the mechanical surface is a crucial technical issue. In order to lower the increasing resistance caused by soil adhesion on the surface of a digging shovel in potato harvesting, a potato digging shovel with a non-smooth surface structure was designed based on bionics theory. Based on testing physical and mechanical properties of soil, a soil groove model corresponding to soil physical properties and particle model physical properties was established through a combination of simulation and physical tests, and a simulation test for evaluating the drag reduction performance was conducted. The simulation comparison test results show that the performance of the bionic digging shovel is better than that of the traditional potato digging shovel, regardless of whether the broken soil rate or the working resistance is reduced, and the soil adhered to the mechanical surface can be effectively reduced by 93.3%. The research results can provide ideas and methods for solving the adhesion problem between machinery and soil.

摘要
考虑到土壤的理化性质和粘附表面的复杂特性，如何改善土壤与机具表面之间的粘附状况是一个非常重要的技术问题。为解决马铃薯收获过程中因土壤粘附于挖掘铲表面造成阻力增大的问题，基于仿生学理论设计了一种具有非光滑表面结构的马铃薯挖掘铲。在测得土壤表征参数的基础上，通过仿真与物理试验相结合的方法，建立了与土壤物理特性和颗粒模型物理特性相对应的土槽模型，通过模拟仿真对减阻效果进行了评估。通过对比仿真与试验，结果表明，无论碎土率还是工作阻力，仿生挖掘铲的效果都优于传统的马铃薯挖掘铲，且土壤和粘附在机械表面的数量可以有效地降低 93.3%。该研究结果可以为解决机具与土壤的粘附问题提供思路和方法。

INTRODUCTION

Potatoes are an important global non-grain food crop, industrial raw material, and feed crop *(Celik et al., 2019)*. In 2018, the total planting area of potatoes worldwide was 1.8×10^7 hm^2, with a total yield of 3.7×10^8 t. China accounts for approximately 27% of all potato planting areas, producing 24% of the total global output, ranking first worldwide *(Tong et al., 2000)*. The planting area of potatoes increases every year as potatoes are the fourth most important food crop in China. Therefore, potato-harvesting machinery has become an urgent necessity in the current Chinese market.

The harvesting shovel, which is utilised in the first step of harvesting operations and is an indispensable part of the potato harvester, is used for soil entry and excavation. Because China's planting area's geographical and soil problems are relatively dispersed, some mountainous and hilly areas have a high planting area, which determines the production mode for harvesting, transportation, and manual labour for picking and separation. The common problems associated with potato harvesting include separating clay from potatoes, potato skin rubbing from sandy soil, and increased back soil resistance. Scholars from various countries who are improving potato harvesting machinery have proposed innovative research and achieved beneficial results *(Babbitt, 2008; Hou et al., 2020)*. Although this lays a foundation for further research, soil adhesion on the shovel surface is gradually changed from mechanical contact to soil-to-soil contact (Fig. 1), energy consumption, specifically in some areas where the soil is relatively humid. Additionally, the soil interface adhesion system's overall mechanical behaviour is more severe during operation *(Zenkov, et al., 2020; Jafar et al., 2021)*.

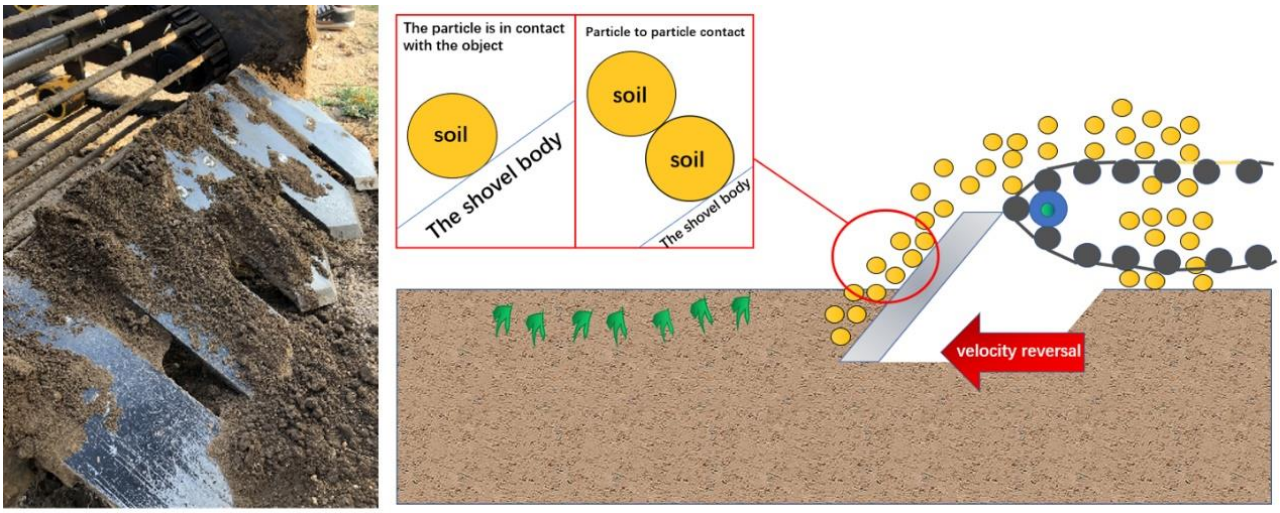

Fig. 1 - Soil stickiness

Therefore, a single force or analytical formula cannot solve the complex soil adhesion problem. There is no accurate and reasonable theoretical basis for the design and research of excavation components, as it is still in the empirical design stage.

In recent years, with the introduction of the advanced concept of bionics by industry peers extensively applying bionic technology and reverse technology in the engineering field *(Junior et al., 2019)*, simulation technologies have proven to be able to solve the problem of insufficient experience in the design of mechanical parts *(Wang et al., 2020)*, such as folding wings of bamboo elephants *(Tong et al., 2015)* and a chicken-like corn seed threshing machine *(Arnell et al., 2007)*.

After several million years of evolutionary optimization, many soil animals move freely in soil or manure without adhering to the outside, such as the armoured pangolin, mole crickets, ants, and moulting. This mobility feature is undoubtedly related to their peculiar body surface morphology. The corrugated surface model analysis shows that a corrugated surface can effectively reduce the soil adhesion area, reduce the negative air pressure at the interface, limit the continuity of the water film, and improve the lubrication of the interface and reduce the viscosity and resistance *(Massah et al.,2020)*.

After years of research, Jilin University in China has divided common geometric shapes into prismatic, concave, convex hull, flake, and spiral *(Zhang et al., 2004)*. The results show that a non-smooth surface has a certain effect on clay reduction and de-soiling *(Ren, et al.,2001; Liu et al.,2016; Junio et al.,2019)*, whereas a ridge structure is relatively easy to control. The pangolin is often found in the humid forest areas of hills, foothills, and plains. Because the pangolin can dig 20~30 cm diameter holes 2~4 m deep in the soil, it is the source of bionic ridge structure. When pangolins use their claws to dig holes through the mountain nail quickly, the pangolin body's scale resists the loosened soil, causing the soil to be pushed out of the hole *(Lee et al., 2001)*. The scale surface on pangolins shows a non-equiangular geometric mesh shape with crisscross changes of longitudinal ridges and transverse grooves. The longitudinal ridges are more prominent and more numerous, with a fan-shaped distribution. The transverse grooves are small and less numerous, and the longitudinal ridge is cut at a certain depth *(Lee et al., 2001; Zhou et al., 2016)*. This biological prototype for a soil removal tool exhibits a satisfactory drag reduction, and its working environment or soil flow on the surface is close to the working condition of the harvesting shovel.

At the same time, it was observed that the scales of pangolins were about 22.5°, while the optimal entry angle of potato harvest shovel was about 24° (Fig. 2).

Combined with the soil digging behaviour of pangolins, the scales would be slightly adjusted with the body surface muscle, so it was thought that they had a lot in common.

This study investigates the attachment of a ridge structure to the potato harvest shovel to reduce viscosity and add a de-soiling to reduce soil adhesion on the shovel surface and minimise resistance to back soil function. This study also provides both mode and method for addressing surface mechanical viscosity reduction and de-soiling that is yet to be solved entirely.

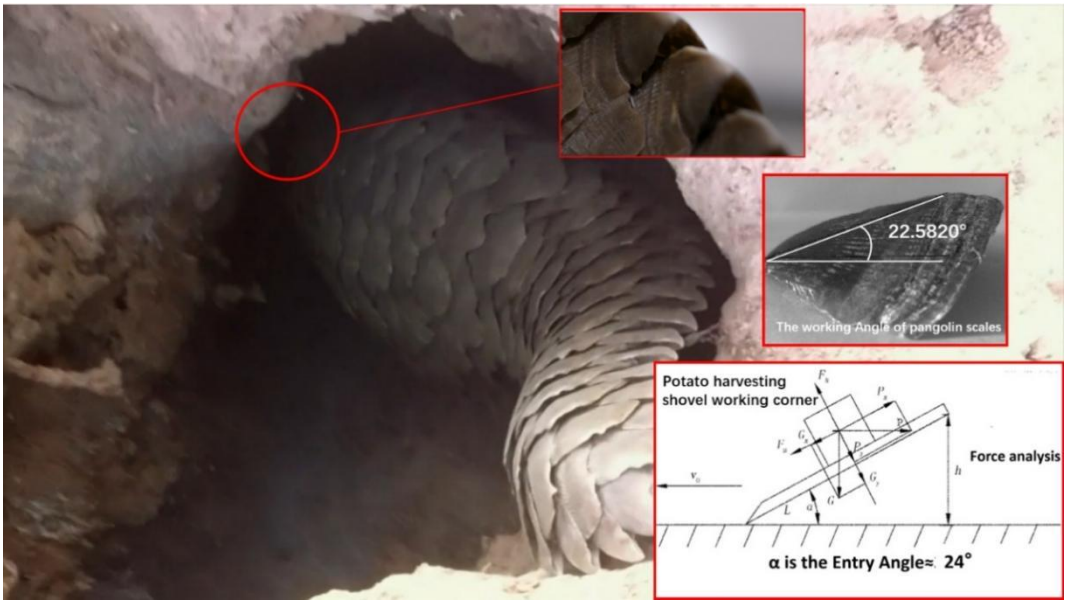

Fig. 2 - Comparison diagram of soil digging behaviour of pangolin and the design of soil digging angle of potato harvesting shovel

MATERIALS AND METHODS

Point cloud data pre-processing and structure feature extraction of target samples

Point cloud data acquisition and processing of squamous perforator

To understand the distribution of ridges on the surface of scales, information on ridge structure characteristics was obtained using reverse engineering technology. Since pangolins are world class protected animals and require research authorization, the choice in this case was to study rare pangolin specimens with the assistance of Shenyang Museum of Natural History, China. The natural death scale of Chinese pangolin *(Heath et al.,1986)* was used as the test material. Before the experiment, the surface of the material was cleaned using 50% alcohol. The ridge spacing was confirmed after observing the surface structure using an ultra-depth scanning electron microscope. To avoid distortion and reflection due to other factors, such as environmental light, an FC-5 contrast enhancer was sprayed on the material's surface while scanning *(Xu et al., 2020)*. After spraying, the data points on the surface of the scale were collected using a three-dimensional scanner VTOP 200 T. Based on pre-processing, such as point cloud multi-view stitching and denoising *(Hao et al., 2021)*, the scale model of the armour was reconstructed by reverse engineering technology, and the error was controlled within the allowable error range of ±5% *(Liu et al.,2016; Hu, 2015)* to ensure the validity of the model. The overall process is as follows (Fig. 3).

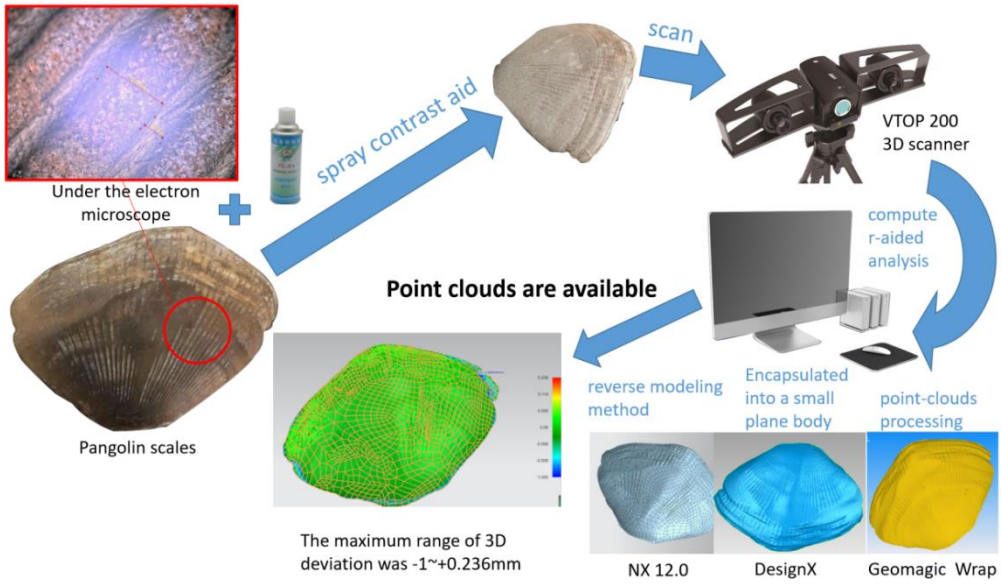

Fig. 3 - Process of point cloud acquisition and checking

Extraction of pangolin scale surface structure characteristics

As bioinspiration should not rely on the mere copying of nature *(Greiner et al., 2015)*. According to the observation, it is impossible to judge which function rule is consistent with the outer contour of pangolin scales, so polynomial fitting method is adopted to fit it. Based on the Curve Fitting function in the Toolboxes directory of MATLAB, surface Fitting (CF Tool) was selected to perform polynomial Fitting on the point cloud data.

Ridge line:

The central ridge is to be extracted by setting a vertical plane through the scale point cloud using Geomagic Control, as shown in Fig. 4.

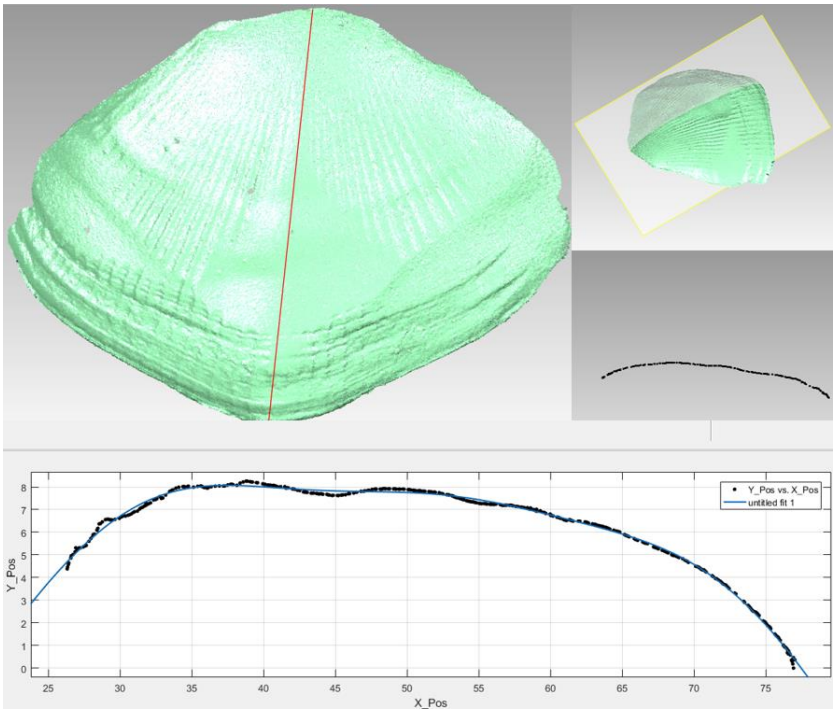

Fig. 4 - Extraction and fitting process of the outer ridge contour

Based on MATLAB, the point cloud data is fitted and its equation is obtained as follows:

$$f(x) = -1.442\times10^{-8}x^6 + 4.557\times10^{-6}x^5 + 6.02\times10^{-4}x^4 + 0.04197x^3 - 1.635x^2 + 33.75x - 280.7 \quad (1)$$

As shown in Table 1, with the exponential of x increasing, the values of SSE and $RMSE$ of MATLAB polynomial surface fitting for the three-dimensional coordinate data of the point cloud are decreasing and the coefficient of determination (R^2) is increasing, indicating that the fitting surface is closer to the actual pangolin surface contour with the exponential increase of x. However, when the index of x increases to 4, the values of SSE, $RMSE$ and R^2 change little for each index of independent variable. For example, when the index of x increases from x^4 to x^5, the square of residual (SSE) decreases from 8.639 to 7.92, and the mean square error ($RMSE$) decreases from 0.1481 to 0.142. The coefficient of determination increased from 0.9947 to 0.9952. For example, when the index of x increases from x^5 to x^6, the square of residual error (SSE) decreases from 7.92 to 5.395, the mean square error ($RMSE$) decreases from 0.1481 to 0.142, and the determination coefficient increases from 0.9952 to 0.9967. When the exponents are 8, the surface fitting result is SSE=4.682, $RMSE$=0.1096, R^2=0.9972, and the determination coefficient is close to 1. For the fitting result of complex biological surface, the fitting accuracy meets the fitting requirements. In summary, the power of x is 6.

Table 1

Fitting results of outer contour lines of different exponents

x^n	SSE	R^2	Adjusted R^2	$RMSE$
4	8.639	0.9948	0.9947	0.1481
5	7.920	0.9952	0.9952	0.1420
6	5.395	0.9967	0.9967	0.1173
7	4.952	0.9970	0.9970	0.1125
8	4.682	0.9972	0.9971	0.1096

Note: x^n means that the highest index of x was n. SSE is residual sum of squares, $RMSE$ is mean square error, the same as below.

Rib texture

As the amount of point cloud data will affect the subsequent surface fitting, the point cloud model processed by the Geomagic Wrap was imported into the Geomagic Control and divided into nine areas for observation. The effective surfaces with clear structure B, C, D, E and F were selected as the research objects, and the rest areas were subdivided. Point cloud is a collection of scattered points in space, which represents the contour feature information of the object surface. Point cloud slices are intersected with point cloud by a group of planes. Through the function of cross section under the start menu, a section perpendicular to the surface was established and the number of external contour lines was exported, as shown in Fig. 5. After the export, the data points were roughly between 380 and 450. The TXT coordinates were exported from the interface dat. file, and the data could be viewed by Excel or MATLAB (Fig. 5).

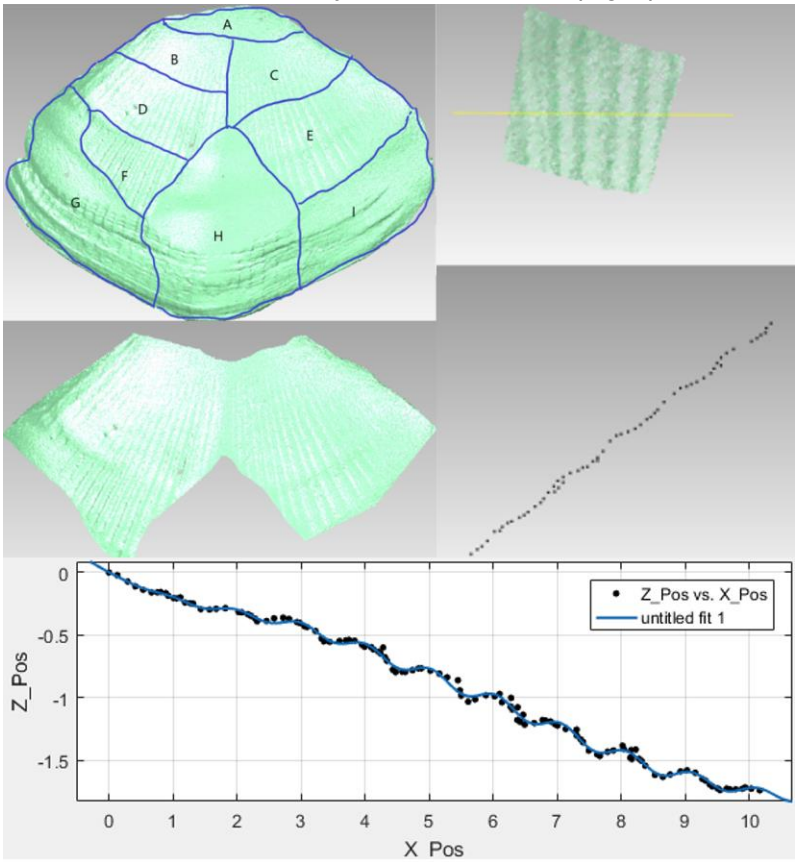

Fig. 5 - Derives the characteristic contour of the surface texture

The ridges on pangolin scales were observed to conform to some function law, so sinusoidal function fitting method was used to fit the ridges. Based on the Curve Fitting function in the Toolboxes directory of MATLAB, CF Tool was selected to perform sum of sin Fitting on the point cloud data. As shown in Table 2, with the exponential of x increasing, the values of SSE and $RMSE$ of MATLAB polynomial surface fitting of the three-dimensional coordinate data of the point cloud are continuously decreasing, and the coefficient of determination (R^2) is increasing. When the exponential of x is 6, it reaches the minimum, and then rises again. In this case, SSE and $RMSE$ are the minimum, R^2 is the maximum, and the determination coefficient is close to 1. As for the surface fitting results, the fitting accuracy meets the fitting requirements. In summary, the power of x is selected as 6, so the fitting equation of the surface texture of ribbed structure is as follows:

$$f(x) = 1.776\sin(0.2177x + 2.92) + 0.5651\sin(0.4075 - 0.7116) + 0.03001\sin(1.232x - 3.094) + 0.02179\sin(1.599x - 2.344) + 0.02896\sin(5.92 - 2.713) + 0.02541\sin(6.403x + 0.4) \quad (2)$$

Table 2

Fitting results of outer contour lines of different exponents

x^n	SSE	R^2	Adjusted R^2	$RMSE$
5	0.08247	0.9976	0.9973	0.02776
6	0.06915	0.9980	0.9976	0.02579
7	0.07028	0.9979	0.9975	0.02638

The expressions of ridges were obtained by function fitting, as shown below: the determination coefficient was approximately 1, and the fitting accuracy of the surface fitting results met the fitting requirements. Ridge line and the outer contour line of the surface rib texture jointly constitute the bionic surface, which provides the design basis for the subsequent bionic modeling.

Design and analysis of potato-digging shovel based on the ridge structure of the armoured pangolin

Design of bionic potato-harvesting shovel

The scale surface of a pangolin was observed, measured, and analysed under a super depth of field microscope (Fig. 6).

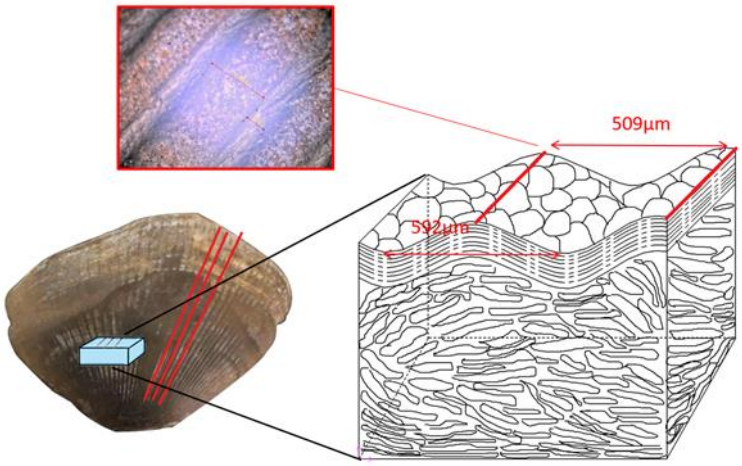

Fig. 6 – The scale surface of pangolin was observed, measured and analysed under a super depth of field microscope

The distance between the two ribbons on the pangolin scales was measured at about 500 to 600 microns. Therefore, in the virtual modelling of rib arrangement, the rib structure was roughly divided into the following three categories (Fig. 7).

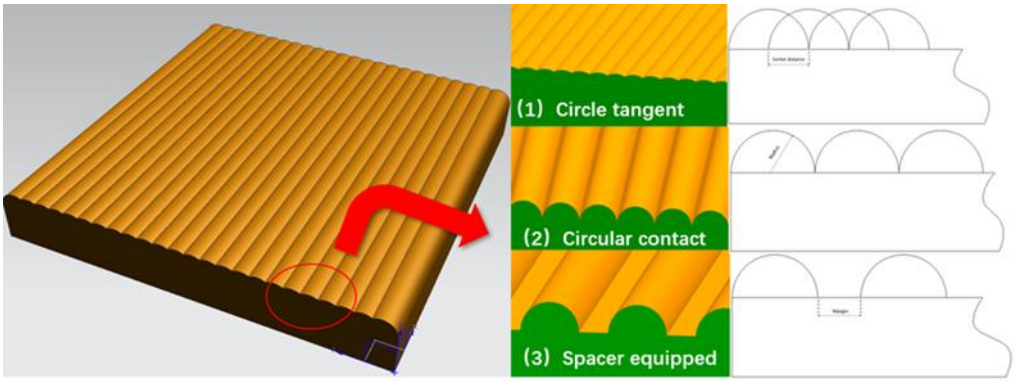

Fig. 7 – Three kinds of ribbed arrangement

(1) Ribbed with tangential boundaries; (2) A closely arranged ribbed structure; (3) Ribbed with certain gaps

Considering that the problem of adhesion is a process of many a little makes a mickle, all the particles in the 15×15 mm soil tank used in the adhesion test were the smallest particles after screening, with radii of 0.3–0.5 mm. According to the above types, nine groups of ribbed surfaces with different radii and a smooth plane were established with dimensions of 10×10×1.5 mm. Based on the radii of 0.3, 0.4, and 0.5 mm, the ribbed edges with tangential edges were designated as C, those with dense edges were denoted as S, and those integrated into the ribbed edges with tangential edges were indicated by V. First, the experimental body was buried under the soil at an angle of 32.5°. In the filling process, the slope of the experimental body was 24°. When the soil particles were stable, the speed of the plane body was set, and the experimental body moved upward by 0.3 m/s. When most of the particles were clearly leaving the experimental surface, the motion of the experimental body was suspended. Inertia was used to remove the soil particles completely from the surface in the computing area. Then, the direction of gravity was reversed, the soil particles that were not attached to the plane body left the calculated area, and the results were compared. This approach reduced the CPU calculation load and accelerated the calculation process.

Fig. 8 depicts this procedure. (In EDEM, the gravity direction of soil particles can be reversed by modifying the gravity in the environment. Instead of dumping the soil by turning over the shovel, the soil left after the above operation is attached to the shovel surface. This method can quickly determine how many soil particles are adhered to the surface of the shovel surface.)

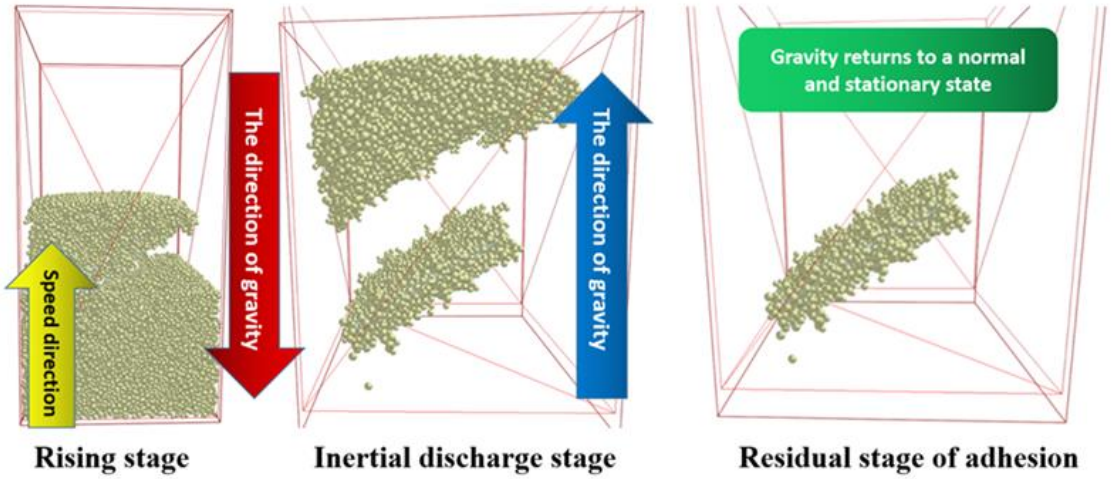

Fig. 8 – Three stages of soil particles

After comparing the simulation results (Fig. 9), it can be concluded that the surface residual soil values of the edge-cut type and the interval type with 0.5 mm radius are respectively 6.51×10^{-6} kg and 6.33×10^{-6} kg, which are less than those of other types.

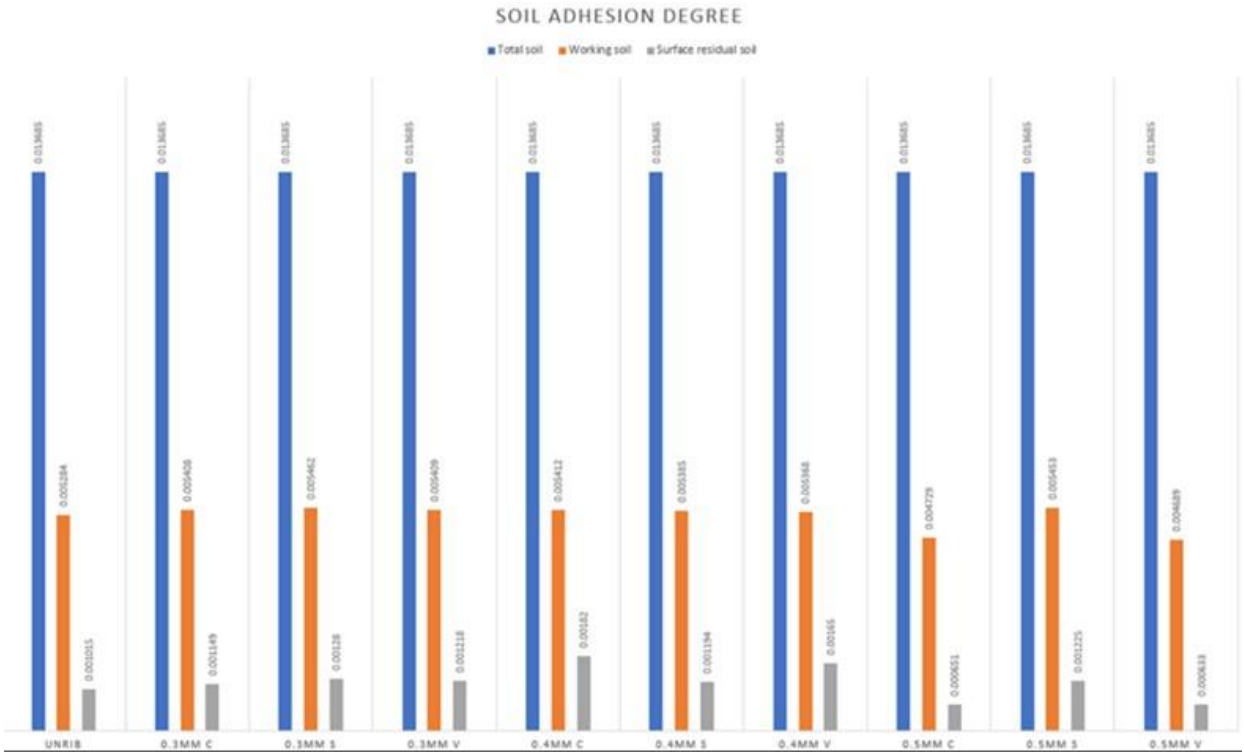

Fig. 9 – Comparison of soil residual conditions of 10 groups of different types of planar bodies

The seven types of potato-harvesting shovels presented in Fig.10 were designed based on the contour curve function obtained by the above software function. Each shovel was 10 mm thick, 335 mm long, and 131 mm wide. In addition to the enlarged ridge-type digging shovel, the ridge spacing of the non-smooth surface was 0.5 mm, and the ridge diameter was 0.5 mm. By establishing the above shovels with different overall shapes or surface smoothness, experimental subjects were provided for subsequent control experiments to explore the optimal arrangement of ribbed patterns.

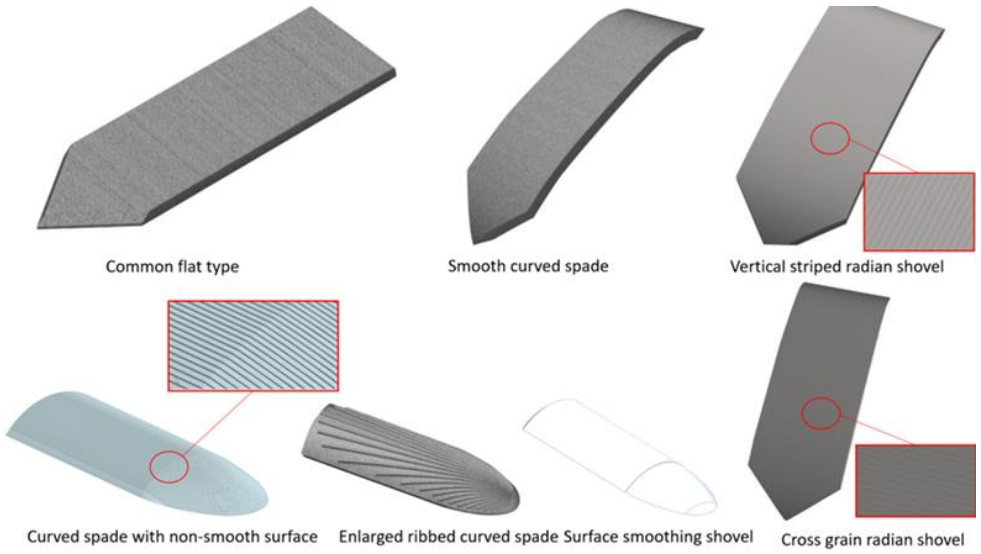

Fig. 10 – Types of shovels

Simulation test analysis

Establishment of soil particle model:

The soil with a moisture content between 13% and 16% in Northeast China was used for simulation in this study. In capillary theory, soil adhesion is related to the interfacial water model tension *(Fisher, 1928)*.

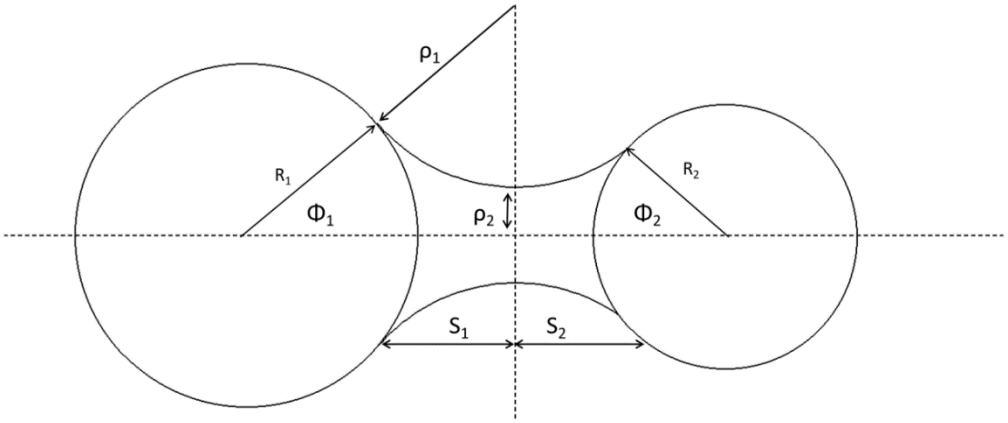

Fig. 11 - Water film tension model between two spherical soil particles

According to the Fisher theoretical model, as shown in Fig. 11, the water model tension, P, between two spherical particles is given by:

$$P = \pi r_2^2 \Delta\rho + 2\pi r_2 \gamma_{LV} \tag{3}$$

Under a certain moisture content, a water ring is formed to combine the particles, where ρ_1 and ρ_2 are the radii of the concave and convex surfaces, respectively; R_1 and R_2 are the radii of the particles; S_1 and S_2 are the distances from the particles to the liquid bridge neck; φ_1 and φ_2 are the wedge angles of the particles.

According to the study of Qiushanfeng and Hengjingzhao *(Yutaka et al., 1972)*, a solid intervention exists when the soil is divided into loose accumulation and dense accumulation. The model is transformed, as demonstrated in Fig. 12.

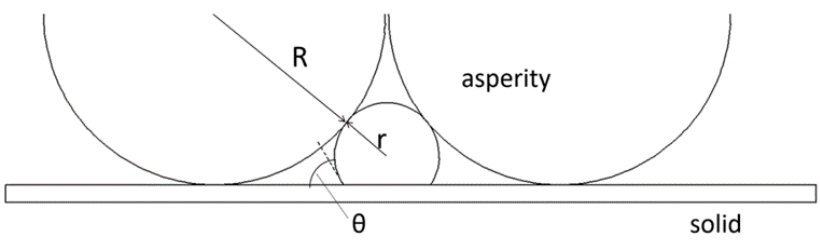

Fig. 12 - Schematic of the capillary channel between two soil particles and solid surface

The adhesion force, F_0, between soil particles and solid materials, which is a small-density accumulation of soil, can be expressed as follows:

$$F_0 = \frac{\pi(1+\cos\theta)\{(1+\cos\theta)(1+\cos\alpha) - \sin\alpha\}(\cos\theta+\cos\alpha)\gamma_{LV}}{4R} \quad (4)$$

The adhesion force between soil particles and solid materials, F_C, is given by

$$F_C = \frac{2}{\sqrt{3}} F_0 \quad (5)$$

The adhesion force is primarily determined by the resultant force, F, of the following five forces:

$$F = F_m + F_e + F_c + F_b - F_p \quad (6)$$

Where F_m is the intermolecular attraction, F_e is the metal surface static attraction, F_c is the capillary force, F_b is the viscous resistance, F_p is the wedge resistance, and F_c plays a decisive role.

$$\gamma_{S/V} = \gamma_{S/L} + \gamma_{L/V}\cos\theta \quad (7)$$

According to the equation, $\gamma_{S/V}$ is the energy of the solid surface, $\gamma_{S/L}$ is the energy of solid/liquid interface, $\gamma_{L/V}$ is the energy of the liquid surface, and θ is the contact angle of the liquid droplet on the solid surface. Therefore, it was attempted to add the Johnson–Kendall–Roberts (JKR) model to the Hertz–Mindlin model to obtain the surface energy formula, expressed as follows:

$$F_{JKR} = -4\sqrt{\pi\gamma E^* \alpha^{3/2}} + \frac{4E^*}{3R^*}\alpha^3 \quad (8)$$

$$\delta = \frac{\sqrt{4\pi\gamma\alpha}}{E^*} + \frac{\alpha^2}{R^*} \quad (9)$$

Where the contact spot radius, E^* and R^* are equivalent to Young's modulus and equivalent radius of the two spheres in contact, respectively, defined in terms of shear moduli of contacting spheres *(Baran et al., 2009)*.

$$F_{Hertz} = \frac{4}{3} E^* \sqrt{R^* * \sigma^{3/2}} \quad (10)$$

Before establishing a soil trough model, the contact parameters and contact model parameters must be calibrated according to the experimental site's intrinsic parameters, and the typical soil in Northeast China must be collected *(Hunt et al., 1984*. (Fig. 13).

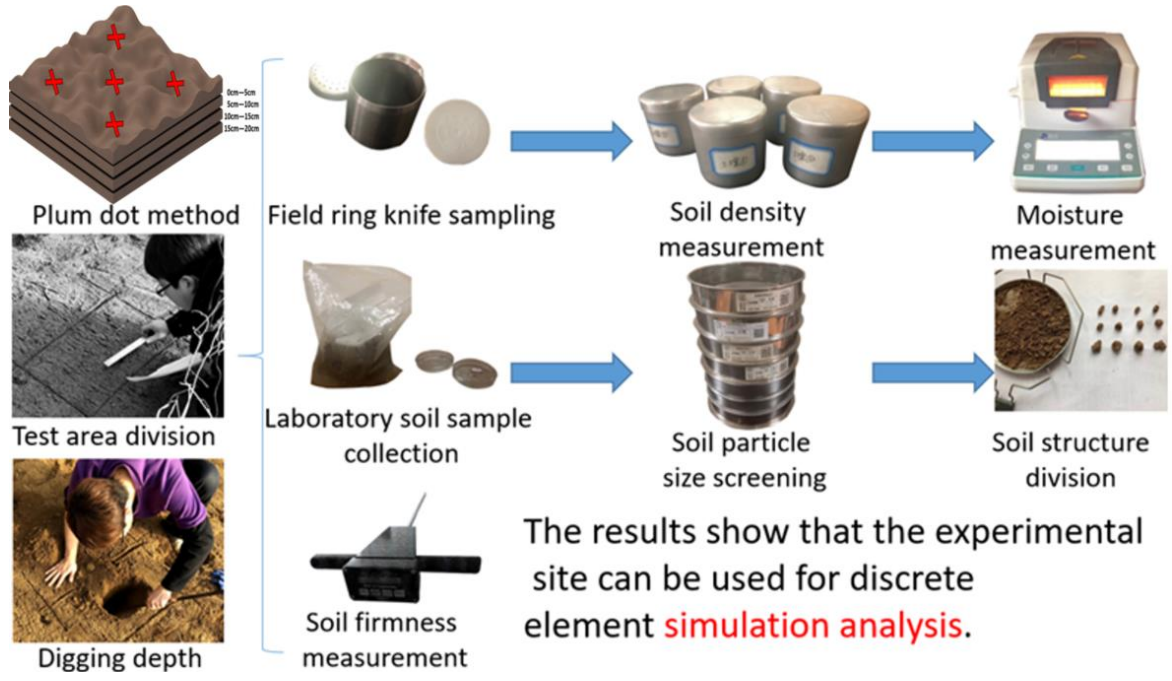

Fig. 13 - Determination of field soil intrinsic parameters

According to the above test steps, the experimental data in the following table can be obtained, as shown in Table 3.

Table 3

Result of soil moisture content

Sampling point/depth	0~5cm	5~10cm	10~15cm	15~20cm
1	15.24%	14.79%	13.41%	14.92%
2	15.68%	15.56%	15.98%	15.75%
3	16.09%	16.08%	14.39%	14.70%
4	15.88%	13.35%	15.66%	15.39%
5	14.46%	14.71%	15.10%	15.43%
Average value	15.47%	14.898%	14.908%	15.238%

The average water content of five samples at different depths was counted. Then it was concluded that the water content was similar between 0 and 20 cm, and there was no preliminary conjecture that the water content of 0~5 cm was significantly greater than that of 15~20 cm, and the soil water content was 15.13%. The direction of movement of water in soil depends on its water potential, as in equation 11:

$$\phi_T = \phi_M + \phi_O + \phi_G + \phi_P \tag{11}$$

That is, the total water potential φ_T is the sum of matrix potential φ_M, solute potential φ_O, gravitational potential φ_G and pressure potential φ_P. Considering that it is a rainy season, the similarity of current moisture content to normal phenomenon is not an error caused by improper operation in the experiment process. There is still a distance from the soil layer with obvious change of moisture content. The moisture content data can provide an important theoretical basis for the selection of contact model in the subsequent discrete element software simulation process.

The test soil in this experiment was obtained from the test field in Heishan County, Jinzhou City, Liaoning Province. The soil samples were collected at 05:00 h. As potatoes are planted at a depth of approximately 20 cm in the ploughing layer, and moisture content is similar from 0 cm to 20 cm, it was not necessary to obtain the samples from different depths. When obtaining the soil samples, the soil around the ring knife was first cut with a paring knife, then the ring knife filled with soil was removed. The excess soil at both ends of the ring knife was removed, and the soil outside the ring knife was wiped. Both ends of the ring knife were covered immediately to prevent the evaporation of the moisture contained in the soil, then weighed (accurate to 0.01 g) and recorded. In the same layer, an aluminium box was used to obtain samples for subsequent experimental research. The ring knife holder was placed on the ring knife of known weight, and the ring knife edge was pressed downward and vertically into the soil until the ring knife barrel was filled with samples. Attention was paid to applying a stable and consistent force while pressing the ring knife. According to the density formula, the mass of the ring cutter is m_0, the total mass of the ring cutter and the soil sample is m_1, and V is the volume of the ring cutter, which is 100 cm^3. The density calculation formula is as follows:

$$\rho = \frac{1000(m_1 - m_0)}{V} \tag{12}$$

The densities of soil samples at depths of 0~20 cm can be obtained according to the above steps. Table 4 shows the test data.

Table 4

Result of soil density

Sampling location	Soil mass / g	Soil volume / cm^3	Soil density / kg/m^3
1	168.01	100	1680
2	146.51	100	1465
3	158.77	100	1588
4	142.10	100	1421
5	154.61	100	1546
Average value	154.00	100	1540

According to the data in Table 4, the soil density of the site is approximately 1540 kg/m^3. After screening, the average value was calculated. Particles with radii exceeding 2 mm account for ~14.975% of all the particles. Those with radii between 1 mm and 2 mm account for ~22.075%. Those with radii between 0.5 mm and 1 mm account for ~12.19%, and those with radii less than 0.5 mm account for ~57.45%. According to the particle angle of repose China National Standard, the measurement device was built vertically from a height of 10 mm to the desktop at 80 mm, and the average angle of repose was measured to be 38.5065°. After establishing the ground using EDEM software, the circular plane with a diameter of 10 mm was set as the particle factory, and the particle radius was divided into four intervals: 2~3, 1~2, 0.5~1, and 0.3~0.5 mm. Design-Expert was used to analyse the data. Table 5 presents the analysis of variance of the angle of repose.

Table 5

Analysis of variance table of the angle of repose Y_1

	Sum of		**Mean**	**F**	**P-value**
Source	Squares	df	Square	Value	Prob > F
Model	2832.55	14	202.32	13.35	< 0.0001***
A-rolling friction	457.57	1	457.57	30.19	< 0.0001***
B-particle density	132.77	1	132.77	8.76	0.0103**
C-surface energy density	1652.92	1	1652.92	109.05	< 0.0001***
D-Poisson's ratio	55.08	1	55.08	3.63	0.0773*
AB	43.22	1	43.22	2.85	0.1134
AC	67.06	1	67.06	4.42	0.054*
AD	12.03	1	12.03	0.79	0.388
BC	3.43	1	3.43	0.23	0.6415
BD	1.35	1	1.35	0.089	0.7697
CD	105.38	1	105.38	6.95	0.0195**
A2	29.84	1	29.84	1.97	0.1824
B2	0.019	1	0.019	1.25 e-03	0.9723
C2	13.3	1	13.3	0.88	0.3649
D2	0.35	1	0.35	0.023	0.8816
Residual	212.21	14	15.16	-	-
Lack of Fit	179.45	11	16.31	1.49	0.4117
Pure Error	32.76	3	10.92	-	-
Cor Total	3044.76	28	-	-	-

**** indicates extremely significant ($P < 0.01$); ** indicates significant ($0.01 < P < 0.05$); * indicates significant ($0.05 < P < 0.1$).*

Table 5 shows that the experimental model is significant ($P < 0.01$). The surface energy density and rolling friction have extremely significant effects on the soil accumulation angle, whereas the particle density and interaction CD (surface energy density and Poisson's ratio) significantly affect the soil accumulation angle. The order of the influence of the various factors and interaction factors on the bulb loss rate is A, C, B, CD, AC, and D, and the regression equation between the index and various factors is:

$$StackingAngle = 19.04809 - 187.02557\alpha + 0.026875\beta + 36.4122\lambda + 11.1048\gamma - 5.13\lambda\gamma \quad (13)$$

where λ is the surface energy density, γ is Poisson's ratio, α is rolling friction between soil particles, and β is soil particle density. The friction angle was calibrated to 38.5° by adjusting the surface energy density and rolling friction parameters, as shown in Fig. 14.

There are many methods for measuring the stacking angle, and the funnel falling device structure was chosen which is more accurate and convenient to control, so that it is more in line with China's national standards for measuring discrete materials. Finally, the surface energy between the material and the particles was found to be 36.5 J/m^2, and the surface energy between the particles was 1 J/m^2.

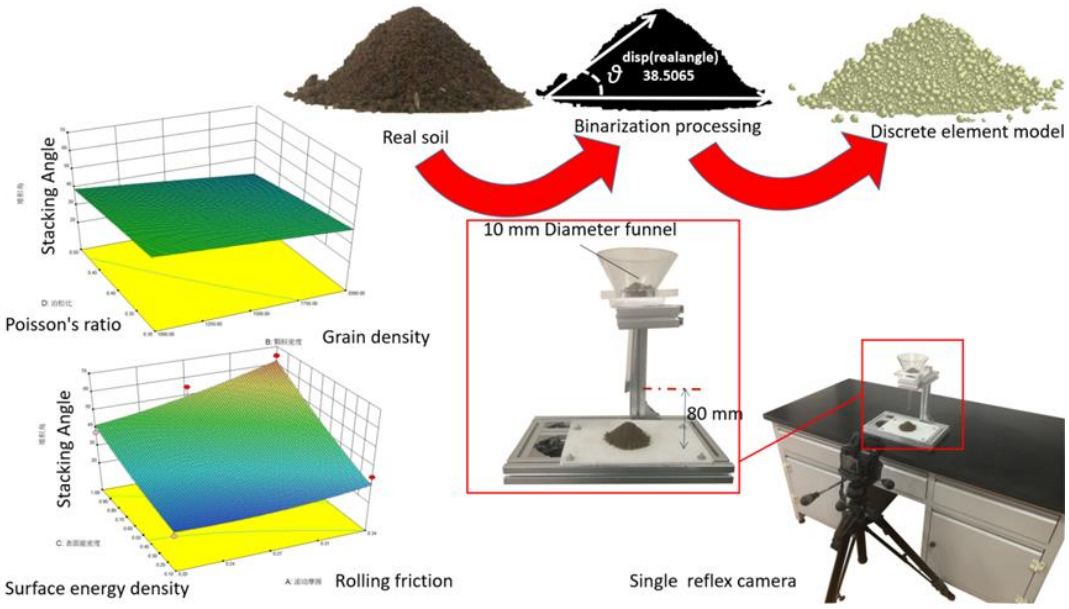

Fig. 14 - Parameter calibration experiment

Table 6 lists the other parameters. Based on these data, a realistic model of the target soil groove was built.

Table 6

EDEM parameter settings

Parameter	Unit	Numerical value
Poisson's ratio of soil particles	-	0.35
Shear modulus of soil particles	MPa	1.06
Density of soil particles	kg/m^3	1540
Poisson's ratio of 65 manganese	-	0.3
Shear modulus of 65 manganese	MPa	1.92
Density of 65 manganese	kg/m^3	7800
Recovery coefficient between particles	-	0.13
Rolling friction factor between particles	-	0.27
Static friction factor between particles	-	0.56
Recovery coefficient between particles and excavating shovel	-	0.16
Rolling friction factor between particles and excavating shovel	-	0.5
Static friction factor between particles and excavating shovel	-	0.43
Simulation time step	S	13.2
Acceleration of gravity	m/s^2	9.81

Establishment of test soil tank model

Owing to the complexity of the soil composition, it is challenging to explain the adhesion problems of machinery in soil disturbance using a single force. With the destruction of the stable soil structure, the total surface area of the particles increases, the surface energy becomes large, and the adhesion becomes severe. Therefore, to accelerate the calculation, a 400×350×330 mm calculation domain was established to move with the shovel and perform the dynamic auxiliary calculation. Soil entry is the initial state of the shovel body. With the accumulation of granular beds, the 350×243×500 mm soil grooves were elongated to 350×243×1200 mm after the granular bed particles were stabilized at 0.5001 s to simulate the actual soil environment. Subsequently, the amount of soil in the space was calculated when the soil grooves moved in the x-direction at a speed of 0.5 m/s, stopped at 4 s, moved in the z-direction at a speed of 0.5 m/s, and stopped at 5 s.

Fig.15 depicts the soil groove model. A completely closed soil groove will cause incorrect soil displacement. Therefore, the wall was dismantled in stages during the simulation process and designed a kind of soil groove model similar to a matchbox, and thus eliminated the rebound force of motion potential energy acting on the wall.

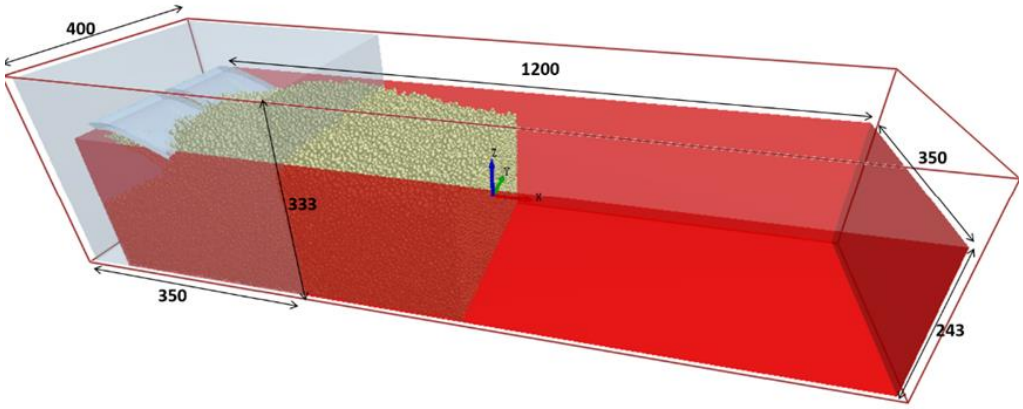

Fig. 15 - Modified soil model

RESULTS

Fig. 16 presents the results of the potato-harvesting simulation. The proposed harvesting shovel with a ridge-type non-smooth (HD) surface is clearly more effective than other harvesting shovels in reducing clay and soil. The soil removal effect directly affects the size of soil particles in the spatial grid of each shovel. After dividing the particles in the region in which the shovel was located, the soil volume attached to the conventional flat-type shovel (PB) surface is 312.9416 mm^3 per unit time after process termination. Compared with the flat type, the single-direction radian shovel designed by the ridge function has 295.693 mm of soil attached to it after process termination because of its unique angle. Therefore, the outer contour has a certain influence on soil removal. Simultaneously, it bends along the function of the pangolin scale from the front and back directions as well as the left and right, but the surface is relatively smooth and has no ridge structure (QG). After the work stops, the attached soil volume is 270.4352 mm^3, which is better than that in the single direction case, further confirming the influence of the outer contour on soil removal.

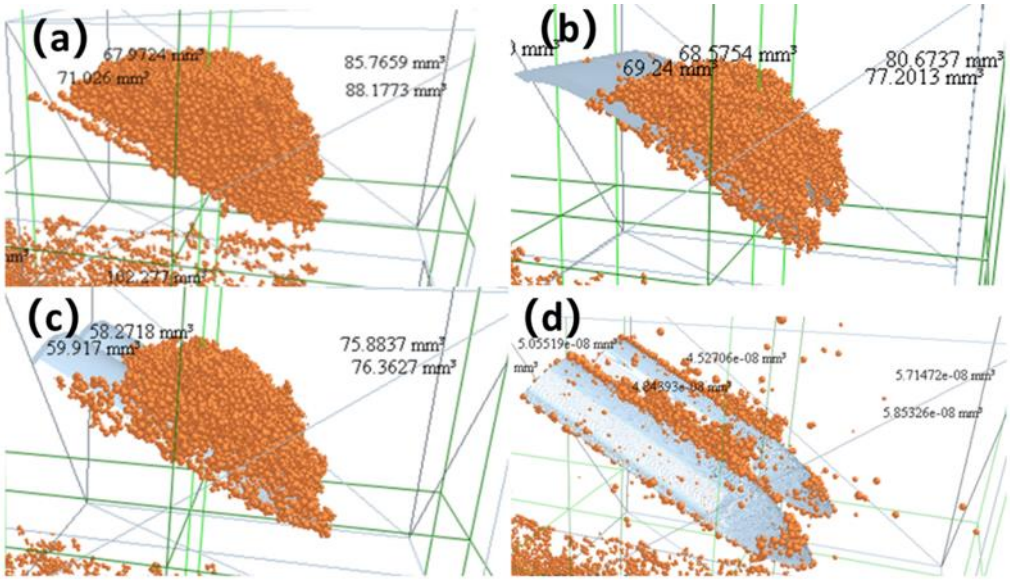

Fig. 16 - Soil adhesion to the surfaces of different types of shovels

(a) Conventional flat-plate harvester; (b) Bionic radian shovel; (c) Bionic smooth-surface shovel; (d) Bionic non-smooth-surface shovel

The bidirectional surface shovel, combined with the texture characteristics of the surface ridges (QL), has a significant effect. After the work stops, the soil volume attached to the shovel body is only 20.93897 E-08 mm^3, indicating that the non-smooth surface has a substantial impact on soil removal. Fig. 17 is a comparison of the pressures of four excavating shovels.

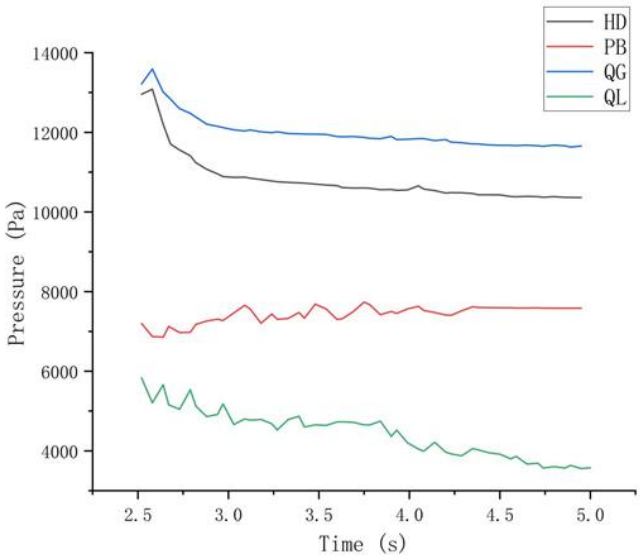

Fig. 17 - Contrast diagram of four kinds of excavating spades subjected to pressure

CONCLUSIONS

In this study, a potato-harvesting shovel based on the texture characteristics of pangolin scales was designed considering the unique external surface profiles of organisms, combined with knowledge of bionics, reverse engineering, soil adhesion mechanics, materials science, and other fields. Soil was collected during the potato-harvesting period and measured on the spot, and the soil groove model was established in stages after calibrating the soil particles parameters. The accuracy and scientific nature of the model were verified by comparing the soil on the surface of the excavating shovel after bionic and conventional shovelling.

(1) Compared with the existing potato-harvesting shovel design methods, the design method proposed in this paper has the following advantages.

Based on the natural behaviour and living environment of the pangolin, pangolin scales were found to be extremely similar to potato-harvesting shovels, providing the best harvest in certain respects. Therefore, according to the depth-of-field microscope observation results to search for a non-smooth ribbed surface with the best arrangement, combined with the discrete element method, the 0.5 mm diameter clearance arrangement was confirmed to be the optimal solution. In addition, the overall profile of the spade face was determined according to reverse fitting, and the mathematical model of the corresponding function was established. Simultaneously, various control groups were established and applied in the subsequent simulation tests.

(2) In calibrating the soil model parameters, it can be concluded from the factorial experiment that the soil accumulation angle is mainly dependent on the surface energy density and rolling friction. The smaller the total particle weight, the larger the surface area and surface energy. Therefore, it is impossible to solve the soil adhesion problem effectively from the perspective of broken soil. Therefore, from the angle of the surface energy, the continuity of water film on the surface is destroyed by making the surface non-smooth. Defining a reasonable calculation domain in the EDEM granular bed calculation could reduce the calculation time without affecting the whole.

(3) This design method can be applied to the design of other soil-touching parts of agricultural machinery, such as deep turning machines, deep loosening machines, and ditch openers. This approach is not limited to potatoes and has strong generality to solve the problem of soil desorption.

This design method can be applied to the design of other soil touching parts of agricultural machinery, such as deep turning machine, deep loosening machine, ditch opener, etc. Crops are not limited to potatoes, and have a strong generality to solve the problem of soil desorption. In order to make better use of bionics to solve the problem of soil adhesion of agricultural machinery, a database matching a variety of soil organisms with the actual production conditions of more agricultural machinery will be established in the future, so as to provide more inspirations for the design of agricultural machinery from the perspective of biology. This method ignores the fibre root agglomeration model of crops because only soil adhesion to the surfaces of shovels was analysed in this study. Therefore, to make our model closer to the actual soil environment, the next steps will be to add the characteristic parameters of the soil swelling force caused by roots and to perform further exploration by coupling the ANSYS and EDEM methods.

ACKNOWLEDGEMENT

We would like to thank Editage (www.editage.cn) for English language editing. The pangolin, an endangered wild animal, is explicitly protected by law in China; thus, it is difficult to obtain its scales even for research purposes. Therefore, we would like to thank the Shenyang Museum of Natural Science in Liaoning Province, China, for providing us with the opportunity to photograph and study pangolin specimens without harming wildlife to the greatest extent possible.

REFERENCES

[1] Arnell, R. D. (2007). Two-body abrasive wear of the surfaces of pangolin scales. *J. Bionics Eng.,* 2, 77–84. DOI: 10.1016/S1672-6529(07)60017-1

[2] Babbitt, D.M. (2008). Seed potato treatment on a large scale. *Am. Potato J.,* 8(12*)*, pp.271-272. DOI: 10.1007/BF02878789

[3] Baran, O., Degennaro, A., Ramé, E., Wilkinson, A., Nakagawa, M., & Luding, S. (2009). DEM simulation of a Schulze ring shear tester. *Paper presented at the Int. Conf. Micromechanics of Granular Media*.

[4] Celik, H. K., Cinar, R., Yilmaz, D., Ulmeanu, M. E., Rennie, A. E. W., & Akinci, I. (2019). Mechanical collision simulation of potato tubers. *J. Food Process Eng.,* 42(5), pp.e13078. DOI: ARTN e1307810.1111/jfpe.13078

[5] Fisher, R. A. (1928). Further note on the capillary forces in an ideal soil. *J. Agric. Sci.,* 18(3). DOI: 10.1017/S0021859600019432

[6] Greiner, C., & Schäfer, M. (2015). Bio-inspired scale-like surface textures and their tribological properties. *Bioinspir. Biomim., 10(4)*. DOI: 10.1088/1748-3190/10/4/044001

[7] Hao, F., Florent, L., Cihui, P., & Hui, H. (2021). Floorplan generation from 3D point clouds: A space partitioning approach. ISPRS J. Photogramm. *Remote Sens*., 175, pp.44-55. DOI: 10.1016/j.isprsjprs.2021.02.012

[8] Heath, M. E., & Hammel, H. T. (1986). Body temperature and rate of O2 consumption in Chinese pangolins. *Am. J. Physiol.,* 250(3 Pt 2). DOI: 10.1152/ajpregu.1986.250.3.R377

[9] Hou, Q., Yang, X., Cheng, J., Wang, S., Duan, D., Xiao, J., & Li, W. (2020). Optimization of performance parameters and mechanism of bionic texture on friction surface. *Coatings, 10(2)*. DOI: 10.3390/coatings10020171

[10] Hu, S. X. (2015). Study on parametric reverse modeling. *Appl. Mech. Mater.*, 3748.

[11] Hunt, R. E. (1984). *Geotechnical engineering investigation manual: Geotechnical engineering investigation manual*. McGraw-Hill Book Company

[12] Jafar, M., Mohsen, R. F., & Hassan, A. (2021). An optimized bionic electro-osmotic soil-engaging implement for soil adhesion reduction. *J. Terramechanics,* 95, pp.1-6. DOI: 10.1016/j.jterra.2021.01.003

[13] Junior, R. A. A., Cheng, L.-Y., & Osello, P. H. S. (2019). An improvement of rigid bodies contact for particle-based non-smooth walls modeling. *Comp*. *Part. Mech.,* 6(4), pp.561-580. DOI: 10.1007/s40571-019-00233-4

[14] Lee, K. H., Woo, H., & Suk, T. (2001). Point data reduction using 3D grids. *Int. J. Adv. Manuf. Tech., 18(3),* pp.201-210. DOI: 10.1007/s001700170075

[15] Liu, S., Wang, Y., Jiang, H., Wei, Q., & Xiao, J. (2016). Aerial survey and scanning point cloud data acquisition & modeling technology for hydropower engineering. *5th Int. Conf. Advanced Materials and Computer Science*, 114-119.

[16] Massah, J., Roubeneh, F.H., Roubeneh, Z. H., &Vakilian, K. A. (2020). Experimental investigation of bionic soil-engaging blades for soil adhesion reduction by simulating Armadillidium vulgare body surface. *INMATEH-Agricultural Engineering*, 60(1), pp. 99-106. DOI:10.35633/inmateh-60-11

[17] Ren, L. Q., Tong, J., Li, J. Q., & Chen, B. C. (2001). SW—Soil and water: Soil adhesion and biomimetics of soil-engaging components: A review. *J. Agric. Eng. Res.,* 79(3), 239-263. DOI: 10.1006/jaer.2001.0722

[18] ****Testing of physical properties of granular materials - Part 3: Measurement of fluidity index*, GB/T 31057.3-2018 C.F.R. (2018).

[19] ****Testing of physical properties of granular materials - Part 2: Measurement of vibrational density*, GB/T 31057.2-2018 C.F.R. (2018).

[20] Tong, J., Ma, Y.-H., Ren, L.-Q., & Li, J.-Q. (2000). Tribological characteristics of pangolin scales in dry sliding. *J. Mater. Sci. Letters,* 19(7), pp.569-572. DOI: 10.1023/A:1006769926391

[21] Tong, J., Zhang, Q., Guo, L., Chang, Y., Guo, Y., Zhu, F., Chen, D., Liu, X. (2015). Compaction performance of biomimetic press roller to soil. *J. Bionic Eng.,* 12(1), pp.152-159. DOI: 10.1016/S1672-6529(14)60109-8

[22] Wang, W., Song, J., Zhou, G., Pan, B., Wang Q., & Chen, L. (2022). Simulations and experiments of the seedbed straw and soil disturbance as affected by the strip-tillage of row cleaner (DEM). *INMATEH-Agricultural Engineering*, 66(1), pp:49-61. DOI: https://doi.org/10.35633/inmateh-66-05

[23] Xu, P. F., Duan, S. Y., & Wang, F. (2020). Reverse modeling and topological optimization for lightweight design of automobile wheel hubs with hollow ribs. *Int. J. Comput. Methods*, 17(09). DOI: 10.1142/S0219876219500646

[24] Yutaka, A., & Hajime, Y. (1972). Study on the adhesion of soil (Part 2): Theoretical analysis on the mechanism of adhesive force at the saturated stage. *Japanese J. Soil Sci. Plant Nutr.,* 43(8).

[25] Zenkov, S. A., & Lkhanag, D. (2020). Use of repair-recovery compositions for reducing the adhesion of soils to working bodies of machines. *IOP Conf. Ser.: Mater. Sci. Eng., 971(5)*. DOI: 10.1088/1757-899X/971/5/052051

[26] Zhang, L., Ren, L., Tong, J., & Shi, Y. (2004). Study of soil-solid adhesion by grey system theory. *Prog. Nat. Sci., 14(2)*, 119-124.

[27] Zhou, G., Ma, S., Han, D., Luo, G., Liu, F., & Zhang, R. (2016). Trafficability of rigid wheel with bionic lug on sand by 3D DEM, *Proceedings of the 2nd international conference on advances in mechanical engineering and industrial informatics,* Vol. 73, pp. 1648-1651.

DESIGN AND EXPERIMENT OF SMALL VEGETABLE SEEDER WITH SINGLE DISC MULTI-ROW SEEDING AND INDEPENDENT AIRWAY

/

小型单盘多行独立气道蔬菜播种机设计与试验

Yinping ZHANG[1)], Xin YANG[1)], Xiaoran LI[2)], Zhenwei WANG[*3)], Hua ZHOU[*1)], Jiasheng WANG[4)]

[1)]School of Agricultural and Food Science, Shandong University of Technology, Zibo (255000), China;

[2)] Collage of Engineering, Huazhong Agricultural University, Wuhan (430070), China;

[3)] Nanjing Institute for Agricultural Mechanization, Ministry of Agricultural, Nanjing (210014), China;

[4)] School of Mechanical and Electrical Engineering, Qingdao Agricultural University (266109), Qingdao, China.

DOI: https://doi.org/10.35633/inmateh-70-03

Keywords: *Facilities greenhouses, vegetable seeding, seed-metering device, airway disc*

ABSTRACT

In this paper, a small pneumatic vegetable precision seeder suitable for facility greenhouses was designed. Based on the traditional positive and negative pressure seed-metering device, the airway disc structure was designed, and the negative pressure air chamber was divided into three separate air chambers. The separate air chambers could solve the problems of high-pressure requirements of traditional seed-metering device with large air chamber and suitable for small power machineries more. One, two, or three rows drill can be completed by replacing the seed plate and divider. The seed discharge process of the seed-metering device was analyzed and the bench test was performed. Results showed that the required pressure of the seed-metering device with the airway disk was 1 kPa less than traditional seed-metering device with large air chamber when the eligible rate of seed discharge was 95%. Field experiments were performed, results showed that the best performance w*ere achieved under the speed of 3 km/h, for 3.72 % missed, 1.93% repeat and 94.35 % of inner ring, and 5.72%, 1.87% and 92.41% respectively of outer, meeting the requirements for vegetable seeding.*

摘要

本文设计了一种适用于设施大棚的小型气力式蔬菜精量播种机，在传统正负压排种器的基础上，设计气道盘结构，将负压气室分为 3 个独立的气室，解决传统正负压排种器气室大，气压要求高，不适合小动力机械的问题。通过更换排种盘和分种器，可以完成 1 行、2 行或 3 行蔬菜播种作业。对排种器排种过程进行了分析和台架实验，结果表明，满足排种合格率 95%时，带有气道盘的排种器所需气压比传统排种器小 1kpa。对设计的小型单盘多行独立气道蔬菜播种机进行田间试验，结果表明：播种速度为 3km/h 时，播种效果最佳，此时内圈漏播指数为 3.72%，重播指数为 1.93%， 合格指数为 94.35%；外圈漏播指数为 5.72%，重播指数为 1.87%，株距合格率为 92.41%，满足蔬菜播种要求。

INTRODUCTION

Facility agriculture is an important part of modern agriculture. At present, China has become a major country in facility agriculture, with the largest planted areas and most output of vegetables in the world *(Xiao et al., 2017; Chen et al., 2018; Yazgi A et al., 2014)*. However, compared with developed countries, the mechanization level of facility agriculture was relatively low, with the comprehensive mechanization level was only about 30% and the planting mechanization level was only 15.2% *(Li et al., 2021; Qi et al., 2020; Li et al., 2014)*. Due to the small space of the facility's greenhouse, large pneumatic vegetable planters could not be brought into operation. Vegetable seeding was usually done by manual or small simple mechanical seeder, which have low accuracy and high labor intensity, severely limiting the level of mechanization in facility farming.

At present, the research of vegetable seeder in developed countries in Europe and America are mainly focused on vegetable seeding machinery in large field, which can realize many functions such as ditching, seeding, soil covering and drip irrigation belt laying, but with large power and high sales price, which is not suitable for facility greenhouses. An air-suction vegetable seeder from Maschio, for example, can produce precise seeds of different sizes by changing seed plates with different apertures. While research in Asian countries like China, Japan and South Korea are focusing on small and medium-sized mechanical vegetable planters, which are compact and lightweight and more suitable for facility greenhouses.

For example, Hu Jingming et al. in China designed the hand-held precision acupoint planter for rapeseed, and the disc vegetable planter produced by Borante in Korea, etc. But mechanical seed planters have a high seed damage rate and low accuracy for irregular seeds and are suitable for granulated seeds *(Hu et al., 2017; Jafari et al., 1991; Maleki et al., 2006)*.

In this paper, for the demands of vegetable precision seeding in facility greenhouses, a vegetable seeder was designed, whose seed-metering devices had single disc but multi-row seeding and independent airway. And the airway disc was innovatively designed base on the traditional positive and negative pressure seed-metering device, which reduced the negative pressure chamber and low pressure needs for seed suction and avoided the problem of miss-seeding caused by insufficient fan speed because of the insufficient power of the small machine. The seeder designed in this paper could improve the accuracy of vegetable sowing and promote the mechanization level of facility agriculture.

MATERIALS AND METHODS

Overall structure and working principle

As shown in Fig. 1, the overall structure of the vegetable seeder mainly includes the frame, seed-metering device, ditching and seed division device, row suppression device, front and back suppression device, depth adjustment device, plant spacing adjustment transmission, fan and power system.

The gasoline engine power was divided into two ways, one through a chain drive back suppression wheel which drives the whole machine, while the front suppression wheel was rotated passively and drove the seed-metering device through the gearbox and chain. When travelling on road, the gearbox was in neutral, and the seed-metering device didn't work. And when seeding in the facility greenhouse, the gearbox was adjusted in the position rely on the seeding space requirements, while the seed-metering device was rotated. The other power part from gasoline engine drove the fan by belt. The fan connected with air pipe, which provided stable air flow to the seed-metering device.

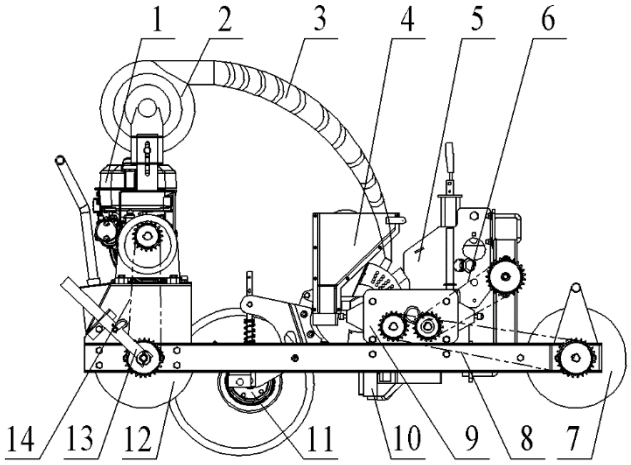

Fig. 1 - Complete machine structure diagram

1. Gasoline engine; 2. Fan; 3. Positive pressure air duct; 4. Seed-metering device; 5. Depth limit and adjustment device; 6. Transmission chain; 7. Front suppression wheel; 8. Seed-metering device drive chain; 9. Gearbox; 10. Ditching and seed division device; 11. Row suppression device; 12. Back suppression wheel; 13. Clutch; 14. Walking driven chain.

Seed-metering device structure and principle

Seed-metering device is the key component of the whole machine, which directly determines seeding accuracy and working efficiency *(Wang et al., 2020; Zhang et al., 2011; Jiang et al., 2014)*. Pneumatic seed-metering devices have been widely used in the vegetable sector due to their good adaptability to seed shapes, little damage, and high accuracy and uniformity. For example, Zhang Kaixing et al. *(Zhang et al., 2019)* designed an air suction seed-metering device with double-disc for vegetable, which can achieve precise seeding for different sizes seeds, but it is easy to produce sticky disk phenomenon when seeds fall by seed weight for light vegetable seeds. Cong Jinling et al. *(Cong et al., 2014)* designed a seed-metering device with positive and negative pressure, which relied on negative pressure to fill seeds, and blew the seeds off through increasing positive pressure at the seed dropping site, thus solving the problem of seed sticking disc. However, conventional air suction seed-metering device could only plant one row, which was difficult to meet the requirements of leafy vegetable seeding with small row spacing. Yan Qiuyan et al. *(Yan et al., 2014)* developed a pneumatic seed-metering device which could realize two-row seeding.

However, the structure of the seed-metering device was complicated with two seed plates and the two seed plates share one air chamber, which requires high pressure. Li Ming et al. *(Li et al., 2013)* developed a pneumatic aggregate precision seed-metering device for rape, which could plant multiple rows by one device, but it was suitable for the field traction vegetable planter, which had a large power demand.

Aiming at the requirement of small row space for vegetable seeding, seed-metering devices having single disc but multi-row and independent airway was designed as shown in Fig. 2. The airway disc was the core component of the metering device. The traditional air chamber shown in Fig. 3a which required higher air pressure to ensure the stability of seed absorption *(Wu et al., 2007)* was divided into independent airway by airway disc shown in Fig 3b which reduced the demand for air pressure, and only negative pressure was passed in the airway corresponding to the seed suction hole but positive pressure was at the seed dropping mouth *shown in Fig 3c*, so as to solve the problem of miss-seeding caused by limited power and insufficient air pressure of the small seeder.

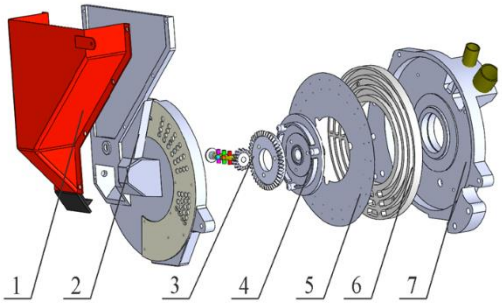

Fig. 2 - Structure diagram of seed meter

1. Seed box; 2. Shell; 3. Seed stirring device; 4. Power plate; 5. Seed arrangement plate; 6. Airway plate; 7. Right shell of seed discharging device

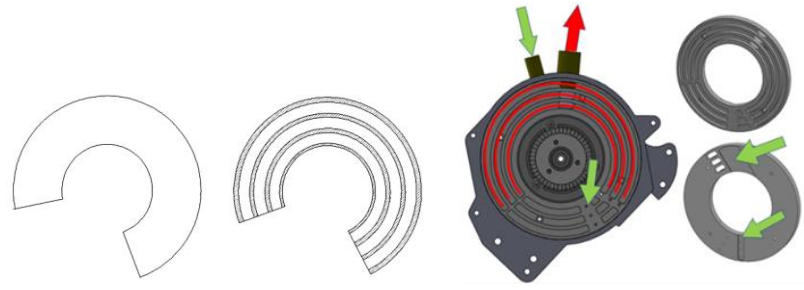

Fig. 3 - Schematic diagram of airway disc structure

1. Negative pressure annular groove; 2. Negative pressure ventilation groove; 3. Positive pressure groove; 4. Positive pressure vent hole; A: Conventional air chamber; B: Independent chamber; C: Airway disk structure and flow route map

Analysis of seeding process

According to the different functions of each region during seeding, the working area of the seed-metering device was divided into four regions: seed filling region, seed clearing region, seed carrying region, and seed unloading region, as shown in Fig.4. According to Bernoulli equation, the pressure was equal everywhere in the constant chamber flow field *(Li et al., 2012; Chen et al., 2007).*

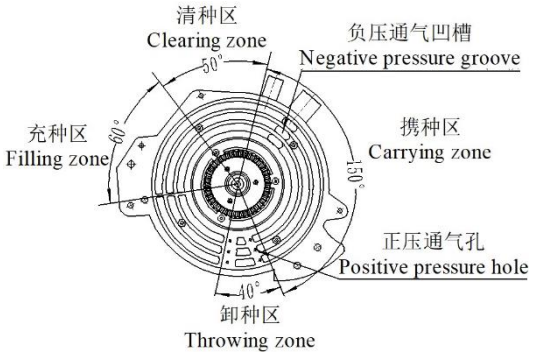

Fig. 4 - Partition of seed-metering device working area

(1) *Seed filling process analysis*

Ignoring the effects of machine vibrations and other factors in the seeding process, rape seeds with a good spherical shape were chosen as the objects of study, and outer ring seeds were used as particle points to establish a Cartesian coordinate system. The direction of the centrifugal force on the seed was taken to be the positive direction of the x axis, the direction of air and friction between seeds was taken as the positive direction of y axis, the direction of the normal vector of the seed plate was taken to be the positive direction of the z-axis, the kinematic analysis of the seed filling process was shown in Fig. 5.

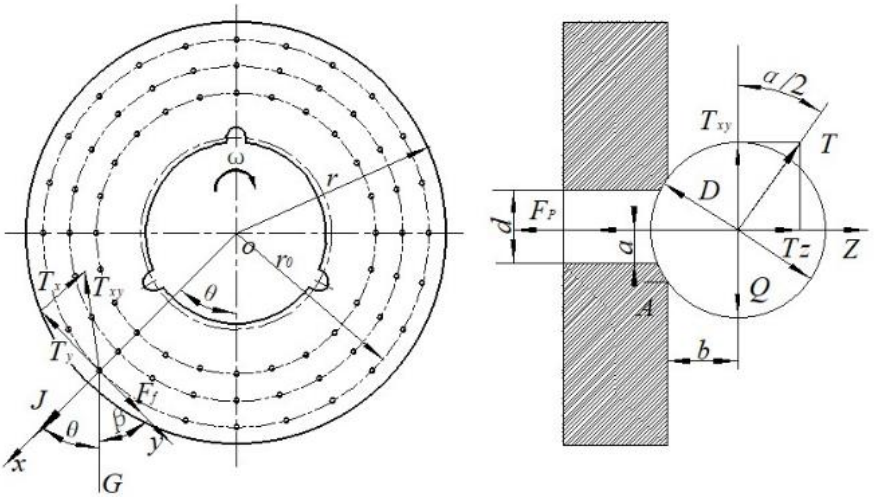

Fig. 5 - Force analysis of suction seed course

Note: G is seed gravity, N; J is centrifugal force of seeds, N; F_f is frictional resistance between air and seeds, N; Q is resultant force of G, J and F_f of seeds, N; T is normal force of suction hole to seeds, N; T_x, T_y and T_z are component force of T on the x, y and z axis, N; T_{xy} is resultant force of T_x and T_y, N; F_p is suction force of seed, N; ω is angular speed of seed-metering plate, rad·s^{-1}; O is center of seed-metering plate; θ is included angle between attachment from seed barycenter to seed-metering plate center and vertical direction, (°); β is included angle between gravity and y-axis, (°); r is radius of seed-metering plate, m; r_0 is radius of the circle surrounded by the outer holes, m; D is diameter of seed, m; a is distance from action point to suction axis, m; b is distance from action point to resultant force Q, N; d is diameter of suction hole, m; α is taper angle of suction hole, (°).

The stress balance equation of rape seeds in the filling process was as in formula (1).

$$\begin{cases} \sum F_x = 0, T_x - G\cos\theta - J = 0 \\ \sum F_y = 0, T_y - G\sin\theta - F_f = 0 \\ \sum F_z = 0, T_z - Fp = 0 \\ \sum M_A = 0, F_p a - Qb = 0 \end{cases} \quad (1)$$

According to formula (1), binding force on seeds in the XY plane during seed filling can be expressed as formula (2).

$$T_{xy} = \sqrt{T_x^2 + T_y^2} = \sqrt{G^2 + J^2 + F_f^2 + 2G\sqrt{(J^2 + F_f^2)}\sin(\theta + \beta)} \quad (2)$$

If the seed was balanced at the suction hole, then:

$$F_p = Qa/b = Q\tan(\alpha/2) = T_{xy}\tan(\alpha/2) = \sqrt{G^2 + J^2 + F_f^2 + 2G\sqrt{(J^2 + F_f^2)}\sin(\theta + \beta)} \times \tan(\alpha/2) \quad (3)$$

The critical value of negative pressure vacuum degree at the seed suction hole was simulated as formula (4).

$$P = \frac{F_p}{S} = \frac{4\sqrt{G^2 + J^2 + 2G\sqrt{(J^2 + F_f^2)}\sin(\theta + \beta)} \times \sin(\alpha/2)}{\pi D^2 \cos^3(\alpha/2)} \quad (4)$$

where:

P - the theoretical negative pressure value at which the seed can be adsorbed in the filling process, kPa;

S - the force region of the seed on the suction hole, m².

In practice, seeds were subject to external factors such as air resistance, self-vibrations, and inconsistent seed sizes and shapes. To ensure the reliability of seed suction, the actual minimum vacuum degree of negative pressure during seed suction was as formula (5).

$$P_{0\min} = K_1 K_2 P = K_1 K_2 \frac{4\sqrt{G^2 + J^2 + 2G\sqrt{(J^2 + F_f^{\ 2})}\sin(\theta + \beta)} \times \sin(\alpha / 2)}{\pi D^2 \cos^3(\alpha / 2)} \quad (5)$$

where:

K_1 is coefficient of external conditions. (The external influence coefficient accounts for air resistance, external vibrations, and other factors that affect the seed suction process, K_1 is generally 1.8 ~ 2, take K_1=1.8);

K_2 is suction reliability coefficient. (To compensate for errors due to seed size, shape, and inter-specific collisions, K_2 is generally 1.8 ~ 2, take K_2=2) *(Li et al., 2009)*.

According to Equation (5), in the process of seed filling, the negative pressure required by the negative pressure gas chamber was related to the angle of seed suction hole, seed linear velocity (determined by the rotation speed of seed disc and the radius of seed suction hole), physical and mechanical characteristics of seeds and other factors.

(2) *Seed charging process analysis*

At seed charging process, the adsorption force of the negative pressure air chamber on the seed vanished, and the positive pressure acted on the seed through the vent hole. At this point, the seed was affected by its own gravity G and barotropic pressure F *(Li et al., 2009)*. Depending on the magnitude of positive pressure on the seed, the seed charging process was divided into active falling and forced falling.

a. Active falling process analysis

If the positive pressure was enough for the seed to fall out of the suction hole and into the *seed division device*, it was an active falling. It took a certain amount of time for the seed leaving the seed plate to enter the *seed division device*. When the positive pressure was low, the horizontal acceleration and horizontal displacement of the seed were small, and the motion trajectory of the seed was dotted line *b* shown in Fig. 6.

The horizontal displacement of the seed was increased by the increasing of positive pressure when the displacement increased to the point where it collided to the shell, the seed bounced back, and the trajectory was dotted line *c*. When the positive pressure continued to increase, the seed had multiple collisions between the *seed plate and the shell, and the* trajectory was dotted line *a*.

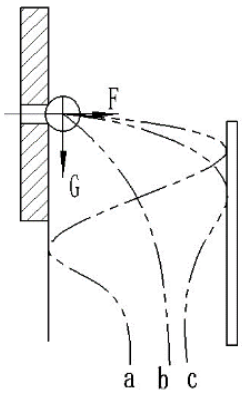

Fig. 6 - Active falling trajectory

Assuming that the positive pressure only generated an instantaneous shock force on the seed during seed dropping, and there was no longer pressure when the seeds removed from the seed suction hole. The velocity of seeds removed from the seed plate was equal to that before *(Yong et al., 2015)*, then according to Newton's second law the trajectory of the seed during seed dropping can be represented by the equation (6).

$$\begin{cases} ma = F \\ \frac{1}{2}at^2 = l \\ vt + \frac{1}{2}gt^2 = H \\ PS = F \\ l < L \end{cases} \quad (6)$$

where:

m is the weight of seed, (kg); F is the instantaneous force of positive pressure on the seed through the suction hole, (N);

t is the time from seed breaking away from the seed plate to getting out of the seed-metering device, (t);

l is the horizontal displacement of the seed, (m);

v is the vertical velocity of the seed at the moment of its release from the seed plate, (m/s);

H is the vertical displacement of the seed, (m);

L is the distance between the two seed outlets, (m);

P is the positive pressure zone, (Pa);

S is the bearing area of seed, (m^2).

According to equation (6), it was deduced that the positive pressure should satisfy equation (7).

$$\begin{cases} 0 < \mathrm{P} < \frac{2mL}{Q^2 S} \\ Q = \frac{-2v \pm \sqrt{v^2 + 2gH}}{g} \end{cases} \quad (7)$$

b. Forced falling process analysis

If the positive pressure couldn't meet the minimum requirement for seed active falling and couldn't blow the seed away from the suction hole, and if the seed could not be dropped by gravity alone, the seed continued to rotate with the seed plate, rotate towards the seed guide plate to forcibly scrape off the seed, and fall tightly into the seed separator below. One, two, or three rows of seeding with a seeder was completed. The structure of the seed guide plate and seeding apparatus is shown in Fig. 7.

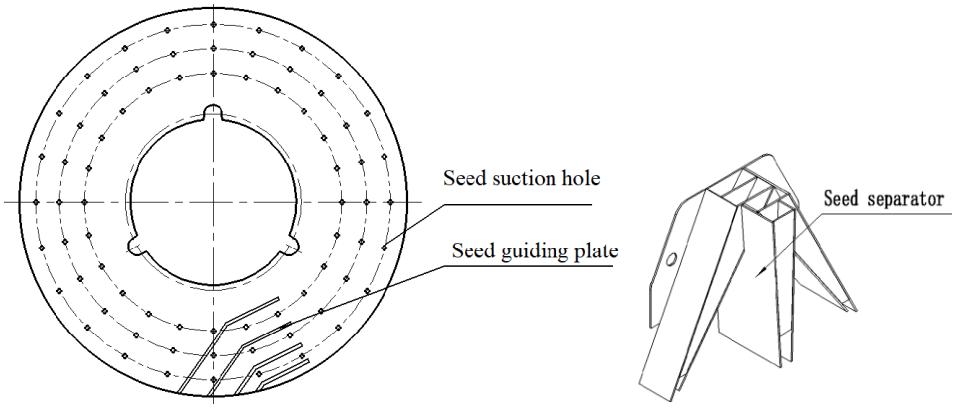

Fig. 7 - The structure of seed guiding plate and seed separator

RESULTS

Bench experiments

In order to explore the effect of the airway disc on reducing the negative pressure, a bench contrast test was carried on the JPS—12 seed-metering device performance testbed, the seed-metering device with and without airway disc was used to make a comparison, as shown in Fig. 8.

Rape seeds and a seed disc with 1 mm suction hole were selected and the experiments were carried under the condition that the seed plate rotational velocity was 15 r/min. Eligibility rates, leaky absorption rates, and re-absorption rates were as the evaluation metrics, and the results of the tests were shown in Table 1.

Fig. 8 - JPS—12 seed-metering device performance testbed

Table 1

Contrast test results of air chamber structure

Air chamber structure	Index (%)	Negative pressure (kPa)				
		1.0	1.5	2.0	2.5	3.0
With airway disc	Qualified rate	94.6	95.22	95.47	93.61	91.38
	Miss-seeding rate	2.89	2.34	0.96	0.45	0
	Reseeding rate	2.51	2.44	3.57	5.94	8.62
With no airway disc	Qualified rate	89.4	90.26	94.63	95.13	95.36
	Miss-seeding rate	10.2	8.61	3.05	2.46	2.03
	Reseeding rate	0.4	1.13	2.32	2.41	2.61

Experimental results shown that for negative pressure of 1 kPa, the qualified rate of seed-metering devices with airway disk reached more than 90% and as the negative pressure increased to 1.5 kPa and 2.0 kPa, the qualified rate was over 95%. However, when the negative pressure reached 2.5 kPa, the reseeding rate was high, resulting in a drop in the qualified rate. In contrast to traditional seed-metering device which with no airway disc, as the negative pressure increased, the miss-seeding rate gradually decreased, the reseeding rate slightly increased, and the qualified rate was in increasing trend. When negative pressure reached 1.5 kPa, the qualified rate reached more than 90%, and more than 95% when the negative pressure reached 2.5 kPa, which pressure was 1kPa higher than that with airway disc. The results indicated that the airway disc structure could effectively reduce the suction negative pressure.

Field experiment

Field tests were carried on in Fuqun Agricultural Machinery Professional Cooperative in Linz on February 29, 2023, the seeder with two seed-metering devices with airway discs and had two circular suction holes on the discs, as shown in Fig. 9. The commercially available cilantro seeds were selected, the theoretical plant spacing was set to 5 cm, and the operating speeds were set to 2 km/h, 3 km/h, and 4 km/h respectively. After seeding, a 2 m long seeding section was randomly selected from each row and 20 measurement points were selected according to "GB/T6973-2005 Testing methods of single seed drills (precision drills), the plant spacing, qualified rate, miss-seeding and reseeding rate were determined, and the test results were shown in Table 2.

Coriander seeds

Seeder

Test after seeding

Fig. 9 - Prototype field test

Table 2

Calculation result of performance index of small pneumatic precision planter for vegetable

Speed Index	2 km/h		3 km/h		4 km/h	
	Inner ring	Outer ring	Inner ring	Outer ring	Inner ring	Outer ring
Qualified rate (%)	93.29	91.59	94.35	92.41	90.61	90.16
Miss-seeding rate (%)	2.84	4.16	3.72	5.72	7.68	8.63
Reseeding rate (%)	3.87	4.25	1.93	1.87	1.71	1.21

The test results showed that all qualified rates reached 90% under three speeds. However, the miss-seeding rates were increasing and the reseeding rates were decreasing as the speeds increased. And the miss-seeding rate increased but reseeding rate decreased dramatically under the speed of 4 km/h. The best performance speed was 3 km/h, but there was certain gap compared to the performance on the bench test, as the actual field operation of the seeder was affected by its own vibrations, soil environment, and other factors. In addition, the qualified rates of the outer ring were lower than that of the inner rings similar with those on the bench test. As the seeds in the outer ring were subjected to a greater centrifugal force, the phenomenon of miss-seeding was easily produced. In order to solve the problem, the size of annular grooves corresponded with the outer ring could increase, to balances the forces and reduce the miss-seeding rates in subsequent improvements.

CONCLUSIONS

(1) A small vegetable seeder with single disc but multi-row seeding was designed. The independent airway disc was innovatively designed base on the traditional pneumatic seed-metering device which could decrease the negative pressure. The bench test results showed that the negative pressure value was lower by 1 kPa when the airway disc was used than that of the traditional pneumatic seed-metering device when qualified rate reached 95%.

(2) Field experiments of the small vegetable seeder were carried on, results shown that it was the optimum operation in a seeding speed of 3 km/h, while the miss-seeding rate was 3.72 %, the reseeding rate was 1.93 % and the qualified rate was 94.35% for the inner ring, and 5.72%, 1.87% and 92.41% respectively for the outer ring. The seeder meets the requirements for vegetable seeding.

ACKNOWLEDGEMENT

This work was supported by the Key R&D program of Shandong Province (No. 2022CXGC010611) and Agricultural machinery equipment innovation research and development plan of Shandong Province (2018YFD005).

REFERENCES

[1] Chen Hong, Chen Juan., (2018). Current situation analysis and development countermeasures of Chinese vegetable industry [J] (我国蔬菜产业现状分析与发展对策). *Changjiang Vegetable*, Vol. (02), pp.81-84, (in Chinese)

[2] Chen Jin, Li Yaoming, Wang Xiqiang, et al., (2007). Finite Element Analysis of Suction Hole Flow Field of Suction Seed drainer [J] (气吸式排种器吸孔气流场的有限元分析). *Transactions of the Chinese Society for Agricultural Machinery*, Vol. 38(9), pp. 59-62.

[3] Cong Jinling, Yu Jiajia, Cao Xiuying, et al., (2014). Pneumatic precision seed dispenser for rape and wheat [J] (油菜小麦兼用型气力式精量排种器). *Transactions of the Chinese Society for Agricultural Machinery*, Vol. (1), pp. 46-52.

[4] Hu Jingming, Yang Mei, Sun Wancang, Liu Zigang, Huang Xiaopeng, Sun Wei, Yao Yaping., (2017). Design and experiment of precision point seeding machine for rape [J] (油菜精量穴播机的设计与试验). *Journal of Agricultural Mechanization Research*, Vol. 39(04), pp. 154-157.

[5] Jafari J.F., (1991) A study of the metering of free flowing particulate solids using multi-flight screws [J]. *Proceedings of Institutionof Mechanical Engineers*, Vol. 205, pp. 113-120.

[6] Jiang Xiniu, Li Xuyi, Chi Zhongzhi et al., (2014). Research on potted-Tray grown rice seedling transplanting by machine [J]. *Agricultural science & technology*, Vol. 15(11), pp. 1923-1927.

[7] Li Hongchang, Gao Fang, Zhao Zhan et al., (2014). Research status and development trend of precision seed meter at home and abroad [J] (国内外精密排种器研究现状与发展趋势). *Chinese Journal of Agricultural Mechanization*, Vol. 35(2), pp. 12-16, 56. (in Chinese)

[8] Li Jibo., (2009). *Simulation analysis and Experimental study on Precision seed drainer of Rapeseed with combined positive and negative Pressure* [D] (正负气压组合式油菜精量排种器的仿真分析及其试验研究). Huazhong Agricultural University/China.

[9] Li Ming, Liu Xiaohui, Liao Yitao, et al., (2013). Pneumatic cylinder precision harvester for rape[J] (气力滚筒式油菜精量集排器). *Transactions of the Chinese Society for Agricultural Machinery*, Vol. 44 (12), pp. 68-73.

[10] Li Xiaoran, Zhang Yinping, Diao Peisong et al., (2021). General situation of Chinese vegetable production and research status of precision planter [J] (我国蔬菜生产概况及精量播种机研究现状). *Journal of Agricultural Mechanization Research*, Vol. 43(5), pp.263-268.

[11] Li Xu., (2012). *Working principle and Experimental study of Pneumatic Rapeseed Precision Metering Device* [D] (气力式油菜精量排种器工作原理与试验研究). Huazhong Agricultural University, Wuhan/China.

[12] Maleki M.R., Jafari J. F., Raufat M.H. et al., (2006). Evaluation of seed distribution uniformity of a multi-flight auger as a grain drill metering device[J]. *Biosystems Engineering*, Vol. 94(4), pp. 535-543.

[13] Qi Yazhuo, Xiang Shu-nan., (2020). Research status and development trend of vegetable planter at home and abroad [J] (国内外蔬菜播种机的研究现状与发展趋势). *Chinese Journal of Agricultural Mechanization*, Vol. 41(01), pp. 205-208. (in Chinese)

[14] Wang Fenghua, Sun Kai, Lai Qinghui, et al., (2020). Design and Experiment of Single row Air-sucking miniature potato Precision seeder [J] (单行气吸式微型薯精密播种机设计与试验). *Transactions of the Chinese Society for Agricultural Machinery*, Vol. 51(01), pp. 66-76.

[15] Wu Futong., (2007). *Research on rapeseed precision direct seeding device with combined positive and negative pressure* [D] (正负气压组合式油菜籽精量直播排种器的研究). Huazhong Agricultural University, Wuhan/China.

[16] Xiao Tiqiong, Cui Siyuan, Chen Yongsheng, et al., (2017). General situation of vegetable production and mechanization development in China [J] (我国蔬菜生产概况及机械化发展现状). *Chinese Journal of Agricultural Mechanization*, Vol. 38(8), pp. 107-111.

[17] Yan Qiuyan, Liao Yitao, Liao Qingxi., (2014). Design and Function Analysis of Pneumatic Seed Harvester with One Machine and Two Rows[J] (油麦气力式一器双行兼用型排种器的设计与功能分析). *Journal of Huazhong Agricultural University*, Vol. 33 (3), pp. 109-114.

[18] Yazgi A, Degirmencioglu A, (2014). Measurement of seed spacing uniformity performance of a precision metering unit as function of the number of holes on vacuum plate [J]. *Mesurement*, Vol. 56(10),pp.128-135.

[19] Yong Kai, Wu Delin, Li Jun, Wu Chongyou, Cao Chengmao., (2015). Determination of Seed Metering Parameter Threshold of Pneumatic Drum Seed metering device with Small Particle Size[J] (小粒径气力滚筒式排种器排种参数阈值确定). *Journal of Agricultural Mechanization Research*, Vol. 37(02), pp. 52-56.

[20] Zhang Kaixing, Li Jinfeng, Song Zhenghe, Liu Xianxi, Liu Lei., (2019). Optimization design and experiment of Variable Particle Size Double Disc air suction precision seed Separator[J] (变粒径双圆盘气吸式精量排种器优化设计与试验). *Transactions of the Chinese Society for Agricultural Machinery*, Vol. 50(6), pp. 52-63. (in Chinese)

[21] Zhang Min, Wu Chongyou, Zhang Wenyi, et al., (2011). Simulation and analysis of suction hole flow field of rice seedling planter with suction cup[J] (吸盘式水稻育秧播种器吸孔气流场仿真分析). *Transactions of the Chinese Society of Agricultural Engineering*, Vol. 27 (7), pp. 162-167.

SIMULATION AND EXPERIMENT ON THE PROCESS OF CASTOR SHELLING BASED ON DISCRETE ELEMENT METHOD

/

可调式蓖麻脱壳机脱壳过程离散元分析与试验

Junming HOU, Zhaotan REN, Hongjie ZHU, Zhi RENDE, Wei WANG
Shenyang Agricultural University, College of Engineering / China;
Tel: +86024-88487116; E-mail: junming_hou@163.com
DOI: https://doi.org/10.35633/inmateh-70-04

Keywords: *castor, stress analysis, experiment, DEM, design optimization*

ABSTRACT

Castor is one of the important oil crop, the shelling process of which directly affects the quality of castor seeds. In the process of shelling, the shelling force of castor is an important index to study its damage. The castor capsule model was established and the shelling test machine was established based on the discrete element method. Then the extrusion law of castor capsule during shelling was analyzed. The shelling process is divided into three stages, which are the Initial stage*,* stable shelling stage *and the* final stage*. The force law of shelling process is analyzed. The results show that with the increase of rotating speed, the maximum force decreases from 68.78 to 68.10 N, the maximum speed increases from 8.92 to 12.99 m/s, the force of inner drum increases from 509.34 to 533.14 N, and then decreases to 456.15 N. The shelling increases from 91.23% to 91.28%, and then decreases to 88.89%. With the increase of filling amount, the maximum force increases from 55.86 to 76.93 N, the maximum speed decreases from 12.99 to 10.86 m/s, the force of inner drum increases from 338.58 to 603.364 N, and the shelling rate changes from 91% to 90.05%. This study can provide theoretical support for the design of castor shelling machine.*

摘要

蓖麻是重要的油料作物，其脱壳过程直接影响蓖麻种子的质量。在脱壳过程中，蓖麻的受力是研究其损伤的重要指标。本研究基于离散元方法，建立了蓖麻蒴果模型并搭建了脱壳试验台。分析蓖麻蒴果在脱壳过程中的挤压规律。该过程分为三个阶段，即开始阶段、稳定阶段和结束阶段。分析了三个阶段的脱壳过程的应力规律。结果表明，随着转速的增加，最大受力从 68.78 N 降至 68.10 N，最大转速从 8.92 m/s 升至 12.99 m/s，内筒应力从 509.34 N 升至 533.14 N，然后降至 456.15 N，脱壳率从 91.23%升至 91.28%，然后降至 88.89%。随着装填量的增加，最大压力从 55.86 N 增加到 76.93 N，最大速度从 12.99 m/s 降低到 10.86 m/s，内筒应力从 338.58 N 增加到 603.364 N，脱壳率从 91%变为 90.05%。本研究可为蓖麻脱壳机的设计提供理论支持。

INTRODUCTION

Castor is one of the ten oil crops in the world. Castor oil extracted from seeds has a high viscosity, ignition point and low freezing point, which is one of the advanced lubricating oils for trains, high-speed lathes, and aerospace (*Huang et al., 2013; Liu et al., 2015*). Shelling is the first step of castor oil processing, which directly affects its quality. The force law of castor is a vital index to affect the damage of castor capsule during the process of shelling.

Güner et al., (2003), determined the fracture force and fracture energy required for hazelnut shell breaking, which provided a reference for the design of hazelnut sheller. The anisotropic behavior of hazelnut was analyzed with numerical simulation (*Delprete et al., 2014*). The significant data of mechanical properties was obtained, which can provide a reference for the design of shelling machine. The effect and shelling mechanism of rubber materials on the shelling performance of grain sheller was studied (*Baker et al., 2012*). The results show that the shear force is the main factor affecting the shelling rate. The mechanical behavior of collision between rice grain and the key parts of shelling machine was studied (*Zhao et al., 2013*). The results show that the difference of normal contact force increased with the increase of particle size ratio. The geometric model and stress model for ginkgo biloba were established, which can analyze the stress based on the finite element method (*Wang et al., 2003*).

The best direction and mode of force application were found, which provides a theoretical basis for the development of shelling equipment. The shelling method of ginkgo fruit was determined, and the force of ginkgo fruit in extrusion working area was analyzed (*Pan et al., 2019*). The finite element model of chestnut shell breaking was established in vacuum. The results show that the wet stress is the main factor of chestnut shell breaking in vacuum (*Yuan et al., 2011*). The mechanical behavior of *Jatropha curcas L.* seeds under compression was studied. The results showed that the stamping speed has a great influence on deformation, deformation energy and oil yield (*Kabutey et al., 2013*). Wang studied the mechanical properties of kenaf capsule (*Wang et al., 2015*). The results showed that the capsule began to break from the middle near the top and then produced cracks to make the seeds come out of the capsule. The nonlinear relationship between water content, loading speed, transverse diameter ratio and shell breaking force of walnut was established, which provided the law of shell breaking conditions and crack variation characteristics (*Zhang et al., 2014*). Liu et al. (*2016*) analyzed the stiffness of walnut shell by mechanical theory of elasticity. The dynamic response of different drop height to the impact of potato rigid plate was supervised (*Gao et al., 2018*). The results show that the maximum impact force and the maximum deformation are positively correlated with the drop height. The mechanical behavior of *Jatropha curcas L.* seeds was studied at different pressing vessel diameters and seed pressing heights under compression loading (*Herak et al., 2013*). The mathematical models can provide the basis for the development of further models. The mechanical properties of the sides and middle parts of the film were enhanced to improve the recovery efficiency of residual film (*Hu et al. 2017*). The results suggested that the film was of tensile strength after its mechanical properties have been reinforced. The force and rate of shelling removal of the inner drum were analyzed (*Hou et al., 2020*). The results provided theoretical support for the design of the castor shelling machine. The minimum fall height of potatoes falling onto steel sheets, steel rods and rubber-steel rods causing unallowable damage to potatoes was studied (*Rady et al., 2015*). The results showed that steel sheet and steel rods resulted in higher bruise volume values compared to the coated steel rods. The design of the seed metering device was optimized (*Shi et al., 2020*). The result showed that the optimized seed plate had a better performance at high speed and vibration conditions. The collision recovery coefficient of soybean seed contact with seed plate, seed wheel and organic glass was determined (*Zhang et al., 2017*). The results showed that the collision recovery coefficients were 0.561, 0.518 and 0.472, respectively.

The critical forces of walnut, the vital forces of shell breaking, and the conditions of crack propagation after fracture were obtained. Considering the related studies, progress has been made in the study of the mechanical law of agricultural materials shelling. However, the process of shelling on agricultural particles based on Discrete Element Method (DEM) has not been studied in detail deeply. Especially, the force parameters of particles in the shelling process were not discussed.

In the study, the model of castor was established based on DEM. The law of force extrusion in the process of shelling was analyzed. The shelling process is divided into three stages, which are the beginning shelling stage, stable stage, and the ending stage. The shelling process and force law of the three stages were analyzed.

MATERIALS AND METHODS

Establishment of castor model

The castor capsule bond model was established. The relationship between the force and displacement of particles in each contact motion was described. Its three axis dimensions are 15.00 mm in length, 14.50 mm in width, and 16.00 mm in height. The contact of particles, center of the area, line between the center point of two particles, and the center point were established.

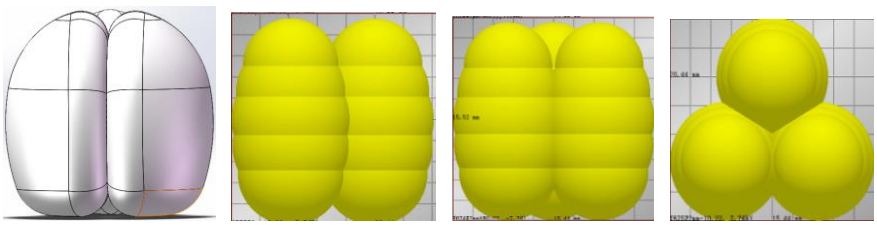

(a) Three-dimensional map (b) Direction X (c) Direction Y (d) Direction Z

Fig. 1 - 3 DEM model of castor fruit

Division of shelling stage for castor capsule

The variety of TongBi No.7 castor was selected as the test material. The replacement effect occurs at 0.395 s during the simulation. At 1.5 s, the particles fell into the shelling drum and began to shell. Fig. 2 shows the process of castor shelling.

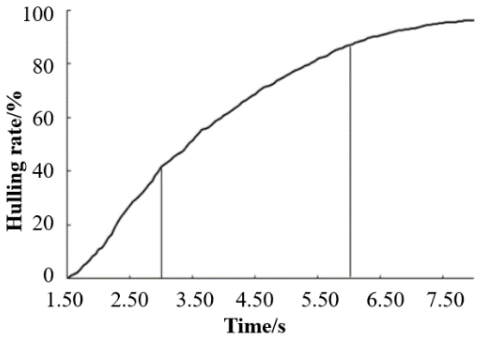

Fig. 2 - The process of castor shelling

It can be drawn that the shelling rate rose rapidly from 1.5 s to 3 s. It ran stably from 1.5 s to 6 s, and ran gently from 6 s to 8 s. It continued to rise from 1.6 s to 6 s, then it ran smoothly from 6 s to 8 s. Therefore, the shelling process was divided into three stages which are the initial, stable, and ending shelling stages. The three stage curve fitting equation and correlation coefficient are shown in Table 1.

Table 1

Regression equation of undamaged bond

Shelling distance process	Fitting equations	The correlation coefficient
Initial stage	Y=1.44X-3.86	0.9939
Stable shelling stage	Y=0.75X+43.66	0.9878
Final stage	Y=0.23X+87.78	0.9630

It can be drawn that the shelling efficiency decreased continuously in the process of shelling. Therefore, the shelling efficiency shows a downward trend. The correlation coefficients of the fitting equation are all close to 1.0. Table 2 shows the division of shelling stages.

Table 2

Division of shelling stages

Shelling distance stage	Feeding	Initial stage	Stable shelling	The end of the shelling
Period of time/s	0~1.5	1.5~3	3~6	6~8

Simulation of castor capsule at the initial stage

The relationship between average velocity and maximum particle force is shown in Fig. 3. It can be drawn that when the average speed of particles reached 1.81 m/s, the maximum force of particles reached a maximum value of 48.86 N. When the average particle velocity reached 1.77 m/s, the maximum particle force reached the minimum value of 10.04 N. When the average speed of particles was from 1.57 m/s to 1.83 m/s, the maximum force of particles fluctuated greatly, and the fluctuation frequency was small. When the average velocity of particles changed from 1.83 m/s to 1.95 m/s, the maximum force fluctuation of particles was low. Because the particles entered the shelling part in a short time, the force changed significantly.

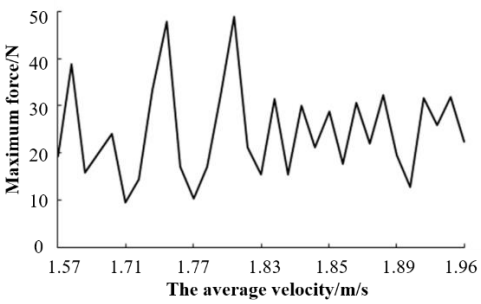

Fig. 3 - Relationship of average velocity and maximum force

The force exerted by the particle groups on the shelling model is shown in Fig.4. It can be seen that with the progress of the shelling process, the force produced by the external drum of particles changes smoothly, reaching the maximum value of 101.53 N at 1.75 s.

The average force at the beginning of the shelling stage was 47.28 N. The force exerted by particles on the inner drum fluctuated greatly, reaching a maximum value of 245.09 N at 2.75 s. The average force was 141.73 N in this stage. At this stage, the particles fall into the shell chamber from the inlet. Comparing the force of particles on the inner with outer drums, it can be seen that the force of the inner drum is higher than the outer drum at the same time. Therefore, the inner drum performs the main shelling work at this stage. The force fluctuation range of the inner drum is extensive, so the shelling effect at this stage is mainly the collision between the particles and the drum.

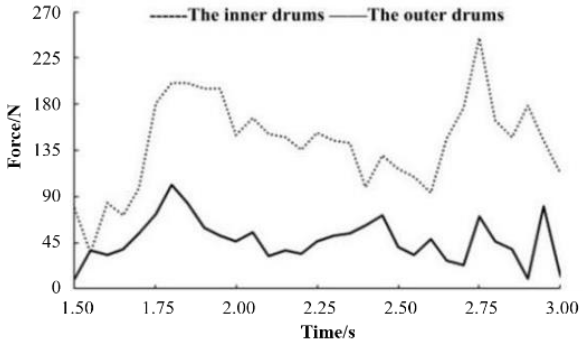

Fig. 4 – Force of particle group to shelling model

The average and tangential force among particles is shown in Fig.5. According to Fig.5 (a), in the X-axis direction, when the average velocity of particle reached 1.81 m/s, the maximum force among particles reached 23.66 N. When the average velocity of particle reached 1.57 m/s, the maximum force among particles reached 5.75 N. When the average particle velocity reached 1.71 m/s, the maximum force among particles reached 6.29 N. When the average particle velocity reached 1.57 m/s, the maximum force among particles reached 4.34 N.

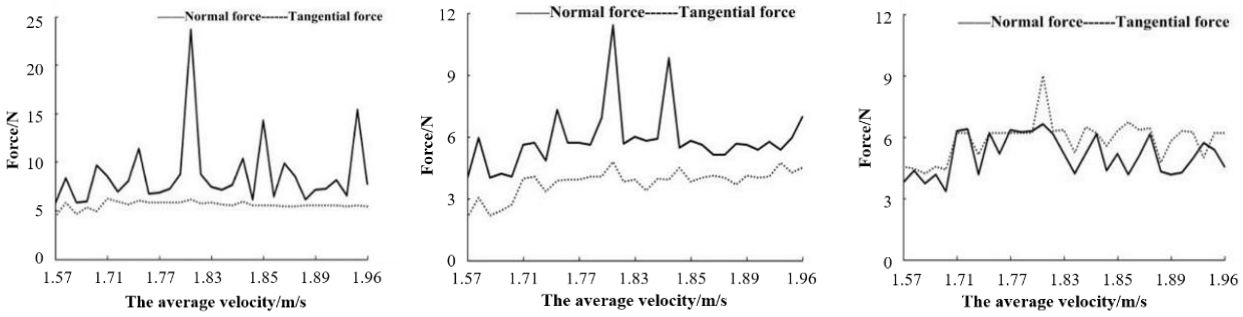

(a)X direction (b)Y direction (c)Z direction

Fig. 5 - Contact forces between particles

Fig.5 (b) shows the results in the Y-axis direction. When the average velocity of particle reached 1.81 m/s, the maximum force among particles reached 11.45 N. When the average speed of particles reached 1.57 m/s, the maximum force among particles reached the minimum value, which is 3.99 N. When the average particle velocity reached 1.81 m/s, the maximum tangential force among particles reached 4.82 N. When the average speed of particles reached 1.57 m/s, the maximum force among particles reached the minimum value, which is 2.06 N.

Fig.5 (c) shows the results in the Z-axis direction. When the average particle velocity reached 1.81 m/s, the maximum normal force among particles reached 6.62 N. When the average velocity of particles reached 1.70 m/s, the maximum force among particles reached the minimum value, which is 3.36 N. When the average particle velocity reached 1.81 m/s, the maximum tangential force among particles reached 9.03 N. When the average speed of particles reached 1.65 m/s, the maximum force among particles reached the minimum value, which is 4.22 N. The results show that the inner and outer rollers jointly provide the shelling effect, and the frequency difference of force fluctuations caused by particles on the inner and outer rollers is small.

Simulation of stable shelling stage

The relationship between average velocity and maximum particle force is shown in Fig. 6. It can be drawn that in the stable shelling stage, when the average velocity of particles reached 1.77 m/s, the maximum force of particles reached a maximum value of 41.39 N.

When the average speed of particles reached 1.51 m/s, the maximum force of particles reached the minimum value, which is 6.98 N. When the average velocity of particles was between 1.44 m/s and 1.59 m/s, the maximum force of particles fluctuates greatly.

When the average velocity of particles was from 1.59 m/s to 1.76 m/s, the maximum force fluctuation of particles was low. When the average velocity of particles was from 1.76 m/s to 1.84 m/s, the maximum force of particles fluctuated greatly. The reason is that particles are uniformly distributed in the inner part of the shelling chamber, and the inner and outer rollers act together to remove the shell.

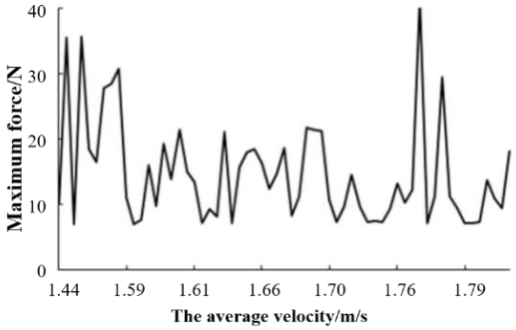

Fig. 6 - Relationship of average velocity and maximum force

The force of particle group in the shelling process is shown in Fig. 7. It can be drawn that the force generated by the particles in the external drum. It presented a downward trend with the progress of the shelling process. The maximum value is 74.39 N when the time is 3.30 s. The average value was 23.87 N in this stage. The force exerted by particles on the inner drum showed a downward trend, reaching a maximum value of 133.80 N at 3.10 s. The average value was 26.79 N in this stage. By comparing the force on the inner and outer drum, it can be drawn that the particles evenly distributed in the interior of the shelling region. Therefore, the outer and inner drum worked together to break the shell in this stage. The particles were impacted, squeezed and rubbed together with the drums.

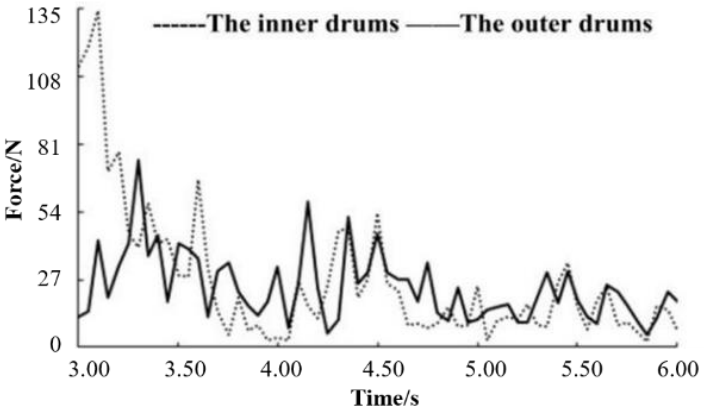

Fig. 7 - Force of particle group in the shelling process

The law of the normal and tangential forces among particles is shown in Fig.8. It can be seen from Fig.8(a) that when the average particle velocity reached 1.67 m/s, the maximum force among particles reached 12.55 N in the X-axis direction. When the average particle velocity reached 1.57 m/s, the maximum normal force among particles reached to the minimum value, which was 5.75 N. When the average particle velocity reached 1.73 m/s, the maximum tangential force among particles reached 6.97 N. When the average speed of particles reached 1.96 m/s, the maximum reasonable force among particles reached the minimum value, which was 5.50 N.

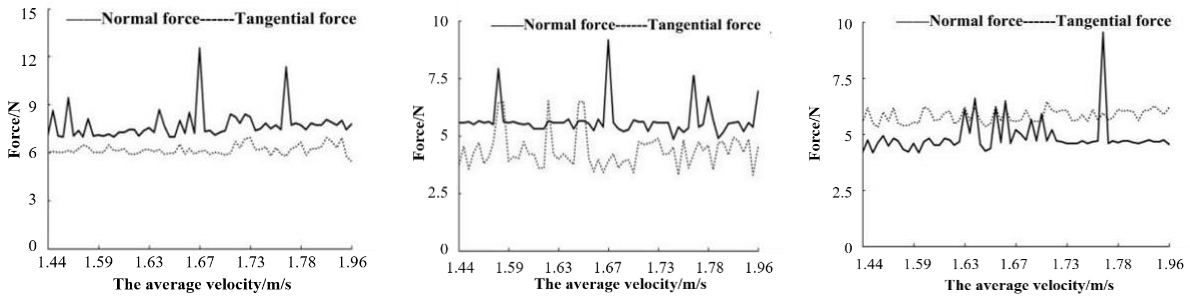

(a) X direction (b) Y direction (c) Z direction

Fig. 8 - Contact force between particles

Fig.8 (b) shows that when the average particle velocity reached 1.67 m/s, the maximum reasonable force between particles reached 9.16 N in the Y-axis direction. When the average particle velocity reached 1.75 m/s, the maximum reasonable force among particles reached the minimum value, which was 4.88 N. When the average particle velocity reached 1.61 m/s, the maximum tangential force among particles reached 6.51 N. When the average speed of particles reached 1.76 m/s, the maximum reasonable force among particles reached the minimum value, which was 3.31 N.

Fig.8(c) shows that when the average particle velocity reached 1.77 m/s, the maximum normal force among particles reached 9.54 N in the Z-axis direction. When the average speed of particles reached 1.51 m/s, the maximum normal force among particles reached the minimum value, which was 4.16 N. When the average particle velocity reached 1.70 m/s, the maximum tangential force among particles reached 6.44 N. When the average speed of particles reached 1.52 m/s, the maximum reasonable force between particles reached the minimum value, which was 5.30 N. The frequency of force fluctuations generated by particles on the external drum is high. At this stage, the collision between the capsules and their forces on the shelling parts cause them to break.

Simulation of final shelling stage

The relationship between average velocity and maximum particle force is shown in Fig.9.

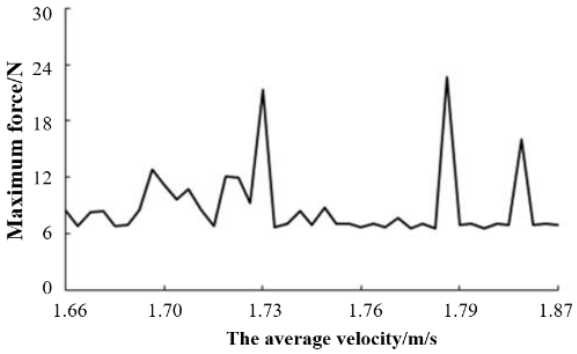

Fig. 9 - Variation of average velocity with maximum force

It can be drawn that when the average particle velocity reached 1.79 m/s, the maximum particle force reached a maximum value of 22.59 N. When the average particle velocity reached 1.78 m/s, the maximum particle force reached the minimum value of 6.56 N. In this stage, with the increase of average speed, the maximum force fluctuation of particles is relatively stable. The collision between the capsules and their forces on the shelling parts cause them to break.

The force exerted by particles group on the shelling model is shown is Fig.10. It can be drawn that the force generated by particles in the external drum. It decreased with process of shelling, reaching a maximum value of 25.87 N at 6.75 s. The force exerted by particles on the inner drum decreased with the prolonging of the shelling process when it reached a maximum value of 21.64 N at 7.80 s. By comparing the force of particles on the internal and external drums, the inner and outer drums provided the shelling effect in this stage. Moreover, the force fluctuation of particles on the inner and outer drums was small. Therefore, the outer and inner drums worked together to complete the shelling in this stage.

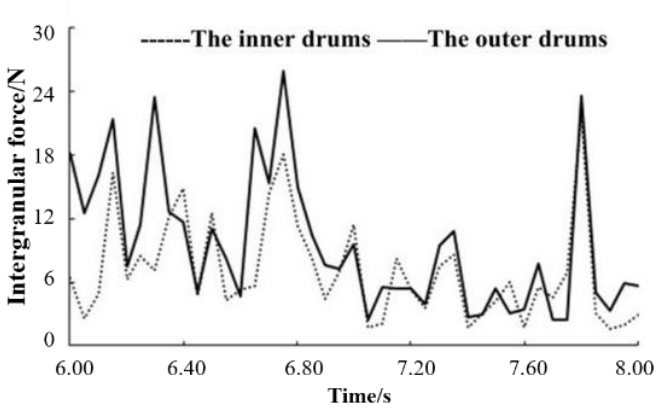

Fig. 10 - Force of particle group on the shelling model

To analyze the interaction among particles during the shelling process, the average and tangential forces of the interaction among particles are shown in Fig.11.

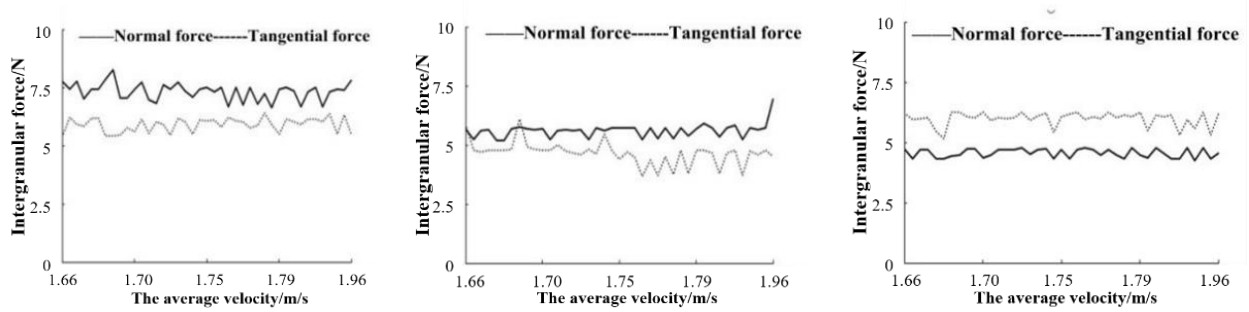

(a) X direction (b) Y direction (c) Z direction

Fig. 11 - Force of the particles

According to Fig.11 (a), when the average particle velocity reached 1.70 m/s, the maximum force among particles reached 8.25 N in the X-axis direction. When the average speed of particles reached 1.78 m/s, the maximum force among particles reached the minimum value, which was 6.65 N. When the average particle velocity reached 1.78 m/s, the maximum tangential force among particles reached 6.40 N. When the average speed of particles reached 1.66 m/s, the maximum force among particles reached the minimum value, which was 5.41 N.

According to Fig.11 (b), when the average particle velocity reached 1.96 m/s, the maximum force between particles reached 6.95 N in the Y-axis direction. When the average particle velocity reached 1.69 m/s, the maximum reasonable force among particles reached the minimum value, which was 5.19 N. When the average speed of particles reached 1.70 m/s, the maximum tangential force among particles reached 6.09 N. When the average velocity of particles reached 1.76 m/s, the maximum reasonable force among particles reached the minimum value, which was 3.70 N.

When the average speed of particles reached 1.76 m/s, the maximum tangential force among particles reached 6.27 N. When the average particle velocity reached 1.69 m/s, the maximum force among particles reached the minimum value, which was 5.15 N.

The extrusion among the particles and the drums worked to complete the shelling. So, the force among the particles changes in the way.

Analysis of transition phase and key grid

Considering the continuity and integrity of the process, there is a transition stage among the three stages. The maximum force, particle normal force, and triaxial displacement of the particles are mostly between the two period of 2.75-3.25 s and 5.75-6.25 s. Table 3 shows the size comparison of the results of particles at the time of 2.75 s, 3.25 s, 5.75 s, and 6.25 s.

Table 3

Statistics of the result size at each moment of the particles

Time	Maximum force	Interparticle normal resultant force	Interparticle tangential resultant force	Displacement
[s]	[N]	[N]	[N]	[mm]
2.75	48.86	27.11	11.94	885.54
3.25	26.01	10.21	8.83	944.95
5.75	9.36	10.84	10.39	1255.75
6.25	7.61	7.12	7.63	1409.6

Fig.12 shows the critical state of particles. The result shows that the distribution grid in the process of shelling.

It showed a trend of growth in the interval from 1.5 s to 2.75 s. The particles number was stable from 2.75 s to 3.25 s. The large number of particles distribution was from 3.25 s to 5.75 s. When the time was between 5.75 s and 6.25 s, the amount of particles was on the decline. Fig.11(b) shows the maximum force in the grid. It can be drawn that the maximum force decreased with the continuation of the shelling process and reached zero gradually with the continuous discharge of particles. Fig.11 (c) shows the maximum velocity of particles in the grid. The maximum speed decreased with the continuation of the shelling process and reached to zero gradually with the continuous discharge of particles.

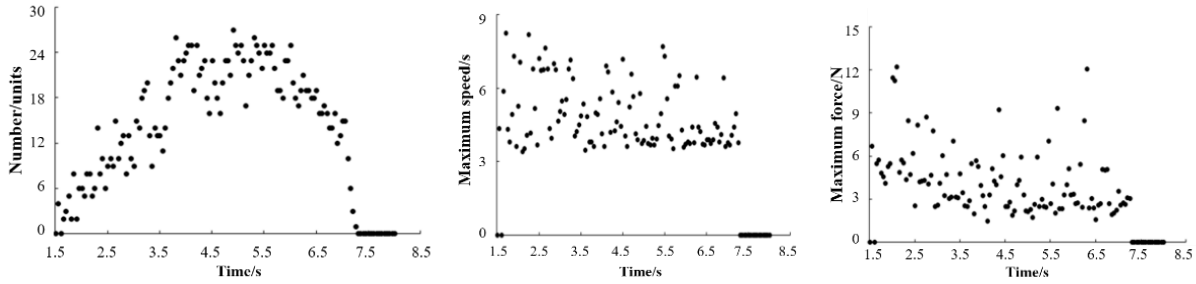

(a) **(b)** **(c)**

Fig. 12 - Critical grid state of particles

Test methods and instruments

The speed of the inner drum, the distance of shell removal and the filling amount were the test factors, while the rate of shell removal, damage rate and productivity were the test indicators. The speed of the inner drum can be changed through the frequency converter, the position of the outer drum was adjusted to change the shell distance, and the amount of feed is adapted to fit the filling amount. The high speed camera was directed towards the observation window, and recorded the status of particles in the drum within 1.5 s to 8 s after feeding through high-speed photography (*Hou et al., 2020)*.

Fig. 13 - Castor Shelling Test Bed

1. Host; 2. Motor; 3. Light source; 4. Adjustment hole; 5. Frequency converter; 6. Adjustment arm; 7. Shelling drum; 8. Feeding hopper; 9. Observation window; 10. Frame; 11. Camera

The experimental material was castor capsule Tongbi No.11, which was dried in Tongliao Academy of Agricultural Sciences, Inner Mongolia. The test equipment includes castor capsule shelling machine, Shuangjie electronic scale (TC-60K) (maximum weighing 60 kg, accuracy 10.0 g). The shelling machine equipment is shown in Fig.13.

RESULTS

Shelling machine design

Based on the parameter setting of the simulation shelling model, the shelling machine was designed. Through changes in the amount of drum rotating speed, the shelling distance and filling amount were taken as the factors, damage rate and productivity were as an index. The schematic diagram of the shelling machine is shown in Fig.14.

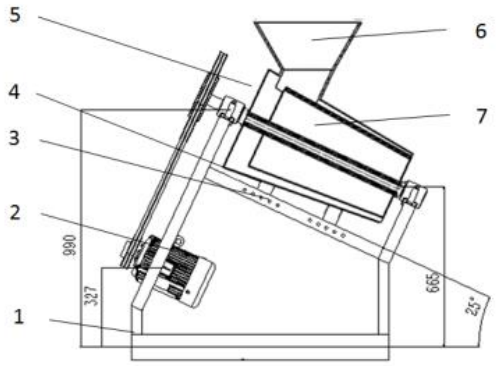

Fig. 14 - Schematic diagram of complete machine

1. Motor; 2. Base frame; 3. Adjustment hole; 4. Adjustment arm; 5. Outer drum; 6. Feed hopper; 7. Inner drum

Analysis of test results

The rotating speed of the inner drum, the shelling distance, and the filling amount are the test factors, and the shelling rate, damage rate, and productivity are the test indicators. The test bench test is conducted. The level table is shown in Table 4.

Table4

Test Factor level

Level	Speed rpm	Shelling distance mm	Filling amount %
-1	250	5	30
0	300	6	40
1	350	7	50

The analysis of variance of shell removal rate is shown in Table 5. The test statistic value *F* represents inter group differences. The significance level is *P* value. It can be drawn that the rotation speed, shelling distance and filling amount have an extremely significant influence on the rate of shelling, among which the shelling distance has the most considerable impact, followed by rotation speed. The filling amount was the smallest.

Table 5

Variance analysis results

Sources of variance	Square sum	Freedom	Mean square	*F* value	*P* value
A	18.29	2	9.15	134.14	<0.01
B	27.59	2	13.79	202.21	<0.01
C	12.14	2	6.07	89.01	<0.05
Error	0.14	2	0.07		
Summation	58.17	8			

Table 6 is the variance analysis of damage rate. It can be seen that the speed and the shelling distance had an extremely significant influence on the damage rate.

Table 6

Variance analysis results

Sources of variance	Square sum	Freedom	Mean square	*F* value	*P* value
A	0.13	2	0.06	134.23	<0.01
B	0.13	2	0.07	139.00	<0.01
C	0.04	2	0.02	43.53	<0.05
Error	9.56×10^{-4}	2	4.78×10^{-4}		
Summation	0.30	8			

Furthermore, the impact of the shelling distance was greater than the speed, and the filling quantity had a considerable influence on the damage rate. Table 7 shows the productivity variance analysis.

Table 7

Variance analysis results

Sources of variance	Square sum	Freedom	Mean square	*F* value	*P* value
A	10672.16	2	5336.08	239.44	<0.01
B	4698.14	2	2349.07	105.41	<0.01
C	424.24	2	212.12	9.52	<0.1
Error	44.57	2	22.29		
Summation	15839.11	8	7919.55		

It can be drawn that the speed and the shelling distance had an extremely significant impact on productivity. The speed had a greater impact than the shelling distance, and the filling amount has a considerable effect on productivity.

Comparison of shelling rate

The significance order of each factor obtained by simulation was the shelling distance, rotation speed and filling amount. The significance order of each factor obtained by experiment was the shelling distance, rotation speed and filling amount. The optimal combination obtained by the simulation was 350.0 r/min, the shelling distance was 5 mm, and the filling amount was 40.0%. The optimal combination obtained by the test was 350.0 r/min, the shelling distance was 5.0 mm, and the filling amount was 30.0%. The speed and the shelling distance were incredibly significant factors, and the filling amount was a substantial factor, which is within a reasonable range.

CONCLUSIONS

(1) The shelling distance and the filling amount have a significant impact on the force of the inner drum, while the rotating speed has no significant impact on the force of the inner drum. With the increase of the shelling distance and the filling amount, the force of the inner drum increased.

(2) The shelling process is divided into three stages. At the initial stage, the maximum force of the particle is generated, which is 48.86 N. The main shelling form is collision. At the stable stage, the force fluctuation frequency of the particle is the highest. The shelling work is completed by the inner and outer drum together. At the final stage, the force fluctuation frequency of the particle on the inner and outer drum is less different. The inner and outer drum work together to complete the shelling. The main form of shelling is extrusion and rubbing.

(3) The optimized within roller cone angle is 4.5°, drum length is 605.0 mm with the highest for shelling rate under the conditions of size parameter adjustment. The rate of shell removal is 96.42% when the size parameters are applied for simulation. There was a difference of 0.39% from the fitting value.

(4) The simulation model is verified on test bed. The shelling rate was significantly affected by the rotation speed, shelling distance and filling amount. The shelling damage rate was significantly affected by the rotation speed. By comparing the shelling rate, it can be seen that the difference ratio between the simulation result and the test result is 8.73% at the maximum and 1.43% at the minimum. The optimal parameter combination obtained by simulation was the rotational speed of 350 r/min, the shelling distance of 5.0 mm, and the filling amount of 40.0%. The results were relatively close, and the difference was within a reasonable range.

ACKNOWLEDGMENTS

The research was supported by China National Natural Science Foundation Project (Grant No. 51457312).

REFERENCES

[1] Baker, A., Dwyer-Joyce, R., Briggs, C., Brockfeld, M. (2012). Effect of different rubber materials on husking dynamics of paddy rice. Proceedings of the Institution of Mechanical Engineers, Part J: *Journal of Engineering Tribology*, Vol.226, Issue 06: 516-528.

[2] Delprete, C., Sesana, R. (2014). Mechanical characterization of kernel and shell of hazelnuts: Proposal of an experimental procedure. *Journal of Food Engineering*, Vol.124, Issue 01: 28-34.

[3] Gao, Y., Song, C., Rao, X., Ying, Y. (2018), Image processing-aided FEA for monitoring dynamic response of potato tubers to impact loading. *Computers and Electronics in Agriculture*, Vol.151:21–30.

[4] Güner M, Dursun E, Dursun İ.G. (2003). Mechanical Behaviour of Hazelnut under Compression Loading. *Biosystems Engineering*, Vol.85, Issue 04: 485-491.

[5] Herak, D., Kabutey, A., Divisova, M., Simanjuntak, S. (2013). Mathematical model of mechanical behaviour of *Jatropha curcas L*. seeds under compression loading. *Biosystems Engineering*, Vol.144, Issue 03:279-288.

[6] Hu, C., Wang, X., Li, H., Wang, L., Li, J., Yang, Y. (2017). Design and test of a new reinforced plastic film collector. *International Agricultural Engineering Journal*, Vol.26, Issue 04: 65-73.

[7] Huang, Z., Cheng, X., Li, C., Xiao, Z., Shi, L (2013). Mechanical model and major influential factors of breaking castor shell. *Journal of Shenyang Agricultural University*, Vol.44, Issue 02: 185-159.

[8] Junming Hou, Zhu Hongjie, Jinpeng Li, Enchao Yao, Hu Weixue. (2020). Analysis and optimization on the process of adjustable double drum castor shelling based on discrete element method, *INMATEH – Agricultural Engineering*, Vol.62, Issue03: 289-298.

[9] Kabutey, A., Herak, D., Chotěborský, R., Dajbych, O., Divišova, M., E. Boatri, W. (2013). Linear pressing analysis of *Jatropha curcas L.* seeds using different pressing vessel diameters and seed pressing heights. *Biosystems Engineering*, Vol.115, Issue 01: 43-49.

[10] Liu, M., Li, C., Zhang, Y., Yang, M., Hou, Y., Gao, L. (2016). Shell crushing mechanism analysis and performance test of flexible-belt shearing extrusion for walnut. T*ransactions of the Chinese Society for Agricultural Machinery*, Vol.47, Issue 07: 267-273.

[11] Liu, R., Cheng, X., Xiao, Z., Li, C., Huang, Z., Ye, H. (2015). Finite element simulation on mechanical property of castor capsule during husking. *Journal of the Chinese Cereals and Oils Association*, Vol.30, Issue 05: 62-66.

[12] Pan, J., Song, W., Liu, H., Shao, N., He, B., Tu, Q. (2019) Research on the Design of Ginkgo Nut Sheller. *Mechanical Engineer*, Vol.01, Issue 04: 92-95.

[13] Rady, A., Soliman, S. (2015). Evaluation of mechanical damage of Lady Rosetta potato tubers using different methods, *International Journal of Postharvest Technology & Innovation*, Vol.05, Issue 02:125-148.

[14] Shi, S., Liu H., Wei, G., Zhou, J., Jian, S., Zhang, R. (2020) Optimization and Experiment of Pneumatic Seed Metering Device with Guided Assistant Filling Based on EDEM-CFD. *Transactions of the Chinese Society for Agricultural Machinery*, Vol.51, Issue 05:54-66.

[15] Wang, L., Quan, Y., Deng, W. (2003). Finite Element Force Analysis of Ginkgo hulling. Journal of Agricultural Engineering, Vol.04, Issue 04: 58-61.

[16] Wang, Z., Xu, J., Li, X., Tian, K., Shen, C. (2015). Mechanical properties test and analysis of Kenaf capsule. *Chinese Journal of agricultural machinery chemistry*, Vol.36, Issue 06: 136-138.

[17] Yuan, Y., Yuan. Y., Dang, X., Xu, Y., Dong, J., Xu, J. (2011). Finite element analysis of mechanical properties of chestnut vacuum cracking. *Journal of Agricultural Machinery*, Vol.42, Issue 05: 136-141.

[18] Zhang, H., Ma, Y., Li, Y., Zhang, R., Zhang, X., Zhang, R. (2014). Prediction model of walnut fracture work based on genetic BP neural network. *Journal of Agricultural Engineering*, 30(18): 78-84.

[19] Zhang, Tao., Liu, F., Zhao, M., Liu, Y., Li, F., Ma, Q., Zhang, Y., Zhou, P. (2017). Measurement of physical parameters of contact between soybean seed and seed metering device and discrete element simulation calibration. *Journal of China Agricultural University*, Vol.22, Issue 09:86-92.

[20] Zhao, Z., Li, Y., Chen, Y., Liang, Z., Liu, L. (2013). Study on the Collision Mechanical properties of rice grains. *Journal of Agricultural Machinery*, Vol.44, Issue 06: 88-92.

CONSTRUCTION OF MAIZE VISUALIZATION MODEL BASED ON BIOMASS
/
基于生物量的玉米可视化模型构建

Lili SUN [1], Yuzhi WANG [2)], Yaoyu LI [2)], Xiaoying ZHANG [3)], Wuping ZHANG [2)], Fuzhong LI [2,*)]

[1)] College of Agricultural Engineering, Shanxi Agricultural University, Taigu, Shanxi / China
[2)] College of Software, Shanxi Agricultural University, Taigu, Shanxi / China
[3)] Department of Basic, Shanxi Agricultural University, Taigu, Shanxi / China
Tel: +8603546287093; E-mail: lifuzhong@sxau.edu.cn
Corresponding author: Li Fuzhong
DOI: https://doi.org/10.35633/inmateh-70-05

Keywords: *biomass, maize, visualization, NURBS surface, OpenGL*

ABSTRACT

Maize is one of the characteristic species in Shanxi Province. It has strong drought and cold tolerance. The study of maize growth and development law through the construction of the model is helpful to accurately understand the growth characteristics of maize, improve the yield, and further provide an important theoretical basis for the realization of precision agriculture. In this paper, "Xianyu 335" maize was taken as the research object. The data of leaf length, leaf width, stem length, stem number and tassel length, as well as leaf, stem, tassel, ear, cob and root organ morphology and biomass of maize during the whole growth period were obtained by field experiment. The maize geometric form structure module was constructed. The dynamic simulation of maize growing process was realized by object-oriented programming in Visual Studio software platform. With the help of 3D OpenGL graphic library Nurbs (Non-Uniform Rational B-Splines) curve and surface simulation technology, the growth visualization of maize organs was realized based on the idea of curve and surface control point selection parameter modeling.

摘要

玉米是山西特色物种之一，具有很强的耐旱性与耐寒性等特点。通过构建模型对玉米生长发育规律研究有助于精准了解玉米生长特性，提高产量，进一步为实现精准农业提供重要的理论依据。本文以“先玉 335”玉米为研究对象，采用田间试验获取玉米全生育期叶片数、叶长、叶宽、节间长、节间数、果穗长，以及叶片、节间、果穗、根器官形态与生物量试验数据，构建玉米几何形态结构模块。采用面向对象的程序设计，在 Visual Studio 软件平台实现玉米生长过程动态模拟。基于曲线曲面控制点选取参数建模思想，借助 3D OpenGL 图形库 Nurbs（非均匀有理 B 样条曲线，Non-Uniform Rational B-Splines）曲线曲面模拟技术，实现玉米各器官生长的可视化。

INTRODUCTION

Global climate changes have threatened the agricultural production in yield stability and increased productivity, along with the increasing population of the world, and have caused great challenges to food security (*Henry E.J. and Eviatar H., 2014*). The widely accepted strategy is to produce more agricultural products on the original arable land, that is, to improve agricultural productivity (*Foley et al., 2011*). The increases in agricultural productivity depend largely on the optimized agronomic management measures and the use of superior varieties of crops (*Henry E.J. and Eviatar H., 2014*). Studies have shown that global climate change will have a significant impact on biodiversity in the 21st century, which, to some extent, also foresees greater uncertainty and difficulties in cultivation of crop varieties with high and stable yields (*Dawson et al., 2011*). So, new technical means are needed to overcome this major challenge in agricultural production systems. In a number of technical solutions, the FSPMs (*Functional-Structural Plant Model*) are a potential to solve or partially solve these problems (*Yan, et al., 2004; Henke et al., 2016; Evers and Bastiaans, 2016*).

[1] *Lili SUN, Ph.D. Eng.; Yuzhi WANG, M.S. Stud. Eng.; Yaoyu LI, M.S. Stud. Eng.; Xiaoying ZHANG, Prof. Ph.D. Eng.; Wuping ZHANG, Prof. Ph.D. Eng.; Fuzhong LI, Prof. Ph.D. Eng..*

The research of crop visualization is helpful to improve the digitalization and visualization level of agricultural growth system expression and lay a foundation for the development of virtual agriculture (*Liu et al., 2009; Yang et al., 2017; Li et al., 2022*) Maize production and planting is of great significance to the development of organic dry farming. The dynamic growth mechanism of maize was studied, the growth process of maize was quantified and digitized, and the relationship model was established (*Guo et al.,2007; Chen et al., 2009; Liu et al.,2021*). It is helpful to optimize decisions, to make predictions through phenotypes, and to overcome the influence of traditional agronomic experiments on weather.

MATERIALS AND METHODS

Experimental design

The maize variety used in the experiment was Xianyu 335, which showed outstanding lodging resistance and drought resistance. The growth period was 98 days, the plant height was 286 cm, the tassel height was 103 cm, and the number of leaves was about 19.

The experimental area is located in Mengjiazhuang (112°30'E, 37°26'N) in Taigu District. The average annual precipitation in Taigu District is 397.1 mm, the average annual sunshine duration is 2527.5 hours, and the frost-free period is 179 days. The soil texture is clay, organic matter is 14.11 g/kg, total nitrogen is 1.19 g/kg, available nitrogen, phosphorus and potassium are 50.49, 33.63 and 206.41 mg/kg, respectively, pH is about 8, field water capacity is 18.5%.

Data Collection

Destructive sampling was carried out after jointing, and 6 maize plants were randomly selected as test subjects every week. Leaf length, leaf width, leaf area, stem volume, tassel length and root number were obtained, and the dry matter mass (biomass) was weighed in the oven.

Model Construction

In the absence of tillering, the upper part of the maize field contains only independent main stems. There are internode, node, node distribution of maize leaves, in the composition structure of the stem. In the later stage of growth, there are female spikes on part of the stem and male spikes on the top of the stem. This paper discusses how to simulate and analyse maize morphology from the biomass of stem, leaf and leaf sheath.

Leaf is one of the key organs of maize photosynthesis, and leaf morphology is closely related to canopy light interception efficiency.

At the Growth Cycle (GC) i, the area $S_b(i,j)$ of the meta-leaf of section j can be obtained according to its cumulative biomass:

$$S_b(i,j) = \frac{q_b(i,j)}{\varepsilon_b} [\text{cm}^2] \tag{1}$$

where, $q_b(i,j)$ is the cumulative biomass of the leaves at the stem j at the GCi, and ε_b is the specific leaf weight. The relationship between leaf length l_b and cumulative biomass can be expressed by the following formula:

$$l_b(i,j) = k_b \cdot q_b(i,j)^{\gamma} [\text{cm}] \tag{2}$$

In the above formula, $k_b$and γ describe the fitting coefficients.

The calculation of blade area is mainly related to length, width and fitting coefficient λ. After the simulation of blade area and length, the expression of blade width can be obtained as follows:

$$w_b(i,j) = \frac{s_b(i,j)}{\lambda \cdot l_b(i,j)} [\text{cm}] \tag{3}$$

where W_b is the width of the leaves, λ is the fitting coefficient.

The position of internode is directly related to the elongation pattern. The position factor should be considered when describing the internode morphology. Internode can be regarded as a similar cylinder, then the stem volume v_e of the stem j at the GC i can be expressed as follows:

$$v_e(i,j) = \frac{q_e(i,j)}{\rho_e(i,j)} = l_e(i,j) \cdot s_e(i,j) [\text{cm}^3] \tag{4}$$

where:

$q_e(i,j)$ describes the cumulative biomass between stems, and $\rho_e(i,j)$ describes the density between stems. $l_e(i,j)$ describes the length of the internodes and $s_e(i,j)$ describes the cross-sectional area of the stems.

The relationship between the two can be expressed as:

$$l_e(i,j) = k_e \cdot s_e(i,j)^{\alpha}[\text{cm}] \tag{5}$$

In the above formula, k_e and α describe the empirical coefficients, and the coefficients k_e and α between stems have obvious differences. The calculation and simulation of internode morphology are mainly related to coefficients β and b_e, as shown below:

$$\begin{cases} \beta = \dfrac{\alpha - 1}{\alpha + 1} \\ b_e = k_e^{1-\beta} \end{cases} \tag{6}$$

Then the length and cross-sectional area between the stem j at the GC i can be calculated:

$$\begin{cases} l_e(i,j) = \sqrt{b_e} \cdot \left(\dfrac{q_e(i,j)}{p_e(i,j)}\right)^{\frac{1+\beta}{2}} [\text{cm}] \\ s_e(i,j) = \sqrt{\dfrac{1}{b_e}} \cdot \left(\dfrac{q_e(i,j)}{p_e(i,j)}\right)^{\frac{1-\beta}{2}} [\text{cm}^2] \end{cases} \tag{7}$$

Since the shape of maize leaves is different, this paper uses Nurbs surface to simulate maize leaves. Nurbs refers to the uniform rational B-spline curve drawing technique, which is a widely used 3D surface model in related fields. It can accurately describe the bending degree of the surface of the target and show the vivid object modeling. In terms of Nurbs theoretical model, it is simple to operate, has high computational efficiency, and can ensure good computational accuracy, which is of great value for the interpretation and presentation of the geometric meaning of objects. This leads to the formula:

$$p(v) = \frac{\sum_{i=0}^{n} \omega_i N_{i,k}(v)\, p(i)}{\sum_{i=0}^{n} \omega_i N_{i,k}(v)} \tag{8}$$

In the above formula: $p(v)$ is different control points, $p_i, i = 0,1 \cdots n$; $\omega_i$is the weight of different control points;

$N_{i,k}$ describe B-spline basis functions generated in different directions.

During the first cycle of maize growth, a growth unit is produced, which is considered to be an approximate cylinder. The geometric dimensions of the organs, such as the radius of the low and top surfaces, and the length of the organs, were obtained according to the allometric growth law. In this study, formula (9) can be used to obtain the spatial coordinate information of the top surface. Assuming that the position and direction of the underside remain fixed, the biomass obtained by plant organs will increase significantly, which can be demonstrated by the dynamic change of growth. The dynamic changes of maize plants include geometric shape and size, which can be reflected by the changes in the radius of the bottom and top surface, as well as the dynamic changes in length extension. The gluCylinder () function in OpenGL can be used to realize visual processing and simulation analysis.

$$\begin{aligned} x_2 &= x_1 + L \cdot \cos\alpha \\ y_2 &= y_1 + L \cdot \cos\beta \\ z_2 &= z_1 + L \cdot \cos\gamma \end{aligned} \tag{9}$$

where: (x_1, y_1, z_1) are the initial position coordinates; (x_2, y_2, z_2) is the end position coordinate at the end; L is the length of growth and development; $(\cos\alpha, \cos\beta, \cos\gamma)$ refers to the cosine of the function in different directions.

RESULTS AND ANALYSIS

Results of geometric model

The relationship between leaf length, leaf width, leaf area and biomass of maize was obtained through measured data. The power exponential equations were obtained as $l_b = 0.0494e^{0.0504}q_b$, $w_b = 0.1058e^{0.357} \cdot q_b$ and $s_b = 0.0018{q_b}^{1.1435}$. The determination coefficients of the equations were 0.87, 0.79 and 0.91, respectively. Stem volume was linearly correlated with internode biomass, whose equation was $v_e = 0.0018{q_b}^{1.1435}$ and coefficient of determination R^2 was 0.86. There was a power exponential relationship between root number and root biomass.

The equation was $y = 0.0005x^{2.6652}$, and the coefficient of determination R^2 was 0.72. The difference was significant (P<0.01), and the fitting effect was good. Figs. 1 to 5 show the fitting effect.

The morphological structure of maize organs in each period was simulated according to the geometric morphological model, and the simulation results were in good agreement with the experimental results.

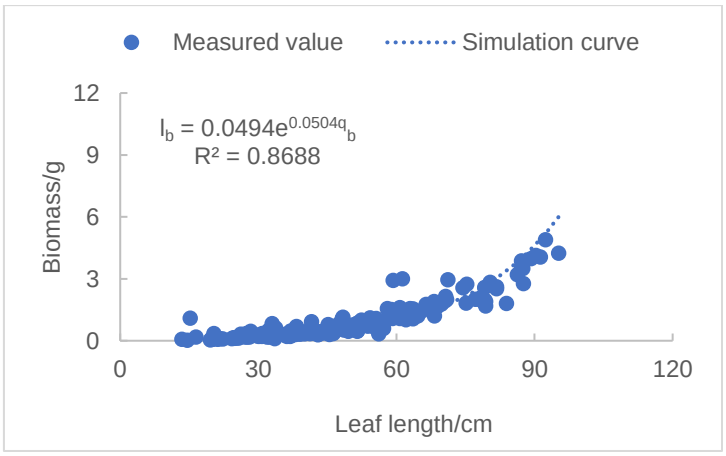

Fig. 1 – Relationship between maize leaf length and biomass

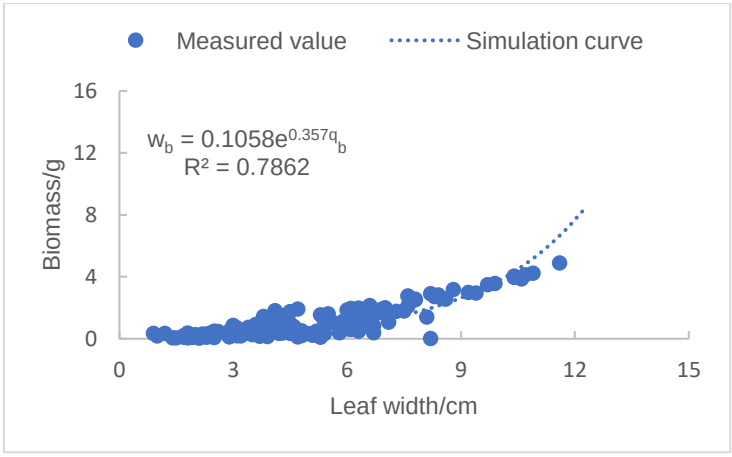

Fig. 2 – Relationship between maize leaf width and biomass

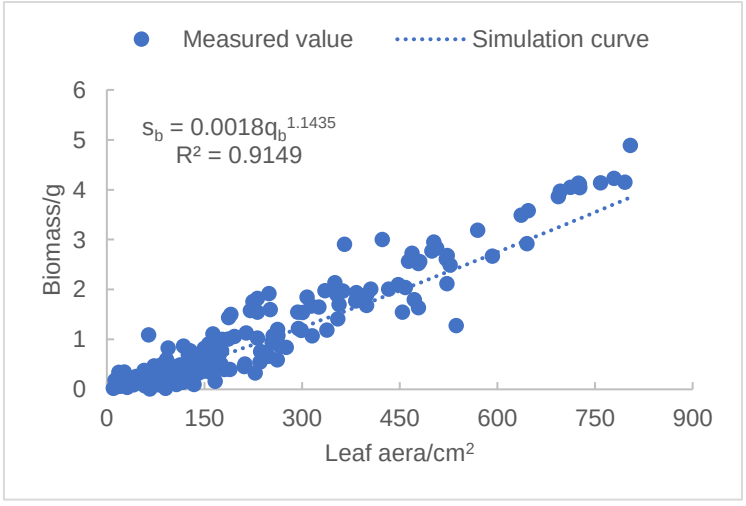

Fig. 3 – Relationship between maize leaf area and biomass

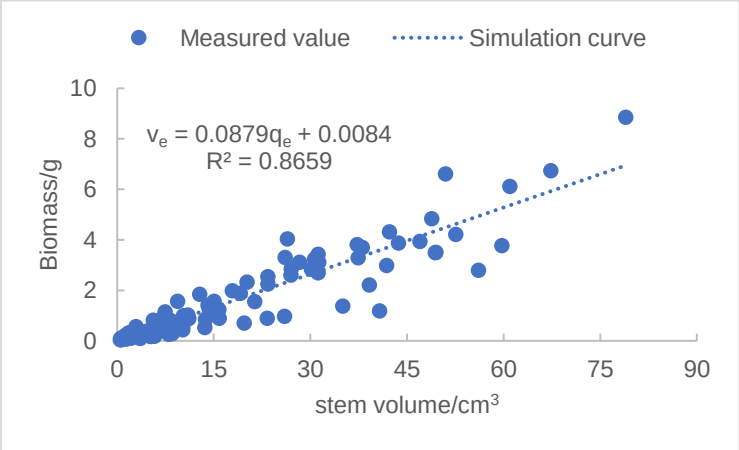

Fig. 4 – Relationship between stem volume and biomass

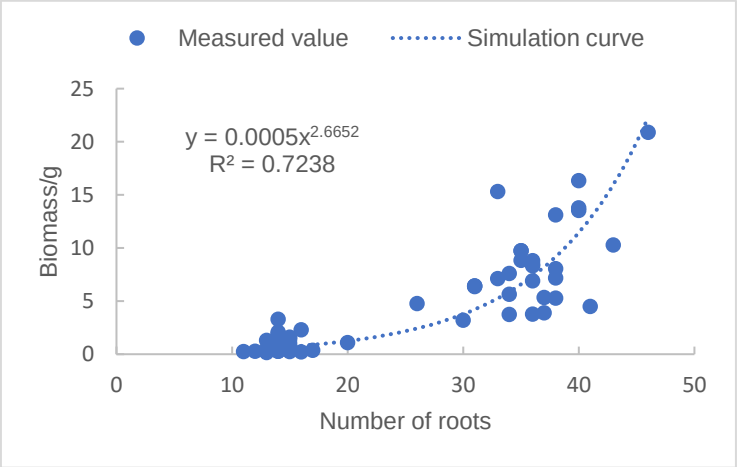

Fig. 5 – The relationship between the number of roots and biomass

Visualization of leaf

Based on the maize morphological data collected in the field experiment and combined with the maize geometric morphological growth simulation model, the maize morphological characteristic parameters were obtained. The surface mesh model of maize leaves was constructed by NURBS surface, and 3D visualization of leaf growth process under different periods was realized based on OpenGL graphic library. The results are shown in Fig. 6.

Fig. 6 – Visualization of maize leaf

Stem visualization

Maize nodes have various forms of internode, and a single internode can be described by columns of different spatial forms. The gluCylinder() library function in OpenGL is used to accurately describe the internode structure morphology and geometric characteristics of maize. The parameters involved include the following: GLU quadric Obj *qobj, which refers to the cylinder drawn by the graphics library; GL double base Radius, which refers to the base radius of the cylinder drawn by the graphics library; GL double top Radius, which refers to the radius of the top surface of a cylinder drawn by the graphics library; Glint stacks refer to the weft lines drawn by the graphics library that surround the Z-axis; GLdouble height, which is the height of the cylinder drawn by the graphics library. After obtaining the simulated values of the bottom surface, top surface and length of internode, a complete maize stem structure can be formed, and the results are shown in Fig.7.

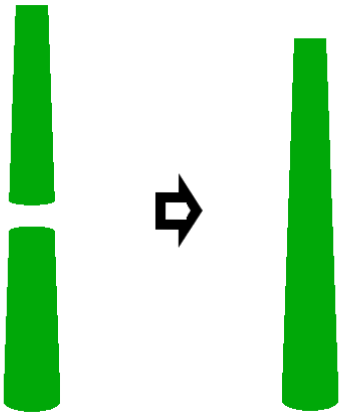

Fig. 7 – Visualization of Maize Stem Nodes

Visualization of ear

The approximate conical shape of the ear can be simulated by a table with different upper and lower surface areas. The experiment is based on the gluSphere() function in the OpenGL graphics library to draw the ear of maize, which mainly includes the following parameters: GLdouble radius, which refers to the radius of the sphere; GLUquadricObj *qob, refers to an instance of an object; Glint stacks refer to the warp lines that surround the Z axis; GLint slices, those are the weft slices that surround the Z axis. After the parameters of gluSphere() function are given, the dynamic simulation of ears in different periods can be realized (Fig. 8).

Fig. 8 – Visualization of Maize Ear

Tassel visualization

Maize tassels are mainly composed of spines, branches and spikelets. The topological structure (number and spatial position of branches) and morphological structure of maize tassels can be programmed to realize visualization. Let the tassel main axis be vertical and overlap with the Z-axis of the coordinate system. The topological parameters of tassel are as follows: length of tassel gh, number of branches i, Angle between branches and main axis θ, and azimuth of branches ϕ.

The tassel morphological structure is composed of two cylinders. The experiment is based on OpenGL graphic library to improve the function required to draw the cylinder, which mainly includes the following parameters: gluCylinder() represents the spatial position and shape size of the cylinder; GLint stacks refer to the warp lines that surround the Z axis; GLint slices, those are the weft slices that surround the Z axis. After the parameters of the gluCylinder() function are given, the dynamic simulation of maize tassels can be realized.

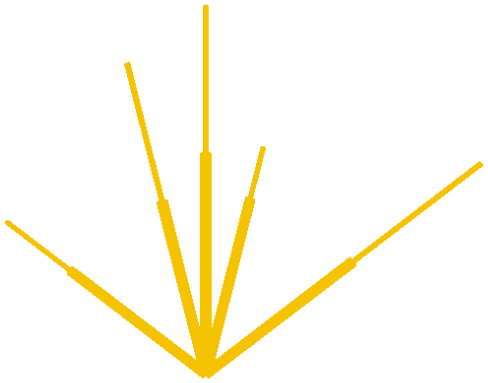

Fig. 9 – Visualization of Maize tassel

Visualization of roots

The visualization of the whole root system can be realized through the visualization of each root element. During each cycle of root growth, all root element individuals are traversed, and each individual is treated as follows. Call the spatial position data of the root element, namely the beginning point and end point of the root element, to carry out spatial translation and rotation. Draw the root by calling the top bottom diameter and the bottom diameter of the root. Realize the visual display of root system in 3D space.

output - txt

File(F) Edit(E) Format(O) View(V) Help(H)

GC	PA	GA	X1	X2	Y1	Y2	Z1	Z2	B0	B1
0	1	0	0.000	0.000	0.000	0.000	-2.000	-2.000	0.00000000	0.00000000
1	6	0	0.000	0.263	0.000	0.313	-2.000	-6.444	0.00076949	0.00076949
5	11	0	0.253	0.497	0.301	0.522	-6.273	-6.254	0.00001101	0.00001101
6	11	1	0.497	0.725	0.522	0.755	-6.254	-6.226	0.00001090	0.00001090
7	11	2	0.725	0.883	0.755	0.934	-6.226	-6.203	0.00000799	0.00000799
8	11	3	0.883	1.027	0.934	1.125	-6.203	-6.190	0.00000797	0.00000797
9	11	4	1.027	1.174	1.125	1.306	-6.190	-6.140	0.00000794	0.00000794

Ln 1, Col 68

Fig. 10 – Data structure for storing the data of BRSU

In the root data, each row represents a root metadata, including the physiological age of the root element, the growth age (the number of root growth cycles minus the number of root generation cycles), the coordinates of the two end points of the root element, the biomass obtained by the axial expansion of the root element, and the accumulative sum of the biomass obtained by the radial expansion of the root element. Call OpenGL graphics library to realize the visualization of root three-dimensional space, as shown in Fig. 11.

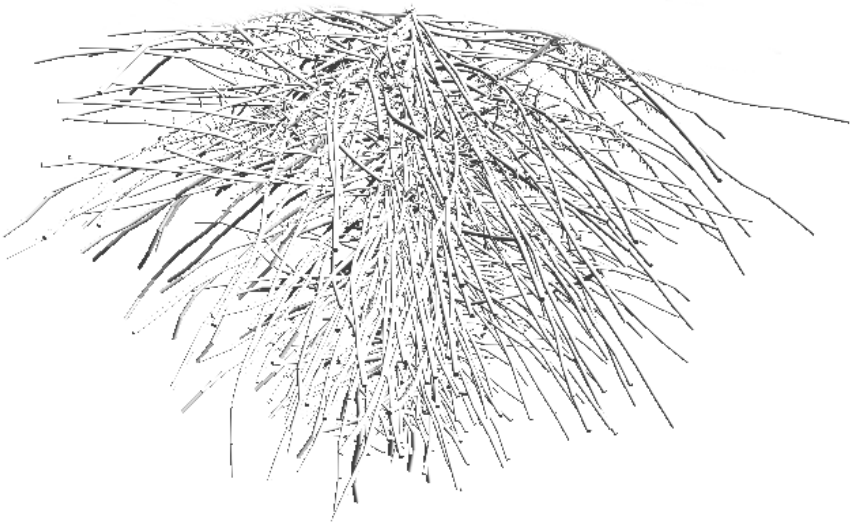

Fig. 11 – Visual simulation to the root of maize based on OpenGL

Visualization processing and simulation analysis of maize growth process

In this experiment, various parameters during the growth and development of maize plants were simulated and analysed, including the number, type and morphological characteristics of organs. After entering the second cycle, the growth and development of two organs of the plant, namely the growth and development of the top and collateral organs, showed specific changes in Fig. 12. Firstly, the corresponding geometric size was simulated according to the degree of organ biomass acquisition. Secondly, the specific spatial location information is determined according to the dynamic linked list. Finally, the visualization and simulation analysis of each vector are carried out by using computer graphics library.

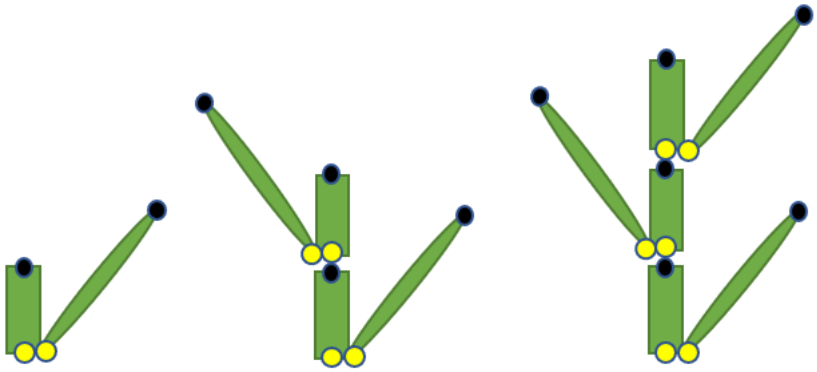

Fig. 12 – Visual processing and simulation diagram of spatial geometric structure changes of various organs during maize plant growth and development

Note: The white circle represents the starting point of growth, while the black circle represents the ending point of growth

Windows, Visual C++ and other tools were used to complete the visual processing and simulation analysis of maize growth. See Figure 13 for details.

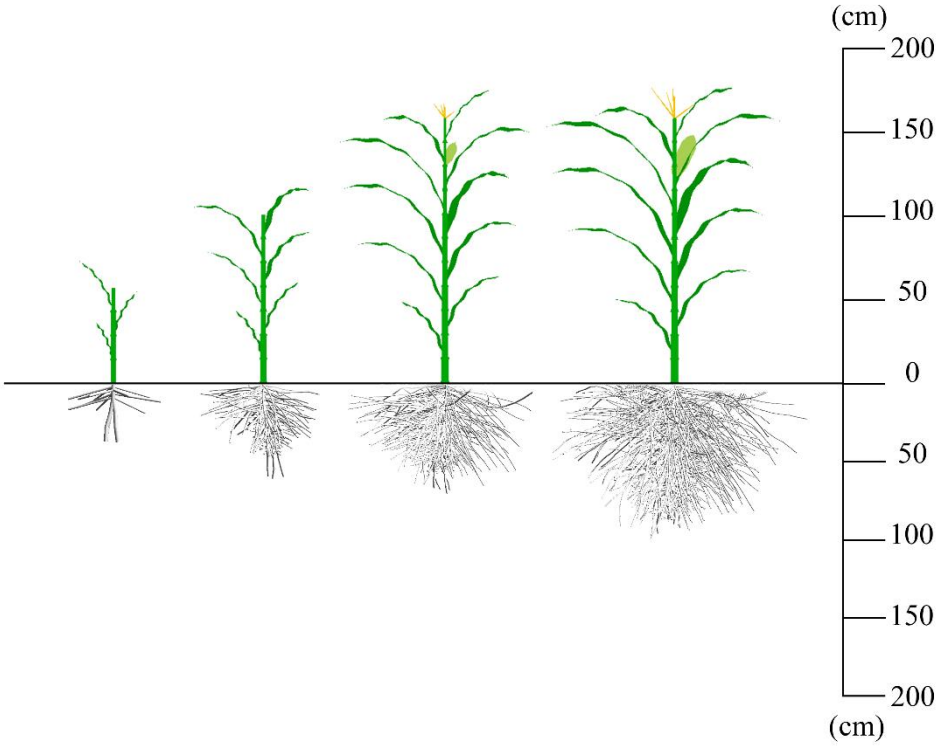

Fig. 13 – Visualization of the growth and development process of maize at different growth times (8, 12, 16, 20 GC)

CONCLUSIONS

In this paper, geometric parameters such as leaf length, leaf width, node length and node diameter of maize were simulated based on the structural function model and the 2019 field experiment data. This model simulated the morphological changes of maize organs during the growth process, and realized the visualization of maize leaves, stems and tassel by using NURBS surface and OpenGL.

ACKNOWLEDGEMENT

The authors were funded for this project by the Major research and development Projects of Shanxi Province, China (2022ZDYF127), and the Basic Research Project of Shanxi Province (202103021224123).

REFERENCES

[1] Chen Guo-qing, Zhang Ji-wang, Dong Shu-ting. (2009). Visualization-Based Growth Simulation System for Super-Maize (基于可视化的超级玉米生长模拟系统). *Scientia Agricultura Sinica*, Vol. 42, pp. 3361-3367, Shandong/China.

[2] Dawson T P, Jackson S T, House J I, et al. (2011). Beyond predictions: biodiversity conservation in a changing climate. *Science,* Vol. 332, pp. 53-58, UK.

[3] Evers J B, Bastiaans L. (2016). Quantifying the effect of crop spatial arrangement on weed suppression using functional-structural plant modelling. *Journal of plant research*, Vol.129, pp. 339-351, Netherlands.

[4] Foley J A, Ramankutty N, Brauman K. A, et al. (2011). Solutions for a cultivated planet. *Nature*, Vol. 478, pp. 337-342, USA.

[5] Guo Xinyu, Zhao Chunjiang, Xiao Boxiang, et al. (2007). Design and implementation of three-dimensional geometric morphological modeling and visualization system for maize（玉米三维重构及可视化系统的设计与实现). *Transactions of the CSAE*, Vol. 23, pp. 144-148, Beijing/China.

[6] Henke M, Kurth W, Buck-Sorlin G H. (2016). FSPM-P: towards a general functional-structural plant model for robust and comprehensive model development. *Frontiers of Computer Science*, Vol.10, pp. 1103-1117, Germany.

[7] Henry R J, Nevo E. (2014). Exploring natural selection to guide breeding for agriculture. *Plant biotechnology journal*, Vol. 12, pp. 655-662, Australia.

[8] Li Dong, Gao Hexuan, He Yuying, et al. (2022). Research on the Visualization Model of Astragalus Growth Based on Open GL. *Tropical agricultural engineering*, Vol. 46, pp. 48-51, Gansu/China.

[9] Liu Hui, Tang Liang, Zhang Wenyu, et al. (2009) Construction and implementation of model-based visual rice growth system. *Transactions of the CSAE*, Vol. 25, pp. 148-154, Jiangsu/China.

[10] LIU Qing, LIU Yang, HU Yang, et al. (2021) Visual Method for Rapid Screening of Transgenic Maize (一种可视化快速筛选转基因玉米的方法研究). *Journal of Maize Sciences*, Vol. 29, pp. 50-59, Jilin/China.

[11] YAN H P, Kang M Z, De Reffye P, et al. (2004). A dynamic, architectural plant model simulating resource‐dependent growth. *Annals of Botany,* Vol. 93, pp. 591-602, China.

[12] Yang Le. (2017). Modeling and Visualization of Rice Root Based on L－System (基于 L 系统的水稻根系模型构建及可视化研究). *Bulletin of science and technology*, Vol. 33, pp. 156-158, Jiangxi/China.

TECHNICAL AND ENVIRONMENTAL EVALUATION OF USING RICE HUSKS AND SOLAR ENERGY ON THE ACTIVATION OF ABSORPTION CHILLERS IN THE CARIBBEAN REGION. CASE STUDY: BARRANQUILLA

/

EVALUACIÓN TÉCNICA Y AMBIENTAL DEL USO DE CÁSCARA DE ARROZ Y ENERGÍA SOLAR EN LA ACTIVACIÓN DE REFRIGERADORES DE ABSORCIÓN EN LA REGIÓN CARIBE. CASO DE ESTUDIO: BARRANQUILLA

Andrés Rodríguez Toscano*[1)], Rafael Ramirez[2)], José M. Sánchez[2)]
[1)]Universidad de la Costa, Energy Department, Cl. 58 #55-66, 080002 Barranquilla, Colombia/ Colombia;
[2)]Universidad del Atlántico, Efficient Energy Management Research Group-Kai, Carrera 30 Número 8-49, 081007 Puerto Colombia/ Colombia.
Tel: +573004162429; E-mail: arodrigu83@cuc.edu.co
DOI: https://doi.org/10.35633/inmateh-70-06

Keywords: *Absorption refrigeration system, solar energy, biogas, biomass, solar cooling, rice husk.*

ABSTRACT

This research presents a thermodynamic analysis of a Thermal LTC-10 single-effect absorption series cooling system using the water/LiBr pair. Four operating scenarios were modeled on an hourly basis (24h) with EES software using mass and energy balances and the environmental conditions of the city of Barranquilla, Colombia. The analysis of the results shows that the system powered only by solar energy obtains the highest COP between 8:00 and 16:00 hours and the lowest greenhouse gas (GHG) emissions, while the system powered by rice husk biogas presents stable operation throughout the day and higher SO_2eq emissions.

RESUMEN

En esta investigación se presenta un análisis termodinámico de un sistema de refrigeración en serie por absorción de simple efecto Thermal LTC-10 utilizando el par agua/LiBr. Cuatro escenarios de operación fueron modelados en una base horaria (24h) con el software EES utilizando balances de masa y energía y las condiciones ambientales de la ciudad de Barranquilla, Colombia. El análisis de los resultados demuestra que el sistema alimentado únicamente por energía solar obtiene el mayor COP entre las 8:00 y las 16:00 horas y las menores emisiones de gases de efecto invernadero (GEI), mientras que el sistema alimentado con biogás de cáscara de arroz presenta un funcionamiento estable durante todo el día y mayores emisiones de SO_2eq.

INTRODUCTION

Despite the efforts to reduce the energy consumption and greenhouse gas emissions, these continue to increase (*IEA, 2019; Li et al., 2022; Saint Kadir et al., 2020*). Therefore, it is very interesting for researchers to analyze the possibility of replacing traditional sources with renewable energy sources (*Ghafoor & Munir, 2015; IEA, 2019; A. R. Toscano et al., 2020*). HVAC systems account for about 40% of the electrical energy consumed in buildings globally (*Aune et al., 2016; Pérez-Lombard et al., 2008; Rodríguez-Toscano et al., 2022a)*. Therefore, these systems are often energy-intensive, especially in the operation of the compressor, which coupled with leaks, lack of maintenance and cleaning can lead to a significant increase in energy consumption (*Adel et al., 2016; Juaidi et al., 2016; Rodríguez-Toscano et al., 2022a*).

In the specialized literature, the solar energy equipment to activate cooling systems has been reported (*Allouhi et al., 2015; Asadi et al., 2018*). Other studies have used these technologies with absorption refrigeration systems to reduce the use of electricity and take advantage of residual thermal energy in the industrial sector (*Asadi et al., 2018; Bellos & Tzivanidis, 2017; United States Department of Energy, 2016*). Further research has demonstrated the feasibility of solar-powered absorption cooling systems in shopping malls by means of different working fluids to improve the heat transfer and COP with computational sources, experiments, and tests in commercial facilities (*Alhamid et al., 2020; Amaris, 2013; Rodríguez-Toscano et al., 2022a; Zapata et al., 2021*). However, there is scarce information available on absorption refrigeration systems installed on the market that involves biomass as another energy source for their activation, along with the use of solar energy (*Ayou et al., 2013; Ghafoor & Munir, 2015; A. D. R. Toscano et al., 2021*).

Colombia has an energy potential from solar and biomass sources *(Sagastume Gutiérrez et al., 2020; UPME, 2015*). In this country, the energy produced with biomass for self-generation and cogeneration purposes is higher than solar and wind energy (*Federación Nacional de Biocombustibles de Colombia, 2018*).

Rice is the third most-produced human-consumable agricultural product in Colombia, with more than 2,463,689 tons/year (*UPME, 2016a*). From this, residual biomass called rice husk is obtained, which has an energy potential of approximately 7,136.53 TJ/year (*UPME, 2016a*). On the other hand, the Colombian Caribbean coast has a high solar energy potential with average solar irradiation of approximately 5 kW-h/m^2, with high relative humidity and average ambient temperatures of up to 35ºC (*Castro, 2010; EPM, 2020; Rodríguez-Toscano et al., 2022b; UPME, 2015; Weather Underground, 2020*). This involves using cooling systems for air conditioning and industrial sector needs. Nevertheless, the potential of this biomass has not been studied in conjunction with solar energy in absorption cooling systems, which generates uncertainty about the use of this energy source in terms of operation, air pollution, and system performance in companies or industries that have these agricultural residues and are located on the Colombian Caribbean coast.

MATERIALS AND METHODS

This section describes the environmental characteristics of the city of Barranquilla, the thermodynamic model, and the economic model of the absorption cooling system using biomass (rice husk) and the solar energy as activation source considering water/LiBr as the working pair in the simulation of the absorption refrigeration system.

ENVIRONMENTAL VARIABLES IN BARRANQUILLA

The city of Barranquilla is characterized by maintaining a high solar potential on the Colombian Caribbean coast. Its ambient temperature is between 24ºC and 35ºC (*Castro, 2010; EPM, 2020; Rodríguez-Toscano et al., 2022b; Weather Underground, 2020*). Figure 1 shows the behavior of the average solar irradiance for a day (24 h) in the months of February and October. Where it is noticeable that February is the month of highest solar irradiance and October the month of lowest solar irradiance. Also, the irradiation peaks occur between 9:00 and 15:00 hours. In this sense, the requirements for activating the solar absorption regeneration system during peak hours will be considered from the month with the lowest solar irradiation.

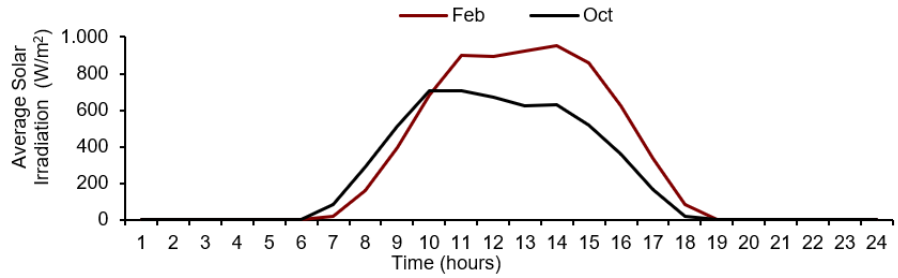

Fig. 1 - Average hourly solar irradiation per month (*IDEAM, 2020*)

RICE HUSK CHARACTERISTICS

Rice husk is a biomass or plant tissue consisting of cellulose, silica, among other elements that allows its use as fuel. This biomass has a great potential for energy in Colombia, due to its large production in the country and in its Caribbean coast (*Jaider et al., 2009*). Table 1 shows the most important characteristics for the technical and environmental analysis of this research.

Table 1

Rice husk characteristics (*Sánchez Lario, 2017; UPME, 2016b*)

% Humidity	$LHV_{biomass}$ (kJ/kg)	LHV_{biogas} (kJ/Nm^3)	Volume biogas per kg of biomass (Nm^3/kg biomass)	Emission factor $C_{em\ biogass}$ (Kg CO_2/kJ)	Emission factor $C_{em SO_2}$ (Kg SO_2/kJ)
10	14090	5330	0.92	0.103	0.000000153

ABSORPTION CHILLER CONFIGURATION

Figure 2 shows the simplified configuration scheme of the single-effect absorption refrigeration system based on the Thermal LTC-10 series, which has a nominal cooling capacity of 352 kW and uses the water/LiBr mixture as the working fluid (*Absorsistem, 2014*). Where this water/LiBr solution is driven by the pump to the desorber. The thermal energy is supplied to the desorber from an external circuit which includes solar thermal collectors and a gasifier.

In stream 7, superheated water vapor exits the desorber and, in stream 4, a lean water/LiBr solution leaves the desorber. Then, in the condenser, the water vapor is cooled by the water corresponding to stream 16. After the water exits the condenser, the fluid passes through the valve and its temperature decreases due to the expansion that occurs. Finally, the water enters the evaporator to cool stream 18, which is water that will extract heat from the conditioned space.

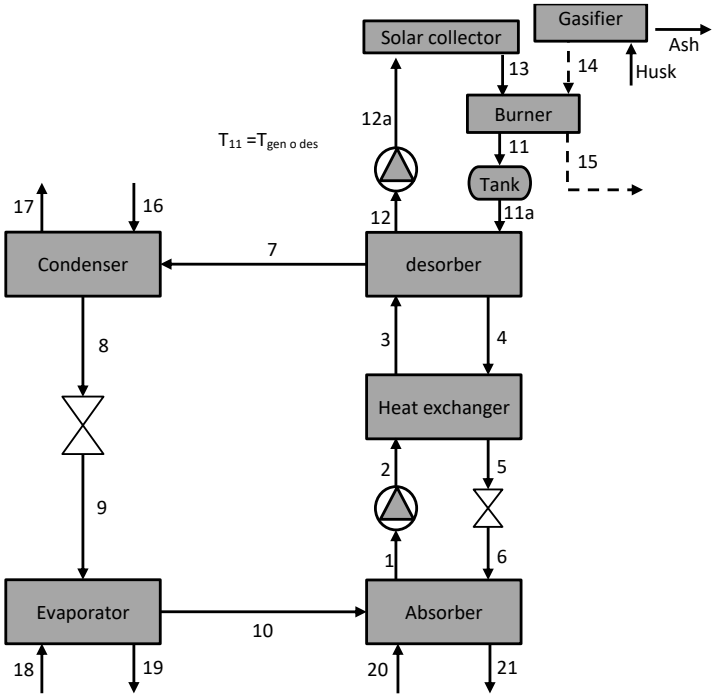

Fig. 2 - Absorption refrigeration system, solar collectors, and gasifier

The scenarios of the absorption refrigeration system are:

1. Solar-powered: The cooling system is solar-powered using Evacuated Tube Thermal Collectors.
2. Activated with rice husk biogas: The absorption refrigeration system is activated only with the biogas produced by rice husk gasification.
3. Activated with solar energy and biogas from rice husk: The absorption cooling system is activated with solar energy using the ETC collectors and the burning of biogas from the gasification of rice husk.
4. Conventional electricity-activated cooling system: This scenario is only evaluated to determine the emissions of greenhouse gases (CO_2 eq) and the equivalent amount of sulfur dioxide due to electrical energy consumed by a conventional system. This to compare the environmental effects of the previous scenarios with the conventional system.

THERMODYNAMIC MODEL

The thermodynamic system was analyzed with EES software. The properties of the working fluid were taken from the previous work of Pátek & Klomfar (*Pátek & Klomfar, 2006*) and provided to the EES software. The considerations of the thermodynamic evaluation are:

1. The temperature of the water at the evaporator inlet (stream 18) is 12 ºC.
2. The temperature of the water at the condenser inlet (stream 16) is 29.4 ºC (*Absorsistem, 2014*).
3. The temperature of the water at the absorber inlet (stream 20) is 29.4 ºC (*Absorsistem, 2014*).
4. The flow of water entering the condenser (50 m^3/h), absorber (50 m^3/h), desorber (74.9 m^3/h) and evaporator (55 m^3/h) is taken from the manufacturer's catalog, and the flows of water to the condenser and coming from the absorber have a parallel configuration (*Absorsistem, 2014*). The mass flow rate is calculated by multiplying the density of the water by the flow rate at the corresponding pressure and temperature.
5. For scenario 2 and 3, the water temperature at the outlet of the gas burner is 90ºC.
6. The water pressure entering the condenser and absorber is 105 kPa.
7. The pressure of the water entering the desorber is 500 kPa.
8. The pressure of the water entering the solar thermal collectors is 454.9 kPa.

9. The mass flow rate $\dot{m}_1$ is 1.681 kg/s.

10. The low system pressure is the saturation pressure of the water at T_{10} and the high system pressure is the saturation pressure of the water at T_8.

11. The refrigerant flow in the desorber (stream 7) is vapor and losses into the pipelines are negligible (*Rodríguez-Toscano et al., 2022b*).

12. The LHV_{biogas} is 14090 kJ/kg, the LHV_{biogas} is 5330 kJ/Nm^3 and the volume biogas is 0.92 Nm^3/kg biomass.

13. Thermal collector area (ETC) is 840.4 m^2.

14. The efficiency of the gasifier is 0.7 (*Sánchez Lario, 2017*).

15. The efficiency of the gas heater (η_{GN}) is 0.85 (*Gomri, 2013*).

16. The length of the heat reservoir is considered equal to its diameter (*Bellos et al., 2017*).

17. The efficiency of the solution pump is 0.6.

18. The effectiveness of the Evaporator is 0.815 (*Rodríguez-Toscano et al., 2022a*), the effectiveness of the condenser is 0.676 (*Rodríguez-Toscano et al., 2022a*), the effectiveness of the absorber is 0.5 *(Rodríguez-Toscano et al., 2022a*), the effectiveness of the desorber is 0.302 (*Rodríguez-Toscano et al., 2022a*) and the effectiveness of the exchanger is 0.64 (*Rodríguez-Toscano et al., 2022a*).

19. The thermal reservoir is adiabatic (*Rodríguez-Toscano et al., 2022a*).

20. Thermodynamic evaluation is performed between 7:00 and 20:00 hours.

21. The thermodynamic model has been previously validated by one of the present authors (*Rodríguez-Toscano et al., 2022a*). Table 2 provides the mass and energy balance equations of the absorption chiller.

Table 1

Mass and energy balances of the absorption chiller

Components	Mass Balance	Eq.	Ref.	Energy balance and	Eq.	Ref.
Solar thermal collector	$\dot{m}_{12a} = \dot{m}_{13}$	1	-	$\dot{Q}_s = A_c I_s$ A_c is the area of thermal solar collectors in m^2. I_s is the solar radiation in W/ m^2	17	(*Kalogirou, 2004*)
				$\eta_c = \frac{\dot{Q}_u}{\dot{Q}_s} = \frac{\dot{m}_{11} c_p (T_{12} - T_{13})}{A_c I_s}$	18	-
				$\eta_c = n_o - \frac{a_1 \Delta T_{avg}}{I_s} - \frac{a_2 (\Delta T_{avg})^2}{I_s}$ n_o=0.82 a_1=2.198 a_2=0	19	(*Asadi et al., 2018; Bellos et al., 2017; Rodríguez-Toscano et al., 2022b*)
Pump	$\dot{m}_1 = \dot{m}_2$	2	-	$\dot{W}_p = \eta_p \cdot \dot{W}_{p\,el}$ where η_p is the pump efficiency	20	-
				$\dot{W}_p = \dot{m}_1 \cdot \upsilon_1 \cdot (P_2 - P_1)$	21	-
Heat Exchanger	$\dot{m}_2 = \dot{m}_3$	3	-	$\dot{Q}_{shx} = \dot{m}_2 \cdot (h_3 - h_2)$	22	-
	$\dot{m}_4 = \dot{m}_5$	4	-	$\dot{Q}_{shx} = \dot{m}_4 \cdot (h_4 - h_5)$	23	-
				$\varepsilon = \frac{T_4 - T_5}{T_4 - T_2}$	24	-
Desorber	$\dot{m}_3 = \dot{m}_7 + \dot{m}_4$	5	-	$\dot{Q}_d = \dot{Q}_u + \dot{Q}_{GN}$	25	(*Gomri, 2013*)
	$\dot{m}_3 X_3 = \dot{m}_7 + \dot{m}_4 X_4$ where X is the concentration of LiBr in the solution.	6	-	$\dot{Q}_{GN} = \frac{\dot{m}_{GN} \cdot LHV_{biogas} \cdot \eta_{GN}}{\rho_{biogas\ per\ kg\ of\ biomass}}$	26	-
				$\dot{Q}_{GN} = \dot{m}_{11} \cdot C_p \cdot (T_{11a} - T_{13})$	27	-
				$\dot{Q}_d = \dot{m}_7 \cdot h_7 - \dot{m}_3 \cdot h_3 + \dot{m}_4 \cdot h_4$	28	-
				$\dot{Q}_d = \dot{m}_{11} \cdot C_p \cdot (T_{11a} - T_{12})$	29	-
				$\varepsilon = \frac{T_4 - T_3}{T_{11a} - T_3}$	30	-

Components	Mass Balance	Eq.	Ref.	Energy balance and	Eq.	Ref.
Absorber	$\dot{m}_{10} = \dot{m}_1 - \dot{m}_6$ $\dot{m}_6 X_6 + \dot{m}_{10} = \dot{m}_{10} X_{10}$. where X is the concentration of LiBr in the solution.	7	-	$\dot{Q}_a = \dot{m}_{10} \cdot h_{10} + \dot{m}_6 \cdot h_6 - \dot{m}_1 \cdot h_1$	31	-
				$\dot{Q}_a = \dot{m}_{20} \cdot C_p \cdot (T_{21}\text{-}T_{20})$	32	-
				$\varepsilon = \frac{T_6 - T_1}{T_6 - T_{20}}$	33	-
Condenser	$\dot{m}_7 = \dot{m}_8$	8	-	$\dot{Q}_{cond} = \dot{m}_7 \cdot h_7 - \dot{m}_8 \cdot h_8$	34	-
				$\dot{Q}_{cond} = \dot{m}_{16} \cdot C_p \cdot (T_{17} - T_{16})$	35	-
				$\varepsilon = \frac{T_7 - T_8}{T_7 - T_{16}}$	36	-
Evaporator	$\dot{m}_9 = \dot{m}_{10}$	9	-	$\dot{Q}_e = \dot{m}_{10} \cdot h_{10} - \dot{m}_9 \cdot h_9$	37	-
				$\dot{Q}_e = \dot{m}_{18} \cdot C_p \cdot (T_{18} - T_{19})$	38	-
				$\varepsilon = \frac{T_{18} - T_{19}}{T_{18} - T_{19}}$	39	-
Valve 1	$\dot{m}_8 = \dot{m}_9$	10	-	$h_8 = h_9$	40	-
Valve 2	$\dot{m}_5 = \dot{m}_6$	11	-	$h_5 = h_6$	41	-
The heat reservoir tank	$V_{tank} = \frac{A_c}{30}$	12	(Asadi et al., 2018)	-	42	(*Bellos & Tzivanidis, 2017*)
Gasifier	$\dot{m}_{GN} = \dot{m}_{14}$	13	-	$\eta_{gasifier} = \frac{\dot{Q}_{gasifier}}{\dot{Q}_{husk}}$ $\eta_{gasifier} = \frac{}{\rho_{biogas\ per\ kg\ of\ biomass}\ LHV_{biogas}}$	43	(*Sánchez Lario, 2017*)
	$\dot{m}_{ash} = 0.005 \frac{kg\ ash}{kg\ biom} \cdot \dot{m}_{husk}$	14	(Sánchez Lario, 2017)	$\dot{Q}_{gasifier} = \frac{\dot{m}_{GN}\ LHV_{biogas}}{\rho_{biogas\ per\ kg\ of\ biomass}}$	44	(*Sánchez Lario, 2017*)
				$\dot{Q}_{husk} = \dot{m}_{husk}\ LHV_{husk}$	45	(*Sánchez Lario, 2017*)
Absorption cooling system	-	15	-	$COP = \frac{\dot{Q}_{ev}}{\dot{Q}_d + \dot{W}_p}$ The COP is the coefficient of performance of the absorption	46	(*Rodríguez-Toscano et al., 2022a*)
Total system	-	16	-	$COP_{system} = \frac{\dot{Q}_{ev}}{\dot{Q}_s + \dot{Q}_{husk} + \dot{W}_{p\ el}}$	47	-

Eq. 48 defines the CO_2eq emissions, and the environmental effects associated to the use of biogas (scenario 3) (*Comisión del Cambio Climático, 2011; Rodríguez-Toscano et al., 2022b*).

$$CO_2\ eq = (\dot{m}_{GN} \cdot C_{em\ biogass} + \dot{W}_e \cdot C_{em\ el}) \cdot time_{use} \quad (48)$$

where: $C_{em\ el}$ is the emission factor of kg of CO_2 associated to the electricity consumption (kW-h) and it is equal to 0.181 kg CO_2 / kWh. The above equation also applies to scenario 2.

In this sense, Eq. 49 calculates the CO_2eq emissions associated to the energy consumption (scenario 4) (*Comisión del Cambio Climático, 2011; Rodríguez-Toscano et al., 2022b*).

$$CO_2eq = (\dot{Q}_e / (COP_{comp}) \cdot time_{use} \cdot C_{em\ el} \quad (49)$$

COP_{comp} is assumed as 3 *(Bellos & Tzivanidis, 2017; Rodríguez-Toscano et al., 2022a*).

Then, Eq. 50 determines the CO_2eq associated with the energy consumption (scenario 1) (*Comisión del Cambio Climático, 2011; Rodríguez-Toscano et al., 2022b*).

$$CO_2\ eq = \dot{W}_e \cdot time_{use} \cdot C_{em\ el} \quad (50)$$

Last but not least, Eq. 51 calculates the SO_2eq associated to the biogas burning (scenario 2 and 3).

$$SO_2\ eq = \dot{Q}_{gasifier} \cdot time_{use} \cdot C_{em SO_2} \quad (51)$$

RESULTS

Figure 3a shows the heat rate used to activate the desorber versus the solar energy potential and the biomass energy of the rice husk. In this figure, scenario 1 has the best ratio between 8:00 and 16:00 hours, since this is the period with the highest solar irradiation and the highest efficiency of the ETC's (0.66). Furthermore, the COP (see Figure 3b.) presents the highest value presented and hence the highest $\dot{Q}e$ of all scenarios. However, this system can only operate until 17:00 hours. Concerning scenario 2, the ratio (see Figure where X is the concentration of LiBr in the solution. 3a) and COP (see Figure 3b) remain constant throughout the operating hours. In general, if the area under the curve is considered, it is in this scenario where the energy potential during the entire operating time is used to the greatest extent. Scenario 3 exceeds the ratio of scenario 2 only between 9:00 and 12:00 hours and throughout the timetable it presents practically the same COP. With this behavior, the system in scenario 3 could improve the heat transfer in the absorber. The above would imply further increasing the biomass mass flow between 07:00 and 08:00 and between 16:00 and 20:00 hours.

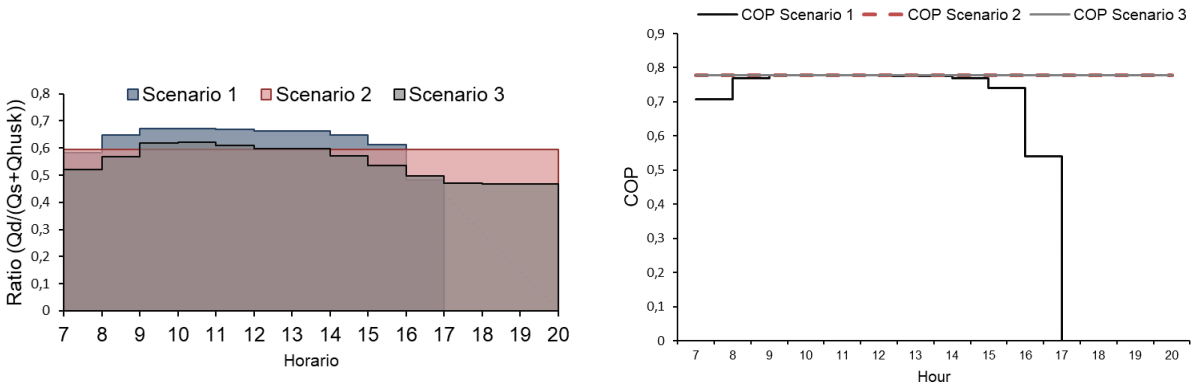

Fig. 3 - Heat rate and COP analysis of the thermodynamic system

a) Desorber rate in relation to the potential of energy sources.
b) COP of the absorption refrigeration system for the different scenarios

After maintaining the highest value, the COP_{system} develops a downward concavity curve as the system increases the amount of $\dot{Q}e$ relative to the amount of $\dot{Q}s$ at peak hours. It should be noted that the COP_{system} is changing continuously due to the indicator variation without a backup (note that $\dot{Q}_e$ has a lower value compared to other scenarios due to the quantity of solar collectors and solar energy at time). For scenario 3, the COP_{system} maintains the highest value during off-peak hours. Between 7:00 and 8:00 hours the COP_{system} is 0.4 and between 15:00 and 16:00 hours the COP_{system} is 1.36. Between 16:00 hours and 17:00 hours, the COP_{system} takes a value of 0.38. After 17:00 hours, this value is equal to 0.37. This behavior is expected because the decrease in the COP_{system} indicator is generated by the participation of rice husk biogas in the constant temperature combustion with the least amount of solar energy available at the same time. The above is supported by comparing the behavior of the scenario 3 with Figure 1. The COP_{system} curve is concaved upward as the amount of solar energy is higher at peak hours for $\dot{Q}_d$. The constant behavior of $\dot{Q}_e$ is because the gas burner works at a constant temperature (this is because the burner operates to maintain a constant temperature in the water at T11).

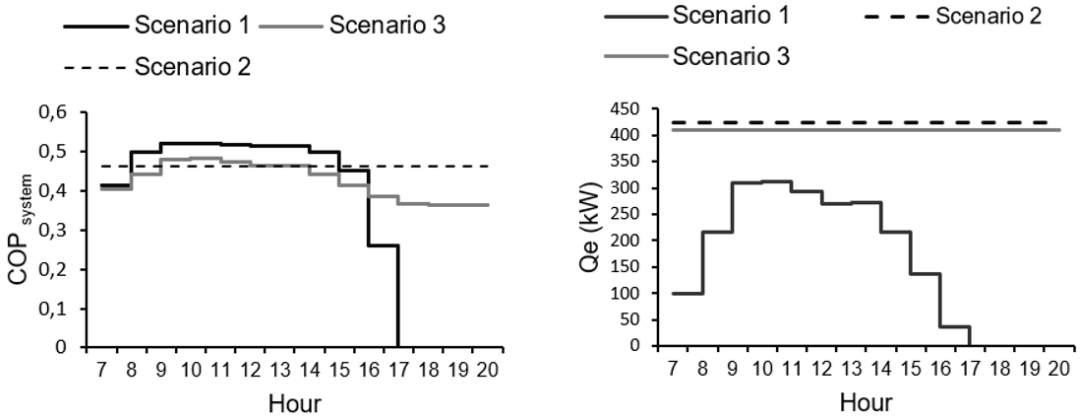

Fig. 4 - Analysis of the COP_{system} and $\dot{Q}_e$ for each scenario

a) COP_{system} of the total system for scenarios 1,2 and 3. b) $\dot{Q}_e$ of the absorption refrigeration system

Figure 5 shows the amount of biomass required to activate the rice husk absorption refrigeration system in the scenarios 2 and 3. In general, to activate the system at nominal capacity, 0.064 kg/s is required. For the scenario 2, the mass flow remains constant value of 0.064 kg/s. In the case of scenario 3, the amount of biomass mass flow decreases due to the significant solar energy input during the hours of sunshine (between 7:00 and 17:00 hours). This allows flexibility in the nominal range of the system using rice husk of up to 71.7%.

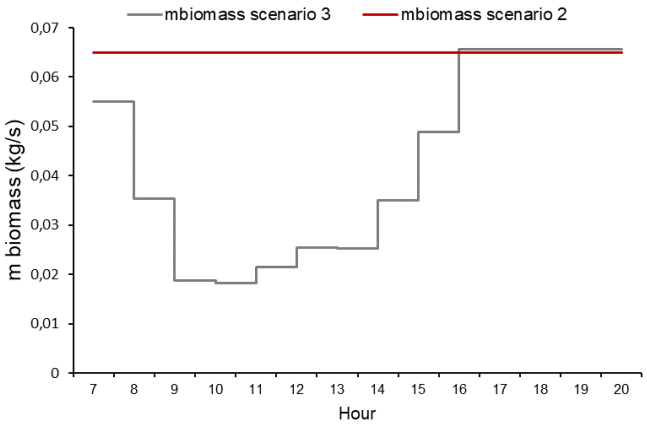

Fig. 5 - Mass flow of rice husk in scenario 2 and 3

GREENHOUSE GASES AND SULFUR DIOXIDE SO_2

Figure 6a shows the GHGs for each scenario. The scenario 4 was evaluated with respect to the other scenarios to propose an objective comparison of the results and determine the decrease of GHGs. The absorption refrigeration system that achieved the greatest reduction in relation to the conventional system was the first described in scenario 1 (99.98%), followed by the scenario 3 (99.6%) and the scenario 2 (99.53%). This behavior is explained using another energy source (rice husk) which causes GHGs in a low amount. Figure 6b shows the amount of sulfur dioxide produced for scenarios 1, 2 and 3. The results show that the System evaluated in scenario 1 does not generate sulfur dioxide. Although scenarios 2 and 3 generate the highest values of sulfur dioxide, these amounts are low and do not tend to significantly pollute the surrounding environment. In these cases, filters should be used according to humidity and particulate matter to avoid the formation of aerosols over time.

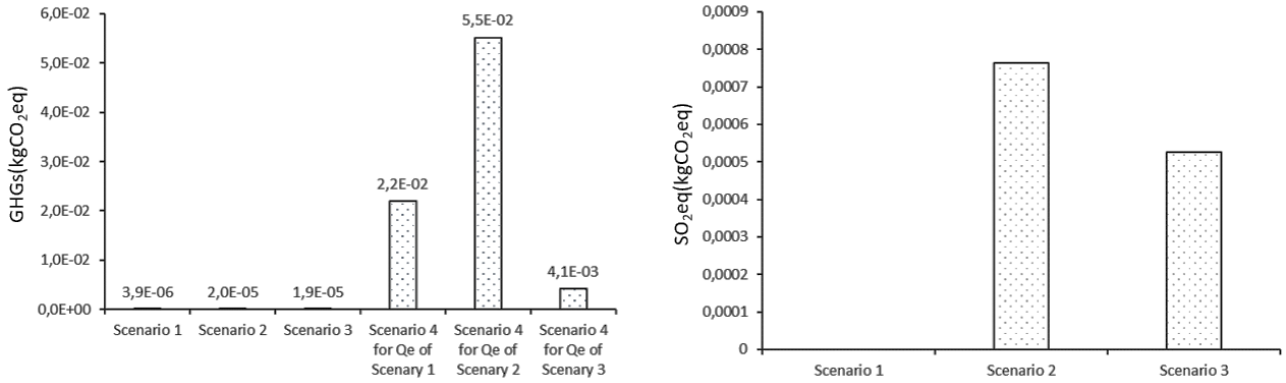

Fig. 6 - Analysis of greenhouse gases and sulfur dioxide emissions

a) GHGs or $CO_2\ eq$ for the various scenarios. b) $SO_2\ eq$ for the several scenarios.

CONCLUSIONS

The absorption cooling systems using solar energy (with ETC) and biomass (rice husk) as energy sources are technically feasible. However, only scenarios 2 and 3 can operate throughout the proposed schedule. The system evaluated in scenario 1 operates between 7:00 and 17:00 hours with the partial or nominal evaporator cooling load for the typical day of the most critical month. The COP and COP_{system} are highest at peak hours. In addition, this is the scenario that provides the greatest reduction in GHGs.

The system evaluated in scenario 1 presented the greatest reduction of GHGs and the maximum COP and COP_{system} in relation to $\dot{Q}_e$. If the technical and environmental benefits such as flexibility or availability of the energy source, the COP, the $COP_{system,}$ the amount of GHGs and the amount of sulfur dioxide are compared and the behavior of a compression (conventional) cooling system is analyzed, the most favorable option is the absorption refrigeration system that uses both energy sources (scenario 3). If only the technical aspects and GHGs are taken into consideration, the best option is the technology that uses solar energy (scenario 1). However, this analysis does not consider the investment and operating costs of the entire system. Therefore, further studies may consider an assessment of these scenarios from an economic perspective.

Concerning the rate of energy used by the desorber and the potential energy for its activation ($\dot{Q}s+\dot{Q}husk$), this variable maintained a constant value in scenario 2. The system evaluated in scenario 3 only surpassed the indicator (ratio) corresponding to the system of scenario 2, between 9:00 and 12:00 hours. As for the scenario 1, in peak hours it outperformed all of them. Therefore, it is identified that a control and resource management strategy can be generated to improve the use of the energy needed to activate the cooling system by reducing the amount of rice husk while using more solar energy during peak hours. Finally, for the absorption refrigeration system of scenario 3, it is recommended to study in future research the amount of ETC to find an optimal operating condition that favors economic feasibility.

ACKNOWLEDGEMENT

The authors are very thankful to the Universidad de la Costa and MINCIENCIAS. This study is part of a research project funded by the named institutions through the INDEX project CONV-13-2018 and CONV-15-2020.

REFERENCES

[1] Adel, J., AlFaris, F., Montoya, F., & Manzano-Agugliaroa, F. (2016). Energy benchmarking for shopping centers in Gulf Coast region. *Energy Policy*, 247–255.

[2] Alhamid, M. I., Coronas, A., Lubis, A., Ayou, D. S., Nasruddin, Saito, K., & Yabase, H. (2020). Operation strategy of a solar-gas fired single/double effect absorption chiller for space cooling in Indonesia. *Applied Thermal Engineering*, *178*. https://doi.org/10.1016/j.applthermaleng.2020.115524

[3] Allouhi, A., Kousksou, T., Jamil, A., Bruel, P., Mourad, Y., & Zeraouli, Y. (2015). Solar driven cooling systems: An updated review. *Renewable and Sustainable Energy Reviews*, *44*, 159–181. https://doi.org/10.1016/j.rser.2014.12.014

[4] Amaris, C. C. (2013). *Intensification of NH 3 Bubble Absorption Process using Advanced Surfaces and Carbon Nanotubes for NH 3 /LiNO 3 Absorption Chillers*.

[5] Asadi, J., Amani, P., Amani, M., Kasaeian, A., & Bahiraei, M. (2018). Thermo-economic analysis and multi-objective optimization of absorption cooling system driven by various solar collectors. *Energy Conversion and Management*, *173*(July), 715–727. https://doi.org/10.1016/j.enconman.2018.08.013

[6] Aune, M., Godbolt, Å. L., Sørensen, K. H., Ryghaug, M., Karlstrøm, H., & Næss, R. (2016). Concerned consumption. Global warming changing household domestication of energy. *Energy Policy*, *98*, 290–297. https://doi.org/10.1016/j.enpol.2016.09.001

[7] Ayou, D. S., Bruno, J. C., Saravanan, R., & Coronas, A. (2013). An overview of combined absorption power and cooling cycles. In *Renewable and Sustainable Energy Reviews* (Vol. 21, pp. 728–748). Pergamon. https://doi.org/10.1016/j.rser.2012.12.068

[8] Bellos, E., & Tzivanidis, C. (2017). Energetic and financial analysis of solar cooling systems with single effect absorption chiller in various climates. *Applied Thermal Engineering*, *126*, 809–821. https://doi.org/10.1016/j.applthermaleng.2017.08.005

[9] Bellos, E., Tzivanidis, C., Symeou, C., & Antonopoulos, K. A. (2017). Energetic, exergetic and financial evaluation of a solar driven absorption chiller – A dynamic approach. *Energy Conversion and Management*, *137*, 34–48. https://doi.org/10.1016/j.enconman.2017.01.041

[10] Castro, A. O. (2010). Análisis del potencial energético solar en la Región Caribe para el diseño de un sistema fotovoltaico. *INGE CUC*, *6*(1), 95–102.

[11] Ghafoor, A., & Munir, A. (2015). Worldwide overview of solar thermal cooling technologies. *Renewable and Sustainable Energy Reviews*, *43*, 763–774. https://doi.org/10.1016/j.rser.2014.11.073

[12] Gomri, R. (2013). Simulation study on the performance of solar/natural gas absorption cooling chillers. *Energy Conversion and Management*, *65*, 675–681. https://doi.org/10.1016/j.enconman.2011.10.030

[13] Jaider, E.C., Aguilar, S., De, U., Facultad, S., & Ingenieria, D. E. (2009). *Alternativas de aprovechamiento de la cascarilla de arroz*.

[14] Juaidi, A., Al Faris, F., Montoya, F. G., & Manzano-Agugliaro, F. (2016). Energy benchmarking for shopping centers in Gulf Coast region. *Energy Policy*, *91*, 247–255. https://doi.org/10.1016/j.enpol.2016.01.012

[15] Kalogirou, S. A. (2004). Solar thermal collectors and applications. In *Progress in Energy and Combustion Science* (Vol. 30, Issue 3, pp. 231–295). Pergamon. https://doi.org/10.1016/j.pecs.2004.02.001

[16] Li, K., Xiong, P., Wu, Y., & Dong, Y. (2022). Forecasting greenhouse gas emissions with the new information priority generalized accumulative grey model. *Science of the Total Environment*, *807*, 150859. https://doi.org/10.1016/j.scitotenv.2021.150859

[17] Pátek, J., & Klomfar, J. (2006). A computationally effective formulation of the thermodynamic properties of LiBr-H2O solutions from 273 to 500 K over full composition range. *International Journal of Refrigeration*, *29*(4), 566–578. https://doi.org/10.1016/j.ijrefrig.2005.10.007

[18] Pérez-Lombard, L., Ortiz, J., & Pout, C. (2008). A review on buildings energy consumption information. *Energy and Buildings*, *40*(3), 394–398. https://doi.org/10.1016/J.ENBUILD.2007.03.007

[19] Rodríguez-Toscano, A., Amaris, C., Sagastume-Gutiérrez, A., & Bourouis, M. (2022a). Technical, environmental, and economic evaluation of a solar/gas driven absorption chiller for shopping malls in the Caribbean region of Colombia. *Case Studies in Thermal Engineering*, *30*, 101743. https://doi.org/10.1016/J.CSITE.2021.101743

[20] Rodríguez-Toscano, A., Amaris, C., Sagastume-Gutiérrez, A., & Bourouis, M. (2022b). Technical, environmental, and economic evaluation of a solar/gas driven absorption chiller for shopping malls in the Caribbean region of Colombia. *Case Studies in Thermal Engineering*, *30*, 101743. https://doi.org/10.1016/j.csite.2021.101743

[21] Sagastume Gutiérrez, A., Cabello Eras, J. J., Hens, L., & Vandecasteele, C. (2020). The energy potential of agriculture, agroindustrial, livestock, and slaughterhouse biomass wastes through direct combustion and anaerobic digestion. The case of Colombia. *Journal of Cleaner Production*, *269*, 122317. https://doi.org/10.1016/j.jclepro.2020.122317

[22] Saint Akadiri, S., Adewale Alola, A., Olasehinde-Williams, G., & Udom Etokakpan, M. (2020). The role of electricity consumption, globalization and economic growth in carbon dioxide emissions and its implications for environmental sustainability targets. *Science of the Total Environment*, *708*, 134653. https://doi.org/10.1016/j.scitotenv.2019.134653

[23] Sánchez Lario, A. (2017). *Diseño de una planta de gasificación con cogeneración para el aprovechamiento energético de la cascarilla de arroz en un proceso industrial*. E.T.S.I. Diseño Industrial (UPM).

[24] Toscano, A. D. R., Torres, D. A. A., Pérez, D. M., Castillo, A. P. P., Herazo, J. C. M., & Rivera, M. H. (2021). Estimation and Trends of the Absorption Refrigeration Global Market. *Smart Innovation, Systems and Technologies*, *205*, 633–643. https://doi.org/10.1007/978-981-33-4183-8_50

[25] Toscano, A. R., Piñeres Castillo, A. P., Mojica Herazo, J. C., López, R. L., & Restrepo, R. R. (2020). Management and Control of Variables for the Generation of Biogas from Pig Zungo. *Procedia Computer Science*, *177*, 261–266. https://doi.org/10.1016/J.PROCS.2020.10.036

[26] Zapata, A., Amaris, C., Sagastume, A., & Rodríguez, A. (2021). CFD modelling of the ammonia vapour absorption in a tubular bubble absorber with NH3/LiNO3. *Case Studies in Thermal Engineering*, *27*, 101311. https://doi.org/10.1016/J.CSITE.2021.101311

[27] ***Absorsistem. (2014). *Plantas enfriadoras de agua por ciclo de absorción, accionadas por agua caliente.* https://absorsistem.com/

[28] ***Comisión del Cambio Climático. (2011). *Guía práctica para el cálculo de emisiones de gases de efecto invernadero (GEI) GUÍA PRÁCTICA PARA EL CÁLCULO DE EMISIONES DE GASES DE EFECTO INVERNADERO (GEI)*.

[29] ***Empresas Públicas de Medellín (EPM). (2020). *Tarifario del mes | Gases del Caribe*. Tarifario Del Mes. https://gascaribe.com/tarifario-del-mes/

[30] ***Federación Nacional de Biocombustibles de Colombia. (2018, January 20). *Federación Nacional de Biocombustibles de Colombia*. Desperdicio Que Sí Sirve. https://www.fedebiocombustibles.com/nota-web-id-3016.htm

[31] ***Instituto de Hidrología, Meteorología y Estudios Ambientales (IDEAM). (2020). *Boletín Climatológico Mensual - CLIMATOLÓGICO MENSUAL - IDEAM*. http://www.ideam.gov.co/web/tiempo-y-clima/climatologico-mensual
[32] ***International Energy Agency (IEA). (2019). *Perspectivas energéticas mundiales 2019 - Análisis - IEA*. Perspectivas Energéticas Mundiales 2019. https://www.iea.org/reports/world-energy-outlook-2019#
[33] ***United States Department of Energy. (2016). *Absorption Chillers for CHP Systems*. 3–6.
[34] ***Unidad de Planeación Minero Energética (UPME). (2015). Integración de las energías renovables no convencionales en Colombia. In *Ministerio de Minas y Energía*. https://doi.org/10.1021/ja304618v
[35] ***Unidad de Planeación Minero Energética (UPME). (2016a). *Atlas del potencial energético de la Biomasa residual en Colombia*. Atlas Del Potencial Energético de La Biomasa Residual En Colombia. https://www1.upme.gov.co/siame/Paginas/atlas-del-potencial-energetico-de-la-biomasa.aspx
[36] ***Unidad de Planeación Minero Energética (UPME). (2016b). *FECOC*. Total de Emisiones CO2 Calculadas. http://www.upme.gov.co/calculadora_emisiones/aplicacion/calculadora.html
[37] ***Weather Underground. (2020). *Barranquilla, Colombia Weather Conditions | Weather Underground*. https://www.wunderground.com/weather/co/barranquilla

RESEARCH ON PIG BODY SIZE MEASUREMENT SYSTEM BASED ON STEREO VISION
/
基于立体视觉的猪只体尺测量系统研究

Yanli GENG*[1)], Xiaodong YUE[1)], Yankai JI[1)], Yanbo LIN[1)], Yanfang FU[2)], Shucai YANG[3)]
[1)]School of Artificial Intelligence, Hebei University of Technology, Tiajin, 300130 / China,
[2)]Hebei Provincial Animal Husbandry Station, Hebei 050035 / China,
[3)]Tianjin Mojieke Technology Development Co., Ltd, Tiajin, 300130 / China;
Tel: +8615320025316; E-mail: gengyl@hebut.edu.cn
DOI: https://doi.org/10.35633/inmateh-70-07

Keywords: *Pig body size measurement, KinectV2 camera, Point cloud, Calibration registration*

ABSTRACT
Body size of pigs is an important evaluation indicator in pig breeding. The traditional method of body size measurement is usually in manual way, which requires more employees and causes stress reactions of pigs. In response to the shortcomings of the traditional methods, this paper designed a system for measuring the body size of pigs based on stereo vision. The point cloud of both the calibration object and the pig was collected using dual KinectV2 cameras. Pre-processing was conducted using filtering and random sample consensus to remove background noise from the point clouds. As there was limited overlap between the two sides of the point clouds, the rotation matrix obtained from registering the calibration object was applied to the pig point clouds. Curve fitting and slicing were then utilized to measure the pig's body dimensions, including length, width, height, and abdominal circumference. The results of the study indicated that the mean absolute percentage error (MAPE) was 2.13% for body length, 1.02% for body width, 1.05% for body height, and 2.21% for abdominal girth. These results demonstrate the high accuracy and practical production value of the system.

摘要
生猪的体尺参数是生猪养殖情况的重要评判指标，传统的猪只体尺参数测量方式通常为直接接触式，需要消耗更多的人力并且易造成猪只的应激反应。针对传统体尺测量方法的缺陷，本文设计了一种基于立体视觉的猪只体尺自动测量系统。首先利用双 KinectV2 相机采集标定物与猪只的点云数据，利用滤波和随机采样一致性算法对采集的点云进行预处理，获取无背景的标定物与猪只点云；然后针对两侧点云重合度低的问题，将标定物配准输出的旋转矩阵应用于猪只点云配准；最后利用曲线拟合与切片处理方法测量猪只体长、体宽、体高和腹围。 试验结果表明，猪只体长测量平均相对误差为 2.13%，体宽测量平均相对误差为 1.02%，体高测量平均相对误差为 1.05%，腹围测量平均相对误差为 2.21%。该系统具有较高的估算准确性，在实际生产中有重要意义。

INTRODUCTION
The outbreak of African swine fever virus in 2018 has made a profound negative impact on pig farming industry (*Liu et al., 2020; Zhang et al., 2021*). The body size parameters are important indicator for evaluating the growth of pigs. In the traditional way, breeders measure the size with a tape measure. In this way, breeders keep close contact with the pig, which will increase the risk of disease in pigs *(Wang et al., 2018； Luo et al., 2018)*. The automatic measurement can effectively reduce the risk of disease in pigs, increase efficiency and accuracy of measurement and improve animal welfare *(Reinke et al., 2021; Cheng et al., 2021).*

In recent decades, two-dimensional cameras have been widely used in the field of computer vision *(Bewley et al., 2008; Chen et al., 2018; Junming et al., 2020)*. However, this technique has limitations in measuring animal body parameters, such as changes in light intensity, difficulty of background separation and image acquisition environment *(Viazzi et al., 2014).* With the development of machine vision and 3D point cloud processing technologies, these technologies are being used in the livestock industry *(He et al., 2020; Salau et al., 2014; Weber et al., 2014).* A visual image analysis system is designed by *White et al. (2005)*. The size and shape information of pig's back is obtained by a camera, which is used to monitor the growth of pigs. A noncontact weight estimation system for pigs is built by *Apirachhai et al. (2015)*. A camera is put on the top of the system, which is used to capture the image of pig's back. The body contour of the pig is extracted and the body length and profile length of the pigs is calculated.

The parameters of pig body size are used as inputs to the weight estimation model, and the MAPE in weight estimation is less than 3%. The interactive measurement software LSSA_CAU is designed by *Guo et al. (2017)* to estimate livestock body size based on point clouds. The point cloud of the pig is obtained by *Liu et al. (2014)* using a non-contact 3D scanner. The surface model of the pig is reconstructed to obtain the coordinates of the measurement points for each parameter. The thorax, surface area and volume of the pig are calculated. The top and side view depth maps of the pig are captured by *Pezzuolo et al. (2018)* using a Kinect depth camera. The coordinates associated with the pig's body parts are efficiently obtained from the point cloud reconstructed by the depth map, and then the body size parameters can be calculated. *Wang et al. (2018)* proposed a method for measuring pig body size based on a single-view point cloud. A complete point cloud of the pig's body is obtained using mirror imaging and body size parameters are measured. This method requires only one camera and reduces the complexity of image acquisition, but the measurement error is large. *Yin et al. (2019)* use the Kinect v2 to collect the local point clouds of pigs from the top, left and right angles simultaneously. The local point cloud is denoised by the neighbourhood curvature change method, and the complete pig body point cloud is obtained by registration. Finally, each body size is measured using an accurate estimation technique of multi-scale data. *Li et al. (2018)* propose a method for the construction of stereo vision. This method set up two cameras on the back to acquire images and automatically extract the body size measurement points of the pig.

In this paper, two KinectV2 cameras were placed symmetrically on the left and right sides of the measured object. The point clouds of calibration object and pigs were collected, which were denoised and segmented. The rotation-translation matrix of the point clouds was obtained by registering the calibration objects, which was used to register the pig point clouds. This method only needs to be calibrated once before collecting the point cloud, which can improve registration accuracy and speed. Finally, each body scale was measured by slicing and curve fitting, as shown in Fig 1.

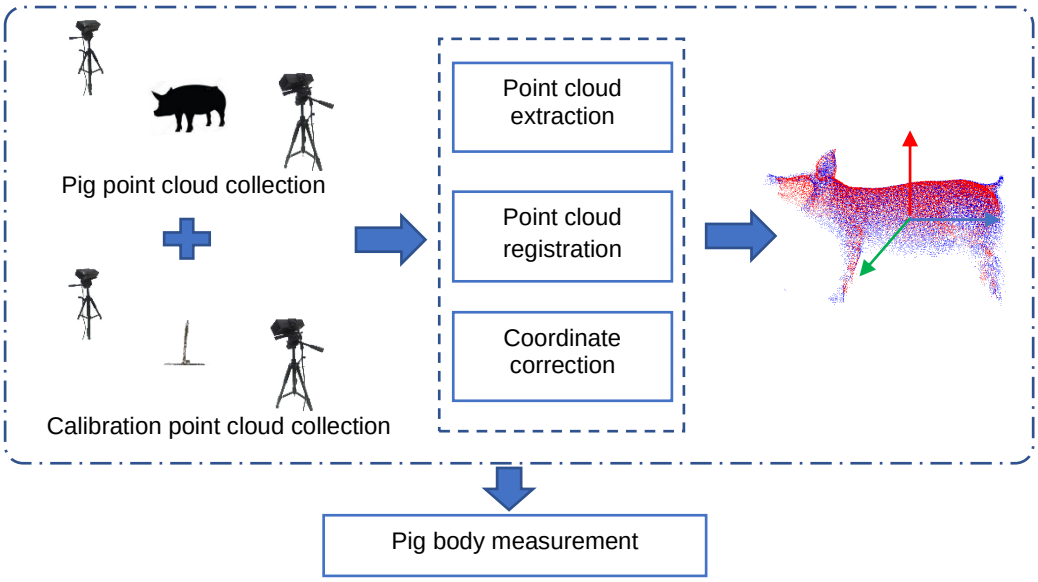

Fig. 1 - Technology Roadmap

MATERIALS AND METHODS

In this paper, a collection platform of point cloud was built in the laboratory. The Kinect cameras are placed symmetrically on both sides of the pig. The camera's height above ground level is 0.9 m. The horizontal distance between the two cameras is 1.2 m. The angle between the camera and the horizontal plane is 45° (as shown in Figure 2.a). The point cloud of pig on both left and right side are collected. The position of the camera must remain constant when collecting the point cloud of the calibration object and pig. In this way, the rotation matrix of the calibration object can be used in pig point cloud registration.

The measurement experiment platform was built in Dabei Farm, Cangzhou (as shown in Figure 2.b). Only one pig was allowed in the collection area. The location and placement of Kinect v2 cameras were same as that of the laboratory.

The breed of the pig is Yorkshire and the age ranged from 90-100 days. Data were collected from 9.30AM to 16.30PM. A total of 3510 point clouds were collected from 100 pigs in the experiment. All manual measurements of body size of pigs were measured by professional testers with tape measures. The measurement accuracy is 1 mm in the laboratory and 1 cm on the farm.

(a) **(b)**

Fig. 2 - Pig point cloud acquisition platform

Pig point cloud extraction

When acquiring point clouds of pigs, noisy points appear in the acquired point clouds due to the accuracy of Kinect v2, experimenter's operation, and environmental problems at the test site. In addition, there are discrete points far away from the main point cloud in the point cloud data due to the infrared diffraction problem and the influence of different surface textures of the measured object. In order to extract the pig point cloud and remove the noise, the following processes are applied to the point cloud.

1) Pass-through filter processing: Among the point clouds captured by Kinect v2, only some of them require subsequent processing. Therefore, with a clear target area, the point cloud is filtered by Pass-through, and the irrelevant point clouds can be quickly removed to obtain the point cloud of the pig area.

2) Statistical filter processing: Statistical analysis is conducted on the neighbourhood of each point in the point cloud obtained in step 1). Then all distances in the point cloud are assumed to form a Gaussian distribution, and its shape is determined by mean μ and standard deviation σ , Let the coordinate of the nth point in the point cloud be $P_n(X_n, Y_n, Z_n)$, The distance from this point to any point is S_i , as shown in Equation (1):

$$S_i = \sqrt{(X_n - X_m)^2 + (Y_n - Y_m)^2 + (Z_n - Z_m)^2} \quad (1)$$

Calculate the mean $\mu = \frac{1}{n}\sum_{i=1}^{n} S_i$ and standard deviation $\sigma = \sqrt{\frac{1}{n}\sum_{i=1}^{n}(S_i - \mu)^2}$ of the distance from each point to any point, when the average distance of a point close to k points is within the standard range $(\mu - x\sigma, \mu + x\sigma)$, the point is retained. If it is not within the standard range, it is defined as an outlier deletion.

3) Random sampling consistency split: Three points are randomly selected in the initial point cloud, and their corresponding plane equations are calculated $ax + by + cz + d = 0$. Calculate the algebraic distance d_i of all points to this plane, as shown in Equation (2):

$$d_i = \left| ax_i + by_i + cz_i + d \right| \quad (2)$$

Pick Threshold $d_{\max}$, if $d_i \le d_{\max}$, then the point is considered to be a point in the plane, otherwise it is an out-of-plane point. Repeat the above steps, setting the maximum number of iterations N and getting the surface with the most plane points. The normal vector n_z of the plane is calculated, and then delete it to achieve the effect of removing the plane. The effect of the point cloud after the above three steps is shown in Figure 3:

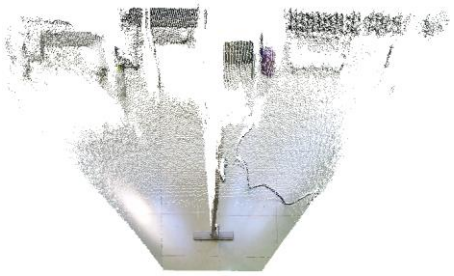

(a) Panoramic point cloud

(b) Point cloud extraction

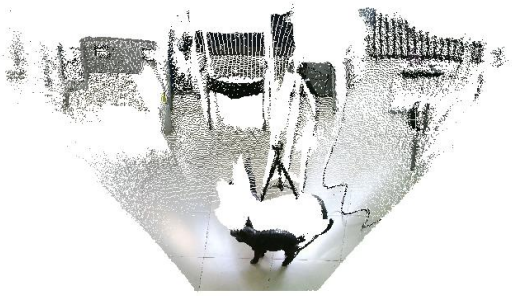

(c) Pig panoramic point cloud

(d) Pig point cloud extraction

Fig. 3 - Point cloud denoising segmentation processing

Calibration-based point cloud registration

The process of converting point clouds to the world coordinate system is called point cloud registration, and the stitching of point clouds is done by screening for overlap. In this paper, point clouds are captured horizontally symmetrically by the KinectV2 camera. The overlap of the pig point clouds is poor, resulting in low registration efficiency and accuracy. Therefore, fine and rough registration methods are designed to deal with the point clouds. The output translation and rotation matrix are used for the registration of the pig point clouds.

First, the calibration object is roughly registered. In the calibration of multiple depth cameras, the process is called rough registration, which involves obtaining the rotation and translation matrices of adjacent sub-regions and calculating the transformation into the same coordinates based on Equation (3).

$$\begin{bmatrix} x_1 \\ y_1 \\ z_1 \end{bmatrix} = R_{rough} \begin{bmatrix} x_2 \\ y_2 \\ z_2 \end{bmatrix} + T_{rough} = \begin{bmatrix} R_1 & R_2 & R_3 \\ R_4 & R_5 & R_6 \\ R_7 & R_8 & R_9 \end{bmatrix} \begin{bmatrix} x_2 \\ y_2 \\ z_2 \end{bmatrix} + \begin{bmatrix} t_x \\ t_x \\ t_x \end{bmatrix} \tag{3}$$

where:

R_{rough} is the space transformation matrix, T_{rough} is the translation vector.

The camera coordinate system of the right camera is set to the world coordinate system, and the point cloud acquired by the left camera is linearly transformed into the world coordinate system. Before the experiment, rotation and translation matrices were obtained by calibrating two KinectV2 cameras. The object is roughly registered by linearly transforming the left point cloud.

The right point cloud is used as the target point cloud, and the object to be registered is the linearly transformed left point cloud. Source point cloud S and target point cloud T are obtained, as shown in Equation (4).

$$\begin{cases} S = \{s_1, s_2, s_3, \cdots, s_n\} s_i \left(x_i, y_i, z_i\right)_{i=1,2,\cdots,n} \\ T = \{t_1, t_2, t_3, \cdots, t_n\} t_j \left(x_j, y_j, z_j\right)_{j=1,2,\cdots,n} \end{cases} \tag{4}$$

Improved ICP is designed for the fine registration of the origin point cloud S and target point cloud T and has a high retrieval speed.

The algorithm steps are as follows:

Step 1: The source point cloud and the target point cloud are inputted, and an Octree bounding box is established.

Step 2: The overlapping areas of the source point cloud *S* and the target point cloud *T* are searched for by Octree.

Step 3: Point clouds of overlapping regions are extracted and the corresponding point S' and T' are calculated, as shown in Equation (5).

$$\begin{cases} S' = \{s_1', s_2', s_3', \cdots, s_n'\}\, s_i'\left(x_i, y_i, z_i\right)_{i=1,2,\cdots,n} \\ T' = \{t_1', t_2', t_3', \cdots, t_n'\}\, t_j'\left(x_j, y_j, z_j\right)_{j=1,2,\cdots,n} \end{cases} \quad (5)$$

The original point cloud normal vector is calculated, and the normal vector angle threshold of the target point cloud is set to be larger than s_i'. The non-standard point cloud is deleted and two groups of corresponding points are obtained, as shown in Equation (6).

$$\begin{cases} S'' = \{s_1'', s_2'', s_3'', \cdots, s_n''\}\, s_i''\left(x_i, y_i, z_i\right)_{i=1,2,\cdots,n} \\ T' = \{t_1', t_2', t_3', \cdots, t_n'\}\, t_j'\left(x_j, y_j, z_j\right)_{j=1,2,\cdots,n} \end{cases} \quad (6)$$

Step 4: After obtaining the corresponding points, the optimal rotation and translation matrix are obtained by the least squares method. The space conversion parameters $R_{accurate}$ and $T_{accurate}$ are calculated between the nearest corresponding point pairs s_i'' and t_j'.

Step 5: The rotation matrix $R_{accurate}$ and the translation vector $T_{accurate}$ are applied to the source point cloud S'' to obtain a new nearest point-to-point set S''', as shown in Equation (7).

$$S''' = \{s_1''', s_2''', s_3''', \cdots, s_n'''\}\, s_i'''\left(x_i, y_i, z_i\right)_{i=1,2,\cdots,n} \quad (7)$$

The mean of Euclidean distance D is calculated between the two point sets S''' and T', as shown in Equation (8).

$$D = \frac{\sum_{i=1}^{n} \sqrt{\left[s_i'''(xi) - t_i'(xi)\right]^2 + \left[s_i'''(yi) - t_i'(yi)\right]^2 + \left[s_i'''(zi) - t_i'(zi)\right]^2}}{n} \quad (8)$$

If $D \le \tau$ (τ is a given distance threshold), the process ends; otherwise, the above steps are repeated until the convergence conditions are met (as shown in Figure 4).

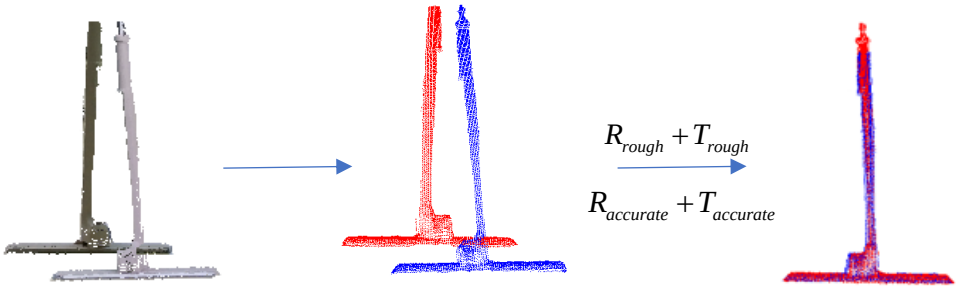

Fig. 4 - Calibration point cloud registration process

The left and right point clouds are rendered in red and blue respectively, according to the rough registration transformation parameters R_{rough} and T_{rough}, as well as the fine registration transformation parameters $R_{accurate}$ and $T_{accurate}$. The left and right point clouds are rendered into red and blue respectively, and the left pig point cloud is spatially transformed to complete the pig point cloud registration (as shown in Figure 5).

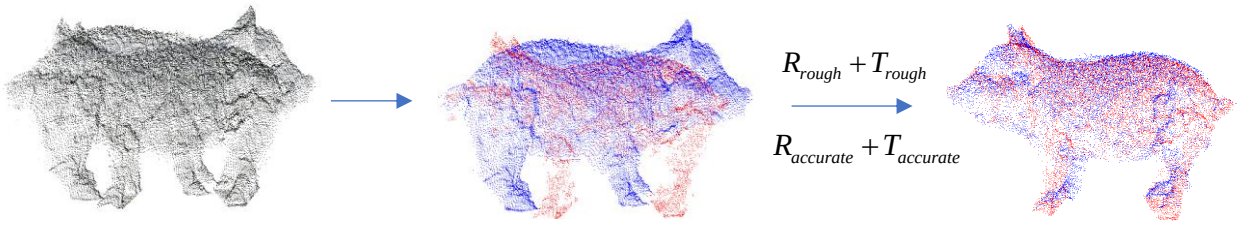

Fig. 5 - Pig point cloud registration process

Coordinate system correction based on plane normal vector

When Kinect v2 acquires the point cloud, it creates a coordinate system with the camera position as the origin. In order to facilitate the measurement of the pig point cloud, the origin of the coordinate system needs to be adjusted to the centre of the point cloud, and make the coordinate system X-axis register with the body width direction, Y-axis register with the body length direction, and Z-axis register with the body height direction.

Firstly, the ground normal vector n_z is used as the Z-axis of the new coordinate system. Then the maximum cross-section of the point cloud along the body length direction is found, and its normal vector n_x as the X-axis of the new coordinate system. The n_y of the new coordinate system is obtained by taking the cross product of n_z and n_x. Finally, the coordinate system is established with the centre of the point cloud as the coordinate origin (as shown in Figure 6).

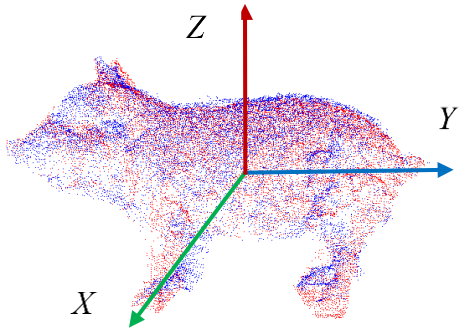

Fig. 6 - Coordinate system correction

Pig body measurement

Body length

The body length of the pig is defined as the length along the curve of its back from the midpoint of each ear to the base of the tail. Only the upper half of the pig's point cloud is needed, so $Z \geq 0$ part is selected. In order to extract the back curve of the pig, the point cloud of the pig was sliced in the range of $-0.01 \leq X \leq 0.01$.

A polynomial fit was applied to the dorsal curve and all extreme points and points of maximum curvature of the curve were calculated. The first extreme point is chosen as the starting point and the point of maximum curvature as the end point, and the length of the curve between these two points is calculated as the body length of the pig. The specific process is shown in figure 7.

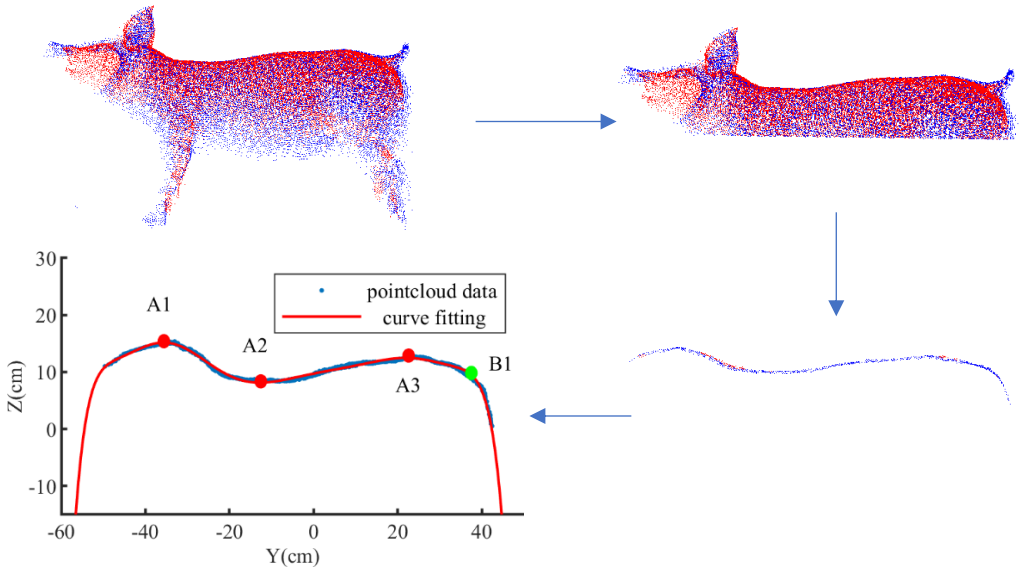

Fig. 7 - Schematic diagram of body length measurement

Body width

The body width is defined as the distance between the widest points of the abdomen. However, the width of the forelimbs and hindlimbs can affect this measurement of body width. To exclude this effect, the point cloud was divided into eight equal parts along the Y-axis direction, and the two parts near the origin were taken.

The difference between the maximum and minimum values of this part in the X-axis direction was calculated as the pig body width. The process is shown in figure 8.

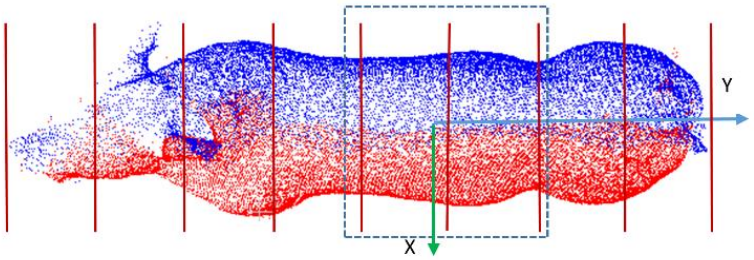

Fig. 8 - Schematic diagram of body width measurement

Body height

The body height of the pig is defined as the distance from the highest point of its back to the ground, which is the same as the body width measurement. However, the head can affect the body height measurement. In order to exclude this effect, the point cloud needs to be divided into eight equal parts along the Y-axis.

The four parts near the origin are selected, and the difference between the maximum and minimum values of the Z-axis is then calculated as the body height of the pig. The process is shown in figure 9.

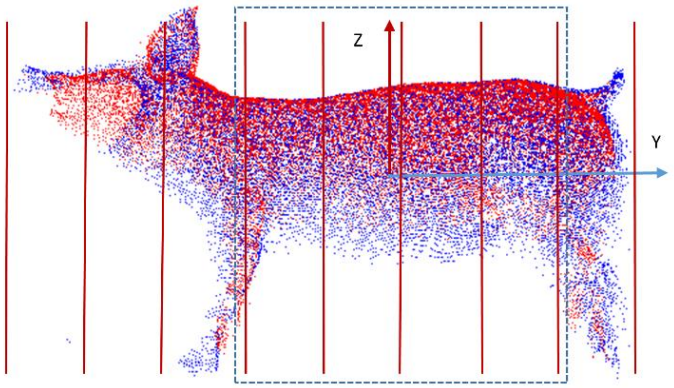

Fig. 9 - Schematic diagram of body height measurement

Abdominal circumference

The abdominal circumference of a pig is defined as the body circumference at the widest point of its abdomen. However, due to the horizontal camera angle, the pig's abdomen may not be fully captured. To compensate for this, the curve needs to be filled in using ellipse fitting, based on a plane perpendicular to the Y-axis and determined by two body width measurement points.

The fitted ellipse circumference was used as the abdominal circumference. The process is shown in figure 10.

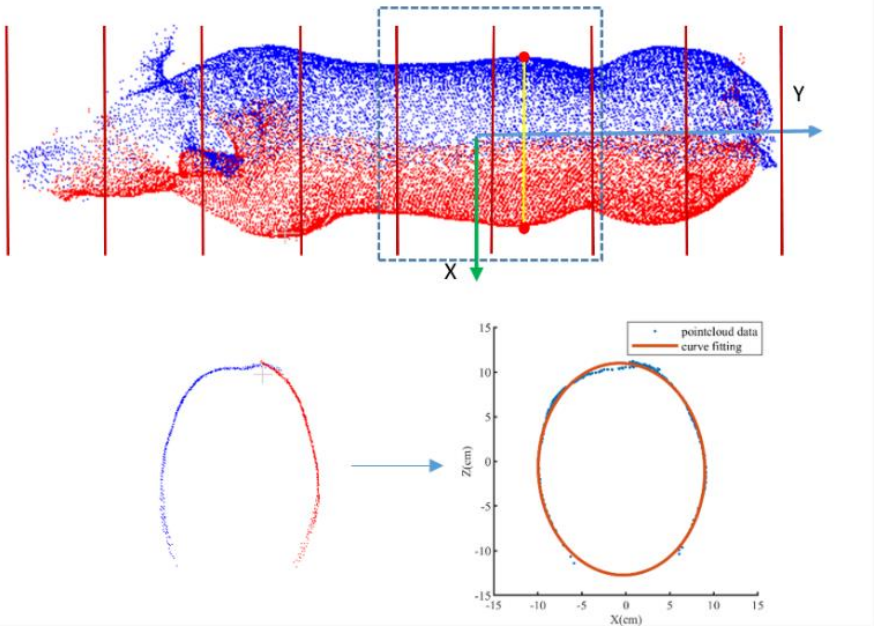

Fig. 10 - Schematic diagram of body Abdominal circumference measurement

RESULTS

In order to verify the accuracy of the algorithm for pig body size detection, a model of 100 pigs was used to register and measure the body size parameters in the experiment. To visually compare the manual and automatic measurements, a comparison graph was created for 20 randomly selected pigs, as shown in Figure 11. The MAPEs of body length, body width, body height and abdominal circumference were found to be 2.13%, 1.02%, 1.05% and 2.21%, respectively, which indicates that the proposed algorithm shows a significant degree of robustness accuracy.

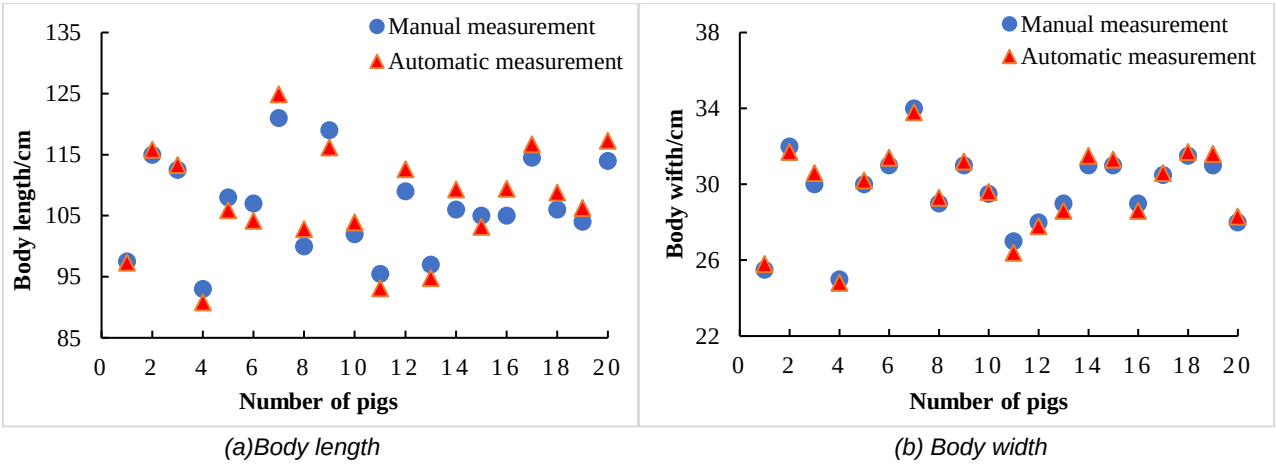

(a)Body length *(b) Body width*

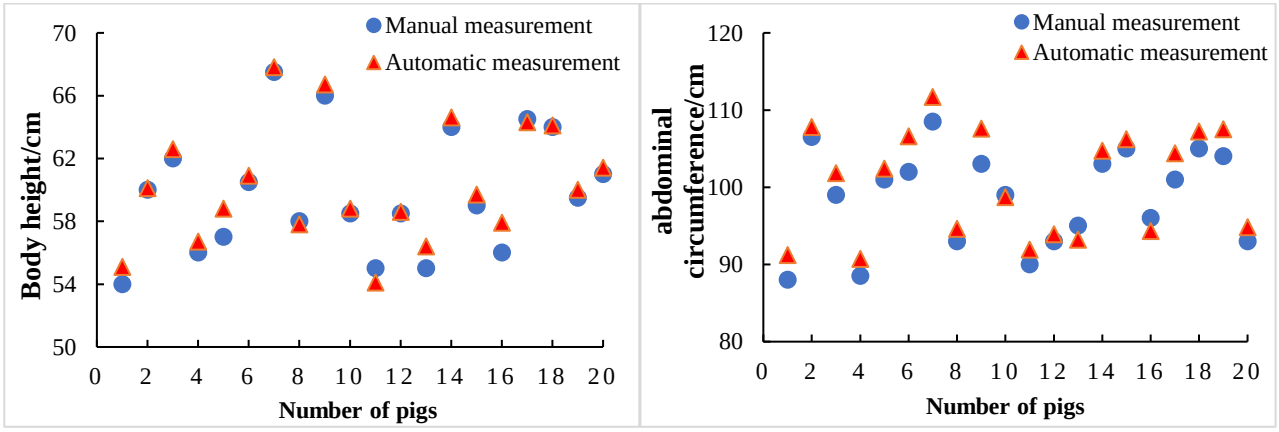

(c)Body height *(d)Body abdominal circumference*

Fig. 11 - Comparison chart of manual measurement and automatic measurement

CONCLUSIONS

In this paper, a curve-fitting-based method was proposed for accurately measuring the body size of pigs through point cloud processing and curve fitting. The method was validated in a measurement experiment involving 20 pigs, which demonstrated high accuracy. However, it is obvious that the MAPE of body width and height is smaller than that of body length and abdominal circumference. During system measurement, body height and body width were directly calculated as the straight-line distance between two points. In contrast, body length and abdominal circumference required curve fitting before their length could be calculated. This curve fitting process increased the potential for error between the actual and measured values. Furthermore, the measurement requires the pig to be in a strict upright posture without bending its body, which limits the system's practical application. Further research should aim to reduce the influence of posture on measurement results and improve the system's practical relevance.

ACKNOWLEDGEMENT

This study was supported by Key R&D program of Hebei Province(20326620D) and National key research and development program (2021YFC0122704).

REFERENCES

[1] Apirachai W., Banchar A., Supachai P., (2015). An approach based on digital image analysis to estimate the live weights of pigs in farm environments. *Computers and Electronics in Agriculture*, Vol.115, pp.26-33, Khon Kaen/ Thailand.

[2] Bewley J.M., Peacock A.M., Lewis O., (2008). Potential for estimation of body condition scores in dairy cattle from digital images. *Journal of dairy science*, Vol.94, Issue 9, pp.3439-3453, West Lafayette/UK.

[3] Chen C., Liu T., Wu W., (2018). Application and development of three-dimensional sensor Kinect in agriculture. *Jiangsu Agricultural Sciences*, Vol.46, Issue 8, pp.11-14, Yangzhou/China.

[4] Cheng H.J., Wang L., (2021). The impact of animal welfare on breeding efficiency. *Journal of Zhejiang Agricultural Sciences*, Vol.62, Issue 10, pp.2084-2086+2090, Zhejiang/China.

[5] Guo H., Ma X., Ma Q., (2017). LSSA_CAU: An interactive 3d point clouds analysis software for body measurement of livestock with similar forms of cows or pigs. *Computers and Electronics in Agriculture*, Vol.138, pp.60-68, Beijing/China.

[6] He X.Y., Zhao S.L., Zhang Z., Zhao T.Y., (2020). Development Trend of the Research and Application of Machine Vision. *Machinery Design & Manufacture*, Issue 10, pp. 281-283+287, Shenyang/China.

[7] Junming H., Hongjie Z., Li J., Yao E., & Weixue H. (2020). Analysis and optimization on the process of adjustable double drum castor shelling based on discrete element method. *INMATEH-Agricultural Engineering, (3).*

[8] Li Z., Du X.D., Mao T.Y., (2018). Pig body size detection system based on depth image. *Swine Industry Outlook*, Issue 4, pp.26-33, Beijing/China.

[9] Liu M.J., (2020). Infection mechanism and epidemic prevention measures of swine disease. *Animal Husbandry and Veterinary Medicine Today*, Vol.36, Issue 3, pp.22, Hunan/China.

[10] Liu T.H., Teng G.H., Zhang S.N., (2014). Reconstruction and application of 3D pig body model based on point cloud data. *Transactions of the Chinese Society for Agricultural Machinery*, Vol.45, Issue 6, pp.291-295, Beijing/China.

[11] Luo W.X., Luo F., Guo Y.J., (2018). Talking about the matters needing attention in the daily work of measuring pigs in the centre. *Northern Animal Husbandry*, Issue 10, pp.19, Hebei/China.

[12] Pezzuolo A., Guarino M., Sartori L., (2018). On-barn pig weight estimation based on body measurements by a Kinect v1 depth camera. *Computers and Electronics in Agriculture*, Vol.148, pp.29-36, Veneto/ Italy.

[13] Reinke N.A., Bogner M., (2021). Non-Contact Measurement for Resource-Efficient Production. *IST International Surface Technology*, Vol.14, Issue 1, pp.48-49, Winterthur/ Schweiz.

[14] Salau J., Haas J.H., Junge W., (2014). Feasibility of automated body trait determination using the SR4K time-of-flight camera in cow barns. *Springer Plus*, Vol.3, Issue 1, pp.1-16, Kiel/Germany.

[15] Viazzi S., Bahr C., Van H.T., (2014). Comparison of a three-dimensional and two-dimensional camera system for automated measurement of back posture in dairy cows. *Computers and Electronics in Agriculture*, Vol.100, pp.139-147, Leuven/Belgium.

[16] Wang D.F., Huang H.N., Zhang H.J., (2018). Current situation and development analysis of engineering technology research on pig breeding facilities. *Transactions of the Chinese Society for Agricultural Machinery*, Vol.49, Issue 11, pp.8-21, Harbin/China.
[17] Wang K., Guo H., Ma Q., (2018). Pig body size measurement method based on mirror reflection of single angle point cloud. *Transactions of the Chinese Society for Agricultural Machinery*, Vol.49, Issue 3, pp.187-195, Beijing/China.
[18] Weber A., Salau J., Haas J.H., (2014). Estimation of backfat thickness using extracted traits from an automatic 3D optical system in lactating Holstein-Friesian cows. *Livestock Science*, Vol.165, Issue 1, pp.129-137, Kiel/Germany.
[19] White R., Schofield C., Green D., Parsons D., Whittemore C., (2004). The effectiveness of a visual image analysis (VIA) system for monitoring the performance of growing/finishing pigs. *Animal Science*, Vol.78, Issue 3, pp.409-418, Bedford/UK.
[20] Yin L., Cai G.Y., Tian X.H., (2019). Three dimensional point cloud reconstruction and body size measurement of pigs based on multi-view depth camera. *Transactions of the Chinese Society of Agricultural Engineering*, Vol.35, Issue 23, pp.201-208, Guangzhou/China.
[21] Zhang L.L., (2021). The impact of African swine fever on my country's pig breeding industry. *Animal Husbandry and Veterinary Science (Electronic Edition)*, Issue 3, pp.158-159, Jilin/China.

STUDY ON THE INFLUENCE OF PCA PRE-TREATMENT ON PIG FACE IDENTIFICATION WITH KNN
/
PCA 前处理对 KNN 识别猪脸的影响研究

Hongwen YAN*, Zhiwei HU, Yiran LIU
College of Information Science and Engineering, Shanxi Agricultural University, Taigu/China
Tel: +86-0354-6288165; E-mail: yhwhxh@126.com
DOI: https://doi.org/10.35633/inmateh-70-08

Keywords: *KNN, PCA, individual identification, intelligent management of pig breeding*

ABSTRACT
To explore the application of traditional machine learning model in the intelligent management of pigs, in this paper, the influence of the Principal Component Analysis (PCA for short) pre-treatment on pig face identification with k-Nearest Neighbor (KNN for short) is studied. With testing method, individual identification test was carried out on 10 different pigs in two testing schemes, in which one adopted KNN alone and the other adopted PCA + KNN, for which the classifier parameter was taken as 3 and 5, respectively. In the optimized scheme, the operating efficiency got significantly increased, also the training time and testing time were reduced to 4.8% and 7% of the original value in the KNN alone scheme, though the accuracy got lowered to a certain extent. With all these factors taken into consideration, PCA pre-treatment is beneficial to individual pig identification with KNN. It can provide experimental support for mobile terminals and embedded application of KNN classifiers.

摘要
为探索传统机器学习模型在生猪智能管理中的应用，本文研究了 PCA 前处理对 KNN 识别猪脸的影响，采用试验方式分别确定仅采用 KNN 以及 PCA+KNN 两种试验方案分类器参数值分别为 3、5，分别对 10 头生猪进行个体识别试验，优化方案运行效率显著提升，训练时间和测试时间缩减为原来的 4.8%、7%，准确率有一定程度降低，综合考虑，使用 PCA 前处理对采用 KNN 进行生猪个体识别具有增益作用，可为 KNN 分类器的移动端和嵌入式应用提供试验支持。

INTRODUCTION
The management of individual identification and behavior analysis of pigs, an important part in the intelligent management of pigs, can be divided into three categories: the first category is based mainly on RFID (Radio Frequency Identification) technology *(Maselyne et al., 2014; Hahnel et al., 2016)*, while the second category is based mainly on traditional machine learning model: LASSO regression and random forest model were used to predict the weight of pigs at 159 days to 166 days under four scenarios *(He et al., 2021)*; random forest and generalized linear regression were used to predict physiological temperature of piglets, though the prediction error was relatively high *(Gorczyca et al., 2018)*; auto-regression (AR) model and improved local linear embedding (LLE) were used to estimate pig weight in actual farm environment *(Wongsriworaphon et al., 2015)*. The third category is based mainly on the application of deep learning model and improved computer vision technology. Tu Shuqing et al. explored a PigMS R-CNN (Region Convolutional Neural Networks) framework based on mask scoring R-CNN (MS R-CNN) to segment the adhesion regions in images for herd pigs as well as identify and locate them. Zhang Jianlong et al. modified DenseNet201, ResNet152 V2, Xception and MobileNet V2 to be a multi-output regression CNN (Convolutional Neural Network) before getting them trained on modeling data, with modified Xception selected as the optimal estimation model. In order to improve the real-time performance of the model, Residual learning structure was introduced in, with its MSE reaching 0.092 *(Zhang et al., 2021)*. Yan Hongwen used the Feature Pyramid Attention (FPA) combined with a Tiny-YOLO model to achieve multi-target detection of herd pigs in different scenarios *(Yan et al., 2020)*. Yan Hongwen realized the detection of different types of face posture of herd pigs by constructing an attention sub-model with which both spatial attention and channel attention information are respectively introduced in on basis of YOLOV3 model *(Yan et al., 2019)*.

[1] *Hongwen Yan*, As. Ph.D. Prof. Eng.; Zhiwei Hu, Lect. Ph.D. Eng.; Yiran Liu, Lect.. Ph.D. Eng.*

Hu Zhiwei constructed a Dual Attention Unit (DAU) which integrates Channel Attention Unit (CAU) and Position Attention Unit (PAU) as one by taking ResNet50 and ResNet101 as the backbone network, and had it used in the Feature Pyramid Network (FPN) structure to realize the pig instance detection in different scenarios (*Hu et al., 2021)*. Marsot *(Marsot et al., 2020)* used the cascade classifier with Haar features to intuitively see how neural network learns to distinguish parameters by using the class activation map generated by grad-CAM, with an accuracy for 320 test images reaching 83%.

Though with the application of GPU, the high precision advantage of computer vision technology has gradually been revealed, in the management of small and medium-sized farms, the needs for mobile terminals and embedded application have gradually been increasing. For the deep learning model has high requirements to hardware, it is difficult to adapt to wide application. In addition, the deep learning model is of weak interpretability, which leads to its weak controllability. That is why it is necessary to study the application of RFID and traditional machine learning model in the management of small and medium-sized farms. However, for the RFID technology is easy to be simulated in the management *(Shi et al., 2012; Zhou et al., 2018)*, also it violates the animal welfare breeding thinking, it has gradually been eliminated. Only the requirements to hardware by traditional machine learning model conform to the standards for mobile terminals and embedded application, though there is still room for improvement in its identification accuracy and running time. With principal component analysis, the main features of the images for pig faces can be extracted *(Lin et al., 2021; Zhang et al., 2021)*, thus reducing the computation burden, improving the interpretability of the model, the operating efficiency, eliminating noise interference and improving identification accuracy. In order to promote the use of traditional machine learning model in mobile terminals and embedded application, in this paper, KNN is adopted for bettering the identification efficiency of pig faces in this study, and its influence on the efficiency of pig face identification is further studied by adding PCA pre-treatment in, which provides experimental support for its use in both mobile terminals and embedded application.

MATERIALS AND METHODS

Sample collection

The data of this study was collected in two times. The first time was collected in Dongsongjiazhuang Village, Jicun Town, Fenyang City, Shanxi Province, China (111º95′ E, 37º27′ N). In order to obtain live pig images of different pig house scenes, it was collected from 9:00-14:00 on June 1, 2019 (fine, strong light). Select 3 pig farms for video capture, each pig farm consists of 10-30 pig pens, the number of each pen varies from 6 to 8, the size of pig pens is about 3.5 m×2.5 m×1 m. A total of 35 videos of 5 pens of breeding pigs aged 20 to 105 days were collected. The second time was from 10:30-12:00 on October 13, 2019 (cloudy, weak light), and the collection site was located in the Laboratory Animal Management Center of Shanxi Agricultural University, Taigu City, Shanxi Province, China (112º59′ E, 37º43′ N). A total of 15 pigs in 6 pens are selected for video collection. In this study, 10 pigs are selected as the research objects, as shown in figure 1, including 768 training samples, 85 validation samples and 250 test samples.

Fig. 1 - Pig Samples

The computer used in the experiment is configured with 64-bit windows system, Intel Core i7-6700, 8GB memory, 6GB video memory capacity, and Program development uses Python V3.5 version language.

Principle of pig face identification with KNN

Among machine learning methods, the nearest neighbor algorithm can be traced back to the study made by Fix and Hodges *(Evelyn et al., 1989)*, and a more detailed content on k-nearest neighbor algorithm was proposed by Dasarathy *(Dasarathy et al., 1991)*. The k-nearest neighbor algorithm aiming to measure the distance between different eigenvalues for classification is also called KNN algorithm. In principle, KNN works in this way: the labeled sample set is used to figure out the data samples of the nearest distance by calculating the features of new data and the corresponding features in the training data, then the category of the samples with the nearest distance is judged before the category of new data is output. In KNN algorithm, k samples with the nearest distance can be chosen, therefore, before using the KNN algorithm to analyze the data, we need to determine the value of the parameter k first. In this study, the KNN algorithm was used to analyze pig face data in the following process:

(1) Data collection. Collect data to obtain image data of pig face;

(2) Data preparation. Prepare the numerical value needed for distance calculation, then normalize the pig face image data, and represent the matrix representing each image as a vector, so as to facilitate the calculation of distances between sample data;

(3) Data analysis. Divide the data into training data and test data by either sampling or proportion segmentation method;

(4) Algorithm training. KNN algorithm is used to train the training sample set of pig face data, in which k is an independent variable, and the KNN is trained by inputting different k values;

(5) Algorithm testing. Calculate the error rate of KNN algorithm for k of different values, so as to determine the optimal k value;

(6) Category determination. Use the algorithm to input the determined optimal k value into the KNN algorithm model, and then run the KNN algorithm on the test sample set of pig face data to determine which category the input pig face data for test respectively belong to.

In KNN, instance-level samples are used for training, so all the data need to be stored in the training process. Usually, a large number of training samples are used, and the corresponding storage cost is relatively high. When the algorithm is running, the distance of each sample needs to be calculated, which causes a certain time cost, for which Euclidean distance is used. The L_p distance is defined in the following way:

$$L_p(x_i, x_j) = \left(\sum_{l=1}^{n} \left|x_i^{(l)} - x_j^{(l)}\right|^p\right)^{\frac{1}{p}} \quad (1)$$

where: $x_i \in R^n$ represents a point in the dataset to be used for classification reference, [dimensionless];

$x_j \in R^n$ represents another point in the dataset to be used for classification reference, [dimensionless];

L_p represents the category parameter of the calculated distance in the KNN algorithm, [dimensionless];

l represents the dimension of the data point, [dimensionless].

p is a variable element.

In this study, p is taken as 2, namely Euclidean distance, corresponding to L_2 norm.

According to the given distance, we can find the k points closest to the data point x in the training set, and the field covering the k points is denoted as $N_k(x)$. In $N_k(x)$, according to the classification decision rules, the algorithm can decide the class of the data point x, which is represented by y, the y is defined in the following way:

$$y = argmax_{c_j} \sum_{c_j \in N_k(x)} I(y_i = c_j) \quad (2)$$

where: I represents the indicator function, when $y_i = c_j$, I is 1, otherwise I is 0, [dimensionless];

$N_k(x)$ represents the area of k points closest to the data point x, [dimensionless].

RESULTS AND DISCUSSION

Pig face identification test carried out with KNN alone

KNN model parameter determination

In the feature space, k features can always be found to have certain similarity with an input sample, which can be measured by the Euclidean distance between vectors. If most of the k samples belong to a certain category, then the sample also belongs to this category, where k is usually an integer not greater than 20. KNN algorithm determines which category the samples to be detected should be divided into according to the category of the selected k samples. Therefore, the selection of k is a key factor for the performance of KNN algorithm.

There is no fixed method for the selection of k value. In accordance with the different distribution of samples, a small value is first selected to test the indicator change of classifier, and k value with better comprehensive effect is selected. In order to determine the value of k, in this paper, it was taken as an independent variable to study the relationship between different k values and KNN's classification accuracy, recall rate as well as *f1* value of original image data. The curve relationship drawn is as shown in figure 2.

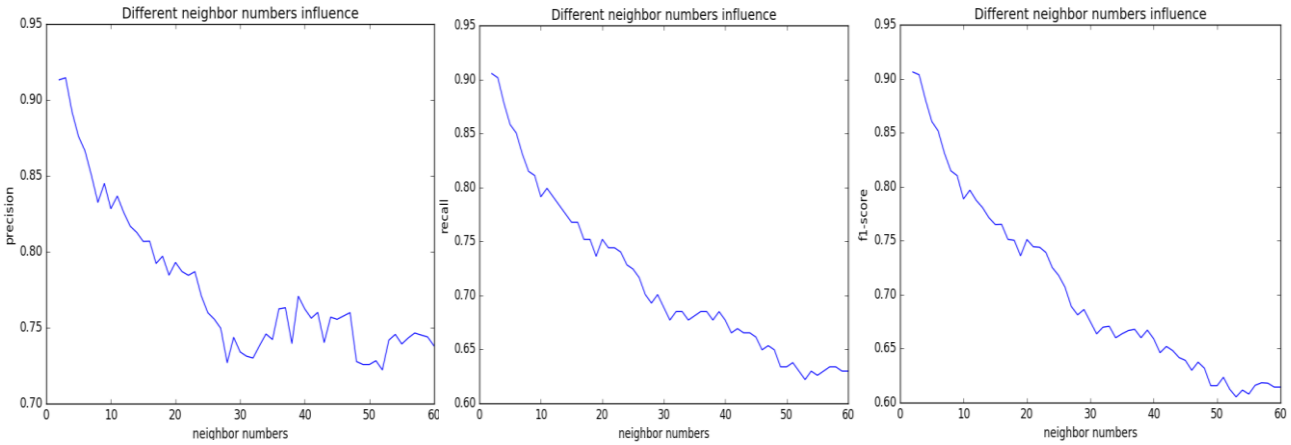

a. accuracy *b. recall rate* *c. f1 value*

Fig. 2 - The relationship between the evaluation index of KNN model and its kernel function and coefficient

Fig. 2(a) shows the relationship between the k value and the accuracy rate, wherein the abscissa represents k value while the ordinate represents the accuracy rate. As can be seen from the figure, when k value was less than 25, the smaller the k value was, the higher the accuracy rate was; when k value was greater than 25, the accuracy rate was low and showed fluctuation; when k value was greater than 55, the accuracy rate was basically smooth and steady. This phenomenon appeared for the reason that in KNN algorithm, the category of the unknown pig face data to be predicted is determined by the label of k data that are nearest to the unknown data. Therefore, the larger the k value is, the more the categories possibly contained in the k comparative values selected are. When the predicted value is equal to the one with the most labels among k samples, the accuracy may decline.

Fig. 2(b) shows the relationship between the k value and the recall rate, wherein the abscissa represents k value and the ordinate represents the recall rate. Different from the results in figure 2(a), the recall rate basically showed a decreasing trend as k value increased. However, when k reached a certain value, the recall rate was close to a fixed value.

Fig. 2(c) shows the relationship between the k value and the *f1* value, wherein the abscissa represents the k value and the ordinate represents the *f1* value. Similar to the results in figure 2(b), as k value changed, the change of *f1* value was basically consistent with the change of recall rate. As can be seen from the figure, different indicators showed different change characteristics under different k values. As for the accuracy index, its value always decreased in the first half stage when k value increased, but when k increased to a certain extent, there was a great fluctuation, while the recall rate and *f1* value basically decreased as k value continued to increase. With a comprehensive consideration of the performance of the three indicators, in this paper, the k value was taken as 3 to be the parameter for the subsequent test set in KNN model.

Evaluation index of KNN model

According to the parameter determined by the above tests, that is, the k value set to be 3 in KNN for the tests to be carried out on the test set, the prediction confusion matrix was drawn according to the test results, as shown in figure 3. The main diagonal element of the matrix represents the sample size of pig face correctly classified. The background color of each data in the matrix changed from light to dark as the value increased, and the darker the color was, the larger the value was. It can be seen from figure 3 that the KNN algorithm achieved good results in the classification of 10 pigs.

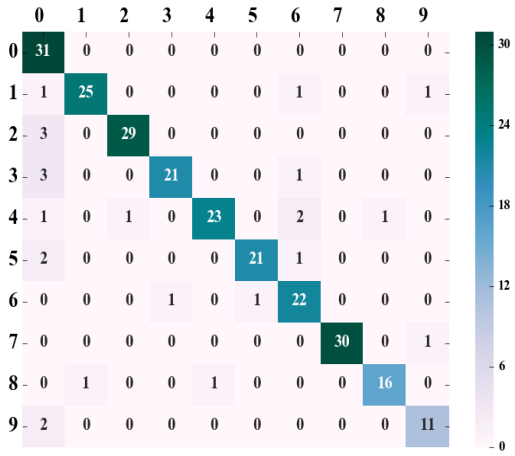

Fig. 3 - KNN prediction result confusion matrix

The prediction accuracy, recall rate and f1 value of each category are calculated in accordance with the confusion matrix, and the calculation formulas are as shown in formula (3) ~ (5). In the classification task, the results were usually divided into true positive cases (TP), false positive cases (FP), true negative cases (TN) and false negative cases (FN). With the number of samples corresponding to TP, FP, TN and FN given, the precision ratio was defined as:

$$precision = \frac{TP}{TP + FP} \tag{3}$$

Recall ratio was defined as:

$$recall = \frac{TP}{TP + FN} \tag{4}$$

Recall ratio was also called recall rate. Recall ratio and precision ratio changed in opposite trend. $f1$-score can measure the different preferences of these two indexes, and the formula was as follows

$$f1 - score = 2 \times \frac{precision \times recall}{precision + recall} \tag{5}$$

where: TP represents the number of positive samples that are actually positive samples, [a];
FP represents the number of positive samples that are actually negative samples, [a];
FN represents the number of negative samples that are actually positive samples, [a].

Table 1

KNN model prediction performance table

Category	*precision* [%]	*recall* [%]	*f1-score* [%]	Count [a]
1	72	100	84	31
2	96	89	93	28
3	97	91	94	32
4	95	84	89	25
5	96	82	88	28
6	95	88	91	24
7	81	92	86	24
8	100	97	98	31
9	94	89	91	18
10	85	85	85	13
average	91.46	90.16	90.36	25

It can be seen from table 1 that the average accuracy rate, recall rate and *f1* value of KNN algorithm for pig face data classification and recognition were up to 91.46%, 90.16% and 90.36% respectively. The effects were good.

Experiment of pig face identification with KNN + PCA pre-treatment

Determine the *k* value in principal component analysis

At the first stage of the experiment, the number of principal components needs to be determined for principal component analysis. Here the k value was taken as 300, with the variance explanation rate reaching over 95%.

Determination of KNN parameters in the optimization plan

Distribution of the data going through PCA dimension reduction may change to some extent, thus the k value determined in the previous stage may not be the optimal value when it is used to be the input for KNN algorithm. Therefore, the k value of KNN algorithm needs to be redetermined. With the testing method in "**KNN model parameter determination**" adopted, the relationships between different k values and the classification accuracy, recall rate as well as *f1* value of KNN to pig face data were measured, and the relationship curves are as shown in figure 4.

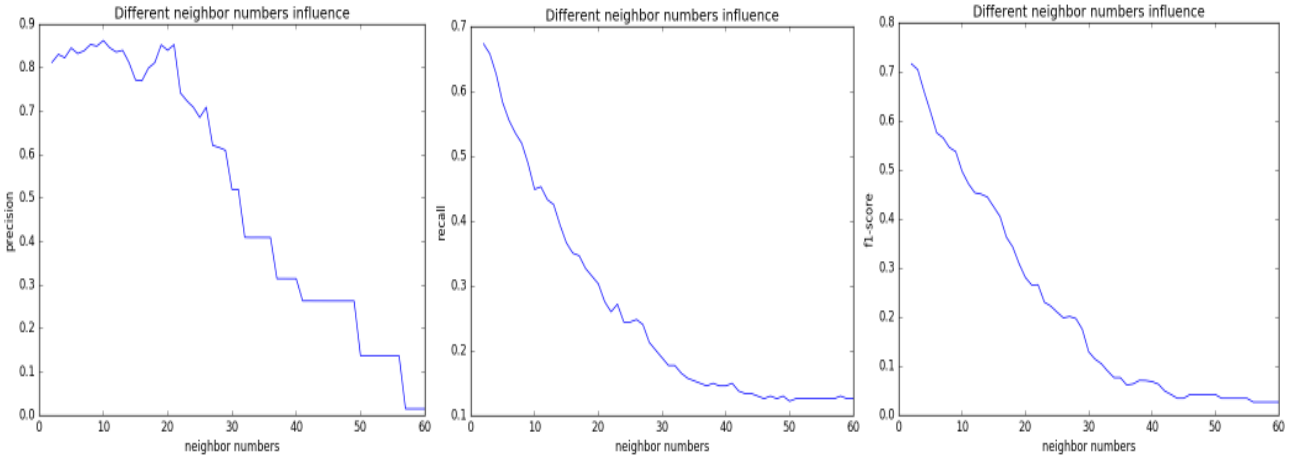

a. accuracy *b. recall rate* *c. f1 value*

Fig. 4 - The relationship between KNN model performance and parameters after PCA pre-processing

In figure 4(a), the abscissa represents k value, and the ordinate represents precision. When k is 0, the image to be tested will not be predicted to belong to any category.

When k is the maximum, the precision value is close to 0, for which the reason is that any image to be tested will be predicted to belong to the category with the largest number of samples in the data set. Obviously, in this way, the accuracy would be very low. It can be seen from the figure that the k value began with 2, and as k value increased, the accuracy fluctuated greatly. As k value increased within the range of 2~12, the precision value gradually increased, reaching 0.85. This is because a small k value makes the training error very small. The prediction can be correct only when the sample to be tested has the same or similar distribution with the training sample. When the generalization error of the classifier increases, the classification model for training will be very complex and over-fitting may occur, so at this stage, the precision increases as k value increases.

When k value exceeded 12, its corresponding precision value started to decrease and reached a stage lowest value of 0.77 when it reached 14. However, the precision value did not always decrease but rebounded and reached the highest value of 0.86 when k value reached 20. This indicates that the precision value decreases for the over-fitting situation caused by noise interference of the sample, thus the precision value may decrease for a while. As k value increases, the training data are enlarged, partly solving the over-fitting problem. Therefore, the precision value rises again.

When k value exceeded 20, its corresponding precision value was always in a declining trend, though rising slightly at 28, while falling continuously after 28. At the ranges of 30~35, 40~48, 50~57 and 58~60, several smooth and steady curves could be seen. At these smooth and steady stages, the highest precision was 0.4 and the lowest was about 0.01, which means that such predictions were meaningless.

In figure 4(b), the abscissa represents k value, and the ordinate represents recall. While precision deals with accuracy, recall solves the problem of incompleteness. An ideal model requires these two values to be high. When recall is 0, it means that all positive examples are not predicted. When recall value is 1, it indicates that all positive instances can be predicted, which is considered to be the most ideal model.

As can be seen from figure 4(b), when k value was 2, its recall value reached the peak, and then it kept declining. When k value was 10, it stayed flat slightly before continuing to decline. When k value was 21, it rose slightly, and then kept declining. The whole declining process gradually got flat and remained unchanged after k value turned 50. When k was 2, recall reached the maximum value of 0.68. According to the probability theory, the more the sample points are, the more categories it is likely to contain; conversely, the fewer the sample points are, the fewer categories it is likely to contain. According to KNN principle, when k value is small, the more probable it can correctly predict positive samples, if stated in the figure, recall will be at a high position. As k value increased, the probability of correctly predicting positive samples got gradually decreasing, and its curve was in a downward trend.

As can be seen from figure 4(a), the precision value was obviously interrupted by noise when k value reached 14. It was not obvious in recall curve showing only being slightly flat. The prediction error rate gradually decreased as k value increased, that is why the curve gradually turned placid. When k exceeded 30, its precision was lower than 0.5, which means that such prediction was meaningless. When k exceeded 50, the prediction was basically wrong, and the curve was basically in a horizontal state with a very small value, which was about 0.12 as in the figure. Considering precision and recall values comprehensively, k should be within 2~8. In this range, it can be ensured that the recall value was greater than 0.5 and the precision value was greater than 0.8 and in an upward trend.

For *f1*, the classification accuracy rate and recall rate needs to be considered. With a value range of 0~1, *f1* score assumes that accuracy and recall rate are equally important, so the one with a bigger value shall be chosen. In figure 4 (c), it can be seen that when the k value was 2, *f1* score was 0.72. As k increased, *f1* score was in decline, though it rose slightly in the middle. After k exceeded 40, the *f1* value remained basically at about 0.02. With all the three factors considered, going through tests on the training set, the k value of KNN was finally selected to be 5 before it got tested on the validation set.

Model evaluation index of optimization plan

The principal component value of principal component analysis measured on the training set was selected to be 300, and the k value of KNN classifier was selected to be 5, and they were tested in the test set. With the test results, the confusion matrix was drawn, as shown in figure 5.

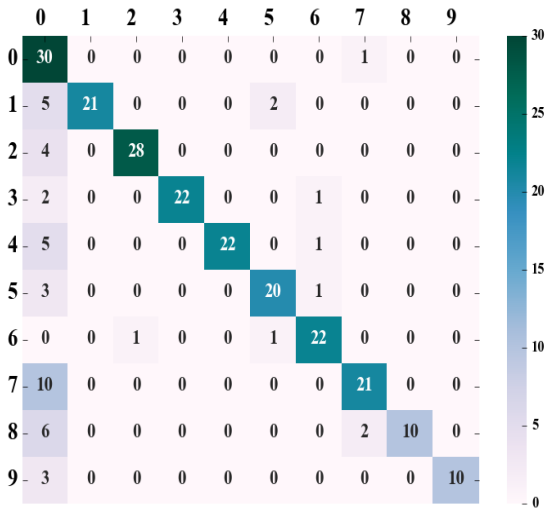

Fig. 5 - PCA+KNN prediction result confusion matrix

The precision, recall and *f1*-core values of 10 different pigs were obtained in accordance with the confusion matrix and formulas (6) ~ (8), as shown in table 2.

Table2

PCA+KNN model prediction performance table

Category	Precision [%]	Recall [%]	f1-score [%]	Count [a]
1	25	100	40	31
2	93	50	65	28
3	78	66	71	32
4	100	52	68	25
5	100	36	53	28
6	67	50	57	24
7	100	54	70	24
8	92	39	55	31
9	100	56	71	18
10	92	85	88	13
average	82.82	57.87	61.86	25

As can be seen from table 2, the average precision of PCA+KNN classifier for 10 classified pig samples reached 82.82% after feature extraction by principal component analysis. With individual pig identification with KNN + PCA pre-treatment, the identification accuracy got reduced to a certain extent, though the training time and test time were greatly improved. The specific test indexes of the two schemes are shown in table 3.

Table3

The optimization result of KNN model by PCA pre-processing

Model	Precision [%]	Precision change	Test_time [ms]	Test_ new / old [%]	Train_time [ms]	Traintest_ new / old [%]
KNN	91.46		1,306		187	
PCA+KNN	82.82	-8.64	93	7	9	4.8

As can be seen from table 3, in the test, in the PCA+KNN test scheme, the training time and the recognition time were 9 ms and 93 ms respectively, while the precision, the training time and the identification time of KNN classifier without feature extraction by principal component analysis were 91.46%, 187 ms, and 1,306 ms respectively, indicating a decrease in the identification accuracy and a great rise in operating speed. The training time was 4.8% of the original value in the KNN alone scheme, while the identification time was 7% of the original value.

PCA+KNN test results showed that the precision decreased from 91.46% to 82.82%, which may be caused by the difference in data distribution between the test set and the training set. The much noise in pig samples in the test set was also one of the reasons for the reduced accuracy. The operating efficiency got significantly improved: the training time and the identification time were reduced to 4.8% and 7% of the original values respectively, much better than the expected test effects. Probably the reason is that going through the PCA feature extraction, on the one hand, pig facial features for calculation got reduced, thus reducing the amount of calculation and enhancing the efficiency of the algorithm; on the other hand, some minor features were eliminated while the main features were extracted, thus the image noise was eliminated and the noise reduction effect was achieved. Theoretically, it is predicted that both the recognition accuracy and the operating efficiency of the algorithm would be improved.

The experimental results showed that the precision was reduced to a certain extent, which was different from the expected effect of the test. It could be adjusted in the distribution of sample types, but the accuracy still remained at 82.82%. With the operating efficiency of the algorithm greatly improved, the loss of accuracy was within an acceptable range.

CONCLUSIONS

In this paper, the influence of PCA pre-treatment mode on the efficiency of identification of 10 different pigs with a KNN classifier employed was studied. The parameter for the classifiers was determined via tests. With the influence of two test methods on identification efficiency compared, in which one adopting the KNN classifier alone and the other adopting PCA+KNN, we got the following conclusions:

(1) When KNN classifier is used for individual pig identification, the selection of kernel function is related to the pre-treatment method. When the KNN alone scheme is adopted, the parameter value can be 3; while the PCA+KNN scheme is adopted, the parameter value can be 5;

(2) PCA pre-treatment can benefit the efficiency of individual pig identification with KNN adopted, with the accuracy decreasing to 82.82% from 91.46%, and the training time as well as testing time reduced to 4.8% and 7% of the original value respectively;

(3) KNN classifier going through PCA pre-treatment is more suitable for the application of mobile terminals and embedded devices, so it suits to the development of a portable and real-time pig face identification system.

ACKNOWLEDGEMENTS

This research, titled 'Study on the Influence of PCA Pre-treatment on Pig Face Identification with KNN', was funded by the National Key Research and Development Plan of China (2016YFD0701801), the Shanxi Province Basic Research Program Project (Free Exploration) (Grant No.20210302124523, 202103021224149, 202103021223141), the Doctor Scientific Research Foundation of Shanxi Agricultural University (2020BQ14). The authors are grateful and honored to have obtained support from the Key Laboratory of Biomechanics.

REFERENCES

[1] Adrion F, Kapun A, Holland E, et al., (2017), Novel approach to determine the influence of pig and cattle ears on the performance of passive UHF-RFID ear tags, *Computers and Electronics in Agriculture*, Vol.140, pp.168–179, Oxford/England;

[2] Dasarathy, B.V., (1991), *Nearest neighbor (NN) norms: NN pattern classification techniques*, IEEE Computer Society, pp.5-20, Hoboken/ USA;

[3] Fix E., Hodges J.L., (1989), Discriminatory analysis-nonparametric discrimination: consistency properties, *Revue Internationale de Statistique*, Vol.57, Issue 3, pp.238-247, California/USA;

[4] Gorczyca M. T., Hugo F. M., Alex S. C., et al., (2018), Machine learning algorithms to predict core, skin, and hair-coat temperatures of piglets*, Computers and Electronics in Agriculture,* Vol.151, pp.286–294, Oxford/England;

[5] Hahnel D, Burgard W, Fox D, et al., (2016), Mapping and localization with RFID technology. *IEEE International Conference on Robotics and Automation*, pp.1015-1020, Los Angeles/USA;

[6] He Y.Q., Tiezzi F., Jeremy H., et al., (2021), Predicting body weight in growing pigs from feeding behavior data using machine learning algorithms, *Computers and Electronics in Agriculture*, Vol.184, pp.106085, Oxford/England;

[7] Hu Z.W., Yang H., Lou T.T., (2021), Dual attention-guided feature pyramid network for instance segmentation of group pigs, *Computers and Electronics in Agriculture*, Vol.186, pp.106140, Oxford/England;

[8] Jarissa M., Wouter S., Petra B., et al., (2016), Methods to construct feeding visits from RFID registrations of growing-finishing pigs at the feed trough, *Computers and Electronics in Agriculture*, Vol.128, pp.9–19, Oxford/England;

[9] Lin H. , Sheng H. , Sun G.X. , et al., (2021), Identification of pumpkin powdery mildew based on image processing PCA and machine learning, *Multimedia Tools Applications*, Vol.80, Issue 14, pp.21085-21099, Dordrecht / Netherlands;

[10] Marsot M., Mei J.Q., Shan X.C., et al., (2020), An adaptive pig face recognition approach using Convolutional Neural Networks. *Computers and Electronics in Agriculture*, Vol.173 pp.105386, Oxford/England;

[11] Maselyne J, Saeys W, Ketelaere B, et al., (2014), Validation of a High Frequency Radio Frequency Identification (HF RFID) system for registering feeding patterns of growing-finishing pigs. *Computers and Electronics in Agriculture*, Vol.102 pp.10-18, Elsevier, Oxford/England;

[12] Shi Y.W., Zhang Y.Q., Liu K.S., (2012), Research on Security Issues Based on RFID System, *Computer Science*, Vol.39, Issue 6A, pp.214-216, Chongqing/China;

[13] Tu S., Yuan W., Liang Y., Wang F., Wan H., (2021), Automatic Detection and Segmentation for Group-Housed Pigs Based on PigMS R-CNN, *Sensors,* Vol.21, Issue 9, pp.3251, Basel/ Switzerland;
[14] Wongsriworaphon A., Arnonkijpanich B., Pathumnakul S., (2015), An approach based on digital image analysis to estimate the live weights of pigs in farm environments*, Computers and Electronics in Agriculture*, Vol.115, pp.26–33, Oxford/England;
[15] Yan H.W., Liu Z.Y., Cui Q.L., et al., (2020), Multi-target Pig Detection Based on Feature Pyramid Attention and Deep Convolutional Network*, Transactions of the Chinese Society of Agricultural Engineering,* Vol.36, Issue 11, pp.193–202, Beijing/China;
[16] Yan H.W., Liu Z.Y., Cui Q.L., et al., (2019), Detection of facial gestures of group pigs based on improved Tiny-YOL, *Transactions of the Chinese Society of Agricultural Engineering,* Vol.35, Issue 18, pp.169–179, Beijing/China;
[17] Yan H.W., Cui Q.L., Liu Z.Y., (2020), Pig Face Identification Based on Improved AlexNet Model, *INMATEH-Agricultural Engineering*, Vol.61, Issue 2, pp.97-104, Bucharest/Romania; https://doi.org/10.35633/inmateh-61-11
[18] Zhang J.L., Zhuang Y.R., Ji H.Y., Teng G.H., (2021), Pig Weight and Body Size Estimation Using a Multiple Output Regression Convolutional Neural Network: A Fast and Fully Automatic Method, *Sensors*, Vol.21, Issue 9, pp.3218, Basel/ Switzerland;
[19] Zhang Y.Z.*,* Guo Y.N.*,* (2021), Train Driver State Detection System Based on PCA and SVM, *Artificial Intelligence and Security - 7th International Conference*, Vol.12736, pp.516-526, Dublin/Ireland;
[20] Zhou J., Lu J.Z., Tu Y.Z., (2018), Discussion on the use of intelligent recognition terminal to promote the management of animal ear tags, *The Chinese Livestock and Poultry Breeding*, Vol,14, Issue 5, pp.33-34, Beijing/China.

ANALYSIS ON THE UNIFORMITY OF SEED SOWING IN THE SPRAYING MACHINE OPERATING ON THE GRASSLAND
/
草地作业喷播机喷播落种均匀性分析

Chen YAN, Wenxia ZHANG*), Guo HUA, Fu SHI, Zhang RUI, Zhang MING [1]
Department of Information Engineering, Ordos Institute of Technology, Compass, Ordos/ China
Tel: +815548555828; E-mail: zhangwenxia100@163.com
Corresponding author: Wenxia ZHANG
DOI: https://doi.org/10.35633/inmateh-70-09

Keywords: *spraying uniformity, falling trajectory, compensation mechanism, opening height*

ABSTRACT
In the process of revegetation of degraded grassland by pneumatic seed sprayer, the working parameters of the sprayer, such as the position of the sprayer and the air velocity of the inlet of the sprayer, have an impact on the uniformity of spraying. In this paper, 4BQD-40C pneumatic sprayer is taken as the research object. The influence of the compensation mechanism on the airflow velocity at the inlet of the barrel nozzle and the spraying quality is analyzed. The conclusions show that: (1) The planting trajectory of the sprayer inlet compensation mechanism is analyzed, and the planting trajectory equation is obtained, which lays a foundation for subsequent research. (2) The influence law of the opening height on the inlet airflow velocity of the nozzle is obtained, and the drop trajectory is adjusted by adjusting the inlet airflow velocity of the nozzle, and the area of the missed seeding area is reduced. (3) The time points of opening height adjustment and reset of the compensation mechanism in one cycle were obtained. At the same time, there is a lag time t_1 due to changing the seed drop trajectory by adjusting the nozzle inlet airflow velocity. Due to this lag time, the compensation mechanism can be used to change the seed drop trajectory when the swing frequency is less than 7.3 min^{-1} to achieve optimization of the reseeded and missed seeding areas.

摘要
气力喷播机对退化草地进行植被修复的过程中，喷播机的工作参数，如喷播机姿态和喷筒入口气流速度对喷播均匀性均有影响。本文以4BQD-40C型气力喷播机为研究对象，分析安装喷筒补偿机构后喷筒入口气流速度对喷播质量的影响。结论表明：(1)分析了喷播机喷筒入口加装补偿机构的落种轨迹，得到了落种轨迹方程，为后续研究奠定基础。(2)得到了补偿机构开口高度对喷筒入口气流速度的影响规律，并且通过调节喷筒入口气流速度，调节落种轨迹，减小漏播区域面积。(3)得到1个周期内补偿机构开口高度调节的时间点与复位的时间点；同时由于通过调节喷筒入口气流速度改变落种轨迹时存在滞后时间 t_1，受限于该滞后时间，当摆动频率小于7.3 min^{-1} 时，可通过补偿机构改变落种轨迹，实现对落种区域重播、漏播面积的优化。

INTRODUCTION
Judging from the early spraying test, the spraying operation is a technical measure to restore grassland vegetation with faster speed and high efficiency under natural climatic conditions. The relevant research on the restoration of grassland vegetation by pneumatic spraying has achieved important research results (*Chen et al., 2022; Wang et al., 2015; Zhang et al.,2013; Xuan et al., 2016; Zhang et al., 2013; Tai et al., 2022; Zhang et al., 2022*). However, in the process of revegetation of degraded grassland by pneumatic seed sprayer, the working parameters of the sprayer, such as the influence of sprayer position, sprayer structure (*Grella et al., 2022)*, reservoir units optimization (*Liu et al., 2019*), sprayer working airflow and spraying amount on spraying uniformity, air speed and liquid flow rate on the droplet size and homogeneity (*Balsari et al., 2018)*, the vertical position and constructional variants of the diffuser (*Gierz et al., 2020)*, shaping air holes (*Li et al., 2019*), surface coverage by impact of droplets (*Dalili, et al., 2020*), and the relationship with the existing grassland vegetation cover were not considered (*Sylvain et al., 2022; Tai et al., 2022*).

[1]*Yan Chen, Lecturer Ph.D. Eng.; Wenxia Zhang, Prof M.S. Eng.; Hua Guo, Prof M.S. Eng.; Shi Fu, Lecturer M.S. Eng.; Rui Zhang, Lecturer M.S. Eng.; Ming Zhang, Lecturer M.S. Eng.*

When 4BQD-40C pneumatic sprayer is spraying, under the action of airflow of the seed delivery pipe, the ice grass seeds go from the seed discharge area to the seed dropper. Seeds in the seed dropper are attracted by the negative pressure of the main air duct throat, suspended and accelerated into the main air duct, and then sprayed out with the high-speed airflow of the barrel nozzle. The sprayer moves forward. At the same time the sprayer barrel nozzle swings from 0° to 180° in the horizontal plane. (*Fan et al., 2013; Chen et al., 2018*).

The inlet airflow velocity of the sprayer canister is provided by the fan. Due to the fact that the fan rotational inertia is large, it takes a long time to adjust the inlet airflow velocity of the sprayer by changing the fan speed, and the swing frequency of the sprayer is faster, so the seed falling trajectory cannot be changed in real time by adjusting the fan speed. In order to further improve the uniformity of spraying and improving the quality of spraying, a spraying uniformity compensation mechanism (hereinafter referred to as the compensation mechanism) is designed and installed at the entrance of the barrel nozzle. The real-time adjustment of the airflow velocity at the inlet of the spray drum is realized by adjusting the opening height of the mechanism. This mechanism can change the seed drop trajectory and improve the uniformity of spraying and falling seed. This paper focuses on the relationship between the position of 4BQD-40C sprayer and the seed drop area, the relationship between the airflow velocity at the inlet of the barrel nozzle and the seed drop area. Adjust the airflow velocity at the inlet of the barrel nozzle by installing a spraying uniformity compensation mechanism. This method changes the trajectory of seed fall, at the same time it can improve the spraying uniformity and improve the quality of spraying.

MATERIALS AND METHODS

Analysis of compensation mechanism location

The 4BQD-40C sprayer can adjust the airflow velocity at the inlet of the nozzle by increasing the airflow channel. Therefore, a compensation mechanism is installed at the inlet of the sprayer to adjust the airflow velocity at the inlet of the sprinkler. The compensation mechanism is shown in Fig.1, h_b is the opening height of that mechanism, ε_b is the angle of the sector area corresponding to the mechanism opening area, r_b is the radius of the mechanism circulation cross-sectional area ($r_b = 25\ mm$), and S_b is the opening area of the mechanism.

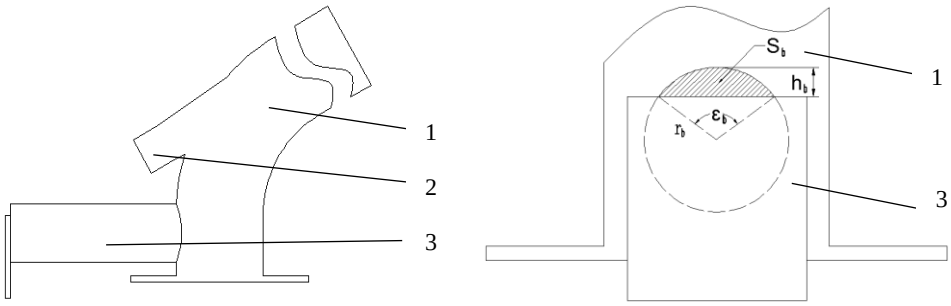

Fig. 1 - Schematic diagram of compensation mechanism
1 – Sprayer; 2 – Seed tube; 3 – Compensation mechanism

The opening height of the compensation mechanism affects the airflow velocity in the barrel nozzle, and its installation position affects the air flow distribution in the barrel nozzle. Therefore, the installation position is numerically simulated to find out its optimal installation position. The air flow enters the nozzle through the throat pipe from the fan outlet, and the seed ejection speed is mainly formed in the seed tube insertion section in the nozzle. Therefore, the compensation mechanism can be installed at the entrance of the nozzle or the sprayer throat to adjust the inlet air velocity.

The airflow distribution in the nozzle corresponding to different installation positions of the compensation mechanism was simulated using Fluent software. In this paper, the diameter of this mechanism is 50 mm, and the mechanism is set to be fully open and the air velocity at the nozzle inlet is 60 m/s. The simulation analysis is carried out for the installation positions of the compensation mechanism at 30 mm, 50 mm and 80 mm away from the connection between the nozzle and the throat. The simulation results are shown in Fig. 2. (*Shivam et al., 2022; Yin et al., 2022; Tao et al., 2020*).

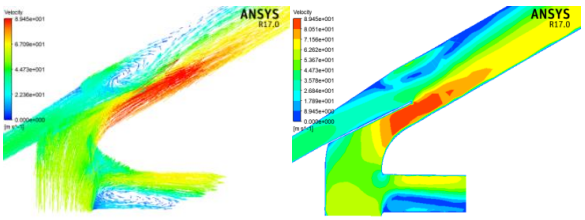

(a) The compensation mechanism is located 30 mm from the connection between the barrel nozzle and the **hose**

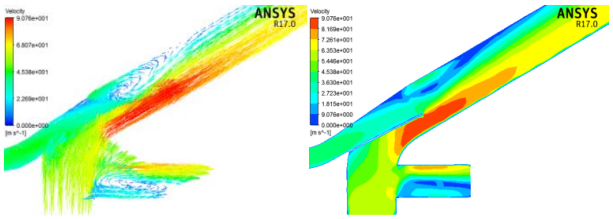

(b)The compensation mechanism is located 50 mm from the connection between the barrel nozzle and the hose

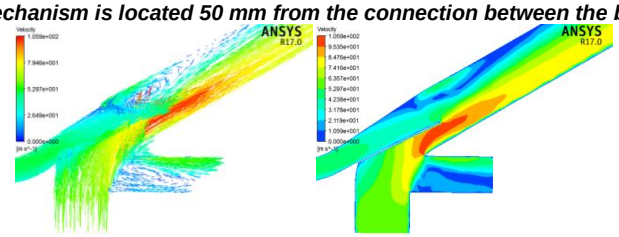

(c)The compensation mechanism is located 80 mm from the connection between the barrel nozzle and the **hose**

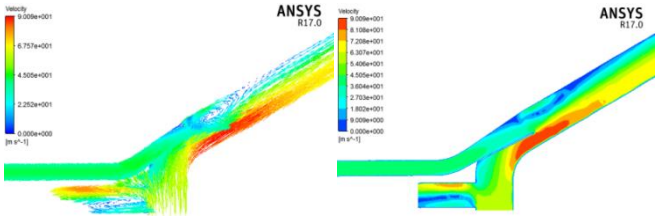

(d)The installation position of the compensation mechanism is opposite to (a)

Fig. 2 - Influence of installation position of the compensation mechanism on air distribution in barrel nozzle

From the numerical simulation results, it can be seen that different installation positions of the compensation mechanism have different effects on the airflow in the barrel nozzle. When the distance of the compensation mechanism from the throat connection is changed from 80 mm to 30 mm, the airflow in the insertion section of the seed tube is reduced from 105.9 m/s to 90.0 m/s. The installation position of the compensation mechanism is closer to the insertion section of the seed tube, which is a big change to the original structure. It is easy to cause the airflow direction to shift from the centre of the nozzle to the edge of the nozzle. This causes the seed to accelerate towards the wall of the nozzle, and at the same time causes seed breakage. Comparing Fig. 2(a) and 3(d), it can be seen that the compensation mechanism has less influence on the direction of the airflow in the nozzle cylinder when it is installed at the position as shown in Fig. 2(d). Therefore, the compensation mechanism is selected to be installed at the mounting position shown in Fig. 2(d).

When the air velocity is 55 m/s, the numerical simulation is carried out for the opening heights of 5 mm, 10 mm, 15 mm, 20 mm, 25 mm, and 32.5 mm, and the simulation results are shown in Fig. 3.

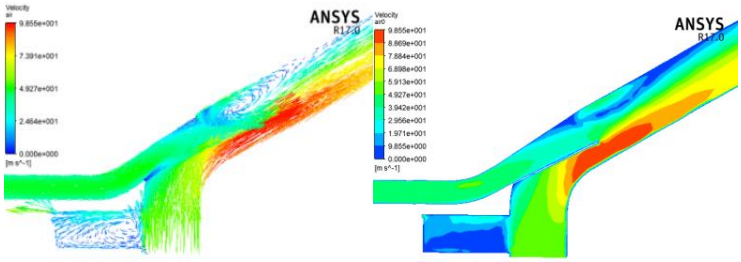

(a) The opening height of 5 mm

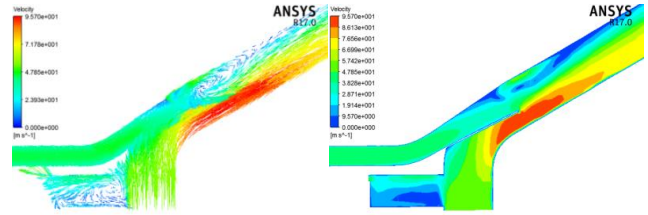

(b)The opening height of 10 mm

(c)

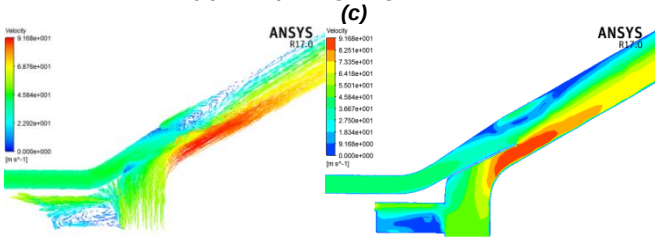

(d)The opening height of 15 mm

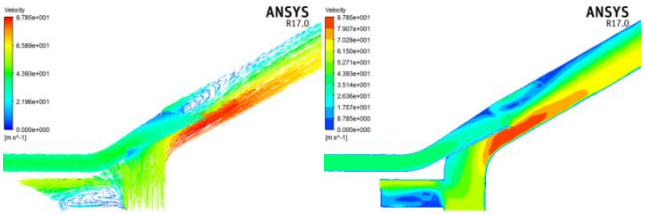

(e)The opening height of 20 mm

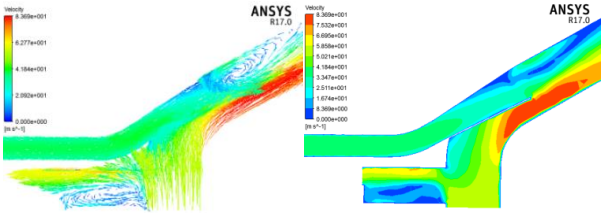

(f) The opening height of 25 mm

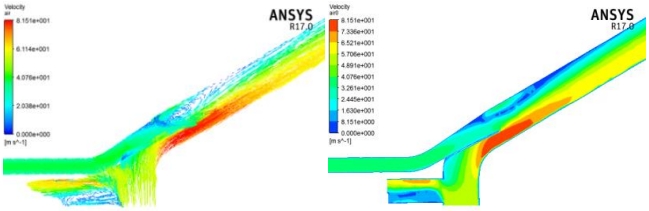

(f) The opening height of 30 mm

Fig. 3 - Influence of opening height of compensation mechanism on gas flow distribution in barrel nozzle inlet

From the numerical simulation results, the relationship between the compensation mechanism opening height and the air velocity at the inlet of the nozzle can be obtained as shown in Table 1. It can be seen from Table 1 that the larger the opening height of that mechanism, the greater the influence on the inlet airflow velocity of the nozzle. But when the opening height exceeds the radius of that mechanism, increasing the opening height has less and less effect on the inlet airflow velocity of the nozzle.

Table 1

Relationship between opening height of compensation mechanism and air velocity at inlet of barrel nozzle after splitting

Compensate for the opening height of the mechanism [mm]	5	10	15	20	25	30
Nozzle inlet airflow velocity after shunting [m/s]	53.8	51.5	49.3	47.5	45.8	44.2
The velocity of the nozzle outlet after shunting [m/s]	67.6	66.1	62.1	59.3	57.0	55.6

It can also be seen from Table 1 that as the opening height increases, the airflow velocity entering the insertion section decreases. However, the proportion of airflow velocity reduction is not proportional to the height of the opening. Due to the fact that the compensation mechanism is a circular pipe, the relationship between the opening height and area of the mechanism installed on the bypass pipe can be converted by equations (1) and (2). The ε_b is the angle of the sector area corresponding to the mechanism opening area.

When the opening height is $h_b \leq r_b$:

$$\begin{cases} \varepsilon_b = 2 \times arccos\left(\frac{r_b - h_b}{r_b}\right) \\ S_b = \frac{\varepsilon_b}{360} \times \pi \times r_b^2 - \frac{1}{2} r_b^2 \times \sin(\varepsilon_b) \end{cases} \quad (1)$$

When the opening height is $r_b < h_b < 2r_b$

$$\begin{cases} \varepsilon_b = 2 \times arccos\left(\frac{h_b - r_b}{r}\right) \\ S_b = \frac{360 - \varepsilon_b}{360} \times \pi \times r_b^2 + \frac{1}{2} r_b^2 \times \sin(\varepsilon_b) \end{cases} \quad (2)$$

After converting the area according to the above formula, the relationship between the opening area of the compensation mechanism and the inlet airflow velocity of the nozzle is shown in Table 2.

Table 2

The relationship between the opening area of the compensation mechanism and air velocity at inlet barrel nozzle after splitting

compensation mechanism opening area [mm²]	102.0	279.3	495.0	732.9	981.2	1229.6
Nozzle inlet airflow velocity after shunting [m/s]	53.8	51.5	49.3	47.5	45.8	44.2
The amount of speed reduction [m/s]	1.2	3.5	5.7	7.5	9.2	10.8

Table 2 shows that when the airflow velocity before adjusting is 55 m/s, the correspondence between the opening area and the inlet airflow velocity of the nozzle after shunting is:

$$\vartheta'_{pr} = 55.0 - 0.0083 \times S_b - 1.0213 \quad (3)$$

In the formula, S_b represents the area of the opening of this mechanism and ϑ'_{pr} represents the inlet airflow velocity of the nozzle after shunting.

From the above analysis, it can be seen that adjusting the opening height of the compensation mechanism can change the inlet airflow velocity of the nozzle. The seed drop trajectory can be changed by adjusting the opening height of the compensation mechanism during spraying. This can further reduce the reseeding and missed seeding area of the seed falling area.

The analysis of the sprayer shows that when the oscillation frequency of the barrel nozzle is optimized, the seeds fall in the same trajectory. At this point, the idea of optimizing the seed drop area is used to determine the compensation mechanism start adjustment time, end adjustment time and opening height.

The opening height of the compensation mechanism is adjusted to reduce the missed seeding area of the seed drop area and to improve the spraying quality. The goal of optimizing the missed seeding area is to minimize it by adjusting the opening height of the compensation mechanism without increasing the reseeding area. From the above analysis, it can be seen that when the swing time of the spray drum is 0.5T~T, the seed drop trajectory is changed by adjusting the opening height of this mechanism. The offset distance of the seed trajectory is d_L, and the d_L<8 m is set.

From the analysis of the seed drop trajectory formula of the sprayer, it can be seen that the optimization of the missed seeding area of the seed drop region should be in the time [0.71T, T]. The seed drop trajectory in the first 1/2 cycle is symmetric with the second 1/2 cycle. Therefore, the missed seeding area is optimized during the [0.29T, 0.5T] time of the first 1/2 cycle.

After the optimization of the seed drop area, the compensation mechanism starts to regulate at 0.34T and 0.84T in 1 nozzle swing cycle, the recovery time is 0.44T and 0.94T. The seed drop trajectory regulation distance $d_L = 2.8\,m$, at this time, the seed drop trajectory curve formula is (*Cao et al., 2023*):

$$\begin{cases} x_1 = R \cdot cos\omega t \\ y_1 = R \cdot sin\omega t - \vartheta \cdot t \end{cases} \quad t \in (0, 0.34T) \cup (0.44T, 0.5T) \quad (4)$$

$$\begin{cases} x_1 = (R + d_L) \cdot cos\omega t \\ y_1 = (R + d_L) \cdot sin\omega t - \vartheta \cdot t \end{cases} \quad t \in (0.34T, 0.44T) \quad (5)$$

$$\begin{cases} x_2 = r \cdot cos\omega t \\ y_2 = r \cdot sin\omega t - \vartheta \cdot t \end{cases} \quad t \in (0,0.34T) \cup (0.44T, 0.5T) \quad (6)$$

$$\begin{cases} x_2 = (r + d_L) \cdot cos\omega t \\ y_2 = (r + d_L) \cdot sin\omega t - \vartheta \cdot t \end{cases} \quad t \in (0.34T, 0.44T) \quad (7)$$

$$y_3 = -\vartheta \cdot t \quad t = 0, x \in [r, R] \quad (8)$$

$$y_4 = -\vartheta \cdot t \quad t = 0.5T, x \in [-r, -R] \quad (9)$$

$$\begin{cases} x_5 = R \cdot cos(\pi - \omega t) \\ y_5 = R \cdot sin(\pi - \omega t) - \vartheta \cdot t \end{cases} \quad x \in (0.5T, 0.84T) \cup (0.94T, T) \quad (10)$$

$$\begin{cases} x_5 = (R + d_L) \cdot cos(\pi - \omega t) \\ y_5 = (R + d_L) \cdot sin(\pi - \omega t) - \vartheta \cdot t \end{cases} \quad t \in (0.84T, 0.94T) \quad (11)$$

$$\begin{cases} x_6 = r \cdot cos(\pi - \omega t) \\ y_6 = r \cdot sin(\pi - \omega t) - \vartheta \cdot t \end{cases} \quad x \in (0.5T, 0.84T) \cup (0.94T, T) \quad (12)$$

$$\begin{cases} x_6 = (r + d_L) \cdot cos(\pi - \omega t) \\ y_6 = (r + d_L) \cdot sin(\pi - \omega t) - \vartheta \cdot t \end{cases} \quad t \in (0.84T, 0.94T) \quad (13)$$

$$y_7 = y_3 - \vartheta \cdot t \quad t = T, x \in [r, R] \quad (14)$$

Based on the above analysis, the opening height of the compensation mechanism can be adjusted to obtain the seed drop trajectory as shown in Fig. 4.

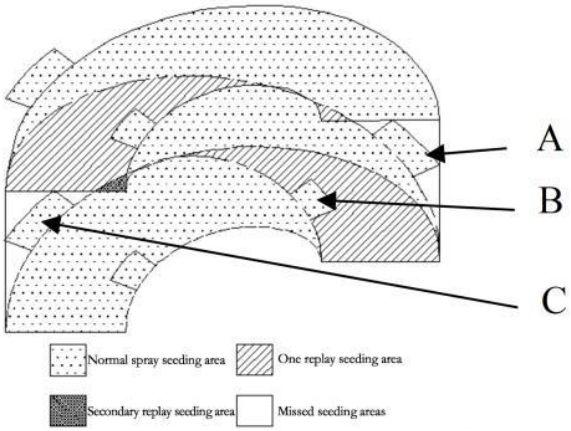

Fig. 4 - Diagram of the seed drop area after adjustment of the compensation mechanism

As can be seen in Fig. 4, there is a large area of missed seeding before the seed drop trajectory is not adjusted. Area A changed from a missed seeding area to a normal spraying area when the seed drop trajectory is adjusted using the compensation mechanism. The missed seeding area of the barrel nozzle was reduced by 28.3% in one swing cycle. Area B changed from a reseeded area to a normal sprayed area and the reseeded area decreased by 14.1%. The optimization of the seed drop area using the compensation mechanism not only reduces the area of missed seeding, but also reduces the area of reseeding. Area C is the new seed drop area after compensating for the missed seeding area in the later swing cycle. The seed drop trajectory of the sprayer has symmetry, so the areas of region A and region C are equal.

Seeds are sprayed onto the land from the seed delivery tube. The spraying time includes the time of acceleration of the seed inside the canister, and the time of movement of the seed from the outlet of the canister to the land. The use of the compensation mechanism to adjust the seed drop trajectory increases the compensation mechanism response time t_{11}, and the transition time t_{12} for the change in velocity of the seed caused by the adjustment of the airflow velocity at the nozzle inlet. In the actual use of the compensation mechanism to regulate the seed drop trajectory, it is necessary to determine t_{11} and t_{12}, which in turn determines the regulation lead time in the actual regulation process t_1.

From the above analysis, it can be seen that when the inlet air velocity of the barrel nozzle is adjusted by the compensation mechanism, the trajectory of the seed drop is changed. In the actual regulation process due to the data transmission and the response of the controller and actuator there is a certain lag, so that the compensation mechanism has a response time t_{11}. This response time is determined by the compensation mechanism and the control system.

The stepper motor type 86BYGH-350E and the ball screw model SFU1204-3 adjust the opening height of the compensation mechanism. This mechanism was tested to obtain the system response time shown in Table 3.

Table 3

Compensation mechanism response time at different opening heights

Compensate for the opening height of the mechanism [mm]	5	10	15	20	25	30
System response time [s]	0.29	0.35	0.37	0.39	0.40	0.41

As can be seen from Table 3, the system response time does not change much when the opening height of the compensation mechanism is increased. The system response time is 0.41 s when the opening height of the compensation mechanism is 30 mm. From the above analysis, the time to adjust the opening height of the compensation mechanism is [0.29T, 0.34T]. The compensation mechanism starts to adjust at 0.29T and adjusts appropriately at 0.34T. The reset time of the compensation mechanism is [0.44T, 0.5T].The compensation mechanism starts to reset at 0.44T and returns to its original position at 0.5T. Therefore, the length of time to adjust the compensation mechanism is 0.05T and 0.06T. When the length of time for adjusting the compensation mechanism 0.05T is greater than the maximum response time of the system 0.41 s, and the oscillation frequency of the barrel nozzle is less than 7.3 min^{-1}, this mechanism can be used to adjust the seed drop trajectory in order to reduce the missed seeding area.

From the simulation analysis, it can be seen that when the airflow velocity at the inlet of the barrel nozzle is changed, the seed velocity inside the barrel nozzle is changed accordingly. There is a transition time t_{12} for the seed to reach the desired velocity from the initial velocity at the nozzle outlet. The speed of seed is continuously changing inside the barrel nozzle. The transition time for the accelerated movement of the seed to the required velocity at the nozzle exit after adjusting the compensation mechanism is t_{12}. Analysing the time t_{12} taken for the seed to move from the insertion section to the exit of the spray canister, the acceleration of the seed inside the spray canister is approximated as a uniformly accelerated process.

The seed acceleration time in the spray canister can be calculated by formula (15).

$$t_{12} = \frac{2l}{v_c + v_r} \tag{15}$$

In the formula l is the length of the barrel nozzle, l= 1.5m, v_c is the speed of movement of the seed in the insertion section of the nozzle, v_r is the speed at which the seed moves at the outlet of the barrel nozzle.

When the compensation mechanism adjusts the airflow rate at the inlet of the nozzle, the airflow rate inside the nozzle changes gradually. The start time for adjusting the opening height of the compensation mechanism should be advanced $t_1 = t_{11} + t_{12}$. At this time, the compensation mechanism opening height adjustment time becomes $0.34T - t_1$,$0.44T - t_1$,$0.84T - t_1$and$0.94T - t_1$, that can ensure the actual seed drop trajectory is the same as the theoretical analysis.

Test

The test was conducted in a flat soil site at Inner Mongolia Agricultural University. The test conditions were wind speed less than 1 m/s and temperature of 15-20°C. The experimental equipment used for this test was: 4BQD-40C pneumatic seed sprayer, a number of coated ice grass seeds, a 9565-P multifunctional air gauge of TSI in the United States, a hot wire wind speed probe, a tape measure, a stopwatch, and a number of white powders.

The designed compensation mechanism is mounted on the lower end of the nozzle. The test is mainly completed by adjusting the opening height of the compensation mechanism to test the air velocity at the outlet of the nozzle in a seedless state. Test the effect of the compensation mechanism on the spraying quality by adjusting the opening height of this mechanism in the presence of seed.

Nozzle outlet air velocity test

Ensure that seed boxes, seed delivery tubes, and barrel nozzle are clear and free of seed prior to test. The frequency converter was adjusted so that the air velocity at the nozzle inlet was 40 m/s during the test. The air velocity at the nozzle outlet was tested when the opening height of the compensation mechanism was adjusted to 0 mm, 5 mm, 10 mm, 15 mm, 20 mm, 25 mm and 30 mm. The probe is placed at the nozzle outlet perpendicular to the nozzle centreline. The probe is faced the direction of the incoming flow. The nozzle outlet air velocity is tested after the anemometer data has stabilized. The centre of the nozzle is selected as the measuring point and 10 instantaneous values are recorded. Then the average value is calculated.

Spray quality test

Follow the test procedure to adjust the sprayer prior to the test. The grid of the test area was also divided. The air velocity at the nozzle inlet was set to 55 m/s by a frequency converter before the test. At the same time, the opening height of the compensation mechanism was adjusted. When the opening height is 13.6 mm, the airflow at the nozzle inlet is reduced from 55 m/s to 50 m/s. The sprayer was loaded with coated ice grass seeds at this time. The sprayer was moved forward at 0.5 m/s and the barrel nozzle started spraying at an oscillation frequency of 1.57 min^{-1}. At the same time, the speed of the seed discharger was set to 0.63 min^{-1}. The opening height of the compensation mechanism was adjusted from 13.6 mm to 0 mm to continue spraying when the oscillation time of the barrel nozzle was 12.5 s. When the oscillation time of the barrel nozzle was 16.3 s and the opening height of the compensation mechanism was adjusted to 13.6 mm the sprayer continues to spray. Adjustment of the seed drop trajectory is done during the first 1/2 cycle of the barrel nozzle oscillation. The barrel nozzle oscillation time was 31.6 s and the opening height of the compensation mechanism was adjusted from 13.6 mm to 0 mm. The sprayer continues to spray. The barrel nozzle oscillation time was 35.4 s and the opening height of the compensation mechanism was recovered 13.6 mm. The sprayer continues to spray. Adjustment of the seed drop trajectory is done during the last 1/2 cycle of the barrel nozzle oscillation. The sprayer reaches the end position and stops working after 1 cycle of barrel nozzle oscillation. At the same time, the test data statistics are carried out in the divided grid.

RESULTS

Nozzle outlet air velocity results

As can be seen from Table 4, the compensation mechanism can adjust the airflow velocity in the barrel nozzle in real time. The spraying quality of the sprayer can be improved by adjusting the opening height of the compensation mechanism during spraying operations. So the basic requirements for designing a compensation mechanism are met. And the nozzle outlet air velocity decreases with the increase of the opening height of the compensation mechanism. However, when the opening height is adjusted from 25 mm to 30 mm, the air velocity at the nozzle outlet decreases from 36.88 m/s to 35.29 m/s. The reduction in nozzle outlet air velocity is small. This is consistent with the numerical simulations obtained when the opening height is greater than the radius of the compensation mechanism. Continuing to increase the height has a decreasing effect on the nozzle outlet air velocity. It is verified that the numerical analysis of the opening height of the compensation mechanism on the airflow is correct. The results of the simulation analysis can be used in the analysis of seed drop trajectory regulation.

Table 4

The relationship between the opening height of the compensation mechanism and the airflow velocity at the outlet of the barrel nozzle

Opening height [mm]	Real-time test value 1/ [m/s]	Real-time test value 2 / [m/s]	Real-time test value 3 / [m/s]	Real-time test value 4 / [m/s]	Real-time test value 5 / [m/s]	Real-time test value 6 / [m/s]	Real-time test value 7 / [m/s]	Real-time test value 8 / [m/s]	Real-time test value 9 / [m/s]	Real-time test value 10/ [m/s]	average value/ [m/s]
0	47.63	47.72	47.61	47.58	47.68	47.57	47.61	47.57	47.63	47.59	47.62
5	45.74	45.73	45.77	45.78	45.74	45.73	45.68	45.75	45.69	45.79	45.75
10	43.35	43.31	43.34	43.28	43.37	43.29	43.34	43.27	43.31	43.38	43.32
15	41.12	41.11	41.09	41.08	41.07	41.08	41.13	41.15	41.08	41.06	41.09
20	38.90	39.01	38.86	38.93	38.98	38.97	38.99	38.96	38.95	38.97	38.95
25	37.01	36.98	36.75	36.80	36.85	36.92	36.78	36.95	36.93	36.87	36.88
30	35.26	35.27	35.33	35.32	35.82	34.93	34.97	34.79	34.87	34.96	35.29

Spray quality results

The forward speed of the sprayer was 0.5 m/s and the oscillation frequency of the barrel nozzle was 1.57 min^{-1}. The seed drop area was adjusted using the compensation mechanism. The amount of seed dropped was counted as shown in Table 5. A comparison of this seed drop with the seed drop before adjustment shows as Table 6. The reseeding area of the seed drop area was reduced from 60 m^2 to 48 m^2 after adjustment with the compensation mechanism.

The area of missed seeding was reduced from 64 m^2 to 40 m^2. Both the reseeded area and the missed seeding area were reduced. The reduction in the area of missed seeding was greater than the reduction in the area of reseeding. It can be seen that the designed and installed compensation mechanism can adjust the seed drop trajectory of the sprayer in real time. Reduce the reseeding and missed seeding area in the seed drop area to improve the spraying quality.

Table 5

The amount of seeds in seed drop area is counted when the oscillation frequency is 1.57 min^{-1}

Vertical distance (m)	Lateral distance(m)																			
	2	4	6	8	10	12	14	16	18	20	22	24	26	28	30	32	34	36	38	40
2	0	0	0	0	0	0	0	0	0	1	1	1	0	1	0	0	0	0	0	0
4	0	0	0	0	0	0	0	2	3	6	5	9	6	6	1	1	0	0	0	0
6	0	0	0	0	0	1	5	11	17	14	15	15	14	12	14	6	1	0	0	0
8	0	0	0	0	2	5	8	12	19	16	19	18	17	19	16	15	12	1	0	0
10	0	0	2	1	7	13	16	19	12	12	14	13	13	17	18	17	14	10	1	0
12	0	1	9	15	13	14	14	14	10	4	4	3	5	3	12	14	17	17	6	1
14	0	8	11	14	18	14	14	12	6	6	1	2	0	1	9	11	21	21	14	1
16	1	7	16	16	23	17	10	14	14	11	11	9	3	1	6	10	17	19	16	2
18	1	8	17	26	22	14	18	17	17	18	14	14	8	6	4	1	0	0	0	0
20	2	9	22	32	19	17	16	17	14	14	18	19	16	12	12	1	0	2	0	0
22	1	11	24	22	18	13	9	8	4	7	10	15	14	19	15	10	14	5	4	0
24	3	19	29	23	17	8	2	1	0	5	1	6	9	17	16	14	17	12	8	0
26	2	28	35	16	20	5	0	0	0	0	0	1	5	9	4	14	15	10	3	2
28	1	15	23	14	13	3	0	0	0	0	0	0	1	0	2	4	16	22	12	1
30	0	0	0	0	0	0	0	0	0	0	0	0	0	0	1	3	11	18	9	1
32	0	0	0	0	0	0	0	0	0	0	0	0	0	0	1	2	9	14	10	1
34	0	0	0	0	0	0	0	0	0	0	0	0	0	0	1	1	12	13	15	3
36	0	0	0	0	0	0	0	0	0	0	0	0	0	0	3	9	12	17	14	1
38	0	0	0	0	0	0	0	0	0	0	0	0	0	0	1	9	14	14	10	2
40	0	0	0	0	0	0	0	0	0	0	0	1	0	0	2	0	0	0	0	0

Table 6

Comparison of reseeding and missed seeding area in the falling area before and after adjustment

Compensation mechanism status	Reseeding area / [㎡]	Missed seeding area / [㎡]	The sum of reseeding and missed seeding areas / [㎡]
Shut down	60	64	124
Open	48	40	88

CONCLUSIONS

Spraying quality is an important indicator to measure the spraying performance of the sprayer. The factors affecting the quality of spraying were analysed by simulation analysis, numerical simulation and test analysis. The following conclusions were drawn:

(1) The seed drop trajectory of a sprayer with a compensation mechanism installed at the nozzle inlet of the sprayer was analysed. The obtained formulas for the seed drop trajectories provide a basis for subsequent studies.

(2) The opening height of the compensation mechanism installed to the nozzle inlet is analysed. The law of the influence with the opening height on the airflow velocity at the nozzle inlet was obtained. By adjusting the air velocity at the nozzle inlet, the seed drop trajectory can be changed to reduce the size of the missed seeding area.

(3) The adjustment time points are 0.34T and 0.84T for the opening height of the compensation mechanism in one cycle. The adjustment time points at which the opening height began to reset were 0.44T and 0.94T. There is a lag time t_1 when changing the seed drop trajectory by adjusting the nozzle inlet air velocity. This time is determined by the response time of the compensation mechanism and the seed acceleration time. The compensation mechanism opening height adjustment time becomes 0.34T-t_1, 0.434T-t_1, 0.84T-t_1 and 0.94T-t_1. The oscillation frequency is limited by the response time of the compensation mechanism. When the oscillation frequency is less than 7.3 min^{-1}, the compensation mechanism can be used to change the seed drop trajectory to achieve the optimization of reseeding and missed seeding area.

ACKNOWLEDGEMENT

The support of the University scientific research projects in Inner Mongolia Autonomous Region (NJZY22207) for this research is greatly appreciated.

REFERENCES

[1] Balsari, P., Grella, M., Marucco, P., Matta, F., Miranda-Fuentes, A., (2018). Assessing the influence of air speed and liquid flow rate on the droplet size and homogeneity in pneumatic spraying. *Pest Management Science*, Vol. 75(2), England.

[2] Chen, Y.H., Lai, J.X., (2022). Application of sprayed grass protection technology in the protection of roadside slopes at the top of the North Ru River embankment (喷播植草防护技术在北汝河堤顶路边坡防护中的应用). *Construction Technology Development*, Vol. 49(18), pp. 24-26, Beijing/China.

[3] Chen, Y., (2018). *Research on Automatic Variable Spraying Technology and Related Parameter Optimization of Spraying Machine Based on Multisource Information* (基于多源信息的喷播机自动变量喷播技术及相关参数优化研究). PhD thesis. Univ. Inner Mongolia agricultural, Hohhot/China.

[4] Cao, A.N., Wu, C.D., Zhang, B., et al., (2023). Simulation and Analysis of Spray Barrel Motion for Unmanned spray Vehicles Replacing Pesticides (替代农药无人喷雾车的喷筒运动仿真及分析). *Journal of Agricultural Mechanization Research*, Vol. 45(08), pp. 10-17, Heilongjiang/China.

[5] Dalili, A., Sidawi, K., Chandra, S. (2019). Surface coverage by impact of droplets from a monodisperse spray. *Journal of Coatings Technology and Research*, Vol. 17(1), pp. 207–217, United States.

[6] Fan, C. M., (2013). *Optimization and experimental verification of nozzle swing frequency of 4BQD-40C vehicle-mounted spraying machine* (4BQD-40C 型车载式喷播机喷筒摆动频率的优化及试验验证). Univ. Inner Mongolia agricultural, Hohhot/China.

[7] Grella, M., Marucco, P., Manzone, M., Gallo, R., Mazzetto, F., Balsari, P., (2022). Indoor test bench measurements of potential spray drift generated by multi-row sprayers. *1st IEEE International Workshop on Metrology for the Agriculture and Forestry (IEEE MetroAgriFor)*, Vol.03 -05, Italy.

[8] Gierz, L., Markowski, P., (2020). The effect of the distribution head tilt and diffuser variants on the evenness of sowing rye and oat seeds with a pneumatic seed drill. *Materials*, Vol. 13(13), pp. 3000. Switzerland.

[9] Liu, C.L., Zheng, Q., Wang, Q., Lin, A.Q., Jiang, Y.T., Luo, M.C., (2019). Sensitivity analysis of multistage compressor characteristics under the spray atomization effect using a CFD Model. *Energies*, Vol. 12(2), pp. 301, Switzerland.

[10] Li, W., Qian, L., Song, S., Zhong, X. (2019). Numerical study on the Influence of shaping air holes on atomization performance in pneumatic atomizers. *Coatings*, Vol. 9(7), pp. 410, Switzerland.

[11] Sylvain, V., Thibault, M., Jean-Philippe, G., (2022). Jean-Paul, D., Assessment of nozzle control strategies in weed spot spraying to reduce herbicide use and avoid under- or over-application. *Biosystems Engineering*, Vol. 219, pp. 68-84, England.

[12] Shivam, S.C.J. R., Bhaskor, J.B., Arjun, D., Nur, A., (2022). Numerical analysis of vertical axis wind turbine blades in ANSYS Fluent. *Materials Today: Proceedings*, Vol. 59(3), pp. 1781-1785, England.

[13] Tai, Z. K., (2022). *Design and experiment of seed metering device for coated caragana seed spray seeder* (包衣柠条种子喷播机排种器设计与试验). Univ. Inner Mongolia agricultural, Hohhot/China.

[14] Tao, T., Wei, X.H., (2020). Numerical simulation and analysis of the flow field of five-finger spray barrel of orchard sprayer (果园喷雾机五指式喷筒流场数值模拟与分析). *Agricultural Mechanization Research*, Vol. 42(05), pp. 40-45, Heilongjiang/China.

[15] Wang, D.G., Gao, Y., Xu, A., Wang, Z., Yu, H., Ren, W., (2015). Effects of Different Improvement Measures on Degraded Sheep grass Pasture (不同改良措施对退化羊草草地的影响). *Journal of Grassland and Livestock*, Vol. 223(6), pp. 22-24, Sichuan/China.

[16] Xuan, C., Chen, Z., Liu, H., Song, T., Xue, J., Liang, T., (2016). Wind erosion resistance of different restoration modes in Siziwang Banner grassland restoration experimental area (四子王旗草地修复试验区不同修复模式的抗风蚀试验). *Transactions of the Chinese Society of Agricultural Machinery*, Vol. 47(8), pp. 164-170, Beijing/China.

[17] Yin, Z.T., Pan, J.R., He, L. et al., (2022). Influence of nozzle position and spray drum pressure on atomization effect of fog machine (喷头位置和喷筒压力对烟雾机雾化效果影响). *Journal of Agricultural Mechanization Research*, Vol. 42(07), pp. 45-49, Heilongjiang/China.

[18] Zhang, W.B., Yan, Y.J., (2013). From the Perspective of "Beautiful China" to Discuss the Significance and Strategy of Ecological Civilization Construction: Starting from the Report of the 18th National Congress of the Communist Party of China (从“美丽中国”的视角论生态文明建设的意义与策略——从党的十八大报告谈起). *Ecological Economy*, Vol. 04, pp. 184-188, Yunnan/China.

[19] Zhang, Y., Fan, C.M., Chen, Z., Wang, J.W., (2013). Optimization and experimental verification of swing frequency of nozzle boom in spraying machine (喷播机喷筒摆动频率的优化及试验). *Transactions of the Chinese Society of Agricultural Engineering*, Vol. 29(7), pp. 24-29, Beijing/China.

[20] Zhang, H.M., Zheng, Y.J., (2022). Analysis of the application of spray seeding grass ecological slope protection technology in municipal landscape engineering (喷播植草生态护坡技术在市政景观工程中的应用分析). *Engineering Construction and Design*, Vol. 478(08), pp. 190-192, Beijing/China.

DISCRIMINATION OF CERASUS HUMILIS FRUIT MATURITY BASED ON HYPERSPECTRAL IMAGING TECHNOLOGY
/
基于高光谱成像技术的欧李果成熟度判别

Bin WANG, Hua YANG*, Lili LI [1]
College of Information Science and Engineering, Shanxi Agricultural University, Taigu/China
Tel: +86-0354-6288165; E-mail: yanghuaxky@126.com
DOI: https://doi.org/10.35633/inmateh-70-10

Keywords: *Cerasus humilis fruit, maturity, hyperspectral imaging, nondestructive examination*

ABSTRACT

In order to realize the rapid and accurate identification of different maturity of Cerasus humilis fruit, this study explored the nondestructive testing method of Cerasus Humilis fruit maturity based on hyperspectral imaging technology. The hyperspectral data of 320 samples of Cerasus humilis fruit were collected by using a hyperspectral imaging system in the range of 895~1700 nm. By comparing the prediction accuracy of the partial least squares (PLS) model established by four preprocessing methods, the competitive adaptive reweighted algorithm (CARS), successive projection algorithm (SPA), and random frog (RF) were used to extract characteristic wavelengths, and partial least squares-discriminant analysis (PLS-DA) and least squares-support vector machine (LS-SVM) discriminant models were established. The results showed that the SPA-LS-SVM model had the highest discrimination accuracy for the four types of maturity samples, and the discrimination accuracy of the correction set and prediction set were 85.00% and 87.50%, respectively. This study provides a theoretical reference for the rapid and nondestructive testing of the maturity of Cerasus Humilis fruit by hyperspectral imaging technology.

摘要

为了实现对不同成熟度欧李果进行快速、准确识别，本研究探讨基于高光谱成像技术对欧李果成熟度进行无损检测研究的方法。利用 895~1700 nm 范围内的高光谱成像系统采集不同成熟时期（转色期、着色期、成熟期、完熟期）的欧李果共 320 个样本的高光谱数据。通过对比 4 种预处理方法建立的 PLS 模型预测精度，应用 CARS、SPA、RF 提取特征波长，并分别建立 PLS-DA 和 LS-SVM 判别模型。结果表明，SPA-LS-SVM 模型对 4 类成熟度样本的判别准确率最高，其校正集和预测集的判别准确率分别为 85.00% 和 87.50%。该研究为高光谱成像技术在欧李果成熟度的快速、无损检测提供了理论参考。

INTRODUCTION

As a unique fruit in China, the Cerasus Humilis fruit is also called “calcium fruit” because it is rich in active calcium and easy to be absorbed by the human body. The fruit is bright in color, unique in flavor and rich in nutrition. It can be eaten as fresh fruit or processed into fruit juice, wine, vinegar and other products. Maturity is an important factor that determines the shelf life, edible quality and postharvest storage of fruits. With the general improvement of social economic level and consumers' purchasing power, people pay more and more attention to the quality and safety of fruits. Determining the optimal maturity is the key to ensure the quality and storage of fruits. At present, the method of distinguishing the mature stage of the Cerasus humilis fruit mainly depends on people's experience and intuition. However, this method is inefficient and subjective, and cannot cope with large-scale production and modern fruit processing. Therefore, it is necessary to explore a fast and nondestructive method for determining the ripeness of Cerasus Humilis fruit to improve the market value and consumer satisfaction.

In recent years, hyperspectral imaging technology, a fusion technology integrating digital image and spectral technology, can provide spatial and spectral information of the target at the same time, and has been widely used in the detection of agricultural product maturity *(Yuan et al., 2021)*. *Shao et al. (2020)* used hyperspectral imaging technology (400~1000 nm) to analyze the maturity of Feicheng peach (green ripening stage, color changing stage).

[1] *Bin Wang, As Lec. Ph.D. Eng.; Hua Yang*, Prof. Ph.D. Eng.; Lili Li, As Lec. Ph.D. Eng.*

The sequential forward selection (SFS) algorithm was adopted to extract three characteristic wavelengths to establish an artificial neural network (ANN) prediction model. The total prediction accuracy of the model was 98.3%. *Li Lili et al. (2019)* used hyperspectral imaging technology (420~1000 nm) to identify Cerasus Humilis fruits with different maturity (immature, semi-mature, mature and over-mature). And the results showed that the established SPA-PLS model had the highest discrimination accuracy, and the accuracy reached 91.25%. *Pu et al. (2019)* used the hyperspectral imaging system to collect hyperspectral images of bananas at different maturity stages (the 2, 4 and 6 stages), and adopted regression coefficient method to choose characteristic wavelengths to establish three classification models (K-nearest neighbor algorithm, SIMCA, PLS-DA). Among them, the accuracy of PLS-DA model was the best (93.3%). *Zhang et al. (2020)* used the 300~1100 nm hyperspectral imaging system to divide bagged red Fuji apples into three maturity levels (immature, harvest maturity, edible maturity) with starch index as the maturity index, and established five discrimination models. The research showed that the RF-SPA-LS-SVM model had the highest classification accuracy (89.05%) for prediction sets. *Zou et al. (2019)* used hyperspectral imaging technology to classify peanuts with different maturity (immature and mature), and established multiple discrimination models (PLS-DA, LS-SVM). The results showed that LS-SVM model had the highest discrimination accuracy for immature and mature peanuts, which were 92.36% and 99.43% respectively. The above studies show that it is feasible to use hyperspectral imaging technology to identify fruit maturity. However, no researchers have used hyperspectral imaging to identify the maturity of Cerasus Humilis fruit in relevant studies.

In this study, the hyperspectral imaging system is used to obtain the hyperspectral image of the “Nongda No. 6” Cerasus humilis fruit samples in the range of 900~1700 nm, and extract the average spectral data of the region of interest (ROI). The effects of five spectral pretreatment methods on the performance of PLS model were analyzed and the optimal pretreatment method was determined. The competitive adaptive reweighted algorithm (CARS), successive projection algorithm (SPA), and random frog (RF) were used to extract the characteristic wavelength, and the partial least squares-discriminant analysis (PLS-DA) and least squares-support vector machine (LS-SVM) discriminant models were established based on the characteristic wavelength, so as to provide a theoretical basis for further development of online sorting equipment of Cerasus Humilis fruits in different mature periods.

MATERIALS AND METHODS

Sample Collection

In this study, fresh edible Cerasus Humilis fruit (Nongda No. 6) was collected from a Cerasus Humilis planting demonstration base in the agricultural high-tech industry demonstration zone (112°29'E, 37°23'N) of Jinzhong, China, July 30, 2020. After harvest, the sample is placed in a cryogenic crisper, transported to the laboratory on the same day as the sampling, to avoid the effects of individual differences on the testing results. A total of 320 samples (include 66 color turning stages, 90 coloring stages, 84 maturity stages, and 80 full ripe stages) without defects, bruises, scar, and relatively uniform shape were selected. Finally, the selected samples were numbered, rinsed, wiped. Prior to hyperspectral image acquisition, the samples were taken out and placed in a laboratory (25°C, 40% relative humidity) for 2h to avoid the effect of temperature on the spectrum and the fruit quality. Samples of Cerasus Humilis fruit at four maturity levels (immaturity, white maturity, early-red maturity, half-red maturity, and full maturity) are shown in Fig.1.

The SPXY algorithm *(Galvao et al., 2005)* was used to divide the Cerasus Humilis fruit dataset into a calibration set (240 samples) and a prediction set (80 samples) with a ratio of 3:1.

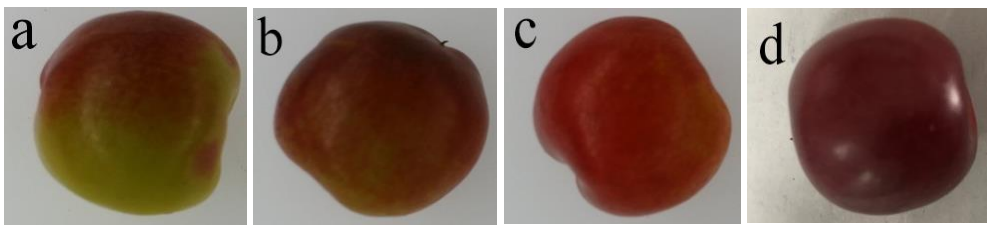

Fig. 1 - Samples of Cerasus Humilis fruit at different maturity stages
a) Color turning stage; b) Coloring stages; c) Maturity stage; d) Full ripe stage

Spectrum Acquisition

In this study, a hyperspectral imaging system (GaiaSorter, Zolix Instruments Co. Ltd., China) was used to collect spectral and image information. The spectral range is 895~1700 nm and the spectral resolution is 5 nm, and the number of pixels is 320×256. The entire system consists of a high-spectrum spectrometer, CCD camera, four 250 W halogen lamps, a precision mobile platform controlled by stepper motors, and a computer, as shown in Fig.2. Among them, four 250 W halogen lamps were placed as a lighting device at a 45°angle.

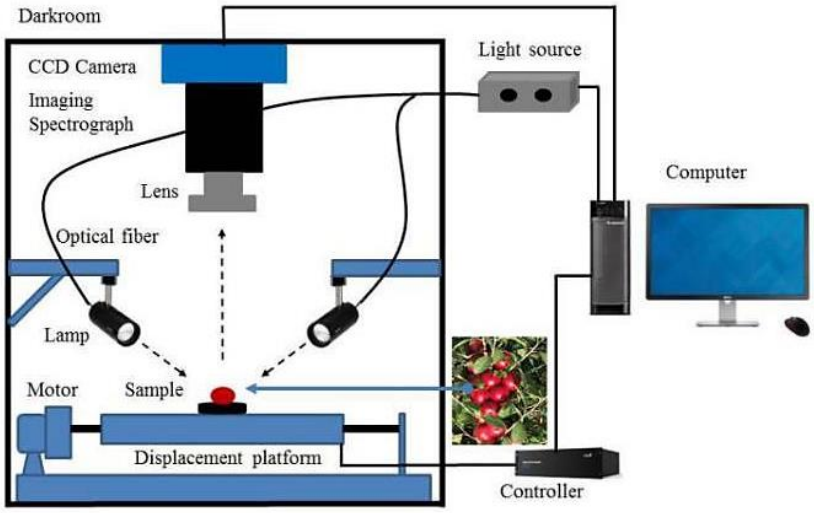

Fig. 2 - The schematic diagram of hyperspectral imaging system

To ensure clear images, avoid information oversaturation and imaging distortion. Based on the system configuration, the equatorial region of Cerasus humilis fruit was facing the camera, and the camera was fixed at a distance of 280 mm from the lens to the samples' surface. Each Cerasus humilis fruit was placed on the sample table to be scanned at an 8 mm/s constant speed line by line using 150 ms exposure time to create a hyperspectral image. Due to the uneven distribution of light intensity and the presence of dark currents in the sensor, the resulting image had high noise. Therefore, the raw images were corrected according to the following equation:

$$I = \frac{R - B}{W - B} \times 100\% \quad (1)$$

where:

I is the corrected image;
R is the original image;
B is the image of the blackboard correction;
W is the image of the whiteboard correction.

Discriminant Model

Partial least squares-discriminant analysis (PLS-DA) is a multivariate statistical analysis method combining partial least square method and linear discriminant analysis method. The optimal number of principal components is obtained by cross validation, and then linear discriminant analysis is carried out to solve the multicollinearity problem of independent variables in regression analysis. In this study, principal components were selected according to the interaction test, the maximum number of principal components was set as 10, and 10-fold interaction test was performed.

Least squares-support vector machine (LS-SVM) is a multivariate statistical method. Its algorithm is the least squares method. Its principle is structural risk minimization, which can effectively implement data classification and processing. It also reduces training time and simplifies computational complexity. In this study, the optimal characteristic wavelength is used as the input, and four maturity categories are used as the output parameters. After optimization, the optimal regular parameter (γ) and square bandwidth (σ^2) were obtained.

Software Tools

In this study, ENVI5.0 (Version 5.0, ITT Visual Information Solutions, Boulder, USA) software was used to analyze hyperspectral images. The Unscrambler X10.1'' (CAMO PROCESS AS, Oslo, Norway) and MATLAB R2009a software (The Mathworks, Inc., Natick, MA, USA) were used to process and analyze data. In addition, Origin Pro 8.0 SR0 (Origin Lab Corporation, Northampton, MA, USA) software was used to design graphs.

RESULTS AND DISCUSSION

Spectral Characteristics Analyses

The ROI with 40×60 pixels was manually extracted from hyperspectral image of equatorial region of each sample. The spectra of each pixel within the ROI were extracted, and then the mean spectrum was calculated, as shown in Fig. 3a. Meanwhile, the average spectra of various samples were obtained, as shown in Fig. 3b. Because of the low signal-to-noise ratios and large noise at 895~945 nm, 1675~1700 nm, the wavelength range of 945~1675 nm (230 bands) were selected for further analysis in this study.

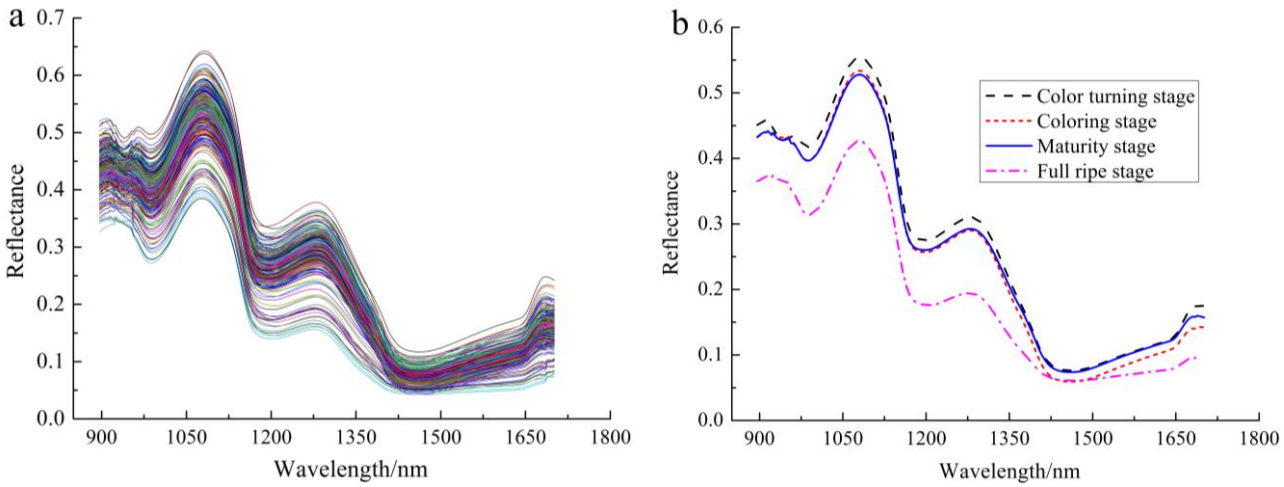

Fig. 3 - Raw reflectance spectra of Cerasus Humilis fruit samples at different maturity

As shown in Fig. 3a, spectra of samples at different maturity stages have some crossover and overlap, but the trend of spectral curves is very similar. It can be seen from Fig. 3a that the spectra have obvious absorption peaks at 980, 1195 and 1460 nm. The absorption peak at around 980 nm and 1195 nm were related to the second overtone of O-H stretching *(Shinzawa et al., 2011)* and the second overtone of C-H stretching, respectively *(Liu et al., 2010)*. There is an obvious absorption peak near 1460 nm, which is related to the first order frequency doubling of the stretching vibration of the O-H bond *(Osborne et al., 2006)*. It can be seen from Fig. 3b that the spectral curves at different maturity stages (color turning stage, coloring stage, maturity stage, and full ripe stage) have similar trends, but the spectral reflectance will vary greatly with the extension of the sample maturity stage, and the spectral reflectance of the sample at maturity stage is the lowest. In the range of 1180~1300 nm, the fruit reflectance varied greatly, and tended to decrease gradually, which may be related to the changes of the contents of chemical components in the fruits of Cerasus Humilis at different maturity stages.

Spectral Pretreatment

Selecting an appropriate spectral preprocessing method can eliminate or weaken the influence of non-target factors on the original spectral information, and improve the signal-to-noise ratio and the detection accuracy and stability of the model *(Chi et al., 2021)*. In the present work, four spectral pre-processing methods, including standard normal variate (SNV), multiplicative scatter correction (MSC), baseline correction (BC), and de-trending (De-T) were used to preprocess the raw spectral data. The PLS prediction models were established respectively, and the optimal pretreatment methods were compared and selected. The prediction results are shown in Table 1.

Table 1

Prediction results of PLS models built by different preprocessing methods

Pretreatment methods	Calibration set		Prediction set	
	Rc	RMSEC	Rp	RMSEP
Original spectra	0.87	0.51	0.88	0.50
SNV	0.76	0.68	0.85	0.54
MSC	0.85	0.58	0.85	0.57
BC	0.88	0.49	0.89	0.48
De-T	0.86	0.52	0.88	0.51

It can be seen from Table 1 that compared with the predicted results of the PLS model established by the original spectrum without pretreatment, the predicted results of the PLS model established by the three pretreatment methods (SNV, MSC, De-T) were poor. The PLS model established after BC method preprocessing has the highest prediction accuracy, with the correlation coefficient (Rc) of the correction set and the correlation coefficient (Rp) of the prediction set being 0.88 and 0.89, respectively. The root mean square error (RMSEC) of the correction set and the mean square error (RMSEP) of the prediction set being 0.49 and 0.48, respectively, both of which are relatively low and close. Therefore, the spectral data processed by BC were used for further analyses in this study.

Effective Wavelength Selection

Competitive Adaptive Reweighted Sampling (CARS)

The CARS algorithm is a feature information filtering method that has been widely used in recent years. It is based on Darwin's theory of evolution and follows the “survival of the fittest” principle. In the CARS procedure, the absolute coefficients of variables in the PLS model are set as an index for evaluating the importance of each variable and the wavelengths with large absolute coefficients were regarded as optimal wavelengths *(Wang et al., 2021)*.

In the process of CARS, the number of Monte Carlo sampling runs was set to 50 and the final variable number to be selected was determined by 5-fold cross validation. Fig. 4a, b and c show the trends of the number of sampled variables, RMSECV values, and regression coefficient paths for each variable as the number of Monte Carlo samples increases for each CARS run, respectively. From Fig. 4a, it can be seen that the number of wavelengths gradually decreases and finally plateaus with the gradual increase of the number of sampling runs, which verifies the fast selection phase and refined selection phase in the wavelength screening process. Fig. 4b showed the changing trends of RMSECV with sampling runs from each sampling. When the number of sampling runs gradually increases to 36, the cross-validation RMSECV gradually decreases and then shows a trend of increasing. When the RMSECV gradually becomes smaller, it means that the useless information in the spectral information was eliminated, when the RMSECV increases, it means that the useful information of the spectral information was eliminated. In Fig. 4c, each curve represents the regression coefficients at different sampling runs for each variable, the position of the vertical line marked with "*" in the Fig. 4c indicates that the RMSECV reaches a minimum value of 0.51 when the number of sampling runs was 36. Finally, the number of selected wavelengths was 14 from 230 wavelengths, these variables were 960, 1027, 1091, 1151, 1161, 1164, 1167, 1173, 1355, 1371, 1374, 1380, 1625, and 1650 nm, respectively.

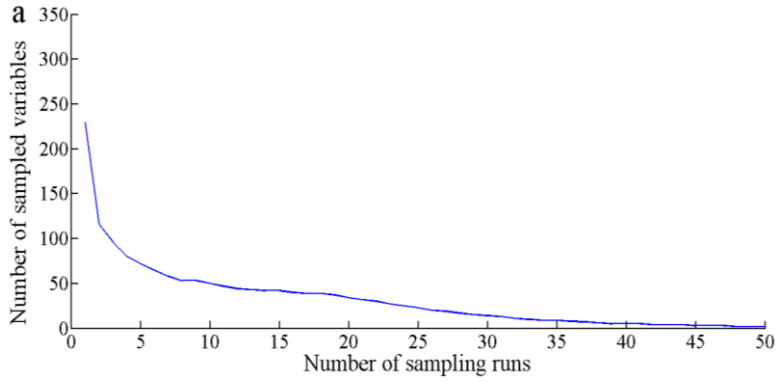

a)

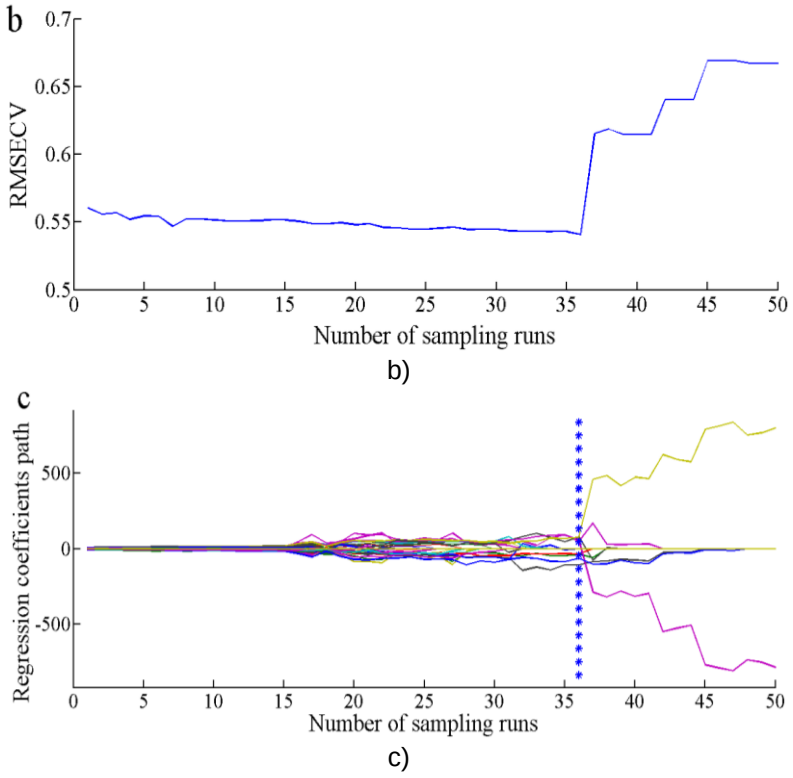

Fig. 4 - Key variables selection results of CARS

Successive Projection Algorithm (SPA)

SPA is a forward selection method proposed by Araújo *(Araújo et al., 2001)*. This algorithm is to avoid the overlap of effective information in spectral variables and eliminate the collinearity between them through multiple variable information iterations, find a group of characteristic variables with low redundant information, minimum collinearity and representativeness, which can represent most spectral information of tested samples, avoid the overlap of information to the greatest extent, and improve the modeling speed.

The SPA algorithm is used to extract the characteristic wavelengths from the pre-processed full spectrum data. In this study, the parameters of the minimum and maximum numbers of variables selected in the SPA procedure were 1 and 30, respectively. Fig. 5 shows the distribution of root mean square errors (RMSE) for the different number of variables chosen by the SPA algorithm. When the 19 variables were selected (marked as open blue square), the RMSEP reached its optimal value (with RMSE=0.46). Fig. 6 shows the selected 19 variables, the nineteen characteristic wave-lengths were 1609, 1377, 1113, 1580, 1068, 1275, 1355, 1212, 1641, 1672, 1141, 953, 1323, 957, 1399, 1488, 1669, 1676, and 1460 nm, respectively. Accounting for 3.91% of the total wavelength, the importance of the wavelength decreases in turn.

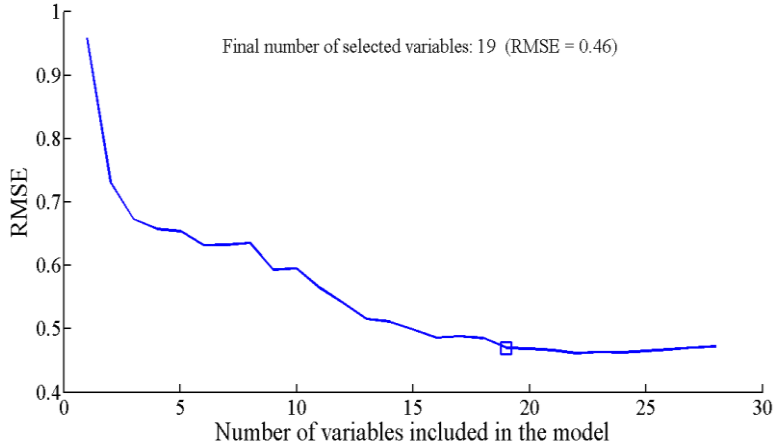

Fig. 5 - The relationship between wave number and root mean square error

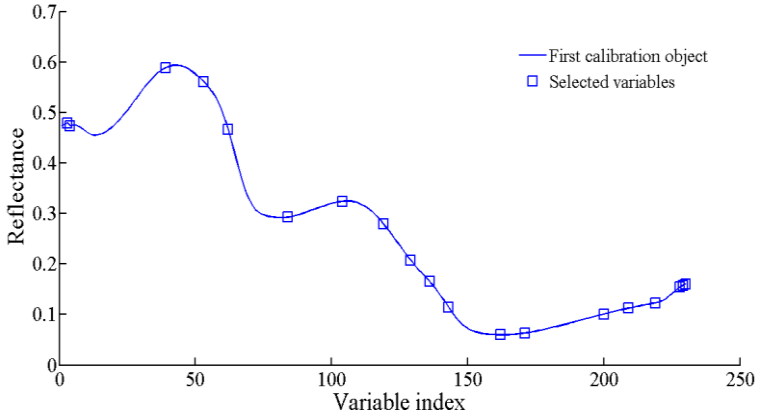

Fig. 6 - Feature wavelength extracted by SPA

Random Frog (RF)

Random Frog (RF) is a mathematically simple method with high computational efficiency. It is similar to reversible jump Markov chain Monte Carlo algorithm, which can iterate multidimensional data variables and calculate the weight value of each variable. The higher the value, the greater the probability of being selected, and the more important the corresponding wavelength *(Yan et al., 2020)*.

In order to reduce the influence of random factors, the algorithm needs to run several times and calculate the results. In this study, the frequency of RF algorithm was set as 2000, and when RMSECV reached the minimum value of 0.48, the threshold was selected as 0.31. The process of using RF algorithm to select characteristic wavelength was shown in Fig. 7. It can be seen from Fig. 7 that the band selection probability ranges from 0.0 to 0.8. Only a few variables have prominent selection probability peaks, which can be identified as characteristic wavelength. The first 10 data coordinate points with large probability values are (133,0.7525), (134,0.4245), (121,0.4135), (151,0.3670), (97,0.3495), (182,0.3460), (52,0.3290), (62,0.3175), (8,0.3135), (53,0.3075), respectively, arranged in descending order. The corresponding characteristic wavelengths are 1367, 1371, 1329,1425, 1253, 1523, 1110, 1142, 969, and 1113 nm respectively, accounting for 4.35% of the original wavelength.

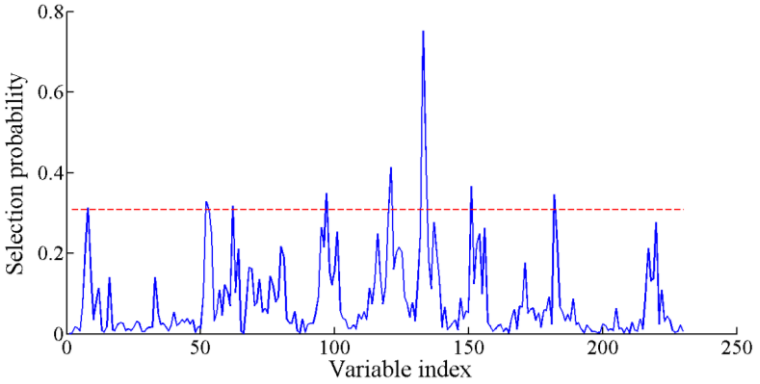

Fig. 7 - Feature wavelength extracted by RF

Establishment of a Maturity Model Using the Feature Wavelengths

The PLS-DA and LS-SVM discrimination models were established by assigning the samples of different maturity periods (color turning stage, coloring stage, maturity stage, and full ripe stage) with values of 1, 2, 3, and 4, respectively.

When the established discriminant model is used to discriminate samples at different mature stages, if the correct prediction value of color turning stage is within the threshold value [0.5, 1.5], it is determined that the prediction category is consistent with the assumed category, that is, the color turning stage. By analogy, the threshold range of the coloring stage is (1.5, 2.5], the maturity stage is (2.5, 3.5], and the full ripe stage is (3.5, 4.5]. Based on the discriminant results of different models of characteristic wavelength analysis, the most effective method of extracting characteristic wavelength and modeling method are determined. Table 2 shows the discrimination results of PLS-DA and LS-SVM models based on the characteristic wavelengths of Cerasus Humilis in different maturity periods.

Table 2

Discriminant results of models by the characteristic wavelength of Cerasus Humilis fruit maturity

Model	Variable selection methods (No. of variables)	Calibration set		Prediction set	
		Number of misjudgments	Discriminant accuracy (%)	Number of misjudgments	Discriminant accuracy (%)
PLS-DA	Original spectra（230）	76	68.33	27	66.25
	SPA（19）	68	71.67	20	75.00
	CARS（14）	70	70.83	25	68.75
	RF（10）	93	61.25	36	55.00
LS-SVM	Original spectra（230）	37	84.58	12	85.00
	SPA（19）	36	85.00	10	87.50
	CARS（14）	41	82.92	14	82.50
	RF（10）	68	71.67	27	66.25

As can be seen from Table 2, among the PLS-DA discriminant models, the RF-PLS-DA model has the worst discriminant results for Cerasus Humilis fruits at different maturity stages, and the accuracy of correction set and prediction set are 61.25% and 55.00%, respectively. Compared with the original spectra data, the discriminant results of the model based on the characteristic wavelengths extracted by SPA and CARS are slightly improved by 8.75% and 2.50% respectively. Among them, SPA-PLS-DA model has the best discrimination result for Cerasus Humilis fruits at different maturity stages. The number of selected characteristic wavelengths accounts for 8.26% of the total spectrum data, and the discrimination accuracy of correction set and prediction set are 71.67% and 75.00%, respectively.

In the LS-SVM discriminant model, compared with the discriminant results of the model established by the original spectrum, the model established by using the characteristic wavelength extracted by CARS and RF methods has significantly reduced the discriminant results of the prediction set, while the prediction set of RF-LS-SVM model has the lowest discriminant accuracy, with a value of 66.25%. It shows that the effective information in the original spectral data is eliminated in the process of extracting characteristic wavelength by RF algorithm. By comprehensive comparison, when $\gamma=6.17\times10^3$, $\sigma^2=71.21$, SPA-LS-SVM model has the best discriminative results for plum fruit at different maturity stages. The number of selected characteristic wavelengths only accounts for 8.26% of the whole spectrum data, and the discriminative accuracy of correction set and prediction set are 85.00% and 87.50%, respectively.

By comparing the discriminant accuracy of the optimal linear model and the optimal nonlinear model, it can be seen that the SPA-LS-SVM model has the highest discriminant accuracy. *Singh et al. (2021)* research on barley seed varieties recognition based on hyperspectral imaging technology combined with convolutional neural network, and discrimination accuracy of the nonlinear convolutional neural network model is superior to that of the linear model, which is consistent with the conclusion of this study. In this study, the accuracy of the optimal discriminant model for the prediction set (87.50%) was slightly lower than that of *Li et al., (2019),* (91.25%) and *Liu et al., (2022),* (90.12%). This may be due to the different research objects, which leads to the deviation of the hyperspectral image information collected. In addition, the 19 characteristic wavelengths extracted by SPA algorithm in this study are consistent with previous research reports *(Riza et al., 2017)*. That is 967~1095 nm is related to the overtone of C-H stretching, 1165~1390 nm is associated with the first overtone of bond O-H, and 1620~1800 nm is associated with the first overtone of bond C-H *(Wang et al., 2021)*. It is further indicated that the characteristic wavelength extracted by SPA can be used as the key variable to reflect the different ripening stages of Cerasus Humilis fruit, which can simplify the model and improve the accuracy of discriminant.

Fig. 8 shows the discriminant results of the prediction set of 4 types of Cerasus Humilis fruits based on the optimal SPA-LS-SVM model. Among them, 3 Cerasus Humilis fruits in the color turning stage were misjudged as the coloring stage, 4 Cerasus Humilis fruits in the coloring stage were misjudged as the color turning stage, and 3 Cerasus Humilis fruits in the maturity stage were misjudged as the coloring stage.

This may be due to the fact that a few Cerasus Humilis fruits in the color turning stage, the coloring stage and the maturity stage had no obvious color changes and the absorption spectrum was consistent, which was easy to cause confusion.

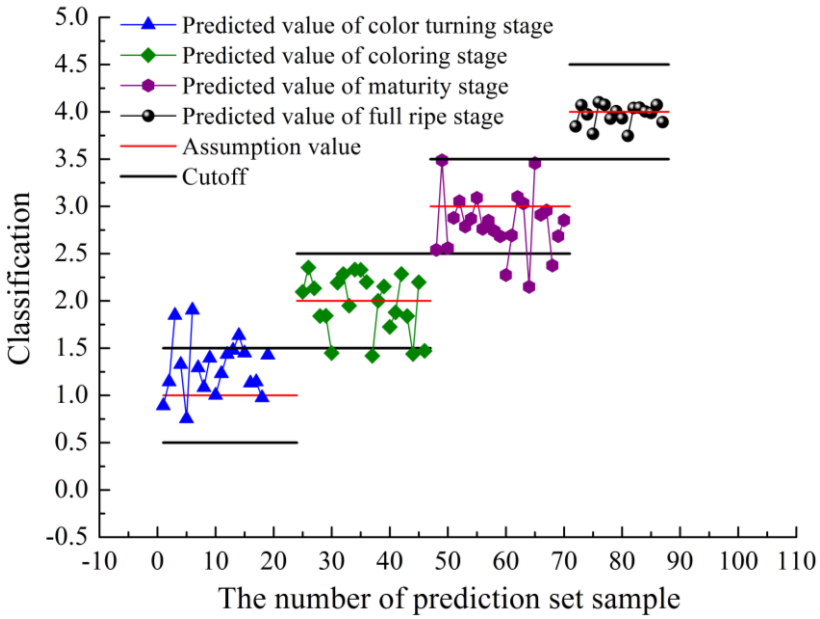

Fig. 8 - The discriminant result of SPA-LS-SVM model

CONCLUSIONS

In this study, hyperspectral imaging technology was used to nondestructive discriminant research of Cerasus Humilis fruit at different maturity stages (color turning stage, coloring stage, maturity stage, and full ripe stage), the effects of different spectral preprocessing methods and characteristic wavelength extraction methods on the accuracy of the model were compared. The main research conclusions are as follows:

(1) Based on the spectral information in the range of 945~1675 nm, the PLS prediction models established by four pretreatment methods (SNV, MSC, BC, De-T) were compared and analyzed. The results showed that the PLS model pretreated by BC method was the best, with Rc and RMSEC of 0.88 and 0.49, Rp and RMSEP of 0.89 and 0.48, respectively.

(2) Based on the original spectrum pretreated by BC method, the characteristic wavelength was extracted by CARS, SPA and RF algorithms, and the PLS-DA and LS-SVM discriminative models were established respectively. Comparative analysis showed that the SPA-LS-SVM model had the best discriminant results for different maturity stages of Cerasus Humilis fruit ($\gamma=6.17\times10^3$ and $\sigma^2=71.21$). The number of selected characteristic wavelengths only accounted for 8.26% of the full spectrum, and the discriminant accuracy of correction set and prediction set were 85.00% and 87.50%, respectively. This study provides a theoretical basis for rapid and non-destructive detection of the ripeness of Cerasus Humilis fruits.

ACKNOWLEDGEMENT

This research was supported by the Province Basic Research Program Project (Free Exploration) (Grant No.20220302123641), the Doctor Scientific Research Foundation of Shanxi Agricultural University (2023BQ63).

REFERENCES

[1] Araújo, M.C.U., Saldanha, T.C.B., Galvao, R.K.H., Yoneyama, T., Chame, H.C., & Visani, V. (2001). The successive projections algorithm for variable selection in spectroscopic multicomponent analysis. *Chemometrics and intelligent laboratory systems*, *57*(2), 65-73. https://doi.org/10.1016/S0169-7439(01)00119-8

[2] Chi, J.T., Zhang, S.J., Ren, R., Lian, M.R., & Mu, B.Y. (2021). Detection of eggplant external defects using hyperspectral technology. *Modern Food Science and Technology*, *37*(9), 279-284+178. https://doi.org/10.13982/j.mfst.1673-9078.2021.9.0034

[3] Galvao, R.K.H., Araujo, M.C.U., José, G.E., Pontes, M.J.C., & Saldanha, T.C.B. (2005). A method for calibration and validation subset partitioning. *Talanta,* 67, 736–740. https://doi.org/10.1016/j.talanta.2005.03.025

[4] Li, L.L., Wang, B., Zhang, X.H., & Zhang, S.J. (2019). Discrimination of plum fruit maturity based on hyperspectral imaging technology. *Modern Food Science and Technology*, *35*(6): 258-263. https://doi.org/10.13982/j.mfst.1673-9078.2019.6.034

[5] Liu, J. X., He, X. W., Luo, H. P., Xu, J. Y., & Shen, L. L. (2022). Maturity discrimination model of little white apricot based on hyperspectral imaging technology. *Food Research and Development*, *43*(15): 158-165. https://doi.org/10.12161/j.issn.1005-6521.2022.15.022

[6] Liu, Y., Sun, X., Zhang, H., & Aiguo, O. (2010). Nondestructive measurement of internal quality of Nanfeng mandarin fruit by charge coupled device near infrared spectroscopy. *Computers and Electronics in Agriculture*, *71*, S10-S14. https://doi.org/10.1016/j.compag.2009.09.005

[7] Osborne, B. G. (2006). Near-infrared spectroscopy in food analysis. *Encyclopedia of analytical chemistry: applications, theory and instrumentation*. https://doi.org/10.1002/9780470027318.a1018

[8] Pu, Y. Y., Sun, D. W., Buccheri, M., Grassi, M., Cattaneo, T. M., & Gowen, A. (2019). Ripeness classification of bananito fruit (Musa acuminata, AA): a comparison study of visible spectroscopy and hyperspectral imaging. *Food Analytical Methods*, *12*(8), 1693-1704. https://doi.org/10.1007/s12161-019-01506-7

[9] Al Riza, D. F., Suzuki, T., Ogawa, Y., & Kondo, N. (2017). Diffuse reflectance characteristic of potato surface for external defects discrimination. *Postharvest Biology and Technology*, *133*, 12-19. https://doi.org/10.1016/j.postharvbio.2017.07.006

[10] Shao, Y., Wang, Y., Xuan, G., Gao, C., Wang, K., & Gao, Z. (2020). Visual detection of SSC and firmness and maturity prediction for feicheng peach by using hyperspectral imaging. *Transactions of the Chinese Society for Agricultural Machinery*, *51*(8), 344-350. https://doi.org/10.6041/j.issn.1000-1298.2020.08.038

[11] Shinzawa, H., Ritthiruangdej, P., & Ozaki, Y. (2011). Kernel analysis of partial least squares (PLS) regression models. *Applied spectroscopy*, *65*(5), 549-556. https://doi.org/10.1366/10-06187

[12] Singh, T., Garg, N. M., & Iyengar, S. R. (2021). Nondestructive identification of barley seeds variety using near infrared hyperspectral imaging coupled with convolutional neural network. *Journal of Food Process Engineering*, *44*(10), e13821. https://doi.org/10.1111/jfpe.13821

[13] Wang, B., He, J., Zhang, S. J., & Li, L. L. (2021). Nondestructive prediction and visualization of total flavonoids content in Cerasus Humilis fruit during storage periods based on hyperspectral imaging technique. *Journal of Food Process Engineering*, *44*(10), e13807. https://doi.org/10.1111/jfpe.13807

[14] Wang, B., He, J. L., & Li, L.L. (2021). On-line detection of cerasus humilis fruit based on VIS/NIR spectroscopy combined with variable selection methods and GA-BP model. *INMATEH-Agricultural Engineering*, *63*(1), 199-210. https://doi.org/10.35633/inmateh-63-20

[15] Yan, L., Pang, L., Wang, H., & Xiao, J. (2020). Recognition of different Longjing fresh tea varieties using hyperspectral imaging technology and chemometrics. *Journal of Food Process Engineering*, *43*(4), e13378. https://doi.org/10.1111/jfpe.13378

[16] Yuan, R., Liu, G. S., He, J. G., Kang, N. B., & Ma, L. M. (2021). Quantitative damage identification of Lingwu long jujube based on visible near-infrared hyperspectral imaging. *Spectroscopy and Spectral Analysis*, *41*(4), 1182-1187. https://doi.org/10.3964/j.issn.1000-0593-1182-06

[17] Zhang, M., Zhang, B., Li, H., Tian, S., Zhang, H., & Zhao, J. (2020). Determination of bagged 'Fuji' apple maturity by visible and near-infrared spectroscopy combined with a machine learning algorithm. *Infrared Physics & Technology*, *111*, 103529. https://doi.org/10.1016/j.infrared.2020.103529

[18] Zou, S., Tseng, Y. C., Zare, A., Rowland, D. L., Tillman, B. L., & Yoon, S. C. (2019). Peanut maturity classification using hyperspectral imagery. *Biosystems Engineering*, *188*, 165-177. https://doi.org/10.1016/j.biosystemseng.2019.10.019

DESIGN OF VISUAL NAVIGATION SYSTEM FOR AGRICULTURAL ROBOTS BASED ON PID-FUZZY CONTROL AND MONOCULAR VISION

/

基于 PID-模糊控制的单目视觉农田机器人视觉导航系统设计

Hanzhuo REN, Wei LI※), Shaobo YE, Bing XU 1)

College of Agricultural Engineering, Shanxi Agricultural University, Taigu 030801 / China;

Corresponding author: Sanmin Sun

Tel: +86-0354-6288339; E-mail: jamesallenlw@163.com

DOI: https://doi.org/10.35633/inmateh-70-11

Keywords: *Monocular vision; Agricultural robots; Vision navigation system; PID-fuzzy control*

ABSTRACT

This study proposes a monocular vision navigation control system based on PID-fuzzy control, which travels along the edge of the path. It collects path image information through monocular vision, identifies the path edge through image processing to determine the preview point, and uses a combination of PID and fuzzy control to design a controller to track the preview point for path navigation. Coordinate calibration and conversion were performed on the monocular camera. According to the navigation strategy of driving along the edge of the path, the world coordinate equation of the path edge is obtained through image processing technology, and the preview point tracked by the navigation system is determined. The navigation parameters are determined based on the position of the preview point. The PID fuzzy controller system designed in this study can switch different control methods based on the position of the preview point. The verification results show that the average error of the navigation control system in tracking the path when driving in a straight line was 0.039 m, the average error when turning left was 0.079 m, and the average error when turning right was 0.121 m. The error range can meet the basic requirements of agricultural robot farmland operations. Research has shown that the navigation strategy based on PID-fuzzy joint controller to track the preview point along the path edge has a good effect on the visual navigation control system of agricultural robots.

摘要

本研究提出了一种沿路径边缘行驶，基于 PID-模糊控制的单目视觉导航控制系统，它通过单目视觉采集路径图像信息，图像处理识别路径边缘确定预瞄点，利用 PID 和模糊控制相结合的方式设计控制器跟踪预瞄点实现路径导航。首先对单目摄像机进行坐标标定与转换，实现了从图像坐标系到世界坐标系的坐标转换，并通过试验验证了标定结果的准确性。根据沿路径边缘行驶的导航策略，通过图像处理技术得到路径边缘的世界坐标方程，确定导航系统追踪的预瞄点，根据预瞄点的位置确定导航参数。本研究设计的 PID-模糊控制器系统，能够根据预瞄点的位置不同切换不同的控制方式。最终对该控制系统的单目视觉导航系统进行了试验验证，验证结果表明该导航控制系统在直线行驶时跟踪路径的平均误差是 0.039 m，左转弯时的平均误差为 0.079 m，右转弯平均误差 0.121 m，误差范围能够满足农业机器人农田作业的基本要求。研究表明，基于 PID-模糊联合控制器控制沿路径边缘追踪预瞄点行驶的导航策略对农田机器人视觉导航控制系统效果良好。

INTRODUCTION

Due to its affordable price, large amount of information available, and flexible guidance, visual navigation has become the fastest developing navigation strategy in recent years, and has also become a hot research topic for navigation strategies both domestically and internationally, with broad application prospects (*Zhang et al., 2022; Yang et al., 2022; Wang et al., 2021*). Robot visual navigation technology can usually be divided into indoor visual navigation and outdoor visual navigation. Generally speaking, the difficulty of outdoor robot visual navigation is much greater than that of indoor robot visual navigation, as indoor robots can achieve regular paths, uniform lighting, and less random interference (*Wang et al., 2022*; *Khan et al., 2022*). In addition to facing irregular paths and constantly changing light intensity, outdoor robot visual navigation also needs to face various interferences that may occur at any time (*Lai et al., 2023*).

Hanzhuo Ren, B.S. Stud. Eng.; Wei Li, Lecturer Ph.D. Eng.; Shaobo Ye, Lecturer Ph.D. Eng.; Bing Xu, Lecturer Ph.D. Eng.

Agricultural robot visual navigation belongs to outdoor visual navigation, and agricultural robots face complex agricultural environments, which further increases the difficulty of visual navigation (*Li et al., 2018; Tai J. et al., 2020*).

The earliest application of visual navigation technology to the agricultural field was Marr's visual Theory of computation in the 1970s. Europe, America and other countries took the lead in carrying out relatively in-depth research and exploration, and achieved certain results (*Li D. et al., 2017; Phalak Y. et al., 2018*). China's research in the field of agricultural robot visual navigation started relatively late and has achieved considerable research results through continuous research and exploration in recent years (*Ren et al., 2021*).

At present, there is no unified, effective and feasible solution for agricultural robot visual navigation technology, which focuses on researching specific navigation strategies for different agricultural environments (*Guan et al., 2020; Liu, 2019*). This article mainly proposes a visual navigation strategy for driving along the edge of a path in agricultural environments with obvious path edges.

The main contributions of this article are as follows:

(1) A visual navigation strategy for driving along the edge of the path is proposed. Due to the frequent need for agricultural robots to operate along the edge of the path in agricultural work environments, this paper proposes a visual navigation strategy for driving along the edge of the path.

(2) A PID-fuzzy controller has been designed, which can freely switch between PID control and fuzzy control methods. PID control has good stability and high accuracy, and fuzzy control guidance is flexible and suitable for nonlinear and complex control. The PID fuzzy controller combines the advantages of both controllers and can adapt well to the designed navigation strategy.

(3) The feasibility of the navigation strategy and the effectiveness of the controller design were verified through experiments. By conducting tests on the agricultural robot testing platform for straight, left turn, and right turn driving, the deviation of the agricultural robot's track from the predetermined track was measured, and a comprehensive evaluation of the navigation strategy and controller was conducted.

MATERIALS AND METHODS

Construction of agricultural robot test platform

The agricultural robot experimental platform mainly includes a frame, hub motor, hub motor controller, power supply, monocular camera, DSP image processing system, STM32 microcontroller, ultrasonic sensor, etc. The agricultural robot experimental platform controls the wheel hub motors of two front wheels for differential steering. The two rear wheels belong to a universal follower wheel and can rotate freely. The CCD camera is responsible for collecting image information and transmitting it to the DSP processor for processing. The DSP image processing controller model is DM642, mainly responsible for image information processing in monocular vision. DSP communicates with STM32 and transmits the DSP image processing results to the STM32 microcontroller. STM32 controls the wheel hub motor speed of the left and right front wheels for navigation based on image information and navigation algorithms. Ultrasonic sensors are mainly used to detect obstacles and achieve obstacle avoidance in agricultural robot testing platforms. Fig. 1 shows the overall structure of the agricultural robot experimental platform.

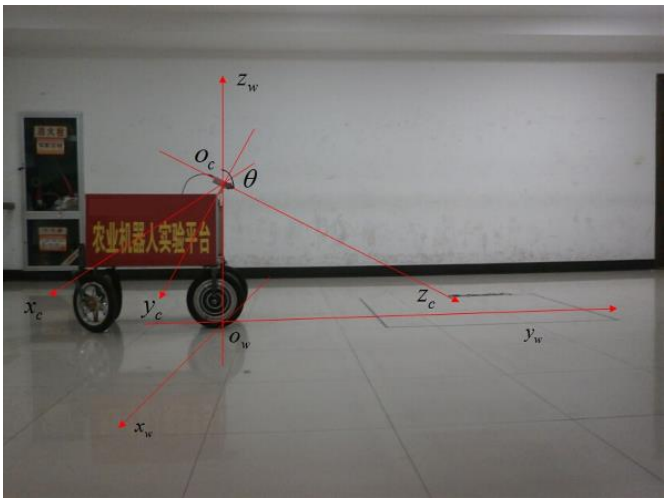

Fig. 1 - The overall structure of the agricultural robot experimental platform

Camera pixel calibration

Conversion relationship between different coordinate systems

The coordinates in the image information processed by the image processing system are the pixel coordinates of the image captured by the CCD camera, and for the navigation system to navigate correctly, it is necessary to use the world coordinate system for navigation (*Zeng et al., 2020*). Therefore, it is particularly important to convert the pixel coordinates of the image to world coordinates (*Liu Y., 2019*). Fig. 2 shows the relationship between different coordinate systems.

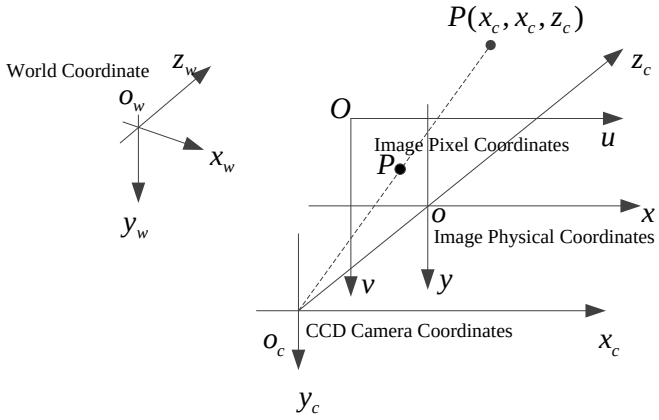

Fig. 2 - The relationship between different coordinate systems

Assuming the camera coordinate system rotates θ clockwise around the axis x_C, moving parallel along the x_C axis $-h_1$, moving parallel along the y_C axis $-h_2$, and moving parallel along the z_C axis $-h_3$ can obtain the world coordinate system. The relationship between the world coordinate system (x_w, y_w, z_w) and the camera coordinate system (x_c, y_c, z_c) is as follows:

$$\begin{bmatrix} x_c \\ y_c \\ z_c \\ 1 \end{bmatrix} = TR \begin{bmatrix} x_w \\ y_w \\ z_w \\ 1 \end{bmatrix} = \begin{bmatrix} 1 & 0 & 0 & -h_1 \\ 0 & \cos\theta & -\sin\theta & -h_2 \\ 0 & \sin\theta & \cos\theta & -h_3 \\ 0 & 0 & 0 & 1 \end{bmatrix} \begin{bmatrix} x_w \\ y_w \\ z_w \\ 1 \end{bmatrix} \quad (1)$$

where:

$$R = \begin{bmatrix} 1 & 0 & 0 & 0 \\ 0 & \cos\theta & -\sin\theta & 0 \\ 0 & \sin\theta & \cos\theta & 0 \\ 0 & 0 & 0 & 1 \end{bmatrix} \quad (2)$$

$$T = \begin{bmatrix} 1 & 0 & 0 & -h_1 \\ 0 & 1 & 0 & -h_2 \\ 0 & 0 & 1 & -h_3 \\ 0 & 0 & 0 & 1 \end{bmatrix} \quad (3)$$

The conversion relationship between the physical coordinate system of the image *(u, v)* and the pixel coordinates stored in the image processing system (x, y) is:

$$\begin{cases} u = u_0 + \dfrac{x}{s_x} \\ v = v_0 + \dfrac{y}{s_y} \end{cases} \quad (4)$$

Based on the above analysis, the final relationship between the pixel coordinates *(u, v)* of the image and the world coordinate system (x_w, y_w, z_w) is:

$$\begin{cases} u = u_0 + \dfrac{f}{s_x} \cdot \dfrac{x_w - h_1}{y_w \cdot \sin\theta + z_w \cdot \cos\theta - h_3} \\ v = v_0 + \dfrac{f}{s_y} \cdot \dfrac{y_w \cdot \cos\theta - z_w \cdot \sin\theta - h_2}{y_w \cdot \sin\theta + z_w \cdot \cos\theta - h_3} \end{cases} \quad (5)$$

where u_0 and v_0 are the camera internal parameters, [pixel number]. h_1, h_3 and h_3 are the distances the camera coordinate system moved along the x, y and z of the world coordinate system, [m]. θ is the camera coordinate system rotate clockwise angle around the x axis of the world coordinate system, [°].

Camera calibration test

The camera calibration process is as follows:

(1) Establish a world coordinate system and a camera coordinate system: The establishment of the world coordinate system is shown in Fig. 1, with the projection point of the camera center to the ground as the origin of the world coordinate system. The forward direction of the agricultural robot test platform is the positive direction of the Y-axis, the upward direction perpendicular to the ground is the positive direction of the Z-axis, and the direction perpendicular to the robot's forward direction and to the right is the positive direction of the X-axis. The camera coordinate system takes the camera optical center as the coordinate origin, with the positive direction of the Z axis along the camera, the positive direction of the Y axis perpendicular to the camera downwards, and the positive direction of the X axis perpendicular to the Y-Z axis plane to the right.

(2) The vertical distance between the optical center of the camera and the ground, measured as 0.85 m, is the angle between the Z axis of the camera coordinate system and the Z axis of the world coordinate system.

(3) Adjust the focal length of the camera to obtain the clearest ground image information and capture images. The world coordinates of the marked points on the ground can be obtained through measurement, and the pixel coordinates of the marked points in the collected image information can be obtained through image information processing.

(4) By incorporating the obtained world coordinates and image pixel coordinates into formula 5, the unknown parameters in the equation can be solved, thereby achieving camera calibration.

The Camera calibration test results is shown in Table 1.

Table 1

The result of camera calibration

Camera external parameters				Camera internal parameters		
h_1	h_2	h_3	θ	(u_0,v_0)	m	n
0.05	0.03	0.91	123	(309.71,242.31)	320.44	354.72

The final conversion relationship between the world coordinate system and the camera pixel coordinates is as formula (6):

$$\begin{cases} x_w = \dfrac{187.7 - 0.565u + 0.068v}{-231.5 - 0.54v} \\ y_w = \dfrac{992.0 - v}{231.5 + 0.54v} \end{cases} \quad (6)$$

where u and v are the camera pixel coordinate system, [pixel number]. x_w and y_w are the world coordinate system.

In order to verify the accuracy of formula (6), twenty points were randomly selected in the world coordinate system to find the corresponding pixel points in the image coordinate system. The world coordinates of the corresponding points in the world coordinate system were calculated using the pixel coordinates of the pixel points and the formula, and the error between the calculated and actual values of the world coordinates was compared. From the error analysis, it can be seen that the maximum error does not exceed 0.11 m, while most errors are mainly concentrated within the range of 0.07 m. Considering the complexity of the agricultural robot operating environment, this error is within the allowable range and can meet the accuracy requirements.

Driving strategy along the edge of the path

Agricultural robots mainly operate in agricultural environments, which are relatively complex. However, there are generally obvious path edges in farmland (*Peng et al., 2018*). Therefore, this article proposes a navigation strategy for agricultural robots to travel by path edges. The agricultural robot determines the world coordinates of the preview point based on the collected path information and the navigation strategy of driving along the edge of the path. Then, the controller controls the hub motor to track the position of the preview point, thereby achieving the navigation of the agricultural robot driving along the edge of the path. The driving strategy along the edge of the path is shown in Fig. 3.

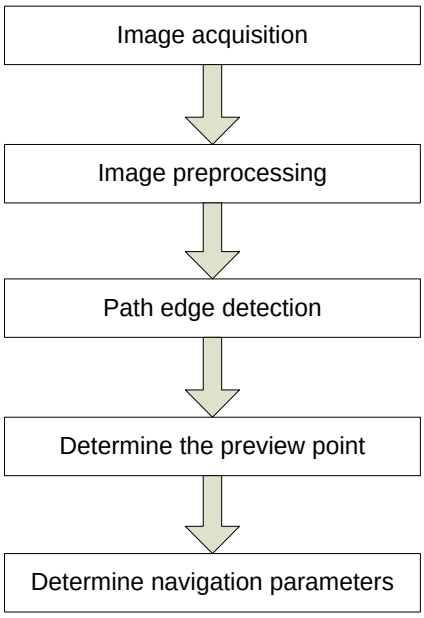

Fig. 3 - The driving strategy along the edge of the path

The image information collected by the camera needs to be preprocessed using DM642, which mainly includes image graying, threshold segmentation, morphological processing, edge detection, line detection, etc. The main image Processing process is shown in Fig. 4.

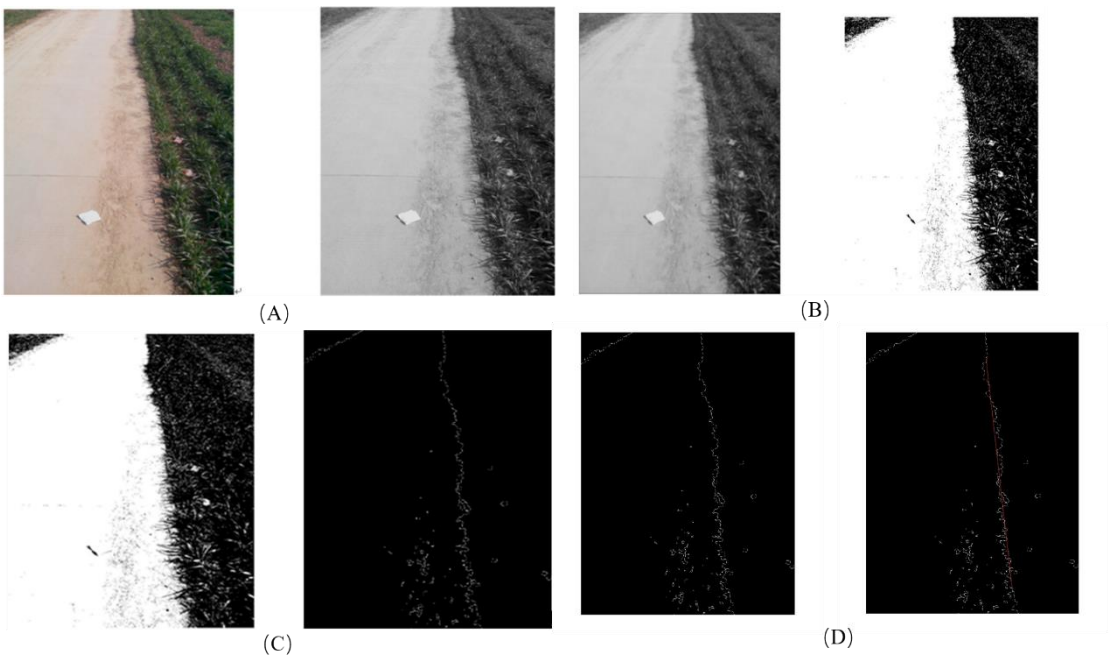

Fig. 4 - The image processing process

Finding the preview point for path tracking

Through the previous image processing, the path edge can be already found in the image and the path edge can be fit with a straight line to obtain the analytical equation of the path edge in the image. This expression is then transformed into the world coordinate system through coordinates, and the expression of the path edge in the world coordinate system is obtained. Then, based on the equation of the path edge in the world coordinate system and the width of the agricultural robot body, the preview point position for path tracking can be determined as the tracking target for navigation. Fig. 5 illustrates the main steps to determinate the preview point.

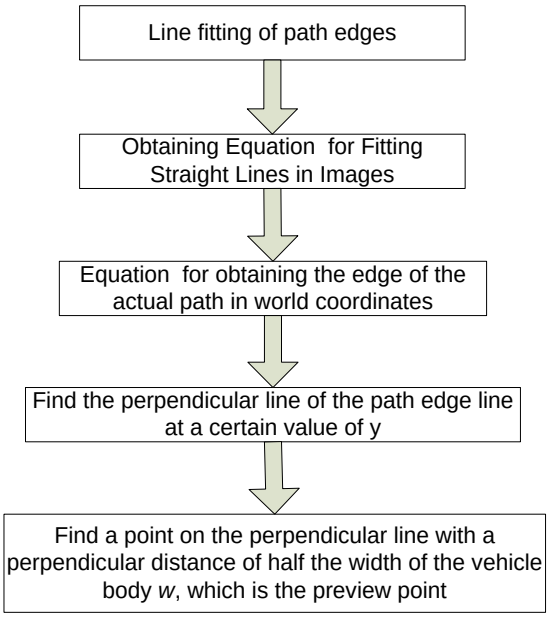

Fig. 5 - The determination of preview point

Assuming the linear equation of the navigation path edge in the pixel coordinate system is:

$$y = k_1 u + b_1 \tag{7}$$

The equation expression for the navigation path edge in the world coordinate system is:

$$y = k_2 x + b_2 \tag{8}$$

After determining the preview point, it is necessary to design a controller to control the agricultural robot experimental platform to track the constantly changing preview point. Navigation parameters that describe the position of the preview point need to be defined.

As shown in Figure 11, the navigation parameters mainly include the following three: preview point lateral offset *d*, path tangent direction angle φ, and preview point direction deviation angle *θ*. The preview point lateral offset *d* refers to the distance between the tracked preview point position and the world coordinate system y axis, while the path tangent direction angle *θ* refers to the angle between the direction of the path edge fitting line and the positive direction x in the world coordinate system. The directional deviation angle φ refers to the angle between the line connecting the tracked preview point position and the world coordinate origin and the world coordinate system y axis.

It should be pointed out that when the tracked preview point position is in the first quadrant of the world coordinate system, the deviation angle φ and the lateral offset *d* of the preview point are both positive, while when the tracked preview point position is in the second quadrant of the world coordinate system, the deviation angle φ and the lateral offset d of the preview point are both negative. During the process of changing the position of the preview point from the first phenomenon to the second quadrant, the tangent angle of the path direction changes from 0° to 180°. The navigation parameters' calculation process are showed in the Tab. 2.

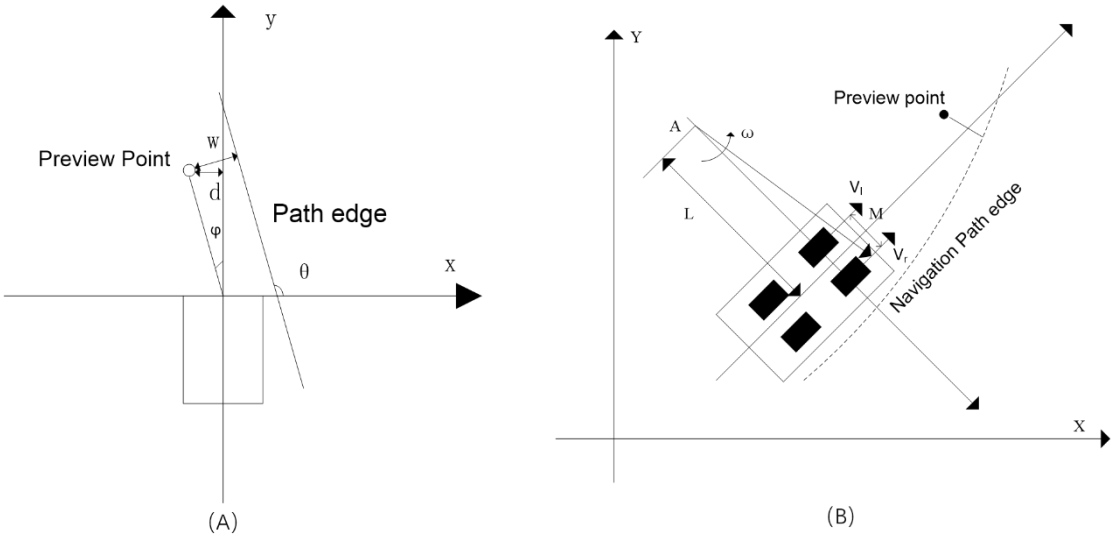

Fig. 6 - Navigation parameter diagram
(A) Straight line path; (B) Curve path

Table 2

Determination of navigation parameters in different situations

Navigation parameter	$0.5 \le \lvert k_2 \rvert \le 300$	$\lvert k_2 \rvert > 300$	$\lvert k_2 \rvert < 0.5$
d	$1-b_2-\frac{wk_2^2}{\sqrt{k_2^2+1}}$	$b-w$	$\begin{cases} l+w-n_1 (x_1>0) \\ w+n_1-l (x_1<0) \end{cases}$
φ	$\arctan\frac{x}{y}$	$\arctan\frac{b-w}{l}$	$\begin{cases} \arctan\frac{l+w-n_1}{n_1+w} (x_1>0) \\ \arctan\frac{w+n_1-l}{n_1-w} (x_1<0) \end{cases}$
θ	$\begin{cases} \arctan k_2 (k_2>0) \\ \pi+\arctan k_2 (k_2<0) \end{cases}$	90	$\begin{cases} 0 \quad (x_1>0) \\ 180 \, (x_1<0) \end{cases}$

Assuming that the direction deviation generated by the agricultural robot test platform after time Δt, that is, the defined path tangent deviation angle θ=Δe_θ, and the generated lateral deviation distance $d=\Delta e_d$, then the Kinematics equation of the agricultural robot test platform can be expressed as follows:

$$\begin{aligned} \frac{\Delta e_\theta}{\Delta e_t} &= \omega = \frac{v_r+v_l}{2L} \\ \frac{\Delta e_d}{\Delta e_t} &= \frac{v_r+v_l}{2}\cdot\sin\Delta e_\theta \end{aligned} \tag{9}$$

where: v_l and v_r are the speeds of left and right wheels, respectively, [m/s]; L is the width of the experimental platform vehicle, [m]; e_θ is the defined path tangent deviation angle, [°]; e_d is the generated lateral deviation distance, [m]; e_t is an extremely short running time, [s].

The kinematics equation of the agricultural robot test platform can be simplified as follows:

$$\begin{aligned} \dot{e}_\theta &= \omega = \frac{v_r+v_l}{2L} \\ \dot{e}_d &= \frac{v_r+v_l}{2}\cdot\sin\Delta e_\theta \end{aligned} \tag{10}$$

Let $v_c=\frac{v_r+v_l}{2L}$.

In this way, the Kinematics equation of the agricultural robot test platform can be further simplified as:

$$\begin{bmatrix} \dot{e}_d \\ \dot{e}_\theta \end{bmatrix} = \begin{bmatrix} 0 & v_c \\ 0 & 0 \end{bmatrix} \begin{bmatrix} e_d \\ e_\theta \end{bmatrix} + \begin{bmatrix} 0 \\ \frac{1}{L} \end{bmatrix} (v_c) + \begin{bmatrix} \Delta_d \\ \Delta_\theta \end{bmatrix} \quad (11)$$

Fuzzy control can achieve control of the controlled object without an accurate model of the controlled object. Fuzzy control can simulate human preview control behavior, especially in the absence of an accurate model of the controlled object, and can achieve good control effects in complex environments such as nonlinearity. The working environment of agricultural robots is generally complex, and choosing a fuzzy controller can adapt to this complex environment.

Fuzzy controllers have their own shortcomings, such as poor stability and difficulty in eliminating static errors. While, classical PID controllers can effectively solve these problems. Therefore, this controller chooses a control method that combines PID control and fuzzy control. When the path turns or the deviation distance of the preview point is large, a robust fuzzy controller is selected, PID controller is chosen in areas where the deviation distance between the straight path or the preview point is small. This can combine the advantages of two control methods, which can meet the stability and robustness demand of the controller.

RESULTS

To verify the tracking effect of the proposed navigation strategy on the agricultural robot test platform on different paths, three types of tracks have been set up, including straight line, left turn, and right turn. The travel trajectory errors of the agricultural robot have been measured. The experimental testing process is shown in Fig. 7.

Fig. 7 - Driving trajectory test

(A) Strait line test; (B) Turn left test; (C) Turn right test; (D) Error data measurement; (E) Driving trajectory leakage bottle; (F) Obstacle avoidance test

The average error of tracking the straight line path is 0.039 m, the average error of left turn is 0.079 m, and the average error of right turn is 0.121 m (Fig. 8).

Considering that the agricultural robot works in an agricultural environment, these errors are not too large, usually within the allowable range. The mean squared error of straight line driving is 0.036 m, the mean squared error of left turn tracking is 0.059 m, and the mean squared error of right turn tracking is 0.070 m.

The mean squared error of straight line driving is significantly smaller than that of left turn and right turn, and the mean squared error of straight line driving is also smaller than that of left turn and right turn. This is because straight line driving uses PID controllers, while left and right turns combines PID and fuzzy control, and PID control accuracy and stability are significantly better than fuzzy control. Fuzzy control can adapt well to complex control with high nonlinearity such as left and right turns, and has good guidance flexibility.

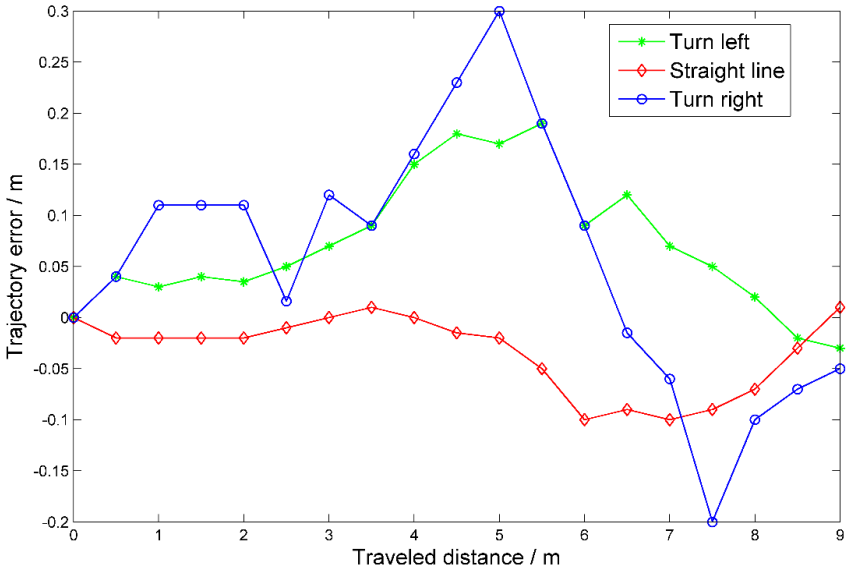

Fig. 8 - Trajectory error curve

CONCLUSIONS

The visual navigation system of the agricultural robot experimental platform was tested by simulating farmland paths. The experimental results show that the agricultural robot experimental platform can accurately track the edges of straight and curved paths on a flat football field, and be able to independently achieve turning path tracking control. When the path is lost, the agricultural robot experimental platform can automatically deflect to the right to find the edge of the path, so it has a certain degree of fault tolerance for short-term path loss. In addition, the ultrasonic sensor module of the agricultural robot testing platform was tested. When encountering obstacles, the agricultural robot testing platform can stop in a timely manner to prevent danger. The driving trajectory of the agricultural robot test platform is relatively smooth, and there are certain overshoots and oscillations in the system during the driving process. Given that the agricultural environment does not require high navigation accuracy, the proposed monocular vision PID-fuzzy navigation strategy can basically meet the design requirements to drive along the edge of the path.

ACKNOWLEDGEMENTS

This research, titled “Design of Visual Navigation System for Agricultural Robots Based on PID-Fuzzy Control and Monocular Vision”, was funded by project: “Design of Ultrasonic Generator and its Application in Facility planting (Grant No. 2016010)”, and project “Study on Detection of organophosphorus Pesticide residues based on Electrochemical biosensor (Grant No. 2022BQ35)”.

REFERENCES

[1] Guan Z.H., Chen K.Y., Ding Y.C., Wu C.Y., Liao Q.X., (2020), Visual navigation path extraction method in rice harvesting, *Transactions of the Chinese Society for Agricultural Machinery*, vol.51, Issue 1, pp.19-28;

[2] Khan D., Cheng Z., Uchiyama H., et al., (2022), Recent advances in vision-based indoor navigation: A systematic literature review, *Computers & Graphics*, Vol.104, pp.24-45, Elsevier, London / England;

[3] Lai H.R., Zhang Y.W., Zhang B., et al., (2023), Design and experiment of the visual navigation system for a maize weeding robot (玉米除草机器人视觉导航系统设计与试验), *Transactions of the Chinese Society of Agricultural Engineering*, Vol.39, Issue 01, pp.18-27, Beijing / China.

[4] Li Y.W., Xu J.J., Wang M.F., et al., (2019), Development of autonomous driving transfer trolley on field roads and its visual navigation system for hilly areas, *Transactions of the Chinese Society of Agricultural Engineering*, Vol. 35, Issue 01, pp.52-61, Beijing / China.

[5] Li D., Xu S., Zheng Y., (2017), Navigation Path Detection for Cotton Field Operator Robot Based on Horizontal Spline Segmentation. *International Journal of Information Technology & Web Engineering*, Vol.12, Issue 3, pp.28-41, USA;
[6] Liu B., (2019), *Research on visual navigation system of citrus picking robot mobile platform, MSc dissertation*, Chongqing University of Technology, Chongqing / China;
[7] Liu Y., Gao G.Q., (2019), Recognition of visual navigation directrix between winter fruit tree row, *Journal of Chinese Agricultural Mechanization*, vol.40, Issue 5, pp.160-166, China;
[8] Peng S.Z., Li J.B., (2018), Design and implementation of jujube garden visual navigation path extraction software, *Jiangsu Agricultural Sciences*, vol.46, Issue 10, pp.213-217;
[9] Phalak Y., Charpe G., Paigwar K., (2018), Omnidirectional Visual Navigation System for TurtleBot Using Paraboloid Catadioptric Cameras. *Procedia Computer Science*, Vol.133, pp.190-196, Netherlands;
[10] Ren X.D., Wang H.C., Shi X., et al., (2021), Research on visual navigation path detection method for dense plum grove, *INMATEH - Agricultural Engineering*, Vol.65, Issue 3, PP. 111-118, Romania;
[11] Tai J., Li H.T., Du Y.F, Mao E.R., Zhang J.N., Long X.J., (2020), Rapid design of maize ear harvester header based on knowledge engineering. *INMATEH - Agricultural Engineering*, Vol.61, Issue 2, pp.263-272, Romania;
[12] Wang T., Chen B., Zhang Z., et al., (2022), Applications of machine vision in agricultural robot navigation: A review, *Computers and Electronics in Agriculture*, Vol. 198, 107085, Ed. Elsevier, London/England;
[13] Wang Z., Cheng X., (2021), Adaptive optimization online IMU self-calibration method for visual-inertial navigation systems, *Measurement*, Vol.180, 109478, Ed. Elsevier, London / England;
[14] Yang Z., Ouyang L., Zhang Z. et al., (2022), Visual navigation path extraction of orchard hard pavement based on scanning method and neural network, *Computers and Electronics in Agriculture*, Vol.197, 106964, Ed. Elsevier, London / England;
[15] Zeng H.W., Lei Z.B., Tao J.F., Zhang W., Liu C.L., (2020), Navigation line extraction method for combine harvester under low contrast conditions, *Transactions of the Chinese Society of Agricultural Engineering*, vol.36, Issue 4, pp.18-25;
[16] Zhang T.Y., Hu X.G., Xiao J. et al., (2022), A survey of visual navigation: From geometry to embodied AI, *Engineering Applications of Artificial Intelligence*. Vol.114, 105036, Ed. Elsevier, London / England;

DESIGN AND EXPERIMENT OF A SINGLE-ROW SMALL GRAIN PRECISION SEEDER [1]

单行小籽粒精少量播种机设计与试验

Jingxin SUN[1)], Liqin YANG[2)], Baohui XU[1)], Yuming GUO*[3)]
[1)] Department of Mechanical and Electrical Engineering, Yuncheng University, Yuncheng 044000, China;
[2)] Planning Finance Office, Yuncheng University, Yuncheng 044000, China;
[3)] College of Agricultural Engineering, Shanxi Agriculture University, Taigu 030801, China;
Tel: +86-0354-6286869; E-mail: guoyuming99@sina.com
DOI: https://doi.org/10.35633/inmateh-70-12

Keywords: *millet, broomcorn millet, precision, seeder*

ABSTRACT

In order to meet the precision seeding of small seeds including millet and broomcorn millet in hilly and mountainous areas, a single-row small grain precision seeder was developed. Static seeding test and seeding test were carried out on the seeder. In this paper, the key parts such as socket wheel-ring groove seed metering device, transmission system and tensioning wheel are designed. The working parts such as arrow shovel furrow opener, plastic seed tube and hollow cast iron press wheel were selected to achieve seed metering. The seed metering wheel has double-row of holes. The results of static seeding test showed that rotational speed had a significant effect on the sowing quantity of millet and broomcorn millet (P < 0.001). The higher the rotational speed, the greater the sowing quantity. With the increase of rotational speed of seed metering wheel, the damage rate of millet and broomcorn millet increased. At the same rotational speed, the breakage rate of broomcorn millet is smaller than that of millet. The field sowing test showed that when the seeder is at a marching speed of about 0.5 m/s, the qualified rate of the hole spacing of millet and broomcorn millet is greater than or equal to 90%, and the qualified rate of the number of grains per hole is greater than or equal to 82%. All indicators meet the requirements of the technical conditions of single-grain (precision) seeder. The design can provide reference for the design and optimization of small grain precision seeder.

摘要

为了满足丘陵山地谷子、黍子等小籽粒种子的精少量播种，研制了单行小籽粒精少量播种机，并对播种机进行了静态排种试验和播种试验。该文设计了窝眼轮-环槽式排种器、传动系统、张紧轮等关键零部件，选用了箭铲式开沟器、塑料导种管、空心铸铁镇压轮等工作部件，排种轮具有双排型孔。静态排种试验结果表明：转速对谷子、黍子的排量有极显著影响显著（P＜0.001），转速越大，排量越大；随着排种轮转速的增大，谷子和黍子的破损率均增大；在同一转速下，黍子的破损率比谷子的破损率均小。田间播种试验表明：当播种机在 0.5m/s 左右的前进速度下，谷子、黍子的穴距合格率均大于等于 90%，穴粒数合格率均大于等于 82%，各项指标均满足单粒（精密）播种机技术条件的要求。该设计可为小籽粒精量播种机设计和优化提供参考。

INTRODUCTION

Millet is one of the characteristic crops in China with drought tolerance and balanced nutrition *(Li et al., 2021; Hou et al., 2017)*. In recent years, driven by the adjustment of industrial structure and the market, *(Li et al., 2021)*, the planting area of millet is increasing, and the development prospect is broad. However, at present, millet sowing mostly uses strip sowing. If the sowing quantity is large, it needs to be artificially interplanted. It wastes seeds, time and labor *(Zhang et al., 2017)*. If the sowing quantity is small，which will appear 'broken seedlings' phenomenon, and artificial seedling replenishment is needed, which limits the rapid development of millet industry to a certain extent. Therefore, the development of a small grain precision seeder can not only save labor and sowing costs, but also promote the whole mechanization of millet.

[1] *JingXin Sun, Associate prof. Ph.D. Eng.; Liqin Yang, Semi-senior accountant. M.B.A.Eng.; BaoHui Xu, Prof. Ph.D. Eng.; YuMing Guo, Prof. Ph.D. Eng.*

The precision sowing machinery in foreign developed countries started early and has perfect technology *(Nikolay et al., 2022; Pareek et al., 2023; Dylan et al., 2013).* Because of its wide sowing width and high sowing speed, the traditional mechanical sowing can't meet the sowing requirements, so it is mainly based on air suction or air blowing sowing *(Arzu et al., 2014; Sujit et al., 2022; Pareek et al., 2021).*

Karayel D studied the depth uniformity of the improved vacuum precision seeder and experimentally determined the optimum vacuum pressure *(Karayel et al., 2009).* The seeding uniformity of vacuum precision seeder was optimized by response surface method (RSM). The optimum combination of variables was obtained and verified *(Arzu et al., 2007).* Cujbescu used the mathematical model to numerically simulate the working process of the pneumatic seed-metering device, and analyzed the movement of the seeds according to the angle of detachment, the height of detachment of the seed, as well as the speed of the seed in its trajectory towards the channel opened by the coulter (*Cujbescu et al., 2022*). Hoque developed a tilt-plate seeder, which has been tested to save 90 % of time and 86 % of cost compared to manual planting, with a payback period of 1.2 years *(Hoque et al., 2016).* However, foreign millet planting area is relatively small. There is not much research on millet precision metering device *(Yi et al., 2021).* Four kinds of suction holes with different structures were compared by Wang. The results showed that the suction effect of the air-suction millet seed metering device was the best when the suction hole was the four-prism platform, and the best working parameters of the seed metering device were obtained *(Wang et al., 2021)*.

In recent years, there are more and more researches on millet and other small grain precision metering device in China. Yi developed positive and negative air pressure and type hole wheel combined millet seed metering device, and obtained the best working parameters of the metering device through the combination test *(Yi et al., 2021).* Zhang designed a pressure-holding precision seed-metering device for maize, and obtained the optimal size of the parts of the seed-metering device and the rotation speed (*Zhang et al., 2023*). Wang combined EDEM discrete element software to optimize the mechanical wheat seeding device, and concluded that when the inner diameter of the seed wheel was 125 mm and the opening inclination angle was 25°, the seeding performance was the best (*Wang et al., 2021*). Zhang designed a millet fluid seed-metering device. The seed-metering device seeded the prepared suspension liquid through the pump pipe and the seed-metering pipe by the conveying pump. The field test showed that the qualified rate of hole spacing and the qualified rate of the number of holes were both above 74% *(Zhang et al., 2017*; *Zhang et al., 2012).* Zhang developed a kind of ring groove millet seed metering device. Liu designed a magnetic pickup finger seed-metering device with magnetic force to complete the opening and closing of the finger-clamp, and optimized the seed-metering device to obtain the optimal operating parameters (*Liu et al., 2021*). Chen designed a vertical disc metering device, and used the quadratic orthogonal rotation center combination design test to optimize the structural parameters of the seed agitators (*Chen et al., 2021*). Tian designed a rotary precision hill direct seeding metering device, and obtained the optimal parameters through test (*Tian et al., 2021*). Mechanical metering device has the problems of seed injury, seed sticking and complex structure. The air suction metering device has high processing precision, high energy consumption and high air tightness requirements *(Wang et al., 2017; Yi et al., 2021).* The fluid metering device has higher requirements for mixed suspension *(Zhang et al., 2017).*

The purpose of this paper is to design and trial-produce a single-row small grain precision seeder with simple structure, low damage rate and low cost, and carry out static seeding and seeding experiments on the seed metering device of the seeder. This study can provide reference for the development of precision sowing technology for millet and other small grains.

MATERIALS AND METHODS

Overall Design of Seeder

The single-row small grain precision seeder is shown in figure 1.

It is mainly composed of ring screw *1*, ground wheel *2*, body frame *3*, scraping blade *4*, seed metering device *5*, big sprocket *6*, chain *7,* hand-push rod *8*, small sprocket *9*, pressing wheel *10*, spring *11*, tension pulley wheel *12*, type *R* opening pin *13*, seed guide tube *14*, furrow opener *15*, butterfly nut *16* and other parts. Ground wheel, furrow opener, pressing wheel through bolts or pins installed on the body frame, adjust the opening pin installation position can adjust the ditching depth. The seed metering device and the hand putter are fixed on the opener by bolts, the big sprocket and the seed tube are installed on the seed metering device, the small sprocket is installed on the pressing wheel, and the tension pulley wheel is installed on the body frame. Adjust the tightness of the tensioning wheel by a spring mounted on the frame. The number of working rows is single, the whole machine size is: 1100mm × 400mm × 960mm.

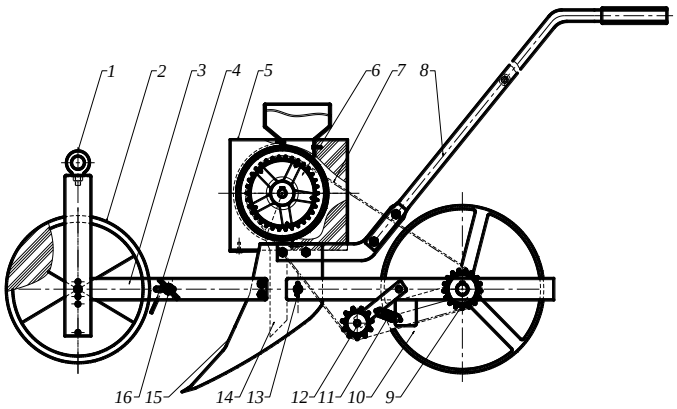

Fig. 1- Schematic diagram of the structure of a single-row small grain precision seeder

1 – Ring screw; 2 – Ground wheel; 3 – Body frame; 4 – Scraping blade; 5 – Seed metering device; 6 – Big sprocket; 7 – Chain; 8 – Hand-push rod; 9 – Small sprocket; 10 – Pressing wheel; 11 – Spring; 12 – Tension pulley wheel; 13 – Type R opening pin; 14 – Seeding guide tube; 15 – Furrow opener; 16 – Butterfly nut

Working principle

When the seeder is working, the forward power is provided by pushing the hand-push rod (*8*) and pulling the ring screw (*1*). The pressing wheel drives the seed metering device shaft to rotate through the chain drive, and the seed metering device shaft drives the seed metering wheel to rotate. The seed is introduced into the seed ditch through the seeding guide tube, and the concave pressing wheel completes the soil covering and pressing operation at the same time. The tensioning wheel can prevent the chain from unchaining under the action of spring tension.

Overall structure design and working principle of seed metering device

The radius R of the seed metering wheel is 70 mm, and the larger diameter of the seed metering wheel can prolong the filling time and filling distance, which is beneficial to improve the filling coefficient. *(Huang et al., 2019)*. The thickness of the seed metering wheel is 30 mm. In order to meet the land with different moisture conditions, the seed metering wheel is a double-row sockets. The single-row or double-row seeding can be determined according to the moisture condition of soil, which effectively improves the utilization rate of the seeding device. The number of double-row sockets of the metering device is designed to be 20, the center line of the two rows of sockets is 14mm apart, and the center of the single-row socket is 8mm from the edge of the seed metering wheel. The minimum diameter of the seeding wheel shaft can be calculated to be 12 mm according to Formulas (1) and (2).

$$d \geq A_0 \sqrt[3]{\frac{P}{n}} \quad \text{[mm]} \tag{1}$$

$$P = \frac{FV}{1000} \quad \text{[kW]} \tag{2}$$

where: d is the minimum diameter of the shaft, [mm];

A_0 is a constant (related to the material and structure of the shaft), and the value is 126;

n is the rotational speed of the metering device, [r/min];

P is power, [kW];

F is the working resistance, [N], the value is 110 N;

V is the speed of the metering device, [m/s].

According to 'GB/T 276-2013', use a 6001 deep groove ball bearing. According to 'GB/T 1096-2003', select 5mm×5mm ordinary flat keys. The cross section of filling port is 50 mm × 8 mm, and the cross section of seeding port is 40 mm × 30 mm. Acrylic plate has the advantages of high transparency, easy processing, so the seed metering wheel, shell and end cover are made of acrylic plate processing. The processed metering device can clearly see its internal structure and the whole seeding process.

The socket wheel-ring groove metering device is mainly composed of seed box *1*, scraping seed brush *3*, seed metering wheel *5*, ring groove *6*, seed clearing brush *8*, seed metering shell *9*, metering device shaft *12*, end cover *13*, etc. the schematic diagram of the seed metering device is shown in Fig. 2.

When working, the pressing wheel drives the metering shaft *12* to rotate clockwise through the chain drive, and the shaft drives the metering wheel *5* to rotate through the key connection.

The seeds in the filling room *2* are filled into socket *4* under the action of gravity. With the rotation of the seed metering wheel, the seed brush *3* removes the excess seeds. In the seed protection area, there is a ring groove *6* at the corresponding part of socket. The ring groove can effectively avoid compression and friction of the seed protection plate on seed, so as to achieve the effect of protecting the seed. After the seed metering wheel is turned about 110° from the vertical direction, seed begins to move from socket to the ring groove. In order to ensure that the seed in the socket can be completely discharged into seed furrow, a seed cleaning brush *8* was installed at the seed outlet *7*.

The conical section of the ring groove seed metering device can only accommodate one seed, which can avoid the self-locking phenomenon of two seeds. The socket wheel seed metering device has a more accurate hole spacing and the number of seeds per hole, the height of seed falling is low, and it can be designed into single and double row sockets *(Li et al., 2018).* Therefore, the seeding method of the seed metering device is the socket wheel ring groove type, that is, the seed metering wheel is socket wheel, and the seed protection plate has a 1/2 ring groove corresponding to the socket.

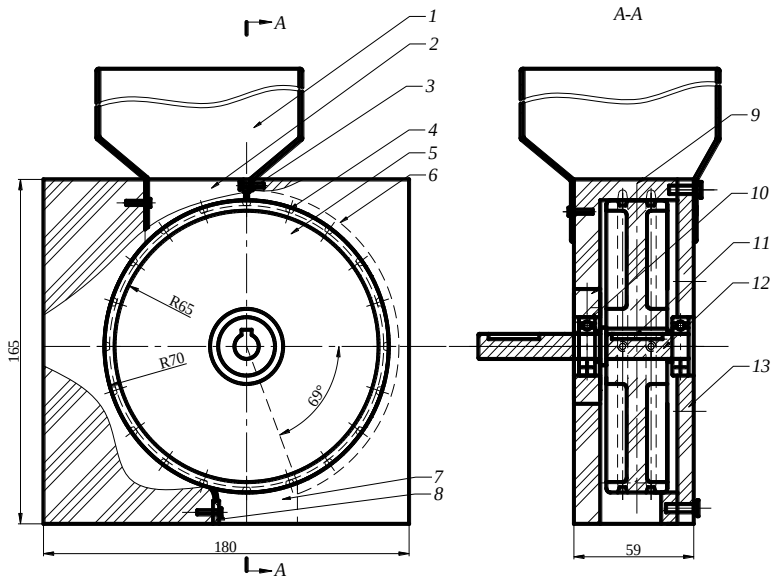

a) Schematic diagram of the seed metering device

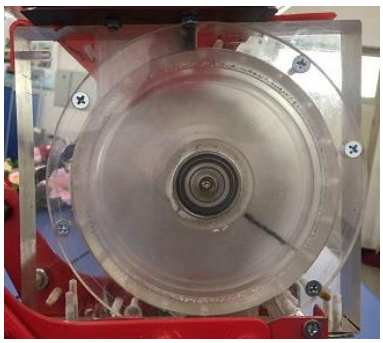

b) The object diagram of the seed metering device

Fig. 2 - The seed metering device

1 – Seed box; 2 – Filling room; 3 – Scraping seed brush; 4 – Socket; 5 – Seed metering wheel; 6 – Ring groove; 7 – Seed outlet; 8 – Seed cleaning brush; 9 – Seed metering shell; 10 – Rolling bearing; 11 – Keyslot; 12 – Seed metering shaft; 13 – End cover

Design of socket section and ring groove section

In order to design the cross-sectional shape and size of the socket, it is necessary to measure the triaxial size of small grains. In this paper, the triaxial size of millet and broomcorn millet were measured by digital vernier caliper (accuracy: ± 0.01mm). The measurement results are shown in table 1.

Table 1

Measurement the triaxial size of the millet and broomcorn millet

Small grain cereal species	Triaxial size/mm	Measurement times					Average value/mm
		1	2	3	4	5	
Millet	Length	2.16	2.21	2.24	2.18	2.15	2.188
	Width	1.81	1.92	1.85	1.89	1.87	1.868
	Height	1.45	1.41	1.38	1.36	1.42	1.404
Broomcorn millet	Length	3.42	3.48	3.53	3.50	3.45	3.476
	Width	2.53	2.51	2.61	2.42	2.48	2.510
	Height	1.87	1.74	1.99	1.78	1.90	1.856

It is known from table 1 that the average size of the three axes of millet is 2.19 mm length, 1.87 mm width and 1.40 mm height. The three-axis average size of broomcorn millet is 3.48 mm in length, 2.51 mm in width and 1.86 mm in height. Therefore, the shape of the socket is designed as an inverted conical table, and the angle between the generatrix and the vertical direction is designed to be 20°.

The cross-section shape is shown in fig.3 The socket can accommodate up to 2~3 seeds. After cleaning and brushing, two seeds can be retained. The two sides of the socket are inclined, which is conducive to both filling and seeding.

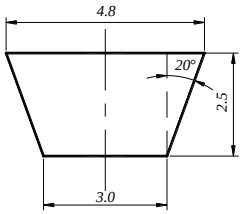

Fig. 3 - The shape of socket section

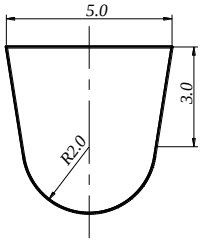

Fig. 4 - The shape of ring groove section

In order to make the ring groove shape suitable for small grains of various shapes and sizes, the cross-section design of the ring groove is shown in figure 4.

Seed metering device cleaning device and brushing device

Commonly used seed cleaning methods include rigid seed cleaning plate, elastic seed cleaning wheel, rubber scraper, brush and air flow seed cleaning. The bristle brush is harder than sponge, but softer than rubber. The cleaning effect is better than that of rubber and felt, and the rate of seed injury is lower. In order to reduce the rate of seed injury, the brush is used to scrape the excess seeds. The brush is fixed with iron sheet and bolt in the filling port and coincides with the central axis of the seed metering wheel. The cleaning device of the seed metering device is to use iron sheet and bolt to fix the brush at the end of the seed metering port, and the seeds remaining in the socket are brushed out of the socket in time and then discharged into the seed furrow, which does not affect the subsequent filling.

Body frame design

In order to reduce the weight of the whole seeder, on the premise of meeting the stiffness requirements of the seeder, the hand-push rod of the frame is connected by steel pipe and fixed by bolt, and the beam spacing of the hand-push rod is 230 mm. While meeting the seeding requirements, in order to facilitate maintenance, the ground wheel, opener, and press wheel are all connected with shafts and opening pins, and the length of the shaft is 90 mm.

In order to meet the characteristics of low cost, convenient disassembly and assembly, adjustable sowing depth, adjustable sowing amount and adjustable hand-held parts of the seeder, at the same time, the space is reserved according to the ground wheel, seed metering device, furrow opener and pressing wheel. The length of the frame is 730 mm, the width is 400 mm, and the height is 840 mm.

Transmission system design

The driving wheel generally adopts the pressing wheel or the ground wheel, and the seeder adopts the pressing wheel drive, and the transmission type is chain drive.

First, the optimal speed of the metering device is obtained by the test. The speed of the seed metering device is adjusted by adjusting the speed of a stepless variable speed motor. Taking millet and broomcorn millet as the test objects, under the static seeding performance test, the optimal speed range of the metering device was measured as: 9 r/min~15 r/min. The theoretical operating speed of the seeder is about 18 r/min~30 r/min. The average transmission ratio of the sprocket can be calculated as about 1:2 by formula (3), and the tooth number ratio of the sprocket is about 2:1.

$$i=\frac{\pi D(1+\delta)}{tz}=\frac{n_1}{n_2}=\frac{z_2}{z_1} \tag{3}$$

where: z_1 is number of teeth of the driving sprocket;

z_2 is number of teeth of the driven sprocket;

n_1 is the rotational speed of the driving sprocket, [r/min];

n_2 is the rotational speed of the driven sprocket, [r/min];

D is the diameter of the press wheel, [m];

δ is he slip rate of the press wheel, [%];

t is the hole spacing, [m];

z is the number of sockets of seeding wheel;

Generally, the number of small sprocket teeth is greater than or equal to 17*(Pu et al., 2019)*. Therefore, the number of teeth of the driving and driven sprockets is: z_1=17, z_2=34.

In order to prevent the chain from loosening and falling off, reduce the wear of the chain and sprocket, and prolong the service life of the chain and sprocket, it is necessary to install the tension wheel. The diameter of the tension wheel should be close to the diameter of the small sprocket *(Pu et al., 2019)*. The number of teeth of the tension wheel is 11. Chain tensioner adopts spring structure. The physical diagram of the single row small grain precision seeder is shown in figure 5.

Fig. 5 - Physical diagram of the single-row small grain precision seeder

Test instrument

Test instruments include: electronic balance, tape measure. SQP electronic balance parameters: Sartorius Scientific Instruments (Beijing) Co., Ltd., operating voltage:12~18V(DC)/0.4A, calibration index value of 10mg.The millet variety is 'Jingu-21', and the broomcorn millet variety is 'Jinshu-8'.

Static seeding test of the seeder

The static seeding test of the seeder is mainly to test the breaking rate and sowing quantity stability of the seed. The method is as follows: the ground wheel and opener of the seeder are fixed on the ground, the pressing wheel is suspended in the air, the pressing wheel is rotated at a constant speed, and the seeds collected in a container below the opener within 1 min are collected as a group. Test five groups, measure their weight with the electronic balance, record the test results and process them with SAS. And the experimental results were analyzed.

Effect of rotational speed on millet and broomcorn millet sowing quantity

The test is carried out according to the above method, and the test results are calculated by the following formula.

$$\bar{q} = \frac{1}{n}\sum_{i=1}^{n} q_i \quad [g] \tag{4}$$

$$S_{\bar{q}} = \sqrt{\frac{1}{n-1}\sum_{i=1}^{n}\left(\bar{q} - q_i\right)^2} \quad [g] \tag{5}$$

$$\alpha_i = \frac{S_{\bar{q}}}{\bar{q}} \quad [\%] \tag{6}$$

where: $\bar{q}$ is the average of five measurements, [g];

n is the total number of measurements;

$S_{\bar{q}}$ is the standard deviation of five measurements, [g];

α_i is the coefficient of variation of sowing quantity, [%];

The rotational speed of the seed metering device is 9 r/min, 10 r/min, 12 r/min, 14 r/min and 15 r/min, respectively. The measurement results are recorded in table 2.

The SAS software was used to analyze the balanced random design test of the samples, and the mean multiple comparisons were performed. The results are shown in table 3.

The test of seeds damage rate

Before the test, five samples of the same quality were randomly selected from the same batch of seeds that were not tested to determine the natural damage rate of the seeds. The test material selected for determining the seeds damage rate is the seeds discharged through the seed metering device.

Five samples of the same quality were randomly weighed, and the samples were placed on an electronic balance to measure their weight, record the data, and calculate the damage rate of the seeds.

Sowing test of the seeder

In order to observe the sowing situation and record the data of millet and broomcorn millet more accurately, this test was carried out on the sand trough. The test method is as follows: the metering device is fixed on the trolley, and the trolley is driven by the motor at a constant speed according to the designed speed. According to the rotation speed of the seed metering wheel, the field test was simulated at 9r/min, 10r/min, 12r/min, 14r/min and 15r/min respectively, and the sowing situation is observed and the hill spacing is recorded. Through comparative analysis, it is concluded that when the rotation speed of the seed metering wheel is 14 r/min, the hill spacing of millet is mostly 50 mm~70 mm, and the number of seeds per hill is mostly 2~4, and the sowing uniformity of millet is the best. The test results are shown in fig.6. When the rotation speed of the seed metering wheel is 12 r/min, the hill spacing of broomcorn millet is mostly 60 mm~90 mm, the number of seeds per hill is mostly 1~2, and the sowing uniformity of broomcorn millet is the best. The test results are shown in Fig.7.

Fig. 6 - The test of millet sowing

Fig. 7 - The test of broomcorn millet

Fig. 8 -The test of field sowing

According to the requirements of precision sowing, the best hill spacing of millet is generally 50 mm~100 mm, and the number of seeds per hill is 2~3. The best hill spacing of broomcorn millet is generally 45mm~60mm, and the number of seeds per hill is 1~2. Therefore, when the rotation speed of the seed metering wheel is 14r/min and 12r/min respectively, millet and broomcorn millet meet the requirements of precision seeding.

Field test of the seeder

According to the requirements of GB/T6973-2005 single grain (precision) seeder test method, the field test was designed and carried out. The field test included sowing uniformity test and sowing depth consistency test. The sowing length is 30 m, and the artificial sowing is carried out at a speed of about 0.5m/s. The ditching depth is set to 40 mm, as shown in Fig.8.

The soil on the seed was gently scraped with a scraper and a brush to make the seed completely leak out, and then the sowing depth was measured with a ruler. At the same time, the number of grains per hill and the distance between hills were measured. When the number of grains per hill of millet was 2-4, it was qualified, and the others were unqualified. When the number of grains per hill of broomcorn millet is 2-5, it is qualified, and the others are unqualified. The theoretical hill spacing value plus or minus 15 mm was qualified. A total of 101 grains per hill, 100 hill spacing, and 50 sowing depths were measured. Record and process the data, calculate the qualified rate of the number of grains per hill, the qualified rate of hill spacing and the average sowing depth.

RESULTS

The results obtained using the designed small grain precision seeder are presented below.

Table 2

Effect of the rotate speed on sowing quantity of millet and broomcorn millet

Small grain cereal species	Rotate speed(r/min)	Measurement times					Average value / g
		1	2	3	4	5	
Millet	9	3.66	3.63	3.59	3.61	3.64	3.626
	10	3.81	3.87	3.79	3.83	3.8	3.820
	12	4.21	4.17	4.25	4.23	4.18	4.208
	14	4.71	4.77	4.8	4.75	4.72	4.750
	15	5.08	5.12	5.14	5.09	5.11	5.108

Small grain cereal species	Rotate speed(r/min)	Measurement times					Average value / g
		1	2	3	4	5	
Broomcorn millet	9	1.91	1.97	1.96	1.89	1.94	1.934
	10	2.13	2.2	2.22	2.18	2.17	2.180
	12	2.66	2.67	2.75	2.69	2.70	2.694
	14	2.95	2.93	2.96	2.94	2.95	2.946
	15	3.19	3.21	3.22	3.2	3.21	3.206

From Table 2 and Table 3, it can be seen that the rotational speed has a very significant effect on the sowing quantity of millet and broomcorn millet ($P < 0.001$). The greater the rotational speed, the greater the sowing quantity. The sample is analyzed by a linear regression model. The regression model is as follows:

$$y_1 = 0.24254x + 1.39194 \quad (7)$$

$$y_2 = 0.20569x + 0.12369 \quad (8)$$

where: y_1 is millet sowing quantity, [g];

y_2 is broomcorn millet sowing quantity, [g];

x is rotation speed of seed metering device, [r/min]

The determination coefficients R^2 of the regression model are 0.9877 and 0.9862, respectively. It shows that the fitting accuracy of the model is high and can be used as the corresponding prediction.

Table 3

The multiple comparison of means about the rotate speed test

Small grain cereal species	Rotate speed(r/min)	Average value/g	Number of observations	Significance	
				0.05	0.01
Millet	9	3.626	5	e	E
	10	3.820	5	d	D
	12	4.208	5	c	C
	14	4.750	5	b	B
	15	5.108	5	a	A
Broomcorn millet	9	1.934	5	e	E
	10	2.180	5	d	D
	12	2.694	5	c	C
	14	2.946	5	b	B
	15	3.206	5	a	A

Table 4

The effect of rotational speed on the damage rate of millet and broomcorn millet

Damage rate	Rotate speed(r/min)				
	9	10	12	14	15
Damage rate of millet	6.83	7.05	7.44	7.78	7.92
Damage rate of broomcorn millet	6.51	6.68	7.02	7.39	7.53

The effect of rotational speed on the damage rate of millet and broomcorn millet is shown in table 4.

It can be seen from table 4 that with the increase of the rotation speed of the seed metering wheel, the damage rate of millet and broomcorn millet increases. At the same speed, the damage rate of broomcorn millet is smaller than that of millet. This is because under the same moisture content, broomcorn millet is harder than millet *(Sun et al., 2017;* Yang *et al., 2016)*, and the seed coat of broomcorn millet is harder than millet and smoother than millet.

Table 5

Field sowing test results

Grain	March-ing speed ($m \cdot s^{-1}$)	Rotation speed of seed metering device ($r \cdot min^{-1}$)	Theoret-ical hole spacing / mm	Average hole spacing / mm	Average number of grains per hole	Qualified rate of hole spacing / %	Qualified rate of the number of grains per hole / %	Average sowing depth / mm
Millet	0.50	19	78	79	3.0	90	82	39.4
Broomcorn millet	0.44	17	91	90	2.4	91	83	41.1

It can be seen from table 5 that at the marching speed of about 0.5 m/s, the average hole spacing of millet and broomcorn millet was 79 mm and 90 mm respectively. The average number of grains per hole was 3.0 and 2.4, respectively. The qualified rate of hole spacing is greater than or equal to 90%. The qualified rate of hole number is greater than or equal to 82%, and the average sowing depth was 39.4 mm and 41.1 mm respectively. All indicators meet the technical requirements of JB/T 10293-2013 single grain (precision) planter.

CONCLUSIONS

By designing a single-row small grain precision seeder and conducting static seeding and seeding tests on the seeder, the following conclusions are obtained.

1. The core component of the single-row small grain precision seeder is the socket wheel-ring groove type precision metering device. It has the advantages of simple structure, low rate of damage and jam seed, convenient disassembly and assembly, adjustable sowing depth, adjustable sowing rate, adjustable hand-held parts, low cost, etc. Small seeds of different sizes can be sown by changing the seed metering wheel.

2. The results of static seeding test showed that the rotational speed had a significant effect on the sowing quantity of millet and broomcorn millet ($P < 0.001$). The higher the rotational speed, the greater the sowing quantity. With the increase of rotational speed of seed metering wheel, the damage rate of millet and broomcorn millet increased. At the same rotational speed, the damage rate of broomcorn millet is smaller than that of millet.

3. When the seeder is at a marching speed of about 0.5 m/s, the qualified rate of the hill spacing of millet and broomcorn millet is greater than or equal to 90%, and the qualified rate of the number of grains per hole is greater than or equal to 82%. All indicators meet the requirements of the technical conditions of single-grain (precision) seeder.

ACKNOWLEDGEMENTS

This research titled ‘Design and experiment of a single-row small grain precision seeder’ was funded by the National Key Research and Development Plan of China (2016YFD0701801), Basic Research Program (Free Exploration) Youth Project of Shanxi Province (20210302124521), '1331' Industrial Information Transformation to Enhance Collaborative Innovation Center Construction Project of Shanxi Province, Science and Technology Innovation Project of Shanxi Province (2020L0568), Yuncheng Science and Technology Plan Project in 2022 (Basic Research) (YCKJ-2022069), Doctoral Research Start Project of Yuncheng University (YQ-2019020) and Students Innovation and Entrepreneurship Training Project of Yuncheng University (202210123004). The authors are grateful and honored to have obtained support from the Laboratory of Agricultural Biomechanics of Shanxi Agricultural University and the Department of Mechanical and Electrical Engineering of Yuncheng University.

REFERENCES

[1] Arzu Y., Adnan D., (2007), Optimisation of the seed spacing uniformity performance of a vacuum-type precision seeder using response surface methodology. *Biosystems Engineering*, vol.97, issue 3, pp. 347-356.

[2] Arzu Y., Adnan D., (2014), Measurement of seed spacing uniformity performance of a precision metering unit as function of the number of holes on vacuum plate, *Measurement*, Vol. 56, pp.128–135.

[3] Chen Y., Zhang M., Liu Z., Lan Y., Yi L., Ji P., Yin X., (2021), Design and experiment of seed agitator for vertical disk seed metering device, *INMATEH - Agricultural Engineering*, Vol. 63 (1), pp. 179–188. DOI: https://doi.org/10.35633/inmateh-63-18

[4] Cujbescu D., Găgeanu I., Persu C., Gheorghe G., (2022), Numerical simulation of seed distribution of a pneumatic seed meter, *INMATEH - Agricultural Engineering*, Vol. 66 (1), pp. 41–48. DOI: https://doi.org/10.35633/inmateh-66-04

[5] Dylan S., Dianne C., Andrew L., (2013), Precision metering of Santalum spicatum (Australian Sandalwood) seeds, *Biosystems Engineering*, Vol. 115 (2), pp. 171–183.

[6] Hoque M., Karim M., (2016), Upscaling and evaluation of BARI inclined plate planter. *Agriculturists*, vol.13, issue 2, pp. 1-8.

[7] Hou H., Cui Q., Zhang Y., Hu X., Chang Z., (2017), Development of 2BZ-2 type fine and small-amount seeder for foxtail millet (2BZ-2 型谷子精少量播种机的研制), *Transactions of the Chinese Society of Agricultural Engineering*, vol.33, issue 3, pp. 16-22.

[8] Huang J., (2019), *Design and test of electromagnetic linear vibration millet essence small amount seeding device (集中型槽孔轮式油菜精量排种器设计及其破碎率试验研究)*. [Unpublished master's dissertation]. Huazhong Agricultural University.

[9] Karayel D., (2009), Performance of a modified precision vacuum seeder for no-till sowing of maize and soybean. *Soil and Tillage Research*, vol.104, issue 1, pp. 121-125.

[10] Li B., (2018), *Agricultural machinery* (second edition) (农业机械学第二版), ISBN 978-7-109-23840-4, China Agricultural Press, pp. 60-80, Beijing/P.R.C.

[11] Li S., Liu F., Liu M., Cheng R., Xia E., Diao X., (2021), Current Status and Future Prospective of Foxtail Millet Production and Seed Industry in China (中国谷子产业和种业发展现状与未来展望). *Scientia Agricultura Sinica*, vol.54, issue 3, pp. 459-470.

[12] Liu F., Lin Z., Li D., Zhang T., (2021), Design optimization and performance test of magnetic pickup finger seed metering device, *INMATEH - Agricultural Engineering*, Vol. 63 (1), pp. 137–144.

[13] Nikolay Z., Nikolay K., Gao X., Li Q., Mi G., Huang Y., (2022), Design and testing of novel seed miss prevention system for single seed precision metering devices, *Computers and Electronics in Agriculture*, Vol. 198, 107048.

[14] Pu L., Chen G., Wu L., (2019), *Machine design (机械设计)*. ISBN 978-7-04-051421-6, Higher Education Press, pp. 177-185, Beijing/P.R.C.

[15] Pareek C., Tewari V., Machavaram R., Nare B., (2021), Optimizing the seed-cell filling performance of an inclined plate seed metering device using integrated ANN-PSO approach, *Artificial Intelligence in Agriculture*, Vol. 5, pp.1–12.

[16] Pareek C, Tewari V, Machavaram R. (2023), Multi-objective optimization of seeding performance of a pneumatic precision seed metering device using integrated ANN-MOPSO approach, *Engineering Applications of Artificial Intelligence*, Vol. 117, 105559.

[17] Sujit H., Hifjur R., (2022), An unmanned wetland paddy seeder with mechatronic seed metering mechanism for precise seeding, *Computers and Electronics in Agriculture*, Vol. 203, 107463.

[18] Tian L, Ding Z., Su Z., Li L., Wang Z., (2022), Design and experiment of rotary precision hill direct seed-metering device for rice, *INMATEH - Agricultural Engineering*, Vol. 66 (1), pp. 311–320.

[19] Wang F., Lv B., Wang H., Zhao M., (2017), Structural design and test of seed-suction hole of air-sucking seed-metering device for millet (气吸式谷子排种装置吸种孔的结构设计与试验). *Transactions of the Chinese Society of Agricultural Engineering*, vol.33, issue 8, pp. 30-36.

[20] Wang Y., Li H., Wang Q., He J., Lu C., Cheng X., Liu P., Yang Q., (2021), Experiment and parameter optimization of seed distributor of mechanical shooting seed-metering device for wheat, *INMATEH - Agricultural Engineering*, Vol. 63 (1), pp. 29–40.

[21] Yi S., Chen T., Li Y., Tao G., MAO X., (2021), Design and test of millet hill-drop seed-metering device with combination of positive-negative pressure and hole wheel (正负气压-型孔轮组合式谷子穴播排种器设计与试验). *Transactions of the Chinese Society for Agricultural Machinery*, vol.52, issue 6, pp. 83-94.

[22] Zhang Y., Cui Q., Wang F., Hou H., Hu X., (2017), Design and test of fluid and small-amount seed metering device for foxtail millet (谷子精少量流体排种装置的设计与试验). *Transactions of the Chinese Society of Agricultural Engineering*, vol.33, issue 12, pp. 20–27.

[23] Zhang Y., Cui Q., Ye S., Wang C., Zhang Z., (2022), Optimization of stirring parameters for millet fluid seed metering based on response surface methodology, *INMATEH - Agricultural Engineering*, Vol. 66 (1), pp. 373–382. DOI: https://doi.org/10.35633/inmateh-66-37

[24] Zhang Y., Cheng J., Zhang X., Shi Z., Wang M., Wu H., Fu H., (2023), Design and experiment of pressure-holding precision seed-metering device for maize, *INMATEH - Agricultural Engineering*, Vol. 69 (1), pp. 159–169. DOI: https://doi.org/10.35633/inmateh-69-14

MEASUREMENT OF PHYSICAL PROPERTY PARAMETERS AND SIMULATIVE CALIBRATION OF DEM PARAMETERS FOR GREEN ONION SEEDS
/
大葱种子物性参数测量及 DEM 参数仿真标定

Chong TAO[1)], Zhiye MO[1)], Fangyuan LU*[1)], Zhihe LI[1)], Dianbin SU[1)], Yinping ZHANG[1)]
School of Agricultural Engineering and Food Science, Shandong University of Technology, Zibo/ China
Tel: +8615288942032; E-mail: fangyuan-lu@foxmail.com
Corresponding author: Fangyuan Lu
DOI: https://doi.org/10.35633/inmateh-70-13

Keywords: *calibration, contact parameters, green onion seed, discrete elements method, small irregular*

ABSTRACT
The contact parameters setting determines the accuracy of discrete element method (DEM) simulation analysis, while there is a lack of research on contact parameters of green onion seed. In this paper, the physical parameters of green onion seeds were measured by experiment, and the DEM parameters were calibrated by simulation. Based on EDEM software, the Hertz-Mindlin no-slip model was used to create the particle model of green onion seeds that takes on the shape of peltate with the irregular surface, and the repose angle was measured by the measurement method of lifted cylinder. Plackett-Burman test was designed to screen the significance of parameters, and the optimal range of significance parameters was further determined through the steepest climbing test. Then the regression model of seeds repose angle was obtained by Box-Behnken test and the optimal parameter combination was calculated: the static friction factor between seeds was 0.424, the rolling friction factor was 0.085, the static friction factor between seeds and steel was 0.310. The optimized repose angle in the simulation had an overall relative error of 0.54%, indicating that the contact parameters of the calibrated green onion seed had high accuracy.

摘要
离散元法（DEM）仿真分析的精度取决于接触参数的设置，而目前缺乏对大葱种子接触参数的相关研究。因此，本文通过实验测量了大葱种子的物理参数，并通过仿真对其离散元参数进行了标定。基于EDEM软件，采用Hertz-Mindlin无滑动接触模型，建立了大葱种子呈盾形且表面不规则的颗粒模型，并采用圆筒提升法测量堆积角。通过 Plackett-Burman 试验筛选参数的显著性，并使用最陡爬坡试验进一步确定显著性参数的最佳范围。然后通过 Box-Behnken 试验得到大葱种子堆积角的回归模型，并计算出最优参数组合:大葱种子间静摩擦系数为0.424，大葱种子间滚动摩擦系数为0.085，大葱种子与钢板静摩擦系数为0.310。经过优化后的仿真堆积角与实际数值的相对误差为0.54%，说明标定出的大葱种子接触参数具有较高的精度。

INTRODUCTION

As a seasoning vegetable and cash crop widely cultivated in China, green onion plays an extremely important role in vegetable production in China *(Liu D. et al., 2017).* The average annual planting area green onion reaches half a million hectares and its annual export share reaches 70% of the world one *(Wang H.X. et al., 2019).* The mechanization level of green onion planting in China is currently low, so the method of green onion planting mainly relies on artificial sowing, which seriously restricts the development of mechanization in the whole process of green onion production. In order to deeply study the movement mechanism between green onion seeds and the seeding mechanism during the sowing process, it is necessary to study the physical parameters and contact parameters of green onion seeds. Due to the small volume, irregular shape and poor fluidity of green onion seeds, it is effective to use physical test to measure the physical parameters and to calibrate the DEM parameters combined with simulation experiment *(Wang W.W. et al., 2021),* that can accurately obtain the parameters of green onion seeds. The research results are of great significance for the theoretical analysis of the precise seeding process and the performance optimization of the sowing device *(Lu F.Y. et al., 2018).*

[1] *Chong Tao, M.S. Stud. Eng.; Zhiye Mo, M.S. Stud. Eng.; Fangyuan Lu, As. Ph.D. Eng.; Zhihe Li, As. Ph.D. Eng.; Dianbin Su, As. Ph.D. Eng.; Yinping Zhang, As. Ph.D. Eng.*

At present, DEM simulation is an effective method to solve the problem of modern agricultural technology, many studies have been carried out on the calibration of discrete element simulation parameters of agricultural materials at home and abroad in order to ensure the accuracy of simulation. *Peng Z. et al., (2022),* calibrated the parametric calibration of cotton straw parameters in Xinjiang through the simulation and actual measurement tests of the repose angle. *Lu F.Y. et al., (2018),* constructed a regression equation for the friction angle of rice bud seeds based on the DEM, and calibrated the main contact parameters with different moisture contents. *Xuejie M. et al., (2022),* calibrated the contact parameters of seed and powder by the repose angle trial and error method. *Ma W.P. et al., (2020),* calibrated the optimal combination of discrete element contact parameters of alfalfa seeds by using a device that can simultaneously measure the repose angle and the repose angle of materials. *Li Y.X et al., (2019),* simplified the irregular wheat flour into soft spherical particles, and adopted the Hertz-Mindlin with JKR model to obtain the accurate contact parameters of wheat flour discrete element simulation. *Zhou H. et al., (2022),* determined the DEM parameters of paddy soil with high moisture content (>40%) by using the Hertz–Mindlin with JKR model. *Yan D. et al., (2022),* measured and calibrated the RFCP-P and RFCP-B of soybean seed particles of three varieties with different sphericity. The above studies have calibrated the key DEM parameters of the particles, which improved the accuracy of related simulation studies, but there is no related study reported on green onion seeds and similar seeds.

In this paper, the intrinsic parameters of green onion seeds were measured, and the physical stacking test and simulation test were conducted on green onion seeds. With the repose angle as the index, Plackett-Burman test was used to screen out the factors that had significant influence on the index, and the steepest climbing test was used to quickly find the interval of the optimal value of each factor. The second-order regression models of the repose angle and the static friction factor between green onion seeds, the rolling friction factor between seeds and the static friction factor between seeds and steel was established by the design-expert optimization module, then, the key contact parameters that had significant influence on the discrete element simulation study of green onion seeds were obtained. Finally, the reliability of the model and simulation parameters was verified by the repose angle test, in order to provide reliable discrete element model parameters for the simulation analysis of the precision sowing of green onion and other mechanized devices. The result provides essential theoretical parameters for the study of the performance of the seeding machinery for green onion.

MATERIALS AND METHODS

Test material and physical parameter determination

For the DEM simulation, physical properties and contact parameters of seeds are required to be set. The physical parameters of green onion seeds include shape, size, density, moisture content, Poisson's ratio, shear modulus and Young's modulus, which could be obtained directly through test measurement. While the recovery coefficient, static friction coefficient and rolling friction coefficient between seed particles or between seed particles and boundary are difficult to measure inaccurately and therefore need to be calibrated.

Determination of triaxial size, 1000-grain weight, density and moisture content

This paper takes the green onion seeds of Zhangyou 006 variety in Shandong Province as the research object, which has the advantages of strong disease resistance, frost resistance and fast growth rate. Green onion seeds belong to bulk materials, and the basic physical property parameters need to be measured include triaxial size, 1000-grain weight, density, moisture content, Poisson's ratio, Young's modulus and shear modulus.

In order to accurately establish the three-dimensional model of green onion seed, 500 seeds of Zhangyou 006 variety were randomly selected. In this paper, it was used to measure the maximum triaxial size of green onion seeds by SZX16 advanced research stereological microscope of OLYMPUS (accuracy is 0.01 mm) (Fig.1). Image View software was used to calibrate the range, added a ruler, and measured the data, which made the data more accurate. The measured results showed that green onion seeds took on the shape of black peltate with the irregular and angular surface (Fig.2), and the average values of the maximum length, width and thickness of the seeds were 3.08, 2.02 and 1.23 mm.

One thousand seeds were randomly selected and weighed with a high-precision electronic analytical balance. The average value was obtained by measuring five times. The thousand seeds of green onion is 2.49 g. Then the density of 100 green onion seeds was measured by the pycnometer method, and the average value was taken ten times, and the density of green onion seeds was obtained as 1085 kg/m^3.

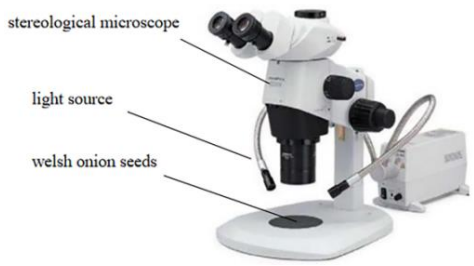

Fig. 1 - Stereological microscope

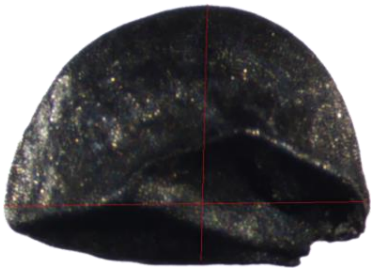

Fig. 2 - Welsh onion seed

The green onion seeds are oil crops, so the electric heating constant temperature drying oven is used to dry the green onion seeds at a low temperature for 8 hours. 500 seeds were selected randomly to measure their weight at room temperature, and then dried continuously for eight hours at a temperature of 103°C ± 2°C. The temperature in the oven was lowered to room temperature before the green onion seeds were taken out and weighed. The moisture content on a dry basis is obtained from Eq.1.

The average moisture content of the dry base of green onion seeds is 6.8% through measurement test and calculation with 5 repetitions.

$$M_a = \frac{m_b}{m_c} \times 100\% \quad (1)$$

where:

m_b is the mass of water contained in the material, g;

m_c is the mass of dry matter contained in the material;

M_a is the dry basis moisture content.

Poisson's ratio determination

As the shape of green onion seeds is small and irregular, professional physical property tester (TA.XT Plus C) from Stable Micro Systems UK was adopted to measure the Poisson's ratio of seeds accurately. First of all, 20 seeds were randomly selected and labeled to measure thickness (axial) and width (transverse), and a cylindrical probe with a diameter of 8 mm that loaded at 0.1 mm/s along the direction of the green onion seed thickness (axial) was used to apply pressure until the seed was cracked to stop it *(Xiangqian D. et al., 2022)*. At the moment the deformation of the positive strain in the direction of seed thickness was measured by the mass spectrometer, and the deformation of the positive strain in the direction of width was measured by the digital vernier caliper. At last, the Poisson's ratio of green onion seeds was calculated from Eq.2. Through measurement test and calculation with 20 repetitions, the average value of Poisson's ratio of green onion seeds was 0.481.

$$t = \frac{|c'|}{c} = \frac{Q_1 - Q_2}{S_1 - S_2} \quad (2)$$

where:

t is Poisson's ratio;

c' - the deformation amount of green onion seed in the width direction, mm;

c - the amount of deformation in the direction of seed thickness, mm;

Q_1 - the seed width of scallion before loading, mm;

Q_2 - the seed width of green onion after loading, mm;

S_1 - the seed thickness of scallion before loading, mm;

S_2 - the thickness of onion seed after loading, mm.

Determination of elastic modulus and shear modulus

20 seeds selected randomly were labeled from 1 to 20 in order. The cylindrical probe with a diameter of 8 mm that loaded at 10 mm/min along the direction of the seeds thickness was used to apply pressure *(Fei L. et al., 2020).* 20 labeled seeds were tested separately, and the average value of the 20 sets of test data was taken. According to the following Eq.3 and Eq.4, the average elastic modulus of the green onion seeds is 29.8 MPa and shear modulus is 10.06 MPa.

$$E = \frac{\alpha}{\varepsilon} \quad (3)$$

$$G = \frac{E}{2(1+t)} \quad (4)$$

where:

E is the elastic modulus of green onion seeds, MPa;

α - the maximum compressive stress;

ε - the line strain;

G - shear modulus, MPa;

t - Poisson's ratio of green onion seeds.

Contact parameter determination

The inclined plane method was used to measure the static friction coefficient between green onion seeds and boundary (the main material of the precision sowing device is steel), and the interspecific static friction coefficient of seeds. The seeds were arranged closely and glued on the cardboard with double-sided adhesive to form a board composed of seeds to eliminate rolling friction caused by seeds on the steel plate *(Zhang W., 2022),* as shown in the Fig.3. The seeds board was placed on the steel plate with the side of the seed in contact with the steel plate. When the test was started, right end of the steel plate was placed on the small experimental lifting platform that was slowly lifted, and the high-speed camera was used to record the operation. When the seed board began to slide, the experimental lifting platform stopped, meanwhile, the tilt angle of the steel plate was recorded with the digital display inclinometer. The above operation was repeated 10 times and the average datum was calculated. According to Eq.5, the static friction coefficient between green onion seeds and steel is 0.326.

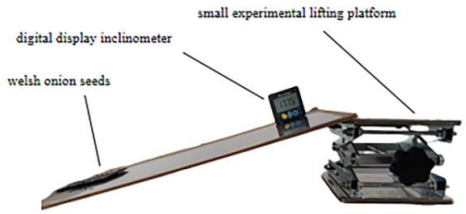

Fig. 3 - Small experimental lifting platform

$$\theta = tan\beta \quad (5)$$

where:

θ is the static friction coefficient;

β is the angle indicated by the digital display Inclinometer, °.

The friction coefficient between green onion seeds was measured using the above method, and seeds were closely arranged and bonded on the plate to make up a seeds surface. At the beginning, green onion seeds were placed on the seeds surface, and the height of the acrylic plate was slowly raised with the experiment platform until the seeds slipping, then the tilt angle of the seeds surface was recorded by a digital angle gauge. The average interspecific static friction coefficient was 0.493 after 10 repetitions.

Physical experiment on the repose angle

The repose angle of green onion seeds was measured by the measurement method of lifted cylinder device consisting of a cylinder with diameter of 100 mm and length of 200 mm and a plate of 2 mm thickness. The steel cylinder filled with a certain amount of seeds was lifted slowly and uniformly. After all the seeds were completely stationary on the steel plate, the high-definition camera was used to take vertical pictures of the positive side of the stacked seeds. The repose angle image obtained by the test was processed by Python to make the result more accurate. Firstly, the image of seeds repose angle was processed by grayscale, then the binarization was processed by threshold method, and the image contour was extracted by the findContours () function in Open CV. After the edge contour was obtained, Python was used to process the image, extract the straight line, and calculate the angle of the straight line *(Zenghui G. et al., 2022).* The average repose angle of green onion seeds was 25.34° after ten repetitions. The original image and edge contour curve image are shown in Fig.4.

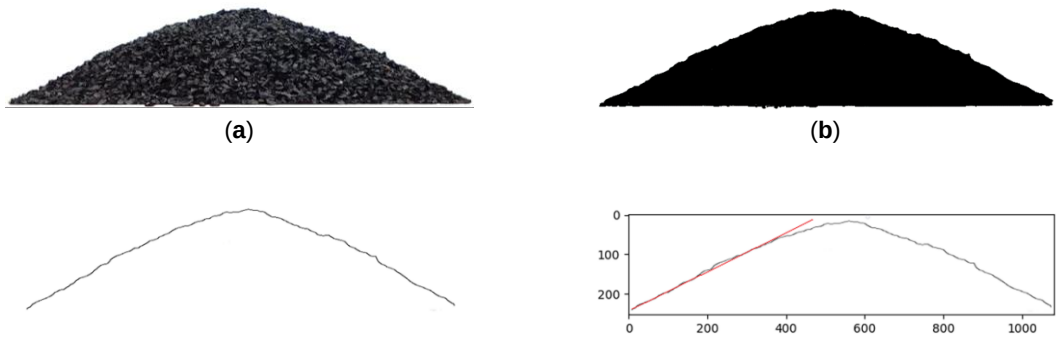

Fig. 4 - Physical stacking test of green onion seeds
(a) Original image; (b) Binarized image contour extraction; (c) Edge contour; (d) Fitting the straight lines.

Simulation experiment on repose angle

Simulation model

EDEM software was used to build the simulation particle model based on the basic physical property parameters of green onion seeds determined by the previous physical test and pre-test. The nine-ball model was used to establish the particle model of green onion seeds in order to establish the shape of peltate with the irregular surface *(Min F. et al., 2023).* The triaxial dimensions of the particle model were consistent with the determined size (Fig.5).

Three-dimensional materialized model of the lifted cylinder device established according to the cylinder size and thickness used in physical test was imported into EDEM software. A particle factory for generating green onion seeds was established above the cylinder, and the generation mode of the particles was set as dynamic generation with a generation rate of 1000 units/s *(Gong X. et al., 2022).* The total number of green onion seeds was set to 2000, and the generation time was set to 2.5 s. Significantly, the sizes of all seeds were generated according to the normal distribution law of determined size. Then motion of the cylinder was the set to move along the vertical upward direction with the uniform speed of 0.1 m/s.

The seeds in the cylinder (Fig.6) are slowly scattered into piles, the repose angle cannot be measured until all seeds are completely stationary. The total simulation time is set to 5 s.

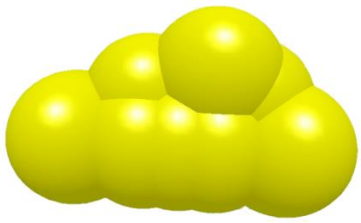

Fig. 5 - Discrete element model of green onion seeds

Fig. 6 - Simulation test of green onion seeds

DEM parameters calibration

Green onion seeds density, Poisson's ratio and Young's modulus were determined according to previous studies. The ranges of density, Poisson's ratio, Young's modulus as well as the recovery coefficient, static friction coefficient and rolling friction coefficient of seed-seed and seed-steel, were selected from pre-experiment and literature (Table 1) *(Xiaolong H. et al., 2022).*

The Plackett-Burman test was used to screen out the parameters that had significant influence on the repose angle by taking the repose angle of the particle model of green onion seeds as the response value.

Table 1

Parameters and corresponding value ranges in the Plackett–Burman test

Symbol	Parameter	Unit	Value	
			Low level (-1)	High level (+1)
S_1	Poisson's ratio of green onion seeds	-	0.28	0.48
S_2	Green onion seeds density	Kg/m³	885	1285
S_3	Young's modulus of green onion seeds	MPa	9.88	49.80
S_4	Collision recovery coefficient of seed-seed	-	0.10	0.20
S_5	Static friction factor of seed-steel	-	0.28	0.38
S_6	Static friction factor of seed-seed	-	0.30	0.60
S_7	Rolling friction factor of seed-seed	-	0.05	0.17
S_8	Collision recovery coefficient of seed-steel	-	0.29	0.49
S_9	Rolling friction factor of seed-steel	-	0.05	0.17
S_{10}, S_{11}	The virtual parameters	-	-1	+1

RESULTS

Plackett-Burman test

The Plackett-Burman test was designed on 15 groups, and the parameters of each group were set according to S_1 to S_{11}, then the repose angle of seed particles was simulated by EDEM software. Each group repeated 5 times. The post-processing clip function was adopted to slice the simulation results with a thickness of 3 mm after each group of simulation tests, and the simulation repose angle of green onion seeds was measured with the angle measuring function (Fig.7). The result of the Plackett-Burman's was shown in Table 2. Design-Expert10.0 software was used to conduct ANOVA on the test results, and the significant results of each simulation parameter were obtained as shown in Table 3. According to the significance screening, the static friction factor of seed-seed (S_6), rolling friction factor of seed-seed (S_7) have the highest significance, and the static friction factor of seeds-steel (S_5) has significant effects. Other factors S_1, S_2, S_3, S_4, S_8 and S_9 have little influence on the angle of repose.

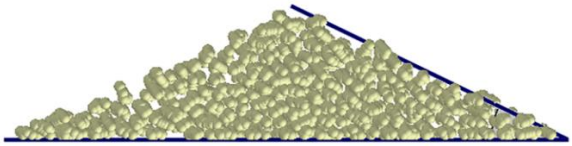

Fig. 7 - Measure the simulation repose angle

Table 2

Plackett-Burman test parameters

No.	Green onion seeds Plackett-Burman test parameter											
	S_1	S_2	S_3	S_4	S_5	S_6	S_7	S_8	S_9	S_{10}	S_{11}	Repose angle (°)
1	0.48	1285	9.88	0.05	0.38	0.30	0.17	0.29	0.20	-1	1	27.41
2	0.38	1085	29.80	0.125	0.33	0.45	0.11	0.39	0.125	0	0	26.15
3	0.48	885	49.80	0.20	0.38	0.30	0.17	0.49	0.05	-1	-1	30.05
4	0.28	1285	49.80	0.05	0.28	0.60	0.17	0.49	0.05	-1	1	33.23
5	0.48	885	49.80	0.20	0.28	0.60	0.05	0.29	0.20	-1	1	28.40
6	0.28	1285	49.80	0.20	0.38	0.30	0.05	0.29	0.05	1	1	23.43
7	0.48	885	9.88	0.05	0.38	0.60	0.05	0.49	0.05	1	1	27.35
8	0.38	1085	29.80	0.125	0.33	0.45	0.11	0.39	0.125	0	0	29.22
9	0.28	885	49.80	0.05	0.38	0.60	0.17	0.29	0.20	1	-1	35.70
10	0.48	1285	9.88	0.20	0.28	0.60	0.17	0.29	0.05	1	-1	30.65
11	0.28	885	9.88	0.05	0.28	0.30	0.05	0.29	0.05	-1	-1	19.80
12	0.48	1285	49.80	0.05	0.28	0.30	0.05	0.49	0.20	1	-1	21.80
13	0.28	1285	9.88	0.20	0.38	0.60	0.05	0.49	0.20	-1	-1	32.30
14	0.38	1085	29.80	0.125	0.33	0.45	0.11	0.39	0.125	0	0	28.12
15	0.28	885	9.88	0.20	0.28	0.30	0.17	0.49	0.20	1	1	24.96

Table 3

Significance analysis of Plackett-Burman test results

Parameters	Sum of squares	Degree of freedom	F values	P values
S_1	1.18	1	0.73	0.4564
S_2	0.55	1	0.34	0.6022
S_3	8.57	1	5.29	0.105
S_4	1.69	1	1.04	0.3825
S_5	25.23	1	15.58	0.029*
S_6	134.54	1	83.06	0.0028**
S_7	69.70	1	43.03	0.0072**
S_8	1.54	1	0.95	0.4013
S_9	3.06	1	1.89	0.263
S_{10}	4.44	1	2.74	0.1963
S_{11}	2.54	1	1.57	0.2993

*Note: ** indicates an extremely significant effect (p<0.01), * indicates a significant effect (p<0.05).*

Analysis of the steepest climbing test

In order to further determine the relationship between S_1, S_2, S_3 and the repose angle of green onion seeds, the steepest climbing test was designed to screen out the optimal value range of three simulation parameters of green onion seeds. The relative error between the measurement and simulation of repose angle was taken as the evaluation index, and the steepest climbing test design scheme was shown in Table 4. The test results show that the 3rd group of data has the smallest relative error.

Table 4

Steepest ascent experiment design scheme and results

No.	Green onion seeds steepest ascent experiment design and results				
	S_5	S_6	S_7	Repose angle	Relative Error (%)
1	0.28	0.3	0.05	21.80°	13.97
2	0.30	0.36	0.074	24.15°	4.70
3	0.32	0.42	0.098	25.02°	1.30
4	0.34	0.48	0.122	26.13°	3.10
5	0.36	0.54	0.146	31.58°	24.60
6	0.38	0.60	0.170	34.70°	36.90

Box-Behnken test

Based on the steepest ascent experiment results, the Box-Behnken test with the test parameter levels shown in Table 5 was conducted. The 3rd group of data from the steepest climb test was set as the central point, the second group of data as the low level, and the fourth of data as the high level to find the optimal results. The design scheme and results of the Box-Behnken test were shown in Table 5. The values of other non-significant factors in the Box-Behnken test were the same as those in the steepest climbing test to ensure the accuracy of the results.

Table 5

Box-Behnken experimental design and results

No.	Green onion seeds test design and results			
	S_5	S_6	S_7	Repose angle (°)
1	0.30	0.42	0.122	26.57
2	0.32	0.42	0.098	25.66
3	0.32	0.42	0.098	25.78
4	0.34	0.48	0.098	27.70
5	0.32	0.42	0.098	25.93
6	0.32	0.42	0.098	25.60
7	0.32	0.48	0.122	28.89
8	0.34	0.42	0.122	30.40
9	0.30	0.36	0.098	24.58
10	0.32	0.36	0.122	26.20
11	0.34	0.42	0.074	27.40

No.	Green onion seeds test design and results			
	S_5	S_6	S_7	Repose angle (°)
12	0.34	0.36	0.098	26.43
13	0.32	0.42	0.098	25.72
14	0.32	0.36	0.074	24.90
15	0.32	0.48	0.074	25.77
16	0.30	0.48	0.098	26.63
17	0.30	0.42	0.074	25.80

The variance analysis of Box-Behnken test is shown in Table 6. The analysis results show that S_5, S_6, S_7, S_5^2 and S_7^2 have highly crucial effects on the repose angle. S_5S_7 and S_6S_7 have significant influence on the repose angle; S_5S_6 and S_6^2 have no marked effect on the repose angle. The response surface of repose angle is shown in Fig.8. The results of Box-Behnken ANOVA shows that S_5S_7 and S_6S_7 had significant effects on the repose angle. It can be seen from the figure that with the increase of static friction coefficient and rolling friction coefficient, the repose angle also increases gradually, and the relative error between simulated repose angle and physical repose angle decreases first and then increases.

Table 6

Analysis of variance for Box-Behnken test results

Analysis of variance for green onion seeds test result					
Source of variance	Sum of Squares	Degree of freedom	Mean Square	F Value	p-value Prob > F
Model	32.6	9	3.62	27.81	0.0001
S_5	8.72	1	8.72	66.92	< 0.0001**
S_6	5.92	1	5.92	45.43	0.0003**
S_7	8.38	1	8.38	64.38	< 0.0001**
S_6S_7	0.83	1	0.83	6.36	0.0397*
S_5S_6	0.15	1	0.15	1.17	0.3156
$S_5 S_7$	1.24	1	1.24	9.55	0.0176*
S_5^2	3.04	1	3.04	23.35	0.0019**
S_6^2	0.27	1	0.27	2.07	0.1938
S_7^2	3.84	1	3.84	29.47	0.0010**
Residual	0.91	7	0.13		
Lack of Fit	0.85	3	0.28	17.63	0.009
Pure Error	0.064	4	0.016		
Cor Total	33.51	16			

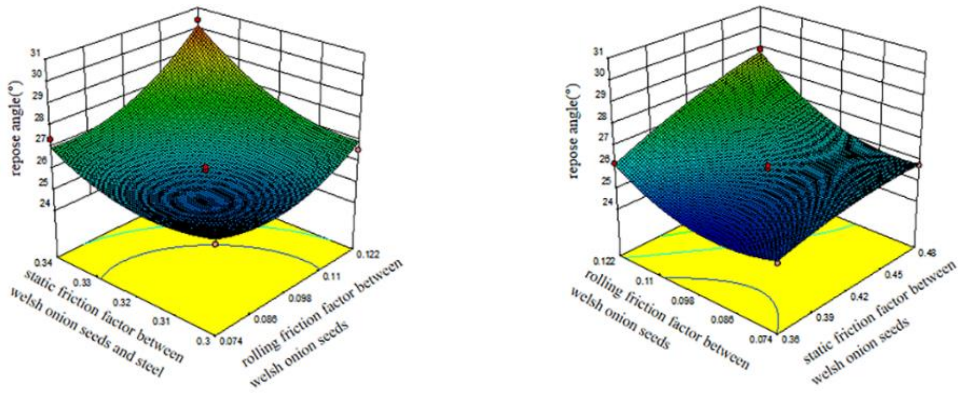

(S_5×S_7) **(S_6×S_7)**

Fig. 8 - Response surface of green onion seeds repose angle. (S_5×S_7) Effect of interaction between S_5 and S_7 on repose angle error. (S_6×S_7) Effect of interaction between S6 and S7 on repose angle error.

The repose angle regression fitting model P=0.0001. The regression model coefficient of determination R^2=0.9728 and Adjusted R^2=0.9378, which is very close to 1, and the coefficient of variation CV=1.36%.

The second-order regression equation of the repose angle of green onion seeds (Eq.6) was obtained by fitting the Box-Behnken test results. In conclusion, the regression model is extremely significant, which is of great significance for analysing and predicting the repose angle of green onion seeds.

$$\theta=+25.74+0.86S_6+1.02S_7+1.04S_5+0.45S_6S_7-0.20S_5S_6+0.56S_5S_7-0.25S_6^2+0.95S_7^2+0.85S_5^2 \quad (6)$$

Simulation parameter calibration and test verification

The data was further optimized with the objective of the physical repose angle (25.34°) of green onion seeds by the optimization module of Design-Expert10.0 software, and the second-order regression equation was solved. The group of optimal parameters closest to the actual value was calibrated: the static friction factor of seed-seed (S_6) was 0.424, the rolling friction factor of seed-seed (S_7) was 0.085, the static friction factor of seeds-steel (S_5) was 0.310, and other non-significant parameters value were determined by measured value. The average value of repose angle with the optimal parameter combination is 25.48° after 5 repetitions of simulation tests, and the error between the value and the physical real repose angle is 0.54%, which further verifies the reliability and authenticity of the simulation experiment. The comparison of simulation test and physical test is shown in Fig.9 and Fig.10. The results showed that the physical repose angle of green onion seeds was similar to the repose angle in the simulation results in morphology and angle, indicating that there was no significant difference between the simulation results and the physical test values.

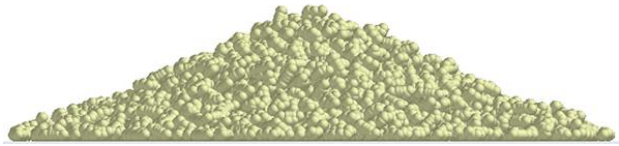

Fig. 9 - Green onion seeds simulation test

Fig. 10 - Green onion seeds physical test

CONCLUSIONS

In this paper, the physical parameters of Zhangyou 006 green onion seeds were determined by physical experiments, and Placket-Burman test, steepest climbing test, Box-Behnken test and the design-expert optimization module were used to calibrate the contact parameters that had a significant impact on the repose angle. The accuracy of the simulation parameters is verified by repose angle test. The conclusions are as follows:

(1) The static friction coefficient of seed-seeds (S_6), the rolling friction coefficient of seed-seeds (S_7), and the static friction coefficient of seed-steel (S_5) had significant effects on the repose angle of green onion seeds and therefore need to be calibrated.

(2) The optimal parameter combination was S_6 of 0.424, S_7 of 0.085, and S_5 of 0.310 and the average value of the simulated repose angle was 25.48° with the optimal parameter combinations.

(3) The verification test shows that the simulated repose angle is similar to the physical repose angle, and the overall relative error of 0.54% is low. The results show that physical parameters measured, the contact parameter calibrated and the seed particle model created by DEM are accurate and reliable.

In conclusion, parameter calibration can help researchers accurately obtain contact parameters that are difficult to measure. The research method in this paper can provide reference for the parameter calibration of other small and irregular seeds. The model of green onion seeds in this study only shows the characteristics of the specific variety Zhangyou 006. In future studies, it should be considered to analyse the commonness and differences of the seed particle models and parameters of different varieties of green onion, and establish a model database of green onion seeds.

ACKNOWLEDGEMENT

This research was supported by the Natural Science Foundation youth programme of Shandong (ZR2022QC159).

REFERENCES

[1] Fei L., Dapeng L., Tao Z., & Zhen L. (2020). Analysis and calibration of quinoa grain parameters used in a discrete element method based on the repose angle of the particle heap. *INMATEH Agricultural Engineering*, vol.61, no.2, pp.77-86. https://doi.org/10.35633/inmateh-61-09

[2] Gong X., Bai X.W., Huang H.B., Zhang F.Y., Gong Y.J., & Wei D.S. (2022). Dem parameters calibration of mixed biomass sawdust model with multi-response indicators. *INMATEH Agricultural Engineering*, vol.65, no.3, pp.183-192. https://doi.org/10.35633/inmateh-65-19

[3] Liu D., Gao H., Wang F., & Zhou J., (2017). Planting Agronomy and Mechanization Production Technology of Scallion in Zhangqiu (章丘大葱种植农艺及机械化生产技术). *Transactions of Agricultural. Engineering*, vol.7, no.1, pp.15-18+47.

[4] Lu F.Y., Ma X., Tan S.Y., Chen L.T., Zeng L.C., & An P. (2018). Simulative Calibration and Experiment on Main Contact Parameters of Discrete Elements for Rice Bud Seeds (水稻芽种离散元主要接触参数仿真标定与试验). *Transactions of the Chinese Society for Agricultural Machinery*, vol. 49, no.2, pp. 93-99.

[5] Lu F.Y., Ma X., Qi L., Xing X.P., Li H.W., & Guo L.J. (2018). Theory and experiment on vibrating small-amount rice sowing device (振动式水稻精密播种装置机理分析与试验). *Transactions of the Chinese Society for Agricultural Machinery*, vol. 49, no.6, pp. 119-128+214.

[6] Ma W.P., You Y., Wang. D.C., Yin S.J., & Huan X.l. (2020). Parameter Calibration of Alfalfa Seed Discrete Element Model Based on RSM and NSGA－Ⅱ (基于 RSM 和 NSGA-Ⅱ的苜蓿种子离散元模型参数标定). *Transactions of the Chinese Society for Agricultural Machinery*, vol.51, no.8, pp. 136 - 144.

[7] Min F., Xiaoqing C., Zefei G., Chengmeng W., Bing X., & Yilin H. (2023). Parameters calibration of discrete element model for crushed corn stalks. *INMATEH Agricultural Engineering*, vol.69, no.1, pp.399-408. https://doi.org/10.35633/inmateh-69-37

[8] Peng Z., Hu Z., Jinming L., Chunlin T., & Jiaxi Z. (2022). Parametric calibration of cotton straw parameters in Xinjiang based on discrete elements. *INMATEH Agricultural Engineering*, vol.67, no.2, pp.314-322.

[9] Wang H.X., Wu Y.Q., Li T.H., Zhang J.Q., & Hou J.L. (2019). Current situation and prospect of research on Welsh onion planting machinery (大葱种植机械研究现状与展望). *Transactions of Journal of Chinese Agricultural Mechanization*, vol.40, no.2, pp.35-39.

[10] Wang W.W., Can D.Y., Xie J.J., Zhang C.L., Liu L.C., & Chen L.Q. (2021). Parameter calibration of discrete element model for dense moulding of corn stalk powder (玉米秸秆粉料致密成型离散元模型参数标定). *Transactions of the Chinese Society for Agricultural Machinery*, vol. 52, no.3, pp. 127-134.

[11] Xiangqian D., Zheng H., Xuan J.I.A., Yonglei L., Jiannong S., & Jicheng W. (2022). Calibration and experiments of the discrete element simulation parameters for rice bud damage. *INMATEH Agricultural Engineering*, vol.68, no.3, pp.659-668. https://doi.org/10.35633/inmateh-68-65

[12] Xiaolong H., Decheng W., Yong Y., Wenpeng M., Lu Z., & Sibiao L. (2022). Establishment and calibration of discrete element model of king grass stalk based on throwing test. *INMATEH Agricultural Engineering*, vol.66, no.1, pp.19-30. https://doi.org/10.35633/inmateh-66-02

[13] Xuejie M., Zhanfeng H., Min L. (2022). Calibration of simulation parameters of coated particles and analysis of experimental results. *INMATEH Agricultural Engineering*, vol.67, no.2, pp.233-242. https://doi.org/10.35633/inmateh-67-23

[14] Yan D., Yu J., Wang Y., Sun K., Zhou L., Tian Y., & Zhang N. (2022). Measurement and Calibration of DEM Parameters of Soybean Seed Particles. *Agriculture*, vol.*12*, no.12, pp.1825-1825.

[15] Zhou H., Zhou T., Wang X., Hu L., Wang S., Luo X., & Ji J. (2022). Determination of Discrete Element Modelling Parameters of a Paddy Soil with a High Moisture Content (> 40%). *Agriculture*, vol.*12*, no.12, pp.2000-2000.

[16] Zhang W., Wang F. (2022). Parameter calibration of American ginseng seeds for discrete element. *International Journal of Agricultural and Biological Engineering*, vol.1, no.6, pp.16-22.

[17] Zenghui G., Shuqi S., Nan X., & Dongwei W. (2022). Parameter calibration of discrete element simulation model of wheat straw-soil mixture in Huang Huai Hai production area. *INMATEH Agricultural Engineering*, vol.66, no.1, pp.201-210. https://doi.org/10.35633/inmateh-66-20

EXPERIMENTAL RESEARCH ON ENERGY CONSUMPTION IN THE LAMINATION AND DRAWING OF DOUGH
/
CERCETĂRI EXPERIMENTALE PRIVIND CONSUMURILE ENERGETICE LA LAMINAREA ȘI TREFILAREA ALUATURILOR

Mariana- Gabriela MUNTEANU [1], Gheorghe VOICU *[1], Gabriel-Alexandru CONSTANTIN [1], Elena –Mădălina STEFAN [1], Paula TUDOR [1], Mihaela NITU[2]
National University of Science and Technology "POLITEHNICA" of Bucharest, Faculty of Biotechnical Systems Engineering / Romania; INMA Bucharest / Romania
Tel: 0040724715585; E-mail: ghvoicu_2005@yahoo.com
DOI: https://doi.org/10.35633/inmateh-70-14

Keywords: *dough, bagels, lamination, drawing, energy consumption*

ABSTRACT
This paper presents an analysis of the variation of energy consumption in the lamination and drawing process of bagel doughs. Also, the paper highlights the farinographic characteristics (water absorption, dough development time, and dough stability, degree of dough softening and farinographic index) of the flour used for the dough preparation for which the energy consumption during lamination and drawing was determined.

REZUMAT
Lucrarea dată prezintă o analiză a variației consumului de energie în procesul de laminare și trefilare a aluaturilor de covrigi. De asemenea, în lucrare se evidențiază caracteristicile farinografice (capacitatea de hidratare, timpul de dezvoltare a aluatului, stabilitatea aluatului, gradul de înmuiere a aluatului și indicele farinografic) ale făinurilor folosite pentru prepararea aluaturilor pentru care s-a determinat consumul de energie la laminare, respectiv trefilare.

INTRODUCTION

Shaping dough for bagels between counter-rotating profiled rollers of the lamination and drawing system, having the same or different diameters, is an operation often used in the bakery industry as a dough forming process. Repeated rolling of the dough is clearly an advantage to produce a structured system of it (*Bousquieres J. et al*., *2014*). This type of operation is performed for a wide range of bakery products, contributing to the development of the dough structure (*Haegens N., 2018; McCann Thu. H. et al., 2013*; *Munteanu et al, 2015; Steffe J.F., 1996; Yao N., 2004).* The deformation of the dough pieces by the mechanical action of rigid elements not only determines the improvement of the physical-mechanical properties of the previously divided dough, but also contributes to defining the aesthetic shape of the finished product (*Băisan I., 2023).*

The evaluation of the dough is made by its consistency, which represents a property of its rheological, complex nature, resulting from the combination of viscosity, plasticity, elasticity and which varies with humidity, temperature and time, with the proportion between the phases of the dough (solid-liquid-gas), with the biochemical composition of the flour, etc. The consistency of the dough is measured organoleptically, by feeling, or with the help of consistometers (with immersion penetrometers or by comparison with a standard kneading installation - farinograph). It influences the yield of the baking technological process. Dough consistency is measured in Brabender units (1 UB ≈ 10-3 daN·m). The dough is considered to have a normal consistency when it requires a maximum kneading time of 500 UB.

In the paper *(Munteanu et al, 2015)*, the lamination process is compared to the calendering process, which is often used in the paper, plastic, steel industry, etc. In this process, the piece of dough, properly dosed, is successively passed through one or more pairs of rollers, which by pressing is compacted and adjusted from greater to lesser thickness, forming a thin dough sheet, (*Yao N., 2004)*. Repeated lamination of the dough results in dough strips of uniform thickness and homogeneous structure, making the dough more plastic and easier to shape (*Băisan I., 2023).*

The mechanical stress behaviour of wheat flour dough is similar to viscoelastic bodies and can be described rheological by various constitutive mechanical models, which estimate the dough more or less accurately, (Burgers body, Bergstrom-Boyce) (*Mohsenin N.N., 2020; Patel M.J. et al., 2013; Chakrabarti Bell S. et al., 2010).*

Drawing process differs from lamination process in that the resulting dough is drawn between two profiled rollers and shaped into wicks/noodles of a certain thickness/width and length. This is due to the drawing rollers which are provided with grooves (circular for breadsticks, rectangular for hooks, etc). The drawing machines are equipped with devices for cutting the dough strands to different length and also have conveyor belts for transporting the strands to the next processing machine in the technological flow (*Băisan I., 2023).*

In specialized literature, the effects of sheeting is intensively researched in bakery, because the operation influences the quality of the finished product. In one of the most recent papers, *(Albasir M.O.S. et al., 2022)*, investigated, using the dynamic dough density technique, the effects of this operation on the development of the doughs used in the bakery, as well as on the baking process. In terms of volume and structure (for bread), the effects of the sheeting regime were examined on various bread doughs and pretzels made with different percentages of bran, having as a control sample a sample of dough without bran, these being laminated to a thickness of 6 , 9 and 12 mm. The results showed that the dough laminated to a thickness of 6 mm had a better gluten development, although the voids of gas development were less and with a larger average diameter.

Many scholars claim that dough lamination is more efficient from an energetic point of view, although from a mechanical point of view it is a complex process *(Kilborn R.H. et al. 1974; Levine L., 1996; Qi F. et al., 2008; Patel M. et al. 2013)*.

As a result of compacting the dough, a number of effects occur during the lamination/drawing process, such as: the evacuation of air from the dough mass, thus avoiding the worsening of its characteristics, an effect which could be produced by enzymatic oxidative processes; the transformation of the dough into a homogeneous and uniform mass with viscoelastic characteristics, characteristics produced as a result of the flour particles sticking together *(Dogan H. et al., 2006).*

In their paper, *Naik H.R. et al., (2007)*, compared bagels made from normal (control) flour dough with bagels made from different levels of added defatted soy flour. So, the second type of bagels had a decrease in moisture, fat, non-reducing sugars and starch. In the same time increased ash, protein, reducing and total sugars. On the other hand, the organoleptic evaluation of the bagels showed that a 5% level of defatted soy flour resulted in bagels with a texture, colour and flavour above the average level of acceptability. At the same time, bagels with added deffated soy flour had a longer shelf life (about 90 days in laminated bags) regardless of the amount of added defatted soy flour.

Response surface methodology (RSM) was used by *Paykary M. et al., (2015),* to study the optimization of leavening agents in extruded gluten-free brewer's rice hard pretzel. Through RSM was optimized the effects of yeast and bicarbonate of soda on several physical and mechanical properties (fracturability, porosity, hardness, expansion ratio, specific length, density, surface colour, water absorption index, water activity, and others). In conclusion, for the gluten-free pretzel is necessary 2.59 g bicarbonate soda and 8.05 g yeast at every 500 g of brewer’s rice flour.

Pretzels are a focused area for the researchers in bakery. In paper *(Schoenauer S. et al, 2019)*, the authors have applied some aroma extract dilution on pretzels to increase the flavour and aroma. The extract was obtained from the crust of freshly baked soft pretzels. *Dhaygude et al.* in their supplemented pretzel dough with barley flour and used as a natural sweetener honey paper *(Dhaygude V. et al., 2017)*. They varied honey between 20 - 40%, wheat flour between 50 and 80 g and barley flour between 20 and 40g. The results were analysed by the same RSM.

Physico-chemical properties, dough manoeuvrability and pretzel properties (as a final product) were investigated in paper written by *Naik H.R. et al., (2014).* The authors added soy flour in wheat dough in percentage of 0, 5, 10, 20 and 30%. The results showed that some properties (as development time for dough, dough stability, water absorption and dough consistency) increased their value, and some properties decreased their value (softening degree, mixing tolerance index, peak viscosity, gelatinization temperature) with addition of soy flour. The authors made also an organoleptic evaluation and found that at 5% soy flour pretzels have the best flavour, colour and texture and recorded an shelf life of 90 days.

The objective of this paper is to present the flour curves for three samples of wheat flour used in the preparation of bagels doughs, which were the samples for which the variation in energy consumption during lamination and drawing was determined. In order to show the variation of energy consumption in lamination and drawing, the experimental data obtained were processed in MS Office Excel.

MATERIALS AND METHODS

The experimental research was carried out at the Department of Biotechnical Systems, Politehnica University of Bucharest. To carry out the experiments, three commercial types of white flour type 650 were used: FA1 with a moisture content of 9.56%, FA2 with a moisture content of 10.45%, FA3 with a moisture content of 11.59%, and the quantities of ingredients used to prepare the doughs were: 1 kg flour, 45% water and 10% oil in relation to the quantity of flour, 12 g salt, 5 g yeast, 100 g sugar. A DitoSima BM20S spiral-arm planetary mixer was used both for mixing the pretzel recipe components and for kneading the dough. The mixing time of the recipe components was 2 minutes in the first gear of the kneading arm, and 10 minutes in the second gear to carry out the dough kneading process.

After preparing the doughs, they were taken out of the kneading trough, rolled out by hand with a wooden roller into a sheet about 13 cm wide, 89 cm long and about 1 cm thick, to ensure an initial thickness of the dough before lamination. The dough sheets obtained were inserted between the lamination and drawing rolls of the dough strand machine. The rolls speed was 40 rpm, the distance between the lamination rolls was set in the 6th step, i.e. 2.7 mm, and the working space for drawing was a rectangle with length L = 6.1 mm and width l = 2.3 mm.

For the flours used in the experiments, farinographic determinations were made using the Brabender Farinograph-E, an electronic apparatus consisting of a special biuret used to measure the amount of water and a mixer with two "∑" shaped kneading arms that rotate in opposite directions. The mixer tank has a capacity of 300 g and is fitted with a double jacket through which distilled water is recirculated at a temperature of 30 ± 1°C. The farinograph software plots, in real time, the farinographic curve. This curve is indicating the rheological characteristics of the dough, which is the basis for assessing flour quality. The flour curve is drawn as a result of the resistance of the dough to the kneader shaft.

Flour farinographic characteristics indicates usually the quality of flours. These characteristics are of particular importance in the technological process of obtaining both bakery and pastry products *(Păucean A. et al., 2015; Qi F. et al., 2008).*

During the kneading operation, flour and water are gradually transformed into a homogeneous viscoelastic dough, the moistened flour particles bind to each other forming, at first, small agglomerations that grow slowly, eventually binding together to form the dough with elasto-visco-plastic properties from which the air has been removed. The mixing process promotes several physical, chemical and physico-chemical changes that lead to the development and formation of dough. Of course, the kneading process is one way to characterize the quality of flour samples.

Not all types of flour are equally suitable for a specific end product. Determining the quality of flour is therefore of particular importance as it relates to the desired end product and its manufacturing process (*Ștefan E.M. et al., 2013).*

The following test steps were carried out with the Brabender electronic farinograph according to the following methods AACC 54-21, ICC 115/1, ISO 5530-1 *(Păucean A. et al., 2015; http://www.maxmixers.com/sigma-mixer/sigma-blade-mixer/hydraulic-tilt-soap-and-dough-sigma-blade.html):*

- 300 g of flour were weighed with a Kern precision 0.1 g balance;
- the flour has been placed in the mixer bowl;
- covered the blender with the transparent plastic protective cover;
- the device was started, and after the flour had been mixed for 60 seconds, water was added from the dough mixer; the volume of water added to form the dough is close to the volume needed to obtain a dough with a consistency of 500 BU;
- during the mixing of the ingredients inside the mixer bowl, the computer screen of the Brabender farinograph software program records and plays back the farinographic curve;
- the plotting of the farinographic curve continues for at least 10 minutes after the close of development time;
- when the "end of test" message appears, switch off the machine and clean the mixer;

An example of a farinographic curve is shown below in Figure 1.

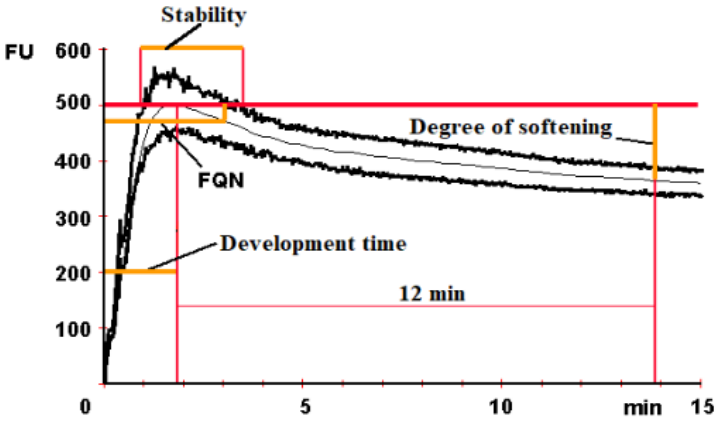

Fig. 1 - Example of farinographic curve and how to interpret it (*Voicu Gh., 1999)*

On the farinographic curve (figure 1), given by the resistance of the dough to kneading, one can read:

- water absorption – the amount of water absorbed by the flour to form the dough with a standard consistency of 500 FU (1 FU = 1 BU - Brabender Units, 1 BU ≈ 10^{-3} daN·m);
- dough development time - indicates the time from when water is added until the dough reaches the maximum consistency of 500 FU;
- dough stability – indicates the length of time the dough retains its normal consistency of 500 FU; stability time is correlated to flour strength;
- degree of softening – indicating when the dough has broken down *(Qi F. et al., 2008)*.

RESULTS

After recording the farinographic curves using the Brabender E-Farinograph (Figure 2), the characteristics of the farinograms obtained were read and noted in Table 1. The data obtained must fall within the ranges of the values of the assessment indicators in Table 2.

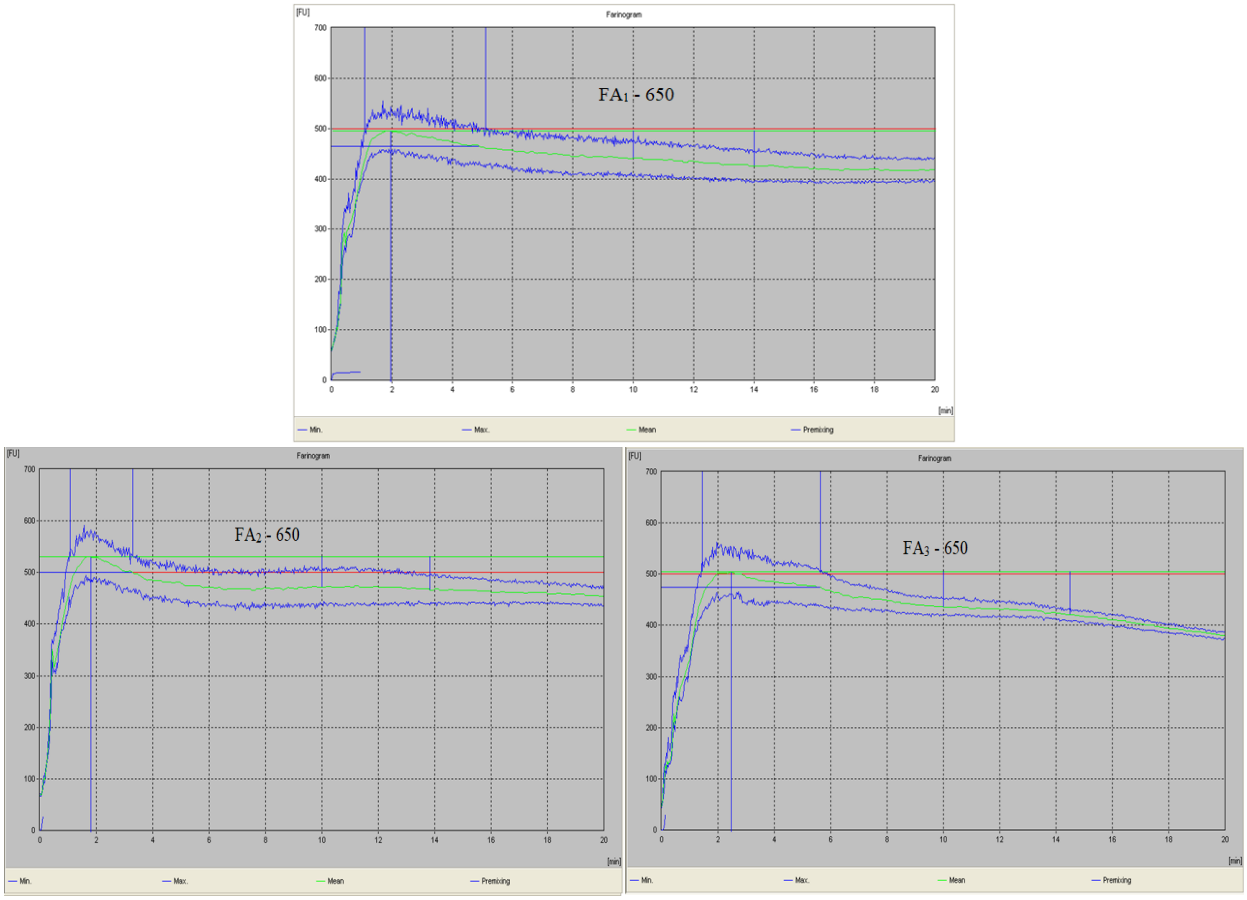

Fig. 2 - Farinograph curves experimentally obtained with the Brabender farinograph for dough made from the three types of FA 650 type of wheat flour (FA_1, FA_2, FA_3)

Table 1

Farinograph characteristics for the three commercial types of wheat flour FA$_1$ 650, FA$_2$ 650, FA$_3$ 650

Farinograph characteristics	Wheat flour FA 650		
	FA$_1$	FA$_2$	FA$_3$
Water absorption [%] **Corrected for 500 [FU]**	65.7 65.6	62.1 62.2	60.1 60.2
Dough development time [min]	2	1.8	2.5
Dough stability [min]	4	2.2	4.2
Degree of softening [FU]	70	59	69
Farinograph index	49	33	56

Table 2

Criteria for assessing flour quality, *(David A.P. et al., 2009)*

Flour	Farinograph characteristics				
	Water absorption [%]	Dough development time [min]	Dough stability [min]	Degree of softening [U.F.]	Farinograph index
Very good	more than 65	more than 3	more than 8	under 60	more than 65
Good	60 - 65	2 - 3	5 - 8	60 - 80	50 - 65
Satisfactory	55 - 60	1.5 - 2	3 - 5	80 - 100	40 - 50
Unsatisfactory	less than 55	less than 1.5	less than 3	more than 100	Sub 40

From the analysis of the curves and farinographic parameters in Figure 2 and Table 1 for the three types of FA 650 wheat flours, it can be seen that the dough development time values vary within narrow limits, from 1.8 minutes to 2.5 minutes, and this observation leads to the fact that the three commercial types of flours fall in terms of development time within the standard values of a satisfactory to good flour.

The standard values of a good flour also include the water absorption values, which have been corrected by the farinograph so that the other farinographic parameters can be properly estimated and interpreted.

Regarding the data obtained for the stability time, it is observed that the lowest value, i.e. 2.2 minutes was recorded for white flour FA$_2$, while for white flour FA$_3$, an average stability time of 4.2 minute was recorded, followed by of a stability time of 4 minutes for FA$_1$ flour. Through this analysis, it can be concluded from the point of view of dough stability time, FA$_2$ flour falls within the standard values of an unsatisfactory flour, and the dough stability time of FA$_3$ and FA$_1$ flour falls within the standard values of some flours satisfying.

Also, in the farinographic curves in Figure 2 and Table 1, both the softening degree of the dough and the farinographic index, index by which the quality of the flour is assessed, are presented. It can be seen that the values of the degree of softening for FA$_2$ flour fall within the standard values of a very good flour, while the farinographic index ranks it as an unsatisfactory flour.

The values of the degree of softening and the farinographic index for the FA$_3$ flour place the flour in the standard values of a good flour, while the values of the degree of softening and the farinographic index for the flour FA$_1$ place it both in a satisfactory and good flour, respectively.

FA$_3$ flour shows the most parameters that correspond to flour from the category of good flours, and FA$_1$ and FA$_2$ flours show values that fall within several standard parameters for several flour categories

The results obtained for the energy consumption in lamination and drawing are presented in Table 3.

Table 3

Dough parameters and energy consumption during lamination and sheeting

Flour	Moisture content (%)	Water absorption, (ch %)	Energy consumption in drawing (x10^3 J)	Specific energy consumption in drawing (x10^3 J/kg)	Energy consumption in lamination (x10^3 J)	Specific energy consumption in lamination (x10^3 J/kg)
FA$_1$	9.56	65.6	9.00	5.39	11.52	6.91
FA$_2$	10.45	62.2	6.84	4.10	10.80	6.47
FA$_3$	11.59	60.2	6.48	3.88	9.72	5.83

From Table 3 and Figure 3, it can be seen that the energy consumed for sheeting and lamination of dough pieces prepared with the three types of flour is different and show that they increase with decreasing moisture content and increasing hydration capacity of the flour.

Considering that the quantities of water in the recipe were respected, 45% water and 10% oil in relation to the quantity of flour, and that the hydrating capacity of the flour and the moisture content were not taken into account, it can be said that the difference in the energy consumption values is due to the small quantities of water and oil used to prepare the dough.

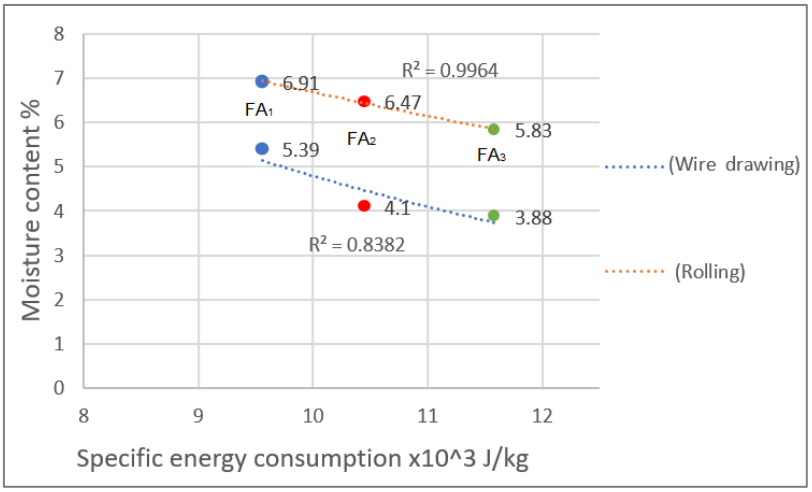

Fig. 3 - Variation of energy consumption in the lamination and drawing of bagel dough

Considering the 11.59% moisture content of FA_3 flour and the water absorption of 60.2%, the quantities of water and oil in 55% of the flour quantity were sufficient to produce a dough that resulted in a consumption of $6.48x10^3$ J in lamination and $9.72x10^3$ J at drawing, compared to the energy consumption recorded for the dough made from FA_2 flour with moisture content of 10.45% and 62.2 % water absorption, respectively for the dough made from FA_1 flour which had a moisture content of 9.56% and 65.6 % water absorption.

For the dough prepared with FA_1 650 flour, the quantities of water and oil were not sufficient to cover the required flour water absobtion of 65.6%, and this led to an increase in energy consumption to 9.00x103 J for lamination and 11.52x103 J for drawing.

CONCLUSIONS

Analysing the data presented, it can be seen that the values of the flour parameters for the three types of flour analysed varied within wide limits, so that the flours fell into several standard parameters of several flour categories (they cannot be placed in a single category/class). The flour that showed the most parameters that met the criteria for a good flour is FA_3 flour (water absorption of 60.1%, dough development time 2.5 minutes, degree softening of 69 FU).

An increase in the moisture content and a lower value of the water absorption of the flour led to a decrease in the energy consumption during drawing from 11.52x103 J to 9.72x103 J, but also to a decrease in the energy consumption during lamination from 9.00x103 J to 6.48x103 J. It should be noted that these values, which were also the lowest, are recorded for FA_3 flour which also showed the best farinographic characteristics.

ACKNOWLEDGEMENT

This work has been funded by the European Social Fund from the Sectoral Operational Programme Human Capital 2014-2020, through the Financial Agreement with the title "Training of PhD students and postdoctoral researchers in order to acquire applied research skills - SMART", Contract no. 13530/16.06.2022 - SMIS code: 153734, and from the project "Development of the practical application base for agricultural, mechatronic and environmental mechanics in vineyards, orchards and solariums (DEMEVILISO)", CNFIS-FDI-2023-F-0277, from the Ministry of Education through the Executive Agency for Financing Higher Education, Research, Development and Innovation.

REFERENCES

[1] Albasir M.O.S., Alyassin M., Campbell G.M., (2022), Development of Bread Dough by Sheeting: Effects of Sheeting Regime, Bran Level and Bran Particle Size, *Foods 2022*, vol. 11;

[2] Băisan I., (2021), *Equipment for milling and baking*, https://mec.tuiasi.ro/wp-content/uploads/2021/12/Utilaje-pentru-morarit-si-panificatie.pdf, (Accessed 2023);

[3] Bousquieres J., Deligny C., Riaublanc A., Lucas T., (2014), CLSM study of layers in laminated dough: Roll out of layers and elastic recoil, *Journal of Cereal Science*, vol. 60, Issue 1, pp. 82-91;

[4] Chakrabarti Bell S., Bergström J.S., Lindskog E., Sridhar T., (2010), Computational modeling of dough sheeting and physical interpretation of the non-linear rheological behavior of wheat flour dough, *Journal Food Engineering*, vol. 100, pp. 278-288;

[5] David A.P., Burnete N., (2009), *Theoretical premises of mathematical modelling of the bread baking process, agriculture* – Science and practice no. 1-2 (69-70);

[6] Dhaygude V., Szedljak I., Somogyi L., Nanda V., (2017) Effect of honey on barley flour supplemented pretzel, *Conference: Chemical Engineering Conference*, VeszpremAt: Pannon University, Veszprem, Hungary;

[7] Dogan H., Kokini J. L., (2006), *Handbook of Food Engineering – Chapter: Rheological Properties of Foods,* Taylor and Francis Group, CRC Press;

[8] Haegens N., (2018), *Baking*, Available from http://www.classofoods.com/page2_3.html, (Accessed 2018);

[9] Kilborn R.H., Tipples K.H., (1974) Implication of the mechanical development of bread dough by means of sheeting rolls. *Cereal Chem.* vol.51, pp. 648–657;

[10] Levine L., (1996), Model for the Sheeting of Dough Between Rolls Operating at Different Speeds. *Cereal Foods World.* vol.41, pp. 690–697;

[11] McCann Thu. H., Day, L., (2013), Effect of sodium chloride on gluten network formation, dough microstructure and rheology in relation to breadmaking, *Journal of Cereal Science*, vol. 57, no.3, pp. 444–452;

[12] Mohsenin N.N., (2020), *Physical properties of plant and animal materials*, vol. I, Gordon and Breach Science, Publisher Routledge, ISBN 9781000122633;

[13] Munteanu M., Voicu Gh., Ștefan E.M., Constantin G.A., (2015) Farinograph Characteristics of Wheat Flour Dough And Rye Flour Dough, *International Symposium ISB-INMA TEH 2015*, *Agricultural and Mechanical Engineering*, vol. 47, no. 3, pp. 645 -650;

[14] Naik H.R., Sekhon K., (2014), Influence of defatted soy flour addition on the quality and stability of pretzel type product, *Journal of Food Science and Technology*, vol.51;

[15] Naik H.R., Sekhon K., Baljit S., Kaur A, Rather A.H., (2007), Influence of triticales and wheat classes on pretzel quality, *Journal of Food Science and Technology*, vol.44, pp.495-499;

[16] Patel M.J., Chakrabarti-Bell S., (2013), Flour quality and dough elasticity: dough sheetability, *of Food Engineering*, vol.115, pp. 371–383;

[17] Paykary M., Karim R., Saari N., Sulaiman R., Shekarforoush E., Aghazadeh M., (2015), Optimization of Leavening Agents in Extruded Gluten-Free Brewer's Rice Hard Pretzel Using Response Surface Methodology, *Journal of Food Process Engineering*, vol. 39;

[18] Păucean A., Man S., Muste S., Pop A., (2015), Physicochemical and Sensory Characteristics of Pretzel with Wheat Bran, *Bulletin UASVM Food Science and Technology*, vol. 72, no. 2;

[19] Qi F., Dai S.-C., Newberry M.P., Love R.J., Tanner R.I., (2008), A simple approach to predicting dough sheeting thickness. *J. Cereal Sci.* 2008, vol.47, pp. 489–495;

[20] Schoenauer S., Schieberle P., (2019), Characterization of the Key Aroma Compounds in the Crust of Soft Pretzels by Application of the Sensomics Concept, *Journal of Agricultural and Food Chemistry*, vol. 67;

[21] Steffe J.F., (1996), *Rheological methods in food process engineering*, Second Edition, Freeman Press, S.U.A;

[22] Ștefan E.M., Voicu Gh., Ipate G., Constantin G.A., (2013), Mathematical model to estimate the energy consumption at wheat grinding with roller mills, *Proceedings of the 41. International Symposium on Agricultural Engineering. Actual Tasks on Agricultural Engineering*, 19th – 22th February, Opatija, Croatia, vol.41, no.1, pp. 279-289;

[23] Voicu Gh., (1999), *Processes and machinery for bakery*, Press Bren, Bucharest;

[24] Yao N., (2004) *Hard Pretzel Characterization and Process Optimization,* A Thesis in Food Science, The Pennsylvania State University;
[25] ***http://www.maxmixers.com/sigma-mixer/sigma-blade-mixer/hydraulic-tilt-soap-and-dough-sigma-blade.html (Accessed 2023).

CFD ANALYSIS OF THE SETTLING PROCESS IN A RADIAL CLARIFIER
/
ANALIZA CFD A PROCESULUI DE DECANTARE ÎNTR-UN DECANTOARE RADIAL

Gabriel Alexandru CONSTANTIN [1)], Bianca Stefania ZABAVA *[1)], Gheorghe VOICU [1)], Georgiana MOICEANU [2)], Irina Aura ISTRATE [1)], Mihaela NITU [3)]

[1)] National University of Science and Technology "POLITEHNICA" Bucharest, Faculty of Biotechnical Systems Engineering / Romania; [2)] National University of Science and Technology "POLITEHNICA" Bucharest, Faculty of Entrepreuneurship, Business Engineering and Management / Romania; [3)] INMA Bucharest / Romania

Tel: 0040731538941; E-mail:bianca.dragoiu@upb.ro

DOI: https://doi.org/10.35633/inmateh-70-15

Keywords: *Computational Fluid Dynamics, fluid velocity, radial clarifier, Reynolds number*

ABSTRACT

The objective of the present study was to make a theoretical study based on a CFD analysis for a conventional radial clarifier. The parameters of the Computational Fluid Dynamics analysis were set in the Ansys software, and after running the simulation, the values for fluid velocity, turbulence intensity and Reynolds number were obtained. Thus, it was obtained a fluid velocity of 0.103 m/s, a turbulence intensity of $3.82 \cdot 10^{-2}$ % and a Reynolds number of 14.7. This work can help researchers in the field, mainly, but also radial clarifier manufacturers to optimise the process.

REZUMAT

Obiectivul prezentului studiu a fost de a realiza un studiu teoretic bazat pe o analiză CFD pentru un clarificator radial convențional. Parametrii analizei dinamicii fluidelor computaționale au fost setați în software-ul Ansys, iar după rularea simulării, au fost obținute valorile pentru viteza fluidului, intensitatea turbulenței și numărul Reynolds. Astfel, s-a obținut o viteză a fluidului de 0,103 m/s, o intensitate a turbulenței de $3,82*10^{-2}$ % și un număr Reynolds de 14,7. Această lucrare poate ajuta cercetătorii din domeniu, în principal, dar și constructorii de clarificatoare radiale în sensul optimizării procesului.

INTRODUCTION

Our planet has witnessed an escalating rate of industrialization, urbanization, and population increase over the past 50 years, which has had a negative influence on the quality of the world's water, air, and soil as well as on environmental degradation. Since it promotes sustainable water reuse while decreasing or eliminating pollution of natural water sources, wastewater treatment has become one of society's most important environmental problems (*Alsina, 2008*).

Current wastewater management techniques result in inefficient nutrient recovery and reuse, which can have negative effects on the ecosystem, including eutrophication, the climate, and world food security *(Hoffmann et al., 2020; Öberg et al., 2020).* Water issues are given a lot of attention in a circular economy, which entails more sustainably managing waste and raw materials (including water) (including wastewater) (*Smol, 2022; Smol and Koneczna, 2021).*

In recent decades, water and wastewater treatment plants have attracted the government's attention, especially through the dangers of wastewater pollution from urban areas *(Chero et al., 2019).* Most municipal wastewater treatment facilities are required by law to provide some type of treatment for all flows that enter their facilities, regardless of volume or duration (*Clarifier Design, 2005*).

In Romania, there is the problem of rainwater collection and reuse without being collected in wastewater treatment stations.

Solids removal is probably the most widely used method of water purification from primary mechanical treatment in wastewater treatment plants. A crucial phase in this process refers to the separation of sludge and suspended solid particles using gravity, a process called sedimentation, the equipment in which the process is carried out is called a clarifier. In these tanks, the wastewater is admitted to the tank at one end and the clarified water is discharged at the other end of the clarifier. For the correct deposition of particles, water should pour into the reservoir for enough time (*Hasim et.al., 2020*).

To eliminate suspended solids from influent raw wastewater, primary clarifiers are frequently used in wastewater treatment facilities (*Gernaey and Vanrolleghem, 2005*).

Primary clarifiers, as the first stage of treatment, have an impact on the following biological and sludge treatment units as well as the production of biogas and electric energy in systems with anaerobic digestion and cogeneration.

As a result, primary clarifiers have a significant impact on the efficiency of the wastewater treatment facility as a whole (Patziger *et.al., 2016; Griborio et.al., 2021*).

In the general case, several distinct zones can be identified in a clarifier: the inlet zone, the sedimentation zone, the sediment accumulation zone (sludge zone) and the sediment discharge zone *(Rus, 2001).* The clarifier, as a major installation in wastewater treatment plants, can limit or define the performance of the treatment plant (Das et.al., 2016). In general, up to 50% of the total pollutant load in wastewater is removed by sedimentation *(Manuals of British Practice in Water Pollution Control, 1980).*

Many different things can have an impact on how well a clarifier is performing to illustrate this, the Reynolds number, the viscosity of the water, the type of movement of the water flow, and also the size and construction of the clarifier are the most important factors in the sedimentation unit *(Chero et.al., 2019; Campbell and Empie, 2006)*.

Conventional clarifier models make up about one-third of the total cost of capital water treatment facilities because of the cost of land and construction. Numerous techniques have been developed to increase the effectiveness of tailing ponds, increase their hydraulic capacity, and reduce construction or operational costs (*Saady, 2012).* Recently, Computational Fluid Dynamics (CFD) analyses have become fast and easy to use. These new generation analyses offer a cheap means of testing and optimizing the hydraulic operation of both existing and design constructions *(Al-Jeebory et al., 2010).* CFD is a quick, low-cost method for assessing engineering systems that are difficult to replicate in a lab or real-world situations. This gives it several benefits over traditional modelling techniques. Construction of more efficient and compact sedimentation tanks for conventional water treatment facilities can relate to a famous example of how CFD can build a "virtual prototype". Using CFD, it is possible to visualize the three-dimensional liquid flow inside a tank, which can increase solids separation and decrease turbulence.

The objective of the present study is to make a theoretical study based on a CFD analysis for a conventional radial clarifier. The parameters of the Computational Fluid Dynamics analysis were set in the Ansys software, and after running the simulation, the values for fluid velocity, turbulence intensity and Reynolds number were obtained.

MATERIALS AND METHODS

This study builds on earlier research that was done to optimize the sedimentation process (*Zăbavă et al., 2021)*. The research started with the simulation of the flow of a liquid-solid mixture in a radial clarifier, with a central supply area, made in ANSYS CFX. It is important to note that a 2D flow analysis inquiry was carried out, because the clarifier is radial, and a symmetry of the results appears. The preceding study's mathematical equations and simplifying hypotheses were applied to the modelling *(Zăbavă et al., 2021; Brennan, 2001; Kohnke, 1999; Parry, 2014; Sharifi et al., 2019).*

It should be noted that was run one simulation for a usual clarifier in which the supply pipe had diameter=1 m over, height=5.5 m (the usual case). A simplified 3D modelling of the radial clarifier was performed (Fig. 1), but also a section through the central area of the clarifier, a section that also passes through the middle area of the supply pipe (Fig. 2), using SolidWorks 2016 SP 0.0.

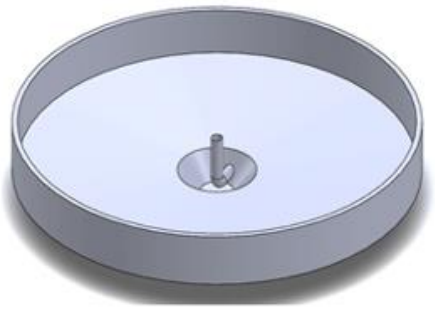

Fig. 1 - Isometric view of a radial clarifier, designed in SolidWorks: 1 m supply line
(Zăbavă et al., 2021)

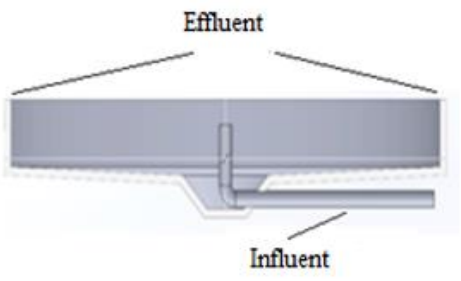

Fig. 2 - Section in the central area for the clarifier with 1 m supply line
(Zăbavă et al., 2021)

The model was drawn in the “Design Modeler” module and are presented in Figure 3.

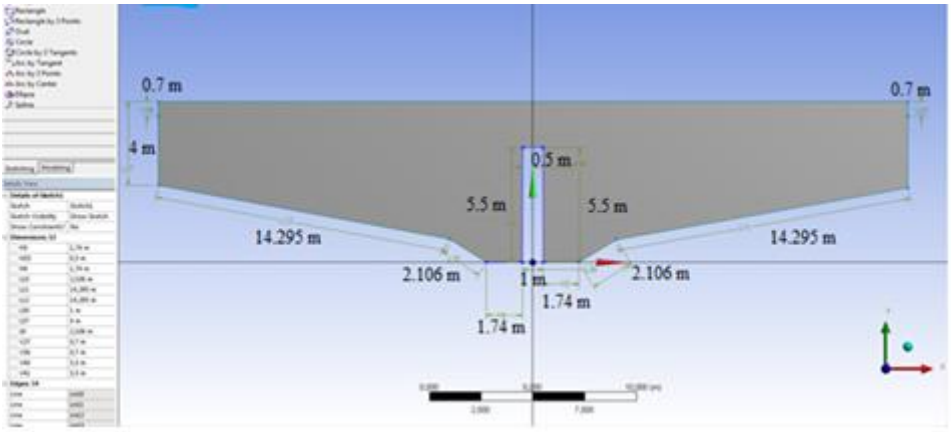

Fig. 3 - Geometric model drawn for the analysis of the clarifier with a feeding pipe with 1 m supply line *(Zăbavă et al., 2021)*

Therefore, 250 divisions have been set for Edge Sizing and for Edge Sizing 2 - 300, basically both groups define the geometry of the model. In these areas, a reasonable level of numerical prediction accuracy was effectively ensured by imposing a considerable number of finite volume divisions, considered delicate for the 1 m feed pipe clarifier. The surface area of the geometric models was then divided into finite volumes using the triangulation method, Quadratic option. Finally, the grid was given a smoothness of grade 3.
After grid generation (which took about 60 minutes), a grid with 372395 elements and 729904 nodes was obtained for the clarifier with 1 m feed pipe (Figure 4).

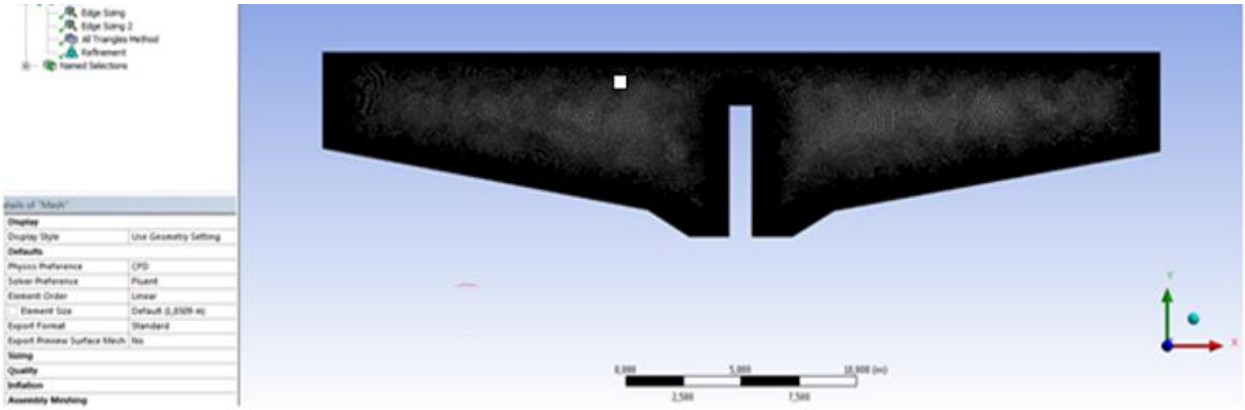

Fig. 4 - Finished volume mesh obtained for the geometric model with 1 m supply line *(Zăbavă et al., 2021)*

Following discretization, the water feed zone and the water outlet zone were configured as independent zones (Figure 5).

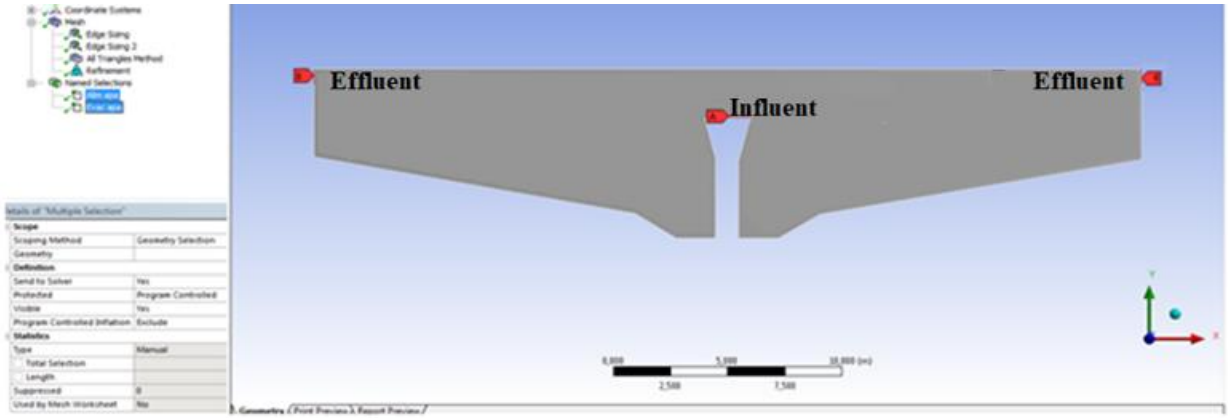

Fig. 5 - Water supply and discharge areas for the clarifier *(Zăbavă et al., 2021)*

With the CFD option as the physical reference, the discretized network cells were automatically assigned to be fluids. Knowing all the values involved in the relation of the Reynolds number, its calculation was performed for the two geometric models, using the calculation formula:

$$Re = \frac{v \cdot \rho \cdot d}{\vartheta} \quad (1)$$

It has a value of 40449.44 for this clarifier, which frames the flow regime as a turbulent one. In order to support the study, the mathematical model k- (2 equations) was used. The RNG (Re-Normalization Group) option was chosen as the k-model to improve study accuracy. This approach to renormalizing the Navier-Stokes equations to account for the effects of motion at lower scales was initially put forth in the publication (*Yakhot, 1992*).

The calcium carbonate to be injected in the water supply area, the injection position, the particle diameter (0.001 m), the flow rate (0.1 kg/s), the time to inject (from 0 to 180 s simulation time), the collision behaviour, and the simulation boundary conditions were all set before the discrete phase was activated. With the velocity-inlet option and a primary fluid feed rate of 0.036 m/s, the water supply area has been configured as the supply region, and the water discharge area has been configured as the outflow. At this point, the operating conditions (pressure and gravitational acceleration) were also established. The analysis approach was then chosen (Figure 6).

The second order equations for pressure, impulse, turbulent kinetic energy, and dissipation rate were selected to achieve the highest calculation accuracy.

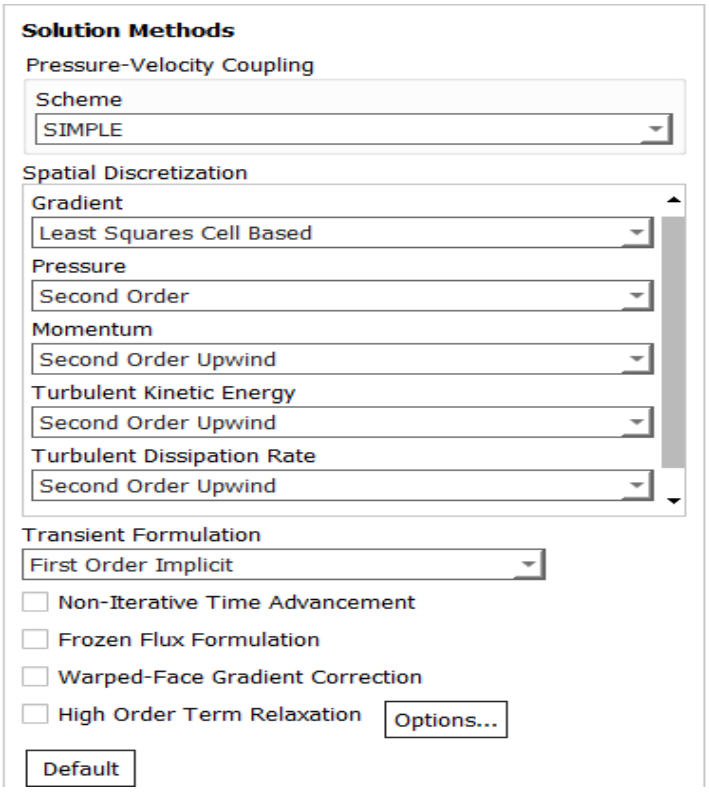

Fig. 6 - Choosing the analysis method in the Ansys program

The following settings were used to finish the calculation: Step size for the calculation was 0.005 seconds, there were 36,000 steps total, and there were 20 iterations for each time step. By dividing the total number of steps (36,000) by the calculation step size (0.005 s), the overall simulation duration (180 s) was determined. The calculation was started by clicking the "Calculate" button. While executing the calculation, the software simultaneously plots the residual value variation curves (Figure 7).

According *to ANALYSIS TOOLS, (2008; Stat Trek)*, this analysis's residual values attained a value of 10^{-4} for this type of clarifier.

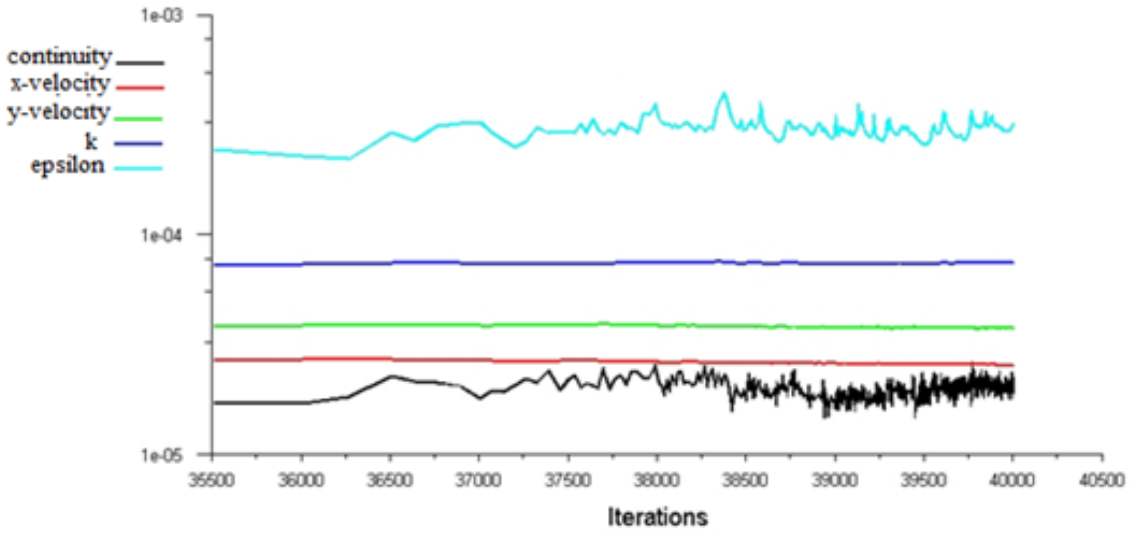

Fig. 7 - Residual values variation curves

RESULTS

The data for velocity, the Reynolds number in each cell, and the intensity of the turbulence at 60 s, 120 s, and 180 s (the simulation time) are reported in this section. It should be noted that a study on a few of the results reported below was conducted by one of the authors of this paper and published in the Ph.D. thesis.

Fluid velocity analysis

Figure 8 displays the velocity distribution for the clarifier with a feeding pipe of 1 m to 60 s, 120 s, and 180 s, as well as specifics of the feeding in those same timeframes.

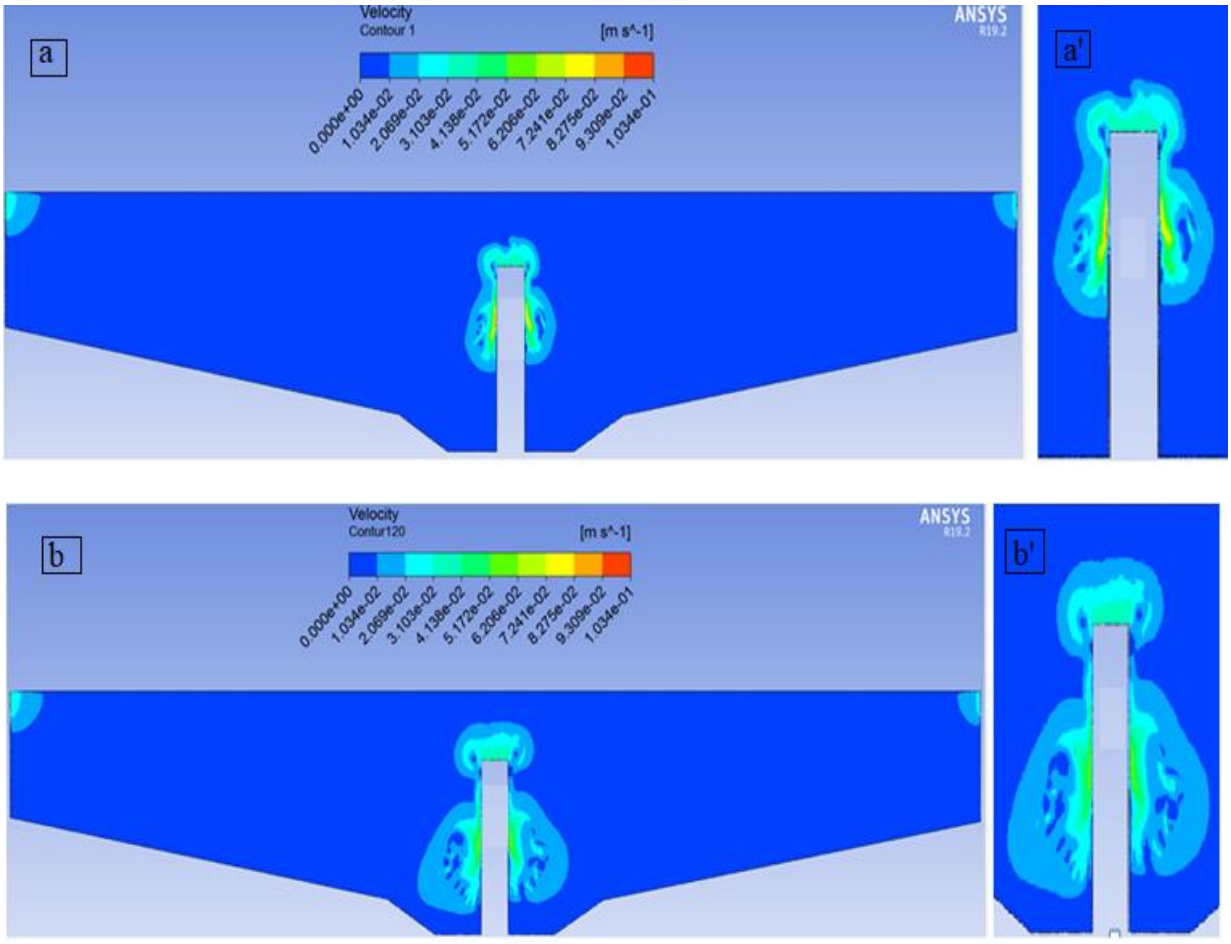

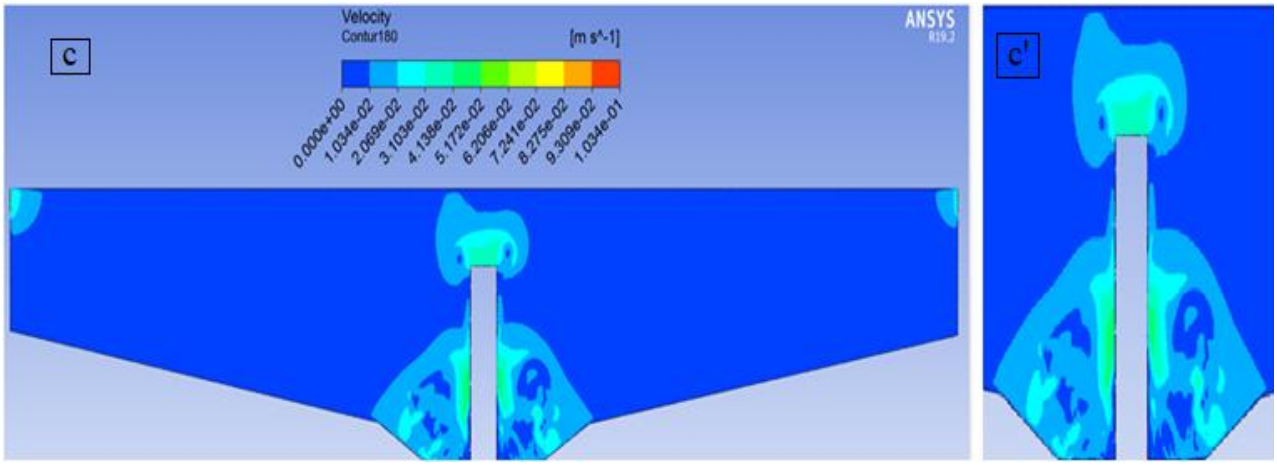

Fig. 8 - Clarifier velocity distribution at 60 s (a), 120 s (b) and 180 s (c), respectively details in the feeding area, in the same time intervals (a'-c')

Figure 9 shows the vector projection of the velocity at t=180 s for the clarifier with the supply pipe of 1m.

The vortex area can be easily observed, and further fluid propagation can be expected. Also, the tendency to move can be expected, at least for another period, in the bottom area of the decanter. This disadvantages the sedimentation process because the sediments are already on the bottom of the sedimentation tank and can be taken up by the water flow and lifted into the fluid mass. This will increase the final sedimentation time.

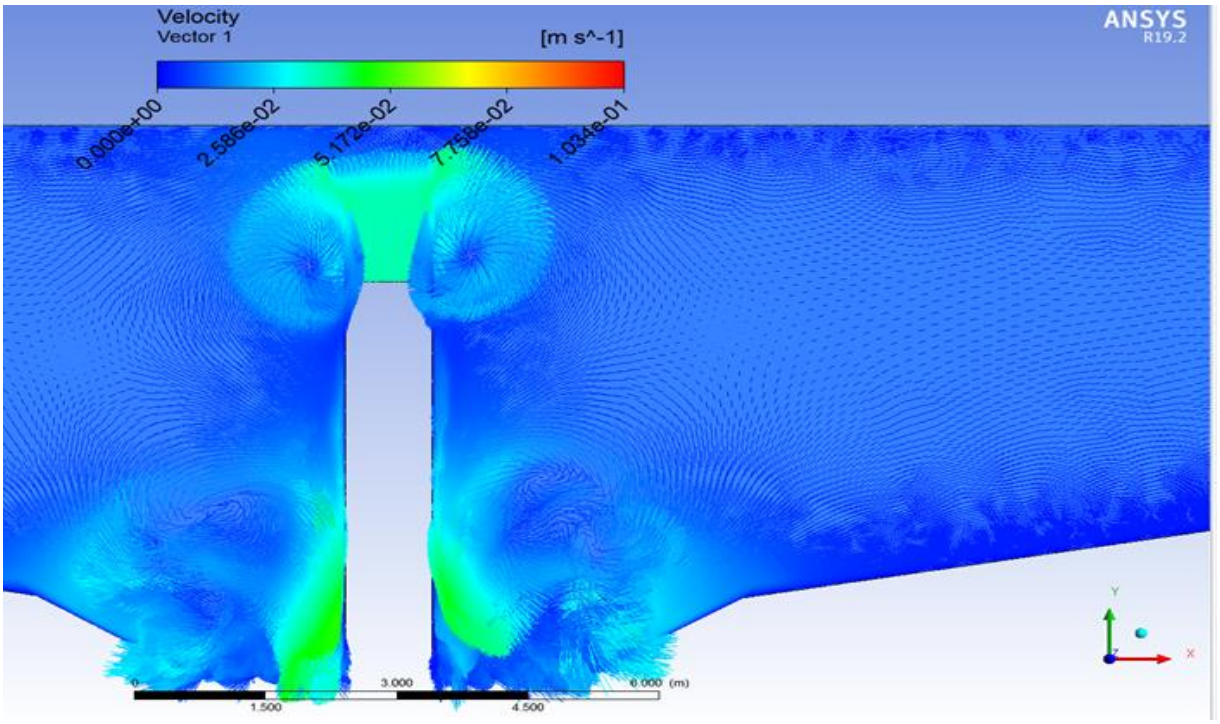

Fig. 9 - Vector projection of the velocity at t=180 s for the clarifier with 1m supply pipe

Reynolds number analysis

Figure 10 displays the Reynolds number's distribution along the diameter of the clarifier with the feeding pipe of 1 m, at 60 s, 120 s and 180 s. Also, details from the feeding zone, for the same time are presented here. Although for the supply area (inside the pipe) the calculated Reynolds number determined a turbulent regime, immediately after the entry of the fluid inside the clarifier, the regime becomes laminar, which favours the sedimentation process.

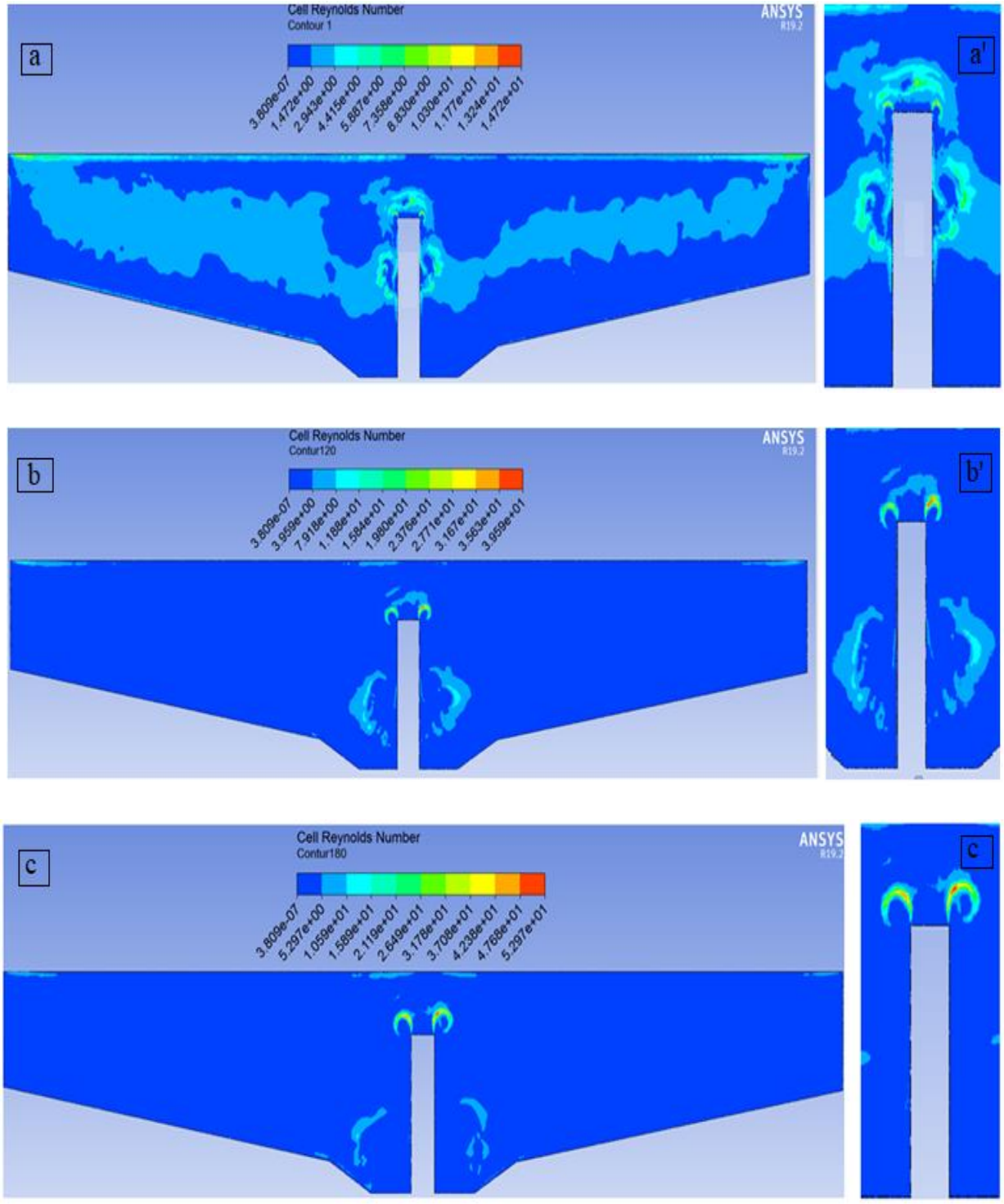

Fig. 10 - Reynolds number's distribution at 60 s (a), 120 s (b) and 180 s (c), respectively details of the feeding area, in the same time intervals (a'-c')

Turbulence intensity analysis

Figure 11 shows the distribution of turbulence intensity along the diameter of the clarifier with the feeding pipe of 1 m, at 60 s, 120 s and 180 s. The literature describes turbulence intensity as the ratio of standard deviation of fluctuating fluid velocity to the mean fluid speed, and it represents the intensity of fluid velocity fluctuation (*Zhang, 2013; Mudde et al., 2005)*.

If the maximum turbulence intensity remains constant at $3.82 \cdot 10^{-2}$ % over the entire length of the simulation time, it is interesting to analyse the evolution in time of the turbulence intensity over the length of the clarifier.

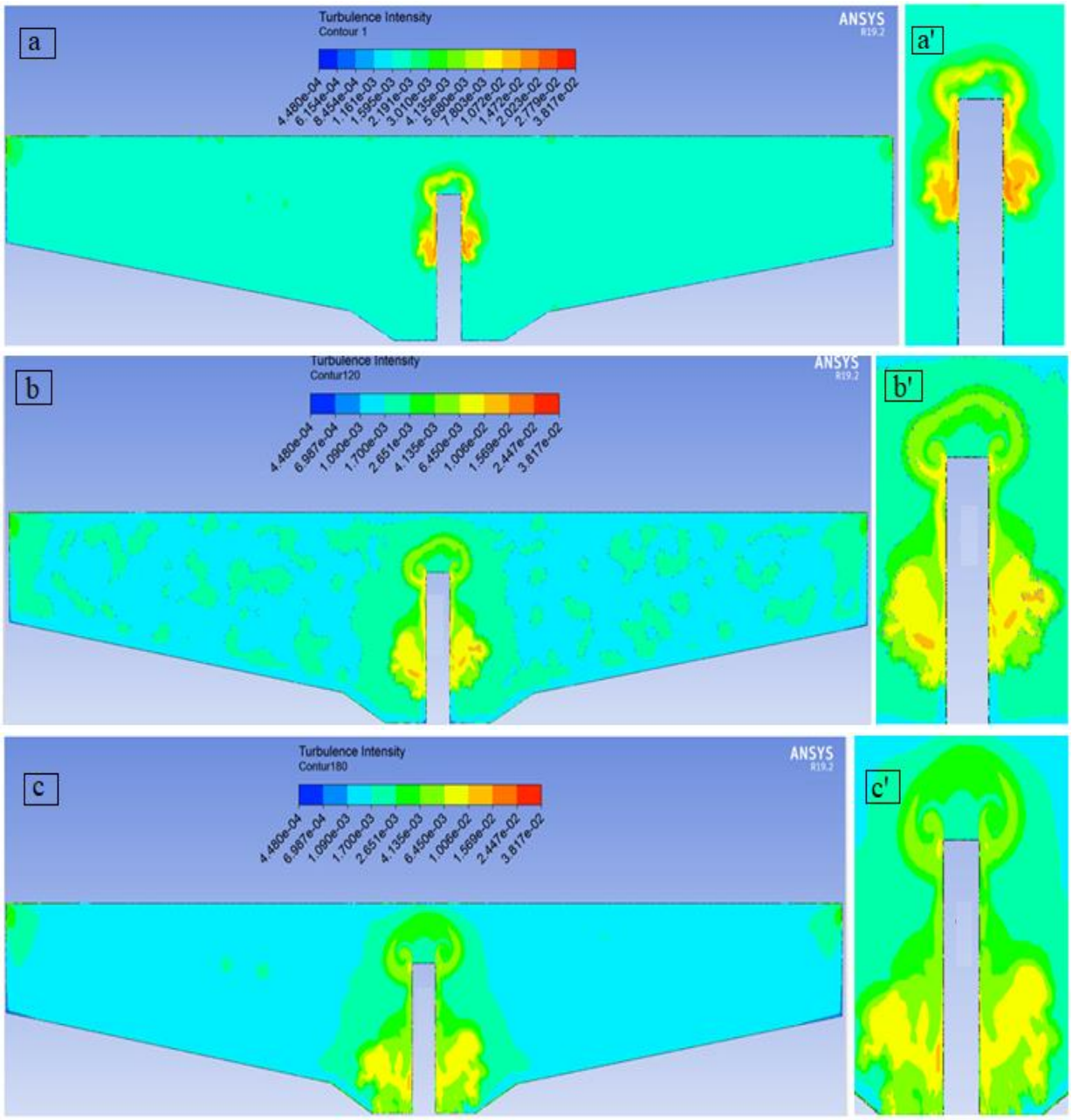

Fig. 11 - Clarifier turbulence distribution at 60 s (a), 120 s (b) and 180 s (c), respectively details of the feeding area, in the same time intervals (a'-c')

Analysing the results obtained for the clarifiers with 1 m supply pipe, regarding the fluid velocity analysis, despite the feeding area's velocity being set to 0.036 m/s, it is apparent from this number that there are locations in the clarifier where the velocity is 0.103 m/s. In the feeding area, velocity values are at their highest values. As presented in Figure 8, it is shown that the direction of travel is typically in the direction of the clarifier's bottom. This is caused by the vortices that form at the supply pipe's left and right corners at the end of the pipe. This results at the bottom of the clarifier in a considerable pressure difference in the fluid mass.

The Reynolds number study's highest values for the clarifier diameter were 14.7 for t=60 s, 39.6 for t = 120 s, and 53 for t=180 s. Although, initially, the tendency to move is towards the water evacuation areas, due to the appearance of vortices in the limit areas of the supply pipe, the fluid velocity increases, and proportionally with it, the Reynolds number also increases. Additionally, it could be seen that the presence of eddies affects the shift in travel direction from "mainly to the outlet" to "largely to the bottom" of the clarifier. Looking at the evolution of the Reynolds over time, an increasing tendency can be seen, but it will not increase so much as to go out of the area of a laminar regime on the diameter of the clarifier.

Also, regarding the turbulence intensity analysis showed that at t=60 s, the average value of the turbulence intensity was $1.70 \cdot 10^{-3}$ % but, with the appearance of vortices, which cause part of the fluid to move to the bottom of the clarifier, the turbulence intensity decreases in the radial direction of the clarifier to $1.09 \cdot 10^{-3}$ % at t=120 s and t=180 s. In time, the zones of maximum for the turbulence intensity are getting closer and closer to the bottom of the clarifier.

It should be mentioned that the results obtained agree with the results obtained by other researchers *(Chero et al., 2019; Griborio et al., 2021; Griborio et al., 2014; Shahrokhi et al., 2013; Czernek et al., 2014; Sharifi et al., 2019).*

CONCLUSIONS

Analysing the results obtained for the clarifiers with 1m supply pipe, regarding the fluid velocity analysis, despite the feeding area's velocity being set to 0.036 m/s, it is apparent from this number that there are locations in the clarifier where the velocity is 0.103 m/s. In the feeding area, velocity values are at their highest values.

In terms of the results of the Reynolds number analysis, the values increased during the three time periods looked at, with the minimum value being 14.7 and the maximum being 53.

Also, regarding the turbulence intensity analysis showed that at t=60 s, the average value of the turbulence intensity was $1.70 \cdot 10^{-3}$ % but, with the appearance of vortices, which cause part of the fluid to move to the bottom of the clarifier, the turbulence intensity decreases in the radial direction of the clarifier to $1.09 \cdot 10^{-3}$ % at t=120 s and t=180 s. The results obtained agree with the results obtained by other researchers. This work may help researchers in the field, mainly, but also the builders of radial clarifiers.

ACKNOWLEDGEMENT

This work has been funded by the European Social Fund from the Sectoral Operational Programme Human Capital 2014-2020, through the Financial Agreement with the title "Training of PhD students and postdoctoral researchers in order to acquire applied research skills - SMART", Contract no. 13530/16.06.2022 - SMIS code: 153734 and from the project "Development of the practical application base for agricultural, mechatronic and environmental mechanics in vineyards, orchards and solariums (DEMEVILISO)", CNFIS-FDI-2023-F-0277, from the Ministry of Education through the Executive Agency for Financing Higher Education, Research, Development and Innovation.

REFERENCES

[1] Alsina X. F. (2008), *Conceptual design of wastewater treatment plants using multiple objectives*. PhD Thesis, Faculty of Sciences at the University of Girona, Spain;

[2] Al-Jeebory A. A., Kris J., Ghawi A.H. (2010), Performance improvement of water treatment plants in Iraq by CFD model. *QJES*, *3*(1), 1-13;

[3] Brennan D. (2001), *The numerical simulation of two-phase flows in settling tanks.* PhD Thesis, University of London, London;

[4] Campbell B.K., Empie, H.J. (2006), Improving fluid flow in clarifiers using a highly porous media*. Journal of Environmental Engineering.*, 132, 1249-1254;

[5] Chero E., Torabi M., Zahabi H., Ghafoorisadatieh A., Bina, K. (2019), Numerical analysis of the circular settling tank Drinking Water Engineering and Science*, 12*, 39–44;

[6] Czernek K., Ochowiak M., Janecki D., Zawilski T., Dudek L., Witczak S., Krupińska A., Matuszak M., Włodarczak S., Hyrycz M., Pavlenko I. (2014), Sedimentation Tanks for Treating Rainwater: CFD Simulations and PIV Experiments*. Energies, 14*, 7852. https://doi.org/10.3390/en14237852;

[7] Das S., Bai H., Wu C., Kao J.H., Barney B., Kidd M., Kuettel M. (2016), Improving the performance of industrial clarifiers using three-dimensional computational fluid dynamics*. Engineering applications of computational fluid mechanics*., 10, 130-144;

[8] Gernaey K.V., & Vanrolleghem P.A. (2005), Modeling of reactive primary clarifier. *Water Science and Technology*., 43(7), 73–81. doi:10.2166/wst.2001.0393;

[9] Griborio G., Rodríguez J.A., Enriquez L. (2021), Use of three-dimensional computational fluid dynamics model for a new configuration of circular primary settling tank McCorquodale*. Water Science and Technology*., *84* (2), 333–348;

[10] Griborio A., McCorquodale J.A., Rodriguez J.A. (2014), CFD Modeling of Primary Clarifiers: The State-of-the-Art. *In: Proceedings of the WEFTEC 87th Annual Technical Exhibition and Conference*. New Orleans, LA. doi:10.2175/193864714815941540;
[11] Hasim A.M.H., El-Hafiz A.A., El Baz A.R., Farghaly S.M. (2017), Study the performance of circular clarifier in existing potable water treatment plant by using computational fluid dynamics. *XVI World Water Congress*, Cancun;
[12] Hoffmann S., Feldmann U., Bach P.M., Binz C., Farrelly M., Frantzeskaki N.A. (2020), Research Agenda for the Future of Urban Water Management: Exploring the Potential of Nongrid, Small-Grid, and Hybrid Solutions. *Environmental Science & Technology*., *54*, 5312–5322. doi: 10.1021/acs.est.9b05222;
[13] Kohnke P. (1999), ANSYS Theory Reference. Eleventh Edition, SAS IP, Inc.;
[14] Mudde R.F., Deutz L., Nievaart V.A., van Maanen H.R.E. (2005), LDA-Measurements of the Turbulence in and Around a Venturi. *Proceedings of the ERCOFTAC International Symposium on Engineering Turbulence Modelling and Measurements*; ETMM6, Sardinia, Italy, 23–25 May, 511-520;
[15] Öberg G., Metson G.S., Kuwayama Y., Conrad S. (2020), Conventional Sewer Systems Are Too Time-Consuming, Costly and In-flexible to Meet the Challenges of the 21st century. *Sustainability, 12*, 6518. doi:10.3390/su12166518;
[16] Parry A. (2014), *Numerical Simulations and Optimisation of Gas-Solid-Liquid Separator. MSc Thesys in Petroleum Engineering,* Imperial College London, London;
[17] Patziger M., Günthert F.W., Jardin N., Kainz H., Londong J. (2016), On the design and operation of primary settling tanks in state-of-the-art wastewater treatment and water resources recovery. *Water Science and Technology., 74 (*9), 2060–2067. doi:10.2166/wst.2016.349;
[18] Rus F. (2001), *Separation operations in the food industry*, (*Operații de separare în industria alimentară*) Publisher: Transylvania University Publishing House, Romania;
[19] Saady N.M. (2012), Effect of inclined plates and polyelectrolyte on the performance of settling tanks. Department of Civil and Environmental Engineering, University of Windsor;
[20] Sharifi Kh., Jafari B.T., Ebrahimi S., Sabeti M., Soflaee S. (2019), A new computational fluid dynamics study of a liquid-liquid hydrocyclone in the two phase case for separation of oil droplets and water, *Brazilian Journal of Chemical Engineering 36*, 1601-1612;
[21] Shahrokhi M., Rostami F.Md., Said M.A., Sabbagh Yazdi S.R., Syafalni S. (2013), Computational investigations of baffle configuration effects on the performance of primary sedimentation tanks. *Water and Environment Journal., 27* (4), 484–494. doi:10.1111/j.1747-6593.2012.00367.x;
[22] Smol M. (2022), Chapter 1 - Circular economy approach in the water and wastewater sector, Editor(s): Alexandros Stefankis, Ioannis Nikolaou, Circular Economy and Sustainability, *Elsevier*, 1-19, ISBN 9780128216644.;
[23] Smol M., Koneczna R. (2021), Economic Indicators in Water and Wastewater Sector Contributing to a Circular Economy (CE). *Resources, 10*, 129. https://doi.org/10.3390/resources10120129;
[24] Yakhot V., Orszag S.A., Thangam S. (1992), Development of turbulence models for shear flows by a double expansion technique. *Physics of fluids. 4*, 1510-1520;
[25] Zăbavă B.Ș., Constantin G.A., Voicu G. (2021), Numerical CFD analysis in a radial decanter. *UPB Scientific Bulletin* Series D, 83 (3).*;*
[26] Zhang L.Z. (2013), Conjugate heat and mass transfer in heat mass exchanger ducts, 1st ed.; Publisher: Academic Press;
[27] ***Analysis Tools, (2008), ANSYS Advantage, Volume 2, no. 4, https://www.ansys.com/content/dam/company/advantage/aa-v2-i4-full-version.pdf ;
[28] ***Clarifier Design: WEF Manual of Practice No. FD-8, Water Environment Federation. (2005), 2nd ed McGraw-Hill Publishing House. https://silo.pub/clarifier-design-wef-manual-of-practice-no-fd-8.html ;
[29] ***Stat Trek, Residual Analysis in Regression. https://stattrek.com/regression/res idual-analysis.aspx;
[30] ***Manuals of British Practice in Water Pollution Control. PRIMARY SEDIMENTATION, (1980), The Institute of Water Pollution Control https://www.ircwash.org/sites/default/files/341.9-80UN-1158.pdf.

THE DESIGN OF JUJUBE IRRIGATION SYSTEM USING LINEAR REGRESSION ANALYSIS, BP NEURAL NETWORK AND RANDOM FOREST

/

利用线性回归分析、BP 神经网络与随机森林的枣树灌溉系统设计

Wenhao DOU, Sanmin SUN *), Pengxiang XU [1]
College of Water Conservancy and Architecture Engineering, Tarim University, Alar, Xinjiang / China
Tel: +8609974680383; E-mail: ssmaqx@126.com
Corresponding author: Sanmin Sun
DOI: https://doi.org/10.35633/inmateh-70-16

Keywords: *Random Forest, BP neural network, Linear regression analysis, Intelligent irrigation system*

ABSTRACT

This paper evaluates linear regression analysis, BP neural network, and a random forest prediction model for the prediction of jujube water demand. The results highlight that the R^2 of the random forest is 0.941 and the residual distribution is the most stable. Hence, the random forest is more suitable for prediction, and therefore, an intelligent irrigation system is established employing random forest, where the cloud server is the upper computer and a Raspberry Pi is the lower computer, and at the same time, a PC and a mobile interface was built to present various information about the developed irrigation system.

摘要

本文搭建线性回归分析、BP 神经网络与随机森林预测模型预测枣树需水量，结果表明随机森林的 R2 为 0.941 且残差分布最稳定，随机森林更适合用于预测。利用随机森林建立一套智能灌溉系统，使用云服务器作为上位机，树莓派作为下位机，同时搭建 PC 端与移动端操作页面。

INTRODUCTION

Water demand data is important for jujube growth, with water demand prediction being a key link to achieving intelligent irrigation, and prediction accuracy directly affecting the water-saving effect. Hence, many experts and scholars apply computer technology to predict water demand to realize intelligent agricultural water-saving *(Friha et al., 2021)*.

With the maturity of artificial intelligence technology, more intelligent algorithms are applied to predict crop water demand *(Liu et al., 2021)*. Given that linear regression analysis, BP neural network, and random forest have extensively been used and proven effective in data analysis *(Abdol et al., 2020),* these three prediction models on water prediction demand for jujube trees were evaluated.

Considering agricultural intelligent irrigation systems, the one based on ZigBee is unsuitable for building sensors in a wide range of farmland due to its small networking range *(Emad Ahmed Mohammed et al., 2023).* Additionally, the intelligent irrigation control system based on NB IoT has a wide coverage and much-connected equipment but requires a very high network *(Cheng et al., 2021; Aqeel-Ur-Rehman at al., 2011).* The LoRa communication system has wide coverage, low energy consumption, and no requirements for the network. Therefore, the developed system uses LoRa communication for data transmission.

Currently, the core controller of most intelligent irrigation systems is a single-chip computer. The development cycle of SCM is quick, but the running speed is slow, the resources are few, and the update code must be rewritten, which is relatively troublesome. Therefore, a new generation of intelligent irrigation systems with Raspberry Pi as the core controller has emerged *(Zhao et al., 2022; Tan et al., 2019)*. Raspberry Pi is a microcomputer that uses an ARM core processor to run the Linux operating system. It can directly program and run programs locally, and after connecting to the Internet, it can directly perform remote operations and complete operations that a microcontroller cannot complete.

Spurred by the above findings, this paper evaluates linear regression analysis, BP neural network, and a random forest prediction model and selects the best model as the irrigation system prediction model. Given the experimental results, an intelligent control system for agricultural irrigation is constructed using Raspberry Pi as the core controller and LoRa communication as the data transmission system.

[1] *Dou Wenhao, M.S. Stud. Eng.; Sun Sanmin, Prof. Ph.D. Eng.; Xu Pengxiang, M.S. Stud. Eng.*

MATERIALS AND METHODS

System architecture

For this intelligent irrigation system, the current sensor technology, Internet of Things technology, wireless communication technology, and artificial intelligence technology were exploited. The developed system comprises a built data acquisition module, control module, irrigation module, cloud server, and online control platform. Solar modules power the system.

Specifically, wind speed, solar radiation, soil temperature, humidity, and other sensors are used to collect various environmental information in the jujube garden. The data are then transmitted via the LoRa communication system, and the Raspberry Pi is the control module that transmits data and provides the appropriate instructions. Besides, the irrigation module comprises a water pump, solenoid valve, and flowmeter and employs LoRa communication technology for data transmission. Additionally, the PC terminal and mobile terminal pages are designed for viewing various sensor data from the jujube garden and controlling the solenoid valve for irrigation. The system can conduct real-time environmental monitoring, data collection, transmission and analysis, water demand prediction, and remote irrigation control. The developed irrigation system is illustrated in Fig.1.

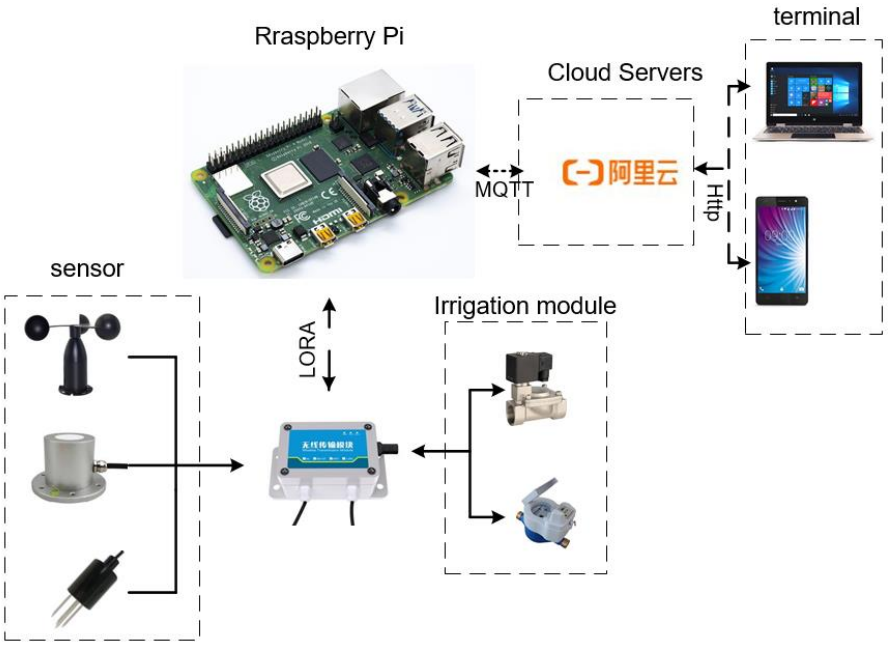

Fig. 1 - System Framework

During irrigation, the system first collects data through the data acquisition module and transmits it to the control module through LoRa communication. Then, the control module uploads the data to the online control page and the cloud server and makes the irrigation decisions, which are passed to the irrigation module for implementation. The actual irrigation system is illustrated in Fig.2.

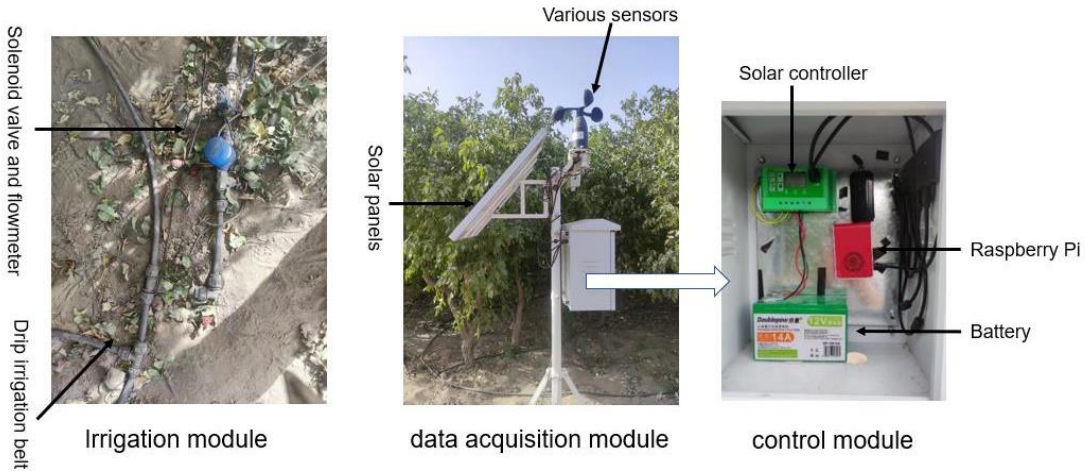

Fig. 2 - Physical system

Irrigation prediction model

The data are independently predicted according to linear regression analysis, BP neural network, and random forest, and the best model is selected for the intelligent irrigation system. The sample data were obtained from various sensors in the Zaoyuan Irrigation Experimental Base of the School of Water Conservancy and Building Engineering of Tarim University in Alar from 2001 to 2021. From the sample data, 80% is allocated to the training set and 20% to the verification set. Examples of raw data are listed in Table 1.

Table 1

Raw data

date	Average temperature X1（℃）	Average wind speed X2（m/s）	relative humidity X3(%)	Sunshine hours X4(h)	Pressure X5(Pa)	solar radiation X6(W/m2)	water demand Y(mm)
20010401	17.38	3.62	18.66	6.62	895.2	177.09	4.13
20010402	16.67	4.69	20.53	5.43	893.7	144.21	4.01
⋮	⋮	⋮	⋮	⋮	⋮	⋮	⋮
20210929	20.31	1.64	19.45	5.21	895.5	143.82	2.98
20210930	22.11	2.28	16.49	5.11	895.7	140.90	3.49

Linear regression analysis

The traditional linear model has a simple structure and a small computational burden. When the time series are in a stable state, the linear model produces good predictions and captures the linear relationship of the time series *(Huang et al., 2022)*.

The regression model considers the water demand of jujube trees as the dependent variable Y in the regression analysis, and the other meteorological factors are the independent variable Xi.

The equation and analysis results are as follows:

$$Y=0.316X_1+0.768X_2+0.023X_3+3.147X_4-0.037X_5-0.093X_6+24.618 \quad (1)$$

Table 2

Results of linear regression analysis

variable	Denormalization coefficient		Standardization coefficient	T	P	R^2	F
	B	Standard error	Beta				
constant	24.618	4.136	—	5.95	0		
X_1	0.316	0.006	0.65	52.99	0		
X_2	0.768	0.019	0.34	39.55	0		
X_3	0.023	0.002	0.13	11.93	0	0.857	F=1987.2
X_4	3.147	0.182	1.819	17.28	0		
X_5	-0.037	0.005	-0.08	-8.08	0		
X_6	-0.093	0.007	-1.49	-14.14	0		

Table 2 reveals that the F value of the regression equation is 1987.2 and the P value of the model is less than 0.01, indicating that the multiple linear regression equation is very significant. However, the fitting effect of R^2 is 0.857, which is not adequate. To further improve the prediction effect, BP neural network and random forest will be used.

BP neural network

A BP neural network is a multi-layer feedforward network with a hidden layer, which is the core of the feedforward network and reflects the essence of an artificial neural network. BP neural network systems solve the learning problem of hidden unit connection weight in multi-layer networks. A typical BP neural network model is depicted in Fig.3, where the input layer is X1~X4, and Y is the output vector.

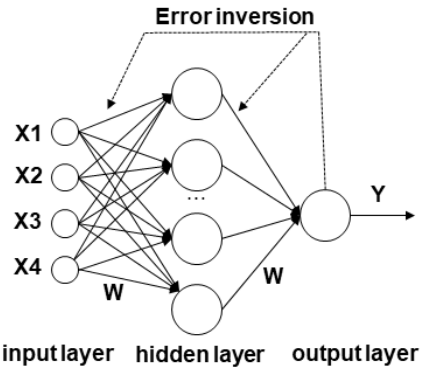

Fig. 3- BP Neural Network Topology

This paper's BP neural network prediction model employs the LM training algorithm. The sample data in this paper comprise 3843 groups of medium-scale data, and the LM algorithm has the fastest training speed. Moreover, 'tansig' is selected as the transfer function, 'trainlm' as the training function, and 'learngdm' as the learning function. The number of iterations is set to 1000, the learning rate is 0.1, and the error precision is 0.001. The hidden layer is determined as 11, according to the determination method of 2N+1 *(Lv et al., 2019)*.

The results highlight that the deterministic parameter R^2 of the BP neural network prediction model is 0.849, indicating that the model's prediction accuracy is insufficient. Table 3 shows that the model's MSE value has a large error, with the training effect not meeting the actual demand.

Table 3

BP Neural network analysis results

MSE	RMSE	MAE	R^2
1.281	1.132	0.926	0.849

Stochastic forest model

The random forest exploits a decision tree as the basic learner through Bootstrap technology. It randomly extracts k samples from the sample set N, with the samples replaced in N. The sample size in the random extraction is the same as the original data and establishes k decision tree models for k samples. Each time a training set is used to obtain a model, the final decision tree model will provide k decision results, and the final results will be voted according to each record. Fig.4 illustrates the principle of a random forest, where D is the sample set, and D1, D2 … Dk are the decision trees formed by random sampling.

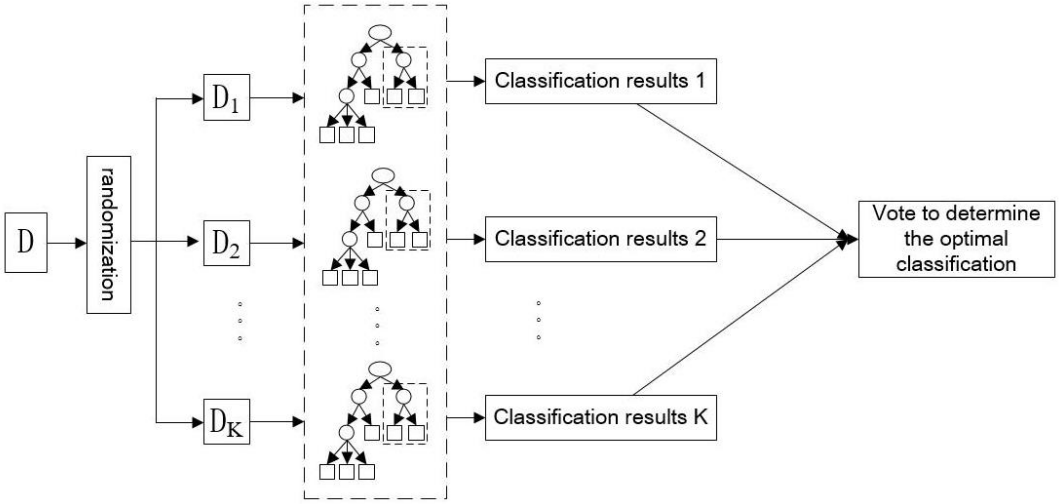

Fig. 4 - Principle of random forest

According to the data sample size, the number of decision trees in the random forest model is set to 100, the maximum depth of the decision tree is 10, and the maximum number of leaf nodes is 50. In this work, sampling with placement is performed. After importing the training data into the model, the corresponding results are reported in Table 1, which reveals that the deterministic parameter R^2 is 0.928, i.e., the model training effect is appealing and meets the requirements of daily use.

Table 4

Random Forest Analysis Results

MSE	RMSE	MAE	R^2
0.359	0.6	0.45	0.928

Comparison and analysis of prediction models

This paper considers the jujube garden as an example to analyze and compare the application of linear regression analysis, BP neural network, and random forest prediction model in water demand. After training the model, 615 groups of sample data are randomly selected from the 3843 groups of experimental data to predict the water demand of jujube trees using the three competitor models, with Table 5 presenting the actual and predicted water demand per model.

Table 5

Partial water demand

Serial No	Actual water demand /(mm·d^{-1})	Predicted water demand /(mm·d^{-1})		
		Linear regression analysis	BP neural network	Random forest
1	4.1340	4.8142	4.7200	4.7825
2	4.0755	4.8334	4.7014	4.3487
⋮	⋮	⋮	⋮	⋮
614	6.9904	5.9874	5.8915	6.0657
615	6.5048	5.3346	5.1512	5.6568

The prediction results are displayed, and the model's predicted values are linearly fitted with the real values. Fig.5 compares the residual error of the fitting curve between some predicted and real water demand values based on linear regression analysis, BP neural network, and random forest prediction model.

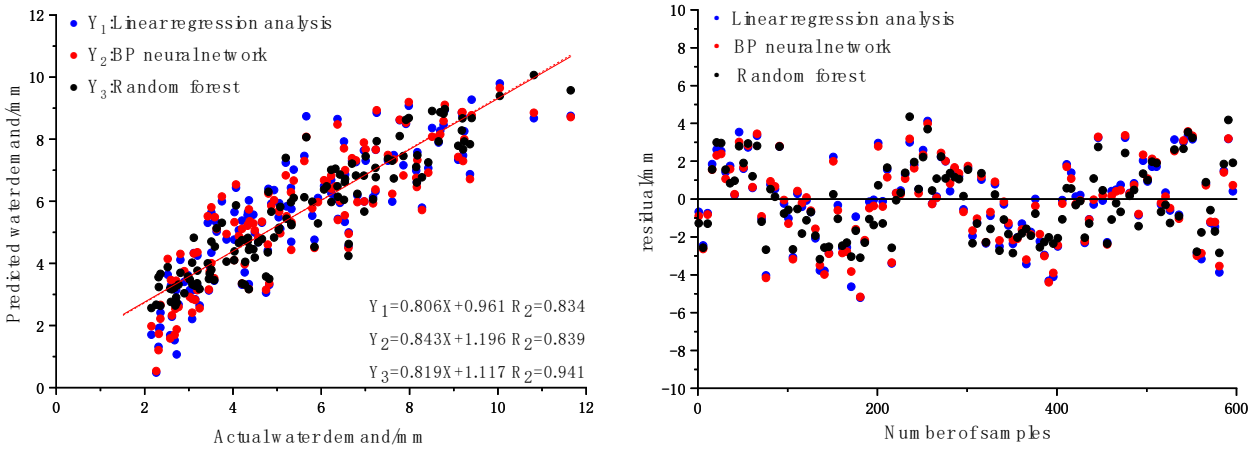

Fig. 5 - Fitting curve and residual

Fig. 5 highlights that the predicted value using the linear regression equation and the actual value have a fit of 0.839. For the BP neural network, the fitting value is 0.834, and for the random forest, the fitting value is 0.941. Considering the residuals, the residuals of the linear regression equation and the BP neural network are relatively large and volatile, while the residuals of the random forest are small and stable. Compared with linear regression analysis and BP neural network, the random forest regression has a better prediction effect on the water demand of jujube trees. Thus, the random forest has higher accuracy and is more suitable for the water storage prediction of jujube trees.

Irrigation control platform

The Alibaba Cloud is utilized for PC and mobile control platforms to facilitate remote control and real-time irrigation system monitoring. Our platform interface displays environmental parameters, sensor status, irrigation control, and equipment positioning. Specifically, the environmental monitoring part displays the real-time environmental data in the orchard, which users can view in real-time. The sensor status part displays the operational status of the sensor to find damaged offline equipment quickly.

The irrigation control allows users to query the crop water demand predicted by the model, realize the remote switch of the user control field solenoid valve, and display the irrigated water volume and the instantaneous flow of the drip irrigation belt through the flowmeter. Besides, the device location displays the device location to prevent the loss of the device. At the same time, to overcome the problem that operators cannot use the PC interface to view farmland environmental information and control the solenoid valve irrigation, a mobile terminal operation interface was also built. The PC end control interface is shown in Figure 6.

Fig. 6 - PC end control interface

The mobile end control interface is illustrated in Figure 7.

Fig. 7 - Mobile terminal control interface

RESULTS

Irrigation experiment

After the system is built, its parts are tested to confirm normal operation. Precisely, the data obtained by the sensors are compared with the data obtained by the weather station in the jujube garden. Moreover, it is tested that the operation interface can display data in real time and that the data transmission is normal. Additionally, it is confirmed that the PC and mobile interfaces can remotely control the solenoid valve, and the remote control switch of the solenoid valve operates normally. The abovementioned tests aim to confirm that the system achieves the expected effect.

The irrigation test site is located in the jujube garden of the irrigation test base of the School of Water Conservancy and Building Engineering of Tarim University in Alar City. The jujube trees are 10 years old, and drip irrigation has been adopted. The irrigation test environment is shown in Fig. 8.

Fig. 8 - The irrigation test environment

During irrigation, first, the Stacking integrated learning prediction model predicts the water demand according to the meteorological data collected by the sensors in the jujube garden. The predicted value is compared with the soil moisture storage calculated by the soil moisture sensor. When the predicted water demand exceeds the soil moisture storage, the system judges whether to conduct irrigation. The irrigation stops when the soil moisture sensor detects that the soil moisture storage exceeds the predicted water demand. Otherwise, irrigation will not be carried out.

The calculation formula of soil water storage is:

$$S = \rho b \times h \times w \tag{2}$$

where:

S — Soil water storage, [mm];

ρb — Soil bulk density, [g/cm^3];

h — Soil thickness, [mm];

w — Soil moisture, [%];

In this experiment, the soil moisture sensor is buried at 20 cm, so h=200 mm. According to the previous experimental data, the soil bulk density of the test site is 1.43 g/cm^3 *(Zhou et al., 2021)*.

Considering our test, the soil water storage is calculated based on the data obtained from the soil humidity sensor, and the system irrigation results are reported in Table 6, revealing that the system operates normally and starts irrigation when the soil water storage is less than the predicted value. No irrigation will be carried out when the soil water storage exceeds the predicted value.

Table 6

Systematic irrigation test

Number of tests	Soil water storage /mm	Model prediction value /mm	Solenoid valve status
1	5.3	6.7	open
2	5.9	6.6	open
3	5.7	8.3	open
4	7.1	6.5	close
5	6.1	5.2	close

CONCLUSIONS

This paper evaluates linear regression analysis, BP neural network, and random forest to predict the water demand of jujube trees. Considering the meteorological factors as independent variables and the jujube water demand as the dependent variable, the results reveal that the fitting coefficient R^2 of the random forest model is 0.972, which is better than the linear regression analysis and BP neural network. Additionally, the residual error of the random forest is stable. Overall, the random forest prediction model is highly accurate and can be used in actual production. At the same time, hardware such as the data acquisition module and the irrigation module and apply LoRa communication technology were developed to solve the problem of RS485 communication requiring a wired connection. Overall, the absolute error between the model-predicted water demand and the actual crop water demand is small, demonstrating that all modules of the irrigation system operate normally in daily production, and the whole system operates stably.

ACKNOWLEDGEMENT

The authors were funded for this project by the science and technology project of Xinjiang Production and Construction Corps (No.2021CB021), and science and technology plan project of the first Division of the City of Alar (No.2022XX01).

REFERENCES

[1] Abdol R. Z., Mohammad R. M., & Ali S. (2021). Investigating of the climatic parameters effectiveness rate on barley water requirement using the random forest algorithm, Bayesian multiple linear regression and cross-correlation function. *Paddy and Water Environment*, Vol. 19, pp. 137-148, Germany.

[2] Aqeel-Ur-Rehman, Abbasi A.Z., Islam N., Shaikh Z.A., (2014). A review of wireless sensors and networks' applications in agriculture, *Comput. Stand. Interfac*, Vol.36, pp. 263–270, Pakistan.

[3] Cheng Z., Xin Y., Yao Y., Hou C., (2021). Design of intelligent irrigation system based on NB IoT (基于 NB-IoT 的智能灌溉系统设计). *Integrated Circuit Applications*, Vol. 6, pp. 44-45, Shanghai/ China.

[4] Emad Ahmed Mohammed., Hakam Marwan Zaidan, Zaid Ghanim Mohammed, (2023). Implementation of WSN based Smart Irrigation System. *Przeglad Elektrotechniczny*, Vol. 6, pp. 27-31, Mosul.

[5] Friha O., Ferrag M.A., Shu L., Maglaras L.A., Wang X. (2021). Internet of things for the future of smart agriculture: a comprehensive survey of emerging technologies, *IEEE CAA J. Autom*, Vol. 8, pp. 718–752, Algeria.

[6] Huang H., Zhang Z., Lin Z., Liu S., (2022) Hourly water demand forecasting using a hybrid model based on mind evolutionary algorithm. *Water Supply*, Vol. 1, pp. 917-927, United Kingdom.

[7] Liu J., Liu X., Wu H., Deng H., Li Z. (2021). Application of support vector machine model based on GA optimization in forecasting water demand of green pepper crops (基于 GA 优化的支持向量机模型在青椒作物需水量预测中的应用). *Water Saving Irrigation*, Vol. 1, pp. 70-76, Hubei/China.

[8] Lv H., Feng Qian., (2019). A review of stochastic forest algorithm research (随机森林算法研究综述). *Journal of Hebei Academy of Sciences*, Vol. 3, pp. 37-41, Hebei/China.

[9] Tan Y., Qin F., (2019). Design and research of indoor intelligent irrigation system based on Raspberry Pi (基于 Raspberry Pi 的室内智能灌溉系统设计与研究). *Water saving irrigation*, Vol. 7, pp.105-108, Hubei/China.

[10] Zhao S., Chen X., (2022). Intelligent irrigation system based on Raspberry Pi and cloud platform (基于树莓派和云平台的智能灌溉系统). *Computer System Application*, Vol. 4, pp.123-129, Beijing/China.

[11] Zhou S., Sun S., Yao B., Li F., He T., Wang W., (2021). Effects of mist irrigation on canopy environment, photosynthetic characteristics, yield and quality of jujube orchards (弥雾灌对枣园冠层环境和光合特性及产量品质的影响). *Journal of Agricultural Machinery*, Vol. 5, pp. 249-257, Beijing/China.

GRASSLAND RAT-HOLE RECOGNITION AND CLASSIFICATION BASED ON ATTENTION METHOD AND UNMANNED AERIAL VEHICLE HYPERSPECTRAL REMOTE SENSING
/
基于注意力网络的无人机高光谱草原鼠洞的识别研究

Xiangbing ZHU[1)], Yuge BI[*1)], Jianmin DU[1)], Xinchao GAO[1)], Eerdumutu JIN[1)], Fei HAO[2)] [1]
[1)] Inner Mongolia Agricultural University, College of Mechanical and Electrical Engineering, Inner Mongolia, China
[2)] Department of Mechanical and Electrical Engineering, Hohhot Vocational College, Hohhot, China
Tel:+86-0471-4309215; E-mail: 2538808294@qq.com
DOI: https://doi.org/10.35633/inmateh-70-17

Keywords: *3D convolutional neural networks, Attention mechanism, Rat-hole identification, UAV hyperspectral remote sensing*

ABSTRACT
Rat-hole area and number of rat holes are indicators of the level of degradation and rat damage in grassland environments. However, rat-hole monitoring has consistently relied on manual ground surveys, leading to extremely low efficiency and accuracy. In this paper, a convolutional block attention module (CBAM) model suitable for rat-hole recognition in desert grassland monitoring, called grassland monitoring-CBAM, is proposed that comprehensively incorporates unmanned aerial vehicle hyperspectral remote-sensing technology and deep-learning methods. Validation results show that the overall accuracy and Kappa coefficient of the model were 99.35% and 98.90%, which were 3.96% and 3.35% higher, respectively, than those of the basic model. This study represents a breakthrough in the intelligent interpretation of rat holes and provides technical support for the subsequent rapid interpretation of grassland rat holes and rat damage evaluation. It also provides a solution for the fine classification and quantitative inversion of similar landscape features.

摘要
鼠洞面积和鼠洞数是监测和评价草原退化分级及草原鼠危害等级的双重指标。然而鼠洞监测一直沿用人工地面勘察，效率和精度极低。本研究综合运用无人机高光谱遥感技术和深度学习方法，首次提出了一种适用于荒漠草原监测中鼠洞识别的卷积块注意力模块（CBAM）模型（GM-CBAM）。经过精度验证，模型的总体精度和 Kappa 系数分别为 99.35%、98.90%，相较于基础模型分别提高了 3.96%、3.35%，解决了小样本、高冗余及混合像元导致的识别精度低、泛化能力差等难题，实现了荒漠草原景观下鼠洞的高精度识别。本研究不仅在鼠洞的智能解译方法上有所突破，为后续快速解译草原鼠洞及鼠害等级评价等研究提供了技术支持，也为其他相似景观地物的精细分类和定量反演提供了解决思路。

INTRODUCTION
Grassland rodents not only degrade grassland ecological environments, which restricts animal husbandry production, but also endanger human health. As an important part of the terrestrial ecosystem, grasslands have a practical significance in building an ecological barrier and promoting the animal husbandry economy *(Torok et al., 2021)*. In recent years, owing to the combined effects of global climate change and overgrazing, large-scale grassland degradation has occurred in Inner Mongolia, China *(Lyu et al., 2020)*. Grassland degradation has improved the suitability of the habitat for rodents, resulting in a sharp increase in the rodent population and eventually leading to frequent rodent damage *(Hua et al., 2022)*. The increase in the number of rodents in a grassland environment leads to the consumption of large amounts of vegetation and causes conflict between rodents and livestock. Their tunnelling behaviour causes large areas of secondary bare land, which weakens the self-healing ability of the grassland ecosystem. In addition, rodents carry pathogens that are a serious threat to human and animal health. Therefore, establishing an effective and dynamic grassland rodent monitoring mechanism to protect the grassland ecology and promote animal husbandry production is of great significance.

1 *Xiangbing ZHU, Ph.D. Stud. Eng.; Yuge BI, Prof. Ph.D. Eng.; Jianmin DU, Prof. Ph.D. Eng.; Xinchao GAO Ph.D. Stud. Eng.; Eerdumutu JIN Ph.D. Stud. Eng.; Fei HAO, Lecturer M.S. Eng.*

Efficient and accurate monitoring of rodent damage is a prerequisite for devising prevention strategies and measures. Traditional carpet-style manual surveys *(Garba et al., 2014)* are a time-consuming and laborious method of counting rat hole numbers and distribution, and cannot satisfy the demands of large-scale rodent monitoring. Satellite remote sensing has low spatial resolution and cannot acquire detailed spatial distribution information about rat holes. It can only indirectly reflect areas affected by rodent damage through vegetation loss *(Chidodo et al., 2020)*, thus limiting its application. Currently, unmanned aerial vehicle (UAV) remote sensing boasts excellent mobility and efficiency, leading to its wide application in fields such as geological mapping *(Villarreal et al., 2022)*, disaster warning *(Ghali et al., 2022)*, and precision agriculture *(Boursianis et al., 2022)*. The combination of UAVs and hyperspectral imaging enhances the discernibility between rodent damage information on the ground and vegetation shadows *(Qin et al., 2020)*, furnishing the fundamental hardware requirements for identifying rat holes in grassland degradation monitoring. However, further research is necessary to intelligently, accurately, and quickly interpret rat holes from UAV hyperspectral images.

Low recognition accuracy and poor generalization capability are currently bottlenecks in remote sensing classification research. Deep learning is considered the most advanced method in hyperspectral image processing at present. However, these bottlenecks remain unsolved because of the influence of small samples, nonlinear high redundancy, and mixed pixels. Classification methods based on spectral features (1D-CNN) or spatial features (2D-CNN), which ignore the interwoven relationship between space and spectrum, result in insufficient feature extraction capability of the network. Subsequent researchers proposed classification methods based on joint spatial–spectral features (3D-CNN), significantly improving classification accuracy. However, 3D-CNNs are limited in generating large-scale 3D-CNN models because of the number of parameters and computational resources required. Moreover, small-sample training sets are more prone to overfitting issues. Recently, researchers have proposed combining attention mechanisms with CNNs to solve small-sample-size and imbalance issues *(Liu et al., 2022; Wang et al., 2022)*. Attention mechanisms can be understood as an information selection method, focusing on different weight distribution based on the importance of given information and filtering out key information for the current task. Most current research regarding attention remains focused on the classification of urban architecture, forests, and crops, without considering the complexity of desert grassland landscapes. When existing models are applied to the identification of objects in desert grasslands, the recognition accuracy is typically far from expectations because of insufficient generalization ability, particularly in cases with complex topography and fragmented object distribution. Therefore, developing models for fragmented desert grassland landscape objects under the influence of small samples, high redundancy, and mixed pixels and realizing effective feature mining to improve object recognition accuracy is crucial.

To achieve high-precision, intelligent recognition of burrows in complex desert grassland landscapes, in this study hyperspectral data were collected of desert grassland burrow sample plots under natural light using UAV-based hyperspectral remote-sensing technology. By comprehensively employing multiscale 3D convolution, convolutional block attention module (CBAM) attention mechanisms, and dual-branch feature fusion, a GM-CBAM model suitable for burrow recognition in desert grasslands is proposed.

The main contributions of this study are as follows:

1. To address the mixed pixel issue, a grassland monitoring base model (GM-B model) was developed by using algorithms such as multiscale 3D convolution and dual-branch feature fusion. The GM-B model extracts global spatial-spectral joint features with adaptive receptive fields through multiscale 3D convolution, effectively overcoming the interference of mixed pixels. The dual-branch feature fusion enables the feature maps to contain more semantic information while optimizing computational efficiency.

2. To address small-sample-size and data-redundancy issues, attention mechanisms were added to the GM-B model, forming the grassland monitoring CBAM (GM-CBAM) model. The GM-CBAM model filters important features through the attention module, reducing data redundancy and mitigating the overfitting problem caused by small sample sizes.

3. Through performance comparisons between 2D-CNN and 3D-CNN, optimization of parameters such as patch size and learning rate, and performance comparisons and exploration of single-attention modules (channel attention, spatial attention) and mixed-attention modules (CBAM), the influence of channel attention and spatial attention ordering in the CBAM module on the model was investigated. The results enabled the development of an optimal model for grassland burrow recognition.

MATERIALS AND METHODS

Research Area Overview and Data Collection

The study area was in the Gegentala grassland in the central Inner Mongolia Autonomous Region. The area is a typical desert steppe. The constructive species of the grassland is *Stipa breviflora* Griseb, and the dominant species is *Artemisia frigida* Willd. The main rodents are *Lasiopodomys brandtii, Meriones unguiculatus, Rhombomys opimus*, and *Spermophilus dauricus (Zhu et al., 2023)*.

The experimental area covers approximately 3 hm². The spectrometer used for data collection (Fig. 1) has a spectral range of 400–1000 nm, a spectral resolution of 3.5 nm, and 256 bands. At a flight altitude of 20 m, the spatial resolution is 1.73 cm/pixel. Data were collected from July 8 to 10, 2021, with the data collection time window set between 10:00 and 14:00 Beijing time. During this period, solar irradiance was stable, and wind speed was less than 5.4 m/s.

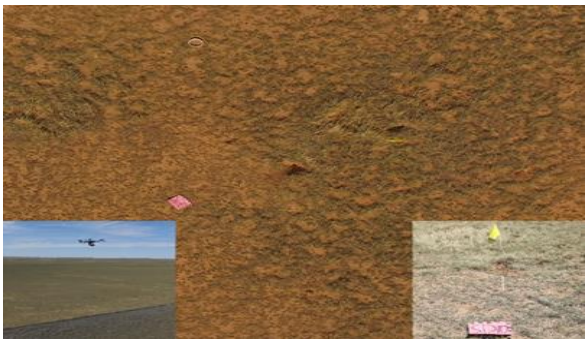

Fig. 1 - UAV hyperspectral data acquisition

Note: Mats and flags in the figure are markers of the rat-hole quadrat.

Data Preprocessing

The raw data were screened for image quality, and distorted and deformed data were removed. After reflectance correction, the standard reflectance images were obtained; the hyperspectral curves for each object are shown in Fig. 2. On the basis of the field investigation, the high-resolution digital images and hyperspectral images were used to create labels for five types of objects: burrows, vegetation, bare soil, sample plot marking foam pads, and sample plot marking flags. The dataset was then divided into training and testing sets at a 4:1 distribution ratio (Table 1).

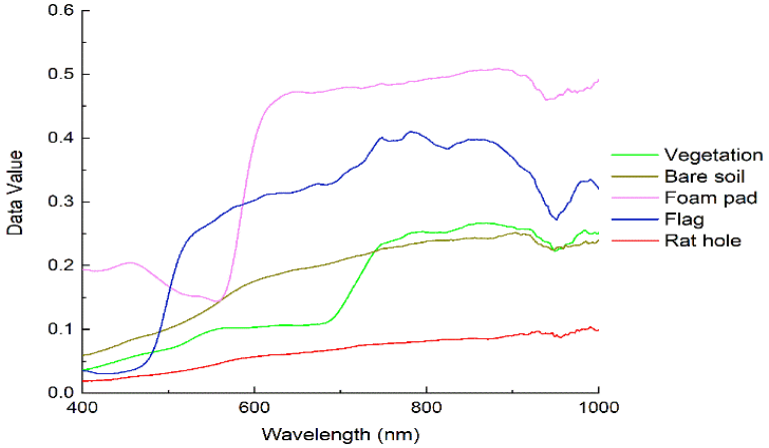

Fig. 2 - Reflectance of different objects

Table 1

Data distribution for training and test sets

NO.	Class name	Training samples	Testing samples
1	Vegetation	9780	2445
2	Bare soil	12220	3056
3	Foam mat	332	83
4	Flag	83	21
5	Rat hole	85	21
	Total	22500	5626

Proposal of GM-CBAM Model

After principal component analysis was applied to the original 256 bands, the first 30 principal components were obtained. To address the mixed-pixel issue, the GM-B model was built using the deep-learning algorithm concept of multiscale 3D convolution and dual-branch feature fusion. To address the small sample size and data redundancy issues a CBAM was added to the GM-B model, forming the GM-CBAM model.

Base Model (GM-B)

The GM-B model first uses 1 × 1 × 1 convolutions for nonlinear enhancement to improve the generalization ability of the model. The model then employs two convolution branches for feature extraction. The first branch uses two layers of 5 × 3 × 3 and 3 × 3 × 3 convolution kernels, whereas the second branch adopts a single layer of 7 × 5 × 5 convolution kernels. Subsequently, the features of the two convolution branches are fused, and finally, a 1 × 1 × 1 convolution operation is applied for nonlinear enhancement again (Fig. 3(a)).

GM-CBAM Model

Built upon the GM-B model, the CBAM is embedded into the convolution branches to form the GM-CBAM model (Fig. 3(b)). The CBAM utilized in this research is essentially a mixed-channel and spatial attention mechanism. Compared to using channel attention mechanisms or spatial attention mechanisms separately, the CBAM module integrates both channel and spatial attention mapping processes, preserving more useful information.

Assuming that the intermediate input feature cube $F \in R^{H \times W \times D \times B}$ is given (where H, W, and D represent the height, width, and spectral band of the feature cube, respectively, and B is the number of channels of the feature cube), the attention weights of different channels are obtained by modeling in the channel dimension, and then the attention weights of different spatial positions are obtained by modeling the feature map F1 (CA output) in the spatial dimension, so as to obtain the dual focus F2 of the target in the channel dimension and the spatial dimension. The mathematical expression of the process is:

$$\begin{cases} F_1 = A_C(F) \otimes F \\ F_2 = A_S(F_1) \otimes F_1 \end{cases} \quad (2)$$

In (2), $A_C(F)$ is the CA feature cube, and $A_S(F_1)$ is the SA feature cube. $\otimes$ is the point multiplication operator, which represents the product of the corresponding elements of the two tensors.

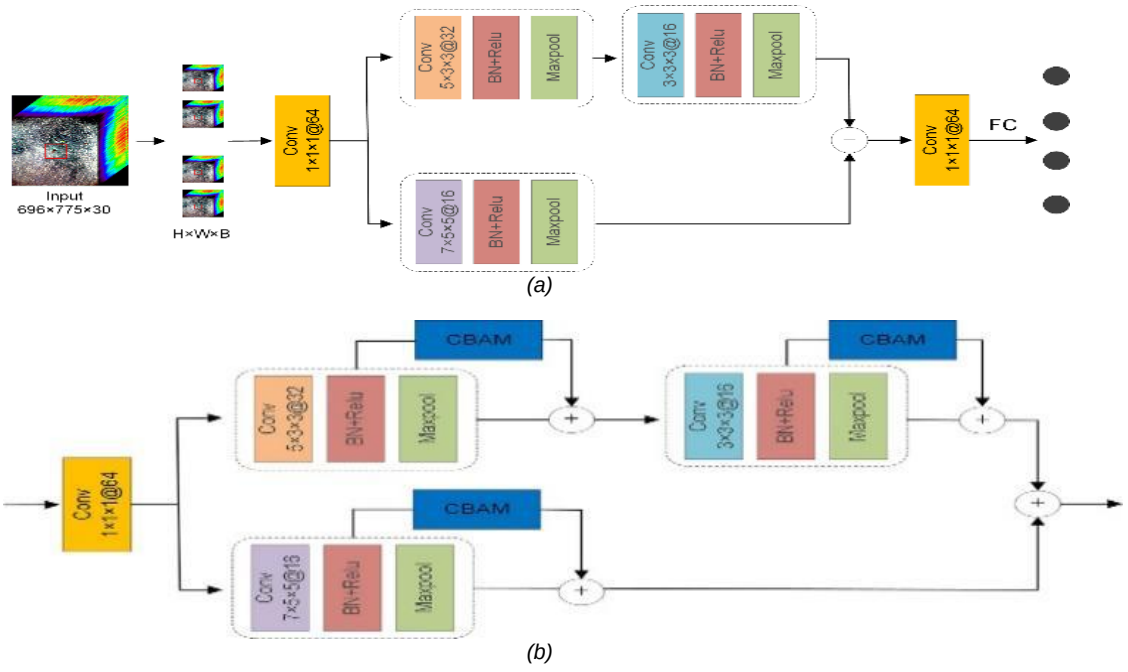

Fig. 3 - Model structure

(a) GM-B model structure; (b) GM-CBAM model

RESULTS AND DISCUSSION

To objectively compare the classification ability of each model, the number of training iterations was set to 100, and the accuracy evaluation index selected the overall accuracy (OA), average accuracy (AA), and Kappa coefficient (K).

Advantages of 3D convolution

To better evaluate the performance of 2D-CNN and 3D-CNN, performance tests under the base network GM-B were conducted. In this test, the patch size was set to 7, the learning rate to 0.001, and the number of fully connected layers to 1024. Figure 4 shows the accuracy results for 2D-CNN and 3D-CNN. Compared with 2D-CNN, 3D-CNN exhibits significant improvements in object recognition rate and OA for all types of objects.

Because hyperspectral images are three-dimensional data, when 2D-CNN is used for classification, the drawback of channel relationship loss exists, preventing 2D-CNN from fully extracting the spectral features required for the classification task. Unlike 2D-CNN, 3D-CNN uses a 3D kernel to extract both spectral and spatial features simultaneously, resulting in features containing more effective and comprehensive high-order semantic information for the classification task. Overall, 3D-CNN demonstrates good classification capabilities in grassland degradation monitoring.

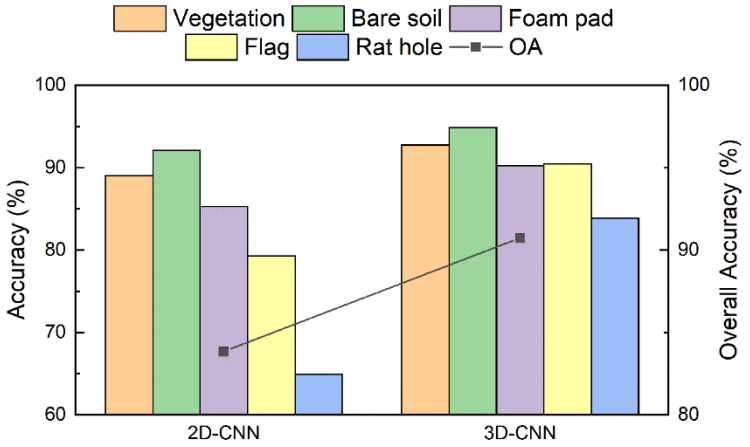

Fig. 4 - Performance comparison between 2D-CNN and 3D-CNN

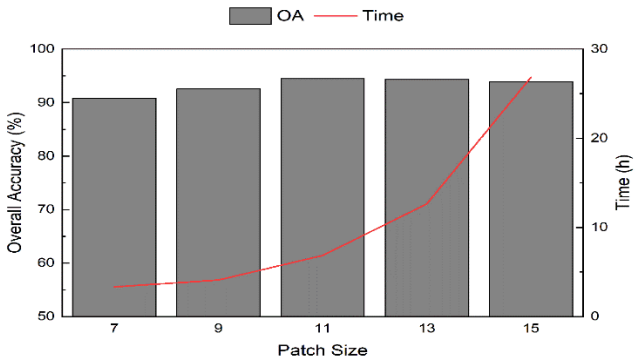

Fig. 5 - Accuracy comparison for different patch sizes

Patch Size Parameter Analysis

The size of the spatial input determines the amount of spatial information in the neighborhood of the central pixel. To evaluate the impact of patch size on model performance, five different patch sizes based on 3D-CNN were set up: 7, 9, 11, 13, and 15. As shown in Fig. 5, the OA value initially increases significantly as the patch size increases, with the best performance resulting when the patch size is 11. When the patch size is greater than 11, the performance improvement is relatively weak, but the training time increases dramatically.

Appropriately increasing the patch size can effectively improve the classification performance of the model, but an overly large patch size may generate substantial noise. In addition, a larger patch size means more training time is required.

Learning Rate Parameter Analysis

Choosing an appropriate learning rate can effectively control the convergence speed and improve the performance of the model. To determine the optimal learning rate, nine different learning rates were set: 0.0001, 0.0003, 0.0005, 0.001, 0.003, 0.005, 0.01, 0.03, and 0.05, on the basis of patch size 11, and the OA values of the model for each learning rate were obtained (Fig. 6). It was found that the model performed best when the learning rate was 0.0005. When the learning rate was greater than 0.005, the performance of the model declined because the larger learning rate made it impossible for the model to reach the global optimum.

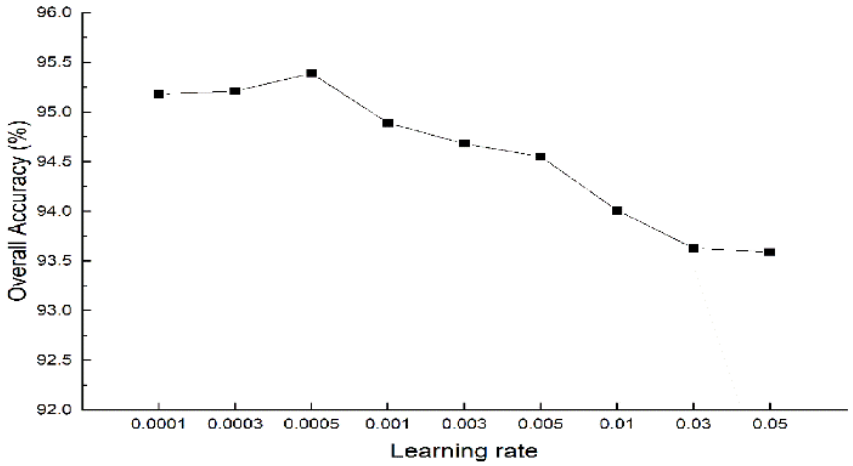

Fig. 6 - Comparison of different learning rates

Comparison of Different Attention Modules and Selection of CBAM Combination

The rat-hole sample is a small sample, and significant imbalance exists among different classes of samples. Moreover, 3D convolution has a large number of parameters. Therefore, attention mechanisms were used instead of data augmentation methods to alleviate the small-sample problem.

To better evaluate the performance of the attention mechanism, the performance of the models were tested including the channel attention (GM-CA), spatial attention (GM-SA), and combined attention (GM-CBAM) modules on the basis of the GM-B model. Three different arrangements are available for the hybrid attention: 1) channel attention prioritized over spatial attention (channel first in CBAM, CBAM_CF); 2) spatial attention prioritized over channel attention (spatial first in CBAM, CBAM_SF); and 3) channel attention and spatial attention in parallel (CBAM_P). As shown in Table 2, all attention modules perform better than the GM-B model, with the hybrid-attention module (GM-CBAM) outperforming the single-attention modules (GM-CA, GM-SA). Among the single-attention modules, GM-CA performs better than GM-SA. Among the three different arrangements in the hybrid attention, CBAM_CF exhibits the best performance, followed by CBAM_P, and CBAM_SF is the worst. At this point, the optimal model GM-CBAM has been obtained; its OA and Kappa coefficient are 99.35% and 98.90%, respectively, an improvement of 3.96% and 3.35% compared to the base model GM-B.

Table 2

Classification results of different models

Class	Methods					
#	GM-B	GM-CA	GM-SA	CBAM_CF	CBAM_SF	CBAM_P
Vegetation	98.04	99.94	99.06	100	100	100
Bare soil	98.87	99. 26	99.01	100	100	100
Mat	96.54	99.02	98.93	99.81	99.21	99.30
Flag	90.11	98.07	97.25	99.92	98.94	99.32
Rat hole	90.48	98.47	95.60	98.86	98.58	98.66
OA (%)	95.39	98.93	98.88	99.35	99.13	99.20
AA (%)	95.27	98.49	98.36	99.31	99.03	99.11
K×100	95.55	97.96	96.83	98.90	98.58	98.63

The comparison between the attention models and the base model shows that the attention mechanism, as an information-selection mechanism, has significant advantages in alleviating the small-sample problem and reducing irrelevant information mapping.

Comparing the combined attention module with the single attention modules proves that the hybrid attention mechanism has a significant advantage in mining spectral–spatial feature information in desert grassland hyperspectral images and demonstrates good classification performance.

Comparing the three different arrangements in the hybrid attention shows that channel attention contributes more to model performance than spatial attention. In addition, the result that GM-CA outperforms GM-SA in single attention modules provides further confirmation. From a spatial perspective, channel attention is global, whereas spatial attention is local. Evidently, the weight of local information is determined by the global feature distribution.

Classification Results Display

To visually verify the rationality of the classification results, Fig. 7 shows the visualization results of the original hyperspectral image (Fig. 7(a)), basic network GM-B (Fig. 7(b)), single-attention module GM-SA (Fig. 7(c)), GM-CA (Fig. 7(d)), mixed-attention network CBAM_SF (Fig. 7(e)), CBAM_P (Fig. 7(f)), and CBAM_CF (Fig. 7(g)). Among them, GM-B and GM-SA have noticeable misclassification; the mixed-attention module has no noticeable misclassification, and CBAM_CF exhibits smoother edge control.

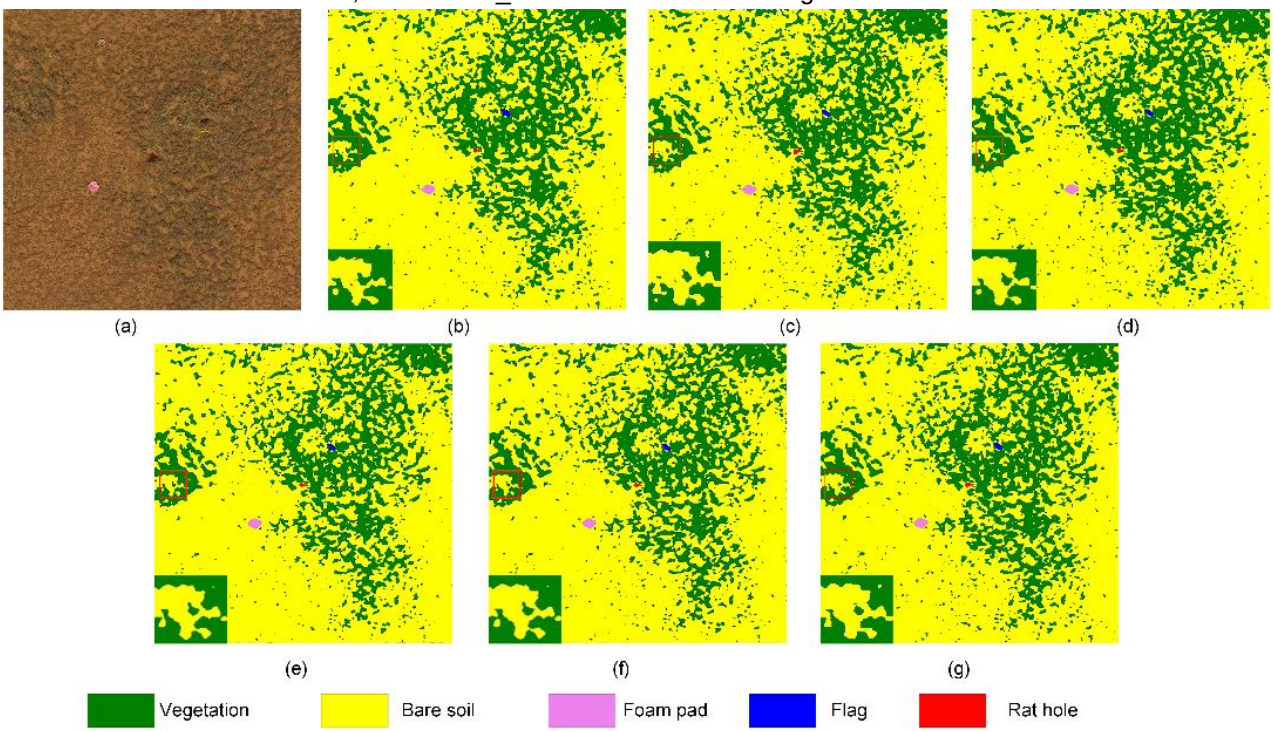

Fig. 7 - Visualization of model classification results

(a) original hyperspectral image, (b) GM-B, (c) GM-SA, (d) GM-CA, (e) CBAM_SF, (f) CBAM_P, and (g) CBAM_CF. Note: Enlarged images in the boxes in Fig. 7 (b)–(g) are shown in the lower left corner.

Limitations and prospects

The classification of desert grassland landscape features based on UAV hyperspectral images is a complex task, and research in this field is still in the primary stages. Although this study has made acceptable progress, subsequent quantitative inversion and degradation grade evaluation work needs further study. In addition, the GM-CBAM model must be further optimized to enable deployment to mobile devices.

CONCLUSIONS

In this study, a low-altitude UAV hyperspectral remote sensing platform was used to collect desert grassland data in central Inner Mongolia, China. The GM-CBAM model was created with multi-scale convolution, double-branch feature fusion, and a CBAM attention mechanism. After optimizing the network structure and parameters, an optimal model suitable for low-altitude UAV hyperspectral remote-sensing desert grassland classification was obtained. Verification experiments based on the OA, AA, and Kappa coefficient demonstrated the superior classification ability and reliability of the model.

This result provides technical support for the subsequent rapid interpretation of grassland rat holes and rat damage evaluation, in addition to providing methods and models for subsequent quantitative inversion studies of desert grassland.

ACKNOWLEDGEMENT

The research leading to these results received funding from the National Natural Science Foundation of China (grant No. 31660137) and the Research Key Project at Universities of the Inner Mongolia Autonomous Region (grant Nos. NJZZ23037 and NJZY21518) and Inner Mongolia Autonomous Region Natural Science Foundation Joint Fund Project (grant No. 2023LHMS06010).

REFERENCES

[1] Boursianis, A. D., Papadopoulou, M. S., Diamantoulakis, P., Liopa-Tsakalidi, A., Barouchas, P., Salahas, G., & Goudos, S. K. (2022). Internet of Things (IoT) and Agricultural Unmanned Aerial Vehicles (UAVs) in smart farming: A comprehensive review. *Internet of Things*, Vol. 18, Netherlands.

[2] Chidodo, D. J., Kimaro, D. N., Hieronimo, P., Makundi, R. H., Isabirye, M., Leirs, H., & Mulungu, L. S. (2020). Application of normalized difference vegetation index (NDVI) to forecast rodent population abundance in smallholder agro-ecosystems in semi-arid areas in Tanzania. *Mammalia*, Vol. 84, pp. 136–143, Germany.

[3] Garba, M., Kane, M., Gagare, S., Kadaoure, I., Sidikou, R., Rossi, J. P., & Dobigny G. (2014). Local perception of rodent-associated problems in Sahelian urban areas: a survey in Niamey, Niger. *Urban Ecosystems*, Vol. 17, pp. 573–584, Netherlands.

[4] Ghali, R., Akhloufi, M. A., & Mseddi, W. S. (2022). Deep Learning and Transformer Approaches for UAV-Based Wildfire Detection and Segmentation. *Sensors*, Vol. 22, Switzerland.

[5] Hua, L. M., & Chai, S. Q. (2022). Rodents pest control on grassland in China: current state, problems and prospects (中国草原鼠害防治现状、问题及对策). *Journal of Plant Protection*, Vol. 49, pp. 415–423, Beijing/China.

[6] Liu, J. X., Zhang, K. F., Wu, S. Q., Shi, H. T., Zhao, Y. D., Sun, Y. Q., & Fu, E. R. (2022). An Investigation of a Multidimensional CNN Combined with an Attention Mechanism Model to Resolve Small-Sample Problems in Hyperspectral Image Classification. *Remote Sensing*, Vol. 14, Switzerland.

[7] Lyu, X., Li, X. B., Gong, J. R., Wang, H., Dang, D. L., Dou, H. S., & Liu, S. Y. (2020). Comprehensive Grassland Degradation Monitoring by Remote Sensing in Xilinhot, Inner Mongolia, China. *Sustainability*, Vol. 12, Switzerland.

[8] Qin, Y., Sun, Y., Zhang, W., Qin, Y., Chen, J. J., Wang, Z. W., & Zhou, Z. Y. (2020). Species Monitoring Using Unmanned Aerial Vehicle to Reveal the Ecological Role of Plateau Pika in Maintaining Vegetation Diversity on the Northeastern Qinghai-Tibetan Plateau. *Remote Sensing*, Vol. 12, Switzerland.

[9] Torok, P., Brudvig, L. A., Kollmann, J., Price, J. N., & Tothmeresz, B. (2021). The present and future of grassland restoration. *Restoration Ecology*, Vol. 29, United States.

[10] Villarreal, C. A., Garzon, C. G., Mora, J. P., Rojas, J. D., & Rios, C. A. (2022). Workflow for capturing information and characterizing difficult-to-access geological outcrops using unmanned aerial vehicle-based digital photogrammetric data. *Journal of Industrial Information Integration*, Vol. 26, Switzerland.

[11] Wang, L. F., Wang, L. G., Wang, Q. M., & Atkinson, P. M. (2022). SSA-SiamNet: Spectral-Spatial-Wise Attention-Based Siamese Network for Hyperspectral Image Change Detection. *IEEE Transactions on Geoscience and Remote Sensing*, Vol. 60, pp. 1–18, United States.

[12] Zhu, X. B., Bi, Y. G., Du, J. M., Gao, X. C., Zhang, T., Pi, W. Q., & Zhang, H. J. (2023). Research on deep learning method recognition and a classification model of grassland grass species based on unmanned aerial vehicle hyperspectral remote sensing. *Grassland Science*, Vol. 69, pp. 3–11, Japan.

PREDICTION OF BIOMASS PELLET DENSITY USING ADAPTIVE NEURO-FUZZY INFERENCE SYSTEM（ANFIS） METHOD

/

基于自适应模糊神经网络算法（ANFIS）的生物质原料颗粒密度预测

Juan LIU[1)], Zhuoyu YAN[2)], Mingze XU[2)], Yudi LIU[2)], XueWei BAI*[2)], Yonghai XIU[3)], DeSheng WEI[2)]

[1)]Liaoning Petrochemical University, School of Civil Engineering, Fushun / China

[2)]Shenyang Agricultural University, College of Engineering, Shenyang / China

[3)]Sunbon Agricultural Machinery Manufacturing Company, Siping / China

Tel: +86-024-88487663; E-mail: bai-xuewei@syau.edu.cn

DOI: https://doi.org/10.35633/inmateh-70-18

Keywords: *biomass material, ANFIS, prediction model, pellet density*

ABSTRACT

Coconut husk powder and corn stover powder were used as raw materials to produce formed particles, and four sets of uniaxial compression moulding devices were used to explore the effects of inner hole diameter of the forming moulds, depth of compression, and depth of conformal depth of the formed particles on the density of the particles. Sampling of the formed particles was carried out at the stage of stable compression force, the maximum pellet density of the coconut coir dust material is 1.53 g/cm³ (1530 kg/m³), and 1.23 g/cm³ (1230 kg/m³) of the corn stalk powder pellets are obtained. At the same time, in the process of the test, failure to compress the two biomass raw materials into pellets also occurred, indicating that the compression parameters studied in the experiment had a significant impact on the pellet quality. On the basis of the obtained pelleting test data, taking into account the nonlinear characteristics between pellet density and processing parameters involved, the adaptive neuro-fuzzy influence system (ANFIS) method was used to predict the pellet density of coconut coir dust and corn stover powder. The results show that the method is effective for predicting the density of biomass particles.

摘要

以椰子椰壳粉和玉米秸秆粉料为原料制取成形颗粒，利用四套单轴压缩成形装置，探索成形模具内孔直径、压缩深度、成形颗粒保形深度对颗粒密度的影响规律，在压缩力平稳阶段对成形颗粒进行取样，得到的椰子椰壳粉原料的最大颗粒密度为 1.53 g/cm³ (1530 kg/m³)*，玉米秸秆粉料颗粒的最大颗粒密度为* 1.23 g/cm³ (1230 kg/m³)*，同时在试验过程中两种生物质原料都出现了未成形的情况，表明了处理所研究压缩参数对颗粒质量影响显著。在已获得的颗粒成形试验数据基础上，考虑到颗粒密度与研究参数间的非线性特点，利用自适应模糊神经网络算法对玉米秸秆和椰子椰壳粉颗粒密度进行预测，结果显示该方法对预测生物质颗粒密度是有效的。*

INTRODUCTION

Accelerating clean energy transformation is critical to ensure timely decarbonization globally, in line with the goals of the Paris Agreement (*Aleluia et al., 2022*). There are many agricultural residues that can be considered as biomass raw materials, which can be densified into pellets or briquettes to replace traditional (fossil) fuels in developing countries (*Nath et al., 2023*). It is proved an effective way to increase biomass density, which has the added benefit of increasing the material's unit density as much as ten-fold (*Kumar et al., 2022; Stolarski et al., 2013*), resulting in a consistent shape and size of products (*Mani et al., 2004*), The biomass pellets were found to characteristically have higher calorific value, higher bulk and energy densities; and lower moisture content (*Kumar et al., 2022*).

Because of rising concerns about environmental pollution, global increases of energy cost and reduction in fossil fuel resources, many researchers have attempted to numerical modeling of biomass pelleting behavior and product quality parameters. In several works of literature, the nature and effects of different operating factors on biomass pelleting have been extensively studied, Saha in Bangladesh found that briquette made of coconut coir dust mixed with rice husk at ratio 1:1 appeared as the impressive economic feasibility (*Saha et al., 2016*). Regarding pellet physical properties, the effect of pelletizing moisture on pellet moisture content, bulk density, single pellet density and durability index were statistically significant (*Yılmaz et al., 2021*).

Die geometry also influences product properties like moisture content, bulk density, and durability (*Jr. & Sokhansanj, 1997*). The L/D (length to diameter) ratio of the pellet die can be a good metric for the degree of compression during pelleting (*Li et al., 2015*). An increase in the length of the pellet die increases the pelleting pressure, whereas an increase in the diameter of the pellet die decreases the pelleting pressure (*Holm et al., 2006*). The finite element modeling was employed to predict damage of biomass pellets (*Awny et al., 2022*), or discrete element method was adopted to simulate the compaction of bulky agricultural residues (*Horabik & Molenda, 2016; Xun et al., 2021*), also the development of constitutive models for the densification of biomass material to describe the mechanical behaviors in pellets production (*Huo L.et al., 2013; Kaliyan & Morey, 2009; Shang et al., 2011*)

Due to the wide divergence in physical and chemical properties of agricultural residues, pelleting conditions and pellet properties need to be determined for effective use. Adaptive neuro-fuzzy inference system (ANFIS), is a type of regression in which the experimental data is modelled by a nonlinear combination of parameters. The applications of ANFIS artificial intelligence in different disciplines have been reported, ANFIS significantly improving its capability to correlate uncertainties associated with computational modeling (*Ani & Agu, 2022*). The non-linear relationship between the dependent parameters like die diameter, compression depth, depth remain (defined as d_r, as illustrated in Fig.2) and feed, encourage usage of the soft-computing methods based on the concept of neural network. Therefore, the experiments used cylindrical pellets of corn stover and coconut coir dust to investigate density that affect handling and storage behavior of pellets. Data of pellet density under different pelleting parameters were collected, then these data were introduced into predicting biomass pellet density, this research attempted to create and implement a sophisticated algorithm to output reasonably density prediction in biomass pellet production.

MATERIALS AND METHODS

Materials

Corn stover and coconut coir were selected as biomass material for obtaining pellets, they were chopped and then ground using a mill (WILEY Laboratory Mill Model 4, ARTHUR H. THOMAS COMPANY). Particle distribution of two biomass material is presented in Table 1.

Table 1

Sieve analysis of corn stover and coconut coir dust

Sieve mesh space / mm	0.85	0.6	0.425	0.355	0.3	0.25	pan
Corn stover /%	100.00	70.55	48.40	24.09	18.07	12.76	7.86
Coconut coir / %	100.00	99.04	98.85	91.65	86.28	66.99	49.42

The moisture content of raw corn stover and coconut coir were both lower than 10% with wet basis for long-term storage under dry condition, it is below the commonly recommended range according to literature. To get the appropriate moisture content for obtaining pellets, raw materials after grinding were wetted by spraying purified water evenly, then the biomass material was put into water-tight bags, and it was being mixed manually for every 8 h to obtain a proper absorption of water and homogeneity. The moisture content in wet basis of corn stover and coconut coir dust is 20%±0.5% and 15%±0.2% respectively, and the initial bulky density under this condition for corn stover and coconut coir dust are 185±5.4 and 307±2.2 kg/m^3 respectively. Material that satisfied the required moisture content was stored in a container placed in ambient temperature of 10-15 ℃ for 48 h prior to pelleting. Raw materials and some pellets with different diameters produced in the test is shown in Fig.1.

Fig. 1 - Raw material of ground corn stover and coconut coir, and pellets

Experimental set-up

Pellets were obtained by using four sets of uniaxial compaction set-ups consisting of a cylinder and piston, the diagram of setup being shown in Fig. 2. The cylinder had an internal diameter *d* span of 6 to 25 mm, and a length span of 23 to 90 mm, in which the symbol d_c represents the depth in compression biomass material, and d_r represents the depth remain of cylinder for newly compacted pellet. During the pelleting process experiment, the support part is placed on the working table of a universal testing machine (MTS Systems Corporation, maximum force provided to 100 kN).

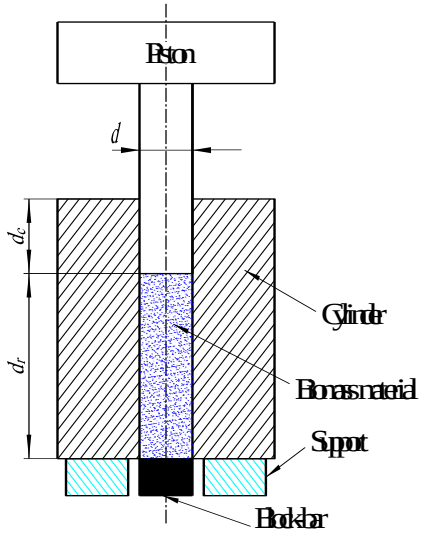

Fig. 2 - Diagram of uniaxial compaction set-up for pellet making

Experimental procedure

Corn stover and coconut coir are used as feedstock, compaction was carried out at different *d* and depth in compression d_c for different pellet obtaining set-up. Biomass material is fed into the cavity of the cylinder orifice, lower cavity end (outlet of hole) was blocked by a bar at first to establish the initial loading condition, also prevent the direct outflow of biomass material. After enough internal stress was set with 5-10 strokes of compression, the block bar is released as the continuous pellets production situation with roller-die biomass pelleting machine. As shown in Fig. 3, corn stover material is compacted into pellet, while the compression force is logged. Change of compression force depends on whether or not fix the part block-bar, it corresponds to three apparent phases of force, namely initial (the block-bar in Fig. 2 is set to close the orifice), transitional (the block-bar in Fig. 2 is removed and pellet start to move out the orifice) and steady phase. To eliminate the influence of initial loading conditions like preloading force etc., the pellet samples were collected in steady phase, the peak compression force in each stroke is close to 13000 N, after a gradual increasing trend of peak force in initial phase and transitional phase.

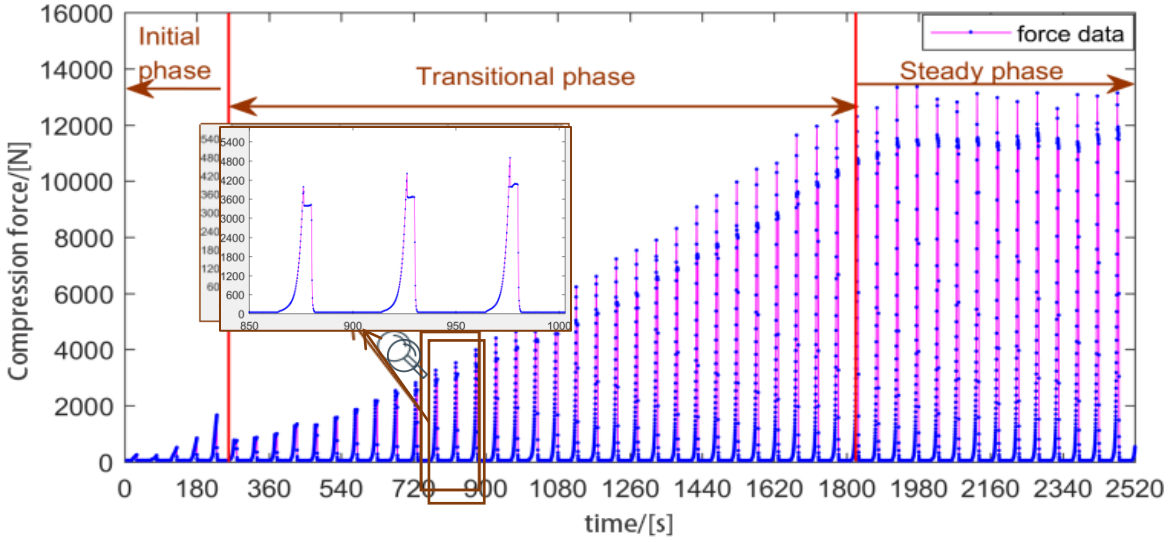

Fig. 3 - Diagram of uniaxial compaction setup for pellet making

The feeding amount *f* of biomass material of every stroke in each trial was the same in experiment, and the constant pushing/loading speed (14 mm/min) was also set in computer-controlled program to run the pelleting experiment.

Samples of biomass pellets produced in steady phase were sealed immediately in water-tight bags. After a week's preserving in a storage cabinet at approximate 18 ℃, then the diameter and height of pellet were measured with a caliper (0.02 mm resolution), and the average value of 5 measurements in different direction is adopted for each sample; the mass of each pellet sample was weighed with an electronic balance (0.01 g resolution, model ML4002E/03, Mettler-Toledo International Inc.). The unit density of pellets was calculated by dividing the mass by the volume of individual pellets.

Architecture of ANFIS model

Adaptive Neuro-Fuzzy Inference System (ANFIS), has been widely employed to represent or approximate a nonlinear system. It is a multilayer feed-forward network composed of nodes connected by directed links, in which each node performs a particular function on its incoming signals to generate a single node output. Figure 4 shows entire system architecture consists of five layers, namely fuzzy layer, product layer, normalized layer, de-fuzzy layer and output layer (*Jang, 1993*). With input/output data for given set of parameters, the ANFIS method models a fuzzy inference system (FIS) whose membership function parameters are tuned (adjusted) using either a backpropagation algorithm alone, or in permutation with a least squares type method. The parameter optimization is done in such a way during the training session that the error between the target and the actual output is minimized. A hybrid algorithm is used for optimization, which is the combination of least square estimate and gradient descent method. The parameters to be optimized in ANFIS are the premise parameters. These parameters define the shape of the membership functions (*Patel et al., 2014*). In order to reduce the error measure, any of several optimization routines can be applied after constituting MFs. The parameters set for an adaptive network allows fuzzy systems to learn from the data they are modeling (*Walia et al., 2015*).

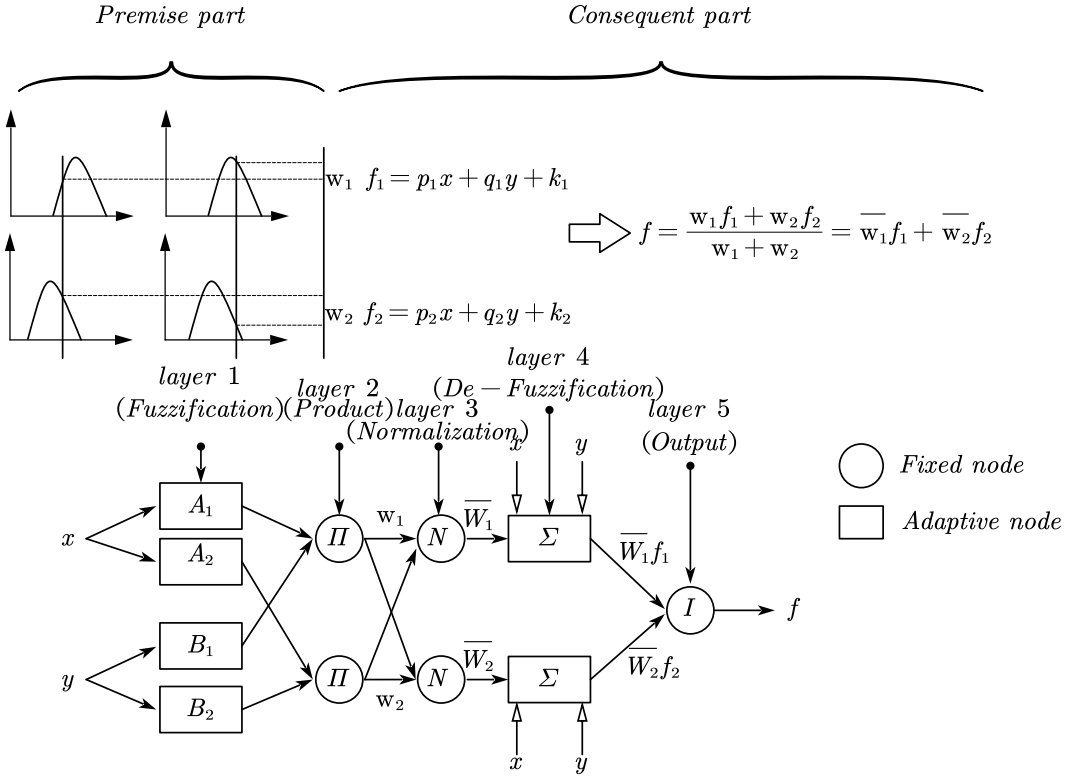

Fig. 4 - Basic architecture of an ANFIS model (Jang, 1993)

The architecture of the ANFIS in this study is shown in Fig. 5. In layer 'input', the die diameter *d*, compress depth d_c, remain depth d_r and feed *f*, are to be fuzzified. Inference process and rules are applied in layer 'inputmf' and layer rule. Calculation of output for each corresponding rules are carried out in layer 'outputmf' and then in layer density all outputs from layer 'outputmf' are combined to get one final 'output'.

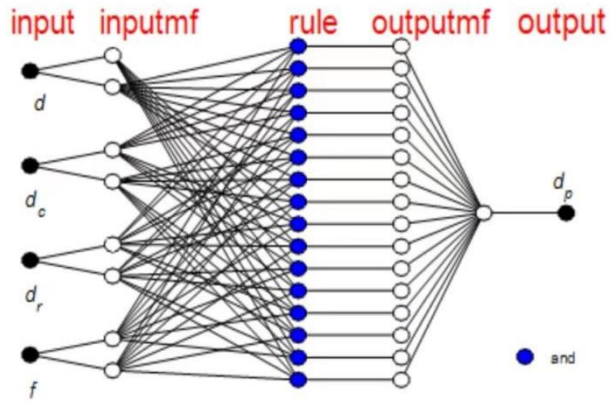

Fig. 5 - Architecture of ANFIS employed in this study

In this work, the membership function that defines how each point in the input space is mapped to a membership value, the generalized bell-shaped membership function is employed for all input variables, as defined in relation (1).

$$f(x;a,b,c)=\frac{1}{1+\left|(x-c)/a\right|^{2b}} \tag{1}$$

where: a, b, c are constant parameters to locate the center and shape of the curve (*Takagi & Sugeno, 1983*).

Fig. 6 shows the diagram of membership function of variables d, d_c, d_r and f in the ANFIS employed in prediction pellet density of both coconut coir dust and corn stover powder.

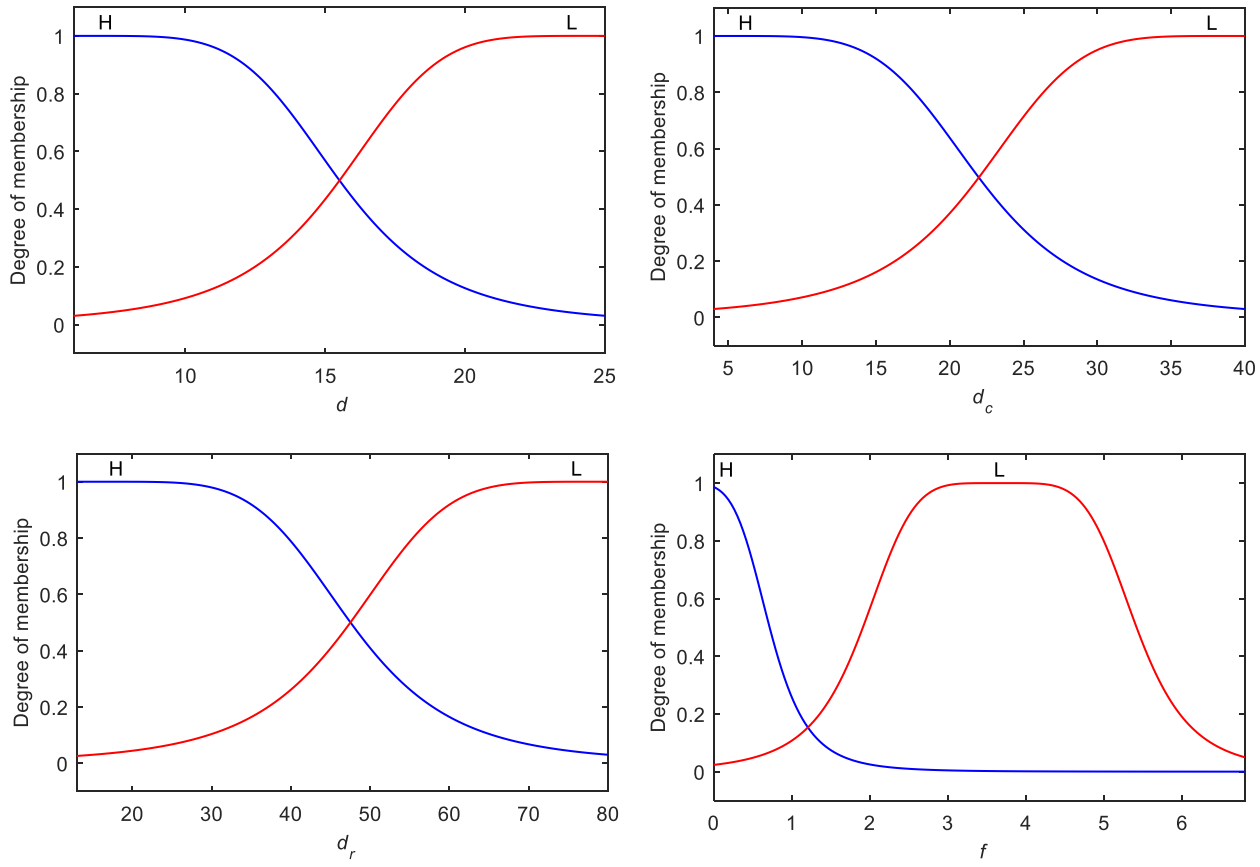

Fig. 6 - Membership function of four input variables in ANFIS model

The fuzzified information is processed using the rule base, composed of the fuzzy IF-THEN rules referred to as fuzzy control rules that must be well defined in order to control the given process (*Precup & Hellendoorn, 2011*). As shown in Table 2, the control rules in the ANFIS model used are given.

Table 2

Control Rules in ANFIS model

d	d_c	d_r	f	d_p
H	**L**	**L**	**L**	1
H	**L**	**L**	**H**	2
H	**L**	**H**	**L**	3
H	**L**	**H**	**H**	4
H	**H**	**L**	**L**	5
H	**H**	**L**	**H**	6
H	**H**	**H**	**L**	7
H	**H**	**H**	**H**	8
L	**L**	**L**	**L**	9
L	**L**	**L**	**H**	10
L	**L**	**H**	**L**	11
L	**L**	**H**	**H**	12
L	**H**	**L**	**L**	13
L	**H**	**L**	**H**	14
L	**H**	**H**	**L**	15
L	**H**	**H**	**H**	16

RESULTS

Pellet density under uniaxial compression

Density of pellets (expressed by the symbol d_p) made of coconut coir dust with uniaxial compression are given in Table 3, in order to get the influence of processing parameters on pellet density; 50 tests were conducted in making pellets of coconut coir dust. Parameters involved in each run are d, d_c, d_r and f, which represents the diameter, depth in compression, depth remain as defined previously in Fig. 2, and feed amount in gram respectively. The maximum pellet density was obtained in run No. 43, namely 1.53 g/cm^3 (1530 kg/m^3), which was produced in cylinder of internal diameter 6 mm with feed 0.11 g per stroke. Under the same conditions, other 2 replications also produced relatively high-density pellets, as indicated in run No. 44 and 45. The minimum density 0.31 g/cm^3 (310 kg/m^3) was obtained in run No. 2, the diameter being 25 mm with feed of 6.79 g per stroke. In the process of compressing biomass material, even though the pellets in initial phase are close to 1.20 g/cm^3, the compression force decreased gradually in transitional phase, and finally got close to 0 N in steady phase, the feeding material run through the cylinder hole in bulky format.

Table 3

Density data of coconut coir dust pellet in uniaxial compression

Run No.	d [mm]	d_c [mm]	d_r [mm]	f [g]	d_p [g/cm^{-3}]	Run No.	d [mm]	d_c [mm]	d_r [mm]	f [g]	d_p [g/cm^{-3}]
1	25	36	54	6.79	0.38	26	20	10	66	1.21	0.57
2	25	36	54	6.79	0.31	27	20	10	66	1.21	0.68
3	20	20	56	2.41	0.79	28	6	8	15	0.09	1.41
4	20	20	56	2.41	0.61	29	6	8	15	0.09	1.06
5	20	40	36	4.83	0.43	30	20	30	46	3.62	0.95
6	20	40	36	4.83	0.43	31	20	30	46	3.62	0.95
7	20	40	36	4.83	0.50	32	20	30	46	3.62	0.90
8	25	16	74	3.02	0.92	33	20	8	68	0.97	0.80
9	25	16	74	3.02	0.95	34	20	8	68	0.97	0.75
10	25	26	64	4.90	0.51	35	20	8	68	0.97	0.67
11	25	26	64	4.90	0.52	36	12	5	46	0.22	1.10
12	25	24	66	4.52	0.54	37	6	8	15	0.09	0.62
13	25	10	80	1.89	0.49	38	12	25	26	1.09	1.10
14	25	10	80	1.89	0.46	39	12	25	26	1.09	0.61

Run No.	d [mm]	d_c [mm]	d_r [mm]	f [g]	d_p [g/cm^{-3}]	Run No.	d [mm]	d_c [mm]	d_r [mm]	f [g]	d_p [g/cm^{-3}]
15	25	10	80	1.89	0.40	40	12	25	26	1.09	0.97
16	6	4	19	0.04	1.36	41	12	15	36	0.65	1.06
17	6	4	19	0.04	1.24	42	12	15	36	0.65	0.98
18	12	20	31	0.87	1.19	43	6	10	13	0.11	1.53
19	12	20	31	0.87	1.39	44	6	10	13	0.11	1.17
20	6	4	19	0.04	1.52	45	6	10	13	0.11	1.50
21	6	4	19	0.04	1.30	46	12	10	41	0.43	1.26
22	6	4	19	0.04	1.47	47	12	10	41	0.43	1.10
23	12	25	26	1.09	1.25	48	6	8	15	0.09	1.24
24	12	25	26	1.09	1.25	49	6	8	15	0.09	1.24
25	20	10	66	1.21	0.65	50	6	6	17	0.07	1.13

Similar behaviors also could be seen in pellet making of corn stover pellet, 52 runs were conducted in the experiment as shown in Table 4. The maximum pellet density obtained in run No.8, namely 1.23 g/cm^3 (1230 kg/m^3), which was produced in cylinder of internal diameter 12 mm with feed 0.29 g per stroke. Under the same conditions, other 2 replications also produced relatively high-density pellet, as indicated in run No. 9 and 10. The minimum density 0.17 g/cm^3 (170 kg/m^3) was obtained in run No. 29 and 43-49.

Table 4

Density data of corn stover pellet in uniaxial compression

Run No.	d [mm]	d_c [mm]	d_r [mm]	f [g]	d_p [g/cm^{-3}]	Run No.	d [mm]	d_c [mm]	d_r [mm]	f [g]	d_p [g/cm^{-3}]
1	12	25	26	0.48	0.68	27	25	26	64	2.17	0.58
2	12	25	26	0.48	0.69	28	25	16	74	1.34	0.49
3	12	25	26	0.48	0.71	29	6	4	19	0.02	0.17
4	12	25	26	0.48	0.68	30	25	10	80	0.83	0.58
5	12	5	46	0.10	1.04	31	25	10	80	0.83	0.68
6	12	5	46	0.10	0.94	32	25	10	80	0.83	0.67
7	12	5	46	0.10	0.76	33	20	20	56	1.07	0.76
8	12	15	36	0.29	1.23	34	20	20	56	1.07	0.76
9	12	15	36	0.29	1.02	35	20	20	56	1.07	0.66
10	12	15	36	0.29	1.17	36	20	20	56	1.07	0.74
11	12	10	41	0.19	1.04	37	25	16	74	1.34	0.57
12	12	10	41	0.19	1.10	38	25	16	74	1.34	0.58
13	12	10	41	0.19	1.05	39	25	16	74	1.34	0.57
14	20	10	66	0.53	1.07	40	6	6	17	0.03	0.89
15	20	10	66	0.53	0.83	41	6	6	17	0.03	0.75
16	20	10	66	0.53	0.91	42	25	16	74	1.34	0.49
17	20	30	46	1.60	0.68	43	20	40	36	2.14	0.17
18	20	30	46	1.60	0.64	44	20	40	36	2.14	0.17
19	20	30	46	1.60	0.65	45	20	8	68	0.43	0.17
20	20	20	56	1.07	0.79	46	20	8	68	0.43	0.17
21	20	20	56	1.07	0.76	47	25	36	54	3.00	0.17
22	25	16	74	1.34	0.66	48	25	36	54	3.00	0.17
23	25	16	74	1.34	0.71	49	25	36	54	3.00	0.17
24	25	16	74	1.34	0.66	50	12	20	31	0.38	0.99
25	25	26	64	2.17	0.54	51	12	20	31	0.38	0.98
26	25	26	64	2.17	0.56	52	12	20	31	0.38	0.90

Prediction of pellet density with ANFIS

Sugeno type of ANFIS (*Michio, 1985*) model was implemented in this work, 35 data were selected from both Table 3 and Table 4 respectively, for training the ANFIS model, and the rest of the data was used in validating the model.

Fig. 7 and Fig. 8 depicts the comparisons of data acquired from compaction experiment and prediction, it can be seen that the ANFIS model provided the most dominant accuracy for describing pellet density with a simpler structure, the average error in training ANFIS model is 0.123 for material coconut coir dust pellet, and the value is 0.056 for corn stover powder, this also indicated that the corresponding data is in good agreement as shown in Fig. 7 and Fig. 8. The average error in checking the ANFIS model is 0.169 for coconut coir dust pellet, and 0.149 for corn stover powder. This also shows that the ANFIS model effectively learned from the experimental data.

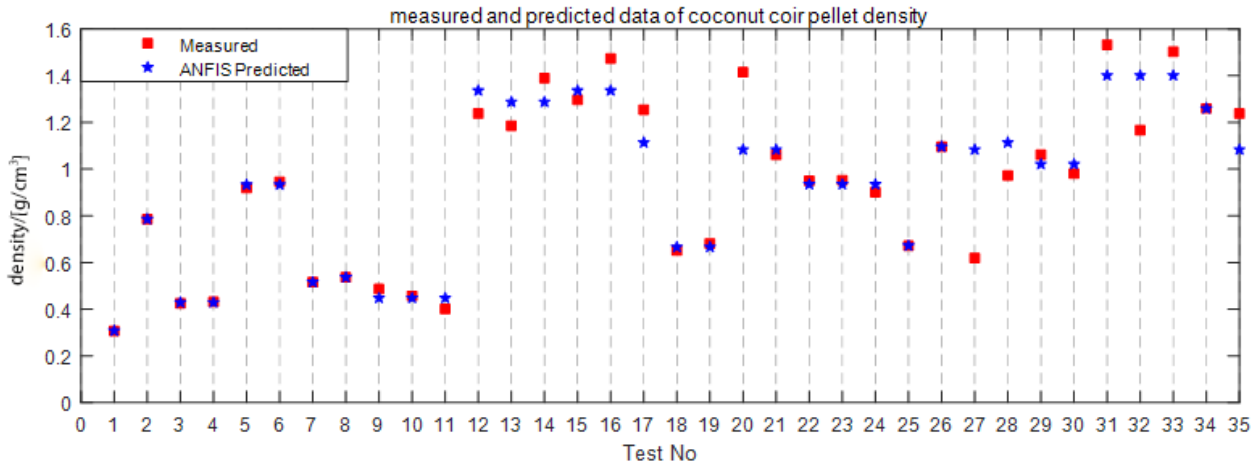

Fig. 7- Comparison of measured and ANFIS predicted values of coco coir pellet density

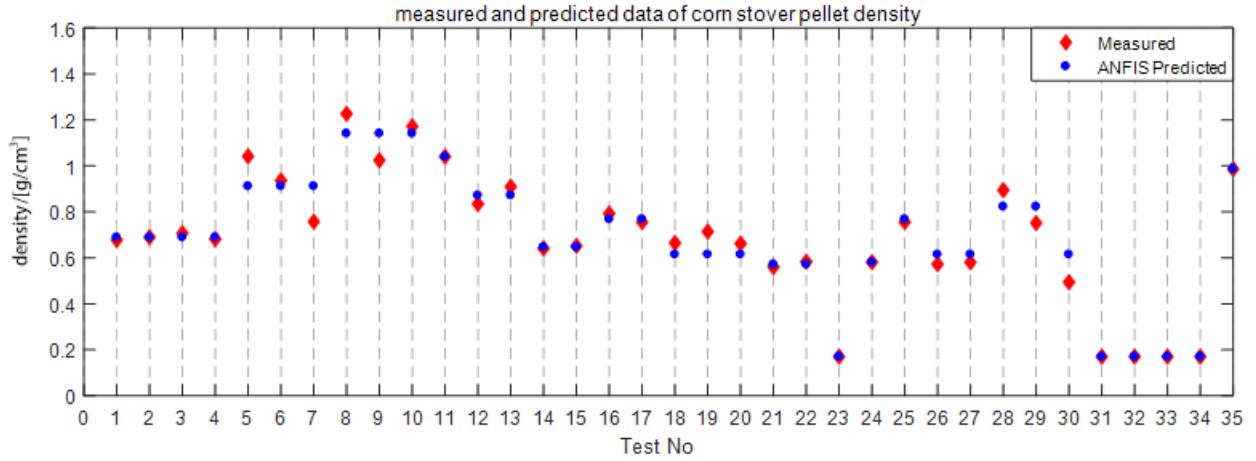

Fig. 8- Comparison of measured and ANFIS predicted values of corn stover pellet density

CONCLUSIONS

This study investigated the feasibility of coconut coir dust and corn stover powder as a suitable biomass material for pellet production, and the experimental data was conducted considering the key factors like cylinder diameter, depth in compression, depth remain and feed, in pellet making process, pellet samples were collected in steady phase, which was more consistent with the actual production situation, the failure in compaction and blocking behaviors were also observed in uniaxial compression. The ANFIS model was introduced to predict the pellet density. It is indicated that ANFIS model gave relatively lower errors for the predicted biomass pellet density and provided good agreements with experimental data, the ANFIS provide a feasible way to describe the nonlinear relationship between quality parameters and processing variables in biomass pellet producing.

ACKNOWLEDGEMENT

This project is supported by National Natural Science Foundation of China (Grant No. 51405311); Liaoning Provincial Education Department (Grant No. LJKZ0425); and by Liaoning Petrochemical University (Grant No. 1100130241).

REFERENCES

[1] Aleluia J., Tharakan P., Chikkatur A.P., et al. (2022), Accelerating a clean energy transition in Southeast Asia: Role of governments and public Policy, *Renewable and Sustainable Energy Reviews*, vol.159, pp.112226;

[2] Awny A., Radwan M.N., Nour M.A. et al. (2022), Finite element modeling of the breakage behavior of agricultural biomass pellets under different heights during handling and storage, *Saudi Journal of Biological Sciences*, 29(3), pp.1407-1415;

[3] Ani K.A., Agu C.M. (2022), Predictive comparison and assessment of ANFIS and ANN, as efficient tools in modeling degradation of total petroleum hydrocarbon (TPH), *Cleaner Waste Systems*, vol. 3, pp. 100052;

[4] Holm J.K., Henriksen U.B., Hustad J.E. et al. (2006), Toward an Understanding of Controlling Parameters in Softwood and Hardwood Pellets Production, *Energy & Fuels,* vol.20(6), pp.2686-2694;

[5] Horabik J, Molenda M., (2016), Parameters and contact models for DEM simulations of agricultural granular materials: A Review, *Biosystems Engineering*, vol.147, pp. 206–225;

[6] Huo L., Zhao L., Tian Y. et al., (2013), Viscoelastic constitutive model of biomass pellet (生物质颗粒燃料成型的黏弹性本构模型), *Transactions of the Chinese Society of Agricultural Engineering (Transactions of the CSAE)*, vol.29(09), pp.200-206;

[7] Jr. L.G.T., Sokhansanj S., (1997), Bulk properties of alfalfa grind in relation to its compaction characteristics, *Applied Engineering in Agriculture*, vol.13(4), pp.499-505;

[8] Jang J.S.R., (1993), ANFIS: Adaptive-network-based fuzzy inference System, *IEEE Transactions on Systems, Man, and Cybernetics*, vol.23(3), pp.665–685;

[9] Kumar P., Subbarao P.M.V., Kala L. et al., (2022), Influence of physical, mechanical, and thermal properties of biomass pellets from agriculture residue: Pearl millet cob and Mix, *Bioresource Technology Reports*, vol.20, pp.101278;

[10] Kaliyan N., Morey R.V., (2009), Constitutive model for densification of corn stover and Switchgrass, *Biosystems Engineering*, vol.104(1), pp.47-63;

[11] Li Yongkui, Sun Yuezhu, Bai Xuewei, (2015), Extrusion process of corn stalk powder in single orifice die processing based on discrete element method (玉米秸秆粉料单模孔致密成型过程离散元模拟). *Transactions of the Chinese Society of Agricultural Engineering (Transactions of the CSAE)*, vol.31(20), pp.212-217;

[12] Mani S, Tabil L G, Sokhansanj S., (2004), Grinding performance and physical properties of wheat and barley straws, corn stover and Switchgrass, *Biomass and Bioenergy*, vol.27(4), pp.339-352;

[13] Michio S., (1985), Industrial Applications of Fuzzy Control. *Elsevier Science Pub. Co.*

[14] Nath B., Chen G., Bowtell L. et al., (2023), Assessment of densified fuel quality parameters: A case study for wheat straw Pellet, *Journal of Bioresources and Bioproducts*, vol.8(1), pp.45–58;

[15] Patel D., Parekh F., (2014), Flood Forecasting using Adaptive Neuro-Fuzzy Inference System (ANFIS), *International Journal of Engineering Trends and Technology*, vol.12(10), pp.510-514;

[16] Precup R.E., Hellendoorn H., (2011), A survey on industrial applications of fuzzy Control. *Computers in Industry,* vol. 62(3), pp. 213-226;

[17] Stolarski M.J., Szczukowski S., Tworkowski J. et al. (2013), Comparison of quality and production cost of briquettes made from agricultural and forest origin Biomass, *Renewable Energy*, vol.57, pp.20-26;

[18] Saha K., Hossain M., Ali M. et al., (2016), Feasibility study of coconut coir dust briquette, *Journal of the Bangladesh Agricultural University*, vol.12(2), pp.369-376;

[19] Shang C., Sinka I.C., Pan J., (2011), Constitutive Model Calibration for Powder Compaction Using Instrumented Die Testing, *Experimental Mechanics*, vol.52(7), pp.903-916;

[20] Takagi T., Sugeno M., (1983), Derivation of Fuzzy Control Rules from Human Operator's Control Actions, *IFAC Proceedings Volumes*, vol. 16(13), pp. 55–60;

[21] Walia N., Singh H., Sharma A., (2015), ANFIS: Adaptive Neuro-Fuzzy Inference System- A Survey, *International Journal of Computer Applications*, vol.123(13), pp. 32-38;

[22] Xun G., XueWei B., HaiBo H. et al., (2021), Dem parameters calibration of mixed biomass sawdust model with multi-response indicators, *INMATEH Agricultural Engineering*, pp.183-192;
[23] Yilmaz H., Çanakci M., Topakcı M. et al., (2021), The effect of raw material moisture and particle size on Agri-pellet production parameters and physical properties: A case study for greenhouse melon Residues, *Biomass and Bioenergy*, vol.150, pp.106125;

DESIGN AND RESEARCH OF COMPOUND DUST COLLECTION AND STERILIZATION DEVICE WITH PHASE-CONTROLLED BUNDLED CONDUCTOR FOR LIVESTOCK AND POULTRY HOUSING SPACE

/

畜禽舍空间相控分裂导线复合除尘杀菌装置设计研究

Jing TIAN[1)], Jiayuan SHAO[1)], Xinyue SONG[2)], Ying WANG[1)], Tingting YANG [2)], Lili NIE [2)], Zhenyu LIU*[1)]

[1)] College of Agricultural Engineering, Shanxi Agricultural University, Taigu / China;

[2)] College of Information Science and Engineering, Shanxi Agricultural University, Taigu / China

Tel: +86-13593101646; E-mail: lzysyb@126.com

DOI: https://doi.org/10.35633/inmateh-70-19

Keywords: *livestock and poultry houses, phase control, bundled conductor, space electric field, COMSOL simulation*

ABSTRACT

Livestock-scale breeding is the inevitable trend of future livestock and poultry husbandry. Closed breeding requires an excellent environment and livestock and poultry housings contain a lot of dust, pathogenic microorganisms and harmful gases, affecting the health of livestock and poultry and breeding personnel. Most of the common sterilization and dust collection devices for livestock and poultry housings on the market are too high energy consumption, and easy to cause secondary pollution. Therefore, an environmental purification device was designed to absorb dust in the air and kill harmful bacteria by using high-voltage pulsed electric field. The device was designed using phase control principle and bundled conductor. COMSOL Multiphysics was used to simulate the layout of single conductor, twin bundled conductor and quad bundled conductor. It was found that when the conductor was designed as twin bundled conductor or quad bundled conductor, the gradient distribution of spatial electric field intensity was more uniform and the downward trend of the electric field was slower, which could effectively improve the dust collection and sterilization efficiency of the device. At the same time, a variety of electric field environments can be set up by using phase differences to meet different environmental requirements of livestock and poultry. The compound dust collection and sterilization device with phase-controlled bundled conductor for livestock and poultry housing space includes a high voltage pulse generator, bundled conductor, high voltage special timer, insulator and other parts, which can effectively reduce the dust content in the air, the concentration of pathogenic bacteria, harmful gases, etc. after assembly test and can also reduce the humidity in the livestock and poultry housings.

摘要

畜禽规模化养殖是未来畜牧养殖的必然趋势，封闭饲养需要优良的环境，畜禽舍内含有大量灰尘、病原微生物和有害气体，影响畜禽动物和养殖人员健康。市面常见畜禽舍杀菌除尘装置大多能耗过高，且容易造成二次污染，为此，设计一款利用高压脉冲电场吸附空气中灰尘，杀灭有害病菌的环境净化装置，该装置设计利用相位控制原理和分裂导线，由 COMSOL Multiphysics 软件模拟仿真单导线、二分裂导线、四分裂导线三种导线布设，发现导线设计为二分裂或四分裂时，空间电场强度梯度分布更均匀且电场下降趋势更缓慢，可有效提高装置除尘杀菌效率；同时利用相位差可设置多种电场环境，满足不同畜禽环境需求。空间相控分裂导线复合除尘杀菌装置包括高压脉冲发生器、分裂导线、高电压专用定时器、绝缘子等部件，组装后经测试可有效降低空气中灰尘含量、致病菌浓度、有害气体等，亦可降低畜禽舍内湿度。

INTRODUCTION

In recent years, the scale of China's poultry breeding industry has grown steadily year by year, and the overall output of poultry meat has shown an upward trend (*Zhang et al., 2021*), with the development of animal husbandry, large-scale livestock and poultry breeding is an inevitable trend of animal husbandry in the future (*Dai et al., 2021*). As of 2020, the large-scale rate of livestock and poultry breeding in China has reached 67.5% (*Wei et al., 2022*), the pattern of breeding entities has undergone profound changes, large-scale breeding has developed rapidly, the quality and safety of livestock and poultry products have remained at a high level, and major animal diseases have been effectively controlled.

The large-scale and intensive breeding mode puts forward higher requirements for the environmental quality of livestock and poultry houses (*Wang et al., 2018*). In the breeding process, livestock and poultry are often raised in a specific closed space, due to the activities of livestock and poultry, feed, manure, etc. will cause dust, harmful gases, pathogenic microorganisms and other environmental pollutants in the air. The environment in the house is also affected by temperature and humidity (*Huynh et al., 2005*), and in a humid environment, pathogenic microorganisms multiply rapidly, which can easily lead to the disease of livestock and poultry herds and affect the healthy growth of livestock and poultry.

For healthy breeding of livestock and poultry, strict disinfection can reduce the incidence of disease on farms by 80%. Doing a good job of disinfection can bring greater economic benefits to the safe production of farms. The commonly used disinfection methods of livestock and poultry housings at home and abroad mainly adopt physical disinfection and chemical disinfection. The air purification equipment of physical disinfection mainly includes mechanical ventilation equipment, spray dust collection equipment, wet dust collection equipment, ventilation filtration equipment, electric dust collector, ozone sterilization disinfector, ultraviolet lamp, etc. The above equipment can maintain the air quality of livestock and poultry housings to a certain extent, but there are problems such as poor comprehensive control ability, large energy consumption, large land area, and easy to cause secondary pollution, which will affect the health of livestock and poultry.

Based on the demand for environmental control of livestock and poultry housings, this paper proposes a new type of research and design program of space phase-controlled bundled conductor compound dust collection sterilization device for livestock and poultry housings. Using pulsed electric field technology (*Pataro et al., 2015; Bonetta et al., 2014; Sui et al., 2016*) and the phase control principle, a stable spatial electric field is formed in the space of livestock and poultry housing, and the bundled conductors are laid under the spatial electric field to improve the efficiency of sterilization and dust collection, which can not only guarantee the air quality in the housing but also take into account the function of dust collection and humidity reduction.

MATERIALS AND METHODS

Main components of the device

The design of the device is simple in structure, and the main components include a high-voltage pulse generator, bundled conductor, high-voltage special timer, insulators and so on. In the livestock and poultry housing, the output end of the high-voltage pulse generator, whose input end is connected to the mains through the timer, can be set to different phase voltage output. The bundled conductors described in this paper are twin bundled conductors or quad bundled conductors, and when the bundled conductor is connected to the output of the high-voltage pulse generator, it can output different phase DC electricity, and the phase difference can form different difference positions such as 60°, 90°, 180°, etc., which can provide a variety of electric field environments such as positive electric field, negative electric field, compound electric field, etc. The different types of spatial electric fields formed by using phase control to realize different conductor connections can be applied to a variety of environmental scenarios.

Technical Principles

Due to the uneven distribution of the electric field in the livestock and poultry housing, more and more free electrons and ions will be produced in the space (*Wang et al., 2020*). Affected by the electric field force, the ions will have directional movement and collide with dust particles in the air (*Liu et al., 2005*). The charged dust particles will have directional removal movement under the action of high voltage and high-frequency electric field force, while harmful gases such as carbon dioxide and ammonia will condense with dust particles in the house. Part of the charged dust particles migrate to the conductor and eventually deposit on the conductor, while the other part of the charged dust particles deposit on the wall, ground, livestock and poultry surface, equipment and facilities in the house, thus playing the purpose of dust collection. After the periodic action of the electric field, most of the pathogenic microorganisms attached to the dust particles are killed and the air quality in the house is improved. With the circulation of the dust collection and sterilization system, the electric field corona can prevent the outside dust particles from entering the livestock and poultry housing (*Wang et al., 2005*), blocking the transmission channel of the disease air. The high-voltage discharge releases ozone ions at the same time (*Gaëtan et al., 2022*), which can kill bacteria and viruses. The microorganisms in the house can be double eliminated, and the whole livestock and poultry housing environment is in a state of fewer bacteria and cleanliness, reducing the incidence of diseases in the respiratory system of livestock and poultry.

The spatial electric field formed in the livestock and poultry housing also has the function of reducing humidity (*Arif-Uz-Zaman et al., 1996; Zhang et al., 2017*). Its principle is to use the internal interaction between the ion beam and water molecules in the air and the external blowing effect. In this process, the random motion of water molecules becomes a directional movement along the direction of the increase in the intensity of the electric field under the action of electric field forces. Water vapor turns into liquid water (*Xie et al., 2003*) under the action of electric field forces and is attached to the surface of the internal structure of the livestock and poultry housing, such as the wall and the ground, and then the air humidity decreases.

Simulation design of phase-controlled bundled conductor

Simulation design process

COMSOL Multiphysics achieves the simulation of real physical phenomena by solving partial differential equations (single field) or partial differential equations (multi-field) based on the Finite Element Method (FEM), which is widely applied in high voltage electric field simulation (*Zhao et al., 2022; Yu Z., 2022; Pataro et al., 2015*). The COMSOL simulation steps of the compound dust collection and sterilization device with phase-controlled bundled conductor for livestock and poultry housing space include module selection, model housing, boundary constraint adding, grid construction, setting research and solution, data post-processing, etc.

The geometric model network division of livestock and poultry housing space is shown in Figure 1. The calculation results were visualized, and the electric potential distribution on the space section plane of the livestock and poultry housing was obtained as shown in Figure 2. The spatial electric field intensity was larger near the bundled conductor, and the further away from the conductor, the smaller the electric field intensity.

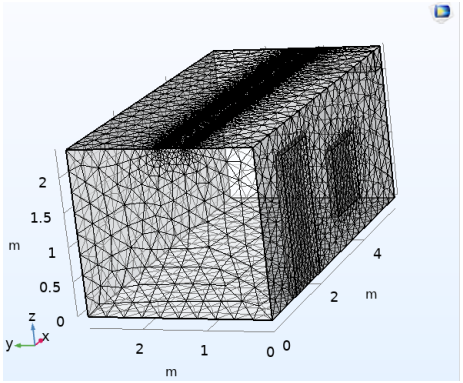

Fig. 1 - The geometric model network division of the livestock and poultry housing

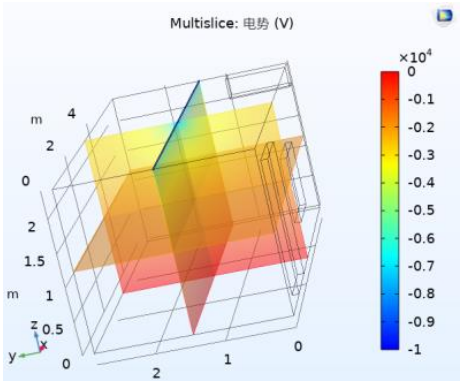

Fig. 2 - The electric potential distribution on the space section plane of the livestock and poultry housing

Simulation study of conductor distribution mode

In order to suppress corona discharge and reduce line reactance, UHV transmission lines usually adopt bundled conductor erection. That is, each phase conductor is composed of several small diameter intraphase conductors, which are spaced a certain distance apart and arranged in a symmetrical polygon. The number of bundled conductors of the UHV transmission line is generally 3 ~ 4. Based on the principle of UHV bundled conductor, the conductors of the compound dust collection and sterilization device with phase-controlled bundled conductor for livestock and poultry housing space are set as twin bundled conductors or quad bundled conductors. The spacing of adjacent conductors is 30 cm-50 cm, and it is connected to the output end of the high-voltage pulse generator. The bundled conductors are introduced by using phase control, which can increase the intensity of the electric field around the livestock and poultry housing, thus improving the sterilization and dust collection efficiency of the device.

In order to study the electric field distribution after the device was connected with bundled conductors, this paper used Comsol Multiphysics software for simulation. The spatial electric field intensity is set to -10kV, and the conductor distributions of electric field are set to three different connection modes, including single conductor, twin bundled conductor, and quad bundled conductor. Figure 3 and Figure 4 respectively show the electric field distribution under the three modes of conductor connection in the space of livestock and poultry housings. Under the same electric field intensity and the same section, the electric field gradient distribution and electric field intensity of the quad bundled conductor is better than that of the twin bundled conductor, and the electric field characteristics of the twin bundled conductor are better than that of the single conductor.

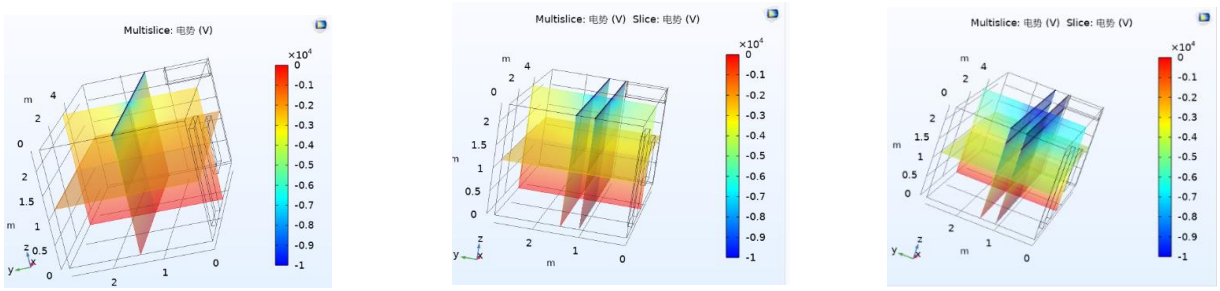

(a)Single conductor - 10kV (b) Twin bundled conductor - 10kV (c) Quad bundled conductor- 10kV

Fig. 3 -10kV space electric field sectional potential distribution

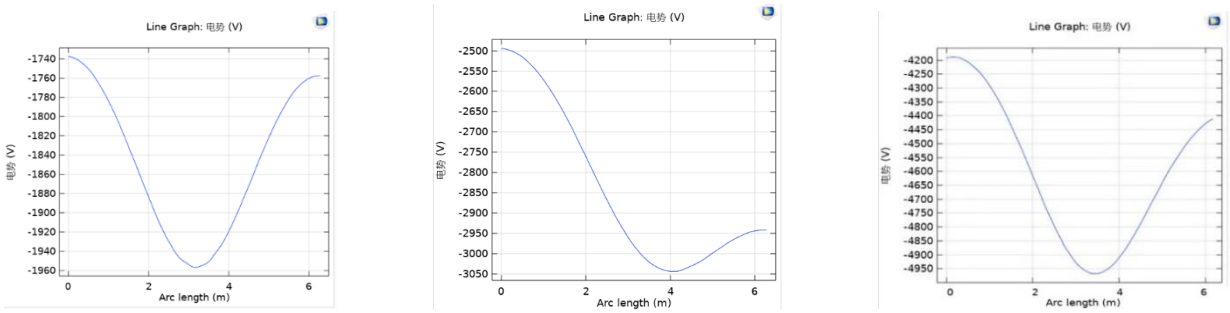

(a) Single conductor - 10kV parallel section potential line diagram (b)Twin Bundled Conductor - 10kV parallel section potential line diagram (c)Quad Bundled Conductor- 10kV parallel section potential line diagram

Fig. 4 - 10kV space electric field parallel section potential line diagram

Simulation study of high voltage positive electric field, negative electric field, compound electric field

The high-voltage pulse generator used in the design and research device has adjustable output voltage (0-70kV), pulse width (0-49μs), frequency (0-990Hz), duty ratio and phase of the output end. The parameters that affect the processing effect of high voltage pulsed electric field are mainly divided into two categories: processing working parameters and microorganisms' own characteristics parameters (*Uchida et al., 2008; S.Monfort et al., 2010; Somolinos et al., 2009).* The processing working parameters include electric field intensity, processing time, pulse waveform, pulse width and processing time, etc.

Comsol Multiphysics software was used to simulate the electric field distribution under high voltage pulse positive electric field, negative electric field and compound electric field, and to investigate the sterilization effect of the device under different electric fields. The output voltage of the compound dust collection and sterilization device with phase-controlled bundled conductor for livestock and poultry housing space was set to 35 kV, and in the simulation test, the voltage on the high voltage conductor was set as positive 35 kV, negative 35 kV and compound 35 kV.

Treatment of Escherichia coli by high voltage pulsed electric field

Escherichia coli is a common pathogenic bacterium in livestock and poultry housings, and its killing degree directly determines whether a sterilization method can meet the requirements of industrial production. Therefore, the effective sterilization method of Escherichia coli has always been the focus of research, and the high-voltage pulsed electric field has been proven to play a certain sterilization effect *(Matra et al., 2020; Tanino et al., 2020).* Therefore, in this paper, in the process of using high voltage pulsed electric field to kill Escherichia coli, factors such as electric field intensity and processing time in the sterilization process were analyzed to verify the sterilization effect of the designed spatial electric field on Escherichia coli in livestock and poultry housings.

The Escherichia coli used in the experiment was provided by the College of Life Sciences of Shanxi Agricultural University. The bacterial suspension of the experimental group was placed in a set electric field for treatment, and the results were counted and recorded by plate counting method, and the average value was taken.

RESULTS

Numerical simulation analysis

Comsol Multiphysics software was used to establish the simplified geometric model of the livestock and poultry housing, and the conductor distribution was set as quad bundled conductors with a distance of 40 cm. Firstly, a positive 35 kV pulse voltage was applied to the space of the livestock and poultry housing, the electric field distribution is shown in Figure 5 (a), and the electric field shows a gradient downward trend from the conductor end to the ground end. The electric field intensity near the conductor reaches 3×10^4 V. Figure 5 (b) shows the electro-potential diagram of the section parallel to the conductor. It can be seen from the diagram that the distribution of the spatial electric field is uneven and changes with the radius within the effective processing area, and the electric field intensity meets the sterilization requirements.

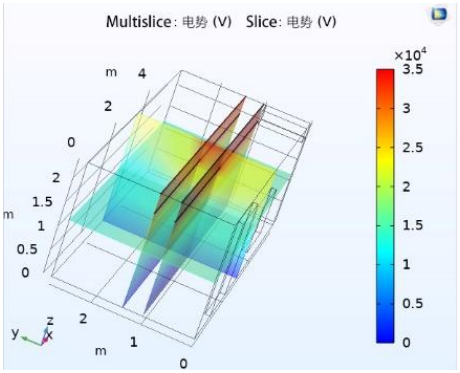

Fig. 5(a)- Quad bundled conductors 35kV positive electric field potential distribution

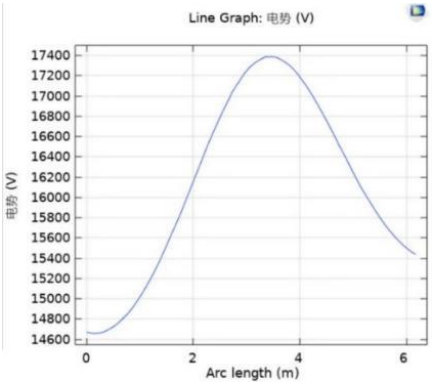

Fig. 5(b)- Quad bundled conductors 35kV positive electric field parallel section potential line diagram

A negative 35 kV pulse voltage is applied to the space of the livestock and poultry housing in the simulation, and its electric field distribution is shown in Figure 6 (a). The electric field shows a gradient downward trend from the conductor end to the ground end, and the electric field intensity near the conductor reaches -3× 10^4V. Figure 6 (b) shows the electro-potential diagram of the section parallel to the conductor. It can be seen from the diagram that the distribution of the spatial electric field is uneven and changes with the radius within the effective processing area, and the intensity of the electric field meets the sterilization requirements.

In the simulation, a compound pulse voltage of 35 kV is applied to the space of livestock and poultry housing, and its electric field distribution is shown in Figure 7 (a). The electric field presents a gradient downward trend from the conductor end to the ground end. The upper conductor is set to positive 35 kV, and the lower conductor is set to negative 35 kV, which corresponds to the phase difference of 180° between the bundled conductors of the physical device, forming a positive and negative compound electric field. Figure 7 (b) shows the electro-potential diagram of the section parallel to the conductor. It can be seen from the diagram that the distribution of spatial electric field intensity is uneven, and compared with electro-potential diagram in Figure 5, and Figure 6, the electric field intensity shown in figure 7 is relatively weaker, but its overall electric field intensity still meets the sterilization requirements.

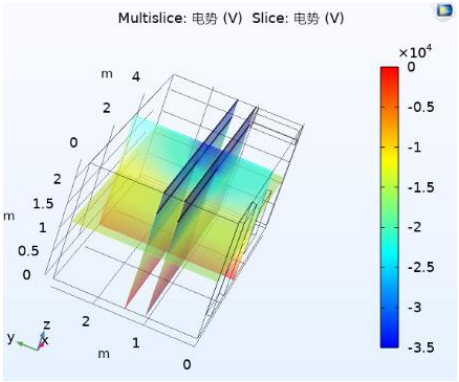

Fig. 6(a)- Quad bundled conductors 35kV negative electric field potential distribution

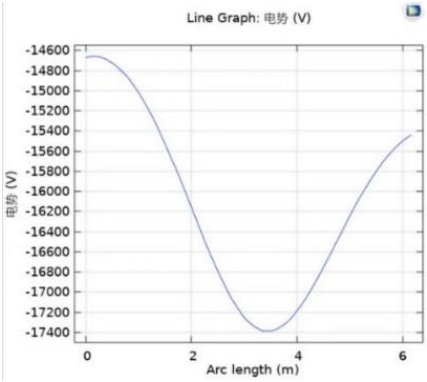

Fig.6(b)- Quad bundled conductors 35kV negative electric field parallel section potential line diagram

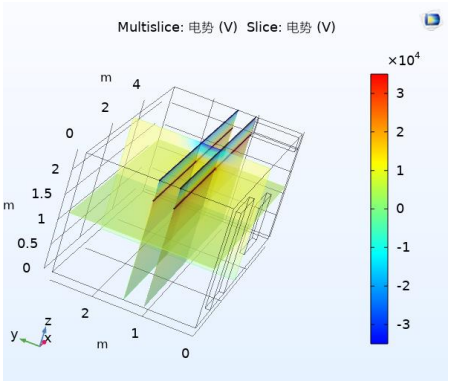

Fig. 7(a)- Quad bundled conductors 35kV composite electric field potential distribution

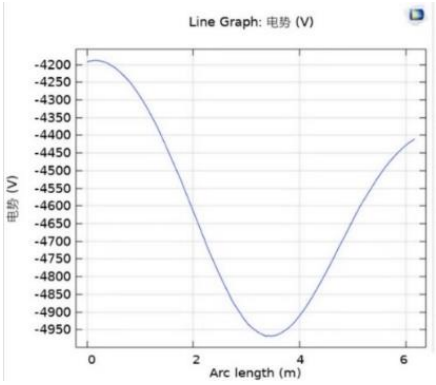

Fig.7(b)- Quad bundled conductors 35kV composite electric field parallel section potential line diagram

The simulation results show that the compound dust collection and sterilization device with phase-controlled bundled conductor for livestock and poultry housing space can meet different scenarios, the conductor connection is set to a twin bundled conductor or quad bundled conductor, the electric field gradient distribution and electric field intensity are optimized, and the sterilization, dust collection and dehumidification efficiency of the device is improved. The high-voltage pulse generator can provide a variety of electric fields at the same time, including positive electric field, negative electric field and compound electric field, and its electric field intensity can meet the sterilization requirements. When the device is activated, different wiring modes are selected according to the air quality in the house. When the concentration of dust particles in the house is high, the phase difference between the bundled conductors of the device can be set to 180°, and the electric field between positive and negative phases can be established with the ground connection point, and the positive and negative charges will be released respectively. Dust particles in the air are respectively charged with positive and negative charges at different levels and after charging, the chances of collision of dust particles increase due to the attraction effect of positive and negative charges and the coagulation effect is enhanced. Under the action of high voltage and high-frequency periodic vibration electric field, dust can be more quickly attached to the conductor or the wall, ground of livestock and poultry housing and the surface of equipment and facilities, and the dust collection efficiency is improved and the air cleaning rate is enhanced.

Analysis of Escherichia coli test results

Relationship between lethality of Escherichia coli and electric field intensity

The test groups were placed under the set positive and negative high voltage pulsed electric field, the test temperature was 20℃, the processing time was 1 h, different electric field voltages of 2 kV, 5 kV and 10 kV were adopted, and the conditions of frequency and duty ratio were set the same. The Escherichia coli bacterial solution was treated, and the origin software was used for analysis. The effects of different voltages on the lethality rate of Escherichia coli are shown in Figure 8. As can be seen from Figure 8, positive and negative high voltage pulsed electric fields have obvious lethal effects on Escherichia coli, and the lethality rate of Escherichia coli increases with the increase of voltage. Under the voltage of 10 kV, the average lethality rates of positive and negative high voltage pulsed electric field against Escherichia coli reach the highest, which are 20.80% and 25.92% respectively. When the voltage is 2 kV, the average lethality rates of positive and negative high voltage pulsed electric field against Escherichia coli are 3.73% and 5.38% respectively. The lethal effect of electric field on Escherichia coli is not obvious. When the voltage is 5 kV, the average lethality rates of positive and negative high voltage pulsed electric field against Escherichia coli are 11.12% and 14.26% respectively, and the lethal effect of the electric field against Escherichia coli is enhanced.

Table 1

Lethality rate of E. coli treated with high-voltage pulsed electric field under different voltage conditions/%

	Voltage /KV	Fatality rate 1	Fatality rate 2	Fatality rate 3	Average fatality rate	Standard deviation
Positive high voltage pulsed electric field	2	3.96	3.78	3.45	3.73	0.258650343
	5	11.53	11.42	10.42	11.12	0.611582646
	10	21.48	20.14	20.79	20.80	0.670099495
Negative high voltage pulsed electric field	2	4.94	5.88	5.33	5.38	0.47226405
	5	14.12	14.62	14.05	14.26	0.313734003
	10	26.78	25.28	25.71	25.92	0.772420438

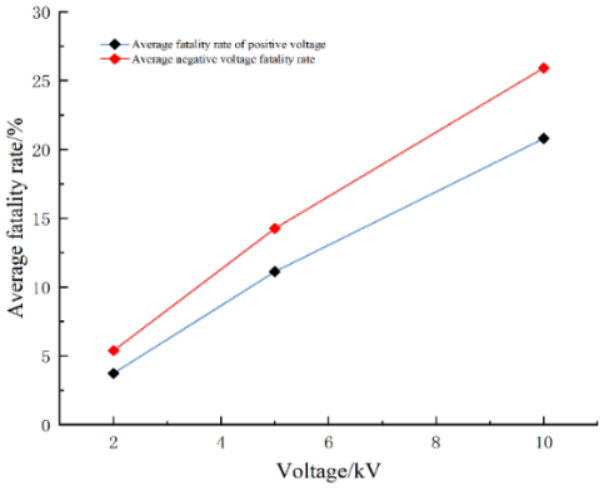

Fig. 8 - Relationship between voltage and average lethality of E. coli

As can be seen from Table 1, with the increase of positive and negative high voltage pulsed electric field voltage, the average lethality rate of Escherichia coli increases, and the standard deviation is all less than 10%, indicating that the test data are stable and the average lethality rate is reliable.

Analyzing the above data results, the intensity of the high voltage pulsed electric field has different effects on the lethality rate of Escherichia coli. When the electric field intensity is low, the lethality rate of Escherichia coli is low, and with the increase of positive and negative electric field intensity, the lethality rate of Escherichia coli increases, and the effect of negative high voltage pulsed electric field on the lethality rate of Escherichia coli is better than that of positive high voltage pulsed electric field.

Relationship between lethality rate of Escherichia coli and processing time

The test groups were placed under the set positive and negative high voltage pulsed electric fields, the test temperature was 20℃, the processing time was 1h, 2h, 3h and 4h, respectively, with different electric field voltages of 2 kV, 5 kV and 10 kV were adopted, and the conditions of frequency and duty ratio were set the same. The Escherichia coli bacterial solution was treated, and the origin software was used for analysis. The effects of different times and voltage on the lethality rate of Escherichia coli are shown in Figure 9 and 10. It can be seen from Figure 9 and Figure 10 that both positive and negative high voltage pulsed electric fields have significant lethal effects on Escherichia coli. As the time of electric field processing increases, the lethality rate of Escherichia coli increases. When the voltage is 2 kV and the processing time is 4 h, the average lethality rates of positive and negative high voltage pulsed electric field against Escherichia coli reach the maximum, which is 40.41% and 42.71% respectively. When the voltage is 5 kV and the processing time is 4 h, the average lethality rates of positive and negative high voltage pulsed electric field against Escherichia coli reach the maximum, which is 54.50% and 58.14% respectively. When the voltage is 10 kV and the processing time is 4 h, the average lethality rate of positive and negative high voltage pulsed electric fields against Escherichia coli reach the maximum, which are 62.36% and 72.14%, respectively.

Table 2

Lethality rate of E. coli treated with high-voltage pulsed electric field under different time and voltage conditions/%

	Time/ h	2 kV Average fatality rate	2 kV Standard deviation	5kV Average fatality rate	5kV Standard deviation	10kV Average fatality rate	10kV Standard deviation
Positive high voltage pulsed electric field	1	9.32	0.7254	16.30	0.4007	27.51	0.4005
	2	20.56	0.7060	28.45	0.8429	37.63	0.5278
	3	29.33	0.4703	44.50	0.4313	57.49	0.4229
	4	40.41	0.8082	54.50	0.4195	62.36	0.5314
Negative high voltage pulsed electric field	1	10.41	0.8549	19.34	0.6635	29.58	0.4541
	2	19.12	1.3807	30.14	0.4767	40.02	2.6006
	3	32.76	0.9404	47.09	0.9660	59.12	1.2971
	4	42.71	0.1323	58.14	0.9061	72.14	1.6783

As can be seen from Table 2, the average lethality rate of Escherichia coli increases with the increase of processing time under the positive and negative high voltage pulsed electric field voltage of 2 kV, 5 kV and 10 kV, and the standard deviation is all less than 2.7, indicating that the test data are stable and the average lethality rate is reliable.

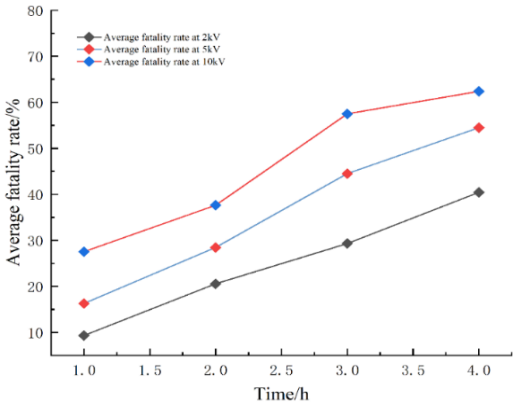

Fig. 9- Relationship between positive high-voltage pulsed electric field time and average lethality of E. coli

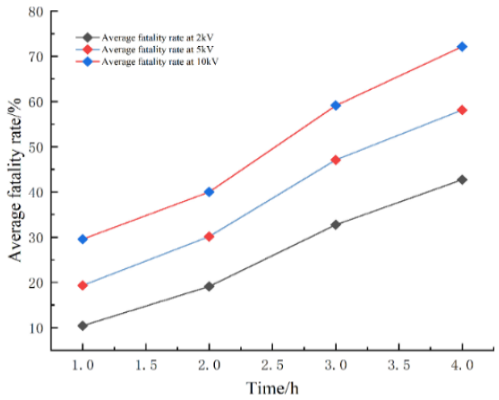

Fig. 10- Relationship between negative high-voltage pulsed electric field time and average lethality of E. coli

Based on the above data results, it is indicated that the processing time of positive and negative high - voltage pulsed electric fields have a very significant influence on Escherichia coli. Escherichia coli has a certain survival rate under the condition of short processing time. Although Escherichia coli can be inactivated after a long processing time, the highly active Escherichia coli can still continue to grow and develop. With the increase of positive and negative high voltage pulsed electric field processing time, the lethality rate of Escherichia coli becomes higher and higher.

The space electric field provided by the device can effectively kill Escherichia coli. The electric field distribution and intensity of the device can meet the actual needs by setting.

CONCLUSIONS

This study focuses on exploring the effect of different electric conductor wiring modes on sterilization and dust collection effect in the electric field of livestock and poultry housing space. It mainly analyzes the electric field distribution of single conductor, twin bundled conductor and quad bundled conductor, and verifies the sterilization effect against Escherichia coli when the electric field intensity is set to 2 kV/cm, 5 kV/cm and 10 kV/cm. From the Comsol simulation results, it can be seen that the electric field gradient distribution and electric field intensity of the quad bundled conductors are better than the twin bundled conductors, and the twin bundled conductors are better than the single conductors. The spatial electric field can be set into a variety of electric field forms, including positive electric field, negative electric field, compound electric field, etc. by the phase regulation of the high voltage pulse generator and the change of the wiring mode of the bundled conductor. The device is designed to be applied to different livestock environmental conditions and meet the daily sterilization and dust collection and dehumidification requirements of livestock and poultry housings. Through this investigation, the wiring mode of the electric conductor of sterilization and dust collection device for the livestock and poultry housing space was optimized and the efficiency of sterilization, dust collection and dehumidification and the stability of the device were enhanced by using the phase control and bundled conductor concept.

ACKNOWLEDGEMENT

This study was supported by Shanxi Key Research and Development Program, Genetic Improvement, Germplasm Innovation and Demonstration of Jinfen White Pig, (No. 202102140601005).

REFERENCES

[1] Arif-Uz-Zaman, M., Rezwan K. M., (1996). A novel dehumidification technique using electric field. *IEEE Transactions on Industry Applications*, Vol. 32, pp. 36-40, USA.

[2] Bonetta, S., Bonetta, S., Bellero, M., Pizzichemi, M., & Carraro, E., (2014). Inactivation of Escherichia coli and Staphylococcus aureus by pulsed electric fields increases with higher bacterial population and with agitation of liquid medium. *Journal of food protection*, Vol. 77, pp. 1219-1223, Italy.

[3] Denoya, G. I., Vaudagna, S. R., Polenta, G., (2015). Effect of high pressure processing and vacuum packaging on the preservation of fresh-cut peaches. *LWT - Food Science and Technology*, Vol. 62, pp. 801-806, Buenos Aires/Argentina.

[4] Dai, Q., (2021). Pollution control strategy of livestock and poultry large-scale breeding based on eco logical circular economy theory (基于生态循环经济理论的畜禽规模化养殖污染治理策略). *Rural science and technology*, Vol. *12,* pp. 112-113, Liaoning/China.

[5] Gaëtan. W., Valentin. F., (2022). Experimental mapping of the ozone distribution in a pulsed positive corona discharge to estimate the efficiency of ozone production. *Physica Scripta*, Vol. 97, France.

[6] Huynh, T. T. T., Aarnink, A. J. A., Verstegen, M. W. A., Gerrits, W. J. J., Heetkamp, M. J. W., & Kemp, B., et al. (2005). Effects of increasing temperatures on physiological changes in pigs at different relative humidities1. *Journal of Animal Science*, Vol. 83, pp. 1385-1396, Vietnam.

[7] Liu, B., Qian, H., Ma, Z., (2005). Air safety design and application of environmentally safe poultry house (环境安全型禽舍的空气安全设计及其应用). *Chinese poultry*, Vol. 24, pp. 35-39, Dalian/China.

[8] Matra, K., Buppan, P., Techaumnat, B., (2020). Analytical and Experimental Studies on the Application of a Series of Treatment Chambers for Escherichia coli Inactivation by Pulsed Electric Fields. *Applied Sciences*, Vol. 10, Thailand.

[9] Monfort, S., Gayán, E., Saldaña. G., Puértolas, E., Condón, S., & Raso, J., et al. (2010). Inactivation of salmonella typhimurium and staphylococcus aureus by pulsed electric fields in liquid whole egg. *Innovative Food Science & Emerging Technologies*, Vol. 11, pp. 306-313, Spain.

[10] Pataro, G., Barca, M. G., Donsì, G., & Ferrari, G., (2015). On the modeling of electrochemical phenomena at the electrode-solution interface in a PEF treatment chamber: methodological approach to describe the phenomenon of metal release. *Journal of Food Engineering*, Vol. 165, pp. 34-44, Italy.

[11] Somolinos, M., García, D., Mañas. P., and, et al. (2009). Organic acids make Escherichia coli more resistant to pulsed electric fields at acid pH. *International Journal of Food Microbiology,* Vol. 136, pp. 381-384, Zaragoza/Spain.

[12] Sui. J., (2016). Application of space electric field technology in livestock and poultry house (空间电场技术在畜禽舍中的应用). *Chinese journal of animal husbandry and veterinary medicine,* Vol. 4, pp.38-39, Liaoning/China.

[13] Tanino, T., Hirosawa, M., Moteki, R., et al. (2020). Engineering of pulsed electric field treatment using carbon materials as electrode and application to pasteurization of sake. *Journal of Electrostatics*, Vol. 104, Japan.

[14] Uchida. S., Houjo. M., Tochikubo, F., (2008). Efficient sterilization of bacteria by pulse electric field in micro-gap. *Journal of Electrostatics*, Vol. 66, pp. 427-431, Japan.

[15] Wei, H., Cui, K., (2022). Agricultural Powerhouse's Connotation Characteristics, Construction Foundation and Promotion Strategies (农业强国的内涵特征、建设基础与推进策略). *Reform*, Vol. 12, pp. 1-11, Beijing/China.

[16] Wang, D., Huang, H., Zhang, H., Liu, J., Dong, X., (2018). Analysis of Research Status and Development on Engineering Technology of Swine Farming Facilities (生猪养殖设施工程技术研究现状与发展分析). *Transactions of the Chinese Society for Agricultural Machinery*, Vol.11, pp.1-14, Heilongjiang/China.

[17] Wang. L., (2020). *Study on removal of fine particulate matter by electrostatic precipitator*(静电除尘器对细颗粒物脱除的研究). Nanchang University, China.

[18] Wang. K., Wu. J., Mei. W., et al. (2020). Research status on particulate reduction technology in livestock houses (畜舍颗粒物减排技术研究现状). *Transactions of the Chinese Society of Agricultural Engineering (Transactions of the CSAE),* Vol. 36, pp. 204-212, Zhejiang/China.

[19] Xie. L., Sun. Q., (2003). Analysis and research on application mechanism of high voltage electric field in dehumidification, deodorization and disinfection of greenhouse and livestock and poultry house (高压电场在温室和畜禽舍中除湿、除臭、消毒应用机理的分析与研究). *Agricultural Equipment &Technology* , Vol. 29, pp. 23-25, Neimenggu/China.

[20] Yu. Z., (2022). Electric field and temperature analysis of high-voltage XLPE cable insulation bubbles based on COMSOL simulation. *International Journal of New Developments in Engineering and Society*, Vol. 6, pp. 50-55, China.

[21] Zhang, H., Wen, C., Li, H., (2021). Development of world pig industry in 2020 and its market trends in 2021. *Swine industry science*, Vol. 38, pp. 34-38, Guangdong/China.

[22] Zhang. Y., Ma. J., (2017). Analysis of dehumidification effect of space electric field on sheep shed after electrolysis water spray disinfection (空间电场对电解水喷雾消毒后的羊舍除湿效果分析). *Heilongjiang Animal Husbandry and Veterinary*, Vol. 20, pp. 147-150, Xinjiang/China.

[23] Zhao. Y., Liu. C., Zhou. D., (2022). Estimation of submarine underwater corrosion electric field based on equivalent circuit and point current source (基于等效电路和点电流源的潜艇水下腐蚀电场估算). *Journal of National University of Defense Technology*, Vol. 44, pp. 176-830, China.

STUDY ON BIODEGRADABLE MATERIALS FROM THERMOPLASTIC STARCH WITH THE ADDITION OF NUTS SHELL
/
BADANIE MATERIAŁÓW BIODEGRADOWALNYCH ZE SKROBI TERMOPLASTYCZNEJ Z DODATKIEM ŁUPIN ORZECHÓW

Tomasz ŻELAZIŃSKI[1)], Adam EKIELSKI[1)], Karol DURCZAK[2)], Magdalena MORAWSKA[3)]
[1)] Institute of Mechanical Engineering, Warsaw University of Life Sciences (SGGW) / Poland;
[2)] Faculty of Environmental and Mechanical Engineering, Poznan University of Life Sciences / Poland;
[3)] Faculty of Manufacturing Engineering, Warsaw University of Life Sciences / Poland
Tel 225934565; E-mail: tomasz_zelazinski@sggw.edu.pl (corresponding author).

DOI: https://doi.org/10.35633/inmateh-70-20

Keywords: *nut shells, biocomposite, thermoplastic starch TPS, mechanical properties, water absorption*

ABSTRACT
The paper presents the results of research on film biocomposites made of thermoplastic starch (TPS) and various types of nut shells. The research involved the use of thermally treated nut shells: hazelnuts, pistachios, walnuts and peanuts. TPS biocomposites were produced by the pour method using non-adherent moulds. The obtained samples were used to test the basic physical properties used in testing biodegradable materials. The following parameters were determined: mechanical strength, colour and colour difference, water contact angle, moisture absorption from water and atmospheric air. Images of biocomposite fractures were also taken using a scanning electron microscope (SEM). It was found that the addition of nut shells enabled the production of homogeneous materials and contributed to the improvement of their strength parameters. The research showed that nut shells can be a prospective raw material for the production of innovative biodegradable materials.

ABSTRACT
W pracy przedstawiono wyniki badań bikompozytów otrzymanych ze skrobi termoplastycznej (TPS) oraz różnego rodzaju łupin orzechów. Do badań wykorzystano poddane obróbce termicznej łupiny orzechów: laskowych, pistacji, włoskich i ziemnych. Biokompozyty TPS wytworzono metodą wylewową z wykorzystaniem form teflonowych. Uzyskane próbki posłużyły do zbadania podstawowych właściwości fizycznych stosowanych badaniach materiałów biodegradowalnych. Określono następujące parametry: wytrzymałość materiałów, barwę, różnicę barw, kąt zwilżania, absorpcję wilgoci z wody i powietrza atmosferycznego. Wykonano również zdjęcia pęknięć biokompozytów za pomocą skaningowego mikroskopu elektronowego (SEM). Stwierdzono, że dodatek łupin orzechów umożliwił uzyskanie materiałów jednorodnych i przyczynił się do poprawy ich parametrów wytrzymałościowych. Badania wykazały, że łupiny orzechów mogą być perspektywicznym surowcem do produkcji innowacyjnych materiałów biodegradowalnych.

INTRODUCTION

Pro-ecological activities observed in the global economy force the search for new solutions limiting the use of plastics in the agri-food industry *(Mangaraj et al., 2019).* At the same time, the constantly growing consumption causes an increasing demand for new and innovative products, including biodegradable materials *(Borowski et al., 2022).* Therefore, current biodegradable products cover a wider range of applications than just plates, drinking straws or other small everyday items. Scientists are increasingly trying to obtain structural biocomposites that could be used in various branches of the agri-food industry. Currently, these trends are widely promoted around the world, which opens up the possibility of implementing innovative biodegradable products on a global scale. There is also an effort to minimize energy consumption, which biocomposites perfectly fit in *(Borowski, 2021).* Therefore, the use of raw materials of completely natural origin and in accordance with the principles of sustainable development and the idea of "zero waste" is an important criterion for the production of modern biocomposites *(Nenciu et al., 2022a).* These raw materials include various by-products from technological processes related to agri-food processing. These can be, for example: fruit pomace, brewer's spent grains, pomace after oil extraction, waste from sugar cane processing and residues from processing nuts *(Ungureanu et al., 2022).* Some of such raw materials are also waste resulting from fruit and vegetables not sold in supermarkets *(Nenciu et al., 2022b).*

These raw materials are usually rich in many natural ingredients that strengthen the structure of biocomposites (e.g. lignocellulosic fibres, pectins, starch, proteins, etc.). The rational use of such raw materials for the production of biocomposites is therefore fully justified and prospective *(Rodriguez et al., 2020).*

Therefore, the essence of modern biocomposite production is to find the right ingredients from which innovative biomaterials can be easily produced. In general, some researchers argue that unsatisfactory physical and mechanical properties are one of the main limitations in the production of biodegradable materials *(Nanthananon et al., 2018).* Therefore, the solution seems to be the search for new components that will improve the properties of such materials as thermoplastic starch biocomposites (TPS). Such raw materials include waste from the processing of nuts. This waste is the shell after the edible part has been dehusked and consists mainly of lignocellulose.

According to some research, walnut shells contain 27.4-52.3% lignin, 25.6-34.5% cellulose and 22.1% hemicellulose *(Queirós et al., 2020)*. In the case of peanut shells, the percentage of these components is: lignin 35.4%; cellulose 26.7 - 40.5%; hemicellulose 12.1%. The composition of hazelnuts was as follows: lignin 27.2 - 40.3%; cellulose 26.7 - 40.5%, hemicellulose 30.4%.

The composition of pistachio shells according to *Kasiri and Fathi, (2018)* is lignin 23.6%, cellulose 38.1%, and hemicellulose 31.4%. An important feature of nut shells is low moisture content, which allows easy storage of shells without drying. This facilitates their use at very low costs. In addition, depending on the variety, the share of shells is from 10 to 70% of the total weight of the nut. Thus, the processing of nuts in industrial conditions leaves significant amounts of this raw material.

More than 3.7 million tons of walnuts are produced annually in the world. The largest producers are China 1.6 million tons, USA 0.6 million tons, Iran 0.4 million tons. In Poland, the production of walnut is about 0.1 million tons. Hazelnuts also account for a significant part of the production of nuts. In general, about 75% of the production of these nuts is produced in Turkey and Italy. The hazelnut shell makes up about 30% of the total weight of the nut. Another widely produced nut is the pistachio, which is produced around 0.6 million tonnes per year. Nearly 81% of total production is in Iran, USA and Iran. Pistachio shells account for over 30% of the dry weight of almond fruit. This means that the residues from nut processing may have great potential for their wider use. In general, the research conducted so far concerned the chemical properties of nut shells, including pistachio shells *(Yang et al., 2006).*

Research was also conducted on the use of almond peels as antioxidants (Mandalari et al., 2013). Nut shells have also been used as fillers for biocomposites for home applications *(Shaik et al., 2022*). Studies have also been conducted on the use of walnut shells as an additive to PLA polylactic acid *(Chaturvedi et al., 2021; Orue et al., 2020).*

Taking into account the above, no research has been carried out on their use in biocomposites made of TPS thermoplastic starch. The aim of this research is to produce a biocomposite from thermoplastic starch with the addition of various types of nut shells and to study their physical properties.

MATERIALS AND METHODS

Material

The following ingredients were used for the production of thermoplastic biocomposites: potato starch (PPZ Trzemeszno, Trzemeszno, Poland), purified vegetable glycerin (ERPOL, Warsaw, Poland) and nut shells: hazelnut, pistachio, walnut and peanut. Nut shells were obtained from purchased nuts on the local market in Poland. The obtained shells were ground into flour using an MKM 6000 impact mill (manufacturer: BOSCH, Gerlingen, Germany). Then the raw material was sieved on a sieve with a mesh size of 0.25 mm using a LPzE-2e screen (manufacturer: MULTISERW-Morek, Brzeźnica, Poland). Before adding the raw material for testing, it was thermally treated in a water bath for 60 s at 100 °C, and then drained on a sieve.

Production of biocomposite

The preparation of the test sample consisted in mixing 50 g of potato starch, 25 g of vegetable glycerin and the addition of nut shells in 500 ml of distilled water. Each time 2 wt% and 5 wt% of ground nut shells were added to the thermoplastic starch. The prepared suspension was placed on the heater and mixed with a CAT-30 stirrer (rotational speed of the stirrer 300 rpm) until the temperature of 85°C was reached. Then the obtained suspension was poured into di-Teflon moulds.

The sample prepared in this way was dried for 24 h at 45°C in a convection dryer Physical and chemical tests of the obtained materials included the determination of the basic parameters of the materials, such as: strength parameters, water contact angle, colour and colour difference, moisture absorption from water and air. The fractures of the samples were analysed using a scanning electron microscope (SEM).

Table 1

Parameters of the mixture for TPS biocomposites

Basic Components of TPS	Addition of Nut Shell to the Mixture (wt%)	Acronym of the Obtained Film/Biocomposite TPS
Starch 50 g + Glycerol 25 g	2 5	Haz_TPS (material with hazelnut shells)
	2 5	Pis_TPS (material with pistachio shells)
	2 5	Wal_TPS (material with walnut shells)
	2 5	Pean_TPS (material with peanut shells)
	0	TPS (thermoplastic starch)

Mechanical Properties

The following tests were selected to determine the strength parameters: elongation stress, elongation at break, Young's modulus and puncture force. Paddles of 6 mm x 80 mm were cut from the prepared TPS biocomposites (foil sheets). For the puncture tests, samples of 100 x 40 mm were prepared. The thickness of the TPS biocomposite in the analysed place was measured with an electronic caliper with an accuracy of 0.01 mm. The tests were performed in accordance with the standards *PN-EN ISO 527-1:2020-01, PN-EN ISO 527-2:2012.* The AXIS 500 universal testing machine with the FA 200 N (0.01 N) measuring head (manufacturer: AXIS, Gdansk, Poland) was used in the tests.

Water Contact Angle

Surface wettability was measured using the "sitting drop" method according to *Giri et al., (2019).* The test stand consisted of a digital camera A2500-14uc (5, Mpix), (manufacturer: Basler, Ahrensburg, Germany), an adjustable table and a syringe for dispensing distilled water. Each time, a drop of 15 µl was dosed on the surface of the tested material. Images were downloaded using the Pylon Viewer software (manufacturer: Basler, Ahrensburg, Germany). Wetting angle measurements were made in Autodesk Autocad Mechanical 2019. Product version: 23.0.46.0.

Colour

The images necessary for colour measurements were taken with an Optatech STX stereoscopic microscope equipped with a 5Mpx colour camera and a LED circular illuminator (colour temperature 7000K) (Opta-Tech, Warsaw, Poland). Prior to the study, the camera was calibrated using a Minolta white guide. CorelDRAW Home Version 17.1.0.572 software (Corel Corporation, Ottawa, Canada) was used in the colour studies, on which the L^*, a, $^*b^*$ colour space values were read.

Changes in the colour ΔE of TPS biocomposites, which occurred as a result of the addition of 2 wt% and 5 wt% nut shells, were also calculated.

$$\Delta E = [(\Delta L^*)^2 + (\Delta a^*)^2 + (\Delta b^*)^2]^{1/2} \quad (1)$$

where ΔL^*, Δa^*, Δb^* were changes in the colour value ΔE after increasing the addition of nut shells to TPS from 2 wt% to 5 wt%. Below in Fig. 1, exemplary photos of the produced TPS biocomposite samples are presented.

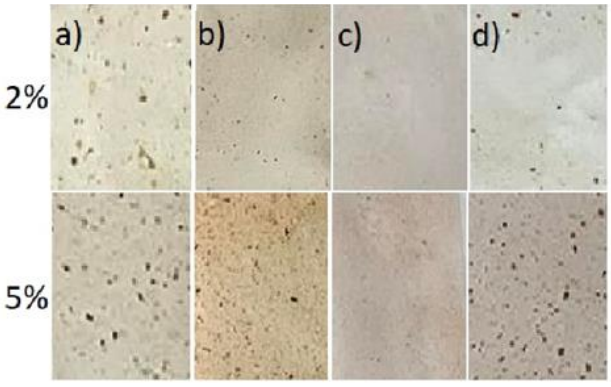

Fig. 1 - Example images of TPS biocomposites with the addition of:
a) peanut shells, b) hazelnut, c) pistachio, d) walnut

Scanning electron microscope (SEM)

Images of the structure of TPS biocomposites were made on a scanning electron microscope (SEM) HITACHI S-3400N at the Accelerating Voltage of 20 kV in a low vacuum of 70 Pa. The fracture of the composites after breaking the biocomposite was analysed.

Moisture absorption from water and air

Before starting the tests, the material samples were cut into pieces of 10 x 8 m and dried in a convection dryer to a constant weight. Then, the samples were placed in 50 ml flacons filled with distilled water at 21 °C. Each time after taking it out of the water, the sample was drained with a dry cloth and weighed on a laboratory scale with an accuracy of 0.001 g. During the test, the initial mass W_o and final mass W_t were recorded for each measurement. Measurements were made every hour for 8 hours.

The percentage absorption was determined on the basis of equation (2).

$$Moisture\ absorption = \frac{W_t - W_o}{W_o} \times 100\% \quad (2)$$

Similarly, tests of moisture absorption from the air were carried out. In this study, samples were placed in a KBK-30 climatic chamber (manufacturer: Wamed, Warsaw, Poland), Relative humidity (RH): 75% at 25°C. The percentage absorption was also determined from equation (2).

Statistical analysis

Statistica 2013 software, version 13.3 (TIBCO Software Inc., Palo Alto, California, USA) was used for statistical analysis. Statistical analysis was performed in the tests of strength tests, wetting angle and general colour changes. The results from the experimental studies were obtained from 5 repetitions. The normality of the data distribution was tested with the Shapiro-Wilk test. The confidence level was 95% ($p < 0.05$). In the next step, the data was analysed by one-way ANOVA with Tukey's test. Significant and non-significant differences are shown in lowercase and uppercase letters above the error bars. Different upper-case letters, e.g., (C, B), indicate significant differences between the biocomposites (the same percentage of added digestate). Different lower-case letters, e.g., (c, d), indicate significant differences between samples with different percentages of components. Lack of significance between homogeneous groups is indicated by, e.g., (a, a, or B, B).

RESULTS

Analysing the results of strength tests, it can be concluded that the addition of crushed nut shells had a significant effect on changes in strength parameters. Observing the results of the elongation stress tests (Fig. 2a), it can be concluded that the TPS biocomposites with the addition of 5% of nut shells were characterized by the highest strength. The biocomposites with the addition of peanut shells (Pean_TPS) had the highest strength, which was 3.4 MPa. Biocomposites with the addition of walnut shells Wal_TPS, which was 3.0 MPa, were also characterized by high strength. Since the strength of a pure TPS sample was 2.6 MPa, the addition of these nuts increased the strength of biocomposites by over 30%. In the case of Pean_TPS biocomposites, the highest strength may result from a good connection of lignocellulosic fibres with the TPS matrix. Generally, lignocellulose was crushed mechanically and thermally treated, which could favour partial release of cellulose (*Delgenés et al., 2002*).

According to various studies, cellulose is a commonly used additive that strengthens the structure of various biocomposites *(Sirviö et al., 2018).*

The share of cellulose in peanut shells may even exceed 40%, which may explain the obtained strength parameters *(Queirós et al., 2020).* Biocomposites with the addition of Haz_TPS hazelnuts and Pis_TPS pistachio nuts had results similar to TPS thermoplastic starch films.

Analysing the results of the sample elongation tests (until breaking), it can be concluded that all samples had a lower elongation than biocomposites made of pure TPS (fig. 2b). This is one of the limitations of the use of lignocellulosic raw materials, which was also indicated *(Teixeira et al., 2012).*

Studies of Young's modulus YM presented in Fig. 2c showed an increase in elasticity for all biocomposites with the addition of nut shells. The highest YM values compared to TPS were found for peanuts (5 wt%) 109.2 MPa. For comparison, the lowest value for this test was 98 MPa for Haz_TPS. The addition of 2 wt% shells contributed to obtaining lower YM values, which ranged from 80.3 to 90.3 MPa.

Comparing these results to commercial foil tests, the obtained results are satisfactory. According to research by *Bilck et al., (2010),* a typical plant covering film has a Young's modulus of 81 - 122 MPa.

Promising results were also obtained when testing the puncture strength of TPS biocomposites (Fig. 2d). In this case, both the addition of 2 wt% and 5 wt% caused a significant increase in the force needed to pierce the sample. In this case, the biocomposite reinforced with peanut shells (5.1 N) was the most puncture resistant.

The puncture force values for the other shell-reinforced biocomposites were similar and ranged from 4.1 to 4.3 N with the shell addition of 5 wt%.

The strength of samples reinforced with 2 wt% of nut shells was lower by almost 1N for all samples. Despite the satisfactory results, the parameters obtained differ from commercial films, e.g. agricultural, whose puncture strength ranges from 8 to about 26 N *(Bilck et al., 2010).*

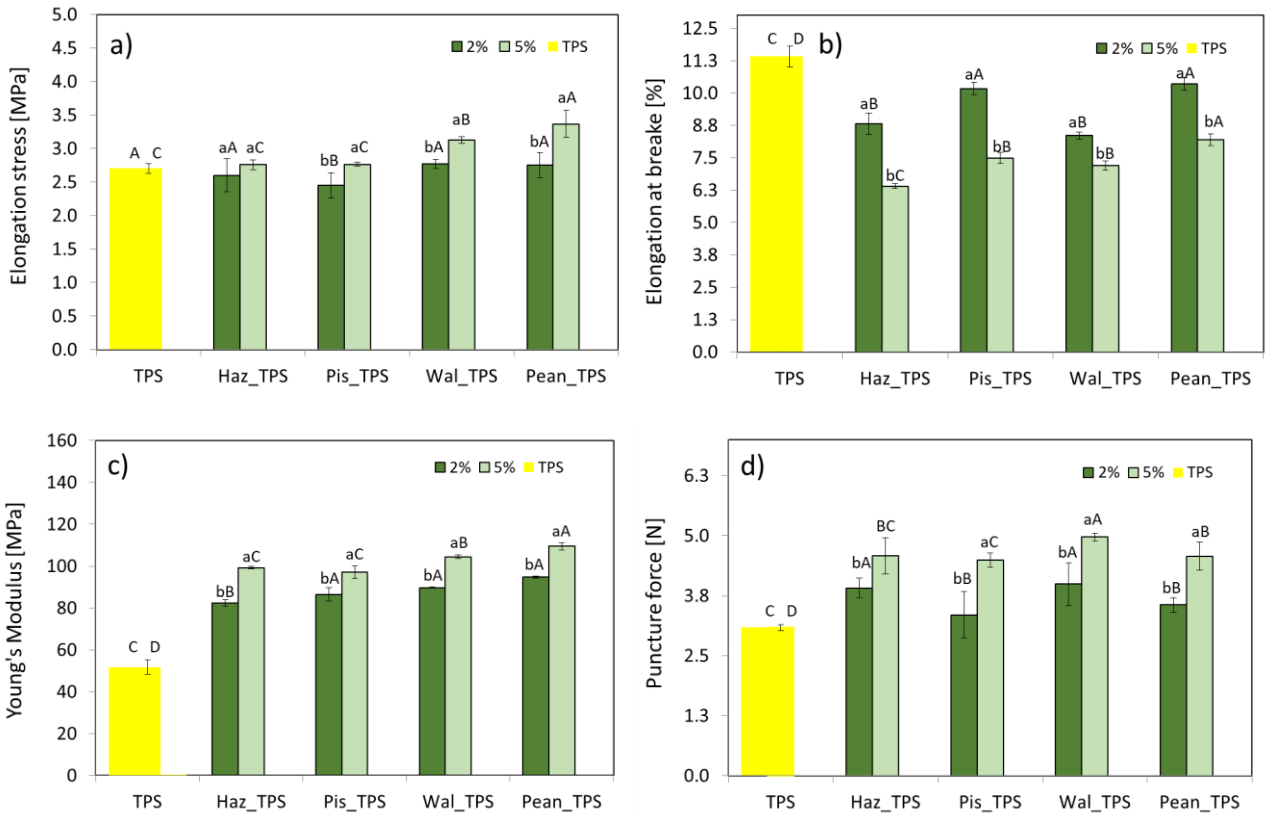

Fig. 2 - Strength tests of biocomposites

(a) elongation stress, (b) elongation at break, (c) Young's modulus, (d) puncture force.

Water contact angle

Analysis of the water contact angle (Fig. 3a) showed that all samples had a contact angle less than 0° < θ < 90°. According to *Valencia et al. (2018)* these samples are hydrophilic. The tests showed that the highest contact angle of 74° had samples with the addition of 2 wt% of Pean_TPS peanuts. Using a 5 wt% addition of these shells, a smaller contact angle of 70° was obtained. In general, all tested samples with 2 wt% shell added had higher values than samples with 5 wt% shell percentage. The samples with the addition of pistachio shells were characterized by the highest hydrophilicity.

The highest values of the contact angle for Pean_TPS may be related to the introduction of significant amounts of lignin found in peanuts into the biocomposite *(Martin et al., 2007).* Lignin is a component that can contribute to the reduction of the water absorption properties of the material.

Peanut shells also contain a small amount of hemicellulose (12%), which is generally considered hydrophilic, which may also contribute to the highest contact angle *(Demirbas, 2006; Aydin and Colakoglu, 2007).* Comparing the obtained results to the studies of other authors, PLA has a contact angle from about 70° to even 118° *(Lovinčić Milovanović et al., 2020; Bhasney et al., 2017).*

The most hydrophobic biodegradable material has a wetting angle of about 160° *(Liu et al., 2022).* It can therefore be concluded that in the case of the tested TPS biocomposites, the contact angle is low.

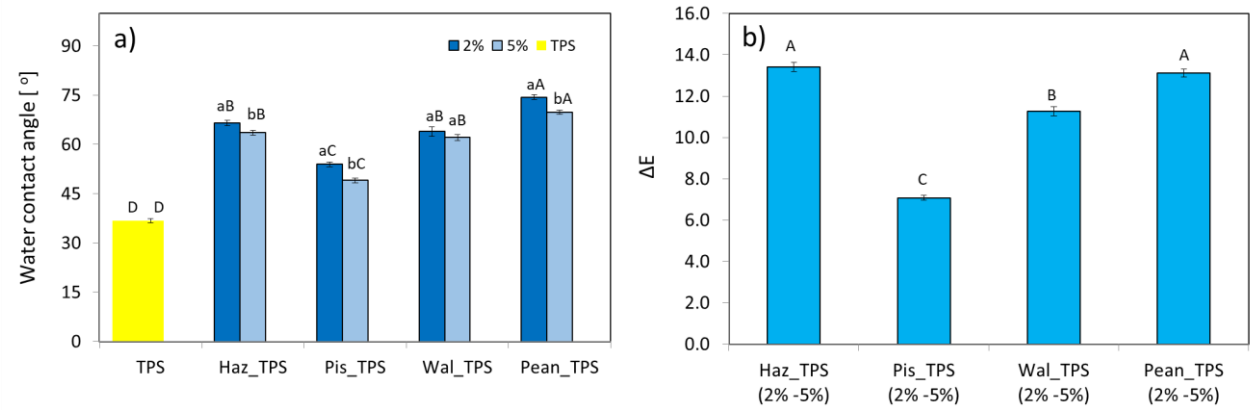

Fig. 3 - Water contact angle charts and colour tests

(a) mean values of the changes in the contact angle.

(b) Mean values of the difference in colour changes ΔE between the TPS with added 2% and 5% nuts shell.

Colour

Colour change studies showed that the TPS biocomposites were characterized by shades of yellow and light brown. This is confirmed by the results of colour changes a* and b*, which in the *L*, a, *b** colour space ranged from -2.02 to 30.22 (Table 2). The intensity of the colours was also affected by the high brightness of the L* samples, which ranged from 61.91 to 79%. By analysing the colour changes, it was found that in each case the addition of 5 wt% shells reduced the brightness of the obtained materials. In general, the overall colour change between the 2 wt% and 5 wt% shell samples was found to be from 7.07 to 13.42 (Figure 3a). Colour changes can therefore be observed even visually. The darkest samples were Haz_TPS and Wal_TPS, which can be explained by the darkest colour of these shells. According to the authors *Khir et al., (2014),* the colour may depend on the moisture content in the nuts and the temperature of the drying process. Therefore, it is to be expected that each batch of nut shells may slightly differ in colour, which may require inspection for industrial applications. The quality and stability of agri-food waste raw materials is one of the main limitations of their industrial use *(Farch et al., 2023).*

Table 2

Average values of *L, *a**, *b** colour components. Five-replicate measurements (p<0.05)**

Sample	Nuts shell addition 2 wt%			Nuts shell addition 5 wt%		
	L*	***a****	***b****	***L****	***a****	***b****
Haz_TPS	69.41 (±0.21)	2.90 (±0.27)	21.11 (±0.15)	61.91 (±0.61)	9.38 (±0.14)	30.22 (±0.35)
Pis_TPS	78.52 (±0.65)	-1.58 (±0.22)	5.97 (±0.12)	77.54 (±0.36)	3.31 (±0.08)	11.02 (±0.43)
Wal_TPS	72.31 (±0.41)	0.93 (±0.32)	8.71 (±0.20)	64.87 (±0.54)	5.73 (±0.10)	15.67 (±0.46)
Pean_TPS	79.05 (±0.32)	-2.14 (±0.52)	7.23 (±0.18)	77.21 (±0.65)	1.11 (±0.08)	19.81 (±0.45)
TPS*	77.15 (±0.12)	-2.02 (±0.09)	4.92 (±0.16)	-	-	-

** - only TPS without the addition of nut shells.*

Moisture absorption in water

Analysing the obtained test results, it can be concluded that the water absorption of TPS biocomposites with the addition of nut shells changed with their addition (fig. 4a). For biocomposites with the addition of 2 wt% nuts, the moisture content increased from 56.5 to 96.3%. In the case of biocomposites with the addition of 5 wt% of nuts, the water absorption of the samples was in the range of 68.9 - 108.9%. Therefore, the research shows that with the increase in the addition of nut shells, the water absorption of the obtained TPS biocomposites also increases significantly. The highest water absorption was found in materials with the participation of Haz_TPS and Wal_TPS, whose water absorption increased from 96.3 to even 109.9%. Such high water absorption may be related to the high content of hemicellulose in these shells, which is considered a hydrophilic material *(Aydin and Colakoglu, 2007).*

In turn, the limitation of water absorption for these samples is lignocellulose, which is hydrophobic *(Gwon et al., 2010).* This may further explain the lowest water absorption for Pean_TPS and Pis_TPS, which have a low content of this component. High water absorption of the obtained materials is generally not a positive feature in the case of utility applications.

A solution to this problem could be to limit the availability of water to hemicellulose by minimizing, for example, thermal and pressure treatment of shells during drying *(Ciemniewska-Żytkiewicz et al., 2014; Bogumił, 2016).*

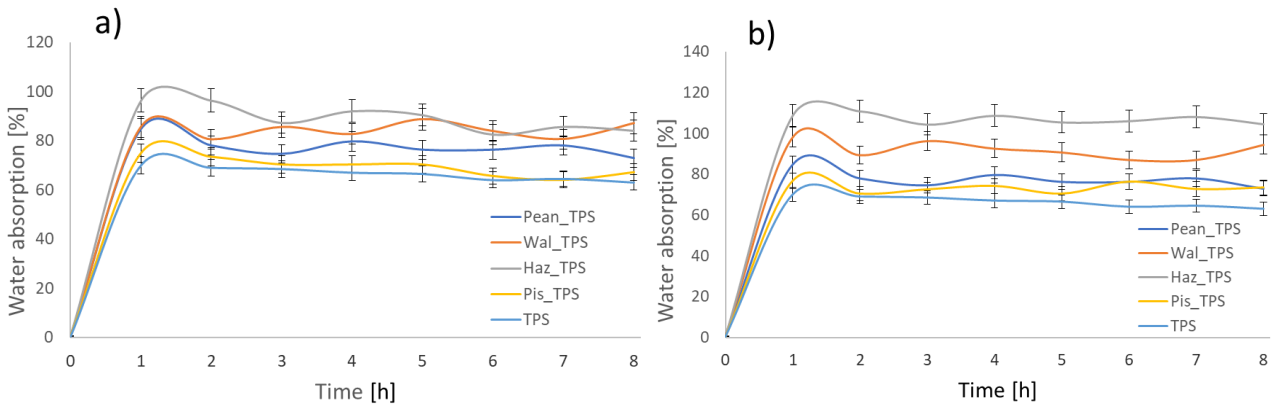

Fig. 4 - Water absorption results for samples with the addition of nut shells
a) 2 wt%, b) 5 wt%

Absorption of moisture from the air

Analysing the results of moisture absorption from the air, it was found that the addition of nut shells also influenced changes in this parameter. As in the above results, biocomposites with Haz_TPS had the highest moisture absorption. In the case of other nutshells, the differences between the obtained results were less visible. In this study, it was found that the water absorption of samples with the participation of Wal_TPS was significantly reduced, which was at the level of pure TPS material. The obtained values were even lower than Pean_TPS and Pis_TPS.

Generally, in this study the maximum moisture absorption was 35.8%. In the case of Wal_TPS it was only 26.7% with the share of this component of 5 wt%. Therefore, the nut components embedded in the TPS matrix did not have access to moisture, as in the case of complete immersion of the material in water. The TPS material, despite its significant hydrophilic properties *(Li et al., 2021),* is a protection against the absorption of moisture from the air for lignocellulosic materials rich in hemicellulose.

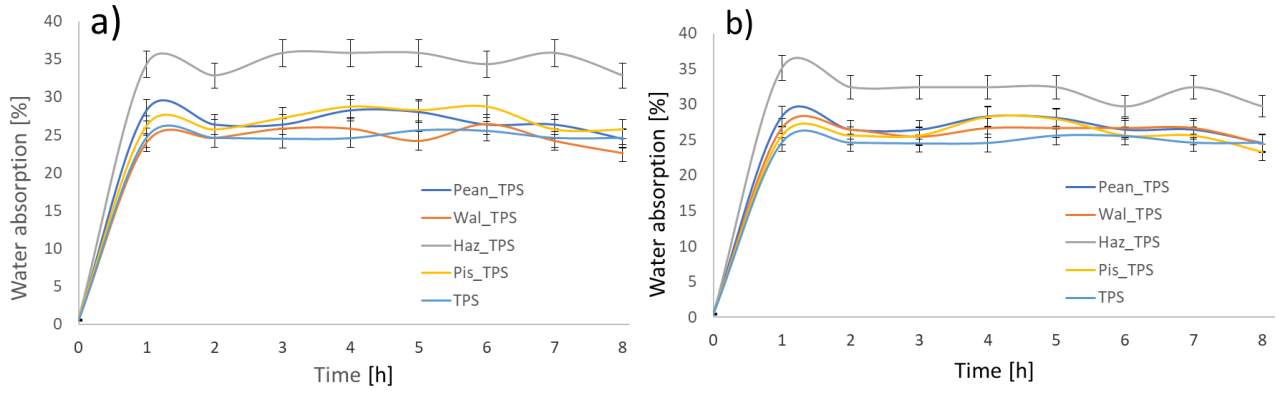

Fig. 5 - Results of moisture absorption from the air for samples with the addition of nut shells
a) 2 wt%, b) 5 wt%.

SEM

The analysis of SEM scanning electron micrographs (fig. 6) showed that all nut shells used as an additive for biocomposites were well embedded in the TPS matrixes. In general, raw materials rich in lignocellulose blend well into the TPS material at the stage of their production, which is confirmed by research *(Ekielski et al., 2021.*

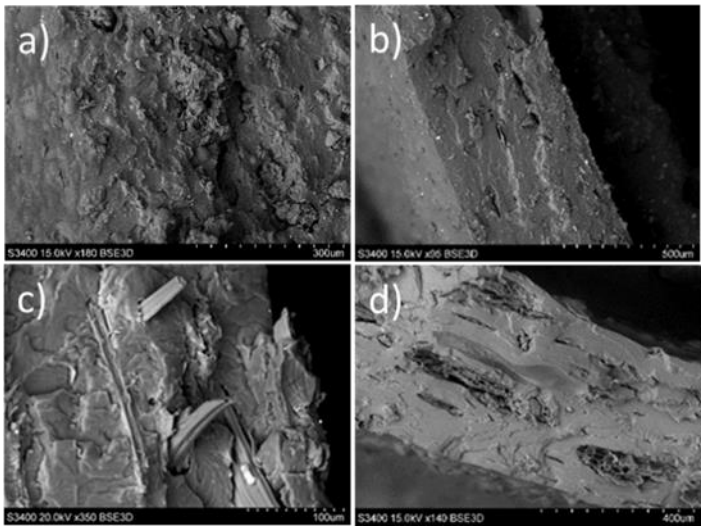

Fig. 6 - Images of fractures of TPS biocomposites
a) material with hazelnut shells, b) material with walnut shells, c) material with pistachio shells, material with peanut shells

In Figure 6a, you can see the porous structure of hazelnut shells. This may explain the increased water absorption found during the tests. Fig. 6b shows the breakthrough of the biocomposite with the addition of walnut shells. The particles of these shells are perfectly embedded in the TPS matrix, and the pores are almost invisible, which may limit the sorption of moisture from the air by these shells. In Figure 6c, particles of pistachio shells that bind the biocomposite are visible, therefore these biocomposites have a high elongation until the sample breaks. In turn, in Fig. 6b, porous particles characteristic of peanut shells can be observed. The air pores that form these shells in the long run may adversely affect the sorption properties of such materials. On the other hand, the fibrous structure of these wastes improves the strength properties found during strength tests. The limitation of the use of these wastes may also be too high buoyancy of such particles, which makes it difficult to sink the shell particles in the TPS suspension. From an ecological point of view, this is beneficial, such materials can be more easily biodegraded *(Irwin, 2018).*

CONCLUSIONS

The obtained test results showed that it is possible to use nut shells as an additive to TPS biocomposites. However, in order to produce a material with a stable structure, previously heat-treated shells must be added to the thermoplastic starch. The raw material prepared in this way enables the use of various types of shells in the amount of 5 wt%, without reducing the quality of the biocomposite. Both the addition of shells 2% and 5% have a positive effect on increasing the puncturing force and increasing the modulus of elasticity YM. However, it is best to use the addition of peanut and walnut shells to improve these parameters. The addition of these shells changes the colour of biocomposites to the greatest extent, which can be observed even visually. The addition of nuts may make the materials more sensitive to moisture, which may limit the use of these materials. The lowest hydrophobicity can be obtained by adding peanut shells to TPS. To sum up, it is worth considering the use of crushed nut shells, especially ground and walnuts, as an addition to TPS biocomposites. When planning applications for these materials, their increased sorption properties should always be taken into account.

REFERENCES

[1] Aydin, I., & Colakoglu, G. (2007). Variation in surface roughness, wettability and some plywood properties after preservative treatment with boron compounds. *Building and Environment, 42*(11), 3837-3840. https://doi.org/10.1016/j.buildenv.2006.11.009

[2] Bhasney, S.M. Patwa, R., Kumar, A. & Katiyar, V. (2017). Plasticizing effect of coconut oil on morphological, mechanical, thermal, rheological, barrier, and optical properties of poly (lactic acid): A promising candidate for food packaging. *J. Appl. Polym. Sci. 134*, 45390. https://doi.org/10.1002/app.45390

[3] Bilck, A. P., Grossmann, M. V., & Yamashita, F. (2010). Biodegradable mulch films for strawberry production. *Polymer testing, 29*(4), 471-476. https://doi.org/10.1016/j.polymertesting.2010.02.007

[4] Bogumił, D. (2016). Effect of methods pretreatment of biomass for yield of biofuels. *Studia Ecologiae et Bioethicae, 14*(4), 191-203.

[5] Borowski, P. F. (2021). Digitization, digital twins, blockchain, and industry 4.0 as elements of management process in enterprises in the energy sector. *Energies, 14*(7), 1885. https://doi.org/10.3390/en14071885

[6] Borowski, P. F., Patuk, I., & Bandala, E. R. (2022). Innovative industrial use of bamboo as key "Green" material. *Sustainability*, *14*(4), 1955. https://doi.org/10.3390/su14041955

[7] Chaturvedi, A., Ranakoti, L., Rakesh, P. K., & Mishra, N. K. (2021). Experimental investigations on mechanical properties of walnut shell and pine needle ash polylactic acid biocomposites. *Composites Theory and Practice*, 21.

[8] Ciemniewska-Żytkiewicz, H., Joanna, Bryś., Andrzej, Bryś., Sujka, K., & Koczoń, P. (2014). Effect of roasting process on moisture content and colour of Polish inshell hazelnuts. *Akademik Gıda*, *12*(1), 6-10.

[9] Delgenés J.P., Penaud V., Moletta R. 2002. Pretreatments for the enhancement of anaerobic digestion of solid wastes Chapter 8. In: Biomethanization of the Organic Fraction of Municipal Solid Wastes. IWA Publishing, pp. 201–228.

[10] Demirbas A (2006) Effect of temperature on pyrolysis products from four nut shells. *J Anal Appl Pyrolysis 76*(1–2):285–289. https://doi.org/10.1016/j.jaap.2005.12.012

[11] Ekielski, A., Żelaziński, T., Mishra, P. K., & Skudlarski, J. (2021). Properties of biocomposites produced with thermoplastic starch and digestate: Physicochemical and mechanical characteristics. *Materials, 14*(20), 6092. https://doi.org/10.3390/ma14206092

[12] Farch, S., Yahoum, M. M., Toumi, S., Tahraoui, H., Lefnaoui, S., Kebir, M., Zamouche, M., Amrane, A., Zhang, J., Hadadi, A., & Mouni, L. (2023). Application of Walnut Shell Biowaste as an Inexpensive Adsorbent for Methylene Blue Dye: Isotherms, Kinetics, Thermodynamics, and Modeling. *Separations, 10*(1), 60. https://doi.org/10.3390/separations10010060

[13] Giri, J.; Lach, R.; Grellmann, W.; Susan, M.A.; Saiter, J.M.; Henning, S.; Katiyar, V.; Adhikari, R. (2019) Compostable composites of wheat stalk micro-and nanocrystalline cellulose and poly (butylene adipate-co-terephthalate): Surface properties and degradation behavior. *J. Appl. Polym. Sci.* 136, 48149. https://doi.org/10.1002/app.48149

[14] Gwon, J.; Lee, S.; Chun, S.; Doh, G.; Kim, J. (2010). Effects of chemical treatments of hybrid fillers on the physical and thermal properties of wood plastic composites. Compos. Part. *A Appl. Sci. Manuf. 41,* 1491–1497. https://doi.org/10.1016/j.compositesa.2010.06.011

[15] Irwin, A. (2018). How to Solve a Problem like Plastics. *New Scientist, 238*(3178), 25-31. https://doi.org/10.1016/S0262-4079(18)30884-4

[16] Kasiri, N., & Fathi, M. (2018). Production of cellulose nanocrystals from pistachio shells and their application for stabilizing Pickering emulsions. *International journal of biological macromolecules*, *106*, 1023-1031. https://doi.org/10.1016/j.ijbiomac.2017.08.112

[17] Khir, R., Atungulu, G. G., Pan, Z., Thompson, J. F., & Zheng, X. (2014). Moisture-dependent color characteristics of walnuts. *International Journal of Food Properties, 17*(4), 877-890. https://doi.org/10.1080/10942912.2012.675610

[18] Li, M., Jia, Y., Shen, X., Shen, T., Tan, Z., Zhuang, W., Zhao, G., Zhu., C., & Ying, H. (2021). Investigation into lignin modified PBAT/thermoplastic starch composites: Thermal, mechanical, rheological and water absorption properties. *Industrial Crops and Products, 171*, 113916. https://doi.org/10.1016/j.indcrop.2021.113916

[19] Liu, C. H., Shang, J. P., Su, X., Zhao, S., Peng, Y., & Li, Y. B. (2022). Fabrication of Superhydrophobic/Superoleophilic Bamboo Cellulose Foam for Oil/Water Separation. *Polymers, 14*(23), 5162. https://doi.org/10.3390/polym14235162

[20] Lovinčić Milovanović, V., Guyon, C., Grčić, I., Tatoulian, M., & Vrsaljko, D. (2020). Modification of Surface Hydrophobicity of PLA/PE and ABS/PE Polymer Blends by ICP Etching and CFx Coating. *Materials, 13*(23), 5578. https://doi.org/10.3390/ma13235578

[21] Mandalari G, Arcoraci T, Martorana M, Bisignano C, Rizza L, Bonina FP, Trombetta D, Tomaino A (2013) Antioxidant and photoprotective effects of blanch water, a byproduct of the almond processing industry. *Molecules 18*(10):12426–12440. https://doi.org/10.3390/molecules181012426

[22] Mangaraj, S., Yadav, A., Bal, L. M., Dash, S. K., & Mahanti, N. K. (2019). Application of biodegradable polymers in food packaging industry: A comprehensive review. *Journal of Packaging Technology and Research*, *3*, 77-96. https://doi.org/10.1007/s41783-018-0049-y

[23] Martin C, Alriksson B, Sjöde A, Nilvebrant NO, Jönsson LJ (2007) Dilute sulfuric acid pretreatment of agricultural and agro-industrial residues for ethanol production. *Appl Biochem Biotechnol 137-140*(1–12):339–352. https://doi.org/10.1007/978-1-60327-181-3_30

[24] Nanthananon, P., Seadan, M., Pivsa-Art, S., Hamada, H., & Suttiruengwong, S. (2018). Reactive Compatibilization of Short-Fiber Reinforced Poly (lactic acid) Biocomposites. Journal of Renewable *Materials, 6*(6), 573-583. DOI: 10.32604/JRM.2018.00129

[25] Nenciu, F., Stanciulescu, I., Vlad, H., Gabur, A., Turcu, O. L., Apostol, T., Vladut, V. N., Cocarta, D. M., & Stan, C. (2022). Decentralized processing performance of fruit and vegetable waste discarded from retail, using an automated thermophilic composting technology. *Sustainability, 14*(5), 2835. https://doi.org/10.3390/su14052835

[26] Nenciu, F., Voicea, I., Cocarta, D. M., Vladut, V. N., Matache, M. G., & Arsenoaia, V. N. (2022). "Zero-Waste" Food Production System Supporting the Synergic Interaction between Aquaculture and Horticulture. *Sustainability, 14*(20), 13396.[b] https://doi.org/10.3390/su142013396

[27] Orue, A., Eceiza, A., & Arbelaiz, A. (2020). The use of alkali treated walnut shells as filler in plasticized poly (lactic acid) matrix composites. *Industrial crops and products, 145*, 111993. https://doi.org/10.1016/j.indcrop.2019.111993

[28] PN-EN ISO 527-1: 2020-01, Plastics—Determination of Mechanical Properties under Static Stretching—Part 1: General Principles; Polish Standardization Committee: Warsaw, Poland, 2020; Available online: https://sklep.pkn.pl/pn-en-iso-527-1-2020-01e.html (accessed on 26 August 2021).

[29] PN-EN ISO 527-2: 2012. Plastics—Determination of Tensile Properties—Part 2: Test Conditions for Moulding and Extrusion Plastics; Polish Standardization Committee: Warsaw, Poland, 2013; Available online: https://www.iso.org/standard/56046.html (accessed on 26 August 2021).

[30] Queirós, C. S., Cardoso, S., Lourenço, A., Ferreira, J., Miranda, I., Lourenço, M. J. V., & Pereira, H. (2020). Characterization of walnut, almond, and pine nut shells regarding chemical composition and extract composition. *Biomass Conversion and Biorefinery*, *10*(1), 175-188. https://doi.org/10.1007/s13399-019-00424-2

[31] Rodriguez, L. J., Peças, P., Carvalho, H., & Orrego, C. E. (2020). A literature review on life cycle tools fostering holistic sustainability assessment: An application in biocomposite materials. *Journal of Environmental Management, 262*, 110308. https://doi.org/10.1016/j.jenvman.2020.110308

[32] Shaik, S. A., Schuster, J., Shaik, Y. P., & Kazmi, M. (2022). Manufacturing of Biocomposites for Domestic Applications Using Bio-Based Filler Materials. *Journal of Composites Science,* 6(3), 78. https://doi.org/10.3390/jcs6030078

[33] Sirviö, J. A., Visanko, M., Ukkola, J., & Liimatainen, H. (2018). Effect of plasticizers on the mechanical and thermomechanical properties of cellulose-based biocomposite films. *Industrial Crops and Products, 122*, 513-521. https://doi.org/10.1016/j.indcrop.2018.06.039

[34] Teixeira, E. D. M., Curvelo, A. A., Corrêa, A. C., Marconcini, J. M., Glenn, G. M., & Mattoso, L. H. (2012). Properties of thermoplastic starch from cassava bagasse and cassava starch and their blends with poly (lactic acid). *Industrial Crops and Products, 37*(1), 61-68. https://doi.org/10.1016/j.indcrop.2011.11.036

[35] Ungureanu, N., Vlăduț, V., & Biriș, S. Ș. (2022). Sustainable Valorization of Waste and By-Products from Sugarcane Processing. *Sustainability, 14*(17), 11089. https://doi.org/10.3390/su141711089

[36] Yang, T., & Lua, A. C. (2006). Textural and chemical properties of zinc chloride activated carbons prepared from pistachio-nut shells. *Materials chemistry and physics, 100*(2-3), 438-444. https://doi.org/10.1016/j.matchemphys.2006.01.039

STUDY ON THE VARIATION OF THERMAL ENVIRONMENT AND PHOTOSYNTHESIS CHARACTERISTICS OF STRAWBERRY IN A SOLAR GREENHOUSE

/

日光温室热环境变化规律及对植物光合特性的影响

Weiwei CHENG [1)], Yu WANG [2)], Changchao WANG [2)], Tao WANG [2)], Junlin HE [2)], Zhouhua LIU [*1)]

[1)] Shanxi Agricultural University, College of Urban and Rural Construction, Taigu / China
[2)] Shanxi Agricultural University, College of Agricultural Engineering, Taigu / China
Tel: +86-0354-6287420; E-mail: lzh6175305@163.com
Corresponding author: Zhonghua LIU

DOI: https://doi.org/10.35633/inmateh-70-21

***Keywords*:** *Sunken solar greenhouse; Stereotypic planting; Vertical temperature change rate; Photosynthesis*

ABSTRACT

The sunken solar greenhouse is suitable for the development of vertical planting, which results in higher yield. In order to investigate the effect of temperature on photosynthesis of plants, an experimental study was conducted on the temperature and photosynthesis of strawberry plants at different heights in the sunken solar greenhouse. The study showed that when the indoor temperature was higher than 25.5°C, the photosynthesis of plants was inhibited; the transpiration rate decreased by 3.89 μmol $m^{-2}s^{-1}$and photosynthesis rate decreased by 3.95 μmol $m^{-2}s^{-1}$ when the air temperature increased from 25.5 °C to 33.3°C and then decreased to 25.4°C at a height of 1.8 m from the indoor floor; there were temperature differences in the vertical direction between the indoor temperatures of the sunken heliostat. The maximum temperatures at 0 m, 0.6 m, 1.0 m, 1.4 m, and 1.8 m height were 20.6°C, 24.1°C, 25.4°C, 25.4°C, 33, and 33.3°C, respectively, and different temperatures would have different photosynthetic characteristics of plants. This study can provide basic support for greenhouse regulation.

摘要

下沉式日光温室适宜于发展竖向种植，从而获得较高收益。温度对植物的光合作用有影响，为探究温度对植物光合作用的影响，对下沉式日光温室不同高度的温度和草莓植株的光合作用展开实验研究，研究显示：室内温度高于 25.5℃时，会抑制植物的光合作用；与室内地面高度为 1.8m 处的空气温度由 25.5℃升高到 33.3℃，然后降低到 25.4℃时，此时间段内蒸腾速率下降了 3.89μmol $m^{-2}s^{-1}$ 光合速率下降了 3.95μmol $m^{-2}s^{-1}$；下沉式日光温室室内温度在竖直方向存在温度差异，室内地面高度为 0m、0.6m、1.0m、1.4m、1.8m 位置处的最高温度分别为 20.6℃、24.1℃、25.4℃、25.4℃、33、3℃，不同温度会对植物的光合特性产生差异。该研究可为温室调控提供基础支撑。

INTRODUCTION

The solar greenhouse is an important agricultural facility in China, supplying more than 30% of the total supply of fruits and vegetables of all facilities in winter, mainly due to the availability of a suitable microclimate in winter (*Chao et al., 2018*). Among the suitable microclimates, the thermal environment is the main reason why year-round cultivation can be achieved. Among the many thermal environment factors, plant body temperature is the most sensitive factor to the healthy growth status of plants, and air temperature is the most synergistic with plant body temperature, both of which have the same change pattern (*Yu, Ming-Han et al., 2015*), thus the temperature in the solar greenhouse can directly respond to the health status of plants. In greenhouse stereo culture, strawberry plants are more sensitive to environmental changes, especially temperature changes have a greater impact on strawberries (*Xu Chuan et al., 2015*).

Plant photosynthesis is also more sensitive to temperature changes, and temperature affects the photosynthetic rate of plants by changing the activity of enzymes (*Lv Huanhuan et al., 2021*), which is also an important factor affecting plant growth and secondary metabolite synthesis (*Zheng Youfeng et al., 2022*).

The penetration of solar light through the plastic trellis film caused an increase in the indoor temperature *(Ahemd et al., 2016*), which can still exceed 30°C for a period of time during midday in winter. Excessive temperatures are a problem in solar greenhouse (*Phunchok Angmo.et al., 2021*). While high temperature was one of the important limiting factors affecting plant physiological processes (*Raja, V. et al., 2020*), high temperature stress disrupted many physiological and biochemical processes, leading to inhibition of photosynthesis (*Mittler et al, 2022*).

The appropriate temperature for many greenhouse plants was 17-27°C (*Shamshiri et al, 2018*), and when the indoor temperature was higher than the maximum value of the appropriate temperature, plants showed to improve the efficiency of photosynthesis in greenhouse plants, the thermal environment of indoor crops should be prevented from being too high. The rate of change of indoor air temperature was in the descending order of: rate of horizontal change > rate of horizontal change > rate of longitudinal change (*Weiwei Cheng et al., 2022*), so the monitoring of vertical temperature is a priority. The greenhouse was a semi-enclosed facility system where the crop interacted with the environment through its own transpiration, respiration and photosynthesis (*Zheng, Rorin et al., 2023*).

The use of ventilation was an important tool for thermal environment regulation in the solar greenhouse (*Xie Di et al., 2010*), and therefore the management system for the regulation of the air outlet should be based on the indoor temperature values (*Ge Jiankun et al., 2021*). In order to investigate the pattern of changes in the thermal environment of the solar greenhouse and to define the effect of different temperatures on photosynthesis of plants, so as to achieve the goal of regulation according to the canopy temperature, the temperature at different heights of the sunken solar greenhouse and the factors related to photosynthesis of strawberries at different temperatures were measured.

MATERIALS AND METHODS

Indoor Environment

Outdoor weather conditions (wind level, temperature, light, carbon dioxide concentration, etc.) were measured using the outdoor weather meter of Shanxi Juxinweiye, and indoor light and temperature were measured using the Shanxi Juxinweiye indoor louvered box agricultural Internet system, with the collector located in the middle of the greenhouse at a height of 4 m from the indoor ground, and indoor and outdoor data stored in the cloud platform. The vertical heights of the upper surface of each layer of substrate and the indoor ground were 1.8 m, 1.4 m, 1 m and 0.6 m, as in Figure 1. Temperature and humidity sensors were arranged at the upper surface of each layer of substrate in the A-frame to record the temperature and humidity values at the corresponding heights.

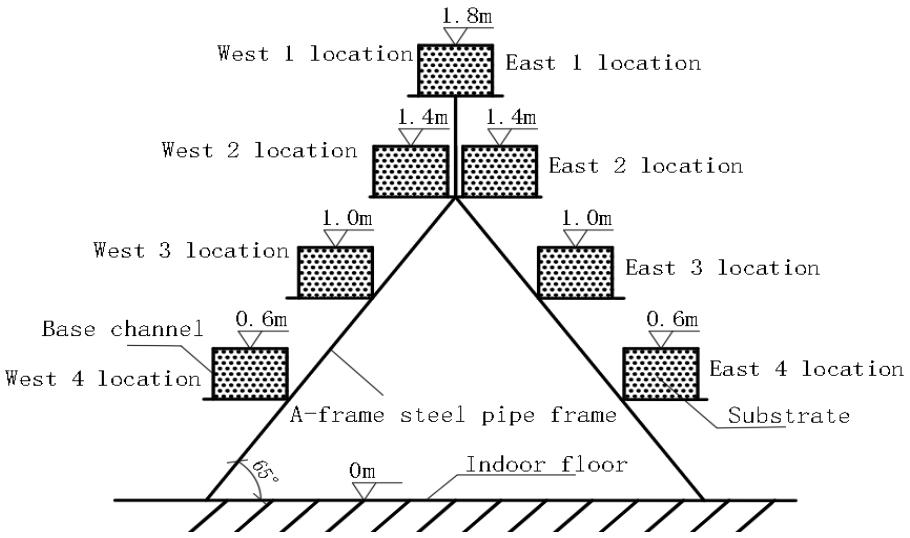

Fig. 1 - Substrates of different heights on A-frame

Experimental materials and methods

To determine the photosynthetic characteristics of strawberry leaves at different heights of strawberries and on the east and west sides of the A-frame, so as to establish the relationship between transpiration rate, photosynthetic rate and temperature at the corresponding heights inside the heliostat. The transpiration rate, photosynthetic rate and stomatal conductance of strawberry leaves in the sunken solar greenhouse were measured during 8:00-17:50 on December 29, 2019, using a portable photosynthesizer Li-6800.

Fig. 2 - Li-6800 photosynthesizer measured in a sunken solar greenhouse

Since a quilt was spread in the middle of the greenhouse film, it was necessary to avoid its influence on indoor light and temperature. The strawberry A-frame in the middle of the greenhouse was selected at 5 m west of the cross-sectional position, and the transpiration rate, photosynthetic rate and stomatal conductance of strawberry leaves were measured in a fixed order: West 1 - West 2 - West 3 - West 4 - East 1 - East 2 - East 3 - East 4, with the strawberry plants at the upper east position and the upper west position were placed in the same basal tank with the distance between plants equal to 15 cm.

Outdoor weather condition

December 29, 2019, all day, sunny, maximum temperature 8°C, minimum temperature -9°C, wind northwest 1 to 2, relative humidity 29%, and the time of sunrise was 7:43 and sunset was 17:20. 8:13 opened the shed, the quilt rose to the full pressure upwind, 11:04 opened the upwind, 14:23 closed the upwind; 15:36 opened the upwind again, 16:00 to close the upwind opening, 17:20 to put down the quilt. Due to the low temperature in winter, the downwind vent was always closed.

RESULTS

Indoor light change and change in indoor carbon dioxide concentration

As can be seen from Figure 3, the indoor light intensity was less than 5000 lx during the time period from closing the shed and putting down the quilts to opening the shed and putting up the quilts the next day; the light intensity gradually increased during the time period from opening the shed to 13:00, and the highest value occurred at 13:00, which was 44440.4lx; the light intensity gradually decreased during 13:00-14:30, increased during 14:30-15:00, and increased after 15:00. After 15:00, the light intensity gradually decreased.

According to Figure 3, the CO_2 concentration of indoor environment decreased from 636 μmol $m^{-2}s^{-1}$ to 296 μmol $m^{-2}s^{-1}$ during 8:30-12:30, which was due to the photosynthesis of plants and CO_2 as the main material of photosynthesis, and the photosynthesis rate was greater than the respiration rate, and the indoor temperature did not inhibit the photosynthesis rate of plants during this period. It meant that the photosynthetic rate of plants decreased, which was due to the increase of indoor temperature between 12:00-13:00, and the increase of temperature to a certain value led to the decrease of enzyme activity in plants and the phenomenon of "lunch break" of the plants, and the highest temperature of 32.9°C at 1.8 m height from the indoor ground in this time period occurred between 13:00-13:20.

The maximum value of CO_2 concentration was 369 during 12:00-15:00, and the temperature was 24.4°C, which was 7°C lower than the maximum temperature of the same measurement point in a day. The minimum value of CO_2 concentration was 340 μmol $m^{-2}s^{-1}$ during this time, and the temperature was 25.4°C, the light intensity was higher during this time, but the CO_2 concentration increased, which indicated that the

temperature had a greater influence on the enzyme activity, and Indoor temperatures between 24 and 25°C have a greater effect on the photosynthetic rate of plant. Therefore, the study of temperature stratification phenomenon in indoor stereoculture was conducted to avoid "lunch break" of strawberry leaves and to increase the yield of strawberry by taking appropriate measures.

The gradual increase of CO_2 concentration between 15:00 and 17:00 was due to the gradual decrease of light intensity, the decrease of photosynthesis, and the decrease of CO_2 consumption by photosynthesis, so that the indoor CO_2 concentration increased.

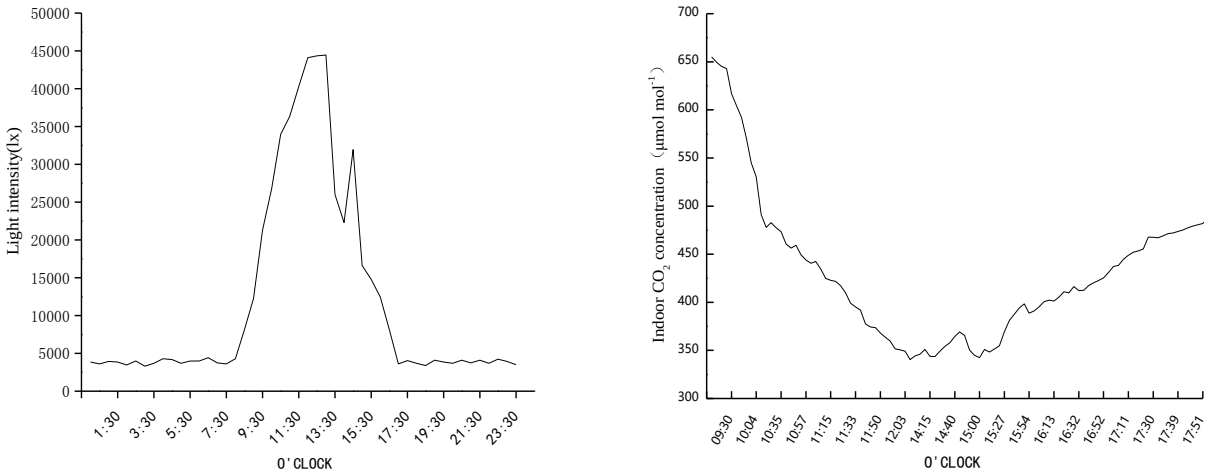

Fig. 3 - Indoor light and CO_2 content curves with time

Variation pattern of temperature with time at different heights

The photosynthetic rate, transpiration rate and stomatal conductance of strawberry leaves at different heights in the central section of the sunken solar greenhouse were measured from 8:54 to 16:54, and the relationship between the temperature values at different heights in this time period was $t_{1.8}>t_{1.4}\geqq t_1>t_{0.6}>t_0$ (t_0 represented the temperature value at the height of 0 m from the indoor floor, i.e., the temperature value at the upper surface of the indoor, the same below); the highest temperature at the height of 0 m, 0.6 m, 1.0 m, 1.4 m and 1.8 m from the indoor floor were 20.6°C, 24.1°C, 25.4°C, 25.4°C, 33.3°C, the highest temperature value at each height did not appear at the same time, the time difference between the highest temperature value at each measurement point was less than 12 min; Within the measurement time period, the maximum temperature difference between t1.8 and t0 at the same time was 13.6°C, the maximum temperature difference between t1.4 and t1 at the same time was 0.5°C, the maximum temperature difference between t1.4 and t0.6 at the same time was 1.6°C, and the maximum temperature difference between t0.6 and t0 at the same time was 3.8°C. It could be seen that the air temperature distribution below 1.8 m from the indoor ground height is not uniform, and there is a large temperature gradient at the same moment. This was mainly due to the uneven solar radiation, which led to large temperature differences in the indoor air layer, i.e., the unevenness of indoor temperature distribution along the vertical space was larger.

During 17:00-18:00, the temperature difference between adjacent measurement points decreased, and the maximum temperature difference between adjacent measurement points was 0.4°C. Due to the weakening of the sunlight intensity, the indoor air absorbed less heat, and the indoor and outdoor air conducted heat conduction due to the temperature difference, resulting in a larger amount of indoor heat loss, so the indoor air temperature value gradually decreased. This was due to the fact that the greenhouse gradually entered the exothermic state and the indoor ground soil, the substrate in the base tank and the indoor walls were gradually in the exothermic state, and the rate of heat gain was faster at the measurement points closer to the ground. Therefore, the study of the vertical distribution of indoor temperature and the maximum value of temperature in the greenhouse during winter could provide the accurate time period of ventilation and heat exchange for stereoculture and the temperature difference data for stereoculture in the vertical height.

Relationship between light intensity and indoor temperature at the same height during the time period of 10:00-14:00

During the period of strong daylight, the indoor ground and the north wall were in the state of heat absorption, while the indoor temperature and the outdoor temperature were exchanging heat due to the temperature difference, but the temperature rising was mainly related to the light intensity, using the light intensity and indoor temperature values collected by the louvered box type data collector at 4 m height of the greenhouse to draw a scatter plot and add a trend line.

To establish the relationship between light intensity and temperature during the period of strong light to provide theoretical data on the corresponding light intensities for temperature calculations in stereoculture.

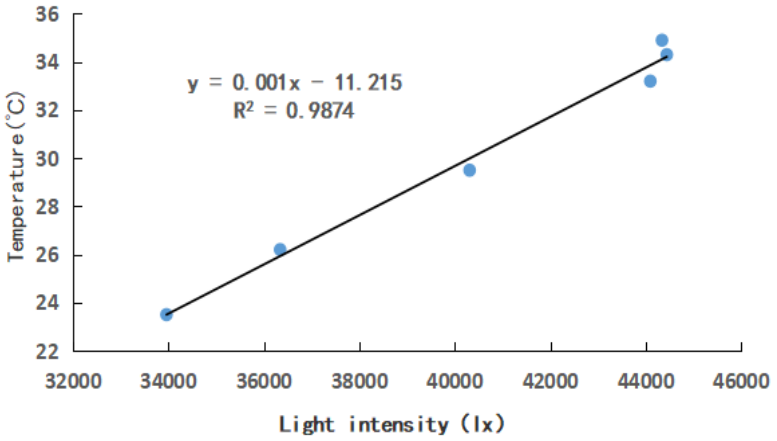

Fig. 4 - Relationship between temperature and light intensity above 30000 Lx

As shown in Figure 4, the temperature increased linearly with the increase of light intensity above 30,000 lx. Fitting with the light intensity and temperature values in the corresponding time period, R2 > 0.98, indicated that there was a significant linear relationship between the increase of indoor temperature and light in the sunken solar greenhouse. Temperature has a significant effect on plant photosynthetic enzyme activity, transpiration rate and stomatal conductance values. Establishing the relationship between indoor temperature and light intensity can reduce the effect of temperature on photosynthetic enzymes by setting automatic shading curtains at the highest part of the stereoculture planting in advance when the temperature was too high at noon and plant photosynthesis was reduced.

Variation of transpiration rate of plants with time

East 1 and West 1 positions refer to the height of 1.8 m from the indoor floor; East 2 and West 2, East 3 and West 3, East 4 and West 4 positions refer to the height of 1.4 m, 1.0 m and 0.6 m from the indoor floor. since the strawberries in East 1 and West 1 positions were located at the same A-frame height of 1.8 m, and the strawberry plants in East 1 and West 1 were spaced 15 cm apart. Therefore, the greenhouse temperature and light environment of strawberries in the east and west positions were the same.

From Figures 3 and 5, the transpiration rate and stomatal conductance of strawberry at 1.8 m height during 8:50-17:00 were as follows: from 8:30 to 12:00, the transpiration rate tended to increase, with the maximum transpiration rate of 0.0086 μmol $m^{-2}s^{-1}$, and the temperature of the corresponding measurement point in the greenhouse increased gradually with time in the form of a curve, with the maximum value of 27.6°C and the minimum value of 10.2°C.

The overall trend of transpiration rate in the time period of 12:00-14:00 was decreasing, and the maximum value of temperature at 1.8 m height in the greenhouse was 33°C and the minimum value was 25°C, and the value of stomatal conductance in this time period was also gradually decreasing, and the strawberry leaves appeared "lunch break" due to the high temperature.

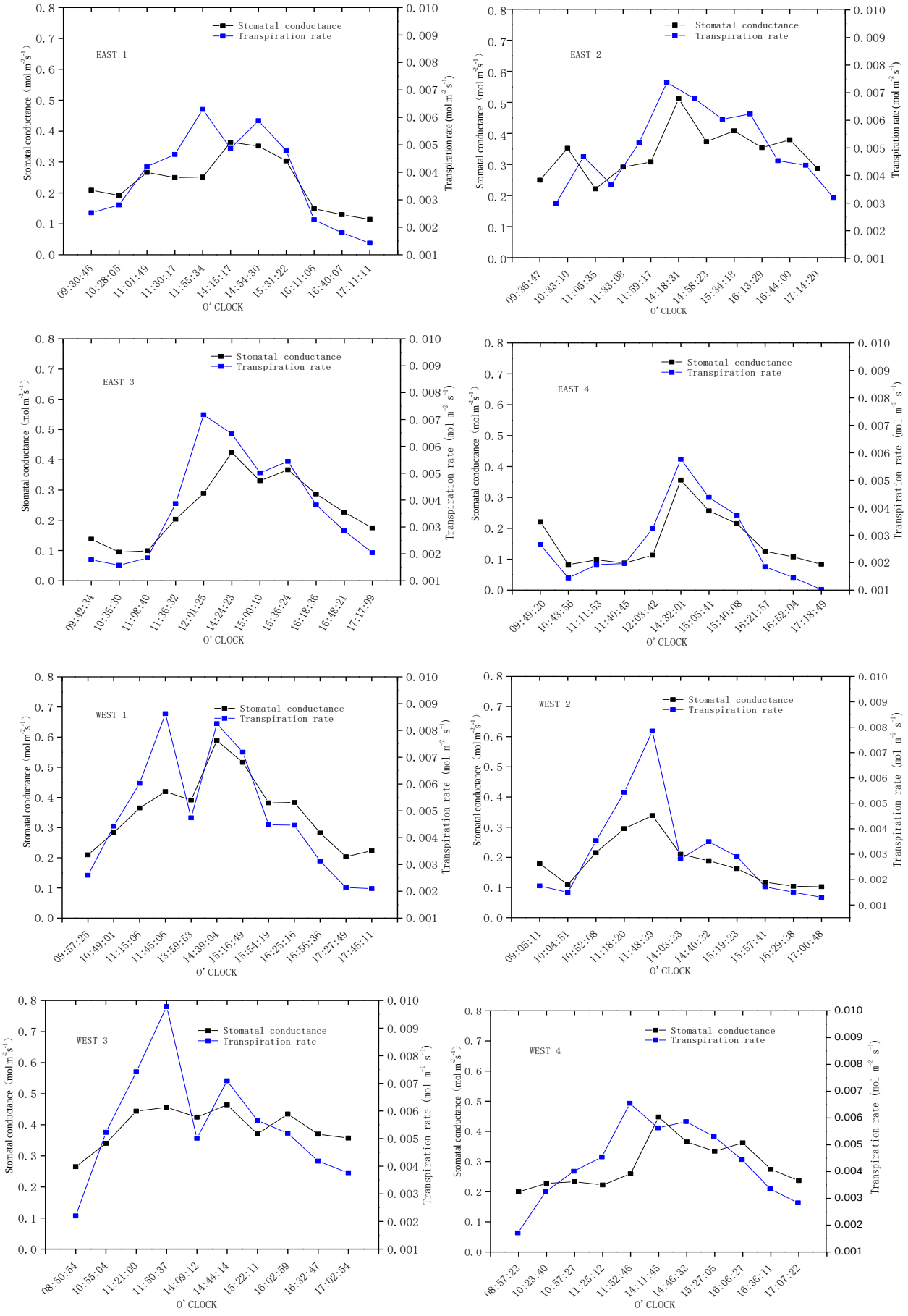

Fig. 5 - Variation curves of transpiration rate and stomatal conductance of strawberry leaves at different heights with time

As it can be seen, the period from 14:00 to 17:09 marked the decrease of the temperature curve in the greenhouse room, and this is caused by the gradual weakening of solar radiation, the heat exchanged between indoor air and outdoor was greater than the heat absorbed by solar radiation, and the transpiration rate and stomatal conductance values of plants gradually decreased during this period; after 17:30, the transpiration rate was maintained at about 0.002 μmol $m^{-2}s^{-1}$, which was more than 40 times different from the maximum transpiration rate, and the difference between the temperature value at this time and the highest temperature value of the same measurement point in a day was 14.3 times. The difference between the temperature value and the highest temperature value of the day at the same measurement point was 14.3°C.

The transpiration rates of strawberry leaves at 0.6 m (West 4), 1.0 m and 1.4 m heights from the indoor floor were the same as those at 1.8 m, but the transpiration rate of strawberry leaves at 0.6 m (West 4) decreased less during the 12:00-14:30 time period, with a maximum of 0.006 μmol $m^{-2}s^{-1}$ and a minimum of 0.003 μmol $m^{-2}s^{-1}$, while the transpiration rate of strawberry leaves at 1.8 m was 0.009 μmol $m^{-2}s^{-1}$ and 0.004 μmol $m^{-2}s^{-1}$. This was due to the fact that the maximum temperature at 0.6 m (West 4) was 24°C and the stomatal conductance did not decrease, so the indoor temperature at this height did not exceed the suitable temperature for photosynthesis of strawberry and the plant did not take a "lunch break", so the transpiration rate at 0.6 m (West 4) was less variable.

The values of transpiration rate and stomatal conductance of strawberry measured at 0.6 m (East 4) did not decrease in the time period of 12:00-13:30, which was due to the change of solar azimuth in this time period, while the strawberry leaves at the lower east position of 0.6 m were in the shade position due to the shading of the adjacent A-frame plants at this time, and the actual temperature was lower, and the temperature values did not make the stomatal conductance decrease, and the strawberry leaves did not show the phenomenon of "lunch break".

It could be seen that: the transpiration rate of strawberry leaves in stereo planting had a greater relationship with the temperature at the corresponding height in the same time period, while the vertical temperature gradient difference in the greenhouse was larger, which had a greater effect on the transpiration of plants.

Variation of stomatal conductance and photosynthetic rate of plants with time

In Figs. 3 and 6, it is showed that the air temperature at different heights increased curvilinearly with time from 8:00 to 12:00, and the photosynthetic rate of strawberry leaves at different heights increased with stomatal conductance from 8:30 to 11:30, which was due to the increase of stomatal conductance, which increased the transport of CO_2, the raw material of photosynthesis, and the photosynthetic rate of each measurement point gradually increased as the light intensity gradually increased.

However, between 11:30-12:00, the photosynthetic rate of strawberry leaves at both the East 1 and West 1 positions were 1.8 m from the indoor ground height, and the photosynthetic rate of strawberry leaves at both the upper east and west positions showed a decreasing trend, and the lowest value of air temperature at the indoor stereoscopic planting height of 1.8 m during this time was 27°C, and the high temperature would inhibit the activity of plant photosynthetic enzymes, so the photosynthetic rate decreased. During 12:00-15:00, the photosynthetic rate of strawberry leaves at different heights decreased during some time, and the outdoor light intensity gradually increased and the stomatal conductance increased, but the photosynthetic rate decreased, because the photosynthetic enzyme activity was affected by the high temperature and the photosynthetic rate decreased.

At 11:45, the air temperature at 1.8 m from the indoor floor height was 25.5°C, at 11:55, the air temperature at 1.8 m from the indoor floor height was 26.5°C, at this time the temperature increased by 1°C, while the transpiration rate decreased by 2.33 μmol $m^{-2}s^{-1}$ and photosynthesis decreased by 1.41 μmol $m^{-2}s^{-1}$; when the indoor temperature was higher than 25.5°C, it would inhibit the photosynthesis of the plant. From 11:45 to 14:00, the air temperature at a height of 1.8 m from the indoor floor increased from 25.5°C to 33.3°C and then decreased to 25.4°C, but the transpiration rate and photosynthesis rate of strawberry leaves at the same height during this time period showed a decreasing trend, with transpiration rate decreasing by 3.89 μmol $m^{-2}s^{-1}$ and photosynthesis rate decreasing by 3.95 μmol $m^{-2}s^{-1}$. Different temperatures affected the quality of strawberry plants, and the photosynthetic and transpiration rates of the plants were inhibited at temperatures above 25.5°C.

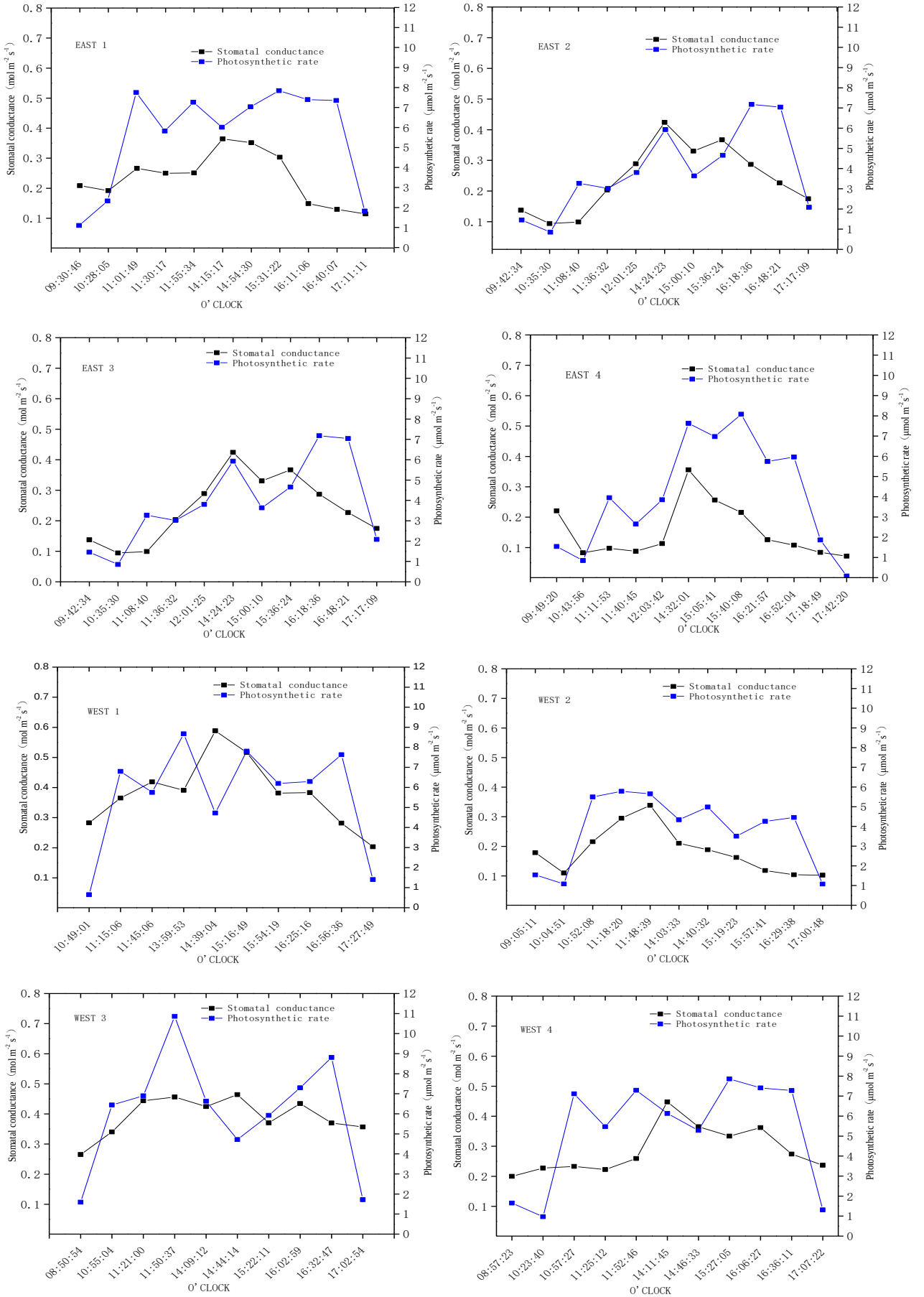

Fig. 6 - Variation curves of photosynthetic rate and stomatal conductance of strawberry leaves at different heights with time

Between 15:00 and 16:00, the photosynthetic rate increased briefly because the enzyme activity was not affected by the high temperature when the indoor temperature was below 25°C and the enzyme activity was not affected by the high CO_2 concentration outside, which led to an increase in photosynthetic material. The photosynthetic rate decreased between 16:00 and 17:30 because the intensity of outdoor light decreased, resulting in lower photosynthetic rate. Strawberry plants at East 1 and West 1 locations were at the same height with a horizontal plant spacing of 15 cm, approximating the same light conditions and the same temperature conditions.

When the outdoor weather was sunny in winter, the indoor air temperature values at different heights showed a trend of rising and then falling with time, and the temperature change was related to the light intensity, while the photosynthetic rate, transpiration rate and stomatal conductance values of strawberry leaves at different heights in the same time period were related to the temperature, and when the temperature was higher than 25.5ºC, it would reduce the transpiration rate and photosynthetic rate of strawberry leaves. Therefore, the study of indoor temperature can provide timely information about the photosynthetic properties of plants.

CONCLUSIONS

The transpiration rate and photosynthesis rate of strawberry leaves were different in different time periods, and were related to the indoor light and temperature. The following conclusions were drawn:

1) When the temperature value at a certain height in the room was above 25.5°C for a certain period of time, the photosynthetic characteristics of the plant were suppressed regardless of the change in the temperature value during this time period.

2) There was variability in temperature at different heights, and when indoor light reached a certain value, there was a linear relationship between indoor light and temperature at different heights.

ACKONWLEDGMENTS

I am very grateful to Prof. Shuangxi Wang, Prof. Junlin He and Associate Prof. Zhonghua Liu. I am very grateful to the College of Urban and Rural Construction for their help during the experiment and to Shanxi Agricultural University for the PhD start-up costs (231258040216003).

REFERENCES

[1] Ahemd H.A., Al-Faraj A.A., Abdel-Ghany A.M. (2016). Shading greenhouses to improve the microclimate, energy, and water saving in hot regions: A review [J]. *Scientia Horticulturae.* 201: 36–45.

[2] Chao Chen, Yin Li, Na Li et al. (2018). A computational model to determine the optimal orientation for solar greenhouses located at different latitudes in China. *Solar Energy*.165:19-26.

[3] Cheng Weiwei, Liu Zhonghua (2022). Study on the change rate of the indoor temperature of a sunken solar greenhouse [J]. *INMATEH - Agricultural Engineering*. 68:119-126 https://doi.org/10.35633/inmateh-68-12

[4] Chuan Xu, Shi-Mei Song, Xue-Jun Zheng et al. (2015). Effect of nighttime root temperature on the growth outcome of strawberry in sunshine greenhouse（夜间根基温度对日光温室草莓生长结果的影响）*Chinese fruit trees*, 4.

[5] Di Xie, Hui Su, Tianlai Li et al. (2010). Effect of top ventilation on the temperature and humidity in a solar greenhouse (顶部通风对日光温室内温湿度的影响). *Jiangsu Agricultural Science,* 6:573-575.

[6] Ge Jiankun, Xin Qingcong, Gong Xuewen, et al (2021). Effects of greenhouse ventilation and water control conditions on water consumption characteristics and yield of tomato [J]. *Transactions of the Chinese Society of Agricultural Engineering*, 37(15): 204-213.

[7] Huanhuan Lv, Yuanyi Niu, Man Zhang et al (2021). Trend analysis of light intensity and air temperature and humidity in daylight greenhouse (日光温室光照强度与空气温湿度变化趋势分析). *Journal of Agricultural Machinery* 52:410-417.

[8] Minghan YU, Guanglei Gao, Guodong Ding et al (2015). A review of plant body temperature studies (植物体温研究综述). *Journal of Ecology*, 34(12):3533-3541.

[9] Mittler, R., Zandalinas, S.I., Fichman, Y. et al (2022). Reactive oxygen species signalling in plant stress responses [J]. *Nat. Rev. Mol. Cell Biol.* 23:663–679.

[10] Phunchok Angmo, Nawang Phuntsog, Desyong Namgail et al. (2021) Effect of shading and high temperature amplitude in greenhouse on growth, photosynthesis, yield and phenolic contents of tomato [J]. *Physiol Mol Biol Plants*. 27(7):1539–1546.

[11] Raja, V., Qadir, S.U., Alyemeni, M.N. et al. (2020). Impact of drought and heat stress individually and in combination on physio-biochemical parameters, antioxidant responses, and gene expression in *Solanum lycopersicum* [J]. 3 *Bioteh*. 10(5): 208.

[12] Ruolin Zheng, Wei Yang, Zhuqing Liu. (2023). Numerical simulation of hygrothermal characteristics of daylight greenhouses with different ventilation forms (不同通风形式日光温室湿热特性的数值模拟). *Journal of China Agricultural University*. 28(03):140-150.

[13] Shamshiri R.R., Jones J.W., Thorp K.R. et al. (2018). Review of optimum temperature, humidity, and vapour pressure deficit for microclimate evaluation and control in greenhouse cultivation of tomato: a review [J]. *Int. agrophysics*. 32.

[14] Youfeng Zheng, Jialan Chen, Fang Xiao. (2022). Effects of different temperatures on photosynthetic properties and photosynthesis-related gene expression in amaranth (同温度对苋菜光合特性及光合作用相关基因表达的影响). *Journal of Plant Resources and Environment.* 31(5):50-57.

FAULT PREDICTION MODEL OF CORN GRAIN HARVESTER BASED ON SELF-CODING NEURAL NETWORK
/
基于自编码神经网络的玉米籽粒收获机故障预测模型

Xin WANG, Guohai ZHANG*), Jia YAO, Jitan LIAN, Xining YANG [1]
School of Agricultural Engineering and Food Science, Shandong University of Technology, Zibo 255091, China
Tel: +86-15965534882; E-mail: guohaizhang@163.com
DOI: https://doi.org/10.35633/inmateh-70-22

Keywords: *corn grain harvester, historical failure data, failure prediction, self-coding neural networks*

ABSTRACT

The corn grain harvester serves as an example of complex farming machinery with a condition monitoring system that collects a lot of working condition data, making it challenging to identify the true change pattern due to the data coming from the equipment in various states. Firstly, the overall structure of the corn grain harvester is analysed, and the common causes and mechanisms of corn grain harvester failures are analysed, leading to the cutting table as the main research object; Secondly, the data is organized and pre-processed by collecting historical fault data as well as real-time fault information from corn grain harvesters. The processed data is trained using a self-coding network to extract internal features related to fault causes, based on feature fusion and prediction networks to construct a mapping between fault causes and fault phenomena; Finally, the future failure phenomena of the corn grain harvester are predicted according to different failure causes. The simulation analysis results show that the self-coding neural network fault prediction model can better predict the occurrence probability and types of faults, and provide data support for fault maintenance and decision making of agricultural machinery.

摘要

以玉米籽粒收获机为代表的复杂农机设备状态监测系统记录了大量的工作状态数据，由于数据来源于不同状态的设备导致其真实变化规律难以发现造成了传统故障预测模型准确率较低，因此我们提出了一种基于自编码神经网络的玉米籽粒收获机故障预测模型。首先分析了玉米籽粒收获机的整体结构，对玉米籽粒收获机故障的常见成因与机理进行分析，引出割台为主要研究对象；其次通过收集玉米籽粒收获机的历史故障数据和实时故障信息，对数据进行整理和预处理。将处理后的数据训练自编码网络，提取故障原因之间的内部特征。基于特征融合和预测网络来构建故障原因与故障现象间的映射；最后根据不同故障原因预测未来玉米籽粒收获机的故障现象。仿真分析结果表明，自编码神经网络故障预测模型能够更好的预测发生的故障概率及种类，为农业机械的故障维修与决策提供数据支持。

INTRODUCTION

Corn grain harvesters are very important equipment in the agricultural industry, and they are widely used in corn harvesting on farmland to help farmers improve harvesting efficiency. Research studies have shown that the direct factors inducing the failure of corn grain harvesters are mainly blockage due to excessive feeding and indirect factors mainly include the problem of parts damage due to aging of parts accumulated over time *(Shi, 2022)*. With the advancement of various instrumentation technologies, more harvester failure data were obtained, and most Chinese machinery companies collected and collated the causes of corn grain harvester failures, and used the collected failure cause data to analyse and improve the reliability of corn grain harvester, which has important engineering practical application value for the failure rate of corn grain harvester.

The approach to failure prediction has evolved rapidly over the last few decades. Firstly, the failure prediction techniques originated from the evolving aerospace systems. Initially, scholars used a series of dynamic equations as the mathematical theoretical basis to develop model-based prediction methods to reason about the mapping relationship between monitoring parameters and equipment failures, and this method of building an accurate model structure to simulate the pattern between parameter changes and equipment performance has many shortcomings.

[1] *Xin Wang,M.S. Stud. Eng.;Guohai Zhang, As. Ph.D. Eng.; Jia Yao,M.S. Stud. Eng.; Jitan Lian,M.S. Stud. Eng.; Xining Yang,B.S. Eng.*

Some scholars *(Xu et al., 2011)* studied the mechanical wear period of CNC machine tools according to the groove curve law, and then established a mathematical model of non-flush Poisson process. Some scholars *(Liu et al., 2015)* obtained the mileage data corresponding to the moment of failure through the whole vehicle durability test, and based on the stochastic process theory, the mathematical model of the failure process of the test vehicle was established with a non-simultaneous Poisson process for reliability evaluation. By analysing the law of equipment failure occurrence and building the corresponding mathematical or physical model to deeply describe the equipment failure evolution mechanism model is more complex and poorly generalized, and it needs to consider the characteristics of different systems and perform task specificity in practical application, which is not universally applicable. In view of the drawbacks of poor generalization and small applicability of the analytical model, researchers have incorporated expert experience and fuzzy logic into fault prediction to form a knowledge-based prediction method, and some scholars *(Liu, 2023)* designed an expert system based on a diagnostic rule reasoner and constructed an experimental environment with the help of AMESim (Advanced Modeling Environment for performing Simulation of engineering systems) hardware to simulate various faults of the robotic arm by injecting different fault signals. The experimental data analysis proves that the designed fault diagnosis expert system can efficiently and accurately detect the faults of the robotic arm. The study improves the generalization of the analytical model by introducing the expert system and fuzzy logic reasoning, which can characterize the equipment fault severity and forecast the possible fault situations in time, and has a greater reference value for the state inference classification of the corn grain harvester in this paper, but the expert system is a rule base constructed by static knowledge, which has certain limitations and cannot express the failure process in time scale.

With the progress of communication technology, a large amount of industrial data can be uploaded to the platform database in time. For example, the corn grain harvester condition monitoring system records a great deal of working condition data, including machine operation status, sensor data, temperature vibration pressure, etc. *(Lian et al., 2022)*. Researchers have continuously modified the model by analysing the data and have proposed a data-driven approach based on it. Initially, signals such as equipment currents and vibrations were converted to the frequency domain range by introducing Fourier transforms to extract the features associated with faults in them and map them to the maintenance and repair of equipment. The development of communication technology laid the foundation for the later development of artificial intelligence.

In order to minimize downtime maintenance time through artificial intelligence learning algorithm research for fault prediction and feature extraction technology development has brought a new idea. Some scholars *(Gu et al., 2022)* proposed a fault diagnosis method of mining excavator engine based on an improved fruit fly optimization algorithm (IFOA) optimized RotGBM. RotGBM is generated by combining Rotation Forest and Light Gradient Boosting Machine (LightGBM), and a new fault diagnosis model is constructed and applied the method to mining excavator engine fault diagnosis with good fault diagnosis effect. Some scholars *(Zhao et al., 2021)* Zhao Hu, (2021). Fault prediction of key components of wind turbine based on BP neural net. *Power System Engineering*, Vol. 37, No. 2, 21-22.used back propagation (BP) neural network fault prediction model to predict the operating parameters of key components of wind turbines, and has good fault prediction effect on gear box bearing temperature. Some scholars *(Zhou et al., 2015)* used the learning method of support vector machine (SVM) to model the gas line failure of gas circuit and verified it with large sample data. Compared with the traditional way of human calculation to deal with faults, the deep learning model can give full play to the advantages of computer arithmetic, through a large amount of data training, gradually reduce the model prediction error, and continuously optimize the prediction results.

In this paper, a fault prediction of corn grain harvester is proposed. The model is a nonlinear mapping between the historical fault cause data and the fault phenomena of corn grain harvester established by self-coding neural network. The model is designed to accurately predict the type of corn kernel harvester failure based on the given fault data. At the same time, the data of failure cause of corn grain harvester were self-coded and analysed, and the internal relationship between the fault cause and maize harvester was obtained.

MATERIALS AND METHODS

Structure and fault analysis of corn seed harvester

As shown in the Fig. 1, the corn grain harvester consists of a cutting table, a lift, a detaching drum, a seed recovery device, an engine, a cab, and a grain bin. The harvesting process includes picking, threshing, separating, scavenging and conveying *(Li, 2016).* When the corn seed harvester is at work, the corn plant is separated from the stalks by cutting the ears through the cutting platform, and the lifters carry the ears into the detaching drum and finally send them to the grain bin *(Li, 2014).*

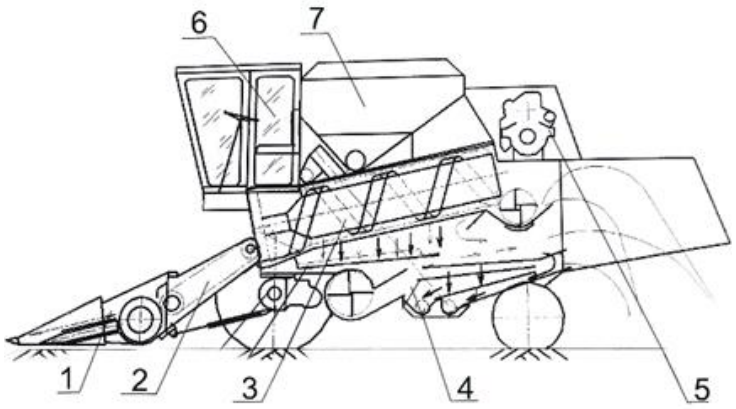

Fig. 1 – Structure of the whole machine of corn grain harvest
1. Cutting platform; 2. Lifting conveyor; 3. Threshing and separation apparatus with axial flow; 4. Grain recovery device; 5. Engine; 6. Cab; 7. Grain bin;

The corn grain harvester cutting table has the role to complete the cutting of corn stalks, clamping and conveying the cob, picking the cob, force feeding the stalk to the chopping mechanism, feeding power to the conveying unit, and providing a mounting platform for the conveying unit, chopping unit, and throwing unit. The structure of the corn grain harvester cutting table is shown in Fig. 2 which mainly includes the grain splitter, the spike picking unit, the conveying churn, the cutting table frame, and related transmission parts and lifting cylinders. The spike picking unit is the main working part of the cutting table, as shown in Fig. 3.

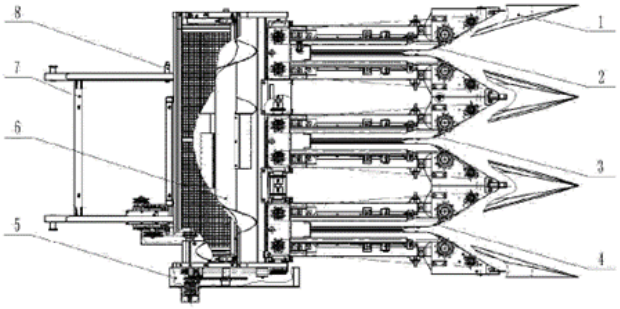

Fig. 2 – Cutting table structure diagram
1. Divider; 2. First unit body; 3. Second unit body; 4. Third unit body; 5. Cutting table rotation; 6. Conveyor churn; 7. Cutter frame; 8. Cutting table structure diagram

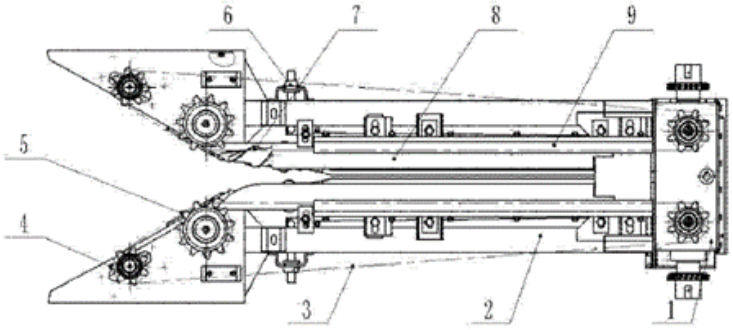

Fig. 3 – Unit structure
1. Spike tine box; 2. Spike rack; 3. Sprocket chain; 4. Tensioning sprocket; 5. Tiller chain driven wheel; 6. Stem pulling roller clearance adjustment handle; 7. Stem pulling roller; 8. Spike plate; 9. Cutting knife

The working process of the cutting table is that the corn plants are first divided by the grain splitter, and under the combined action of a set of paddle chains, the corn plants in front of the machine are guided to the stalk pulling rollers, fed into the working gap between the two stalk pulling rollers, and the ears are picked under the pulling force of the stalk pulling rollers and the blockage of the picking plate, and the ears are conveyed by the paddle chains, which pass the ears to the conveying churn and into the elevator. The rest of the picked ears of stems are drawn down for crushing.

There are many types of corn grain harvester failures, and the cutting platform is a fault-prone part of the corn grain harvester, the causes of failure are relatively complex, and the failure rate of the cutting platform accounts for a high percentage of the whole machine failure. The common failure of the cutter includes blockage of cutter parts, broken and aged parts, etc. *(Zhou, 2021).* The main reason for the above-mentioned failure of the cutter is the improper operation of the employees, which makes the feeding volume too large. The continuous high-intensity work of corn grain harvester makes the parts accelerate deformation and aging, making the harvest quality worse. Other failure mechanisms include inappropriate tension of the chain causing jumping or too tight making the chain and chain teeth wear seriously. The mismatch between the speed of the working parts and the forward speed of the machine can also cause a reduction in harvesting quality, blockage of the cutting table parts and excessive breaking of the corn kernels.

Therefore, this paper takes the corn grain harvester cutting table as the main fault research object, and predicts and classifies its faults.

Methodology Overview

The proposed method framework as shown in Fig. 4, which combines the selection of the fault phenomena of the corn seed harvester and the expected achievement of the fault prediction, is used to partition the difficult to learn by machine recognition data matrix into training and test segments, and the training data are used to train the self-coding neural network model to build a multi-scale fault prediction network *(Xu at al., 2020)*. The test dataset was validated; a fully connected layer with SoftMax classifier was used thereby establishing a mapping of fault data to corn seed harvester faults.

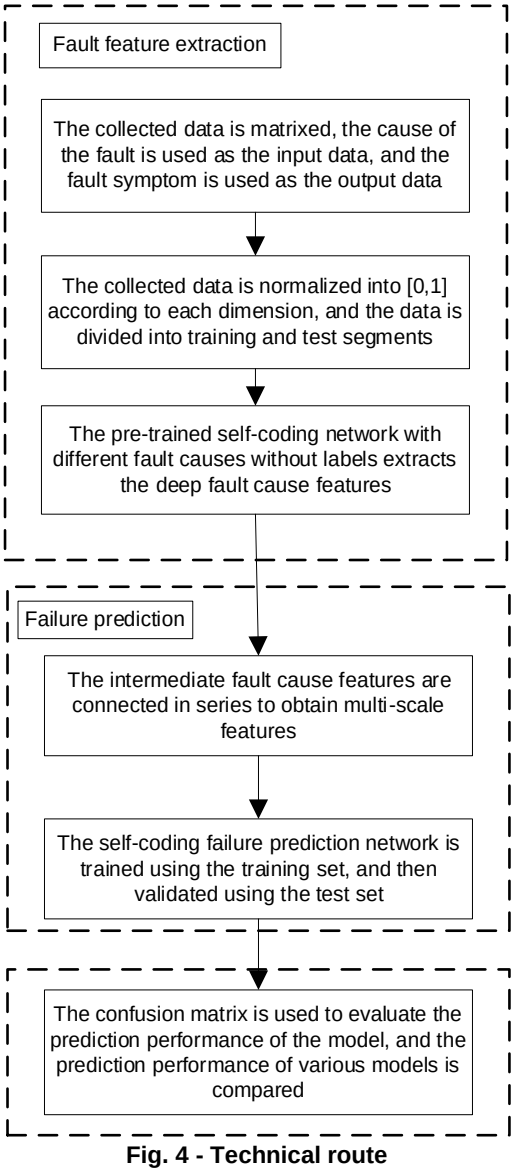

Fig. 4 - Technical route

Self-coding Network-based fault prediction of corn grain harvester

The research object of this paper is the corn grain harvester, through the field investigation of Shandong Dongfeng Agricultural Machinery Co., Ltd., combined with the historical fault database of the harvester obtained by some scholars *(Yang et al., 2022)* through data mining. Take this as the object of study, because the corn grain harvester is a large and complex mechanical equipment, the technician cannot collect all the status information, and the failure causes of the corn grain harvester are varied, this paper selects some fault causes and phenomena of the header for research, through the collection of a large number of historical faults in the corn grain harvester, the cause and symptom data determine the data types of the input and output, as shown in Table 1.

Table 1

Failure matrix

Sequence 1	Cause of fault (input data)	Sequence 2	Fault phenomenon (output data)
1	Excessive tool clearance	1	Cutter winding
2	Too small tool clearance	2	Harvest chain winding
3	The cutting platform rack is too high	3	Clogged rollers
4	The cutting platform rack is too low	4	Bridge blockage
5	The rolling speed is too high	5	Uneven chopping length
6	The rolling speed is too low	6	Stalk guide groove pulling roller is entangled by the plant
7	The chain tension is not appropriate	7	The churn clutch is disengaged, and the churn is not rotating
8	Chain deformation or wear	8	Stem churn conveyor is clogged
9	The speed of the working parts does not match the forward speed of the machine	9	Stem leaves accumulate in front of the stem churn
10	Unstable lifting speed of working parts	10	Corn grain broken too much
11	Cutting table row spacing and crop row spacing are not in line		
12	Large feeding volume		
13	Belt slippage		
14	Tool breakage		
15	Parts aging		
16	Loose parts		
17	Crop collapse		
18	Debris winding around the stem puller		
19	Fields weeds are unusually high		
20	Improper driving operation by staff		

As can be seen from Table 1, this paper uses 20 failure causes as input data and the resulting 10 failure phenomena as output data for the failure prediction of corn grain harvesters. In order to make the failure causes and failure phenomena data recognized by the computer, this paper constructs a matrix; the failure causes are input in a 1×20 matrix and output in a 1×10 matrix.

Pre-processing of database data, the collected historical fault information as well as database data are pre-processed, including the removal of outliers, normalization processing, feature dimensionality reduction, etc., to reduce the interference of noise to the model. For example, the size of the feed is scored by experts, the rest of the data are processed uniformly, and finally the data of each dimension collected is normalized, and the expression formula of normalization is:

$$x_{n'} = \frac{x_n - x_{min}}{x_{max} - x_{min}} \quad (1)$$

For example: $x = [x_1, x_2, \cdots x_n]$ for corn harvester feeding amount of the data collection; After x for normalization of data; x_{max} and x_{min} for corn harvester is one of the biggest feed rate and minimum feed rate.

Self-coding neural network

Autoencoder (AE) is a deep learning technique for learning the hidden representation of data for data generation and dimensionality reduction *(Wang et al., 2022)*. The Autoencoder network consists of an encoder and decoder that learns the hidden representation by minimizing the input-output error *(Yu et al., 2020).* The encoder encodes the input data into a hidden representation and the decoder decodes the hidden representation into the output data.

Assuming the input data $\{A^{(1)}, A^{(2)}, \cdots A^{(n)}\}, A^{(i)} \epsilon R^n$, the self-coding network is trained unsupervised so that the encoding and decoding process makes the input data $A^{(i)}$ and the output data $B^{(i)}$ as identical as possible. A three-layer self-coding network structure contains an input layer, an implicit layer and an output layer as shown in Fig 5. The goal of the learning of the network is to approximate a constant function so that $A^{(i)} = B^{(i)}$. The corresponding coding and decoding process equation is expressed as:

$$h = f_c(A) = S(W_c A + d_c) \tag{2}$$

$$h = f_b(A) = S(W_b A + d_b) \tag{3}$$

$$B = f_e(A) = S(W_e A + d_e) \tag{4}$$

$$S(t) = \frac{1}{1+\exp(-t)} \tag{5}$$

Including f_c、f_b、f_e respectively encoding layer, hidden layer and decoding.

$S(t)$ as the Sigmoid activation function; W is the connection weight matrix; d is biased.

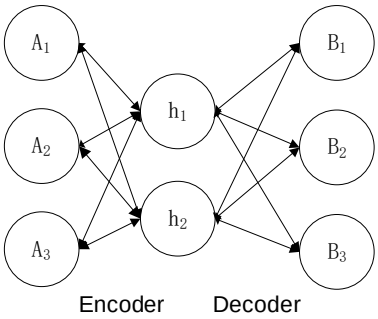

Fig. 5 - Three-layer autoencoding networks

In order to make the input data $A^{(i)}$ and the output data $B^{(i)}$ as identical as possible the cross-entropy error function is used to reconstruct the error $L(x, y)$ function *(Yan et al., 2023)* expressed as:

$$L(x,y) = -\frac{1}{n}\sum_{i=1}^{n}[x_i \ln y_i + (1-x_i)\ln(1-y_i)] + \frac{m}{2}\sum_{k=1}^{n_k}\sum_{j=1}^{s^l}\sum_{i=1}^{s^l+1}\left(W_{ij}^k\right)^2 \tag{6}$$

In the formula, $\frac{m}{2}\sum_{k=1}^{n_k}\sum_{j=1}^{s^l}\sum_{i=1}^{s^l+1}\left(W_{ij}^k\right)^2$ is a regular item, m as the attenuation coefficient of weight, each node weights between neurons for W_{ij}^k. By reducing the weight, overfitting is prevented when extracting deep features from self-coding.

The data selected in this paper have certain correlation, but the input data correlation features are not obvious. By using the fault causes as the input data for training, the deep feature relationships between the fault causes are extracted. The structure of multi-layer self-coding network contains several layers such as coding layer, feature transformation layer, and decoding layer. In this network, each layer consists of multiple neurons that are connected to each other to form a fully connected layer. Each neuron in the fully connected layer is connected to all neurons in the previous layer, and each neuron has a corresponding weight. These weights are used to convert the input data of the previous layer into the output data of the next layer. In this network, the Sigmoid activation function is used to map the output data of the fully connected layer to a range between 0 and 1 to produce probability distributions *(Lin et al., 2016)*.

These probability distributions can be used to represent the correlation between different features, thus helping the network for feature extraction and dimensionality reduction. As shown in Fig. 5, this paper uses a multilayer self-coding network. Input layer: for the dataset $x = [x_1, x_2, \cdots x_n]$ with n combined features, two coding layers are used for feature extraction and dimensionality reduction to obtain the dataset $\bar{x} = [\bar{x}_1, \bar{x}_2, \cdots \bar{x}_n]$. Feature exchange layer: deep feature mapping is extracted by feature transformation of the feature exchange layer data. Decoding layer: two decoding layers change the data into the resolution of the original signal. The network parameters are shown in Table 2.

In this paper, the two-layer coding layers and the two-layer decoding layers are used, and the network settings of each layer are shown in the Fig. 6.

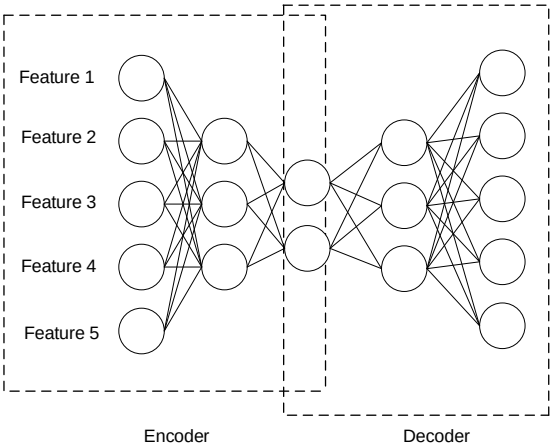

Fig. 6 - Basic structure of DAE

Among them, the two-layer coding layer performs feature extraction and dimensionality reduction on the data. The two-layer decoding layer reduces the original data type. In this paper, a total of 20 types of input data are taken, containing both 20 types of neurons. The input signal type differences are used to train the self-coding network using error functions so as to reconstruct the input signal to extract multi-scale features. The purpose of the self-coding network is to reconstruct the fault cause data to extract multi-scale features between fault causes. The self-coding network is trained by cross-entropy error function, considering that the input data are greatly influenced by the collection process and errors are unavoidable, making the network performance reduced. The self-coding network uses increasing noise perturbation to enhance the robustness of the network.

Table 2

Network parameter settings

One floor	two floors	three floors	four floors	five floors
{20,10}	{10,4}	{4,4}	{4,10}	{10,20}

Maize grain harvester fault prediction network

The internal feature relationships between the 20 causes of failure were obtained by the above feature extraction of the input data using a self-coding network but the phenomena of corn grain harvester failure could not be predicted. Next, the mapping between the causes of corn grain harvester failure and the phenomena of failure was established through fault prediction based on a self-coding neural network.

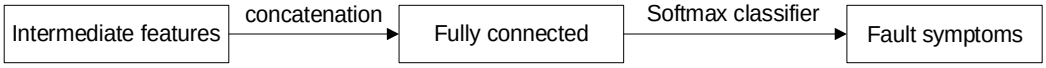

Fig. 7 - Prediction networks of Corn grain harvester

The maize seed harvester fault prediction network diagram is shown in Fig 7, for the constructed maize seed harvester fault prediction network firstly extracts the intermediate features of the cause of the maize seed harvester fault using a self-coding network, secondly concatenates the intermediate features to get the multi-scale features then uses a fully connected layer and a SoftMax classifier to get the phenomenon of the fault and the corresponding probability.

The 20 fault data outputs in the input table of the corn seed harvester fault prediction network are 10 fault phenomena, namely, cutter winding, harvest chain winding, clogged rollers, bridge blockage, uneven chopping length, stalk guide chute pulling stalk roller tangled by plant, disengaged churn clutch, churn not rotating, stalk churn conveyor clogged, stem leaves accumulate in front of the stem churn, and corn grain is broken too much. The coding and decoding layers of the fault prediction network use a self-coding network, and the fully connected part is trained using classification loss.

Simulation experiment

In order to verify the accuracy of self-coding neural network for fault prediction of corn grain harvester the corn grain harvester was tested in simulation experiments, the corn grain harvester was used as the test object for simulation experiments, the test platform was MatlabR2022a simulation software, and the method of fault prediction involved in this paper was input into the simulation software. A total of 500 sets of data were collected in this paper of which 450 sets were used as the training set and the remaining 50 sets were used as the test set. The historical failure data of the existing corn grain harvester was collected through research and data mining techniques to build a database. After normalizing the data, a self-coding network is used to mine the internal characteristics of the cause of the failure of the corn grain harvester, and a failure prediction network is used to predict the failure phenomena caused by the cause of the failure.

Establishing a confusion matrix and verifying the performance of corn grain harvester failure prediction by confusion matrix *(Wang et al., 2021).*

Table 3

Confusion matrix

Confusion Matrix		True Value	
		Positive	Negative
Predicted value	Positive	TP	FP
	Negative	FN	TN

Each column in Table 3 indicates the predicted category, and the numbers of data in each column indicates the number of data predicted to belong to that category. Each row indicates the real category to which the data belongs, and the numbers of data in each row indicates the number of instances of data in that category. The value in each column indicates the number of instances of the actual data predicted to belong to that category. TP, TN, FP, and FN in the table are the first-level base indicators of the confusion matrix with the following concepts: TP is the probability that a positive category is predicted to be positive; FP is the probability that a negative category is predicted to be positive; FN is the probability that a positive category is predicted to be negative; TN is the probability that a negative category is predicted to be negative. The formula and meaning of the confusion matrix are shown in Table 4.

Table 4

Equations and significance of confusion matrix

Abbreviation	Formula	Implication
Recall	$R = \frac{TP}{\lvert TP + FN \rvert}$	Model predicted positive class weights in all results where positive class is positive.
Precision	$P = \frac{TP}{\lvert TP + FP \rvert}$	Weight of model prediction positive class among all results with positive model prediction class
F1 score	$F = 2\frac{PR}{R + P}$	Coordinated average of model accuracy and recall, which reflects the stability of the model
Fowlkes-Mallows index	$FM = \sqrt{\frac{TN}{TN + FP} * \frac{TP}{TP + FN}}$	The geometric mean of the correct results of the classification samples, which can evaluate the overall classification performance of the algorithm.

RESULTS

Analysis of fault prediction results

In this paper, the final prediction of failure was made by comparing the probability of occurrence of the 10 conditions, i.e., cutter winding, harvest chain winding, clogged rollers, bridge blockage, uneven chopping length, stalk guide chute pulling stalk roller tangled by plant, disengaged churn clutch, churn not rotating, stalk churn conveyor clogged, stem leaves accumulate in front of the stem churn, and corn grain is broken too much. Fig. 8 shows the prediction results obtained by testing data from two different scenarios using the algorithm in this paper.

Fig. 8a shows that the probability of occurrence of the 10 fault phenomena for the given operating state of the fault cause condition is 2.7%, 28.17%, 48%, 12.33%, 3.54%, 1.9%, 2.03%, 0.32%, 0.14%, and 0.87%, respectively, which indicates that the probability of corn seed harvester cutter winding is the highest in the current state. Therefore, the output of the fault prediction is corn seed harvester cutter winding. Compared to the actual situation, the predicted results match the actual occurrence of the fault. Fig. 8b shows that the probability of occurrence of the 10 fault phenomena for the fault cause conditions of the given operating condition is 49.94%, 8.14%, 7.93%, 30.06%, 1.25%, 0.15%, 0.49%, 1.04%, 0.32%, and 0.68%, respectively, which indicates that the probability of bridge blockage and cutter winding of the corn seed harvester in the current condition is the highest. Therefore, the output of the fault prediction is that the corn seed harvester has overbridge blockage and cutter tangle. Compared with the actual situation, the predicted results match with the actual occurrence of faults. This shows that the prediction results of the self-coding neural network are consistent with the actual situation.

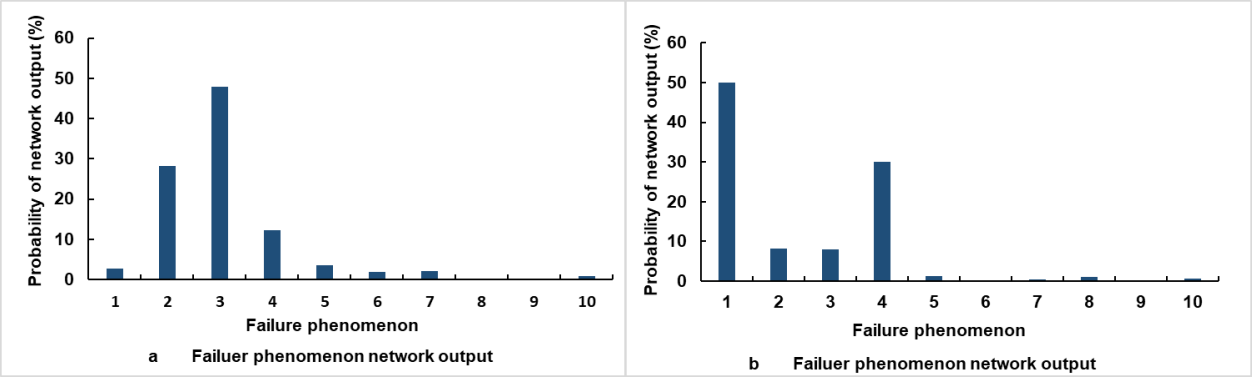

Fig. 8 - Output results of fault phenomenon networks with different data

a-Failure phenomenon network output; b-Failure phenomenon network output;

Algorithm comparison

To verify the effectiveness of the self-coding neural network algorithm, the algorithm was compared with the traditional self-coding network support vector machine classification, sparse self-coding, and Bayesian classification algorithms, using the same training data and test data in order to ensure the accuracy of the experiment. The prediction accuracy of the four models is shown in Table 5. From the table, it can be seen that the correct prediction of corn seed harvester faults by the self-coding neural network outperformed the other fault prediction models. Thus, it shows that the prediction results of the self-coding neural network have a greater improvement using multi-scale feature representation can improve the prediction accuracy of the network.

Table 5

Identification results of different models

Model	Accuracy rate	F	FM
Self-coding network	0.8668	0.8364	0.8472
Support vector machine	0.8507	0.8035	0.7963
Sparse self-coding network	0.9032	0.9079	0.9107
Bayesian classification algorithm	0.8319	0.8632	0.8768
Self-coding neural network	0.9384	0.9476	0.9197

CONCLUSIONS

In this paper, the cause of the fault is matrices, so that the computer can recognize and learn fault data better. Through a self-programmed network, the relationship between the fault causes can be understood, which can lead to a single failure phenomenon or multiple faults, so as to better explore the relationship between failure phenomena fault causes and failure phenomena, and to a certain extent predict the failure of corn grain harvester.

The shortcoming of this paper is that the limited data cannot predict the occurrence of malfunction to some extent, which provides new ideas for failure prediction, relevant references for the health management and maintenance of agricultural machinery, and new ideas for the development of corn grain harvester reliability.

A fault prediction model of corn grain harvester based on self-coding neural network is designed and simulation experiments are performed. Experimental results show that the error is less than a certain amount in different iterations of the test. Experimental results show that the proposed fault prediction model can not only improve the accuracy of prediction, but also reduce the time of fault repair and provide data support for the fault repair and reliability of agricultural machinery.

ACKNOWLEDGEMENT

The work was supported by the High Efficiency and Low Loss Single Longitudinal Axial Flow Threshing and Separation Technology and Development of Intelligent Flexible Threshing Device, (Grant No.2021YFD200050204), and the Development of Intelligent Multifunctional Wheat Corn Grain Combine Harvester, (Grant No.2016YF026).

REFERENCES

[1] Shi Lichun, (2022). The use of corn combine harvester points and maintenance methods (玉米联合收获机的使用要点与维修方法). *Agricultural Machinery Using & Maintenance*, No. 03, 82-84.

[2] Xu Binbin, Yang Zhaojun, Chen Fei et al. (2011). Reliability model of CNC machine tools based on non-homogenous Poisson process (非齐次泊松过程的数控机床可靠性建模). *Journal of Jilin University* (Engineering and Technology Edition), Vol. 41, No. S2, 210-214.

[3] Liu Zhen, Chen Zhen, Shi Weicheng, (2015). Evaluation of vehicle durability test reliability based on non-homogeneous Poisson process and fuzzy theory (基于非齐次泊松过程及模糊理论的整车耐久试验可靠性评价). *Machinery*, Vol. 42, No. 08, 53-57.

[4] Liu Wen, (2023). Optimal design of manipulator fault diagnosis expert system based on inference engine (基于推理机的机械臂故障诊断专家系统优化设计). *Hydraulics Pneumatics & Seals*, Vol.43, No. 02, 03-06.

[5] Lian Yi, Gong Shaojun, Sun Meiyan, (2022). Sampling box with damper for grain condition monitoring device of combine harvester (联合玉米收获机谷物状态监测装置采样盒及其减振器). *Chinese Hydraulics & Pneumatics*, Vol. 46, No. 4, 71-78.

[6] Gu Qinghua, Sun Wenjing, LI Xuexian, (2022). Fault diagnosis of mining excavator engine based on IFOA-RotGBM (基于 IFOA-RotGBM 的矿用挖掘机发动机故障诊断). Metal Mine.

[7] Zhao Hu, (2021). Fault prediction of key components of wind turbine based on BP neural net. *Power System Engineering*, Vol. 37, No. 2, 21-22.

[8] Zhou Dengji, Zhang Huisheng, Weng Shilie, (2015). A new gas path fault diagnostic method of gas turbine based on support vector machine. *Journal of Engineering for Gas Turbines and Power*. Vol.137, No. 10.

[9] Li Shanshan, (2016). *Study on the methods of layout optimization design and virtual verification of self-propelled corn harvester* (自走式玉米籽粒收获机总体结构布局优化设计与虚拟验证方法研究). China Agricultural University.

[10] Li Qinghua, (2014). *Study on reliability prediction method of corn harvest machine* (玉米收获机可靠性预测方法研究). Shandong University of Technology.

[11] Zhou Xueguang, (2021). Corn harvester common failures and troubleshooting methods (玉米收获机常见故障及排除方法). *South China Agriculture*, Vol. 15, No. 33, 183-185.

[12] Xu Lijuan, Wang Yong, Liu Peiqi et al., (2020). Black box failure of electric power metering device based on data matrix (基于数据矩阵化的电力计量装置黑盒故障研究). *Information Technology*, Vol.44, No.11, pp.29-33.

[13] Yang Xiaohui, Zhang Guohia, Yao Jia et al., (2022). Reliability analysis of grain combine harvesters based on date mining technology. *INMATEH-Agricultural Engineering*, Vol. 67, No. 2, 211-220. https://doi.org/10.35633/inmateh-67-21

[14] Wang Yajie, (2022). *Research on rolling bearing fault diagnosis method based on deep auto-encoder and transfer learning* (基于深度自编码与迁移学习的滚动轴承故障诊断方法研究). China University of Mining and Technology.

[15] Yan Yuping, Xiao Zhanhui, (2023). Fault prediction algorithm based on autoencoding neural network for power grid (基于自编码神经网络的电网故障预测算法). *Journal of Shenyang University of Technology*, Vol. 45, No.1, 1-5.

[16] Lin Xia, (2016). *Optimizing Deep Learning Algorithm Based on Noisy Autoencoder* (基于全噪声自动编码器的深度神经网络优化算法). Wuhan University of Science and Technology.

[17] Wang Li, Liu Shuo, Lv Dianji et al, (2021). Multi-sensor signal acquisition and date procession analysis of combine harvester. *INMATEH-Agricultural Engineering*, Vol. 63 No. 1, 335-344. https://doi.org/10.35633/inmateh-63-34

STUDY OF THE TURNING PROCESS OF THE BRIDGE TYPE MACHINES
/
ДОСЛІДЖЕННЯ ПРОЦЕСУ СИЛОВОГО (БОРТОВОГО) ПОВОРОТУ МОСТОВИХ МАШИН

Volodymyr BULGAKOV[1)], **Semjons IVANOVS**[2)], **Volodymyr KUVACHOV**[3)], **Valerii ADAMCHUK**[4)], **Viktor KAMINSKIY**[5)]

[1)] Department of Mechanics, Faculty of Construction and Design, National University of Life and Environmental Sciences of Ukraine, Kyiv, Ukraine
[2)]Faculty of Engineering, Latvia University of Life Sciences and Technologies, Jelgava / Latvia
[3)]Department of Machine-Using in Agriculture, Dmytro Motornyi Tavria State Agrotechnological University, Melitopol / Ukraine
[4)]Institute of Mechanics and Automation of Agricultural Production of the National Academy of Agrarian Sciences of Ukraine, Kyiv / Ukraine
[5)]National Scientific Centre, Institute of Agriculture of NAAS of Ukraine, Kyiv Region / Ukraine

E-mail: semjons@apollo.lv
DOI: https://doi.org/10.35633/inmateh-70-23

Keywords: *agricultural wide span vehicle (gantry), controlled traffic farming, side turn, power, research.*

ABSTRACT
One of the ways to improve the manoeuvrability of wheeled axle machines when they move along the tracks of a constant technological track is the use of onboard turning. This simplifies the layout, increases the useful volume of the machine due to the release of niches in the machine body, necessary for placing the steering wheels when turning. However, the question of the efficiency of onboard turning of axle machines by the criterion of power input remains insufficiently studied. The aim of the research is to substantiate the criterion of the power required to implement on-board turns of an overhead machine. Theoretical research, synthesis of design schemes, parameters and modes of operation of bridge machines have been carried out by simulating on a personal computer the conditions of their functioning. The basics of theoretical mechanics and tractor theory were the basis of the research methods. As a result of the research, it has been established that power (onboard) turning is widely used for wheeled machines and has a prospect of application on bridge machines used in the track farming system. Approbation of the developed methodology of determining power inputs for power (onboard) turning of wheeled axle machines has shown that under the accepted conditions of turning the power required for turning of the axle machine is 28% of the engine power at a speed of 5 km·h^{-1}. As the gauge of the bridge machine increases, the total power required for the power (onboard) turn increases exponentially.

АНОТАЦІЯ
Одним із шляхів підвищення маневреності колісних мостових машин при їх русі по слідах постійної технологічної колії є використання бортового повороту. Це спрощує компоновку, збільшує корисний об'єм машини за рахунок звільнення в корпусі машини ніш, необхідних для розміщення рульових коліс при поворотах. Проте залишається недостатньо вивченим питання ефективності бортового повороту мостових машин за критерієм енергоспоживання. Метою дослідження є обґрунтування критерію потужності, необхідної для здійснення бортових поворотів мостової машини. Теоретичні дослідження, синтез розрахункових схем, параметрів і режимів роботи мостових машин здійснено шляхом моделювання на персональному комп'ютері умов їх функціонування. В основу методів дослідження покладені основи теоретичної механіки та теорії трактора. В результаті проведених досліджень встановлено, що силовий (бортовий) поворот широко використовується для колісних машин і має перспективу застосування на мостових машинах, які використовуються в системі колійного землеробства. Апробація розробленої методики визначення енергозатрат на силовий (бортовий) поворот колісних буксових машин показала, що за прийнятих умов повороту потужність, необхідна для повороту мостової машини, становить 28% потужності її двигуна на швидкості 5 км·год$^{-1}$. Зі збільшенням ширини колії мостової машини загальна потужність, необхідна для силового (бортового) повороту, зростає експоненціально.

INTRODUCTION

A perspective direction of further development of agriculture in the world is the introduction of innovative technologies, which should include the tracked farming system (*Pedersen H.H. et al., 2016*; *Chamen W.C.T. 2013; Onal I. 2012; Thomsen M. et al., 2018*). The effectiveness of the practical implementation of this farming strategy is determined by the use of a new power tool in the form of the so-called «wide span vehicle» (gantry) (*Pedersen H.H. et al., 2016*; *Chamen W.C.T. 2013; Onal I. 2012*).

Bridge machines for Controlled traffic farming (CTF) should be equipped with a wheeled propeller, which should be considered the most acceptable. The use of tracked or other type of propulsion for driving on the tracks of a permanent technological track is not appropriate.

The theory of movement and controllability of wheeled traction-transport machines is sufficiently studied (*Nadykto V. et al., 2015; Bulgakov V. et al., 2022; Bulgakov V. et al., 2020; Ivanovs S. et al., 2020; Bulgakov V. et al., 2018; Ivanovs S. et al., 2018; Bulgakov V. et al., 2016; Szakács T., 2010; Bulgakov V. et al., 2021; Fashutdinov M. et al., 2020; Panchenko, A., 2015*). The operation of any wheeled machine takes place under conditions of a large number of disturbing factors (forces and their moments) that change the position of the machine in space and deviate its movement from the specified trajectory. Constant monitoring and intervention by the operator is required to keep the axle-wheeled machine within the trace of a constant tramline.

The steering of most modern wheeled machines is adapted to manual steering and is based on the kinematic or power steering principle (*Nadykto V. et al., 2015; Bulgakov V. et al., 2022*; *Demšar I. et al., 2012; Bulgakov V. et al., 2020; Ivanovs S. et al., 2020; Bulgakov V. et al., 2018; Ivanovs S. et al., 2018; Bulgakov V. et al., 2016; Bulgakov V. et al., 2021*). Kinematic steering involves turning the steered wheels (front, rear or both front and rear) relative to the carcass or changing the position of one part of the mobile machine relative to the other in the horizontal plane (articulated frame). Power (onboard) turning is realized by rotation of wheels of different sides of the machine with different speed.

The use of onboard (power) turning on an axle machine is the simplest solution technically in terms of simplicity of the chassis and steering drive (*Zhao D. et al., 2020; Bulgakov V. et al., 2015; Bulgakov V. et al., 2017)*. With this method of turning the bridge machine, its motor wheels are mounted on two unguided axles, and its turning in the horizontal plane is performed by different rotation frequency of front and rear wheels of the right and left side.

It is also known that the use of onboard turning on a wheeled vehicle, is one of the ways to improve its manoeuvrability. This simplifies the layout, increases the useful volume of the machine due to the release of niches in the body of the machine required to place the steerable wheels when turning. However, the disadvantage of this turning method is increased tire wear and increased power required to turn the wheeled machine.

Many scientists have considered the issues of controlling vehicles with non-swivel wheels and power (onboard) steering (*Bulgakov V. et al., 2015; Bulgakov V. et al., 2017; Kazachenko G., 1982; Kolesnikovich A., 2019; Gurudatta M. et al., 2018; Zhuravel D. et al., 2022).* Today, onboard steering is widely used in military vehicles, such as armoured vehicles and armoured personnel carriers (Fig. 1a), amphibious all-terrain vehicles (figures 1b and 1c), as well as various small loaders (Fig. 1d) and overhead vehicles (Fig. 1e) (*Kazachenko G., 1982; Kolesnikovich A., 2019; https://www.army-technology; http://www.atv-quad.org; https://pmto-agrosoyuz.com.ua)*.

a) b) c) d) e)

Fig. 1 – Wheeled machines with non-swivel wheels and power steering

a – armoured vehicles and armoured personnel carriers; b – amphibious all-terrain vehicles ARGO; c – amphibious all-terrain vehicle; d – small loader; e – overhead vehicles

Scientists' studies of power (onboard) turning of traction vehicles have shown that the manoeuvrability of a wheeled machine depends on the ratio of its base and track dimensions $L \cdot B^{-1}$, where L – machine base, B – machine track, the number and location of axles on the base, specific power, and other factors (*Bulgakov V. et al., 2015; Bulgakov V. et al., 2017; Kazachenko G., 1982; Kolesnikovich A., 2019; Song P. et al., 2014)*.

However, the issue of the efficiency of on-board turning of bridge machines by the criterion of power input remains insufficiently studied.

The purpose of the research is to determine the variation of forces and power required for turning with constructive and operating parameters of the running system, for machines equipped with non-pivotal wheels.

MATERIALS AND METHODS

The objects of the study are vehicles with onboard turning: AMX-10RC armoured vehicle (*https://www.army-technology*), ARGO amphibious all-terrain vehicle (*http://www.atv-quad.org*), GEHL R150 small loader (*https://pmto-agrosoyuz.com.ua*), vehicles with onboard turning (*Kazachenko G., 1982; Kolesnikovich A., 2019)*, an overhead vehicle of our design (*Bulgakov V. et al., 2018*).

As a physical model to analyse the power consumption for turning, a prototype of an overhead vehicle was used (Fig. 1e) (*Bulgakov V. et al., 2018*). This problem was solved using a PC and Mathcad software.

Theoretical studies, synthesis of design schemes, parameters and modes of operation of bridge machines were carried out by modeling on a personal computer the conditions of their functioning. The basics of theoretical mechanics and tractor theory were the basis of the research methods.

Based on the technical characteristics of the wheeled vehicles with onboard turning, taken as objects of research, the dependence of their estimated parameters obtained experimentally was plotted (Fig. 2).

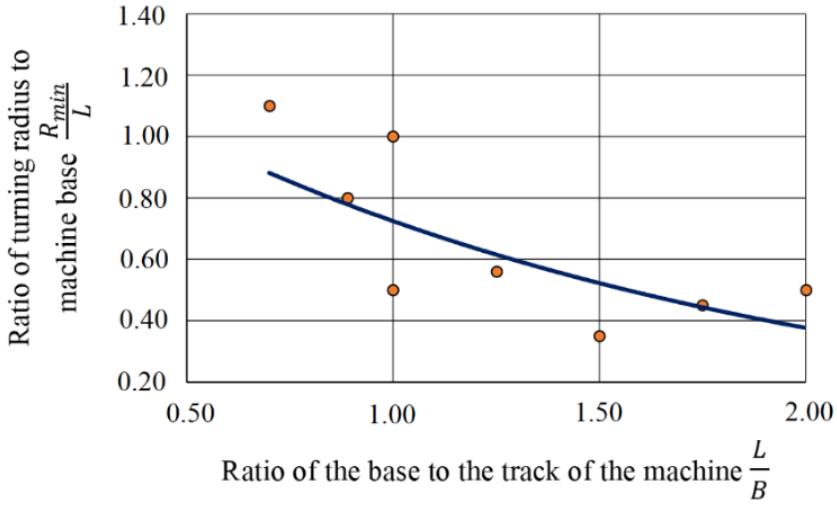

Fig. 2 – Estimation of the relationship between the constructive parameters of the running system and those of turning for wheeled machines

R_{min} – minimum turning radius of a wheeled vehicle; L – wheelbase of the machine; B – machine track

Analysing the curve shown in Fig. 2, it follows that for the considered wheeled machines with a sideways turn their minimum turning radius R_{min} depends considerably on the base *L* and the track width B.

This is especially relevant for overhead machines in the tracked farming system. Since it is known that increasing the track width of axle machines improves land use, i.e. increases the ratio of the area of the agricultural zone of the field to the total area of the land plot.

However, increasing the turning radius will require a proportional increase in the engineering area of the field on the turning lane, which reduces the productive part of the field. At the same time, the power consumption for turning the bridge machine will also increase.

To analyse the power consumption for turning the bridge machine, let's make a computational scheme of forces acting on it (Fig. 3).

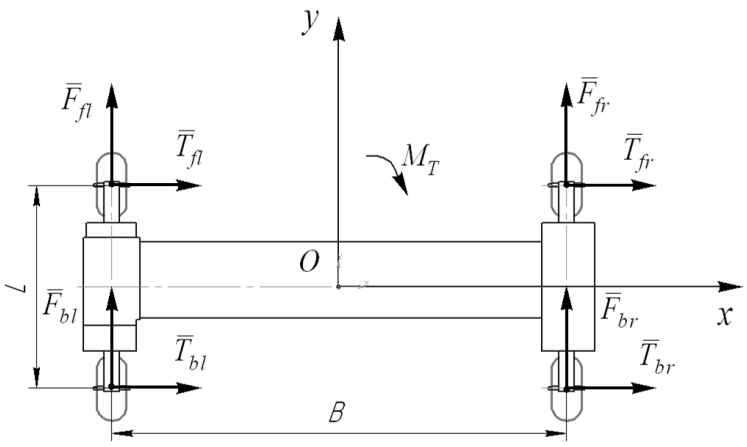

Fig. 3 – Forces acting on a machine when making a turn

xOy – is the system of fixed coordinates; F_{fr}, F_{br} – tangential forces applied to the front and rear wheels of the left side of the bridge machine; F_{fl}, F_{bl} – tangential forces applied to the front and rear wheels of the left side of the bridge machine; B – bridge track gauge; L – wheelbase of the machine; M_T – turning moment of the bridge machine

Power N_T, spent to make an overhead machine turn can be calculated as the product of multiplying the known turning moment M_T at the rate of turn ($d\varphi/dt$):

$$N_T = M_T \cdot \frac{d\varphi}{dt} \tag{1}$$

where:

M_T – moment of rotation of an overhead machine (N·m);

$d\varphi/dt$ – turning speed of the overhead machine (s^{-1}).

The rectilinear motion of the bridge machine along the traces of the constant tramline is preserved when:

– there is absence of disturbing forces and moments acting on the bridge machine;

– there is equality of the sum of the leading moments wheels of the overhead machine right and left sides;

– there is identity of the dimensions and elastic characteristics of the wheels of the bridge machine and the supporting surface of the traces of a permanent technological track in the area of its interaction with the wheel.

Violation of any of these conditions leads to the appearance of the moment of forces in the horizontal plane:

$$M_T = \frac{B}{2} \cdot \left(F_{fr} + F_{br} - F_{fl} - F_{bl}\right) \neq 0 \tag{2}$$

where:

B – track width of the overhead machine;

F_{fr}, F_{br} – tangential forces applied to the front and rear wheels of the right side of the overhead machine;

F_{fl}, F_{bl} – tangential forces applied to the front and rear wheels of the left side of the overhead machine.

Resistance to rotation of the bridge machine is caused by the moment of lateral forces T of interaction of the wheels with the supporting surface M_S, which can be considered the stabilizing moment and the moment of inertial forces M_J:

$$M_T = M_S + M_J = \frac{L}{2} \cdot \left(T_{fr} + T_{fl} - T_{br} - T_{bl}\right) + J_M \cdot \frac{d_2\varphi}{dt^2} \tag{3}$$

where:

T_{fr}, T_{br} – side forces applied to the front and rear wheels of the right side of the overhead machine;

T_{fl}, T_{bl} – side forces applied to the front and rear wheels of the left side of the overhead machine.

J_M – moment of inertia of the machine in the horizontal plane;

$d^2\varphi/dt^2$ – angular acceleration of the machine in the horizontal plane, which takes place at the entrance to the turn and exit from the turn and is equal to zero at the steady-state turn, i.e. at the turn with a constant radius.

For mathematical description of side interaction of the wheeled machine with the supporting soil surface, the "side input" hypothesis in linear interpretation is most often used (*Bulgakov V. et al., 2018; Ivanovs S. et al., 2018; Bulgakov V. et al., 2016*). In this case, to determine side horizontal forces at the points of contact between the wheels and the ground, the resistance coefficients to side departure of tires are used:

$$T_{fr} = k_{fr} \cdot \delta_{fr}$$

$$T_{fl} = k_{fl} \cdot \delta_{fl} \quad (4)$$

$$T_{br} = k_{br} \cdot \delta_{br}$$

$$T_{bl} = k_{bl} \cdot \delta_{bl}$$

where:

k_{fr}, k_{fl}, k_{br} and k_{bl} – coefficients of resistance to wheel entry of the left and right sides of the overhead machine, respectively;

δ_{fr}, δ_{fl}, δ_{br} and δ_{bl} – left and right wheel angles of the overhead machine.

RESULTS

It is known that the coefficients of k_{fr}, k_{fl} and k_{br}, k_{bl} of the resistance to wheel escape of machines depend on the ratio of the following parameters (*Bulgakov V. et al., 2018*):

$$\frac{h}{D_0} = 0.42 \cdot \frac{Q}{p_w \cdot D_0^2} \cdot \sqrt{\frac{D_0}{b_0}} \quad (5)$$

where:

h – is the depth of the footprint formed by the machine wheel in the soil;

D_0 – static tire diameter of the machine wheel;

b_0 – tire width of the machine wheel;

p_w – air pressure in the tire of the machine wheel;

Q – vertical load on the tire of the machine wheel.

At the physical object of research under consideration, which is an overhead machine, tires of size 9.5R32 were used, for which D_0 = 1.245 m and b_0 = 0.241 m. Taking into account the parameters of the indicated tires, the ratio h/D_0 < 0.0885, so, the coefficients of resistance to tire deflection in the process of mathematical modeling, k_i, were calculated according to this dependence:

$$k_i = 60 \cdot \rho_w \cdot {b_0}^2 \left[1.75 \cdot \left(\frac{h}{D_0}\right) - 12.27 \cdot \left(\frac{h}{D_0}\right)^2\right] \quad (6)$$

Taking into account values of air pressure in tires of the overhead machine p_w within 0.14...0.16 kPa, the value of its tire deflection coefficients by expression (6) became 25.6…27.0 kN·rad^{-1}.

When calculating the power required to turn the bridge machine coefficient of traction of its wheels with the bearing surface of the tracks of a constant technological track was taken equal to 0.6, and the speed of movement 5 km·h^{-1}.

The result of calculating the power consumption for the implementation of onboard turning of the bridge machine from the width of its track is shown in Fig. 4.

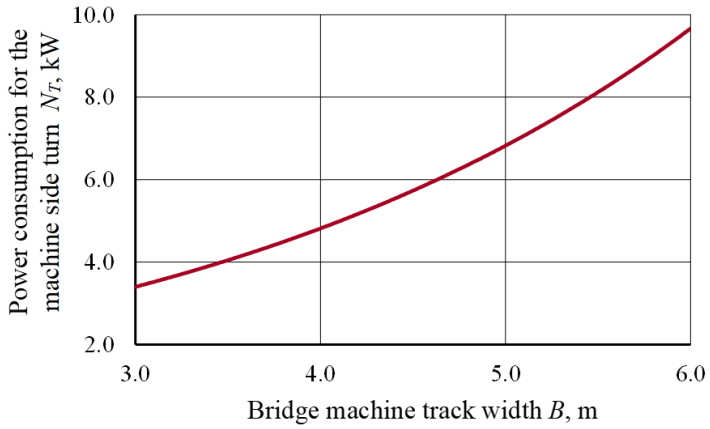

Fig. 4 – The influence of the track width of a vehicle on the traction power during the turn

N_T – power expended on the implementation of the turn of the bridge machine; B – machine track

Analysis of Fig. 4 shows that with increasing the track width of the bridge machine by 2 times, the total power, spent on the power (onboard) turn at the specified parameters, increases exponentially. It can be explained by the fact that with increasing the track width of the bridge machine its mass increases, which increases the moment of inertia JM according to expression (3), the parameters of its wheels also increase, resulting in an increase in the drag coefficients according to (6). Specific power consumption for turning of the bridge machine is at least 28% of the total power of its power plants and essentially depends on the speed of its turning.

CONCLUSIONS

Power (onboard) turning is widely used in wheeled machines and has a prospect of application on bridge machines used in the track system of farming.

Testing of the developed methodology of determining power consumption for power (onboard) turning of wheeled axle machines has shown that under the accepted turning conditions the power required for turning of the axle machine is 28% of the engine power at speed 5 km·h^{-1}.

As the track width of an overhead machine increases, the total power spent on the power (onboard) turn increases exponentially. Therefore, from the point of view of reducing energy costs for operation of bridge machines, only their optimal parameters (track width, base, weight, wheel tire parameters, as well as driving mode on the turn) will allow to have minimum power consumption, spent by them for making power (onboard) turn.

REFERENCES

[1] AMX 10RC *Wheeled Armoured Reconnaisance Vehicle* (2008). France. https://www.army-technology.com/projects/amx/.

[2] Bulgakov V., Aboltins A., Beloev H., Ruzhylo Z., Ivanovs S. (2022). Theoretical Investigation of Selection (Calculation) of Design Parameters of Modular Draft Device in Aggregation of Semitrailers. *Applied Sciences*, Switzerland, 12(20), 10267.

[3] Bulgakov V., Aboltins A., Ivanovs S., Nadykto V., Beloev H. (2020). A mathematical model of plane-parallel movement of the tractor aggregate modular type. *Agriculture, Switzerland*, 10(10). 1–22, 454.

[4] Bulgakov V., Adamchuk V., Kuvachov V., Ivanovs S. (2017). Theoretical justification of the turn of a wide span tractor (vehicle) for controlled traffic farming. *INMATEH – Agricultural Engineering*, 53(3), 1–9.

[5] Bulgakov V., Holovach I., Kuvachov V. et al. (2018). Theoretical investigation of a rear-mounted linkage for wide-span tractors. *Mechanization in agriculture & Conserving of the resources*, 1, pp. 11–14.

[6] Bulgakov V., Ivanovs S., Adamchuk V., Nadykto V. (2016). Theoretical investigation of turning ability of machine and tractor aggregate on basis of ploughing and intertilling wheeled tractor. *Engineering for Rural Development*, 2016-January, 1077–1084.

[7] Bulgakov V., Ivanovs S., Kuvachov V., Prysiazhniuk D. (2021). Investigation of the Influence of Permanent Traffic Lane Properties on Rolling of Bridge Agricultural Equipment Wheels. *Acta Technologica Agriculturae*, 24(2), 97–102.

[8] Bulgakov V., Ivanovs S., Nadykto V., Kuvachov V., Masalabov V. (2018) Research on the turning ability of a two-machine aggregate. *INMATEH – Agricultural Engineering*, 54(1), 139–146.
[9] Bulgakov V., Kuvachov V., Nozdrovický L., Smolinskyi S., Ihnatiev Y. (2018). The study of movement of the wide span tractor-based field machine unit with power method of its control. *Acta Technologica Agriculturae*, 21(4), 160–165.
[10] Bulgakov V., Pascuzzi S., Nadykto V., Ivanovs S. (2018). A mathematical model of the plane-parallel movement of an asymmetric machine-and-tractor aggregate. *Agriculture*, Switzerland, 8(10), 151.
[11] Chamen W.C.T. Wide Span CTF. (2013). http://ctfeurope.co.uk/ WhatIs /Wide–Span–CTF.aspx.
[12] Demšar I., Bernik R., Duhovnik J. (2012). A mathematical model and numerical simulation of the static stability of a tractor. *Agriculturae Conspectus Scientificus*, 77 (3). 143–150.
[13] Fashutdinov Marat, Khafizov Kamil, Galiev Ilgiz, Gabdrafikov Fanil and Khaliullin Farit (2020). Research of dynamics of turning of machine-tractor aggregate with tractor on wheeled-crawler mover. *International Scientific-Practical Conference «Agriculture and Food Security: Technology, Innovation*, Markets, Human Resources» (FIES 2019). 17. 00056.
[14] Gurudatta M. Anche, Velmurugan M.A., Arun Kumar S., Shankar C. (2018). Subramanian Model Based Compensator Design for Pitch Plane Stability of a Farm Tractor with Implement. *IFAC-PapersOnLine*. Vol. 51. Issue 1. 208–213.
[15] Ivanovs S., Bulgakov V., Nadykto V., Kuvachov V. (2018). Theoretical investigation of turning ability of two-machine sowing aggregate. *Engineering for Rural Development*, 17, 314–322.
[16] Ivanovs S., Bulgakov V., Nadykto V., Smolinskyi S., Kiernicki Z. (2020). Experimental study of the movement controllability of a machine-and-tractor aggregate of the modular type. *INMATEH – Agricultural Engineering*, 61(2), 9–16.
[17] Nadykto V., Arak M., Olt J. (2015). Theoretical research into the frictional slipping of wheel-type undercarriage taking into account the limitation of their impact on the soil. *Agronomy Research*, 13(1), 148–157.
[18] Onal I. (2012). Controlled traffic farming and wide span tractors. *Agricultural Machinery Science*, 8(4), 353–364.
[19] Panchenko, A.; Voloshina, A.; Milaeva, I.; Luzan, P. (2019). Operating conditions' influence on the change of functional characteristics for mechatronic systems with orbital hydraulic motors. Modern Development Paths of Agricultural Production: *Trends and Innovations*. 169-176. DOI: 10.1007/978-3-030-14918-5_18.
[20] Pedersen H.H., Oudshoorn F.W., McPhee J.E. (2016) Wide span–re-mechanising vegetable production. *XXIX International horticultural congress on horticulture: sustaining lives, livelihoods and landscapes: international symposia on the physiology of perennial fruit crops and production systems and mechanisation, precision horticulture and robotics Book Series: Acta Horticulturae*, 1130, 551–557.
[21] Song P., Zong C.-F., Tomizuka M. (2014). A terminal sliding mode based torque distribution control for an individual-wheel-drive vehicle. *Journal of Zhejiang University*: Science A. 15 (9), 681-693.
[22] Szakács T. (2010). Developing stability control theories for agricultural transport systems. *Acta Polytechnica Hungarica*, 7 (2), 25–37.
[23] Thomsen Maria Nygård, Tamirat Tseganesh, Pedersen Søren Marcus et al. (2018) Farmers perception of Controlled Traffic Farming (CTF) and associated technologies. *IFRO working paper*. 2018/12.
[24] Zhao Ding, Yaoming Li, Zhong Tang (2020). Theoretical Model for Prediction of Turning Resistance of Tracked Vehicle on Soft Terrain. *Mathematical Problems in Engineering*. 1–9.
[25] Zhuravel D., Samoichuk K., Petrychenko S. et al. (2022). Modeling of Diesel Engine Fuel Systems Reliability When Operating on Biofuels. *Energies*. 15(5). 1795. DOI: 10.3390/en15051795.
[26] Kazachenko G.V. (1982). *The study of the rotation of wheeled vehicles with an onboard control scheme: abstract of the dissertation of a candidate of technical sciences*. Belarus, 21 p.
[27] Kolesnikovich A. N., Vygonny A. G., Goncharko A. A. (2019). Analysis of the use of skid steer of wheeled vehicles, Belarus, Working Paper. https://rep.bntu.by/bitstream/handle/data/60329/64-69.pdf?sequence=1&isAllowed=y.
[28] ***http://www.atv-quad.org/de/fahrzeuge/argo_amphibienfahrzeuge/.
[29] ***https://pmto-agrosoyuz.com.ua/ua/p679231165-mini-pogruzchik-bortovym.html

DESIGN AND EXPERIMENT ON THE SINGLE-DITCH AND DOUBLE-ROW OPENER FOR NARROW ROW FLAT SEEDER
/
单沟双行播种开沟器设计与试验分析

Qichao LI[1,*], Jinlong FENG[1], Xianglan MING[1]
[1] College of Mechanical and Electrical, Lingnan Normal University, Zhanjiang, 524048, China
Corresponding authors. Email: qc_lee@126.com

DOI: https://doi.org/10.35633/inmateh-70-24

Keywords: *agricultural machinery; single-ditch and double-row; narrow row flat; opener; seeder*

ABSTRACT
In order to improve the opener of the seeder and its lightweight structure, a new type of opener is designed. The overall structure and working principle of a single-ditch double-row opener are analyzed, and the structural parameters of machete cutting soil and the soil guide board are designed and optimized. Using the penetration angle of machete cutting soil and the included angle of the soil guide board as test factors, field experiments were conducted. As the test indexes, the working resistance, the sowing coefficient of variation, and the depth coefficient of variation were used to analyze the effect of the opener. The results showed that in terms of working resistance, the penetration angle of the machete cutting edge and the included angle of the soil guide board were extremely significant, and the included angle was greater than the penetration angle regarding the influence degree. In terms of the sowing coefficient of variation, the penetration angle was significant, and the included angle was extremely significant. Regarding the depth coefficient of variation, the penetration angle was extremely significant, and the included angle of the guide soil board was significant. Based on the optimization analysis by using the Design Expert 8.0.6, it is found that the performance of the opener is optimal when the penetration angle and the included angle are 50.03° and 42.36°, respectively. The working resistance, the sowing coefficient of variation, and the depth coefficient of variation are 61.47N, 6.49% and 4.22%, respectively. After verification, the results are basically consistent, and the seeding and trenching performance meets the agronomic requirements. This study can provide a basis and technical reference for the design and development of the ditching technology and opener.

摘要
为提高播种机开沟器开沟作业功能及轻量化结构，设计了一种单沟双行播种开沟装置，阐述分析了开沟器总体结构及工作原理，并设计了开沟器切土弯刀和分土板等关键部件的结构参数。以切土刀刃入土角和分土板夹角为试验因素，开沟工作阻力、播种变异系数和开沟深度变异系数为开沟器作业性能试验指标，进行田间试验。结果表明，对工作阻力影响，两因素均为极显著，且切土刀刃入土角>分土板夹角；对播种性能影响入土角为显著，夹角为极显著；对开沟深度变异系数影响，入土角为极显著，夹角为显著。运用 Design-Expert 8.0.6 软件进行优化分析，得出入土角 50.03°，夹角 42.36°时，播种开沟作业性能最优，工作阻力、播种变异系数和开沟深度变异系数分别为 61.47N、6.49%和 4.22%。进一步通过田间试验验证，结果基本一致，播种开沟性能完全满足要求。该研究为播种机开沟器的设计研发提供了研究基础与技术参考。

INTRODUCTION
The opener is an important part of the seeding machinery. During the sowing process, it is an in-soil component that is in direct contact with the soil to prepare the seedbed. Its role is to build the seed ditch, guide seeds into the soil layer of the ditch and provide a favorable environment for stable planting of seeds. The seedbed quality and seeding quality are affected by the work performance of the opener *(Collins and Fowler, 1996; Barr et al., 2018a; Botta et al., 2010).*

There are many types of openers, such as hoe-shovel type, core share type, ship-shaped shovel type, sliding knife type, and disc type *(Lu 2020; Zhan et al., 2021)*. The shape of seeding ditches is mostly V-shaped, which can improve the seeding accuracy, but the disturbance to the soil is large.

[1]*Qichao Li, Associate Professor; Jinlong Feng, Lecturer; Xianglan Ming, Lecturer*

The wet soil layer of trenching soil is easy to mix with the dry soil layer, resulting in the mixed wet and dry soil covering the seeds when returning to the soil. This is not conductive to soil moisture retention and will affect seed germination. Openers have been studied deeply *(Singh et al., 2016, Singh et al., 2017; Ozmerzi et al., 2022). Jia et al (2017)* designed a sliding knife opener, which can improve the seeding accuracy by opening a V-shaped ditch, and is suitable for the ditching of seeds with small particle size. *Zhao et al, (2022*), designed a serration opener for double-row on ridges, which can cut the root system of maize for no-tillage operation with better working stability. *Lü et al, (2018),* designed a split sliding knife opener to analyze the movement law of soil particles on the ditcher during ditching and backfilling. *Li et al, (2022),* designed a combined opener for sugarcane lateral planting, with effective seed dropping depth. The power consumption and trenching resistance of rotary tillage were studied. *Mustafa et al, (2017a); (2017b)* established a dynamic simulation model of the interaction between the trench cutter and soil. It is more accurate to simulate the contact model of soil particles by combining the delay elastic model and the linear cohesion model. *Barr et al, (2018b),* used the discrete element simulation method to study the influence of structural parameters of the ditcher on soil movement and mechanical performance. *Vamerali et al, (2006),* designed a wide-airfoil no-till opener with acute angle to solve the lack of soil compactness in seedbed. *Saeys et al, (2018),* studied the sliding cutting and hewing cutting methods of the ditcher, and found that the sliding cutting method had less operating resistance. *Sahu et al, (2018),* compared the trenching performance and fuel of different ditchers for the research of power saving. *Ahmad et al, (2020),* used computer technology to conduct discrete element simulation of disk ditcher and studied the influence law of ditching resistance. *Vilaseca et al, (2013),* carried out hot stamping of PVD coating on trenching materials to reduce the friction and drag.

Most of the openers are single row V-shaped, which can improve the seeding accuracy. However, there are few researches on double-row seeding openers. To this end, a sliding knife single-ditch and double-row seeding opener is studied. The soil layer is first cut with a single sliding knife, and then the soil guide board pushed into a seed trench, by a middle partition board to separate the double row seedbed belt. The working principle of the opener and the structural parameter design of key components are explained through the kinematic analysis of the contact between soil particles and the opener. The optimal operating parameters were determined through field tests and the design was validated with the aim of optimizing the structural parameters of the opener. Thereby a theoretical support and technical reference is provided for the innovative design of the opener.

MATERIALS AND METHODS

Structure and working principle of the seed metering device

The integral structure of narrow row flat seeder is shown in Fig. 1.

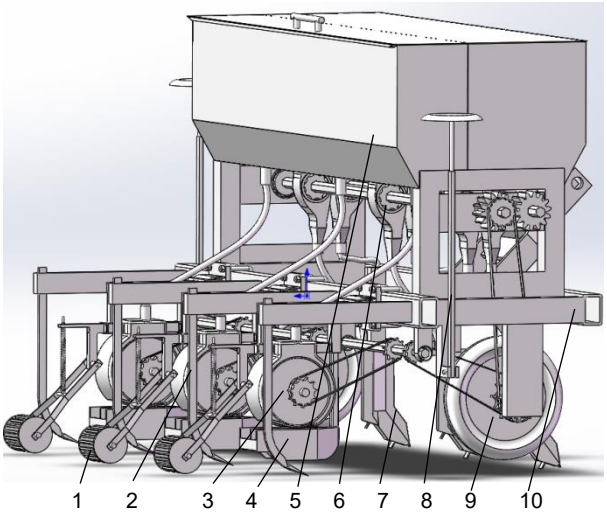

Fig. 1 - Structure of narrow row flat seeder

1. Compacting device; 2. Subsoiling and covering shovel; 3. Seed metering device; 4. Seed opener; 5. Seed and fertilizer box; 6. Fertilizer apparatus; 7. Fertilizer opener; 8. Mark scraper device; 9. Drive support wheel; 10. Mainframe

It consists of mainframe, seed and fertilizer box, fertilizer apparatus, fertilizer opener, seeding monomer (seed metering device, seed opener, compacting device), subsoiling and covering shovel, drive support wheel, and mark scraper device. A partition is designed inside the seed and fertilizer box to separate the seed and fertilizer with a volume ratio of 4:1. It is installed on the mainframe.

The fertilizer apparatus is installed in forequarter of the baseboard of the seed and fertilizer box, and it is connected with a fertilizer opener installed on the front beam of the mainframe by a telescopic hose to complete the fertilization operation. The seeding unit is arranged on the rear beam of the mainframe, with adjustable line spacing in the range of 30-50 cm. The connection is configured in a single hinged form, which has independent replication function and can also shorten the length of the machine to move the machine center of gravity forward. The seeding unit is arranged with the seed metering device, seed opener, and compacting device. The subsoiling and covering shovel is installed on the back beam support of the mainframe. The drive support wheel, mark scraper device are installed on the beam of the mainframe.

Seed opener is an important part of narrow flat bottom of seeding device. Its role is to build seed ditches and provide favorable environment for the smooth implantation of seeds. Its structural rationality will directly affect the sowing quality. The single-slide knife double-row flat-bottom opener is mainly designed for the crops that can be planted in narrow row and close flat. The opener is mainly composed of a soil cutting knife, a divide soil board, a guide soil board, a soil resistance board, a middle partition board, and a support board, as shown in Fig. 2.

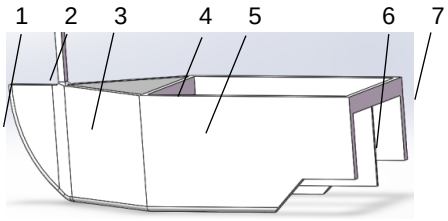

Fig. 2 - Structure diagram of seed opener

1. Soil cutting knife; 2. Handle; 3. Soil guide board; 4. Support board; 5. Soil resistance board; 6. Middle partition board; 7. Connecting board

During operation, the front machete penetrates the soil, guiding the soil board cut through the soil. The soil is separated by the soil resistance board on both sides to form a rectangular groove, opening a flat seed furrow. The cutting surface illustrating the relationship between the furrow shape and the seed is shown in Fig. 3. The notched structure is designed at the end of soil resistance board, so that the moist soil can fall back to the covering seed belt in time and the seeds can contact fully with the moist soil for germination. The middle partition board of the opener can separate two rows of seed ditches, with the functions of strengthening and isolating restriction, ensuring the planting of seeds in the intended seed belt, and reducing the reseeding and miss-seeding caused by seed bouncing. The support board and the connecting board play the role of supporting and reinforcing the soil resistance board on both sides.

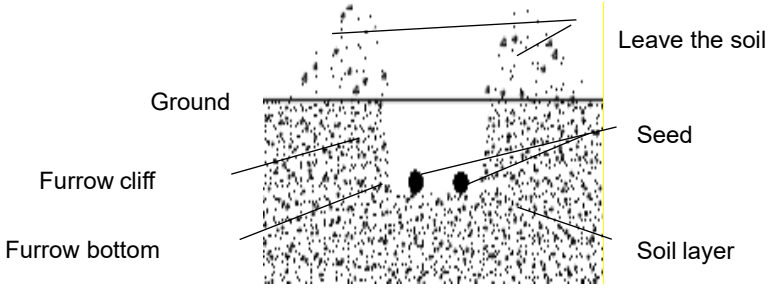

Fig. 3 - Diagram of the furrow shape and seed distribution

Design of the curve for machete cutting edge

The soil resistance arising when the machete cuts into the soil is closely related to the shape of the cutting edge curve. During the cutting process, the soil is subjected to the cutting of the machete, and the soil particles undergo a relative displacement, sliding down along the cutting edge curve of the machete. Since the cutting resistance decreases with the increase of the cutting angle and increases with the increase of the friction angle, as well as the entry resistance increases with the increase of the entry angle, the curved cutting edge is more advantageous in labor than the straight one. As the speed increases, the growth rate of traction resistance of the ditcher is linear > parabola > exponential curve > arc curve *(Liu et al., 2021; Liu et al., 2019)*. In the design, the edge curve is formed by the intersection of symmetrically arranged soil breaking surface. The curve of the arc function is selected as the curve of the machete cutting edge, and the coordinate system is established for the analysis, as shown in Fig. 4.

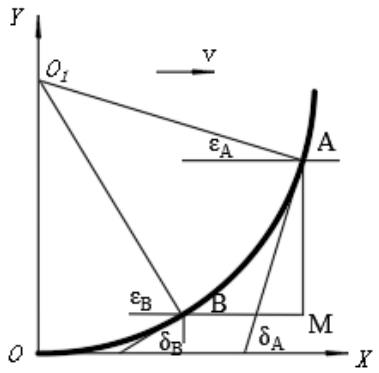

Fig. 4 - Diagram of machete curve

The curve equation *AB* of the machete cutting edge follows the relationship:

$$y = R + \sqrt{R^2 - x^2} \tag{1}$$

Taking two points, $A\ (x_A, y_A)$ and $B\ (x_B, y_B)$ on the arc function curve of the radius R, point A is the upper vertex of the machete curve, and point B is the bottom termination point of the machete curve. The slope of the machete cutting edge at points A and B can be expressed as:

$$\begin{cases} \frac{d_{y_A}}{d_{x_A}} = \frac{x_A}{\sqrt{R^2 - x_A^2}} = tan\delta_A = \tan\left(\frac{\pi}{2} - \varepsilon_A\right) \\ \frac{d_{y_B}}{d_{x_B}} = \frac{x_B}{\sqrt{R^2 - x_B^2}} = tan\delta_B = \tan\left(\frac{\pi}{2} - \varepsilon_B\right) \end{cases} \tag{2}$$

where, ε_A is the cutting angle at A, °; ε_B is the cutting angle at B, °; δ_A is the tangent with a forward direction angle at A, °; δ_B is the tangent with a forward direction angle at B, °; ε_A and δ_A are the complementary angles, and similarly, ε_B and δ_B are the complementary angles.

The difference L_{AM} between points A and B in the vertical direction, i.e., the height of cutting into the soil, is as follows:

$$L_{AM} = y_A - y_B \tag{3}$$

Thus, the simultaneous Equations (1) - (3) can be obtained

$$y = \frac{L_{AM}}{sin\varepsilon_B - sin\varepsilon_A} + \sqrt{\frac{L_{AM}^2}{(sin\varepsilon_B - sin\varepsilon_A)^2} - x^2} \tag{4}$$

Equation (4) shows that the shape of the curve *AB* of the machete cutting edge is determined by the parameters of the cutting angle sε_A and ε_B and the height difference L_{AM}. To make the opener more versatile and wear resistance, the sliding machete is made of cast steel. Considering the agricultural requirements of soybean seeding, the maximum depth of sowing l_{AM} is set to 80 mm, and the curve height of the machete is set to 100 mm. The condition for soil particles to slip downward in ditching is that the cutting angle should be greater than the friction angle. The relationship between the two cutting angles and the friction angle is $\varepsilon_B > \varepsilon_A > \varphi$. The parameter ε_B is an important factor affecting the working resistance. When the machete cuts into the soil, its movement direction is vertically downward. At this time, the cutting angle of point B is not too small, to prevent difficulty in cutting into the soil. To meet the conditions for cutting into the soil, too large resistance, the angle should be greater than the friction angle φ. The friction angle is generally between 15° - 38°.Φ is set to 23° to determine the maximum range of the cutting angle, 23° < ε < 67°.

Design of the guide soil board and soil resistance board

To ensure that two rows of seeds are sown smoothly in their respective seeding row areas, the ditching width is large. Considering the requirement of saving electricity, reducing soil disturbance, not too wide ditching, combined with the requirements of planting multiple crops, it is generally designed to 100-120 mm. According to the requirements of crop growth, the row spacing is not less than 50 mm, and the width of the opener is designed as 100 mm. That is, the end span of the soil guide board is equal to the span of the soil resistance board on both sides, and it is 100 mm. The front span of the soil guide board is equal to the thickness of the back end of cutting soil of the machete. Length L, included angle β and groove width b follows the relationship:

$$L = \frac{b}{2\sin\ (\beta/2)} \tag{5}$$

It can be seen that the length of the soil guide board increases with the decrease of the included angle *β*. According to the law that the smaller the included angle of the soil guide board is, the smaller the resistance of the furrow soil, the included angle of the soil guide board is designed. However, the longer the soil guide board, the stronger the soil disturbance, and the more the relative movement of soil particles is intensified. The wet and dry soil is mixed, with the dry soil interlayer directly covering the seeds, which affects the water absorption of seeds, and it is not easy to germinate. The angle of the soil guide board is thus needed to be designed and analyzed. Soil particles are treated as loose particles and kinematics analysis is carried out on the guide soil board. During the ditching, the ditching device is set to move at a constant speed, and the tillage depth is stable. The analysis of the movement of soil particles on the soil plate and retaining plate of the ditching device is shown in Fig. 5. Soil particles on the contact surface of the soil guide board are subject to supporting the force N and the friction force f. The supporting force is decomposed into N_1 along the contact surface and N_2 along the forward velocity direction. The angle between the forward velocity direction and the normal line is *θ*. The soil particles slide on the contact surface, and the soil squeezing angle is *α*. Since the tangential force is greater than the friction resistance, the contact surface of the ditcher has a sliding and cutting effect on the soil.

The resultant force on soil particles is R, and the direction is the same as the motion of soil particles. In this case, the differential equation of the motion of soil particles is as follows:

$$m\frac{d^2x}{dt^2} = N(tan\theta - tan\varphi) \tag{6}$$

$$m\frac{d^2y}{dt^2} = 0 \tag{7}$$

$$N = \frac{mg}{2tan\alpha} \tag{8}$$

The velocity *v* and displacement *s* of soil particles on the contact surface is as follows:

$$v = \frac{gt}{2}\frac{tan\theta - tan\varphi}{tan\alpha} \tag{9}$$

$$s = \frac{gt^2}{2}\frac{tan\theta - tan\varphi}{tan\alpha} \tag{10}$$

When the soil particles move to the back edge of the soil guide board, they begin to move along the soil resistance board. Soil particles are subjected to the friction f_1 of the soil resistance board and the friction f_2 of the soil edge layer, extruding N '. The friction angle between soil particles is φ '.

In this case, the motion differential equation of soil particles is as follows:

$$m\frac{d^2x}{dt^2} = N'(tan\varphi' - tan\varphi) \tag{11}$$

The instantaneous velocity *v'* of the soil particle escaping from the soil resistance board is as follows:

$$v' = \sqrt{\frac{Lg[(tan\varphi' - tan\varphi) + tan\varphi' - tan\varphi)sin\theta}{tan\alpha}} \tag{12}$$

Where, the included angle *θ* between the forward velocity and the normal, the included angle *β* of the soil guide board of the opener, the relationship between the included angle is *θ+β/2=π/2*. According to the design method of ship-type trenching plough *(Wang et al., 2019)*, the value range of the included angle of the soil guide board is determined as 30°<*β*<70°, shown in Fig. 5. When the soil particles moved to both sides under the action of soil guide board, the rectangle furrow is formed, the bottom of the furrow is flat and the seeding depth is consistent. After the soil resistance board passes, the wet soil particles naturally fall back to the seed groove to ensure that the seeds are fully in contact with the wet soil, thereby improving the regularity of seedlings.

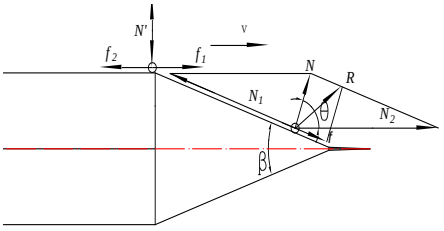

Fig. 5 - Kinematic diagram of soil particles at soil guide board and soil resistance board of the opener

Testing material and equipment

The testing material used is soybeans that are widely grown in Heilongjiang Province. The test was conducted from May 4 to 11, 2022, in the test base of Northeast Agricultural University. The relative humidity of soil was 26% and the hardness was 359 kPa. The test equipment narrow row flat seeder is as shown in Fig.6.

Fig. 6 - Field test of narrow row flat seeder

Testing method

Based on the agronomic requirements of soybean, the spacing between single rows of seeds was set as 80 mm, and the sowing depth as 50 mm to ensure the uniform sowing speed during operation. According to *GB/T6973-2005 Test Method of Simple Grain (Precision) Seeders* and *JB/T10293-2001 Technical Conditions of Simple Grain (Precision)* Seeders, *NY/T740-2003 Field Ditching Machinery Operation Quality*, the seeding performance index and trenching depth performance index of seeder were studied through theoretical analysis and field experiments. The test process is shown in Fig. 7(a) ~(c). The variable coefficient C_b of the seeding is as follows:

$$\bar{X} = \frac{\sum_{i=1}^{m} X_i}{m} \tag{13}$$

$$C_b = \sqrt{\frac{\frac{1}{\text{m-1}}\sum_{i=1}^{m}(X_i - \bar{X})}{\bar{\text{x}}}} \tag{14}$$

where, X_i is the seed spacing of two adjacent seeds in each row, mm; $\bar{X}$ is the average of the seed spacing of two adjacent seeds in each row, mm, and m is the times of tests.

The formula for the variable coefficient C_h of trenching depth is as follows:

$$\bar{h} = \frac{\sum_{i=1}^{n} h_i}{n} \tag{15}$$

$$C_h = \sqrt{\frac{\frac{1}{n}\sum_{i=1}^{n}(h_i - \bar{h})}{\bar{h}}} \times 100\% \tag{16}$$

where, h_i is the sowing depth difference value, mm; $\bar{h}$ is the average of sowing depth difference value, mm, and n is the times of tests.

The main factors affecting the trenching performance and working resistance of the trencher are the penetration angle of the cutting edge of the machete and the angle of the soil guide plate. As a test factor, through the quadratic regression rotary orthogonal combination test, the change law of the influencing factors on the working resistance, the variation coefficient of sowing and variation coefficient of the depth of trenching is analyzed.

(a) (b) (c)

Fig. 7- The process test of performance for the opener

(a) Working status of the opener; (b) The measurement of seeding spacing; (c) The measurement of trenching depth

RESULTS AND ANALYSIS

Performance test of the opener

The machine works at a uniform speed of 2 m/s and the trenching depth is 50 mm. On the basis of the design and analysis of the machete cutting edge and the soil guide board, combined with the seeding distance, the value range of each test factor is determined. The penetration angle ε of the machete cutting edge of the opener is 23°-67°. The included angle β of the guide soil board of the opener is 30°-70°. The two-factor five-level quadratic regression orthogonal combination design is used to seek the best combination of working parameters of the seeding opener. The coding of experimental factors and level is shown in Table 1, and the design scheme and results of the test are shown in Table 2. The measured data of the test are analyzed by using the design-Expert 8.0.6 software regression analysis and factor variance analysis, as shown in Table 3.

Table1

Coding of experimental factors and level

Code number	Penetrating angle ε (°)	Included angle β (°)
1.414	67	70
1	61	64
0	45	50
-1	29	36
-1.414	23	30

Table 2

Experimental design and results

Number	Experimental factor		Performance index		
	Penetrating angle x_1 / °	Included angle x_2 / °	Resistance y_1 / N	Variable coefficient of sowing y_2 / %	Variable coefficient of depth y_3 / %
1	-1	-1	68	9.86	3.05
2	+1	-1	60	6.18	6.61
3	-1	+1	85	13.94	5.45
4	+1	+1	72	8.95	5.34
5	-1.414	0	79	9.05	3.56
6	+1.414	0	66	8.64	6.87
7	0	-1.414	69	6.98	3.67
8	0	+1.414	89	11.56	6.74
9	0	0	61	7.34	3.96
10	0	0	60	8.86	4.72
11	0	0	59	6.91	3.11
12	0	0	66	8.15	4.01
13	0	0	71	6.92	3.07
14	0	0	67	5.45	2.68
15	0	0	70	6.63	4.98
16	0	0	63	7.94	4.35

Table 3

Variance analysis

Index	Source	Sum of squares	df	Mean square	*F*	*P*
Resistance	Model	967.64	5	193.53	10.33	0.0011
	x_1	193.90	1	193.90	10.35	0.0092
	x_2	410.19	1	410.19	21.90	0.0009
	$x_1 x_2$	6.25	1	6.25	0.33	0.5763
	x_1^2	63.28	1	63.28	3.38	0.0959

Index	Source	Sum of squares	df	Mean square	*F*	*P*
	x_2^2	294.03	1	294.03	15.70	0.0027
	Residual	187.29	10	18.73		
	Lack of Fit	41.42	3	13.81	0.66	0.6009
	Pure Error	145.88	7	20.84		
	Cor Total	1154.94	15			
Variable coefficient of sowing	Model	51.70	5	10.34	6.13	0.0075
	x_1	10.73	1	10.73	6.36	0.0303
	x_2	22.63	1	22.63	13.41	0.0044
	$x_1 x_2$	0.43	1	0.43	0.25	0.6250
	x_1^2	7.33	1	7.33	4.35	0.0637
	x_2^2	10.58	1	10.58	6.27	0.0312
	Residual	16.87	10	1.69		
	Lack of Fit	9.14	3	3.05	2.76	0.1214
	Pure Error	7.73	7	1.10		
	Cor Total	68.57	15			
Variable coefficient of depth	Model	22.15	5	4.43	6.98	0.0047
	x_1	8.26	1	8.26	13.03	0.0048
	x_2	3.74	1	3.74	5.90	0.0355
	$x_1 x_2$	3.37	1	3.37	5.31	0.0440
	x_1^2	3.41	1	3.41	5.38	0.0428
	x_2^2	3.36	1	3.36	5.30	0.0441
	Residual	6.34	10	0.63		
	Lack of Fit	1.50	3	0.50	0.72	0.5704
	Pure Error	4.85	7	0.69		
	Cor Total	28.49	15			

As shown in Table 3, in terms of the working resistance, the penetrating angle of the machete cutting edge and the included angle of the soil guide board of the influencing factors are extremely significant. The included angle of the soil guide board is greater than the penetrating angle of the machete cutting edge regarding the influence degree. In terms of the variation coefficient of sowing, the penetrating angle of the machete cutting edge is significant, and the included angle of the soil guide board is extremely significant.

In terms of the variation coefficient of depth, the penetrating angle of the machete cutting edge is extremely significant, and the included angle of the soil guide board is significant. The regression equation between the fitting performance index and the factor coding value is selected.

The regression equations for the working resistance coefficient of variation, seeding coefficient of variation, and depth coefficient of variation are:

$$y_1 = 64.63 - 4.92x_1 + 7.16x_2 - 1.25x_1x_2 + 2.81x_1^2 + 6.06x_2^2 \quad (17)$$

$$y_2 = 7.28 - 1.16x_1 + 1.68x_2 - 0.33x_1x_2 + 0.96x_1^2 + 1.15x_2^2 \quad (18)$$

$$y_3 = 3.86 + 1.02x_1 + 0.68x_2 - 0.92x_1x_2 + 0.65x_1^2 + 0.65x_2^2 \quad (19)$$

To more intuitively analyze the relationship between the performance indicators and test factors, Design-Expert 8.0.6 software is used to establish the corresponding surface between each indicator and factor, as shown in Fig.8 - Fig.10.

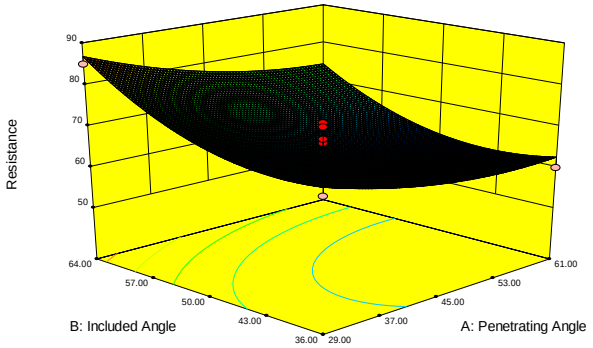

Fig. 8 - Effects of factors on the resistance

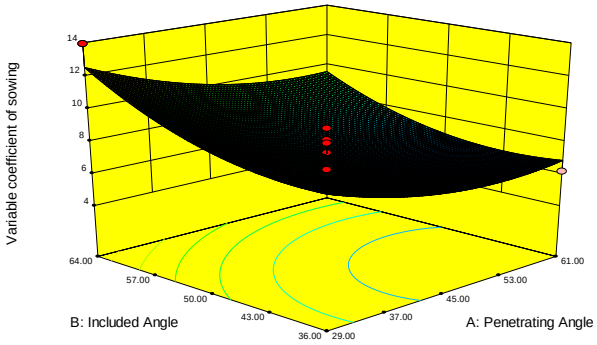

Fig. 9 - Effects of factors on the variable coefficient of sowing

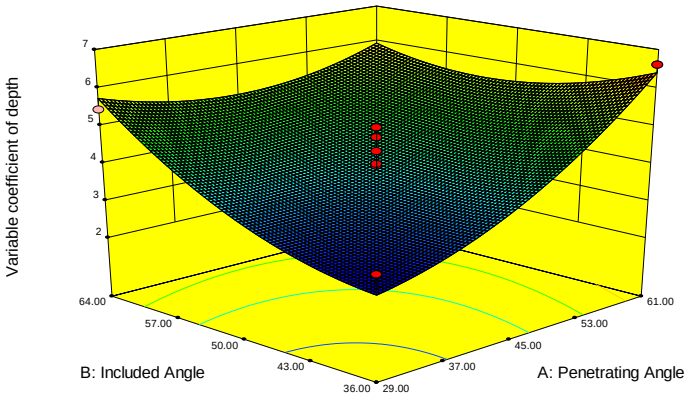

Fig. 10 - Effects of factors on the variable coefficient of depth

Influence analysis of various factors on the performance index of opener

According to Eq. (17) and Fig. 8, the working resistance decreases first and then increases with the increase of the penetration angle, and increases with the increase of the included angle. When the penetrating angle was about 50° and the included angle was 40~45°, the working resistance was the minimum.

According to Eq. (18) and Fig. 9, the variation coefficient of sowing decreases first and then increases with the increase of the penetration angle, and decreases first and then increases with the increase of the included angle. When the penetration angle was 45-53° and the included angle was about 43°, the variation coefficient of sowing was the minimum.

According to Eq. (19) and Fig.10, the variation coefficient of depth increases with the increase of the penetration angle, and increases first and then decreases with the increase of the included angle. When the penetrating angle was 45-53° and the included angle was 38~43°, the variation coefficient of depth was the minimum.

Optimization of test results

As shown in the test data, the optimal combination of working parameters is obtained, and the design for each factor is optimized. According to the agronomic requirements for crop sowing, and combined with the boundary conditions of various factors, the parameterized model is optimized.

According to *GB/T6973-2005 Test Method of Simple Grain (Precision) Seeders* and *JB/T10293-2001 Technical Conditions of Simple Grain (Precision)* Seeders, *NY/T740-2003 Field Ditching Machinery Operation Quality*, Using the multi-objective variable optimization method, the working resistance, seeding coefficient of variation, depth coefficient of variation and regression equation parameters of the nonlinear programming model are established:

$$\begin{cases} \min y_1 \\ \min y_2 \\ \min y_3 \\ s.t. \quad 23° \le x_2 \le 67° \\ \quad 30° \le x_2 \le 70° \\ \quad 0 \le y_1 \le 70 \\ \quad 0 \le y_2 \le 15\% \\ \quad 0 \le y_3 \le 10\% \end{cases} \tag{20}$$

According to the principle of optimization, and the Design Expert8.0.6 optimization analysis, it is concluded that the penetrating angle is 50.03°, and the included angle is 42.36°. The sowing opener was optimal, the working resistance, the variation coefficient of sowing, the variation coefficient of depth was 61.47 N, 6.49% and 4.22%, respectively. The optimal parameter combination interval is obtained according to the optimization analysis, as shown in Fig.11. When the penetrating angle is 28.09~83.94°, the included angle is 25.54 - 60.16°; the working resistance is less than 70 N; the sowing coefficient of variation is less than 15%, and the depth coefficient of variation is less than10%.

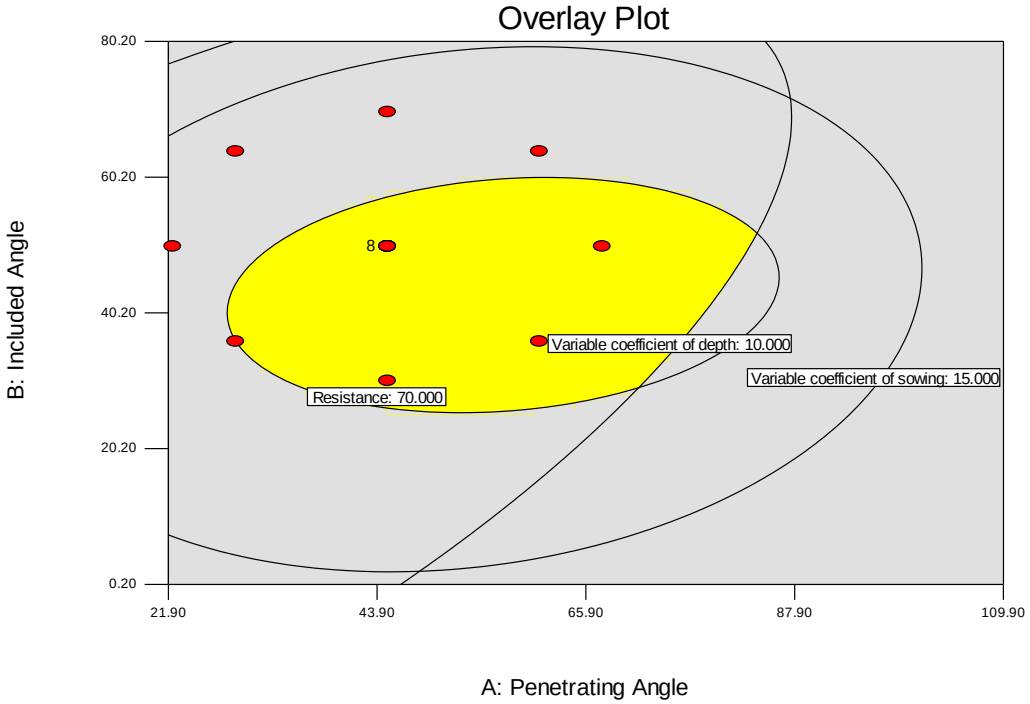

Fig. 11 - Diagram of parameters analysis

Verification of optimization results

According to the optimal parameter range obtained by the optimization analysis, two sets of data are selected for validation testing. The test data of each group were repeated for five times and the mean value is as shown in Table 4.

Table 4

Results of verification experiment

Number	penetrating angle x_1/°	included angle x_2/°	working resistance y_1/N	variation coefficient of sowing y_2/%	variation coefficient of depth y_3/%
1	50	42	62.26	6.81	4.56
2	51	43	63.33	6.99	5.05

From Table 4, it is found that the verification test results are consistent with the theoretical optimization results, and the trenching performance meets the agronomic requirements.

CONCLUSIONS

(1) In this study, a single-trench double-row machete flat bottom opener was designed for precision seeding, and its structure and working principle were elucidated. Based on the equation of arc curve, the machete cutting edge was designed. The theory of kinematic analysis was used to design the soil guide board and soil resistance board to enhance the drag reduction performance and the quality of trenching.

(2) Taking the penetrating angle of machete cutting edge and the included angle of the soil guide board as the influencing factors, a multi-factor quadratic regression orthogonal rotation combined test was conducted to study the effects of various factors on the working resistance, the sowing coefficient of variation, and the depth coefficient of variation. The results showed that: in terms of the working resistance, the penetrating angle of machete cutting edge and the included angle of the guide soil board of the influencing factors were extremely significant, and the included angle of the soil guide board was greater than the penetrating angle of machete cutting edge regarding the influence degree. In terms of the sowing coefficient of variation, the penetrating angle of machete cutting edge was significant, and the included angle of the soil guide board was extremely significant. In terms of the depth coefficient of variation, the penetrating angle of machete cutting edge was extremely significant, and the included angle of the soil guide board was significant.

(3) A multi-objective optimization analysis was performed to establish an optimization model. The optimal combination of the working parameters of the opener was determined using the Design Expert 8.0.6 software. The results showed that when the penetrating angle was 50.03° and the included angle was 42.36°, the sowing opener performance was optimal. The working resistance, the sowing coefficient of variation, and the depth coefficient of variation were 61.47N, 6.49% and 4.22%, respectively. After verification, the results are basically consistent, and the sowing and trenching performance meets the agronomic requirements.

ACKNOWLEDGEMENTS

Thanks to Innovation team of intelligence and key technology research for agricultural machinery and equipment in Western of Guangdong province (GrantNo.2020KCXTD039), University Special talent projects (Grant No. ZL22023).

REFERENCES

[1] Ahmad, F., Qiu, B.J., Ding, Q.S., Ding, W.M., Khan, Z.M., Shoaib, M., Chandio, F.A., Khaliq, A.R.A. (2020). Discrete element method simulation of disc type furrow openers in paddy soil. *International Journal of Agricultural and Biological Engineering,* Vol. 13*,* pp. 103-110. DOI: 10.25165/j.ijabe.20201304.4800

[2] Barr, J.B., Desbiolles, J.M.A., Fielke, J.M. (2018a). Minimising soil disturbance and reaction forces for high speed sowing using bentleg furrow openers. *Biosystems Engineering,* Vol.151(7), pp.53-64. https://doi.org/10.1016/j.biosystemseng.2016.08.025

[3] Barr, J. B., Ucgul, M., Desbiolles, J. M. A., Fielke, J. M.(2018b). Simulating the effect of rake angle on narrow opener performance with the discrete element method. *Biosystems Engineering,* Vol. 171*,* pp. 1-15. https://doi.org/10.1016/j.biosystemseng.2018.04.013

[4] Botta, G.F., A. Tolon-Becerra, A., Lastra-Bravo, X., Tourn, M. (2010). Tillage and traffic effects (planters and tractors) on soil compaction and soybean (Glycine max L) yields in Argentinean pampas. *Soil and Tillage Research,* Vol. 110, pp. 167-174. https://doi.org/10.1016/j.still.2010.07.001

[5] Collins, B. A., Fowler, D. B. (1996). Effect of soil characteristics, seeding depth, operating speed and opener design on draft force during seeding. *Soil and Tillage Research,* Vol.39*,* pp. 199-211. https://doi.org/10.1016/S0167-1987(96)01062-8

[6] Jia, H.L., Zheng J.X., Yuan, H.F., Guo, M.Z., Wang, W.J., Jiang, X.M. (2017b). Design and experiment of profiling sliding-knife opener (仿形滑刀式开沟器设计与试验). *Transactions of the Chinese Society of Agricultural Engineering (Transactions of the CSAE),* Vol. 33*,* pp. 16-24. Beijing/China.

[7] Li, S.P., Pan J.F., Zhong, J.Q., Huang, Z.X., Gan, F.F. (2022). Design and Experiment of Furrow Opener for Transversal Sugarcane Planter Based on Effective Seeding Space (基于有效落种空间的甘蔗横向种植机开沟器设计与试验). *Transactions of the Chinese Society for Agricultural Machinery*, Vol. 53, pp. 162-170. Beijing/China.

[8] Liu, R., Li, Y.J., Liu, C.X., Liu, L.J. (2021). Design and Experiment of Shovel Type Wide Seedling Belt Oat Seeding Furrow Opener (铲式宽苗带燕麦播种开沟器设计与试验). *Transactions of the Chinese Society for Agricultural Machinery (Transactions of the CSAM)*, Vol. 52*,* pp. 89-96. Beijing/China.

[9] Liu, X.P., Zhang, Q.S., Liu, L.C., Wei, G.L., Xiao, L.W.(2019). Surface optimization of ship type ditches based on differential geometry and EDEM simulation (基于微分几何与 EDEM 的船型开畦沟装置触土曲面优化). *Transactions of the Chinese Society for Agricultural Machinery,* Vol. 50, pp. 59-69. Beijing/China.

[10] Lü, J.Q., Yi, S.J., Tao, G.X., Mao. X. (2018). Parameter optimization and experiment of splitter sliding-knife opener for potato planter (马铃薯播种机分体式滑刀开沟器参数优化与试验). *Transactions of the Chinese Society for Agricultural Machinery,* Vol. 34, pp. 44-54. Beijing/China.

[11] Lu, Y. (2020). Design and experimental study of high speed bionic trench opener (高速仿生开沟器设计与试验研究). Changchun: Jilin University. Jilin/China.

[12] Mustafa, U., Chris, S., John, M. F. (2017a). Discrete element modelling of tillage forces and soil movement of a one-third scale mouldboard plough. *Biosystems Engineering,* Vol. 155, pp. 44-54. https://doi.org/10.1016/j.biosystemseng.2016.12.002

[13] Mustafa, U., Chris, S., John, M. F. (2017b). Discrete element modelling of top soil burial using a full scale mouldboard plough under field conditions. *Biosystems Engineering,* Vol. 160, pp.140-153. https://doi.org/10.1016/j.biosystemseng.2017.06.008

[14] Ozmerzi, A., Karayel, D., Topakci, M. (2002). PM-Power Machinery: Effect of Sowing Depth on Precision Seeder Uniformity. *Biosystems Engineering*, Vol. 82, pp. 227-230.https://doi.org/10.1006/bioe.2002.0057

[15] Saeys, W., Wallays, C., Engelen, K., Ramon, H., Anthonis J. (2018). An automatic depth control system for shallow slurry injection, Part 2: Control design and field validation. *Biosystems Engineering,* Vol. 99, pp. 161-170. https://doi.org/10.1016/j.biosystemseng.2007.10.011

[16] Sahu, S. K., Tiwari, K. B., Shrivastava, P. and Namdeo R. (2018). Optimization of the kinematic parameter and fuel consumption for the side-shift offset rotavator using L and J-shape soil cutting blades. *International Journal of Current Microbiology and Applied Sciences*, Vol. 7, pp. 1970-1982. https://doi.org/10.20546/ijcmas.2018.708.227

[17] Singh, K. P., Agrawal, K. N., Dilip J., Manish K., Kushwaha, H. L., Prateek S., Himanshu, T. (2016). Design, development and evaluation of furrow opener for differential depth fertilizer application. *Indian Journal of Agricultural Sciences,* Vol. 86, pp. 250 - 255. http://epubs.icar.org.in/ejournal/index.php/IJAgS/article/download/55999/23526

[18] Singh, S., Tripathi, A. & Singh, A.K. (2017). Effect of Furrow Opener Design, Furrow Depth, Operating Speed on Soil Characteristics, Draft and Germination of Sugarcane. *Sugar Tech,* Vol. 19, pp. 476-484. https://doi.org/10.1007/s12355-016-0499-x

[19] Vamerali, T., Bertocco, M., Sartori L. (2006). Effects of a new wide-sweep opener for no-till planter on seed zone properties and root establishment in maize (Zea mays, L.): A comparison with double-disk opener. *Soil and Tillage Research*, Vol. 89, pp. 196-209. https://doi.org/10.1016/j.still.2005.07.011

[20] Vilaseca, M., Pujante, J., Ramírez, G., Casellas, D. (2013). Investigation into adhesive wear of PVD coated and uncoated hot stamping production tools. *Wear,* Vol. 308, pp. 148-154. https://doi.org/10.1016/j.wear.2013.07.003

[21] Wang, L., Liao, Y.T., Zhang, Q.S., Yao, L., Fu, Y.K. (2019). Design on profile chisel opener of precision broad-width no-tillage planter for rapeseed and wheat. *Transactions of the Chinese Society for Agricultural Machinery,* Vol. 50, pp. 63-73. Beijing / China.

[22] Zhao, S.H., Gu, Z.Y., Yuan, Y.W., Lü, J.Q. (2021). Bionic Design and Experiment of Potato Curved Surface Sowing Furrow Opener (马铃薯曲面式播种开沟器仿生设计与试验). *Transactions of the Chinese Society for Agricultural Machinery,* Vol. 52, pp. 32-42, 64. Beijing / China.

[23] Zhao, S.H., Yang, L.L., Zhang, X., Hou, L.T., Yuan, Y.W., Yang Y.Q. (2022). Design and Experiment of Zigzag Opener for Double-row No-tillage Seeding on Soybean Ridge (大豆垄上双行免耕播种机锯齿式开沟器设计与试验). *Transactions of the Chinese Society for Agricultural Machinery*, Vol. 53(1), pp. 74-84. Beijing / China.

DESIGN AND EXPERIMENT OF A SELF-PROPELLED JUJUBE COLLECTION STRIP PICK-UP MACHINE
/
自走式红枣集条捡拾机的设计与试验

Fengkui ZHANG[1,2], Wenxi SHAO [1,2], Jikui ZHU [1,2], Ting ZHANG[1,3], Shijie ZHAO[1,3], Ping LI [1,2*]
[1)] College of Mechanical and Electrical Engineering, Tarim University, Alar 843300, Xinjiang, China;
[2)] Modern Agricultural Engineering Key Laboratory at Universities of Education Department of Xinjiang Uygur Autonomous Region, Tarim University, Alar 843300, Xinjiang, China
[3)] Key Laboratory of Tarim Oasis Agriculture (Tarim University), Ministry of Education, Tarim University, Alar 843300, Xinjiang, China
Corresponding Author: Ping Li, Email: lpdyy716@163.com

DOI: https://doi.org/10.35633/inmateh-70-25

Keywords: *Collection strip, Harvesting machinery, Jujube, Pick-up, Pneumatic*

ABSTRACT
Aiming at the problems of single mechanical performance, multi-person operation and low operation efficiency of air-suction jujube harvesting in China, combined with the requirements of mechanized jujube harvesting in Xinjiang, this study designed a self-propelled jujube collection strip pick-up machine. The machine is mainly composed of crawler chassis, landing jujube collection strip device, separation and impurity removal device and hydraulic system. According to the jujube planting mode, the size of the crawler chassis is 1780 mm × 1650 mm × 310 mm. In order to simulate the effect of artificial collecting strips, a reciprocating collecting strip blowing head was designed with a height of 15 cm from the ground, a horizontal and vertical angle of 35° and 15° respectively. The model of the collecting fan is selected as 9-19-4A; the fluid simulation analysis of the separation and impurity removal box is carried out to verify the rationality of the box structure design. The performance of the picker was tested by pick-up efficiency, cleanliness, breakage, and impurity rates. The results show that when the forward velocity was about 0.40 m·s^{-1}, the average pick-up efficiency could reach 752.7 km·h^{-1}, the average pick-up cleanliness rate was 95.66 %, the average breakage rate was 2.68 %, and the average impurity rate was 3.64 %. The self-propelled jujube collection strip pick-up machine designed in this experiment meets the requirements of mechanized harvesting of jujube and can realize single-person remote control operation.

摘要
针对我国气吸式红枣收获机械性能单一、需多人同时操作以及作业效率低等问题，结合新疆红枣机械化收获作业要求，本研究设计一种自走式红枣集条捡拾机。该机主要由履带底盘、落地红枣集条装置、分离除杂装置和液压系统等组成。根据红枣种植模式设计履带底盘外形尺寸为 1780 mm×1650mm×310 mm；为模拟人工集条效果，设计往复式集条吹头距地高度 15cm、水平和竖直夹角分别为 35°和 15°；选取集条风机型号为 9–19–4A；对分离除杂箱箱体进行流体仿真分析，验证箱体结构设计合理性；通过捡拾效率、拾净率、破损率和含杂率来检验捡拾机作业性能。结果表明：前进速度约为 0.40m·s-1 时，平均捡拾效率可达 752.7 km·h-1，平均捡净率为 95.66%，平均破损率为 2.68%，平均含杂率为 3.64%。本试验设计的自走式红枣集条捡拾机符合红枣机械化收获作业要求，可实现单人远程遥控操作。

INTRODUCTION
Currently, landing jujube harvest operations in China are mainly comprised of the sectional type operation mode of gathering strips, followed by concentrated harvest, which first uses domestic fire fans to collect scattered jujubes on the ground into heaps or strips. Finally, air-absorbing jujube harvesting machinery and equipment were used to gather the harvest *(Zhang et al., 2021)*. This operation method improved the mechanization level and efficiency of landing jujube harvesting to a certain extent and reduced the cost of production. Still, there are problems, such as the need for multiple people to operate the machine and the working link being verbose simultaneously *(Chen et al., 2020; Yuan et al., 2022)*.

Fengkui Zhang, Master, Lecturer; Wenxi Shao, Graduate student; Jikui Zhu, Lecturer; Ting Zhang, Graduate student; Shijie Zhao, Graduate student; Ping Li, PhD, Professor.

The research on foreign forest fruit harvesting equipment started earlier than that in China. There are many studies on shaking forest fruit harvesting equipment *(Homayouni, 2021; Sola-Guirado, et al., 2017; Afsah–Hejri, et al., 2022)*, such as blueberry, citrus and so on *(Brondino et al., 2021; Ghonimy et al., 2019)*. When harvesting fruits with small particle size, the principle of negative pressure suction is generally used to reduce the damage rate of fruit epidermis *(Shuib et al., 2018)*. The development of modern agriculture is transforming from manual harvesting to sustainable automation *(Kootstra et al., 2021)*. Especially in the mechanization of fruit harvesting, it has begun to focus on economic performance research *(Bernardi et al., 2021; Grupioni et al., 2020)*. With the rapid development of orchard intelligence, orchard picking robots have made positive progress in fruit recognition and positioning *(Kim et al., 2020)*, path planning *(Kurtser and Edan, 2020)*, pose adjustment *(Yeshmukhametov et al., 2020)*, and flexible grasping *(Ben-Shahar et al., 2020)*. However, there are still problems such as low efficiency and difficulty in meeting the actual needs of fresh fruit picking *(Davidson et al., 2020; Fu et al., 2020; Davidson et al., 2020)*.

The planting area and yield of jujubes in China rank first in the world. There is relatively much research on jujube harvesting machinery and equipment. However, the harvesting principle and device structure are similar to those of foreign forest fruit harvesting machinery and equipment due to the late research on forest fruit harvesting machinery and equipment. For the harvesting operation of ground jujube, there are many problems, such as poor applicability and a single function *(Wang et al., 2021)*. Compared with mechanical principle harvesting machinery and equipment, its advantages are: good applicability and flexibility, low picking, and low breakage rates *(Yuan et al., 2021)*. However, most of them are small jujube harvesting machinery, and productivity cannot meet the requirements when working in the field. Before the operation, the landing jujube must be artificially gathered into piles or strips, and the function only meets picking, transportation, separation, and impurity removal. Therefore, it is necessary to improve and optimize such mechanical equipment according to the local conditions and human resources *(Yamin et al., 2022; Yamin et al., 2022)*.

A self-propelled jujube-collecting strip picker was designed in this study based on the analysis of the problems mentioned above and connected with the previous research basis and research data. It can complete the harvesting operation of jujube between under the tree and row middle using the air-blowing principle and the reciprocating collection strip mechanism. The performance parameters of the pick-up machine were verified by the operation performance test of the pick-up machine to provide references for research on jujube harvesting machinery.

MATERIALS AND METHODS

Main planting pattern and mechanized harvesting operation requirements

The planting area and yield of Xinjiang jujube are the first in China. The jujube planting industry uses 4/5 of the available planting regions in Xinjiang, mainly distributed in southern Xinjiang *(Editorial Committee of Xinjiang Statistical Yearbook, (2021))*. In the harvest time, landing jujube is more than 60% of the total, and finally, the artificial tap down on the ground to collect together and complete the harvest operation. The parameter table of the jujube planting pattern is shown in Table 1. Wide-row close planting (trunk shape) and wide-narrow intercropping (open center shape) are two main planting patterns in the jujube high-quality producing areas of Southern Xinjiang for convenient mechanized operation and management. There are characterized by wide row spacing, high crown height and fixed stem, and sparse lateral branches. These two planting patterns benefit the mechanized process and improve the final fruit quality. The wide-row close planting (trunk shape) and wide-narrow intercropping (open center shape) planting modes were selected as the design basis to improve the applicability and versatility of the designed self-propelled jujube collection strip pick-up machine.

Table 1

The parameter table of the jujube planting pattern

Tree shape	Seed spacing /(m $^{-1}$)	Row spacing /(m $^{-1}$)	Crown height /(m $^{-1}$)	Heading height /(m $^{-1}$)
Trunk shape	0.8–1	1.6–2	< 1.5	0.4–0.6
Open Center shape	1.5–2	3–3.5	2.5–3	0.5–0.8

The operation process of landing jujube mechanical harvesting conduct an inter-row landing jujube collection strip and jujube under the tree blow to the inter-row firstly. Then, pick-up, transportation, separation, and impurity removal for the jujube of the collection strip are performed. Finally, the jujube was collected into the fruit collection box.

The whole structure and technical parameter

The structure of the self-propelled jujube collection strip pick-up machine is shown in Figure 1. The apparatus mainly comprises a crawler walking system, chassis frame, hydraulic system, remote control operating system, landing jujube collection strip device, jujube under the tree blowing device, a separation and impurity removal device, picking and conveying pipe, suction blower, transmission mechanism, etc. The landing jujube collection strip device comprises a collection strip blowing head, collection strip fan, reciprocating collection strip mechanism, and copying collection stripboard. The jujube under the tree blowing device is composed of under-tree jujube blowing head, flexible pipe, blowout fan, etc. The main technical parameters of the whole machine are shown in Table 2.

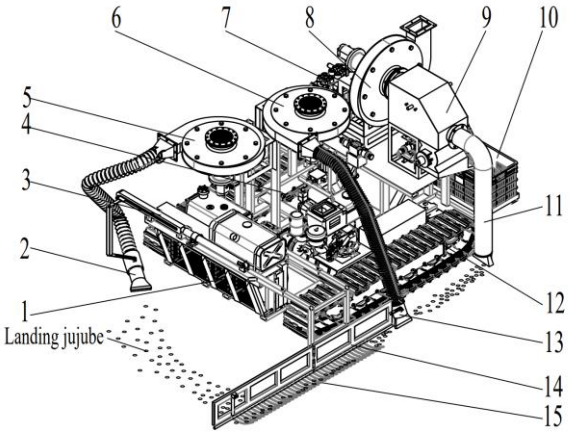

Fig. 1 - Structural diagram of the self-propelled jujube collecting strip pick-up machine

1. chassis frame; 2. collection strip blowing head; 3. reciprocating collection strip mechanism; 4. hydraulic system; 5.collection strip fan; 6. blowout fan; 7. remote control operating system; 8. suction blower; 9. separation and impurity removal device; 10. fruit collection box; 11. picking and conveying pipe; 12. crawler walking system; 13. under-tree jujube blowing head; 14. copying collection stripboard; 15. lock chain

Table 2

Key technical parameters of the self-propelled jujube collecting strip pick-up machine

Parameters	Design Values
Machine size (L × W × H)/ (mm × mm × mm)	2000 × 1500 × 1300
Overall weight / kg	1250
Matched power / kW	23
Operation width / mm	1500–2000
Operating speed / km·h $^{-1}$	0–5
Pick-up efficiency / kg·h $^{-1}$	≥ 700
Pick-up cleanlily rate / %	≥9 0
Breakage rate / %	≤ 3
Impurity rate / %	≤ 5

Working principle

When the self-propelled jujube collecting strip pick-up machine works between rows in the jujube garden (Figure 2), the effect is best when the copying collection strip board of the pick-up machine is adjusted to 3-5 cm from the left jujube trunk between rows. The collection strip blowing head in the front of the pick-up machine blows the landing jujube in the front working area from the right side to the bottom of the left copying collection strip board under the action of the reciprocating collection strip mechanism and intercepts. It collects the strip through the lock chain. The jujube of the collection strip is picked up by picking and conveying pipes and transported to the separation and impurity removal device. The jujube is separated from the impurities under airflow, self-weight, and obstructive board and is discharged into the fruit collection box through the unloading impeller.

The lightweight impurities with small floating speed, such as blades and others, move with the suction airflow, and are discharged from the outlet of the suction blower after being broken by the choppy roll. Heavy impurities, such as soil and others can be discharged through the railing gap of the discharge port during the jujube removal process. During the whole operation process, the under-tree jujube blowing head on the left side of the pick-up machine blows out the jujube under-tree under the action of the blowout fan to the left row of the landing jujube harvest operation. After completing the left side of the inter-row landing jujube harvesting operation, the pick-up machine can be turned to the right side of the inter-row operation and finally achieve the landing jujube harvesting operation of the inter-row.

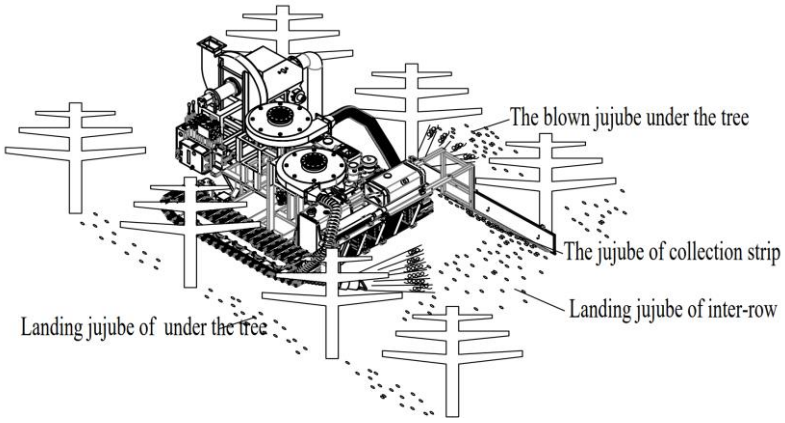

Fig. 2 - Working principle of the self-propelled jujube collecting strip pick-up machine

Design of critical components

Self-propelled crawler chassis

The crawler chassis has the advantages of reducing ground pressure and improving traffic ability *(Zhang et al., 2023)*, and it can better adapt to the operating conditions of sand-land in Southern Xinjiang. The pick-up machine must overcome the driving resistance and steering resistance at the same time. The power consumed by the steering resistance was much larger than the linear driving resistance. Steering of the crawler chassis is achieved by changing the driving force on the driving wheels on both sides to achieve different speeds *(Wang et al., 2021; Du et al., 2023; Vladislav, 2023)*. Figure 3 shows the force analysis of the contact area with the ground when the chassis turns. O is the steering center point of the crawler chassis, and O' is the geometric center point of the crawler chassis.

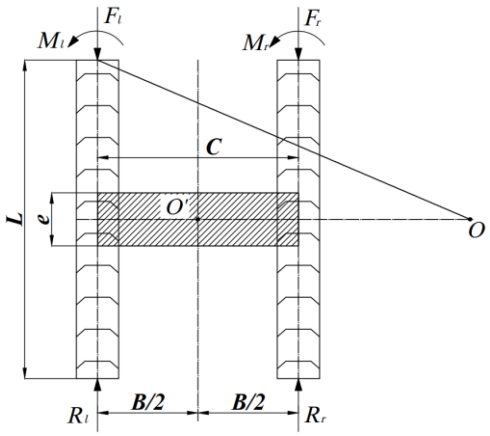

Fig. 3 - Force analysis of the contact area with the ground

The equilibrium conditions for turning are as follows:

$$F_l = \frac{fG}{2}\left(1+\frac{2C}{B}\right) \quad (1)$$

$$F_r = \frac{fG}{2}\left(1-\frac{2C}{B}\right) \quad (2)$$

where:

F_l is the crawler steering resistance of the left side, Pa;

F_r is the crawler steering resistance of the right side, Pa;
f is the coefficient of rolling resistance, it is 0.12;
G is the total gravity of the crawler chassis, N;
C is the transverse eccentric distance, it is 0.708 m; B is the center distance of crawler, it is 1.416 m.

The grounding pressure of the crawler on both sides is as follows:

$$P_{al} = \frac{G}{2bL}\left(1+\frac{2C}{B}\right) \tag{3}$$

$$P_{ar} = \frac{G}{2bL}\left(1-\frac{2C}{B}\right) \tag{4}$$

where:

P_{al} is the crawler grounding pressure of the left side, Pa,
P_{ar} is the crawler grounding pressure of the right side, Pa,
b is the width of crawler contact ground, it is 0.24 m,
L is the length of crawler contact ground, it is 1.4 m.

The steering torque moment of crawler chassis M is:

$$M = M_l + M_r \tag{5}$$

$$M_l = \frac{\mu GL}{8}\left(1+\frac{2C}{B}\right)\left[1-\left(\frac{2e}{L}\right)^2\right]^2 \tag{6}$$

$$M_r = \frac{\mu GL}{8}\left(1-\frac{2C}{B}\right)\left[1-\left(\frac{2e}{L}\right)^2\right]^2 \tag{7}$$

where:

M is the steering torque moment of the crawler chassis, N·m;
M_l is the steering torque moment of the crawler chassis of the left side, N·m;
M_r is the steering torque moment of the crawler chassis of the right side, N·m;
μ is the coefficient of steering resistance, it is 0.7; e is the longitudinal eccentricity distance, it is 0.297 m.

The steering torque moment and power of the drive wheel when the crawler drive chassis turns left are as follows:

$$F_l = \frac{fGL}{2}\left(1+\frac{2C}{B}\right)+\frac{\mu GL}{4B}\left[1-\left(\frac{2e}{L}\right)^2\right]^2 \tag{8}$$

$$F_r = \frac{fGL}{2}\left(1-\frac{2C}{B}\right)-\frac{\mu GL}{4B}\left[1-\left(\frac{2e}{L}\right)^2\right]^2 \tag{9}$$

$$M_{max} = \left(F_{lmax}+F_{rmax}\right)r \tag{10}$$

$$W_{max} = \left(F_{lmax}+F_{rmax}\right)v \tag{11}$$

where:

M_{max} is the maximum driving moment of the crawler driving wheel, N·m;
W_{max} is the maximum driving power of the crawler driving wheel, kW;
r is the pitch radius of the driving wheel, it is 0.12 m;
v is the line speed of the driving wheel, it is 0.415 m·s^{-1}.

The full load quality of the pick-up machine is 1250 kg. According to the calculation, the maximum driving moment of the chassis drive wheel is 649.27 N·m, and the maximum power is 10.82 kW.

The self-propelled crawler chassis comprises a hydraulic motor, driving wheel, tensioning wheel, bearing wheel, etc., as shown in Figure 4.

Two hydraulic motors drive the driving wheel with a power of 6 kW and an operating speed of 155 – 775 $r \cdot min^{-1}$ to realize the movement and spot turn of the pick-up machine. The driving wheel adopts the rear type to reduce the height of the entire machine. The pitch tooth meshing mode fixes the crawler and the driving wheel to ensure that the track does not fall off. According to the row spacing of the wide-row close planting (trunk shape) and wide-narrow intercropping (open center shape) planting modes, the dimension of the crawler chassis was designed to be 1780 mm × 1650 mm × 310 mm (L × W × H).

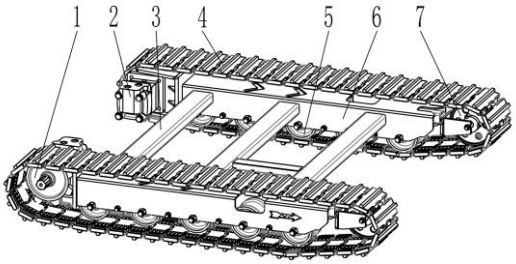

Fig. 4 - Structure diagram of self-propelled crawler chassis

1. Driving wheel; 2. Hydraulic motor; 3. Balance beam; 4. Crawler; 5. Bearing wheel fixing plate; 6. Bearing wheel; 7. Tensioner wheel

The landing jujube collection strip device and under-tree jujube blowing device

The landing jujube collection strip and under-tree jujube blowing device are composed of a collection strip blowing head, reciprocating frame, adjusting mechanism, collecting strip fan, expansion frame, copying collection strip board, blowout fan, under-tree jujube blowing head, etc., as shown in Figure 5. The landing jujube collection strip device realizes reciprocating motion by controlling the hydraulic cylinder to make the adjusting mechanism on the reciprocating frame drive the collection strip blowing head to simulate the effect of a manual collection strip. The adjusting mechanism can adjust the height and horizontal and vertical angle of the collection strip blowing head from the ground. The expansion frame can adjust the protrusion distance of the copying collection strip board to control the width of the collection strip operation to apply to different work plots. The under-tree jujube blowing device discharges the positive pressure airflow through the blowout fan and the under-tree jujube blowing head. According to the previous research results of the team, the design of the strip blowing head was 15 cm from the ground height, the horizontal and vertical angles were 35° and 15°. The operation effect is the best when the forward speed is 1.5 km/h, and the picking rate can reach 93.99 %. The landing jujube under the tree is blown to the row under positive pressure airflow to realize the blowing operation of the jujube under the tree. The under-tree jujube blowing head is installed on the left side of the end of the copying collection strip board to prevent the reduction of picking efficiency caused by blowing out the collected jujube.

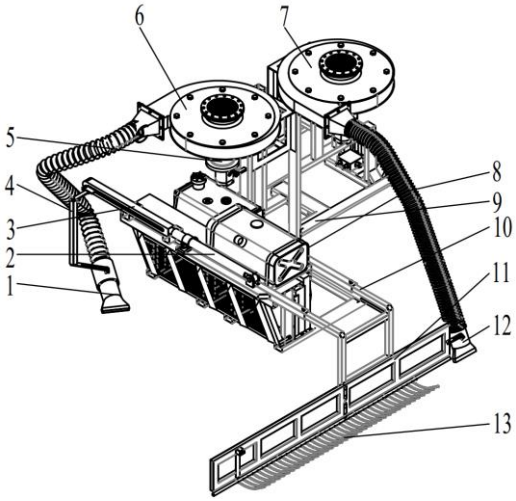

Fig. 5 - The landing jujube collection strip and under-tree jujube blowing device

1. Collection strip blowing head; 2. Hydraulic cylinder; 3. Reciprocating frame; 4. Adjusting mechanism; 5. Hydraulic motor; 6. Collecting strip fan; 7. Blowout fan; 8. Flexible pipe; 9. Frame; 10. Expansion frame; 11. Copying collection stripboard; 12. Under-tree jujube blowing head; 13. Lock chain

By setting up the air-blowing collection strip test device and conducting the orthogonal test in the soil through the laboratory of Tarim University, the orthogonal test showed that the operation effect was the best when the collection strip blowing head from the ground was 15 cm, and the horizontal and vertical angles were 35° and 15°. The forward velocity was 1.5 km·h^{-1}, and the pick-up cleanlily rate could reach 93.99%. The air-blowing collection strip test device is shown in Figure 6.

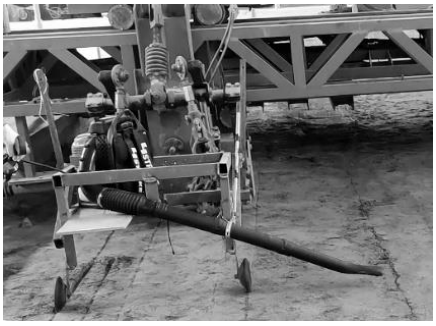

Fig. 6 - Air-blowing collection strip test device

Collection strip fan type selection

The model of the collecting fan can be selected by the air volume required for the operation. The operating air volume includes the operating loss air volume and the air volume required to move the landing jujube to the baffle *(Zhang et al., 2022; Yu et al., 2020)*. The operation air volume can select the model of the collection strip fan. The operation air volume includes the operational waste air volume, and the air volume of the landing jujube moves to the collection stripboard.

(1) Operating air volume calculation

The previous experimental observation found that when the jujube is affected by airflow, the jujube with different initial states will eventually roll with the long axis as the axis. Therefore, the long-axis section is used as the wind surface for calculation, and the air volume is as follows:

$$Q_0 = K \cdot L \cdot \rho \cdot v \cdot Q \tag{12}$$

where: Q_0 is the demand air volume of the collector bar, m^3·h^{-1};

K is the airflow coefficient, due to fan losses and airflow losses in the air, so the airflow coefficient is introduced, generally 1.3–1.6;

ρ is the concentration of landing jujube, pcs/m^2;

v is pick-up machine forward speed, km·h^{-1}.

The air volume required for a single jujube to roll to the baffle is:

$$Q = v_0 \tag{13}$$

where:

v_0 is airflow velocity, m·s^{-1};

A is the cross-sectional area of jujube subjected to wind, m^2.

(2) Wind pressure calculation of fan operation

The total pressure of the fan is composed of static and dynamic pressures. Thus, there are the following formulas:

$$P = P_S + P_D \tag{14}$$

$$P_S = \frac{\varepsilon v_0 \rho_a}{2} \tag{15}$$

$$P_D = \frac{{v_0}^2 \rho_a}{2} \tag{16}$$

where:

P is the full pressure of the fan, Pa;

P_S is the static pressure of the fan, Pa; P_D is the dynamic pressure of the fan, Pa;

ε is the inherent resistance coefficient *(Yang and Wang, 2016)*, 1.35;

v_0 is the airflow velocity, m·s^{-1}; ρ_a is the air density, kg·m^{-3}.

The pressure loss along the way should also be considered in the fan type selection, and it can be obtained from the following formula:

$$\Delta P_m = \frac{\lambda}{de} \cdot \frac{v^2}{2} \rho l \tag{17}$$

$$\lambda = K \cdot \frac{0.0134}{D^{\wedge 0.284}} \tag{18}$$

where:

de is the equivalent diameter of the blowing pipe, m, round blowing pipe de = d; v is airflow velocity in the tube, m·s^{-1}; ρ is the air density, kg·m^{-3}; l is the length of the blowing pipe, m; λ is resistance friction coefficient, as the blowing pipe is in the resistance square zone (it is the ratio of velocity to kinematic viscosity greater than 2.7×10^6); K is the equivalent friction coefficient of the inner wall of the blowing pipe, according to the roughness of the value, here is 0.15; D is the diameter of blowing pipe, m.

The dynamic pressure loss of the fan was 1506.25 Pa, the static pressure loss was 2033.44 Pa, and the pressure loss along the way was 90.26 Pa when the length of the blowing pipe was 1.5 m and the total pressure was 3629.95 Pa. Therefore, the air volume and total pressure of the collection strip fan should be higher than the calculated data *(Chen et al., 2022).* The fan model was 9–19–4A, which was selected during the “Fan Selection” stage.

Separation and impurity removal device

The separation and impurity removal device comprises a discharge fence, discharge impeller, separation and impurity removal box, chain wheel drive mechanism, suction, and supply fan, fan connecting shaft, and hydraulic motor, as shown in Figure 7. During the operation, the suction blower rotates to generate negative-pressure suction airflow inside the separation and impurity removal box. The jujube enters the separation and impurity removal box from the gathering process, conveying hoses and falling into the unloading impeller. From the unloading outlet through the fence the jujube falls into the fruit collection box. In the gathering process and conveying, the floating speed of lightweight impurities, such as blades and others are small, move with suction airflow, and are discharged from the outlet of the suction blower after being broken by the choppy roll. Heavy impurities, such as soil and others can be discharged through the railing gap of the discharge port during the jujube removal process.

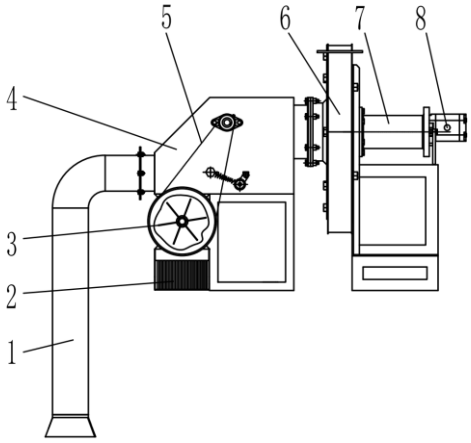

Fig. 7 - Separation and impurity removal device

1. picking up and conveying hoses; 2. unloading fence; 3. unloading impeller;4. separation and impurity removal box; 5. chain wheel drive mechanism; 6. suction blower;7. fan connecting shaft; 8. hydraulic motor

Hydraulic transmission system

The hydraulic transmission system consists of walking and activity systems, as shown in Figure 8. Two traveling motors are connected in parallel in the hydraulic transmission system, and the walking dual pump supplies the oil. The throttle size can control motor speed. The driving motor of the suction strip fan is parallel to the driving motor of the blowout fan. The unloading driving motor is similar to the driving motor of the suction blower, and the speed control valve can control the hydraulic flow rate. The speed of the hydraulic motor can be controlled, and the dual-activity pump supplies the oil.

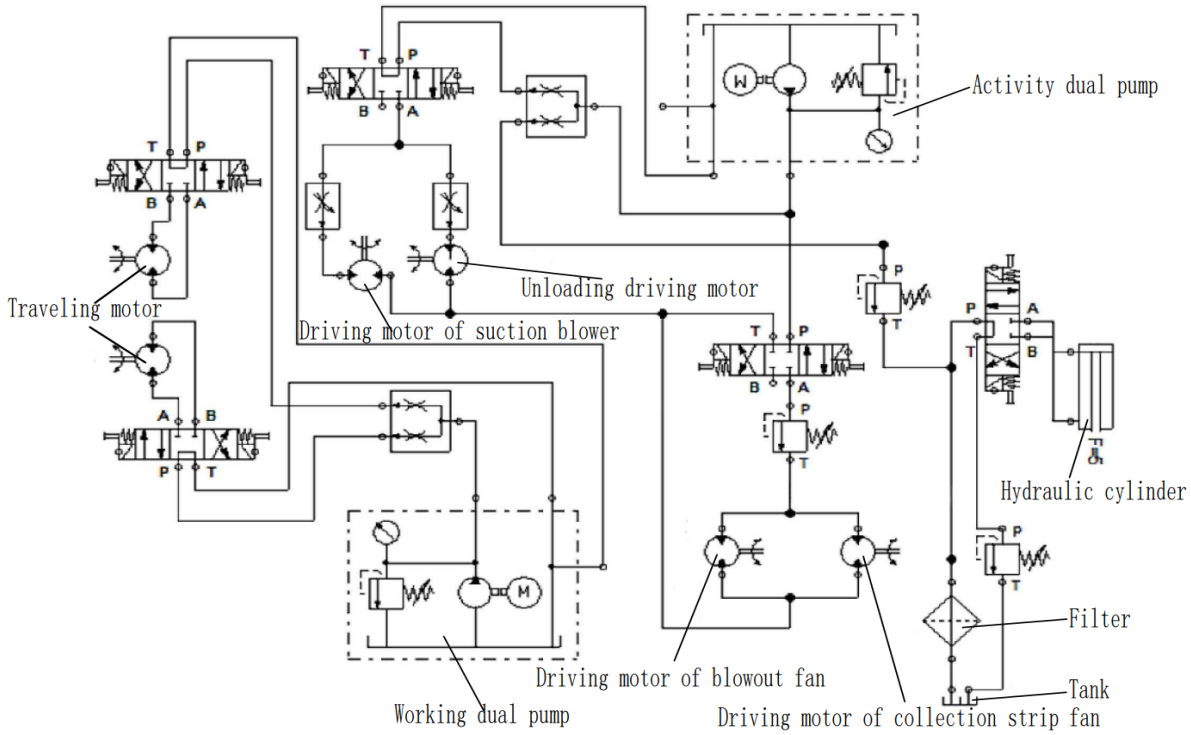

Fig. 8 - Hydraulic transmission system

The reciprocating collection strip mechanism realizes automatic reciprocating linear motion by pushing and pulling the hydraulic cylinder. A three-position four-way electromagnetic directional valve and travel switch control the pushing and pulling of the hydraulic cylinder. When the switch is started during operation, the three-position four-way electromagnetic directional valve is powered at the left valve position, the hydraulic oil enters the left chamber of the hydraulic cylinder, and the hydraulic cylinder is extended at this time. When switch two is fully extended, the right valve of the three-position four-way electromagnetic directional valve is electrified, and the hydraulic oil enters the rod cavity and lets the piston rod return. When the piston rod of the hydraulic cylinder is completely returned, switch one is touched to control the hydraulic cylinder to return, and an operation cycle process is completed.

Separation and impurity removal box

The separation and impurity removal box comprises three parts: a separation chamber, a crushing impurity chamber, and an unloading chamber. The separation chamber reduces the airflow velocity by suddenly increasing the volume and cooperates with the baffle plate to separate the jujube from the impurities. The choppy roll in the crushing impurity chamber crushes the light impurities, such as jujube leaves, through high-speed rotation to be discharged from the outlet of the suction blower. The unloading chamber separates the jujube and heavy impurities through the unloading fence and puts them into the fruit collection box, while ensuring the airtightness of the box. The separation and impurity removal box is shown in Figure 9.

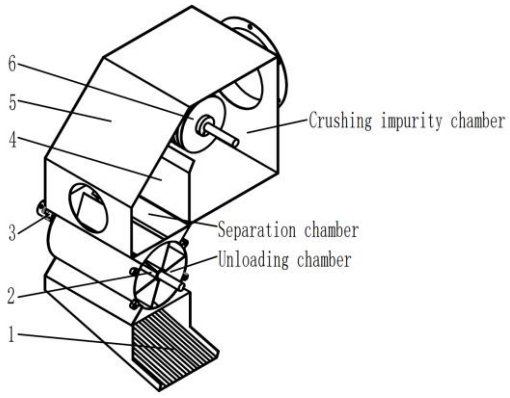

Fig. 9 - Separation and impurity removal box

1. Unloading fence; 2. Unloading impeller; 3. Servo motor; 4. Baffle plate; 5. Box shell; 6. Choppy roll

Operation performance test

Experiment conditions

The operation performance test of the self-propelled jujube collection strip pick-up machine (Figure 10) was carried out in the experimental center of Tarim University of Alar city, Xinjiang Province, China, on 15 August 2022. A flat ground with a length of 50 m and a width of 5 m was selected as the test area for operation performance, and three repeated tests were conducted. Before the experiment, the forward velocity of the pick-up machine was adjusted to about 0.4 m·s^{-1}. A 30 m × 1.5 m landing jujube working belt was arranged in the test area of operational performance. The mass ratio of jujubes to impurities was 4:1. The jujubes with pests and surface damage need to be removed to reduce the impact on the test and reflect the actual performance parameters of the pick-up machine.

Fig. 10 - The operation performance test of the self-propelled jujube collection strip pick-up machine

Test methods

According to the test method of *DG/T 188–2019 "Fruit Picker," (2019)* test indexes, such as picking efficiency, picking rate, damage rate, and impurity rate, were proposed as the performance assessment criteria of the self-propelled jujube collection strip pick-up machine.

(1) Picking efficiency γ

The pick-up machine was operated to harvest the jujube in the selected operation area. After the operation, the jujube in the fruit collection box was weighed and recorded as x_i. Due to the uneven distribution of scattered jujubes on the ground, the time spent on harvesting operations within the area of the completed work was recorded by a timer s_i.

$$\gamma = \frac{x_i}{s_i} \tag{19}$$

where:

γ is picking efficiency, kg·h^{-1};

x_i is weighing the quality of jujube in the fruit collection box, kg;

s_i is time spent on harvesting operations, h.

(2) Pick-up cleanlily rate λ

After the operation of the pick-up machine is completed, the landing jujube that is not collected strip and picked up by the pick-up machine in the operation area, has the weight recorded as $y_{i.}$

$$\lambda = 1 - \frac{y_i}{x_i + y_i} \times 100\% \tag{20}$$

where:

λ is pick-up cleanliness rate, %;

y_i is weighing the quality of un-collected strip and un-picking jujube, kg.

(3) Breakage rate ε

The jujube fruit in the fruit collecting box was selected, weighed and recorded as z_i.

$$\varepsilon = \frac{j_i}{z_i} \times 100\% \quad (21)$$

where:

ε is the breakage rate, %; j_i is weighing the quality of broken jujube, kg.

(4) Impurity rate μ

The mixture in the fruit collection box was weighed and recorded as a_i.

$$\mu = \frac{z_i}{a_i} \times 100\% \quad (22)$$

where:

μ is the impurity rate, %; z_i is the impurity weighing quality, kg.

RESULTS AND ANALYSIS

Numerical simulation of internal airflow field in the box

A fluid simulation analysis of the box was conducted to verify the rationality of the design of the separation and impurity removal box. Only the grids at the unloading chamber and the baffle plate are encrypted when meshing to explore the airflow state of the box and the conveying hoses and reduce the simulation time. The grids at the unloading chamber, the outer wall of the box, and the conveying hoses were sparse, and the number of grids divided was 246,000. The standard k-ε model was used to set the parameters, the inlet pressure was 0 Pa, the outlet pressure was -1200 Pa, the unloading chamber was set as the rotating area, the speed was 30 r·min^{-1}, and the rest areas were the static area. The simulation results are shown in Figure 11.

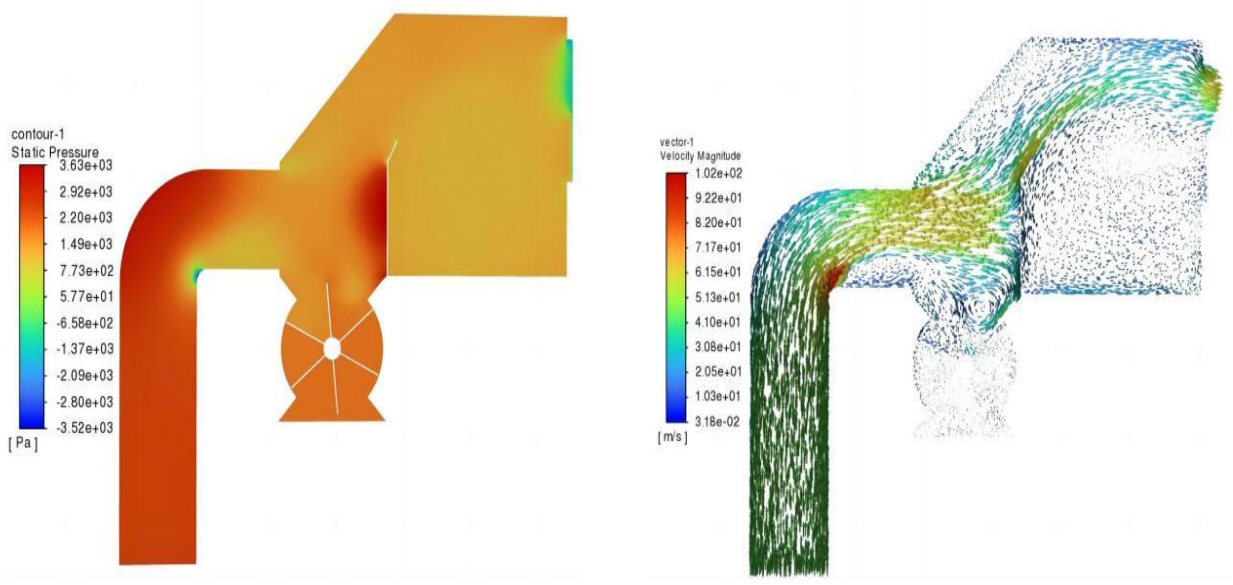

a) b)

Fig. 11 - Distribution diagram of pressure and velocity in the center section of the separation and impurity removal box

a) Pressure nephogram; b) Air velocity trajectory vector diagram

The airflow velocity and pressure distribution of the separation and impurity removal box and the pick-up conveying pipe are relatively uniform, as shown in Figure 11. There are slight losses at the bend pipe, baffle plate, and unloading chamber, which can be ignored. The overall airflow trajectory vector distribution of the unloading chamber is reasonable, and the vortex phenomenon appears on the upper right of the unloading chamber, which is more convenient for the jujube to enter the unloading chamber. The airflow vector in the unloading chamber is weak, which has little effect on the movement of the jujube, indicating that the influence of the rotation of the unloading impeller on the airflow inside the box can be ignored. In summary, the design of the box structure is reasonable.

Experiment results and analysis

The prototype operation performance test showed that the overall performance of the pick-up machine was relatively stable, and each device could work normally. The general operation effect was good, as it could meet the harvesting requirements.

According to the above pick-up machine test method, the picking efficiency, net pick-up rate, breakage rate, and impurity rate of each test area were calculated, and the average values of the three test results were taken. The average picking efficiency of the jujube garden of the pick-up machine is about 752.7 kg·h^{-1}, the average pick-up cleanlily rate is approximately 95.66%, the average breakage rate is about 2.68%, and the average impurity rate is about 3.64%, which meets the design requirements. The experimental results are shown in Table 3.

Table 3

Experimental results

Area Number	Pick-up efficiency (kg·h^{-1})	Pick-up cleanlily rate /%	Damage rate/%	Impurity rate/%
1	749.6	94.61	2.67	3.58
2	756.3	96.46	2.85	3.71
3	752.2	95.93	2.52	3.64

CONCLUSIONS

(1) Aiming at the problems of a single function of air-suction jujube harvesting machinery and equipment, simultaneous operation of multiple people, and low efficiency of field operation, combined with the planting mode and mechanized harvesting requirements of jujube high-quality production areas in Southern Xinjiang, a self-propelled jujube collection strip pick-up machine was designed. The whole machine had a compact structure and could be operated by a single person. It could complete the collection strip, picking, separation, and impurity removal of the landing jujube. It could be remotely controlled to reduce the harm of dust to people during operations.

(2) Through the design calculation and test of the critical devices and components, the size of the crawler chassis was designed to be 1780 mm long, 1650 mm wide, and 310 mm high to ensure the suitable trafficability of the pick-up machine in the garden. Through experiments, it is concluded that when the collection strip blowing head from the ground was 15 cm, the horizontal was 35°, the vertical angle was 15°, and the forward velocity was 1.5 km·h^{-1}, the pick-up cleanlily rate could reach 98.84%. The internal flow field of the separation and impurity removal box was simulated and analyzed to verify that the box structure design was more reasonable.

(3) The operation performance test of the pick-up machine shows that the overall performance is stable and the operation effect was satisfactory. It can meet the requirements of the mechanized harvesting operation of the landing jujube, and the performance index parameters meet the design requirements. The picking efficiency was 752.7.2 kg·h^{-1}, the pick-up cleanliness rate was 95.66%, the breakage rate was 2.68%, and the impurity rate was 3.64%.

ACKNOWLEDGEMENTS

This work was financially Supported by Bingtuan Science and Technology Program (Grant No. 2021CB018), and the Master Talent Project of the Tarim University Presidents Fund (Grant No. TDZKSS202110) for supporting this research. The authors are grateful to anonymous reviewers for their comments.

REFERENCES

[1] Afsah−Hejri, L., Homayouni, T., Toudeshki A., Ehsani, R., Ferguson, L., Castro-García, S. (2022). Mechanical harvesting of selected temperate and tropical fruit and nut trees. *Horticultural Reviews*, vol. 49, pp. 171-242. Belgium.

[2] Ben-Shahar, O., Edan, Y., Hellström, T., Hemming, J., Kurtser, P., Ringdahl, O., Tielen, T., Tuijl, B. v. (2020). Development of a sweet pepper harvesting robot. *Journal of Field Robotics,* vol. 37(6), pp. 1027-1039. United States.

[3] Bernardi, B., Falcone, G., Stillitano, T., Benalia, S., Bacenetti, J., De Luca, A.I. (2021). Harvesting system sustainability in Mediterranean olive cultivation: Other principal cultivar. *Science of the Total Environment*, vol. 766, 142508. Netherlands.

[4] Brondino, L. Borra, D., Giuggioli, N. R., Massaglia, S. (2021). Mechanized Blueberry Harvesting: Preliminary Results in the Italian Context. *Agriculture,* vol. 11(12), 1197. Switzerland.

[5] Chen, B., Pan, J., Wang, L., Wu, Y., Li, X. (2020). Research Status and Prospect of Ground Jujube Picking Machinery (落地红枣捡拾机械的研究现状与展望). *Agric. Eng. Eqpt*, vol. 47, pp. 4-7. Hunan/China.

[6] Chen, C., Zhang, J., Li, J., Bian, Y., Liu, H., Lv, L., Li, S. (2022). Parameter Optimization and Test of Pneumatic Conveying Air Inlet Device for Apple Picking Pipeline (苹果采摘管道气力输送进风装置参数优化). *J. Fruit Sci,* vol. 39, 1308-1322. Henan/China.

[7] Davidson, J. K., Bhusal, S., Mo, C., Karkee, M., Zhang Q. (2020). Robotic manipulation for specialty crop harvesting: A review of manipulator and end-effector technologies. *Global Journal of Agricultural and Allied Sciences,* vol. 2(1), pp. 25-41. Canada.

[8] Davidson, J., Bhusal, S., Mo, C., Karkee, M., Zhang, Q. (2020). Robotic manipulation for specialty crop harvesting: A review of manipulator and end-effector technologies. *Global Journal of Agricultural and Allied Sciences*, vol. 2(1), pp. 25-41. Canada.

[9] Du, X., Ning, C., Yang, Z., Ma, C., He, L., Han, X. (2023). Design and test of crawler chassis walking hydraulic system for cross-type camellia fruit harvester (跨式油茶果收获机履带底盘行走液压系统设计与试验). *Agricultural Machinery Journal,* vol. 54(03), pp. 139-147. Beijing/China.

[10] Fu, L., Majeed, Y., Zhang, X., Karkee, M., Zhang, Q. (2020). Faster R-CNN-based apple detection in dense-foliage fruiting-wall trees using RGB and depth features for robotic harvesting. *Biosystems Engineering*, vol. 197, pp. 245-256. England.

[11] Ghonimy, M., Alzoheiry, A., Abdelrhman, E. (2019). Citrus harvesting by vibrating action. *Misr Journal of Agricultural Engineering,* vol. 36(1), pp. 25-26.

[12] Grupioni, C. M. D.F., Santos, F.L., Velloso, N. S., Valentea, D. S. M., Pinto, F. A. D. C. (2020). Macaw palm supply chain: Evaluation of a semi-mechanized fruit harvesting system. *Industrial Crops and Products*, vol. 151, 112444. Netherlands.

[13] Homayouni, T. (2021). *Enhancing Mechanical Fruit Harvesting Machines Based on Vibration Analysis* [D]. University of California, Merced. DOI:10.5555 › AAI28775445. USA.

[14] Kim, W.-S., Lee, D. -H., Kim, Y.-J., Kim, T., Hwang, R.-Y., Lee, H.-J. (2020). Path detection for autonomous traveling in orchards using patch-based CNN. *Computers and Electronics in Agriculture*, vol. 175, 105620. England.

[15] Kootstra, G., Wang, X., Blok, P.M., Hemming, J., van Henten, E. (2021). Selective Harvesting Robotics: Current Research, Trends, and Future Directions. *Current Robotics Reports,* vol. 2, pp. 95-104. Switzerland.

[16] Kurtser, P, Edan, Y. (2020). Planning the sequence of tasks for harvesting robots. *Robotics and Autonomous Systems,* vol. 131,103591. Netherlands.

[17] Shuib, A. R., Khalid, M. R., Bakri, M. A. M., Deraman, Mohd. Solah. (2018). Development of Oil Palm Loose Fruit Collecting Machine with Elevated Discharge Mechanism (Mark Iii). *International Journal of Engineering and Technical Research,* vol. 7(10). (October-2018). India.

[18] Sola-Guirado, R. R., Ceular-Ortiz, D., Gil-Ribes, J. A. (2017). Automated system for real time tree canopy contact with canopy shakers. *Computers and Electronics in Agriculture*, vol. 143, pp.139-148. England.

[19] Vladislav, G. (2023). Determination of the Critical Speed of Tracked Vehicles on the Trajectory of Skidding. *Transportation Research Procedia*, vol. 68, pp. 761-765. *Russian Federation.* Russian.

[20] Wang, C., Ding, L.; Dou, F., Kan, Z., Li, F., Li, J. (2021). Design and Experiment of Comb-tooth Landing Jujube Picking Device (梳齿式落地红枣捡拾装置的设计与试验). *J. Shihezi Univ: Nat. Sci. Ed,* vol. 39, pp. 409-414. Xinjiang/China.

[21] Wang, W., Xie, J., Chen, L., Liu, L., Quan, L., Liu, L. (2021). Design and Experiment of 3YZ 80A Crawler Self-propelled Corn Interrow Sprayer (3YZ-80A 型履带自走式玉米行间喷雾机设计与试验). *Trans. Chin. Soc. Agric. Mach*, vol. 52, pp. 106-104. Beijing/China.

[22] Yamin, M., Ismail, W.I.b.W., Aziz, S.A., Kassim, M.S.b.M., Akbar, F.N., Ibrahim, M. (2022). Design considerations of variable rate liquid fertilizer applicator for mature oil palm trees. *Precision Agriculture,* vol. 23, pp. 1413-1448. Netherlands.

[23] Yamin, M., Hamid, S., Ali, M.A., Bashir, S., Iqbal, M., Ashraf, M. (2022). Performance optimization and knife dynamics of power tiller operated reaper during wheat harvesting. *Pakistan Journal of Agricultural Sciences*, vol. 59, pp. 261-268. Pakistan.

[24] Yang, S., Wang, X. (2016). Pump and Fan (泵与风机). China Electric Power Press: Beijing/China.

[25] Yeshmukhametov, A., Khaleel, L. A., Koganezawa, K., Yamamoto, Y., Amirgaliyev, Y., Buribayev, Z. (2020). Designing of CNC based agricultural robot with a novel tomato harvesting continuum manipulator tool. *International Journal of Mechanical Engineering and Robotics Research*, vol. 9(6), pp. 876-881. USA.

[26] Yu, F., Li, P., Zhang, F., Li, Z., Zhang, H., Fan, X. (2020). Experimental Determination and Analysis of Suspension Speed Characteristics of Red Dates (红枣悬浮速度特性试验测定与分析). *J. Chin. Agric. Mach.* vol. 41, pp. 99-1. Jiangsu/China.

[27] Yuan, P., Li, S., Han, C., Zhang, J., Xu, Y. (2021). Design and Test of Hydraulic System of Cleaning-air Suction Jujube Picker (清扫—气吸式红枣捡拾机液压系统设计与试验). *J. Chin. Agric. Mach,* vol. 42, pp. 28-33. Jiangsu/China.

[28] Yuan, Y., Bai, S., Niu, K., Zhou, L., Zhao, B., Wei, L., Xiong, S., Liu, L. (2022). Advances in Mechanized Harvesting Technology and Equipment for Forest and Fruit (林果机械化采收技术与装备研究进展). *Trans. Chin. Soc. Agric. Eng,* vol. 38, pp. 53-63. Beijing/China.

[29] Zhang, F., Ran, J, Li, Z., Wang, D., Li, P. (2021). Optimization of Working Parameters of Air- suction Machine for Picking up Ground Jujube (气吸式落地红枣捡拾机作业参数优化). *J. Fruit Sci*, vol. 38, pp. 1190-1200. Henan/China.

[30] Zhang, G., Dong, Z., Chen, L., Liu, H., Zhang, N., Chen, L., Zhang, Q. (2023). Design and experiment of 4BZ-800 Eleocharis dulcis harvester (4BZ-800 型荸荠收获机设计与试验). *Journal of Huazhong Agricultural University,* vol. 42 (01): pp. 219-226. Hubei/China.

[31] Zhang, Y., Wang, J., Wang, Z., Zhang, H., Liu, Y., Hai, P., Niu, H., Ma, J., Zhang, Z. (2022). Development and Test of Air-driven Sprayer for Walnut in Southern Xinjiang (南疆核桃风送式喷雾机的研制与试验). *J. Agric. Biol.* Eng. vol. 44, pp. 56-62. Heilongjiang/China.

[32] ***DG/T 188-2019 “Fruit Picker”. Available online: https://www.csres.com/notice/53315.html (accessed on 3 December 2019).

[33] ***Editorial Committee of Xinjiang Statistical Yearbook. (2021). Xinjiang Statistical Yearbook 2021 (新疆统计年鉴-2021). China Statistical Publishing House: Beijing/China.

EXPERIMENTAL STUDY ON THE EFFECTS OF DIFFERENT PRESSURE METHODS ON THE GROWTH CHARACTERISTICS OF BUCKWHEAT
/
不同镇压方式对荞麦生长特性影响的试验研究

Yun LIU[1)], Weiran LV[1)], Lihong LI[2)], Bing Xu[1)], Decong ZHENG[1)], Qi LU[*1,3)]
[1)] College of Agricultural Engineering, Shanxi Agricultural University, Taigu / China
[2)] Hangzhou Dianzi University information Engineering College, Hangzhou / China
[3)] Chinese Academy of Agricultural Mechanization Sciences Group Co., Ltd., Beijing / China
Tel: +86-13593060095; E-mail: sxndluqi@163.com
DOI: https://doi.org/10.35633/inmateh-70-26

Keywords: *buckwheat, pressure methods, growth characteristics, effect*

ABSTRACT
In order to fully explore the influence of different pressure methods on the growth characteristics of buckwheat, a pressure test device with adjustable press force, and easy to replace the press wheel was designed. Using the dry matter quality of buckwheat roots, stems, leaves at seedling stage, plant height, number of main stem nodes, number of main stem branches, grain number per plant, grain weight per plant, and yield as evaluation indexes, single factor test on press force was carried out, and three-factor and three-level orthogonal test was carried out too with press wheel outer diameter, press force and press wheel type as factors. The results showed that the index values of buckwheat showed a trend of first increasing and then decreasing with the increase of press force. When the press force was 450 N, the growth and development of buckwheat performed best. The effects of press wheel outer diameter, press force, and press wheel type on growth characteristics of buckwheat was different. The effects of press force and press wheel type on the indexes were greater than that of press wheel outer diameter. The optimal pressure methods of buckwheat sowing are as follows: the press wheel outer diameter is 300 mm, the press force is 450 N, and the press wheel type is conical combined wheel. The results of this study could provide reference for the improvement of high-yield mechanized sowing technology of buckwheat and the design of rational pressure device.

摘要
为全面探究不同镇压方式对荞麦生长特性的影响，设计一种镇压力可调、镇压轮便于更换的镇压试验装置。以荞麦苗期根茎叶干物质量、株高、主茎节数、主茎分枝、单株粒数、单株粒重等农艺性状和产量为评价指标，开展了镇压力单因素试验。以镇压轮外径、镇压力、镇压轮型式为试验因素开展了三因素三水平正交试验。试验结果表明：荞麦各指标值随镇压力的增大呈先增大后减小的趋势。 当镇压力为 450 N时， 荞麦生长发育情况表现最佳。 镇压轮外径、 镇压力、 镇压轮型式对荞麦生长特性的影响差异性较大， 镇压力和镇压轮型式对指标的影响比镇压轮外径大。荞麦播种的最优镇压方式为镇压轮外径为 300 mm， 镇压力为 450 N， 镇压轮型式为锥形组合轮。 该研究结果可为荞麦高产机械化播种技术的提升、 合理镇压装置设计提供参考。

INTRODUCTION
Buckwheat is a crop of the genus Buckwheat in the Polygonum family, which is internationally recognized as a versatile economic crop with functions such as nutrition, health, medicine, feed, etc. *(Xu et al., 2021; Lu et al., 2022)*. Buckwheat is one of the main multigrain crops in China. It has the characteristics of cold tolerance, drought tolerance, poverty tolerance, strong stress resistance and short growth period. It has become an important food crop and cash crop in hilly and alpine areas of China *(Huang et al., 2018)*.

Pressure is an important part in mechanized seeding, which mainly serves to compact the soil during the seeding process, prevent water evaporation, and make the soil particles tightly combine. Reasonable pressure can effectively improve the soil environment, play a role in preserving and increasing soil moisture, and have a positive impact on crop emergence, growth, and yield *(Lu et al., 2022)*. Jia Honglei et al. conducted an in-depth study on the structure design and function mechanism of the pressure device (*Jia et al., 2015; Jia et al., 2015; Guo et al., 2017*).

Yun Liu, Lecturer; Weiran Lv, Assistant professor; Lihong Li, Lecturer; Bing Xu, Lecturer; Decong Zheng, Professor; Qi Lu, Ph.D. student*

Wang Jingli et al. developed a variable pressure seedling belt compactor for precision seeder, and conducted post-seeding pressure tests on maize. The effects of different press forces on soil water content, soil pressure strength, germination, growth and yield of maize after seeding were analyzed, and the optimal pressure strength for crop emergence and growth was 0.5-0.7 kg/cm^2 *(Wang et al., 2009)*. Dang Hongkai et al. studied the effects of moisture creation and pressure after sowing on water consumption and growth of wheat before winter, and the results showed that suitable moisture content is the basis of pressure after sowing, and pressure is the guarantee for raising moisture and strengthening seedlings. After sowing wheat in Hebei region, a 95 kg/m compactor is easy to operate in the field, and has a good compaction effect *(Dang et al., 2016*). Lv Guangde et al. carried out field test to determine the influence of pressure at different periods on yield and dry matter quality of wheat, and found the best pressure method *(Lv et al., 2021)*. Yu Xichen et al. studied the effects of different pressure methods on the growth, development and yield of maize, and the results showed that pressure could improve soil water content and soil capacity, which was conducive to the accumulation of dry matter quality and the improvement of yield *(Yu et al., 2002)*. In summary, at present, Chinese scholars only study the influence of pressure treatment on crop growth characteristics of corn, wheat and other major food crops, and there are few studies on buckwheat, so it is necessary to carry out such experimental studies.

In this paper, a pressure test device was designed to study the effects of different press forces, press wheel outer diameter and type on the growth characteristics of buckwheat, such as the dry matter quality of roots, stems and leaves at seedling stage, plant height, number of main stem nodes, number of main stem branches, grain number per plant, grain weight per plant, and yield. The optimum pressure methods were determined in order to provide reference for the improvement of mechanized sowing technology and the design of rational pressure device of buckwheat.

MATERIALS AND METHODS

Test conditions

The test was carried out from August 13 to October 24, 2022 at Shenfeng Village Experimental Base in Taigu District, Jinzhong City, Shanxi Province. The test soil was sandy loam with medium fertility level. The soil moisture content during sowing was 10.77%. The previous crop was oat.

The test equipment included walking crawler seeder, pressure device, steel ruler, electronic scale, sample bag, aluminum box, drying oven, shovel, dustpan and cleaning screen, etc.

Design of test device

In order to explore the influence of pressure on the growth of buckwheat, eliminate the influence of other parts of the planter, a pressure test device was designed, as shown in Figure 1. The device is mainly composed of handle push rod, counterweight box, press wheel, etc., which can easily replace the press wheel, and adjust the press force. During the test, the operator drove the whole test device forward at a constant speed through the handle push rod. The weight box always kept vertical during the movement. By replacing different press wheels and changing the weight of the weight box, the pressure conditions could be changed to meet the requirements of the test design.

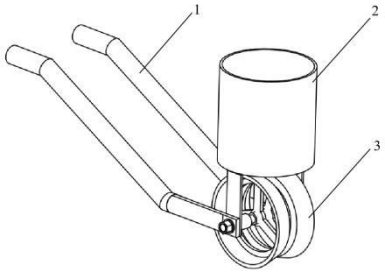

Fig. 2 - Pressure test device

1. Handle push rod; 2. counterweight box; 3. Press wheel

The press wheel is one of the important components of the pressure test device. Changing the type and size of the press wheel will have different pressure effects, which will have different impacts on crop growth and development. This study adopted three types of wheels: flat wheel, convex wheel, and conical combination wheel, the plane wheel, convex wheel and conical combined wheel. Each type is designed and processed with three different outer diameter sizes, as shown in Figure 2.

The outer diameters D_1=200 mm, D_2=300 mm, and D_3=400 mm. The width of the press wheel B=150 mm. For the conical combination wheel, the horizontal width of a single conical surface b = 65 mm, the distance between two conical wheels h = 20 mm, and the inclination angle ε = 17^0.

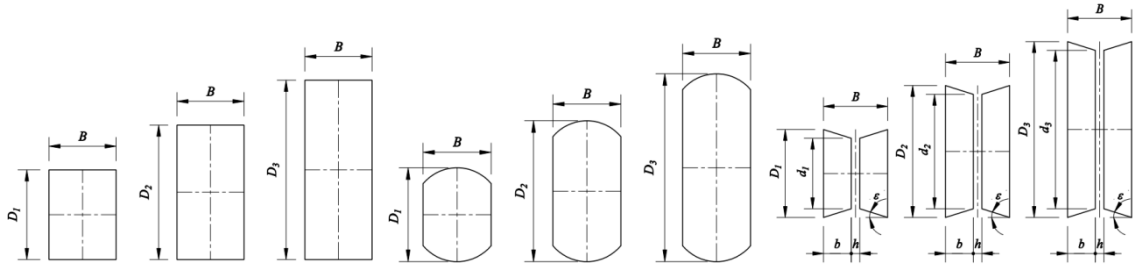

Fig. 2 - Structure of press wheel

a) Plane wheel; b) Convex wheel; c) Conical combined wheel

Test methods

Sowing test

The buckwheat variety used in the test was Hongshan buckwheat. The average 1000-grain weight was 34 g, and the moisture content of the seed was 13.2%. The Sowing text selected plot sowing method, plot area was 2 m × 5 m = 10 m^2. According to the requirements of agronomy, each plot was sown 5 rows. The sowing amount of buckwheat is generally 45-60 kg/hm^2, and the sowing amount in the plot was calculated based on the sowing amount of 53 kg/hm^2. When sowing, the walking crawler seeder was used to sow seed. The sowing depth was 5 cm. After sowing, the pressure text was carried out according to the experimental design scheme.

Test Design

(1) Single factor test design

In the process of crop sowing, low press force does not have the effect of increasing soil moisture, while excessive pressure could cause soil compaction, causing changes in soil particle structure, poor air permeability, and affecting seedling emergence *(Obour et al., 2018; Zuo et al., 2017; Shahrayini et al., 2018*). To explore the optimal press force, a conical combined wheel with an outer diameter of 300 mm was selected as the press wheel for the single factor test. During the test, the change in press force is achieved by changing the counterweight of the counterweight box. There were 6 treatments (0, 250, 350, 450, 550, and 650 N), and each treatment was repeated 3 times. The control group was selected when the press force was 0 N.

(2) Orthogonal test design

The purpose of this test was to explore the effects of different suppression methods on the growth characteristics of buckwheat. Therefore, a three-factor and three-level orthogonal test was designed. The press force, press wheel outer diameter and type were selected as test factors, and three levels were taken for each factor. To ensure the accuracy of the test, each treatment was repeated 3 times.

The experimental factors and levels are shown in Table 1.

Table 1

Factor-level table of test

Levels	Factors		
	press wheel outer diameter	press force	press wheel type
	[mm]	[N]	-
1	200	350	plane wheel
2	300	450	convex wheel
3	400	550	conical combined wheel

Determination of experimental indexes

The main indexes tested in single factor and orthogonal test included the dry matter quality of buckwheat roots, stems, and leaves at seedling stage, agronomic traits (including plant height, number of main stem nodes, number of main stem branches, grain number per plant, and grain weight per plant), and yield. The determination methods were as follows.

(1) Determination of dry matter quality at seedling stage

During the seedling stage of buckwheat, five individual plants in each plot were selected by five-point method, and the completeness of the samples was ensured. After sampling is completed, the soil at the root is cleaned, and then the roots, stems, and leaves of buckwheat were separated and dried in the dryer respectively. Finally, the dry matter quality of roots, stems and leaves was measured by electronic balance and the data was recorded. Repeat 3 times and take average value as evaluation data.

(2) Determination of agronomic traits

After maturity, 5 representative plants were selected in each plot by five-point method for seed testing, including plant height, number of main stem nodes, number of main stem branches, grain number per plant, and grain weight per plant. Repeat 3 times and take average value as evaluation data.

(3) Determination of yield

Firstly, the method of artificial harvesting was used to harvest in sequence according to the plot, and the marks were made. Secondly, clean buckwheat grains were obtained by artificial threshing and clearing in the field. Finally, the plot yield is weighed and converted into yield per hectare.

RESULTS AND ANALYSIS

Single factor test results and analysis

(1) Effects of different press forces on the dry matter quality at seedling stage

The effect of different press forces on the dry matter quality of buckwheat roots, stems, and leaves at the seedling stage is shown in Figure 3. The corresponding press forces for dry matter quality from high to low are 450, 350, 550, 250, 650 and 0 N, respectively. Without pressure, the roots dry matter quality is the lowest at 0.43 g/plant; When the press force is 450 N, the roots dry matter quality is the highest at 0.82 g/plant, which is 1.91 times higher than that without pressure. The roots dry matter quality at seedling stage of buckwheat shows a trend of first increasing and then decreasing with the increase of press force. This is because moderate pressure can make seeds better contact with soil, provide adequate nutrients and a suitable soil environment for seeds, promote roots growth and development. But when the press force is too high, the soil porosity decreases, and the growth of seed roots is hindered, resulting in a decrease in dry matter quality.

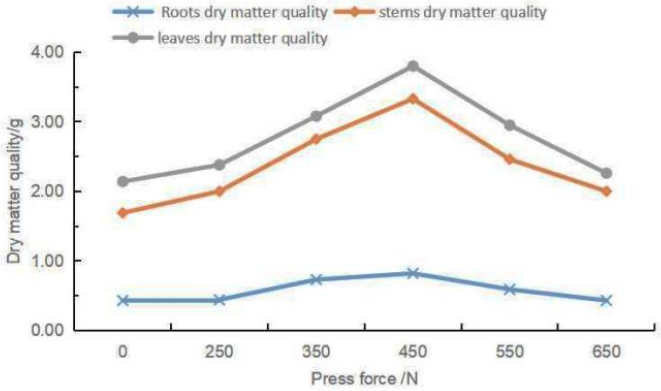

Fig. 3 - Variation curve of dry matter quality at seedling stage with press force

The variation trend of stems and leaves dry matter quality at seedling stage of buckwheat is consistent with that of roots. Without pressure, the stems and leaves dry matter quality is the lowest, at 1.69 and 2.14 g/plant, respectively. When the press force is 450 N, the stems and leaves dry matter quality is the highest, at 3.33 and 3.80 g/plant, respectively, which is 1.97 and 1.78 times higher than that without pressure. Overall, the growth and development of buckwheat after pressure should be better than those without pressure. Press treatment is conducive to the development of buckwheat seedling. Moderate pressure provides a good soil environment for the growth and development of buckwheat, promotes its growth, and is easy to grow into strong seedlings. But when the press force is too high, the soil is too dense, which is not conducive to seed emergence and rooting. The seeds consume a large amount of nutrients during the soil breaking process, which can also make the seeds appear more slender after emergence, leading to a decrease in the dry matter quality during the seedling stage.

(2) Effects of different press forces on the agronomic traits of buckwheat

Five agronomic characters of buckwheat under different press forces are analyzed, and the results are shown in Table 2.

In general, the growth trend of various agronomic traits of buckwheat is consistent with the dry matter quality at seedling stage. When the press force is 450 N, the agronomic characters of buckwheat show significant advantages. Without pressure, the agronomic characters are poor. The highest plant height is 744.44 cm, which is 14.53% higher than that without pressure. The press force has significant effects on the plant height, the grain number per plant and the grain weight per plant, but has no significant effects on the number of main stem nodes and the number of main stem branches.

There are differences in agronomic characters of buckwheat under different press forces. The agronomic trait with the greatest variation is the grain weight per plant, which is as high as 25.30%. The coefficient of variation of grain number per plant is also relatively high at 24.32%. This indicates that these two agronomic traits vary greatly with press force. The number of main stem branches is followed by the coefficient of variation of 19.21%. The coefficients of variation of the plant height and number of main stem nodes are relatively low, which are 9.22% and 10.87%, respectively. These two agronomic traits have relatively high stability in production.

Table 2

Results of agronomic trait analysis

Press force [N]	Plant height	Number of main stem nodes	Number of main stem branches	grain number per plant	grain weight per plant
	[mm]	-	-	-	[g]
0	650.00±69.69 b	7.33±0.50 a	5.33±0.71 a	29.44±6.09 c	0.94±0.20 c
250	703.22±52.41ab	7.78±1.30 a	5.56±1.42 a	30.56±6.84 c	1.00±0.22 c
350	723.33±62.65 a	8.11±0.60 a	6.11±1.27 a	38.56±9.07 ab	1.24±0.29 b
450	744.44±45.65 a	8.11±0.93 a	6.22±0.67 a	43.00±5.27 a	1.84±0.20 a
550	712.22±38.74ab	7.89±0.78 a	5.44±0.73 a	35.56±7.21 b	1.13±0.23bc
650	681.89±84.10ab	7.56±0.73 a	5.33±1.41 a	28.89±6.49 c	0.95±0.21 c
SD	64.79	0.85	1.09	8.35	0.28
Mean	702.52	7.80	5.67	34.33	1.12
C·V	9.22%	10.87%	19.21%	24.32%	25.30%

Note: Different letters indicate significant differences (P<0.05), the same below.

(3) Effects of different press forces on buckwheat yield

The effect of different press forces on buckwheat yield is shown in Figure 4. The yield shows a trend of first increasing and then decreasing with the increase of press force. The press force has significant effects on the yield. When the press force is 450 N, the yield is the highest, at 2401.20 kg/hm^2, which is significantly higher than that under other press forces. When the press force is 350, 550 and 220 N, the yield is 2092.75, 1867.60 and 1775.90 kg/hm^2, respectively, which is 49.41%, 33.33% and 26.79% higher than that without pressure, respectively. When the press force is 0 and 650 N, the yield is 1400.70 and 1567.45 kg/hm^2, respectively, significantly lower than that under other press forces.

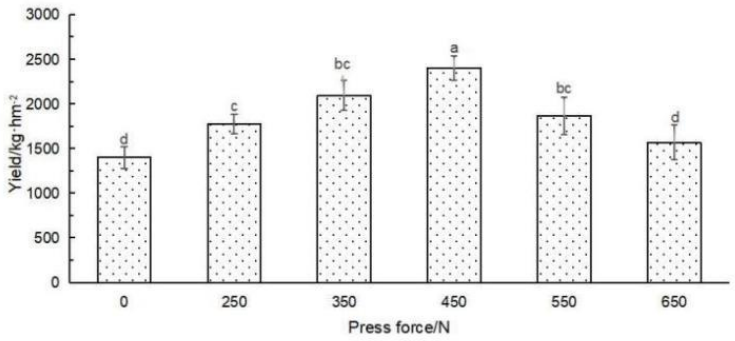

Fig. 4 - Buckwheat yield under different press forces

Orthogonal test results and analysis

The measurement results of Orthogonal test are shown in Table 3. In the table, A, B and C are the coded values for the press wheel outer diameter, press force and press wheel type, respectively. The results of variance analysis are shown in Table 4.

Table 3

Orthogonal test results of growth characteristics

Groups	Factors			Dry matter quality at seedling			Agronomic traits					Yield
	A	B	C	roots	stems	leaves	Plant height	number of main stem nodes	number of main stem branches	grain number per plant	grain weight per plant	
				[g]	[g]	[g]	[g]	-	-	-	[g]	[kg/hm^2]
1	1	1	1	0.27	1.98	2.11	703.33	7.56	4.89	19.89	0.38	800.40
2	1	2	2	0.38	2.04	2.74	704.44	7.64	5.44	32.44	0.88	1245.62
3	1	3	3	0.52	1.75	2.85	724.44	7.88	5.63	38.89	1.12	1960.98
4	2	1	2	0.39	2.41	2.53	705.00	7.86	5.43	23.89	0.85	955.48
5	2	2	3	0.75	2.42	3.22	774.22	8.05	6.08	54.56	2.00	2626.31
6	2	3	1	0.58	1.88	2.79	694.44	7.690	5.56	35.33	1.04	1815.91
7	3	1	3	0.46	2.28	2.39	741.11	8.11	5.56	32.44	0.92	1880.94
8	3	2	1	0.56	2.25	2.43	732.22	7.89	6.24	39.89	1.22	2111.06
9	3	3	2	0.50	1.85	2.42	665.56	7.71	5.76	23.22	0.56	1275.64

Table 4

Results of variance analysis of dry matter quality at seedling stage

Index	Source	SS	DF	MS	F	P	k1	k2	k3	R	Optimization level	Optimal combination
Roots dry matter quality	A	0.05	2	0.03	31.00	0.031*	0.39	0.57	0.51	0.18	A_2	$A_2B_2C_3$
	B	0.06	2	0.03	37.56	0.026*	0.37	0.56	0.53	0.19	B_2	
	C	0.04	2	0.02	22.24	0.043*	0.47	0.42	0.58	0.15	C_3	
	Error	0.002	2	0.001								
	Total	0.15	8									
Stems dry matter quality	A	0.15	2	0.08	18.90	0.050*	1.92	2.24	2.13	0.31	A_2	$A_2B_2C_3$
	B	0.33	2	0.16	40.59	0.024*	2.22	2.24	1.83	0.40	B_2	
	C	0.02	2	0.01	2.41	0.293	2.04	2.10	2.15	0.11	C_3	
	Error	0.008	2	0.004								
	Total	0.51	8									
Leaves dry matter quality	A	0.29	2	0.15	58.46	0.017*	2.57	2.85	2.41	0.43	A_2	$A_2B_2C_3$
	B	0.34	2	0.17	67.70	0.015*	2.34	2.80	2.69	0.45	B_2	
	C	0.22	2	0.11	44.83	0.022*	2.44	2.56	2.82	0.38	C_3	
	Error	0.005	2	0.002								
	Total	0.29	8									
Plant height	A	330.19	2	165.09	3.61	0.217	710.74	724.56	712.96	13.81	A_2	$A_2B_2C_3$
	B	2665.22	2	1332.61	29.13	0.033*	716.48	736.96	694.81	42.15	B_2	

Table 4
(continuation)

Index	Source	SS	DF	MS	F	P	k1	k2	k3	R	Optimization level	Optimal combination
	C	4691.63	2	2345.82	51.28	0.019*	710.00	691.67	746.59	54.93	C_3	
	Error	91.492	2	45.746								
	Total	7778.53	8									
Number of main stem nodes	A	0.05	2	0.02	2.92	0.255	7.73	7.83	7.90	0.18	A_3	$A_3B_2C_3$
	B	0.04	2	0.02	2.69	0.271	7.84	7.89	7.73	0.17	B_2	
	C	0.18	2	0.09	10.95	0.084	7.68	7.77	8.01	0.33	C_3	
	Error	0.016	2	0.008								
	Total	0.29	8									
Number of main stem bran-ches	A	0.45	2	0.22	4.47	0.183	5.32	5.69	5.85	0.53	A_3	$A_3B_2C_3$
	B	0.59	2	0.30	5.92	0.145	5.29	5.92	5.65	0.63	B_2	
	C	0.08	2	0.04	0.83	0.546	5.56	5.55	5.76	0.21	C_3	
	Error	0.100	2	0.050								
	Total	1.22	8									
Grain number per plant	A	95.56	2	47.78	22.93	0.042*	30.41	37.93	31.85	7.52	A_2	$A_2B_2C_3$
	B	431.67	2	215.84	103.59	0.010**	25.41	42.30	32.48	16.89	B_2	
	C	370.77	2	185.38	88.98	0.011*	31.70	26.52	41.96	15.44	C_3	
	Error	4.167	2	2.084								
	Total	902.17	8									
Grain weight per plant	A	0.42	2	0.21	19.48	0.049*	0.79	1.30	0.90	0.50	A_2	$A_2B_2C_3$
	B	0.67	2	0.34	30.93	0.031*	0.72	1.37	0.91	0.65	B_2	
	C	0.57	2	0.29	26.39	0.037*	0.88	0.76	1.35	0.58	C_3	
	Error	0.022	2	0.011								
	Total	1.69	8									
Yield	A	393352.81	2	196676.41	20.75	0.046*	1335.67	1212.27	1575.79	463.57	A_2	$A_2B_2C_3$
	B	930500.48	2	465250.24	49.08	0.020*	1799.23	1994.33	1158.91	782.06	B_2	
	C	1504853.48	2	752426.74	79.38	0.012*	1755.88	1684.18	2156.08	997.17	C_3	
	Error	18958.516	2	874.12								
	Total	2847665.29	8									

Note: * indicates significant difference (0.01<P<0.05), * * indicates extremely significant difference (P ≤ 0.01)

(1) Effects of pressure methods on the dry matter quality at seedling stage

It can be seen from Table 4 that the press wheel outer diameter, press force and press wheel type have significant effects on the roots dry quality at seedling stage, and the optimal combination is $A_2B_2C_3$. The press wheel outer diameter and press force have significant effects on the stems dry quality at seedling stage, but the press wheel type has no significant effects on that. The optimized combination is $A_2B_2C_3$. The three factors have significant effects on the leaves dry matter quality at seedling stage, and the optimal combination is $A_2B_2C_3$. The order of influence from large to small is the press force, the press wheel outer diameter, and the press wheel type.

(2) Effects of pressure methods on the agronomic traits of buckwheat

It can be seen from Table 4 that the press force and press wheel type have significant effects on the plant height of buckwheat, but the press wheel outer diameter has no significant effects on that. The order of influence from large to small is the press wheel type, the press force, and the press wheel outer diameter. The optimal combination is $A_2B_2C_3$. The press wheel outer diameter, press force and press wheel type have no significant effects on the number of main stem nodes, and the number of main stem branches. The optimal combination is $A_3B_2C_3$. The press force has extremely significant effects on the grain number per plant, and it has significant effects on the grain weight per plant. The press wheel outer diameter and press wheel type have significant effects on the grain number per plant and the grain weight per plant, and the order of influence from large to small is the press force, the press wheel type, and the press wheel outer diameter. The optimal combination is $A_2B_2C_3$.

(3) Effects of pressure methods on buckwheat yield

The effects of pressure methods on buckwheat yield are shown in Table 3 and 4. The press wheel outer diameter, press force and press wheel type have significant effects on the yield. The order of influence from large to small is press wheel type, press force and press wheel outer diameter. The optimal combination is $A_2B_2C_3$, with a yield of up to 2626.31 kg/hm^2.

DISCUSSION

Effects of different press forces on the growth characteristics of buckwheat

Yang Xiaojuan et al. showed that unreasonable mechanical operations in farmland would increase soil compactness, and mechanical compaction would not only affect root growth, but also limited the growth of above-ground parts of plants *(Yang et al., 2008)*. Dauda et al. found in two years of experiments that serious soil compactness affected the yield of cowpea *(Dauda et al., 2002)*. Jiang Yecheng et al. showed that the application of seeding weight pressure technology significantly improved the emergence rate, plant dry matter and yield of maize *(Jiang et al., 2022)*. The results of this experiment showed that the growth characteristics of buckwheat were significantly affected by press force. The dry matter quality, agronomic traits and yield showed a trend of first increasing and then decreasing with the increase of press force. These was consistent with the above research conclusions.

Before the start of the test, the test field was tilled by rotary tiller, and the surface soil was relatively weak. After pressure, the soil of the seed bed changed from loose state to compact state, improving the soil compactness and increasing the ability of the seedling soil to absorb underground water. Timely pressure after sowing can make the seed bed compact appropriately, and also make the seeds closely connected to the surrounding wet soil, playing a role in increasing, preserving, and supplying soil moisture, which is conducive to the growth and development of buckwheat and the increase of yield.

However, when the ballast pressure is too high, the soil is too dense, affecting the porosity and moisture content of the soil, which is not conducive to the growth and extension of roots. Thus the growth and development of crops are hindered.

Effects of different pressure methods on the growth characteristics of buckwheat

In addition to the soil condition in the field, the main factors affecting the pressure quality include the press force, press wheel diameter and type, and speed of the pressure operation etc. *(Wang et al., 2009)*. Liu Hongjun showed that the press wheel type had significant effects on maize seedling emergence rate, plant height consistency, and seedling growth status. The optimal combination of press wheel type and operation speed is obtained *(Liu et al., 2019)*. Lu Qi et al. found that the pressure strength, press wheel type and sowing depth had significant effects on seedling emergence rate, growth, and yield of oats. The optimum sowing conditions of oat were as follows: pressure strength was 50 kPa, sowing depth was 5 cm, and press wheel type was conical combined wheel *(Lu et al., 2022)*. The results of this experimental study indicated that press wheel outer diameter, press force, and press wheel type had significant effects on the dry matter quality, plant height, and yield of buckwheat, which was consistent with the above research conclusions. In terms of the press wheel outer diameter, 300 mm is the optimal level. In terms of press force, 450 N is the optimal level. The press wheel outer diameter and press force have comprehensive effects on the strength of the soil compaction by the compactor. Excessive or insufficient pressure strength will affect soil performance, thereby affecting the growth of buckwheat. In terms of the press wheel type, the conical combined wheel exhibited the best compaction effect, which was consistent with the research results obtained by *Lu Q, Zheng D.C., Li L.H., Liu Y, (2022)*.

Perhaps it is because the conical combination can suppress the two sides of the seedling belt, playing a role in water storage and moisture preservation, while forming a soft small soil pile in the middle, which is conducive to the emergence and growth of seeds. In terms of the importance of influencing factors, the press force and press wheel type had greater effects on the indexes than press wheel outer diameter. The three factors comprehensively reflected the compaction effect of the pressure device on the soil.

Overall, the optimal pressure method for buckwheat sowing is $A_2B_2C_3$, which means that the press wheel outer diameter is 300 mm, the press force is 450 N, and press wheel type is a conical combined wheel.

The above experimental results are only data from one-year field trials, and a large number of field trials need to be tracked and demonstrated for many years.

CONCLUSIONS

(1) In this paper, a pressure test device was designed with adjustable pressure control, 9 different structural sizes of press wheels were designed and processed. The results of the single factor test showed that the index values of buckwheat showed a trend of first increasing and then decreasing with the increase of press force. When the pressure is 450 N, the growth and development of buckwheat performed best. The dry matter quality of roots, stems, and leaves was 0.82, 3.33, and 3.80 g/plant, respectively, which was increased by 1.91, 1.97, and 1.78 times compared to that without compaction. The press force had significant effects on the plant height, grain number per plant, and grain weight per plant of buckwheat, but had no significant effects on the number of main stem nodes and number of main stem branches. The agronomic traits with the largest coefficient of variation were grain weight per plant and grain number per plant, which were 25.30% and 24.32%, respectively. When the press force was 450 N, buckwheat yield was the highest at 2401.20 kg/hm^2, which was significantly higher than that under other press forces.

(2) The results of orthogonal test showed that the press wheel outer diameter had significant effects on the dry matter quality of buckwheat roots, stems, and leaves, grain number per plant, grain weight per plant, and yield, but had no significant effects on the plant height, number of main stem nodes, and the main stem branching. The press force had significant effects on the dry matter quality of buckwheat roots, stems, and leaves, plant height, grain weight per plant, and yield. It had extremely significant effects on the grain number per plant. But it had no significant effects on the number of main stem nodes and number of main stem branches. The press wheel type had significant effects on the dry matter weight of buckwheat roots and stems, plant height, grain number per plant, grain weight per plant and yield, but had no significant effects on the dry matter weight of stems, number of main stem nodes and number of main stem branches. In terms of the importance of influencing factors, the press force and press wheel type had greater effects on growth characteristics than the press wheel outer diameter. The optimal pressure methods of buckwheat sowing are as follows: the press wheel outer diameter is 300 mm, the press force is 450 N, and the press wheel type is conical combined wheel.

ACKNOWLEDGEMENT

This research, titled ‘Experimental Study on the Effects of Different Pressure Methods on the Growth Characteristics of Buckwheat’, was funded by the Science and Technology Innovation Project of Shanxi Colleges and Universities (No. 2020L0153), and the Youth Science and Technology Innovation Project of Shanxi Agricultural University (No. 2020QC05).

REFERENCES

[1] Dang H.K., Cao C.Y., Zheng C.L., Ma J.Y., Guo L., Wang Y.N., Li W., Li K.J. (2016). Effects of pre-sowing irrigation and post-sowing soil compaction on water use and growth of winter wheat (造墒与播后镇压对小麦冬前耗水和生长发育的影响). *Chinese Journal of Eco-Agriculture,* China, 24(08), 1071-1079. https://doi.org/10.13930/j.cnki.cjea.160079

[2] Dauda A., Samari A. (2002). Cowpea yield response to soil compaction under tractor traffic on a sandy loam soil in the semi-arid region of northern Nigeria. *Soil and Tillage Research*, NL*,* 68(01), 17-22. https://doi.org/10.1016/S0167-1987(02)00064-8

[3] Guo H., Chen Z., Jia H.L., Zheng T.Z., Wang G., Wang Q. (2017). Design and experiment of soil-covering and soil-compacting device with cone-shaped structure of wheel (锥形轮体结构的覆土镇压器设计与试验). *Transactions of the Chinese Society of Agricultural Engineering (Transactions of the CSAE),* China*, 33(12)*, 56-65. https://doi.org/10.11975/j.issn.1002-6819.2017.12.008

[4] Huang X.N., Zhang W.G., Dang W.L., Zhang K.K., Feng S.K., Liu Z.J., Yang Z.F. (2018). Research status and development trend of buckwheat harvesting machinery (荞麦收获机械研究现状及发展趋势). *Farm Machinery, China, 850(10)*, 84-90. https://doi.org/10.16167/j.cnki.1000-9868.2018.10.023

[5] Jia H.L., Guo H., Guo M.Z., Wang L.C., Zhao J.L., Fan X.H. (2015). Finite element analysis of performance on elastic press wheel of row sowing plow machine for covering with soil and its experiment (行间耕播机弹性可覆土镇压轮性能有限元仿真分析及试验). *Transactions of the Chinese Society of Agricultural Engineering, (Transactions of the CSAE), China, 31(21)*, 9-16+315. https://doi.org/10.11975/j.issn.1002-6819.2015.21.002

[6] Jia H.L., Wang W.J., Zhang J., Luo X.F., Yao P.F., Li Y. (2015). Design and experiment of profiling elastic press roller (仿形弹性镇压辊设计与试验). *Transactions of the Chinese Society for Agricultural Machinery, 46(06)*, 28-34+83. https://doi.org/10.6041/j.issn.1000-1298.2015.06.005

[7] Jiang Y.C., Sun H.Q., Deng A.Y., Wang S., Gao Y.S., Jiang Y. (2022). Influence of Seedling Belt Heavy Repression Technology on Maize Yield and Comprehensive Index (苗带重镇压对土壤环境、玉米生长及产量的影响). *Journal of Maize Sciences, China, 30(06),* 118-123. https://doi.org/10.13597/j.cnki.maize.science.20220616

[8] Liu H.J. (2019). *Research on key technologies of press device for planter in hilly region of northeast China* (东北丘陵地区播种机镇压装置关键技术研究) [Doctoral dissertation]. Northeast Agricultural University, *China.* https://cdmd.cnki.com.cn/Article/CDMD-10224-1019176357.htm

[9] Lu Q., Wang L., Liu Y., Li L.H., Liu L.J., Zheng D.C. (2022). Effects of different suppression intensity on growth characteristics of oat (不同镇压强度对燕麦生长特性的影响). *Agricultural Engineering,* China, 12(07), 88-94. https://doi.org/10.19998/j.cnki.2095-1795.2022.07.017

[10] Lu Q., Zheng D.C., Li L.H., Liu F.J., Liu Y. (2022). Research status of mechanized production technology and equipment of buckwheat in China. *INMATEH Agricultural Engineering,* Romania, 67(2), 487-496. https://doi.org/10.35633/inmateh-67-48

[11] Lu Q., Zheng D.C., Li L.H., Liu Y. (2022). Experimental study on the effects of different pressure and sowing depths on the growth characteristics of Oat under dry farming conditions. *INMATEH Agricultural Engineering,* Romania*,* 67(2)*,* 293-305. https://doi.org/10.35633/inmateh-67-30

[12] Lv G.D., Lv P., Ju Z.C., Pang H., Zhao Q., Wu K., Qian Z.G. (2021). Effect of suppression on yield and dry matter accumulation and transport of wide- sowing winter wheat (镇压对宽幅播种冬小麦产量和干物质积累转运的影响). *Journal of Triticeae Crops,* China, 41(08)*,* 997-1004*.* https://doi.org/10.7606/j.issn.1009-1041.2021.08.

[13] Obour P.B., Kolberg D., Lamandé M., Brrebseb T., Munkholm L.A. (2018). Compaction and sowing date change soil physical properties and crop yield in a loamy temperate soil. *Soil and Tillage Research*, NL*,* 184, 153-163. https://doi.org/10.1016/j.still.2018.07.014

[14] Shahrayini E., Mahboobeh F., Shabanpour M., Ebrahimi E., Saadat S. (2018). Investigation of soil compaction on yield and agronomic traits of wheat under saline and non-saline soils. *Archives of Agronomy and Soil Science,* England, 64(10), 1329-1340. https://doi.org/10.1080/03650340.2018.1431832

[15] Wang J.L., Ma X., Lu B., Xu J. (2009). Experimental study on seeding strip press roller with variable pressure of precision planter (精密播种机可变力苗带镇压器的试验研究). *Journal of Jilin Agricultural University, China, 31(04),* 472-475. https://doi.org/10.13327/j.jjlau.2009.04.007

[16] Xu B., Zhang Y.Q., Cui Q.L., Ye S.B., Zhao F. (2021). Construction of a discrete element model of buckwheat seeds and calibration of parameters. *INMATEH Agricultural Engineering,* Romania, 64(2), 175-184. https://doi.org/10.35633/inmateh-64-17

[17] Yang X.J., Li C.J. (2008). Impacts of mechanical compaction on soil properties, growth of crops, soil-borne organisms and environment (机械压实对土壤质量、作物生长、土壤生物及环境的影响). Scientia Agricultura Sinica, China, 07, 2008-2015. https://doi.org/10.3864/j.issn.0578-1752.2008.07.018

[18] Yu X.C., Sun Z.X., Zheng J.M, Zhang P., Yang H.Z. (2002). The effect of different suppression methods on the growth, development and yield of maize (不同镇压方式对玉米生长发育及产量的影响). *Rain Fed Crops,* China, 2002(05)*, 271-273.* https://www.cnki.com.cn/Article/CJFDTotal-GNZL200205008.htm

[19] Zuo Q.S., Kuai J., Zhao L., Hu Z., Wu J.S., Zhou G.S. (2017). The effect of sowing depth and soil compaction on the growth and yield of rapeseed in rice straw returning field. *Field Crops Research,* NL*,* 203*,* 47-54. https://doi.org/10.1016/j.fcr.2016.12.016

DESIGN AND PERFORMANCE TEST OF REMOTE CONTROL SYSTEM FOR SMALL VEGETABLE PLANTER BASED ON ARDUINO

/

基于 Arduino 的小型蔬菜播种机远程控制系统设计与性能试验

Yinping ZHANG[1)], Bin WANG[1)], Xin LI[1)], Hua ZHOU[1,*)], Fangyuan LU[1)], Jiasheng WANG[2)]

[1)]School of Agricultural and Food Science, Shandong University of Technology, Zibo (255000), China;

[2)]School of Mechanical and Electrical Engineering, Qingdao Agricultural University, Qingdao (266109), China;

Tel: +86-15071259850; E-mail: zhouhua688@163.com

Corresponding author: Hua Zhou

DOI: https://doi.org/10.35633/inmateh-70-27

Keywords: *vegetable, electric seeder, differential steering, remote control system*

ABSTRACT

Facilities greenhouses are relatively narrow and airtight, and the machine operation turns frequently. The existing vegetable seeders is supported by manual hand, and the straightness of operation is poor, Turning around is time-consuming and laborious. This paper designs a remote control system of small vegetable seeder based on Arduino microcontroller, the Arduino single-chip microcomputer remote control technology, multi-motor synchronous drive technology, differential-electric push rod combined with lifting and steering control and other methods are adopted. Through remote control, the forward, speed regulation, lifting of the whole machine and field line change and steering of the seeder during vegetable sowing are realized. The differential steering model and brushless motor speed control model are established, and the android human-computer interaction APP is designed to realize the remote precise control of vegetable seeder. The performance test of the accuracy of the control system was carried out with the accuracy and steering accuracy of the seeder. The results showed that: under the condition of medium speed and medium and low speed operation, the seeding level of vegetable seeder is the most stable and reliable, the speed deviation rate of the seeder is 1.59 %, after starting the drive motor for 2s, the actual speed is close to the target speed, differential steering is relatively accurate, the qualified rate of steering is more than 89.8 %, the synchronous speed error of the lifting mechanism tends to be stable. This study can provide reference for the development of intelligent equipment for facility agriculture.

摘要

设施大棚空间相对狭小、密闭，机器作业掉头转弯频繁，现有的蔬菜播种机多由人工手扶，作业直线性差，掉头费时费力，本文基于 Arduino 单片机微控制器设计了小型蔬菜播种机远程控制系统，采用了 Arduino 单片机远程控制技术、多电机同步驱动技术、差速-电动推杆结合的升降转向控制等方法，通过远程遥控的方式来实现蔬菜播种时播种机前进、调速、整机升降和田间换行转向等作业。建立了差速转向模型与无刷电机调速模型，设计了 android 端人机交互 APP，实现对蔬菜播种机的远程精确控制。以播种机的作业行走准确度和转向准确度为指标进行对控制系统运行的准确性的性能测试，结果表明：在中速及低速运行状态下，蔬菜播种机的播种水平最为稳定可靠，播种机行驶速度偏差率为 1.59%，启动驱动电机 2s 后实际转速接近目标转速，差速转向相对准确，转向合格率大于 89.8%，升降机构同步速度误差变化趋于稳定。本研究可为设施农业智能装备的发展提供参考。

INTRODUCTION

China ranks first in vegetable production and consumption in the world, and is the world's largest vegetable exporter (*Qi et al, 2020*). However, there is still a big gap in the level of comprehensive mechanization compared with developed countries (*Li et al,2019;Richard, 2005; Xiao et al, 2017*), especially in facilities greenhouses vegetables sowing, the space is narrow, the working distance is short and the manual dependence is strong (*Narang et al, 2012; EL-Ghobashy et al, 2016; Du et al, 2017; Jin et al, 2019*), with the shortage of rural labor force, the problem of expensive labor and difficult labor in vegetable production is becoming more and more prominent. Therefore, it is of great significance to study efficient intelligent equipment to improve the production efficiency of facilities greenhouses vegetables, reduce manual dependence and improve the mechanization level of vegetable production.

The research on sowing technology and equipment in developed countries such as Europe and America is relatively mature, with high sowing quality, fast operation speed and simple control (*Zhang et al, 2022; Mei et al, 2016; Zhang et al, 2022*). For example, the automatic seeding and weeding robot for vegetables produced by FarmDroid Company in Denmark, which is driven by solar energy and based on high-precision GPS positioning system, realizes automatic seeding and weeding in the field. The Omnipower seeding platform produced by Raven Company in the United States realizes autonomous operation through remote control of farmers' handheld tablet computers (*Raven, 2021*). In China, the intelligent control of seeder is still in the research stage and has not been widely used. Yuan Yongwei et al. applied laser collimation technology and PLC control system to vegetable seeder to realize linear walking and flexible steering of vegetable seeder (*Yuan et al, 2014*). Xu Qimeng et al. from the College of Engineering of China Agricultural University designed a self-propelled agricultural mobile seeding platform. GNSS positioning and speed measurement technology is used to realize automatic seeding, and multi-motor synchronous drive, electric push rod and differential speed are used to realize the walking and steering of the platform (Xu *et al, 2021*). A plot seeder row control system was designed by Cheng Xiupei et al., the STM32 microcontroller as the main control center, and the Android terminal was used for human-computer interaction (C*heng et al, 2019)*. The solenoid valve was used to control the lifting of the seed tube, the stepper motor was used to drive the cone grille, and the DC brushless motor was used to drive the seeder, the problems of difficult adjustment of seeding operation parameters and poor seeding accuracy were solved. Ding et al. developed an electric drive corn precision seeder control system based on GPS speed measurement. The system also uses STM32 as the main controller and Android mobile phone as the control terminal to set the operating parameters such as planting spacing. The GPS receiver is used to collect the forward speed of the tractor, and the speed of the metering device is adjusted in real time according to the speed information provided by GPS, so as to realize the real-time matching of the speed of the metering device and the forward speed of the tractor (*Ding et al, 2018*). The above examples have good effects on wheat and corn sowing operations, but they do not meet the agronomic requirements of narrow space in facilities greenhouses and vegetable sowing.

Based on the current situation of vegetable sowing in facilities greenhouses, this study designed a remote control system for vegetable seeder. The Arduino single-chip microcomputer was used as the main control core, and the human-computer interaction was carried out through Bluetooth communication and Android terminal, remote control of vegetable seeder walking, speed regulation and lifting steering operations, to achieve long-distance remote control of vegetable seeder operations, reduce labor intensity, improve vegetable seeding efficiency, and provide technical reference for the intelligent development of facility agricultural equipment.

MATERIALS AND METHODS

The structure and working principle of the whole machine

The whole structure of the small vegetable seeder is shown in Fig. 1, which is mainly composed of frame, seeding unit, front and rear pressing device, lift steering mechanism, transmission system, battery and remote control system.

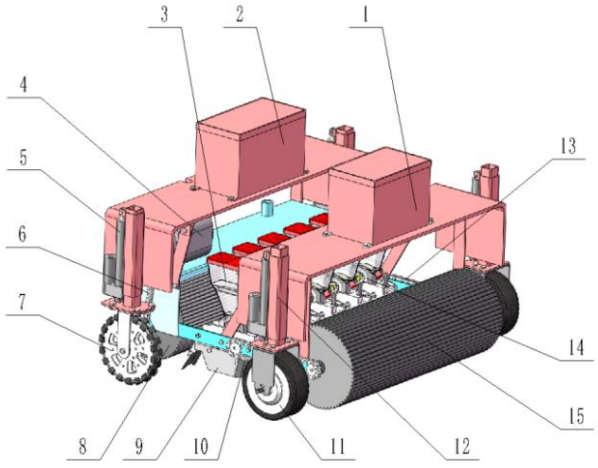

Fig. 1 - Small electric remote control vegetable seeder machine structure diagram

1 – Electric control box; 2 – Battery box; 3 – Seed box; 4 – Travel drive motor; 5 – Electric push rod; 6 – 1st drive chain; 7 – Driven wheel; 8 – Rear press wheel; 9 – Trenching device; 10 – 3rd drive chain; 11 – Drive steering wheel; 12– Front lifting frame; 13 – 2nd drive chain; 14 – Seed rower; 15 – Front press wheel

During the operation, the electric push rod of the lifting steering device is in a low position, and the front and rear press wheels contact the ground. The power is driven by the first-stage chain drive to drive the rear press wheel, and the rear press wheel drives the whole machine forward; the front press wheel obtains power through the second-stage chain drive, and then drives the metering device through the third-stage chain drive to realize the seeding operation. During the steering, the seeding operation mode is switched to the steering mode, the seeding drive motor stops, the seed metering device stops rotating, the lifting drive motor starts, the electric push rod of the lifting mechanism elongates, the steering drive wheel and the driven wheel drop, the whole machine is lifted, the front and rear pressing wheels leave the ground, the steering drive motor starts, and the left and right produce differential speed to achieve steering. The main parameters of the whole machine are shown in Table 1.

Table 1

Main parameters of remote control vegetable seeder

Projects	Parameter
Overall dimensions L×W×H (mm)	1000×900×600
Weight of the whole machine (kg)	102
Number of seeding rows	6
Row spacing (mm)	18-25 Adjustable
Type of seed metering device	Nest round wheel
The whole machine lifting height range/mm	0-150
Drive power (W)	576
Operating voltage (V)	48

The overall design of the remote control system

The composition of the remote control system is shown in Fig. 2, which mainly consists of three parts: control unit, interaction unit and execution unit. The interaction unit consists of Android terminal and Bluetooth module; the control unit consists of Arduino microcontroller, data transmission module, motor driver and relay; the execution unit mainly consists of motor driver, DC brushless motor, relay and electric push rod.

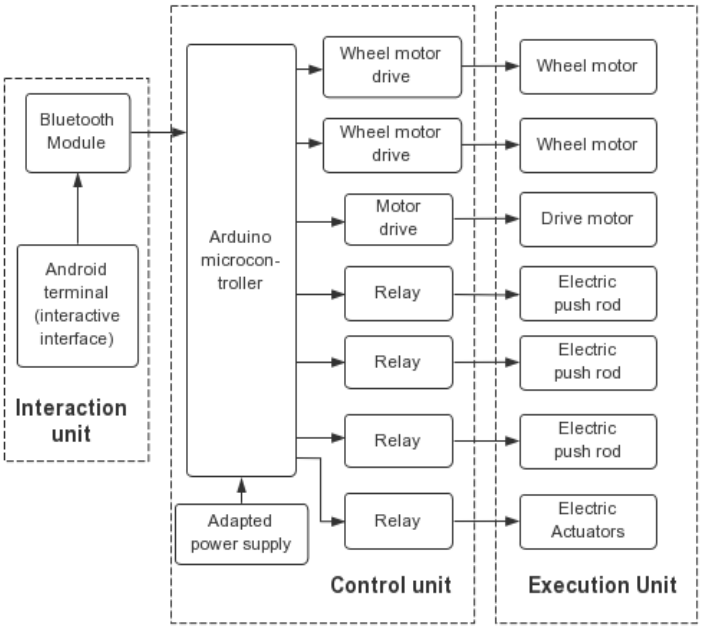

Fig. 2 - Structure diagram of control system

When working, the resetting button is selected in the Android terminal, the Android terminal transmits the status signal to the Arduino microcontroller through the Bluetooth module, the status signal is converted to low level, the relay is disconnected, the electric pusher is reset, and the front and rear press wheels touch the ground; select the sowing button in the Android terminal, the Android terminal transmits the seeding command to the Arduino microcontroller through the Bluetooth module, the Arduino microcontroller outputs the PWM signal to the drive motor driver, and controls the speed of the drive motor by changing the duty cycle of the PWM control signal, thus controlling the operating speed of the seeder. When road walking or steering change, select the lift button in the Android terminal, which is converted into a high level signal by Arduino microcontroller to control the relay suction, the electric pusher extends, the whole machine leaves the ground, select the in/out or steering button, the Arduino microcontroller transmits the road walking or steering command to the front-end steering wheel driver, and the wheel drive wheel starts or generates differential speed to realize road walking or steering change. When changing the sowing site and needing to modify parameters such as turning radius and operating speed, the operating parameters can be set directly through the PC upper computer on the Arduino IDE platform, solving the problem that the traditional vegetable seeder operating mode changes require manual adjustment of the mechanical structure, which is time-consuming and laborious, and can adapt to the sowing needs of different seeds, different plant spacing and different monopoly heights according to the agronomic requirements.

Hardware design

The remote control system of vegetable seeder is based on Arduino microcontroller as the main control core, Bluetooth communication as the data transmission method, and Android platform as the control terminal to complete the operation speed adjustment lift and steering control of the seeder, and the hardware composition of the system is shown in Fig. 3.

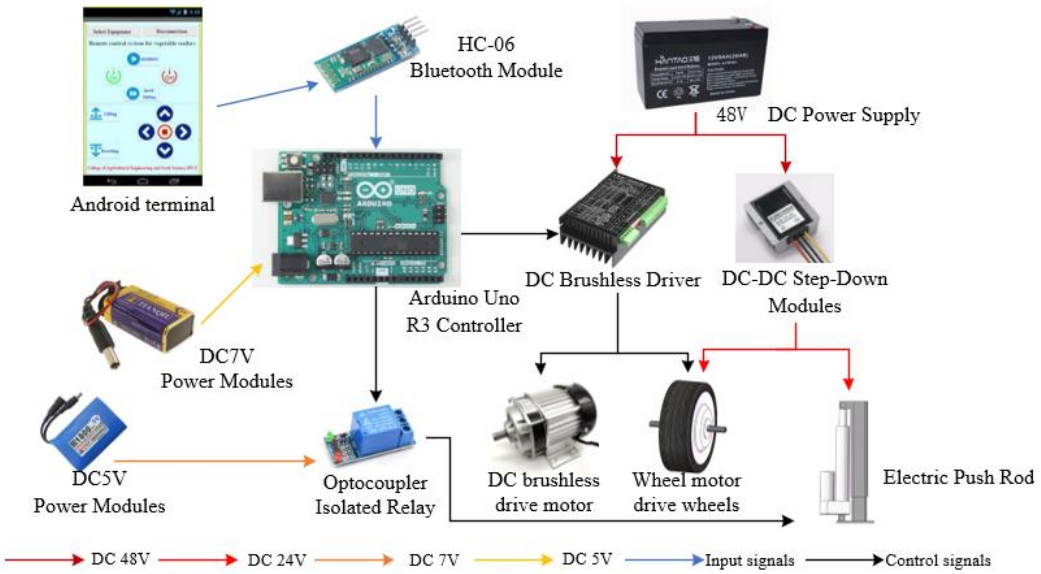

Fig. 3 - Hardware composition

As the core of the control system, the main role of the Arduino microcontroller is to accept the command signals from the host computer and make feedback to control the speed of the drive motor, the wheel motor and the state of the electric push rod. The model Uno R3 Arduino microcontroller with ATmega 328P as the main chip, operating voltage of DC 5V and current of 50mA, has the advantages of high performance, rapid response to real-time communication, low cost and low power consumption, with 6 analog input interfaces and 14 digital input and output interfaces (*Xu et al, 2021*), to meet the system building requirements for multi-target precise control of vegetable seeders.

The communication interface circuit of the system is shown in Fig. 4, where port IN1 on the driver is the input of PWM1 and PWM2 that control the rotational speed of the left and right hub motors, and is connected to ports 5 and 6 of the Arduino main controller; IN2 is the forward and reverse rotational control of the hub motors, and will be connected to ports 7 and 8 of the Arduino main controller; Hall signal ports 5V0, HU, HW, HV, COM are connected to the hub motor Hall signal port; the controller controls the speed and forward and reverse rotation of the two hub motors to achieve the purpose of precise control of the motor working state;

port 9 is the generation port of the PWM3 pulse signal that controls the speed of the DC brushless motor, which also uses the way of changing the duty cycle to drive the motor speed; D2 and D3 are the control ports of the relays, which control four groups of eight D2 and D3 are relay control ports, which control the suction and disconnection of relays by controlling the high and low level conversion of 4 groups of 8 relays, so as to precisely control the state of the electric push rod, and finally realize the lifting and resetting of the whole machine with the lifting device. It is equipped with RS485 communication module, which can be connected to the host computer, and the operating parameters such as turning radius can be adjusted by the host computer terminal to adapt to the changing operating environment; after connecting to the host computer, the speed of the drive motor, the received PWM duty cycle and the high and low potentials can be displayed in detail, which is convenient for system debugging and data collection of the test (*Jiang et al, 2016*).

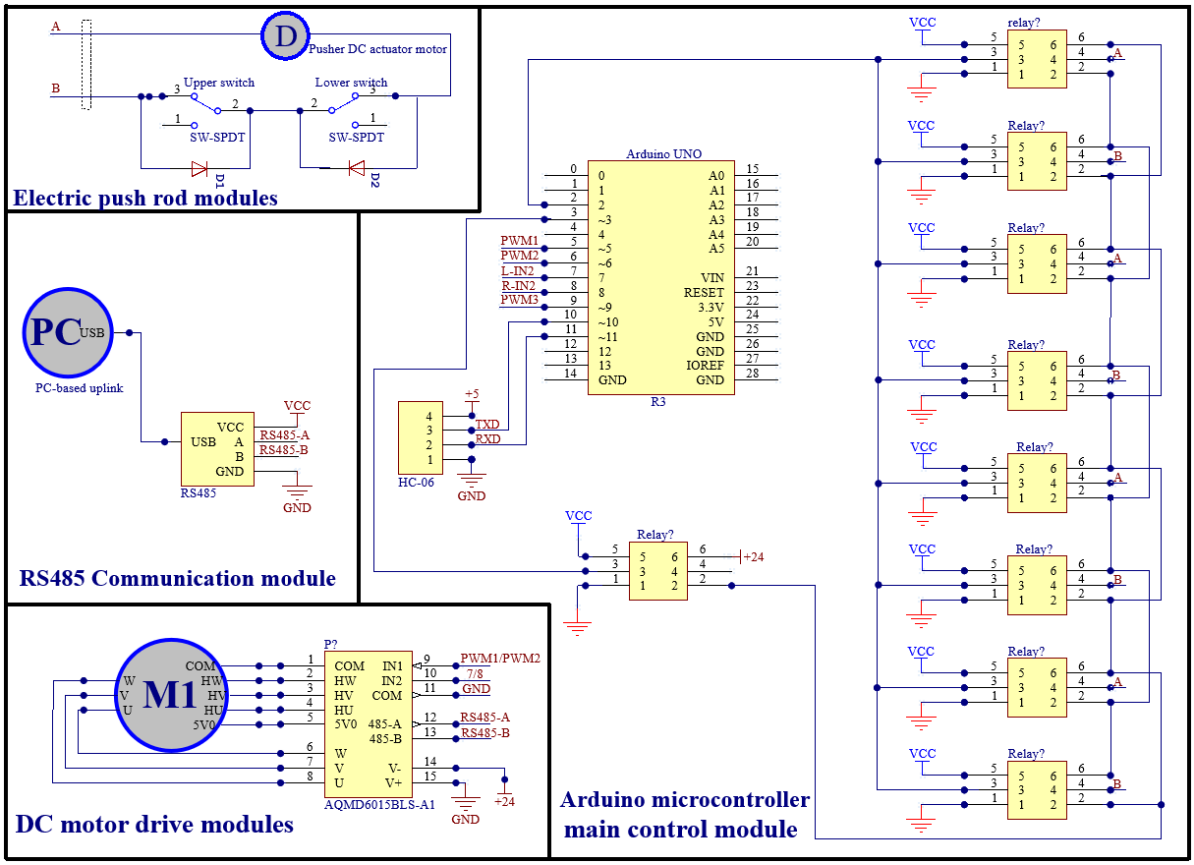

Fig. 4 - Design of communication interface circuit of the system

The data transmission between Android terminal and Arduino microcontroller uses wireless Bluetooth communication, and HC-06 Bluetooth serial module is selected. The principle is shown in Fig. 4 Bluetooth communication circuit part. The module is compatible with a variety of different voltage microcontroller motherboard, comes with 5V to 3.3V circuit, the maximum transmit power is 4dBm, the reception sensitivity is -85dBm (*Chao et al, 2013*), comes with LED lights, can judge whether the Bluetooth is successfully connected through the LED light off, comes with the transmission function, can be connected with cell phones, computers and other kinds of upper computer to communicate with each other, pairing quickly, simple operation, relatively stable.

Description of lifting and steering mechanism

The lifting and steering control mechanism consists of lifting sleeve, supporting frame and electric actuator, driving wheel and universal driven wheel, etc., as shown in Fig. 5. The bottom end of the electric actuator is fixed on the support frame, and the upper end is fixed on the lifting sleeve. The built-in motor drives the actuator to do vertical telescopic movement, and drives the whole machine to lift and reset through the lifting sleeve. The front lifting mechanism is the driving steering mechanism, the walking wheel is the wheel motor, the rear lifting mechanism is the driven steering mechanism, the walking wheel is the universal wheel.

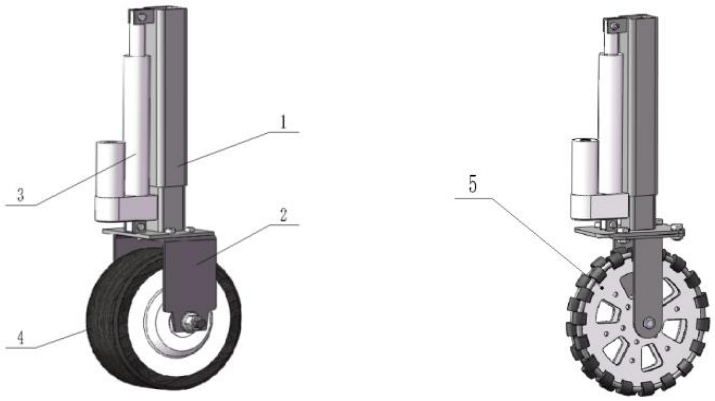

(a) Front lift drive steering device (b) Rear lift slave steering device

Fig. 5 - Lifting and steering mechanism

1 – Lifting sleeve; 2 – Wheel support frame; 3 – Electric push rod; 4 – Wheel motor drive wheel; 5 – Slave universal wheel

Electric push rods should be selected based on parameters such as thrust, stroke and push rod speed. When the vegetable seeder road travel, the press wheels, openers, etc. should be completely off the ground, and the minimum ground clearance should be more than 110 mm (Xu *et al, 2021*), considering the requirement of working monopoly height and the minimum stroke that does not interfere with the sowing operation, the stroke of the push rod is determined to be 150 mm. Select the small silent electric push rod from Dongguan Yiheng Electronics Co., Ltd. as shown in Fig. 6(a). The built-in motor torque of the push rod is 105kg·cm, the reduction ratio is 46.8, the thrust force of the push rod is 900N, the linear speed is 12mm/s, the total thrust force of the four push rods is 3600N, which meets the thrust force requirement of lifting the whole machine. The working voltage of the electric push rod is 24V DC, and the main power supply converts 48V DC to 24V through the step-down module for the use of the push rod.

The positive and negative terminals of the electric push rod are connected to the relay, and the Arduino microcontroller controls the switch of the relay by outputting high and low level signals to control the forward and reverse rotation of the built-in motor of the push rod, so as to control the lift of the electric push rod. The relay itself operates at 5V, which requires an additional power supply or a step-down module. In this study, a DC 5V power supply module is used to power the relay, as shown in Fig. 6(b).

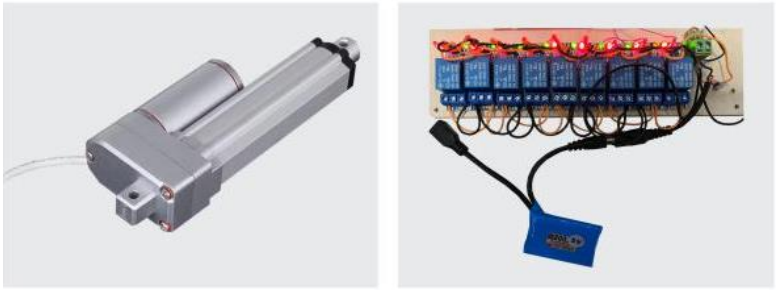

(a) Electric push rod (b) Relay modules

Fig. 6 - Electric push rod and relay modules

The driving steering wheel is a wheel motor of type HB-200 with embedded DC brushless motor, DC power supply 24V, rated power 250W, no-load speed 125r/min, and built-in reduction gear with a reduction ratio of 1:5, as shown in Fig. 7(a).

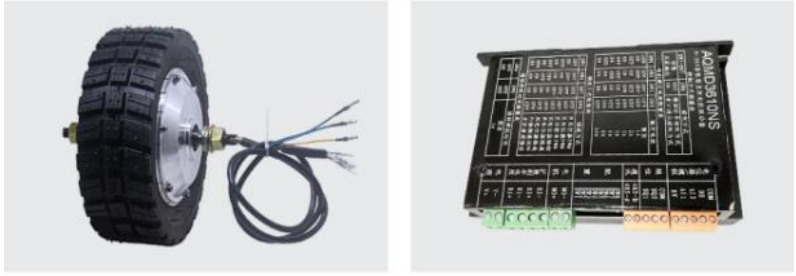

(a) Wheel drive steering wheel (b) Motor drive

Fig. 7 - Drive motor wheels and their drives

Steering control test method

Using the turning radius as the test factor, the Arduino controller sends PWM pulse signals to the driver of the steering drive wheel to control the speed of the drive wheel, and the speed ratio of the two wheels is calculated by equation (2) to adjust the turning radius of the seeder.

The actual turning radius of the planter was tested to ensure the accuracy of the row effect and turning radius when the planter was actually sown, and to verify the accuracy of the differential steering of the planter based on this control system. Set the target steering angle of the planter to 180°, set the theoretical turning radius of the test to 0, 400mm, 500mm, 600mm, 700mm, 800m, and measure the actual turning radius corresponding to the different theoretical turning radii of the planter, each group of turning radius is tested once clockwise and once counterclockwise, and each test is repeated three times to measure the actual turning radius and take the average value to analyze the control accuracy of the seeder steering system. The steering passing rate is calculated as:

$$E = 1 - \frac{|R - R_0|}{R_0} \times 100\% \quad (2)$$

where:

R is actual measurement of turning radius, mm; R_0 is theoretical turning radius, mm; E is steering pass rate, %.

Software design

Arduino control program design

During sowing operation, enter commands on the interactive interface of the Android terminal, the command information is transmitted to the Arduino microcontroller through the Bluetooth serial port, and the Arduino microcontroller parses the protocol and obtains different control commands to complete the control of the seeder actuator. Under normal operating conditions, the Arduino microcontroller can output PWM signals and high and low level signals to each driver and relay to control the forward and reverse rotation and speed of the drive wheel, the speed of the drive motor and the expansion and retraction of the electric push rod separately, and the different commands are not affected by each other; in addition, an emergency stop button is set up to directly override the three-way control signal and emergency stop in case of emergency to avoid accidents. The workflow of the control system is shown in Fig. 8.

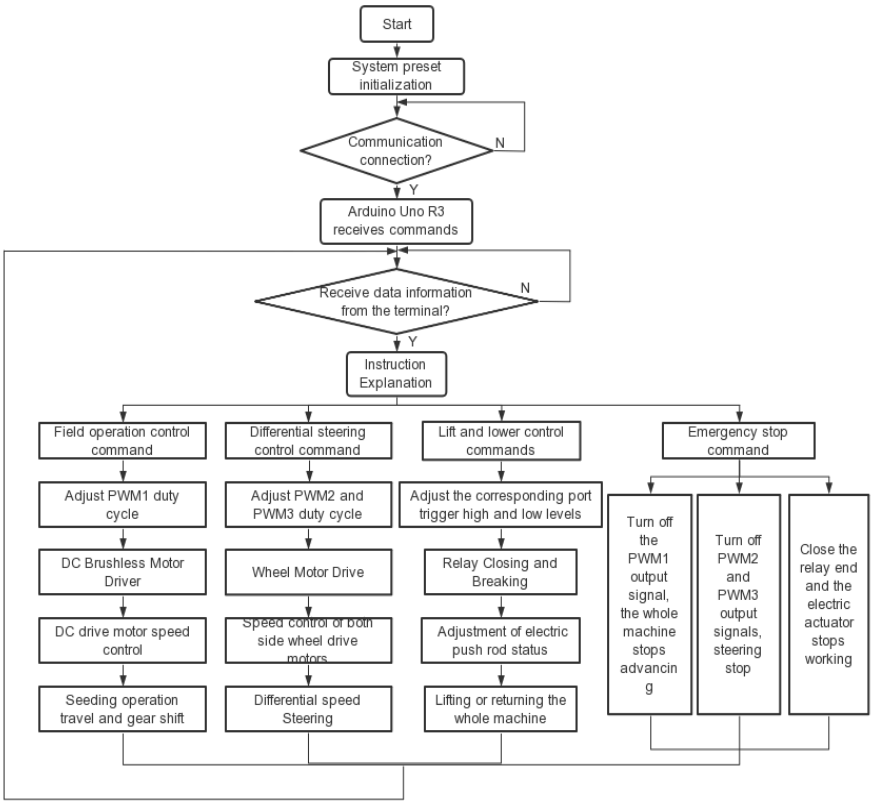

Fig. 8 - Control system workflow

Design of differential steering control model

Differential steering is used to control the planter for steering and row change operation (*Yang et al, 2013*). The Arduino main controller sends PWM duty cycle to regulate the speed of the drive wheels on both sides respectively, and the drive wheels on both sides form a differential speed so as to complete the steering and row change, and the differential steering model, as shown in Figure 9.

It is assumed that the body of the seeder is rigid and the wheels are purely rolling with the ground, without considering the relative sliding of the driving wheels.

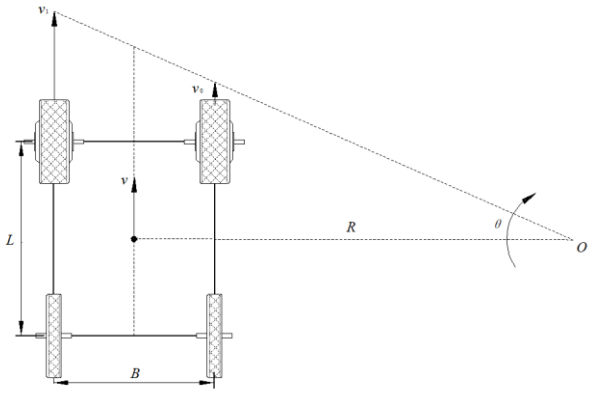

Fig. 9 - Differential steering model

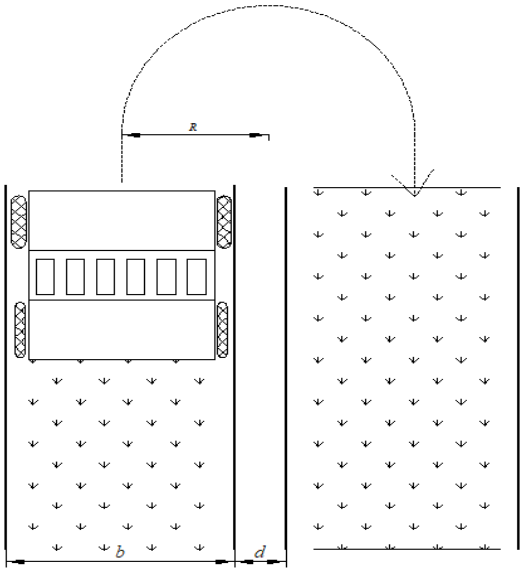

Fig. 10 - Steering diagram

From Fig. 9, it can be seen that the speed ratio of the two driving wheels during the turn is

$$\frac{v_1}{v_0} = \frac{R + B/2}{R - B/2} \quad (1)$$

where:

v_0 is the inside wheel speed, m/s; v_1 is the outside wheel speed, m/s; B is the wheelbase of two driving wheels, mm, here 990 cm is taken; R is the turning radius when steering, mm.

From the above equation, it can be seen that by adjusting the ratio of the speed of the two driving wheels, the demand for different turning radii can be met. When the turning space is narrow, the turning radius $R<B/2$ can be achieved when $R=0$. At this time, the speed of the two driving wheels is the same size and the direction is opposite; when the sowing operation changes rows and turns, $R \geq B/2$ is required in order not to reseed, as shown in Fig.10, the width of the monopoly is b and the distance between the monopoly is d. At this time, the turning radius $R=(b+d)/2$. The turning radius is determined according to the agronomic requirements, and the speed ratio of the two driving wheels is adjusted by PWM duty cycle signals.

Design of Android Remote Control Terminal

The system program is written in Arduino IDE, and the parameters such as communication connection, steering motor speed, drive motor speed, state of electric push rod and emergency stop switch are bound to the keys of Android terminal interaction interface respectively, and the control interaction interface is shown in Fig. 11. During operation, open the Android terminal APP, connect to the control system, click the On button to turn on the power, through the Resetting button, the whole machine descends, the front and rear suppression wheels touch the operating ground, the four steering wheels of the lifting and steering mechanism do not touch the ground, select the Sowing operation button, the sower carries out sowing operation, adjust the operating speed through the Gear shifting button, the gear speed is set according to the actual sowing agronomic requirements, from low speed to high speed cycle change gear; at the end of sowing, the whole machine is lifted off the ground by the Lifting button, and the 4 directional buttons of the lower lift and steering mechanism control the road walking or turning to change rows and turn around in place; after the sowing operation is finished, click the off button to turn Off the power and end the sowing operation. In case of emergency, click the emergency stop button below, the command can override all the commands and realize emergency stop.

Fig. 11 - Android terminal human-machine interaction interface

RESULTS AND ANALYSIS

The test design of system control accuracy and results analysis

In order to ensure that the vegetable seeder travels smoothly and smoothly during the working process, the reliability and stability of the control system are verified, and the parameters of the drive motor speed are optimized, and the no-load driving test based on this control system is carried out.

According to the literature (*Li et al, 2022; Wang et al, 2022*), the reference of the no-load pre-test results of the drive motor, it is found that the operation driving speed of vegetable sowing is generally in 0.6~1.0m/s when the effect of sowing is more ideal, that is, the operation driving speed of the sower is set to three gears of 0.6m/s, 0.8m/s and 1.0m/s respectively, and the operation parameters are set through Arduino IDE. During the test, the driving speed of the seeder was measured in real time by the tachometer. During the test, the control accuracy of the seeder control system was measured under various driving conditions such as three gear speeds and random acceleration and deceleration, and the test data is shown in Fig.12.

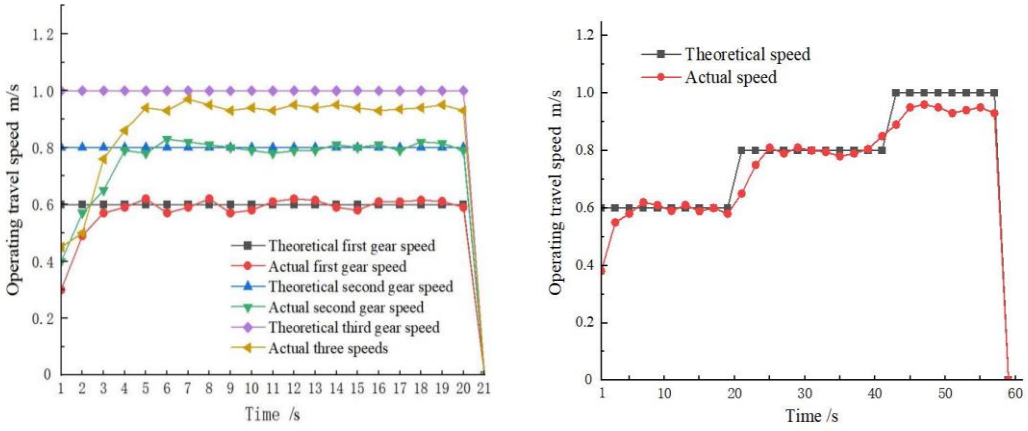

(a) Different gears driving status (b) Random acceleration and deceleration driving status

Fig. 12 - Variation curves of some operating speed parameters under different states

After the system is in stable state, the measured actual speed is compared with the theoretical speed of driving, and the data is shown in Table 2.

Table 2

Deviation of theoretical speed and actual speed under different driving conditions

Driving status	Maximum deviation rate (%)	Minimum deviation rate (%)	Average deviation rate (%)
First gear	6.57	0.93	3.57
Second gear	2.54	0.75	1.59
Third gear	7.16	3.06	5.06
Random gears	6.83	4.57	5.89

From the speed change curve in Fig. 12, it can be seen that the drive motor running start time is about 2s, and the seeder is more unstable in this time period, and the speed deviation rate is larger. After the control system is stabilized, the actual speed of the planter is close to the theoretical speed, and there is no stuck phenomenon; when the driving speed is 0.8m/s, the driving state of the planter under the control system is most stable based on the control system, and the average value of deviation rate is 1.59% at this time, and the control accuracy is higher and the stability is better to meet the control accuracy requirement of the control system.

The test design of steering control and result analysis

In order to ensure the accuracy of the seeder's actual seeding to the row effect and turning radius, to verify the accuracy of differential steering of the planter based on this control system, the actual turning radius of the planter is tested.

Table 3

Steering control test results

Target theoretical turning radius(mm)	Average actual turning radius (mm)	Standard deviation (mm)	Steering pass rate (%)
0	87	31	93.42
400	369	33	94.50
500	547	45	94.10
600	679	86	92.10
700	909	114	91.25
800	941	137	89.80

During the different turning radius tests, the planter was kept driving smoothly, the steering inner measuring wheel speed was kept constant, and the outer wheel speed was changed to vary the actual turning radius. From the analysis of the data in Table 3, it can be seen that the maximum standard deviation is 137 mm, the minimum steering pass rate is 89.8%, and the error value of the turning radius basically meets the target control requirement of the steering system during the test to ensure the planter achieves 180° steering. The error value of turning radius basically meets the target control requirement of steering system. However, as the turning radius becomes larger, the turning radius error gradually increases and the steering qualification rate gradually becomes smaller, which is caused by the vibration of the machine body and the unevenness of the seeding operation road during the seeding process. The larger the turning radius is, the more obvious the above problem is.

CONCLUSIONS

The remote control system of small vegetable seeder was designed with Arduino microcontroller as the control core. Through remote control, the planter can move forward, adjust speed, change line and turn in the field. Through the lifting device and the differential steering device, the vegetable seeding operation is separated from the three modes of road walking and lane changing, it solves the problem of seed waste caused by the fact that the seeding operation of the traditional vegetable seeder is not independent of the mode of road walking and lane changing, and the seed metering device is still rotating during road walking and steering. The Android terminal remote control APP is designed, and the Android terminal is connected through Bluetooth for human-computer interaction.

The operation is simple and the operation parameter setting is convenient, the precision control of vegetable sowing in facilities greenhouse was realized, the quality of vegetable sowing was improved, and the greenhouse vegetable sowing with high precision, high strength and strong repeatability could be completed.

The accuracy of the control system and the qualified rate of steering were tested. The test shows: the control system is stable and reliable, the speed deviation rate of the seeder is 1.59 %, the differential steering is relatively accurate, the qualified rate of steering is more than 89.8 %, and the synchronous speed error of the lifting mechanism tends to be stable, which meets the accuracy requirements of the control system. The designed remote control system is stable, reliable and has good adaptability.

ACKNOWLEDGEMENTS

This work was financially supported by the Shandong Province Key R&D Program (Grant No. 2022CXGC010611).

REFERENCE

[1] Chao Feijuan, Zhao Youliang, Chen Jun, et al. (2013). Design and experimental research on the integrated water and fertilizer hole application machine in orchard (苹果园水肥一体化穴施机设计与试验研究). *Journal of Agricultural Mechanization Research,* Vol. 45, No. 2, 92-97.

[2] Cheng Xiupei, Li Hongwen, Wang Qingjie, et al. (2019). Design and experiment of wheat seeding control system in plot seeder (小麦小区播种机排种控制系统设计与试验). *Transactions of the Chinese Society for Agricultural Machinery,* Vol. 50, No. 7, 30-38.

[3] Ding Youqiang, Yang Li, Zhang Dongxing, et al.(2018). Control system of motor-driving maize precision planter based on GPS speed measurement (基于 GPS 测速的电驱式玉米精量播种机控制系统). *Transactions of the Chinese Society for Agricultural Machinery,* Vol. 49, No. 8, 42-49.

[4] Du Zheng, Shu Hongjie, Lu Zeming, et al. (2017). Design and manufacture of seed planter for small grain vegetable (小粒径蔬菜电动播种机的研制). *Journal of Agricultural Mechanization Research*, Vol. 43, No. 11, 5-10.

[5] EL-Ghobashy H., Mohamed T., EL-Ashker A., et al. (2016). Development of a locally vacuum vegetable seeder for nursery trays. *Journal of Soil Sciences and Agricultural Engineering*, Vol. 7, No. 8, 595-602.

[6] Jiang Huanyu, Zhang Lijun, Shi Weinan. (2016). Effects of operating parameters for dynamic PWM variable spray system on spray distribution uniformity. *Ifac Papersonline*, Vol. 49, No.16, 216-220.

[7] Jin Xin, Li Qianwen, Zhao Kaixuan, et al. (2019). Development and test of an electric precision seeder for small-size vegetable seeds. *International Journal of Agricultural and Biological Engineering*, Vol. 12, No. 2, 75-81.

[8] Li Xiaoran, Zhang Yinping, Diao Peisong, et al. (2019). General situation of vegetable production and research status of precision seeder in China (我国蔬菜生产概况及精量播种机研究现状). *Journal of Agricultural Mechanization Research*, Vol. 43, No. 5, 263- 268.

[9] Li Xiaoran, Zhang Yinping, Diao Peisong, et al. (2022). Design and test of small pneumatic precision seeder for vegetables (小型气力式蔬菜精量播种机设计与试验). *Journal of Agricultural Mechanization Research*, Vol. 44, No. 4, 54-62.

[10] Mei Yincheng, Qi Lijun, Ji Ronghua et al. (2016). Design and experiment of remote control system of greenhouse self-propelled mist sprayer (温室自走式弥雾机远程控制系统的设计与试验). *Journal of China Agricultural University*, Vol. 20, No. 1, 170-175.

[11] Narang M. K., Dhaliwal I. S., Singh Manes G. (2012). Development and evaluation of a two-row revolving magazine type vegetable transplanter. *Journal of Agricultural Engineering*, Vol. 48, No. 3, 1-7.

[12] Qi Yazhuo, Xiang Shunan. (2020). Research status and development trend of vegetable seeder at home and abroad (国内外蔬菜播种机的研究现状与发展趋势). *Journal of Chinese Agricultural Mechanization*, Vol. 41, No. 1, 205-208.

[13] Richard L. Parish. (2005). Current developments in seeders and transplanters for vegetable crops. *HortTechnology*, Vol. 15, No. 2, 346-351.

[14] Raven provides OMNIPOWER™ platform for world' s first omni farm enterprise[EB/OL]. (2021). *Raven company official website, Jun.,* 15th. https://ravenprecision.com/news/ raven-provides-mnipower-platform-for-worlds-first-omni-farm-enterprise.

[15] Wang Fangyan, Yang Liang, Wang Hongti, et al. (2022). Design and test of electric driving pneumatic carrot planter in greenhouse (温室大棚电驱气力式胡萝卜播种机设计与试验). *Journal of Agricultural Mechanization Research*, Vol. 53, No. 8, 64-73+131.

[17] Xu Qimeng, Li Hongwen, He Jin, et al. (2021). Design and experiment of the self-propelled agricultural mobile platform for wheat seeding (小麦播种自走式农用移动平台设计与试验). *Transactions of the Chinese Society of Agricultural Engineering*, Vol. 37, No. 14, 1-11.

[18] Yang Xuefeng, Cai Zhigang, Fang Ming, et al. (2013). Steering styles and features of construction machinery (工程机械车辆的转向形式及其特点). *Construction Machinery,* No. 13, 67-72.

[19] Yuan Yongwei, Yi Jinggang, Cui Baojian, et al. (2014). Greenhouse vegetable planter go straight laser system design and test (温室蔬菜播种机激光走直系统设计与试验). *Journal of Agricultural Mechanization Research,* Vol. 36, No. 12, 147-150.

[20] Zhang Aoqi, He Qinghai, Zhang Guihai, et al. (2022). Equipment and experiment of greenhouse high-pressure atomization spraying based on PLC (基于 PLC 的温室高压雾化喷药设备及试验). *INMATEH Agricultural Engineering,* Vol. 68, No. 3, 147-155.

[21] Zhang Liang, Li Ming, Yao Limin, et al. (2022). Design of farmland area measuring instrument based on BeiDou satellite navigation system (基于北斗导航系统的农田面积测量仪设计). *INMATEH Agricultural Engineering,* Vol. 68, No. 3, 99-109.

RESEARCH AND EXPERIMENT ON EFFICIENT MIXING MODES OF DIFFERENT FORMS OF WATER AND FERTILIZER
/
不同形态水肥高效混合模式研究与试验

Tianhua LI [1,3], Siqi ZHANG [1], Chaofan ZHANG[1], Guanshan ZHANG[1,3], Min WEI[2], Hongen GUO[4], Guoying SHI [1,3*]

[1] Shandong Agricultural University, College of Mechanical and Electrical Engineering/ China;
[2] Shandong Agricultural University, College of Horticultural Science and Engineering/ China;
[3] Shandong Provincial Key Laboratory of Horticultural Machinery and Equipment/China;
[4] Shandong Academy of Agricultural Machinery Science/China
E-mail: sgy509@sdau.edu.cn

DOI: https://doi.org/10.35633/inmateh-70-28

Keywords: *Integration Water and Fertilizer; Stir; Circumfluence; Computational Fluid Dynamics; Numerical Simulation*

ABSTRACT

This paper proposes a fertilizer mixing device that combines pressure relief return and mechanical agitation to address the issues in the current water-fertilizer integration equipment related to limited fertilizer mixing methods and inconvenient irrigation pressure regulation. The device employs different mixing modes for various fertilizer forms and uses pressure relief return to adjust irrigation pressure, thereby enhancing the efficiency of water-fertilizer mixing and optimizing energy consumption. The experimental results indicate that the reflux mode is suitable for liquid-type fertilizers which are fast dissolving and easy to diffuse, and its EC value is stable at about 6.60 mS/cm, which is close to the calibrated value of 6.80 mS/cm. The stirring paddle mode compensates for the reflux mode's weak mixing effect, making it suitable for solid powder-type fertilizers' mixing operation. The EC value remains stable at approximately 8.60 mS/cm when calibrated at 8.70 mS/cm. The "stirring paddle + two-way reflux" mode demonstrates the most robust mixing effect and is suitable for mixing solid granular fertilizers. When calibrated at 8.20 mS/cm, it stabilizes at approximately the calibration value after 105 s. This research provides technical support and a theoretical basis to accomplish efficient, energy-saving, and rational application of water-fertilizer integration across diverse fertilizer forms.

摘要

本文提出了一种泄压回流与机械搅拌相结合的混肥装置，旨在解决水肥一体化设备在混肥方式和灌溉调压方面存在的问题。该装置针对不同形态的肥料采用不同的混肥模式，通过泄压回流调节灌溉压力，提高水肥混合效率和能源利用效率。试验结果表明，回流模式适合溶解快、易扩散的液态型肥料，其 EC 值稳定在 6.60mS/cm 左右，与标定值 6.80mS/cm 接近。搅拌桨模式弥补了回流模式混肥作用较弱的缺点，适合固态粉末型肥料的混肥作业，当标定值为 8.70mS/cm 时，EC 值稳定在 8.60mS/cm 左右。"搅拌桨+双向回流"模式混肥作用最强，适合固态颗粒型肥料的混肥作业，当 EC 标定值为 8.20mS/cm 时，经过 105s 稳定在标定值左右。该研究为实现不同形态肥料的水肥一体化合理、高效、节能应用提供了技术支撑和理论依据。

INTRODUCTION

Water-fertilizer integration equipment is extensively used in agricultural production. Its principle involves mixing fertilizer and water and delivering the mixture to the crop roots area through drip irrigation equipment, thereby conserving both water and fertilizer (*Kapoor et al., 2022; Singh et al., 2023*). Efficient integration of water and fertilizer is a prerequisite for integrated irrigation and fertilizer application. A reliable and efficient fertilizer mixing device is thus an important guarantee for effective fertilizer integration. Currently, artificial fertilizer mixing is expensive and not very efficient. Additionally, water-fertilizer mixing uniformity often fails to meet the demands of precise fertilizer application. Traditional industrial mixing methods such as high-speed mixing, mixing tanks, or blenders are unsuitable for agricultural applications because of their high-power consumption *(Yin et al., 2017).*

Tianhua Li, Professor; Siqi Zhang, Postgraduates; Chaofan Zhang, Undergraduate; Guanshan Zhang, Doctoral students; Min Wei, Professor; Hongen Guo, Researcher; Guoying Shi, Senior experimentalist.

Thus, it is necessary to thoroughly study the mechanical characteristics of the fertilizer-mixing process, and develop suitable fertilizer-mixing devices for agricultural production. This will meet the requirements of precise fertilizer application and help conserve energy.

As the importance of sustainable development of global agriculture gradually increases, water and fertilizer integration has become one of the focuses of agricultural research at home and abroad *(Garcia et al., 2023).* Priva B.V., a Dutch company, has developed three different types of irrigation and fertilizer applicators - the Priva NutriFit, Priva NutriFlex, and Priva NutriJet - all capable of performing sprinkler, drip, and tidal irrigation while accommodating various fertilizer distribution programs as needed (*Wang et al., 2016*). Meanwhile, Israel's NETAFIM company has created an automatic water and fertilizer control system that includes a pumping station, filtration centre, fertilizer irrigation system, valve control system, and field irrigation network. This innovative technology automatically mixes liquid fertilizers with filtered water in specific proportions before entering the field's drip irrigation network (*Zhang et al., 2011*).

Domestic fertilization equipment is also developing, Zhang Zhiyang et al. designed two solid fertilizer dissolution mixed application of water and fertilizer integration device, which can directly apply solid fertilizer, can effectively reduce the cost of integrated use of water and fertilizer (*Zhang et al., 2019*). Liu Lin et al. developed a field mobile precision fertilizer irrigation and fertilization integrated machine for applying solid fertilizer, which realized the precise regulation of mother liquor concentration and automatic irrigation and fertilization (*Liu et al., 2019*). Li Jianian et al. combined pulse width technology to control the solenoid valve, which improved the fertilizer absorption control accuracy of the venturi tube (*Li et al., 2012*). Li Zhizhong et al. research on embedded irrigation controller to improve the water-saving effect of integrated irrigation of water and fertilizer (*Li et al., 2006*). Liu Yonghua et al. applied CFD numerical calculation to the key core components affecting the performance of fertilizer suction to carry out a one-factor performance optimization design, which improved the fertilizer suction flow rate (*Liu et al.,2015*). Chen Feng et al. designed a PLC-based irrigation water-saving controller, which provides a new device for water-saving irrigation technology (*Chen et al., 2010*). The existing integrated water and fertilizer facilities mostly adopt mechanical mixing fertilizer mixing method (*Liu et al., 2018*), while different forms of fertilizer are often applied in actual production in China, and the unified fertilizer mixing method is bound to fail to meet the requirements of reasonable, efficient and energy-saving.

Therefore, this paper designs a fertilizer mixing device combining pressure relief reflux and mechanical stirring to realize the fertilizer mixing operation of different types of fertilizers. Firstly, the numerical solution model of the fertilizer mixing process is established, and the numerical simulation of different types of fertilizer mixing operations is carried out. Then, the relevant flow field parameters such as speed, vortex and flow line are extracted, the hydrodynamic characteristics of different fertilizer mixing modes are analysed, and the fertilizer mixing modes matched by different material forms and fertilizers are proposed. Finally, the reliability of the numerical model and mechanical analysis, and the rationality of the fertilizer mixing device are verified by experiments.

MATERIALS AND METHODS

General structure and operational principle

The fertilizer mixing device is shown in Figure 1a, the device is mainly composed of fertilizer mixing barrel, water pump, six-blade disc *stirring* paddle, mixing motor, fertilizer output pipeline, return pipe group, irrigation pipeline, water injection pipeline, solenoid valve, ball valve, PH sensor, EC sensor, flow meter, etc., which can realize three fertilizer mixing working modes of return, *stirring* paddle and "stirring paddle + two-way reflux".

The internal layout of the fertilizer mixing device is shown in Figure 1b, the stirring paddle is installed inside the fertilizer barrel, the first reflux outlet group and the second reflux outlet group are opened at the bottom, the reflux outlet group is composed of two reflux ports placed at 180°, the first reflux outlet group is placed in a counterclockwise direction, the second reflux outlet group is placed clockwise, and the direction of the reflux elbow is tangentially consistent with the barrel wall, which enhances the guiding effect on the water flow movement. The main return pipeline connects two tributaries, distributed on both sides of the fertilizer barrel, and the tributaries on each side are then divided into two small tributaries and connected with the return port on the side wall of the fertilizer barrel, and the first return pipe and the second return outlet group are connected respectively.

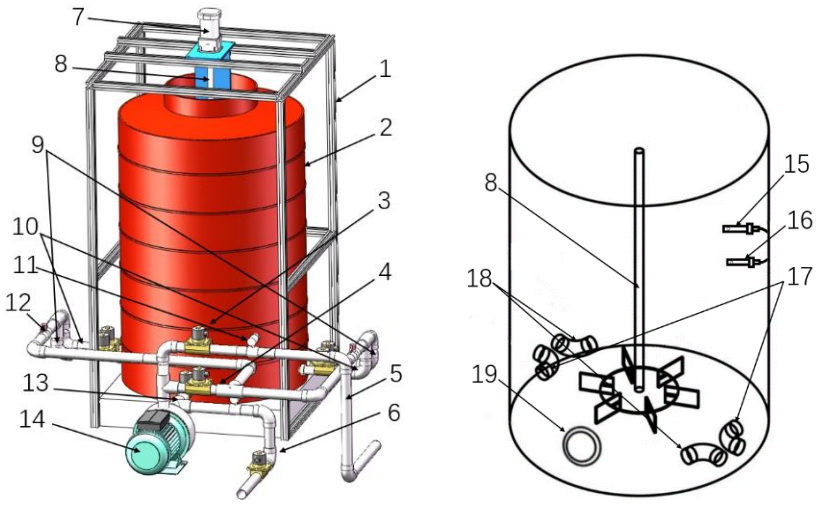

Fig. 1 - The schematic of fertigation

a) Device structure diagram; b) Layout diagram

1. Bracket; 2. Fertilizer buckets; 3. Solenoid valve; 4. Main reflow pipe; 5. Irrigation pipes; 6. Water injection pipes; 7. Stirring motor; 8. Stirring paddle; 9. First return pipe; 10. Second return pipe; 11. Flowmeter; 12. Ball valve; 13. Fertilizer pipe; 14. Water pump; 15. PH sensor; 16. EC sensors; 17. First return port group; 18. Second return port group; 19. Fat outlet

Operational principle

When the fertilizer mixing device is in operation, the water pump is started first, and the electromechanical valves on the main reflux pipeline, water injection pipeline, and the first reflux pipeline are opened. The water pump begins injecting water into the water injection pipeline. The water flows through the water injection pipeline and enters the fertilizer mixing tank, causing the water and fertilizer inside the tank to rotate counterclockwise, completing the initial stirring. Simultaneously, the water injection flow meter is responsible for monitoring the amount of water injected. When the set value of water injection is reached, the electromechanical valve on the water injection pipeline is closed to complete the water injection process.

Upon completing the water injection, the electromechanical valve on the fertilizer outlet pipeline is opened, enabling the mixture of water and fertilizer to enter the water pump and return to the fertilizer mixing tank through the first reflux pipeline. The counterclockwise rotation of water and fertilizer in the mixing bucket achieves reflux work. In reflux mode, activate the stirring motor to rotate counterclockwise so that "stirring paddle + reflux" occurs simultaneously. After a period of stirring, close the solenoid valve on the first return line and open that on the second return line. This will cause a clockwise rotation of water and fertilizer in the mixing bucket while still maintaining counterclockwise stirring by mixing the paddle, thereby achieving "stirring paddle + reverse reflux". If the mechanical stirring mode is selected, all solenoid valves are closed, the stirring motor is started, and the mixing paddle is stirred counterclockwise. The sensor on the inner wall of the fertilizer barrel detects the pH and EC value of the water and fertilizer to determine whether it meets the standard of the fertilizer. After finishing the fertilizer mixing work, close the mixing paddle and all solenoid valves.

When carrying out irrigation work, open the solenoid valve on the fertilizer outlet pipe and the irrigation pipe, and the water and fertilizer in the fertilizer barrel are transported to the irrigation area through the irrigation pipeline through the pump. If it is necessary to adjust the irrigation pressure, open the solenoid valve on the main return pipeline and the first return pipeline, currently, the water and fertilizer coming out of the fertilizer pipeline enter the irrigation pipeline to complete the fertilization work. The other part re-enters the fertilizer mixing barrel through the reflux pipeline, which regulates the irrigation pressure and promotes the flow of fertilizer liquid in the barrel to prevent the crystallization of fertilizer during fertilization, and the ball valves on both sides are used to control the amount of water and fertilizer entering the reflux pipeline.

Build numerical model

Ignoring the influence of free liquid on fertilizer mixing, the geometric model of fertilizer mixing device is established under the three-dimensional modelling platform. Considering the fluid-structure interaction between the paddle and the fluid, the motion of the impeller is defined and embedded by a user-defined function (UDF) of the fluid analysis software Fluent. The dynamic grid setting is performed by the fluid-structure interaction method (FSI) near the *stirring* paddle and the return port, and the position is updated according to the preset speed of each time step.

The corresponding fluid domain grid is redivided by tetrahedral elements to simulate the change process of the fluid calculation region and express the flow characteristics in the flow field *(Banu et al., 2019; Ferrari et al., 2022).* To verify the rationality of meshing, 1×10^5, 2×10^5, 5×10^5, 7×10^5, 8×10^5 and 1×10^6 meshes were carried out for the fluid domain, respectively. By comparing and analysing the numerical results under various mesh densities, it is proved that the numerical results of the fluid domain meshing of 7×10^5, 8×10^5 and 1×10^6 are less different. With the further increase of the number of grids, the computing resources and computing time consumption increase significantly, so the grid division scheme of 7×10^5 is suitable.

The viscous and non-compressible fluids covered in this paper can be described using the Navier-Stokes (N-S) equation. Under the Fluent platform, the finite volume method is used to solve the N-S equation discretely. Since the finite volume method can use various irregular control body units, it has great advantages for dealing with complex dynamic boundary problems in the fertilizer mixing process.

The N-S equation is shown in the following equation:

$$\rho\left(\frac{\partial u}{\partial t}+u\cdot\nabla u\right)=-\nabla p+\mu\nabla^2 u \tag{1}$$

$$\nabla\cdot u=0 \tag{2}$$

where u is the velocity vector of the flow field; ρ is the density of the fluid; p is the fluid pressure; μ is the kinetic viscosity of the fluid; ∇ is the Hamiltonian operator. In the actual fertilizer dissolution and mixing process, the physical characteristics of different types of fertilizers vary greatly, and the research focus of this paper is to analyse the flow field characteristics and mechanical characteristics of the fertilizer mixing process, so the fluid is treated as a single-phase fluid in numerical modelling, ignoring the dissolution of fertilizer and the interaction between different components. In the numerical modelling, the aqueous medium is used as the research object, the fertilizer bucket and the stirring paddle are set as the wall boundary conditions without slip, and the turbulence model adopts the *k-ε* model *(Song et al., 2018; Murthy et al., 2012)*.

In the *k-ε* model, the k-equation for turbulent kinetic energy and the equation for the dispersion of turbulence energy dissipation ε are expressed as follows:

$$\frac{D(\rho k)}{Dt}=P-\rho\varepsilon+D_k \tag{3}$$

$$\frac{D(\rho\varepsilon)}{Dt}=C_1\frac{P\varepsilon}{k}-C_2\rho\frac{\varepsilon^2}{k}+C_3\rho\varepsilon(\nabla\cdot u)+D_\varepsilon \tag{4}$$

In equations (3) and (4), D/Dt is the derivative of matter and u is the average velocity vector; D_k and D_ε are turbulent kinetic energy diffusion terms, respectively:

$$D_k=\frac{\partial}{\partial x_j}\left(\alpha_k\mu\frac{\partial k}{\partial x_j}\right) \tag{5}$$

$$D_\varepsilon=\frac{\partial}{\partial x_j}\left(\alpha_\varepsilon\mu\frac{\partial \varepsilon}{\partial x_j}\right) \tag{6}$$

In the equation μ is the effective viscosity coefficient $\mu=\nu_0+\nu_t$, ν_0 is the molecular viscosity coefficient, and ν_t is the eddy current viscosity coefficient $\nu_t=C\mu k^2/\varepsilon$.

In equations (3) and (4), P is the turbulent kinetic energy generation term, and the equation is:

$$P=-\rho u_i u_j S_{ij} \tag{7}$$

$$u_i u_j-\frac{2}{3}k\delta_{ij}=-2\nu_t\left(S_{ij}-\frac{1}{3}(\nabla\cdot\overline{u})\delta_{ij}\right) \tag{8}$$

In equations (7) and (8), $S_{ij}=(\partial u_i/\partial x_j+\partial u_j/\partial x_i)/2$ is the average strain rate tensor of the fluid; δ_{ij} is the Kronek symbol (δ_{ij}=1 when i=j; δ_{ij}=0 when i≠j); C_μ is the empirical constant of the turbulence model. In the equation, C_1, C_2, C_μ, α_k, α_ε are empirical constants, and coefficient C_3 is a correction term that considers the effect of turbulent compressibility.

In the solution process, the time term adopts the first order fully hidden format discrete, the convection term and viscous term adopt the second order windward discrete format, and the pressure-velocity coupling algorithm adopts the SIMPLE algorithm. One rotation period of the *stirring* paddle is about 2.512 s, divided into 100-time steps, each with 0.02512 s.

Numerical simulation analysis

Based on numerical models, different types of fertilizer mixing processes are numerically simulated. Set the capacity of the fertilizer drum to be 150 L, the diameter is 530 mm, and the height is 720 mm. The diameter of the bottom opening is 40 mm, and the centre of the opening is 50 mm from the bottom of the barrel. The diameter of the *stirring* paddle shaft is 17 mm, the diameter of the disc part is 160 mm, the thickness is 3 mm, the length, width and thickness of the blade are 70 mm, 40 mm and 3 mm, and the size of the blade and the disc part is 25 mm. The speed of the stirring motor can be adjusted from 0-10 rad/s, and the flow rate of liquid return is adjustable from 0-1.5 m/s. By extracting the flow field data such as the moment of the *stirring* paddle, speed, vortex amount, streamline line and pressure, the flow field characteristics of different fertilizer mixing modes are analysed and compared, which provides theoretical support for the applicability of different fertilizer mixing methods and future structural optimization.

Analysis of fertilizer mixing process in stirring paddle mode

For medium and low speed stirring, set the speed of the *stirring* paddle to 2.5 rad/s. The vortex structure of the fluid in the fertilizer barrel is shown in Figure 2a, there is a more regular three-dimensional vortex structure around the *stirring* paddle, the fluid tends to flow to the inside of the paddle, and the liquid movement near the *stirring* paddle blade is more intense, which is easy to form a vortex. The flow chart of the fluid in the fertilizer barrel is shown in Figure 2b, from which the stirring process is the liquid rotating around the axis and churning up and down coupling motion, to achieve the effect of mixing and mixing liquid and fertilizer. However, under the action of viscous resistance, the intensity of movement decreases sharply when the fluid movement spreads near the barrel wall, and laminar flow is formed near the barrel wall, which is not conducive to mixing fertilizer and water in the fertilizer mixing barrel.

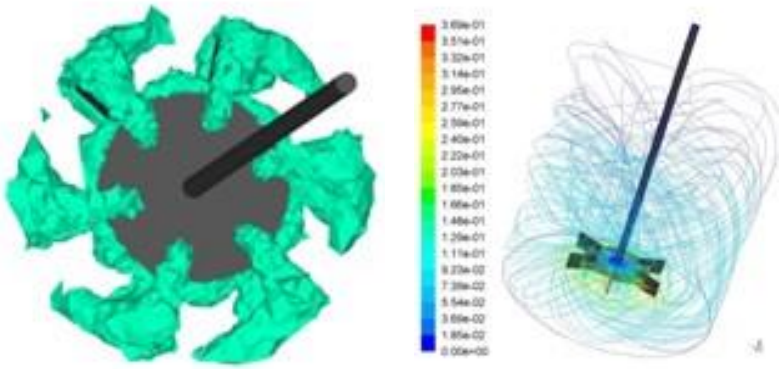

a) Vortex structure b) Streamline

Fig. 2 - Flow Field Characteristic around *Stirring* Paddle

The radial and axial velocity vectors of the fluid in the fertilizer tank are shown in Figure 3a. It can be seen from the radial vector diagram that due to the viscosity of the liquid, the energy loss during the motion transfer process is achieved, the intensity of the movement gradually decreases, and the movement speed of the fluid near the barrel wall is seriously attenuated. It can be seen from the axial vector figure 3b that the fluid in the barrel has tumbling movement in the axial direction, but the range of movement is limited to the middle and lower parts of the barrel, and the movement intensity of the upper solution of the barrel is low, which is not conducive to the uniformity of fertilizer.

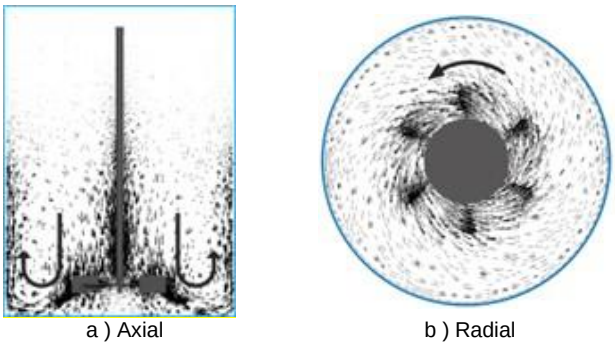

a) Axial b) Radial

Fig. 3 - Velocity vector of flow field

Analysis of fertilizer mixing process in " stirring paddle + two-way reflux " mode

The mixing process of "stirring paddle + two-way reflux" was numerically simulated, and the rotation direction of the reflux was selected in the same direction and reverse with the rotation direction of the stirring paddle, respectively. By extracting the corresponding flow field characteristics, the fluid behaviour and mechanical characteristics of the two modes were analysed.

Stress analysis

Referring to the mixing process of the stirring paddle mode, set the reflux speed of the liquid to 0.4 m/s, the speed of the stirring paddle to 2.5 rad/s, and set the rotation direction of the return flow to be opposite and consistent with the rotation direction of the impeller. The pressure distribution of the stirring paddle mode, "stirring paddle + co-directional reflux" mode and "stirring paddle + reverse reflux" mode is in the same coordinate bar, as shown in Figure 4. It can be seen from the pressure cloud diagram that the negative pressure zone value at the bottom of the stirring paddle is the largest, followed by near the blade, and the value of the upper negative pressure zone gradually decreases with the increase of height. A range of pressure differences are formed between the negative pressure zone and the positive pressure area, which provides power for liquid exchange in different areas, thereby promoting fertilizer dissolution and mixing. Compared with the stirring paddle mode, the axial range of "stirring paddle + co-directional reflux" mode increases in the low-pressure area, and the axial distribution level of the pressure zone is more obvious, which promotes the connection between axial liquids. Compared with the stirring paddle mode, the radial range of "stirring paddle + reverse reflux" mode increases in the low-pressure area, the pressure difference between each pressure zone increases, the pressure gradient distribution is obvious and there is high pressure at the edge, which promotes the fierce exchange of liquid in the radial direction, so that the solute collides with the stirring paddle.

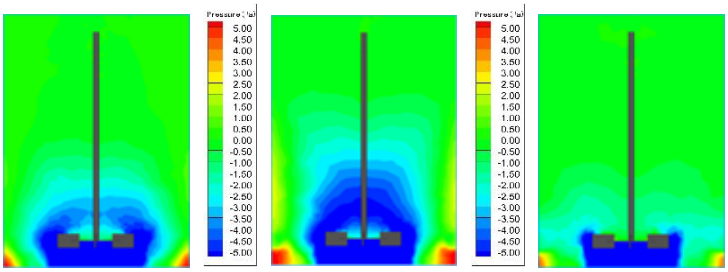

a) Stirring paddle b) Stirring paddle + co-directional reflux circumfluence
c) Stirring paddle + reverse reflux circumfluence

Fig. 4 -Comparison of pressure

Speed vector analysis

The axial velocity vectors for the "Stirring Paddle + Co-directional reflux" mode and the "Stirring Paddle + Reverse reflux" mode are shown in Figure 5. As can be seen from the axial vector diagram, the velocity of the fluid area in the barrel is mainly axial velocity. The axial speed promotes the churning of the liquid in the fertilizer barrel, so that the overall concentration of the fertilizer liquid in the barrel tends to be uniform. The radial velocity is mainly distributed around the paddles and converted into axial velocity after forming a vortex under the action of the barrel wall.

Compared with the stirring paddle mode, the axial velocity vector size and action area of the "stirring paddle + co-directional reflux" mode are significantly increased, which means that the movement of the liquid along the axial direction in the barrel is more violent, which better promotes the range and strength of the liquid churning up and down. The radial velocity vector size increases significantly in the "stirring paddle + reverse reflux" mode, especially near the bottom corner of the barrel, forming a violent tumble and winding the liquid again towards the paddle.

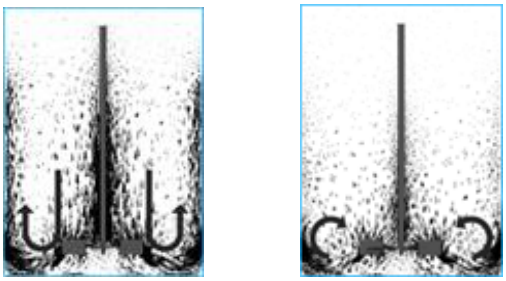

a. Co-rotating *b. Counter-rotating*

Fig. 5 - Comparison of Axial Velocity Vector

Analysis of flow field characteristics around the blade

The radial velocity vector plot and two-position vortex plot around the blade in the "stirring paddle + co-directional reflux" mode and the "stirring paddle + reverse reflux" mode are shown in Figure 6. It can be seen from the velocity vector diagram that the co-directional reflux enhances the overall velocity vector of the cross-section, enhances the rotational motion of the fluid, and promotes the axial convection of the liquid. The reverse reflux intensifies the convection of the liquid in the radial direction, the turbulent effect of the fluid is obvious, and the mixing effect of small scale is enhanced. It can be seen from the two-dimensional vortex diagram that the forward vortex is mostly in the flow field after superimposed co-directional reflux, and the positive vortex intensity increases compared with the positive vortex intensity in the reverse reflux, which enhances the overall rotational motion of the liquid. The eddies in different rotation directions in the flow field after superimposed reverse reflux increase, mainly around the blades and reflux ports. Positive and negative vortices exist in pairs, enhancing the shear effect of the liquid. The jet directly induced by the positive and negative vortex can collide with the barrel wall or paddle blade at high speed, accelerate the dissolution speed of granular fertilizer, and improve the dissolution efficiency of fertilizer.

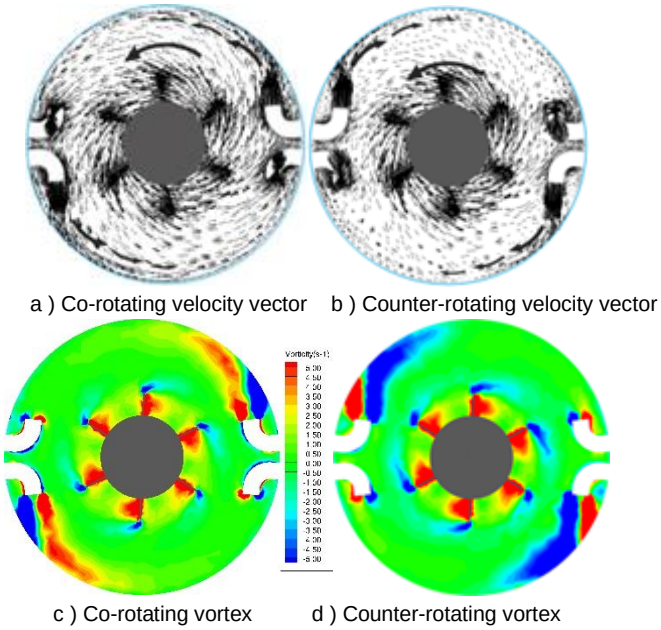

Fig. 6 - Flow field characteristic around stirring paddle

Through numerical simulation analysis, it can be concluded that the reflux direction has a significant influence on the fertilizer mixing process. The "stirring paddle + co-directional reflux" mode can promote the overall convection of liquid and improve the efficiency of fertilizer-liquid mixing operation; The "stirring paddle + reverse reflux" mode promotes the entry of deposited solutions or particles around the paddle at the bottom of the barrel for intensive dissolution. From this, the "stirring paddle + two-way reflux" mode not only improves the efficiency of fertilizer mixing, but also prevents granular fertilizer from accumulating on the wall of the barrel.

RESULTS

Trial design and analysis of results

In order to verify the rationality of numerical model, solution method and fluid analysis, different fertilizer mixing methods were experimentally studied. The implementation site is shown in Figure 7a. Based on MCGS industrial control configuration software, the data acquisition system and motor, solenoid valve and pump control system are built for data collection and the realization of different fertilizer mixing operation modes. The data acquisition system stores data every 1 s to record the EC value of the fertilizer liquid in the fertilizer barrel during different tests. The layout of the barrel is shown in Figure 7b, the test parameters are consistent with the simulation parameters, and EC (conductivity) sensors are placed at the distance of 60 mm, 420 mm and 580 mm from the bottom of the barrel, corresponding to the three different positions of the upper, middle and lower fertilizer barrel in turn, which are used to detect the EC value of the fertilizer liquid in the fertilizer barrel.

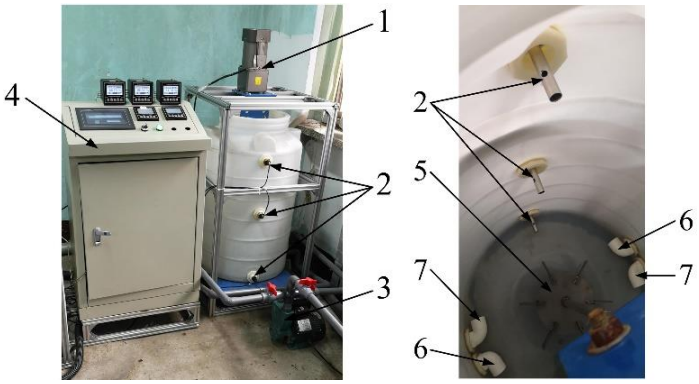

a) Device diagram b) Layout diagram

Fig. 7 - Photo of test site

1. Motor; 2. Conductivity sensors; 3. Pump; 4. Electrical cabinet; 5. Stirring paddle; 6. Inlet; 7. Outlet

In the experimental design, the diffusion of liquid fertilizer is used to achieve the ideal fertilizer mixing effect by stirring, so only the reflux mode test is set; The difficulty of dissolving solid powder fertilizer is increased compared with liquid fertilizer, but the difficulty of dissolution is low compared with solid granular fertilizer, and two sets of tests are set up: reflux mode and stirring paddle mode. Due to its special spherical structure, solid granular fertilizer is more difficult to dissolve, so two sets of tests are set up in the stirring paddle mode and the "stirring paddle + two-way reflux" mode to verify the rationality of the "stirring paddle + two-way reflux" mode. The experimental fertilizers are liquid, solid and granular. The fertilizers with different physical forms are shown in Figure 8.

a) Liquid fertilizer b) Powder fertilizer c) Granular-fertilizer

Fig. 8 - Fertilizer of Different Forms

Liquid fertilizer mixing test

Drip irrigation fertilizer was selected as the test material, and the reference mode of drip irrigation was 200-250 times dilution. According to the fertilizer application guidance method, 150 L of water requires 5.0 kg of fertilizer for dissolution and dilution. Before the test, 50 g of test liquid fertilizer was dissolved in 1.5 L clean water, and the EC value of the solution was stable at about 6.80 mS/cm after manual stirring. During the test, 5.0 kg of liquid fertilizer was added to the fertilizer tank at a uniform speed through the funnel device, and the reflux mode of the fertilizer mixing device was started, and the sensor measured the EC value of the fertilizer liquid at different positions of the fertilizer barrel in real time. The data acquisition system stores the data, makes the EC value change curve, and compares the change trend of the EC value of liquid fertilizer at various positions in the fertilizer barrel in the reflux mode. The test results are shown in Figure 9.

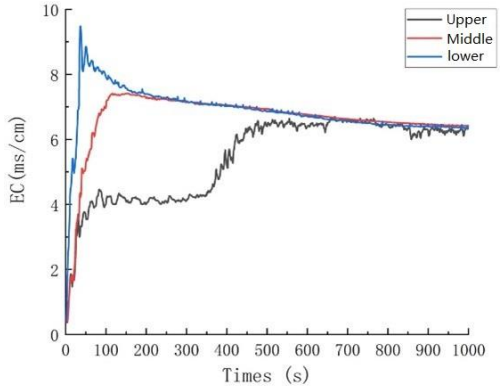

Fig. 9 - Conductivity Graph of Liquid fertilizer

It can be seen from the figure that at the initial stage, the EC value of fertilizer liquid in the upper middle and lower positions of the fertilizer barrel increased significantly. The top position of the fertilizer tank only relies on liquid diffusion to increase the concentration of fertilizer, so the fertilizer EC is stable at a low level. The bottom of the fertilizer barrel was deposited obviously, so the EC of the bottom fertilizer liquid increased the most rapidly and the value was the highest. Part of the liquid fertilizer deposited at the bottom of the fertilizer barrel moves with the water flow under the action of reflux, which accelerates the diffusion of liquid fertilizer in water, resulting in a gradual decrease in the EC value at the bottom of the fertilizer barrel, and a slow decrease after the intermediate position of the fertilizer liquid EC increases to a certain value. With the progress of reflux fertilizer mixing, the bottom reflux gradually affected the top position after a certain period of time, and the EC of the top fertilizer solution in the corresponding test results gradually increased after 350 s until it was consistent with the EC value of the bottom and middle fertilizer solution. After full mixing, the EC value of fertilizer liquid at different positions of the fertilizer mixing barrel was stable at about 6.60 mS/cm, which was basically consistent with the data measured by manual full stirring before the test.

Solid powder fertilizer mixing test

Potassium sulphate water-soluble fertilizer is selected as the test material, the product is bagged white solid powder, according to the fertilizer application method, 1.2 kg fertilizer needs 150 L of water for dissolution and dilution. Before the test, 12 g of test powder fertilizer was dissolved in 1.5 L of clean water, and the EC of the solution was stable at about 8.70 mS/cm after manual stirring. During the test, the reflux mode and stirring paddle mode fertilizer mixing tests were carried out respectively, and 1.2 kg of potassium sulphate powder was added to the fertilizer tank filled with 150 L of water, and the sensor measured the EC value of the fertilizer liquid in the upper, middle and lower positions of the fertilizer barrel in real time. According to the change curve of EC value, the change trend of EC value of fertilizer liquid in the fertilizer barrel was analysed, and the mixing characteristics of fertilizer liquid in reflux mode and stirring paddle mode were compared. The test results are shown in Figure 10.

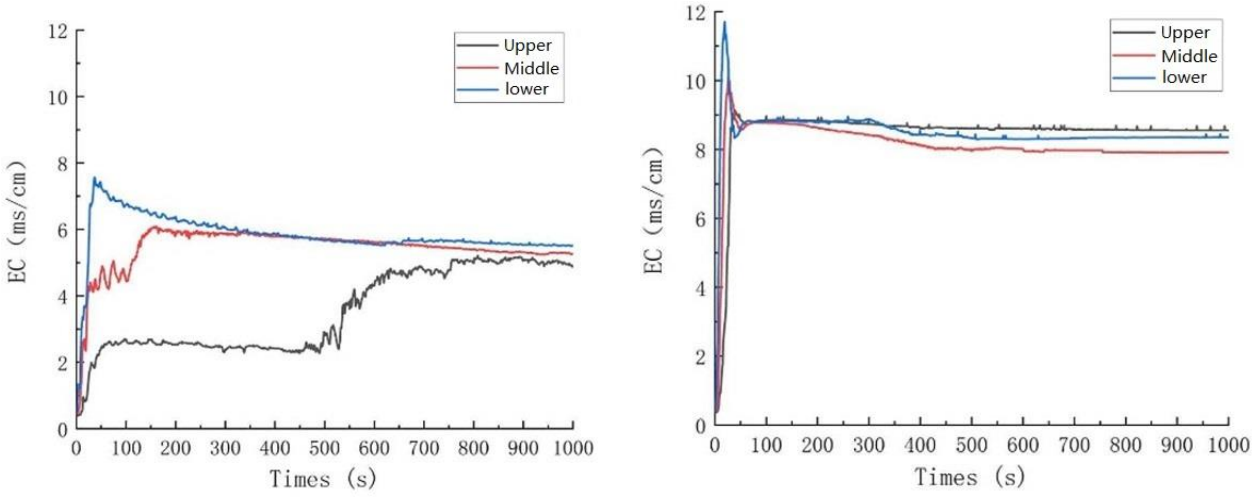

a) Circumfluence b) *Stirring* Paddle

Fig. 10 - Conductivity Graph of Powder fertilizer

In the process of dissolving and mixing, solid powder fertilizer needs to go through the process of first dissolving and then diffusion, which is lower than that of liquid fertilizer. It can be seen from the test results that the EC value of solid powder fertilizer and liquid fertilizer in the mixing process of solid powder fertilizer and liquid fertilizer in the reflux mode is similar, the bottom EC value increases the most rapidly, the top EC value increases the slowest, and finally the EC of the three positions reaches the same value when it is stable. In the stirring paddle mode, the EC values of fertilizer liquid in the upper, middle and lower positions of the fertilizer barrel increased rapidly, and quickly converged. Compared with the test data of reflux mode and stirring paddle mode, it was found that the EC value of fertilizer liquid in the fertilizer barrel was stable at about 5.50 mS/cm in the reflux mode, and the EC value of fertilizer liquid in the fertilizer barrel in the stirring paddle mode was stable at about 8.60 mS/cm.

Solid granular fertilizer mixing test

The compound potassium fertilizer with white spherical particles was selected as the test material, and according to the fertilizer application guidance method, 150 L of water needed 1.3 kg of fertilizer for dissolution and dilution. Before the test, 13g of test granular fertilizer was dissolved in 1.5 L of clean water, and the EC of the solution was stable at about 8.20 mS/cm after manual stirring. The mixing test of mixing paddle mode and "stirring paddle + two-way reflux" mode were carried out respectively. The "stirring paddle + two-way reflux" fertilizer mixing test changes the reflow direction every 10 s. During the test, take 1.3 kg of compound potassium fertilizer and add it to a fertilizer barrel filled with 150 L of clean water at a uniform rate. The sensor measures the EC value of the fertilizer liquid in real time at the upper, middle and lower positions of the fertilizer mixer barrel. Comparing the mixing characteristics of fertilizer liquid in the stirring paddle mode and the "stirring paddle + two-way reflux" mode, the test results are shown in Figure 11.

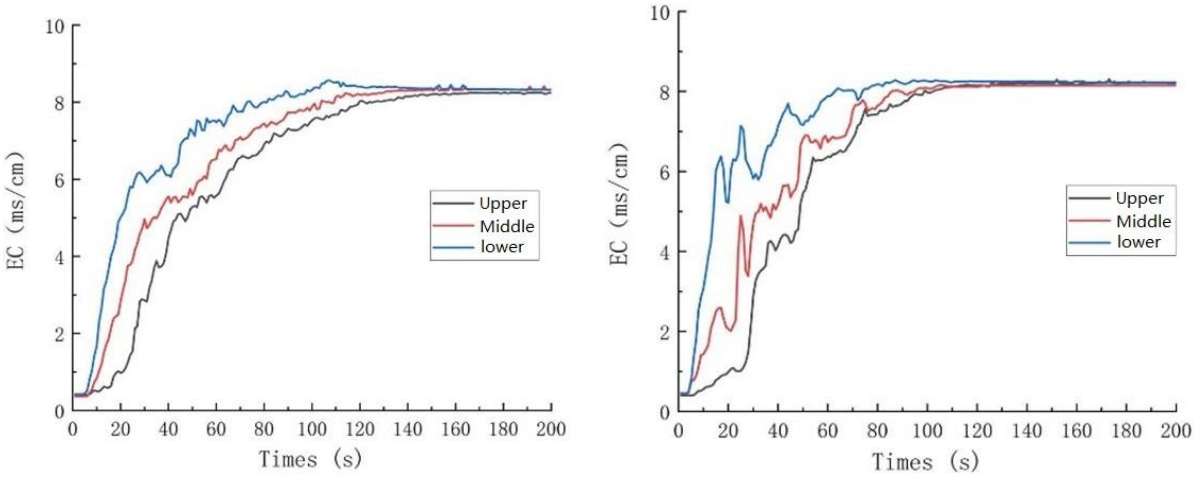

a) Stirring Paddle b) Stirring paddle + two-way reflux

Fig. 11 - Conductivity Graph of Granular fertilizer

From the analysis of the test results, after the granular fertilizer is added to the fertilizer drum, the particles are dissolved and deposited, resulting in different EC values in the upper, middle and lower positions in the fertilizer drum, the EC value of the fertilizer liquid at the bottom position is the highest, and the EC value of the fertilizer in the top position is the lowest. With the progress of the mixing operation, the EC value of the fertilizer liquid in different positions of the mixing barrel increased, and finally stabilized at about 8.20 mS/cm. In the "stirring paddle + two-way reflux" mode, every time the reflow direction is changed, the EC value curve in the corresponding figure fluctuates once, indicating that there is fertilizer accumulation at the bottom of the fertilizer barrel. Comparing the mixing curves of stirring paddle mode and "stirring paddle + two-way reflux" mode, it is found that the EC value tends to be stable at about 150 s in the stirring paddle mode, and the EC value tends to be stable at about 105 s in the "stirring paddle + two-way reflux" mode.

Experimental analysis

The experiment shows that the EC value of the liquid-type fertilizer in reflux mixing mode was stable at approximately 6.60 mS/cm when the liquid reflux speed was set at 0.4 m/s, which is close to the calibrated value of 6.80 mS/cm. The results demonstrate that the reflux mixing achieves the desired fertilizer mixing effect. It only requires the original pump for power and does not require the activation of other functional modules, resulting in low energy consumption costs.

Solid powder-type fertilizer in reflux mode and stirring paddle mode, the liquid reflux speed was set to 0.4 m/s and the stirring paddle speed to 2.5 rad/s. When the calibration value is 8.70 mS/cm, the EC value is stable at around 5.50 mS/cm and 8.60 mS/cm respectively. The test results show that the solid powder fertilizer is more difficult to dissolve than a liquid fertilizer, and it is difficult to achieve the ideal fertilizer mixing effect in reflux mode. While using the stirring paddle mode for fertilizer mixing, the axial and radial liquid velocity formed by the stirring paddle can quickly make the fertilizer liquid converge to a uniform state.

Solid granular fertilizers in stirring paddle mode and "stirring paddle + two-way reflux" mode, the liquid reflux speed was set at 0.4 m/s and the stirring paddle speed at 2.5 rad/s. When the EC calibration value was 8.20 mS/cm, it was stabilized around the calibration value after 150 s and 105 s respectively.

The test results showed that solid granular fertilizers are the most difficult to dissolve, due to their special spherical structure, the mixing process needs to destroy their spherical physical properties before mixing the concentration uniformity of the whole liquid area. A single mixing paddle works to achieve the fertilizer mixing requirements, but the mixing time is long. When using the "stirring paddle + two-way reflux" mode, radial high-intensity mixing is carried out first in the "stirring paddle + reverse reflux" mode.

The use of jets between positive and negative vortices causes the particles to collide with the barrel walls or paddles, thus destroying the spherical shape of the particles. The mixing is then carried out in the axial direction through the "stirring paddle + co-directional reflux" mode so that the concentration of the fertilizer in the drum tends to be homogenized. Alternating between reverse and co-directional modes can effectively solve the problem of low dissolution efficiency and uneven mixing of solid granular-type fertilizers.

CONCLUSIONS

This article presents a hybrid fertilizer mixing device that combines pressure relief reflux with mechanical agitation. The contributions of this device are mainly reflected in three aspects.

(1) The structure and working principle of the entire machine are determined, and three mixing modes of the fertilizer mixing device are designed and explained.

(2) A numerical simulation analysis was conducted to investigate the flow field characteristics and mechanical attributes of the fertilizer mixing process. The findings suggest that the direction of reflux has a notable influence on the efficiency of the fertilizer mixing process. Specifically, employing the “stirring paddle + same direction return” mode enhances the overall convection of the liquid, resulting in improved fertilizer-liquid mixing efficiency. On the other hand, employing the “Stirring Paddle + Reverse Reflux” mode facilitates the dissolution of sedimentary solution or particles by directing them to enter around the stirring paddle.

(3) A mixture of three forms of fertilizer was tested using a development prototype. The experimental results indicate that the reflux mode is suitable for liquid-type fertilizers which are fast dissolving and easy to diffuse, and its EC value is stable at about 6.60 mS/cm, which is close to the calibrated value of 6.80 mS/cm. The stirring paddle mode compensates for the reflux mode's weak mixing effect, making it suitable for solid powder-type fertilizers' mixing operation. The EC value remains stable at approximately 8.60 mS/cm when calibrated at 8.70 mS/cm. The” stirring paddle + two-way reflux” mode demonstrates the most robust mixing effect and is suitable for mixing solid granular fertilizers. When calibrated at 8.20 mS/cm, it stabilizes at approximately the calibration value after 105 s.

ACKNOWLEDGEMENT

This work was supported by the Major Science and Technology Innovation Project of Shandong Province (2022CXGC020708); Shandong Vegetable Industry Technology System Project (SDAIT-05-11); Major agricultural application technology innovation project in Shandong Province.

REFERENCES

[1] Banu, J. P., Mani, A., (2019). Numerical studies on ejector with swirl generator, *International Journal of Thermal Sciences*, Vol.137, pp. 589-600.

[2] Chen, F., Zhao, C., Zheng, W., Shen, C., (2010). Design and application of automatic controller for agricultural water-saving irrigation based on PLCC technology (基于 PLC 技术的农业节水灌溉自动控制器的设计与应用). *Water-saving Irrigation*, Vol.2, pp. 13-16.

[3] Ferrari, C., Beccati, N., (2022). Mixing Phase Study of a Concrete Truck Mixer via CFD Multiphase Approach, *Journal of Engineering Mechanics*, Vol.148.

[4] Garcia, M. M., Cabral, S. R., Zuniga, R. P., et al., (2023). Automatic Equipment to Increase Sustainability in Agricultural Fertilization, *Agriculture-Basel*, Vol.13, pp. 17.

[5] Gyurik, L., Ulbert, Z., Molnar, B., et al., (2020). CFD Based Nozzle Design for a Multijet Mixer, *Chemical Engineering and Processing-Process Intensification*, Vol.157.

[6] Kapoor, R., Kumar, A., Sandal, S. K., et al., (2022). Water and nutrient economy in vegetable crops through drip fertigation and mulching techniques: a review, *Journal of Plant Nutrition*, Vol.45, pp. 2389-2403.

[7] Li, J., Hong, T., Feng, R., et al, (2012). Design and experiment of Venturi variable fertilization device based on pulse width modulation (基于脉宽调制的文丘里变量施肥装置设计与试验) *Transactions of the CSAE*, Vol.28, pp. 105-110.

[8] Li, Z., Teng, G., Jiang, J., Ma, L., (2006). Design of irrigation controller based on embedded Web Server (基于嵌入式 Web Server 灌溉控制器的设计). *China Rural Water Resources and Hydropower*, Vol.9, pp. 1-3.

[9] Liu, L., Li, Y., Yang, K., et al. (2019) Design and test of field-type mobile precision fertilizer and irrigation and fertilization integrated machine (大田移动式精量配肥灌溉施肥一体机设计与试验). *Transactions of the CSAM*, Vol.50, pp. 124－133.

[10] Liu, N., Jiang, X., Cheng, J., et al, (2018). Current situation of foreign organic greenhouse horticulture and its inspiration for sustainable development of Chinese protected agriculture (国外有机设施园艺现状及对中国设施农业可). *Transactions of the CSAE*, Vol.34, pp. 1-9.

[11] Liu, Y., Shen, M., et al. (2015). Structure optimization of suction device and performance test of integrated water and fertilizer fertigation machine (水肥一体化灌溉施肥机吸肥器结构优化与性能试验). *Transactions of the Chinese Society for Agricultural Machinery*, Vol.46, pp. 76-81.

[12] Murthy, Y. R., Bhaskar, K. U., (2012). Parametric CFD studies on hydrocyclone, *Powder Technology*, Vol.230, pp. 36-47.

[13] Singh, J., Sandal, S. K., Yousuf, A., et al., (2023). Effect of Drip Irrigation and Fertigation on Soil Water Dynamics and Productivity of Greenhouse Tomatoes, *Water*, Vol.15.

[14] Song Yuepeng, Zhang Shuai, Li Tianhua, et al. (2018), Design and Numerical Simulation Analysis of Orchard Fertilizer Mixer (果园混肥器设计与数值模拟分析). *Transactions of the Chinese Society for Agricultural Machinery*, Vol.49, pp. 181-188.

[15] Sonnenwald, F., Guymer, I., Stovin, V., (2019). A CFD-Based Mixing Model for Vegetated Flows, *Water Resources Research*, Vol.55, pp. 2322-2347.

[16] Wang, Y., Deng, B., Zhang, L., (2016). Present situation and development prospect analysis of fertilizer distributor in fertigation system (施肥机在水肥一体化系统中的研究现状及发展 前景分析). *Journal of Irrigation and Drainage*, Vol.35, pp. 34-36.

[17] Xia, J., Liu, X., Li, M., et al. (2018). Analysis of the Stirred Reactor's Flow Distribution Based on CFD and the Optimization Design of the Stirred Reactor Simulation (基于 cfd 模拟的搅拌反应釜流场分析及优化设计). *Journal of NanJing Normal University (Engineering and Technology Edition),* Vol.18, pp. 87-92.

[18] Yin, P., Deng, Y., Dai W., et al. (2018). Numerical simulation of the mixing efficiency of water and fertilizer solution in fertigation (水肥一体化中水肥混合效果数值模拟研究). *Journal of China Agricultural University*, Vol.23, pp. 122-130.

[19] Zhang, C., (2011). Modern irrigation agriculture in Israel (以色列的现代灌溉农业). China Agricultural Means of Production, Vol.9, pp. 53.

[20] Zhang, Z., Li, H., Cheng C., et al. (2019). Experimental study on fertilization performance of water fertilizer integrated device of dissolution and mixed application (溶解混施水肥一体化装置施肥性能试验研究). *Journal of drainage and irrigation machinery engineering*, Vol.36, pp.1115－1119.

DEM COMPUTATIONAL SIMULATION OF THE POLISHING OF THE TAGUA (PHYTELEPHAS AEQUATORIALIS) PALM NUTS
/
SIMULACIÓN COMPUTACIONAL EN MED DEL PULIDO DE LAS NUECES DE PALMA DE TAGUA (PHYTELEPHAS AEQUATORIALIS)

Carlos MONTES-RODRÍGUEZ[1*)], Miguel HERRERA-SUÁREZ[2)], María LÓPEZ-ZAMORA[3)], Julio PÉREZ-GUERRERO[2)], Roberto TORRES-RODRÍGUEZ[2)]

[1)] Technical University of Manabi, Institute of Admission and Leveling, Department of Career Leveling / Ecuador;
[2)] Technical University of Manabi, Faculty of Mathematical, Physical and Chemical Sciences, Department of Mechanics / Ecuador;
[3)] Educational Unit Paulo Emilio Macías, Department of Mathematics and Statistics / Ecuador
Tel: +593 959086234; E-mail: carlos.montes@utm.edu.ec
DOI: https://doi.org/10.35633/inmateh-70-29

Keywords: *tagua, coefficient of friction, angle of repose, particle collision, discrete element method*

ABSTRACT

For tagua, the quality of the polishing process is analyzed according to the surface finish of the material, which is obtained manually or through empirically developed machinery that does not include the study of the behavior of the material during the process, which generates an inefficient work. The objective of the work is to determine the macro structural properties of tagua nuts to simulate polishing using the discrete element method. Virtual models were developed and the corresponding physical and mechanical properties were assigned. Among the main results, a tagua nut model was achieved, with m=30.22 g and ρ=1327.3±11.23 kg/m^3, friction coefficient for wood of μ_e = 0.411±0.0006 and angle of repose of β=24.644^o±0.201^o. These properties are the variables used as input data for the DEM model. Finally, the suitability of the Hertz-Mindlin model to simulate the process of mechanized polishing of tagua nuts is demonstrated.

RESUMEN

Para la tagua, la calidad del proceso de pulido se analiza en función del acabado superficial del material, el cual se obtiene manualmente o a través de maquinaria desarrollada empíricamente que no incluye el estudio del comportamiento del material durante el proceso, lo que genera un trabajo ineficiente. El objetivo del trabajo es determinar las propiedades macro estructurales de las nueces de tagua para simular el pulido mediante el método de elementos discretos. Se elaboraron los modelos virtuales y se asignaron las propiedades físicas y mecánicas correspondientes. Entre los principales resultados, se logró un modelo de nuez de tagua, con m=30.22 g y ρ=1327.3±11.23 kg/m^3, coeficiente de fricción para la madera de μ_e = 0.411±0.0006 y ángulo de reposo de β=24.644^o±0.201^o. Estas propiedades son las variables utilizadas como datos de entrada para el modelo MED. Finalmente, se demuestra la idoneidad del modelo Hertz-Mindlin para simular el proceso de pulido mecanizado de nueces de tagua.

INTRODUCTION

Tagua is a product obtained from Phytelephas aequatorialis palms, which grow in the humid forests of Ecuador, Colombia, Peru, Panama, among others. The nuts are composed of a white endosperm, as they are exposed to the sun, this hardens and through polishing a product visually similar to ivory is obtained, so it is also called with the name of vegetable ivory *(Pánchez et al., 2017*).

This material is transformed by artisans (micro-entrepreneurs who make handicrafts) into buttons, figures, key chains, ornaments, among others (*Torres et al., 2019; Vélez, et al., 2018)*. To obtain the tagua nuts, the cluster of nuts is subjected to natural drying by solar radiation, during an interval of 35 to 40 days, this time allows to obtain a hardening or maturation of the nuts, generating the vegetable ivory. With smaller time intervals, tagua nuts are obtained crystalline or hollow inside, which generates considerable economic losses to the artisans. *(Vélez et al., 2018*). The previous processes for the polishing of tagua nut, can be enunciated in, drying, classification, cutting or turning and binding.

Polishing is a very laborious task, especially when it is done manually, which is why the more resourceful producers have empirically developed machines to carry out this task. The design and construction of these machines have not taken into account the characteristics or properties of the material to be processed, which causes the accumulation of material on the walls of the polishing machines, prolonged work time, energy costs and consequently a decrease in the quality of the polished tagua nuts.

With the development of computational means, the application of numerical methods has allowed the solution of problems related to the agricultural sector *(Espinosa, 2017; Marín Cabrera and García de la Figal Costales, 2019; Velloso et al., 2018*).

Within these methods, the discrete element method (DEM) is (*Maamer et al., 2019*) seen as one of the most promising ones, since it has made possible the study of granular materials subjected to different processes in the agricultural sector, such as cutting, mixing, packaging, and transportation, among others *(Ghodki and Goswami, 2017; Romuli et al., 2017; Scheffler et al., 2018*). The increase in computational capabilities over the last decade has increasingly broadened the scope of this method, as fluid-coupled or thermodynamic (CFD) models have begun to be introduced, as well as solid and particle DEM and FEM problems *(Ambaw et al., 2017; Du et al., 2019; Gao et al., 2018*).

During the strength analysis of a given material using the discrete element method, the properties and parameters that define its strength at the microstructure level, which are closely related to the material's macrostructure properties, are taken as input variables (*Roselló et al., 2016*). The properties to be used will depend on the model describing the characteristics of the material to be simulated and the contact *(Araújo et al., 2015; Jiménez et al., 2018*).

The formulation of a discrete element model requires the prior definition of the models of the materials to be simulated, as well as the particle-particle or particle-geometry contact models *(Cundall and Strack, 1979*). The Hertz-Mindlin (no-slip) contact model assumes that during collisions between particles or particle-geometry a no-slip friction arises in the tangential direction which is governed by the Coulomb creep criterion $F_y \leq \mu_p F_n$. This property at the micro level is related to the angle of repose, properties that define the frictional behavior of the material at the macrostructure level.

In this model, the contact between particles at the microstructure level will be governed by the stiffness of the particles in tangential stiffness (k_s) and normal stiffness (k_n), variables that are related to the elasticity of the material at the macrostructure level, which is quantified through Young's modulus (E) and Poisson's coefficient (υ). The shear modulus (G) allows relating both variables.

Finally, the Hertz-Mindlin contact model understands that during the tangential contact between both particles at the micro level there is a damping (ξ_n) that characterizes the degree of conservation of kinetic energy in a collision between particles. The damping constant is related to the critical damping coefficient (β) and the coefficient of restitution (e), parameters that can be determined directly at the macrostructure level.

Namely, the properties and parameters included in the Hertz-Mindlin contact model have not been investigated so far, so the present work aims to determine the macro structural properties of tagua nuts, required for the simulation of the polishing process using the discrete element method *(Maamer et al., 2019*).

MATERIALS AND METHODS

The experimental investigations were carried out in the Physics laboratory of the Institute of Basic Sciences (ICB) of the Technical University of Manabí. For the determination of the macrostructural properties of tagua nuts, initially the sample size was determined, for which 30 experiments were conducted with three replicates each. The selection of tagua nuts is done randomly from a cluster of tagua nuts (Figure 1).

Fig. 1 - Set of tagua nuts after the sanding process

With the data from the analysis of descriptive statistics of the properties, the confidence interval is calculated for 95% for the density of the material, according to equation 1, we have:

$$\vartheta = \bar{X} \mp Z_{\alpha/2} \frac{\sigma}{\sqrt{n}} \quad (1)$$

where:

$\bar{X}$ - is the average;
$Z_{\alpha/2}$ - confidence level;
n - the sample;
σ - standard deviation;
$\vartheta =$ range of values.

Methodology to determine the macrostructural properties of tagua nuts (Phytelephas aequatorialis):
Length (l) *and equatorial diameter* (d)

Measurements were made with a WEZU brand caliper of 250 mm±0.05 mm of error, the length comprised the distance between the farthest ends of the nut (Figure 2a), as for the equatorial diameter is considered the width of the nut, (Figure 2b).

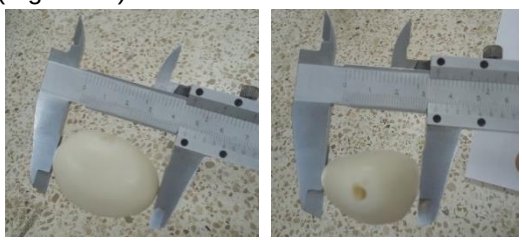

Fig. 2 - Length (a) and equatorial diameter (b)

Mass (m) *and volume* (v)

A precision balance AE ADAM CQT601 of 600g±0.1g of error is used, which has a digital indicator to show the weight (Figure 3a). For the volume, a measuring cylinder with a measurement in cm^3 is used; the value of this variable is obtained by means of the difference in volume that occurs when the tagua nut is submerged in a known volume of water (Figure 3b). With the collection of mass and volume data, the real average density of the sample can be known.

Fig. 3 - Nut mass (a) and volume (b)

The actual density of a material is denoted by the following equation:

$$\rho = \frac{m}{v} \tag{2}$$

where:

ρ - density, [kg/m^3];
m - mass of the particle, [kg];
v - volume of particle, [m^3].

Mechanical properties:
Static friction coefficient (μ_e)

It was determined using the inclined plane method, the instrument used has a scale to measure the angle of inclination, and three sliding surfaces were used: wood, stainless steel and aluminum (Figure 4).

Fig. 4 - Inclined plane for the determination of static friction angles

A particle is placed on the sliding surface of the plane and the angle of inclination is varied progressively, until displacement is caused, by increasing the weight component $(m \cdot g \cdot sen\,\theta)$. Since a system of equations is generated when a particle or body slides along an inclined plane and the same starts from rest, the static coefficient of friction can be determined by:

$$\mu_e = tan(\theta) \quad (3)$$

where:

$\mu_e =$ is the static coefficient of friction, [dimensionless];

$\theta =$ angle of inclination, [°].

Angle of repose (β)

A rectangular surface base is used and a container filled with tagua material resting on the base, the container is removed in an ascending manner so that the nuts form a conglomerate in the center, with a tape measure the height of the material as a whole is indicated (Figure 5). The measurement of this variable is made by means of the trigonometric tangent function, taking the data of the right triangle that is formed (height and base). A total of 435 elements (nuts) are used for the measurement.

Fig. 5 - Measurement of the angle of repose of tagua nuts

Restitution coefficient

When a body is dropped from a known height, it collides with a surface (wood), being possible to determine the value of the coefficient of restitution by knowing the height it reaches after the first rebound (Pavioni and Ortega, 2015; Peña, 2015; Pérez et al., 2017). Considering that, in an inelastic shock, the initial height will be greater than the height after rebound. The coefficient of restitution is established as the quotient between the heights, then:

$$C_r = \left(\frac{h_1}{h_o}\right)^{\frac{1}{2}} \quad (4)$$

where:

h_1 - is the maximum height after rebound, [m];

h_o - is the initial height, [m];

C_r - coefficient of restitution, [dimensionless].

By means of a sequence of photographs, the height (h_1) reached by the particle after hitting the surface, which is dropped from a known height (h_o), is recorded. This procedure is carried out with different tagua nut particles in order to obtain a more accurate measurement.

Methodology for MED simulation of tagua nut polishing.

Computational tool.

The computer has an Intel® Core (TM) i7-8550 CPU @ 1.80GHz 1.99GHz, 32 GB RAM, 64-bit operating system, x64 processor and a video graphics card with dedicated memory of 4096 MB GDDR5. EDEM® Academic software was used, which has a virtual simulation environment based on the discrete element method, allowing the design or import of complex geometries, assigning properties to materials and linear or rotational dynamics to each of the geometries (*Yuan et al., 2016*).

Particle generation

The tagua nuts have an irregular ovoid shape. The creation of the virtual model is performed using the multi-sphere method with the Creator component of the EDEM® Academic software, these spheres are arranged in a row one behind the other, allowing interference or overlapping up to one third of their volume (Figure 6).

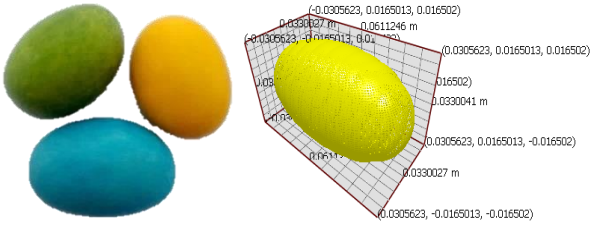

Fig. 6 - Virtual model of the tagua nut particle

The polishing material, consisting of small elements of balsa wood (Ochroma Pyramidale), its main function is to eliminate the roughness of the surfaces of the tagua, they are also used as a means of transport for polishing creams. For the creation of the virtual models of this material, the online multi-sphere creation option is used (Figure 7).

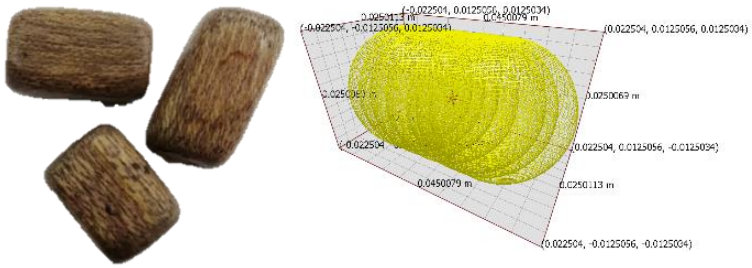

Fig. 7 - Virtual model of the raft

A two-dimensional geometric figure resides inside the rotating vessel and has the function of generating the tagua and balsa particles according to the designed virtual models, the parameters such as, aggregate velocity, generation range and so on for both materials are detailed below (Table 1).

Table 1

Particle generation data.

Name	Tagua factory	Raft factory
Type	Dynamic	Dynamics
Dimensions	0.2 m x 0.6 m	0.2 m x 0.6 m
Total or mass of particles	400	25 kg
Generation range	125 particles·second^{-1}	6.25 kilogram·second^{-1}
Position	Random	Random
Velocity	Direction -y, -1m·s^{-1}	Direction -y, -1m·s^{-1}

Geometry generation

As a reference, the handmade machines for the polishing process are used (Figure 8). The geometry consists of a rotary drum built from oak wood. The length, thickness and type of material were used to elaborate the virtual model and imported in ".x_t" format for the EDEM® Academic software. The developed model considers an octagonal vessel, this characteristic in its geometry allows maximizing the interaction between the tagua nut particles optimizing the process. The design material for the vessel is oak wood (Quercus rubra) with a density of 710 kg·m^{-3} at 12% humidity.

Fig. 8 - Handmade tagua polishing machine with its virtual drum model

Border conditions

A total of 400 tagua units and 25 kg of polishing material are generated (Figure 9). Free movement is allowed for the particles within the geometry. In addition, a rotational kinematics is added to the geometry that simulates the mechanical energy delivered by an electric motor, which starts once the particle generation is finished. The generated particles can rotate and displace due to the impulsion of the polishing drum faces or by free fall due to the action of the force of gravity. The geometry rotates at a rate of 60 revolutions per minute.

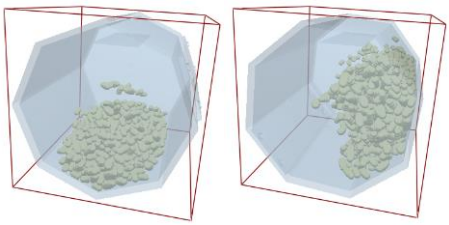

Fig. 9 - Initial particle generation and rotational motion

RESULTS

Physical properties

The results of the experimental determination of the properties are shown as the main variables that characterize the physical structure of the tagua nuts. Table 2 shows the most relevant descriptive statistics.

Table 2

Descriptive statistics of the physical structure of the Tagua nut.

Variable	Unit	Mean	E.E. of mean	Std. Dev.	Variance	Coeff. Var.	Minimum	Maximum
l	mm	39.767	0.446	2.445	5.978	6.15	36.000	46.000
d	mm	31.867	0.400	2.193	4.809	6.88	29.000	39.000
m	g	25.690	0.369	2.020	4.080	7.86	21.600	30.900
v	cm^3	19.353	0.265	1.451	2.106	7.49	16.500	22.500
ρ	kg/m^3	1327.164	5.730	31.390	985.777	2.36	1289.220	1396.980

Equatorial length and diameter

For the tagua nuts, the average length is $l = 39.77 \pm 0.45$ mm, with a deviation of 2.45 mm, this statistic assures that the data collected for the length variable does not show great dispersion. With respect to the equatorial diameter, the mean of the variable corresponds to $d = 31.87 \pm 0.37$ mm. The range for both variables is 1 cm.

Mass y volume

The sample has a mean of m=25.69±0.37g, and the deviation is 2.02 g due to the variations in length and width, and a range of 9.30 g is also obtained. The volume variable presents a deviation with a value of 1.45 cm^3 with respect to the average of $v = 19.35 \pm 0.27$ cm^3 and the range is 6 cm^3.

Actual density

A mean for the density of $\rho = 1327.3 \pm 5.73$ kg/m^3 is obtained, the value for the deviation is justified due to the chemical composition (percentage of water retained) and physical characteristics (dimensions) of the tagua nut. When estimating the mean of the variable with a reliability percentage of 95%, a confidence interval of $\rho = 1327.3 \pm 11.23$ kg/m^3 is obtained. The density value is assigned to the tagua particle material and as a result the mass of the tagua particle is obtained as a function of the volume of the model (Figure 10).

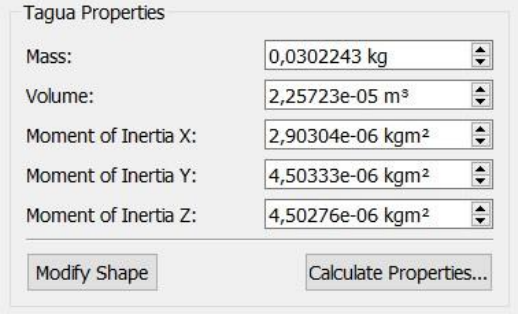

Fig. 10 - Mass and volume of the processed particle

As we can see, the mass and volume of the tagua nut particle are within the range of values of the descriptive statistics calculated for both variables.

Mechanical properties

These values show the behavior of the particles as they interact with each other or with the geometry used as a rotating vessel (Table 4).

Table 4

Descriptive statistics of the mechanical properties of tagua nuts.

Variable	Mean	E.E. of mean	Std. Dev.	Variance	Coeff. Var.	Minimum	Maximum
μ_e, steel	0.314	0.005	0.027	0.00073	8.59	0.26790	0.36400
μ_e, wood	0.411	0.006	0.035	0.00122	8.51	0.36400	0.48770
μ_e, stainless steel	0.401	0.006	0.031	0.00097	7.77	0.32490	0.46630
β	24.644	0.201	1.100	1.21000	4.46	21.73000	26.74000
C_r	0.064	0.001	0.007	0.00005	11.33	0.04800	0.07300

Coefficient of friction

In wood, the highest friction coefficient is determined, with an average of μ_e = 0.411±0.006. When evaluating the stainless-steel surface, averages of μ_e =0.401±0.006 are obtained and for steel, it is observed that sliding can be obtained with a lower amount of force, the friction coefficient on this surface is μ_e=0.314±0.005. The deviations of the data in this variable take small values. The range for stainless steel is 0.1414, wood 0.1237 and for steel 0.0961.

Angle of repose

Angle of repose. The average maximum angle of the conglomerate of the particles studied in a horizontal plane is β =24.644°±0.201° the deviation of the data is 1.1°, while the range is 5.01°. This property is considered of relevance for the design of machinery involving mass flow of material, such as conveying and storage.

Restitution coefficient

The shock that occurs between the tagua nut and a non-deformable surface, is an inelastic shock, since its value is between $0 \leq C_r < 1$, the average of this variable takes values of C_r = 0.064±0.001, this value denoted in an approximation is C_r =0.1 which is close to be considered as a perfectly inelastic shock, the deviation of the data of the coefficient of restitution does not exceed 0.007 and its range is only 0.025.

Discrete element method simulation

Kinetic energy

The kinetic energy of the tagua particles depends largely on the work done by the drum, when analyzing the graph (Figure 11), in the instant t =4s it is observed that the maximum angle of rest of the conglomerate is overcome producing significant material avalanches which registers high magnitudes of kinetic energy, progressively from the instant t =10.5s the particles share a collective rotation and the times between avalanches are reduced until establishing a continuous surface flow, the equilibrium of this state comprises energy values within the range of (6.8 to 8.5)J.

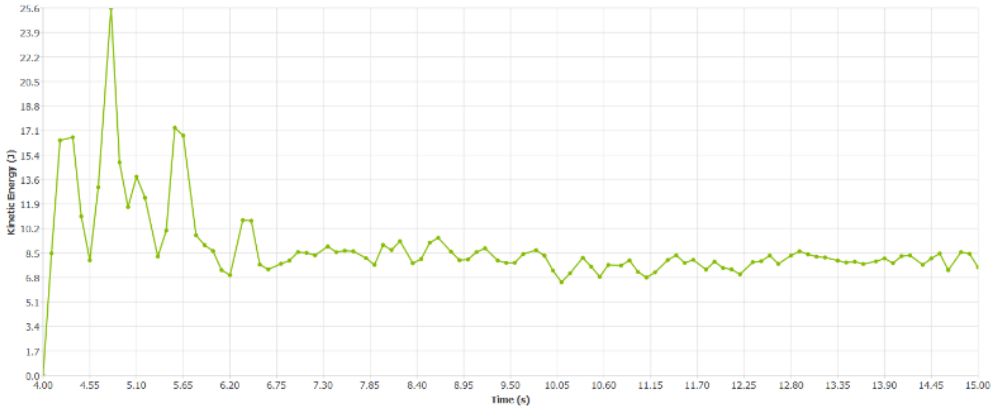

Fig. 11 - Kinetic energy of the tagua particle

Potential energy

Initially, the potential energy grows instantaneously as a result of the impulse given by the drum during the start-up stage where, in order to overcome the inertial forces (Figure 12), part of this energy is transformed into kinematic energy due to the working conditions of the vessel. In addition, during the rotation of the drum, the particles at the upper ends have higher potential energy than those at the lower ends.

The energy values when the flow is in equilibrium are in the range of (-26.2 to -29.7) J. The negative value indicates that the particles interact with the geometry surface, changing position with respect to the control level, in a correct mixing.

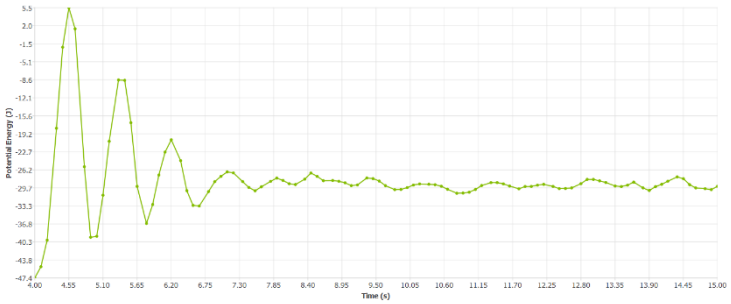

Fig. 12 - Potential energy of the tagua particle

Particle velocity

The variation of the drum speed modifies the flow of the particles inside the vessel, from this it is possible to obtain flow regimes such as sliding, cascade, waterfall and centrifugation *(Lima, 2017; Uribe et al., 2015; Yang et al., 2003*).

A high working speed generates that the particles remain adhered to the internal surface of the drum by the action of the inertia force, making the polishing process impossible, since there are not enough interactions, being determined as a centrifugation regime. For low velocities there is a greater number of collisions between particles and geometry, resulting in a smooth surface of the tagua nut and a particular brightness.

With the simulation of the discrete element method, frequent velocity levels are observed for the particles, it is possible to denote that the particles that are farther away from the center of the conglomerate move with higher velocities than the particles that are in the center, this is because several particles are in direct contact with the wall of the container that gives them a certain amount of movement, they in turn transmit movement to the others that are near the center of the rotation (Figure 13).

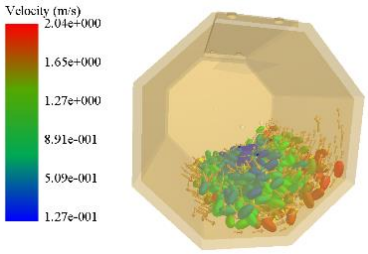

Fig. 13 - Particle velocity within the geometry

The red particles, moving at a velocity of 2.04 m/s, reside mainly on the outside of the conglomerate in direct contact with the vessel. The green particles move at a rate of 1.27 m/s, they are mainly dispersed in the center of the conglomerate, and finally we have the blue particles with velocities of 0.509 m/s, which reside in the center. The particle velocities vary over time, but remain within the values shown. The average velocity of the tagua particle when the flow is kept constant is in the range of (0.749 to 0.842) m/s (Figure 14).

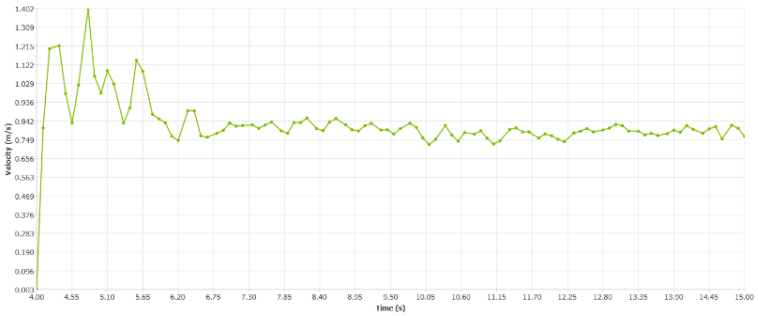

Fig. 14 - Average tagua particle velocity

CONCLUSIONS

The physical properties determined serve as a reference to generate a virtual model of the tagua particle, considering important aspects such as size and average shape to obtain the real density of the material, these variables in conjunction with the mechanical properties allow assigning to the material behavioral characteristics within the polishing process and effects on the geometry or the particles involved, besides becoming relevant parameters to determine the limits of the rotational speed of the vessel.

The simplified Hertz-Mindlin model properly describes the behavior of tagua nuts, being of great utility for the study of the efficiency of the polishing process. The developed model can be used to study the behavior of particles of different geometries of the same material that are currently marketed nationally and exported as tagua handicrafts and adjust the operating parameters of the rotary machines according to this behavior.

The virtual model of the tagua particle shows similarity with the real particle when comparing the values of mass and volume, whose values barely differ by 14.99% and 14.26% respectively for a 95% of reliability and the error for the stated values is not higher than 0.37. This allows to guarantee that the simulated behavior of the interactions between the particles and the container will have a great coincidence with the real behavior.

The properties determined allow simulating the interaction process between the tagua particles, tagua-balsa and both elements with the polishing drum, managing to compute the contacts, energy consumption and particle trajectories, showing results consistent with those described during the processing of this and other agricultural materials.

REFERENCES

[1] Ambaw, A., Dekeyser, D., Vanwalleghem, T., Van Hemelrijck, W., Nuyttens, D., Delele, M., Ramon, H., Nicolai, B., Bylemans, D., Opara, U., Verboven, P. (2017). Experimental and numerical analysis of the spray application on apple fruit in a bin for postharvest treatments. *Journal of Food Engineering, 202*, 34-45. https://doi.org/10.1016/j.jfoodeng.2017.01.026

[2] Araújo, B., Francisquetti, M., Barrozo, M., & Santos, K. (2015). Simulação dem do empacotamento de sementes de acerola. *Blucher Chemical Engineering Proceedings, 1*(3), 2505-2510.

[3] Cundall, P. A., & Strack, O. D. (1979). A discrete numerical model for granular assemblies. *Geotechnique, 29*(1), 47-65. https://doi.org/10.1680/geot.1979.29.1.47

[4] de Lima, R. F. a., Khatchatourian, O., Binelo, M. O. r., Faoro, V., Antoniazzi, R. L., Balbinot, E. J. P. S. o. t. B. S. o. C., & Mathematics, A. (2017). Validação do Método dos Elementos Discretos para o escoamento de grãos de soja. *Proceeding Series of the Brazilian Society of Computational Applied Mathematics, 5*(1). https://doi.org/10.5540/03.2017.005.01.0409

[5] Du, D., Wang, B., Wang, J., Yao, F., & Hong, X. (2019). Prediction of bruise susceptibility of harvested kiwifruit (Actinidia chinensis) using finite element method. *Postharvest biology technology, 152*, 36-44. https://doi.org/10.1016/j.postharvbio.2019.02.013

[6] Espinosa, B. G. G. (2017). Determinación de modos y frecuencias de vibración para la cosecha del mango variedad Manila. *Revista Ingeniería Agrícola, 5*(2), 29-33.

[7] Gao, Y., Song, C., Rao, X., & Ying, Y. (2018). Image processing-aided FEA for monitoring dynamic response of potato tubers to impact loading. *Computers Electronics in Agriculture, 151*, 21-30. https://doi.org/10.1016/j.compag.2018.05.027

[8] Ghodki, B. M., & Goswami, T. (2017). DEM simulation of flow of black pepper seeds in cryogenic grinding system. *Journal of Food Engineering, 196*, 36-51. https://doi.org/10.1016/j.jfoodeng.2016.09.026

[9] Jiménez, N., Barrios, G. K., & Tavares, L. M. (2018). Comparison of breakage models in DEM in simulating impact on particle beds. *Advanced Powder Technology, 29*(3), 692-706. https://doi.org/10.1016/j.apt.2017.12.006

[10] Maamer, B., Boughamoura, A., El-Bab, A. M. F., Francis, L. A., & Tounsi, F. (2019). A review on design improvements and techniques for mechanical energy harvesting using piezoelectric and electromagnetic schemes. *Energy Conversion Management, 199*, 111973. https://doi.org/10.1016/j.enconman.2019.111973

[11] Marín Cabrera, L. O., & García de la Figal Costales, A. E. (2019). Modelo de la interacción suelo herramienta de labranza estrecha utilizando el Método de Elementos Finitos. *Revista Ciencias Técnicas Agropecuarias, 28*(4).

[12] Pánchez, J. P., Vargas, J. G., Rodríguez, K. V., & Polo, I. C. (2017). Estudio para la creación del centro de procesamiento y taller artesanal para la elaboración de productos derivados del marfil vegetal (tagua), en la comuna las Núñez provincia de Santa Elena. *Revista Científica y Tecnológica UPSE, 4*(1), 7-15. https://doi.org/10.26423/rctu.v4i1.234

[13] Pavioni, O., & Ortega, F. (2015). Obteniendo los coeficientes de restitución y arrastre en un solo experimento. *Revista mexicana de física E, 61*(1), 11-16.

[14] Peña, F. (2015). Modelo simplificado para el estudio del balanceo asimétrico de cuerpos rígidos esbeltos. *Revista Internacional de Métodos Numéricos para Cálculo y Diseño en Ingeniería, 31*(1), 1-7. https://doi.org/10.1016/j.rimni.2013.10.005

[15] Pérez, C. S., Aguilera, C. Y., Hurtado, C. J., & Vargas, N. J. (2017). Modelación y simulación fluido-dinámica computacional de sistema de enfriamiento de gases para fundición de cobre mediante Convertidor Teniente con enfriador evaporativo. *Revista Internacional de Métodos Numéricos Para Cálculo y Diseño En Ingeniería, 33*(3-4), 179-187. https://doi.org/10.1016/j.rimni.2016.04.007

[16] Romuli, S., Karaj, S., & Müller, J. (2017). Discrete element method simulation of the hulling process of Jatropha curcas L. fruits. *Biosystems Engineering, 155*, 55-67. https://doi.org/10.1016/j.biosystemseng.2016.11.009

[17] Roselló, V. R. L., Pérez, M. I. P., & Díaz, G. C. H. (2016). Modelación geométrica de microestructuras granulares poliédricas. *Revista Cubana de Ciencias Informáticas, 10*, 186-194.

[18] Scheffler, O. C., Coetzee, C. J., & Opara, U. L. (2018). A discrete element model (DEM) for predicting apple damage during handling. *Biosystems Engineering, 172*, 29-48. https://doi.org/10.1016/j.biosystemseng.2018.05.015

[19] Torres, O. X., Guerrero, C., Silvana, M., Burbano, J. P., & Castro, L. G. (2019). Emprendimientos artesanales en Tagua, una alternativa de fuente de ingresos para mujeres cabeza de hogar. *Dilemas Contemporáneos: Educación, Política y Valores, 6*.

[20] Uribe, C. C., Rodríguez, M. M., Sarmiento, L. F. P., & Cañon, A. M. R. (2015). Aplicabilidad de la energía cinética en el inicio de la inestabilidad de materiales granulares en un tambor rotador mediante la técnica PIV (Particle Image Velocimetry). *Ingeniería y Región, 13*, 9-18. https://doi.org/10.25054/22161325.704

[21] Vélez, N. J. J., Doval, Y. R., & Enrique, L. E. P. (2018a). Análisis prospectivo del proceso de reconversión en la comunidad Sosote, Manabí, Ecuador. *ReHuSo: Revista de Ciencias Humanísticas y Sociales,* 126-142. https://doi.org/10.33936/rehuso.v2iESPECIAL.1252

[22] Vélez, N. J. J., Doval, Y. R., & Enrique, L. E. P. (2018b). La asociatividad para el fortalecimiento de los artesanos productores de las semillas de la tagua en la comunidad de Sosote, Manabí, Ecuador. *Universidad&Ciencia, 7*(2), 248-263.

[23] Velloso, N. S., Costa, A. L. G., Magalhães, R. R., Santos, F. L., & de Andrade, E. T. (2018). The Finite Element Method Applied to Agricultural Engineering: A review. *Current Agriculture Research Journal, 6*(3), 286-299. http://dx.doi.org/10.12944/CARJ.6.3.08

[24] Yang, R., Zou, R., & Yu, A. (2003). Microdynamic analysis of particle flow in a horizontal rotating drum. *Powder Technology, 130*(1-3), 138-146. https://doi.org/10.1016/S0032-5910(02)00257-7

[25] Yuan, J., Yao, H., Hu, Z., & Zhou, J. (2016). The new discharge hopper and EDEM simulation analysis for particles flat accumulation after free falling. International Conference on Advanced Electronic Science and Technology (AEST 2016). https://dx.doi.org/10.2991/aest-16.2016.132

OBSTACLE AVOIDANCE METHOD FOR ELECTRIC TRACTOR BASED ON IMPROVED DYNAMIC WINDOW APPROACH WITH PRIORITY OF ENERGY CONSUMPTION
/
基于能耗最优的改进动态窗口法的电动拖拉机避障方法

Huang TIANYI [1)], Florentina BADEA [2*)], Xiao MAOHUA [1*)], Zhao SHANHU [3)], Sorin-Ionut BADEA [2)], Cristian-Radu BADEA [2)]

[1)]College of Engineering, Nanjing Agricultural University, Nanjing 210031, China;
[2)]National Institute of Research-Development for Mechatronics and Measurement Technique, Bucharest, Romania;
[3)]Jiangsu Yueda Intelligent Agricultural Equipment Co. LTD, Yancheng 224100, China
Badea Florentina Tel: +40724587744.; E-mail: florentina.badea@incdmtm.ro
Maohua Xiao Tel: +86 13951756153.; E-mail: xiaomaohua@njau.edu.cn
DOI: https://doi.org/10.35633/inmateh-70-30

Keywords: *Barrier avoidance; Improve dynamic window approach; Energy consumption model; Path planning*

ABSTRACT
In order to solve the real-time obstacle avoidance problem in electric tractor operation, an improved dynamic window approach (DWA) based on optimal energy consumption is proposed for electric tractor obstacle avoidance. Firstly, energy consumption model of tractor is established based on the transmission system of electric tractor, then energy consumption evaluation sub-function is introduced to improve the evaluation function of original DWA algorithm, and finally, the trajectory is evaluated and the optimal solution of the trajectory is determined by using new evaluation function. Based on the kinematics model of YL254ET electric tractor in Yancheng Yueda, a model predictive controller is designed. The obstacle avoidance planning and tracking control of electric tractor are simulated jointly on Simulink and CarSim simulation platform. Finally, the obstacle avoidance planning test is carried out. The simulation and experimental results show that after the algorithm improvement, the energy consumption of electric tractors is reduced, the generated path is smoother, and the lateral error is smaller.

摘要
为解决电动拖拉机作业时的实时避障问题，提出一种基于能耗最优的改进动态窗口法（DWA）的电动拖拉机避障方法。首先基于电动拖拉机的传动系统建立拖拉机的能耗模型，接着引入能耗评价子函数来改进原始 DWA 算法的评价函数，最后使用新的评价函数对轨迹进行评价并确定轨迹的最优解。基于盐城悦达 YL254ET 电动拖拉机的运动学模型设计一种模型预测控制器，在 Simulink 与 CarSim 联合仿真平台上对电动拖拉机的避障规划及跟踪控制进行联合仿真，最后进行避障规划试验。仿真及试验结果表明：算法改进后电动拖拉机能耗降低，生成的路径更加平滑，横向误差更小。

INTRODUCTION
Unmanned tractors are increasingly widely used in agricultural production and have become key equipment in intelligent agricultural production (*Li et al., 2019; Hu et al., 2015; Gan-Mor et al., 2007; Kaivosoja et al., 2015*). The types of obstacles in farmland are complex, such as wells, pump houses, power poles, trees, etc. When there are obstacles in front of the unmanned tractor during operation, if the tractor does not have the function of real-time autonomous planning of obstacle avoidance paths, the obstacles will hinder the normal operation of the unmanned tractor. Therefore, obstacle avoidance path planning technology is an essential technology for unmanned tractors.

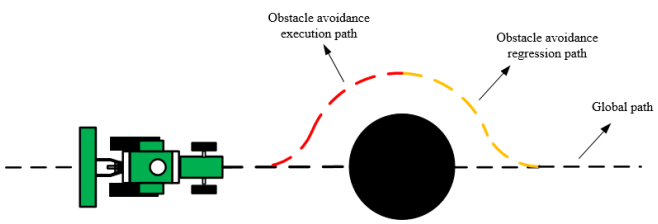

Fig. 1 - Tractor obstacle avoidance model

When an unmanned tractor encounters obstacles during operation, it is necessary to plan a collision free obstacle avoidance path. At present, some scholars have conducted research on obstacle avoidance path planning algorithms for unmanned tractors. Xi Xiaobo et al. proposed a third-order Bezier curve to smooth the obstacle avoidance path of tractors, improving the continuity between the shortest tangent path curves (*Xi et al., 2019*); Yang et al. based on Xi Xiaobo's research and improved Bezier curve, and finally got a lower curvature of obstacle avoidance path (*Yang et al., 2022*). Zhao et al. proposed an obstacle avoidance method based on the minimum capture algorithm, which enables tractors to achieve point-to-point navigation (*Xin et al., 2022*); Guo Chengyang et al. proposed a tractor obstacle avoidance method based on an improved artificial potential field method using LiDAR as a sensor, enabling the artificial potential field method to be applied to tractor obstacle avoidance (*Guo et al., 2020*); Li Guohui et al. achieved obstacle avoidance path planning for agricultural machinery by establishing a motion model and using fuzzy control algorithms (*Li et al., 2021*). Lu Xianglong et al. proposed an obstacle avoidance algorithm for orchard spray robot based on improved A * algorithm and dynamic window method (*Lu et al., 2022*).

Based on this, this paper proposes an improved DWA real-time obstacle avoidance path planning algorithm for electric tractors. Firstly, an energy consumption model for electric tractors is established, then an energy consumption evaluation subfunction to improve the evaluation function of the original DWA algorithm is introduced. Finally, a new evaluation function is used to evaluate the trajectory and determine the optimal solution. Based on the Yancheng Yueda unmanned electric tractor, a vehicle model is established. The obstacle avoidance and tracking control of the electric tractor are jointly simulated using the MTALAB and CarSim joint simulation platform, and the feasibility of path tracking is studied. Finally, a real vehicle obstacle avoidance planning experiment is conducted using the YL254ET electric tractor.

MATERIALS AND METHODS

Establishment of tractor energy consumption model

Simplify the tractor steering model to an ideal bicycle model, assuming that the two front and rear wheels of the tractor are in the same motion state. But in reality, the turning angle of the inner steering wheel is greater than that of the outer steering wheel, causing the vehicle to rotate around the midpoint between the rear wheel axles. The steering motion model is shown in Figure 2.

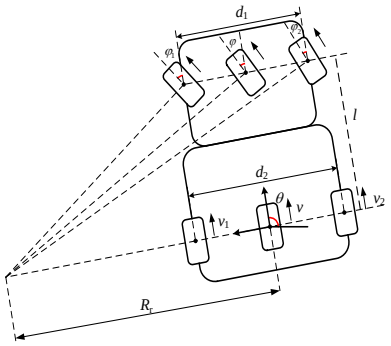

Fig. 2 - Tractor Steering Motion Model

Based on a simplified bicycle model, the tractor steering equation can be derived by considering the triangle formed by the front and rear wheelbase of the tractor l and the side R_r, and adding or subtracting the front and rear wheelbase of the tractor:

$$\begin{aligned} \dot{x} &= v\cos\theta \\ \dot{y} &= v\sin\theta \\ \dot{\theta} &= v\frac{\tan\varphi}{l} \end{aligned} \tag{1}$$

where:

v is the linear velocity of the rear wheel center point, θ is the angle between the linear velocity and the x-axis direction, and φ is the steering angle at the center point of the simulated front wheel; $\dot{x}$ is the linear velocity in the x-axis direction of the tractor motion coordinate system, $\dot{y}$ is the linear velocity in the y-axis direction, and $\dot{\theta}$ is the angular velocity.

Obtain the degree of rotation of the tractor's inner and outer steering wheels:

$$\tan\varphi = \frac{l}{R_r}$$

$$\tan\varphi_1 = \frac{l}{R_r - d_1/2} \tag{2}$$

$$\tan\varphi_2 = \frac{l}{R_r + d_1/2}$$

where:

d_1 is the front track width, φ_1 is the steering inner wheel angle, and φ_2 is the steering outer wheel angle. Obtain the angles of the inner and outer wheels as:

$$R_r = \frac{l\cos\varphi}{\sin\varphi} \tag{3}$$

$$\varphi_1 = \tan^{-1}\left(\frac{2l\sin\varphi}{2l\cos\varphi - d_1\sin\varphi}\right)$$

$$\varphi_2 = \tan^{-1}\left(\frac{2l\sin\varphi}{2l\cos\varphi + d_1\sin\varphi}\right) \tag{4}$$

where:

v_1 and v_2 are the translational velocities of the inner and outer wheels at the linear velocity of the rear wheel navigation center point, and ω is the angular velocity of the inner and outer drive wheels.

When the tractor is in motion, the angular velocity of the inner and outer rear wheels is the same, which can be used to obtain the linear velocity of the inner and outer rear wheels:

$$v_1 = \omega\left(R_r - \frac{d_2}{2}\right) = v\left(1 - \frac{d_2}{2R_r}\right)$$

$$v_2 = \omega\left(R_r + \frac{d_2}{2}\right) = v\left(1 + \frac{d_2}{2R_r}\right) \tag{5}$$

where:

$\omega = v/R_r$, R_r is the distance from the instantaneous center of velocity at the intersection of the vertical line of the inner and outer steering wheel plane and the vertical line of the rear wheel plane to the center point of the rear wheel navigation.

By adding and subtracting from the above equation, v and R_r can be obtained:

$$v = \frac{v_1 + v_2}{2}$$

$$R = \frac{d_2 v}{v_2 - v_1} = \frac{d_2(v_2 + v_1)}{2(v_2 - v_1)} \tag{6}$$

From $\tan\varphi = l/R_r$, it can be concluded that φ:

$$\varphi = \tan^{-1}\left(\frac{2l(v_2 - v_1)}{d_2(v_2 + v_1)}\right) \tag{7}$$

According to equation (1), equation (8) can be obtained.

$$\dot{x} = \frac{v_1 + v_2}{2}\cos\theta$$

$$\dot{y} = \frac{v_1 + v_2}{2}\sin\theta \tag{8}$$

$$\dot{\theta} = \frac{v_1 + v_2}{2}\cdot\frac{\tan\varphi}{l}$$

where:

φ can be obtained through equation (7).

The main electrical energy consumed by driving a tractor comes from the electric motor of the driving wheel and the steering motor. The angular velocity of the inner and outer drive wheels can be obtained from the linear velocity of equation (5):

$$\omega_1 = \frac{v_1}{r2} = \frac{v}{r2}(1 - \frac{d_1 \tan\varphi}{2l})$$
$$\omega_2 = \frac{v_2}{r2} = \frac{v}{r2}(1 + \frac{d_1 \tan\varphi}{2l}) \quad (9)$$

where:

r_2 is the radius of the rear drive wheel.

The driving power of an electric tractor is an electric battery. The tractor contains three motors. There are two Rear-wheel drive motors and one front wheel center steering motor. Set U as the driving voltage of the battery, and U_1 and U_2 are the armature voltages of the inner and outer drive wheel drive motors, respectively. This voltage is controlled by the Pulse Width Modulation (PWM) duty cycle of the driver. Therefore, the real-time armature voltage of the internal and external drive motors is:

$$U_1 = U \cdot D_1$$
$$U_2 = U \cdot D_2 \quad (10)$$

where:

D_1 and D_2 are the PWM duty cycles of the internal and external drive motors, respectively.

The armature voltage consists of two parts, one is the back electromotive force that drives the wheel to rotate, and the other is the voltage of the internal resistance. From this, it can be concluded that:

$$U \cdot D_1 = i_1 R_n + K_n g \omega_1$$
$$U \cdot D_2 = i_2 R_n + K_n g \omega_2 \quad (11)$$

where:

i_1 and i_2 are the armature current of the driving motor, R_n is the internal resistance of the driving motor, K_n is the back electromotive force constant, and g is the motor deceleration ratio.

The energy consumption during the tractor driving process is mainly evaluated by the power consumption of the driving and steering motors. The energy consumption model during the tractor driving process is determined by analyzing the consumption of the driving and steering motors. Assuming P_1 and P_2 are the power of the internal and external drive motors, it can be concluded that:

$$P_1 = U_1 \cdot i_1 = U \cdot D_1 \cdot i_1$$
$$P_2 = U_2 \cdot i_2 = U \cdot D_2 \cdot i_2 \quad (12)$$

where the armature currents i_1 and i_2 can be obtained from equation (12).

$$P_1 = (U^2 D_1^2 - U \cdot D_1 K_r g \omega_1) / R_n$$
$$P_2 = (U^2 D_2^2 - U \cdot D_2 K_r g \omega_2) / R_n \quad (13)$$

From this, it can be concluded that the total energy consumption E_1 of the two drive motors is:

$$E_1 = \int (P_1 + P_2) dt \quad (14)$$

Assuming that the steering angular velocity of the tractor's front wheel steering motor is constant ω_c, D_c is the PWM duty cycle of the steering motor, and the power of the front wheel steering motor is:

$$P_c = \frac{(U_2 D_c^2 - U D_c K_c g \omega_c)}{R_c} \quad (15)$$

where: K_c is the back electromotive force constant of the front wheel steering motor, and R_c is the internal resistance of the front wheel steering motor.

$$E_C = P_C \cdot \Delta t = P_C \cdot \frac{\Delta\varphi}{\omega_C} = \frac{UD_C \Delta\varphi (UD_f - K_C g \omega_C)}{R_C \omega_C} \quad (16)$$

$$E = E_1 + E_C \quad (17)$$

Equation (17) is the total energy consumption of the tractor, where: E_1 is the energy consumption of the Rear-wheel drive motor; E_C is the energy consumption of the front wheel steering motor.

Optimize DWA algorithm

The DWA algorithm is a local path obstacle avoidance algorithm (*Xin et al., 2023; Lin et al., 2022; Abhishek et al.,2020; Christian et al.,2016*). It sets the maximum and minimum values of the speed, acceleration, angular velocity, and angular acceleration key parameters, and sets the sampling resolution. Through the sampling resolution, it samples multiple groups of speeds within the adjustable range during the movement of the vehicle, simulates the movement track of the vehicle within the parameter limit for a certain time, evaluates all tracks within the range through the set evaluation function, and selects the group of tracks with the highest score. The DWA algorithm sets the sampling space based on a vehicle's motion performance, so this obstacle avoidance algorithm can be used for electric tractors in field work environments to achieve safe operation of the tractor. This article adjusts the evaluation function of the DWA algorithm, adds an energy consumption evaluation subfunction, and changes the weight coefficients of the original evaluation subfunctions to reduce the energy consumption of the tractor during obstacle avoidance under the premise of real-time dynamic obstacle avoidance.

- **Tractor Motion Model and Speed Sampling**

The first step of DWA algorithm realization is to establish the kinematics model of the tractor (*Lai et al., 2023*), as shown in Formula (1). Electric tractors are affected by motors and have inherent speed and acceleration limitations, which can be expressed as:

$$V_1 = \left\{(v, \omega) \middle| v_{\min} \le v \le v_{\max}, \omega_{\min} \le \omega \le \omega_{\max}\right\} \quad (18)$$

where:

$v_{\min}$ and $v_{\max}$ are the minimum and maximum linear speeds of the tractor, respectively, $\omega_{\min}$ and $\omega_{\max}$ is the minimum and maximum angular velocity of the tractor, respectively.

Ultimately obtain the speed constraint for the tractor is:

$$V_2 = \left\{(v, \omega) \middle| v \in \left[v_1 - \dot{v}_a \Delta t, \dot{v}_1 + \dot{v}_b \Delta t\right], \omega \in \left[\omega_1 - \dot{\omega}_a \Delta t, \omega_1 + \dot{\omega}_b \Delta t\right]\right\} \quad (19)$$

where:

v_1 is the current linear speed of the tractor, ω_1 is the current tractor corner speed, $\dot{v}_a$ and $\dot{\omega}_a$ are the maximum deceleration of the tractor, $\dot{v}_b$ and $\dot{\omega}_b$ are the maximum acceleration of the tractor.

Based on collision safety factors, to prevent the tractor from colliding with obstacles due to speed reasons, and to increase speed control constraints.

$$V_3 = \left\{(v, \omega) \middle| v \le \sqrt{2dist(v, \omega)\dot{v}_a}, \omega \le \sqrt{2dist(v, \omega)\dot{\omega}_a}\right\} \quad (20)$$

where:

$dist(v,\omega)$ is the shortest distance from the corresponding tractor trajectory to the obstacle.

- **DWA algorithm evaluation function**

In the sampled speed vector space, through speed sampling and discretization of vector space $V_1 \cap V_2 \cap V_3$ with continuous speed constraints, feasible speed sets are obtained, and track prediction is generated according to these speed sets and track prediction time periods. After obtaining the trajectory of a robot, it is usually feasible to have multiple sets of trajectories corresponding to the speed, and the trajectory is evaluated through an evaluation function.

The evaluation function is defined as follows:

$$G(v, \omega) = \sigma\left(\alpha \cdot heading(v, \omega) + \beta \cdot dist(v, \omega) + \gamma \cdot velocity(v, \omega)\right) \quad (21)$$

where:

$heading(v,\omega)$ is the azimuth evaluation function, representing the azimuth deviation between the trajectory and the target point at the current speed, $dist(v,\omega)$ is the closest distance between the trajectory and the static obstacle, and $velocity(v,\omega)$ is the evaluation function of the current speed. σ is the smoothing coefficient. α, β, and γ are the weighted coefficients of each item.

- **Optimize evaluation function**

The three evaluation sub functions of the traditional DWA algorithm evaluation function are relatively independent, and there are significant differences in the optimal weight coefficients of the three sub functions under different operating environments. In response to the operating conditions of electric tractors, the evaluation function of the traditional DWA algorithm has been adjusted and a tractor energy consumption evaluation subfunction $E(v,\omega)$ has been added to the original $G(v,\omega)$.

$$E(v,\omega) = E \tag{22}$$

where the value of E can be obtained by formula (17).

This equation represents the energy consumption of the evaluation trajectory.

The new evaluation function obtained is:

$$G(v,\omega) = \sigma\left(\alpha \cdot heading(v,\omega) + \beta \cdot dist(v,\omega) + \gamma \cdot velocity(v,\omega) + \delta \cdot E(v,\omega)\right) \tag{23}$$

where: δ is the weighting coefficient of the tractor energy consumption evaluation subfunction.

The purpose of the evaluation function $G(v,\omega)$ is to score the trajectory and select the optimal solution.

To avoid a large proportion of any item in the indicator, it is necessary to normalize each item in the objective function:

$$\begin{aligned}
n_heading(v,\omega) &= \frac{heading(v,\omega)}{\sum_{i=1}^{n} heading(v_i,\omega_i)} \\
n_dist(v,\omega) &= \frac{dist(v,\omega)}{\sum_{i=1}^{n} dist(v_i,\omega_i)} \\
n_velocity(v,\omega) &= \frac{velocity(v,\omega)}{\sum_{i=1}^{n} velocity(v_i,\omega_i)} \\
n_E(v,\omega) &= \frac{E(v,\omega)}{\sum_{i=1}^{n} E(v_i,\omega_i)}
\end{aligned} \tag{24}$$

where: n is the number of trajectories to be evaluated; i is the current evaluated trajectory.

The subfunction for evaluating tractor energy consumption refers to the fact that the smaller the obstacle avoidance speed and vehicle speed, the smaller the function value during the process of selecting the obstacle avoidance path. It also indicates that the path is smoother at this time, reducing the speed jump and significant steering of the tractor when approaching obstacles, and improving the economy of tractor movement. δ is the impact coefficient, and its value is related to energy consumption. If the energy consumption of the path is higher, the value of δ will be smaller.

Simulation analysis

- **Tractor Path Tracking Controller**

Use a model predictive controller as the path tracking controller for unmanned tractors to verify the traceability of the path. Gong Jianwei's method in "Model predictive control of Unmanned Vehicles" is adopted (*Gong et al., 2020*).

The unmanned tractor has low working speed. The path tracking controller designed based on kinematics model has reliable control performance and real-time performance, and has low requirements for hardware equipment, which is suitable for the requirements of low-cost and high reliability of unmanned tractors. At the next moment, repeat the above steps to loop through the path tracking of the unmanned tractor.

- **MTALAB and CarSim Joint Simulation**

Build a joint simulation platform of MATLAB and CarSim for obstacle avoidance path planning and tracking control of unmanned electric tractors. The working speed of Yancheng Yueda electric tractor during plowing is 4-8 km/h. Based on this model of electric tractor, a tractor model is established on the CarSim simulation platform. Table 1 shows the actual parameters of the tractor used.

Table 1

Tractor parameters

Variable	Meaning	Unit	Value
$L*W*H$	Length*Width*Height	mm	3195*1240*2340
l	Wheelbase	mm	1585
d_1/d_2	Front/Wear track width	mm	1000/1040
r_1/r_2	Front/Wear wheel radius	mm	330.2/546.1
U	battery voltage	V	76.8
g	Motor reduction ratio		25
R_n	Internal resistance of drive motor	Ω	0.32
R_c	Internal resistance of steering motor	Ω	0.448
K_n	Rear wheel motor back electromotive force constant	V/rmin^{-1}	0.014
K_c	Steering motor back electromotive force constant	V/rmin^{-1}	0.006

In the simulation, the radius of the obstacle is 2.5 m, and the geometric center of the obstacle is located 10 meters forward of the original path. Four stone pillars are simulated to form the obstacle, as shown in the figure. The basic parameters of the model tracking controller are set as follows: prediction step N_p=60, control step N_C=30, control cycle T=0.01 s, simulation time set to 9.00 seconds, and the simulation results are shown in the figure.

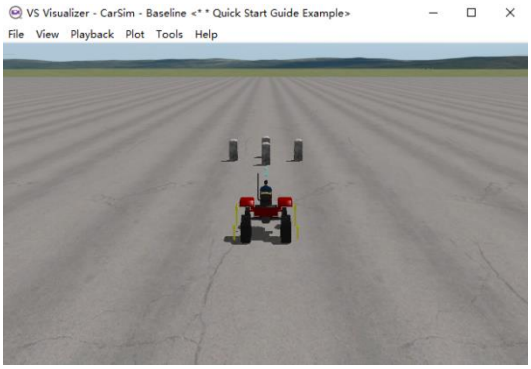

Fig. 3 - CarSim simulation model scenario

RESULTS

Joint simulation results

The original DWA obstacle avoidance algorithm and the improved DWA obstacle avoidance algorithm in the paper are used for simulation comparison, and both use the same trajectory tracking controller.

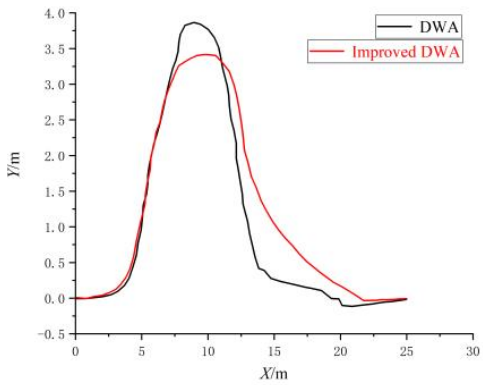

Fig. 4 - Simulation trajectory results

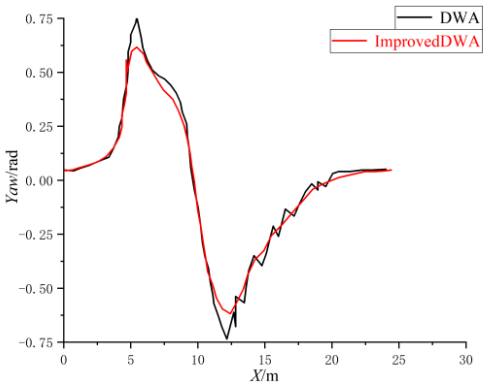

Fig. 5 - Simulation heading angle results

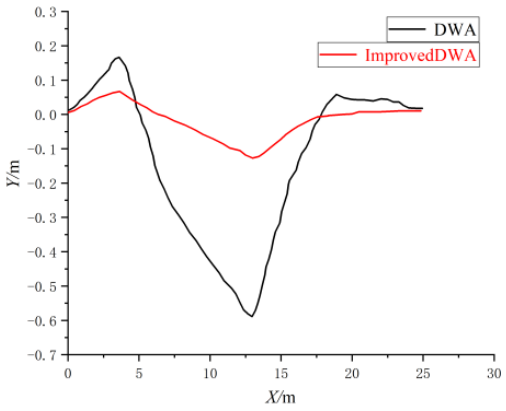

Fig. 6 - Lateral error simulation results

From the simulation results, it can be seen that the improved DWA algorithm is smoother when turning, with smaller curvature when transitioning from the global path to the obstacle avoidance path and the obstacle avoidance regression path back to the global path. The original DWA algorithm has significant fluctuations in heading angle, resulting in a longer steady-state time. The improved DWA algorithm for obstacle avoidance in electric tractors has a maximum lateral error of 0.13 m and a maximum heading angle of 0.557 rad, which is 77.6% and 25.65% less than the original DWA algorithm's maximum lateral error and heading angle, respectively.

Real tractor test

To verify the effectiveness of the improved DWA Algorithm Based on Optimal Energy Consumption, obstacle avoidance tests are conducted on the Yancheng Yueda YL254ET electric tractor as a testing platform. Install the navigation system as shown in the figure7 on the tractor. The system is developed based on the ROS platform. The upper computer uses NVIDIA Jetson TX2, and the lower computer uses a microcontroller for steering wheel and speed control. The system uses CAN bus for data communication. The system uses LiDAR and BeiDou signal receiver as sensors. The BeiDou system obtains the longitude and latitude information of the electric tractor, and uses dotting to obtain the longitude and latitude information of the field boundary and conduct global path planning. The model is Huace PA-3, which also includes an IMU sensor. Lidar perceives obstacle information, which model is Leishen C32-151A, with horizontal and vertical field of view angles of 360° and 30°, respectively.

Fig. 7 - Electric tractor obstacle avoidance test platform

When conducting obstacle avoidance experiments, obstacles are placed in the global path as shown in Figure 8, and the tractor is tracked and navigated along the global path. When the LiDAR scans the obstacles, the upper computer plans the obstacle avoidance path according to the algorithm, and the electric tractor completes the obstacle avoidance operation, Figure 9 shows the process of tractor obstacle avoidance.

The topic recording function in ROS is used to record the speed and heading angular velocity of the tractor during obstacle avoidance, and equations 15-17 are used to calculate the energy consumption of the tractor during obstacle avoidance.

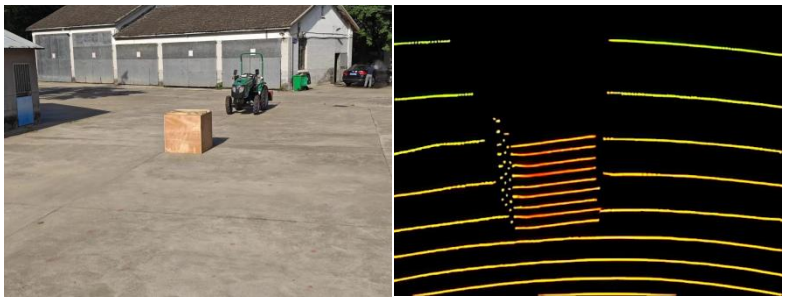

Fig. 8 - Lidar obstacle recognition results

Fig. 9 - Tractor obstacle avoidance process

The starting point of the longitudinal and latitudinal information of the global path planning line is (118° 6957363, 32° 1324537), and the ending point is (118° 6954802, 32° 1324377). A total of 10 meters were recorded from the beginning of the obstacle avoidance path to the node, and obstacles were placed 5 meters away from the starting point. The radius of the obstacle feature circle is 2.5 meters.

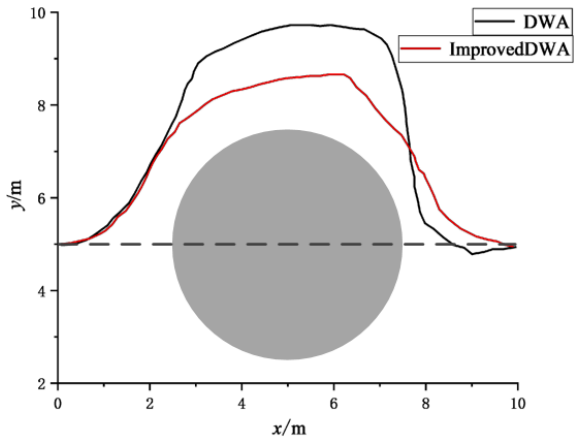

Fig. 10 - Comparison of experimental obstacle avoidance path results

By comparing the method proposed in this article with the original DWA algorithm, Figure 10 shows the running trajectories of the two. The shaded part is the result of fitting the outer contour of the obstacle. Use the BeiDou signal dotter to dot the path of the tractor and record the longitude and latitude information of the path.

Record every 0.1 m, recording the trajectory information using the original DWA algorithm and the algorithm proposed in this article. The dashed line in the figure represents the straight line for the global path planning operation of the tractor. From the figure, it can be seen that the trajectory of the improved algorithm is 1.1 m shorter than the original algorithm in terms of lateral distance.

Table 2

Experimental scenario test results

Algorithm	Length	Planning Spending Time	energy consumption
	[m]	[ms]	[KJ]
DWA	17.97	201	21.14
Improved DWA	15.69	194	19.77

Table 2 shows the results of obstacle avoidance tests on electric tractors. It can be concluded that the improved DWA algorithm can effectively reduce the energy consumption of the tractor during obstacle avoidance, reducing by about 6.47% compared to the original DWA algorithm and shortening the path length by 12.69%. From the table, it can also be seen that the improved algorithm has a slightly shorter path planning time than the original algorithm. The reason may be due to the continuous oscillation of the heading angle in the obstacle avoidance regression path of the original algorithm. The improved DWA algorithm achieves steady-state earlier, therefore it takes less time.

CONCLUSIONS

This paper optimizes the evaluation function of the DWA algorithm by establishing an energy consumption model for electric tractors and adding an energy consumption evaluation subfunction, thereby reducing turning points and excessive turning on obstacle avoidance paths.

The simulation results show that compared with the original DWA algorithm, the improved DWA algorithm based on the optimal energy consumption has a maximum lateral error of 0.13 m and a maximum heading angle of 0.557 rad for the electric tractor obstacle avoidance method. Compared with the original DWA algorithm, the maximum lateral error and heading angle are reduced by 77.6% and 25.65%, respectively. The front wheel steering angle changes smoothly without significant changes, indicating that the obstacle avoidance path control method has high control accuracy and the tractor can travel according to the preset trajectory.

The experimental results show that the length of the generated path is reduced by 12.69%, the total energy consumption for obstacle avoidance can be reduced by about 6.47%, and the planning time for obstacle avoidance paths is shorter. The experimental results demonstrate the effectiveness of this method.

ACKNOWLEDGEMENT

This work was supported by the National key research and development program (Grant No. 2022YFD2001204), the Jiangsu Province International Science and Technology cooperation project (Grant No. BZ2021007) and the Jiangsu Province modern agricultural Machinery equipment and technology demonstration and extension project (Grant No. NJ2021-06). This work was also supported by the project "Increasing INCDMTM performance and international involvement by supporting expertise in advanced mechatronic technologies - PERFORM-MECH", financed by The Ministry of Research, Innovation, and Digitalization, in the framework of Program 1 – Development of the national research and development system, Sub-program 1.2 – Institutional Performance – Projects for financing excellence in Research, Development and Innovation, Contract no. 3PFE/2021.

REFERENCES

[1] Abhishek Kumar Kashyap, Dayal R. Parhi, Manoj Kumar Muni, Krishna Kant Pandey. (2020). A hybrid technique for path planning of humanoid robot NAO in static and dynamic terrains. *Applied Soft Computing Journal*, Vol. 96, pp. 1-18, India.

[2] Borrelli F., Falcone P. (2005). MPC-based Approach to Active Steering for Autonomous Vehicle Systems. *International Journal of Vehicle Autonomous Systems*, Vol. 4, pp. 265-291, England.

[3] Gan-Mor S., Clark R.L., Upchurch B L. (2007). Implement lateral position accuracy under RTK-GPS tractor guidance. *Computers and Electronics in Agriculture*, Vol. 59, pp. 31-38, United States.

[4] Gong J.W., Liu K., Qi Y.J. (2020). Model Predictive Control for Unmanned Vehicles. 2nd edition. Beijing: Beijing University of Technology Press, China.
[5] Guo C.Y., Liu M.C., Gao Z.N. (2020). Research on agricultural machinery obstacle avoidance method based on improved artificial potential field method. *Journal of Chinese Agricultural Mechanization*, Vol. 41, pp. 152-157, China.
[6] Henkel Ch, Bubeck A., Xu Weiliang. (2016). Energy Efficient Dynamic Window Approach for Local Path Planning in Mobile Service Robotics. *IFAC-Papers*, Vol. 49, pp. 32-37, England.
[7] Kaivosoja J., Linkolehto R. (2015). GNSS error simulator for farm machinery navigation development. *Computers and Electronics in Agriculture*, Vol. 119, pp. 166-177, Finland.
[8] Khurshid Aliev, Emiliano Traini, Mansur Asranov, Ahmed Awouda, Paolo Chiabert. (2021). Prediction and estimation model of energy demand of the AMR with cobot for the designed path in automated logistics systems. *Procedia CIRP*, Vol. 99, pp. 116-121, Uzbekistan.
[9] Kuhne F., Lages W.F., et al. (2004). Model Predictive Control of a Mobile Robot Using Linearization. IEEE Proceedings of Mechatronics and Robotics, Vol. 4, pp. 525-530, Brazil.
[10] Li D.D., Shi Y., Li H.B., et al. (2018). Review on the progress of agricultural robot research. *China Agricultural informatics*, Vol. 30, pp. 1-17, China.
[11] Li G.H. (2021). Research on intelligent planning of agricultural robot obstacle avoidance path. *Journal of Agricultural Mechanization Research*, Vol. 43, pp. 236-239, China.
[12] Li S.B., Wang J.Q., Li K.Q. (2010). Stabilization of linear predictive control systems with softening constraints. *Journal of Qinghua University (Science and Technology)*, Vol. 11, pp. 1848-1852, China.
[13] Li S.C, Xu H.Z, Ji Y.H, et al. (2019). Development of a following agricultural machinery automatic navigation system. *Computers and Electronics in Agriculture*, Vol. 158, pp. 335-344, China.
[14] Lu X.L., Wu C.D., Yang G.X. (2022). Path planning of orchard spray robot based on improved A * and DWA algorithms. *Computer Engineering and Applications*, pp. 1-8, China.
[15] Muhannad Mujahed, Dirk Fischer, Barbel Mertsching. (2018). Admissible gap navigation: A new collision avoidance approach. *Robotics and Autonomous Systems*, Vol. 103, pp. 93-110, Germany.
[16] Oğuz Mısır. (2023). Dynamic local path planning method based on neutrosophic set theory for a mobile robot. *Journal of the Brazilian Society of Mechanical Sciences and Engineering*, pp. 1-16, Brazil.
[17] Tonja Heinemann, Oliver Riedel, Armin Lechler. (2019). Generating Smooth Trajectories in Local Path Planning for Automated Guided Vehicles in Production. *Procedia Manufacturing*, Vol. 39, pp. 98-105, Germany.
[18] Xi X.B., Shi Y.J., Dan X. (2019). Obstacle avoidance path control method for agricultural machinery automatic driving based on optimized Bezier. *Transactions of the Chinese Society of Agricultural Engineering (Transactions of the CSAE)*, Vol. 35, pp. 82-88, China.
[19] Xin Lai, Dan Wu, Di Wu, Jia He Li, Hang Yu. (2023). Enhanced DWA algorithm for local path planning of mobile robot. *Industrial Robot*, pp. 186-194, China.
[20] Xin Lai, Dan Wu, Di Wu, Jia He Li, Hang Yu. (2023). Enhanced DWA algorithm for local path planning of mobile robot. *The Industrial Robot*, Vol. 50, pp. 186-194, China.
[21] Xin Zhao, Ke Wang, Sixian Wu, Long Wen, et al. (2023). An obstacle avoidance path planner for an autonomous tractor using the minimum snap algorithm. *Computers and Electronics in Agriculture*,107738, China.
[22] Yang Y., Wen X, Ma Q.L. (2022). Real time planning of the obstacle avoidance path of agricultural machinery in dynamic recognition areas based on Bezier curve. Transactions of the Chinese Society of Agricultural Engineering (Transactions of the CSAE), Vol. 38, pp. 34-43, China.

ALGORITHM FOR OPTIMIZING THE MOVEMENT OF A MOUNTED MACHINE-TRACTOR UNIT IN THE HEADLAND OF AN IRREGULARLY SHAPED FIELD
/
АЛГОРИТЪМ ЗА ОПТИМИЗИРАНЕ ДВИЖЕНИЕТО НА НАВЕСЕН МАШИННО-ТРАКТОРЕН АГРЕГАТ В ИВИЦАТА ЗА ЗАВИВАНЕ НА ПОЛЕ С НЕПРАВИЛНА ФОРМА

Krasimir TRENDAFILOV*[1)], Galin TIHANOV[2)], Vanya STOYKOVA[3)], Galya SHIVACHEVA[3)]
[1)] Trakia University – Stara Zagora, Faculty of Technics and Technologies – Yambol, Department of Mechanical Engineering / Bulgaria;
[2)] Trakia University – Stara Zagora, Faculty of Agriculture, Department of Agricultural Engineering / Bulgaria;
[3)] Trakia University – Stara Zagora, Faculty of Technics and Technologies – Yambol, Department of Electrical Engineering, Electronics and Automatics / Bulgaria.
Tel: +359 887 708 603; E-mail: krasimir.trendafilov@trakia-uni.bg
DOI: https://doi.org/10.35633/inmateh-70-26

Keywords: *Algorithm, T-turn, headland, machine tractor unit, field of irregular shape*

ABSTRACT
Increasing the productivity of machine tractor units when cultivating the field is achieved by reducing the work time, which usually relates to seeking the shortest path of the unit in the field. Reducing the length of headland turns, which account for the largest proportion of the unit non-working moves, will result in higher productivity as well as less soil compaction in the headland. The article presents an algorithm for selection of a turn in the headland of a field of irregular shape. Existing theoretical correlations have been used to determine the length of the non-working move and the headland width when making T-turns. The selection of a turn is made on the basis of the minimum length of the non-working move, after which the width of the needed headland for the selected turn is calculated. This algorithm can be added to the on-board computer of the unit thus providing a more efficient way of moving, automatically generating a headland and following the trajectory of the selected turn by the unit.

РЕЗЮМЕ
Повишаването на производителността на машинно-тракторните агрегати при обработка на полето се извършва чрез намаляване на времето за работа, което обикновено се свежда до търсене на най-краткия път на агрегата в полето. Намаляването на дължината на завоите в края на полето, които са с най-голям дял от неработните ходове на агрегата, ще доведе до по-висока производителност, както и по-малко уплътняване на почвата в ивицата за завиване. В статията е представен алгоритъм за избор на завой в ивицата за завиване на поле с неправилна форма. Използвани са съществуващи теоретични зависимости за определяне на дължината на неработния ход и на широчината на ивицата за завиване при извършване на гъбовидни завои. Изборът на завой се прави на база минимална дължина на неработния ход, след което за избрания завой се определя широчината на необходимата за извършването му ивица за завиване. Този алгоритъм може да бъде добавен в бордовия компютър на агрегата и да осигури по-ефективен начин на движение, автоматично генериране на ивица за завиване и следване на траекторията на избрания завой от агрегата.

INTRODUCTION
The application of information technologies in agriculture allows to achieve complete automation of the operations performed by the agricultural machinery depending on the working conditions, as well as automatic guidance of the machine tractor units along certain trajectories in the field. These technologies enable the development of fully autonomous units that will be the basis for remote controlled agricultural production in the future (*Freyberger and Jahns, 2000*). Autonomous units must be able to make decisions about the way of their movement in the field depending on the specific conditions so as to achieve high efficiency of the operations performed.

To increase the efficiency of performing the mechanized operations, it is necessary to minimize the processing time, which is usually done by seeking the shortest path travelled by the machine tractor unit in the field. *Kroulik et al.* present an algorithm to search for the shortest path of movement in the field by choosing among 180 directions with a step of 1 degree. According to this algorithm, the shortest path is found, but the final decision is made by the farmer depending on the characteristics of the field. The optimization of the trajectory of the machine tractor unit results in reduction in the total length of the travelled path, where the greatest change is in the length of the non-working moves (*Kroulik et al., 2018*). When optimizing the direction of movement in a field of irregular shape not only the size and shape of the field have to be taken into consideration, but also slope, soil conditions, point of entry into the field, and other constraints. The direction in which the ratio between working and non-working moves is the greatest is considered to be the optimum one (*Chyba et al., 2013*).

An increase in efficiency is usually achieved by reducing the number and length of non-working moves. They mainly include the turns made at the end of the field and the moves to load the units. Jin and Tang propose an algorithm to search for the minimum number of turns in the field by determining the direction of movement. With a shuttle mode of movement, the algorithm reduces the number of turns by 16% and the time for making them by 25% (*Jin and Tang, 2010*). Other authors propose an algorithm that can be used to determine the headland points in fields of different shape. The principle is to measure the angle between each field border and the direction of movement. If the angle is greater than 10 degrees, that edge of the field is assumed to have a headland (*Aurbacher and Dabbert, 2009*). According to other authors, the headland is not needed when the angle is below 15 degrees (*Oksanen, 2018*).

The optimization of non-working moves is reduced to minimizing their length in the automatic generation of the moves (*Sabelhaus et al., 2013*). Algorithms used for minimization of the turns must be able to automatically determine the way of turning in the headland and the parameters of the turn depending on the data received from the navigation system about the position of the unit, the headland and the type of unit (*Freyberger and Jahns, 2000; Oksanen, 2018*).

There are different methods for determining the way travelled when making a turn, but the most commonly used is a geometric method, where the turn is represented using straight sections and curved sections of constant radius (*Backman et al., 2015*). In the computational methods, the trajectory of movement is presented as equations of spirals, clothoids, etc. in combination with simple shapes, but the complex calculations to create the required shape of the turn make these methods more difficult to apply (*Khan et al., 2017*). Backman et al. present an algorithm for generating a trajectory in the headland using arcs of variable curvature to transition between arcs of constant radius and/or straight lines. This algorithm is suitable for real-time use, as an average computation time of 0.36 s per turn has been achieved (*Backman et al., 2015*).

Hameed et al. used a method for geometric presentation of the field, which provides a map on which operative planning of the mechanized operations can be put in place. This method is supplied with methods for optimization of the unit's mode of movement. The little time required for calculation makes it possible to use the method in real time for fully automated agricultural units (*Hameed et al., 2010*). Usually, existing algorithms for optimization do not include changing the width of the headland for different direction of movement. *Yatskul et al.* proposed an algorithm for determining the width of the headland that allows adding trajectories to replicate the drivers' behaviour. This allows for a 7.5% reduction of the headland width compared to the actual field measurement and a 5.1% reduction of the largest width of the pear-shaped turn (*Yatskul et al., 2014*).

The headland width as well as the time to make the turn should be minimal. Tu uses a method to calculate the minimum required headland width depending on the angle it makes with the perpendicular to the direction of movement of the unit. The required headland width at the minimum time to make a turn is thus determined (*Tu, 2013*).

Automatic turning will allow the operator to focus more on performing the relevant technological operation (*Freyberger and Jahns, 2000*). Existing navigation systems for automatic turning make it possible for the machine tractor unit to follow different optimal movement patterns. Various algorithms can be added to modern navigation systems to optimize the mode of movement and plan the route of the units (*Bochtis and Vougioukas, 2008*). Such a system for movement in the headland can be successfully coupled with a device performing repetitive actions on the machine tractor unit (e.g. towbar control, PTO, hydraulic valves), allowing for full automation of operations (*Cariou et al., 2010 a, b*).

The objective of the present paper is to propose an algorithm for selecting a trajectory for movement when making a T-turn in a field of irregular shape and determine the headland width, to be applied in automatic control systems of agricultural units.

MATERIALS AND METHODS

The algorithm for selection of a turn has been developed for five types of T-turns made by machine tractor units. Each turn is in two variants - open and closed and is performed in two directions - from left to right and from right to left. A total of 20 turns have been described as shown in Table 1. The turns have been created by a geometric method using lines and arcs of circles of equal radius.

Table 1

Types of T-turns

Name of the turn	Type and direction of execution			
	Open turns		Closed turns	
	left to right	right to left	left to right	right to left
T-turns with straight-line backward move parallel to the field border				
T-turns with straight-line backward move not parallel to the field border				
T-turns with arc-shaped backward move				
T-turns with straight-line move upon entering the headland				
T-turns with straight-line move upon exiting the headland				

To develop the algorithm, the analytical correlations for determining the length of T-turns and the headland width have been used as described in (*Trendafilov and Tihanov, 2022 a, b*). A geometric method was used in the modeling of the turns, where the turn is represented by straight sections and curved sections of constant radius.

Input parameters are: the angle between the direction of movement and the field border (α); working width of the machine tractor unit (B); the kinematic length of the machine tractor unit (l_a); the turn radius of the machine tractor unit (R); the tractor wheel track (M); the longitudinal base of the tractor (H).

Figure 1 presents a diagram of one of the T-turns. The other designations on the figure are: the headland width (E); the beginning of the turn (point A); the end of the turn (point B); the centre of the corresponding curvilinear movement within the turn (point O_1 and point O_2); the rectilinear idle move length (l_g) when entering the headland.

The output parameters of the algorithm are: type of turn, length of the non-working move (l_n), headland width. The length of the non-working move in the headland is the sum of the length of the turn (l_T - the distance between point A and point B) and the length of the rectilinear non-working move l_g before or after making the turn. The criterion for the selection of a turn is the minimum length of the non-working move. For the selected turn, the actual headland width (E) and the number (k) of the unit moves required to handle it, which is a multiple of the working width of the machine tractor unit, have to be calculated.

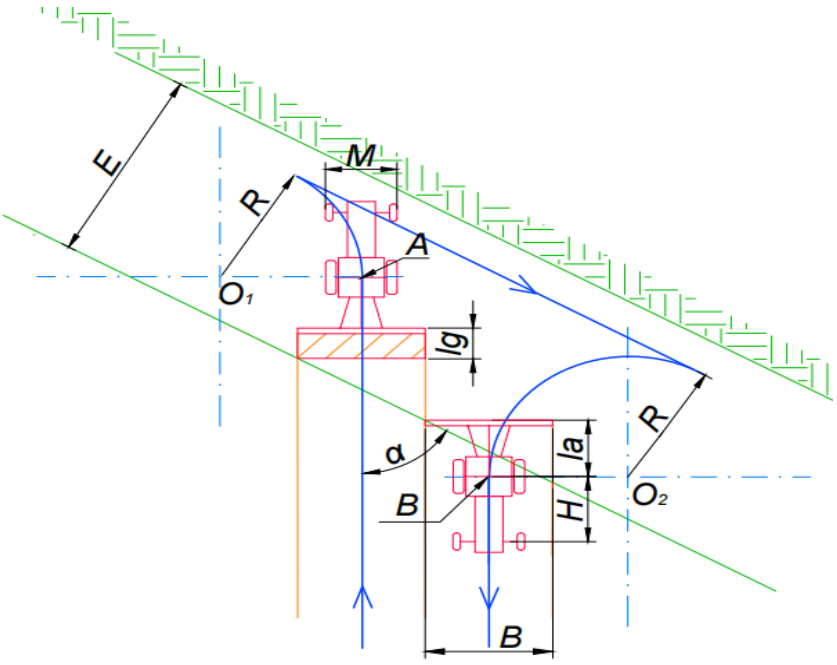

Fig. 1 – Diagram of an open T-turn

RESULTS

Figure 2 presents the block diagram of the algorithm, comprising the following steps:

1. Setting the input parameters: α, B, l_a, R, M and H.
2. Determining the idle move length when the machine tractor unit makes turns on a field of irregular shape and saving the obtained lengths in a database l_n with 20 elements and indices from 0 to 19 according to the set formulas (Fig. 3 - subalgorithm No. 1).
3. Finding the index of the first minimal element of the database l_n.
4. Calculating the whole part when dividing the index by 5. The resulting values determine the variant and direction of the turn (0 - open from left to right, 1 – open from right to left, 2 – closed from left to right, 3 – closed from right to left).
5. Calculating the remainder when dividing the index by an integer of 5. The resulting values determine the type of T-turn (0 – T-turn with a rectilinear reverse move parallel to the field border, 1 – T-turn with a rectilinear reverse move not parallel to the field border, 2 – T-turn with an arched reverse move, 3 – T-turn with a rectilinear move upon entering the headland, 4 – T-turn with a rectilinear move upon leaving the headland).
6. Visualization of the type of T-turn that corresponds to the index of the first minimal element (Fig. 4 - subalgorithm No. 2).
7. Determining the number of moves of the unit and the headland width (Fig. 5 - subalgorithm No. 3).

The block diagram for subalgorithm No. 1 (Fig. 3) presents the calculation of the length of the non-working move in an open T-turn with a rectilinear reverse move parallel to the field border when moving from left to right. The lengths of the other turns are calculated according to the analytical correlations described in (*Trendafilov and Tihanov, 2022 b*).

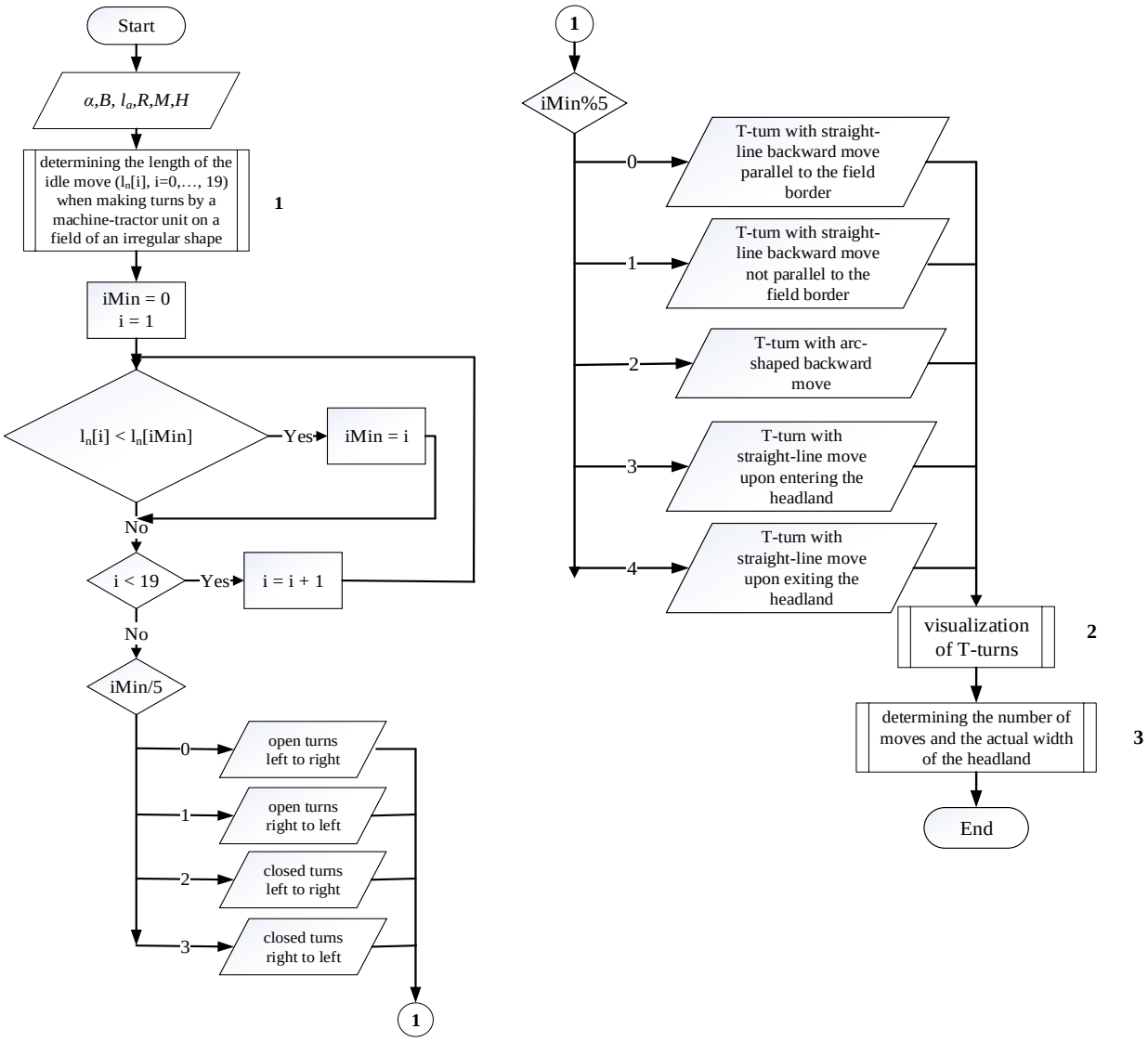

Fig. 2 – Block diagram of an algorithm for selection of a turn

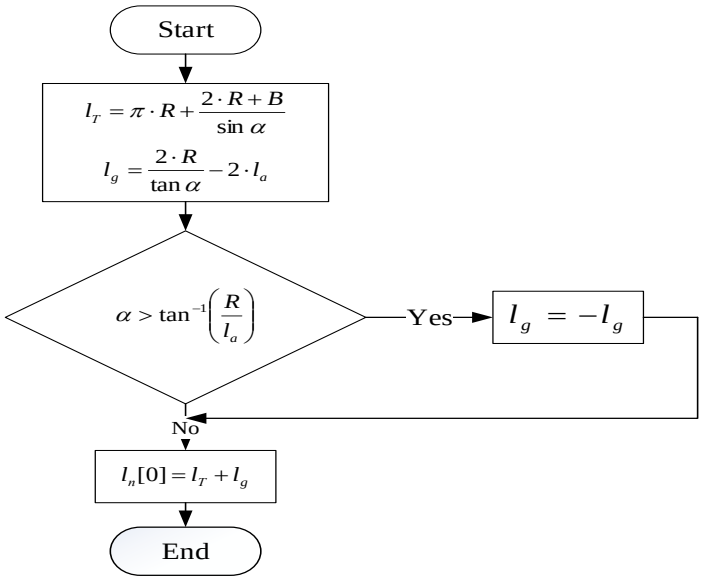

Fig. 3 – Block diagram of subalgorithm No. 1 for calculating the length of the non-working move when making a turn

The block diagram for subalgorithm No. 2 (Fig. 4) visualizes the selected turn of minimum length, and according to its number, the corresponding graphic image from Table 1 is presented.

The block diagram for subalgorithm No. 3 (Fig. 5) defines the number of moves k and the headland width for an open T-turn with a rectilinear reverse move parallel to the field border when traveling from left to right. The widths of the other turns are calculated according to the analytical correlations described in (*Trendafilov and Tihanov, 2022 a*). The number of moves has to be the smallest integer greater than or equal to the quotient of the theoretical headland width (E) and the working width of the machine tractor unit (B). The actual headland width is calculated as the product of the specified number of moves and the working width of the machine tractor unit.

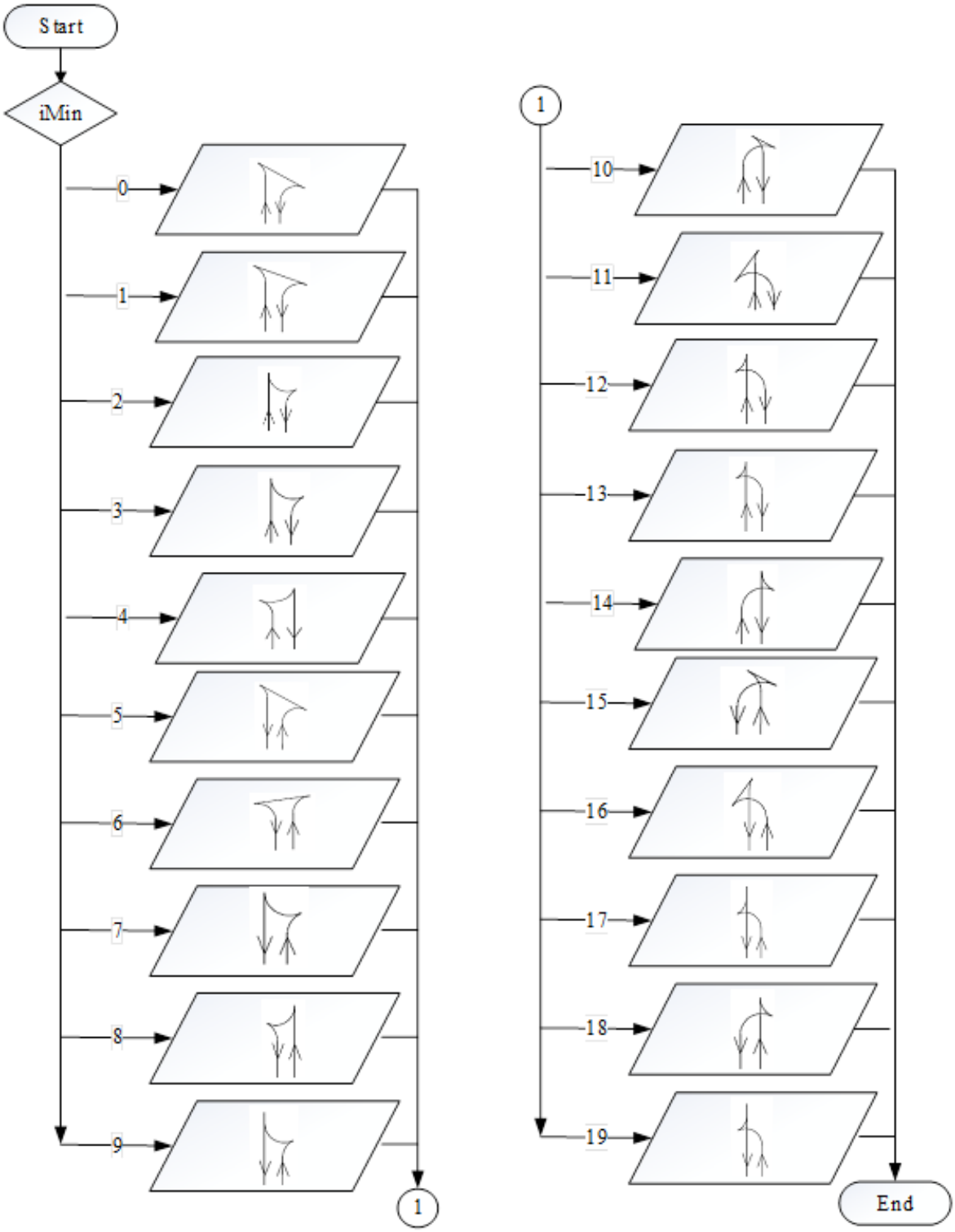

Fig. 4 – Block diagram of subalgorithm No. 2 for visualization of the selected turn

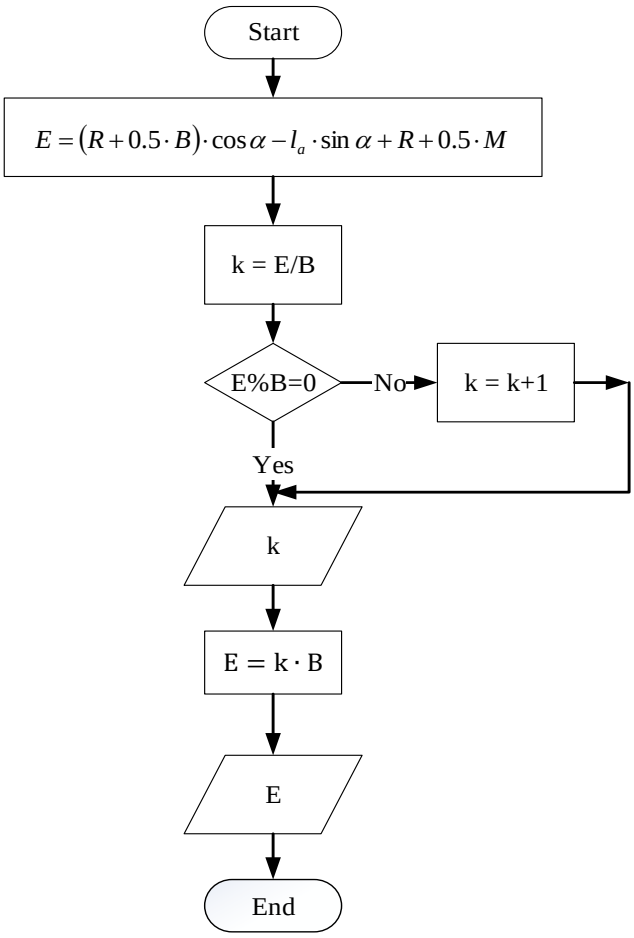

Fig. 5 – Block diagram of subalgorithm No. 3 for headland width and number of moves in it

CONCLUSIONS

An algorithm has been developed for selection of a turn in the headland of a field of irregular shape based on existing theoretical correlations for determining the length of 5 types of turns with a total of 20 variants of their execution. The selection of a is made on the basis of the minimum length of the non-working move, after which the headland width necessary for its execution is determined for the selected turn. The algorithm includes multiple subalgorithms, and in this case only subalgorithms for determining the non-working move and the headland width in one of the 20 types of turns have been demonstrated. This algorithm can be added to the on-board computer of the machine tractor unit and based on the characteristics of the unit and the angle between the direction of movement and the field border to determine the turn with the smallest length of the non-working move, visualize it on the screen and determine the width of the needed headland. This will allow the operator to use the most efficient way of movement, and when combined with the navigation system, the trajectory of the unit in the headland could be generated and followed. For this purpose, it is necessary to develop a computer program based on the presented algorithm, which is the subject of future work.

ACKNOWLEDGEMENT

This work was supported by the Bulgarian Ministry of Education and Science under the National Research Programme “Smart crop production” approved by Decision of the Ministry Council № 866 / 26 November 2020.

REFERENCES

[1] Aurbacher J., Dabbert S. (2009). Integrating GIS-based field data and farm modeling in a watershed to assess the cost of erosion control measures: An example from southwest Germany, *Journal of soil and water conservation*, *64* (5), 350-362;

[2] Backman J., Piirainen P., Oksanen T. (2015). Smooth turning path generation for agricultural vehicles in headlands. *Biosystems engineering*, 139, 76-86;

[3] Bochtis DD., Vougioukas SG. (2008). Minimising the non-working distance travelled by machines operating in a headland field pattern, *Biosystems engineering*, 101, 1-12;
[4] Cariou C., Lenain R., Thuilot B., Humbert T., Berducat M. (2010a). Maneuvers automation for agricultural vehicle in headland. *AgEng 2010 Conference, 2010*, September 6-8, Clermont-Ferrand, France;
[5] Cariou C., Lenain R., Berducat M., Thuilot B (2010 b). Autonomous maneuvers of a farm vehicle with a trailed implement in headland, ICINCO 2010, *Proceedings of the 7th International Conference on Informatics in Control, Automation and Robotics*, Volume 2, Funchal, Madeira, Portugal, June 15-18, 109-114;
[6] Chyba J., Kroulik M., Vitek P., Kumhala F. (2013). Proposals for field work rides and their optimization according to shape of land, *12th International Scientific Conference Engineering for Rural Development*, Jelgava, Latvia, 111-114;
[7] Freyberger F., Jahns G. (2000). Symbolic course description for semiautonomous agricultural vehicles, *Computers and Electronics in Agriculture*, 25, 121-132;
[8] Hameed IA., Bochtis DD., Sørensen CG., Nøremark M. (2010). Automated generation of guidance lines for operational field planning, *Biosystems engineering*, 107, 294-306;
[9] Jin J., Tang K. (2010). Optimal coverage path planning for arable farming on 2D Surfaces, *Transactions of the ASABE*, *53* (1), 283-295;
[10] Khan A, Noreen I., Habib Z. (2017). On complete coverage path planning algorithms for non-holonomic mobile robots: survey and challenges, *Journal of Information Science and Engineering*, *33*(1), 101-121;
[11] Kroulik M., Hula J., Brant V. (2018). Field trajectories proposals as a tool for increasing work efficiency and sustainable land management, *Agronomy Research*, 16 (4), 1752-1761;
[12] Oksanen T. (2018). Path Planning Algorithms for Agricultural Machines, Helsinki University of Technology, *Automation Technology Laboratory, Series A: Research Reports* No 31, Espoo;
[13] Sabelhaus D., Röben F, M. zu Helligen LP, Lammers, PS. (2013). Using continuous-curvature paths to generate feasible headland turn manoeuvres. *Biosystems engineering*, 116, 399-409;
[14] Trendafilov K., Tihanov G. (2022 a). Comparative analysis of the headland width when making T-turns by a mounted machine-tractor unit on an irregularly-shaped field, *INMATEH - Agricultural Engineering*, *67* (2), 221-232, doi: https://doi.org/10.35633/inmateh-67-22
[15] Trendafilov K., Tihanov G. (2022 b). Comparative analysis of the idle move length when making T-turns by a mounted machine tractor unit in a field of irregular shape, *INMATEH - Agricultural Engineering*, *68* (3), 457-470, doi: https://doi.org/10.35633/inmateh-68-45
[16] Tu X. (2013). Robust navigation control and headland turning optimization of agricultural vehicles, *Graduate Theses and Dissertations*, Paper 13188;
[17] Yatskul A., Lemiere JP, Delion C. (2014). On an automated headland turn of wide width air seeders, RHEA, *Second International Conference on Robotics and associated High-technologies and Equipment for Agriculture and forestry*, 21-23 May 2014, Madrid, Spain, 239-246.

IMPROVEMENT DESIGN AND SIMULATION ANALYSIS ON CENTRIFUGAL DISC ORGANIC FERTILIZER SPREADER
/
离心圆盘式有机肥撒施机改进设计与仿真分析

Bing XU [1,2], Qingliang CUI *[1,2], Decong ZHENG [1,2]
[1)] College of Agricultural Engineering, Shanxi Agricultural University, Taigu 030801 / China;
[2)] Dryland Farm Machinery Key Technology and Equipment Key Laboratory of Shanxi Province, Taigu 030801 / China
Tel: +86-0354-6288339; E-mail: qlcui@126.com
DOI: https://doi.org/10.35633/inmateh-70-32

Keywords: *organic fertilizer, spreader, crushing unit, discrete element method*

ABSTRACT
Aiming at the poor efficiency in crushing a handful of caking organic fertilizers spraying from the traditional disc spreader, an improved disc spreader equipped with spike-tooth crushing unit was designed with the introduction of its structural composition and working principle. Also simulation experiments were carried out based on the discrete element method according to the solutions made before and after the structural improvement. Firstly, a granular organic fertilizer model was established based on the EDEM and a caking organic fertilizer bonding model was built based on the HMB (Hertz-Mindlin with bonding) contact model. Then two organic fertilizer spreading models corresponding to the solutions were respectively established, based on which simulation experiments were repeated three times on the spreading process. The analysis on the particle velocity vector diagram revealed the interaction relationship between organic fertilizers with the toothed shaft, external wall and disk, verifying the crushing mechanism of crushing unit. By calculating the total number of the bonds generated and broken in the spreading process in both of the spreading models, the average broken rate of bonds in the spreading process was separately 58.87% and 98.05% based on each solution, revealing that the improved solution outperformed the traditional solution in terms of the efficiency in crushing the caking organic fertilizers. This research will be a reference in designing the critical components or improving the overall performance of disc spreader.

摘要
针对传统圆盘式撒施机在撒施有少量结块的有机肥时，对块状有机肥破碎效果差的问题，改进设计了一种带有钉齿式破碎装置的圆盘式撒施机，阐述了其结构组成和工作原理。基于离散元法对结构改进前、后的两种方案开展模拟试验，首先用 EDEM 软件建立粒状有机肥模型，以 Hertz-Mindlin with bonding（HMB）接触模型为基础建立块状有机肥粘结模型，然后分别建立两种方案对应的有机肥撒施模型，并对撒施过程进行三次重复模拟试验。通过对颗粒运动速度矢量图的分析，明晰了有机肥与钉齿轴、外壁、圆盘之间的作用关系，验证了破碎装置的破碎机理；通过统计两种撒施模型在撒施过程中粘结键生成总数及断裂数，计算得出两种方案在撒施过程中粘结键平均断裂率分别为 58.87%、98.05%，表明改进后的方案对块状有机肥的破碎效果优于传统方案。本研究可为圆盘式撒施机关键部件设计及整机性能提升提供参考。

INTRODUCTION

As an important part in agricultural production, fertilization provides nutrients necessary for crop growth to accelerate the growth and development. The commonly used fertilizers include chemical and organic fertilizers. In recent years, the overuse of fertilizers have led to many problems, such as soil hardening, air and water source pollution, which have become more and more serious. Hence it is very necessary and pressing to apply less fertilizer *(Ma et al., 2019; Wen et al., 2023)*. Researches have shown that organic fertilizer can efficiently improve and increase soil fertility with less environmental pollution, it is a necessity in developing green agriculture *(Sun et al., 2019)*. Therefore, scientifically reduced application of fertilizer and reasonable application of organic fertilizers have become an important approach to improve the quality of cultivated land, increase crop yield and enhance the quality of agricultural products *(Du et al., 2020; Jiang et al., 2023; Fang et al., 2021)*.

[1] *As Lec .M.S.Eng.Bing XU; Qingliang CUI, Prof. Ph.D. Eng.; Decong ZHENG, Prof. Eng.*

Due to the strong bonding force, easy caking and poor fluidity between organic fertilizer granules, organic fertilizer can hardly be spread and this is also one of the main reasons for the low usage of it *(Li et al., 2022)*. As the premise for the wide application of organic fertilizer is the availability of a spreading device with excellent crushing performance, even spreading and high efficiency, the study on an efficient spreading device with good performance is of great significance to accelerate the development of green agriculture.

Currently, according to the different structures, spreaders can be classified into different types, including hammer-shape, roll-type and centrifugal disc spreaders in domestic and overseas market for the spreading of organic fertilizers with different physical properties *(Xu et al., 2022)*. Numerous researches have been made by scholars at home and abroad on the key technologies, such as the structural design of spreader components and the optimization of working parameters during the spreading of organic fertilizers. By taking MG5 organic fertilizer spreader as the research object, Ștefan et al. established a regression model covering the effective working width, effective working quota, rotor speed, conveyor flow, the angle of inclination of the rotors and density of scattered material after the experiment *(Ștefan et al., 2019; Cârdei et al., 2019)*.

Aiming at the problem of poor crushing effect during the spreading of organic fertilizers with high viscosity by traditional spreaders, Lv et al designed a vertical screw spreader with the optimization of structure and working parameters based on the experimental indexes of spreading uniformity and working width *(Lv et al., 2020)*. Based on the discrete element method, Zinkevičienė R et al. built a centrifugal spreading model for cylindrical granular organic fertilizers to evaluate the lateral uniformity of fertilizers over field *(Zinkevičienė et al., 2021)*. In order to increase the uniformity of lateral spreading by organic fertilizer spreader, Liu et al. managed to control the shape of jet flow by innovating the components and optimizing the structural parameters based on the quantitative representation of the shape of jet flow from the spreading device *(Liu et al., 2022)*. Wu et al. designed a spreading device for organic fertilizer spreader by selecting the number of spiral lines on the spreader roll, the screw pitch of blade, the blade angle and the rotation speed as the experimental factors. In the field experiment made based on the variable coefficient of fertilization, which had also served as an evaluation index, the optimal combination of parameters for the spreader roll was obtained *(Wu et al., 2022)*.

Generally, due to the excellent crushing performance, crushing roll-type spreader is applicable to the spreading of barnyard manure that is of high humidity in block structure. With great working width, centrifugal disc spreader is applicable to the spreading of granular or powdered organic fertilizer due to the poor crushing effect. When it is used for the spreading of organic fertilizers, among which most of them are powdery or granular with the mixture of a small number of caking organic fertilizers, the spreading effect will be affected as the caking fertilizers can hardly be crushed efficiently. In view of this, a centrifugal disc spreader equipped with crushing unit was designed in this paper after the structural improvement based on the traditional disc spreader. Also based on the discrete element method, two organic fertilizer spreaders were separately built before and after the structural improvement. Through numerical simulation, both of the solutions had been compared in terms of the crushing of caking organic fertilizers during the operation with an aim to provide a reference to improve the overall performance of spreader.

MATERIALS AND METHODS

Structural composition and principle of disc spreader

In traditional disc spreader, spreading disk serves as the main working component during the operation. Fertilizers have been conveyed backward to the spreading disk via the chain conveying unit and the high-speed rotation of spreading disk contributes to the even spreading of fertilizers to the field. It is applicable to the spreading of powdery or granular fertilizers *(Ma et al., 2019)*.

However for the spreading of a handful of caking organic fertilizers, it doesn't work efficiently in crushing them. Therefore a centrifugal disc spreader equipped with crushing unit has been designed after the structural improvement based on the traditional disc spreader.

As indicated in Figure 1, it mainly consists of traction frame, chain conveying unit, toothed crushing unit, disc spreading unit and universal drive shaft. It is driven by the tractor, whose conveyor driven shaft drives the disk to rotate via the universal drive shaft. During the operation, firstly the organic fertilizers in the fertilizer box will be conveyed to the crushing unit for crushing via the chain conveying unit and then be spread to the field through the disc spreading unit after the crushing.

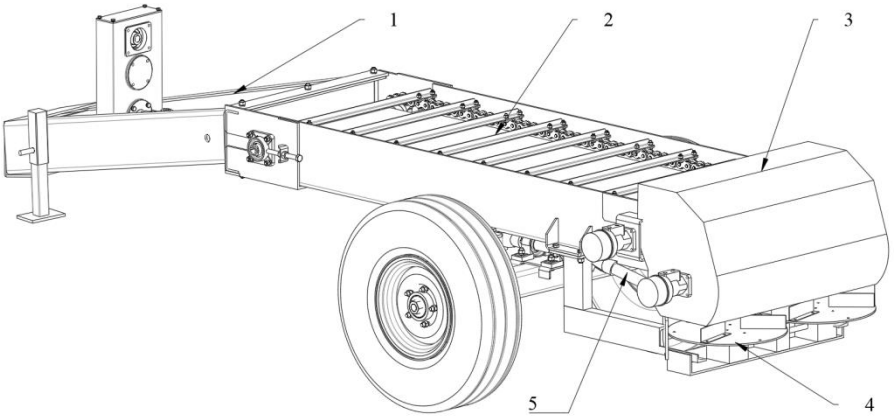

Fig. 1 - Structural composition of disc spreader equipped with crushing unit

1- traction frame; 2- chain conveying unit; 3- toothed crushing unit; 4- disc spreading unit; 5- universal drive shaft

As shown in Figure 2(a) and (b), the spike-tooth crushing unit mainly consists of toothed shaft and external wall. During the operation, organic fertilizers will be conveyed via the chain conveying unit to the inlet of the crushing unit, where the organic fertilizers with smaller particle size will drop to the outlet through the gaps between the spike teeth or between the teeth and the external wall. However, the caking organic fertilizers with larger particle size won't pass directly through the gaps and most of them will interact with the spike teeth and the external wall in the crushing unit with the high-speed rotation of the toothed shaft. They will be broken up due to the impact, collision and squeezing effect and a handful of organic fertilizers will be crushed when they collide with the disk at high speed due to the acceleration effect of the toothed shaft.

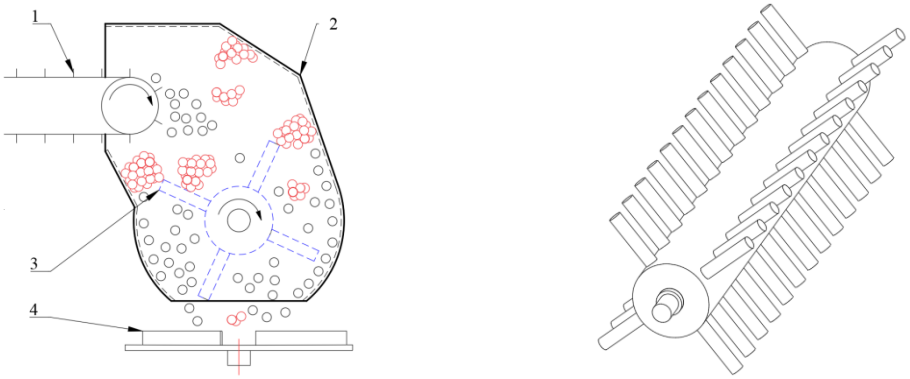

(a) Schematic diagram of crushing unit (b) toothed shaft

Fig. 2 - Structural composition and principle of toothed crushing unit

1- chain conveying unit; 2- external wall; 3- toothed shaft; 4- disk

Construction of discrete element model

Construction of organic fertilizer model

Based on the EDEM software, granular and caking organic fertilizer models were separately built, among which the granular model was constituted by various spheroidal particles in a radius of 8 mm, as shown in Figure 3(a), while the caking fertilizer model that was built based on the HMB (Hertz-Mindlin with bonding) contact model was constructed through the bonding of several above-mentioned spheroidal particles through the bonds. The main factors affecting the bonds include the normal stiffness per unit area, shear stiffness per unit area, critical normal stress, critical shear stress and bonded disk radius *(Wang et al., 2010)*. The bonds can work under a certain normal force or tangential force, but they will break when the outside force exceeds the critical stress of bonds and then the block-shaped particles will be broken into some smaller blocky particles or spheroidal particles. Due to the caking, the organic fertilizers vary in shape and size. Hence in order to simplify the modeling process, only a type of caking organic fertilizer model was built with the process as below: Firstly, based on the 3D modeling software, a 3D caking organic fertilizer model was constructed, which was also introduced into the EDEM to serve as the contour of the organic fertilizer. Then based on the HMB contact model, the spheroidal particles with a radius of 8 mm made a full profile with the setting of bonding parameter to generate the bonds. With reference to the literature, the bonded disk radius was generally 1.2~2 times the radius of particles *(Li et al., 2021)*.

In this paper, it is set to be 10 mm. In order to verify the efficiency in crushing the organic fertilizers based on the improved solution to cater for the crushing and spreading of the organic fertilizers with different bonding forces, the values of the HMB bonding parameters were properly increased based on the existing researches *(Wu, 2016)* in terms of the critical normal stress and critical shear stress, as shown in Table 1.

Table 1

Bonding parameters of HMB

Parameters	Values
Normal stiffness per unit area	1×10^{8} N/m^{-3}
Shear stiffness per unit area	5×10^{7} N/m^{-3}
Critical normal stress	0.55 MPa
Critical shear stress	0.55 MPa
Bonded disk radius	10 mm

Figure 3(b) and (c) showed the caking organic fertilizer bonding model, where every caking model consisted of 40 spheroidal particles and 100 bonds. Figure 3 (d) showed the distribution of the bonds within the caking model. Finally, the position of every spheroidal particle within the caking model was exported and saved as the particle template.

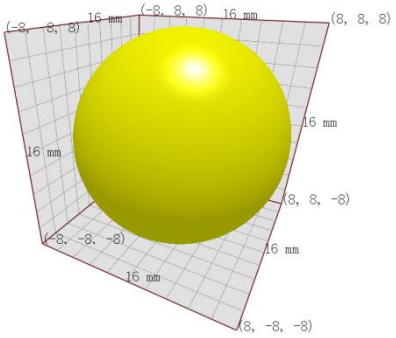

(a) granular organic fertilizer model

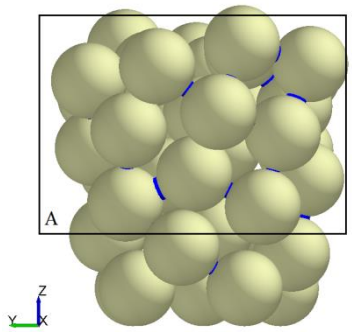

(b) caking organic fertilizer model

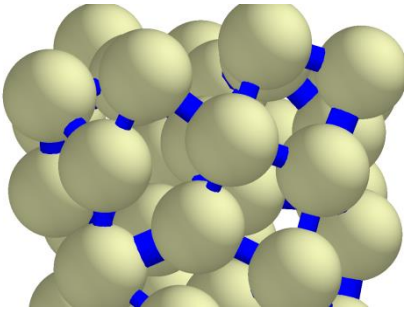

(c) partial enlarged view of area A in Figure 3 (b)

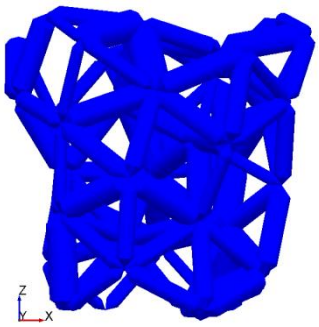

(d) distribution of the bonds within the caking model

Fig. 3 - Discrete element model of organic fertilizer

Construction of organic fertilizer spreading model

Two organic fertilizer spreading models before and after the structural improvement of spreader were separately built based on the discrete element method. Through numerical simulation, both of the structural solutions were compared and analysed in terms of the efficiency in crushing organic fertilizers. But during the construction of both spreading models, none of them were built with the modelling of conveying unit. The organic fertilizer spreading model equipped with crushing unit was constructed according to the following process: Based on the 3D modelling software, the 3D models for the spreading unit and the crushing unit were built, which then were saved in stp format and exported into the EDEM. After referring to the design manual *(China Academy of Agricultural Mechanization Sciences, 2007)*, the rotation speed of disk was set to be 540 r/min and 1200 r/min for the toothed shaft. As provided in Table 2 and 3, the intrinsic parameters and the contact parameters of the materials involved in the spreading model had been set according to the relevant references *(Li et al., 2022; Liu et al., 2022; Wu, 2016)* and combining simulation practice.

Table 2

Material intrinsic parameters

Material	Poisson's ratio	Shear modulus/Pa	Density/ (kg·m^{-3})
Organic fertilizer	0.315	5.5×10^{6}	1.25×10^{3}
Steel	0.30	7.90×10^{10}	7.90×10^{3}
Soil	0.3	5×10^{7}	2.60×10^{3}

Table 3

Material contact parameters

Material	Restore collision coefficient	Static friction coefficient	Rolling friction coefficient
Organic fertilizer -Organic fertilizer	0.01	1.2	1
Organic fertilizer-Steel	0.01	0.5	0.5
Organic fertilizer-Soil	0.01	0.8	0.6

Particle factory was set up at the inlet of the crushing unit to simulate the conveying of the granular organic fertilizer via the conveying unit. In the particle factory, two particle models separately for granular and caking organic fertilizers were generated, among which the granular model was generated at the moment of 0.05 s and lasted to the end of the simulation at a generating rate of 3000 s.

The caking fertilizer model was generated as follows. Firstly, 15 spheroidal particles with a radius of 40 mm were generated in the period of 0~0.05 s within the particle factory. After reading the data of the particle templates from the caking fertilizer model via the EDEM API at the moment of 0.052 s, the spheroidal particles with a radius of 40 mm were replaced by the block-shaped particles. The initial velocity of both particles was 0.1 m/s in the direction of the negative Z-axis. Figure 4(a) showed the organic fertilizer spreading model equipped with crushing unit, while Figure 4(b) showed the traditional centrifugal disc spreading model established in the same way.

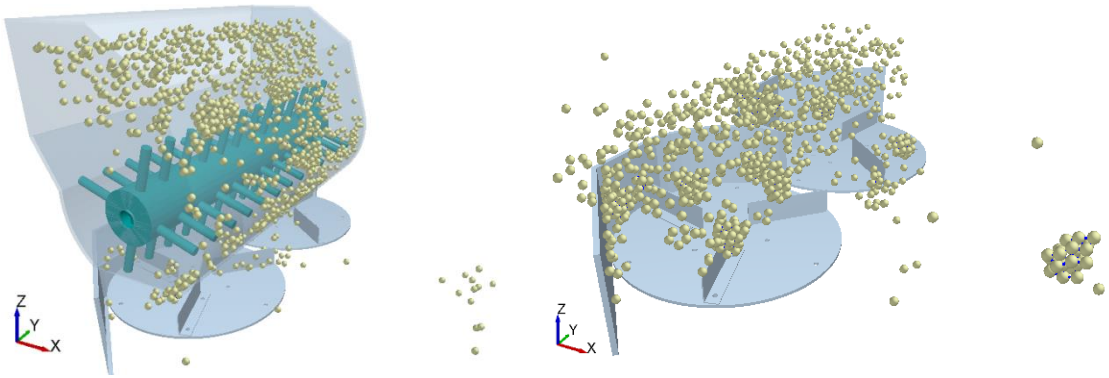

(a) organic fertilizer spreading model equipped with crushing unit (b) traditional centrifugal disc spreading model

Fig. 4 - Organic fertilizer spreading model

Numerical simulation and post-processing method

Simulation experiments on both spreading models were separately repeated three times with the simulation duration set to be 1 s, and data had been saved every 0.01 s.

In order to specify the interaction relationship between the organic fertilizer with the toothed shaft, the external wall and the disk in the improved spreading model, the velocity vector diagram of the granules moving at different moments was exported to observe the velocity vector direction of the organic fertilizer granules and the motion trend in the crushing unit to explore the crushing mechanism of the unit. To facilitate the quantitative analysis on the effect of crushing organic fertilizers in both spreading models during the spreading process, the total number of the bonds generated at the beginning of the simulation and the number of the bonds broken at the end of the simulation were calculated and then the average broken rate of the bonds was separately calculated in each spreading models.

RESULTS

After the simulation, the velocity vector diagram of the granules moving at different moments in the crushing unit was exported in the improved spreading model, as shown in Figure 5, where the direction of arrow, colour and length separately represented the direction of particle velocity, velocity and kinetic energy.

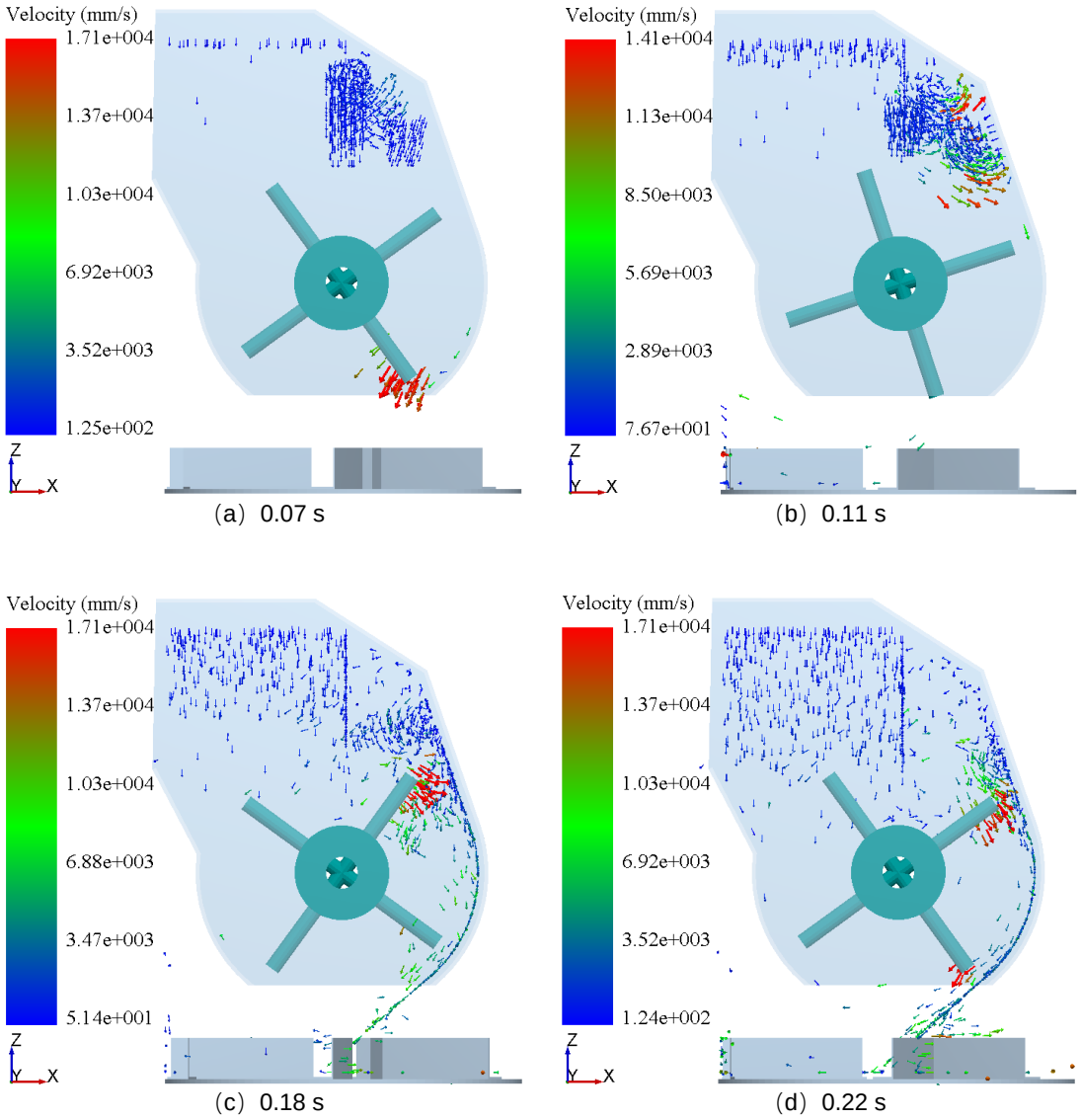

Fig. 5 - The velocity vector diagram of the granules

Figure 5(a) showed that at the outlet of the crushing unit, some granules still moved at high speed towards the disk, indicating the acceleration effect of the toothed shaft on those organic fertilizers that failed to pass through the gap between the teeth.

As shown in Figure 5(b), some granules collided with the external wall at high speed under the acceleration effect of the toothed shaft in the crushing unit. Also Figure 5 (c) and (d) showed the impact and squeezing actions between a handful of granules with the toothed shaft and the external wall. In conclusion, the high-speed collision, impact and squeezing actions between the organic fertilizer and the relevant components in the crushing unit had made a contribution to the crushing of caking organic fertilizers. To observe directly the breakage of the bonds and the crushing process of the block-shaped granules, the distribution variation diagrams of the bonds and the granules at different moments in the crushing unit were exported, as shown in Figures 6 and 7.

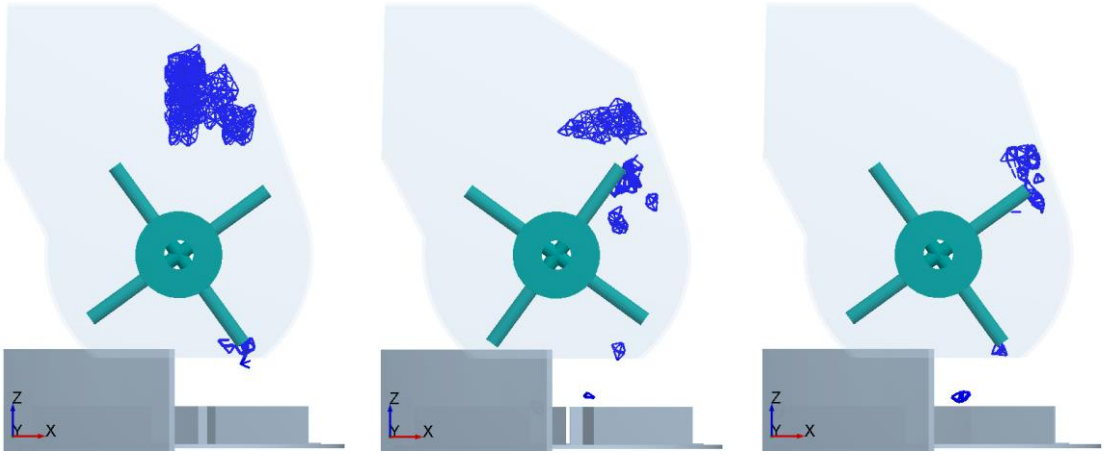

(a) 0.07 s (b) 0.18 s (c) 0.22 s

Fig. 6 - The distribution variation diagrams of the bonds

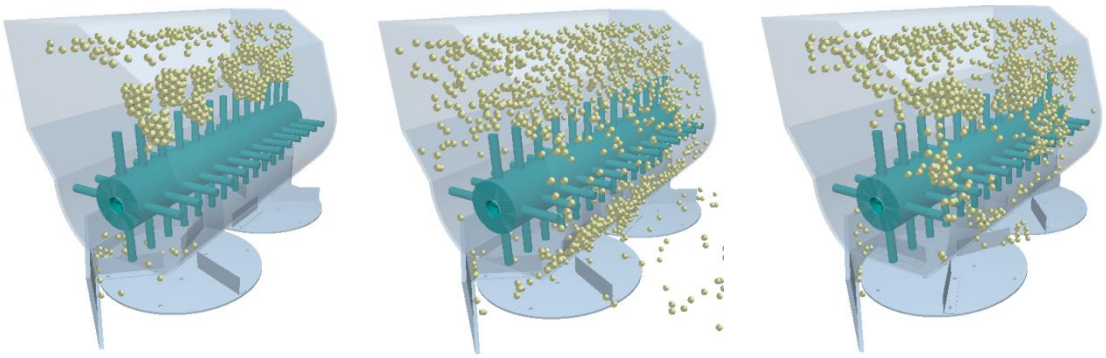

(a) 0.1 s (b) 0.15 s (c) 0.25 s

Fig. 7 - The distribution variation diagrams of the granules

Figures 6 and 7 showed that in the initial stage of the simulation, both of the bonds and the block-shaped granules were relatively intact. But in the period of 0.15~0.18 s, some bonds were broken and the block-shaped granules were crushed into smaller block-shaped particles or spheroidal particles. In the period of 0.22~0.25 s, the bonds were further broken up and the particles were separated into more pieces in smaller granular size.

Figure 8 showed the curves of the changes in the number of the broken bonds over time during the spreading process in each spreading model.

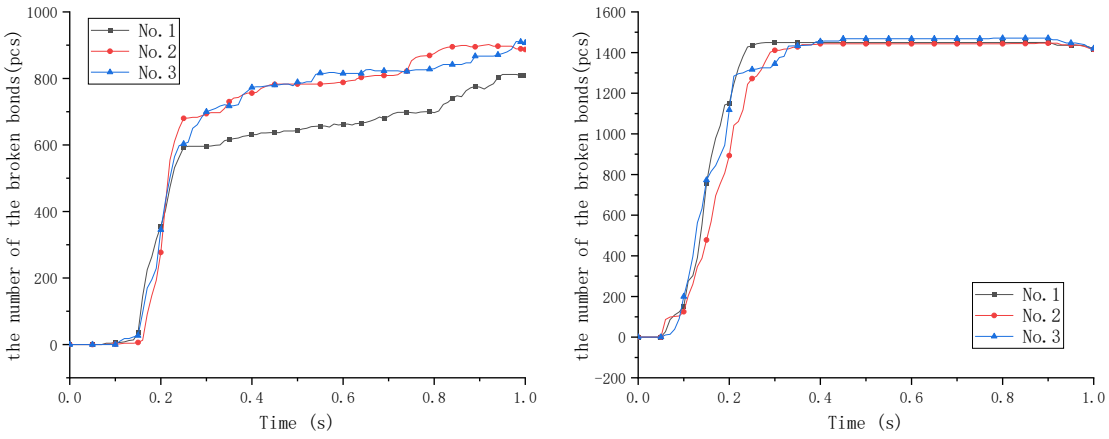

(a) traditional solution (b) improved solution

Fig. 8 - The curves of the changes in the number of the broken bonds over time

As shown in Figure 8, bonds were broken mainly before 0.25 s in both of the spreading models. Also in the experiments that had been repeated several times, the improved solution outperformed the traditional solution regarding the number of the broken bonds.

To facilitate the quantitative evaluation on both solutions in terms of the crushing of organic fertilizers, the total number of the bonds generated in the simulation process and the number of broken bonds at the end of simulation were separately calculated based on each solution to calculate the broken rate of bonds, as indicated in Table 4.

Table 4

Bonds data

solution	No.	total number of bonds/pcs	number of broken bonds/pcs	the broken rate of bonds/%	average value/%
traditional solution	1	1487	812	54.61	58.87
	2	1487	902	60.66	
	3	1485	911	61.35	
improved solution	1	1485	1452	97.78	98.05
	2	1476	1446	97.97	
	3	1495	1471	98.39	

As shown in Table 4, the average broken rate of bonds was separately 58.87% and 98.05% in both spreading models, proving that the improved solution outperformed the traditional solution in terms of the efficiency in crushing caking organic fertilizers.

CONCLUSIONS

(1) Aiming at the poor efficiency in crushing a handful of caking organic fertilizers spraying from the traditional disc spreader, an improved disc spreader equipped with spike-tooth crushing unit was designed with the introduction of its structural composition and working principle.

(2) The organic granular fertilizer model was built based on the EDEM software. Also based on the HMB (Hertz-Mindlin with bonding) contact model, the caking organic fertilizer bonding model and the organic fertilizer spreading models established before and after the structural improvement had been constructed with the running of the numerical simulation.

(3) Based on the analysis on the velocity vector diagram of the granules, the interaction relationship between the organic fertilizers with the toothed shaft, the external wall and the disk as well as the crushing principle were clearly specified. In order to compare the efficiency in crushing organic fertilizers during the spreading process based on both solutions, the total number of the bonds generated and broken in each spreading model was calculated, showing that the average broken rate of the bonds was separately 58.87% and 98.05% after the calculation made based on each solution. It proved that the improved solution was better than the traditional solution in terms of the efficiency in crushing caking organic fertilizers.

ACKNOWLEDGEMENT

This research, titled “Improvement Design and Simulation Analysis on Centrifugal Disc Organic Fertilizer Spreader”, was supported by “Key R&D Program of Shanxi Province, China” (201903D211002-04).

REFERENCES

[1] Cârdei P., Ştefan V., Popa L., Ciuperca R., (2019), Statistical models for the working process carried out by the organic fertilizer spreading machine. *INMATEH Agricultural Engineering*, Vol.58, Issue 2, pp.121-128, Bucharest/Romania.

[2] Du W.Y., Tang S., Wang H., (2020), The status of organic fertilizer industry and organic fertilizer resources in China. *Soil and Fertilizer Sciences in China*, Vol.287, Issue 3, pp.210-219, Beijing / China.

[3] Fang P.P., Abler D., Lin G.H., Sher A., Quan Q., (2021), Substituting Organic Fertilizer for Chemical Fertilizer: Evidence from Apple Growers in China. *Land*, Vol.10, Issue 8:858, Basel/ Switzerland.

[4] Jiang S.T., Li H., Peng H.Y., Mei X.L., Chen T.S., Xu Y.C., Dong C.X., Shen Q.R.,(2023), Effects of partial substitution of chemical fertilizer with organic fertilizer on arbuscular mycorrhizal fungal community of Mangifera indica. *Chinese Journal of Applied Ecology*, Vol.34, Issue 2, pp.481-490, Shenyang / China.

[5] Li J.G., Liu X.M., Zou L.L., Yin R.G., Yang K., Yuan J., (2021), Discrete Element Modeling Method and Experimental Verification of Spinach Main-root. *Journal of Agricultural Mechanization Research*, Vol.43, Issue 08, pp.181-185+191, Harbin/China.

[6] Li L., Cui Q.L., Zhang Y.Q., Hou H.M., Xi P., Hao C., (2022), Experimental Study on Scattering Performance of Organic Fertilizer Spreader Based on EDEM. *Agricultural engineering*, Vol.12, Issue 3, pp.88-94, Beijing / China.

[7] Liu H.X., Du C.L., Yin L.W., Zhang G.F., (2022), Shooting Flow Shape and Control of Organic Fertilizer Side Throwing on Inclined Opposite Discs. *Transactions of the Chinese Society for Agricultural Machinery*, Vol.53, Issue 1, pp.168-177, Beijing / China.

[8] Lyu J.Q., Sun Y.K., Li J.C., Li Z.H., Liu Z.Y., (2020), Design and test of vertical spiral organic fertilizer spreading device. *Transactions of the Chinese Society of Agricultural Engineering (Transactions of the CSAE*), Vol.36, Issue 24, pp.19-28, Beijing / China.

[9] Ma B., Fu J.J., Xu B.X., Wu A.B., Xie H., Chen Y.S., (2019), Research on manure spreader technology and equipment. *Journal of Chinese Agricultural Mechanization*, Vol.40, Issue 08, pp.1-6, Nanjing/China.

[10] Sun D.X., Li M.J., Wu A.B., Liang Q., Zhang A.M., (2019), Research progress of organic fertilizer and its supporting mechanization technology. *Journal of Chinese Agricultural Mechanization*, Vol.40, Issue 02, pp.72-80, Nanjing/China.

[11] Ştefan V., Cârdei P., Popa L., David L., Ciupercă R., (2019), Influence of the manure spreading machines' working parameters on the qualitative performances of the fertilization process. *INMATEH Agricultural Engineering,* Vol.58, Issue 2, pp.115-120, Bucharest/Romania.

[12] Wen C.Y., Xiong Y.H., Wang P. Zhang Z.Y., Yao X.Y., Peng Z.Q., Chen J., Wu Y.S., (2023), Effects of Reduced Chemical Fertilizer with Organic Fertilizer Application on Yield and Quality of High-quality Indica Rice. *Soils*, Vol.55, Issue 02, pp.280-287, Nanjing/China.

[13] Wu H., Liu X.F., Zhang H.B., Chen W.X., (2022), Design and Test of the Spreading Device of Organic Fertilizer Spreader. *Journal of Agricultural Mechanization Research*, Vol.44, Issue 11, pp.113-118, Harbin/China.

[14] Wu N., (2016), *Research and Design of 2F50 Manure Spreader.* Master thesis. Chinese Academy of Agricultural Mechanization Sciences, Beijing/China.

[15] Xu B.X., Chen Y.S., Chen M.J., Ma B., Gao Q.M., Wu A.B.,(2022), Research status and development trend of organic fertilizer application equipment for field crops in China. J*ournal of Chinese Agricultural Mechanization,* Vol.43, Issue 12, pp.20-25, Nanjing/China.

[16] Zinkevičienė R., Jotautienė E., Juostas A., Comparetti A., Vaiciukevičius E., (2021), Simulation of Granular Organic Fertilizer Application by Centrifugal Spreader. *Agronomy*, Vol.11, Issue 2:247, Basel/ Switzerland.

[17] ***China Academy of Agricultural Mechanization Sciences, (2007), Agricultural Machinery Design Manual (农业机械设计手册). ISBN 9787802333352, *China Agricultural Science and Technology Press*, Beijing/China.

[18] ***Wang G.Q., (2010), Discrete element method and its application in EDEM (离散单元法及其在 EDEM 上的实践), ISBN 9787561227978, *Northwestern Polytechnic University Press*, Xi'an/China.

IMPROVED DESIGN AND EXPERIMENT OF ANTI-CLAY ADHESION FOR NO-TILLAGE MAIZE PLANTER SEEDING MONOMER
/
玉米免耕机播种单体防黏土改进设计与试验

Min FU*[,1)], Rongfeng LI[1)], Yilin HAO[1)], Fanhua MENG[2)], Jiacheng ZHOU[1)], Chengmeng WANG[1)]
[1)] Northeast Forestry University, College of Mechanical and Electrical Engineering, Harbin / China;
[2)] Heilongjiang DEWO Technology Development Co., Ltd, Harbin / China
Tel: +86 15663688203; E-mail: fumin1996@163.com
DOI: https://doi.org/10.35633/inmateh-70-33

Keywords: *no-tillage seeding; seeding monomer; soil-contacting part; clay soil; TRIZ (Theory of Inventive Problem Solving)*

ABSTRACT
When the seeding monomer of no-tillage maize planter operates in sticky and wet soil, soil bonding and blocking of soil-touching parts will occur to different degrees, leading to functional failure and affecting the quality of seeding operation. Aiming to improve the anti-adhesion property with minimum cost, a seeding monomer is modified to operate in sticky and wet soil with the support of TRIZ (Theory of Inventive Problem Solving). There are two major scheme adjustments, including self-cleaning seedbed collating device and split gauge wheel. The Su-field model of seedbed collating device is constructed, and the design scheme of smaller wavy coulter and dirt scraper is proposed on the basis of the standard-solution tool and water-film theory. And the parameters of the wave are determined on account of force analysis of soil particles and bionic earthworm. Based on the systemic-functional analysis of the seeding depth-limiting device and the force analysis of gauge wheel during operation, a split type of depth-gauge wheel with large lug hole is designed. As a result, the field trial demonstrates that the improved monomer could meet the operation requirements of clay soil with the water content of 15%-25%. Compared with the original model, the residual clay content is decreased (seedbed collating device 57.5%, gauge wheel seeding depth-limiting device 10%). This study can provide reference for the anti-adhesion design of soil-contacting parts of agricultural machinery.

摘要
玉米免耕播种机的播种单体在黏湿土壤中作业时，各触土部件会发生不同程度的土壤粘结与堵塞，导致功能失效，影响播种作业质量。以最小代价提高抗粘性能为目标，应用 TRIZ 理论辅助分析求解改进方案，设计了一种适于黏湿土壤作业的具有自清洁式种床整理装置、分体式播种限深轮的播种单体。构建了种床整理装置的问题“物-场模型”，基于“标准解工具”和水膜理论提出小波纹形破茬刀盘组合刮土刀的设计方案；通过波纹圆盘破茬刀运动时土壤质点受力分析，结合仿生蚯蚓确定波纹形状参数。基于播种限深装置的“系统功能分析”和限深轮作业过程受力分析，设计了分体式大腰孔限深轮。田间试验表明，改进后的播种单体能够满足含水量在 15%~25%黏壤土的播种作业要求，与原机型相比，种床整理装置和限深装置的残留粘土量分别下降 57.5%、10%。该研究可为农机触土部件抗土壤粘附设计提供参考。

INTRODUCTION
No-tillage Maize Planter is a key tool for the conservation tillage of maize, the composition mainly includes seedbed collating device, seeding depth-limiting device, soil-covering device, etc *(Yalcin et al., 2005; Jia et al., 2017)*. And the operation quality of each soil-contacting device of seeding monomer directly affects the maize yield. During the spring ploughing period in Heilongjiang Province, China, the soil is sticky and wet, hence the soil-contacting parts of the seeding monomer may have different degrees of soil bonding and blocking, which leads to the decline of operation quality.

In recent years, many companies and scholars have conducted in-depth research on seeding monomers. The 1950 series no-tillage maize planter, produced by John Deere in the United States, has seeding monomer with side-position depth-gauge wheel, which can ensure the consistent seeding depth *(Morrison et al., 2002).* The YP series no-tillage maize planter produced by Great Plains has the seeding monomer with wavy coulter and the double-disc furrow opener with non-isometric dislocation arrangement, making the effects of soil-breaking and stubble-breaking better *(Triplett et al., 2008)*.

[1] *Min Fu, Prof.; Rongfeng Li, M.S.Stud.Eng; Yilin Hao, M.S.Stud.Eng; Fanhua Meng, Engineer; Jiacheng Zhou, M.S.Stud.Eng; Chengmeng Wang M.S.Stud.Eng;*

The ED series no-tillage maize planter produced by Amazone in Germany has the seeding monomer adopting the stubble-cutting mode of gravity double-disc furrow opener, and the scalpriform furrow opener installed directly behind the disc can determine the seeding position and the embedment direction of seeds *(Fuentes-Llanillo et al., 2021).* Meanwhile, scholars have also conducted detailed research on the problem of preventing soil adhesion in the soil-touching parts of no-tillers. Jafar Massah, Iran et al. designed corrugated blades by simulating the body geometry of armadillo (*Massah et al., 2020)*. Massah Jafar et al. optimized the design of soil tilling components based on the bionic electro osmosis technology and the biometric features of animal body surface to reduce the adhesion of soil (*Massah et al., 2021)*.

In the 1990s, the no-tillage maize planter was introduced in China, and local improvements were made according to actual demands. Zhao et al. designed a profiling compacting device of seeding monomer that is suitable for hilly areas and established an interaction model between compacting device and soil, which combined with the characteristics of the soil *(Zhao et al., 2017)*. Gao et al. proposed a method of down-force control of seeding monomer based on the pressure of airbag and the dip angle of profiling four-bar linkage, which was used to precisely control the seeding depth *(Gao et al., 2019)*. Jia et al. designed an anti-blocking stubble-breaking machine for inter-row no-tillage, using the intermittent arrangement of cutter teeth with high cutting effect and low soil adhesion *(Jia et al., 2013)*. Hou et al. designed the seeding monomer of double-DOF multi-articulated profiling no-tillage machine, with ploughshare-type furrow opener and separate soil-covering device as well as compacting device *(Hou et al., 2019).* The soil-covering and compacting wheel of seeding monomer designed by Guo et al. adopted the conical wheel structure, which can realize soil-covering and compacting at one time *(Guo et al., 2017).*

The above research provides useful references for the improved design of no-tillage maize planter seeding monomer, however, the research on the causes of failure of soil-contacting parts in sticky and wet soil as well as the anti-adhesion design of seeding monomer are still not sufficient. In this paper, TRIZ (Theory of Inventive Problem Solving) is used to analyse the failure causes, identify critical imperfections and improving directions *(Altshuller, 1984).* Combined with the force analysis of the seeding process, the seeding monomer with self-cleaning seedbed collating device and split gauge wheel is designed. The implementation effect of the improved scheme is verified by field trials.

MATERIALS AND METHODS

Overall Structure

The seeding monomer structure of commonly used traction-type no-tillage maize planter is shown in Fig. 1, which is mainly composed of wavy coulter, four-bar linkage, double-disc furrow opener, depth-gauge wheel, support arm, soil-covering wheel, etc.

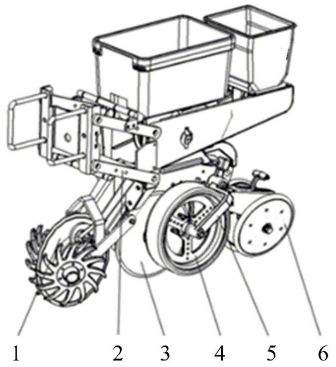

Fig. 1 - Schematic diagram of the seeding monomer of no-tillage maize planter

1. wavy coulter; 2. four-bar linkage; 3. double-disc furrow opener; 4. gauge wheel; 5. support arm; 6. soil-covering wheel

Operating Principle

The seeding monomer of no-tillage maize planter is hooked up to the whole machine frame and is towed by the tractor for work *(Lin et al., 2015).* During the seeding operation, the wavy coulter cuts into the soil, as well as cuts the stubble and straw on the seeding path to complete the collation of seedbed. Then, the double-disc furrow opener cuts the soil along the seeding path to form a seeding furrow, and the seed-metering device sends maize seeds to the bottom of the seeding furrow to complete the seeding operation. The soil-covering wheels arranged in a V-shape squeezes the soil on both sides of the seeding path into the seeding furrow. The soil-covering wheel rolls and compacts to complete the operation.

Problems in the Operation of Sticky and Wet Soil

The seeding monomer can successively realize the functions of seedbed collating, depth-limiting furrow seeding, and soil-covering compacting, etc. The soil-contacting parts include wavy coulter, gauge wheel, double-disc furrow opener and soil-covering wheel *(Wang et al., 2021; Fu et al., 2022).* When working in the sticky and wet soil, each soil-contacting part is in direct contact with the soil, resulting in different degrees of soil adhesion problems (see Fig. 2).

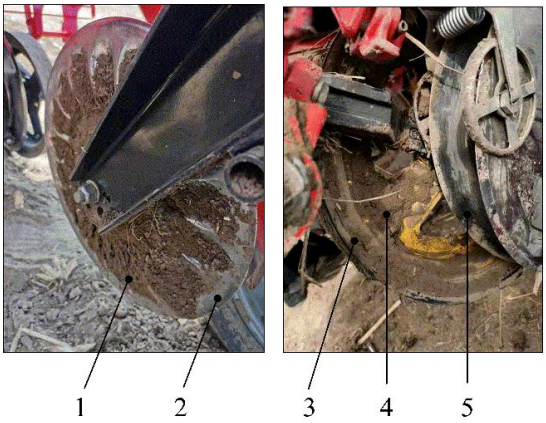

*(**a**) Actual bonding situation of corrugated cutter head* *(**b**) Actual bonding situation of gauge wheel*

Fig. 2 - Actual bonding situation in soil-contacting parts of seeding monomer.

1. clay on wavy coulter; 2. wavy coulter; 3. gauge wheel; 4. clay on gauge wheel; 5. double-disc furrow opener

Improved Design of Seeding Monomer Based on TRIZ

TRIZ is a systematic and structured innovation methodology *(Altshuller, 1984)*. It is effective in breaking through inertial thinking, inspiring innovative consciousness, expanding design ideas, assisting innovation designs, and solving technical problems *(Kang et al., 2022; Fu, 2021)*. In this paper, TRIZ is applied to analyse the soil-adhesion problem of the soil-contacting part of seeding monomer, with the goals of improving the anti-adhesion property at the minimum cost and solving the scheme of improved design.

Improved Design of Wavy Coulter Based on Su-Field Analysis

Coulter is the core component of seedbed collating device, and its function is to cut stubble and straw on the seeding path, so as to provide a favourable seedbed for the germination and growth of seeds *(Gao, 2002; Gao et al., 2008; Liao et al., 2004).* When operating in clay soil, the wavy coulter bond to the soil and accumulate continually, leading to the increase of soil movement and power consumption. The Su-field model of the problem, as shown in Fig. 3, shows that the clay soil has a harmful adhesion effect on the wavy coulter.

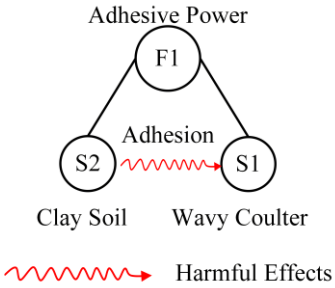

Fig. 3 - Analysis of Su-Field model of the wavy coulter

The standard solution S1.2.2 in TRIZ, that is, the introduction of the deformation of S1 or S2, is applied to eliminate the harmful effects *(Fu, 2021)*, and the improved conceptual scheme 1, that is, the change of configuration and parameter of the wavy coulter (i.e. deformation of S1) is proposed. According to the water-film theory, the adhesion of soil to metal is related to the contact area of soil and metal parts, the larger the contact area, the easier it is to form a water-film layer and the greater the adhesion of clay soil *(Zuo et al., 1997; Zheng, 2019)*. The smaller wavy coulter can reduce the contact area with the clay soil and avoid the formation of a continuous water film interface, thus reducing the adhesion amount of soil.

The standard solution S1.2.1 in TRIZ, that is, the introduction of S3, is applied to eliminate the harmful effects *(Fu, 2021)*, and the improved conceptual scheme 2, that is, adding a scraper, is proposed to scrape away the attached clay soil on the disc surface.

Design on Structure and Key Parameters of the Improved Scheme

1) Overall Structure and Anti-adhesion Operating Principle

The structure of the seedbed collating device with anti-adhesion property designed by the improved conceptual solution is shown in Fig. 4. The rack and weeding machine of improved seedbed collating device adopt original structure, and change the configuration and parameter of the wavy coulter so as to reduce the contact area with soil. Besides, cambered scraper is added to the racks on both sides of wavy coulter, aiming to scrape away the clay attached on the disc surface.

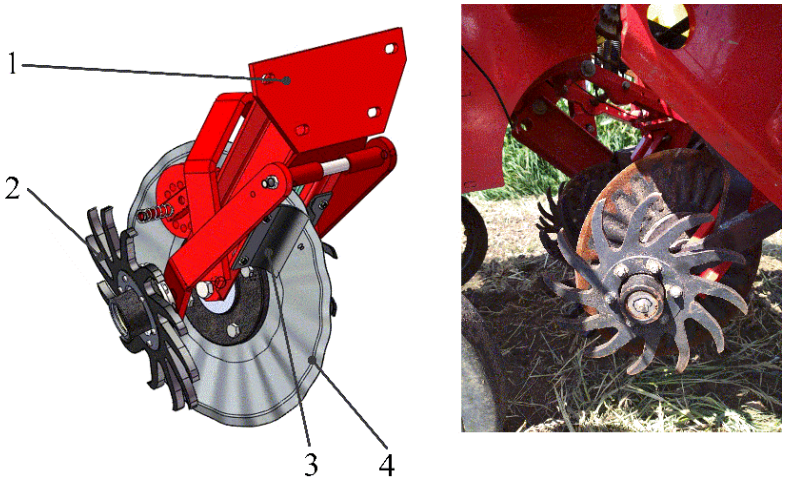

(a) 3D model *(b) Physical model*

Fig. 4 - Structure of improved wavy coulter

1. racks; 2. assembly of weeding wheel; 3. cambered scraper; 4. modified-wavy coulter

2) Design of Key Parameters of Improved Scheme

According to the agronomic requirements of stubble cutting and rod cutting, the modified-wavy coulter is determined as 400 mm in diameter, 4 mm in thickness and 65 Mn in material. The corrugation on the surface of coulter is formed by stamping. In this paper, the corrugation parameters are determined by the force analysis of soil particles *(Wan et al., 2014; Bai et al., 2014)* (see Fig. 5) during the movement of soil and the wavy coulter.

The resultant force at the force point Q is mainly generated by the friction between clay soil and the wavy coulter as well as the mutual extrusion of the two. From Fig. 5, the three component forces of the resultant force F_n are:

$$F_c = F_n \cos\alpha \cos\beta \quad (1)$$

$$F_a = F_c \tan\beta \quad (2)$$

$$F_z = \frac{F_c \tan\alpha}{\cos\beta} \quad (3)$$

When the no-tillage machine is operating at a constant speed, the angular velocity at point Q is invariable, hence the torque at point Q is unchanged. As a result, the circumferential force F_c at point Q is constant. To reduce the amount of soil adhesion, the lateral force F_z and radial force F_a should be reduced.

It can be seen from Equation (2) that the smaller the angle β, the smaller the radial force F_a. If the angle $\beta = 0°$ then the radial force $F_a = 0$, which can eliminate the adhesive attraction of soil to the wavy coulter along the radial direction.

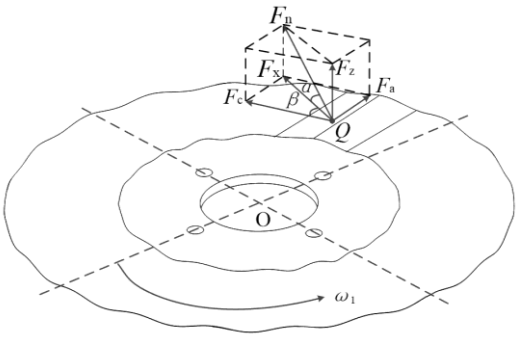

Fig. 5 - Force analysis of soil particles during the movement of wavy coulter

1. raised corrugation; 2. wavy coulter; Q is the force point, O is the centre of rotation.

F_c is circumferential force; F_a is radial force; F_z is lateral force; F_n is the resultant force at the point Q; F_x is the horizontal component of the force F_n; α is the angle between the force F_n and the force F_x. β is the angle between force F_c and force F_v.

The configuration of wave crest directly affects the anti-adhesion property and operation resistance *(Zeng et al., 2018)*. At present, the commonly used corrugated configuration is cambered wave crest. Since the area of arc between two points (lines) is larger than the area of plane, it is easier to form water-film to produce the adhesion phenomenon. In this paper, the plane shape of wave crest is used for structural design. When the angle β = 0 °, the stress state of the two crest surfaces is shown in Fig. 6.

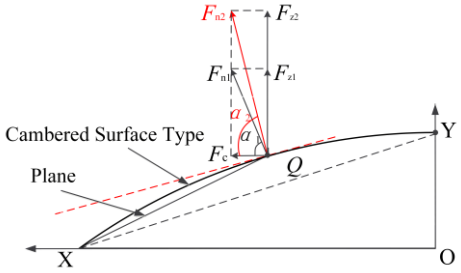

Fig. 6 - Stress states of two wave crests surfaces

Q is the force point, O is the centre of symmetry. F_c is the circumferential force; F_{n1} is the resultant force at point Q of the plane wave crest; F_{n2} is the resultant force at the point Q of the cambered wave crest; F_{c1} is the lateral force at the point Q for plane wave crests; F_{c2} is the lateral force at the point Q for cambered wave crests; α_1 is the angle between the force F_{n1} and the force F_c. α_2 is the angle between the force F_{n1} and the force F_c.

From Equation (3), it can be seen that the smaller the angle α , the smaller the lateral force F_z on the Q point. It can be seen from Fig. 6 that since the angle α_1 is smaller than the angle α_2, the lateral force F_{z1} on the plane wave crest is smaller than the lateral force F_{z2} on the cambered wave crest, which can reduce the soil adhesion to the wavy coulter along the normal direction.

The structure of the plane wave crest is determined by the wave height h and the wave width b. The local structure and stress state of the plane wave crest are shown in Fig. 7.

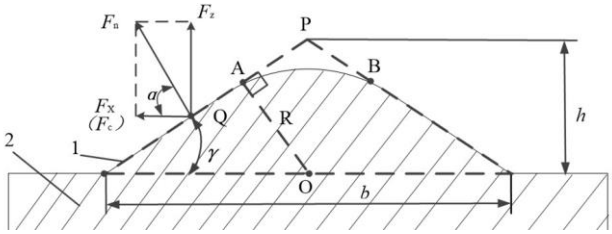

Fig. 7 - Local structure and stress state of the plane wave crest

1. surface of wave crest; 2. coulter

Q is the force particle; h is the wave height; b is the wave width; F_n is the resultant force at the point Q; F_x is the horizontal component of the force F_n; F_c is the circumferential force; α is the angle between the force F_n and the force F_x. γ is the angle between the crestal plane of corrugation and the horizontal plane. O is the arc centre of wave crest. R is the arc radius of wave crest.

From Fig. 7, it can be seen that the angle between the crestal plane of corrugation and the horizontal plane γ is:

$$\gamma = \arctan\frac{2h}{b} \quad (4)$$

Earthworm, as a soil organism, has excellent anti-adhesion property. This paper uses bionic earthworm to determine the corrugation configuration parameters.

According to the characteristics of earthworm skin shape, the ratio of wave height h to wave width b is 1:3 *(Ma et al., 2014)*. Take h=9 mm *(Wei et al., 2017)*, b=27 mm, and substitute them into Equation (4) to get $\gamma \approx 34^{o}$.

Considering the requirements of stamping process and reducing operation resistance, the wave crest needs to be chamfered, and the radius of chamfering arc R is:

$$R = \frac{b}{2}\sin\gamma \quad (5)$$

Substituting b=27 mm, $\gamma \approx 34^{o}$ into Equation (5) yields R=7.55 mm.

The structural parameters of the modified-wavy coulter are compared with the original coulter, as shown in Table 1. The comparison of the physical drawing is shown in Fig. 8.

Table 1

Parameters of wavy coulter

Structural style	Cutter diameter (mm)	Wave height (mm)	Wave width (mm)	Corrugated surface Form
Original-wavy coulter	400	15	30	Cambered type
Modified-wavy coulter	400	9	27	Plane type

(a) original-wavy coulter *(b) modified-wavy coulter*

Fig. 8 - The Physical drawing comparison

Improved Design of Seeding Depth-limiting Device Based on Systemic-Functional Analysis

The function of the seeding depth-limiting device is to carry the operating weight of the seeding monomer and to control the depth of the furrow opener cutting into the soil. In this paper, the systemic-functional analysis in TRIZ is used to analyse the functional structure of the depth-limiting device, identify critical defects, and search for improved scheme on solving the problem of soil adhesion.

Name of system: seeding depth-limiting device.

Function of system: control the depth of seeding.

Object of system: soil.

Components of system: seeding monomer racks, double-disc furrow opener, integrated gauge wheel, support arm, depth-adjusting handle, scraper on seeding furrow opener, scraper on gauge wheel circumference.

Components of super-system: whole machine racks, sticky soil.

The functional relationships among functional objects, system components and super-system components are analysed, and the systemic-functional model diagram of seeding depth-limiting device is established (see Fig. 9).

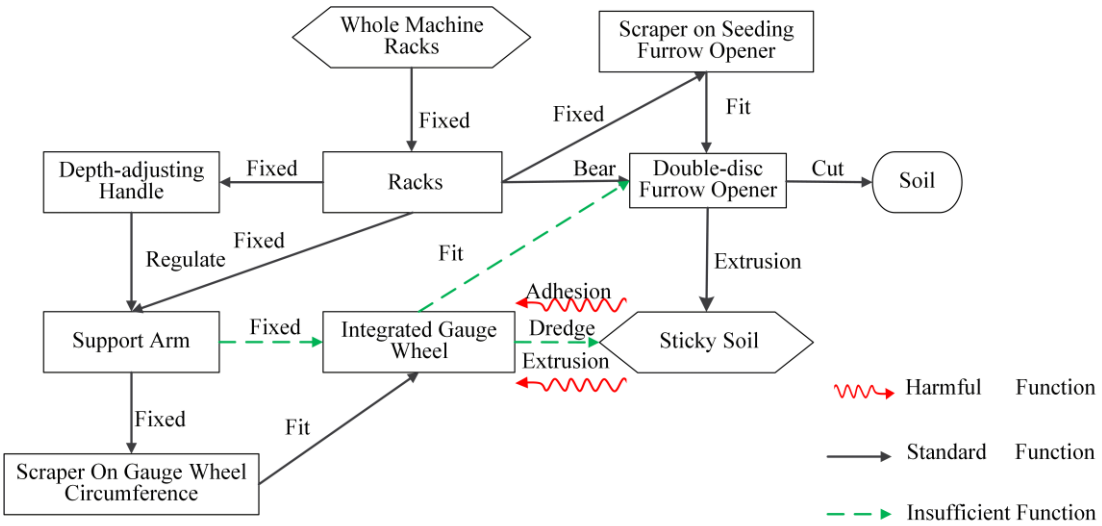

Fig. 9 - Systemic-functional analysis of depth-limiting device

From Fig. 9, it can be seen that the seeding depth-limiting device has five critical defects. The integrated gauge wheel is a key component to solve the anti-adhesion problem of seeding depth-limiting device. Therefore, conceptual scheme 3 is proposed to improve the structure of the integrated gauge wheel and its manner of supporting and fixing.

Improved Design of the Structure of Gauge Wheel

(1) Integrated Gauge Wheel Structure of the Original Model

The structure of the integrated gauge wheel of the original model is shown in Fig. 10. The hub and spokes are formed all-in-one by stamping steel plate, and the wheel body is covered with three lug holes.

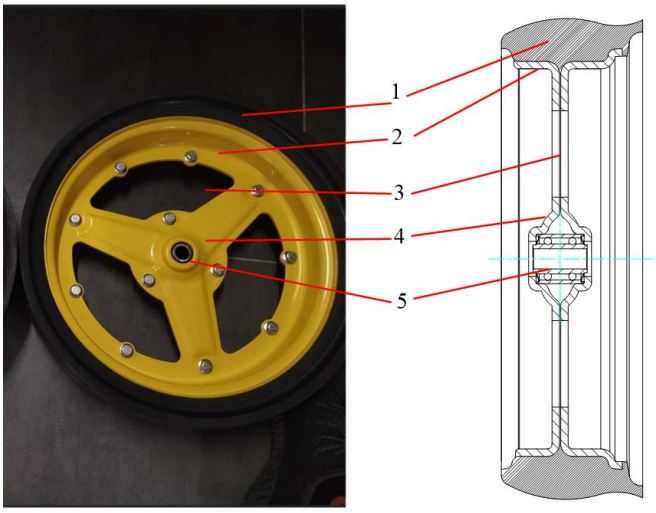

(a) Physical model *(b) Cutaway view*

Fig. 10 - Structure of integrated gauge wheel

1. tire; 2. wheel hub; 3. lug hole; 4. wheel spokes; 5. bearing

(2) Force Analysis of Integrated Gauge Wheel during Operation

When operating on sticky and wet soil, the position of clay soil of the integrated gauge wheel is located between the furrow opener and gauge wheel, and the maximum extrusion force of clay soil on the hub of the gauge wheel is formed at the maximum soil-separation position of the furrow opener (see Fig. 11a.).

In order to balance the maximum extrusion force, a pair of equilibrium moments around point O are generated at the connection points A and C of the gauge wheel. After decomposition and transmission, radial extrusion force is formed on points A and C, and axial extrusion force is formed on points B and D. The force analysis is shown in Fig. 11 (b).

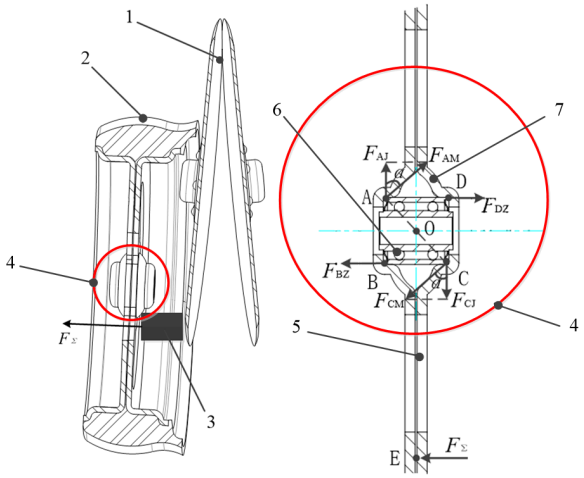

(a) Position of soil extrusion force *(b) Force analysis of connection position*

Fig. 11 - Soil-adhesion position and force analysis of integrated gauge wheel

1. double-disc furrow opener; 2. integrated gauge wheel; 3. clay soil; 4. connecting parts; 5. lug hole; 6. Bearing; 7. integrated hub

A, B, C, D are the four force points. O is the centre of deflection torque. E is the action point of extrusion force. F_{Σ} is the soil extrusion force. F_{AJ} is the radial force at A. F_{AM} is the deflecting force at A. F_{BZ} is the axial force at B. F_{BJ} is the radial pressure at B. F_{CM} is the deflecting force at C. F_{CJ} is the radial-deflecting component force at C. F_{DZ} is the axial force at D.

Assuming that the fixed axis of the gauge wheel is absolutely rigid. Set the distance between OE as L_1, $OC = OA$ as L_2, the following relationship can be obtained from Fig. 11(b).

$$F_{\Sigma} L_1 = F_{AM} L_2 = F_{CM} L_2 \tag{6}$$

According to Fig. 11(b) and Equation (6), the forces acting on each local contact position can be obtained as follows.

Radial force at point A:

$$F_{AJ} = \frac{F_{\Sigma} L_1}{L_2} \cos\alpha \tag{7}$$

Axial force at point B:

$$F_{BZ} = \frac{F_{\Sigma} L_1}{L_2} \sin\alpha \tag{8}$$

Radial force at point C:

$$F_{CJ} = \frac{F_{\Sigma} L_1}{L_2} \cos\alpha \tag{9}$$

Point D axial force:

$$F_{DZ} = \frac{F_{\Sigma} L_1}{L_2} \sin\alpha \tag{10}$$

As can be seen from Fig. 11 (a), the extrusion force of sticky soil is generated by the small area of lug hole on the gauge wheel and the weak dredging ability of sticky soil, which in turn forms the deflection torque. As shown in Fig. 11 (b), since the bearing hole of the integrated gauge wheel spoke is in local contact with both ends of the bearing, deformation occurs at the fit of the two ends under the extrusion force of constantly changing size and direction, resulting in a larger aperture at the fitting location, as well as making the gauge wheel detach from the fixed support arm.

From Equation (7) to Equation (10), it can be seen that the harmful extrusion forces on the integrated gauge wheel and the fitting location of bearings are all formed by the conversion of the extrusion force F_{Σ} of sticky soil.

Through the above analysis, it can be clear that the following weaknesses are supported to be improved: ① the fitting forms of the depth-limiting spoke and bearings need to be improved to enhance the connection strength. ② the form of the lug hole of the gauge wheel needs to be improved to enhance the dredging ability of sticky soil, hence reduce or eliminate the extrusion force F_{Σ}.

(3) Structure of Split Gauge Wheel

The structure of the improved split gauge wheel is shown in Fig. 12. In view of the two weaknesses mentioned in the previous section, the gauge wheel spoke and hub adopt split structure. The hub and spoke are joint by bolt groups to maximize the area of the lug hole. According to Newton's Third Law, as the area of the lug hole increases, the obstruction to clay soil decreases. Therefore, no clay soil can be formed between the gauge wheel and the double-disc furrow opener, and no extrusion force on the gauge wheel can be generated, thus the stability of the depth-limiting device in the operation of sticky and wet soil can be improved.

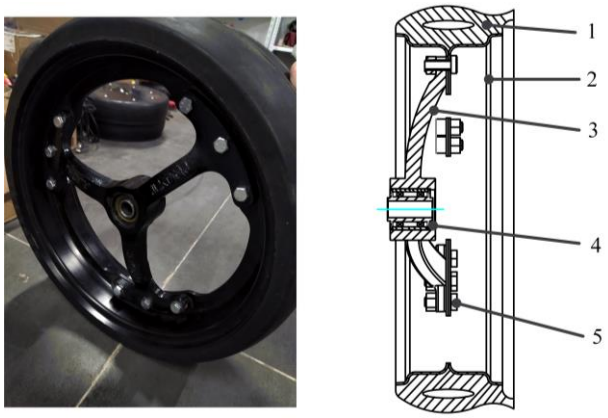

(a) Physical drawing *(b) Cutaway view*

Fig. 12 - Structure of split gauge wheel

1. tires; 2. hubs; 3. spokes; 4. bearings; 5. bolts

Improved Design of the Overall Structure of Seeding Monomer

The improved 3D model of the seeding monomer is shown in Fig. 13(a), and the physical prototype is shown in Fig. 13(b). The weight of the seeding monomer is 160 kg, and the boundary dimensions are 1580 mm × 1127 mm × 343 mm.

(a) 3D model *(b) Physical model*

Fig. 13 - Improved seeding monomer

For the improved seeding monomer, the configuration and parameters of the wavy coulter is changed, and a cambered scraper to remove the sticky soil on the disc surface is added. The integrated gauge wheel of the depth-limiting device is improved into a split gauge wheel, that is, the spoke and hub of the gauge wheel adopt a split structure, while the contact area between the mating hole of spoke bearing and the outer-ring of bearing is increased to improve the strength of the connection support. The area of the lug hole is increased to reduce the obstruction of sticky soil, and the independent regulation of left and right gauge wheels is changed into an integrated linkage mode.

Conditions for Trials

In April 2022, the verification trial was conducted in the experimental field of Devo Group, Shuangcheng District, Harbin City, Heilongjiang Province (126°52′, 45°53′), China. The original and improved seeding monomers were hooked up to the 2BMQ-2 no-tillage maize planter at the same time, and field trials were conducted in designated areas of the experimental field.

Method for Trials

Due to the different functions of each soil-contacting part, different experimental methods should be adopted. A comparative trial is carried out on the seedbed collating device. The two improved schemes of modified-wavy coulter as well as modified-wavy coulter and dirt scraper are compared with the original model, and the clay weight of the wavy coulter for three schemes are recorded.

A mixed orthogonal test with three factors and three levels is used for the seeding depth-limiting device, with 17 sets of tests for each device. Each group of tests is operated continuously for one hour. After collecting the residual clay soil inside the gauge wheel hub, the weight statistics are made. The improved performance of seeding depth-limiting device is evaluated according to the weight of the residual clay soil.

The seeding depth-limiting device takes the clay amount y_1 inside the wheel hub as the test index. The relative water content of soil A, the operating speed B, and the lug hole area of gauge wheel C are selected as the test factors. According to agronomic requirements, the range of relative water content of soil is from 15% to 25%, so the level of test factor A is proposed to be 15%, 20%, and 25%. The speed range of field operation of 2BMQ-2 no-tillage maize planter is from 6 km/h to 8 km/h, so the level of test factor B is proposed to be 6 km/h, 7 km/h, 8 km/h. The current gauge wheel is mainly no-lug hole or integrated semi-open lug hole structure. The improved split open-lug hole is designed in this paper, whose area is 5×10^4 mm^2, so the level of test factor C is proposed to be 0 mm^2 (no-lug hole), 2.7×10^4 mm^2 (lug hole area of the original model), 5×10^4 mm^2. The level coding of test factors is shown in Table 2.

Table 2

Coding table of factor levels

Level	1	2	3
Water content A/ (%)	15	20	25
Operating speed B/(km/h)	6	7	8
Lug hole area C/ (mm^2)	0	2.7×10^4	5×10^4

Test method of test index: Take the amount of soil-adhesion as the test index. After each test, use a soil-spade to clear and collect the clay soil at the inner side of the gauge wheel hub, then use spring scales to weigh separately. Each group of tests should be repeated three times to get the mean value.

RESULTS

Trial Results

The results of comparative trials of seedbed collating device are shown in Table 3. The results show that the amount of soil-adhesion adopted by scheme of modified-wavy coulter and dirt scraper is reduced by 57.5%, compared with that of original model.

Table 3

The clay amount of seedbed collating device

Time/h	0.5	1	1.5
Modified-wavy coulter combination scraper/ (g)	708	787	852
Modified-wavy coulter /(g)	721	973	1250
Original- wavy coulter / (g)	924	1632	1978

The results of comparative trials of gauge wheel of the depth-limiting device is shown in Fig. 14.

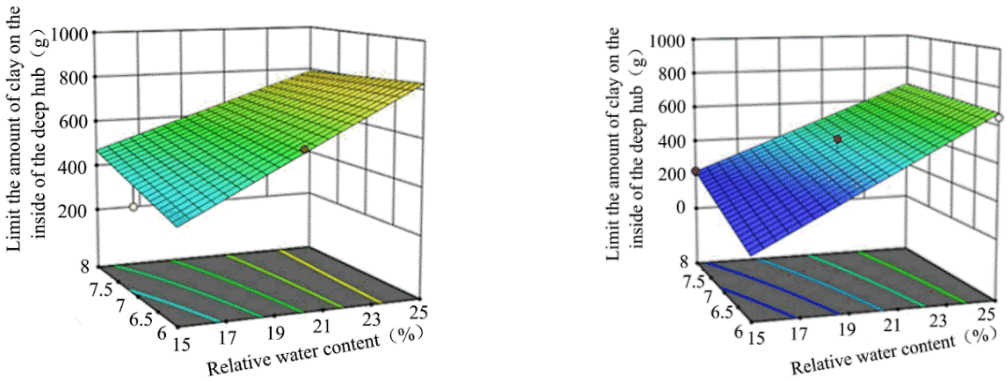

(a) Lug hole area is 5×10^4mm^2 *(b) Lug hole area is 2.7×10^4mm^2*

Fig. 14 - Response surface diagram of clay with different lug hole areas

The results show that when the lug hole area of the gauge wheel is 5×10^4 mm^2, the amount of soil-adhesion decreases by about 10%, compared with 2.7×10^4 mm^2 of the original model.

CONCLUSIONS

Regarding soil-adhesion problem of no-tillage maize planter in black soil area of China, a reformed design of seeding monomer of no-tillage maize planter was constructed with minimum cost and support of TRIZ analysis. In contrast with original version planter, the level of soil adhesion decreased 57.5% in seedbed collating device and 10% in seeding depth-limiting device. This result fulfils the prerequisite for seeding in sticky and wet soil.

The main contributions of the current research can be concluded as follows.

(1) Aiming at the problem that the soil-adhesion of wavy coulter leads to an increase in the disturbance of soil and a loss of crushing function on the surface soil, a self-cleaning seedbed collating device is designed based on Su-field analysis of TRIZ. In the design, a small wavy coulter is used, and a scraper is added on the surface of blades. The parameters of wavy coulter are determined by combining bionic earthworms and the force analysis of soil particle in motion. The results of field trials demonstrate that the modified coulter with scraper has the least amount of clay soil.

(2) Focusing on the problem that the depth-gauge wheel loses its function due to the accumulation and extrusion of clay, the spoke and hub are designed in a split type based on the systemic-functional analysis of TRIZ and the force analysis of the depth-gauge wheel operation process. The depth-gauge wheel of the structure increases the area of lug hole to reduce the adhesion and compression of the soil and changes the independent regulation of the left and right gauge wheels into an integrated linkage mode. The results of field trials show that the most significant factors affecting the soil-adhesion of gauge wheel are the water content of soil as well as the area of lug hole, and the improved split large-lug hole gauge wheel has the least amount of soil-adhesion.

Field trials demonstrate that, the designed self-cleaning seedbed collating device and large-lug hole gauge wheel, can effectively improve the operation performance of no-tillage maize planter, which has market promotion value in the black soil area of northeast China, and also has been recognized by the vast number of customers in China (Qingdao) Agricultural Machinery EXPO. However, China has a vast territory with large land differences and low degree of large-scale agricultural mechanization. The future research and development of no-tillage maize machines and tools are supposed to be closely related to soil conditions in various regions, which will certainly bring great challenges to the product versatility of agricultural equipment enterprises. The author will further study the generalization, modularization and adaptation of equipment based on the agronomic differences of soil and maize seeding in different regions.

ACKNOWLEDGEMENT

This paper was funded by the National Natural Science Foundation of China [Grant No. 51975114] and the Natural Science Foundation of Heilongjiang province of China [Grant No. LH2019E003].

REFERENCES

[1] Altshuller, G.S. (1984). *Creativity as an exact science: the theory of the solution of inventive problems*. Gordon and Breach Science Publishers: New York, USA, pp.15-20.

[2] Bai, X.H., Lin, J., Lv, C.Y., & Hu, Y.Q. (2014). Analysis and experiment on working performance of disc coulter for no-tillage seeder (免耕播种机圆盘破茬刀工作性能分析与试验). *Transactions of the Chinese Society of Agricultural Engineering*, China, 30(15), 1-9.

[3] Fu M. (2021). *Systematic Innovation Approach - TRIZ Practical Tutorial* (系统化创新方法-TRIZ 实用教程); Northeast Forestry University Press: Harbin, China, pp.5-10.

[4] Fu, M., Hao, Y.L., Gao, Z.F., Chen, X.Q., & Liu, X.Y. (2022). User-Driven: A Product Innovation Design Method for a Digital Twin Combined with Flow Function Analysis. *Processes*, Switzerland, 10(11), 2353.

[5] Fuentes-Llanillo, R., Telles, T. S., Junior, D. S., de Melo, T. R., Friedrich, T., & Kassam, A. (2021). Expansion of no-tillage practice in conservation agriculture in Brazil. *Soil and Tillage Research*, Netherlands, 208, 104877.

[6] Gao, Y.Y., Wang, X., Yang S., Zhao, X.G., Dou, H.J., & Zhao, C.J. (2019). Design and test of pneumatic downforce control system for planting (播种机气动式下压力控制系统设计与试验). *Transactions of the Chinese Society for Agricultural Machinery*, China, 50(07), 19-29+83.

[7] Gao, H. (2022). *Agricultural mechanization production science* (农业机械化生产学); China Agricultural Press: Beijing, China, 2002; pp.20-25.

[8] Gao, H.W., Li, H.W., & Yao, Z.L. (2008). Study on the Chinese light no-till seeders (我国轻型免耕播种机研究). *Transactions of the Chinese Society for Agricultural Machinery*, China, 39(04), 78-82.

[9] Guo, H., Chen, Z., Jia, H.L., Zheng, T.Z., Wang, G., & Wang, Q. (2017). Design and experiment of soil-covering and soil-compacting device with cone-shaped structure of wheel (锥形轮体结构的覆土镇压器设计与试验). *Transactions of the Chinese Society of Agricultural Engineering*, China, 33(12), 56-65.

[10] Hou, S.Y., Chen, H.T., Shi, N.Y., Zou, Z., Ji, W.Y., & Wang, Y.C. (2019). Design and experiment of two-degree-of-freedom multi-articulated profiling no-tillage precision design and experiment of two-degree-of-freedom multi-articulated profiling no-tillage precision drill unit (双自由度多铰接仿形免耕精量播种单体设计与试验). *Transactions of the Chinese Society for Agricultural Machinery*, China, 50(04), 92-101.

[11] Lin J., Qian W., Li B.F., & Liu, Y.F. (2015). Simulation and validation of seeding depth mathematical model of 2BG-2 type corn ridge planting no-tillage maize planter (2BG-2 型玉米垄作免耕播种机播种深度数学模型的仿真与验证). *Transactions of the Chinese Society of Agricultural Engineering*, China, 31(09), 19-24.

[12] Jia, H.L., Wang, W.P., Chen, Z., Zheng, T.Z., Zhang, P., & Zhuang, J. (2017). Research status and prospect of soil-engaging components optimization for agricultural machinery (农业机械触土部件优化研究现状与展望). *Transactions of the Chinese Society for Agricultural Machinery*, China, 48(07), 1-13.

[13] Jia H.L., Zhao J.L., Jiang X.M., Jiang, T.J., Wang, Y., & Guo, H. (2013). Design and experiment of anti-blocking mechanism for inter-row no-tillage seeder (行间免耕播种机防堵装置设计与试验). *Transactions of the Chinese Society of Agricultural Engineering*, China, 29(18): 16-25.

[14] Jin, Y.F., Qin, H.T., Zhang, R.H., Wang, M.Y., Liao, H., & Zhu, S. (2014). Design and test of biaxial rotary duplex operation machine for paddy field and dry-land (水旱两用双轴旋耕复式作业机的设计与试验). *Journal of Chinese Agricultural Mechanization*, China, 35(06), 13-16.

[15] Kang, C. Q., Ng, P. K., & Liew, K. W. (2022). A TRIZ-Integrated Conceptual Design Process of a Smart Lawnmower for Uneven Grassland. Agronomy, Switzerland, 12(11): 2728.

[16] Liao, Q.X., Gao, H.W., & Shu, C.X. (2004). Present situations and prospects of anti-blocking technology of no-tillage planter (免耕播种机防堵技术研究现状与发展趋势). *Transactions of the Chinese Society of Agricultural Engineering*, China, 20(01), 108-112.

[17] Ma, Y.H., Ma, S.H., Jia, H.L., Liu, Y.C., Peng, J., & Gao, Z.H. (2014). Measurement and analysis on reducing adhesion and resistance of bionic ripple opener (仿生波纹形开沟器减黏降阻性能测试与分析). *Transactions of the Chinese Society of Agricultural Engineering*, China, 30(05), 36-41.

[18] Massah, J., Fard, M.R., & Aghel, H. (2021). An optimized bionic electro-osmotic soil-engaging implement for soil adhesion reduction. *Journal of Terramechanics*, Switzerland, 95, 1-6.

[19] Massah, J., Roudbeneh, F.H., Roudbeneh, Z.H., & Vakilian, K.A. (2020). Experimental investigation of bionic soil-engaging blades for soil adhesion reduction by simulating Armadillidium vulgare body surface. *INMATEH-Agricultural Engineering*, Romania, 60(1), 99-106.

[20] Morrison, J.E. (2002). Development and future of conservation tillage in America. *Journal of Research and Applications in Agricultural Engineering*, Poland, 47(1), 5-13.

[21] Triplett Jr, G. B., & Dick, W. A. (2008). No-tillage crop production: A revolution in agriculture! *Agronomy journal*, USA, 100, S153-S165.

[22] Wang, Q.J., Cao, X.P., Wang, C., Li, H.W., He, J., & Lu, C.Y. (2021). Research progress of no /minimum tillage corn seeding technology and machine in northeast black land of China (东北黑土地玉米免少耕播种技术与机具研究进展). *Transactions of the Chinese Society for Agricultural Machinery*, China, 52(10), 1-15.

[23] Wei, L.J., Ku, G.H., & Yin, X.P. (2017). Design and optimization of a new wavy coulter (新型波纹式圆盘破茬刀的设计与优化). *Jiangsu Agricultural Sciences*, China, 45(04), 166-168+176.

[24] Yalcin, H., Cakir, E., & Aykas, E. (2005). Tillage parameters and economic analysis of direct seeding, minimum and conventional tillage in wheat. *Journal of Agronomy*, Pakistan, 4(4): 329-332.

[25] Zeng, Z.W., & Chen, Y. (2018). The performance of a fluted coulter for vertical tillage as affected by working speed. *Soil and Tillage Research*, Netherlands, 175: 112-118.

[26] Zhao, S.H., Liu, H.J., Tan, H.W., Yang, Y.Q., & Zhang, X.M. (2017). Design and experiment of bidirectional profiling press device for hilly area (丘陵地区双向仿形镇压装置设计与试验). *Transactions of the Chinese Society for Agricultural Machinery*, China, 48(04), 82-89.

[27] Zheng, K. (2019). Research status and prospect of soil anti-adhesion technology for tillage equipment (耕整机械土壤减粘脱附技术研究现状与展望). *Journal of Anhui Agricultural University*. China, 46(04), 728-736.

[28] Zuo, C.C., Zhang, S.Q., Ma, C.L., & He, H.P. (1997) The study on the adhesion-decreasing and resistance-reducing of disc opener (圆盘开沟器减粘降阻的试验研究). *Transactions of the Chinese Society for Agricultural Machinery*, China, 28(S1), 41-44.

DEVELOPMENT OF ADVANCED METHODOLOGY OF EXPERIMENTAL RESEARCH ON OSCILLATION PROCESSES INTENSITY FOR MACHINE-TRACTOR UNITS
/
РОЗРОБКА НОВОЇ МЕТОДИКИ ЕКСПЕРИМЕНТАЛЬНИХ ДОСЛІДЖЕНЬ ІНТЕНСИВНОСТІ КОЛИВАЛЬНИХ ПРОЦЕСІВ МАШИННО-ТРАКТОРНИХ АГРЕГАТІВ

Volodymyr BULGAKOV[1)], Semjons IVANOVS [*2)], Volodymyr KUVACHOV[3)], Lucretia POPA[4)], Igor SIVAK[1)], Oleksandra TROKHANIAK[1)], Yevhen IHNATIEV[3)]

[1)] Department of Mechanics, Faculty of Construction and Design, National University of Life and Environmental Sciences of Ukraine;
[2)] Faculty of Engineering, Latvia University of Life Sciences and Technologies, Jelgava / Latvia;
[3)] Department of Machine Operation and Technical Service, Dmytro Motornyi Tavria State Agrotechnological University, Melitopol, Ukraine;
[4)] National Institute of Research—Development for Machines and Installations Designed for Agriculture and Food Industry—INMA, Bucharest / Romania
Tel: +380972288905; E-mail: vbulgakov@meta.ua; semjons@apollo.lv
DOI: https://doi.org/10.35633/inmateh-70-34

Keywords: *machine-tractor units, smoothness of motion, technics, vertical oscillations, intensity, accelerometer*

ABSTRACT
An important operational indicator of agricultural machine-tractor units is the smoothness of movement, which significantly affects the traction and dynamic performance of their work, productivity, agronomic qualities of the operation, traffic safety, durability and efficiency. This article presents an improved method and results of experimental assessment of the smoothness of the modular agricultural unit movement, which moves in the footsteps of a constant technological track. Studies of the modular agricultural unit smoothness showed that the graphs of normalized correlation functions of vertical oscillations of the modular agricultural tool developed by us in its motion in the wake of a constant technological track is characterized by a function containing, along with random components, harmonics, which are expressed by attenuating periodic oscillations. The range of oscillations frequencies of the modular agricultural unit frame is concentrated in the range from 0 to 20 s^{-1}, which is consistent with the frequency range 0…0.3 s^{-1} in which the dispersion of fluctuations of profile irregularities is concentrated in traces of the technological track. The developed technique of mathematical modelling and experimental determination of vertical oscillations of the machine-tractor unit can be used to study the dynamics of other agricultural machines and units.

АНОТАЦІЯ
Важливим експлуатаційним показником сільськогосподарських машинно-тракторних агрегатів є плавність ходу, яка суттєво впливає на тягово-динамічні показники їх роботи, продуктивність, агротехнічні якості експлуатації, безпеку руху, довговічність і економічність. У статті наведено нову методику та результати експериментальної оцінки плавності руху модульного сільськогосподарського агрегату, який рухається по слідах постійної технологічної колії. Дослідження плавності модульного агрегату показали, що розроблений нами графік нормованих кореляційних функцій вертикальних коливань модульного сільськогосподарського знаряддя при його русі по слідах постійної технологічної колії характеризується функцією, що містить поряд із випадковими складовими гармонічні, які виражаються загасаючими періодичними коливаннями. Діапазон частот коливань рами сільськогосподарського знаряддя зосереджено в діапазоні від 0 до 20 $с^{-1}$, що узгоджується з діапазоном частот 0…0.3 $с^{-1}$, в якому дисперсії коливань нерівностей профілю зосереджено слідів технологічної колії. Розроблена методика математичного моделювання та експериментального визначення вертикальних коливань машинно-тракторного агрегату може бути використана при дослідженні динаміки інших сільськогосподарських машин та агрегатів.

INTRODUCTION

The quality of many technological processes in agriculture is connected with uniform (smooth) movement of the working bodies for their implementation *(Lou et al., 2021; Shahgoli et al., 2010; Woźniak et al., 2019; Enlai et al., 2019)*. Agricultural machine-tractor units in the process of their working movement are transmitted inclinations, shocks and impacts caused by unevenness of the longitudinal profile of the track, uneven traction resistance and other factors *(Kuvachov et al., 2021)*. In general, the energy and technological parts of agricultural machine-tractor units carry out the oscillations that determine their smooth motion. Smoothness of agricultural units movement is one of the important operational indicators of their work, which is assessed by the impact of oscillations (translational vertical, transverse, angular longitudinal, etc.), mainly on the physical condition and health of the operators who operate them *(Bulgakov et al., 2022; Hac et al., 2009; Szakács et al., 2010; Jazar, 2008)*. At the same time, there are other important indicators of machine-tractor units, which depend on the smoothness of movement: traction and dynamic performance, productivity, agronomic qualities of the operation, traffic safety, durability and efficiency *(Bulgakov et al., 2022)*.

It is known from the theory on the tractor and the car *(Bulgakov et al., 2022)* that the main influence on the movement smoothness and driver's physiological state is exerted by two types of oscillations: translational vertical (jumping) and angular longitudinal (galloping). In turn, the movement smoothness depends on the microrelief of the surface, the skill of the driver, the layout of the unit, the type of running gear, speed, imbalance of parts, uneven rotation.

The research on the dynamics of agricultural tractor-implement units has been the subject of quite a number of studies *(Bulgakov et al., 2016; Xu et al., 2015; Rabbani et al., 2011; Mitsuoka et al., 2008; Mircea et al., 2014; Karkee, 2009)*.

These techniques consider a bunch of heterogeneous indicators for assessing the movement smoothness of mobile vehicles:

– the largest vertical displacement of the centre of elasticity and angular oscillation of the frame;

– largest and average angular or linear accelerations;

– the largest elementary changes in angular or linear accelerations attributed to the corresponding elementary time intervals;

– an indicator of the intensity of shocks on the driver's body, in Piles;

– vibration load and more.

From the position of high versatility, any machine-tractor unit should be aggregated with almost all trailed, semi-mounted and mounted agricultural machines and implements. In addition, the technological part of the unit, regardless of the method of its aggregation, can cause a redistribution of the coupling weight on the front and rear wheels of the tractor, and, with vertical tillage, the weight of the tractor is used to create a cutting force, as a result of which the reaction of the movers to the ground is reduced. At the same time, according to the results of our experimental studies, the unevenness of the longitudinal profile in the traces of a constant technological track has a different frequency spectrum than the usual agricultural background *(Kuvachov et al., 2021; Mitkov, et al., 2021; Bulgakov et al., 2021)*. Therefore, the vertical oscillations of a dynamic system are caused by different characteristics of the perturbations. The latter, on the one hand, are caused by irregularities in the traces of a constant technological track when the tractor propellers move along it, and on the other hand, from the irregularities of the agricultural background, along which the supporting wheels of agricultural machines move.

The dynamics of the movement of the machine-tractor units in the vertical plane is determined by the incoming disturbing influences. The latter include irregularities in the longitudinal profile of traces of a constant technological track and uneven traction resistance of agricultural machines and implements. It is clear that the nature of the internal structure of the tramline longitudinal profile certainly affects tractor smoothness and fluctuations in its tractive effort with all the negative consequences *(Deynichenko et al., 2018; Bulgakov et al., 2021)*.

It is known that the quality of processing by any dynamic system of the input variables depends on its characteristics. Regarding the machine-tractor unit, these are its scheme, as well as design and other parameters. Therefore, the correct choice of the latter from the standpoint of the desired movement smoothness provides it with optimal transformation of the disturbing impacts affecting it.

To conduct scientific research of a machine-tractor unit movement in a longitudinal-vertical plane, one should use the methods of statistical dynamics, described in detail by A.B. Lurie, as used in (*Bulgakov et al., 2016; Bulgakov et all., 2021)*.

According to these methods it is known that the transforming properties of a dynamic system may be expressed by the transfer functions and frequency characteristics *(Kuvachov et al., 2021; Mitkov, et al., 2021; Bulgakov et al., 2021)*.

It is these characteristics, according to many scientists, that give the most complete and physical idea of the agricultural unit reactions to various disturbances, as well as the transient and stable processes of its operation.

The theoretical analysis of the transfer functions and frequency characteristics requires a system of corresponding differential equations, relating the input variables, to input disturbances, that is, a mathematical model of the process itself. At this stage of research, it is purposeful to consider it by means of a system of linear equations. Such idealization is quite efficient in this case since the dynamics of the movement of complex multielement aggregates has not yet been studied enough. And the knowledge gained about it makes it possible to physically comprehend the result obtained, and accumulate experience of designing.

The general method for solving the dynamics problems of a mechanical system in this case are vertical oscillations of the tractor frame and its technological part, which is a system of fairly complex differential equations, built on the basis of the Lagrange equations of the second kind *(Kuvachov et al., 2021; Mitkov, et al., 2021; Bulgakov et al., 2021)*. To construct an equivalent scheme of a tractor with an agricultural implement, hung on it, it is expedient and sufficient to consider the vibrations of a flat figure that has the shape of its lateral projection in one vertical plane, coinciding with the longitudinal area of symmetry of its frame and the agricultural implement.

When studying the uniformity of an agricultural unit movement in longitudinal-vertical plane when it moves along field surface unevenness, it becomes necessary to assess this movement smoothness, for which it is necessary and sufficient to determine some specific indicators of "smoothness" from among generally accepted units of physical measurements: amplitude, frequency, speed and oscillations acceleration. The development and improvement of methods for determining these indicators is an important task in the field of research into dynamics of agricultural units movement.

The purpose of the article is to study the smoothness of the modular agricultural unit movement, which moves in the footsteps of a constant technological track by using a new method of estimating the intensity of vertical oscillations system based on a tablet computer with Android operating system with built-in accelerometer sensors and Accelerometer Meter application.

MATERIALS AND METHODS

For experimental studies, an arable modular machine-tractor aggregate was used, which consisted of an energy module (tractor), a technological module to it, and an attached plough (Figure 1). The design and properties of a modular machine-tractor aggregate are described in *(Bulgakov et al., 2021)*. The movement of the modular agricultural unit took place along the dirt traces of the constant technological track.

Fig. 1 – Modular agricultural unit as part of a mounted plough

To record the vertical accelerations of the agricultural machine frame in the process of its movement during the experimental studies, a tablet computer with the Android operating system was used (Figure 2). In this software environment, a special application Accelerometer Meter (version 1.32) received digitized output signals and their frequency spectrum from the accelerometer sensors (Figure 2).

The obtained digital signals from the accelerometer sensors of the tablet computer (see Figure 2) were imported into the Mathcad software environment to determine their statistical characteristics *(Zhiltsov, 2015; Borysova, 2021; Mazhayskiy et al., 2021; Hassan et al., 2022; Khadim et al., 2023)*.

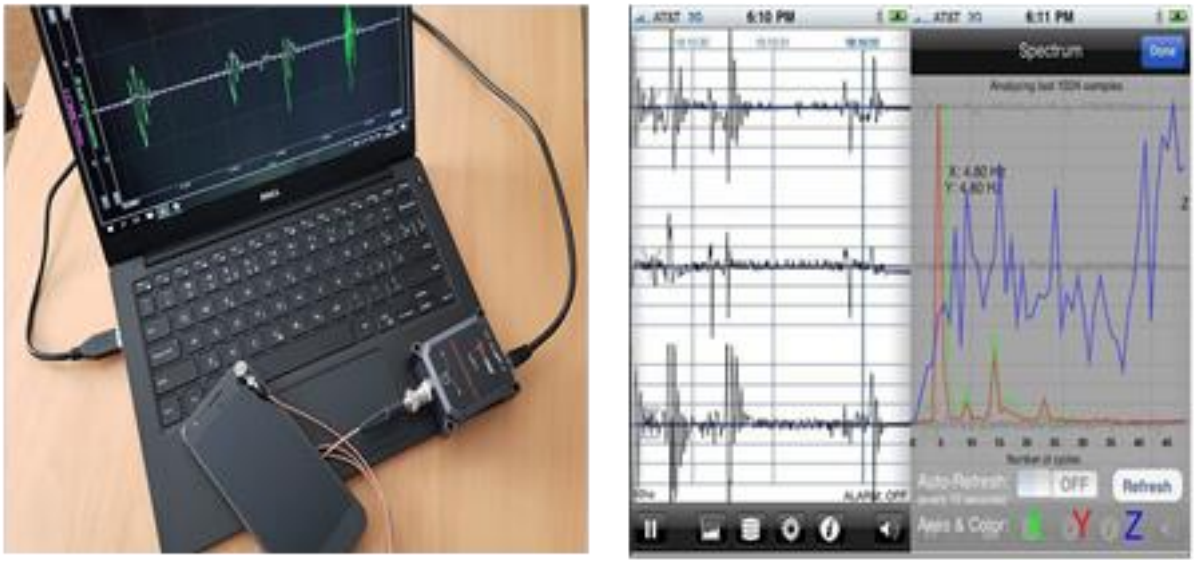

a) b)

Fig. 2 – Accelerometer Meter software environment interface based on Android
a) the measuring system as part of the PC; b) measurement of vertical acceleration (marked Z).

Experimental ordinate of the spectral density of the vertical frame accelerations oscillations of the modular agricultural unit has a unit of measurement m·s^{-2}, which is the implementation of signals from the accelerometer sensors, then at the transition to a linear amplitude z_y (m) the ordinates of the points of spectral density, were determined as follows *(Zhiltsov, 2015)*:

$$z_y = \frac{\ddot{Z} \cdot T^2}{2} \text{ [m]} \quad (1)$$

where:

$\ddot{Z}$ – acceleration of vertical oscillations, m·s^{-2};

T – time equal to the length of the correlation of the density of vertical oscillations accelerations, s.

The theoretical spectral density of frame oscillations of modular agricultural unit was found from the next expression *(Kuvachov et al., 2021)*:

$$S_T(\omega) = \frac{[A_t(\omega)]^2 \cdot S_{pr}(\omega) \cdot D_{pr}}{D_e} \text{ [m]} \quad (2)$$

where: $S_{pr}(\omega), D_{pr}$ – normalized spectral density (m) and variance (m^2) path profile fluctuations;

$A_t(\omega)$ – theoretical amplitude-frequency characteristic which is transmitted to the frame of the unit from the field profile *(Bulgakov et al., 2021)*;

D_e – oscillation dispersion of machine-tractor aggregate.

The accuracy of measurements of the vertical displacements amplitude of a modular agricultural unit frame was evaluated by the value of the root-mean-square error *(Deynichenko et all., 2018)*:

$$\sigma_z = \sqrt{\left(\frac{T^2}{2}\right)^2 \cdot \sigma_{\ddot{Z}}^2 + \left(\ddot{Z} \cdot T\right)^2 \cdot \sigma_t^2} \text{ [m·s}^{-2}\text{]} \quad (3)$$

where:

$\sigma_{\ddot{Z}}$ and σ_t – standards for deviations of measurement errors of vertical frame acceleration of an agricultural machine and time.

The results of the studies showed that the reliability of the results obtained is such that the number of cases in which deviations from the patterns established in the course of experimental studies could occur did not exceed 10%.

RESULTS AND DISCUSSION

For mathematical modelling of the dynamics of the plane-parallel motion of a tractor as part of a machine-tractor unit, it is represented as an equivalent dynamic model (Fig. 3).

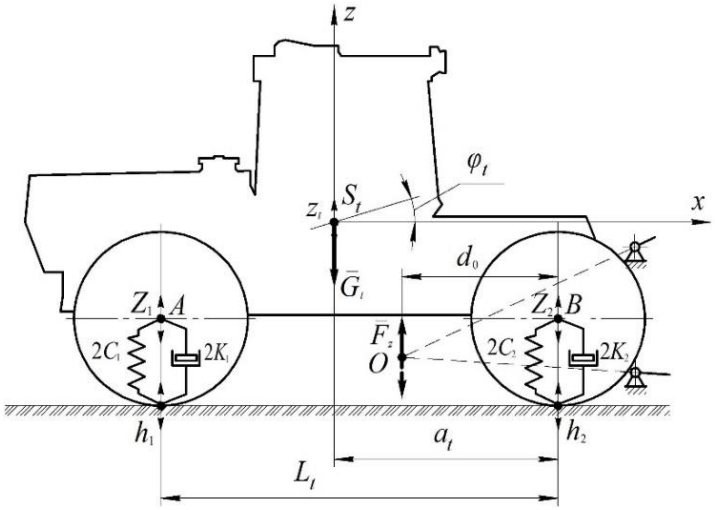

Fig. 3 – Scheme of fluctuations of the tractor in a longitudinal-vertical plane

Z_1, Z_2 – vertical movements of the front and rear axles of the tractor, respectively; h_1, h_2 – the height of the supporting surface unevenness under the front and rear wheels of the tractor; L_t, a_t – basis and the longitudinal coordinate of the tractor centre of gravity; M_t, J_t – mass and the moment of inertia of the tractor in a longitudinal-vertical plane; C_1, C_2 – the coefficients of elastic elements for the tractor front and rear axles, respectively; K_1, K_2 – the resistance coefficients of the dissipative elements of the tractor front and rear axles, respectively.

The mutual influence of the tractor and its technological part, according to the generally accepted principle of replacing rejected bonds by reactions, is expressed through the force F_z, which is concentrated in the instantaneous centre of rotation of the tractor rear mounted mechanism (point *O*, Fig. 3).

The calculated dynamic model of the plane-parallel movement of the tractor in a vertical plane has two degrees of freedom: vertical displacement (Z_t) of its centre of mass (point S_t) and angular fluctuations of the frame φ_t (Fig. 3).

Using the Lagrange equation of the second kind, the mathematical model of the tractor vertical fluctuations has the form:

$$\left.\begin{aligned} A_{11}\cdot\ddot{Z}_1 + A_{12}\cdot\dot{Z}_1 + A_{13}\cdot Z_1 + A_{14}\cdot\ddot{Z}_2 &= f_{11}\cdot\dot{h}_1 + f_{12}\cdot h_1 + f_{13} \\ A_{21}\cdot\ddot{Z}_2 + A_{22}\cdot\dot{Z}_2 + A_{23}\cdot Z_2 + A_{24}\cdot\ddot{Z}_1 &= f_{21}\cdot\dot{h}_2 + f_{22}\cdot h_2 + f_{23} \end{aligned}\right\} \quad (4)$$

where:

$$A_{11} = \frac{M_t\cdot a_t^2 + J_t}{L_t^2}$$
$$A_{12} = 2\cdot K_1$$
$$A_{13} = 2\cdot C_1$$

$$f_{11} = 2\cdot K_1$$
$$f_{12} = 2\cdot C_1$$
$$f_{13} = \frac{F_z\cdot d_0}{L_t}$$
$$A_{21} = \frac{[M_t\cdot(L_t - a_t)^2 + J_t]}{L_t^2}$$
$$A_{22} = 2\cdot K_2$$
$$A_{23} = 2\cdot C_2$$

$$f_{21} = 2\cdot K_2$$
$$f_{22} = 2\cdot C_2$$
$$f_{23} = F_z\cdot\left(\frac{1 - d_0}{L_t}\right)$$

Z_1, Z_2 – vertical movements of the tractor front and rear axles, respectively;

h_1, h_2 – the unevenness height of the supporting surface under the front and rear wheels of the tractor;

L_t, a_t – basis and the longitudinal coordinate of the tractor centre of gravity;

M_t, J_t – mass and the moment of inertia of the tractor in a longitudinal-vertical plane;

C_1, C_2 – the coefficients of elastic elements for the tractor front and rear axles, respectively;

K_1, K_2 – the resistance coefficients of the dissipative elements of the tractor front and rear axles, respectively.

As a result of experimental research it is established that the graphs of normalized correlation functions of vertical oscillations of the modular agricultural unit during its movement on the traces of a constant technological track are characterized by a function containing, along with random components, harmonics, which are expressed by attenuating periodic oscillations (Fig. 4).

The irregularities fluctuations of the traces profile of the constant technological track have the same character. The length of the correlation relation is about 0.16 s, which is equal to 0.35 m when the speed of the modular agricultural unit is within 2.2 m·s^{-1}. The obtained result is explained by the fact that the main spectrum of oscillations of the profile irregularities has a periodicity corresponding to the pitch of the ground hooks of the wheels tires of the modular agricultural unit *(Hac et al., 2009; Szakács, 2010; Jazar, 2008)*.

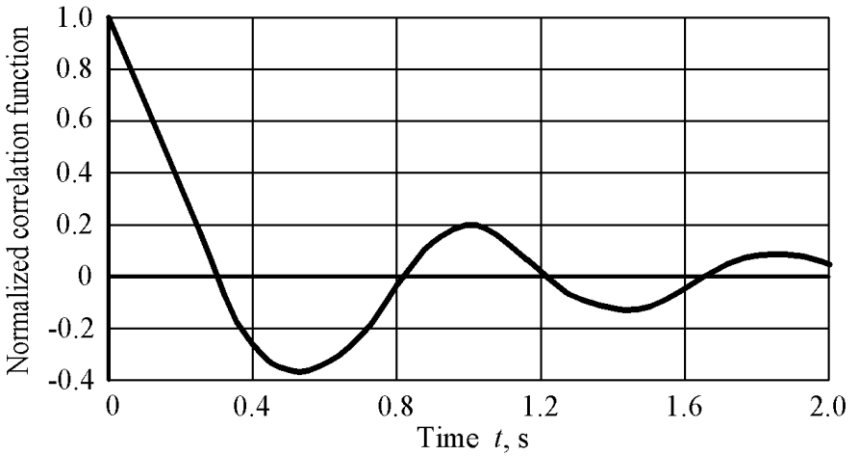

Fig. 4 – Normalized correlation function of accelerations of frame vertical oscillations of modular agricultural unit during its movement on a constant technological track

The experimental normalized spectral density of frame oscillations of modular agricultural unit during its movement on a constant technological track of field, which was measured using a developed methodology, is presented in Fig. 5.

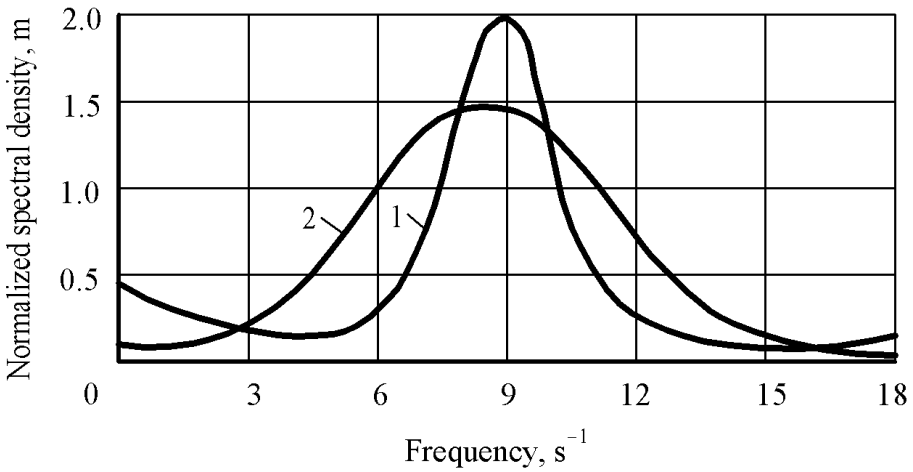

Fig. 5 – Theoretical (1) and experimental (2) normalized spectral densities of frame vertical vibrations of investigated machine and tractor unit

Fig. 5 shows the theoretical dependence of the normalized spectral density of the characteristics of the traces longitudinal profile irregularities of a constant technological track. Spectral density is conveniently displayed in time units (s^{-1}). Since the argument of this function is the frequency ω (m^{-1}), then in order to switch to time units (s^{-1}), the abscissa of the points of the mentioned spectral density must be multiplied by the speed of modular agricultural unit, and the ordinates on the contrary are divided by this speed.

When comparing the theoretical and experimental normalized spectral densities of the tractor frame vertical vibrations, it can be seen that both processes have a similar nature of the change in the frequency range. This testifies to the correct approach to the development of a mathematical apparatus and assumptions about the nature of forced oscillations. Also, the adequacy of the mathematical model and experimental data is confirmed by the results of testing the null hypothesis about the equality of the theoretical dispersion D_t = 1.18 cm^2 and the experimental D_e = 1.42 cm^2 according to Fisher's F-criterion at a significance level of 0.05.

The frequency spectrum of frame vibrations of the investigated machine and tractor unit is concentrated in range from 0 to 18 s^{-1}(see. Fig. 5), which is consistent with the frequency range of 0...0.35 cm^{-1}, in which the dispersion of fluctuations in the profile irregularities of a constant technological track is concentrated.

The conducted studies confirm that for experimental registration of the initial data of movement and acceleration of agricultural units in the vertical plane, it is sufficient to use modern mobile devices with built-in accelerometer sensors and use an application with direct access to them.

CONCLUSIONS

1. Dependencies of normalized correlation functions of vertical oscillations for the investigated machine and tractor unit during its movement along constant technological track are characterized by a function that contains, along with random components, harmonic ones, which are expressed by attenuating periodic oscillations. The correlation length is approximately 0.16 s, when the velocity of the modular agricultural unit is within 2.2 $m \cdot s^{-1}$ which is equal to 0.35 m. The result obtained is explained by the fact that the main spectrum of fluctuations of the profile irregularities has a periodicity corresponding to the step of the grounding hooks of the wheels tires of the modular agricultural unit and the type of basic tillage.

2. The frequency spectrum of frame vibrations of the investigated machine and tractor unit is concentrated in range from 0 to 18 s^{-1}, which is consistent with the frequency range of 0...0.35 cm^{-1}, in which the dispersion of fluctuations in the profile irregularities of a constant technological track is concentrated.

3. When comparing the theoretical and experimental normalized spectral densities of the tractor frame vertical vibrations, it can be seen that both processes have a similar nature of the change in the frequency range. This testifies to the correct approach to the development of a mathematical apparatus and assumptions about the nature of forced oscillations. Also, the adequacy of the mathematical model and experimental data is confirmed by the results of testing the null hypothesis about the equality of the theoretical dispersion D_t = 1.18 cm^2 and the experimental D_e = 1.42 cm^2 according to Fisher's F-criterion at a significance level of 0.05.

4. The proposed method for the theoretical and experimental determination of the vertical vibrations of a machine-tractor unit can be used in experimental studies of agricultural machines and units.

5. The conducted studies confirm that for experimental registration of the initial data of movement and acceleration of agricultural units in the vertical plane, it is sufficient to use modern mobile devices with built-in accelerometer sensors and use an application with direct access to them.

REFERENCES

[1] Borysova, V., Karnaukh, B. (2021). Standard of proof in common law: Mathematical explication and probative value of statistical data. *Journal of the National Academy of Legal Sciences of Ukraine*, 28(2), 171-180. https://www.researchgate.net/publication/353491841.

[2] Bulgakov V., Aboltins, A., Hristo Beloev, H., Nadykto, V., Kyurchev, V., Adamchuk, V., Kaminskiy, V. (2021). Experimental Investigation of Plow-Chopping Unit. *Agriculture*, 11, 30. https://www.mdpi.com/2077-0472/11/1/30/review_report

[3] Bulgakov, V., Aboltins, A., Beloev, H. et al. (2022). Theoretical investigation of selection (calculation) of design parameters of modular draft device in aggregation of semitrailers. *Applied Sciences*, 12(20), 10267. https://www.mdpi.com/2076-3417/12/20/10267

[4] Bulgakov, V., Adamchuk, V., Arak M., Nadykto, V., Kyurchev, V., Olt, J. (2016). Theory of vertical oscillations and dynamic stability of combined tractor-implement unit. *Agronomy Research*, 14(3), 689-710. https://www.researchgate.net/publication/303790342.

[5] Bulgakov, V., Kuvachov, V., Ivanovs, S. et all. (2021). Experimental investigations in vertical vibration damping of agricultural aggregate of block-modular type. *Engineering for Rural Development*, 20, 635-642. https://www.tf.lbtu.lv/conference/proceedings2021/Papers/TF136.pdf

[6] Bulgakov V., Kuvachov V., Solona O., Boris M. Experimental research intensity of oscillations agricultural machine-tractor units. Vibrations in engineering and technology. 2021. №3 (102). P. 24-33.

[7] Bulgakov, V., Olt, J., Ivanovs, S. et all. (2021). Research into dynamics of motion performed by modular power unit as part of ploughing tractor-implement unit. *Annals of DAAAM and Proceedings of the International DAAAM Symposium*, 32(1), 576–585. https://www.researchgate.net/publication/357046111.

[8] Deynichenko, G., Samoichuk, K., Yudina, T., Levchenko, L., Palianychka, N., Verkholantseva, V., Dmytrevskyi, D., Chervonyi, V. (2018). Parameter optimization of milk pulsation homogenizer. Journal of Hygienic *Engineering and Design*, 24, 63-67. https://www.researchgate.net/publication/342649429.

[9] Enlai Zheng, Song Cui, Yuanzhao Yang, Jinlin Xue, Yue Zhu, Xiangze Lin. (2019). Simulation of the Vibration Characteristics for Agricultural Wheeled Tractor with Implement and Front Axle Hydropneumatic Suspension. *Hindawi Shock and Vibration*, Article ID 9135412, 19.

[10] Hac, A., Fulk, D., Chen, H. (2009). Stability and Control Considerations of Vehicle-Trailer Combination. *SAE Int. J. Passeng. Cars - Mech*. *Syst*., 1(1), 925-937.

[11] Hassan, A., Lone, M.A., Dar, I.H., Ahmad, P.B. (2022). A new continuous probability model based on a trigonometric function: Theory and applications. *Reliability: Theory and Applications*, 17(3), 261-272. https://www.gnedenko.net/Journal/2022/032022/RTA_3_2022-21.pdf https://www.researchgate.net/publication/268398123_2008-01-1228 https://www.sciencedirect.com/science/article/abs/pii/S1537511011001280

[12] Jazar, R.N. (2008). *Vehicle Dynamics: Theory and Applications*, 1015. DOI: https://doi: 10.1007/978-0-387-74244-1.

[13] Karkee, M. (2009). *Modelling, identification and analysis of factor and single axle towed implement system*. [Graduate Theses and Dissertations, Iowa State University]. 10875, 246. https://scholar.google.com/citations

[14] Khadim, A., Hussain, T., Bakouch, H.S., Saghir, A. (2023). A probability distribution for precipitation data analysis. *Mathematical Methods in the Applied Sciences*, 46 (2), 2709-2728. https://www.researchgate.net/publication/363268947

[15] Bulgakov, V., Sevostianov, I., Kaletnik, G., ...Holovach, I., Ihnatiev, Y. Theoretical Studies of the Vibration Process of the Dryer for Waste of Food. *Rural Sustainability Research*, 2020, 44(339), pp. 32–45.

[16] Kuvachov, V., Kiurchev, S., Nurek, T., Chorna, T., Mitkov, V., et al. (2021). *Scientific bases of increase movement smoothness of the machine-tractor units on base of modular power means*. [Monograph, Warszawa]. 136. http://www.tsatu.edu.ua/tstt/wp-content/uploads/sites/6/scientific-bases-of-increase-movement-smoothness-of-the-machine-tractor-units-on-base-of-modular-power-means-1..12-2021.pdf DOI: 10.22630/SGGW.IIM.9788375839975.

[17] Lou, S., He, J., Li H., Wang, Q., Lu, C., Liu, W., Liu, P., Zhang, Z. (2021). Current knowledge and future directions for improving subsoiling quality and reducing energy consumption in conservation fields. *Agriculture*, 11 (7), 575. https://www.mdpi.com/2077-0472/11/7/575

[18] Mazhayskiy, Y., Rokochynskiy, A., Lukianchuk, O., Turcheniuk, V., Chernikova, O. (2021). Research of energy capacity of structural comminution in deep loosing of sandy and loamy soil. *Engineering for Rural Development*, 20, 57-62. https://www.semanticscholar.org/paper

[19] Mircea, N. & Nicolae, I. (2014). Study on the dynamic interaction between agricultural tractor and trailer during braking using Lagrange equation. *Applied Mechanic and Materials*, 659, 515-520. https://www.researchgate.net/publication/280952077

[20] Mitkov, V., Kiurchev, S., Nurek, T., Chorna, T., Ihnatiev, Y., Kuvachov, V., Głowacki, S., et all. (2021). *Scientific bases of the combined units aggregation based on arable and row-crop tractor (second edition)*. [Monograph, Warszawa]. 150. http://www.tsatu.edu.ua/tstt/wp-content/uploads/sites/6/scientific-bases-of-the-combined-units-aggregation-based-on-arable-and-row-crop-tractor-1-14-2021.pdf

[21] Mitsuoka, M., Fukushima, T., Okayasu, T., Ioue, E. & Okuda, Y. (2008). Investigation of nonlinear vibration characteristics of the half-track tractor. Proceedings of the 4th international symposium on machinery and mechatronics for agriculture and Biosystems engineering (ISMAB), Taichung, Taiwan. https://agronomy.emu.ee/wp-content/uploads/2016/05/Vol14No3.pdf

[22] Mitsuoka, M., Inaba, S., Inoue, E., Fukushima, T., et al. (2008). Prediction and evaluation of vibration characteristics of an agricultural rubber crawler vehicle equipped with movable track rollers. *Journal of the Japanese Society of Agricultural Machinery*, 70(5), 41-47.

[23] Rabbani, M., Tsujimoto, T., Mitsuoka, M., Inoue, E. & Okayasu, T. (2011). Prediction of the vibration characteristics of half-track tractor considering a three-dimensional dynamic model. *Biosystem Engineering*, 110(2), 178-188.

[24] Shahgoli, G., Fielke, J., Desbiolles, J., Saunders, C. (2010). Optimising oscillation frequency in oscillatory tillage. *Soil and Tillage Research*, 106 (2), 202-210.

[25] Szakács, T. (2010). Developing stability control theories for agricultural transport systems. *Acta Polytechnica Hungarica*, 7(2), 25-37. http://uni-obuda.hu/journal/Szakacs_23.pdf

[26] Woźniak, A. (2019). Chemical properties and enzyme activity of soil as affected by tillage system and previous crop. *Agriculture*, 9(12), 262. https://www.mdpi.com/2077-0472/9/12/262

[27] Xu, H., Zhang, Y., Liu, H., Qi, S., Li, W. (2015). Effects of configuration parameters on lateral dynamics of tractor-two trailer combination. *Advances in Mechanical Engineering*, 7(11). https://www.researchgate.net/publication/285752326

[28] Zhiltsov, O.B. (2015). *Probability theory and mathematical statistics in examples and problems*. Textbook. way. Kyiv: University named after B. Hrinche, 336.

DEVELOPMENT AND EVALUATION OF AN IoT-BASED PORTABLE WATER QUALITY MONITORING SYSTEM FOR AQUACULTURE
/
基于 IoT 的便携式养殖水质监测系统的开发与评估

Yin XU[1)], Jiadong JIN[2)], Songwei ZENG[*2)], Yun ZHANG[*2)], Qinglai XIAO[*3)]
[1)] College of Mathematics and Computer Science, Zhejiang A&F University, Hangzhou / China;
[2)] College of Optical, Mechanical and Electrical Engineering, Zhejiang A&F University, Hangzhou / China;
[3)] Songyang County Natural Resources and Planning Bureau, Lishui / China
Tel: +86-0571-13758280718; E-mail: zsw@zafu.edu.cn
DOI: https://doi.org/10.35633/inmateh-70-35

Keywords: *water sensors, portable, IoT, RTOS, water quality evaluation*

ABSTRACT
In this paper, the development of a portable, multifunctional water quality monitoring system for aquaculture that is based on IoT technology is presented. The system integrates a main control module, sensor module, Human Machine Interface (HMI) module, Wi-Fi module and power module, and is equipped with system software based on Real Time Operating System (RTOS) for scheduling tasks. The main control module collects crucial water quality information, including water temperature (WT), dissolved oxygen (DO), ammonia nitrogen (NH3-N), and pH, through the sensor module and facilitates data interaction with the HMI module. The proposed aquaculture water quality evaluation model utilizes water quality parameters as input to assign a grade based on the evaluation result. These parameters are transmitted wirelessly to the OneNet cloud platform using Wi-Fi modules, enabling users to remotely monitor the water quality through a visual interface. The system structure has been meticulously designed to accommodate both portable and fixed-point remote monitoring applications. The experimental results demonstrate that the system is accurate, stable, and cost-effective, providing a reliable and efficient solution for intelligent aquaculture in small and medium-sized enterprises.

摘要
在本文中，我们介绍了一种基于物联网技术的便携式多功能水产养殖水质监测系统的开发。该系统集成了主控模块、传感器模块、人机交互模块（HMI）、Wi-Fi 模块和电源模块，并配备了基于实时操作系统（RTOS）的系统软件来调度任务。主控制模块通过传感器模块收集关键的水质信息，包括水温（WT）、溶解氧（DO）、氨氮（NH3-N）和 pH 等，并负责与 HMI 模块进行数据交互。提出的水产养殖水质评价模型利用水质参数作为输入，根据评价结果进行水质分级。这些水质参数通过 Wi-Fi 模块远程传输到 OneNet 云平台，使用户可以通过可视化界面远程实时监测水质情况。该系统结构经过特定设计，可以支持便携式使用和定点远程监测使用，实现多功能。实验结果表明，该系统准确率高、稳定性好、成本低，为中小型水产养殖企业的智能水产养殖发展提供了可靠、高效的解决方案。

INTRODUCTION
As the Agriculture 4.0 era continues to evolve, the application of IoT technologies in aquaculture is becoming increasingly prevalent *(Prapti et al., 2022)*. The quality of rearing water is critical for the growth, development, and survival of aquaculture species, while poor water quality increases the incidence of disease among species, leading to significant economic losses and environmental pollution *(Giacomazzo et al., 2020; Hongpin et al., 2015).* Hence, monitoring water quality for aquaculture is of utmost importance.

Recent years have seen continuous research into environmental monitoring systems using IoT technology *(Zhenfeng et al., 2023; Irfan et al., 2022),* resulting in significant advancements in water quality monitoring, as summarized in Table 1.

Yin Xu, M.S. Stud. Eng.; JiaDong Jin, M.S. Stud. Eng.; SongWei Zeng, Prof. Ph.D. Eng.; Yun Zhang*, Lecture M.S. Eng.; QingLai Xiao*, Sr. Engineer.*

The low power consumption, long transmission distance, and easy networking capabilities of NB-IoT and LoRa communication technologies make them ideal for large-scale, multi-node water quality monitoring applications. *Jamroen et al. (2023)* proposed a water quality monitoring system based on NB-IoT, which is powered by both photovoltaic energy and battery energy storage (BES). *Huiying et al. (2021)* proposed a multi-node aquaculture environment monitoring system based on LoRa technology. Despite their relatively short communication distance, technologies such as Wi-Fi and Bluetooth are frequently used in water quality remote monitoring studies due to their cost-effectiveness, high stability, and ease of installation. *Lin et al. (2021)* developed a wireless multi-sensor system using an ESP32 Wi-Fi module to monitor temperature, pH, DO, and EC in freshwater aquaculture. *Kelechi et al. (2021)* designed a Bluetooth-based IoT water quality monitoring system that transmitted data to a mobile application for analysis. Water quality monitoring systems are increasingly incorporating various evaluation methods in addition to remote monitoring of water quality parameters, providing a more comprehensive assessment of water quality. *Le Phuong Truong (2021)* developed a water quality monitoring, evaluation, and warning system for fish farming that includes a mobile phone short message service and web-based alert function. *Sung et al. (2021)* developed an IoT-based water quality monitoring system for water sources, proposing a flowing water quality model based on diversion-method-related experiments.

Table 1

Different studies on water quality monitoring system

Reference number	Main control platform	Measurement parameters	Network technology	Remote monitoring platform
[10]	Arduino Mega 2560	DO, pH, EC	NB-IoT	Grafana
[7]	stm32f103c8t6	T, DO, pH	LoRa	Software platform
[13]	ESP32 Wi-Fi	T, pH, DO, EC	Wi-Fi	ThingSpeak
[11]	ATmega328p	T, pH, turbidity	Bluetooth	Mobile app
[14]	Arduino Mega 2560	T, pH, DO	Wi-Fi and GSM	ThingSpeak
[19]	Arduino UNO board	T, pH, turbidity, conductivity, TDS	Wi-Fi	ThingSpeak

Numerous studies have demonstrated the efficiency, cost-effectiveness, and ease of deployment of IoT-based water quality monitoring systems. DO is one of the water quality parameters most directly related to water pollution, as well as to aquatic biota *(Csábrági et al., 2019)*. High concentrations of NH3-N can significantly impact the quality of water, and pH and WT are also critical indicators in water quality monitoring *(Santos et al., 2022; Jiaqi et al., 2019)*. In this study, the monitoring efforts were focused on four key water quality parameters: DO, NH3-N, WT, and pH. High-yield, large-scale aquaculture facilities typically use WSN technology to monitor water quality, using a set of sensors at each monitoring point to measure data and transmit it to a central monitoring center for real-time online monitoring. However, the cost of these sensors makes it unaffordable for medium and small-scale aquaculture operations to equip each breeding pool node with its own set of sensors *(Aldo et al., 2022)*.

After considering the above factors, a portable and multifunctional water quality monitoring system for aquaculture, which is based on IoT technology, was developed. To enable functional customization, our own system control circuit was designed instead of utilizing commercial development boards like Arduino. Compared with traditional water quality monitoring systems, this system is structurally designed to be portable, making it easy to transport and use. Additionally, a number of sensor interfaces are reserved for functional expansion according to requirements and IoT technology was incorporated to enable fixed-point remote real-time monitoring, allowing for long-term online monitoring of potential problematic aquaculture areas. To improve the overall assessment of water quality, an aquaculture water quality evaluation model was developed based on relevant standards. This model allows for a more comprehensive and accurate evaluation of water quality in aquaculture settings.

MATERIALS AND METHODS

System architecture

The complete system architecture is illustrated in Fig. 1, which consists of three main components: the perception layer, the network layer, and the application layer. The perception layer comprises the microprocessor and various water quality sensors. It executes multiple tasks using RTOS to collect water quality information, evaluate water quality, and transmit resulting data. The network layer connects remotely to the OneNet cloud platform via Wi-Fi. It uses the Message Queuing Telemetry Transport (MQTT) protocol to upload water quality parameters acquired by the sensing layer to the cloud platform. The client-oriented application layer enables users to interact with the system and view water quality information through the HMI. It also provides visual monitoring interfaces on PC and mobile terminals, allowing users to remotely monitor water quality information via mobile app and PC.

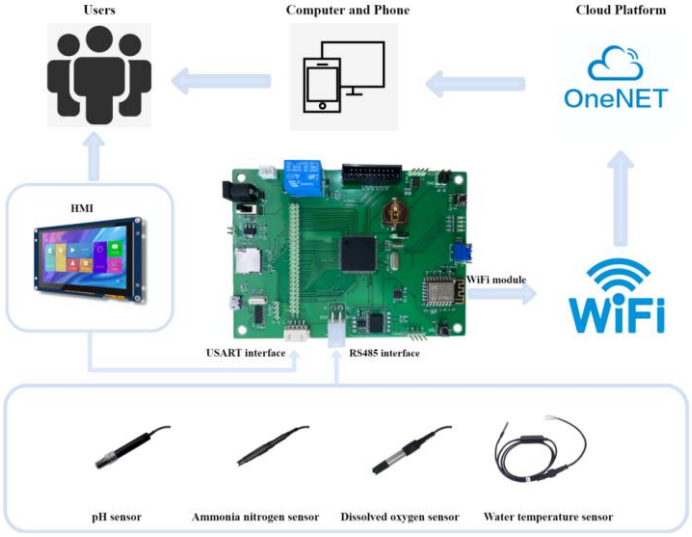

Fig. 1 - System architecture

Sensors for water monitoring

High-precision water quality monitoring sensors from SINO IoT Company (China) were chosen to measure DO, NH3-N, and pH, and a temperature sensor manufactured by DALLAS Semiconductor Company (USA) to measure WT. Table 2 displays the sensors' parameters that support the Modbus transmission protocol and meet the system requirements with high accuracy. Implementing and maintaining Modbus is simpler than other standards and allows multiple devices to connect to the same cable, facilitating communication and enhancing convenience in design *(Miao et al., 2022)*. Modbus also enables the addition of more sensor types in the future while imposing minimal constraints.

Table 2

Parameters of water quality sensors

Sensor types	Measurement range	Accuracy	Resolution	Transmission protocol	Power supply mode
Temperature sensor	-55~80℃	±0.5℃	0.1℃	Modbus	DC 5V
Dissolved oxygen sensor	0~20mg/L	±5%	0.01 mg/L	Modbus	DC 5V
pH sensor	0~14PH	±3%	0.01PH	Modbus	DC 5V-9V
Ammonia nitrogen sensor	0~18g/L	±5%	0.01 mg/L	Modbus	DC 5V-12V

Hardware design

Figure 2 illustrates the hardware architecture of the system, which comprises a single-chip microcontroller module, a RS485 module, an ESP8266 module, and a power module. The GD32F303 series main control produced by GigaDevice Semiconductor Inc. is adopted as microsystem controller (it is a 32-bit general microcontroller based on Arm Cortex-M4 core, with abundant peripheral resources and low cost). The RS485 module transmits the data collected from the sensors to the system master control.

The ESP8266 module enables a connection to a Wi-Fi network, allowing for the remote transmission of data. The power module supplies two power sources of 5V and 3.3V to the system to power the various modules. A design for the connection interface of the HMI module and the debugging download interface, which facilitates the connection and program debugging of the HMI module, was proposed. In addition, some functions and input/output (IO) ports are reserved, such as SD card module, relay module and some of the main controller IO ports, to facilitate the subsequent system function upgrade. The peripheral circuit design of each functional module is implemented and integrated into a single Printed Circuit Board (PCB).

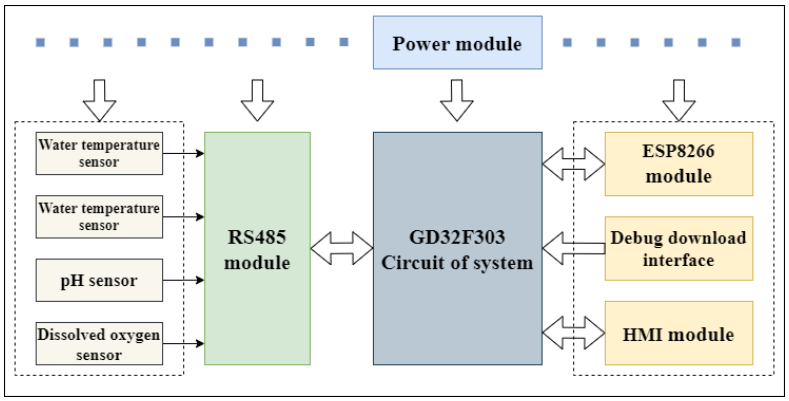

Fig. 2 - Design block diagram of main control board

The main functional circuits of the system hardware include Wi-Fi communication circuit, 485 communication circuit and power supply circuit. Figure 3a shows the Wi-Fi communication circuit, the controller transmits AT commands through serial port 0 to the ESP8266 module to establish a Wi-Fi connection. Figure 3b illustrates the 485-communication circuit. The RS485 to UART_TTL module is used to communicate between the master controller via Serial Port 1 and the external sensors to obtain digital signals. The main controller board requires an external input voltage of 5V, as well as a 3.3V voltage to power the necessary modules. The voltage conversion circuit based on AMS1117 chip is shown in Fig. 3c. Adding decoupling capacitors at the input and output can enhance the transient current response time, minimize output voltage noise and ripple, and promote a stable 3.3V output.

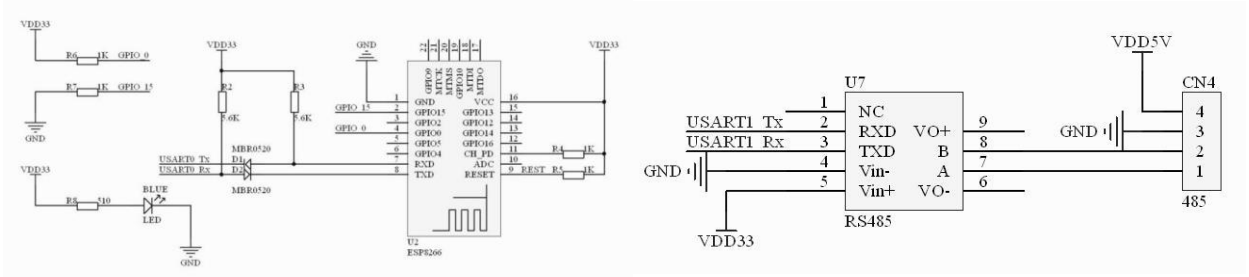

(a)Wi-Fi communication circuit *(b)485 communication circuit*

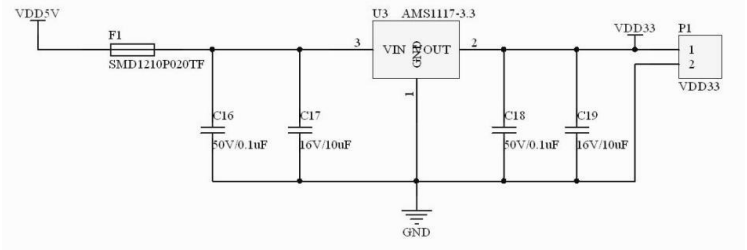

(c)voltage conversion circuit

Fig. 3 - Schematic diagram of main functional circuits

The PCB design of the main control board was completed using Altium Designer (AD) software, and all components were reasonably laid out according to the functional modules, in order to facilitate wiring and ensure the stability of the circuit board, a double-sided board was used in this design. According to the reasonable electrical rules, the PCB Layout diagram is shown in Fig. 4a, and the actual circuit board is shown in Fig. 4b. SolidWorks and CAD software were utilized to design the device's structure. This design allows for both portable and fixed-point usage, as demonstrated in Fig. 5.

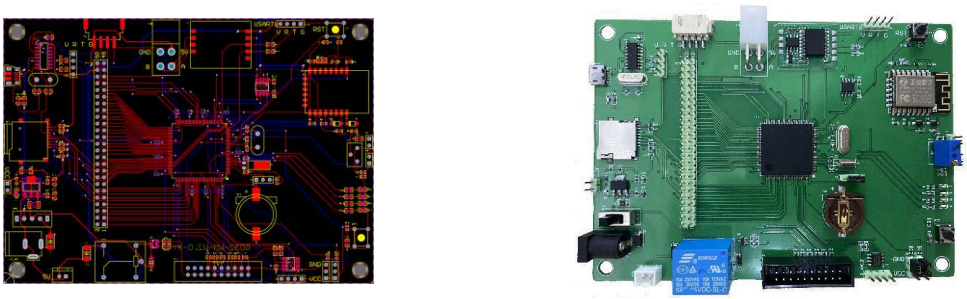

(a)PCB layout (b)real product

Fig. 4 - The electronic board

(a)for portable usage (b)fixed point of usage

Fig. 5 - A 3D view of the structure of equipment

Software development

The system software process is shown in Fig. 6, which is developed based on the lightweight system OpenHarmony. OpenHarmony uses a preemptive scheduling mechanism and includes 32 priority task modules. High-priority tasks can preempt low-priority tasks, while low-priority tasks can only be scheduled after high-priority tasks have been blocked or completed *(OpenAtom)*.

Upon system startup, hardware initialization is performed, which primarily involves setting the parameters for GPIO, serial port, timer, and other modules. After, the system kernel is launched, and three threads with varying priorities are created, from high to low, respectively: (1) the sensor data acquisition thread: This thread acquires water quality parameter information from temperature, DO, pH, and NH3-N sensors, based on the sampling frequency set by the timer. (2) water quality assessment thread: This thread processes the sensor values obtained by the data acquisition thread, using them as inputs to the water quality assessment model and calculates the pollution index and water quality grade. (3) the Wi-Fi communication thread: Establishes a connection to a designated Wi-Fi network through HMI, ensures accurate data transmission using CRC verification algorithm, accesses OneNet cloud platform, and remotely transmits data using MQTT protocol at a specified frequency.

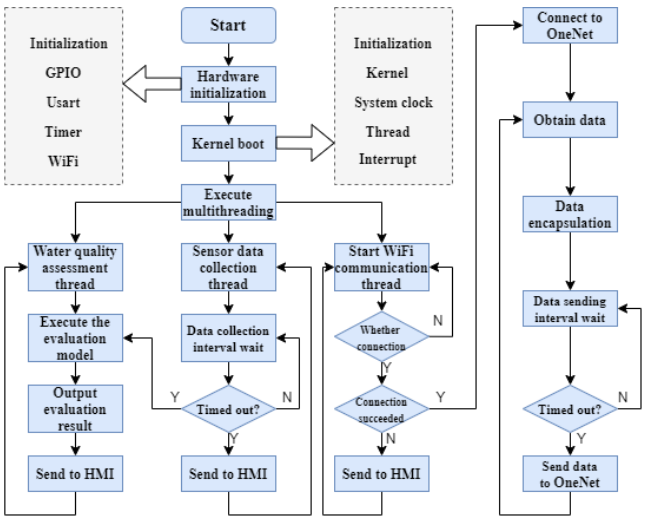

Fig. 6 - System software flowchart

As a leading country in aquaculture, China has maintained its position as the world's top producer of aquaculture for several years *(Kangshun et al., 2021)*. China has developed a range of aquaculture standards based on extensive breeding experience and input from numerous experts. Our team established an aquaculture water quality evaluation model for obtaining the comprehensive pollution index and water quality grade by calculating the single-item pollution index according to the *Specification for Monitoring Environmental Quality of Farm Water Sources (NY/T 396-2000)*.

The single-item pollution index of water quality is calculated according to Eq. (1). To calculate the single-item pollution index for indicators such as DO, which decrease in concentration with increasing pollution, Eq. (2) was used. For the indicator with limited range (the allowable range of pH is 6~9), the single-item pollution index is calculated according to Eqs. (3) and (4). The comprehensive pollution index of water quality is calculated using Eq. (5).

$$W_i = \frac{P_m}{P_s} \tag{1}$$

$$W_i = \frac{P_t - P_m}{P_t - P_s} \tag{2}$$

$$W_i = \frac{P_m - A_{avg}}{A_{min/max} - A_{avg}} \tag{3}$$

$$A_{avg} = \frac{A_{min} + A_{max}}{2} \tag{4}$$

$$W_c = \sqrt{\frac{(W_{avg})^2 + (W_{max})^2}{2}} \tag{5}$$

where:

W_i refers to single-item pollution index of water quality, P_m is a measured value of water pollutant, P_s refers to pollutant quality standard, P_t refers to the theoretical maximum value of a pollutant, A_{avg} is an average value of allowable range, $A_{min/max}$ refers to the maximum or minimum of allowable range, W_c refers to composite pollution index, W_{avg} is a value of average single-item pollution index, W_{max} is a value of Maximum single-item pollution index.

If the single-item pollution index is less than 1, its value is equal to the calculated value. However, if the single-item pollution index is greater than or equal to 1, it is recalculated using Eq. (6).

$$W_i = M + P * lg\ (W_i) \tag{6}$$

where P is a constant 5, M is a constant 1.

In the above formula, the standard limit values of each item (P_s, P_t, $A_{min/max}$) are determined according to *the Basic Standard Limit Values of Environment Quality of Surface Water (GB 3838-2002)* Ⅲ indicators (applicable to aquaculture and other fishing waters). According to the *Fishery Water Quality Standards (GB 11607-89)*, and *NY/T 396-2000*, the water quality is classified based on the comprehensive pollution index (CPI), as shown in Table 3, divided into three water quality levels (WQL).

Table 3

Water quality classification standard

Classification of grades	Composite pollution index	Water quality level
1	≤0.5	Good
2	0.5~1.0	Qualified
3	≥1.0	Poor

***Interface design of HMI and remote* visualization**

The HMI design is based on the system's requirements, which consists of four main interfaces: function selection, water quality monitoring, network connection, and system setting. The function selection interface allows users to choose the desired system functions. The water quality monitoring interface provides a clear and intuitive display of water quality parameters. The network connection interface enables users to connect to a Wi-Fi network. Lastly, the system settings interface allows users to calibrate the system's time setting. The HMI interface, as depicted in the in Fig. 7, was tailored to support the portable use of the system effectively.

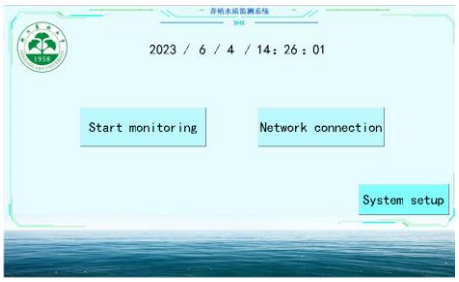

(a)function selection

(b)water quality monitoring

(c)network connection

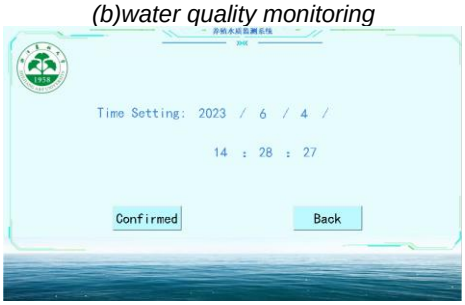

(d)system setting

Fig. 7 - Interface design of HMI

A remote visualization interface for water quality parameters was developed using the data visualization View service provided by the OneNet cloud platform. The PC-side visual interface comprises several modules, including the weather module, pollution index module, monitoring module, and parameter display module, as illustrated in Fig. 8a. This interface allows remote monitoring of the trend of each water quality parameter over time and provides latest access to key water quality information. Users can also access weather conditions for the current day and the following three days, as well as individual and composite pollution indices of the water quality.

To provide a mobile solution, a visualization interface for smartphones was also developed, as depicted in Fig. 8b. With this interface, users can view the main parameters of the breeding water quality as long as their mobile device is within network range.

(a)visualization interface on PC

(b)mobile visualization interface

Fig. 8 - Visual interface design

RESULTS

The sensors have been pre-calibrated by the manufacturer. A physical prototype of the equipment is displayed in Fig. 9 and the sensors are connected to the device through the aviation interface located at the bottom of the device. Figure 9a displays the front of the device, which primarily comprises the HMI interface. Figure 9b depicts the internal circuit of the device. The system is powered by a 15V lithium battery, which outputs a stabilized 5V voltage to the main control board through a voltage stabilized module.

To test the accuracy of the measurement data in the system, standard solutions with three different values for NH3-N and pH parameters were used. The corresponding sensors in the system were used to measure standard solutions, and the measurement average value (MAV) was calculated for each solution by measuring it five times. The accuracy of the data was compared by comparing the DO and WT parameters with the AR8010 device (the AR8010 is a high precision DO analyzer produced by SMART SENSOR company in China, and the DO measurement range is 0-20mg/L, with a resolution of 0.01mg/L). Three different measurement points in a water body were selected and the DO and WT values were measured using both the AR8010 device and the system. Each point was measured five times and the average value was calculated for each measurement separately. The accuracy of the measurement data was evaluated by calculating the relative error (RE) and the mean relative error (MRE). The final test results are shown in Table 4. The MRE for pH and WT parameters were respectively 0.37% and 0.7%. The MRE for NH3-N and DO parameters were 1.73% and 1.93%, respectively. These results indicate that the overall measurement error of the system was low, demonstrating its high accuracy.

(a)equipment front *(b)internal circuit*

Fig. 9 - Physical view of the system

Table 4

System accuracy analysis of measurement

Items	Reference objects	Reference values	MAV	RE/%	MRE/%
NH3-N	NH3-N standard solution	0.5mg/L	0.51mg/L	2	1.73
		1mg/L	1.02mg/L	2	
		5mg/L	5.06mg/L	1.2	
pH	pH standard solution	4.0	4.02	0.5	0.37
		6.86	6.88	0.29	
		9.18	9.21	0.33	
DO	AR8010	5.62mg/L	5.54mg/L	1.42	1.93
		6.21mg/L	6.12mg/L	1.45	
		6.88mg/L	6.68mg/L	2.91	
WT	AR8010	22.6℃	22.5℃	0.44	0.7
		23.8℃	23.6℃	0.84	
		24.2℃	24℃	0.83	

In OneNet, a device is created for the system, and device information and number are added. After the unique authentication information assigned by OneNet is successfully bound to the system, it can store the data sent by the system, such as pH, DO, NH3-N and WT. As shown in Fig. 10, the platform can receive real-time data from the system and query historical data based on a specified time period. Additionally, all data can be synthesized into exportable files, facilitating storage, viewing, and processing of the data. A stability test of the platform's data reception capabilities was conducted. During the test, the system sent four parameters to the platform every 5 seconds, resulting in a total of 150 sets of data. The data received by the cloud platform were collected and analyzed, and the results are shown in Table 5. The NH3-N and DO parameters did not experience any data loss, while the pH and water temperature parameters had a data loss rate of 0.7% and 1.3%, respectively. The high overall data reception rate and minimal data loss indicate strong platform stability.

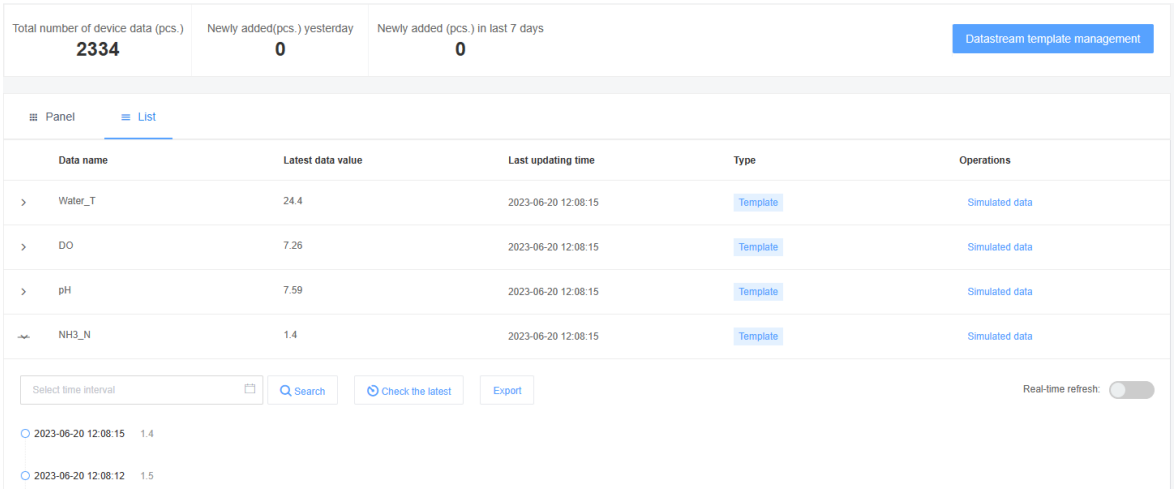

Fig. 10 - The data management interface of platform

Table 5

Cloud platform stability testing

Items	Send data volume	Received data volume	Lost data volume	Data loss rate / %
NH3-N	150	150	0	0
pH	150	149	1	0.7
DO	150	150	0	0
WT	150	148	2	1.3

CONCLUSIONS

This paper proposes a portable multi-functional aquaculture water quality monitoring system based on IoT, which integrates four sensors to measure WT, DO, NH3-N and pH. The system uploads water quality information to the OneNet cloud platform through Wi-Fi communication. The portable structure design of this system simplifies the arrangement of multiple sets of sensors, reducing hardware costs associated with water quality monitoring. This design better suits the monitoring needs of small and medium-sized aquaculture bases, while still allowing for fixed-point remote monitoring. The visualization interface designed for PC and mobile devices clearly and effectively conveys water quality information to aquaculture personnel, enabling timely detection of any issues in the water area. The establishment of a breeding water quality evaluation model enables personnel to accurately assess water quality and make necessary improvements. This system also has some shortcomings, with fewer types of water quality sensors used, but multiple 485 interfaces have been reserved, and other sensors supporting Modbus protocol can be quickly connected to the system. Experimental results demonstrate that the system provides accurate measurements, stable data transmission, and is user-friendly and easy to maintain, which can effectively address water quality monitoring needs for small and medium-sized aquaculture bases.

ACKNOWLEDGEMENT

This work was supported by Zhejiang Provincial Natural Foundation Public Welfare Project of China (LGN18C200017).

REFERENCES

[1] Aldo G.O.L., Des C.M., Mauricio L., et al. (2022). Monitoring of water quality in a shrimp farm using a FANET. *Internet of Things*, 18, https://doi.org/10.1016/j.iot.2020.100170

[2] Csábrági A., Molnár S., Tanosa P., et al. (2019). Estimation of dissolved oxygen in riverine ecosystems: Comparison of differently optimized neural networks. *Ecological Engineering*, 138, 298-309, https://doi.org/10.1016/j.ecoleng.2019.07.023

[3] Giacomazzo M., Bertolo A., Brodeur P., et al. (2022). Linking fisheries to land use: How anthropogenic inputs from the watershed shape fish habitat quality. *Science of The Total Environment*, 717, https://doi.org/10.1016/j.scitotenv.2019.135377

[4] GB 3838-2002. 360doc:http://www.360doc.com/content/21/0522/22/34836513_97850878.shtml (accessed December 2022)
[5] GB 11607-89. DOC88: https://www.doc88.com/p-1018031552042.html (accessed December 2022)
[6] Hongpin L., Guanglin L., Weifeng P., et al. (2015). Real-time remote monitoring system for aquaculture water quality. *International Journal of Agricultural and Biological Engineering*, 8(6), 136-143, https://doi.org/10.3965/j.ijabe.20150806.1486
[7] Huiying C., Fangzhen L., Peng L., et al. (2021). Intelligent aquaculture environment monitoring system based on LoRa communication technology. *INMATEH - Agricultural Engineering*, 63(1), 109-120, https://doi.org/10.35633/inmateh-63-11
[8] Irfan A., Ryan G.C., Nurpilihan B., et al. (2022). An IoT-enabled design for real-time water quality monitoring and control of greenhouse irrigation systems. *INMATEH - Agricultural Engineering*, 69(1), 417-426, https://doi.org/10.35633/inmateh-69-39
[9] Jiaqi W., Bian C., Yang L., et al. (2019). A multi-parameter integrated chip system for water quality detection. *International Journal of Modern Physics B*, 33(7), https://doi.org/10.1142/S02-17979219500413
[10] Jamroen C., Yonsiri N., Odthon N., et al. (2023). A standalone photovoltaic/battery energy-powered water quality monitoring system based on narrowband internet of things for aquaculture: Design and implementation. *Smart Agricultural Technology*, 3, https://doi.org./10.1- 016/j.atech.2022.100072
[11] Kelechi A.H., Alsharif M.H., Anya A.C., et al. (2021). Design and Implementation of a Low-Cost Portable Water Quality Monitoring System. Computers, *Materials & Continua*, 69(2), 2405-2424, https://doi.org/10.32604/cmc.2021.018686
[12] Kangshun Z., Min Z., Kang W., et al. (2021). Aquaculture Impacts on China's Marine Wild Fisheries Over the Past 30 Years. *Frontiers in Marine Science*, 8, https://doi.org/10.338-9/fmars.2021.710124
[13] Lin J.Y., Tsai H.L., Lyu W.H. (2021). An Integrated Wireless Multi-Sensor System for Monitoring the Water Quality of Aquaculture. *Sensors*, 21(24), https://doi.org/10.3390/s21248179
[14] Le P.T., (2021). Cost-effective Evaluation, Monitoring, and Warning System for Water Quality based on Internet of Things. *Sensors and Materials*, 33(2), 575-583, https://doi.org/10.18494/1-0.18494/SAM.2021.2442
[15] Miao H.Y., Yang C.T., Kristiani E., et al. (2022). On Construction of a Campus Outdoor Air and Water Quality Monitoring System Using LoRaWAN. *Applied sciences*, 12(10), https://doi.org/10.3390/app12-105018
[16] NY/T 396-2000. China Standards Online Service: https://www.spc.org.cn/online/262bfcff8828244c7b-68b08dc7c32c4d.html (accessed December 2022)
[17] OpenAtom: https://docs.openharmony.cn/pages/v3.1/zh-cn/OpenHarmony-Overview_zh.md / (accessed December 2022).
[18] Prapti D.R., Shariff A.R.M., Man H.C., et al. (2022). Internet of Things (IoT)-based aquaculture: An overview of IoT application on water quality monitoring. *Reviews in Aquaculture*, 14(2), 979-992, https://doi.org/10.1111/raq.12637
[19] Sung W.T., Fadillah N., Hsiao S.J., (2021). IoT-based Water Quality Monitoring. *Sensors and Materials*, 33(8), 2791-2983, https://doi.org/10.18494/SAM.2021.3342
[20] Santos D., Martins A.C., Silva K.M., et al. (2022). Identifying water factors that are related to ammonia nitrogen concentrations in Columbia River using a reversed hazard exponential model. *River Research and Applications*, 38(2), 256-266, https://doi.org/10.1002/rra.3902
[21] Zhenfeng X., Jiajian Y., Huan Z., et al. (2023). A wireless remote monitoring sensor for agricultural environment based on NB-IoT. *INMATEH-Agricultural Engineering*, 69(1), 285-294, https://doi.org/10.35633/inmateh-69-26

DIFFERENTIAL AND INTEGRAL SLIDING MODE ADAPTIVE CONTROL ALGORITHM FOR DRAFT AND POSITION INTEGRATED CONTROL OF ELECTRO-HYDRAULIC HITCH IN AGRICULTURAL TRACTOR
/
基于微分与积分自适应滑模的拖拉机电液悬挂力位综合控制

Changqing LIU[1)], Jinheng GU[3)], Xin DU[1*)], Chengwen LIU[1)], Yuefeng DU[2)], Enrong MAO[2)]
[1)] School of Mechanical Engineering, Jiangsu Ocean University, Lianyungang 222005 / China;
[2)] College of Engineering, China Agricultural University, Beijing 100083 / China
[3)] School of Mechatronic Engineering, China University of Mining and Technology, Xuzhou 221116/ China
Tel: 0086-0518-85895322; E-mail: xindu@jou.edu.cn
Corresponding author: Xin Du
DOI: https://doi.org/10.35633/inmateh-70-36

Keywords: *Agricultural Tractor; Draft-position integrated; Sliding Mode Controller; Field Test*

ABSTRACT
The accuracy of tractor plowing is an important link to ensure the quality of agricultural crops. The integrated control of draft-position in plowing is an effective plowing precision control technology which can be used to improve the tractor's plowing efficiency. The hydraulic system of the tractor hitch has the characteristics of large load and complex working environment. A differential and integral sliding mode adaptive controller (DI-SMAC) is designed for the tractor hitch hydraulic system with strong nonlinearity, uncertainty and time-varying parameters. Compared with the traditional PID controller, integral sliding mode adaptive controller(I-SMAC) and differential and integral sliding mode adaptive controller (DI-SMAC) in the electro-hydraulic hitch control system, the numerical simulation verifies the advantages of the differential and integral sliding mode adaptive controller. The real test platform of the agricultural tractor is built. The test results show that the DI-SMAC can realize the integrated control function of draft-position. In the position control mode, there is no static error, and the anti-interference ability is strong; Under the draft control mode, compared with the traditional PID controller, the range of traction error of differential and integral sliding mode controller is reduced by 32.9%, and the standard deviation is reduced by 38.6%; When the weight coefficient is changed, the traction force and tillage depth fluctuation are different with different weight coefficients. It is shown that the DI-SMAC is stable and effective, and the developed method is expected to provide technical support for the fine plowing operation of tractors.

摘要
拖拉机犁耕作业精度是保证农业作物种植质量的重要环节。犁耕作业中的力位综合控制是一种有效的犁耕作业精度控制技术，可用于提高拖拉机的犁耕作业效率。本研究以拖拉机电液悬挂为研究对象，综合考虑拖拉机位姿状态和地面起伏和土壤沉陷对电液悬挂控制的影响，建立拖拉机机组电液悬挂动力学数学模型。拖拉机悬挂装置液压系统的负载质量大，作业环境复杂。针对拖拉机悬挂装置液压系统的强非线性、不确定性和参数时变性等特点，设计了微分与积分自适应滑模控制器。通过仿真对比传统 PID 控制器、积分滑模自适应控制器和微分与积分滑模自适应控制器，验证了微分与积分滑模自适应控制器的优越性。搭建实车试验平台，结果表明：采用微分与积分滑模自适应控制器，在位置控制模式下，基本无静差，抗干扰能力强；力控制模式下，相比传统 PID 控制器，微分与积分滑模控制器牵引力误差的极差降低了 32.9%，标准方差降低了 38.6%；力位综合控制模式下，不同权重系数牵引力和耕深波动也不同。说明微分与积分滑模自适应控制器是稳定有效的，所开发的方法有望为拖拉机精细犁耕作业提供技术支持。

INTRODUCTION
The hydraulic hitch control system is an essential device for large agricultural tractors. Hydraulic pressure is used as the power to lift and control agricultural tools. The hydraulic hitch is the core component to realize the power transmission and intelligent control of high-power tractors in the field.

Changqing Liu, Lecturer Ph.D. Eng.; Jinheng Gu, Lecturer Ph.D. Eng.; Xin Du, Lecturer Ph.D. Eng.; Chengwen Liu, Prof. Ph.D. Eng.; Yuefeng Du, Prof. Ph.D. Eng.; Enrong Mao, Prof. Ph.D. Eng.*

The tractor electro-hydraulic hitch control system is helpful to improve the quality of plowing operation (*Bentaher et al*., *2008*; *Janulevičius et al., 2019; LeeKim et al., 2016*). The performance of hydraulic hitch control directly affects the operation of the tractor and the energy consumption of the unit in the field *(Bacenetti, et al., 2018; Balsari et al., 2021; Pranav et al 2012)*. The hydraulic hitch control modes of agricultural tractors mainly include position control (*Saeys et al., 2004*), draft control (*Treichel et al., 1984*) draft-position integrated control *(Wang et al., 2021*), pressure control *(Liu et al., 2020*), slip rate control (*Gupta et al., 2019*) and vibration reduction control *(Cheng et al., 2017)*.

Draft-position integrated control is a common mode of tractor plowing operation. Scholars have carried out extensive research on draft-position integrated control mode of tractor electro-hydraulic hitch during plowing operation. *Lee et al. (1998)* proposed a control system for the depth of tillage of agricultural tractors to improve the precision of the depth of tillage during operation. They tested the dynamic characteristics of the control system. With the maturity of mechatronics, the electrical control system is gradually applied in tractors, and the hydraulic hitch of tractors is further developed. *Luo et al. (2015)* used an electric push rods for hydraulic hitch system control and passed the test to meet the automatic operation requirements of the tractor hydraulic hitch system. *Lu et al. (2013)* studied the automatic control method for the tillage depth of tractor electro-hydraulic hitch system, and put forward an automatic control method for tillage depth of the electro-hydraulic hitch system based on fuzzy control and the concept of integrated coefficient. *Li et al. (2013)* introduced the fuzzy PID control algorithm into the integrated draft-position control mode and carried out the position control and draft control experimental research, respectively, which improved the draft-position integrated control performance and control precision. *Li et al. (2018)* obtained better potential control performance by introducing soil-specific resistance parameters to change the draft-position integrated control weight of potential. In the above research, most of the draft-position integrated control focuses on the change of weight coefficient. Still, less attention is paid to the non-linear factors of the hydraulic hitch system. At present, the non-linear controller is gradually applied in agricultural equipment. *Song et al. (2022)* carried out research on tractor roll-over prevention by introducing a variable structure sliding mode control algorithm. *Li et al. (2014)* put forward an adaptive sliding mode control method based on a non-linear integral sliding surface for steering control of agricultural vehicles and achieved satisfactory steering control performance. *Zhou et al. (2021)* converted the original motion task into a common tracking control problem and introduced LQR optimal control and integral sliding mode control to design a robust tracking controller for TTWMS.

At present, fuzzy PID controller has been widely used in draft-position integrated control (*Li et al., 2013; Wang et al., 2018*). The parameter adjustment process is complicated and the control effect is totally dependent on the experience of the designer. In this paper, a controller is designed based on the mathematical model of hydraulic system with stronger robustness and adjustable control law parameters, which provides new ideas and methods for the design of nonlinear controller of hydraulic hitch tillage system. In this paper, it would be shown that there is a suitable nonlinear controller, and affect the dynamic response. The problem with analyzing the hitch system is that the effect of these is not easily generalized. The focus of this paper is to analyze and describe the various types of draft-position integrated control, and to provide control effect for different draft-position weight. A differential and integral adaptive sliding mode controller is designed and the control performance of tractor hydraulic hitch force level integrated control is verified by simulation. An agricultural tractor real-vehicle test platform is built to verify the effectiveness of the controller designed.

MATERIALS AND METHODS

DESIGN OF ELECTRO-HYDRAULIC HITCH SYSTEM CONTROLLER

Mathematical model of hydraulic system

The principle of the electro-hydraulic hitch hydraulic system is shown in Figure 1, which is composed of the proportional lifting valve, proportional lowering valve, safety valve, and single-acting cylinder.

In the figure, x_v is the spool displacement (m); p_s is inlet pressure (Pa); p_0 is return port pressure (Pa); A_p is the piston area without rod cavity of hydraulic cylinder (m^2); m_L is equivalent load; k_L is equivalent stiffness of hydraulic system (N/m); B_L is equivalent damping for hydraulic system; h_P is ploughing depth (m).

In the process of establishing the mathematical model of the hydraulic system, assuming that there is no elastic load in the design, ignoring the viscous damping coefficient on the piston, ignoring the influence of oil density and compressibility, the return oil pressure is 0.

(1) Pressure flow characteristic equation of electro-hydraulic proportional hitch control valve

To simplify the analysis and explanation, the influence of nonlinear factors, such as the insensitive area of the electro-hydraulic proportional control valve, is temporarily ignored, and it is approximately regarded as a linear system (i.e., approximate linearization).

$$q_L = K_{sv} i - K_c p_L \tag{1}$$

where: i is the control current of the proportional control valve of the electro-hydraulic hitch (A), K_{sv} is the flow coefficient of the electro-hydraulic proportional control valve ($m^3\ s^{-1}\ A^{-1}$), K_c is the flow-pressure coefficient of the electro-hydraulic proportional control valve ($m^3\ s^{-1}\ Pa^{-1}$), and p_L is the load pressure (Pa).

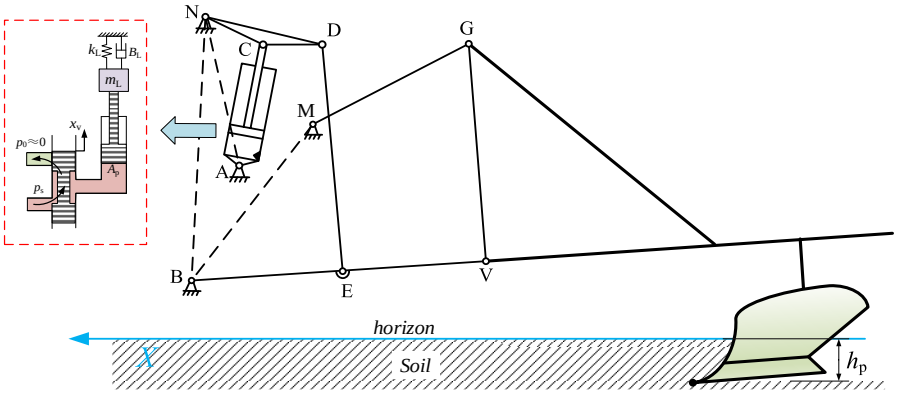

Fig. 1 –Schematic diagram of electro-hydraulic hitch

(2) Electro-hydraulic hitch system is a single-acting cylinder, lifting the flow continuity equation of the cylinder.

$$q_L = A_L \frac{dx_L}{dt} + C_t p_L + \frac{V_L}{\beta_e} \frac{dp_L}{dt} \tag{2}$$

where A_L is the effective area of the hitch system hydraulic cylinder (m^2), x_L is the motion displacement of the hitch system hydraulic cylinder (m), C_t is the total leakage coefficient of the hitch system hydraulic cylinder, V_L is the total volume of two cavities of the hitch system hydraulic cylinder (m^3) and β_e is the effective volume elastic modulus of hitch system hydraulic oil (Pa).

(3) The force balance equation of the cylinder load is:

$$A_L p_L = m_L \frac{d^2 x_L}{dt^2} + B_L \frac{dx_L}{dt} + k_L x_L + F_L \tag{3}$$

where, F_L is the accidental load force of the hydraulic cylinder of the hitch system (N).

Control Principle

Draft-position integrated control is a control method to integratedly deal with the variation of farm implements position and draft. The principle of draft-position integrated control is shown in Figure 2.

The controlled object of this system is the weighted comprehensive value of the traction force and the plowing depth of the implement. Feedback signals from angle displacement sensor of lifting arm and draft sensor are weighted and fed back to the controller for comparison. The controller outputs reasonable control quantities according to the deviation of the feedback signal to realize the lifting and lowering of agricultural implements. It can be seen from the control schematic that when the weight coefficient a=1, the system is in position control mode. When the weight coefficient a=0, the system is in draft control mode. Therefore, the performance of position control and draft control can be analyzed dynamically by draft-position integrated control simulation.

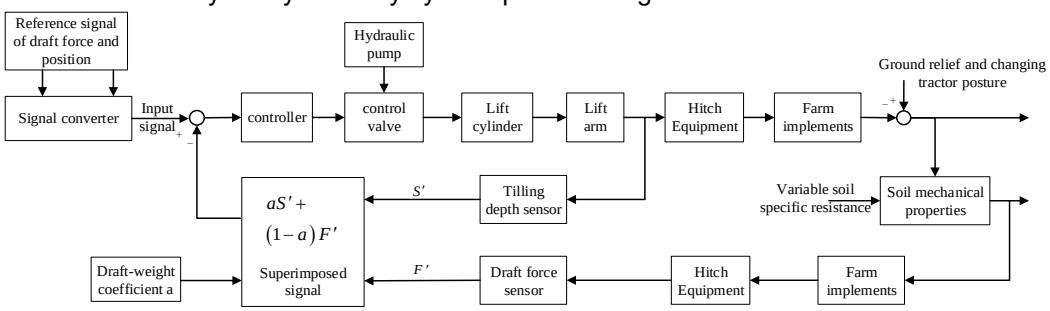

Fig. 2 –Schematic diagram of the draft- position integrated control

The draft-position integrated control converts the input signal into the lift arm displacement angle signal. The draft signal is converted into a lifting arm angular displacement signal reflecting the value of tillage depth. The actual feedback angular displacement is obtained by mixing the angular displacement of the lifting arm converted from the traction signal, and then the force position can be controlled comprehensively by only controlling the angular displacement of the lifting arm. The displacement control of the hydraulic cylinder can be carried out by using the proportional relationship between the angle of the lifting arm and the displacement of the hydraulic cylinder. The displacement control of hydraulic cylinder can be developed as a non-linear controller based on the mathematical model of the hydraulic system, and the draft- position integrated control algorithm is designed by control strategy. The hydraulic system of tractor hitch has a large load, complex operation environment, strong nonlinearity, uncertainty, and parameter variability. Traditional PID is widely used because of its simple principle and stable operation (*Khodayari Balochian, 2015*). Still, its adaptability is poor when it is applied to a nonlinear electro-hydraulic hitch systems, and its parameter tuning is cumbersome.

In addition, the faster response speed is often accompanied by a larger overshoot and a larger number of shocks, which easily causes the vibration of tractor machinery, resulting in a larger pitch movement of the entire unit, and it is difficult to achieve the preset control performance. Sliding mode variable structure control, as a control method which is suitable for both linear and non-linear systems (*HungGao Hung, 1998*), has the advantages of fast response, insensitivity to parameters and disturbances, simple realization and is very suitable for the control of non-linear tractor hitch system. In this study, adaptive control is added to the nonlinear differential and integral sliding mode controller (DI-SMAC), and the uncertain parameters of the hydraulic hitch system are identified by using the adaptive law (*RenLin Yin, 2005*). Thus, the controller can automatically adapt to the control requirements of different operating conditions. The tractor hydraulic hitch system has better robustness in different operating environments.

To verify the control performance of the tractor hydraulic hitch nonlinear differential and integral sliding mode variable structure adaptive control algorithm, PID controller for tractor hydraulic hitch system is also designed (*Chiriță et al, 2023*). The control performance of PID, I-SMAC and DI-SMAC are compared and analyzed by numerical simulation.

Control algorithm

The expression of a traditional PID controller is:

$$u = k_{\mathrm{p}} e_{\alpha_{\mathrm{ANC}}} + k_{\mathrm{i}} \int e_{\alpha_{\mathrm{ANC}}} dt + k_{\mathrm{d}} \dot{e}_{\alpha_{\mathrm{ANC}}} \tag{4}$$

where, u is the output voltage of the controller (V), $e_{\alpha\mathrm{ANC}}$ is the lifting arm angular displacement deviation (deg), k_{p}, k_{i}, and k_{d} are proportional, integral and differential coefficients, respectively.

Different from the traditional sliding mode control, the integral sliding mode variable structure control introduces the integral term of the tracking error into the switching function (*Cheng Zhu, 2005)*, and uses the state variable to replace the error term, so that the derivative terms of the tracking signal of the displacement output of the hydraulic cylinder can be eliminated. The switching function is defined as:

$$s_1 = c_1 x_1 + c_2 x_2 + x_3 + c_0 \int_0^t \left(x_1 - x_d \right) d\tau \tag{5}$$

where x_d is the reference signal for cylinder displacement in electro-hydraulic control system (m).

The expression of the differential integral sliding mode adaptive control law is:

$$u = -\frac{1}{K_{\mathrm{sv}} \hat{\beta}_1} \left(c_1 x_2 + c_2 x_3 + \hat{a}_1 x_3 + \hat{a}_2 x_2 + \hat{d} + c_0 \left(x_1 - x_{\mathrm{d}} \right) + k s_1 + u_0 \right) \tag{6}$$

where u_0 is the differential controller quantity, and it can be obtained:

$$\begin{aligned} \dot{s}_1 &= c_1 x_2 + c_2 x_3 + (\hat{\beta}_1 + \tilde{\beta}_1) K_{\mathrm{sv}} u + (\hat{a}_1 + \tilde{a}_1) x_3 + (\hat{a}_2 + \tilde{a}_2) x_2 + \hat{d} + \tilde{d} + c_0 \left(x_1 - x_{\mathrm{d}} \right) \\ &= \tilde{\beta}_1 K_{\mathrm{sv}} u + \tilde{a}_1 x_3 + \tilde{a}_2 x_2 + \tilde{d} - k s_1 - u_0 \\ &= \tilde{\beta}_1 K_{\mathrm{sv}} u + \tilde{a}_1 x_3 + \tilde{a}_2 x_2 + \tilde{d} - k s_1 - \varphi(e) \dot{s}_1 \end{aligned} \tag{7}$$

Then:

$$\dot{s}_1 = \frac{\tilde{\beta}_1 K_{\mathrm{sv}} u + \tilde{a}_1 x_3 + \tilde{a}_2 x_2 + \tilde{d} - k s_1}{1 + \varphi(e)} \tag{8}$$

The Lyapunov function is defined as:

$$V = \frac{1}{2} s_1^2 - \frac{1}{2\gamma_1} (\beta_1 - \hat{\beta}_1)^2 - \frac{1}{2\gamma_2} (a_1 - \hat{a}_1)^2 - \frac{1}{2\gamma_3} (a_2 - \hat{a}_2)^2 - \frac{1}{2\gamma_4} (d - \hat{d})^2 \tag{9}$$

The law of adaptive control system is:

$$\begin{cases} \dot{\hat{\beta}}_1 = \dfrac{s_1\gamma_1 K_{sv} u}{1+\varphi(e)} \\ \dot{\hat{a}}_1 = \dfrac{s_1\gamma_2 x_3}{1+\varphi(e)} \\ \dot{\hat{a}}_2 = \dfrac{s_1\gamma_3 x_2}{1+\varphi(e)} \\ \dot{\hat{d}} = \dfrac{s_1\gamma_4}{1+\varphi(e)} \end{cases} \quad (10)$$

Substituting the adaptive law formula (10) into the formula (9), it can be obtained:

$$\dot{V} = -\frac{k s_1^2}{1+\varphi(e)} \le 0 \quad (11)$$

It can be seen from the above formula that the system is still asymptotically stable when differential control variables are introduced.

COMPARATIVE ANALYSIS OF CONTROL ALGORITHM SIMULATION

When the tractor is working in the field, it will sometimes change different plows and adjust the length and position of each link, especially the adjustment at the lifting rod and the pull-down rod. The transmission ratio and load quality of the linkage will change, and long-term operation will also lead to leakage of the hydraulic system. To verify the superior performance of the differential integral sliding mode adaptive controller (DI-SMAC) proposed for the tractor electro-hydraulic hitch system in this study, MATLAB is used to establish simulation models to compare different equivalent masses under different control algorithms and the dynamic response characteristics of the system.

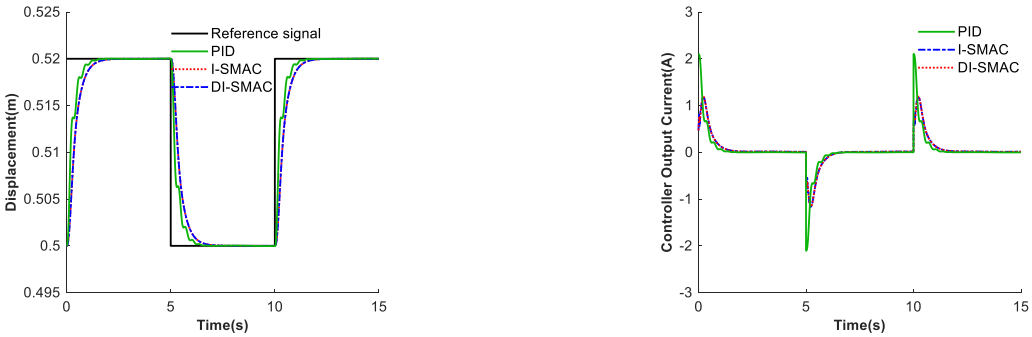

(a) Displacement response curve of hydraulic cylinder (b) Controller input curve

Fig. 3 – Dynamic response diagram with the equivalent mass of 55000 kg

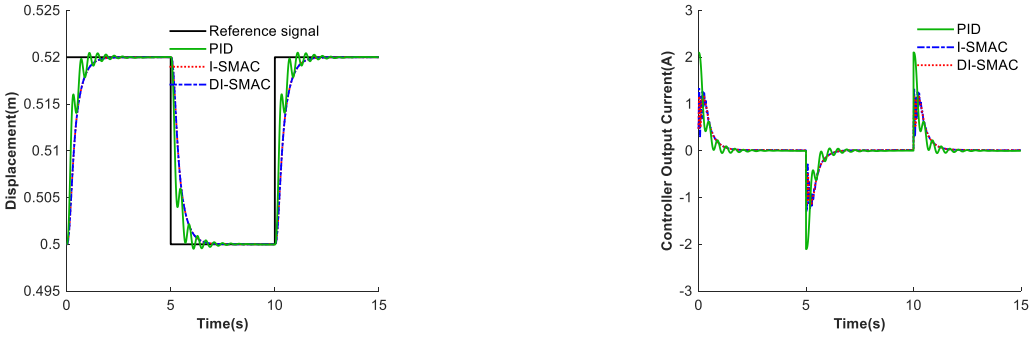

(a) Displacement response curve of hydraulic cylinder (b) Controller input curve

Fig. 4 – Dynamic response diagram with the equivalent mass of 85000 kg

It can be seen from the curve comparison in the above figures that when the PID controller, integral sliding mode adaptive controller (I-SMAC) and differential and integral sliding mode controller (DI-SMAC) are designed according to the equivalent mass of 55000 kg, the three controllers have good control performance. However, when the equivalent mass is changed to 85000 kg (this exists in the actual operation condition, flip plow and non-flip plow), the step response curve of the PID controller begins to shake, and the system oscillates upward, slightly overshooting.

Although the dynamic response curve of the integral sliding mode adaptive controller (I-SMAC) is consistent with that of the differential and integral sliding mode adaptive control (DI-SMAC), the controller input jitters, while the DI-SMAC have good dynamic performance, and the controller output does not jitter.

Thus, compared with the traditional PID controller, the DI-SMAC designed for the tractor electro-hydraulic hitch system can overcome the influence of changing parameters on the system performance when the equivalent mass changes, and has stronger adaptability.

RESULTS AND DISCUSSIONS

TRACTOR FIELD TEST AND RESULT DISCUSSION

Construction of tractor real vehicle test platform

To verify the control performance of the differential integral adaptive sliding mode controller (DI-SMAC) proposed in this study for tractor electro-hydraulic suspension systems, comparative tests were conducted on the traction and position control systems using PID controllers and DI-SMAC controllers. At the same time, the real vehicle test research of the draft-position integrated control was carried out, and a tractor test platform was built based on a certain type of tractor, as shown in Figure 5.

Fig. 5 – Field test platform of tractor electro-hydraulic hitch control system

1. Upper computer; 2. Power supply; 3. Controller; 4. Proportional amplifier; 5. CAN series module; 6. Lift arm angle sensor; 7. Displacement sensor; 8. Pressure sensor; 9. Force measuring pin; 10. Electro-hydraulic proportional valve; 11. Front wheel speed measurement encoder; 12. Rear wheel speed measurement encoder

The main hardware parameters of field test platform for tractor hydraulic hitch control system are shown in Table 1.

Table 1

Hardware parameter table of electro-hydraulic hitch test platform

Type	Model	Operating parameters
Force measuring pin	YZC-9	Working voltage: 24V, output: -10V~10V analog signal, customized measuring range -50000N~50000N, comprehensive error <0.05
Displacement sensor	LWH-0250	Working voltage: 12V, output: 0~10V analog signal, measuring range 0-250mm, resolution > 0.01mm
Pressure sensor	MIK-P300	Working voltage: 24V, output: 0-5V analog signal, accuracy 12 bits, customized range 0-20MPa
Controller	TMS320F28335	Working voltage: 3.3V, with strong signal processing and communication capability, two ways to enhance eCAN, support floating point operation, support external serial communication
Proportional amplifier	AEG-12A-02	Working voltage: 24V, CAN bus input interface, maximum output current adjustable, 0.2~3A

Field test of tractor electro-hydraulic hitch position control system

The test plot is a typical northern China field in Shangzhuang Test Station of China Agricultural University (116.1 ° E, 40.07 ° N). The soil firmness of 20 cm below the surface is about 130.5 kPa on average, and the soil hardness of the plot changes greatly. The plot is uncultivated land after corn harvest, and the ground undulates greatly.

The fitting formula between tillage depth and displacement of hydraulic cylinder is:

$$h_p = 8.81 x_L - 0.866 \tag{12}$$

The tractor is set in B1 gear and the engine is maintained at 2000 r/min. After plowing into the soil, carry out relevant control according to control instructions. During the field test of the tractor, keep the speed stable. To prevent excessive skidding of the tractor during plowing, the four-wheel drive mode is adopted. After the plow body is stabilized in the soil, set the plow depth to a step change of 30 cm to 24 cm, and use the upper computer to conduct real-time monitoring and data recording on the message information transmitted on the CAN network during the plowing period. Intercept the test data within 35 s, and obtain the plow depth change curve, as shown in Figure 6.

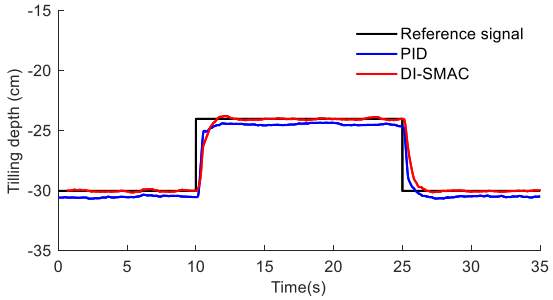

Fig. 6 – Response curve of position controlled tillage depth

From Figure 6 it can be seen that the lifting process using the PID controller and DI-SMAC has no overshoot, and the response time is about 1.7 s. However, the static error of the depth control using the PID controller is about 0.5 cm, while the DI-SMAC has no static error basically. In the descent process, the response time of the PID is about 1 s, while that of DI-SMAC is about 1.6 s. The DI-SMAC can overcome the influence of nonlinear factors of control valve lifting and lower on the hitch system, and the control performance is better.

Field test of tractor electro-hydraulic hitch control system

During the field draft control test, keep the tractor speed stable. When the plow body is stable in the soil, the draft setting value is 5000 N. The upper computer monitors and records the message information transmitted on the CAN network in the real time during the plowing period, intercepts the test data within 120 s, and obtains the test results as shown in Figure 7.

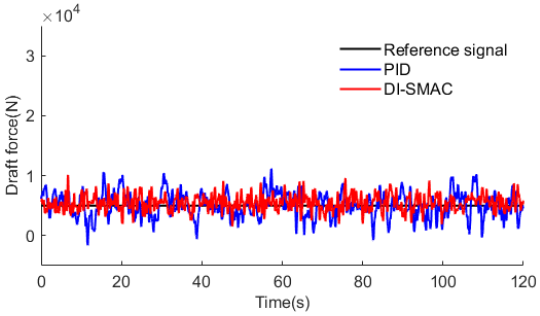

(a) Draft response curve

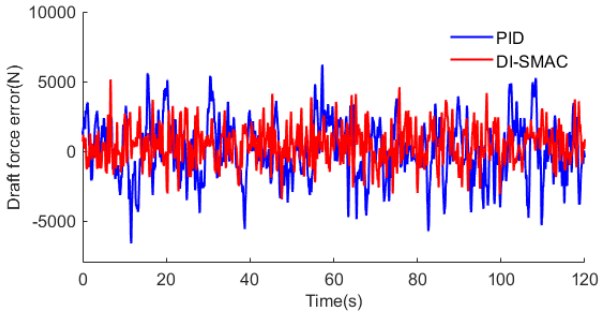

(b) Draft tracking error of different control algorithms

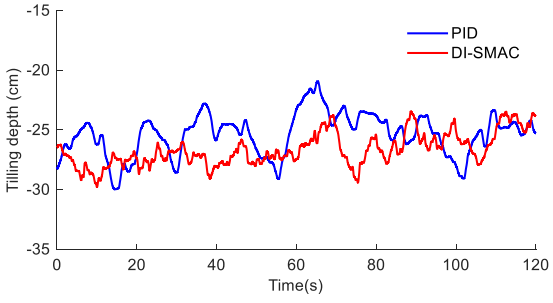

(c) Response curve of tillage depth

Fig. 7 – Response curve of tillage depth under draft control

From Figure 7 (a) it can be seen that when the draft control mode is adopted, the draft fluctuates up and down at the set value. Under different set of the draft values, the fluctuation range of the draft controlled by the PID is 12820 N, and the standard deviation of the draft is 2076 N; the fluctuation range of the draft using differential and integral sliding mode adaptive control (DI-SMAC) is 8590 N, and the standard deviation of draft is 1275 N. When the DI-SMAC is used, the range of draft is reduced by 32.9%, and the standard deviation of the draft is reduced by 38.6%. The DI-SMAC can improve the control performance of the tractor electro-hydraulic hitch draft control system. By comparing the effects of the PID controller and derivative and integral sliding mode adaptive controller (DI-SMAC) of position control and draft control system, it can be seen that the derivative and integral sliding mode adaptive controller (DI-SMAC) designed for tractor electro-hydraulic hitch has better tracking characteristics and higher control accuracy than the traditional PID controller.

Field test of draft and position integrated control

The reference signal of draft is set as 5000 N, the plowing depth is 30 cm, and the draft-weight are set as 30% and 70%, respectively. The DI-SMAC is used for experimental research. During the field test, the upper computer monitors and records the message information transmitted on the CAN network in real time during plowing, intercepts the test data within 120 s, and obtains the test results, as shown in Figure 8.

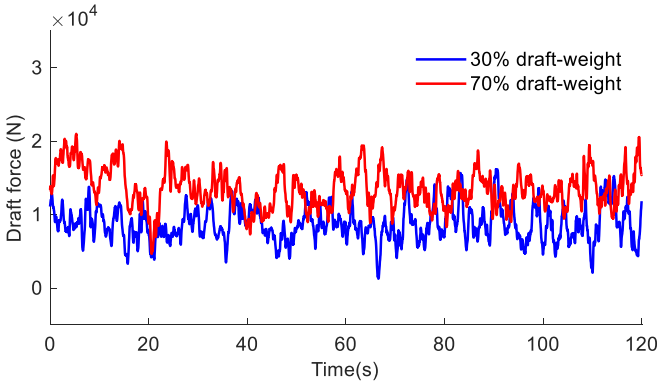

(a) Draft response curve

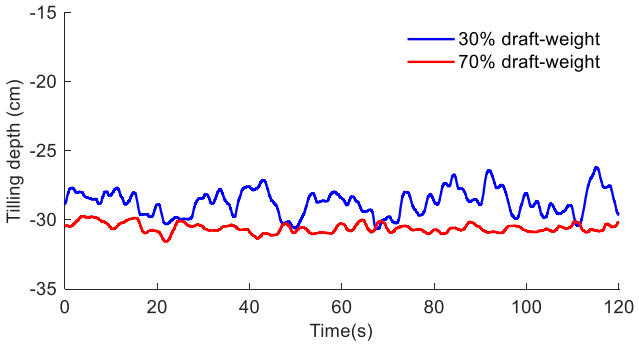

(b) Response curve of tillage depth

Fig. 8 – Response curve of draft and position integrated control

From Figure 8 it can be seen that when the draft and position integrated control mode is adopted, the variation range of draft fluctuation and tillage depth is different under different draft-weight. When the draft-weight is 30%, the fluctuation range of draft is 14890 N, the standard deviation of draft is 2350 N, and the average value of draft is 8717 N; the fluctuation range of tillage depth is 4.47 cm, the standard deviation of tillage depth is 0.947 cm, and the mean value is -26.1 cm. When the draft-weight is 0.7, the fluctuation range of draft is 16350 N, the standard deviation of draft is 2640 N, and the average value of draft is 13550 N; the fluctuation range of tillage depth is 1.84 cm, the standard deviation of tillage depth is 0.339 cm, and the mean value is -29.7 cm.

When the draft-weight is 0, it is in draft control mode. It can be seen from Figure 7 that when the draft-weight is more minor, the draft fluctuation is smaller, and the tillage depth fluctuation is more significant, which is more consistent with the simulation results.

CONCLUSIONS

The control effect of the tractor electro-hydraulic hitch directly determines the quality of the plowing operation. Based on analyzing the dynamics of the plowing operation of the tractor unit, this study designed a DI-SMAC for the electro-hydraulic hitch system, and different controllers are compared and verified through simulation and field test of the tractor. A more comprehensive mathematical model of the plow unit considering the factors such as tractor pitching motion and ground undulation is established. The feasibility and effectiveness of the designed controller are verified by numerical simulation and tractor field tests. The field tests of the tractor show that the DI-SMAC can realize the draft and position integrated control. In the position control mode, the DI-SMAC has basically no static error and strong anti-interference ability; under the draft control mode, compared with the traditional PID controller, the range of traction error of DI-SMAC is reduced by 32.9%, and the standard deviation is reduced by 38.6%; Under the draft and position integrated control, the fluctuation of traction force and tillage depth is different with different draft-weight. The controller designed for the electro-hydraulic hitch system in this study can provide a method to improve the quality of field work, and provide guidance for further research.

ACKNOWLEDGEMENT

The author would like to thank for the support by the National Key Research and Development Program (2017YFD0700101), Jiangsu Ocean University Talent Introduction Research Fund Project (KQ22018), and Natural Science Foundation of the Jiangsu Higher Education Institutions of China (23KJB210007).

REFERENCES

[1] Bacenetti, J., Lovarelli, D., Facchinetti, D., Pessina, D. (2018). An environmental comparison of techniques to reduce pollutants emissions related to agricultural tractors. *Biosystems Engineering*, 171, 30-40.

[2] Balsari, P., Biglia, A., Comba, L., Sacco, D., Eloi Alcatrão, L., Varani, M., Mattetti, M., Barge, P., Tortia, C., Manzone, M., Gay, P., Ricauda Aimonino, D. (2021). Performance analysis of a tractor - power harrow system under different working conditions. *Biosystems Engineering*, 202, 28-41.

[3] Bentaher, H., Hamza, E., Kantchev, G., Maalej, A., & Arnold, W. (2008). Three-point hitch-mechanism instrumentation for tillage power optimization. *Biosystems engineering*, 100(1), 24-30.

[4] Guan, C., & Zhu, S. A. (2005, February). Derivative and integral sliding mode adaptive control for a class of nonlinear system and its application to an electro-hydraulic servo system. *In Zhongguo Dianji Gongcheng Xuebao* (Proc. Chin. Soc. Electr. Eng.) (Vol. 25, No. 4, pp. 103-108).

[5] Cheng, J., Chi, R., Lai, Q., Yang, Y., Mao, E. (2017). Active vibration control of tractor based on electro-hydraulic hitch system. *Transactions of the Chinese Society of Agricultural Engineering*, 33(5), 82-90.

[6] Gupta, C., Tewari, V. K., Ashok Kumar, A., Shrivastava, P. 2019. Automatic tractor slip-draft embedded control system. *Computers and Electronics in Agriculture*, 165, 104947.

[7] Hung, J. Y. Gao, W. Hung, J. C. (1998). Variable Structure Control: A Survey. *IEEE Transactions on Industrial Electronics*, 40(1), 2-22.

[8] Janulevičius, A., Šarauskis, E., Čiplienė, A., Juostas, A. (2019). Estimation of farm tractor performance as a function of time efficiency during ploughing in fields of different sizes. *Biosystems engineering*, 179, 80-93.

[9] Khodayari, M. H. Balochian, S. (2015). Modeling and control of autonomous underwater vehicle (AUV) in heading and depth attitude via self-adaptive fuzzy PID controller. *Journal of Marine Science and Technology*, 20(3), 559-578.

[10] Lee, J., Yamazaki, M., Oida, A., Nakashima, H., Shimizu, H. (1998). Electro-hydraulic tillage depth control system for rotary implements mounted on agricultural tractor Design and response experiments of control system. *Journal of Terramechanics*, 35(4), 229-238.

[11] Lee, J. W. Kim, J. S. Kim, K. U. (2016). Computer simulations to maximise fuel efficiency and work performance of agricultural tractors in rotovating and ploughing operations. *Biosystems Engineering*, 142, 1-11.

[12] Li, M. S., Zhao, J. J., Zhu, Z. X., Xie, B., Chi, R. J., & Mao, E. R. (2013). Fuzzy-PID self-adaptive control method in electro-hydraulic hitch system. *Transactions of the CSAM*, 44(Z2), 295-300.

[13] Li, T., & Hu, J. (2014). Adaptive sliding mode control method based on nonlinear integral sliding surface for agricultural vehicle steering control. *Mathematical Problems in Engineering*, 2014.

[14] Liu, C., Zhao, J., Gu, J., Du, Y., Mao, E. 2020. Pressure Control Algorithm Based on Adaptive Fuzzy PID with Compensation Correction for the Tractor Electronic Hydraulic Hitch. *Applied Sciences*, 10(9), 3179.
[15] Lu, Z. Guo, B. Gao, Q. (2013). Study on auto-control method and experiment for tractor depth based on fuzzy control. *Transactions of the Chinese Society of Agricultural Engineering*, 29(23), 23-29.
[16] Xiwen, L., Penghui, S., Zhigang, Z., Jixun, Z., Zhaopeng, L., & Yajiao, Z. (2015). Electrohydraulic hitch control system for tractor based on linear actuator. *Nongye Jixie Xuebao/Transactions of the Chinese Society of Agricultural Machinery*, 46(10), 1-6.
[17] Pranav, P. K., Tewari, V. K., Pandey, K. P., Jha, K. R. (2012). Automatic wheel slip control system in field operations for 2WD tractors. *Computers and Electronics in Agriculture*, 84, 1-6.
[18] Ren, F. Lin, C. Yin, X. (2005). Design a congestion controller based on sliding mode variable structure control. *Computer communications*, 28(9), 1050-1061.
[19] Song, Z., Wang, L., Liu, Y., Wang, K., He, Z., Zhu, Z., ... & Li, Z. (2022). Actively steering a wheeled tractor against potential rollover using a sliding-mode control algorithm: Scaled physical test. *Biosystems Engineering*, 213, 13-29.
[20] Treichel, R., & Moon, S. (1984). U.S. Patent No. 4,438,818. Washington, DC: U.S. Patent and Trademark Office.
[21] Saeys, W., Mouazen, A. M., Anthonis, J., & Ramon, H. (2004). An automatic depth control system for online measurement of spatial variation in soil compaction, part 2: Modelling of the depth control system. *Biosystems engineering*, 89(3), 267-280.
[22] Wang, L., Wang, Y., Dai, D., Wang, X., Wang, S. (2021). Review of electro-hydraulic hitch system control method of automated tractors. *International Journal of Agricultural and Biological Engineering*, 14(3), 1-8.
[23] Wang, S. Y., Liu, Z., Li, R. C., Xu, J. K., & Liu, Y. J. (2018). Variable weight force-position mixed control of high-power tractor based on soil specific resistance. *J. Agric. Mach*, 49, 351-357.
[24] Zhou, Y. Wen, X. Xu, Q. (2021). Precise motion control of tractor-trailer wheeled mobile structures via a newly observed key motion law. *Nonlinear Dynamics*, 103(1), 833-848.
[25] Chiriță, A. P., & Pavel, C. (2023). Agricultural platform equipped with a hydrostatic transmission capable of continuously adjustable travel velocity and non-linear disturbance compensation capabilities. *INMATEH-Agricultural Engineering*, 69(1), 427-436. https://doi.org/10.35633/inmateh-69-40

DESIGN AND EXPERIMENT OF FILM LAYING QUALITY MONITORING SYSTEM FOR COTTON PRECISION PLANTER
/
棉花精量播种机铺膜质量监测系统设计与试验

Shenghe BAI[1,2], Yanwei YUAN[1,2], Gaoyong XING[1,2], Liang WEI[1,2], Kang NIU[1,2], Liming ZHOU[1,2], Bo ZHAO[1,2], Liguo WEI[1,2], Lijing LIU[1,2]

[1] China Agricultural University, Beijing 100083, China

[2] Chinese Academy of Agricultural Mechanization Sciences Group Co., Ltd, National Key Laboratory of Agricultural Equipment Technology, Beijing 100083, China

Tel: +86-13815375524; E-mail: 13815375524@163.com

DOI: https://doi.org/10.35633/inmateh-70-37

Keywords: *Cotton precision planters; Film; Film laying quality; Monitoring accuracy; System*

ABSTRACT

To realize real-time monitoring of film laying process of cotton precision planter and improve intelligent level of cotton precision planter, based on advanced morphological filtering method and graphical programming of Labview software, a film laying quality monitoring system of cotton precision planter is designed. Using the Vision Assistant visual assistant, the system uses a color extraction function to convert colors to grayscale images. It uses LOOKup Table function and FFT filter function to perform grayscale transformation, binarization and advanced morphological filtering on it respectively. It then uses basic morphology to acquire various components in the plastic film image. It realizes the monitoring of parameters such as the width of the daylighting surface, the side length or seam length of the mechanical damaged part, and the width of the film edge covering soil. The performance test results of the film laying quality monitoring system showed that the system worked stably and reliably, the average monitoring accuracy of the width of the lighting surface and the width of the film edge covering soil reached more than 95%, and the average monitoring accuracy of the side length or the length of the seam at the mechanical damage part reached more than 88%. It solved the problems of difficulty in recognizing the similarity between the plastic film and the background interferer (soil, etc.) and could accurately detect the quality of the cotton film in real time. It effectively improved the operation quality and working efficiency of the cotton precision planter and met the practical requirements of film laying monitoring.

摘 要

为了实现棉花精量播种机铺膜作业过程的实时监测，提高棉花精量播种机智能化水平，基于高级形态学滤波方法，采用 Labview 软件图形化编程，设计了棉花精量播种机铺膜质量监测系统。系统运用 Vision Assistant 视觉助手，使用颜色提取函数将彩色转换为灰度图像，通过 LOOKup Table 函数和 FFT 滤波函数分别对其进行灰度变换、二值化与高级形态学滤波，再运用基本形态学获取地膜图像中的各个成分，实现对采光面宽度、机械破损部位的边长或缝长、膜边覆土宽度等参数监测。铺膜质量监测系统台架性能试验结果表明：该系统工作稳定可靠，采光面宽度、膜边覆土宽度平均监测精度达到 95%以上，机械破损部位的边长或缝长平均监测精度达到 88%以上，解决了地膜与背景干扰物（土壤等）相近识别难度大等问题，能实时准确地检测棉花铺膜质量，有效提高了棉花精量播种机的作业质量和工作效率，满足铺膜监测实际要求。

INTRODUCTION[1]

Cotton is the main economic crop in Xinjiang. According to statistics, in 2021, Xinjiang's cotton planting area reached 2.61 million hm^2 (accounting for 83% of the country), and its output was 5.13 million t (accounting for 89% of the country) (*National Bureau of Statistics of the People's Republic of China, 2011; Bureau of Statistics of Xinjiang Uygur Autonomous Region Xinjiang statistical Yearbook, 2021*). Xinjiang has become the largest cotton producing region in China. At present, cotton planting has generally adopted the technique of mulching precision cave-seeding. Among them, mulching film has the functions of increasing soil temperature and preserving soil moisture, improving soil and inhibiting weeds, which has become a key means to reduce diseases and insect pests and increase crop yield (*Zhai Z.Q. et al., 2022; Zhang S., 2008; Xing J.F. et al, 2021)*.

Shenghe BAI, Ph.D. Stud. Eng.; Yanwei YUAN, Prof. Ph.D. Eng.; Gaoyong XING, Ph.D. Stud. Eng.; Liang WEI, M.S. Stud. Eng.; Kang NIU, Prof. Ph.D. Eng.; Liming ZHOU, Prof. Ph.D. Eng.; Bo ZHAO, Prof. Ph.D. Eng.; Liguo WEI, Prof. Ph.D. Eng.; Lijing LIU, Prof. Ph.D. Eng.*

Due to the harsh working environment in the field, the working parts are more complex, easy to appear film tearing, insufficient lighting surface and other problems. Drivers understand the quality of the film needs to stop, relying on the naked eye to judge. If the fault cannot be found and indicated in time, it will seriously affect the yield and benefit of cotton, and it is difficult to meet the current demand for rapid detection of film laying quality. Therefore, it is of great practical significance to realize real-time monitoring of film laying quality of cotton precision planter to improve operation quality and promote mechanization informatization.

With the continuous development and improvement of science and technology, in modern agricultural production, intelligence is an important development direction of agricultural machinery equipment, and has become a new trend of sustainable agricultural development (*Kong Y.L. et al., 2012*). The detection technology of plastic film mainly includes ultrasonic technology (*Zhang Q. et al., 2013*), polarized light technology (*Zhang C. et al., 2017; Peng B. et al., 2015*), infrared technology (*Zhang D.W. 2019; Lu L. et al., 2015*), low altitude drone imaging (*Banerjee B. et al., 2020; Adão T. et al., 2017*), machine vision (*Zhang X., 2020*), etc. Among them, ultrasonic technology is easily disturbed by external environmental noise and produces misjudgment; The precision of polarized light technology is not high and its performance is unstable; Infrared technology and low altitude drone imaging are easily affected by ambient temperature and humidity, and the maintenance cost is high; Machine vision plays the role of "eyes". Based on the color, contour and distribution characteristics, the specific area of the target or non-target crop is expanded and corrode to achieve the purpose of highlighting. It has the characteristics of high precision, fast speed and non-destructive, which is widely used in various fields and has a broad prospect (*Li Q.L. et al., 2020; Qin C.B. et al., 2019; Diao Z.H. et al., 2014; Hou J.L. et al., 2020*).

With the increasing maturity of machine vision technology *(Bu L.X. et al., 2020)*, it has also developed rapidly in farmland plastic film recognition, and scholars have carried out a lot of research on it. Lu et al. was based on spectral characteristics to extract geomembrane information from the influence of Landast satellite time series (*Lu L. et al., 2014*). Liang Changjiang et al (*Liang C.J. et al., 2019*) used the traditional image segmentation algorithm to identify the farmland plastic film image collected by the UAV, and the results showed that the iterative threshold segmentation algorithm had the best effect; Zhang Xuejun et al (*Zhang X.J. et al., 2021*) optimized Faster R-CNN convolution neural network and used double threshold algorithm to reduce the influence of threshold on model performance; Wu Xuemei et al (*Wu X.M. et al., 2020*) put forward a recognition method based on color characteristics, using pulse coupled neural network to realize the recognition of plastic film in different periods. *Zhai Zhiqiang et al* proposed a method for detecting the coverage of cotton field surface residues before sowing based on pixel blocks and machine learning (*Zhai Z.Q. et al., 2022*). Most of the above-mentioned documents are in the stage of algorithm research and are not combined with hardware. They are all based on the recognition of plastic film images under experimental conditions. There are high requirements for the recognition environment, and the related technologies are still immature. And it is reported that the quality monitoring of film laying has not been explored yet. Therefore, it is necessary to carry out further research on real-time monitoring technology of film laying quality aiming at the complex operating environment of cotton precision planter.

In order to realize real-time monitoring of film laying quality of cotton precision planter, an advanced morphological filtering method is proposed to realize film laying image recognition. In this study, Labview is used to build and develop the quality monitoring system of film laying, and the performance tests are carried out to improve the precision sowing quality of cotton.

MATERIALS AND METHODS

Image acquisition system

The film laying image acquisition system of cotton precision planter includes high-definition network camera (Logitech, C920e), bracket and upper computer. Among them, the camera's field of view angle is 72°, the acquisition capacity is 30 frames/s, and it can automatically zoom and expose. It has the characteristics of clear image, strong adaptability and low cost. The software and hardware of the upper computer are configured as Windows 11 64-bit system, with 16 GB of RAM, Intel Core i9-12900H CPU, and 2.50 GHz main frequency. LabView software is selected for graphical programming, and Vision Assistant is used for image morphology processing. It has a complete image processing function library, rich and powerful functions, and can process images efficiently and quickly (*Hou Z.F. et al., 2022; Zhang, X.W. et al., 2022*).

The shooting object distance is 80 cm (that is, the height of the camera from the ground), and keep the camera vertically downward, the image size is 1280 pixels × 960 pixels, image format is. jpg; Get high-quality images.

The upper computer collects, processes, identifies and displays the film image once through the camera to obtain real-time film samples, so as to realize online monitoring of film laying quality. The image acquisition system is shown in Figure 1.

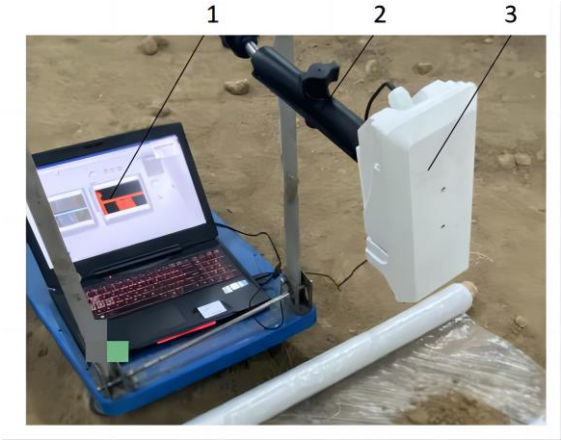

Fig. 1 - Image acquisition system

1. Upper computer; 2. Bracket; 3. HD network camera

Image data acquisition and processing

- **Image data acquisition**

The experimental area of this study is located in the cotton planting area of Tiemenguan City, Xinjiang, China. It is covered with plastic film to sow cotton all year round. The cotton variety is Xinluzao 78. The image acquisition time was April 20, 2022, as shown in Figure 2. The camera was connected with the host computer through USB interface, and the image acquisition system described in this paper was used to collect the film image in real time. The corresponding physical size of the ground was 60 cm×45 cm, a total of 50 near-ground original images of the sampling area were taken. The software interface is shown in Fig. 3.

(a) Test area scenario *(b) Sampling area image*

Fig. 2 - Schematic diagram of study area

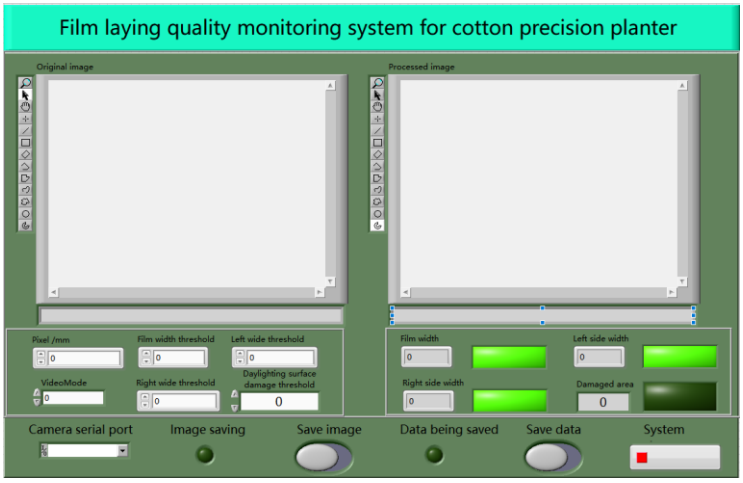

Fig. 3 - Software diagram

Figure 4 shows the collected film image samples, mainly including film and soil. This paper mainly realizes the recognition of the above two components, and constructs a quantitative model to judge the film laying quality of cotton precision planter.

Fig. 4 - Physical picture of plastic film sample

- **Image recognition process**

The image system collects the film image of the mechanized film laying process. Because the surface of the residual film is attached with soil, soil reflection and other phenomena, it is necessary to accurately identify the film and the main components of soil from the complex image. The image collected in this study is RGB image, and the RGB components of the original image are obtained, and then the color is converted into gray image using color extraction function; It uses the LOOKup Table function to transform its gray level and filter it through the FFT filter function. Then it is binarized and advanced morphological filtering. Basic morphology is used to obtain the recognition results of each component in the film image. The image recognition process is shown in Figure 5.

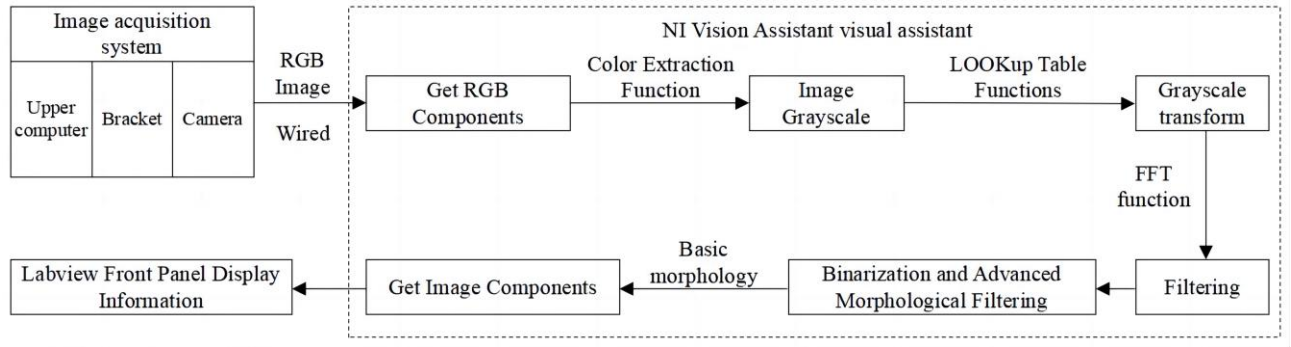

Fig. 5 - Flow chart of image recognition

- **Image preprocessing**

The effect of image preprocessing directly affects the recognition error of subsequent film sample images. In order to facilitate feature extraction and improve recognition accuracy, it is necessary to carry out color plane extraction, filtering, threshold segmentation and morphological analysis on image samples.

(1) Color plane extraction

Since the background of the film sample image is gray soil, the debugging shows that extracting the red plane can better highlight the film contour and eliminate background interference. First, the color image is converted into a grayscale image through the color extraction function, and then the Lookup Table function is used for grayscale transformation.

In this paper, the commonly used color feature RGB is selected in image processing, and the color moments in the color feature are statistically analyzed to achieve effective classification of the film sample image. The color distribution information is mainly concentrated in the first moment (Mean), second moment (Variance) and third moment (Skewness). The first order moment uses the first order origin moment (mean value) to reflect the overall shading procedure of the image. The larger the value, the brighter the image; The second order moment uses the square root of the second order center distance (standard deviation) to reflect the color distribution range of the image. The larger the value, the wider the color distribution range.

The cubic root (deviation) of the third-order center distance is adopted for the third-order moment to reflect the symmetry of image color distribution (*Chen M. et al., 2021*).

Then the calculation formula of the first moment, second moment and third moment is:

$$\begin{cases} \delta_a = \frac{1}{B}\sum_{b=1}^{B} P_{ab} \\ \mu_a = \sqrt{\left(\frac{1}{B}\sum_{b=1}^{B}\left(P_{ab}-\delta_a\right)^2\right)} \\ \eta_a = \sqrt[3]{\left(\frac{1}{B}\sum_{b=1}^{B}\left(P_{ab}-\delta_a\right)^3\right)} \end{cases} \quad (1)$$

where:

δ_a —the color mean value of the a-th color channel of all pixels;

P_{ab}—the color value of the b- th pixel on the a-th color channel;

μ_a —the standard deviation of the a color channel;

η_a —the color deviation of the a color channel.

Grayscale image is shown in Figure 6.

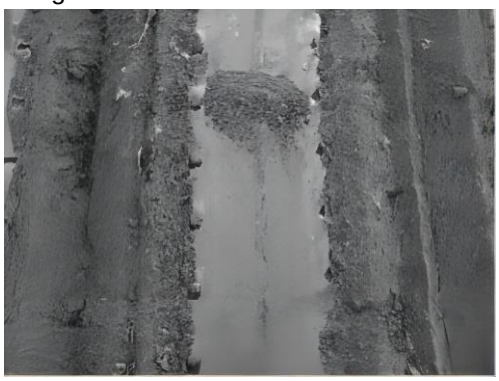

Fig. 6 - Grayscale image

(2) Image filtering

Image filtering has the characteristics of improving image quality, enhancing recognition effect and enriching details. As the surface of the plastic film is attached with soil, soil block, and reflection, it increases the difficulty of treatment. To this end, FFT function and efficient morphological filtering are used first, and details are highlighted. This method can effectively highlight the details of the film, strengthen the high-frequency information such as the contour and edge of the target, and sharpen the image. The filtering effect is shown in Figure 7.

Fig. 7 - Filtered image

(3) Threshold segmentation

The image segmentation is divided into different sub-regions according to the parameters such as image gray level and shape, so as to ensure that the parameters are similar in the same region and show obvious differences between different regions (*Gao L., 2016*). The automatic threshold segmentation method is based on the gray histogram of the image to determine the gray threshold, and has strong applicability.

The minimum uniformity measurement method supported by Ni Vision (LabView built-in visual development kit) (*Jiang L.L. et al., 2019*) is selected (assuming that the image is divided into target A and background B, and the pixel value distribution of the same category should be uniform). The class uniformity can be measured by variance. Then the algorithm steps are as follows:

Given the initial threshold *S*, the pixel values of the image to be segmented are expressed in m (width) and *n* (height) respectively. Then the calculation formula of gray mean value and intra-class variance corresponding to D_1 and D_2 after segmentation is:

$$\begin{cases} \mu_1 = \dfrac{1}{N_{D_1}} \sum\limits_{(x,y)\in D_1} f(x,y) \\ \mu_2 = \dfrac{1}{N_{D_2}} \sum\limits_{(x,y)\in D_2} f(x,y) \\ \sigma_1^2 = \sum\limits_{(x,y)\in D_1} \left(f(x,y)-\mu_1\right)^2 \\ \sigma_2^2 = \sum\limits_{(x,y)\in D_2} \left(f(x,y)-\mu_2\right)^2 \end{cases} \quad (2)$$

It selects the threshold that meets the condition λ^*, and ensures that the image is divided into D_1 and D_2, and meet the following requirements:

$$\begin{cases} \left[P_1\sigma_1^2 + P_2\sigma_2^2\right]_{\lambda=\lambda^*} = \min\left(P_1\sigma_1^2 + P_2\sigma_2^2\right) \\ P_1 = \dfrac{N_{D_1}}{mn} \\ P_2 = \dfrac{N_{D_2}}{mn} \end{cases} \quad (3)$$

where:

μ_1—the gray mean value corresponding to D_1;

μ_2—the mean gray value corresponding to D_2;

σ_1—the intra-class variance corresponding to D_1;

σ_2—the intra-class variance corresponding to D_2;

$F(x, y)$—the gray level at any point (x, y) on the original image;

N_{D1}—the number of pixels in category 1;

N_{D2}—the number of pixels in category 2;

P_1—the distribution probability in the Class 1 image;

P_2—the distribution probability in the class 2 image.

The film image processing after threshold segmentation is shown in Figure 8.

Fig. 8 - Threshold segmentation image

(4) Morphological analysis

After thresholding, the binary image is processed by mathematical morphology denoising method, and then eroded and expanded. It also performs an open operation (local modification) to remove unnecessary information (noise, overlapping areas, etc.) from the image.

At the same time, it guarantees not to destroy the details of the image edge contour, and improves the accuracy of the algorithm (*Tai H.J., 2019; Kang S., et al., 2021*). Then the gray-level morphology processing formula is as follows:

$$\begin{cases} (f\Theta b)(x,y) = \min\limits_{(s,t)\in bN}\{f(x+s,y+t)-b_N(s,t)\} \\ [f\oplus b](x,y) = \min\limits_{(s,t)\in bN}\{f(x-s,y-t)+b_N(s,t)\} \\ f\circ b = (f\Theta b)\oplus b \end{cases} \quad (4)$$

where:

$(f\Theta b)(x,y)$—gray-level morphological corrosion treatment;

f—the original image correlation matrix;

Θ—consistent with corrosion operation;

min—the minimum value operation symbol;

b_N—the structure range element;

（s，t）—the coordinate element;

$(f\oplus b)(x,y)$—gray-level morphological expansion processing;

$f\circ b$—an open operation processing of gray-level morphology;

$\circ$—an open operation symbol;

$\oplus$—the expansion operation compliance;

b—a non-flat structural element.

The film image processing after morphological analysis is shown in Figure 9. It uses the particle analysis function of NI Vision Assistant to obtain the sample coordinate value. It obtains the image data such as the width of the lighting surface of the plastic film, the length of the side or seam of the mechanical damaged part, and the width of the soil covering on the film side through calculation.

Fig. 9 - Morphological analysis image

Performance test design of monitoring system

With reference to the national machinery industry standard JB/T 7732-2006 "Film Planter" (*National Agricultural Machinery Standardization Technical Committee, 2007*) and the national agricultural industry standard GB/T5262-2008 "Operation quality of film planter" (*National Agricultural Machinery Standardization Technical Committee, 2009*), the evaluation index of the film laying quality of cotton precision planter is determined. On the measured plot, five survey areas are randomly and equidistant along the diagonal, with each survey area having a width of 1 working width and a length of 10 m.

Take 5 measuring points at random in each measuring area and measure the width of the lighting surface (within the range of (B-300 mm) to (B-150 mm), which is qualified (B is the width of the film), the side length or seam length of all mechanical damaged parts of the film on the lighting surface in each measuring area, and the width of the soil covering on the film side (between 50 and 100 mm, which is qualified).

Then the calculation formula of the qualified rate of the width of the lighting surface, the mechanical damage degree of the lighting surface, and the qualified rate of the width of the covering soil at the edge of the film is as follows (*Feng W.H., 2012*):

$$\begin{cases} S_a = \dfrac{N_1}{N_2} \times 100\% \\ Sc = \dfrac{1000 \sum_{i=1}^{n} L_i}{LB} \\ S_d = \dfrac{N_d}{N_o} \times 100\% \end{cases} \quad (5)$$

where:

S_a—the qualified rate of daylighting surface width, %;

N_1—the number of qualified points of daylight surface width;

N_2—the total number of points measured for the width of the daylighting surface;

S_c—the mechanical damage degree of the daylighting surface, mm/m^2;

L_i—the side length or seam length of the ith mechanical damaged part in the survey area, mm;

L—the length of the survey area, m;

B—the average value of the film width of the mining surface in the survey area, mm;

S_d—the qualified rate of the width of soil covering on the membrane side, %;

N_d—the number of qualified points for the width of soil covering on the membrane side;

N_o—the total number of measuring points.

The qualified rate of the width of the daylight surface, the mechanical damage degree of the daylight surface, and the qualified rate of the width of the covering soil beside the film calculated by formula (5) are compared with the preset theoretical values to determine the quality of the film. If the monitoring value is greater than the threshold, the alarm will be given, and vice versa, it will work normally.

In order to verify the accuracy of the monitoring system, a bench test bench was built in the State Key Laboratory of Soil and Plant Machinery System Technology of the Chinese Academy of Agricultural Mechanization. The test was carried out in July 2022, and the accuracy monitoring test of the width of the daylighting surface, the length of the side or seam of the mechanical damaged part, and the width of the film side covering soil were carried out respectively. The polyethylene transparent agricultural film with a film thickness of 0.005 mm was selected as the test sample, without adhesion and damage. The test device includes bench, trolley, monitoring system, tape measure, etc. The test bench is shown in Figure 10.

Fig. 10 - Test bench

- **Daylighting surface width monitoring test**

The purpose of the test was to evaluate the accuracy of the image acquisition system in the monitoring system in monitoring the width of the daylight face (that was, the accuracy of the monitoring of the qualified points of the width of the daylight face, and then calculate the qualified rate of the width of the daylight face).

In the test, the lighting surface width of 130, 170, 210, 250 and 290 mm was set respectively. Start the system, open the data and image saving button, and move forward 5 m.

Select 3 time points randomly from the monitoring test results of the width of each daylighting surface, and call up the images and data corresponding to each time point. Record the actual value and monitoring value in the test table, and calculate the monitoring error of the width of the daylighting surface.

- **Monitoring test for side length or seam length of mechanical damaged parts**

In order to evaluate the accuracy of the monitoring of the side length or seam length of the mechanical damaged part of the system (that was, the accuracy of the monitoring of the mechanical damage degree of the daylighting surface), the artificial damage of the plastic film in the test was set as 15, 20, 25, 30 and 35 mm for the side length or seam length of the mechanical damaged part, and the repeatability test was conducted for 3 times. The monitoring accuracy was calculated by comparing the side length or seam length of the mechanical damaged part with the actual value, and the average value of three tests was taken as the monitoring test result of the side length or seam length of the mechanical damaged part.

- **Monitoring test on the width of soil covering at the edge of the membrane**

In order to further evaluate the accuracy of the system's monitoring of the width of soil covering at the edge of the membrane (that was, the number of qualified points of the width of soil covering at the edge of the membrane, and then calculate the qualified rate of the width of soil covering at the edge of the membrane), the width of soil covering at the edge of the membrane was set as 130, 160, 190, 220, and 250 mm respectively in the test. Start the system, open the data and image saving button, and move forward 5 m. In this test, three time points were randomly selected from the monitoring test results of the width of the soil covering around the membrane, and the corresponding images and data of each time point were retrieved. The actual values and monitoring values were recorded in the test table, the monitoring accuracy of the width of the soil covering around the membrane was calculated, and the average value of three tests was taken as the monitoring test results of the width of the soil covering around the membrane.

RESULTS AND ANALYSIS

The monitoring test results of different daylighting surface widths were shown in Table 1. The test showed that the monitoring range of daylighting width was 94.12%~97.60%, and the average monitoring accuracy was 95.99%. The side length or seam length monitoring test results of different mechanical damaged parts were shown in Table 2. The results showed that the monitoring range of side length or seam length of mechanical damaged parts was 85.71%~93.33%, and the average monitoring accuracy was 88.74%. The results of the monitoring test on the width of soil covering at different membrane edges were shown in Table 3. The results showed that the monitoring range of the width of the covering soil beside the membrane was 95.00%~96.82%, and the average monitoring accuracy was 95.61%.

Table 1

Test results of daylighting width monitoring

Actual daylighting surface width/mm	Monitoring daylighting surface width/mm	Monitoring accuracy/%	Average monitoring accuracy/%
130	124	95.38	95.99
170	160	94.12	
210	217	96.67	
250	244	97.60	
290	301	96.20	

Table 2

Monitoring test results of side length or seam length of mechanical damaged parts

Side length or seam length of the actual mechanical damage part/mm	Monitor the side length or seam length of mechanical damaged parts/mm	Monitoring accuracy/%	Average monitoring accuracy/%
15	13	86.67	88.74
20	22	90.00	
25	28	88.00	
30	28	93.33	
35	40	85.71	

Table 3

Results of monitoring test on the width of soil covering around the membrane

Actual width of soil covering at the membrane edge / mm	Monitoring the width of soil covering at the edge of the	Monitoring accuracy/%	Average monitoring accuracy / %
130	136	95.38	95.61
160	152	95.00	
190	181	95.26	
220	227	96.82	
250	261	95.60	

The average monitoring accuracy of the width of the daylighting surface and the width of the film edge covering soil was more than 95%, and the average monitoring accuracy of the edge length or the length of the seam at the damaged part of the machinery was more than 88%. The analysis of its error mainly includes two aspects: The first is that due to the influence of natural light intensity, the daylighting surface reflects too brightly, and the morphological analysis has not completely realized identification; Second, in image segmentation, some areas are identified as soil or impurities. After the segmentation error is accumulated into image recognition, the average recognition rate is reduced accordingly. However, the monitoring accuracy of the width of the daylighting surface, the width of the film edge covering soil, and the edge length or the length of the seam at the damaged part of the machine meet the requirements of the monitoring system. The above results show that the quality monitoring system of film laying of cotton precision planter can accurately judge the width of daylight surface, the width of film edge covering soil, and the side length or seam length of mechanical damaged part, which can be used for evaluation and reference of film laying quality.

CONCLUSIONS

This paper designs a kind of film laying quality monitoring system suitable for cotton precision planter, puts forward an advanced morphological filtering method to realize film laying image identification, and tests the monitoring performance of the monitoring system on the width of daylight surface, the edge length or seam length of mechanically damaged parts and the accuracy of film edge covering width.

(1) A high-definition network camera with clear image and strong adaptability is adopted and a film laying quality monitoring system is designed based on LabView software graphic programming. The system uses the Vision Assistant visual assistant to quickly collect, process, identify and display plastic film images to obtain real-time plastic film samples. It realizes the monitoring of parameters such as the width of the daylighting surface, the side length or the length of the seam at the damaged part of the machine, and the width of the film edge covering soil. It also has alarm and storage functions of data such as alarm information and data monitoring information, and can accurately detect the quality of cotton film laying in real time.

(2) The software system uses a color extraction function to convert colors to grayscale images. It uses the LOOKup Table function to perform grayscale transformation and FFT filter function to binarize it and filter it with advanced morphology. It then uses the basic morphology to obtain the recognition results of each component in the plastic film image. The system solves the problems of difficulty in recognizing the similarity between the plastic film and the background interferer (soil, etc.), and accurately identifies the main components of the plastic film and the soil.

(3) The bench test of the film laying quality monitoring system of cotton precision planter showed that the average monitoring accuracy of the width of the daylighting surface and the width of the film edge covering soil was more than 95%, and the average monitoring accuracy of the edge length or the length of the seam at the damaged part of the machinery was more than 88%. The system works stably and reliably and meets the requirement of quality monitoring of cotton precision burrowing film laying.

Further field tests are carried out to further verify the performance and reliability of the system monitoring, and other programming languages are considered to be introduced, and the development characteristics of other high-level programming languages are taken into account in LabView. This can fully measure analysis and processing, enrich the functional modules, improve the accuracy and adaptability of the algorithm, and enhance the monitoring performance and image data processing capabilities of the system.

This will collect more diversified data to enhance the robustness and adaptability of the model, ensure more stability, reduce monitoring accuracy errors, and improve the environmental adaptability and operational reliability of the system. In the future, high-precision Beidou positioning technology and mobile Internet technology can be combined to form field film laying quantity maps, operation quality status maps and variable film filling prescription maps. This provides support for improving the film laying quality of cotton precision planters and automatically sets film laying parameters, which makes the system functions more in line with actual production conditions and adapts to different operating scenarios.

ACKNOWLEDGEMENT

This work was supported by the National key research and development plan project (Project No. 2022YFD2002401), Xinjiang agricultural machinery R & D manufacturing promotion and application integration project (Project No. YTHSD2022), Autonomous Region Regional Collaborative Innovation Special (Science and Technology Aid to Xinjiang Program) Project of China (Project No. 2021E02055) and Jiangsu Province and Education Ministry Co-sponsored Synergistic Innovation Center of Modern Agricultural Equipment (Project No. XTCX2020).

REFERENCES

[1] Adão, T., et al. (2017). Hyperspectral imaging: A review on UAV-based sensors, data processing and applications for agriculture and forestry[J]. *Remote Sensing*, 9(11): 1110, Basel / Switzerland.;

[2] Bureau of Statistics of Xinjiang Uygur Autonomous Region. (2021). Xinjiang Statistical Yearbook[M]. *China Statistics Press*, Beijing / P.R.C.;

[3] Bu, L.X., et al. (2020). Technological development of robotic apple harvesters: a review[J]. *INMATEH Agricultural Engineering*, 61(2), 151-164, Bucharest / Romania.;

[4] Banerjee, B., et al. (2020). UAV-hyperspectral imaging of spectrally complex environments[J]. *International Journal of Remote Sensing*, 41(11): 4136-4159, Leicester / UK.;

[5] Chen, M., et al. (2021). Online Monitoring Method of Mechanized Soybean Harvest Quality Based on Machine Vision[J]. *Transactions of the Chinese Society for Agricultural Machinery (Transactions of the CSAM)*, 52(01): 91-98, Beijing / P.R.C.;

[6] Diao, Z.H., et al. (2014). Summary of research on machine vision application in agricultural production[M]. *Journal of Agricultural Mechanization Research*, 36(03): 206-211, Heilongjiang / P.R.C.;

[7] Feng, W.H. (2012). Evaluation and testing method of working quality index of film laying machine[J]. *Agricultural Machinery Using & Maintenance*, 05: 47-49, Heilongjiang / P.R.C.

[8] Gao, L. (2016). Determination of kapok/cotton blended content of non-woven web based on image processing technology[D]. *Donghua University*, Shanghai / P.R.C.;

[9] Hou, Z.F., et al. (2022). Design and Experiment of Identification and Detection System for Pelleted Coated Seeds[J]. *Transactions of the Chinese Society for Agricultural Machinery (Transactions of the CSAM)*, 53(06): 62-69+183, Beijing / P.R.C.;

[10] Hou, J.L., et al. (2020). Design and experiment of test bench for garlic bulbil adjustment and seeding based on bilateral image identification[J]. *Transactions of the Chinese Society of Agricultural Engineering (Transactions of the CSAE)*, 2020, 36(01): 50-58, Beijing / P.R.C.;

[11] Jiang, L.L., et al. (2019). High precision measurement method of relay yoke based on machine vision[J]. *Science Technology and Engineering*, 19(13): 181-185, Beijing / P.R.C.;

[12] Xing, J.F., et al. (2021). Design and operation parameters optimization of 4sgms-220 plough layer residual film recovery machine[J]. *INMATEH Agricultural Engineering*, 64(2), 317-326, Bucharest / Romania; https://doi.org/10.35633/inmateh-64-31

[13] Kang, S., et al. (2021). Infrared image enhancement of wind turbine blades based on adaptive differential multi-scale morphology[J]. *China Mechanical Engineering*, 32(07): 786-792, Wuhan / P.R.C.;

[14] Kong, Y.L., et al. (2012). Potato grading method of mass and shapes based on machine vision[J]. *Transactions of the Chinese Society of Agricultural Engineering (Transactions of the CSAE)*, 28(17): 143-148, Beijing / P.R.C.;

[15] Lu, L., et al. (2015). Threshold model for detecting transparent plastic-mulched landcover using moderate-resolution imaging spectroradiometer time series data: a case study in southern Xinjiang, China[J]. *Journal of Applied Remote Sensing*, 9(01): 097094, Bellingham / WA USA.;

[16] Li, Q.L., et al. (2020). The design of ground air dual purpose agricultural information acquisition robot [J]. *INMATEH Agricultural Engineering*, 62(3), 259-268, Bucharest / Romania; https://doi.org/10.35633/inmateh-62-27
[17] Lu, L., et al. (2014). A decision-tree classifier for extracting transparent plastic-mulched landcover from Landsat-5 TM images[J]. *IEEE Journal of Selected Topics in Applied Earth Observations and Remote Sensing*, 7(11): 4548-4558, New York / USA.;
[18] Liang, C.J., et al. (2019). Field film identification algorithm based on UAV[J]. *Zhejiang Agricultural Journal*, 31(06): 1005-1011, Zhejiang / P.R.C.;
[19] Lövdahl, L., et al. (2008). Effects of mulching and catch cropping on soil temperature, soil moisture and wheat yield on the Loess Plateau of China[J]. *Soil & Tillage Research*, 102(01): 78-86, Netherlands / Amsterdam.;
[20] National Agricultural Machinery Standardization Technical Committee. (2007). JB/T 7732-2006 Film planter[S]. *China Agriculture Press*, Beijing / P.R.C.;
[21] National Agricultural Machinery Standardization Technical Committee. (2009). GB/T5262-2008 Operation quality of film planter[S]. *China Agriculture Press*, Beijing / P.R.C.;
[22] National Bureau of Statistics of the People's Republic of China. (2021). China Statistical Yearbook[M]. *China Statistics Press*, Beijing / P.R.C.;
[23] Peng, B., et al. (2015). Detection of colorless plastic contaminants hidden in cotton layer using chromatic polarization imaging[J]. *Chinese Optics Letters*, 13(09), 092901, Shanghai / China.;
[24] Qin, C.B., et al. (2012). The control system design of automatic weeding robot based on visual navigation[M]. *2012 IEEE International Conference on Robotics and Biomimetics (ROBIO)*, 956-961, New York / USA.;
[25] Tai, H.J. (2019). Research on defect detection technology of self-adhesive printing based on linear array camera[D]. *Zhongbei University*, Taiyuan / P.R.C.;
[26] Wu, X.M., et al. Identification method of plastic film residue based on UAV remote sensing images[J]. *Transactions of the Chinese Society for Agricultural Machinery (Transactions of the CSAM)*, 51(08): 189-195, Beijing / P.R.C.;
[27] Zhang, X.J., et al. Identification Method of Agricultural Film Residue Based on Improved Faster R-CNN[J]. *Journal of Hunan University (Natural Sciences)*, 48(08): 161-168, Hunan / P.R.C.;
[28] Zhai, Z.Q., et al. (2022). Detecting surface residual film coverage rate in pre-sowing cotton fields using pixel block and machine learning[J]. *Transactions of the Chinese Society of Agricultural Engineering (Transactions of the CSAE)*, 38(06): 140-147, Beijing / P.R.C.;
[29] Zhang, Q., et al. (2013). Development of Detection System for Cotton Plastic Covering Using Ultrasonic[J]. *Applied Mechanics and Materials*, 411: 1439-1444, Baech / Switzerland.;
[30] Zhang, C., et al. (2017). Design and Test of Foreign Fiber Removal Machine Based on Embedded System[J]. *Transactions of the Chinese Society for Agricultural Machinery (Transactions of the CSAM)*, 48(08): 43-52, Beijing / P.R.C.;
[31] Zhang, D. (2019). Analysis on Detection Technology of Plastic Film Foreign Fiber in Raw Cotton[J]. *Cotton Textile Technology*, 47(05): 73-76, Shanxi / P.R.C.;
[32] Zhang, X. (2020). Research on sorting system of film on seed cotton based on deep learning[D]. *Nanjing Forestry University*, Nanjing / P.R.C.;
[33] Zhang, X.W., et al. (2022). Design and experiment of recognition system for coated red clover seeds based on machine vision[J]. *INMATEH Agricultural Engineering*, 66(1), 62-72, Bucharest / Romania. https://doi.org/10.35633/inmateh-66-06

DESIGN AND TEST OF QUANTITATIVE FERTILIZER FEEDING DEVICE FOR POINT-APPLIED FERTILIZATION DEVICE
/
穴施肥装置精量供肥器设计与试验

Xin DU, Changqing LIU*, Xuhui LI, Wei ZHU, Qixin SUN, Shufa CHEN
School of Mechanical Engineering, Jiangsu Ocean University, Lianyungang 222005/ China
Tel: 0086-0518-85895322; E-mail: lyg_lcq@163.com
Corresponding author: Changqing Liu
DOI: https://doi.org/10.35633/inmateh-70-38

Keywords: *Quantitative feeding device; Grooved wheel; Discrete element method; Uniformity of particle flow*

ABSTRACT
To ensure accurate and consistent fertilizer application, the key component of the fertilizer feeding device, the grooved wheel, was designed and theoretically analyzed, and the number of grooves of the fertilizer wheel was determined to be 9. The effects of grooves inclination angle, grooves length and operating speed on the fertilizer feeding performance were analyzed by single-factor tests, and the appropriate range of factors was determined. The effect of the interaction between groove length and operating speed on the amount of fertilizer discharged from the groove was investigated by a full factorial test, and a quadratic regression was fitted to the test results to establish the regression equations of groove length and operating speed on the average fertilizer application per groove and the coefficient of variation of the average fertilizer application per groove, which can be used to predict the average fertilizer application per groove and the coefficient of variation of the average fertilizer application per groove to solve for groove length and operating speed.

摘要
为保证穴施肥的施肥量准确、一致，本研究对供肥器中的关键零部件供肥轮进行了设计和理论分析，确定了供肥轮槽数为 9。通过单因素试验分别分析了槽孔倾角、槽孔长度和作业速度对供肥性能的影响，并确定了合适的因素范围。通过全因子试验研究了槽孔长度和供肥轮转速间交互影响对穴排肥量的影响，对试验结果进行二次回归拟合，建立槽孔长度和供肥轮转速对每穴平均施肥量和每穴平均施肥量变异系数的回归方程，可以使用该公式预测给定每穴平均施肥量和每穴平均施肥量变异系数求解槽孔长度和供肥轮转速。

INTRODUCTION

Fertilizer application is an effective way to improve soil fertility and increase crop yields (*Cisternas et al.*, *2020*), and the continuous application of chemical fertilizers has led to high and stable grain yields over the years, ensuring food security in China (*Shemi et al.*, *2021*). It was found that cavity application of fertilizer to the root zone of plants can greatly improve fertilizer utilization (*Adu-Gyamfi et al.*, *2019*), and for this reason, a wide range of researchers have developed a cavity fertilizer discharger suitable for mechanized operation (*Du et al.*, 2023a; *Du et al.*, *2022*). Fertilizer feeding device are needed to ensure that the amount of fertilizer applied to the root zone of the plant in the cavity is precise and consistent (*Ma et al.*, *2022*).

The fertilizer feeding device is mainly in the form of external grooved wheel structure (*Jafari*, *1991*), and according to the shape and direction of the groove teeth, the external grooved wheel fertilizer feeder can be divided into straight groove, oblique groove and spiral groove, etc. (*Kara et al.*, *2010*; *Nukeshev et al.*, *2017*). The straight groove fertilizer feeding device is simple in structure and easy to adjust the discharge volume, *Ding et al.,* (*2018*), used a straight groove feeding device to supply a continuous stream of fertilizer granules when applying fertilizer in layers. Although the structure of the oblique groove fertilizer feeding device is more complicated, it can effectively reduce the coefficient of variation of fertilizer supply and is more widely used (*Bangura et al.*, *2020*). The spiral groove fertilizer feeding device has the most complicated structure, and the fertilizer supply can only be adjusted by controlling the speed of the grooved wheel, but it supplies the highest uniformity of fertilizer flow (*Zheng et al.*, *2020*; *Gao et al.*, *2022*; *Sun et al.*, *2020*). In addition, there are some peg-tooth fertilizer feeding devices (*BoydasTurgut*, *2007*; *Sugirbay et al.*, *2020*; *Kim et al.*, *2008*), which are more complex in structure and difficult to machine.

Xin Du, Lecturer Ph.D. Eng; Changqing Liu, Lecturer Ph.D. Eng; Xuhui Li, Lecturer Ph.D. Eng; Wei Zhu, B.S Stud.; Qixin Sun, Prof. Ph.D. Eng; Shufa Chen, Prof. Ph.D. Eng.*

This study takes the straight groove fertilizer feeding device as the research object, and adjusts the transmission ratio and initial installation angle between the feeding device and the point-applied application fertilizer discharging device from the transmission system, so that the grooved holes of the fertilizer wheel correspond to the chambers of the fertilizer discharging wheel one by one, thus achieving the consistency of fertilizer discharge per cavity. The discrete element simulation software EDEM was used to optimize and analyze the fertilizer supply performance to ensure the accurate and consistent fertilizer volume of point-applied application, in order to provide a theoretical basis for the promotion and application of fertilizer point-applied application technology.

MATERIALS AND METHODS

STRUCTURE AND KEY PARAMETERS

The structure of fertilizer feeder is shown in Figure 1, which consists of brush, grooved wheel, shell, fertilizer outlet and fertilizer supply pipe. When working, fertilizer particles fill the space above the grooved wheel, and when the wheel rotates, some fertilizer particles fill the grooved hole under the action of gravity and pressure of fertilizer layer above, and then the excess fertilizer particles above the grooved hole are removed under the action of brush, and then the fertilizer particles in the grooved hole are poured out by rotating to the unloading area, and enter the fertilizer supply pipe through the fertilizer outlet.

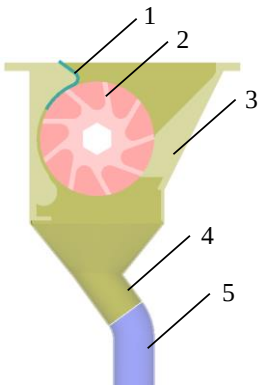

Fig. 1 – Structure of fertilizer feeding device

1. brush; 2. grooved wheel; 3. shell; 4. fertilizer outlet; 5. fertilizer supply pipe

According to GB/T 37088-2018 technical guide for one-time fertilization of corn, 58.33-66.67 kg/667 m^2 of slow-release compound fertilizer with N-P_2O_5-K_2O 24-6-10 needs to be applied, and the amount of fertilizer applied per point is calculated to be 9.84-11.25 g with a bulk density of fertilizer particles of 1.08 g/cm^3 at a maize row spacing of 60 cm×25 cm. The volume of fertilizer granules per point is 9.11-10.42 cm^3, and the grooved wheel per groove is 2.5-15 g, which corresponds to 14.815-88.890 kg/667 m^2, which can basically meet the fertilization requirements of most crops. When the fertilizer application rate is 2.5-15 g per groove, the length of the grooved hole of the fertilizer wheel is 10-60 mm, and the cross-sectional area of the corresponding grooved hole is 231.48 mm^2. The diameter of the fertilizer wheel is 67.5 mm, and the thickness of the grooved hole spacer is 3 mm.

To determine the cross-sectional structural dimensions of a grooved hole, a single grooved hole is considered to be composed of several parts, as shown in Figure 2.

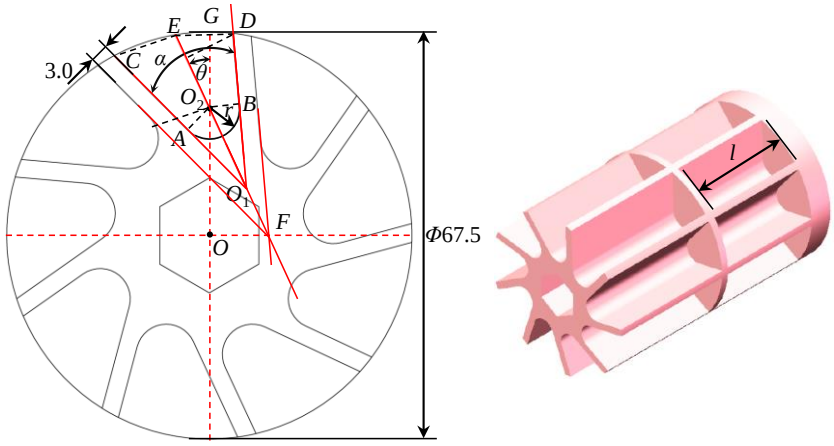

Fig. 2 – Structure of fertilizer grooved wheel

To calculate the cross-sectional area of the grooved hole, the grooved hole cross-section *ABDC* is considered as the difference between the sum of the areas of the two triangles *CEO*$_1$ and *EDO*$_1$ and the area of the curved surface *ABO*$_1$, where:

$$S_{ABO_1} = S_{AO_1BO_2} - S_{ABO_2} = \frac{r^2}{\tan\frac{\alpha}{2}} - \frac{(180^\circ - \alpha)\pi r^2}{360^\circ} \quad (1)$$

From the geometric relationship, it is known that:

$$\frac{O_1O_2}{FO_2} = \frac{BO_2}{BO_2 + 3} \Rightarrow FO_2 = \frac{O_1O_2(BO_2 + 3)}{BO_2} = \frac{r+3}{\sin\frac{\alpha}{2}} \quad (2)$$

In the triangle *OO*$_2$*F:*

$$OO_2 = FO_2 \cos\theta = \frac{(r+3)\cos\theta}{\sin\frac{\alpha}{2}} \quad (3)$$

Therefore, for the line *OG:*

$$GO_2 = GO - OO_2 = \frac{67.5}{2} - \frac{(r+3)\cos\theta}{\sin\frac{\alpha}{2}} \quad (4)$$

Since triangles *EGO*$_2$ and *OFO*$_2$ are similar triangles:

$$\frac{EO_2}{FO_2} = \frac{GO_2}{OO_2} \Rightarrow EO_2 = \frac{GO_2 \times FO_2}{OO_2} = \frac{67.5}{2\cos\theta} - \frac{r+3}{\sin\frac{\alpha}{2}} \quad (5)$$

Therefore, it is possible to obtain:

$$S_{CEO_1} = CO_1 \times \frac{EO_1 \times AO_2}{O_1O_2} = CO_1 \times \frac{(EO_2 + O_1O_2)r}{O_1O_2} = CO_1 \times \left(\frac{67.5\sin\frac{\alpha}{2}}{2\cos\theta} - 3\right) \quad (6)$$

Similarly, it can be obtained:

$$S_{EDO_1} = EO_1 \times \frac{EO_1 \times AO_2}{O_1O_2} \quad (7)$$

After sorting, the following is obtained:

$$S_{ABDC} = S_{CEO_1} + S_{EDO_1} - S_{ABO_1} \quad (8)$$

According to equation (8), the relationship between the inclination angle *θ* and the cross-sectional area *S* of the grooved holes is shown in Figure 3 for the number of grooved holes 8 and 9.

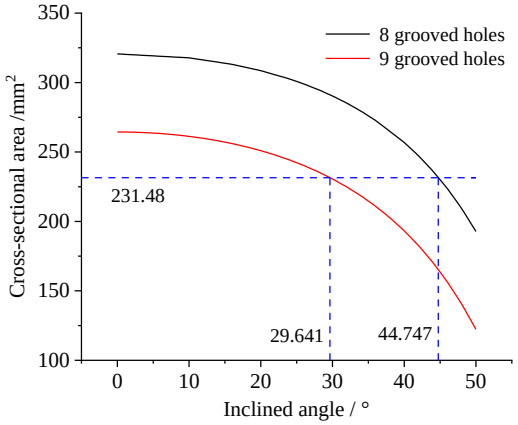

Fig. 3 – Relationship between the number of grooved holes and the inclined angle of the grooved holes on the cross-sectional area of the grooved holes

From the figure, it can be seen that when the number of grooved holes is 8, the grooved hole inclination angle θ is 44.747° and the grooved hole cross-sectional area S is 231.48 mm^2; when the number of grooved holes is 9, the grooved hole inclined angle θ is 29.641° and the grooved hole cross-sectional area S is 231.48 mm^2. When the number of grooved holes is 10, the inclined angle θ of the grooved holes is less than 231.48 mm^2, so the graph is not analyzed; the situation when the number of grooved holes is 7 is also not analyzed, because the smaller the number of grooved holes, the larger the increase in the speed of the grooved wheel when the operating speed is increased, and the grooved wheel filling performance will be significantly reduced. In order to improve the fertilizer filling performance of the grooved wheel, the number of grooved holes of the wheel is set to 9, and the grooved hole tension angle is 40°, and the grooved hole inclined angle is decided according to the simulation test later.

Simulation model construction

To investigate the mechanism of the influence of the above factors on the fertilizer application amount per point, the discrete element simulation software EDEM2020 was used to simulate the grooved wheel filling and fertilizer application process in order to optimize the best structural parameters. The fertilizer feeding device was modeled using SolidWorks 2016, saved in .step format, and imported into EDEM2020, as shown in Figure 4. The total simulation time was 10 s, and the data was saved every 0.01 s.

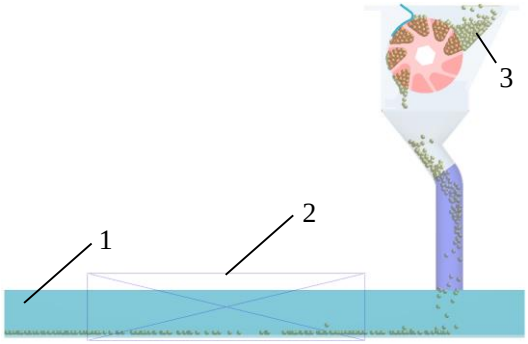

Fig. 4 – Modeling and simulation diagram of fertilizer feeding device

1. Conveyor belt; 2. Geometry bin; 3. Fertilizer granules

The EDEM simulation model of fertilizer granules was established by using Bekosh coated controlled release fertilizer (N-P_2O_5-K_2O 24-6-10) produced by Shandong Nongye Biotechnology Co. The intrinsic parameters and contact parameters used in the simulation are shown in Table 1 (*Du et al.*, *2023b*; *Du et al.*, *2022*).

Table 1

Simulation parameters table

Parameters	Fertilizer granules	ABS	Conveyor belt
Poisson's ratio	0.225	0.394	0.3
True Density (kg/m^3)	2474	1060	2500
Shear modulus (Pa)	1.528×10^8	8.9×10^8	1.0×10^6
Coefficient of restitution	0.509	0.475	0.02
Coefficient of static friction	0.176	0.425	1.25
Coefficient of rolling friction	0.0332	0.0951	1.24

Test indicators

To evaluate the performance of the grooved wheel, select Add Selection in the Setup Selections sub-panel of the EDEM post-processing and add a Geometry bin, adjusting its position so that it is on the upper left side of the conveyor belt, with a length of 250 mm (i.e., the amount of fertilizer required for one corn plant), and a width and height of 80 mm and 60 mm, respectively, so that the length is set to 250 mm (i.e., the amount of fertilizer needed for one corn plant), and the width and height are set to 80 mm and 60 mm, respectively, to cover the conveyor belt. To ensure that fertilizer particles are not counted repeatedly when using the Geometry

bin, it is necessary to ensure that the product of the time interval between each count and the speed of the conveyor belt (i.e., operating speed) is greater than or equal to 250 mm, and then calculate the average fertilizer application per point (AFA), the coefficient of variation of the average fertilizer application per point (COVAFA), and the error of the average fertilizer application per point (EOAFA) according to the following equations.

$$Q_{average} = \frac{\sum_{i=1}^{k} Q_i}{k} \times 100\% \tag{9}$$

$$C_Q = \frac{\sqrt{\frac{1}{k}\sum_{i=1}^{k}\left(Q_i - Q_{average}\right)^2}}{Q_{average}} \tag{10}$$

$$q = \frac{\sum_{i=1}^{k} \frac{|Q_i - Q_0|}{Q_0}}{k} \times 100\% \tag{11}$$

Where: $Q_{average}$ is the average fertilizer application per point, g; Q_i is the *i*-th hole fertilizer application, g; *k* is the total number of points counted; C_Q is the coefficient of variation of the average fertilizer application per point; *q* is the error of the average fertilizer application per point, %; Q_0 is the standard fertilizer discharge per point, g.

RESULTS

Effect of grooved hole inclination on the amount of fertilizer applied to the point

The effect of groove inclined angle on the amount of fertilizer applied to the point is shown in Figure 5 for an effective working length of 30 mm, a rotation speed of 40 r/min and groove inclined angles of 20°, 22.5°, 25°, 27.5° and 30°, respectively.

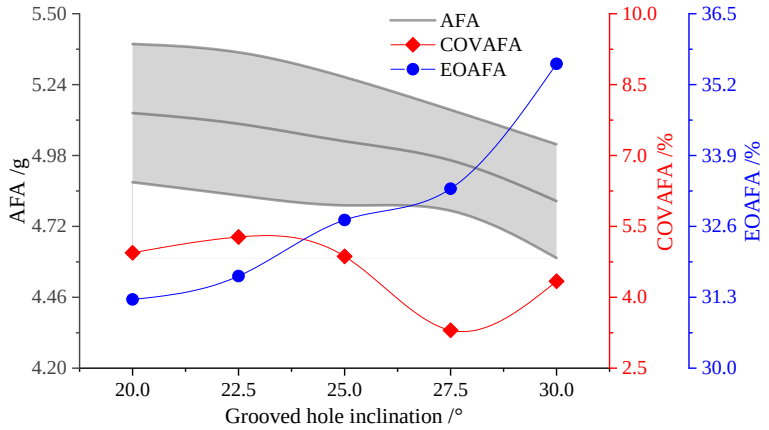

Fig. 5 – Effect of grooved hole inclination on the amount of fertilizer applied to the point

From Figure 5, the AFA gradually decreases when the inclination of the grooved hole gradually increases, probably due to the increase of the grooved hole opening caused by the increase of the inclination angle, although it is easier to fill the fertilizer particles, some particles are found to be easily cleared out of the grooved hole when passing through the brush, because the increase of the grooved hole opening leads to more particles above the edge of the grooved hole, and there is a greater probability that the fertilizer particles inside the grooved hole will be taken out of the grooved hole when passing through the brush. Therefore, the AFA is reduced. As the inclination of the grooved hole gradually increases, the EOAFA gradually increases, because the AFA gradually decreases and the difference between the AFA and the theoretical AFA increases. The COVAFA was basically maintained at 3.3%~5.3% when the inclination angle of the grooved hole was 20°~30°, and the COVAFA was the smallest when the inclination angle of the grooved hole was 27.5°, which was 3.3%. From the standard deviation of AFA (shaded area in the figure), it can be seen that the standard deviation is also the smallest when the grooved hole inclination angle is 27.5°.

From the above analysis, it can be seen that the inclination angle of the grooved hole affects the AFA, and then affects the EOAFA, and the coefficient of variation and standard deviation of the average fertilizer application per hole are the smallest when the tilting angle of the grooved hole is 27.5°, so the stability of the AFA can be improved by appropriately reducing the tilting angle of the grooved hole. Therefore, the final selection of grooved hole inclination angle was 27.5°.

Effect of grooved hole length on the amount of fertilizer applied to the point

The effect of grooved length on the amount of fertilizer applied to the point is shown in Figure 6 for an inclination angle of 30°, a rotation speed of 40 r/min, and effective working lengths of 10 mm, 20 mm, 30 mm, 40 mm, and 50 mm, respectively.

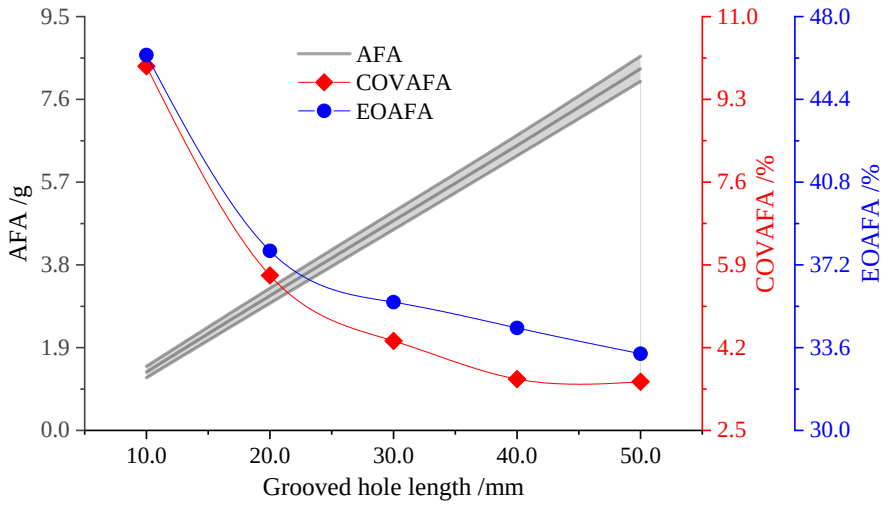

Fig. 6 – Effect of grooved hole length on the amount of fertilizer applied to the point

As shown in the figure 6, when the length of the grooved hole gradually increases, the AFA gradually increases and the EOAFA gradually decreases, because the AFA increases when the length of the grooved hole increases, the opening area of the grooved hole becomes larger, and fertilizer particles can easily fill the grooved hole space, while it is difficult for fertilizer particles to fill the grooved hole when the length of the grooved hole is small, and the difference between the theoretical AFA and the AFA increases, resulting in the COVAFA and the EOAFA being large. When the length of grooved hole was 30 mm~40 mm, the COVAFA was less than 4.3%.

From the above analysis, it can be seen that the length of the grooved hole affects the AFA, and the coefficient of variation and standard deviation of the average fertilizer application per hole are smaller when the grooved hole length is greater than 30 mm, so the stability of the average fertilizer application per hole can be improved by appropriately increasing the grooved hole length.

Effect of operating speed on the amount of fertilizer applied to the point

The effect of the rotation speed of the fertilizer wheel on the amount of fertilizer applied to the point is shown in Figure 7 for an inclination angle of 30°, an effective working length of 30 mm, and rotation speeds of 13.3, 26.7, 40, 53.3, and 66.7 r/min, respectively.

As can be seen from the figure 7, when the speed of the fertilizer supply wheel gradually increases, the AFA gradually decreases, because the fertilizer granule filling time becomes shorter due to the increase in the speed of the fertilizer supply wheel, and it is difficult for the fertilizer granule to fill the grooved hole smoothly. The EOAFA gradually increases when the speed of the fertilizer supply wheel gradually increases, because the AFA gradually decreases and the difference between the AFA and the theoretical fertilizer AFA increases. The COVAFA was 0.4%~7.4% when the speed of the fertilizer wheel was 13.3 r/min~66.7 r/min, and the COVAFA increased sharply at the speed of the fertilizer wheel. From the standard deviation of AFA (shaded area in the figure), it can be seen that the standard deviation gradually increased when the fertilizer supply wheel speed was less than 40.0 r/min, but the standard deviation increased rapidly when the fertilizer supply wheel speed was greater than 40.0 r/min.

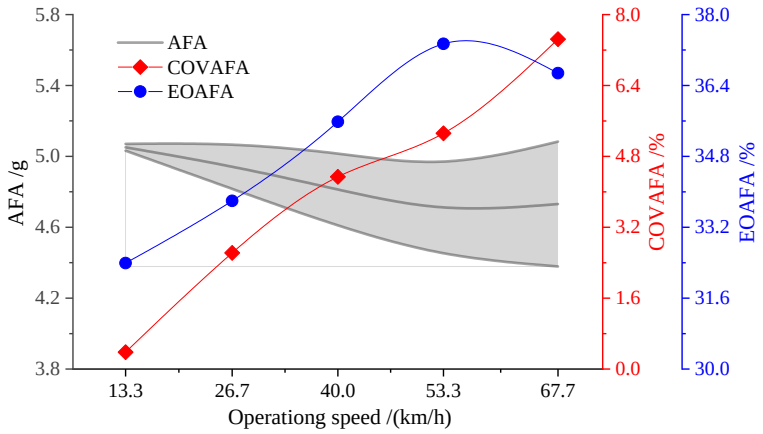

Fig. 7 – Effect of operating speed on the amount of fertilizer applied to the point

From the above analysis, it can be seen that the speed of the fertilizer supply wheel affects the AFA, and then affects the EOAFA, and the coefficient of variation and standard deviation of the average fertilizer application per hole gradually increase when the speed of the fertilizer supply wheel increases.

Modeling the amount of fertilizer applied to the point

Based on the above analysis, the inclination angle of the grooved hole was determined to be 27.5°. In order to study the effect of the interaction between grooved hole length and wheel speed on point discharge, a full factorial test was designed with grooved hole length and fertilizer wheel speed as the study factors, and the COVAFA and AFA were used as the study objectives, and a quadratic regression was fitted to the test results to establish the regression equations of the AFA and the COVAFA were established.

The test scheme and test results are shown in Table 2.

Table 2

Full factorial test program and results

No.	Length *l* / mm	Speed *n* / (r/min)	AFA $Q_{average}$ / g	COVAFA C_Q / %
1	10	13.3	1.513319	7.427964
2	10	26.7	1.385602	7.429568
3	10	40.0	1.33648	9.979386
4	10	53.3	1.284328	13.66198
5	10	66.7	1.296442	14.94868
6	20	13.3	3.286889	2.522676
7	20	26.7	3.204958	3.054150
8	20	40.0	3.097446	5.685218
9	20	53.3	3.076655	6.365773
10	20	66.7	3.093146	9.211046
11	30	13.3	5.050821	0.381679
12	30	26.7	4.945997	2.620881
13	30	40.0	4.812601	4.338091
14	30	53.3	4.681243	5.319122
15	30	66.7	4.730656	7.446586
16	40	13.3	6.805114	1.577270
17	40	26.7	6.765353	3.154584
18	40	40.0	6.528549	3.553546

No.	Length *l* / mm	Speed *n* / (r/min)	AFA $Q_{average}$ / g	COVAFA C_Q / %
19	40	53.3	6.465926	4.341058
20	40	66.7	6.572815	7.111936
21	50	13.3	8.597962	2.115242
22	50	26.7	8.467234	2.886364
23	50	40.0	8.300637	3.499694
24	50	53.3	8.197033	5.255946
25	50	66.7	8.304938	8.007886

A quadratic multiple regression fit to the coefficient of variation of average fertilizer application per hole and average fertilizer application per hole yields the regression equation

$$\begin{aligned} Q_{average} &= -0.0525 + 0.1774l - 0.01539n + 4.066\times10^{-6}l^2 - 6.667\times10^{-5}ln + 0.0001504n^2 \\ C_Q &= 11.05 - 0.6305l + 0.07844n + 0.00909l^2 - 0.001398ln + 0.001065n^2 \end{aligned} \quad (12)$$

Where: $Q_{average}$ is the average fertilizer application per hole, g; C_Q is the coefficient of variation of the average fertilizer application per hole; *l* is the length of the grooved hole, mm; n is the speed of the fertilizer supply wheel, r/min.

The summed variance *SSE*, root mean square *RMSE* and coefficient of determination R^2 of the average fertilizer application rate per hole $Q_{average}$ were 0.04572, 0.04906 and 0.9997, respectively; the summed variance *SSE*, root mean square *RMSE* and coefficient of determination R^2 of the average fertilizer application rate per hole C_Q were 13.9, 0.8555 and 0.955, respectively, indicating that the regression model was significant and it is feasible to use this formula to predict the grooved hole length and fertilizer wheel speed for a given average fertilizer application per hole and the coefficient of variation of average fertilizer application per hole.

The interaction effects of grooved hole length and grooved wheel operating speed on the average fertilizer application per hole and the coefficient of variation of the average fertilizer application per hole are shown in Figure 8.

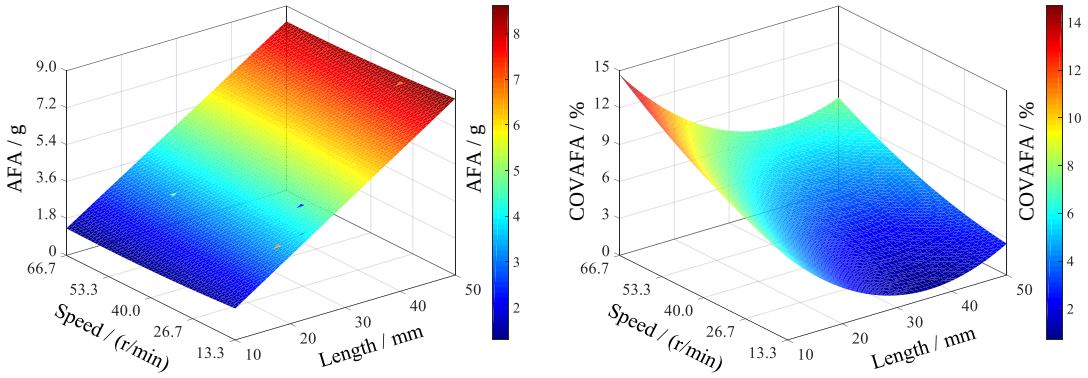

Fig. 8 – Response surface analysis of the interaction effects of factors

CONCLUSIONS

In this study, the key component of the fertilizer feeding device, the grooved wheel, was designed and theoretically analyzed, and the number of grooves of the fertilizer wheel was determined to be 9. The effects of grooves inclination angle, grooves length and operating speed on the fertilizer feeding performance were analyzed by single-factor tests, and the appropriate range of factors was determined. The effect of the interaction between groove length and operating speed on the amount of fertilizer discharged from the groove was investigated by a full factorial test, and a quadratic regression was fitted to the test results to establish the regression equations of groove length and operating speed on the average fertilizer application per groove and the coefficient of variation of the average fertilizer application per groove, which can be used to predict the average fertilizer application per groove and the coefficient of variation of the average fertilizer application per groove to solve the groove length and operating speed.

ACKNOWLEDGEMENT

This work was financially supported by Natural Science Foundation of the Jiangsu Higher Education Institutions of China (23KJB210007).

REFERENCES

[1] Adu-Gyamfi, R., Agyin-Birikorang, S., Tindjina, I., Manu, Y., Singh, U. (2019). Minimizing nutrient leaching from maize production systems in northern Ghana with one-time application of multi-nutrient fertilizer briquettes. *Science of the Total Environment*, *694*, 133667. http://doi.org/https://doi.org/10.1016/j.scitotenv.2019.133667.

[2] Bangura, K., Gong, H., Deng, R., et al. (2020). Simulation analysis of fertilizer discharge process using the Discrete Element Method (DEM). *Plos One*, *15*(7), e235872. http://doi.org/10.1371/journal.pone.0235872.

[3] Boydas, M. G., Turgut, N. (2007). Effect of vibration, roller design, and seed rates on the seed flow evenness of a studded feed roller. *Applied Engineering in Agriculture*, *23*(4), 413-418. http://doi.org/10.13031/2013.23482.

[4] Cisternas, I., Velásquez, I., Caro, A., Rodríguez, A. (2020). Systematic literature review of implementations of precision agriculture. *Computers and Electronics in Agriculture*, *176*, 105626. http://doi.org/https://doi.org/10.1016/j.compag.2020.105626.

[5] Ding, S., Bai, L., Yao, Y., et al. (2018). Discrete element modelling (DEM) of fertilizer dual-banding with adjustable rates. *Computers and Electronics in Agriculture*, *152*, 32-39. http://doi.org/https://doi.org/10.1016/j.compag.2018.06.044.

[6] Du, X., Liu, C. (2023a). Research on the performance of particles distribution of fertilizer point-applied device in root-zone. *Journal of Applied Science and Engineering*, *26*(8), 1063-1072. http://doi.org/10.6180/jase.202308_26(8).0002.

[7] Du, X., Liu, C. (2023b). Prediction of DEM parameters of coated fertilizer particles based on GA-BP neural network. *Engenharia Agrícola*, *43*(spe). http://doi.org/10.1590/1809-4430-eng.agric.v43nepe20210099/2023.

[8] Du, X., Liu, C., Jiang, M., Yuan, H. (2022). Design and development of fertilizer point-applied device in root-zone. *Applied Engineering in Agriculture*, *38*(3), 559-571. http://doi.org/10.13031/aea.14846.

[9] Du, X., Liu, C., Jiang, M., et al. (2022). Research on DEM calibration of contact parameters of coated fertilizer. *INMATEH-Agricultural Engineering*, 101-110. http://doi.org/10.35633/inmateh-66-10.

[10] Gao, X., Xie, G., Xu, Y., Yu, Y., Lai, Q. (2022). Application of a staggered symmetrical spiral groove wheel on a quantitative feeding device and investigation of particle motion characteristics based on DEM. *Powder Technology*, *407*, 117650. http://doi.org/10.1016/j.powtec.2022.117650.

[11] Jafari, J. F. (1991). Study of the metering of free flowing particulate solids using multi-flight screws. *Proceedings of the Institution of Mechanical Engineers. Part E, Journal of process mechanical engineering*, *205 no.E2*(1991), 113-121.

[12] Kara, M., Bayhan, A. K., Ozsert, I., Yildirim, Y. (2010). Performance of fluted roll metering devices in seed drills with ammonium sulphate and diammonium phosphate. *Applied Engineering in Agriculture*, *26*(2), 197-201. http://doi.org/10.13031/2013.29537.

[13] Kim, Y. J., Kim, H. J., Ryu, K. H., Rhee, J. Y. (2008). Fertiliser application performance of a variable-rate pneumatic granular applicator for rice production. *Biosystems Engineering*, *100*(4), 498-510. http://doi.org/10.1016/j.biosystemseng.2008.05.007.

[14] Shemi, R., Wang, R., Gheith, E. M. S., et al. (2021). Effects of salicylic acid, zinc and glycine betaine on morpho-physiological growth and yield of maize under drought stress. *Scientific Reports*, *11*(1). http://doi.org/10.1038/s41598-021-82264-7.

[15] Ma, W., Zhang, S., Jin, C., et al. (2022). Optimization design of an alfalfa seed airflow collection and drainage system based on numerical simulation. *Processes*, *10*(11), 2281. http://doi.org/10.3390/pr10112281.

[16] Nukeshev, S., Eskhozhin, K., Eskhozhin, D., Syzdykov, D. (2017). Justification of design and parameters of seeding unit for fertilizers. *Journal of the Brazilian Society of Mechanical Sciences and Engineering*, *39*(4), 1139-1149. http://doi.org/10.1007/s40430-016-0588-5.

[17] Zheng, W. Q., Zhang, L. P., Zhang, L. X., Zhou, J. P. (2020). Reflux problem analysis and structure optimization of the spiral grooved-wheel fertilizer apparatus. *International Journal of Simulation Modelling*, *19*(3), 422-433. http://doi.org/10.2507/IJSIMM19-3-522.

[18] Sun, J., Chen, H., Duan, J., Liu, Z., Zhu, Q. (2020). Mechanical properties of the grooved-wheel drilling particles under multivariate interaction influenced based on 3D printing and EDEM simulation. *Computers and Electronics in Agriculture*, *172*, 105329. http://doi.org/https://doi.org/10.1016/j.compag.2020.105329.

[19] Sugirbay, A. M., Zhao, J., Nukeshev, S. O., Chen, J. (2020). Determination of pin-roller parameters and evaluation of the uniformity of granular fertilizer application metering devices in precision farming. *Computers and Electronics in Agriculture*, *179*, 105835. http://doi.org/10.1016/j.compag.2020.105835.

OPTIMIZED DESIGN AND TESTING OF A PEANUT-PICKING DEVICE WITH A LARGE FEEDING VOLUME

/

花生大喂入量摘果装置优化设计与试验

Xu LI[1)], Shuqi SHANG[1)], Xiaoning HE[1)], Zelong Zhao[1)], Ning ZHANG[1)], Yaxiu HOU[1)], Jinbiao ZHANG[1)],) Dongwei WANG*[1)]

[1)] Qingdao Agricultural University, College of Mechanical and Electrical Engineering / China;

Tel: +86-0532-58957391; E-mail: 200701031@qau.edu.cn

DOI: https://doi.org/10.35633/inmateh-70-39

Keywords: *peanut-picking device, large feeding volume, simulation, optimized design, test*

ABSTRACT

For a peanut-picking device with a feeding rate greater than 5 kg/s, the problem of low picking rate and high damage rate will occur during the picking process. A discrete element model is developed to determine the range of values of the main influencing factors affecting the peanut picking device. A three-factor, three-level orthogonal combination test was carried out with feeding volume, drum speed, and peanut-picking gap as test factors to investigate the effects of the main influencing factors on the quality of peanut picking operation of the peanut-picking device. The results of the field trials showed that the best results were achieved at the optimum combination of drum speed of 508 r/min, peanut-picking gap of 22 mm, and feeding volumes of 6.3 kg/s. At this time, the peanut picking rate was 99.17%, and the peanut breakage rate was 0.91, meeting the standard technical requirements for mechanized peanut harvesting. The study results provide a theoretical basis for further enhancing the development of peanut combine harvesting equipment.

摘要

针对喂入量大于 5kg/s 的摘果装置在摘果过程中会产生摘果装置摘净率低、破损率高的问题。建立离散元模型，确定影响花生摘果装置的主要影响因素的取值范围。以喂入量、滚筒转速、摘果间隙为试验因素开展三因素三水平正交组合试验，探究主要影响因素对摘果装置摘果作业质量的影响。田间试验验证，结果表明，在最优参数组合滚筒转速为508r/min，摘果间隙为36mm，喂入量为6.3kg/s时，摘果作业效果最佳，此时摘果率为99.17%，破损率为0.91，满足花生机械化收获标准技术要求。研究结果为进一步提升花生联合收获机具研发提供了理论依据。

INTRODUCTION

Peanut is an important oilseed crop and cash crop in China, which not only meets the country's rigid demand for edible oil but also provides a strong guarantee for the healthy development of the agricultural economy (*Li et al., 2020*). However, China's peanut mechanization harvesting technology is relatively lagging, seriously affecting the development of China's peanut industry (Jaime et al., 2015). Peanut picking is a key part of peanut mechanized harvesting, but also the core technology of the peanut combine harvester, peanut picking device structure design and operating parameters directly determine the operational performance of the peanut combine harvester (*Shang et al., 2004; Hu., 2011*).

Improving the operational quality of the picking device is a key part of the picking process and an important measure to improve peanut picking rates and reduce breakage (*Chen et al., 2017*). In recent years, in order to improve the operational quality of peanut-picking devices, scholars at home and abroad have carried out systematic research on peanut-picking devices for root crops such as peanuts and oilseed beans, studying and analyzing the problem from various aspects (*Shang et al., 2004; Chen et al., 2016; He et al., 2022*). Wang Dongwei et al. have designed a spiral-arc panel structure that generates an axial thrust on the peanut during the picking operation and eliminates the need for picking teeth, avoiding roller blockage and reducing breakage rates (*Wang et al., 2013*). Fang Qingliu et al. applied the TRIZ principle to innovate the design of the peanut-picking device, using U-shaped springs to achieve flexible peanut picking, avoiding high-speed impact blows, reducing broken and shattered peanuts, and removing peanuts cleanly (*Fang et al., 2021*). Shang Shuqi et al. used a full-feed axial flow type peanut picking device to improve the peanut picking rate of fresh wet peanuts and reduce the breakage rate by using the shake and stroke working principle (*Shang et al., 2009*).

Guan Meng et al. studied a multi-drum combination peanut picking device, analyzed the peanut picking mechanism of the cutting and axial flow picking drums, determined the basic parameters of each drum, and solved the problem of low picking efficiency and high pod damage rate of the full-feed axial flow single-drum peanut picker (*Guan et al., 2015*).

This paper addresses the problem that peanut picking devices with large feed volumes can produce blockage and entanglement, resulting in low peanut picking rates and high breakage rates, and optimizes the design and picking performance of the peanut picking device structure (*Omori H et al., 2008*). The EDEM software was used to simulate and analyze the peanut picking process to determine the optimum operating parameters of the picking device, thereby achieving an improved peanut picking rate and reduced breakage rate and also providing a theoretical basis for the study of peanut picking devices with large feed volumes (*Shmulevich I et al., 2010; Xie G J et al., 2012; Chen et al., 2020*).

MATERIALS AND METHODS

Overall Structure

The peanut-picking device is a longitudinal full-feed type connected to the feed inlet of the peanut combine. The main working parts are the peanut picking drum, the concave sieve, the top cover of the peanut-picking drum, the deflector plate, the feeding baffle, the feeding blade, the peg teeth, the fixed toothed rod, and the central axis, all in a longitudinal configuration. The overall structure is shown in Fig 1.

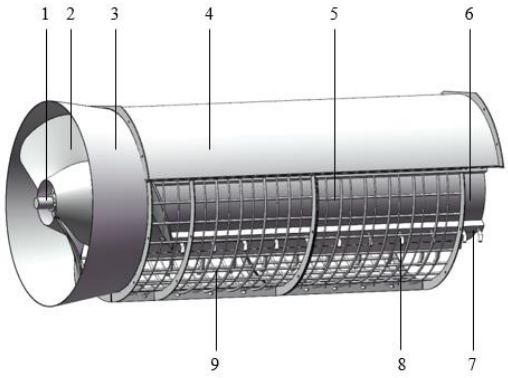

Fig. 1 - Overall structure chart of peanut-picking device

1. central axis; 2. feeding blade; 3. Feeding baffles; 4. Peanut picking drum top cover; 5. concave sieve; 6. peanut picking drum; 7. fixed toothed rod; 8. peg teeth; 9. deflector plate

Working Principle

At work, the dried peanut plants are fed by the feeding blade into the peanut-picking drum, which is rotated by the drive of the central shaft (Zheng et al., 2023). The peanut plant is guided by the deflector plate and the peanut-picking peg teeth, which create a tendency for the peanut plant to move in an axial direction, with the peanut plant wrapped around the high-speed rotating peanut-picking peg teeth (Xu et al., 2020). As the peanut plant is subjected to centrifugal force, the peanut pods face towards the side of the concave plate sieve, which generates a shearing force on the moving peanut pods, thus separating the pods from the peanut seedlings and realizing the peanut-picking process. There is also a part of the peanut pod when entering the drum, subject to peanut picking peg teeth friction, dragging, hitting, rubbing, and falling to achieve the peanut picking process.

Optimized design of peanut-picking roller structure

The performance parameters of the peanut-picking drum have the most direct impact on the quality of peanut-picking operations and are the core components of the peanut-picking device. Therefore, taking into account the peanut picking performance and the cost of construction, a single-cylinder axial flow type peanut picking device is used *(Zheng et al., 2023)*. To achieve a large number of peanuts feeding into the peanut picking operation, a large number of peanut plant movements driven by the peanut picking peg teeth is the strength of the peg teeth and the number of driven seedling vines put forward higher requirements (*Yue et al., 2021*). The design of the peanut-picking peg teeth in this paper is more reasonable in structure and can meet the requirements of a large number of winding peanut plants. The cross-flow peanut-picking device has a low space utilization rate for the whole machine, and it is not convenient to replace parts. In view of the space utilization of the machine and the replacement of parts at a later stage, a longitudinal axial flow type peanut picker has been chosen for this study. The longitudinal axial flow peanut picking drum is shown in Figure 2.

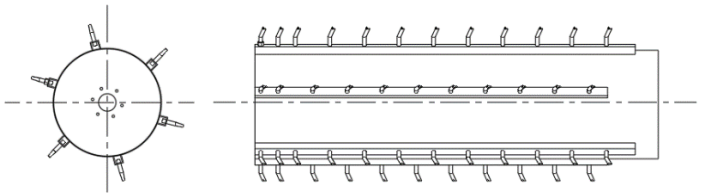

Fig. 2 - Structural Sketch of Picking Drum

Determination of the basic parameters of the peanut-picking drum

The diameter, length, and speed of the peanut-picking drum, as well as the type and order of the included picking elements, have an important influence on the performance indicators and operational quality of the picking unit. The arrangement of the peanut-picking elements is spiral in response to the blockage and entanglement that can occur with peanut-picking devices with large feed volumes. The spiral arrangement increases the axial force on the peanut plant in the peanut picking drum and avoids clogging and entanglement of the peanut plant *(Wang., 2013)*.

For the calculation of the distance between its adjacent plucking nail teeth on the fixed tooth stem, the formula is：

$$E = \frac{XB}{N} \tag{1}$$

where:

E is the distance between adjacent peanut-picking peg teeth, (mm);

B is for the similar nail teeth axial spacing, often taken from 50 to 80 mm, (mm);

X is the number of fixed-toothed rods needed to peanut-picking peg teeth, often taken from 4 to 8;

N is the number of spirals; tests have shown that n ≤ 5.

The length of the rollers is calculated as：

$$L = B\left(\frac{I}{N} - 1\right) + 2\mathrm{h} \tag{2}$$

where:

L is the length of the peanut picking drum, (mm);

B usually between 50 and 80 mm, B = 65 mm, (mm);

I is the total number of peanut-picking peg teeth, I = 84;

h is the distance from the peanut-picking peg teeth to the bottom of the fixing slot, (mm).

According to the formula for the diameter of the peanut-picking drum:

$$D = \frac{X\mathrm{s}}{\pi} + 2\mathrm{h} \tag{3}$$

where:

D is the diameter of the drum, (mm);

s is the distance between adjacent fixed toothed rod, (mm).

The diameter of the peanut-picking drum has an important influence on the performance index of the peanut-picking device. The force analysis of the peanut-picking drum is shown in Fig. 3.

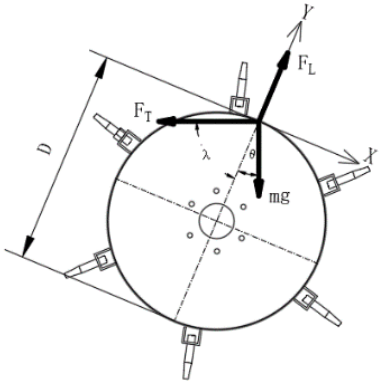

Fig. 3 - Peanut picking roller force analysis diagram

To determine the diameter of the peanut picking drum, the forces at each position are simplified and analyzed as follows: when the peanut plant acts up to the uppermost end, the centrifugal force exerted is the greatest, i.e., the diameter of the drum is the largest, then there is:

$$\begin{cases} F_T - F_L \cos\varphi \cos\lambda - mg\cos\theta > 0 \\ F_L = \mathrm{m}\omega^2 \dfrac{D}{2} \\ F_T = F_{拉} \cos\varphi \end{cases} \quad (4)$$

Where：

F_{pull} for peanut plants subjected to roller tension, F pull = 7 to 20 N, (N);

F_T is the force projected onto the two-dimensional plane by the pulling force, (N);

F_L is the centrifugal force generated by the rotation of the drum, (N);

m is the mass of the peanut plant, m = 7 to 20 g, (Kg);

g is the acceleration of gravity, taken as 10m/s^{-2}, (m/s^{-2});

γ is the angle between F_L and drum diameter, (°);

ω is the angular velocity of the drum, (rad/s);

φ is the angle between the peanut plant and the two-dimensional plane, (°);

θ is the angle between the gravity of the peanut plant and the diameter of the drum, (°).

In order for the peanut picking drum not to produce seedling blockage, it is necessary to satisfy γ = θ = φ = 0, i.e., to satisfy the relation:

$$\mathrm{D} > 2\left(\frac{F_{拉} + \mathrm{mg}}{\mathrm{m}\omega^2}\right) \quad (5)$$

From the above equation, the diameter of the drum should be greater than 350 mm. With reference to the dimensional parameters of commercially available peanut picking devices, analysis of the working performance of existing longitudinal flow picking devices and the performance requirements of this picking device, the picking diameter was determined to be approximately 480 mm (Without spike teeth size).

From the analysis of the above calculations, it follows that: D=480 mm, B=65 mm, N=3, X=6, I=80 pieces, i.e., E=130 mm, L=1800 mm, h=100 mm.

Optimized design of peanut-picking peg teeth

The peanut-picking peg teeth designed in this paper are used to pick the peanut seedlings by rotating the drum through the peg teeth during the picking action (*Kim N.K., 2006*). The top of the peg teeth collide with the peanut pods, as shown in Fig 4.

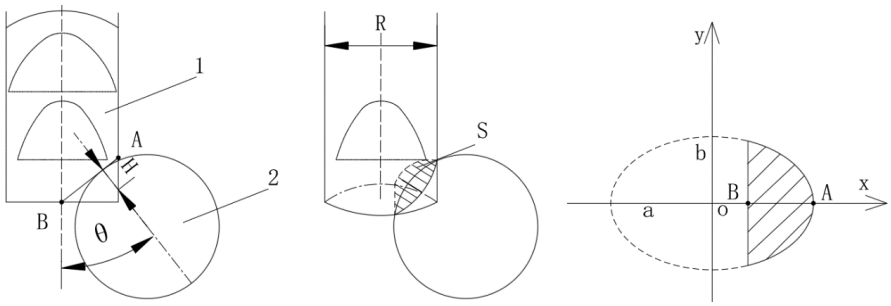

Fig. 4 - Collision diagram

It is assumed that the peanut pod collides with the top of the peg teeth at an angle θ. Taking the direction of the long axis of the ellipse as the x-axis, the direction of the short axis as the y-axis, and the center point of the ellipse as the origin to establish a right-angle coordinate system, the collision areas S are, respectively:

$$S = \int_{-\mathrm{a}}^{-\mathrm{a}+2H} b\sqrt{1-\frac{x^2}{a^2}}dx, \quad x \in (-a, a) \quad (6)$$

where:

H is the compression of the peanut pod when it collides with the peg teeth, (mm);

a is the length of the semi-axis of the elliptical section, (mm).

b in Fig. 5 shows the length of the semi-short axis of the elliptical section, the length of which is equal to the diameter R at the cylinder of the peg tooth. That is, the relationship between a and b is:

$$a = \frac{R}{2\cos\theta} \tag{7}$$

where:

R is the diameter of the peg teeth at the cylinder, (mm).

The cylindrical diameter of the peg teeth, R, is 17 mm, which, when substituted into equation (7), $a = \frac{17}{2\cos\theta}$.

When the peanut pods are impacted by the peanut-picking peg teeth, the impact occurs at an angle of 45° with the greatest force on the peanut pods. The impact of the pods on the peg teeth at an angle of 45°, i.e., θ = 45° is, therefore, analyzed, which gives:

$$S = \frac{289\sqrt{2}}{4}\pi + \left(4\sqrt{2}H - 34\right) \bullet \sqrt{\frac{17\sqrt{2}}{2}H - H^2} + \frac{289\sqrt{2}}{2} \bullet \arcsin\left(\frac{2\sqrt{2}}{17}H - 1\right) \tag{8}$$

Through peanut pod compression tests, the moisture content of peanut plants was between 10% and 20% when the peanuts were dried for 3 to 5 days after starting to be dug. Pod splitting occurred in the widely grown Luhua 12 peanut pods in Shandong with a compression deformation of between 0.95 and 3.25 mm. The amount of compression of the peanut pods without cracking the pods during the operation of the peanut picking peg teeth is H ≤ 0.95 mm, i.e., the contact area between the peanut pods and the peanut-picking peg teeth is S ≤ 4.62 mm^2.

The vertical part of the peanut picking peg teeth is 70 mm long, the curved part is 45 mm long, and the bending angle is 45°. The peg teeth are made from high tensile steel, heat treated to 50 HRC, and galvanized to meet the stiffness and strength requirements of high infeed peanut picking operations.

The peanut plant rotates in the drum with the peanut picking peg teeth, and its forces in the drum are shown in Fig. 5.

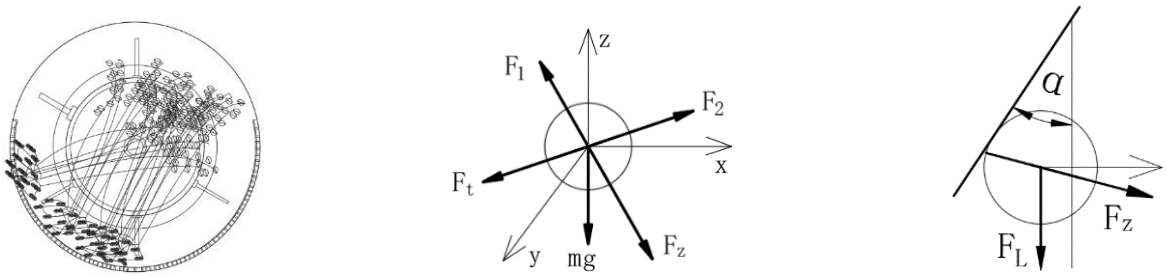

Fig. 5 - Force analysis of peanut pods

The thrust of the peanut plant, F_Z:

$$\begin{cases} F_z = F_1 - G\cos\gamma \\ G = mg \\ F_L = F_z \sin\alpha \\ F_1 = \mu F_2 \\ F_2 = \dfrac{mv^2}{R} - mg\sin\gamma \end{cases} \tag{9}$$

where:

F_Z is the thrust on the peanut plant in the drum, (N);

F_1 is the frictional force on the peanut plant, (N);

F_t is the centrifugal force on the peanut plant, (N);

F_2 is the pressure of the peanut plant on the peanut plant by the concave plate screen and the drum, (N);

F_L is the lateral force on the peanut plant, (N);

G is the gravity of the peanut plant, (N);

R is the radius of the peanut picking drum, (mm);

α is the angle between the concave plate screen and the drum axis, (°);

γ is the quadrant angle of the peanut plant when it is in circular motion, (°);

ν is the linear speed of the drum, (m/s);

μ is the coefficient of friction.

To avoid clogging the roller, the lateral force on the peanut vine after picking is greater than the frictional force on the vine. i.e., $F_L > F_1$

$$F_1 \sin\alpha - mg\cos\gamma\sin\alpha \geqslant F_1 \tag{10}$$

Substituting equation (10) into equation (11) yields:

$$\mu\left(\frac{mv^2}{R} - mg\sin\gamma\right)(\sin\alpha - 1) \geqslant mg\cos\gamma\sin\alpha \tag{11}$$

From the above, it can be seen that the drum speed is 450-500 r/min and the radius of the drum is 240 mm, further simplified to give:

$$mv^2 / R - mg\sin\gamma \geqslant 0 \tag{12}$$

Because $\sin\alpha \in [0,360°]$, therefore, $\sin\alpha - 1 \leq 0$, So the left-hand side of the inequality is negative. If the inequality is made to hold, i.e., satisfies, $\cos\gamma < 0$, then the lateral force on the peanut vine after picking is greater than the frictional force on the vine.

Concave plate screen design

In this paper, the design of the concave plate screen has a certain frictional conveying effect to meet the large feeding volume of peanut seedlings after picking to convey to the seedling discharge mechanism. The overall structural dimensions of the concave sieve are compatible with the peanut picking drum, with a length L of 1800 mm and a width D of 800 mm. A schematic diagram of the concave plate sieve structure is shown in Fig 6.

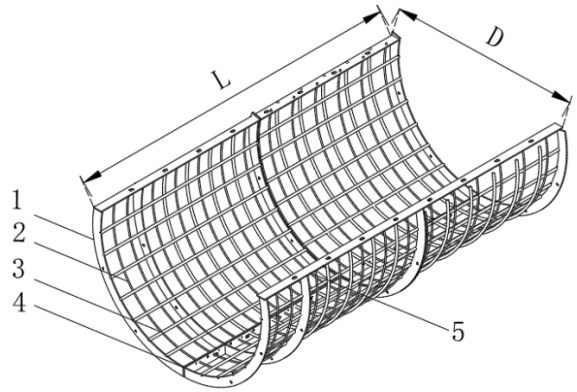

Fig. 6 - Schematic diagram of concave sieve structure

1. lateral arcuate plate 2. horizontal partition 3. round crossbar 4. connection plate 5. mounting plate

Peanut-picking gap design

The peanut-picking gap is an important parameter affecting the quality of peanut-picking operations once the peanut-picking gap parameters are selected unreasonably, directly affecting the peanut-picking performance indicators, which in turn affects the overall performance of the peanut combine harvester. The peanut-picking gap parameter is, therefore, an extremely important working parameter, and the impact of the size of the peanut-picking gap on the picking performance index has to be measured in order to make a reasonable design. A diagram of the peanut picking gap is shown in Fig 7.

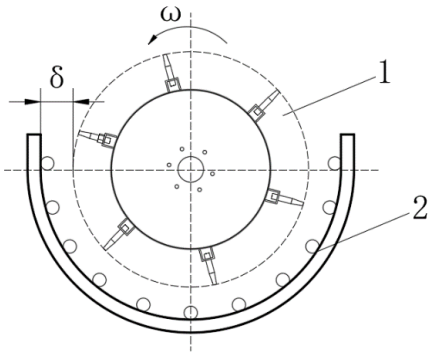

Fig. 7 - Schematic diagram of peanut picking gap

1. peanut picking drum; 2. concave sieve

Considering the movement of the peanut plant during the picking operation, the size of the peanut pods, and the analysis of the existing models, the peanut picking gap of the large feeding volume picking device was designed. The length of the peanut pods is approximately 35 mm, and the adjustable peanut picking gap is designed to be 35 to 55 mm to meet the requirements of different peanut varieties and feeding volumes.

Peanut picker model

Apply Solidwork2019 to build a 1:1 scale model of the peanut picking device, save it in STL format, and import it into EDEM2021. The simulation model is shown in Fig. 8.

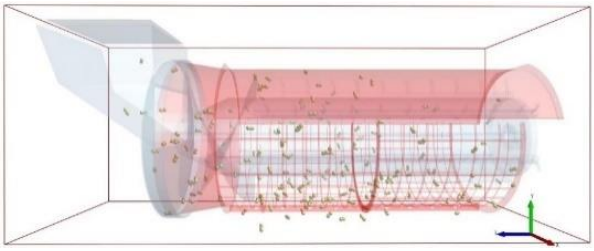

Fig. 8 - *Peanut picker model*

Peanut model construction

Apply Solidwork2019 to build a peanut model according to a 1:1 scale, save it in STL format, and import it into EDEM2021. The discrete element model is shown in Fig 9.

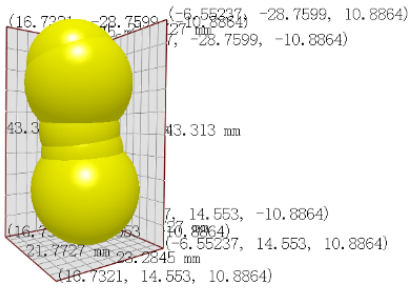

Fig. 9 - *Peanut model*

Table 1

Basic parameters of discrete element simulation

Parameters	Numerical value
Peanut Poisson's ratio	0.32
Peanut shear modulus（MPa）	7
Peanut density（kg/m^3）	257

Parameters	Numerical value
Steel Poisson's ratio	0.27
Steel shear modulus（MPa）	8240
Steel density（kg/m^3）	7850
Coefficient of restitution between peanut particles	0.50
Coefficient of static friction between peanut particles	0.30
Coefficient of dynamic friction between peanut particles	0.20
Coefficient of restitution between peanut and steel	0.37
Coefficient of static friction between peanut and steel	0.40
Coefficient of dynamic friction between peanut and steel	0.10

Peanut-Picking Simulation Results and Analysis

In order to investigate the range of values of the main influencing factors affecting the quality of peanut picking operation, the peanut picking rate and breakage rate were taken as indicators, and the feeding volume, drum speed, and peanut picking gap were taken as experimental factors. The simulation analysis is shown in Fig. 10.

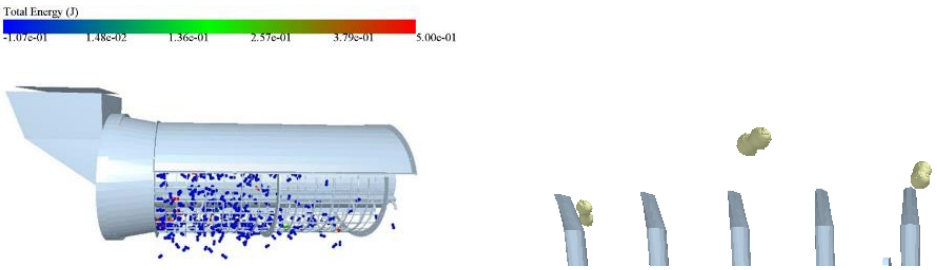

Fig. 10 - Peanut Picking Simulation Schematic

In this paper, theoretical calculations have been carried out to analyze the laws affecting the stress on peanut pods. For further validation, therefore, the simulation test was carried out according to different factors. Depending on the factors, the operating parameters affecting the factors feed, drum speed, and peanut picking gap are changed. Apply the controlled variable method to explore more intuitively the changing law of force on peanut pods.

(1) Influence of feeding volume on peanut-picking operations

Determine the drum speed as 500 r/min and the peanut picking gap as 45 mm. Observe the changing pattern of force on peanut pods by varying the size of the feeding volumes. The resulting comparison is shown in Fig 11:

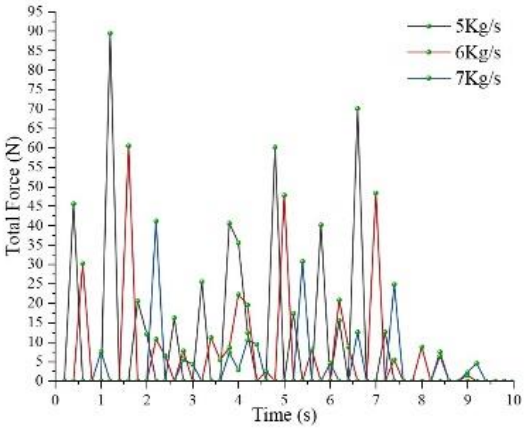

Fig. 11 - Comparison of force analysis of peanuts with different feeding levels

(2) Effect of drum speed on peanut-picking operations

Determine the feeding volumes of 6 kg/s and the peanut picking gap of 45 mm. By changing the size of the rotational speed of the drum, observe the change rule of the force on the peanut pods. The resulting comparison is shown in Fig. 12:

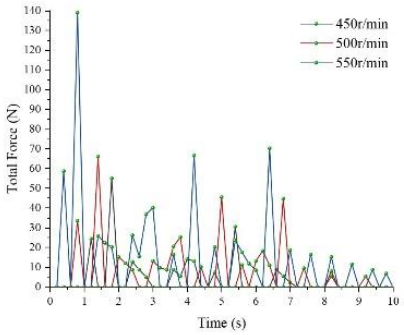

Fig. 12 - Comparison of force analysis of peanuts at different rotational speeds

(3) Influence of peanut picking gaps on peanut picking operations

Determine the feeding volume 6 kg/s, drum speed 500 r/min. By changing the size of the peanut picking gap, observe the changing law of peanut pod force. The resulting comparison is shown in Fig. 13:

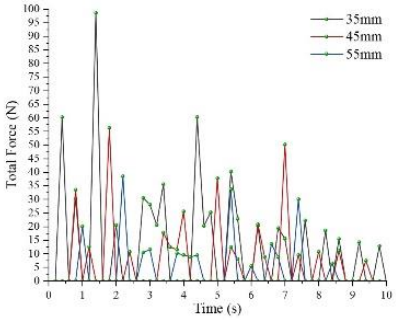

Fig. 13 - Comparative force analysis of peanuts with different picking gaps

Field Test

The quality of the peanut used in the experiment was Luhua 12, which is widely grown in Shandong. The experimental site was selected in Yishui County, Shandong Province, China. After spreading and after three days of drying, the combined water content of the seedling peanut reached 20-30 percent, which satisfied the test conditions.

Fig. 14 - Field test chart

Test program

In order to explore the effects of drum speed, peanut picking gap and feeding volume on the performance index of peanut-picking device. The drum speed X_1, picking gap X_2, and feeding volume X_3 were selected as three test factors, while peanut picking rate Y_1 and breakage rate Y_2 were selected as test indexes to carry out orthogonal rotating combinatorial design tests on the peanut picking device. The feeding volume was selected to be 5.0-7.0 kg/s, the drum speed to be 450-550 r/min, and the peanut picking gap to be 35-55 mm. The experimental data were analyzed by quadratic regression orthogonal rotating combination experimental design using Design-Expert 10 software. Analytical tests were designed according to the Central Composite Design principle. The coded list of test factors is shown in Table 2, and the experimental program and results are shown in Table 3:

Table 2

Experimental factors and levels

Factor level	—1	0	1
Drum speed	450	500	550
Peanut picking gap	15	25	35
Feed rate	5.0	6.0	7.0

Table 3

Test plan and results

Serial number	X_1 Drum speed r/min	X_2 Peanut picking gap mm	X_3 Feed rate Kg/s	Y_1 Peanut picking rate %	Y_2 Breakage rate %
1	-1	-1	0	99.27	1.74
2	1	-1	0	99.01	1.97
3	-1	1	0	99.10	0.92
4	1	1	0	98.71	1.41
5	-1	0	-1	99.24	1.54
6	1	0	-1	98.89	1.53
7	-1	0	1	99.15	0.97
8	1	0	1	98.84	1.41
9	0	-1	-1	99.21	2.04
10	0	1	-1	99.06	1.43
11	0	-1	1	99.12	1.65
12	0	1	1	98.94	0.85
13	0	0	0	99.17	1.58
14	0	0	0	99.21	1.55
15	0	0	0	99.15	1.52
16	0	0	0	99.27	1.61
17	0	0	0	99.18	1.54

It can be derived from Table 3: drum speed and peanut picking gap and feed are used as test factors to explore the findings that affect the peanut picking rate and breakage rate of peanut picking devices. The peanut picking rate Y_1 generally ranged from 98.71 to 99.27 percent, and the breakage rate Y_2 ranged from 0.85 to 2.04 percent.

Quadratic multiple regression was fitted to the data in Table 3. After processing by Design-Expert 10.0 software, the results of ANOVA regarding the rate of peanut picking rate and breakage rate were obtained, as shown in Tables 4 and 5.

Table 4

Analysis of variance for peanut picking rate

Sources	Squares	DF	MS	F value	P
Model 1	0.40	9	0.045	26.62	0.0001
X_1	0.21	1	0.21	127.31	<0.0001
X_2	0.080	1	0.080	47.48	0.0002
X_3	0.015	1	0.015	9.09	0.0195
X_1X_2	4.225E-0.03	1	4.225E-0.03	2.51	0.1573
X_1X_3	4.000E-0.04	1	4.000E-0.04	0.24	0.6410
X_2X_3	2.250E-0.04	1	2.250E-0.04	0.13	0.7256
X_1^2	0.054	1	0.054	31.91	0.0008
X_2^2	0.015	1	0.015	9.15	0.0193
X_3^2	0.012	1	0.012	7.02	0.0330
Residual	0.012	7	1.685E-0.03		
Lack of Fit	3.075E-0.03	3	1.025E-0.03	0.47	0.7193
Pure Error	8.720E-0.03	4	2.180E-0.03		
Cor Total	0.42	16			

Note: highly significant (P<0.01); significant (P<0.05).

Table 5

Analysis of variance for breakage rate

Sources	Squares	DF	MS	F value	P
Model 2	1.65	9	0.18	50.48	<0.0001
X_1	0.17	1	0.17	45.51	0.0003
X_2	0.97	1	0.97	267.89	<0.0001
X_3	0.34	1	0.34	94.83	<0.0001
X_1X_2	0.017	1	0.017	4.65	0.0679
X_1X_3	0.051	1	0.051	13.94	0.0073
X_2X_3	9.025E-0.03	1	9.025E-0.03	2.48	0.1590
X_1^2	0.034	1	0.034	9.39	0.0182
X_2^2	6.737E-0.03	1	6.737E-0.03	1.85	0.2154
X_3^2	0.049	1	0.049	13.40	0.0081
Residual	0.025	7			
Lack of Fit	0.020	3		5.45	0.0676
Pure Error	5.000E-0.03	4			
Cor Total	1.68	16			

Note: highly significant (P<0.01); significant (P<0.05).

Using Design-Expert 10.0 software, the three insignificant terms in the test were removed, and the quadratic term regression model for peanut picking rate Y_1 was obtained as:

$$Y_1 = 99.20 - 0.16X_1 - 0.10X_2 - 0.044X_3 - 0.11X_1^2 - 0.053X_3^2 \quad (13)$$

Using Design-Expert 10.0 software, the three insignificant terms in the test were removed, and the quadratic term regression model for peanut picking rate Y1 was obtained as:

$$Y_2 = 1.56 + 0.14X_1 - 0.35X_2 - 0.21X_3 - 0.11X_1X_3 - 0.090X_1^2 - 0.11X_3^2 \quad (14)$$

RESULTS

Response surface analysis

Response surface analysis of the experimental results using the software can demonstrate more intuitively the effects of drum speed, peanut picking gap, and feeding volume on peanut picking rate and breakage rate.

(1) Interaction analysis of the effects of drum speed, picking gap, and feeding volume on peanut picking rate:

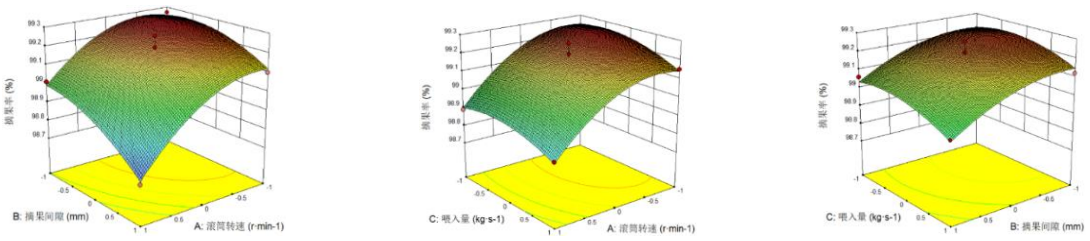

(a) (b) (c)

Fig. 15 - Interaction effects on peanut picking rate

The trend analysis of the response surface change of peanut picking rate in two two-factor intersection operations is shown in Fig. 15. It shows that the peanut picking rate increases with the increase of drum speed X_1, first increases and then decreases with the increase of peanut picking gap X_2, and first increases and then decreases with the increase of feeding volume X_3.

(2) Interaction effects of drum speed, picking gap, and feeding volume on breakage rate

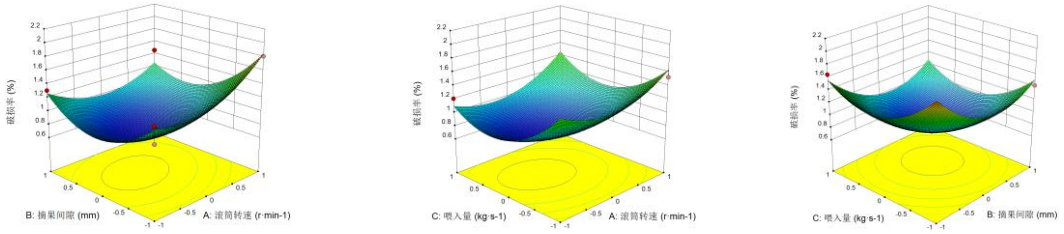

(a) (b) (c)

Fig. 16 - Interaction effects on breakage rate

Trend analysis of response surface variation of peanut breakage rate in two two-factor intersection operations is shown in Fig. 16. It shows that the peanut picking rate increases with the increase of drum speed X_1 decreases with the increase of peanut picking gap X_2, and decreases first and then increases with the increase of feeding volume X_3.

Determination of optimal operating parameters

In order to obtain the best performance index of the peanut large feeding volume picking devices. Based on the results of the above analysis, the quadratic regression model for the peanut picking rate and breakage rate of the peanut picking operation was optimally solved under the constraints using Design-Expert 10.0 software. The objective function of the peanut picking performance index is:

$$\begin{cases} \max Y_{1i} = f\left(X_1,\ X_2,\ X_3\right) \\ \min Y_{2i} = f\left(X_1,\ X_2,\ X_3\right) \\ 0 \le Y_{1i} \le 1 \\ 0 \le Y_{2i} \le 1 \\ X_i \in [-1,1],\quad (\mathrm{i}=1,\ 2,\ 3) \end{cases} \tag{15}$$

The optimal combination was obtained as drum speed 508 r/min, peanut picking gap 22 mm, feeding volume 6.3 kg/s, at which time the peanut picking rate was 99.18%, and the breakage rate was 0.91%.

CONCLUSIONS

(1) The optimized design of the large feeding volume picker is characterized by its high feeding volume and high efficiency. To a certain extent, it solves the problem that the currently existing ordinary peanut picking device is prone to cause a low peanut picking rate and high breakage rate when there is a large feeding volume.

(2) Through the EDEM software on the peanut picking device picking operation process simulation analysis, were determined the drum speed in the 500 r/min or so, picking gap of 25 mm or so, feeding volume of 6 kg/s or so of the optimal range of work values.

(3) Verified by field trials, the optimal working parameters were determined by a three-factor, three-level combination method using drum speed, peanut picking gap, and feeding volume as test factors and peanut picking rate and breakage rate as evaluation indexes. The results of the field test showed that the best peanut-picking operation was achieved when the drum speed was 508 r/min, the peanut-picking gap was 36 mm, and the feed rate was 6.3 kg/s. At this time, the peanut picking rate is 95.01%, and the breakage rate is 0.91%, which meets the requirements of the peanut picking operation.

ACKNOWLEDGEMENT

This research was funded by Shandong Province Collaborative Innovation Centre for Mechanized Production Equipment of Major Crops (2115002).

REFERENCES

[1] Chen Mingdong, Zhai Xinting, Zhang Huan, et. (2020). Study on control strategy of the vine clamping conveying system in the peanut combine harvester[J]. *Computers and Electronics in Agriculture*, 178.

[2] Chen Zhongyu, Gao Lianxing, Chen Charles, Butts C.L. (2017). Analysis of the current status and development of peanut harvest mechanization technology in China and the United States[J](中美花生收获机械化技术现状与发展分析). *Journal of Agricultural Machinery*, 48(04): 1-21.

[3] Chen Zhongyu, Guan Meng, Gao Lianxing, Chen Lijuan, Ma Fang, Dong Huashan. (2016). Design and test of two-stage harvesting peanut screw curved tooth axial picking device[J](两段收获花生螺杆弯齿式轴流摘果装置设计与试验). *Journal of Agricultural Machinery*, 47(11):106-113.

[4] Guan Meng, Chen Zhongyu, Gao Lianxing et al. (2015). Research on multifunctional combined full-feed peanut picking test device [J]（多功能组合式全喂入花生摘果试验装置研究）. *Journal of Agricultural Machinery*, 46(11):88-94.

[5] Hu Zhichao. (2011). *Research on key technology of semi-feed peanut combine harvester[D]（半喂入花生联合收获机关键技术研究）*. Nanjing Agricultural University.

[6] Jaime Cuauhtemoc Negrete. (2015). Current status and strategies for harvest mechanization of peanut in Mexico[J]. *SRG International Journal of Agriculture & Environmental Science (SSRG-IJAES)*, 2 (1): 7-15.

[7] Li Kunpeng, Jiang Ping, Ma Genzhong, Luan Xueyan. (2020). Solution for the whole mechanization of peanut production in Shandong Province[J]（山东省花生生产全程机械化解决方案）. *Agricultural Engineering*, 10(09): 1-7.

[8] Kim N.K., Hung Y.C. (2006). Mechanical Properties and Chemical Composition of Peanuts as Affected by Harvest Date and Maturity[J]. *Journal of Food Science*, (56):1378-132.

[9] Omori H, Hayakawa T, Nakamura T. (2008). Locomotion and turning patterns of a peristaltic crawling earthworm robot composed of flexible units [C] *International Conference on Intelligent Robots and Systems. IEEE*, 1630-1635.

[10] Shang Shuqi, Wang Fangyan, Liu Shuguang, Zhao Zhonghai, Wang Jianchun. (2004). Research status and development trend of peanut harvesting machinery [J]（花生收获机械的研究现状与发展趋势）. *Journal of Agricultural Engineering*, (01):20-25.

[11] Shmulevich I, Horn R. (2010). State of the art modeling of soil-tillage interaction using discrete element method[J]. *Soil & Tillage Research*, 111(1):41-53.

[12] Shang Shuqi, Wang Yanyao, Zhou Yalong. (2004). Application status and promotion of peanut harvesting machine [J]（花生收获机的应用现状与推广）. *Agricultural Machinery Science and Technology Promotion*, (08):10-11.

[13] Wang Dongwei. (2013). *Research on key devices of peanut combine harvester [D]（花生联合收获机关键装置的研究）*. Shenyang Agricultural University.

[14] Wang Dongwei, Shang Shuqi, Han Kun. (2013). Design and test of 4HJL-2 type peanut picking and plucking combine harvester[J](4HJL-2 型花生捡拾摘果联合收获机的设计与试验). *Journal of Agricultural Engineering*, 29(11):27-36+294.

[15] Xie G J, Liu B F, Ren N Q. (2012). The kinetic characterization of photo fermentative bacterium Rhodopseudomonas faecalis RLD-53 and its application for enhancing continuous hydrogen production [J]. *International Journal of Hydrogen Energy*, 37:13718-13724.

[16] Xu Nan, Shang Shuqi, Wang Dongwei et al. (2020). Design and experimental study of peg-tooth type longitudinal flow peanut picking device [J]（钉齿式纵轴流花生摘果装置的设计与试验研究）. *Agricultural Mechanization Research*, 42(08):197-201.

[17] Yue Dansong, Wang Dongwei, Shang Shuqi, He Xiaoning, Gao Zenghui. (2021). Design and test of 4HL-6 three-row and six-row intelligent peanut combine harvester[J] (HL-6 型三垄六行智能花生联合收获机的设计和试验). *Agricultural Mechanization Research*, 43(09):109-112+120. 09.020.

[18] Yu Zhaoyang, Hu Zhichao, Cao Mingzhu, Wang Shenying, Zhang Peng, Peng Baoliang. (2019). Design of clearing mechanism of cut-flow peanut full-feed combine harvester [J]（切流式花生全喂入联合收获机清选机构设计）. *Journal of Agricultural Engineering*, 35(09):29-37.

[19] Zheng Jinming, Wang Dongwei, Shang Shuqi et al. (2023). Design and test of feeding conveyor of peanut picker combine harvester[J](花生捡拾联合收获机喂入输送装置的设计与试验). *Agricultural Mechanization Research*, 45(04):81-87+94.

[20] Zhang Jinming, Shang Shuqi, Wang Dongwei et al. (2023). Design and test of feeding device of longitudinal flow peanut picking system[J](纵轴流花生摘果系统喂入装置的设计与试验). *Agricultural Mechanization Research*, 45(01):183-189.

SIMULATION MODELS OF TECHNOLOGICAL OPERATIONS IN MACHINE MILKING IN PARALLEL TYPE PARLOUR
/
СИМУЛАЦИОННИ МОДЕЛИ НА ТЕХНОЛОГИЧНИТЕ ОПЕРАЦИИ ПРИ МАШИННО ДОЕНЕ В ДОИЛНИ ЗАЛИ ПАРАЛЕЛ

Dimitar GEORGIEV[1)], Galina DINEVA[*1)], Dimitar KARASTOYANOV[2)], Kancho PEYCHEV[1)], Vania DIMOVA[1)]

[1)] Trakia University - Stara Zagora, Faculty of Agriculture, Department of Agricultural Engineering / Bulgaria;
[2)] Bulgarian Academy of Sciences – Sofia, Institute of Information and Communication Technologies / Bulgaria
Tel: +359879020197; E-mail: galinats@abv.bg
DOI: https://doi.org/10.35633/inmateh-70-40

Keywords: *simulation model, milking parlours, milking machine, technological operations*

ABSTRACT

The hourly productivity of the milking parlour is significantly influenced by the organization of the technological process. Milkers perform a series of sequential operations (entry on the platforms, washing, drying, placing the milking units, removing them, disinfecting the teats, exiting the platforms of the milking parlour) the duration of which is a large part of the total milking time. The duration of the latent period from the release of oxytocin to its contact with the myoepithelial cells in the glandular part of the udder is from 30 s to 90 s (average 60 s). In this line of thought, the following questions arise: "in what time interval should the preparatory operations for milking be performed and what is their permissible duration". The aim of the present study is to develop methodologies (models) for simulating the work of milkers in "Parallel" type parlours. It was found that under the initially set working conditions of only two milkers in the milking parlour, all developed models are applicable for capacities up to 2x8. Models II, III and IV are unacceptable for capacities above 2x8, as the total duration of preparation of milking cows exceeds the time frame by between 30-80%. This finding proves that for a capacity over 2x8 it is necessary to perform technological operations with a larger number of milkers.

РЕЗЮМЕ

Часовата производителност на доилната зала се влияе значително от организацията на технологичния процес. Доячите извършват поредица от последователни операции (влизане на платформите, измиване, изсушаване, поставяне на доилните апарати, свалянето им, дезинфекция на цицките, излизане от платформите на доилната зала), чиято продължителност е голяма част от общото време на доене. Продължителността на латентния период от освобождаването на окситоцин до контакта му с миоепителните клетки в жлезистата част на вимето е от 30 s до 90 s (средно 60 s). В този ред на мисли възникват следните въпроси: „в какъв интервал от време трябва да се извършват подготвителните операции за доене и каква е допустимата им продължителност“. Целта на настоящото изследване е да се разработят методики (модели) за симулиране работата на доячите в зали тип „Паралел”. Установено е, че при първоначално зададените условия на работа само на двама доячи в доилната зала, всички разработени модели са приложими за капацитети до 2x8. Модели II, III и IV са неприемливи за капацитети над 2x8, тъй като общата продължителност на подготовката на дойните крави надвишава времевата рамка с между 30-80%. Тази констатация доказва, че при капацитет над 2x8 е необходимо извършването на технологични операции с по-голям брой доячи.

INTRODUCTION

One of the main trends in the development of milking equipment is the constant search for innovative solutions aimed at greater profitability of the farm, precision in the implementation of processes and at the same time reduce the duration of technological operations. Milking installations are increasingly tolerated, creating conveniences for service personnel, animal welfare and the possibility of continuous improvement of the technological process (*Da Borso et al., 2022; Douphrate et al., 2013; Reinemann, 2019*).

Although, in practice different configurations of milking parlours are offered, the technological operations in the process of machine milking do not differ significantly (*Chiumenti et al., 2022; Jakob, 2019; Sandrucci et al., 2019*).

The hourly productivity of the milking parlour is significantly influenced by the organization of the technological process (*Kic, 2015*). Milkers perform a series of sequential operations (entry on the platforms, washing, drying, placing the milking units, removing them, disinfecting the teats, exiting the platforms of the milking parlour) the duration of which is a large part of the total milking time (*Douphrate et al., 2013;Dzidic et al., 2019; Reinemann, 2019*).

In this sense, modern "good practices" emphasize the qualification of service personnel in order to optimize the work process, reduce milking time, increase the hourly productivity of the milking parlour and reduce stress for animals (*Dineva, 2016; Palmer, 2005; Wagner et al., 2001; Uzunova et al., 2017*).

The total time for milking the animals can be divided quite conditionally into two phases - "preparation of the animals for milking" and "actual milking". In the practice of modern intensive animal husbandry, those factors that lead to a maximum increase in the hourly productivity of the installed equipment are considered as priorities (*Peychev et al., 2019; Wagner et al., 2001; Stewart et al., 2002*). Such a concept can lead to an unjustified reduction in the duration of those technological operations that form the stage of preparation of animals for machine milking. The presumed consequence of such an approach is incomplete milking of cows and increased risk of udder health problems (*Rasmussen et al., 1992; Thomas et al., 1997; Marinova et al., 1989*).

The analysis of the above statements raises the following questions: "in what time interval should the preparatory operations for milking be carried out and what is their permissible duration".

According to literature data, the duration of the latent period from the release of oxytocin to its contact with the myoepithelial cells in the glandular part of the udder is from 30 s to 90 s (average 60 s). It follows from the stated physiological regularity that the average duration of the preparatory operations (entrance, washing, drying/massage) must correspond to the duration of the latent period. Any reduction or prolongation of the duration of preparatory operations below and above the latency period calls into question the concentration of oxytocin in the blood and the complete milking of the animals (*Peychev et al., 2019; Kokorina, 1986*).

The aim of the present study is to analyse the time structure of the performed manual operations in machine milking of cows in order to develop models for optimizing the work of milkers.

MATERIALS AND METHODS

The object of the study are "Parallel" type halls with a capacity of 2x8, 2x10 and 2x12 milking parlours.

The subject is an analysis of the duration of the manually performed technological operations during milking and the way of movement of the milkers in the technological corridor between the milking platforms.

The following operations related to the preparation of animals for machine milking were studied - washing, drying and massage, placement of the milking unit and actual milking.

The following boundary conditions are accepted during the derivation of the models:

- the duration of all operations for preparation of the udder for milking (washing, drying and placement of the milking units) - 30 to 90 s (physiologically determined);
- washing time - 2 s (average value from experimental timing);
- drying time - 2 s (average value from experimental timing);
- time for placing the milking unit - 4 s (average value from experimental timing);
- time for movement of the milker between two neighbouring animals - 1 s (average value from experimental timing);
- time for movement of the milker between two adjacent platforms - 2 s (average value from experimental timing);
- travel time (idling) - from 1 ÷ 8 animals - 3 s; from 1 ÷ 10 animals - 5 s; from 1 ÷ 12 animals - 8 s (average value from experimental timing).

The proposed models are simulative and are based on the limit values set by us for the duration of each of the technological operations of the milking process. In this study, no real measurements of the duration of the technological operations were made. Our long-term experience as researchers of the machine milking process shows that the set times are quite sufficient. The statement is valid for milkers possessing the necessary qualification and routine. The derived simulation models are yet to be implemented in real working conditions and will be compared with the theoretical ones in a future experiment. This type of comparison would show whether there are significant differences. This would provide additional up-to-date information to refine our proposed milker work patterns.

RESULTS

The values of the duration of the preparatory operations recommended by Westfalia separator and set in the “Stimopuls C” system (Fig. 1) are in the range of 30-90 s (average 60 s). The probable consequences of a deviation from the recommended values of the udder preparation time would have a negative impact on the course of the neuro-hormonal phase of milk secretion and a decrease in the concentration of oxytocin in the blood. The finding necessitates rethinking and introduction of new methods and methods of work in which the duration of the preparatory operations (timed to the placement of the milking unit) is about 60 s/cow.

Fig. 1 - General view of Westfalia Separator Stimopuls C pulsator

Four simulation models have been developed for the way of milking operator movement in compliance with the technological sequence of operations in machine milking.

Model I - (one milker serves one platform)

In this model the sequence is as follows: the milker washes the udders of all the animals one after the other, then returns to the first at idle. Dry them in the same order and return again (second idle) to place the units from the first to the last cow on the platform (Fig. 2). Analogously to the described circuit works second milker which serves cows on the opposite platform.

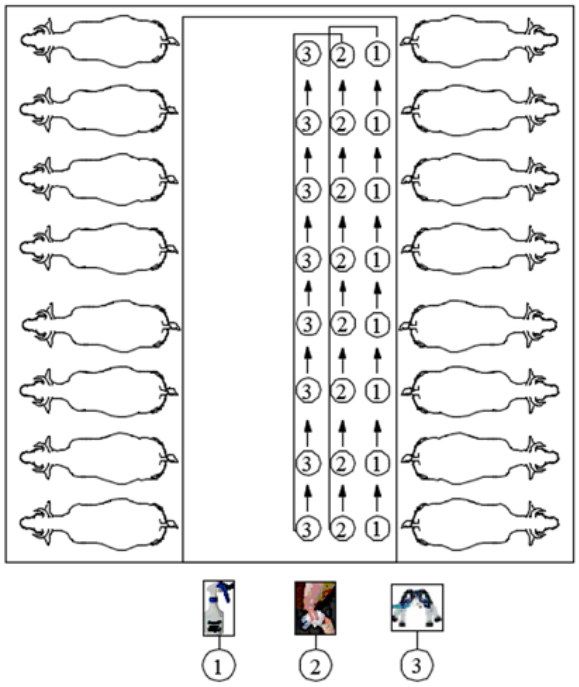

Fig. 2 - Movement and sequence of work of the milkers in Model I

Model II - It is accepted that in the longitudinal direction the milking parlour is divided into two parts. Each milker serves the animals from his corresponding "half" at the same time as shown in Figure 3.

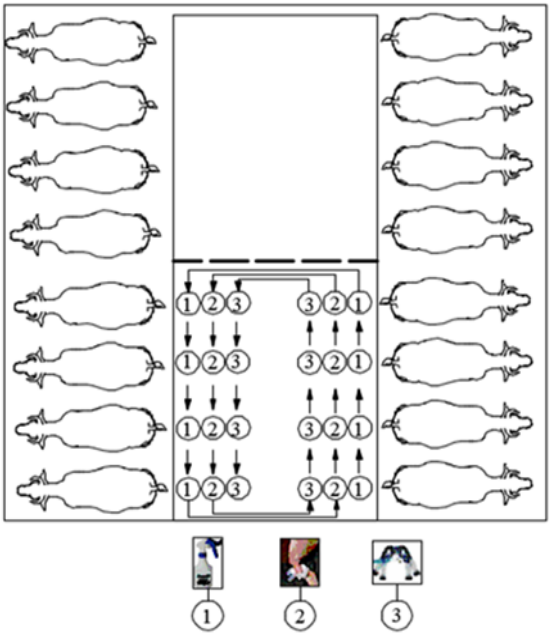

Fig. 3 - Movement and sequence of work of milkers in Model II

The way the service staff works is as follows: the first milker washes the udders of cows from №1 to №4 on the first "left" platform. Similarly, it serves the animals (from №5 to №8) from the "right" platform. He turns to the "left" again, dries the udders of cows from №1 to №4, goes to the "right" and manipulates the animals from №5 to №8 in the same order. It is transferred for the third time to the animals from the "left" platform and according to the established course of work it puts the milking units from №1 to №4. He turns to the "right" platform and performs the same activity with cows from №5 to №8. The work of the second milker is analogous to that described.

Model III- (one milker serves one platform)

The first milker washes the udders of the all cows on the platform (from №1 to №10). He returns to №1 (idle), dries the udder, immediately places the milking unit, then switches to №2, №3, etc. performing the same operations (Fig. 4). The second milker serves the cows from the opposite platform analogously to the described scheme.

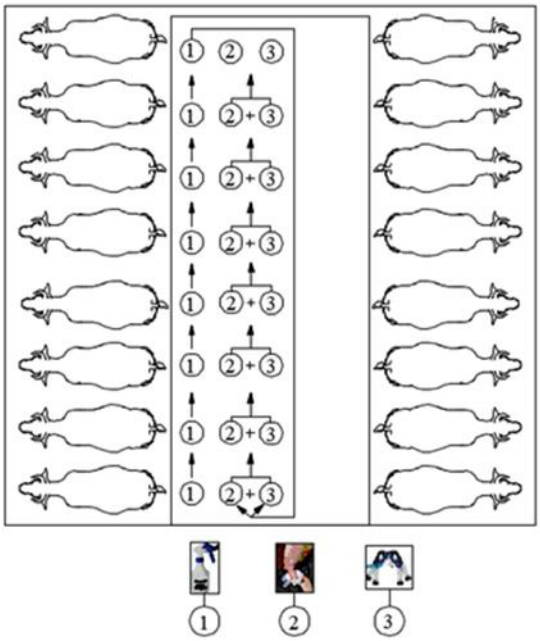

Fig. 4 - Movement and sequence of work of milkers in Model III

Model IV - The milking parlour is conditionally divided into two parts in the longitudinal direction. Each milker works in the corresponding part of the parlour according to Figure 5.

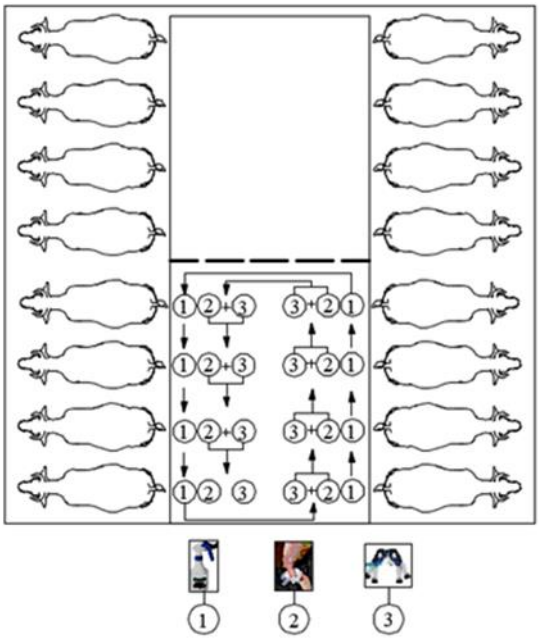

Fig. 5 - Movement and sequence of work of milkers in Model IV

The milker washes the udders of the animals from №1 to №4 from the "left" platform. Moves to the "right" and serves cows from №5 to №8. He returned and dried the udders, immediately placing the milking units successively on cows from №1 to №4 on the "left" platform. He continues his work with the cows on the "right" platform in a similar order.

The hypothetical results from the use of the presented variant modeling are systematized in Figure 6. The same are referred to "Parallel" type milking parlours with a capacity of 2x8, 2x10 and 2x12.

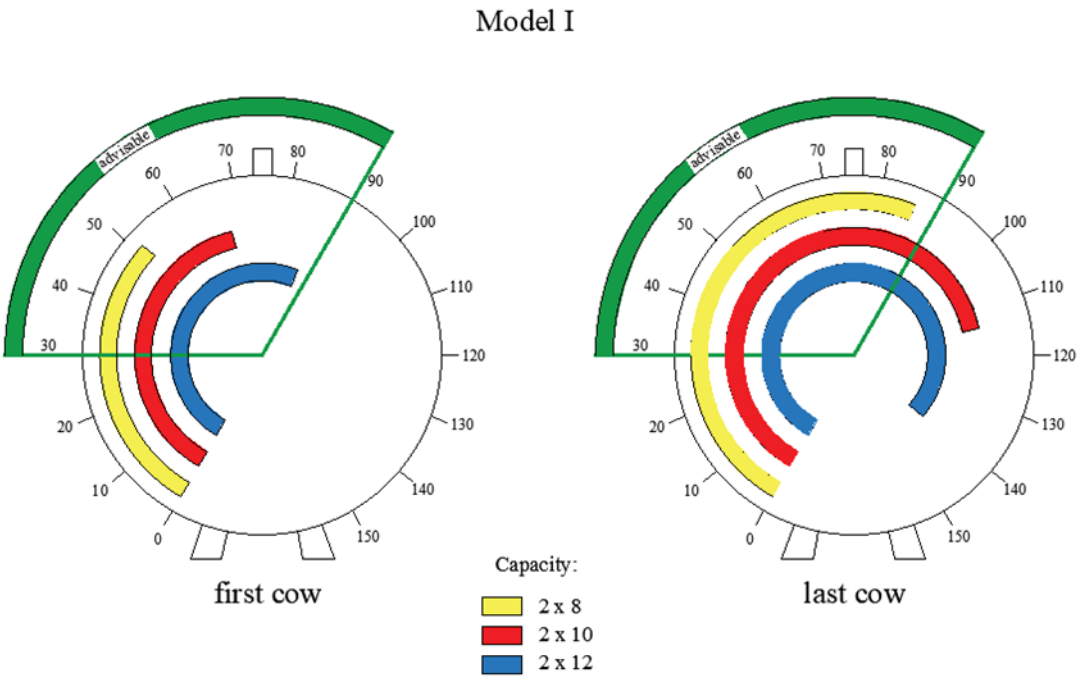

Fig. 6 - Time structure (s) of the technological operations (performed by the milkers) in machine milking referred to Model I

The graphic interpretation of Fig. 6 shows how long after the first irritation (after washing the udder) the milking units are placed on the first and last animal from the milking platform for the considered capacities. For milking parlours with a capacity of 2x8, the placement of the milking units for the first and last animal is within the recommended range (30-90 sec). Model I is unsuitable for 2x10 and 2x12 capacities as the time for placing the milking units of the last animals on the platform significantly exceeds 90 seconds.

Figure 7 illustrates the time structure of the performed technological operations performed by the milkers in simulation Model II.

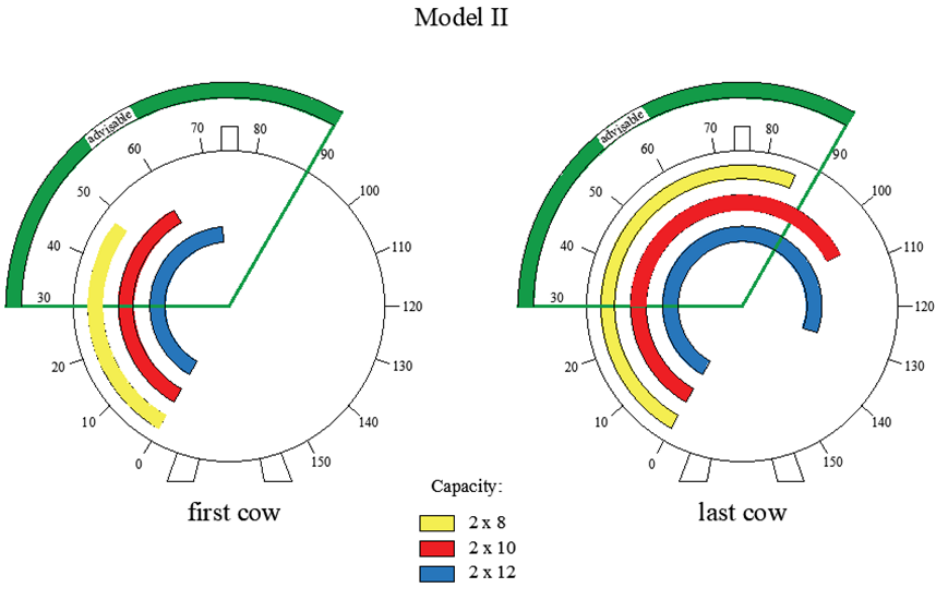

Fig. 7 - Time structure (s) of the technological operations (performed by the milkers) in machine milking referred to Model II

Although in model II the milking parlour is divided into two parts (Fig. 3) the sequence of technological operations is analogous to Model I (washing all animals, returning to the first animal, drying all serviced cows and placing the milking unit of the first animal). The results are close in terms of time spent.

Figures 8 and 9 show the duration of the technological operations performed by the milker respectively for the simulation models III and IV.

The time component of the technological operation "placement of the milking machine" of the first animal is within the recommended values for all considered capacities in both models.

The simulation models III and IV, developed for 2x12 capacity, are unsuitable for practical application, as the time for placing the milking unit on the last animal exceeds by more than 30% the upper limit of the reference values (90 sec).

Only as a compromise option for implementation in real production conditions can model IV for 2x10 capacity be accepted. The graph shows that in this simulation arrangement for performing technological operations the placement of the milking machine on the last animal is 96 seconds. This value is very close to the maximum (of the pre-set time frame).

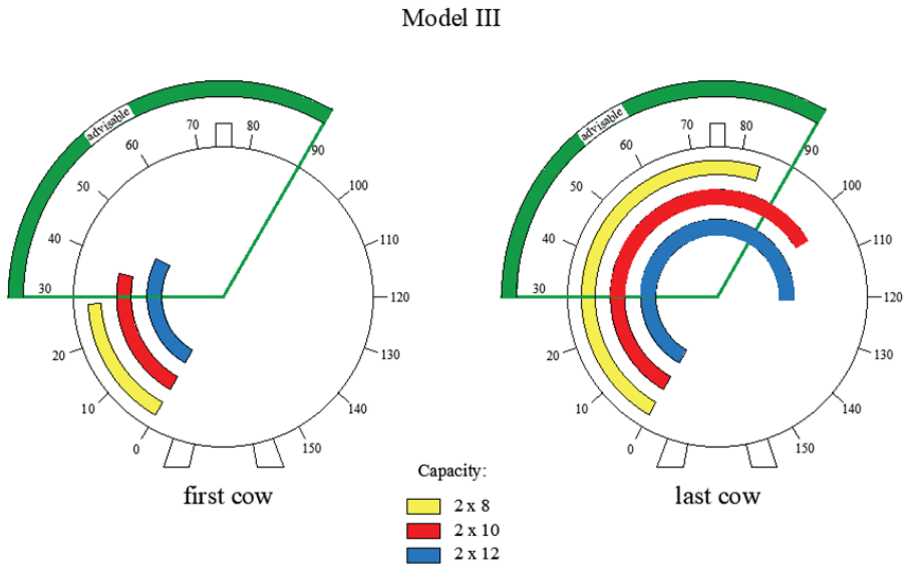

Fig. 8 - Time structure (s) of the technological operations (performed by the milkers) in machine milking referred to Model III

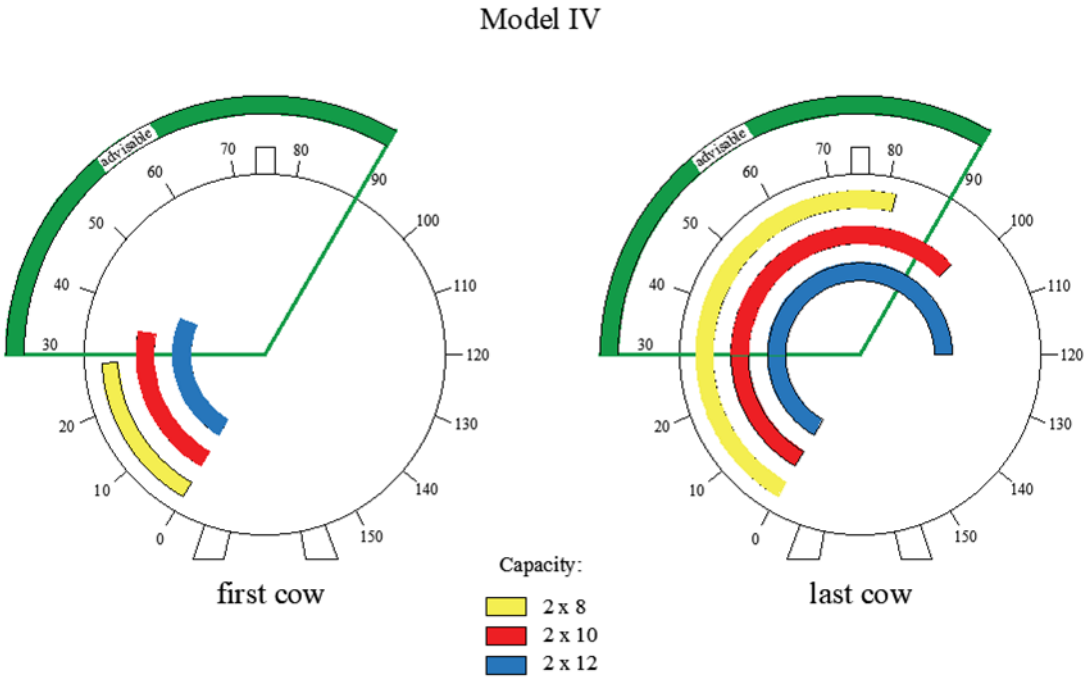

Fig. 9 - Time structure (s) of the technological operations (performed by the milkers) in machine milking referred to Model IV

CONCLUSIONS

The organization of the work of the milkers in "Parallel" type parlour significantly influences the time for preparation of the animals before the "actual milking".

All simulation models are suitable for use in milking parlours type "Parallel" type parlour with a capacity of up to 2x8.

Model IV may be used in "Parallel" type parlour with a capacity of up to 2x10.

All developed models are unsuitable (except for model IV with capacity 2x10) for milking parlours type "Parallel" with capacity over 2x8 as the time for preparation of animals significantly exceeds the maximum 90s.

The models may be used in case the number of milkers is increased or they perform the preparatory operations in a shorter time.

Recommendation: It is necessary to achieve a "kind of optimum" between the productivity of technical equipment and the overall productive and healthy status of animals. This is feasible by properly organizing the work of milkers so as to ensure the duration of the preparatory operations (until the placement of the milking machines) before the "actual milking" in the interval 30-90 s.

ACKNOWLEDGEMENT

The research leading to these results has received funding from the Ministry of education and science under the National science programme “INTELLIGENT ANIMAL HUSBANDRY”, grant agreement n°D01-62/18.03.2021.

REFERENCES

[1] Chiumenti, A., da Borso, F., Chiumenti, R. & Kic, P. (2020). Applying a Mathematical Model to Compare, Choose, and Optimize the Management and Economics of Milking Parlors in Dairy Farms. *Journal of Agriculture,* 10, 472, https://doi.org/10.3390/agriculture10100472

[2] Da Borso, F., Kic, P. & Kante, J. (2022). Analysis of Management, Labor and Economics of Milking Systems in Intensive Goat Farms. *Agriculture,* 12(4), 513, https://doi.org/10.3390/agriculture12040513

[3] Dineva, G., Peychev, K., Vlashev, V., Georgiev, D. & Georgieva V. (2016). Investigation of the functional dependencies between milking unit pulsation parameters and pressure on an artificial teat. *Applied Researches in Technics, Technologies and Education,* 4, 7-13

[4] Douphrate, D. I., Kolstrup, C., Nonnenmann, M., Jakob, M. & Pinzke S. (2013). Ergonomics in Modern Dairy Practice: A Review of Current Issues and Research Needs. *Journal of Agromedicine,* 18(3):198-209, doi: 10.1080/1059924X.2013.796900

[5] Dzidic, A., Rovai, M., Poulet, J., Leclerc, M. & Marnet, P. (2019). Review: Milking routines and cluster detachment levels in small ruminants. *Journal of Animals,* 13, 86–93, https://doi.org/10.1017/S1751731118003488

[6] Jakob, M. (2019). Evaluation of a Physical Ergonomic Intervention for Milking Parlor Operatives – A Case Study. *Journal of Agromedicine,* 24, 1-9

[7] Kic, P. (2015). Mathematical model for optimal arrangement of milking parlor. *Agricultural Engineering International: CIGR Journal,* 71–79, http://www.cigrjournal.org

[8] Kokorina, A. E. (1986). *Conditional reflexes and animal production*. *Agropromizdat,* 335, (Bg).

[9] Marinova, A., Balnikova, A. & Trendafilov, L. (1989). Manual on milking cows. *Zemizdat, Sofia,* (Bg).

[10] Palmer, R. (2005). *Dairy Modernization*, *Thomson Delmar Learning, Canada, NY 12065-2919, 316.*

[11] Peychev, K. V., Georgiev, D., Dineva, G. & Dimova, V. (2019). Structure-time analysis and development of dairy cows machine milking models in “Herringbone” milking parlors. *Bulgarian Journal of Agricultural Science,* 25, 3, 196–200

[12] Rasmussen. M., Frimmer. E., Galton. D. & Peterson, L. (1992). Influence of premilking teat preparation and attachment delay on milk yield and milking performance. *Journal of Dairy Science,* 75, 21-31

[13] Reinemann, D. (2019). Chapter 10 - Milking Machines and Milking Parlors. *Handbook of Farm, Dairy and Food Machinery Engineering (Third Edition),* 225-243

[14] Sandrucci, A., Bava, L., Tamburini, A., Gislon, G. & Zucali, M. (2019). Management practices and milk quality in dairy goat farms in Northern Italy. *Italian Journal of Animal Science,* 18, 1–12, https://doi.org/10.1080/1828051X.2018.1466664

[15] Stewart, S., Godden, S., Rapnicki, P., Reid, D., Johnson, A. & Eicker, S. (2002). Effects of Automatic Cluster Remover Settings on Average Milking Duration, Milk Flow and Milk Yield. *Journal of Dairy Science,* 85, 818-823

[16] Thomas, C., DeLfrenzo, M., Bray, D., Weldon, R., Bucklin, R. & Martin, J. (1997). A Stochastic Economic Analysis of Large Herringbone and Parallel Milking Parlors. *Journal of Dairy Science,* 80, 2418–2428

[17] Uzunova, K., Halil, M. & Tosheska M. (2017). Bulgarian Contributions to Animal Welfare. *Albanian journal of agricultural science,* 397-390

[18] Wagner, A., Palmer, R., Bewley, J. & Smith, D. (2001). Producer Satisfaction, Efficient of Different Milking Systems. *Journal of Dairy Science,* 84, 1890–1898

DESIGN AND EXPERIMENT OF SELF-PROPELLED HIGHLAND BARLEY HARVESTING AND BINDING MACHINE
/
自走式青稞收割打捆一体机的设计与试验

Chengyi ZHONG[1,2], Wenqing YIN [1], Dejiang LIU[2*],Keheng YAO [2], Wei CHEN[2], Zitao XING[3], Fan Jin [2]
[1] College of Engineering, Nanjing Agricultural University, Nanjing 210014, China
[2] Nanjing Institute of Agriculture Mechanization, Ministry of Agriculture and Rural Affairs, Nanjing 210014, China
[3] Ministry of Agriculture and Rural Agricultural Mechanization station, Beijing 100125, China
Tel: +86 025-84346278; E-mail: zhongchengyi@caas.cn
DOI: https://doi.org/10.35633/inmateh-70-41

Keywords: *highland barley harvest, cutting device, bundling, field experiment*

ABSTRACT
In view of the complex agronomic technology of highland barley production and the lack of special machinery for harvesting and bundling highland barley, the harvesting of highland barley is basically done manually. There is a seriously reduced degree of mechanization of highland barley harvesting. Therefore, this paper designs a self-propelled highland barley harvesting and bundling machine, which realizes a single operation process to complete mechanized complex operations such as harvesting, bundling and laying highland barley. By designing the highland barley harvesting method and cutting platform, the height of the cutting platform can be adjusted stepless, and the highland barley bundle knotter is designed to realize the regulation and control of the baling diameter of the highland barley. According to the design of the rope feeding mechanism, the gathering mechanism and the baling mechanism, the main parameters of the baling device are determined. The stubble cutting height of the machine is 325 mm, the average diameter of the highland barley bundles is 195 mm, the average weight per bundle is 5.08 kg, bale formation rate is 97.8%, the qualification rate of the straw bundle reaches 95.6%, drop resistance rate is 92.6%, operating efficiency is 0.82 ha/h. The harvest baler runs in low speed 1 gear, the machine has high operation efficiency, high bundling rate of highland barley, good paving effect, reduced labor intensity, provides the mechanized efficiency of highland barley harvesting. Fuel consumption per hectare is 8.05 kg.hm^{-2}, and the three shifts are without fault, to sum up, it can meet the requirements of highland barley harvesting and baling. The above research can provide a reference basis for the design of the highland barley harvesting baler.

摘要
针对青稞生产农艺技术复杂且青稞收割打捆无专用机械，目前青稞收获基本靠人工背负式收割器割倒青稞后，人工打捆后用拖拉机拉到场地上晾晒，劳动强度非常大，且效率低下，严重降低了青稞收获的机械化作业程度。因此本文设计了自走式青稞收割打捆一体机，该机具实现了一个作业流程即可完成青稞收割、打捆、铺放等机械化复式作业。该机具通过设计青稞收割方式和割台，可无级调整割台高度，设计了青稞成捆打结器，实现了对青稞打捆捆径的调节控制，通过对送绳机构、集禾机构、放捆机构进行设计，确定了打捆装置的主要参数。该机作业后的割茬高度 325mm，青稞捆平均直径为 195mm，每捆平均重量为 5.08 kg，成捆率 97.8%，草捆合格率达到 95.6%，草捆抗摔率 92.6%，作业效率 0.82 公顷/小时，收割打捆机行驶速度挂在低速 1 挡，该机具作业效率高，青稞成捆率高，铺放效果好，降低了劳动强度，提供了青稞收获的机械化效率，每公顷燃油消耗量 8.05kg·hm^{-2}，并且三班次作业无故障，综上，可满足青稞收割打捆一体化机械作业需求，以上研究可为青稞收割打捆机的设计提供参考依据。

INTRODUCTION

Highland barley is an annual herb of the gramineae family and the barley family. It is erect, smooth and up to 100 cm tall. It is the main food, fuel and livestock feed for the inhabitants of Tibetan areas in China, and it is also the raw material for the production of beer, medicine and health products. Agricultural mechanization is an important basis for changing the mode of agricultural development and improving rural productivity, as well as an important symbol and inevitable way of agricultural and rural modernization. In 2021, the highland barley planting area is 2.163 million mu, and the output exceeds 825,000 tons *(Dai F, 2019)*. Highland barley has been planted in Tibet, China for many years, the planting agronomy is complicated, the agricultural machinery research and development investment is small, and there are many problems in mechanized harvesting.

First, the wheat combine harvester introduced in the mainland cannot meet the technical needs of highland barley mechanization harvesting in our area. Highland barley needs to go through a period of time after harvesting (*Dai Fei, 2021*), in order for the grain to be fuller, easier to eat , of better quality. This characteristic of plateau barley led to the introduction of wheat combine harvesters from the mainland, which could not mechanize the harvest of plateau barley *(Jiang Chunyan, 2010)*. At present, the farmers and herdsmen in Tibet in the highland barley harvesting operation, basically use the piggyback harvester. After dragging the field with a tractor for a period of time, the threshing, harvesting or collection of wheat combine harvesters are completed manually or by small machinery, which greatly reduces the efficiency of mechanized harvesting and seriously limits the level of mechanized barley harvesting. With the problems of "difficult labor" and "expensive labor" in agriculture intensifying year by year *(Li H.C., 2012)*, the traditional planting methods of low efficiency and high labor cost input make the comparative benefits of highland barley production continue to decline, and the research, development and improvement of new efficient highland barley mechanized harvesting technology and equipment are imminent *(Liu Kai, 2020)*.

At present, there are few researches on highland barley processing technology and mechanized production equipment in various countries. This project is mainly based on the existing mechanized harvesting equipment for rice and wheat and according to the highland barley special agronomic technology and mechanized production it is necessary to carry out technological innovation, research and development of highland barley special harvesting equipment (*Liu Kai, 2020*). From the formulation of technical regulations for mechanized barley harvesting, the research and development of mechanized packaging equipment and the research and development of mechanized mining and stripping equipment, the status quo and expected analysis of existing technologies, intellectual property rights and technical standards at home and abroad are analyzed.

The research and development of foreign harvesting and baling equipment began in the 1920s, and the German CLAAS company began to study the bundling machine knotter in 1927, and used it with the company's first cutting and binding machine. The popularization and use of the knotter has also further promoted the research and development of straw cutting and binding machine. In order to meet the production needs of straw transportation and mechanical unbaling, the technology of baling has been continuously developed in the aspects of baling density uniformity, rope tightness and knot performance stability. At present, AGCO (AGCO), New Holland (New Holland), Krone and other world's top agricultural machinery equipment manufacturing companies, in the field of straw baling and harvesting technology patent quantity and quality are in the world's leading position. Domestic baling equipment research and development began in the 1960s, because the market demand is not large, there are not many research results. In recent years, with the government's attention to the environmental pollution caused by straw incineration and the increasing utilization value of straw resources, more and more scientific research institutions and agricultural machinery enterprises began to deeply study the straw bundling mechanism and achieved certain scientific research results (*Qiang Xiaolin, 2008*). The Nanjing Institute of Agricultural Machinery of the Ministry of Agriculture and Rural Affairs, the China Agricultural Machinery Institute and Shandong Leiwo and other scientific research institutes and agricultural machinery enterprises in rice and wheat and other bulk crops pick up institutions, feeding institutions, baling rooms, bundling systems and so on have more research results. For highland barley and other small grains baling and baling equipment the research is still in the initial stage, because the highland barley straw is all used as feed in the grazing area, in order to facilitate transportation and storage, the height of cutting stubble, the affordability of the rope, the tightness of the bale, the loss of ear head to special needs, highland barley mechanized baling equipment research and development results will be more and more numerous (*Peam Ba, 2015*).

Based on the above research and development, the Nanjing Institute of Agricultural Mechanization of the Ministry of Agriculture and Rural Affairs and Xizang Huacheng Industrial Co., Ltd. established a research and development team to conduct in-depth investigation and research, and through repeated comparison and demonstration, extensively collected information and materials of similar products in China and abroad, digested and absorbed advanced technologies. According to the current Chinese research, the mechanical structure of rice and wheat combine harvester and baler has basically the same characteristics (*Tian Bin, 2021*), aiming at the agricultural requirements of highland barley, the self-supporting highland barley harvesting and binding machine is developed. The machine can complete one operation process to complete the highland barley harvesting, baling, laying and other processes, mechanical efficient cutting and drying, baling and field placement. According to the preliminary calculation of the technical parameters of the machine, the machine can improve the operation efficiency by 50% ~ 60% compared with the traditional artificial harvesting highland barley, each machine can replace 20-25 labor force, and the work efficiency can be increased by 15 ~ 20 times.

MATERIALS AND METHODS

Whole structure and working principle - Whole structure

4 KL-1200 highland barley harvesting and binding machine is mainly composed of rack, cutter, knot cutter, rope feeder, baling mechanism, transmission system, walking mechanism and so on, as shown in Figure 1. The frame part is composed of a front gearbox and a rear drive box. The front gearbox is designed to advance third, second, first and reverse gears. The countershaft of the front transmission serves as the power input for the rear drive (*Geert Craessaerts, 2009*; *Wang Baoai, 2021*). The whole machine is rear-wheel drive, front-wheel steering. The front gearbox and the rear drive box are divided into upper and lower layers, and special connecting parts are designed to connect them. The folding steering rotation center is designed at a suitable position between the front gearbox and the rear drive box. The steering mechanism of the five Signs agricultural vehicle, the ball head pull rod and the steering wheel are selected as the bending steering mechanism. Total frame length: 1586 mm, total frame width: 718 mm, total frame height: 1227 mm.

Fig. 1 – Overall highland barley harvesting and binding machine

Fig. 2 – Appearance

For operation, as shown in Figure 3, the highland barley stalk is cut down by the cutting mechanism of the binding machine, it is transported from the right side of the cutting platform to the left side through the picking teeth of the conveyor chain, and enters the baling device. The driving wheel of the baling device continuously rotates, and the highland barley rod transported by the picking teeth is transferred to the baling mechanism through the collecting and compression mechanism, and the retaining rake is continuously squeezed (*Wang Bao'ai, 2020*). When the accumulated highland barley rod reaches a certain amount. The stop pull rod of the baling mechanism is removed to complete a baling cut, and then the above work content is repeated to enter the next working cycle. The binding machine can complete the cutting of highland barley stalk and the baling of highland barley stalk in one workflow. When working, the parts operate flexibly, and the rotating parts have safety tips and protective covers. The baling effect of highland barley harvesting is shown in Figure 4. The main parameters of the highland barley harvesting and binding machine are shown in Table 1.

Fig. 3 – Field operation

Fig.4 - Highland barley harvesting and baling effect

Planting agronomic qualification

Table 1

Highland barley harvesting and binding machine technical parameter table

No.	Project	Technical parameters
1	Version	4KL-1200
2	Type of power	Single cylinder diesel
3	Tractor power（kW）	25.7
4	Cut width (tunable, mm)	1200
5	Harvesting line number	4
6	The harvesting way	Cutting type
7	Number of cutting knives (put)	8
8	Cutting knife width (mm)	90
9	Cutting knife length: (mm)	2200
10	Outline dimensions length × width × height: (cm)	1586 x 718 x 1227
11	Operation speed（km·h）	3.5
12	Machine weight/kg	~ 1200 kg
13	Number of operators (including tractor driver)	1
14	Block digits	4

Design analysis of key highland barley harvesting and binding machine

Design of whole structure

The overall arrangement of the machine is "soil" type structure, as shown in Figure 5 below. The cutting table, driving seat, binding conveyor, feeding mechanism, compression device and diesel engine are all symmetrically arranged along the longitudinal axis of the main engine, and the load balance of the left and right walking wheels is balanced (*Mekonnen Gebreslasie, 2010; Wang Baoai, 2018*). In the process of operation, the highland barley stalk material flows along the vertical direction of the binding machine, reducing the resistance of picking and feeding, making the highland barley material flow smooth and continuous, reducing the harvesting loss rate, enhancing the highland barley bundling rate, and ensuring the mechanized productivity and operation quality of the highland barley harvesting and bundling machine.

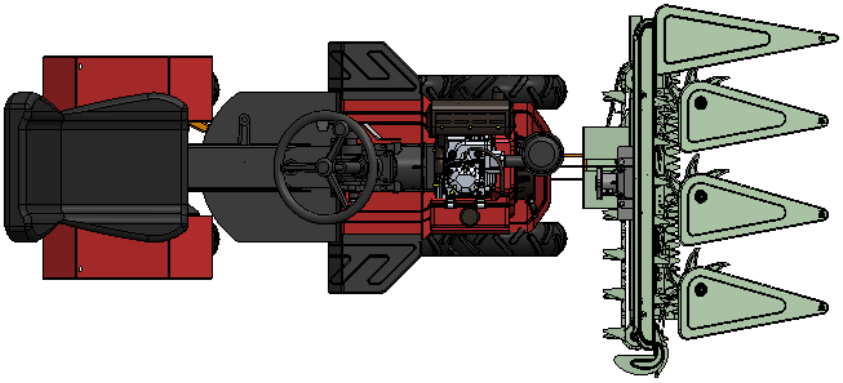

Fig. 5 - Layout diagram of highland barley harvesting and binding machine

The highland barley cutting table is arranged in front of the machine, close to the driving wheel driven by the diesel engine, which shortens the total length of the unit and improves the shape copying effect of the cutting table (*Hermann D., 2016*; *Yang Wenmin, 2019*). The steering wheel and 192FE single cylinder diesel engine are located in the middle of the machine, and the driving seat is located behind the machine, which facilitates the driving of the harvest baling operation and also facilitates the later maintenance. The cutting table, cutting knife, binding conveying device, feeding mechanism, compression device, etc. are arranged in the front of the machine and installed on the front frame.

Design of walking chassis and walking system of highland barley harvesting and binding machine

The chassis frame is the supporting part of the equipment, which carries all the component parts, as well as the assembly and connection positions between the parts. The highland barley harvesting and binding machine uses a single cylinder diesel engine to drive the front wheel drive, frame articulated shaft connects the front and rear frame together, two steering cylinders are installed on the left and right sides of the frame articulated shaft (*Yong-Joo Kim, 2013*), the driver rotates the steering wheel, the steering cylinder begins to work.

Under the action of the steering cylinder, the hinged shaft of the rear frame rotates to drive the subsequent steering, so as to realize the steering of the entire integrated machine. The chassis and walking system of the machine are shown in Figure 6 below.

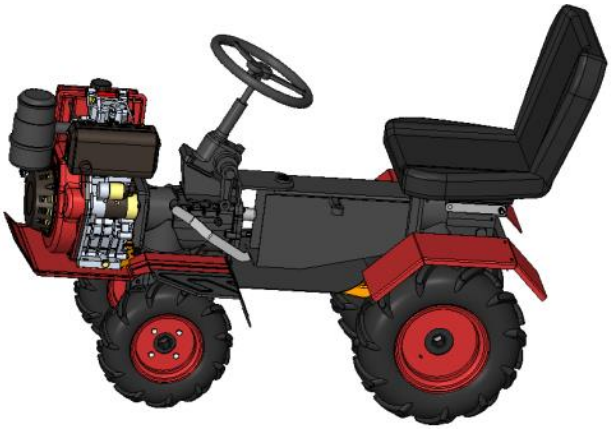

Fig. 6 - Highland barley harvesting baler walking chassis 3 D general map

The driving power of the machine is 192FE single-cylinder diesel engine, which transmits the power to the driving wheel through the driving wheel bridge, which is rigidly fixed on the tube beam of the driving bridge, and is composed of the clutch, gearbox, central transmission, differential and brake. The drive wheel bridge is equipped with 4 gears and stepless gear components, each of which realizes stepless transmission by moving the gear handle to adjust the driving and working speed to meet the needs of harvesting highland barley in the field (*Zhang Shilin, 2020*).

The power required for the operation of the machine is related to the weight of the baler, the operation speed of the baler and the soil condition. The calculation formula can be obtained by consulting the relevant information as follows:

$$P_v = \frac{G \cdot \mathrm{v} \cdot f}{\tau} \times 10^{-3} \quad (1)$$

where: G - represents the total weight of the machine, N;

P_V - power required for machine operation, kW;

V - machine operating speed, m/s;

f - the dynamic friction resistance coefficient of the wheel driving is 0.35;

τ - the driving efficiency coefficient of the traveling system is 0.95.

It can be seen from equation 1 that the power required by the machine to travel is positively correlated with the traveling speed. Therefore, it should be calculated according to the highest forward speed during the operation of the machine and the maximum v=5.5 km/h=1.53 m/s. The transmission efficiency coefficient of the traveling system is 0.95. According to the calculation, the total weight of the machine in full load operation is m=1200 kg, G=mg=5880 N. Bring into the above equation 1 to obtain, the power required by the walking system during machine operation is P_V=6.63 kW.

Design of the highland barley cutting device

Harvester cutter is divided into reciprocating cutter, rotary cutter. Rotary cutting speed is relatively high, cutting ability is strong, but not suitable for wide operation, more used in lawn mowers, harvesting machinery widely used reciprocating cutter, reciprocating cutter by moving blade, knife rod, fixed blade, blade press, gasket, upper and lower friction pieces and other parts of the composition, as shown in Figure 7. The advantages of reciprocating cutter is stable cutting performance. The highland barley binding machine cutting device designed in this paper is a reciprocating cutter, and the cutting mechanism is composed of a cutter and a cutting tool transmission device (*Streicher E.A., 2007*; *Zhang Shilin, 2020*). The function of the cutting mechanism is to cut off crop stalks for cutting width 0.5~5 m. The cutting width designed in this paper is 1.2 m, and the average cutting speed is less than 2.5 m/s. The cutting mechanism performs low and neat cutting, there is no leakage cutting phenomenon, small power consumption, small vibration, easy maintenance and wide adaptability.

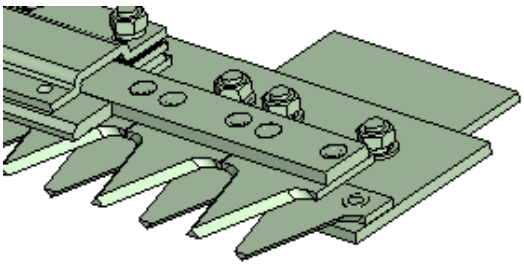

Fig. 7 – Harvesting baler cutter

Speed and forward speed of the cutter

The cutting process of harvesting machinery is the synthesis of cutting motion and the advancing speed of the machine, and the advance distance is the time for the cutting tool to complete a stroke, which can be expressed as the relationship between the cutting tool speed and the advancing speed, expressed as follows:

$$L = V_1 \frac{\pi}{\omega} \tag{2}$$

where:

L - the time for the cutter to complete a stroke the distance for the machine to advance, m;

V_1 - tool forward speed, m/s;

ω - cutter speed, rad;

The ratio of the average cutting speed to the forward speed is the cutting speed ratio:

$$\frac{v_{\text{average}}}{v_1} = \frac{sn/30}{Hn/30} = \frac{S}{H} \tag{3}$$

where:

$v_{average}$ - average speed of the cutter, m/s;

v_1 - tool forward speed, m/s;

S - cutter stroke, mm;

H - cutter drive, mm;

n - cutter shaft speed, rad/min;

ω - Cutter axis angular speed, rad.

In the process of harvesting and baling highland barley, too small cutting speed ratio will cause the highland barley stalk to break, resulting in unequal cutting height, and too large cutting speed ratio is easy to cause leakage, reduce harvesting efficiency, and increase the wear of the cutter. The relevant literature tests show that when the cutting speed ratio is between 0.85 and 3.5 (*Zhang Shilin, 2020*), the quality of the highland barley is better, so that the rotating speed of the cutting cutter is determined to be 450 r/min.

Field experiment and data analysis

Test site and equipment

In August 2022, the highland barley harvesting and binding machine prototype test was carried out in Zhangba Village, Baiba Town, Bayi District, Nyingchi City. The barley used in the test was highland barley, and the varieties of highland barley planted are Zangqing 2000, with an average plant height of 1100 mm. The tying rope used in the knotter was a special nylon bundling rope for the bundling machine, and the speed of the speed regulating motor was set at 450 r/min. The highland barley after harvesting was bundled and pushed to the left side of the bundling machine, and was spread on the ground. Stop to measure bale diameter and weight and related performance indicators.

Test instruments and equipment

Stopwatch, leather tape, steel tape, steel tape and post are used in the test, which can meet the test requirements.

Test time and place

The prototype was tested on August 5, 2022. The test site was conducted in the field of Zhangba Village, Baiba Town, Bayi District, Nyingchi City, China. The test plot was flat with a length of 900 m and a width of 800 m. The weather was fine on the day of the test, which could meet the test requirements.

RESULTS

Test items and test results

In order to understand and master whether the prototype can meet the design requirements and technical performance indexes, the barley bale diameter, stubble height, bale rate, bale pass rate, bale fall resistance rate, fuel consumption per hectare and operation efficiency were tested. The measurement results are shown in Table 2.

Table 2

Test result of miniature ridge mulcher

No.	Project	Agronomic and technical requirements	Determination results	Determinant
1	Binding rate（%）	≥80	97.8	qualified
2	Barley bale qualified rate（%）	≥75	100	qualified
3	Drop resistance of bale（%）	≥70	92.6	qualified
4	Barley bale diameter（mm）	100-300	195	qualified
5	Highland barley stubble height (mm)	300-500	325	qualified
6	Working performance （hm^2/h）	0.82		
7	Fuel consumption per hectare（$kg \cdot hm^{-2}$）	8.05		
8	Fault situation	Three shift operation without fault	meet the requirement	qualified

Through the field test, the main performance index of the machine meets the design requirements, and can meet the agronomic requirements of highland barley harvesting and binding.

CONCLUSIONS

(1) The working parts of the highland barley harvesting and bundling machine designed in this paper are arranged in the front of the self-propelled highland barley harvesting and bundling machine, which is mainly composed of a frame, a cutter, a knotter, a rope feeding mechanism, a baling mechanism, a transmission system, and a walking mechanism. The highland barley harvesting and bundling function completes the highland barley harvesting, bundling, laying and other mechanized compound operations at one time. The average diameter of the highland barley bundle is 195 mm, the average weight is 5.08 kg, and the bundling rate is 97.8%.

(2) The highland barley harvesting and binding machine will cut the highland barley into bundles in the post-ripening period and transfer it out of the field in a timely manner, this way it can be harvested 10-15 days in advance. Compared with the highland barley picking threshing machine, the highland barley harvesting and binding machine will bale the highland barley before the maturity period, avoiding the loss of the barley dropping. Compared with the highland barley combine harvester, barley cutting and bundling machines will simplify the labor intensity of traditional hand harvesting. However, after the barley matures, in order to ensure the quality of the barley and increase the yield, the barley stem can also be used as livestock feed.

(3) The cutting width of the highland barley harvester designed in this paper is 1.2 m, the total transverse size of the machine is 1.58 m, the stubble height after operation is 325 mm, the baling rate of highland barley bales is 97.8%, the pass rate of straw bales is 95.6%, the fall resistance rate of straw bales is 92.6%, and the working efficiency is 0.82 ha/h. Fuel consumption per hectare is 8.05 kg·hm-2, three shifts without failure. According to the summary, the designed highland barley harvesting and bundling machine meets the agronomic requirements of highland barley harvesting in sections.

ACKNOWLEDGEMENT

This research was supported by Tibet Autonomous Region Science and technology plan project - highland barley mechanized low-loss harvesting equipment research and development and improvement (XZ202201YD0016C), the Science and Technology plan project of Tibet Autonomous Region - Research and development and application of equipment for key links of highland barley mechanized production （XZ202301ZY0015N-1), the National technical system of barley and highland barley industry (CRAS-05-04A-01).

REFERENCES

[1] Dai F., Song X F., Zhao W.Y. (2019). Motion simulation and test on threshed grains in tapered threshing and transmission device for plot wheat breeding based on CFD－DEM. *International Journal of Agricultural and Biological Engineering*, 12(1), pp.66-73.

[2] Dai Fei, Zhang Shilin, Zhao Wuyun, (2021). Parameter optimization and test of self-propelled highland barley combined harvesting and binding machine (自走式青稞联合收获打捆一体机参数优化与试验). *Agricultural Research in arid Areas*, 39 (06), pp. 248-256.

[3] Hermann D., Bilde M.L., Andersen N.A., Ravn O., (2016). A Framework for Semi-Automated Generation of a Virtual Combine Harvester. *IFAC PapersOnLine,* 13(4), pp. 11-19.

[4] Streicher E.A., Stroshine R.L., Krutz G.W., Hinkle C.N. (2007). Cleaning Shoe Air Velocities in Combine Harvesting of Wheat. *Transactions of the ASAE*, 15(1), pp.211-220.

[5] Geert Craessaerts, Josse de Baerdemaeker, Bart Missotten, Wouter Saeys, (2009). Fuzzy control of the cleaning process on a combine harvester. *Biosystems Engineering*, 68(3), pp.15-22.

[6] Jiang Chunyan, Tan Jin, (2010). Research progress and application status of highland barley (青稞的研究进展及应用现状). *Xizang Science and Technology*, 2010 (02), pp. 14-16.

[7] Li H.C., Li Y.W., Gao F., (2012). CFD-DEM simulation of material motion in air-and-screen cleaning device. *Computers and Electronics in Agriculture*, 88(2), pp. 111-119.

[8] Liu Kai, Cui Qingliang, Hou Huaming, (2020). Selection test of highland barley crop threshing materials (青稞作物脱粒物料清选试验). *Agricultural Engineering*, 10 (09), pp. 71-76.

[9] Liu Kai, (2020). Experimental study on the clearance characteristics of highland barley mechanical harvest effluent (青稞机械收获脱出物清选特性试验研究). *Shanxi Agricultural University.*

[10] Mekonnen Gebreslasie, Josse De., (2010). Numerical and experimental study of a cross-flow fan for combine cleaning shoes. *Martine Baelmans. Biosystems Engineering*, 45 (01): 26-38.

[11] Qiang Xiaolin, Chi Deshao, Feng Jilin. (2008). Highland barley production and development status in the Qinghai-Tibet Plateau region (青藏高原区域青稞生产与发展现状). *Xizang Science and Technology*, 2008 (3), pp.11-17.

[12] Peam Ba, (2015). Discussion on the status quo and countermeasures of highland barley mechanized production. *Xizang Agricultural Science and Technology*, 37 (02): 46-48.

[13] Tian Bin, (2021). Self-propelled crawler highland barley combined harvesting and binding machine. Gansu Province (自走式履带青稞联合收获打捆一体机), *Gansu Agricultural University*.

[14] Wang Baoai, Zhang Qin, Ding Xiaobin, (2021). Current status and existing problems of highland barley mechanized harvesting (青稞机械化收获现状及存在问题). *Guangdong Silkulture*, 55 (01), pp. 57-58.

[15] Wang Bao'ai, Dai Fei, Xin Shanglong, (2020). Test and analysis of the cutting force of highland barley stalk at mature stage (成熟期青稞茎秆切割力的测试与分析). *Journal of Gansu Agricultural University*, 55 (02), pp.201-208.

[16] Wang Baoai, Zhang Qin, Xin Shanglong, (2018). Structural design of key components of the harvest stage (青稞穗茎分流双层收获割台关键部件的结构设计). *Mechanical Research and Application*, 31(03), pp.108-110.

[17] Yang Wenmin, He Ming, Wu Bei, (2019). Design and test of rape cutter baling parts (油菜割捆机打捆部件的设计与试验). *China Agriculture Bulletin*, 35 (31), pp. 129-133.

[18] Yong-Joo Kim，Sun-Ok Chung，Chang-Hyum Choi. (2013). Effects of gear selection of an agricultural tractor on transmission and PTO load during rotary tillage. *Soil & Tillage research,* 134, pp. 90-96.

[19] Zhang Shilin, Dai Fei, Zhao Wuyun, (2020). Design and test of threshing device of highland barley combined harvester (青稞联合收获机脱粒碎芒装置设计与试验). *China Agricultural Machinery Chemical News*, 41 (11), pp.18-25.

[20] Zhang Shilin, Dai Fei, Zhao Wuyun, (2020). Design and test of straw baling device for highland barley combine harvester (青稞联合收获机配套秸秆打捆装置设计与试验). *Zhejiang Journal of Agriculture*, 32 (07), pp. 1289-1301.

[21] Zhang Shilin, (2020). Design and test of highland barley combined harvesting and binding machine (青稞收割打包机的设计与试验). *Gansu Agricultural University*.

NON-DESTRUCTIVE PREDICTION OF SOLUBLE SOLID CONTENT IN KIWIFRUIT BASED ON VIS/NIR HYPERSPECTRAL IMAGING
/
基于可见/近红外高光谱成像无损预测猕猴桃可溶性固形物含量

Shibang MA*[1)], Ailing GUO [2)] [1]

[1)] School of Mechanical and Electrical Engineering, Nanyang Normal University, Nanyang / China;
[2)] Library, Nanyang Normal University, Nanyang / China
Tel: +86 13503774059; E-mail: mshibang@126.com
DOI: https://doi.org/10.35633/inmateh-70-42

Keywords: *nondestructive and rapid detection, kiwifruit, soluble solid content, Vis/NIR hyperspectral imaging, genetic algorithm*

ABSTRACT
Soluble solid content (SSC) is a major quality index of kiwifruits. Visible near-infrared (Vis/NIR) hyperspectral imaging with the genetic algorithm (GA) was adopted in this study to realize the non-destructive prediction of kiwifruit SSC. A laboratory Vis/NIR hyperspectral imaging system was established to collect the hyperspectral imaging of 120 kiwifruit samples at a range of 400–1100 nm. The average reflectance spectral data of the region of interest of the kiwifruit hyperspectral imaging were obtained after different preprocessing method, namely, Savitzky–Golay smoothing (SG), multiplicative scatter correction (MSC), and their combination method. The prediction models of partial least squares regression, multiple linear regression, and least squares support vector machine (LS-SVM) were built for determining kiwifruit SSC by using the average reflectance spectral data and effective feature wavelength variables selected by GA, respectively. The results show that SG+MSC is the best preprocessing method. The precisions of the prediction models built using the effective feature wavelength variables selected by GA are higher than that established using full average reflectance spectral data. The GA-LS-SVM prediction model has a best performance with correlation coefficient for prediction (R=0.932) and standard error of prediction (SEP=0.536° Bx) for predicting kiwifruit SSC. The prediction accuracy has been improved by 5.6% compared with that of the prediction models established by using the full-band reflectance spectral data. This study provides an effective method for non-destructive detection of kiwifruit SSC.

摘要
可溶性固形物含量是猕猴桃的主要品质指标。本研究采用可见/近红外高光谱成像结合遗传算法实现猕猴桃可溶性固形物含量的无损检测。构建了可见/近红外高光谱成像系统，采集了 120 个猕猴桃样品 400-1100 nm 的高光谱图像。获取猕猴桃高光谱图像感兴趣区域平均反射光谱，采用 Savitzky-Golay 平滑、散射校正及其组合预处理方法对其进行预处理。分别利用全波段反射光谱和遗传算法选取的有效特征波长光谱建立猕猴桃可溶性固形物含量的偏最小二乘回归、多元线性回归和最小二乘支持向量机预测模型。结果表明，Savitzky-Golay 组合散射校正是最好的预处理方法。利用遗传算法选择有效特征波长建立的预测模型精度高于全波段反射光谱建立的预测模型。GA-LS-SVM 预测模型预测猕猴桃可溶性固形物含量的相关系数(R=0.932)和标准误差(SEP=0.536°Bx)最好，相对于全波段反射光谱建立的预测模型，预测精度提高了 5.6%。本研究为无损检测猕猴桃可溶性固形物含量提供了有效的方法。

INTRODUCTION
A fruit with rich nutritional value is one of the most popular and favourite agricultural products worldwide. Kiwifruit, which contains a lot of vitamins, minerals, sugar, and other nutrients, has become a global agricultural commodity *(Berardinelli et al., 2019)*. It is loved by many consumers and called as the “fruit king”. Nowadays, consumers pay more attention to the internal quality of fruits *(Eunhee et al., 2018)*. Soluble solid content (SSC) is a major internal quality attribute index of a fruit. It is an important factor in the timing of fruit ripening and harvesting *(Umer et al., 2020)*. It also determines the taste or quality of the kiwifruit and affects the price and consumers’ purchasing intention *(Xu et al., 2020)*. Moreover, SSC affects the commercial value and market competitiveness of fruits *(Jiang et al., 2019)*.

[1] *Shibang Ma*, Associate Prof. Ph.D.; Ailing Guo, Assistant Librarian*

Predicting fruit SSC has an important reference value for the evaluation of a fruit harvest time, quality, and grading sale. The conventional measurements using a refractometer are reliable and objective. However, they are laborious, destructive, time-consuming and require experience. They cannot meet the demands for non-destructive and online real-time detection of fruits. Moreover, the requirement of consumers and the market such as non-destructive, rapid and easy operating cannot be met. Consequently, a rapid, nondestructive, and easy-to-operate evaluation method is required for evaluating fruit SSC. Hyperspectral imaging is a relatively emerging tool that can provide spectral data information and spatial information from the examined object *(Rosalba et al., 2017)*. Its detection principle is based on the interaction of the light with the examined object. The reaction strength of various objects to light at different wavelengths variable varies. The spectrum variation in each object is determined by its microstructure and chemical composition; thus, the SSC can be reflected by the intensity change in the relevant wavelength of examined object using chemometric methods *(Zhang et al., 2020)*. An examined object image obtained from a hyperspectral imaging system can be taken as a three-dimensional spectral data matrix *(Santosh et al., 2016)*. In recent years, hyperspectral imaging has been broadly recognized as an emerging technology for rapidly and non-destructively assessing the attributes, quality, and safety of fruits *(Ebrahiema et al., 2018)*. *Li et al. (2018)* used short-wave and long-wave near-infrared hyperspectral imaging technologies coupled with an improved watershed segmentation algorithm to detect early bruises on peaches rapidly and nondestructively. The results showed that short-wave NIR hyperspectral imaging model was highly suitable for detecting early bruises on peaches. Its detection results indicated that 96.5% of the bad peaches and 97.5% of the good peaches were accurately detected from all the test peaches. *Reddy R. et al. (2021)* used hyperspectral imaging and multivariate statistics to assess the SSC and flesh firmness of fresh cherry fruits nondestructively by developing a partial least squares regression (PLSR) model and Gaussian process regression (GPR) model. The test dataset results highlighted that GPR model can be used to detect SSC and firmness of cherry with correlation coefficients (R) of 0.88 and 0.60, respectively, and root mean standard errors (RMSE) of prediction of 0.43% and 0.38, respectively. Thus, hyperspectral imaging can be considered as a reliable and robust technology for estimating cherry fruit quality attributes. However, the GPR models showed low certainty with a prediction interval coverage probability of 0.90–0.97. *Ma et al. (2021)* built a NIR hyperspectral imaging detection system combined with a sample rotation holder to scan the whole kiwifruit surfaces and acquire the hyperspectral imaging with key wavelengths within the 1002–2300 nm range. Then, they constructed SSC calibration models via PLSR analysis. The results showed that the coefficient of determination (R_{cv}^2) and RMSE of the cross-validation set were 0.74 and 0.7%, respectively. However, *Ma et al. (2021)* only established a PLSR model. Moreover, the robustness and stability of the model is unknown.

These aforementioned studies showed that Vis-NIR hyperspectral imaging technology can predict the SSC and other qualities of different fruits, such as peach, plum, cherry, and kiwifruit. Those studies established prediction models mainly using the full wavelength spectrum data. The studies on the influence of different prediction model, different preprocessing methods and variable selection method on the prediction accuracy are few. Moreover, studies on the non-destructive prediction of kiwifruit SSC via Vis/NIR hyperspectral imaging with variable selection method are also fewer. The stability and accuracy of a SSC prediction model greatly affect its practical application and cost. Therefore, the stability and accuracy of the prediction model must be improved.

In the previous research process, the authors have explored the feasibility of using visible near infrared spectroscopy to detect the SSC of kiwifruit, and achieved good results. In this study, the authors further studied the feasibility of using hyperspectral imaging technology for non-destructive detection of kiwifruit SSC on the basis of the previous studies. Some experimental methods referred to the previous research process *(Ma, 2021)*.

The present study aimed to establish the approach of using Vis/NIR hyperspectral imaging combined with GA for the non-destructive prediction of kiwifruit SSC. Moreover, the influences of different spectral preprocessing methods, full wavelength variables, effective feature wavelength variables selected by GA, and the accuracy of different prediction models were studied. The best spectral preprocessing method and best prediction model for kiwifruit SSC were also determined. This study provides an effective method for non-destructive detection of fruit quality.

MATERIALS AND METHODS

Vis/NIR hyperspectral imaging system

A Vis/NIR hyperspectral imaging system in the wavelength range of 400–1100 nm was built and used to collect the hyperspectral imaging of the kiwifruit samples in the process of experiment. The schematic diagram of the Vis/NIR hyperspectral imaging system is shown in Fig. 1. The Vis/NIR hyperspectral imaging system comprised a charge coupled device camera, hyperspectral spectrograph, halogen lamp, a sample holder, DC power, power cable, a computer, data cable, and frame.

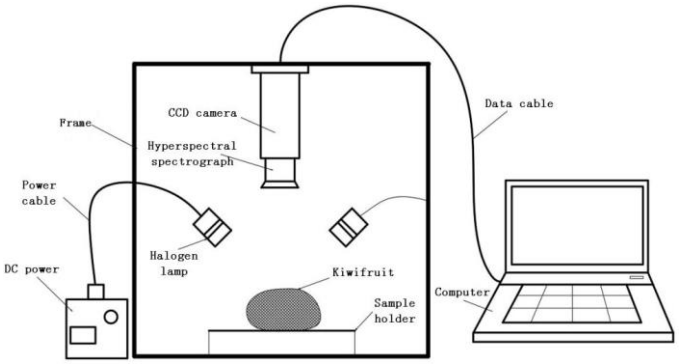

Fig. 1 - Schematic diagram of the Vis/NIR hyperspectral imaging system

Kiwifruit samples

One hundred and twenty fresh kiwifruit samples at the same maturity stage were collected from a kiwifruit orchard. All the samples were transferred to the optical testing laboratory room in a freshness preservation box, and stored under cold conditions at $0-3^{\circ}C$. The experiment was completed in four days. Every time before the experiment, the cold-stored samples were removed to room temperature conditions ($22\pm2^{\circ}C$) for approximately 8 h to reduce collection data variations caused by different temperature of kiwifruits. First, the hyperspectral imaging of each fruit sample was acquired by the Vis/NIR hyperspectral imaging system, then, the SSC values of each fruit sample were measured by the digital refractometer.

Vis/NIR hyperspectral imaging acquisition

Figure 2 shows a scene of the Vis/NIR hyperspectral system. The Vis/NIR hyperspectral imaging of each kiwifruit sample was acquired using the Vis/NIR hyperspectral imaging system. The experimental kiwifruit samples were placed on the sample tray for scanning and the hyperspectral imaging was collected. Each sample was scanned two times from the upper surface and bottom surface, and two Vin/NIR hyperspectral images were collected for each sample. The mean of two images was taken as the final imaging data. Before scanning, the parameters of exposure time, scanning speed and lens focusing distance were set. The raw Vis/NIR hyperspectral imaging was corrected by using the white reference image and dark reference image before each measurement to reduce the influences of external interference and dark current noise. The dark reference image was acquired by recording the Vis/NIR hyperspectral image after the lens was covered with black cap, whereas, the white reference image was acquired by collecting the Vis/NIR hyperspectral image of a white background plate.

The final calibrated Vis/NIR hyperspectral image of sample was calculated based on the following formula:

$$l_c = \frac{l_0 - l_d}{l_w - l_d} \quad (1)$$

where: l_c means the calibrated Vis/NIR hyperspectral image, l_0 indicates the raw Vis/NIR hyperspectral image, l_w represents the white reference images, and l_d denotes the dark reference images.

Spectral profile extraction

The calibrated Vis/NIR hyperspectral images of the samples were further analysed using the ENVI 5.3 software. The scanned region of kiwifruit was selected as the region of interest (ROI). The spectral profile was extracted from the ROI of each sample Vis/NIR hyperspectral image. The spectral profile extraction process is shown in Fig. 3.

The mean intensity of all pixels of each kiwifruit sample in the ROI was calculated and regarded as the full average reflectance spectrum for further constructing prediction model and wavelength variable selection.

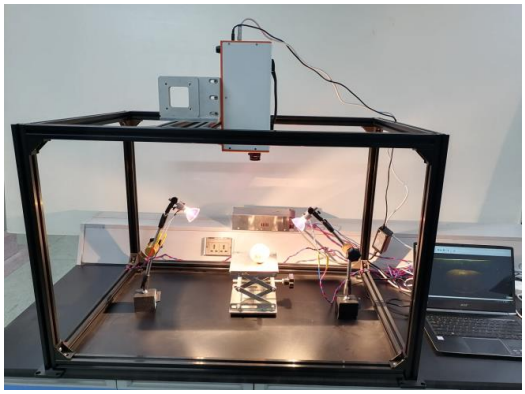

Fig. 2 - The scene of the Vis/NIR hyperspectral imaging system.

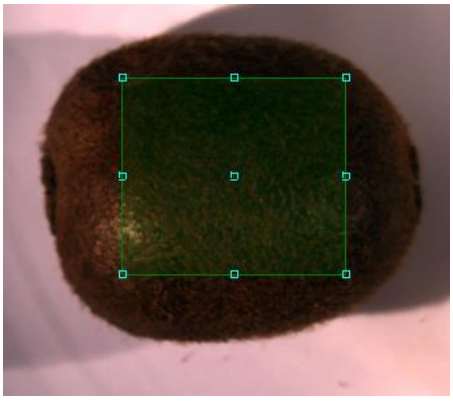

Fig. 3 - ROI selection and spectral profile extraction

Kiwifruit SSC real value

The SSC real value of each kiwifruit sample was measured after the Vis/NIR hyperspectral image collection. First, the kiwifruit sample was peeled and cut into flesh slices in its upper surface and bottom surface, respectively. Second, the flesh slices were squeezed into juice using a fruit juicer (HY-160, Joyoung, China). Then, the SSC of each kiwifruit sample was tested using a digital Brix refractometer (PR-101; ATAGO Co., Ltd., Japan). The average of the SSC real values of the upper and bottom scanned surface was regarded as the real value of kiwifruit SSC.

Data analysis and model establishment

Data preprocessing and model establishment methods

On the one hand, the kiwifruit is similar sphere. Its surface curvature affects the absorption and reflection of light. On the other hand, there are a lot of fluffs on the surface of kiwifruit. Scattering occurs when light hits the surface of kiwifruit. These affect the quality of the spectral data. The raw spectra of samples should be pretreated to improve their qualities. There are many kinds of spectral preprocessing methods. The spectra of samples were pretreated by Savitzky–Golay smoothing (SG) and multiple scattering correction (MSC) to eliminate noise interference and reduce analysis error. The detailed explanation and instruction of the SG algorithm can be found in literature *(Chen et al., 2011)*, whereas that of the MSC algorithm can be found in literature *(Tom et al., 2009)*. The prediction models of the SSC were developed by PLSR, MLR, and the least squares support vector machine (LS-SVM). Prediction model was optimized based on the optimal method to improve predictive ability by eliminating the useless information and redundant variables in the raw spectral data by using an effective variable selection algorithm. GA was used to decide optimized feature wavelength variables. Finally, the best pretreatment method and the best prediction model were determined.

Around 1975, the PLSR was proposed by Herman Wold to build complicated model. It is a widely used to solve the problem of multivariate linear regression. PLSR can be thought of relating two data matrices, X (predictors; i.e., spectrum of kiwifruits in this study) and Y (response; i.e., SSC in this study), through a linear multivariate model. In the present study, PLSR analysis method was used to build a prediction model for detecting kiwifruit SSC. The latent variables (LVs) were considered as an important parameter in establishing a PLSR model. They were considered potential eigenvectors of the raw spectra. LVs can compress the raw spectral data and reduce the dimensionality. The LVs were taken as the input variables of PLSR and simplified the PLSR model. The reasonable number of LVs helps avoid underfitting or overfitting the model. In general, full cross-validation is used to determine the reasonable number of LVs by using the root-mean-square error of cross-validation in establishing a PLSR model *(Li et al., 2019; Nturambirwe et al., 2019)*.

MLR is a well-known statistical analysis method *(Hamid et al., 2012)* that attempts to develop the relationship between an output variable with two or more input variables by fitting a linear regression equation.

The equation of MLR model is:

$$y_i = a_0 + a_1 x_{i,1} + a_2 x_{i,2} + \ldots + a_j x_{i,j} + e_i \quad (2)$$

where:

y_i is the output variable, a_0 is a constant, is an input variable, a_j is the regression coefficient vector, and e_i is a random measurement error.

Support vector machine (SVM) is an effective analysis tool for classification problem. However, the training problem of SVM model is a complex and thorny problem. Suykens and Vandewalle proposed a modified and simplified SVM algorithm called LS-SVM. LS-SVM can simplify the training process and improve the convergence rate of regression equation. Therefore, LS-SVM has been widely used to solve complex regression and classification problem and achieved acceptable results *(Xu et al., 2015)*. Establishing prediction model with LS-SVM belongs to a regression problem. In order to solve the regression problems with LS-SVM, suppose $T=(x_i, y_j)$ is the training set, and m is the sample number, where $i=1,2,3,\ldots,m$; x_i is the independent variable, and y_j is the dependent variable. The prediction regression problem of LS-SVM can be described as follows:

$$\begin{cases} \min J(w,a,\xi)=\frac{1}{2}w^T w+\frac{1}{2}\gamma\sum_{i=1}^{m}\xi_i^2 \\ s.t y_i[w^T\varphi(x_i)+b]=1-\xi_i,\ i=1,\ldots,m \end{cases} \quad (3)$$

where:

w is the weight vector, a is a partial vector, y is the penalty parameter used in adjusting the proportion of empirical risk and the confidence interval of LS-SVM ξ_i is the slack variable for x_i.

The LS-SVM parameters and proper kernel function are two important factors that influence the performance of LS-SVM. Therefore, the parameters and proper kernel function should be determined before using LS-SVM. The frequently used kernel functions include radial basis function (RBF), polynomial kernel, and linear kernel in LS-SVM. RBF is a nonlinear function that can simplify the training process and deal with the nonlinear relationships between input variables and output variables. RBF was selected as the kernel function of LS-SVM in present study. The parameter σ^2 and the penalty parameter γ of the RBF kernel function are two key parameters that should be determined. They affect prediction ability and prediction accuracy of LS-SVM. In this study, the γ and σ^2 were determined by using K-fold cross-validation method.

GA (genetic algorithm)

GA is one of the most popular methods for selecting effective features. GA can be regarded as computer simulations of evolutionary process from biological systems. It is able to find an optimal solution in dealing with the search problems and suitable for solving nonlinear complex optimization problems. GA starts with an initial population. Then, a new population is generated by crossover and mutation operations with the selected chromosomes of current population. The population and chromosomes are generated or chosen in term of their fitness at each stage. The selection of initial population, fitness function, chromosome, crossover rate and mutation rate are important steps in GA. The number of initial population is determined according to the training set and the number of extracted features. A new population is generated from the current population by chromosome selection, crossover, and mutation. A detailed description and computer program explanation of the GA can be found in Literature *(Leardi et al., 1998)*. GA has been widely used to select the feature variable and develop predictions. In present study, the GA was used to select the effective feature wavelength variables and develop prediction models.

Model performance criteria

The performance of prediction model was assessed based on calculating the differences between the real measured value and predicted value of kiwifruit SSC by the correlation coefficient and the standard error. The correlation coefficient of calibration set (R_C), the standard error of calibration (SEC), the correlation coefficient of prediction set (R_P), and the standard error of prediction (SEP) were defined as shown in Equations (4)–(7). The four indices were used to assess the performance of the prediction models.

$$Rc = \sqrt{\sum_{i=1}^{n_c}(\hat{y}_i - y_i)^2} \Big/ \sqrt{\sum_{i=1}^{n_c}(\hat{y}_i - y_m)^2} \quad (4)$$

$$Rp = \sqrt{\sum_{i=1}^{n_p}(\hat{y}_i - y_i)^2} \Big/ \sqrt{\sum_{i=1}^{n_p}(\hat{y}_i - y_m)^2} \quad (5)$$

$$SEC = \sqrt{\frac{1}{n_c - 1}\sum_{i=1}^{n_c}(\hat{y}_i - y_m)^2} \quad (6)$$

$$SEP = \sqrt{\frac{1}{n_p - 1}\sum_{i=1}^{n_p}(\hat{y}_i - y_m)^2} \quad (7)$$

where: $\hat{y}_i$ is the predicted value of the i^{th} kiwifruit sample, y_i is the real value of the i^{th} kiwifruit sample, y_m is the average value of the calibration or prediction set, n_C is the number of samples in the calibration set, and is the number of samples in the prediction set. In general, a good prediction model should have high values n_P of R_C and R_P, low values of SEC and SEP. In present study, the processing and analysis of all data were done by using MATLAB R2013 software (The Mathworks, Inc., USA).

RESULTS AND DISCUSSION

Spectral analysis of sample and SSC real values

The outliers of the samples' spectra and SSC measured values affect the accuracy and robustness of the prediction model. In order to improve the stability and precision of the prediction model, Mahalanobis distance outlier detection algorithm was used to eliminate the outliers of the samples' spectra and SSC measured values *(Christophe et al., 2018)*. Six outlier SSC value samples were determined and removed from 120 samples. The average reflectance spectra in the ROI of the hyperspectral image of the 114 kiwifruit samples are shown in Fig. 4 (a).

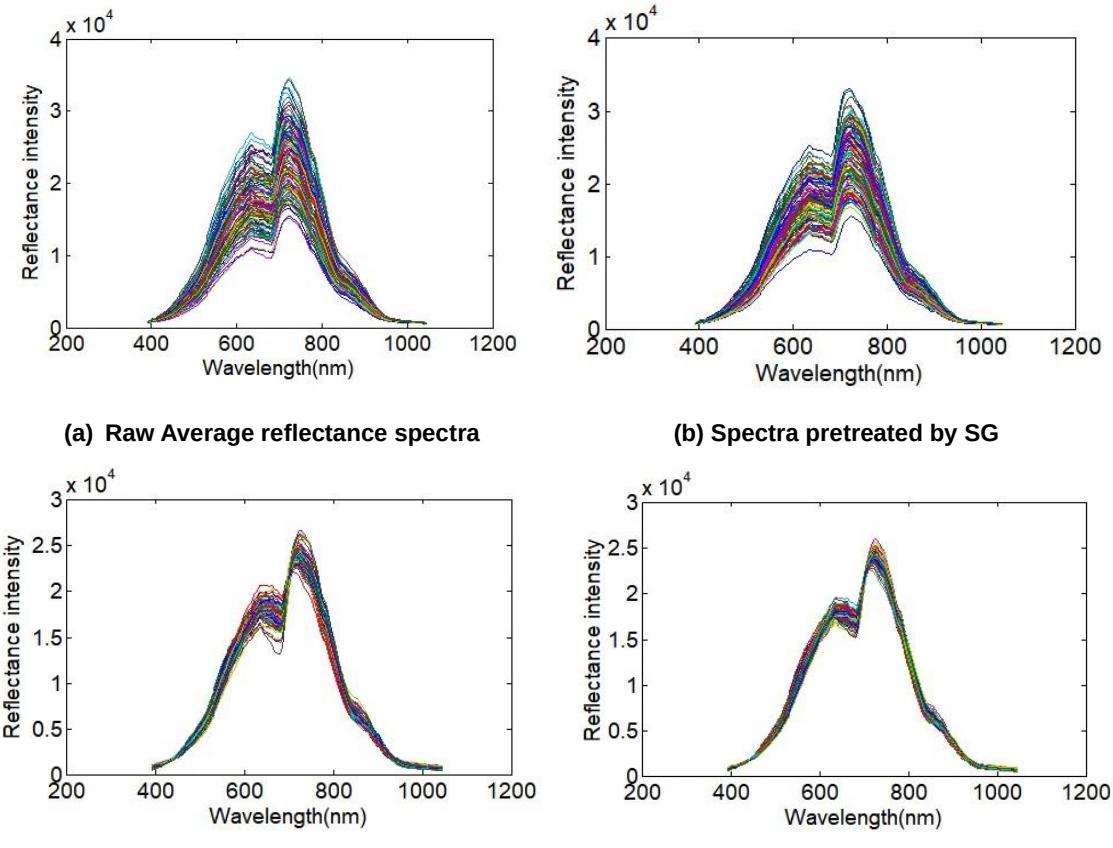

(a) Raw Average reflectance spectra **(b) Spectra pretreated by SG**

(c) Spectra pretreated by MSC **(d) Spectra pretreated by SG+MSC**

Fig. 4 – Raw average reflectance spectra and pretreated spectra of all kiwifruit samples

The reflection spectral curves of the samples had high similarity; the overall trends of the spectral curves were basically the same. Obvious absorption peaks existed at 713, 746, and 870 nm, which were principally due to C–H stretch third overtone and fourth overtone; they were mainly associated with the carbohydrate absorption bands in the kiwifruit *(Hu et al., 2017)*. The average reflection spectra exhibited obvious baseline drift and scattering. Therefore, pretreatment methods of SG, MSC, and SG+MSC were used to pretreat the average reflection spectra. The pretreatment spectra shown in Figs. 4(b) – 4(d) had no baseline drift and scattering.

One hundred and fourteen samples were randomly divided into two sets, namely, the calibration set and the prediction set. The calibration set was used to construct the prediction model, and the prediction set was used to verify the accuracy and robustness of established prediction model. All kiwifruit samples were randomly divided into the calibration set and prediction set according to the ratio of 3:1 by using Kenard-Stone algorithm. The calibration set has 86 kiwifruit samples and the prediction set has 28 kiwifruit samples. Table 1 summarizes the SSC measured values of kiwifruits in the calibration set and the prediction set. Measures of SSC ranged from 8.3 to 13.8 °Bx in the calibration set, and from 7.9 to 13.5 °Bx in the prediction set. The mean values of SSC in the calibration set and the prediction set were 10.5 °Bx and 10.4 °Bx, respectively. The SDs of SSC in the calibration and prediction sets were 1.23, 1.21, respectively. This shows the sample division was reasonable.

Prediction models built using full average reflectance spectrum

Before establishing prediction model, the full average reflectance spectra of samples in calibration and prediction sets were pretreated using the SG, MSC, and SG+MSC methods. Then, they were taken as the input variables to establish the prediction models of kiwifruit SSC. The kiwifruit SSC prediction models of PLSR, MLR, and LS-SVM were built based on the full average reflectance spectra, respectively. Table 2 shows the results of the prediction. The performance of the three prediction models pretreated with SG+MSC was better than that pretreated with SG or MSC only. Therefore, SG+MSC was taken as the pretreatment method for establishing the prediction models. The accuracy of the LS-SVM prediction model was the best in the three prediction models, with R_C = 0.893, SEC = 0.621, R_P = 0.882, and SEP = 0.752. Moreover, the performance of PLSR model was better than that of the MLR model. However, on the whole, the performances of the three prediction models were relatively low. The key reason may be that the full average reflectance spectra contain a lot of redundant, useless wavelength information, thereby reducing the prediction accuracy of the model. Thus, some measures should be taken to eliminate useless wavelength information. Moreover, effective feature wavelength variables should be picked out from the full average reflectance spectra to establish the prediction models and improve their prediction precision.

Prediction models established using effective wavelength variables

In order to optimize and simplify the prediction model and improve the prediction precision, the GA method was used to select the effective feature wavelength variables from the full average reflectance spectra of kiwifruit samples. The selected effective feature wavelength variables by GA were used as input variables to build the PLSR, MLR, and LS-SVM prediction model of SSC. GA parameters were set in term of the number of the spectral domains. The size of population and chromosome of GA was set to 30. Moreover, the probabilities of cross-over and mutation were set to 50% and 1%. The number of run times of GA was set to 100 for every model. At every run time, the initial chromosome population was generated randomly. The GA was randomly run five times to select the effective feature wavelength variables for every prediction model. Fig. 5 shows one of the five times variable selection processes. The wavelengths above the dotted line were selected feature variables by GA.

Overall, the GA-selected variables were mainly concentrated at the wavelengths of 420, 520, 600, 715, 750, and 870 nm. Moreover, the useless information and the number of variables for establishing the prediction model were greatly reduced. Fig. 6 illustrates the distribution of the effective feature wavelength variables picked out by GA at 400–1100 nm. The selected variables were used to establish the GA–PLSR, GA–MLR, and GA–LS-SVM prediction models of SSC. The results of the three different kind prediction models of SSC are shown in table 3. The results prove that the prediction precisions of the models established using the effective feature wavelength variables were better than those of the models established with the full-average reflectance spectra (Table 2).

The prediction accuracies of GA–LS-SVM are the best with R_C = 0.948, SEC = 0.403, R_P = 0.931, and SEP = 0.536 (Fig. 7).

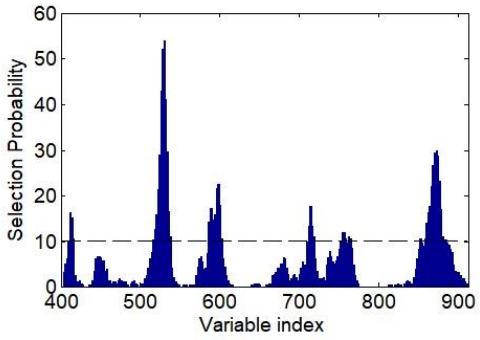

Fig. 5 - Frequencies of the variables selected by GA

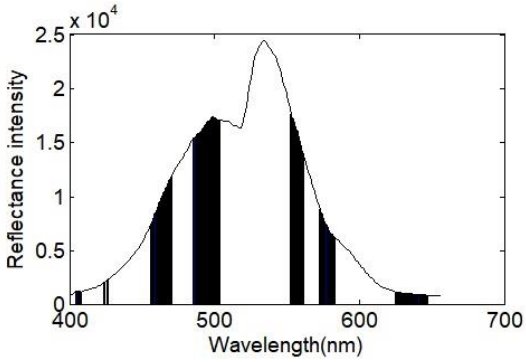

Fig. 6 - Distribution of the GA-selected effective wavelength variables

The prediction accuracy has been improved by 5.6% compared with the LS-SVM model established by using the full-band reflectance spectra. These results also proved that GA is an effective method for extracting effective feature wavelength variables and improving the prediction accuracy of the model.

Table 1

Statistics of the SSC real values

Set	Amount of sample	Maximum	Minimum	Mean	SD
Calibration set	86	13.8	8.3	10.5	1.23
Prediction set	28	13.5	7.9	10.4	1.21

Table 2

Prediction SSC values of different preprocessing methods and models

Preprocessing method	PLSR				MLR				LS-SVM			
	Rc	SEC	Rp	SEP	Rc	SEC	Rp	SEP	Rc	SEC	Rp	SEP
SG	0.846	0.702	0.844	0.783	0.837	0.715	0.834	0.872	0.855	0.662	0.835	0.876
MSC	0.865	0.633	0.822	0.818	0.866	0.675	0.845	0.783	0.877	0.648	0.799	0.920
SG +MSC	0.886	0.602	0.855	0.764	0.872	0.670	0.869	0.736	0.893	0.621	0.882	0.752

Table 3

Prediction results of GA–PLSR, GA–MLR, and GA–LS-SVM models

Run Times	GA–PLSR				GA–MLR				GA–LS-SVM			
	R_c	SEC	R_p	SEP	R_c	SEC	R_p	SEP	R_c	SEC	R_p	SEP
1	0.913	0.488	0.911	0.606	0.905	0.539	0.895	0.641	0.913	0.495	0.890	0.633
2	0.912	0.499	0.912	0.596	0.917	0.498	0.902	0.738	0.919	0.504	0.917	0.566
3	0.925	0.473	0.915	0.565	0.912	0.521	0.892	0.662	0.920	0.515	0.918	0.635
4	0.916	0.485	0.909	0.703	0.906	0.570	0.886	0.715	0.927	0.439	0.911	0.547
5	0.916	0.498	0.914	0.681	0.920	0.505	0.894	0.674	0.948	0.403	0.931	0.536

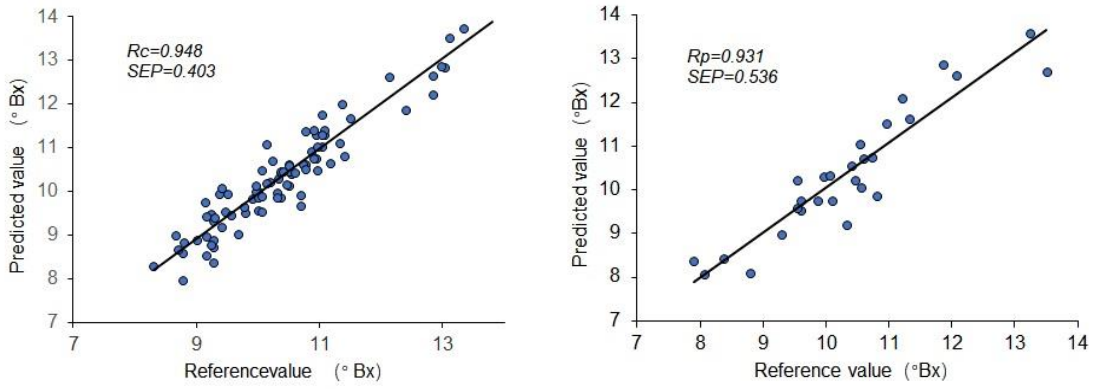

(a) Calibration set **(b) Prediction set**

Fig. 7 - Prediction SSC using GA–LS-SVM model by Vis/NIR hyperspectral imaging

CONCLUSIONS

GA-LS-VM prediction model based on Vis/NIR hyperspectral imaging was successfully utilized for non-destructive detection SSC of kiwifruit. The different preprocessing methods and prediction models were studied. GA was applied to select the effective feature wavelength variables to improve the precision of the prediction model. The conclusions are as follows:

(1) The GA is an effective method for selecting effective feature wavelength variables. The Vis/NIR hyperspectral imaging with GA can non-destructively determine the SSC of kiwifruits.

(2) The SG+MSC is the best pretreatment method among SG, MSC and SG+MSC in improving spectral quality.

(3) The precisions of the prediction models established with the effective feature wavelength variables selected are higher than that established with full wavelength variables. GA-LS-SVM is the best prediction model of kiwifruit SSC among PLSR, MLR, and LS-SVM. It shows a better accuracy with R_C = 0.948, SEC = 0.403 °Bx, R_P = 0.931, and SEP = 0.536 °Bx.

This study offers a non-destructive and rapid method of predicting kiwifruit SSC using Vis/NIR hyperspectral imaging with GA. However, this detection technique also has certain limitations, for example, it may need to construct different prediction models or modify the models for different varieties of fruit. When fruit farmers apply this technology, the prediction results may have errors due to the influence of temperature environment, and the prediction model needs to be constantly revised. In future studies, prediction models for different varieties and different internal quality indicators of kiwifruit should be further established, and detection methods should be further promoted and applied through cooperation with farms and factories.

ACKNOWLEDGEMENT

The authors grateful thank the financial support provided by the Science and Technology Research Project of Henan Province (Project No.222102110262)

REFERENCES

[1] Berardinelli A., Benelli A., Tartagni M., Ragni L. (2019). Kiwifruit flesh firmness determination by a NIR sensitive device and image multivariate data analyses. *Sensors and Actuators A*, 296, 265–271. https://doi.org/10.1016/j.sna.2019.07.027

[2] Chen H. ZH, Pan T., Chen J. M., Lu Q. P. (2011). Waveband selection for NIR spectroscopy analysis of soil organic matter based on SG smoothing and MWPLS methods. *Chemometrics and Intelligent Laboratory Systems*, 107, 139-146. http://dx.doi.org /10.1016/j.chemolab.2011.02.008

[3] Christophe L., Olivier K., Yves D., Christophe L. (2018). Detecting multivariate outliers: Use a robust variant of the Mahalanobis distance. *Journal of Experimental Social Psychology*, 74, 150-156. http://dx.doi.org/10.1016/j.jesp.2017.09.011

[4] Ebrahiema A., Olaniyi A. F., Lembe S. M., Umezuruike L. O. (2018). Non-destructive prediction of internal and external quality attributes of fruit with thick rind: A review. *Journal of Food Engineering*, 217, 11-23. http://dx.doi.org/10.1016/j.jfoodeng.2017.08.009

[5] Eunhee P., Yaguang L., Sasha C. M., Kathryne L. E., Shirley A. M., Samantha B., John S. (2018). Consumer preference and physicochemical evaluation of organically grown melons. *Postharvest Biology and Technology*, 141, 77–85. https://doi.org/10.1016/j.postharvbio.2018.03.001

[6] Hamid G., Golasa M., Hakimeh F. (2012). Spectroscopic studies on Solvatochromism of mixed-chelate copper (II) complexes using MLR technique. *Spectrochimica Acta Part A*, 85, 25-30. http://dx.doi.org /10.1016/j.saa.2011.08.042

[7] Hu W. H., Sun D. W., Jose B. (2017). Rapid monitoring 1-MCP-induced modulation of sugars accumulation in ripening 'Hayward' kiwifruit by Vis/NIR hyperspectral imaging. *Postharvest Biology and Technology*, 125, 168-180. http://dx.doi.org/10.1016/j.postharvbio.2016.11.001

[8] Jiang B., He J. R., Yang SH. Q., Fu H. F., Li T., Song H. B., & He D. J. (2019). Fusion of machine vision technology and AlexNet-CNNs deep learning network for the detection of postharvest apple pesticide residues. *Artificial Intelligence in Agriculture*, 1, 1-8. https://doi.org/10.1016/j.aiia.2019.02.001

[9] Leardi R., & Amparo L. G. (1998). Genetic algorithms applied to feature selection in PLS regression: how and when to use them. *Chemometrics and Intelligent Laboratory Systems*, 41,195-207.

[10] Li J.B., Chen L.P., & Huang W. Q. (2018). Detection of early bruises on peaches (*Amygdalus persica L.*) using hyperspectral imaging coupled with improved watershed segmentation algorithm. *Postharvest Biology and JeanTechnology*, 135, 104–113. http://dx.doi.org/10.1016/j.postharvbio.2017.09.007

[11] Li J. B., Zhang H. L., Zhan B. SH., Wang ZH. L, & Jiang Y. L. (2019). Determination of SSC in pears by establishing the multi-cultivar models based on visible-NIR spectroscopy. *Infrared Physics and Technology*, 102, 103066. https://doi.org/10.1016/j.infrared.2019.103066

[12] Ma SH. B. (2021). Nondestructive Determination of Kiwifruit SSC using Visible/Near-Infrared Spectroscopy with Genetic Algorithm. *Journal of Engineering Science and Technology Review*, 14 (1), 100-106. https://doi.10.25103/jestr.141.11

[13] Ma T., Xia Y., Tetsuya I., & Satoru T. (2021). Non-destructive and fast method of mapping the distribution of the soluble solids content and pH in kiwifruit using object rotation near-infrared hyperspectral imaging approach. *Postharvest Biology and Technology,* 174, 111440. https://doi.org/10.1016/j.postharvbio.2020.111440

[14] Nturambirwe J.F.I., Nieuwoudt H.H., Perold W.J.P., Opara U.L. (2019). Non-destructive measurement of internal quality of apple fruit by a contactless NIR spectrometer with genetic algorithm model optimization. *Scientific African*, 3, e00051. https://doi.org/10.1016/j.sciaf.2019.e00051

[15] Reddy R. Pullanagari, S. R. O., Mo L. & Research O. (2021). Uncertainty assessment for firmness and total soluble solids of sweet cherries using hyperspectral imaging and multivariate statistics. *Journal of Food Engineering,* 289, 110177. https://doi.org/10.1016/j.jfoodeng.2020.110177

[16] Rosalba C., Jose M. A., & Alessandro U. (2017). Transferring results from NIR-hyperspectral to NIR-multispectral imaging systems: A filter-based simulation applied to the classification of Arabica and Robusta green coffee. *Analytica Chimica Acta*, 967, 33-41. http://dx.doi.org/10.1016/j.aca.2017.03.011

[17] Santosh S., Matej K., Uros Z., Lise C. D., & René G. (2016). Single seed near-infrared hyperspectral imaging in determining tomato (Solanum lycopersicum L.) seed quality in association with multivariate data analysis. *Sensors and Actuators B: chemical*, 237, 1027–1034. http://dx.doi.org/10.1016/j.snb.2016.08.170

[18] Tom F., Cecilia R., Ana G., & José E. G. (2009). On the geometry of SNV and MSC. *Chemometrics and Intelligent Laboratory Systems*, 96, 22-26. http://dx.doi.org /10.1016/j.chemolab.2008.11.006

[19] Umer M. J., Lei G., Haileslassie G., Luqman B. S., Pingli Y., Zhao SH. J., Lu X. Q., He N., Zhu H. J., & Liu W. G. (2020). Expression pattern of sugars and organic acids regulatory genes during watermelon fruit development. *Scientia Horticulturae,* 265, 109102. https://doi.org/10.1016/j.scienta.2019.109102

[20] Xu J. C., Ren Q. W., & Shen ZH. ZH. (2015). Prediction of the strength of concrete radiation shielding based on LS-SVM. *Annals of Nuclear Energy*, 85, 296-300. http://dx.doi.org/10.1016/j.anucene.2015.05.030

[21] Xu L. J., Zhang L. N., Huang P., Chen H., & Kang ZH. L. (2020). Detection of kiwifruit dry matter content based on hyperspectral technology using uninformed variable elimination coupled with successive projection algorithm. *DYNA-Ingenieria e Industria,* 95(6), 654-660. https://doi.org/10.6036/9837

[22] Zheng W., Bai Y. H., Luo H., Li Y. H., Yang X., & Zhang B. H. (2020). Self-adaptive models for predicting soluble solid content of blueberries with biological variability by using near-infrared spectroscopy and chemometrics. *Postharvest Biology and Technology*, 169, 111286. https://doi.org/10.1016/j.postharvbio.2020.111286

VEHICLE PATH OPTIMIZATION OF AGRICULTURAL PRODUCTS COLD CHAIN LOGISTICS BASED ON GREEN EVALUATION

/

基于绿色评价的农产品冷链物流车辆路径优化分析

Jinhui YU[1)]*, Lili CHENG[1)]

[1)] Department of Basic Education, Luohe Vocational College of Food, Luohe, Henan, China.

[2)] Department of Food Engineering, Luohe Vocational College of Food, Luohe, Henan, China.

**E-mail: lhspzyxyyjh@163.com*

Corresponding author: Jinhui YU

DOI: https://doi.org/10.35633/inmateh-70-43

Keywords: *AHP-TOPSIS, vehicle evaluation, improved SA algorithm, agricultural product logistics*

ABSTRACT

With the development of the economy and society and the improvement of living standards, the demand for fresh products is increasing, and the huge demand has driven the rapid growth of fresh products in China. However, fresh products are prone to spoilage and wear, and higher transportation requirements are put forward to ensure product quality. Based on this, the transportation function of cold chain logistics vehicles on farm products cold chain logistics greatly improves the cold chain transportation efficiency of agricultural products. Aiming at the vehicle path problem of cold chain logistics distribution and under multiple refrigerated trucks, a single distribution center, and multiple commodity types, a path optimization model of cold chain logistics vehicles was established with the optimal evaluation of total distribution cost and distribution vehicles as the objective considering the economy, greenness, and sustainability of vehicles. Then, an evaluation index system of refrigerated trucks consisting of cost index, environmental index and quality index was established, an AHP-TOPSIS (Analytic Hierarchy Process, Technique for Order Preference by Similarity to an Ideal Solution) evaluation model of refrigerated trucks was constructed, and the comprehensive evaluation value of refrigerated trucks was obtained. On the basis of vehicle evaluation results, the corresponding vehicle path optimization model of agricultural cold chain logistics was established, the large-scale neighborhood search SA algorithm was designed to solve an example, and the optimization model was compared with the optimization model without considering vehicle evaluation. The experimental results show that considering the vehicle evaluation factors can effectively reduce the distribution cost, and increasing the vehicle evaluation weight can effectively improve the greenness and sustainability of the distribution fleet.

摘要

随着经济社会的发展和生活水平的提高，人们对生鲜产品的需求量越来越大，巨大的需求量推动了中国生鲜产品的快速增长。然而生鲜产品具有易腐易损性，为了保证产品的品质对运输提出了更高的要求。基于此，冷链物流车辆对农场品冷链物流的运输作用大大提升了农产品冷链运输效率。针对冷链物流配送的车辆路线问题，在多冷藏车、单配送中心、多商品类型的条件下，考虑车辆的经济性、绿色与可持续性，以配送总成本和配送车辆的最优评价为目标，建立冷链物流车辆路线优化模型，建立由成本指标、环境指标和质量指标组成的冷藏车评价指标体系，构建 AHP-TOPSIS 法的冷藏车评价模型，得到了综合考虑的冷藏车评价值。在车辆评价结果的基础上，建立相应的农业冷链物流车辆路线优化模型，设计改进蚁群算法求解算例，并将优化模型与不考虑车辆评价的优化模型进行比较。实验结果验证，考虑车辆评价因素可以有效降低配送成本，增加车辆评价权重可以有效提高配送车队的绿色和可持续性。

INTRODUCTION

The green and low-carbon transformation of logistics industry is an important bridge and channel for the comprehensive green transformation of industrial chain and supply chain. The International Energy Agency (IEA) released a piece of data—transportation carbon emissions accounted for 26% of global carbon emissions in 2020.

According to the research of Green Logistics Branch of CPAG GROUP, the carbon emission of the logistics industry in China reached 880 million tons in 2020, and the carbon emissions of transportation and distribution activities accounted for about 85% of the carbon emissions of logistics industry in China, where loading/unloading and warehousing activities accounted for about 10% and auxiliary logistics activities for about 5%. It is predicted that the carbon emissions of the logistics industry will continue to show an upward trend in a long time. Thus, the low-carbon development of the logistics industry plays a vital role in the implementation of China's double-carbon (peak carbon and carbon neutral) strategy. With the social and economic development and the improvement of living standards, people's demand for fresh products is increasing, which has promoted the rapid growth of fresh products in China *(He M. et al., 2021)*. Fresh products are perishable and vulnerable, and higher requirements are put forward for transportation in order to ensure the quality of products *(Fan H.M. et al., 2018)*. Cold chain logistics has obvious advantages in ensuring product quality and reducing product loss by effectively controlling the temperature. Cold chain logistics has received more attention and development, and meanwhile, it has also put forward new requirements for cold chain logistics enterprises.

According to the statistics of China Mobile Source Environmental Management Annual Report (2021), by 2020, among the 281 million motor vehicles (automobiles) in China, the traditional fuel vehicles were the main force to carry out the traditional agricultural products cold chain distribution and transportation business with the ultra-high data of 98.25%. The data showed that trucks in China emitted 2.073 million tons of carbon monoxide (CO), 5.178 million tons of nitrogen oxides (NOx), 460,000 tons of hydrocarbons (HC), and 58,000 tons of particulate matter (PM), accounting for 29.8%, 84.3%, 26.6%, and 90.9% of the total automobile emissions *(Chen W.Z. et al., 2020)*. High-carbon emission and greenhouse effect are not conducive to environmental development, which is largely attributed to the use of fuel vehicles in quantity. At the same time, for logistics enterprises, the rising oil price and fuel tax expenditure have further squeezed the industry profits under pressure due to changes in the competitive pattern. Under the dual pressures of environmental protection and industrial upgrading, in recent years, the state is actively introducing policies to develop green logistics and vigorously promoting the application of new energy vehicles represented by electric vehicles in the logistics field *(Chen S. et al., 2018)*. For instance, nine departments like the Ministry of Commerce and the Ministry of Transport jointly issued the "Special Action Plan for High-quality Development of Commercial Logistics (2021-2025)", which required to vigorously promote energy-saving and clean energy transportation tools and logistics equipment and guide logistics distribution enterprises to use new energy vehicles or clean energy vehicles. In addition, by 2021, the target, i.e., the proportion of new energy bus stops for logistics distribution vehicles in the key areas of air pollution prevention and control and the national ecological civilization experimental zones was higher than 80%, was put forward in the "New Energy Automobile Industry Development Plan (2021-2035)" issued by the State Council.

STATE OF THE ART

As an important link in cold chain logistics, the distribution of fresh agricultural products plays a vital role in the path programming of distribution vehicles, so it has been widely studied. The existing literature is mainly based on basic model settings, e.g., a single distribution center, the same refrigerated vehicle, a single product, and each customer is served by only one vehicle, with time window constraints *(Shukla M., 2013; Wu H. et al., 2021; Dorigo M. et al., 2006; Pérez-Rodríguez R. et al., 2019)*. In Literature *(Bauernhansl T., 2016; Chiang W.C. et al., 1996; Li B. et al., 2019)*, a heterogeneous fleet was adopted in the model, and in Literature *(LI Z. et al., 2019)*, the model was solved using a threshold algorithm, but the time window constraint was not considered. In Literature, it was verified that a heterogeneous fleet could effectively reduce the distribution cost and improve the capacity utilization rate of distribution vehicles *(Aggarwal D. et al., 2018)*. In Literature, a green vehicle routing problem model of joint distribution was established, in which cold chain logistics enterprises completed the distribution task by considering carbon tax policy and cooperating with each other. It was found that joint distribution could effectively reduce the total cost and carbon emissions compared with single distribution *(Govindan K. et al., 2014)*. In Literature, the vehicle routing problem under multiple distribution centers was considered, and a semi-open joint distribution mode with multiple distribution centers was proposed and solved by designing the ant colony algorithm *(Nwakaire C.M. et al., 2015)*. The conclusion proves that the distribution process in this mode is better than that in case of a single distribution center.

In Literature, carbon emissions were transformed into costs in the path optimization model of cold chain logistics with multiple distribution centers, and the multi-distribution center model was transformed into a single distribution center model by introducing virtual parking lots and solved using an improved genetic algorithm *(Ellabib I. et al., 2007)*. Energy conservation and emission reduction have become a global consensus, and low-carbon technology and low-carbon economy have attracted widespread attention around the world *(Han X. et al., 2019)*. As a major consumer of fuel and carbon emissions, logistics industry, especially cold chain logistics, needs to consume more energy to ensure the quality of products compared with normal temperature logistics *(Zhou X. et al., 2011)*. The environment is more prominently affected by the high energy consumption and high carbon emission characteristics of cold chain logistics, so it is very important to reduce the energy consumption of cold chain logistics and realize green and sustainable development *(Cordeau J-F. et al., 2001)*. With the development of the automobile industry and the response to the low-carbon policy in recent years, in addition to the traditional diesel fuel refrigerated trucks, pure electric refrigerated trucks and refrigerated trucks using mixed fuels, biodiesel, and natural gas have also developed rapidly and are widely used in the cold chain transportation of fresh products.

In cold chain transportation, logistics companies need to make decisions over the use of different vehicle types, and vehicle evaluation mainly provides valuable information for vehicle selection. Vehicle evaluation mainly refers to the establishment of a relevant evaluation system, and the quantitative ranking calculation of vehicle performance and vehicle transportation process indexes by using some evaluation methods. Based on the basic characteristics of green design, in Literature, a comprehensive evaluation system was established for the green design of construction vehicles and the ideas for the green evaluation of engineering vehicles were provided *(Shaw P., 1998)*. In Literature, the drivers' psychological and physiological loads during driving were considered, and the comfort and safety of vehicles were evaluated through heart rate variability *(Mohammed M.A. et al., 2017)*. In Literature, the fuzzy analytic hierarchy process (AHP) was adopted to comprehensively evaluate the performance of armored vehicles *(Venkata N.K. et al., 2013)*.

In Literature, an evaluation index system composed of five aspects—trafficability, dynamic performance, operability, safety, and economy—was established, the TOPSIS method was applied to evaluate the scheme and make fuzzy operation, and the evaluation result of large transport vehicles were acquired *(Liu H. et al., 2014)*.

Through the recent literature research on vehicle path optimization and vehicle evaluation of agricultural cold chain logistics, it is found that vehicle system evaluation has been involved in few literature documents, and the vehicle path optimization of agricultural cold chain logistics is mainly based on a single distribution center and a single vehicle type. In this paper, the economy and sustainability of vehicles were comprehensively considered, and a green vehicle routing problem model with multiple vehicles and commodity types was established under the background of cold chain logistics. Firstly, the vehicle evaluation was performed using the AHP-TOPSIS method, and an evaluation index system of vehicles was constructed from three dimensions, namely, environmental index, cost index, and quality index. Given the vague judgment on complex things, the qualitative evaluation results were quantified by triangular fuzzy numbers, and the comprehensive evaluation model of vehicles was established by combining AHP and TOPSIS methods. The vehicle evaluation value and the total distribution cost were obtained to constitute the objective and establish a model, which was then solved by designing an improved simulated annealing (SA) algorithm. Finally, the effectiveness and feasibility of the models and algorithms established in this paper were verified through a practical example, providing methodological guidance and decision-making support for the distribution process and management.

MATERIALS AND METHODS

In this paper, the vehicle routing problem of a single agricultural products cold chain logistics distribution center with soft time window constraint and capacity restriction was explored. In the model, different types of refrigerated vehicles completed the distribution work of a variety of commodities using the distribution strategy of split delivery. The vehicle distribution route that may exist in multiple distribution centers under the split delivery mode is shown in Fig. 1.

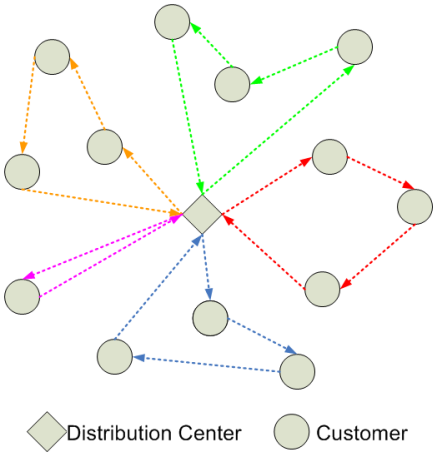

Fig. 1 - Vehicle path network model of agricultural products

The assumptions of the vehicle path optimization model of agricultural products cold chain logistics are as follows:

(1) There is one distribution center, multiple refrigerated vehicles for transportation, and multiple customers in the model.

(2) The distribution center has different quantities and models of refrigerated vehicles, each of which has a certain capacity limit.

(3) The geographical locations of the distribution center and customers are known, the demand of customers is fixed and known, and the distribution center has no demand.

(4) In all distribution processes, the starting point must be the agricultural product distribution center, and the distribution process must end with completing the agricultural product distribution task and returning to the agricultural product distribution center.

(5) Each customer has its own prescribed time window and acceptable time window, and each customer is served by at least one vehicle.

(6) Agricultural products are divided into many types, the storage and transportation temperature conditions of each agricultural product are the same, and the distribution mode of split delivery is adopted.

Mathematical Model

To transform the constrained optimization problem into the unconstrained optimization problem, the penalty function method was used in this paper. A penalty cost was added to this relaxation mechanism, and the solutions violating the capacity and time window constraints were accepted by means of penalty, so as to enhance the diversity of solutions *(LI Z. et al., 2019)*. The penalty coefficient for violating the time window constraint could be set according to the compensation mechanism formulated by the enterprise. Because it was not allowed to violate the capacity constraint in the actual transportation process, the penalty coefficient for violating the capacity constraint should be as large as possible. The sets, parameters, and variables are defined as follows:

Sets: N is a customer set, N={1, 2, 3, ..., n}; V is a node set, $V=\{0\}\cup N$, and 0 represents the distribution center; M is a vehicle set $M=\{1,2,3,...,k\}$.

Parameters: Q is the maximum loading capacity of the vehicle $k(k\in M)$; c_k denotes the fixed cost of each vehicle; c_{ij} is the driving cost generated by a unit distance; q_i is the cargo quantity demanded by the customer $i(i\in N)$; d_{ij} is the Euclidean distance between nodes i and j $(j\in N)$; v is the vehicle velocity; e_i is the earliest service time designated by the customer $i(i\in N)$; l_i is the latest service time designated by the customer i; e_0 and l_0 are the earliest opening time and deadline of the distribution center, respectively; S_i is the service time needed by the customer $i(i\in N)$; α $(\alpha\in N^+)$ represents the penalty coefficient of violating the capacity constraint; $\beta(\beta\in N^+)$ is the penalty coefficient of violating the time window constraint.

Decision variables: x_{ij}^k is the driving variable of the vehicle k, $x_{ij}^k=1$ if the vehicle k drives from the node i to the node j, otherwise, $x_{ij}^k=0$; t_{ki} is the arrival time of the vehicle k at the node i; t_i is the starting service time for the node i; w_{ik} is the waiting time for the vehicle k earlier than e_i; l_{ik} is the delay time of the

vehicle k later than l_i; q is the sum of the exceeding part of the total demand of each path from the maximum vehicle load in the solution, $q=\sum_{k=1}^{K}\max\{0,(\sum_{i=1}^{n}q_i x_{jk}-Q)\}\ \ (\forall k\in M,\forall i\in N)$; w is the sum of the delayed part of vehicle arrival time from the latest service time in the solution, $w=\sum_{k=1}^{K}l_{ik}(\forall k\in M,i\in V)$.

$$f=c_k\sum_{j=1}^{n}\sum_{k=1}^{K}x_{0j}^{k}+c_{ij}\sum_{i=0}^{n}\sum_{j=0,j\neq i}^{n}\sum_{k=1}^{K}d_{ij}x_{ij}^{k}+\alpha q+\beta_W \tag{1}$$

$$s.t. \tag{2}$$

$$\sum_{j=1}^{n}x_{ij}^{k}=\sum_{i=1}^{n}x_{i0}^{k}\left(\forall k\in M\right)$$

$$\sum_{k=1}^{K}\sum_{j=1,j\neq i}^{n}x_{ij}^{k}=1,\left(\forall i\in V\right) \tag{3}$$

$$\sum_{i=0,i\neq j}^{n}\sum_{j=0}^{n}x_{ij}^{k}\leq 1,(\forall k\in M) \tag{4}$$

$$t_{ij}=\frac{d_{ij}}{v},\left(\forall i,j\in V,i\neq j\right) \tag{5}$$

$$t_i=t_{ik}+w_{ik},(\forall i\in N,\forall k\in M) \tag{6}$$

$$t_{0k}=e_0,\left(\forall k\in M\right) \tag{7}$$

$$w_{ik}=max\{0,(e_i-t_{ik})\},\left(\forall i\in N,\quad \forall k\in M\right) \tag{8}$$

$$l_{ik}=max\{0,(l_i-t_{ik})\},(\forall i\in N,\forall k\in M) \tag{9}$$

$$\sum_{i=1}^{n}q_i x_{ij}^{k}\leq Q,\left(\forall j\in V,i\neq j,\forall k\in M\right) \tag{10}$$

$$l_{0k}=max\{0,\sum_{j=0}^{n}\sum_{i=0,j\neq j}^{n}x_{ij}^{k}(t_i+s_i+t_i j)-l_0)\},\left(\forall k\in M\right) \tag{11}$$

where in Formula (1) is an objective function; Constraint (2) ensures that each vehicle leaves and returns to the distribution center only once; Constraints (3) and (4) ensure that each customer is served by one vehicle only once; Constraint (5) represents the travel time from node i to node j; Constraint (6) indicates the starting service time of the node; Constraint (7) ensures that each vehicle starts service within the opening hours of the distribution center; Constraint (8) represents the waiting time of each vehicle at the node; Constraint (9) represents the delay time of each vehicle at the node; Constraint (10) indicates that the total demand of customer points served by each vehicle cannot exceed the maximum carrying capacity of the vehicle; Constraint (11) indicates the delay time of the vehicle in the distribution center after completing the service.

Vehicle Evaluation Model Based on AHP-TOPSIS

A model integrating TOPSIS and AHP was used to construct an evaluation index system of agricultural product distribution vehicles, and the weight of each index was determined. Refrigerated vehicles were evaluated based on the AHP-TOPSIS method, and the evaluation results were incorporated into the multi-center vehicle path optimization model of cold chain logistics.

In this paper, 6 types of refrigerated vehicles commonly used in distribution centers, namely electric refrigerated trucks, mixed fuel refrigerated trucks, gasoline refrigerated trucks, diesel refrigerated trucks, biodiesel refrigerated trucks, and natural gas refrigerated trucks, were used for the distribution center. The greenness, sustainability, and economy of vehicles were comprehensively considered when evaluating refrigerated vehicles, and a vehicle evaluation index system as seen in Table 1 was established.

Table 1

Vehicle evaluation index system

Objective layer	Level-II indexes	Symbol	Level-III indexes	Symbol
Vehicle evaluation	Cost index	C1	Vehicle cost	C11
			Fuel cost	C12
			Maintenance cost	C13
	Environmental index	C2	Carbon emission	C21
			Vehicle life	C22
			Noise	C23
			Fuel efficiency	C24
			Fuel availability	C25
	Quality index	C3	Safety	C31
			Comfort	C32
			Dynamic performance	C33

The system consists of three dimensions: cost, environment, and quality. In the process of vehicle evaluation, the economy of the vehicle should be considered first, that is, the operating cost of the vehicle, which mainly includes fuel cost, vehicle cost, and maintenance cost. Secondly, the green and sustainability of the vehicle are taken into account. The greenness of the vehicle is mainly reflected in its fuel emission and fuel efficiency. The fuel emission mainly refers to the impact of carbon dioxide and other gases emitted by the vehicle on the environment. The higher the fuel efficiency, the greener the fuel vehicle. Indexes related to vehicle sustainability include vehicle life and fuel availability, in which fuel availability refers to the availability of fuel; meanwhile, the noise pollution of vehicles during operation is considered. Finally, the quality of the vehicle mainly includes the safety and comfort of the vehicle during driving. The safety is evaluated mainly based on the accident rate of the vehicle. The lower the accident rate of the vehicle, the higher the safety. Comfort is evaluated mainly based on the criteria of improving the driving performance and operating performance.

In the establishment of the model, the objective layer, criterion layer, and measure layer are usually used as the hierarchical structure of the AHP method. Firstly, the judgment matrix can be easily constructed according to the hierarchical structure. Each factor with a downward membership (called criterion) is the first factor of the judgment matrix (located in the upper left corner), and the factors subordinate to it are arranged in the first row and the first column in turn, as shown in Formula (12).

$$A=(a_{ij})=\begin{bmatrix} a_{11} & a_{12} & \cdots & a_{1n} \\ a_{21} & a_{22} & \cdots & a_{2n} \\ \vdots & \vdots & \vdots & \vdots \\ a_{i1} & \cdots & a_{ij} & \cdots \\ \vdots & \vdots & \vdots & \vdots \\ a_{n1} & a_{n2} & \cdots & a_{nn} \end{bmatrix} \tag{12}$$

In Formula (12), n refers to the number of factors in the present layer, which are related to one criterion in the previous layer, and a_{ij} indicates the fuzzy scale. Then, the factors in each row of matrix A are continuously multiplied, and an n-order root is extracted, as shown in Formula (13).

$$w_i^*=\sqrt[n]{\prod_{j=1}^{n} a_{ij}}, i=1,2,\cdots,n \tag{13}$$

The weight w_i is solved as per Formula (14).

$$w_i=\frac{w_i^*}{\sum_{i=1}^{n} w_i^*}, i=1,2,\cdots,n \tag{14}$$

Afterward, the indexes in each column of matrix A are summed, as seen in Formula (15).

$$S_j = \sum_{i=1}^{n} a_{ij}, j = 1,2,\cdots,n \tag{15}$$

Then, λ_{max} is solved as seen in Formula (16).

$$\lambda_{max} = \sum_{i=1}^{n} w_i s_i \tag{16}$$

The eigenvalue of the judgment matrix A is solved to get the eigenvector W, which becomes the ranking weight of the attribute after normalization. To avoid weight errors and make the result of judgment matrix more realistic, a consistency test is needed. The specific formula for the consistency index is shown in Formula (17).

$$CI = {}^{\lambda_{max} - n}\!\!\diagup\!\!_{n-1} \tag{17}$$

In Formula (17), n is the order of judgment matrix A. Table 2 presents the average random consistency index (CI) value of 1-9-order judgment matrices.

Table 2

Average random consistency index of 1-9-order judgment matrices

Matrix order	1	2	3	4	5	6	7	8	9
CI	0	0	0.52	0.89	1.12	1.26	1.36	1.41	1.46

The TOPSIS method is a method of ranking schemes by taking the “ideal solution” and “negative ideal solution” of multi-objective decision-making problems as standards, which is called the integrated distance evaluation method. The “ideal solution” is an optimal solution envisaged in the standardized original data matrix, while the “negative ideal solution” is the worst scheme. The relative closeness between the best and worst schemes is calculated to rank the evaluation results. The TOPSIS method removes the dimensional effect of different indexes by normalizing and co-trending the original data, which can objectively reflect the real gap between schemes. Firstly, m objectives (finite objectives) and n attributes are set, the evaluation value given by an expert to the attribute j of the objective i is x_{ij}, and then the initial judgment matrix V is:

$$V = \begin{bmatrix} x_{11} & x_{12} & \cdots & x_{1n} \\ x_{21} & x_{22} & \cdots & x_{2n} \\ \vdots & \vdots & \vdots & \vdots \\ x_{i1} & \cdots & x_{ij} & \cdots \\ \vdots & \vdots & \vdots & \vdots \\ x_{m1} & x_{m2} & \cdots & x_{mn} \end{bmatrix} \tag{18}$$

However, because the dimensions may vary from index to index, it is necessary to normalize the initial judgment matrix V to obtain the judgment matrix V' and get the Formula (19).

$$V' = \begin{bmatrix} x'_{11} & x'_{12} & \cdots & x'_{1n} \\ x'_{21} & x'_{22} & \cdots & x'_{2n} \\ \vdots & \vdots & \vdots & \vdots \\ x'_{i1} & \cdots & x'_{ij} & \cdots \\ \vdots & \vdots & \vdots & \vdots \\ x'_{m1} & x'_{m2} & \cdots & x'_{mn} \end{bmatrix} \tag{19}$$

In Formula (19),

$$x'_{ij} = x_{ij} \Big/ \sqrt{\sum_{k=1}^{n} x_{ij}^2}, i = 1,2,\cdots,m; j = 1,2,\cdots,n \tag{20}$$

Then, the information weight matrix B of the expert group for attributes is acquired through the AHP method to form the weighted judgment matrix Z, as seen in Formula (21).

$$Z = V^{'}B = \begin{bmatrix} x_{11}^{'} & x_{12}^{'} & \cdots & x_{1n}^{'} \\ x_{21}^{'} & x_{22}^{'} & \cdots & x_{2n}^{'} \\ \vdots & \vdots & \vdots & \vdots \\ x_{i1}^{'} & \cdots & x_{ij}^{'} & \cdots \\ \vdots & \vdots & \vdots & \vdots \\ x_{m1}^{'} & x_{m2}^{'} & \cdots & x_{mn}^{'} \end{bmatrix} \begin{bmatrix} w_{11} & w_{12} & \cdots & w_{1n} \\ w_{21} & w_{22} & \cdots & w_{2n} \\ \vdots & \vdots & \vdots & \vdots \\ w_{i1} & \cdots & w_{ij} & \cdots \\ \vdots & \vdots & \vdots & \vdots \\ w_{m1} & w_{m2} & \cdots & w_{mn} \end{bmatrix} = \begin{bmatrix} f_{11} & f_{12} & \cdots & f_{1n} \\ f_{21} & f_{22} & \cdots & f_{2n} \\ \vdots & \vdots & \vdots & \vdots \\ f_{i1} & \cdots & f_{ij} & \cdots \\ \vdots & \vdots & \vdots & \vdots \\ f_{m1} & f_{m2} & \cdots & f_{mn} \end{bmatrix} \quad (21)$$

The positive ideal solution f^*_j and negative ideal solution $f^{'}_j$ of the evaluation objective are obtained as per the weighted judgment matrix, as seen in Formula (22).

$$\begin{aligned} f_j^* &= \begin{cases} max(f_{ij}), j \in J^* \\ min(f_{ij}), j \in J^{'} \end{cases}, j = 1,2,...,n \\ f_j^{'} &= \begin{cases} min(f_{ij}), j \in J^* \\ max(f_{ij}), j \in J^{'} \end{cases}, j = 1,2,...,n \end{aligned} \quad (22)$$

In Formula (22), J^* is a benefit-type index and J' is a cost-type index. The Euclidean distance between each objective value and ideal value is solved as seen in Formula (23).

$$\begin{aligned} S_i^* &= \sqrt{\sum_{j=1}^{m}(f_{ij} - f_j^*)^2}, j = 1,2,...,n \\ S_i^{'} &= \sqrt{\sum_{j=1}^{m}(f_{ij} - f_j^{'})^2}, j = 1,2,...,n \end{aligned} \quad (23)$$

Finally, the relative closeness C_i^* of each objective is calculated as seen in Formula (24).

$$C_i^* = \frac{S_i^{'}}{S_i^* + S_i^{'}}, i = 1,2,...,m \quad (24)$$

The objectives are ranked based on the relative closeness C_i^* to form a decision-making basis.

Algorithm Design

In this paper, the large-scale neighborhood SA algorithm was implemented starting from a higher temperature. In the current neighborhood, the bi-directional random search technology based on probability was used, and a better solution in the neighborhood was guaranteed by the Metropolis sampling stability criterion. If the calculated optimal solution was not better than this solution, the random solution would continue to be generated in the neighborhood in the next cycle after annealing. On the other hand, the next larger neighborhood was calculated, and it was repeated with the continuous decrease of temperature until the termination criterion was met. The basic steps of the SAVN algorithm are as follows:

(1) The initial temperature t_0 is determined, and the current temperature is set to $t=t_0$; the neighborhood structure is represented by the set $\{N_k, k = 1, 2, \ldots, k_{max}\}$, and k=1 is set; an initial solution S_0 is generated; the current solution is set to $S=S_0$ and the historical optimal solution to $S_b=S_0$. (2) Whether the scheme reaches the algorithm termination criterion is judged, if yes, turn to (8), otherwise, the current optimal solution is set to $S_c=S$, and turn to (3). (3) Whether the sampling stability criterion is satisfied if judged, if yes, turn to (6), otherwise, a new solution S^* is randomly generated in the k-th neighborhood structure of S, $s^* \in N_k(s)$, and turn to (5). (4) If $min\{1, exp[-(f(s^*)-f(s))/t]\} \geq randrom[0,1]$, $S=S^*$ is set, and turn to (5), otherwise, turn to (3). (5) If $f(s)<f(S_c)$, $S_c=S$ is set, and turn to (3); otherwise, sc is unchanged, and turn to (3). If $f(s)<f(S_b)$, $S_b=S_c$ is set, and turn to (7); otherwise, $k=(k \bmod k_{max})+1$, and turn to (6). (6) Annealing is performed, $t=update(t)$ is set, and turn to (2). (7) The current optimal solution is output.

Before applying the meta-heuristic algorithm, a high-quality feasible solution can be searched using a small-scale heuristic algorithm as the initial solution of the meta-heuristic algorithm. In this paper, the basic steps of the Push-Forward Insertion Heuristic (PFIH) algorithm are described as follows:

(1) k=0 is set, an empty path is newly built, and k=k+1. According to the cost function of seed customers (Formula 16), a customer with the minimum cost is chosen as the seed from all the undistributed customers and inserted into the current path k.

(2) In the presence of any undistributed customer, turn to (3), otherwise, the algorithm is terminated.

(3) If an undistributed customer has feasible insertion points in the current path k, its insertion cost is calculated as per the insertion cost function (Formula 17), the undistributed customer with the minimum insertion cost is selected and inserted into the current path k, and turn to (2); otherwise, any undistributed customer fails to find any feasible insertion point in the current path, and turn to (1).

For the customer i to be inserted into an empty path, the cost function of the seed customer is set as follows:

$$c_i^{(1)} = -\alpha t_{0i} + \beta l_i + \gamma\left(\frac{|p_i - p_j|}{2\pi} \times t_{0i}\right) \tag{25}$$

Where p_i is the polar angle of the customer i relative to the station; p_j denotes the polar angle of the last served customer j on the previous vehicle path relative to the station; t_{ij} is the running time of the vehicle k on the path (i,j); l_i stands for the latest service starting time of the customer i. Generally, the three weight factors are set to $\alpha = 0.7, \beta = 0.2, \gamma = 0.1$.

For the customer w to be inserted into the arc (i,j), the insertion cost function consists of four parts: additional path cost, service cost, waiting cost, and subsequent waiting cost variation, as shown in Formula (26):

$$c_i^{(2)} = \left(c_{iw} + c_{uj} - c_{ij}\right) + c_{wait} \times wt_i + c_{serne} \times st_i + c_{wait} \times \sum_{\sigma \in V_j} \left(wt_\sigma^* - wt_\sigma\right) \tag{26}$$

Where c_{ij} is the cost of the path on the arc (i,j); w_t is waiting time; S_t stands for service time; V_j is the set of customer nodes on the current path j and those after j; w^*_t is the new waiting time of subsequent customer nodes after new customers are inserted.

The initial solution obtained by the above method is feasible, but the SAVN algorithm allows the existence of infeasible solutions, which endows the algorithm with a wider search space and increases the possibility of finding a better solution. When setting the objective function, the algorithm increases the penalty value of time window violation, and the penalty value gradually increases with the decrease of temperature, so the algorithm will gradually converge to the feasible solution in the subsequent iteration process.

STASA algorithm replaces the greedy criterion of the state transition algorithm with the Metropolis criterion of the SA algorithm, which can avoid falling into a local optimum and premature convergence very well *(AGGARWAL D. et al., 2018)*. The STASA algorithm can successfully solve combined optimization problems such as the traveling salesman problem and multi-traveling salesman problem. The unified form of the STASA algorithm is as shown in Formula (27):

$$\begin{cases} x_{k+1} = A_k x_k + B_k u_k \\ y_{k+1} = f(x_{k+1}) \end{cases} \tag{27}$$

where $x_k, x_{k+1} \in R^n$ is the new candidate solution generated by the current solution and transform; $A^k, B^k \in R^n$ is a transform operator; $u_k \in R^n$ is the expression of the objective function; $f()$ stands for the objective function. There are three discrete transform operators in the STASA algorithm: exchange, translation, and symmetry, and the calculation formulas are shown in (28)-(30), respectively.

$$x_{k+1} = A_k^{swap}(m_a)x_k \tag{28}$$

$$x_{k+1} = A_k^{shift}(m_b)x_k \tag{29}$$

$$x_{k+1} = A_k^{sym}(m_c)x_k \tag{30}$$

The updating strategy of solutions: During the search process based on the Metropolis criterion, if the new solution is better than the current solution, the new solution is accepted, otherwise, the new solution is accepted at a probability of $P = e^{-(f(x_{k+1}) - f(x_k))/T} \geq \eta$, where $\eta \in [0,1]$. With the reduction of temperature $t = t * \gamma$, the probability tends to be 0, and the algorithm gradually reach convergence.

In this paper, the relocation operation was implemented by combining the relocation operator, the generalized exchange operator, and the correlation removal operator and farthest insertion heuristic method

in LNS, and the global optimal solution of each iteration was locally searched. Correlation removal operator: One customer is randomly chosen from removed customer points, and the correlation between this customer point and customer points in the distribution scheme is calculated. Distribution schemes are ranked in a descending order according to the correlation, the customer point ranked at $\lceil rand^{D} * nip \rceil$ is removed, $rand \in [0,1]$, and nip is the number of customer points in the distribution scheme. The random factor D can work in a considerably large scope, and the solving effect is favorable. The correlation is calculated via $R(i,j) = \frac{1}{C_y + V_y}$, $C_{ij} = \frac{d_{ij}}{*max\{d_{i1}, d_{i2}, ..., d_{in}\}}$, and d_{ij} is the running distance. If the customers i and j are served by the same vehicle, V_{ij}=1, otherwise, V_{ij}=0.

The farthest insertion heuristic method is adopted to perform the reinsertion operation and find the customer point with the priority to be reinserted and its optimal insertion point.

RESULTS

In the experiment, the Solomon criterion was selected as a CVRPSTW test example to verify whether the algorithm worked. According to the difference between time window and vehicle capacity, the Solomon criterion was divided into series 1(C1, R1, RC1) and series 2(C2, R2, RC2) test example sets. Series 1 had a smaller vehicle capacity and a narrower customer time window, while Series 2 had a larger vehicle capacity and a wider time window, and one vehicle could serve more customers.

Vehicle Evaluation Based on AHP-TOPSIS

Refrigerated vehicles were evaluated based on the established AHP-TOPSIS model, and 4 experts from the field of transportation and logistics were invited to form an evaluation group.

After the original data of AHP was obtained, Matlab2014b was used for programming, and the RI value was 0.520 by looking up the table, so the calculated CR values were 0.009 and 0.000, both of which were less than 0.1. The CI value calculated by the fourth-order judgment matrix was 0.048, and the RI value was 0.890 by looking up the table, so the calculated CR value was 0.054<0.1, that is, the judgment matrix of this paper met the consistency test, and the calculated weights were consistent. The calculated AHP results are listed in Table 3.

Table 3

Weight calculation results of AHP

Objective layer	Level-II index	Symbol	AHP weight	Level-III index	Symbol	AHP weight	Weight
Vehicle evaluation	Cost index	C1	0.2302	Vehicle cost	C11	0.3868	0.0891
				Fuel cost	C12	0.3214	0.0740
				Maintenance cost	C13	0.2918	0.0672
	Environmental index	C2	0.4868	Carbon emission	C21	0.2737	0.1333
				Vehicle life	C22	0.1294	0.0630
				Noise	C23	0.2439	0.1188
				Fuel efficiency	C24	0.1875	0.0913
				Fuel availability	C25	0.1655	0.0806
	Quality index	C3	0.2828	Safety	C31	0.2737	0.0774
				Comfort	C32	0.1294	0.0366
				Dynamic performance	C33	0.2439	0.0690

The TOPSIS method ranks the evaluation objects according to the distance from the positive and negative ideal solutions, so as to evaluate the relative advantages and disadvantages. First, the evaluation indexes are determined and ensured to keep a forward trend (the greater the value, the better), and the results in Table 4 are calculated.

Table 4

Positive ideal solution and negative ideal solution

Item	Positive ideal solution A	Negative ideal solution A-
C11	0.102	0.083
C12	0.111	0.011
C13	0.025	0.01
C21	0.333	0.1
C22	15	15
C23	0.05	0.01
C24	1	0.78
C25	1	0.8
C31	1	1
C32	1	0.8
C33	1	0.8

The positive and negative ideal solutions in Table 4 are intermediate process values when calculating the positive and negative distances (D+ and D-), and their significance is relatively small. The positive ideal solution A+ represents the maximum value of the evaluation index; the negative ideal solution A- denotes the minimum value of the evaluation index.

Table 5

TOPSIS evaluation and calculation results

Item	Positive ideal solution D	Negative ideal solution D-	Relative closeness C	Ranking result
Diesel refrigerated vehicle	0.125	0.067	0.348	3
Gasoline refrigerated vehicle	0.109	0.075	0.407	2
Electric refrigerated vehicle	0.006	0.149	0.962	1
Biodiesel refrigerated vehicle	0.142	0.016	0.099	6
Mixed fuel refrigerated vehicle	0.12	0.04	0.249	5
Natural gas refrigerated vehicle	0.109	0.054	0.331	4

The evaluation indexes of various vehicles were ranked based on AHP, and then the results obtained by the AHP-TOPSIS method are shown in Table 5. The evaluation values of such vehicles were ranked as electric refrigerator > gasoline refrigerator > diesel refrigerated vehicle > natural gas refrigerated vehicle> mixed fuel refrigerated vehicle > biodiesel refrigerated vehicle. The evaluation results of vehicles were taken into account in the multi-center vehicle path optimization model of cold chain logistics to ensure that vehicles with higher evaluation values were given the priority and the quality of the distribution fleet was guaranteed.

Experiment and Comparative Analysis

The evaluation results were multiplied with normal numbers to form the weight of vehicle evaluation, which was then considered into the objective function of the optimization model. By changing the weight of vehicle evaluation, the value of the objective function changed significantly. The greater the weight of vehicle evaluation, the better the greenness and sustainability of the distribution fleet. In this paper, an example in the Solomon Benchmark test set was used to test the algorithm. The examples in the Solomon Benchmark test set could be divided into six categories according to the node position relationship and time scheduling level: R1, R2, C1, C2, RC1, and RC2, and the customer scale of each example was 100. Among them, the node positions in R1 and R2 were randomly generated, and an example R101 with a scale of 100 customers was adopted in this paper.

The fixed cost of vehicles is $P_k = 100$ and the maximum carrying capacity is q_k =4 tons; the path cost of the vehicle k on the arc (i, j) in the time period τ is $c_{ijk}(\tau) = c_{trans} \times distance_{ij}$, where $T0 = 500$, $r = 0.997$, $Ts = 1$, $\text{iter} = 300$, and $\text{maxIterate} = 2100$; Without considering the road congestion, it is assumed that the vehicle is driving at a constant speed of 50 km /h, the average price of agricultural products is 6 yuan /kg, the refrigeration cost of unit product per unit time is 0.5 yuan/(h·kg), the corruption rate during transportation is 0.002, the corruption rate during loading and unloading is 0.003, the penalty coefficient for vehicles arriving

in advance is 20 yuan /h, the penalty coefficient for vehicles arriving late is 30 yuan /h, the service time of each customer is 15 min, and the number of vehicles in the distribution fleet is restricted to 10.

In this paper, the large-scale neighborhood search SA algorithm was used to solve the vehicle path optimization model of agricultural products cold chain, and the maximum number of iterations was set to 2100. A satisfactory solution could be obtained by solving the model, that is, 4 electric refrigerated trucks were needed to complete the agricultural product distribution task, and the total cost was 1548.94 yuan.

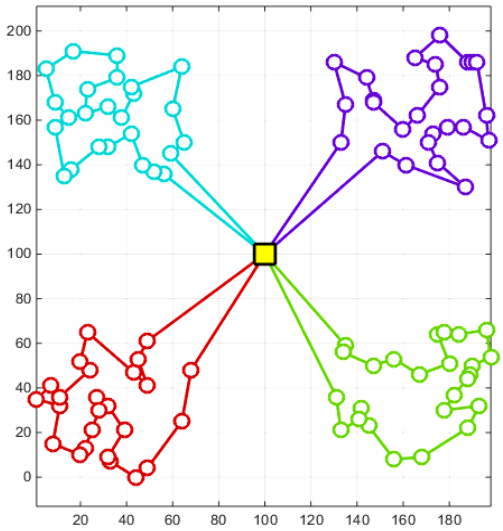

Fig. 2 - Path diagram of the large-scale neighborhood search SA algorithm

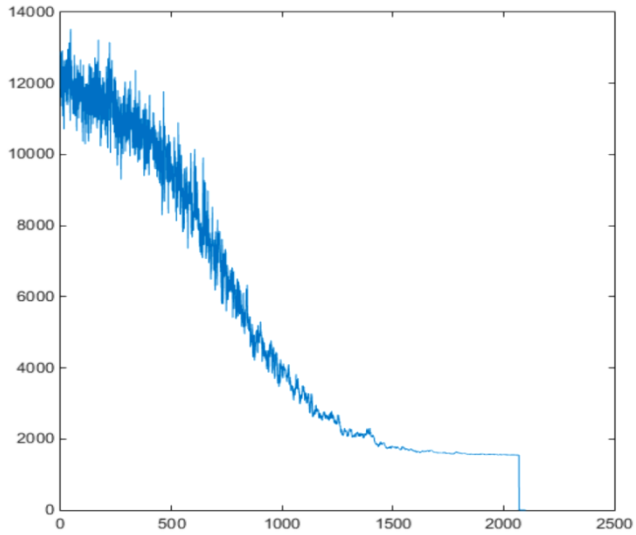

Fig. 3 - Convergence curve of the large-scale neighborhood search SA algorithm

The algorithm spent 413.81 seconds. The path diagram of the large-scale neighborhood search SA method is shown in Fig. 2. The convergence curve of the large-scale neighborhood search SA algorithm is shown in Fig. 3, and the calculation results are listed in Table 3.

To further verify the effectiveness of the large-scale neighborhood search SA algorithm, the model was also solved by designing the traditional SA algorithm in this paper. Under unchanged initial cost and parameters, a total of 5 electric refrigerated vehicles were needed to solve the path optimization model, with a total cost of 1688.6455 yuan and time consumption of 574.48 s. Fig. 4 is the path diagram of the traditional SA algorithm and Fig. 5 displays the convergence curve of the traditional SA algorithm.

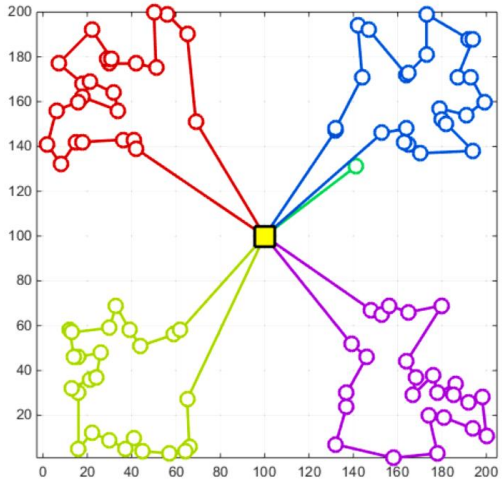

Fig. 4 - Path diagram of the traditional SA algorithm

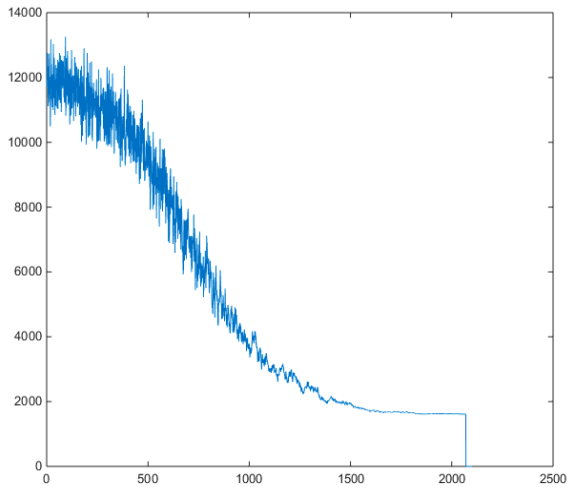

Fig. 5 - Convergence curve of the traditional SA algorithm

As shown in Table 6, compared with the traditional SA algorithm, the large-scale neighborhood search SA algorithm is strongly exploratory and convergent, with a better value of the objective function. The large-scale neighborhood search SA algorithm displays advantages over the traditional SA algorithm in the quantity of refrigerated vehicles, driving distance, total cost, and algorithm time consumption. Therein, the traditional SA algorithm needs 5 electric refrigerated vehicles to complete the agricultural product cold chain

transportation task, while the large-scale neighborhood search SA algorithm only requires 4 electric refrigerated vehicles to complete the same task, with the efficiency improved by 20%. The *large-scale neighborhood search SA algorithm* spends 413.81 s in convergence, while the *SA* algorithm embedded with a genetic operator spends 574.48 s, so the algorithm efficiency is improved by 27.96%.

Table 6

Algorithm comparison

Algorithm	Total Cost (RMB)	Total Mileage (Km)	Number of Vehicle	Algorithm Time (s)
Large scale neighborhood search SA algorithm	1548.93	51.631	4	413.81
Traditional SA algorithm	1688.6455	56.288	5	574.48

CONCLUSIONS

Aiming at the route problem of agricultural cold chain vehicles with multiple models and single distribution center, firstly, considering the green, sustainability and economic requirements of refrigerated trucks, as well as the ambiguity, complexity and uncertainty of objective things, the AHP-TOPSIS method was used to evaluate all kinds of refrigerated trucks. Then, an objective function is established based on the assessed value of the vehicle as well as the transportation costs, fixed costs, cargo damage costs, cooling costs and fines incurred during the distribution process. Secondly, the corresponding cold chain logistics vehicle route optimization model is constructed, and the designed genetic algorithm is used to solve the problem, and the route of the batch arriving vehicles is obtained. The model can change the weight of vehicle evaluation, and a larger weight value means that the distribution process is more environmentally friendly and sustainable, and logistics companies can choose the right distribution scheme according to their needs.

The evaluation results of six kinds of refrigerated trucks, such as electric refrigerated trucks, mixed fuel refrigerated trucks, diesel refrigerated trucks, gasoline refrigerated trucks, biodiesel refrigerated trucks and natural gas refrigerated trucks, take into account the cost and green indicators, and provide a reference for cold chain logistics companies to select and integrate distribution vehicles. Taking Daliandili fresh food distribution as an example, the feasibility of the model and algorithm established in this paper is verified. In addition, it has been proven that considering vehicle assessment factors will increase distribution costs to some extent, but it can effectively improve the green and sustainable distribution process. By comparing with the model under the non-divided distribution mode, it is found that the divided distribution mode achieves lower distribution cost than the non-divided distribution mode. This study provides a new way of thinking for multi-vehicle and multi-distribution center cold chain logistics vehicle routing problem, and provides a certain reference for logistics enterprises to make distribution decisions.

REFERENCES

[1] Aggarwal D., Kumar V. (2018). An improved firefly algorithm for the vehicle routing problem with time windows. *International Conference on Advances in Computing, Communications and Informatics (ICACCI)*. pp. 222-229. Bangalore, India;

[2] Bauernhansl T. (2016). Exact method for the vehicle routing problem with mixed line haul and back haul customers, heterogeneous fleet, time window and manufacturing capacity. *Procedia CIRP*, Vol. 41, Issue 06, pp. 573-578. Netherlands;

[3] Chen S., Chen R., Wang G-G, et al. (2018). An adaptive large neighborhood search heuristic for dynamic vehicle routing problems. *Computers & Electrical Engineering*, Vol. 67, pp. 596-607. England;

[4] Cordeau J-F, Laporte G, Mercier A. (2001). A unified tabu search heuristic for vehicle routing problems with time windows. *Journal of the Operational Research Society*, Vol. 52, Issue 8, pp. 928-936. England;

[5] Chen W Z, Jiang F, Liu P. (2020). Research on path planning of highly perishable agricultural product based on improved ant colony algorithm (基于改进蚁群算法的易腐农产品配送路径规划研究). *Journal of Hebei Agricultural University*, Vol. 43, Issue 3, pp. 130-135. China;

[6] Chiang W-C, Russell R.A. (1996). Simulated annealing metaheuristics for the vehicle routing problem with time windows. *Annals of Operations Research*, Vol. 63, Issue 1, pp. 3-27. Netherlands;

[7] Dorigo M., Birattari M., Stutzle T. (2006). Ant colony optimization. *IEEE Computational Intelligence Magazine*, Vol. 1, Issue 4, pp. 28-39. England;
[8] Ellabib I., Calamai P., Basir O. (2007). Exchange strategies for multiple ant colony system. *Information Sciences*, Vol. 177, Issue 05, pp. 1248-1264. United States;
[9] Fan H.M., Liu W.Q., Xu Z.L. et al. (2018). Solving VRPSPD problem with a soft time window using hybrid particle swarm algorithm (混合粒子群算法求解带软时间窗的 VRPSPD 问题). *Computer Engineering and Applications*, Vol. 54, Issue 9, pp. 221-229. China;
[10] Govindan K., Jafarian A., Khodaverdi R. (2014). Two-echelon multiple-vehicle location-routing problem with time windows for optimization of sustainable supply chain network of perishable food. *International Journal of Production Economics*, Vol. 152, Issue 02, pp. 9-28. Netherlands;
[11] Han X., Dong Y., Yue L., et al. (2019). State transition simulated annealing algorithm for discrete-continuous optimization problems. *IEEE Access*, Vol. 7, pp. 44391-44403. United States;
[12] He M., Wei Z., Wu X., et al. (2021). An adaptive variable neighborhood search ant colony algorithm for vehicle routing problem with soft time windows. *IEEE Access*, Vol. 9, pp. 21258 -21266. United States;
[13] Liu H., Liu Y.Z. (2014). A fuzzy TOPSIS-based comprehensive evaluation method of purchasing agents (一种基于模糊 TOPSIS 的采购商综合评价模型). *Statistics & Decision*, Issue 16, pp. 4-6. China;
[14] Li Z., Li W.X., Ju Y.X., et al. (2019). Hybrid ant colony algorithm for solving vehicle routing problem with soft time window (混合蚁群算法求解带软时间窗的车辆路径问题). *Journal of Wuhan University of Technology (Transportation Science & Engineering)*, Vol. 43, Issue 4, pp. 761-766. China;
[15] Li B., Yang X., Xuan H. (2019). A Hybrid Simulated Annealing Heuristic for Multistage Heterogeneous Fleet Scheduling with Fleet Sizing Decisions. *Journal of Advanced Transportation*, Vol. 2019, Issue 10, pp. 1-19. United States;
[16] Mohammed M.A., Gani M.K., Hamed R.I. (2017). Solving vehicle routing problem by using improved genetic algorithm for optimal solution. *Journal of Computational Science*, Vol. 21, pp. 255-262. Netherlands;
[17] Nwakaire C.M., Keirstead J. (2015). Assessing the sustainability of meat transport mode choices in abattoir logistics using the analytic hierarchy process. *ARPN Journal of Engineering and Applied Sciences*, Vol. 10, Issue 20, pp. 9331-9338. Pakistan;
[18] Pérez-Rodríguez R., Hernández-Aguirre A. (2019). A hybrid estimation of distribution algorithm for the vehicle routing problem with time windows. *Computers & Industrial Engineering*, Vol. 130, pp. 75-96. England;
[19] Shukla M. (2013). Agriculture fresh produce supply chain management: a state-of-the-art literature review. *International Journal of Operations & Production Management*, Vol. 33, Issue 2, pp. 114-158. England;
[20] Shaw P. (1998). Using constraint programming and local search methods to solve vehicle routing problems, *International Conference on Principles and Practice of Constraint Programming*, pp. 417-431. Berlin, Heidelberg.
[21] Venkata N.K., Kivelevitch E., Sharma B. (2013). Ant colony optimization technique for solving min-max multi-depot vehicle routing problem. *Swarm and Evolutionary Computation*, Vol. 13, Issue 12, pp. 63-73. Netherlands;
[22] Wu H., Gao Y, Wang W., et al. (2021). A hybrid ant colony algorithm based on multiple strategies for the vehicle routing problem with time windows. *Complex & Intelligent Systems*, pp. 1-18. Saudi Arabia;
[23] Zhou X., Yang C., Gui W. (2011). Initial version of state transition algorithm, *2011 Second International Conference on Digital Manufacturing & Automation*, pp. 644-647. Zhangjiajie, China.

ANALYSIS ON HANDLING PATH OPTIMIZATION OF AGRICULTURAL ROBOTS BASED ON IMPROVED ANT COLONY ALGORITHM

/

基于改进蚁群算法农业机器人搬运路径优化分析

Zhen WANG[1)], Keqing QIAN[1)], Xiaoli ZHU[1)], Xinyu HU[1)], Xinran LI[2)]*

[1)]College of Biological and Food Engineering, Huanghuai University, Zhumadian, Henan, China;

[2)]Zhumadian City Yicheng District Agricultural and Rural Bureau, Zhumadian, Henan, China.

**E-mail: ycqnyjnjg@163.com*

Corresponding author: Xinran Li

DOI: https://doi.org/10.35633/inmateh-70-44

Keywords: *agriculture robot, path optimization, transport, intelligent agricultural machinery equipment*

ABSTRACT

With the rapid development of agricultural machinery intelligence and informatization, agricultural robots are becoming the protagonist, promoting standardized production in agriculture, improving efficiency, and reducing labor costs. However, how to quickly plan an efficient and safe path for agricultural transport robots is currently a hot topic in path planning research. In this study, the path optimization problem of agricultural robots handling agricultural products (such as Edible Fungi) in and out of warehouses, which served as the study object, was solved. First, the number of agricultural handling robots was initialized based on the scanning method, and the geometric center of sub-path nodes was set as the virtual node. Secondly, the optimal path of the virtual node was solved using the improved ant colony algorithm embedded with a genetic operator, and the optimal result of sub-paths was acquired. Thirdly, the optimal solution meeting constraint conditions was obtained with the launch cost, transportation cost, and time cost of agricultural robots as objective functions. Lastly, the effectiveness of the optimization model and the improved ant colony algorithm was verified through the instance analysis. This study is of certain significance to the ex-warehousing path optimization of agricultural robots under the sustainable development concept of agricultural automation.

摘要

随着农业机械智能化和信息化的飞速发展，农业机器人正在成为主角，推动农业实现标准化生产，提高效率，减少人工成本。然而农业搬运机器人如何快速规划出一条高效、安全的路径是目前路径规划研究的热点问题。本文以农业机器人仓库运输路径优化为研究对象，解决农业机器人搬运农产品(例如食用菌)进出仓库场景下的路径优化问题。首先，基于扫描法初始化农业搬运机器人初始数量，并将子路径节点的几何中心设置为虚拟节点；其次，采用嵌入遗传算子的改进蚁群算法求解连接虚拟节点的最优路径，求解子路径的最优结果。第三，以农业机器人启动成本、运输成本和时间成本为目标函数，最终得到满足约束条件的最优解。最后，通过实例分析验证优化模型和改进蚁群算法的有效性，对农业自动化可持续发展理念下农业机器人出库路径的优化研究具有一定的意义。

INTRODUCTION

Agricultural robots refer to multi-degree-of-freedom autonomous operating equipment with sensing, decision-making, control, and execution capabilities for agricultural production, including an information perception system, a decision-making control system, an operation execution mechanism, and an autonomous mobile platform, namely “eyes, brain, hands, and feet”. At present, the labor force engaged in agricultural production in China is decreasing and the labor cost is increasing, so the demand for agricultural robots grows rapidly. In the future, with the development of urbanization, the rural labor force will continue to decrease. According to the characteristics and needs of agriculture, the research on agricultural robots has been carried out. A lot of research work has been done in autonomous tractors, small agricultural mobile platforms, grafting robots, loading robots, fruit sorting robots, picking robots, farmland information monitoring robots, and plant protection drones, which have been well applied in autonomous agricultural machinery, plant protection drones, and milking robots. China should vigorously promote the deep integration of informatization and industrialization, and speed up the process of intelligent production. As we all know, agricultural products warehouse is the key link in the circulation of agricultural products.

Improving the intelligent management level of workshops, tapping the potential, saving costs, and reducing energy consumption are topics of concern to both academia and industry.

With the rapid development of artificial intelligence and robot technology, agricultural robots are gradually replacing human beings to complete the task of handling agricultural products in and out of warehouses. `Driving path optimization of agricultural robots is the core problem encountered in the application of warehouse operations *(Li G H., 2021)*. In the environment with uncertain obstacles, the path planning of agricultural robots is the focus of research, that is, the collision-free path optimization from the starting point of movement to the target end point. When agricultural robots handle agricultural products in and out of a warehouse, the working environment directly affects their working state *(Jiang N. et al., 2020)*. Because agricultural product warehouses are generally characterized by narrow handling channels and many uncertain obstacles, the working efficiency of agricultural robots will often be reduced due to the poor optimization ability of path planning algorithms during dynamic path planning *(Yin J. et al., 2019)*. Therefore, robot path optimization algorithms have gradually become one of the research hotspots. Given this, agricultural robots were required to complete the task of handling agricultural products in and out of warehouses simultaneously, and the sum of robot start-up cost, transportation cost, and time cost was taken as the objective function to solve the modeling and algorithm research on the agricultural robot path optimization problem.

State of the art

The genetic algorithm (GA) is one of the earliest heuristic algorithms used to solve the path optimization problem of robots. *Panchu et al* solved the shortest time for robots to complete tasks using GA *(Panchu K P. et al., 2018)*. *Li et al* optimized the driving path of the robot based on the received dynamic information. Some scholars have also proposed to use GA to optimize the sequence of tasks to be completed by robots *(Li Y F. et al., 2014)*, to design an improved GA based on the roulette and optimal preservation strategy to solve the robot path optimization problem *(Qian Z. et al., 2015)*, and to use the dual-population genetic ant colony algorithm to solve the robot path problem *(Gang L I. et al., 2015; Pei Z B. et al., 2015)*. By analyzing the role of GA in solving the path optimization problem of robots, it is found that the algorithm can solve the optimal value problem of path optimization of small-scale robots, but its convergence speed is slow, failing to meet the agile demand of the workshop production mode. *Zhao et al* proposed to establish an interlocking relationship between α and β to define pheromone update rules *(Zhao H C. et al., 2018)*. Some scholars have proposed to solve the high-quality distribution route problem based on the ant colony algorithm *(Lu E H C. et al., 2016)*, and a hybrid ant colony algorithm has been put forward to solve the robot path optimization problem *(Kober J. et al., 2013)*. Based on the above analysis, it is found that the ant colony algorithm has obvious distribution characteristics, strong robustness, and high reliability when solving robot path optimization problems, but the disadvantage is that it will fall into a local optimal solution at a certain probability. In recent years, the reinforcement learning algorithm has also been applied to path optimization *(Polydoros A S. et al., 2017)*. Some scholars have designed an improved fuzzy Q learning algorithm to solve the problem of path planning strategies *(Duguleana M. et al., 2016)*. Some scholars have adopted the firefly optimization algorithm to solve the problem of vehicle path optimization *(Wang H F. et al., 2012)* and the tabu search algorithm to solve the problem of vehicle path optimization *(Wang C. et al., 2013)*. The above literature constructs the mathematical model of the robot carrying path respectively, selects different platforms to solve the robot path optimization problem, and most heuristic methods solve the path optimization problem of the carrying robot in the solution algorithm. The selection strategy of heuristic action improves the solution efficiency, and can obtain the optimal solution of the model. However, based on this, the path optimization search of the carrying robot has a high total distance and high consumption.

Some scholars have conducted in-depth research on the path optimization technology of handling robots in terms of technology, such as，*Faina, A. et al. (2020)* who describe the EvoBot modular design and through scientific experiments such as basic liquid handling, nurturing of microbial fuel cells, and droplet chemotaxis experiments document how functionality is increased in one module at a time with a significant amount of reuse. Gürel S. et al. studied the trade-off between cycle time and energy consumption of robots in robot units producing the same parts (*Gürel S. et al., 2019).* Gultekin et al. proposed a Second-order cone programming formula to find Pareto efficient solutions *(Gultekin et al., 2021)*.

A heuristic algorithm that can find a set of approximate Pareto efficient solutions was also developed, and the cone formula can find robot scheduling for small units with fewer machines in a reasonable computational time.

Santos et al solved the path optimization model of agricultural robots based on the point cloud transformation algorithm. When the robot encounters obstacles, the local path is re-planned through the point cloud transformation algorithm, thus improving the path safety of agricultural robots *(Santos L. et al., 2020)*. *Cernicchiaro et al* optimized the driving path of agricultural robots based on D* algorithm, and the example proved that the algorithm can improve the working efficiency of agricultural robots and shorten the movement time between execution points *(Cernicchiaro C. et al., 2019)*. *Azzabi et al* optimized the robot path based on the potential field method. In the process of moving, obstacles will repel the robot, which will help the robot avoid obstacles and improve the efficiency and safety of robot execution *(Azzabi A. et al., 2017)*. *Zhang et al* optimized the path of the robot by combining the improved ant colony algorithm and the potential field method *(Zhang Q. et al., 2019)*. The potential field method is used to plan the main path of the robot, and the improved ant colony algorithm to avoid obstacles and plan the path based on the main path. In addition, there are path planning strategies based on ant colony-particle swarm optimization *(Wang Z W. et al., 2018)*, robot path planning strategies based on longicorn search optimization algorithm *(Jiang X.Y. et al., 2014)*, and robot path planning strategies based on the improved longicorn search algorithm *(Xue J.K. et al., 2020)*. The above algorithms improve the robot path planning algorithm in terms of optimization accuracy, convergence speed, and running distance. In complex working environments, however, there are many breakpoints in the path of agricultural handling robots, and the path planning algorithm is prone to local optimization, slow convergence speed, and low result accuracy.

To sum up, Chinese and foreign scholars have made great achievements in robot path optimization research, mainly focusing on theories, models, and algorithms. However, there are few research results on multi-robot operation path optimization in the specific scenes of handling agricultural products in and out of warehouses simultaneously. In related research, meanwhile, intelligent bionic algorithms such as GA and particle swarm optimization have been mostly adopted, which, however, are generally subjected to low efficiency and slow convergence when solving the path optimization problem of robots. And the robot path optimization problem for agricultural product warehouses has been rarely solved using the improved ant colony algorithm. In the existing results, moreover, the path optimization problem under static environments has been mainly considered, not in line with the actual situation of many uncertain factors in agricultural product warehouses. Given this, this problem was solved in this study by proposing an ant colony algorithm embedded with a genetic operator. And the crossover and mutation mechanisms of the genetic operator were introduced to jump out of the local optimal solution combining the strong robustness and high reliability of the ant colony algorithm. In the meantime, the deficiency of a single algorithm was effectively compensated by organically combining GA and ant colony algorithm. The ant colony algorithm with a genetic operator could solve the driving path of agricultural handling robots, capture the dynamic collision information in agricultural product warehouse on the driving path, and realize dynamic obstacle avoidance. Finally, the path optimization problem with the objective of total cost minimization was solved.

MATERIALS AND METHODS

In the process of entering and leaving the agricultural product warehouse, each order contains different varieties and quantities of commodities. Therefore, agricultural robots need to pick according to the order requirements during the operation of entering and leaving the warehouse, and at the same time, complete the related tasks such as product warehousing. Otherwise, the inventory will increase, and even equipment shutdown will be induced, reducing inventory efficiency.

There is a certain physical distance between the product storage areas in the agricultural product warehouse, ensuring that the handling robot can shuttle back and forth and assume the position of each product storage location and the position of the warehouse-in and out operation area. The maximum load capacity of the agricultural handling robot is known, the maximum load capacity of the agricultural handling robot is greater than the weight or volume of products entering and leaving each cargo location each time, and each cargo location can only have one agricultural handling robot. Because the agricultural handling robot has strong dynamic endurance and the time window limit is not considered, the maximum running distance of the robot is no longer taken into account. According to the specific situation of the warehouse-in and out tasks of agricultural products, the number of agricultural handling robots is reasonably arranged. While completing the warehousing tasks of agricultural products, the objective function is to minimize the total cost of agricultural handling robots, such as start-up cost, transportation cost, and time cost. There is only one warehouse-in and out operation area in the workshop, and the robot returns to this operation area after completing the warehouse-in and out task, forming a closed running track, as shown in Fig. 1.

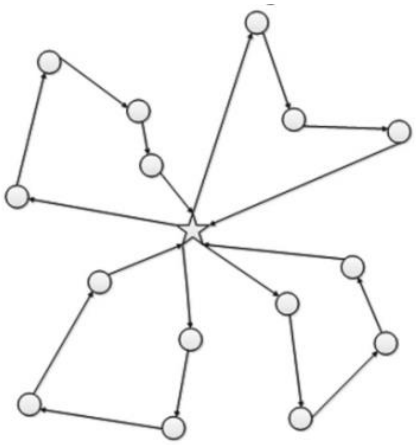

Fig. 1 - Schematic diagram of the running path of the agricultural handling robot

The robot sensor sends signals to the control system in time to adjust the distribution route. Therefore, considering the particularity of the warehouse environment and the problem of handling agricultural in and out of the warehouse, the dynamic obstacle avoidance problem was the main reason why the ant colony algorithm was improved by embedding a genetic operator in GA.

Model Building

In an agricultural product warehouse, there are R agricultural robots with the maximum load carrying capacity of Q that provide warehouse-in and out services for this warehouse. Therein, d_i stands for the warehouse-out quantity needed by the cargo location i; p_i is the warehouse-in quantity needed by the cargo location i; e_{ij} is the total warehouse-out quantity after the agricultural handling robot passes the cargo location i; f_{ij} represents the total warehouse-in quantity after the agricultural handling robot passes the cargo location i, and the sum of the warehouse-in and out quantities of the agricultural handling robot should not exceed its maximum load carrying capacity at any time; d_{ij} indicates the distance from the cargo location i to j, and the warehouse-in and out positions and the spatial position of each cargo location are already known and expressed by the corresponding coordinates; Q_{rij} is a decision variable, representing whether the agricultural handling robot r experiences a collision when moving from the cargo location i to j; both x_{ijr} and y_{ir} are decision variables defined as follows:

$$x_{ijr} = \begin{cases} 1, robot\ R\ moves\ from\ the\ cargo\ bay\ i\ to\ the\ j \\ 0, else \end{cases} \quad (1)$$

$$y_{ir} = \begin{cases} 1, Robot\ R\ to\ provide\ service\ for\ the\ Goods\ i \\ 0, else \end{cases} \quad (2)$$

The mathematical models for the agricultural robot's handling path optimization problem are as follows:

$$min \sum_i \sum_j \sum_r d_{ij} \times x_{ijr} \quad (3)$$

$$s.t. \quad (4)$$

$$\sum_{r=1}^{R} y_{or} = R$$

$$\sum_{i=1}^{M} y_{i0r} = 1 (r = 1, \cdots, R) \quad (5)$$

$$\sum_{i=1}^{R} y_{ir} = 1 (r = 1, \cdots, M) \quad (6)$$

$$\sum_{i=1}^{M} x_{ijr} = y_{jr} (j = 1, \cdots, M; r = 1, \cdots, R) \quad (7)$$

$$\sum_{j=0}^{M} x_{ijr} = y_{jr} (i = 1, \cdots, M; r = 1, \cdots, R) \quad (8)$$

$$\sum_{j=0}^{M} e_{ij} - \sum_{j=0}^{M} e_{ji} = p_i (i = 1, \cdots, M) \quad (9)$$

$$\sum_{j=0}^{M} f_{ij} - \sum_{j=0}^{M} f_{ji} = d_i (i = 1, \cdots, M) \quad (10)$$

$$e_{ji} + f_{ji} \le Q \sum_{j=0}^{R} x_{jir} (i, j = 1, \cdots, M) \quad (11)$$

$$Q_{rij} = \begin{cases} 1, Collide \\ 0, else \end{cases} \quad (12)$$

In this model, Equation (3) represents the objective function, that is, the minimum warehouse-in and out cost; Equation (4) indicates that all robots start from the working area of the warehouse; Equation (5) means that the robot returns to the warehouse operation area after completing the task; Eqs (6), (7), and (8) indicate that only one robot arrives at a certain cargo location and provides services; Equation (9) represents the constraint on the quantity of agricultural products required by the warehouse; Equation (10) denotes the inventory constraint of products required by the warehouse; Equation (11) indicates the limit of the carrying capacity of the robot; in Equation (12), Q_{ij}=1 indicates whether the robot r experiences a collision when moving from the cargo location i to j, and Q_{ij}=0 means that no collision occurs.

Improved Ant Colony Algorithm

The position of a cargo location was acquired through the scanning method, i.e., its position was expressed by polar coordinates. The warehouse-in and out operation area of the warehouse served as the starting point, with its angle set to 0. Then, the equipment nodes were segmented with the robot's maximum carrying capacity as the constraint to obtain several subregions conforming to the carrying capacity limit.

The basic idea of the improved ant colony algorithm is described as follows: to solve the problem of pheromone shortage and slow convergence in the early stage of the ant colony algorithm, multiple feasible solutions are obtained by using GA in the initial stage, and the formula is transformed into an initial pheromone distribution. Then, the ant colony algorithm is used to further optimize the search and give full play to the positive feedback mechanism to facilitate the algorithm to converge quickly. In the pheromone update stage, high-quality solutions are selected from the candidate set using the Metropolis criterion of the simulated annealing algorithm, and only these high-quality solutions will update the pheromone concentration.

GA starts from the initial feasible solution, so it has a high convergence speed in the early stage. The process of obtaining the initial pheromone distribution by GA is as follows:

(1) Coding: According to the characteristics of the robot path optimization problem for handling agricultural products in and out of the warehouse, the real number coding method was adopted in this study, where the number 0 represents the warehouse-in and out operation area, and the numbers 1, 2, 3, and n represent the positions of goods. The number of robots in and out of the warehouse was set to k, so the chromosome length should be set to $k+n+1$, so that all customer points could be served in extreme cases. The code $0, i_1, \cdots, i_e, 0, i_f, \cdots, i_k, 0$ represents a possible chromosome.

(2) Population initialization: A total of n cargo locations were arranged randomly, the number 0 was inserted in the arrangement according to the model constraint, and another number 0 was added to the starting point and end point to indicate that both the robot's starting point and end point were inside and outside the warehouse operation area. Then, a chromosome (a feasible solution) was generated. This process was repeated m times, where m stands for the population.

(3) Determination of the fitness function: The objective function $minz$ of the path optimization model for robots handling agricultural products was achieved at the minimum total cost. Since the fitness function was in a direct proportion to the individual survival rate, the fitness function value was determined in this study as seen in Equation (13).

$$f = 1 / min Z \quad (13)$$

(4) Improved selection operation. In this study, the population was selected by means of roulette selection, and the principle of steady-state replication was introduced based on the traditional roulette selection method so as to skip the links of crossover and mutation and directly enter the next iteration, thereby ensuring that the optimal gene of each generation would not be lost.

(5) Crossover operation. The crossover operation was completed through multiple rounds of selecting crossover individuals, and a random number rand was generated between crossover individuals in each round. If the random number rand was less than the crossover probability, the genetic crossover operation was carried out by using two-point crossover. However, an infeasible solution might be generated by the direct crossover operation, as shown in Fig. 2, and two new offspring chromosomes were obtained. The two offspring were illegal solutions: gene 0 appeared twice in offspring A, but gene 3 did not exist; gene 3 appeared twice in offspring B, but gene 0 did not exist. On this basis, to avoid the direct crossover of infeasible solutions, the following idea was adopted in the implementation of the algorithm: for example, when the offspring $A1$ was obtained, the first three genes A (1-3):012 and the last three genes A(8-10): 789 of the parent A were kept unchanged, while the 6 genes retained in A were deleted in the parent B in turn, leaving 4 genes B(4): 6543 in B, then the offspring $A1$= A(1-3)+ B(4)+ A(8-10) was acquired, namely A1:0126543789, and the offspring $B1$ could be obtained similarly.

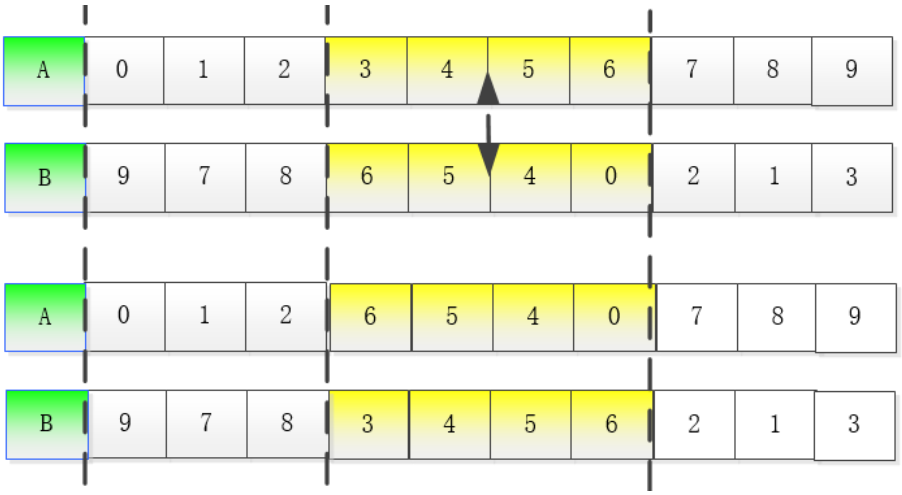

Fig. 2 - Schematic diagram of chromosome crossover operation

(6) Mutation operation. According to the probability of the mutation operation, the result of Step (5) was subjected to the mutation operation, which was specifically implemented by local reversed order.

(7) Generation of an initial pheromone distribution. When the set evolutionary generation Gen_{max} was reached, the iteration was terminated, the solution obtained at this time was regarded as the initial solution of the ant colony algorithm, and the initial concentration of pheromones on each path was calculated according to Equation (14).

$$\tau_{ij} = \sum_{k=1}^{m} \frac{Q}{L_k} \tag{14}$$

where the additional strength coefficient of pheromones is usually set as a constant, which is expressed by Q; the total length of ant k's walking route in this iteration is expressed by L_k.

After the initial pheromone distribution was generated, the ant colony algorithm was used to further optimize the search and generate the candidate set route, which had a common solution. Then, the pheromone concentration on the path needed to be updated.

If the pheromone was updated by the global method without considering the quality of the solution, the pheromone concentration on the better path and the worse path would not be much different, which then interfered with the subsequent optimization search of ants, led to a large number of invalid handling paths in the search, and then affected the convergence speed of the algorithm.

Therefore, after the candidate set Routh was obtained, the Metropolis criterion of the simulated annealing algorithm was introduced to filter the solutions of the candidate set, and a high-quality solution set Routh_New was generated, and only the pheromone concentration was updated.

Firstly, the objective function value z_i of candidate set solutions was calculated one by one; then, according to the acceptance probability formula of the simulated annealing algorithm, as shown in Equation (15), whether the current solution was added to the latest solution set was determined.

$$P_i = \begin{cases} 1, & z_i < z_{best} \\ exp(-\frac{z_i - z_{best}}{kT}), & z_i \geq z_{best} \end{cases} \quad (15)$$

where the objective function value of the robot's optimal driving path is expressed by z_{best}; the current temperature value of the simulated annealing algorithm is expressed by T, which decreases at a certain proportion as the iteration process of the ant colony algorithm continues; k is a constant. When $z_i < z_{best}$, this solution is directly added to the latest set. When $z_i > z_{best}$, a random number rand between $(0,1)$ is generated. If $rand < \exp(-\frac{z_i - z_{best}}{kT})$, this solution is added into the latest set. At high temperature, the greater the T value, the greater the calculation result of $\exp(-\frac{z_i - z_{best}}{kT})$. In this way, more high-quality solutions in the candidate set will be added to the *Routh_New* solution set, thus increasing the diversity of understanding and avoiding prematurity and stagnation to some extent. At low temperature, if the value of $\exp(-\frac{z_i - z_{best}}{kT})$ is small, the calculation result is small, which reduces the number of high-quality solutions added to the *Routh_New* solution set, thus accelerating the convergence speed of the algorithm.

When the value of ρ—an important factor affecting the pheromone concentration on the handling path of agricultural robots—is small, the pheromone evaporation speed is slow, which leads to too many pheromone residues on the handling path of agricultural robots, expands the search range of ant colony, and produces a large number of invalid paths, which in turn leads to the slow convergence speed of the ant colony algorithm. When the evaporation factor ρ is too large, the pheromone on the path evaporates rapidly, and the pheromone concentration difference between the better path and the worse path is obvious, which narrows the search range of the ant colony and makes the ants gather on the better path quickly. In the early search, the main purpose is to get the optimal solution as soon as possible, so a larger value of ρ should be taken. When the algorithm is at a standstill, it may fall into a local optimal solution. At this time, it is necessary to reduce this value, expand the search range of the ant colony, and jump out of the local optimal solution.

Based on the above analysis, the numerical formula in this study is displayed in (16).

$$\rho(t+1) = \begin{cases} max[0.7 * \rho(t), \rho_{min}], & x = x_{max} \\ \rho(t), & else \end{cases} \quad (16)$$

where:

x stands for the number of consecutive cycles of the optimal solution;

x_{max} is a constant value, and the minimum value of ρ is expressed as ρ_{min}.

To avoid too much attenuation of ρ from influencing the algorithm performance, a limit is added to ρ_{min}.

When $x = x_{max}$, the value of ρ is reduced based on $0.7\rho(t)$, and x is set to 0, followed by counting again. Such cycles are continued until ρ attenuates to the minimum value ρ_{min}.

The flow of the improved ant colony algorithm solving the optimization model in this study is shown in Fig. 3.

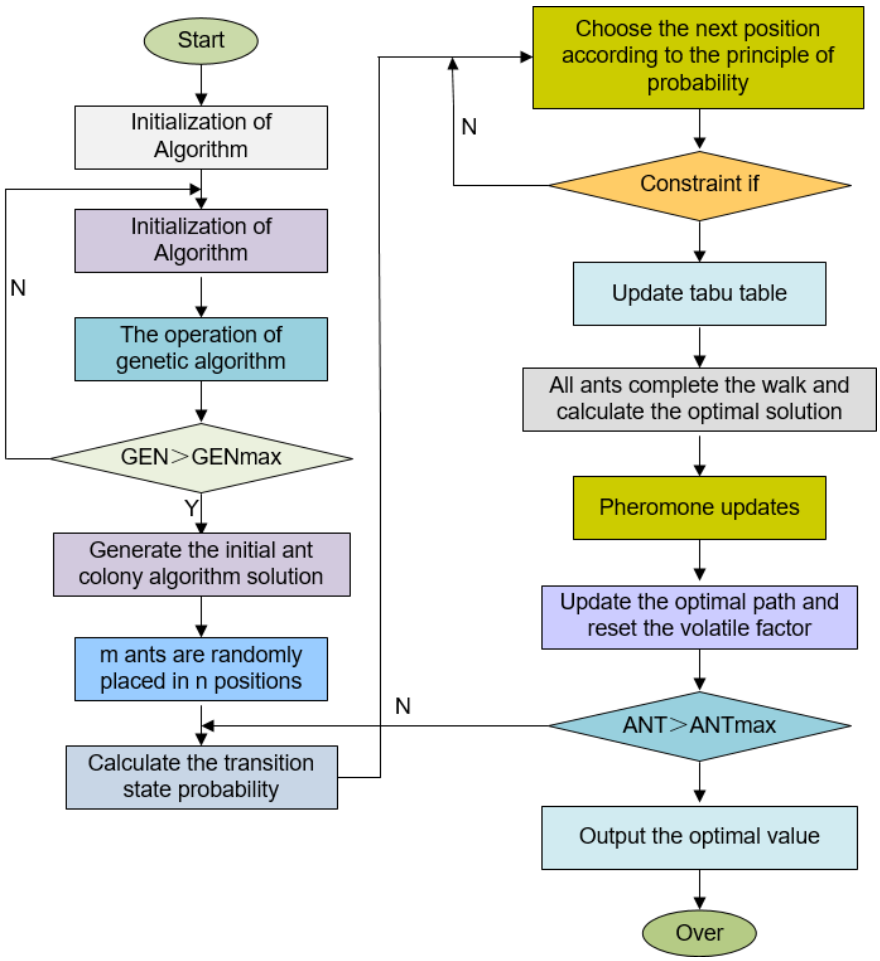

Fig. 3 - Flowchart of the improved ant colony algorithm for solving the optimization model

RESULTS

Experimental Environment and Parameter Setting

In this study, Intel i7 processor and Matlab2014b were adopted for the experiment. The mutation probability, crossover probability, and genetic gap of GA were 0.1, 0.9, and 0.7, respectively. In the ant colony algorithm, the important factor of pheromone was 1, the constant coefficient Q was 1, the evaporation factor of information was 0.1, and the important factor of the heuristic function was 5. The discount factor and learning rate of the reinforcement learning algorithm were 0.9 and 0.2, respectively. The three cost parameters are listed in Table 1.

Table 1

Cost parameters

Parameter type	Parameter name	Value
Basic cost	Basic cost of dispatched robots	300 yuan (CNY)
Transportation cost	Unit distance loss of robots	5 yuan (CNY)
Time cost	Robot operating speed	10 m/min
	Robot handling/unloading time	1 min
	Maximum carrying capacity of robots	200 kg

In this study, the operation area inside and outside the agricultural product warehouse served as node o with coordinates of (40,50). In the warehouse, there were 29 cargo locations, which were expressed by the corresponding coordinate values X and Y, and the number of agricultural products in and out of each cargo location was known, as seen in Table 2.

Table 2

Warehouse-in and out information of cargo locations

Cargo location No.	Coordinate X	Coordinate Y	Warehouse-out quantity	Warehouse-in quantity	Cargo location No.	Coordinate X	Coordinate Y	Warehouse-out quantity	Warehouse-in quantity
0	40	50	0	0	13	22	75	15	15
1	45	68	4	6	14	22	85	6	4
2	45	70	10	20	15	20	80	17	23
3	42	66	7	3	16	20	85	16	24
4	42	68	8	2	17	18	75	10	10
5	42	65	4	6	18	15	75	8	12
6	40	69	2	18	19	15	80	7	3
7	40	66	11	9	20	30	50	8	2
8	38	68	12	8	21	30	52	18	2
9	38	70	6	4	22	28	52	3	17
10	35	66	4	6	23	28	55	2	8
11	35	69	7	3	24	25	50	1	9
12	25	85	10	10	25	25	52	31	9

Experiment and Comparative Analysis

In this study, the warehouse-in and out path optimization model for agricultural handling robots was solved using the improved ant colony algorithm embedded with a genetic operator, the maximum number of iterations was set to 200, and the start-up cost of agricultural handling robots was 300 yuan. A satisfying solution could be obtained by solving the model, namely, the warehousing and unloading task of agricultural products was completed needing three mobile robots, the total travel distance of robots was 191.81 m, and the total cost was 1533.61 yuan (CNY). To complete the task of agricultural product delivery and improve the ant colony algorithm, 3 robots are required, and the driving path of each robot is shown in Figure 3. This algorithm took 448.81 s. The path diagram of the improved ant colony algorithm embedded with GA is displayed in Fig. 4. The convergence curve of the improved ant colony algorithm embedded with GA is exhibited in Fig. 5, and the calculation results are listed in Table 3.

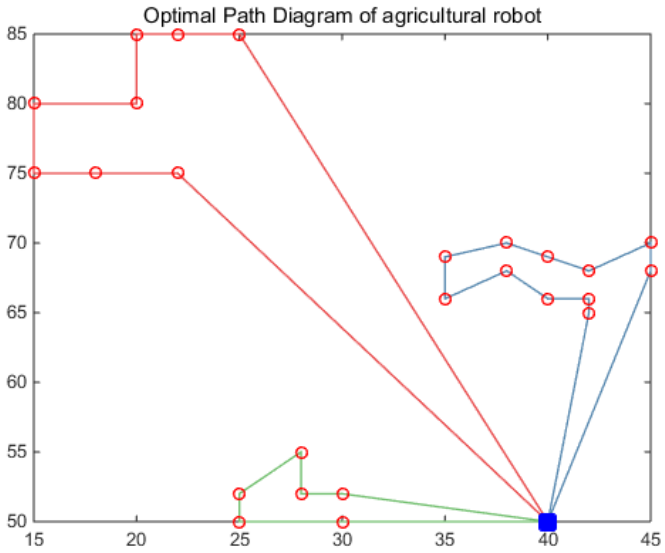

Fig. 4 - Path diagram of the ant colony algorithm embedded with GA

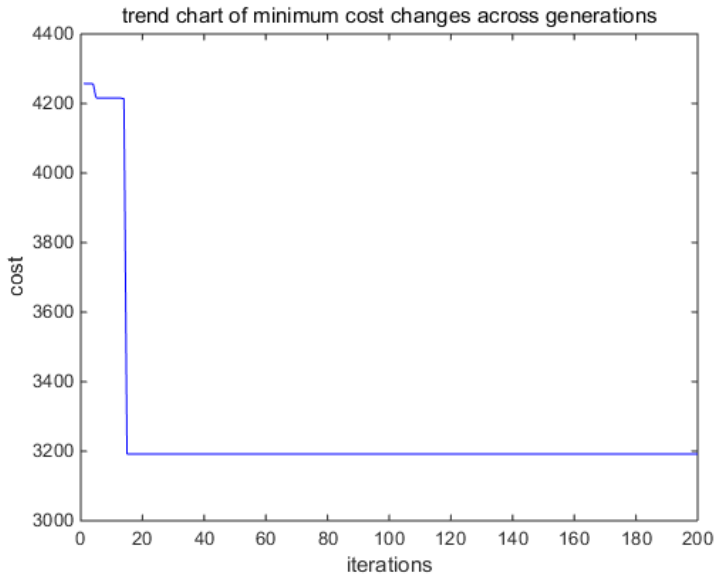

Fig. 5 - Convergence curve of the improved ant colony algorithm embedded with GA

Table 3

Optimal service path (improved ant colony algorithm)

Service path	Actual carrying capacity	Maximum carrying capacity	Full load rate
0→5→3→7→8→10→11→9→6→4→2→1→0	160	200	80%
0→13→17→18→19→15→16→14→12→0	170	200	85%
0→20→24→25→23→22→21→0	110	200	55%

To further verify the effectiveness of the ant colony algorithm embedded with a genetic operator, the traditional ant colony algorithm was also designed in this study to solve the model. Under the constant initial cost and parameters, a total of 4 mobile robots were required to solve the agricultural robot path optimization model, with a total driving distance of 277.32 m, a total cost 2004.64 yuan (CNY), and time consumption of 604.48 s. To complete the task of agricultural product delivery, the traditional ant colony algorithm requires four robots, and the driving path of each robot is shown in Figure 6. The path diagram of the traditional ant colony algorithm is displayed in Fig. 6, the convergence curve of the traditional ant colony algorithm is displayed in Fig. 7, and the calculation results are listed in Table 4.

Compared with the traditional ant colony algorithm, the improved ant colony algorithm embedded with a genetic operator displayed strong exploration and convergence, accompanied by a better objective function value. The comparison of the two algorithms is shown in Table 5.

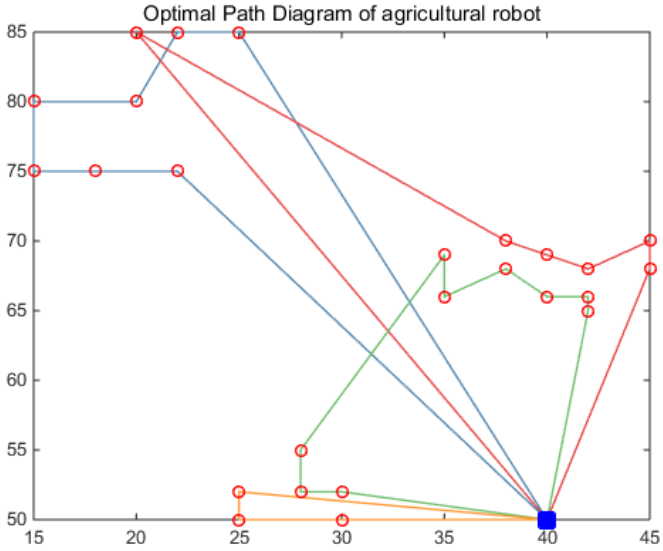

Fig. 6 - Path diagram of the traditional ant colony algorithm

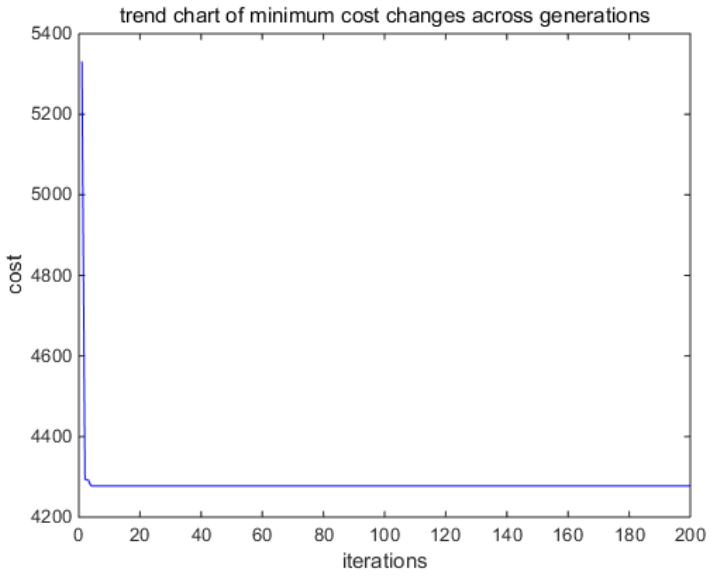

Fig. 7 - Convergence curve of the traditional ant colony algorithm

Table 4

Optimal service path (ant colony algorithm)

Service path	Actual carrying capacity	Maximum carrying capacity	Full load rate
0→13→17→18→19→15→14→12→0	150	200	75%
0→16→9→6→4→2→1→0	120	200	60%
0→5→3→7→8→10→11→23→22→21→0	130	200	65%
0→20→24→25→0	60	200	30%

Table 5

Comparison of the two algorithms

Algorithm	Number of robots	Average full load rate	Driving distance (m)	Total cost (yuan, CNY)	Algorithm time consumption (s)
Improved ant colony algorithm	3	73.33%	191.81	1533.61	448.81
Traditional ant colony algorithm	4	57.5%	277.32	2004.64	604.48

From Table 5, it can be seen that the improved ant colony algorithm embedded with a genetic operator is superior to the traditional ant colony algorithm in the number of robots, average full load rate, driving distance, total cost, and time consumption. The traditional ant colony algorithm needs 4 robots to complete the task of handling agricultural products in and out of the warehouse, while the improved ant colony algorithm embedded with a genetic operator only needs 3 robots to complete the same task, which improves the efficiency by 25%.

The average full load rate of agricultural robots obtained by the traditional ant colony algorithm is 57.5%, while that by the improved ant colony algorithm embedded with a genetic operator is 73.33%, with an increase of 15.83%. In terms of robot driving distance, the total driving distance of agricultural robots obtained by the traditional ant colony algorithm is 277.32 m, while that by the improved ant colony algorithm embedded with a genetic operator is 191.81 m. The total cost of agricultural robots obtained by the traditional ant colony algorithm is 2004.64 yuan, while that by the improved ant colony algorithm embedded with a genetic operator is 1533.61 yuan. In terms of time consumption, the convergence time of the traditional ant colony algorithm is 604.48 s, while that of the improved ant colony algorithm embedded with a genetic operator is 448.81 s, indicating an efficiency improvement of 25.75%.

CONCLUSIONS

In the process of large-scale transfer of rural surplus labor force, the shortage of young labor force and strong labor force has gradually become prominent in the field of agricultural production. Since the appearance of agricultural robots, both speed and variety have developed very well, which has gradually changed the traditional agricultural labor method and improved the level of agricultural modernization. However, many problems have been exposed in the wide application of agricultural robots. On this basis, the path optimization problem of moving robot entering and leaving warehouse is studied. In addition, an ant colony algorithm embedded with genetic operators is designed to optimize the path of agricultural transport robots. The main findings are as follows:

(1) Establish an optimization model, and establish a path optimization model of agricultural handling robot with full consideration of start-up cost, transportation cost and time cost. The simulation results show that the optimized model can achieve lower overall delivery cost.

(2) Algorithm optimization. An ant colony algorithm embedded with genetic operator was proposed to solve the path optimization problem of agricultural product handling robot in agricultural product warehouse. By using sequence decision making and reinforcement learning environment perception, pheromone initialization effectively improves the problem of insufficient initial pheromone in ant colony algorithm. The Metropolis pheromone update strategy proposed in this paper can accelerate the convergence of the algorithm while ensuring the quality of the solution.

(3) Algorithm performance comparison. By comparing the improved ant colony algorithm with the traditional ant colony algorithm, it is verified that the ant colony algorithm with genetic operator embedded in this study can effectively reduce the comprehensive allocation cost and has high convergence efficiency.

REFERENCES

[1] Azzabi A., Nouri K. (2017). Path planning for autonomous mobile robot using the potential field method. *International Conference on Advanced Systems & Electric Technologies. IEEE,* pp.389-394. Hammamet, Tunisia;

[2] Baizid K., Chellali R., Yousnadj A., et al. (2010). Genetic algorithms-based method for time optimization in robotized site. *IEEE/RSJ International Conference on Intelligent Robots and Systems (IROS),* pp. 1359-1364. Taibei, Taiwan;

[3] Cernicchiaro C., Gaspar P.D., Aguiar M.L. (2019). Fast return path planning for agricultural autonomous terrestrial robot in a known field. *International Journal of Mechanical and Mechatronics Engineering*, Vol. 13, Issue 2, pp. 79-87. Pakistan;

[4] Duguleana M., Mogan G. (2016). Neural networks-based reinforcement learning for mobile robot obstacle avoidance. *Expert Systems with Applications an International Journal*, Issue 62, pp. 104-115. England;

[5] Faina, A., Nejati, B., & Stoy, K. (2020). Evobot: An open-source, modular, liquid handling robot for scientific experiments. Applied Sciences, 10(3), 814.

[6] Gultekin, H., Gürel, S., & Taspinar, R. (2021). Bicriteria scheduling of a material handling robot in an m-machine cell to minimize the energy consumption of the robot and the cycle time. Robotics and Computer-Integrated Manufacturing, 72, 102207.

[7] Gürel, S., Gultekin, H., & Akhlaghi, V. E. (2019). Energy conscious scheduling of a material handling robot in a manufacturing cell. Robotics and computer-integrated manufacturing, 58, 97-108.

[8] Jiang X.Y., Li S. (2018). Beetle antennae search algorithm for optimization problems. *International Journal of Robotics and Control*, Vol. 1, Issue 1. Canada;

[9] Jiang N., Si L.N., Cai Z.Y. (2020). Automatic obstacle avoidance system of agricultural robots based on wireless network security (基于无线网络安全的农业机器人自动避障系统). *Journal of Agricultural Mechanization Research*, Vol. 42, Issue 2, pp. 238-242. China;

[10] Kober J., Peters J. (2013). Reinforcement learning in robotics: a survey. *International Journal of Robotics Research*, Vol. 32, Issue 11, pp. 1238-1274. England;

[11] Li Gang, Yu Jia-xin, Guo Dao-tong, et al. (2015). ROBOT route planning and simulation based on improved genetic algorithm (基于改进遗传算法的机器人路径规划与仿真). *Computing Technology and Automation*, Vol. 34, Issue 2, pp. 24-27. China;

[12] Li G.H. (2021). Research on intelligent planning of agricultural robot obstacle avoidance path (农业机器人避障路径智能规划研究). *Journal of Agricultural Mechanization Research*, Vol. 43, Issue 3, pp: 236-239. China;

[13] Lu E.H.C., Yang Y.W., Su Z.L.T. (2016). Ant colony optimization solutions for logistic route planning with pick-up and delivery. *2016 IEEE International Conference on Systems, Man, and Cybernetics (SMC)*, pp. 000808-000813. Budapest, Hungary;

[14] Pei Z.B., Chen X.B. (2015). Improved ant colony algorithm and its application in obstacle avoidance for robot (改进蚁群算法及其在机器人避障中的应用). *CAAI Transactions on Intelligent Systems*, Vol. 10, Issue 1, pp. 90-96. China;

[15] Polydoros A.S., Nalpantidis L. (2017). Survey of model-based reinforcement learning: applications on robotics. *Journal of Intelligent & Robotic Systems*, Issue 86, pp.1-21. Netherlands;

[16] Panchu K.P., Rajmohan M., Sumalatha M.R, et al. (2018). Route planning integrated multi objective task allocation for reconfigurable robot teams using genetic algorithm. *Journal of Computational and Theoretical Nanoscience*, Vol. 15, Issue 2, pp. 627-636. United States;

[17] Qian Z., Wang G., Wang J., et al. (2015). Route planning of UAV based on improved ant colony algorithm. *International Conference on Logistics Engineering, Management and Computer Science (LEMCS 2015)*, pp. 1421-1426. France;

[18] Santos L., Santos F., Mendes J., et al. (2020). Path planning aware of robot's center of mass for steep slope vineyards. *Robotica*, Vol. 38, Issue 4, pp. 684-698. England;

[19] Wang H.F., Chen Y.Y. (2012). A genetic algorithm for the simultaneous delivery and pickup problems with time window. *Computers & Industrial Engineering(S0360-8352)*, Vol. 62, Issue 1, pp. 84-95. England;

[20] Wang Z.W., Xu J.C., Li Y.H. et al. (2018). Simulation study of agricultural robot path planning based on PSO-EACO (基于 PSO-EACO 的农业机器人路径规划仿真研究). *Journal of Chinese Agricultural Mechanization*, Vol. 39, Issue 10, pp. 103-106. China;

[21] Wang C., Zhao F., Mu D., et al. (2013). Simulated annealing for a vehicle routing problem with simultaneous pickup delivery and time windows. *IFIP International Conference on Advances in Production Management Systems*, pp. 170-177. Berlin, Heidelberg;

[22] Xue J.K., Shen B. (2020). A novel swarm intelligence optimization approach: sparrow search algorithm. *System Science and Control Engineering an Open Access Journal*, Vol. 8, Issue 1, pp. 22-34. England;

[23] Yin J.J., Dong W.L., Liang L.H. et al. (2019). Optimization method of agricultural robot path planning in complex environment (复杂环境下农业机器人路径规划优化方法). *Transactions of the Chinese Society for Agricultural Machinery*, Vol. 50, Issue 5, pp.17-22. China;

[24] Zhang Q., Chen B.K., Liu X.Y. et al. (2019). Optimal path planning of mobile robots based on improved potential field ant colony algorithm (基于改进势场蚁群算法的移动机器人最优路径规划). *Transactions of the Chinese Society for Agricultural Machinery*, Issue 5, pp. 23-32. China;

[25] Zhao H.C., Guo J.L., Xu X.J. et al. (2018). Mobile robot path planning research based on fuzzy ant colony algorithm (基于模糊蚁群算法的移动机器人轨迹规划研究). *Computer Simulation*, Vol. 35, Issue 5, pp. 318-321. China.

WHITE TEA BUD DETECTION BASED ON DEEP LEARNING RESEARCH
/
基于深度学习的白茶嫩芽检测研究

Weiqiang PI[1)], Rongyang WANG*[1)], Qinliang SUN[1)], Yingjie WANG[1)], Bo LU[1)], Guanyu LIU[1)], Kaiqiang JIN[1)]

[1)] Huzhou Vocational and Technical College, College of Mechatronics and Automotive Engineering, Huzhou / China
Tel:15849125756; E-mail: piweiqiang20171@163.com
DOI: https://doi.org/10.35633/inmateh-70-45

Keywords: *White tea, Image detection, YOLOv5, Deep learning, Algorithm*

ABSTRACT
The quality of white tea buds is the basis of the quality of finished tea, and sorting white tea buds is a laborious, time-consuming, and key process in the tea-making process. For intelligent detection of white tea buds, this study established the YOLOv5+BiFPN model based on YOLOv5 by adding a Bidirectional Feature Pyramid Network (BiFPN) structure to the neck part. By comparing the YOLOv5 and YOLOv3 through the ablation experiment, it was found that the YOLOv5+BiFPN model could extract the fine features of white tea buds more effectively, and the detection average precision for one bud and one leaf was 98.7% and mAP@0.5 was 96.85%. This study provides a method and means for white tea bud detection based on deep learning image detection, and provides an efficient, accurate, and intelligent bud detection model for high-quality white tea sorting.

摘要
白茶嫩芽品质是成茶品质的基础，白茶嫩芽分选是制茶工序中费工、费时且关键的工序。为了实现白茶嫩芽智能化检测任务，本文通过建立白茶鲜叶数据集，基于 YOLOv5 模型，在 Neck 加入双向特征金字塔网络（BiFPN）结构，得到了 YOLOv5+BiFPN 模型。通过烧蚀实验对比 YOLOv5 模型和 YOLOv3 模型，发现 YOLOv5+BiFPN 模型可以更有效的提取白茶嫩芽中的细小特征，对一芽一叶的检测精度达 98.7%，mAP@0.5 达 96.85%。本研究为白茶嫩芽检测提供了一种基于深度学习图像检测的方法与手段，为名优白茶分选提供了一种高效、准确、智能化的嫩芽检测模型。

INTRODUCTION
In terms of the size of its tea plantations and annual production, China ranks first in the world and is one of the largest producers and consumers of tea. White Leaf No. 1, commonly known as Anji White Tea, is a rare kind of Chinese tea tree that only produces white tea with albino leaves. It was discovered in Anji, Zhejiang, China, in the 1980s. The Anji White Tea has a huge consumer market because of its high amino acid content, the finished tea with white leaves and green veins, fragrant and mellow taste. Anji white tea has a planting area of more than two hundred and ten thousand acres and an annual output value of more than 3.4 billion. With a national planting area of about two hundred and seventy thousand hectares, it has been widely planted by Guizhou, Jiangxi, Hubei, Sichuan, and other provinces. It also has a high nutritional and economic value *(Wang et al., 2023)*.

The quality of white tea buds is the basis of the quality of the tea, and white tea bud sorting is an important part of the tea production process. The white tea production process is mainly divided into three steps: picking, withering, and drying. Among them, the tea picking and sorting process accounts for more than 60% of the total workload of tea making, and the cost is more than 50%. The quality of tea leaves is determined by the experience and attitude of the tea picker, which is uneven and requires manual secondary sorting. With the development of agricultural machinery and the increase in labor costs, mechanized tea harvesting technology and equipment are now becoming more mature and gradually applied *(Yi et al., 2020)*.

However, mechanized tea picking can mix a large number of different types of tea leaves and impurities, and the quality varies, so it cannot directly enter the next step of the tea production process, and still needs tea fresh leaves sorting. Therefore, there is an urgent need for an efficient, intelligent, accurate, and low-cost tea fresh leaf sorting technology and method.

With the gradual improvement of the quality of life and the upgrading of consumption, consumers' requirements for the quality of Anji white tea have become higher and higher, and there is a huge price gap between the price of famous Anji white tea and the price of bulk Anji white tea. In the past two decades, scholars developed the sorting process according to the physical characteristics of tea leaves, such as rolling sieve *(Wang et al., 2016)*, round sieve *(Zhao et al., 2014)*, wind sieve *(Zhang et al., 2014)*, etc., which can separate the debris of tea fresh leaves (incomplete leaves, leaf stalks, etc.), but it is difficult to carry out the precise bud grade division of white tea buds so that one bud and one leaf, a bud and two leaves, a bud and three leaves and other types of tea fresh leaves are mixed together, reducing the quality of tea, so that only artificial sorting methods can be used to produce famous tea or directly producing low-priced bulk tea.

In recent years, with the development of machine vision and deep learning technology, precision agriculture is gradually moving towards the era of intelligence. Machine vision has been widely used in the fields of tea bud detection, quality identification, category recognition, and pest control due to its non-destructive and highly automated characteristics. Traditional machine vision methods were first applied in tea classification research, such as applying a support vector machine to Wuyi rock tea fresh leaf classification *(Lin et al., 2019)*; then using a support vector machine to extract texture features combined with distance matrix further improved tea fresh leaf classification accuracy *(Mao et al., 2020)*.

With the outstanding performance of deep learning models in image detection, the YOLOv3 model was gradually applied in tea detection, and scholars used the YOLOv3 model to achieve better detection results for single bud targets (one bud and one leaf) in tea fresh leaves *(Yang et al., 2019; Li et al., 2021)*, but due to the Feature in the YOLOv3 model YOLOv5 is rapidly coming into the view of scholars because of its excellent detection speed and accuracy for small targets, and is currently applied to the detection on Cucumber *(Zhao et al., 2022)*, Green asparagus *(Hong et al., 2023)*, green pepper *(Nan et al., 2023)*, and other crops, but few studies have been reported on the detection of white tea buds.

MATERIALS AND METHODS

Dataset Production

White tea No. 1 producing region in Anji County, Zhejiang Province (30°28′N, 119°42′E), is where the fresh white tea leaves were gathered. The fresh white tea leaves were returned to the lab in sealed preservation bags and placed on the experimental table the same day they were harvested. A dataset of fresh white tea leaves was created by manually selecting 1200 photos of the test bed's fresh white tea leaves taken with a Canon 6D II camera.

The white tea fresh leaf dataset has four categories: one bud and one leaf, one bud and two leaves, one bud and three leaves, and the other (incomplete leaves and other buds). Table 1 lists the number of samples for each of the four categories. The image size and the category labeling of white tea fresh leaves using labeling, as shown in Figure 1.

Table 1

The sample size for the fresh white tea leaves dataset

category	Train	Test	Total
One bud and one leaf	422	106	528
One bud and two leaves	157	39	196
One bud and two leaves	262	66	328
Other	119	19	148

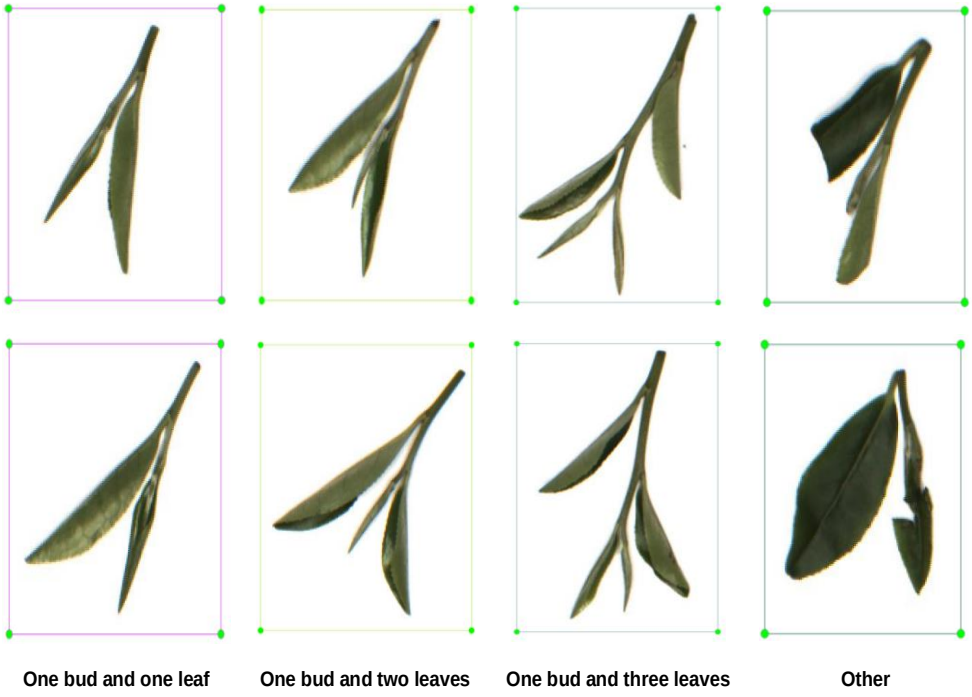

Fig. 1 - White tea fresh leaf category labelling

ALGORITHM PRINCIPLE

For the purpose of detecting white tea buds, this study will combine two original deep learning models—YOLOv3 and YOLOv5—and enhance the Neck layer on top of the YOLOv5 model. The core components of the original YOLOv3 and YOLOv5 models are Backbone, Neck, and Head, with Backbone retrieving picture data, the Neck doing feature fusion, and the Head performing prediction.

Darknet-53 serves as the YOLOv3 model's backbone. One DBL module, five Residual Blocks, and 53 convolutional layers make up Darknet-53. The DBL module is the tiniest one of them all in Darknet-53. In order to address the overfitting issue, the DBL module first convolves the image features before adding Batch Normalization processing and using the activation function Leaky Rectified Linear Unit; each Residual Block is made up of Zero Padding, DBL, and x Res Units. The DBL module uses convolution to complete the downsampling, and the Res Units follow suit to achieve jump connection using consecutive Conv (1*1) and Conv (3*3), which improves the gradient disappearance problem as the network depth increases. Darknet-53's final three Residual Block outputs are used to feed three different feature scales into the Neck Feature Pyramid Networks structure (FPN) for feature fusion and reconstruction, and the Head Convolution operation is then applied to the three feature maps that have been fused by the FPN structure (*Deng et al., 2021*). The structure of the YOLOv3 model is shown in Figure 2.

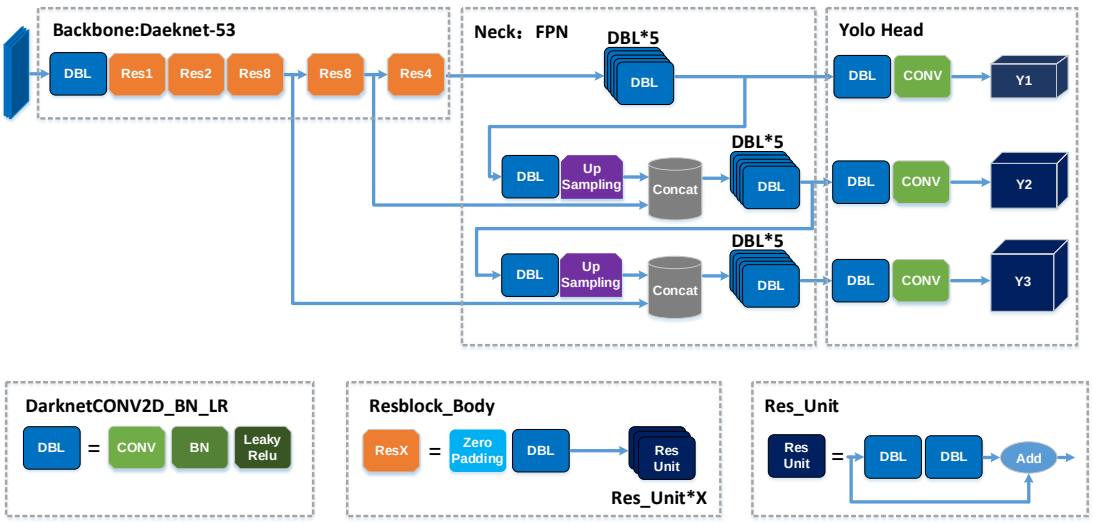

Fig. 2 - Model structure of YOLOv3

CSP Darknet-53, which includes the Focus module, DBL module, CSP module, and SPP module, serves as the skeleton of the YOLOv5 model. The Focus module divides the input picture into slices before entering the DBL module, the SCP1_X module splits the base layer mapping feature into two pieces, jump convolution is then used to fuse the features, and finally, the SPP module increases the ability of Backbone to extract features from MaxPool; to further enhance the feature fusion capabilities, the YOLOv5 model combines the SCP2_X module in Neck with the DBL module to construct the structure of Feature Pyramid Networks and Perceptual Adversarial Networks (FPN_PAN). Finally, the three feature maps from the fusion are applied to the Head. The structure of the YOLOv5 model is shown in Figure 3.

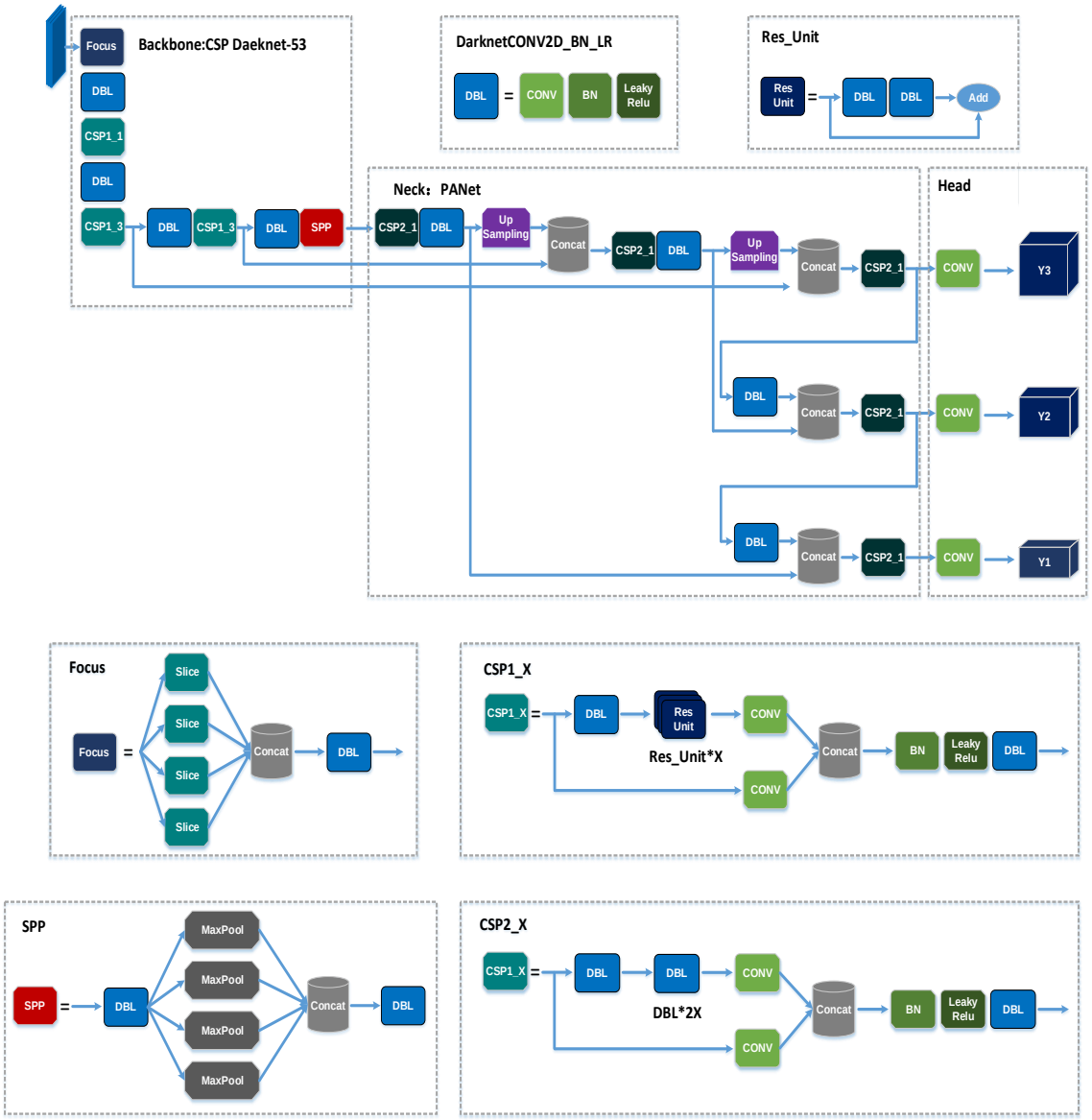

Fig. 3 – Model structure of YOLOv5

IMPROVED YOLOV5 MODEL

This study will improve the Neck portion of YOLOv5 and transform the FPN_PAN structure into a Bidirectional Feature Pyramid Network (BiFPN) structure (Qiu et al., 2023). The traditional FPN structure down-samples the image features before resampling them, which increases the feature level and makes it harder to detect small targets in the large feature layer. In contrast, the FPN_PAN structure adds a bottom-up channel to the FPN to fix the problem of one-way feature information transfer but does so at the expense of higher computational costs. By adding learning weights, the BiFPN structure outperforms the FPN_PAN structure by learning the relative weights of various input features and performing top-down and bottom-up feature fusion with fewer parameters. The schematic diagram of the three feature pyramid structures is shown in Figure 4, and the structure of the improved YOLOv5-BiFPN model structure is shown in Figure 5.

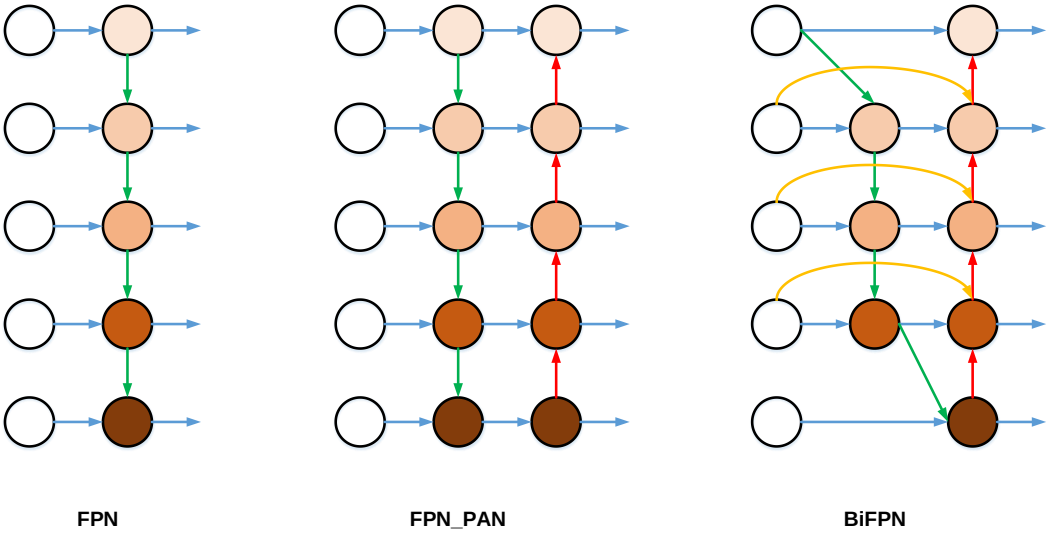

Fig. 4 – The structure of FPN, FPN_PAN and BiFPN module

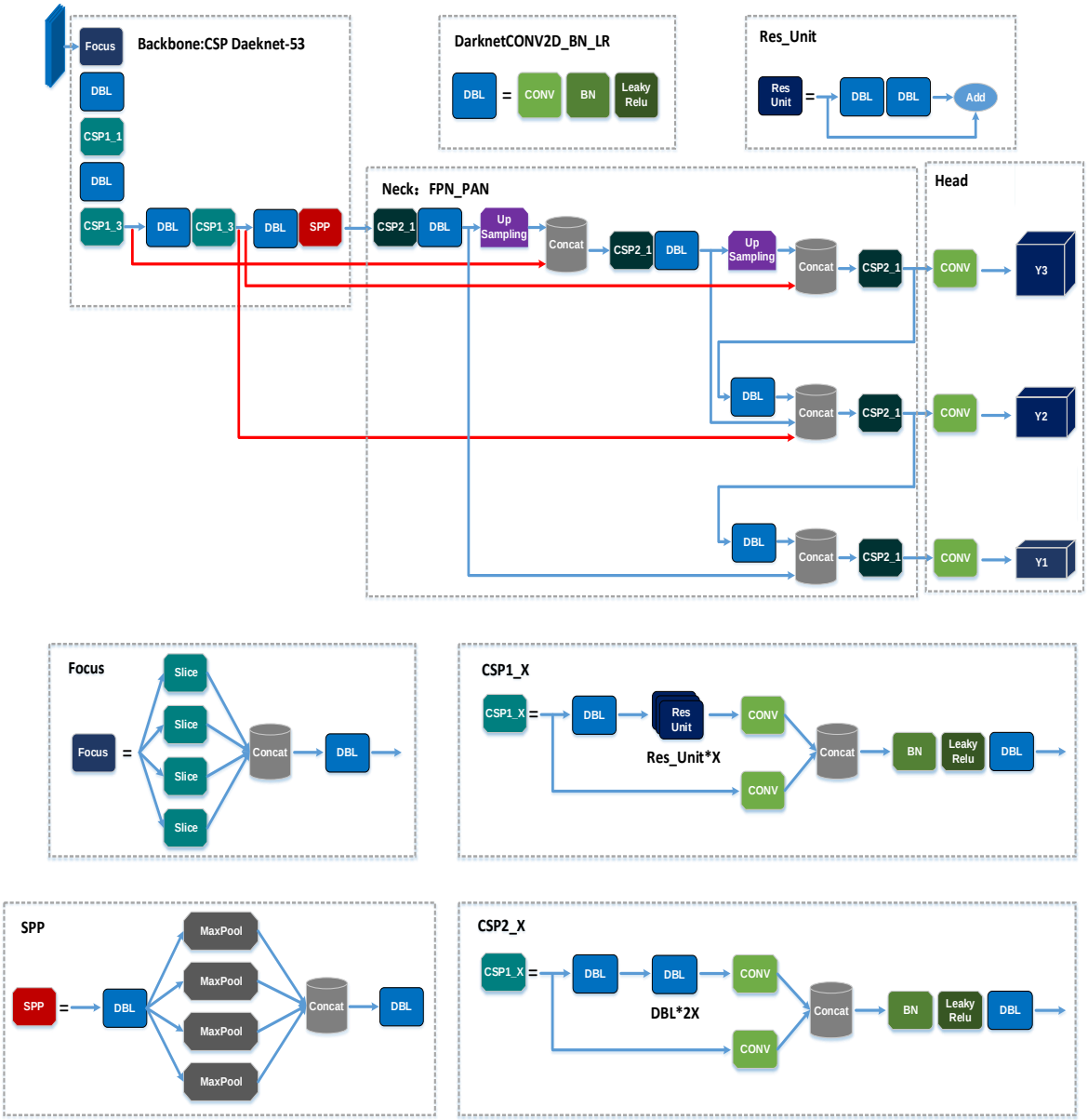

Fig. 5 – Model structure of improved YOLOv5-BiFPN

TEST ENVIRONMENT

Test environment configuration: Programming language Python3.7, deep learning framework Pytorch, graphics card Nvidia GeForce GTX1660 with 6GB video memory, processor Inter Core i7-9700K 3.60GHz octa-core, memory 32GB, and relevant libraries such as Torch, Torchvision, Opencv, Numpy, Scipy, Pillow, Matplotlib, Tqdm, H5py, etc.

NETWORK TRAINING

With 960 photos for the training dataset and 240 images for the validation dataset, three deep learning models—YOLOv3, YOLOv5, and YOLOv5-BiFPN—were trained on a graphics processing unit (GPU). The image sizes were then adjusted to 640 x 640. A total of 300 epochs were trained using Stochastic Gradient Descent (SGD), with an initial learning rate of 0.001 and a reduction to 0.0001 at the 200th epoch with a Batch Size of 4. The training loss rate curve of the three models is shown in Figure 6.

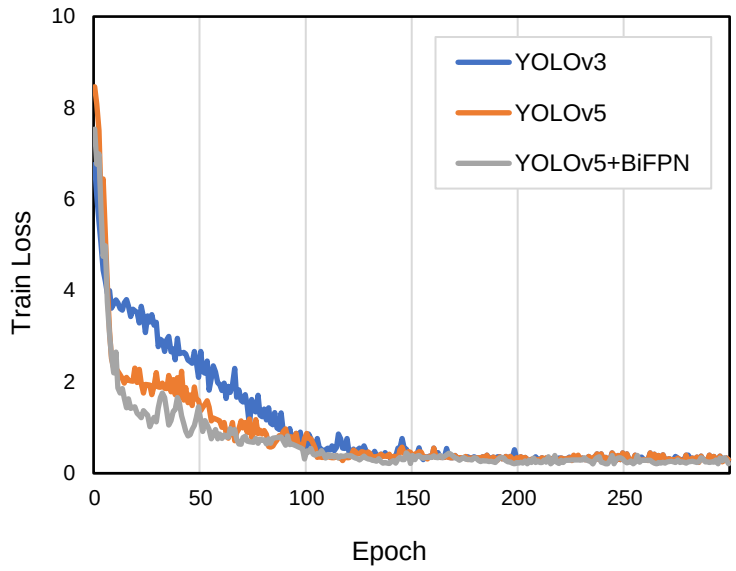

Fig. 6 - The training loss rate curve of the three models

Figure 6 shows that all three models produce positive training results. YOLOv3 has the lowest initial loss, followed by YOLOv5+BiFPN and YOLOv5 has the highest initial loss rate. As Epoch rises, the training loss of the three models eventually falls and stabilizes. Among them, YOLOv5+BiFPN converges the quickest and eventually converges between 0.20-0.24; YOLOv5 converges the second-fastest and eventually converges between 0.23-0.27; while YOLOv3 converges the slowest and ultimately converges between 0.26-0.29.

Evaluation Indicators

In this study, Recall (R), Average Precision (AP), and mean Average Precision (mAP) will be used as target detection evaluation indexes for white tea buds.

The precision and recall are respectively expressed by Equations (1) and (2):

$$Precision = \frac{TP}{TP+FP} \quad (1)$$

$$Recall = \frac{TP}{TP+FN} \quad (2)$$

where: TP (true positives) represents the number of positive samples correctly predicted by the model, FP (false positives) represents the number of positive samples incorrectly predicted by the model, and FN (false negatives) represents the number of negative samples incorrectly predicted by the model (*Li et al., 2022*).

AP and mAP are defined by Equations (3) and (4),

$$AP = \int_0^1 P(R)dR \quad (3)$$

$$mAP = \frac{\sum_{i=1}^{N} AP_i}{N} \quad (4)$$

where:

P represents Precision, AP_i represents the i-th category of target detection average precision, AP_i represents the average precision of the target detection for the i-th category, and N represents for the category of markers.

RESULTS

Comparison of Actual Detection Effects

In order to verify the actual detection effect of the YOLOv5+BiFPN model, the YOLOv5 model and the YOLOv3 model were used to test the images of the white tea fresh leaf dataset with four types of samples randomly selected, and the detection results are shown in Figure 7.

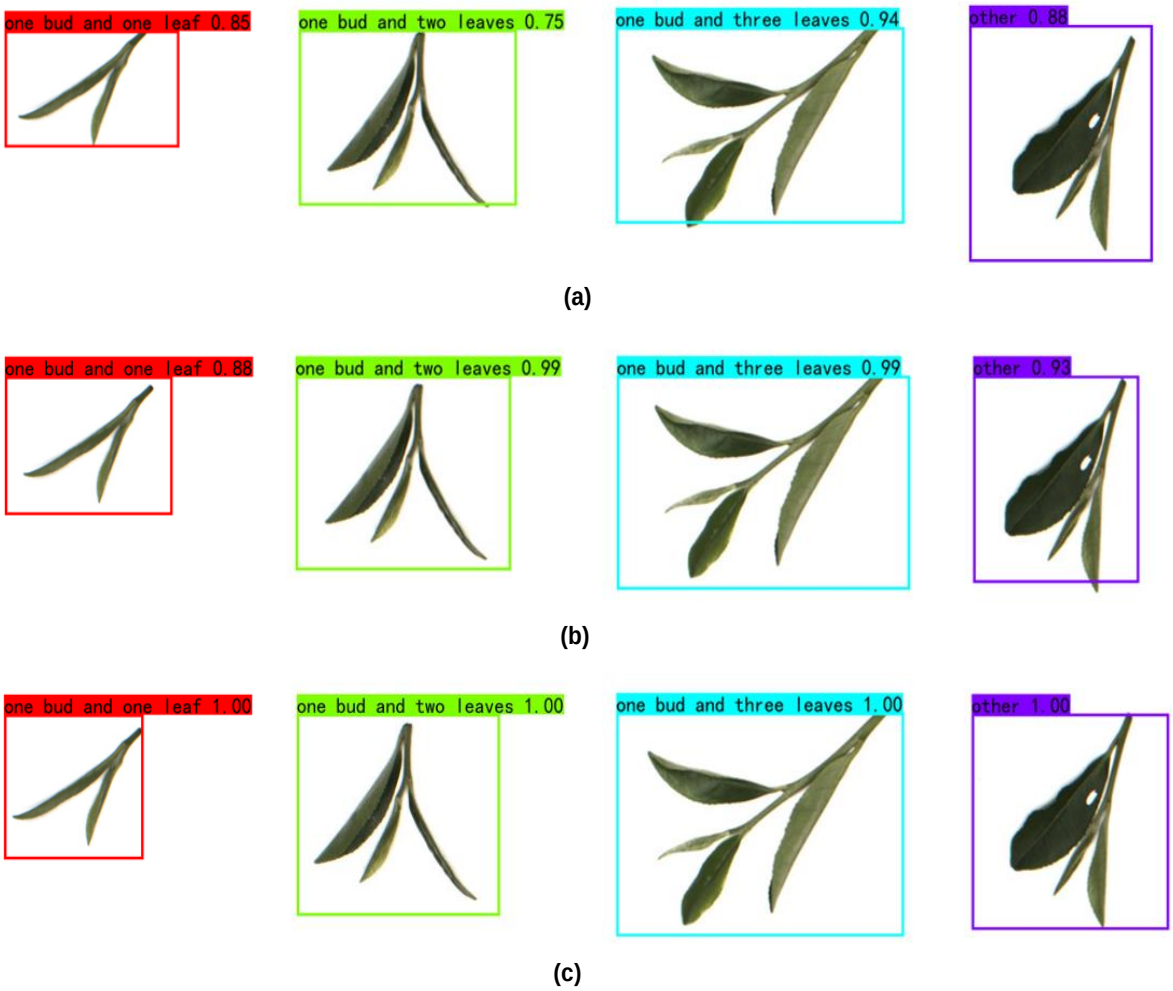

Fig. 7 - Comparison of detection effects of three models on white tea fresh leaves dataset. (a) YOLOv3 model; (b) YOLOv5 model; (c) YOLOv5-BiFPN model

It can be seen from Figure 7 that the improved YOLOv5+BiFPN model has the highest confidence score and the best overall prediction box, but there is still room for optimizing the prediction box for others; The YOLOv5 model has the next best confidence score and the prediction box is better overall, but inaccurate for Other's prediction box; The YOLOv3 model had the lowest confidence score, the prediction box was not effective overall, the prediction box for one bud and two leaves, one bud and three leaves was inaccurate, and there was still room for optimization of the prediction box for other.

Comparison of Different Object Detection Models

In this study, the effectiveness of the improved model was verified by conducting ablation experiments on three models, and the results were compared on the same test data, and the experimental results are shown in Table 2.

Table 2

Comparison of detection performance for different algorithms

Model	AP				mAP@0.5
	one bud and one leaf	one bud and two leaves	one bud and three leaves	other	
YOLOv3	92.3%	89.6%	90.1%	86.4%	89.60%
YOLOv5	95.6%	92.3%	93.3%	89.9%	92.78%
YOLOv5+BiFPN	98.7%	96.4%	97.7%	94.6%	96.85%

Table 2 shows that the improved YOLOv5+BiFPN model has the highest average detection precision for all four types of buds in the white tea fresh leaf dataset, with the highest average detection precision of 98.7% for the one bud and one leaf category. mAP@0.5 was 96.85%. The average detection precision of all three models for the other class was the lowest among the four classes, which shows that there is still some difficulty for the model to detect the fine features in the bud incomplete leaves of the other class. The YOLOv5+BiFPN model improved the average detection precision of the other class by 4.7% compared to the YOLOv5 model and 8.2% compared to the YOLOv3 model, and combined with the YOLOv5+BiFPN model, the YOLOv5+BiFPN model improved the average detection precision of the other class by 4.7% compared to the YOLOv5 model. BiFPN model for one bud and one leaf class shows that the improved YOLOv5+BiFPN model has the advantage of extracting small features of white tea buds.

CONCLUSIONS

In this paper, the YOLOv5+BiFPN model was improved based on the YOLOv5 model, realized the high-precision detection of white tea buds in the established white tea fresh leaf dataset. The main results of this study are as follows:

1) The white tea fresh leaf dataset and YOLOv5+BiFPN white tea buds detection model were established, and the detection average precision of four categories of buds in the white tea fresh leaf dataset was 98.7%, 96.4%, 97.7%, and 94.6%, respectively. The mAP@0.5 was 96.85%.

2) The ablation experiment analysis showed that the YOLOv5+BiFPN white tea bud detection model improved mAP@0.5 with 4.07% higher than the YOLOv5 model and 7.25% higher than the YOLOv3 model.

3) The addition of the Bidirectional Feature Pyramid Network structure to the Neck in the YOLOv5 model can extract the small features in the fresh leaves of white tea more effectively, and its dual-channel and multi-scale feature fusion has more potential for the detection of buds such as one bud and one leaf and other.

In this study, the improved YOLOv5+BiFPN model is effectively combined with white tea fresh leaf images to provide a method and means for white tea bud detection based on deep learning image detection. The BiFPN structure can effectively improve the model's ability to extract the small features of white tea buds, providing an efficient, accurate, and intelligent buds detection model for the sorting of famous white tea.

ACKNOWLEDGEMENT

This work was supported by the National Natural Science Foundation of China (52105283), Huzhou Public Welfare Application Research Project (2020GZ01), Huzhou Natural Science Foundation Project (2022YZ54), Huzhou Vocational and Technical College Application of Special Public Welfare Technology for High-Level Talents (2022022GY08) and Teacher Professional Development Project for Domestic Visiting Scholars in Universities (FX2022113).

REFERENCES

[1] Dario L., Oscar P., Ruben U., et al., (2021), Cost-Performance Evaluation of a Recognition Service of Livestock Activity Using Aerial Images. *Remote Sensing*, 13(12), 2318. https://doi.org/10.3390/rs13122318

[2] Deng X., Yan X., Hou Y., et al., (2021), Detection of Behavior and Posture of Sheep Based on Yolov3. *INMATEH Agricultural Engineering*, 64(02), 457-466. https://doi.org/10.35633/inmateh-64-45

[3] Hong W., Ma Z., Ye B., et al., (2023), Detection of Green Asparagus in Complex Environments Based on the Improved YOLOv5 Algorithm. *Sensors*, 23, 1562. Sensors 2023, 23, 1562. https://doi.org/10.3390/s23031562
[4] Li X., Wang C., Ju H., et al., (2022), Surface Defect Detection Model for Aero-Engine Components Based on Improved YOLOv5.*Applied Sciences*, 12(14), 7235. https://doi.org/10.3390/app12147235
[5] Li Y., He L., Jia J., et al., (2021), In-field tea bud detection and 3D localization using an RGB-D camera. *Computers and Electronics in Agriculture*, 185: 106149. https://doi:10.1016/j.compag.2021.106149
[6] Lin L., Li C., Yang S., et al., (2019), Automated classification of Wuyi rock tealeaves based on support vector machine. *Concurrency and Computation practice & Experience*, 31(23):3.
[7] Mao YT., Huang Y., Wen XG., et al., (2020), Research on classification of fresh tea based on multiple features and multiple classifiers. *Journal of Chinese Agricultural Mechanization*, 41(12), 75-83. https://doi:10.13733/j.jcam.issn.2095-5553.2020.12.014
[8] Nan Y., Zhang H., Zeng Y., et al., (2023), Detection of Green Asparagus in Complex Environments Based on the Improved YOLOv5 Algorithm. *Computers and Electronics in Agriculture*, 23, 1562. Sensors 2023, 205, 107536. https://doi.org/10.1016/j.compag.2022.107563
[9] Qiu M., Huang L., Tang B., et al., (2023), Bridge detection method for HSRRSIs based on YOLOv5 with a decoupled head. *International Journal of Digital Earth*, 16(01), 113-129. https://doi.org/10.1080/17538947.2022.2163514
[10] Wang C., Zhang T., Zheng Y., et al., (2016), Simulation Study on the Screening of the Reciprocating Roller Screen with Two Degrees of Freedom for Tea. *Journal of Tea Science*, 36(06), 613-620. https://doi:10.13305/j.cnki.jts.2016.06.008
[11] Wang Z., Li S., Jin Z., et al., (2023), Accurate prediction technique of meteorological index relevant to frost damage for Anji white tea based on current planting zone. *Chinese Journal of Ecology*, 42(04), 1018-1024. https://doi:10.13292/j.1000-4890.202304.023
[12] Yang H., Chen L., Chen M., et al., (2019), Tender tea buds recognition and positioning for picking robot using improved YOLO-V3 model. *IEEE Access*, 23(11):180998-181011. https://doi:10.1109/ACCESS.2019.2958614
[13] Yi W., Cheng F., Qiu Y., et al., (2020), Research status and development trend of single tea-picking machine. *Journal of Chinese Agricultural Mechanization*, 41(11), 33-38. https://doi:10.13733/j.jcam.issn.2095-5553.2020.11.006
[14] Yuan H., Hua J., Deng Y., et al., (2016), Optimization of grading and classification technology for machine-picking leaves based on YJY-2 type classifier. *Transactions of the Chinese Society of Agricultural Engineering*, 32(06), 276-282. https://doi:10.11975/j.issn.1002-6819.2016.06.038
[15] Zhao F., Zhang J., Zhang N., et al., (2022), Detection of Cucurbits' Fruits Based on Deep Learning. *INMATEH Agricultural Engineering*, 66(01), 231-330. https://doi.org/10.35633/inmateh-66-32
[16] Zhang H., Xiao H., Mei S., et al., (2014), Status Quo and Future of Tea Sorting Technology. *Journal of Agricultural Engineering*, 04(05), 59-63. https://doi:10.13733/j.jcam.issn.2095-5553.2020.11.006
[17] Zhao Z., Zhang L., Wang X., et al., (2014), Condition Analysis and Numerical Simulation of Tea Plane Circular Sieve. *Journal of Tea Science*, 34(01), 1-8. https://doi:10.13305/j.cnki.jts.2014.01.001

OPTIMIZATION OF DRYING PARAMETERS FOR DESICCATED COCONUT POWDER USING CENTRAL COMPOSITE DESIGN
/
OPTIMASI PARAMETER PENGERINGAN KELAPA PARUT KERING MENGGUNAKAN DESAIN KOMPOSIT SENTRAL

Muhammad Nashir EFFENDY[1)], Siti NURHASANAH[2)], Asri WIDYASANTI[1*)]

[1)] Department of Agricultural Engineering and Biosystems, Faculty of Agro-Industrial Technology, Universitas Padjadjaran, Jln. Raya Bandung-Sumedang km. 21 Jatinangor, Sumedang, West Java 45363, INDONESIA

[2)] Department of Food Industrial Technology, Faculty of Agro-Industrial Technology, Universitas Padjadjaran, Jln. Raya Bandung-Sumedang km. 21 Jatinangor, Sumedang, West Java 45363, INDONESIA

**E-mail*: *asri.widyasanti@unpad.ac.id*

DOI: https://doi.org/10.35633/inmateh-70-46

Keywords: *Desiccated Coconut, Drying, Optimization, RSM*

ABSTRACT

Desiccated Coconut (DC) is a product rich in fat, protein, carbohydrates and fiber. It is widely used as an additive for the snack industry. As a potential food additive product, every process needs to be considered to produce a good quality DC. The effort to maintain the quality of DC is to optimize the main process of making DC, namely the drying process. In several studies, the drying condition of DC was carried out differently, that is why an optimization process on DC drying is needed. This study aims to determine the temperature and drying time combination that produces DC with the optimum moisture content, fat content, and yield. The drying process used a food dehydrator with a temperature combination of 50°C to 70°C and a time of 2 to 4 hours. The research method used was a laboratory experimental method with Response Surface Methodology (RSM) optimization using Central Composite Design (CCD). It was presented that the optimum drying conditions given by RSM were obtained by drying at 70°C for 2 hours. The results obtained from the validation of a water content of 1.279% wet basis (wb), a fat content of 64.855% wb, and a yield of 42.363%, were following CODEX STAN 177-1991. Based on this study, it can be concluded that the combination of temperature and drying time affects moisture content, fat content, and DC yield.

ABSTRAK

Kelapa Kering (DC) merupakan produk yang kaya akan lemak, protein, karbohidrat, dan serat. Produk ini banyak digunakan sebagai bahan aditif untuk industri makanan ringan. Sebagai produk bahan tambahan makanan yang potensial, setiap proses perlu diperhatikan untuk menghasilkan DC yang berkualitas baik. Upaya menjaga kualitas DC adalah dengan mengoptimalkan proses utama pembuatan DC yaitu proses pengeringan. Terdapat perbedaan kondisi pengeringan terbaik pada beberapa penelitian sebelumnya, sehingga perlu dilakukan optimasi proses pengeringan DC. Penelitian ini bertujuan untuk menentukan kombinasi suhu dan waktu pengeringan yang menghasilkan DC dengan kadar air, kadar lemak, dan rendemen yang optimum. Proses pengeringan menggunakan food dehydrator dengan kombinasi suhu 50°C hingga 70°C dan waktu 2 hingga 4 jam. Metode penelitian yang digunakan adalah metode eksperimen laboratorium dengan optimasi Response Surface Methodology (RSM) menggunakan Central Composite Design (CCD). Dipaparkan bahwa kondisi pengeringan optimum yang diberikan oleh RSM diperoleh dengan pengeringan pada suhu 70°C selama 2 jam. Hasil yang diperoleh dari validasi kadar air 1,279% basis basah, kadar lemak 64,855% basis basah, dan rendemen 42,363% yang sudah sesuai dengan CODEX STAN 177-1991. Berdasarkan penelitian ini dapat disimpulkan bahwa kombinasi suhu dan waktu pengeringan berpengaruh terhadap kadar air, kadar lemak, dan rendemen DC.

INTRODUCTION

The coconut plant *(Cocos nucifera)* is a plant that belongs to the Palmae family and is a tropical plant. Coconut plants are believed to be native plants from the Indo-Malaysia region or originating from the Southeast Asian region so coconut plants are plants that are often found in Indonesia (*Chan and Elevitch, 2006)*. In 2018, Indonesia managed to export coconuts of more than 1.3 billion USD or the equivalent of 2.17 million tons and became one of the sectors contributing to the country's foreign exchange (*Ditjenbun, 2021*).

In addition, in 2020 according to data taken from (*Statista, 2022*), Indonesia is one of the largest coconut-producing countries in the world. Directorate General of Estate Crops also declared that Indonesia has a total area of coconut plantations reaching 3,401,893 Ha and many of them are scattered in coastal areas

Coconut is also known as the "tree of life" because coconut has an important role both from a socio-cultural and economic perspective (*Lo et al.,* 1997). Almost every part of the coconut plant has benefits for humans. One of the coconut products that is currently being developed is Desiccated Coconut (DC). DC is grated old coconut meat that is dried to a certain moisture content to extend shelf life (*Heathcock and Chapman*, *1983)*. This dry-grated coconut is in the form of granules with various levels of fineness, this form will facilitate packaging and storage. The more diverse the snack food industry such as bread, biscuits, and other processed foods, the need for grated coconut is also increasing. Adding dry-grated coconut to biscuit products will increase the levels of fat, protein, carbohydrates, and fiber needed by the body to add nutritional value to these biscuits (*Lubis et al., 2014*).

As an additive in various food products, DC is a product that has a high fat content. Therefore, fat content is generally used as an indicator to determine the quality of desiccated coconut because it is related to nutritional value and shelf life (*Yuvita et al.,* 2022). The water content in DC is also related to the quality of the product. According to Chen *(Chen, 201*9), there is a linear relationship between water content and water activity so there is a tendency that the higher the water content, the higher the a_w value. The water content will determine the amount of water in the material, while the water activity describes how the water content in the material will react with microorganisms. The higher the activity water content will increase microbial activity which can shorten the shelf life of the DC (*Serin et al., 2*018). The effort to maintain the quality of DC is to optimize the main process of making DC, namely the drying process. The main purpose of drying food products is to reduce the water content to a certain moisture content, allowing longer storage (*Yahya et al., 2020*). Temperature and drying time have a significant effect on the quality of the DC produced because the drying process will affect the moisture content, fat content, color, and aroma of the product (*Fennemas et al., 2017*).

The difference in optimal conditions for DC drying results in the need for an optimization process carried out for DC drying to produce products with quality according to applicable standards but with the most efficient time. The study was designed to determine the optimum drying conditions for DC manufacturing by the effects of temperature and drying time using the Response Surface Methodology (RSM). RSM was chosen because this method does not require large amounts of experimental data and does not take a long time to determine the optimum conditions for a process *(Majdi et al., 2019*). Data processing with RSM is done with the help of Design Expert version 13 software. In this study, there are two factors: temperature expressed by X_1, and drying time expressed by X_2. The lower and upper temperature limits used are 50°C and 70°C respectively. The lower and upper limits of drying time used were 2 hours and 4 hours, respectively. The main parameters to be analyzed in this study are moisture content, fat content, and partial drying yield. The research objective was to identify the temperature and drying time combination that yields DC with the best possible yield, fat content, and moisture content.

MATERIALS AND METHODS

1. Instrumentation

The tools used in this research were a coconut grater, sprayer, freezer, blanching tool, food dehydrator, Tyler sieve, mesh filter number 14, cup, oven, soxhlet apparatus set, and analytical balance. The food dehydrator used was the PAPALOLO Drying Stainless Steel Food Dehydrator Machine 10 Trays SS-10H brand. This tool has dimensions of 35x40x43 cm with a power consumption of 800 W. This tool has a temperature setting between 30-90℃ and a time setting between 30 minutes to 24 hours. There were 10 trays with a tray size of 30x28 cm.

2. Raw Material

The main raw material used in this research was old coconut with a hybrid variety obtained from the Bandung Gedebage Market, where the coconut was supplied from the Cipatujah, Tasikmalaya (West Java, Indonesia). Another material used was Natrium Metabisulfite ($Na_2S_2O_5$).

3. Method

The method used in this study was a laboratory experimental method where the number and combination of treatments (running) will be obtained from the design expert application version 13 using the DoE (Design of Experiment) design with the central composite design (CCD) type.

There were two numerical independent variables used in this research. The first independent variable used in this analysis was the drying temperature with the selected lower limit of 50℃ and the selected upper limit of 70℃. The second independent variable used was the length of drying time with the selected lower limit of 2 hours and the selected upper limit of 4 hours. The stages in determining the number of treatments (runs) in this study were 13 runs. The combination of these treatments was obtained from a randomized experimental design expert design.

4. The Process of Drying Desiccated Coconut with A Food Dehydrator

Before the drying process, the preparation of raw materials is made by choosing old coconut. Then the white meat preparation process and the grating process are carried out. Then, the coconut will undergo a process of administering 50 ppm of Natrium Metabisulfite ($Na_2S_2O_5$). The addition of Natrium metabisulfite is given as much as 0.0005% of the coconut mass used *(Mohpraman & Siriphanich, 2012*). The use of sodium metabisulfite can be anti-browning because the browning reaction catalyzed by the phenolase enzyme can be inhibited by the sulfite content. The sulfite content can also prevent the formation of *5 hydroxyl methyl furfural* compounds from D-glucose which can cause browning reactions (*Suryani et al., 2*016). Grated coconut is then blanched with steam at 90℃ for 5 minutes (Siriwongwilaichat et al., 2014). This blanching process serves to deactivate unwanted enzymes that can change the flavor, texture, and color. In addition, for the processing of materials to be dried, the blanching process will speed up the drying process because the cells will be made permeable to water movement (*Waisundara et a*l., 2007). Drying grated coconut using the drying conditions according to the design. 300 grams of sample is dried per run in a thin layer (S*angamithra et al*., 2013) and the process of exchanging tray positions is carried out every half of the drying process.

5. Response Measurement

DC moisture content testing was carried out using the thermogravimetric method (*AOAC, 2005*). The use of the thermogravimetry method also refers to research by Ogawa (O*gawa et al., 2012)*.

The equation for calculating the water content is as follows:

$$MC=\frac{b-(c-a)}{b}x100\% \quad (1)$$

where:

MC is the moisture content (% wb)
a - weight of empty cup (g)
b - mass of wet sample (g)
c - weight of the cup with the sample that has been dried

Measurement of fat content refers to SNI 01-2891-1992 regarding the method of testing food and beverages and refers *(Hewavitharana et al., 202*0) where measuring fat content on DC using the Soxhlet method. The Soxhlet method is a traditional technique used for extracting lipids in foods.

The equation for calculating the fat content is as follows:

$$FC=\frac{W_2-W_1}{W_{fc}}\ x\ 100\% \quad (2)$$

where:

FC is the fat content (%b/b)
W_{fc} - sample weight for measuring fat content (g)
W_1 - weight of fat before extraction (g)
W_2 - weight of fat desiccated coconut after extraction (g)

To find out the yield of drying is done with the following equation:

$$Yield\,(\%)=\frac{M_b}{M_a}x\ 100\% \quad (3)$$

where:

Yield is the partial drying yield (%)
M_b - mass of desiccated coconut (g)
M_a - mass of grated coconut (g)

6. Data Optimization

From the response measurement results obtained, the data was inputted and processed into the RSM program. Then the response target was determined based on the quality standard for desiccated coconut, namely CODEX STAN 177-1991 which was correlated with the results of measurements of water content, fat content, and yield. All response data were then processed using Design Expert®13 software. The results obtained were then translated into an equation model of the response function to the selected independent variables. Model selection analysis was carried out using the ANOVA test, namely model significance value, inappropriateness test, coefficient of determination (predicted R-squared, adjusted R-squared), and VIFs test using the Design Expert ® 13 program (*Pan et al., 2010*).

RESULTS

1. Independent Variables and Responses

A total of 13 samples with different temperature and drying time treatments have been tested and obtained the responses as shown in Table 1. These responses determine the model that can be used to obtain the optimum combination of temperature and drying time to produce DC which has a moisture content, fat content, and yield drying according to the specified criteria.

Table 1

Central Composite Design: Independent Variables and Responses

Run	Factor 1 A: Temperature (℃)	Factor 2 B: Drying time (Hours)	Response 1 Yield (%)	Response 2 Water Content (%wb)	Response 3 Fat Content (%wb)
1	70	2	42.448	1.196	64.839
2	45.857	3	44.202	3.593	63.673
3	60	4.414	40.020	1.382	64.044
4	60	3	42.272	1.878	64.152
5	60	3	42.193	2.075	63.247
6	50	4	42.036	2.411	63.479
7	60	3	42.251	1.515	63.321
8	60	3	41.152	1.293	64.099
9	50	2	43.260	2.677	63.196
10	74.142	3	42.051	1.148	64.456
11	70	4	40.352	1.129	63.688
12	60	3	42.183	1.825	63.932
13	60	1.585	42.053	3.195	63.994

Based on Table 1, it can be seen that the drying yield ranges from 40.020–44.202%. The difference in the yield values obtained indicates that the drying time and temperature affect the resulting yield values (Tontul a*nd Topuz, 2017)*. The higher the drying air temperature and the longer the drying time tends to have a lower yield value. The smallest yield is obtained from run 3 and the largest yield is obtained from run 2. The standard deviation value at 5 center points is 0.482, this shows that the deviation at the center point is quite low and the data does not have wide variations. Lower yield values are caused by more water content being evaporated. Based on Table 1 it can be seen that the drying water content ranges from 1–3.5%. The higher the drying air temperature and the longer the drying time tends to have a lower moisture content value. This is under Toledo (*Toledo et al., 20*07), that the higher the temperature and the longer the drying time given, can have a very large influence on the speed of water transfer so that the water content in the material will be lower. The smallest water content value is obtained from run 11 and the largest water content is obtained from run 2. The standard deviation value at the center point is 0.3108, this indicates a small deviation or the variation at the center point is not wide. Each treatment sample met the water content criteria specified by CODEX STAN 177-1991, namely a water content of less than ±3%.

Based on Table 1 it can be seen that the drying fat content ranges from 61–64%. The results obtained in this study the smallest fat content value was obtained from run 9 with drying conditions of 50℃ for 2 hours and the highest fat content was obtained from run 1 with drying conditions of 70℃ for 2 hours. The standard deviation value at 5 center points is 0.370, this indicates a small deviation or variation at a small center point. According to (*Zouari et al.,* 2019) an increase in drying time and temperature will result in an increase in the fat content on the wet basis due to a decrease in the water content on the wet basis. Each treatment sample met the fat content criteria specified by CODEX STAN 177-1991, namely fat content of more than 60%.

2. Mathematical Model Analysis of Response

The first step of RSM is to find the right approximation function to see the relationship between response Y and factor X through the first-order model. If the form of the relationship is quadratic, then for the function approach a higher-degree polynomial is used second-order model *(Erbay & Icier, 20*09). The relationship between the independent variables (drying temperature and drying time) to the dependent variable or response (moisture content, fat content, and yield) can be described by the linear, 2FI, and quadratic models which can be seen in Table 2. After the mathematical model of the response has been determined, an analysis of the model obtained is carried out. If the most suitable surface is found through a sufficient approximation, then the results of this analysis will be close to the actual function. The fit between the data distribution and the model is shown by the results ANOVA test, namely, model significance value, lack of fit test, coefficient of determination (predicted R-squared, adjusted R-squared), and VIFs test using the Design Expert ® 13 programs (*Pan et al., 2*010).

Table 2

Mathematical Model Analysis of Response

Response	Mathematical Models	F-Value	p-Value	Lack of Fit	R^2	Adj R^2 Model	Pred R^2 Model	Adeq Precision	VIFs each variable
Yield (%)	Quadratic	0.0027	0.9566	0.9566	0.9299	0.8798	0.8636	16.258	<10
Water Content (%wb)	Linear	0.001	0.1749	0.1749	0.7493	0.6991	0.5322	10.691	<10
Fat Content (%wb)	2FI	0.0749	0.8216	0.8216	0.5966	0.4622	0.2836	7.374	<10

The first analysis is the recommendation of the model used to determine the effect of the variables on the response. Based on Table 2, the model analysis values for the yield response are obtained using the quadratic model with an F-value of 0.0027, lack of fit 0.9566, adjusted R^2 0.8798, and predicted R^2 0.8636. Model analysis for moisture content response uses a linear model as suggested by the design expert application which can be seen in Table 2 with an F-value of 0.001, lack of fit 0.1749, adjusted R^2 0.811,6 and predicted R^2 0.3814. Meanwhile, the model analysis for response to fat content used the 2FI model as suggested by the design expert application with an F-value of 0.0749, lack of fit 0.8216, adjusted R^2 0.4622, and predicted R^2 0.2836. The selected model for each response is used based on the model with a significant F-value, in significant lack of fit, and the highest R^2 value. The Lack of fit F-value obtained (P> 0.05) indicates that it is not significant relative to the pure error. There is a 95.66% possibility that the Lack of fit F-value of this magnitude can occur due to noise. A significant model and a non-significant Lack of fit are good model condition because it shows the suitability of the response data. This gives a good picture of the fit of the model with the response. In other words, the model was fit with the responses data collected. With the fulfilment of these conditions, each response can be explained properly by the model and is suitable for describing the response data (*Karimifard & Alavi Mogha*ddam, *2018*).

The R^2 obtained in this study for the yield response was 0.9299. This value is quite good because the value is close to 1. The smaller R^2 value indicates a large deviation in the data or an error in the study (*Hadiyanto, 2*016). This value indicates that the data that can be described by the model is 92.99% and the temperature and drying time factors affect the response by 92.99% and 7.01% are influenced by other factors not examined. Meanwhile, for the response to water content, based on Table 2, it can be seen that the R^2 value obtained in this study was 0.7493. This value is quite low compared to the yield response value. This value indicates that the data that can be described by the model is 74.93% and it can be interpreted that the temperature and drying time factors affect the response by 74.93% and 25.07% are influenced by other factors not examined. As for the response to fat content, based on Table 2, it can be seen that the R^2 value obtained in this study was 0.5966. This value is quite low compared to the response value of the yield and water content. This value indicates that the data that can be described by the model is 59.66% and it can be interpreted that the temperature and drying time factors affect the response by 59.66% and 40.34% are influenced by other factors not examined.

The response model for drying yield, moisture content, and fat content stated a reasonable agreement, where the resulting model met the criteria. These criteria are the difference between Adj R-squared and Pred R squared less than 0.2 and Adequate Precision > 4.

The test results show that the equation formed by Design Expert ® 13 to predict the response of drying yield, moisture content, and fat content indicates that the model can be accepted and used in the design space. Based on Table 2 it can be seen that the model is good because it has a difference between adjusted R^2 and predicted R^2 below 0.2. The Adequate precision value for each response also shows a value greater than 4. Adequate precision measures the ratio of signal to noise. A good model is a model that has a ratio greater than 4 so that the model can be accepted and used in the design space (*Nguyen Tram Anh et al., 2021*).

Based on Table 2, it can be seen that the VIF value of each factor and the response has shown a value of <10. The VIF value is a factor that can determine how much the variance of the regression estimator coefficients increases compared to the orthogonal variables if they are connected linearly. The VIF value is used to test whether the non-multicollinearity assumption is met. The greater the correlation between the independent variables, the greater the VIF value. If the VIF value of the variable exceeds 10, it can be assumed that multicollinearity occurs. Multicollinearity symptoms will result in a regression model that is biased, unstable, and possibly far from the predictive value *(Daoud, 2018)*.

3. Mathematical Model of Each Response

3.1. Yield Response Model:

RSM equation or model for process optimization DC powder drying to yield response is shown in equation 4:

$$Yield\ (\%) = +59.627 - 0.656(A) + 3.540(B) - 0.021(AB) + 0.005(A^2) - 0.500(B^2) \quad (4)$$

It can be seen that the quadratic model shows that the yield response is influenced by drying temperature and drying time, as well as the quadratic interaction between the two. The influence exerted by time is greater on yield than that of drying temperature. This can be seen from coefficient B which has a greater value of 3.54 when compared to coefficient A with a value of 0.656. This equation also illustrates that the drying temperature has an inverse effect on the response. This is indicated by a negative (-) constant. In contrast to time, which has a directly proportional effect on the response indicated by a constant positive (+) value.

In Figure 1a, a visual appearance of the yield results is presented which is marked by color differences. The bluer the area, the lower the yield, while the redder the area, the higher the yield. In Figure 1b, the shape of the three-dimensional graph is in the form of a parabola because the model used is quadratic. The yield values with blue or the lowest yield were obtained by the drying treatment which used the highest temperature and the longest drying time, whereas the graph with green, yellow, and red colored areas or the high yield was obtained from the drying with the lowest temperature and the shortest time.

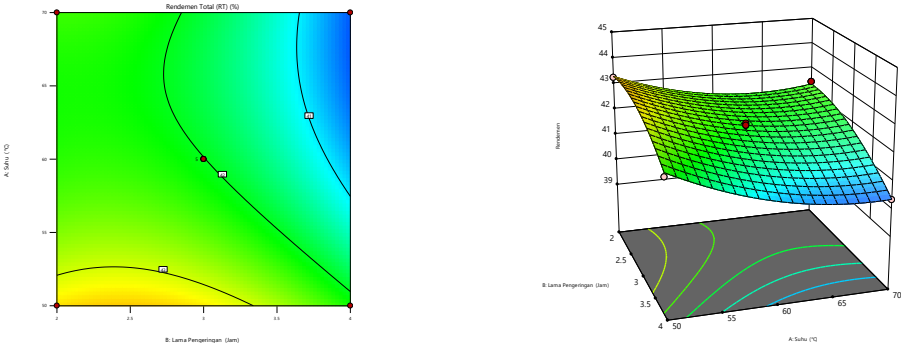

(a) (b)

Fig. 1 - Contour Plot for Yield (a), 3D Plot for Yield (b)

3.2. Moisture Content Response Model:

The selected RSM equation or model for optimizing the drying temperature and drying time in the DC drying process for the response to water content can be identified by equation 5:

$$Moisture\ Content\ (\%\ wb) = 7.699 - 0.077(A) - 0.362(B) \quad (5)$$

The water content response model obtained is a first-order model (linear). This indicates that the response to water content is only influenced by drying temperature and time and not the interaction between them. The influence given by time is more dominant on the response of water content than the effect of drying temperature. This can be seen from coefficient B with a value of 0.362 indicating a value that is greater than coefficient A, namely with a value of 0.07.

The equation illustrates that the effect of drying temperature and time is inversely proportional to the response of water content. The moisture content response will have a lower value when the temperature and drying time are added. This is also indicated by a negative sign (-) on the coefficients A and B which are opposite to the constants in the model.

In Figure 2a. The above shows the surface contour graph of the model from the temperature factor and drying time to the water content. The conditions of the factors with the maximum response value are marked in the yellow area, while the minimum response is marked in the blue area. Figure 2b showed a 3D graph of the water content response. Because the model obtained is linear, the graph is not a parabola. The higher the temperature factor and the longer the drying time, the less water content will be.

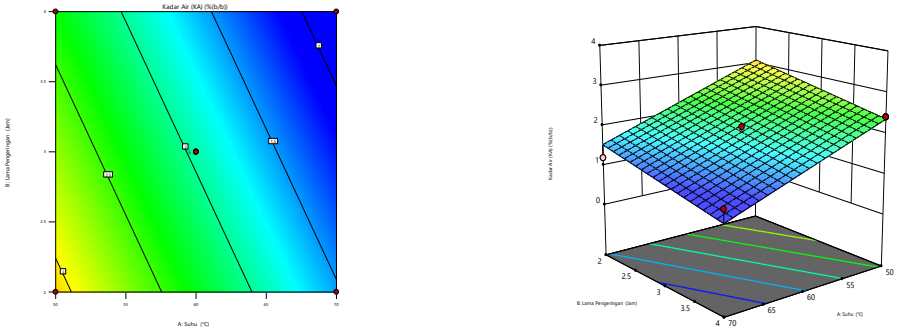

(a) (b)

Fig. 2 - Contour Plot for Water Content (a), 3D Plot for Water Content (b)

3.3. Fat Content Response Model

The selected RSM equation or model for optimizing drying temperature and drying time in the DC drying process for the response of fat content can be identified by equation [6]:

$$Fat\ Content\ (\%wb)=5.481+0.144(A)+2.051(B)-0.035(AB) \quad (6)$$

The fat content response model obtained is the 2FI model. This shows that the response of fat content is influenced by drying temperature and time and the interaction between them. The effect given by time is more dominant on the response of fat content than the effect of drying temperature. This can be seen from coefficient B with a value of 2.0513 indicating a greater value than coefficient A, namely with a value of 0.144. The equation illustrates that the effect of drying temperature and time is directly proportional to the response of fat content. While the interaction between temperature and time is inversely proportional to the response of fat content. The response of fat content will have a higher value when the temperature and drying time are added. This is also indicated by a negative sign (+) on the coefficients A and B which are opposite to the constants in the model.

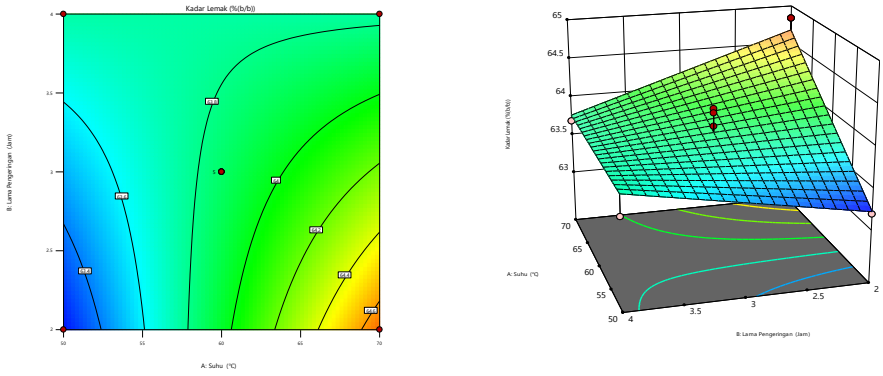

(a) (b)

Fig. 3 - Contour Plot for Fat Content (a), 3D Plot for Fat Content (b)

In Figure 3a, the above shows the surface contour graph of the model from the temperature factor and drying time to the water content. The conditions of the factors with the maximum response value are marked with red areas, while the minimum response is marked with blue areas. Figure 3b shows a 3D graph of the fat content response. Because the model obtained is 2FI, the graph is not a parabola. The longer the drying time, the more intact fat content is formed, and the fat content can be measured.

4. Optimization of Desiccated Coconut Drying Process

After obtaining a mathematical model for each response, the optimization process is carried out. The optimization design carried out on DC drying can be seen in Table 3. The determination of the upper and lower limits on the response is the result of recommendations based on the model that has been obtained from each response. The level of importance is determined based on CODEX STAN 177-1991.

Table 3 shows the target values, upper limit, lower limit, and importance of each optimization variable. The yield response is determined to have the maximum target. This target was set because it was desired that a drying process with optimal conditions still produce a high yield. Setting targets on the response of water content set a minimum target. The target is to comply with CODEX STAN 177-1991. High water content tends to cause the DC to agglomerate and will result in a high a_w value so that microbial activity increases. The fat content response is determined to have a maximum target, where the fat content is expected to have a value that exceeds 60% to comply with CODEX STAN 177-199. Therefore, desiccated coconut with a high-fat type can be produced from this optimization process.

Table 3

Criteria For Determining the Optimum Drying Condition of Desiccated Coconut

Response	Target	Lower Limit	Upper Limit	Importance
Yield (%)	*Maximize*	40.02	44.202	+++++
Water Content (%wb)	*Minimize*	1.129	3.593	+++++
Fat Content (%wb)	*Maximize*	63.196	64.839	+++++

The results of recommendations for optimum condition solutions for DC drying based on Design Experts can be seen in Table 4. The determination of optimum conditions is based on the highest desirability value. If this value is higher, it shows that every constraint or requirement previously arranged is increasingly being fulfilled (*Witek-Krowiak et al., 2014*). In addition to the accuracy of the data obtained for all runs, the desirability value depends on the required optimization design where the more complicated the conditions are, the smaller the desirability value. Therefore, the optimal conditions chosen in this study were factor 1 (temperature) 70 ℃ and factor 2 (time) 2 hours

Table 4

DC Drying Optimum Conditions Recommendations

No	Temperature (℃)	Drying Time (Hour)	Water Content (%Wb)	Fat Content (%wb)	Yield (%)	*Desirability*	
1	**70**	**2.000**	**1.532**	**64.683**	**42.353**	**0.750**	***Selected***
2	70	2.009	1.529	64.679	42.353	0.750	
3	70	2.035	1.519	64.667	42.353	0.749	
4	70	2.052	1.513	64.660	42.352	0.748	
5	70	2.333	1.411	64.531	42.301	0.732	
6	50	4.000	2.363	63.744	42.189	0.442	

5. Model Verification

The validation stage of RSM is used to determine the level of accuracy of the formula from the prediction results given by Design expert 13 with RSM-Central Composite Design. Based on Table 4, it is known that the optimal drying conditions are factor 1 (Temperature) 70 ℃ and factor 2 (Time) 2 Hours, so for the validation process, two repetitions are used which consist of the input run 1 sample value under the same conditions and re-drying under the same conditions. optimal. The water content values (%wb) for the two validation processes were 1.196%wb and 1.363%wb, the values for the fat content (%wb) obtained for the two validation processes were 64.839%wb and 64.872%wb, while for the drying yield values (%) for each validation process was 42.448% and 42.278%.

The validation confirmation results can be seen in the RSM optimum solution confirmation table in Table 5, where it can be seen that the results of the validation values for each response are still in the prediction range of 95% PI low and 95% PI high. In Table 5 it can be seen that the average response value for water content is lower, namely 1.279% than previously predicted, 1.531%. The water content validation results are also within the prediction range, namely between 0.632% (95% Low PI) to 2.431 (95% High PI). The fat content response obtained from the validation results was 64.855%, which was higher than predicted, namely 64.683%.

Table 5

RSM Optimum Solution Confirmation

Solution	*Predicted*	Std Dev	n	SE Pred	95% PI low	Data Mean	95% PI high
Water Content	1.531	0.443	2	0.403	0.632	1.279	2.431
Fat Content	64.683	0.356	2	0.369	63.847	64.855	65.519
Yield	42.352	0.377	2	0.399	41.407	42.363	43.298

The validation results are still in the range of PI 95% Low and PI 95% High, namely 63.847% to 65.519%. Finally, the validation results on the yield response were 42.363%, higher than the predicted 42.352%. The values obtained in the yield validation are in the range of PI 95% Low and PI 95% High, namely 41.407% – 43.298%. All validation results are still within the lowest and highest predictive ranges, so it can be said that the solutions offered by RSM were good (*Pan et al., 2010)*.

CONCLUSIONS

In the DC drying process, there is an interaction between temperature and drying time variables which results in different moisture content, fat content, and yield for each treatment. Based on the research result obtained a linear equation for the response to water content, a 2FI equation for the response to fat content, and a quadratic equation. In addition, it can be seen that optimization using the Design expert 13 program with RSM-Central Composite Design produces an optimization formula with a temperature of 70°C for 2 hours in a food dehydrator dryer resulting in a moisture content of 1.279% wb, fat content of 64.855% wb, and a yield of 42.363%, which complies with CODEX STAN 177-1991.

ACKNOWLEDGEMENT

The authors are grateful for the research facilities and publication fee provided by Universitas Padjadjaran.

REFERENCES

[1] Chan, E., & Elevitch, C. R. (2006). Cocos nucifera (coconut). species profiles for pacific island agroforestry. hōlualoa. In *Permanent Agriculture Resources* (Issue April).

[2] Chen, C. (2019). Relationship between water activity and moisture content in floral honey. *Foods*, *8*(1). https://doi.org/10.3390/foods8010030

[3] Daoud, J. I. (2018). Multicollinearity and Regression Analysis. *Journal of Physics: Conference Series*, *949*(1). https://doi.org/10.1088/1742-6596/949/1/012009

[4] Ditjenbun. (2021). Tree Crop Estate Statistics of Indonesia 2017-2019. In *Directorate General of Estate Crops*.

[5] Erbay, Z., & Icier, F. (2009). Optimization of hot air drying of olive leaves using response surface methodology. *Journal of Food Engineering*, *91*(4), 533–541. https://doi.org/10.1016/j.jfoodeng.2008.10.004

[6] Fennemas, O. R., Damodaran, S., & Parkin, K. L. (2017). *Fennema's food chemistry.* (S. Damodaran & K. L. Parkin (eds.)). CRC Press Taylor & Francis Group.

[7] Hadiyanto, S. H. (2016). Response surface optimization of ultrasound assisted extraction (UAE) of phycocyanin from microalgae Spirulina platensis. *Emirates Journal of Food and Agriculture*, *28*(4), 227–234. https://doi.org/10.9755/ejfa.2015-05-193

[8] Heathcock, J.F., Chapman, J.A. (1983). The Structure of Fresh Desiccated Coconut. *Food Structure*, *2*(1).

[9] Hewavitharana, G. G., Perera, D. N., Navaratne, S. B., & Wickramasinghe, I. (2020). Extraction methods of fat from food samples and preparation of fatty acid methyl esters for gas chromatography: A review. *Arabian Journal of Chemistry*, *13*(8), 6865–6875. https://doi.org/10.1016/j.arabjc.2020.06.039

[10] Karimifard, S., & Alavi Moghaddam, M. R. (2018). Application of response surface methodology in physicochemical removal of dyes from wastewater: A critical review. *Science of the Total Environment*, *640–641*, 772–797. https://doi.org/10.1016/j.scitotenv.2018.05.355

[11] Lo, A., Atran, S., Coley, J. D., Medin, D. L., & Smith, E. E. (1997). *The Tree of Life : Universal and Cultural Features of Folkbiological Taxonomies and Inductions*. *295*, 251–295.

[12] Lubis, Y. M., Satriana, Fahrizal, & Darlia, E. (2014). The formulation of desiccated coconut biscuits by roasting and without roasting. *Jurnal Teknologi Dan Industri Pertanian Indonesia*, *6*(2), 39–43. https://doi.org/10.17969/jtipi.v6i2.2065

[13] Majdi, H., Esfahani, J. A., & Mohebbi, M. (2019). Optimization of convective drying by response surface methodology. *Computers and Electronics in Agriculture*, *156* (December 2018), 574–584. https://doi.org/10.1016/j.compag.2018.12.021

[14] Mohpraman, K., & Siriphanich, J. (2012). Safe use of sodium metabisulfite in young coconuts. *Postharvest Biology and Technology*, *65*, 76–78. https://doi.org/10.1016/j.postharvbio.2011.11.006

[15] Nguyen Tram Anh, M., Van Hung, P., & Thi Lan Phi, N. (2021). Optimized Conditions for Flavonoid Extraction from Pomelo Peel Byproducts under Enzyme- And Ultrasound-Assisted Extraction Using Response Surface Methodology. *Journal of Food Quality*, *2021*. https://doi.org/10.1155/2021/6666381

[16] Ogawa, T., Kobayashi, T., & Adachi, S. (2012). Prediction of pasta drying process based on a thermogravimetric analysis. *Journal of Food Engineering*, *111*(1), 129–134. https://doi.org/10.1016/j.jfoodeng.2012.01.011

[17] Pan, H. F., Bao, W. N., Xie, Z. P., & Zhang, J. G. (2010). Optimization of medium composition for cis-epoxysuccinate hydrolase production in Escherichia coli by response surface methodology. *African Journal of Biotechnology*, *9*(9), 1366–1373. https://doi.org/10.5897/ajb10.952

[18] Sangamithra, A., Swamy, G. J., Sorna, P. R., Chandrasekar, V., Sasikala, S., & Hasker, E. (2013). Coconut- value added products coconut : an extensive review on value added products. *Indian Food Industry Magazine*, *32*(6), 1–9. https://www.researchgate.net/publication/262740332_Coconut-_Value_Added_Products

[19] Serin, S., Turhan, K. N., & Turhan, M. (2018). Correlation between water activity and moisture content of Turkish flower and pine honeys. *Food Science and Technology (Brazil)*, *38*(2), 238–243. https://doi.org/10.1590/1678-457X.31716

[20] Siriwongwilaichat, P., Thongart, K., & Thaisakornphan, P. (2014). The effect of blanching on texture and color of frozen young coconut meat. *Food and Applied Bioscience Journal*, *2*(2), 143–151.

[21] Statista. (2022). *Coconut production in the Asia-Pacific region in 2020, by country*. https://www.statista.com/statistics/661690/asia-pacific-coconuts-production-by-country/

[22] Suryani, L., Abbas Zaini, M., & Yasa, I. (2016). The effect of the concentration of sodium metabisulfite and drying method toward vitamin c and organoleptic of banana slice (sale). *Jurnal Ilmu Dan Teknologi Pangan*, *2*(1), 85–93.

[23] Toledo, R. T., Singh, R. K., & Kong, F. (2007). Fundamentals of Food Process Engineering. In *Springer* (Fourth Edi, Vol. 44, Issue 1). Springer. https://doi.org/10.1111/j.1365-2621.2007.01646.x

[24] Tontul, I., & Topuz, A. (2017). Spray-drying of fruit and vegetable juices: Effect of drying conditions on the product yield and physical properties. *Trends in Food Science and Technology*, *63*, 91–102. https://doi.org/10.1016/j.tifs.2017.03.009

[25] Waisundara, V. Y., Perera, C. O., & Barlow, P. J. (2007). Effect of different pre-treatments of fresh coconut kernels on some of the quality attributes of the coconut milk extracted. *Food Chemistry*, *101*(2), 771–777. https://doi.org/10.1016/j.foodchem.2006.02.032

[26] Witek-Krowiak, A., Chojnacka, K., Podstawczyk, D., Dawiec, A., & Pokomeda, K. (2014). Application of response surface methodology and artificial neural network methods in modelling and optimization of biosorption process. *Bioresource Technology*, *160*, 150–160. https://doi.org/10.1016/j.biortech.2014.01.021

[27] Yahya, S., Mohd Shahrir, A., Amir Syariffudden, M. A., Shafie, A., Mohammad Shukri, J., Mohd Zaimi, Z. A., & Amir Redzuan, S. (2020). A study of drying parameters on drying time and colour quality of grated coconut using tumbling mechanism in convective dryer. *Food Research*, *4*, 64–69. https://doi.org/10.26656/fr.2017.4(S6).023

[28] Yuvita, L. V. A., Budiastra, I. W., & Hasbullah, R. (2022). Evaluation of chemichal content of desiccated coconut using ft-nir spectroscopy. *IOP Conference Series: Earth and Environmental Science*, *1024*(1), 0–10. https://doi.org/10.1088/1755-1315/1024/1/012020

[29] Zouari, A., Perrone, Í. T., Schuck, P., Gaucheron, F., Dolivet, A., Attia, H., & Ayadi, M. A. (2019). Effect of outlet drying temperature and milk fat content on the physicochemical characteristics of spray-dried camel milk powder. *Drying Technology*, *37*(13), 1615–1624. https://doi.org/10.1080/07373937.2018.1526189

IoT-BASED EVAPOTRANSPIRATION ESTIMATION OF PEANUT PLANT USING DEEP NEURAL NETWORK

/

ESTIMASI EVAPOTRANSPIRASI TANAMAN KACANG TANAH BERBASIS IoT MENGGUNAKAN DEEP NEURAL NETWORK

Suhardi[1,2], Bambang Marhaenanto[1], Bayu Taruna Widjaja Putra[1,*], Sugeng Winarso[2]
[1] Agricultural Engineering, Faculty of Agricultural Technology, University of Jember, Jember, Indonesia 68121
[2] Doctoral study program in agricultural science, Faculty of Agriculture, University of Jember, Jember, Indonesia 68121
*Corresponding Author E-mail: bayu@unej.ac.id
DOI: https://doi.org/10.35633/inmateh-70-47

Keywords: *DNN, evapotranspiration, NDVI, sensors, temperature, humidity*

ABSTRACT

The water availability in soil strongly influences crop growth by sustaining photosynthesis, respiration, and the maintenance of plant temperature. The water availability will decrease due to crop evapotranspiration (ETc) which is influenced by reference evapotranspiration (ETo) and crop coefficient (Kc). During water shortage, Kc is strongly influenced by soil evaporation coefficient (Ke) and basal crop coefficient (Kcb) which can be calculated using the Blue Red Vegetation Index (BRVI). The purpose of this study was to apply and evaluate a new method of estimating ETo, Ke, and Kcb at a research site using a Deep Neural Network (DNN) with minimum requirements. The results of the ETo estimation using DNN shows a good output with a determinant coefficient (R^2) being 0.774. Meanwhile, the estimates of Ke and Kcb show excellent results with the determinant coefficient (R^2) being 0.9496 and 0.999 respectively.

ABSTRAK

Ketersediaan air dalam tanah sangat mempengaruhi pertumbuhan tanaman untuk mempertahankan fotosintesis, respirasi, dan pemeliharaan suhu tanaman. Ketersediaan air akan berkurang akibat evapotranspirasi tanaman (ETc) yang dipengaruhi oleh evapotranspirasi referensi (ETo) dan koefisien tanaman (Kc). Pada saat kekurangan air, Kc sangat dipengaruhi oleh koefisien penguapan tanah (Ke) dan basal crop koefisien (Kcb) yang dapat dihitung dengan menggunakan Normalized Difference Vegetation Index (NDVI). Tujuan dari penelitian ini adalah untuk menerapkan dan mengevaluasi metode baru estimasi ETo, Ke, dan Kcb di lokasi penelitian menggunakan Deep Neural Network (DNN) dengan persyaratan minimum. Hasil estimasi ETo menggunakan DNN menunjukkan output sangat baik dengan koefisien determinan (R^2) 0.774. Sementara itu, estimasi Ke dan Kcb menghasilkan luaran sangat baik dengan koefisien determinan (R^2) secara berurutan adalah 0.9496 dan 0.999.

INTRODUCTION

One of the factors that affect crop growth is the availability of water which functions as a solvent and medium for biochemical reactions, a raw material for photosynthesis, and a determinant to maintain constant crop temperature. Water availability is extremely dependent on rainwater because some of the rainwater that seeps into the ground will be stored in it. However, water in the soil will be increasingly limited during the dry season due to increased temperature which subsequently raises evapotranspiration. Likewise, solar radiation and wind speed are likely to increase evapotranspiration (*Luo et al., 2021; Dong et al., 2020; Kiefer et al., 2019*). On the other hand, relative humidity (RH) is the ratio between actual water vapor pressure and saturated water vapor pressure at a specific temperature which affects the decrease in evapotranspiration when RH increases *(Fu et al., 2022*). Other factors that affect evapotranspiration are environmental factors, such as the nature of vegetation and anthropogenic management (*Jiao et al., 2019)*. Given these driving factors to water availability, researchers generally analyze temperature, solar radiation, humidity, wind speed, and rainfall to estimate evapotranspiration using Artificial Neural Networks (ANN) *(Vulova et al., 2021; Ferreira & França, 2020; Elbeltagi et al., 2020; Ferreira et al., 2019; Saggi and Jain, 2019)*.

The estimation of evapotranspiration using an ANN with a big dataset produces very good results. However, ANN-based evapotranspiration estimation with small dataset can also be a promising option in the absence of big datasets (*Feng et al., 2019*).

In this direction, this study investigated the use of the minimum dataset requirement involving Tmean and RHmean to estimate evapotranspiration. In addition, Tmean and RHmean datasets, BRVI, and basal crop coefficient (Kcb) from the FAO table in one growing season were used as input parameters to estimate the Kcb of sample crops and soil evaporation coefficient (Ke) on the research site.

In this scenario, this study aimed to apply and evaluate a new model of evapotranspiration estimation using DNN with a minimum dataset requirement based on the Internet of Things (IoT).

MATERIALS AND METHODS

Research site

The research site was located at the University of Jember, East Java, Indonesia, located at -8.16346° and 113.71305° with a tropical climate and two seasons, the rainy season and dry season. The beginning of the rainy season occurs in September, while the dry season begins in April. In this dry season, the water availability in the soil decreases, so some crops do not receive sufficient water supply through irrigation. This has an impact on crop growth and yields.

Datasets

This study used data on temperature (T), relative humidity (RH), Kcb from the FAO table, and BRVI from crop images recorded by cameras based on the Internet of Things (IoT) from January 2022 to April 2022. Peanut plants were used as samples in this study. Tmean and RHmean generated through a 4-hour data recording served as input data for DNN-based ETo estimation. Meanwhile, ETo from the IoT-based lysimeter measurement was compared against the estimated output of ETo. The Tmean, Rhmean, and Kcb from the FAO table and BRVI in one growing season were used as input data to estimate the soil evaporation coefficient (Ke) and Kcb of crops on the research site. Temperature and humidity sensors were used to record T and RH. Meanwhile, the load cell sensor was used as an IoT-based grass crop weight sensor to measure ETo. The change in the weight of grass and soil was considered as the weight of evapotranspiration of water and converted to the actual ETo height. Temperature and humidity sensors were placed around the crop while the growing media and crops were placed on top of the load cell. The node MCU ESP8266 module which functioned as an internet connection microcontroller was used for recording T, RH, and ETo and sending these data to a cloud server.

Peanut images were captured using a camera sensor placed above the crop canopy by attaching it to a pole. The camera was put next to the crop to capture RGB data directly on the crop leaves *(Putra et al., 2020*). Red (R) and blue (B) bands in the image crops were used for BRVI calculations *(Delalieux et al., 2023*). The specifications of camera sensor, T and RH sensor, and load cell sensor are presented in Table 1, and the equipment arrangement is shown in Figure 1.

Table 1

Specification of the camera sensor, temperature sensor, humidity sensor, and load cell sensor

Sensor	Specification
Camera sensor module	• Connectivity using WiFi 802.11b/g/n, Bluetooth 4.2 with BLE. • Microcontroller computing power up to 600 DMIPS. • The memory storage of 520KB SRAM + 4MB PSRAM + SD card slot. • A 9-pin GPIO port. • 2MP camera with JPEG image format. • An external FTDI adapter to connect the camera, sensor module to the mini-USB port.
Temperature (T) and relative humidity (RH) sensors	• Measuring range of 20-90% RH and temperature 0-50°C. • Measurement accuracy of ±5% RH and ±2°C. • Voltage source of 5V DC. • Current consumption of 0.5mA-2.5mA.
Load cell	• Aluminum alloy as basic material • Dimensions 8x1.25x1.25 cm • Operating temperature range of -20°C – 65°C • Output of 0.1mV - 1mV/V • The margin of error ≤1.5%

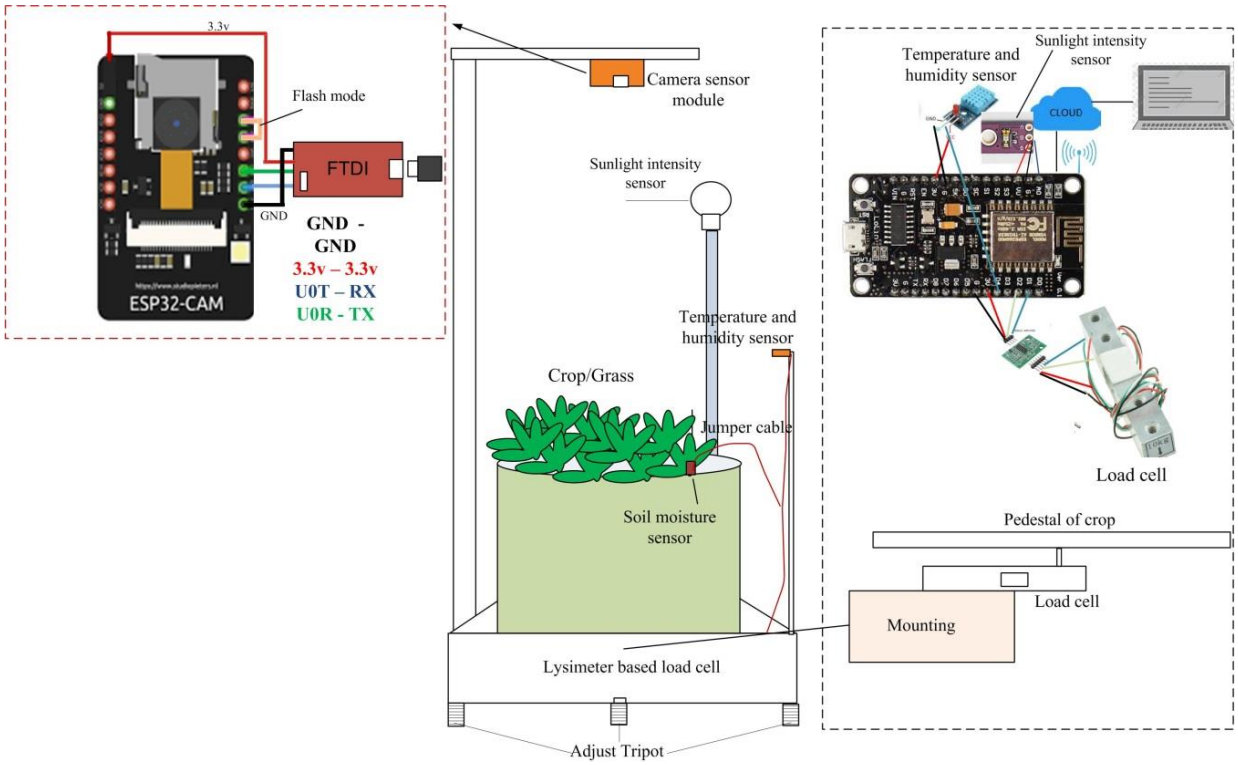

Fig. 1 - The arrangement of camera sensor equipment, weighting lysimeter device, IoT-based temperature, and humidity sensor

The estimation of Kcb using BRVI

The estimation of Kcb of peanut plants on the research site was done by identifying a linear relationship between the NDVI and the FAO Kcb of peanut plants, while the NDVI of peanut plants was calculated by equation 1. Furthermore, the NDVI was plotted with the Kcb from the FAO table (Kcb-FAO) at the same plant phase and age *(Reyes-gonzález et al., 2018; Sánchez et al., 2021; de Oliveira et al., 2020)*. The relationship between NDVI and Kcb was based on the fact that NDVI will tend to increase until the development stage and decrease at the late season stage (harvest). Likewise, Kcb tends to rise in the initial stage up to the development stage, but it is likely to decrease in the late season stage. As an alternative, a scatter plot in the form of a triangle between Land Surface Air Temperature (LST) and NDVI can be used to estimate Kcb *(Chen and Liu, 2020)*. The resultant linear equation was used as the basis for calculating the Kcb-NDVI value *(Niu et al., 2020*). On the other hand, the use of RGB cameras for taking plant images has been widely used to diagnose plant physiological characteristics including leaf chlorophyll content *(Liu et al., 2021)*. B and R bands on the RGB camera image are used to calculate the Blue Red Vegetation Index (BRVI) which functions to assess the biophysical properties of the vegetation index. Therefore, BRVI is identical to the NDVI value calculated using the NIR and R band (*Putra and Soni, 2017*).

$$BRVI = \frac{(B-R)}{(B+R)} \quad (1)$$

The accuracy rate of Kcb estimation can be justified by referring to the correlation coefficient. A very good correlation is marked by coefficient index ranging from 0.9 to 1.0, a range of 0.70 to 0.89 is a good correlation, a range of 0.40 to 0.69 denotes a moderate correlation, and a range of 0.1 – 0.39 indicates weak correlation (*Schober et al., 2018*).

The estimation of ETo using DNN

The estimation of evapotranspiration using DNN employed an architecture involving 1 input layer, 4 hidden layers, and 1 output layer with a Rectified Linear Unit (*ReLU*) activation function. The *ReLU* activation function was chosen because it has a better performance than sigmoid logistics (*Huang et al., 2019)*. Meanwhile, the data compositions for DNN modeling at the training and testing stages were 70% and 30% respectively.

The DNN-based estimation of ETo using minimum dataset requirement

This research engaged minimum dataset requirements comprising Tmean, RHmean, and the actual ETo measurement results of an IoT-based lysimeter within 7 days of data recording, with a duration of 4 hours each day. The input data were Tmean and Rhmean while ETo was used as comparison data against DNN output.

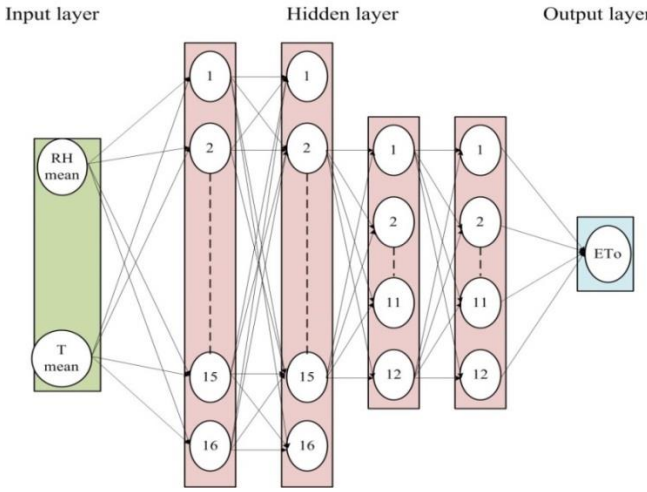

Fig. 2 - DNN architecture for ETo estimation using minimum dataset requirement.

The estimation of Kcb and Ke

Changes in crop growth from the initial planting to harvesting were indicated by Kcb. The Kcb at the initial stage was constant and started to rise during the development stage. The Kcb remained constant until the mid-season stage, but it sank until the late season stage. Meanwhile, the Ke can be derived from NDVI and a fraction of vegetation cover (Fc), such as equations 3 and 4 (*Zhang et al., 2019; Wang T. et al., 2021*). In general, the Fc value of FAO (Fc-FAO) in each crop stage was described as follows: (a) initial stage (0 – 0.1); (b) crop development stage (0.1 – 0.8); (c) mid-season stage (0.8 – 1); and (d) late season stage (0.8 - 0.2) (*Allen et al., 1998*).

$$Ke = 0.9 * (1 - Fc) \quad (2)$$

$$Fc = 1.19 * (NDVI - NDVImin) \quad (3)$$

$$Fc = 1.26 * NDVI - 0.18 \quad (4)$$

Based on this description, Tmean, RHmean, and BRVI of the peanut plants were used as input data to estimate Kcb and Ke with the aid of DNN. The target data which included Kcb-BRVI and Ke-FAO served as comparative data against the DNN output. Kcb-BRVI was generated from the linear equation between Kcb, FAO tables, and BRVI, while Ke was generated from equation 2. The DNN architecture is shown in Figure 3.

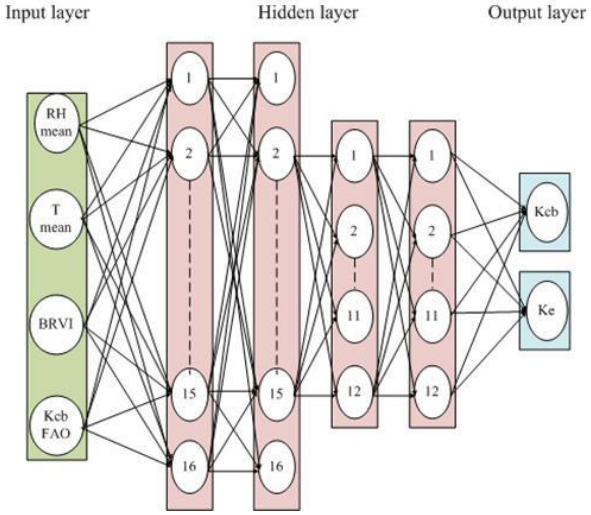

Fig. 3 - DNN Architecture of Kcb and Ke Estimation

RESULTS

RGB camera sensor calibration

RGB camera sensor was calibrated by calculating the relationship between the BRVI of the RGB camera sensor (BRVI-camera sensor) and the NDVI spectrometer (NDVI-spectrometer). The NDVI was generated by calculating the reflectance rate of the red and blue bands in the leaf samples. Meanwhile, the combination of RGB bands from the camera sensor had to be extracted first to produce red and blue bands, and then the red and blue band reflectance rate was calculated to estimate the BRVI. The calibration results demonstrate a very satisfactory accuracy with R^2 of 0.8973 (see Figure 4).

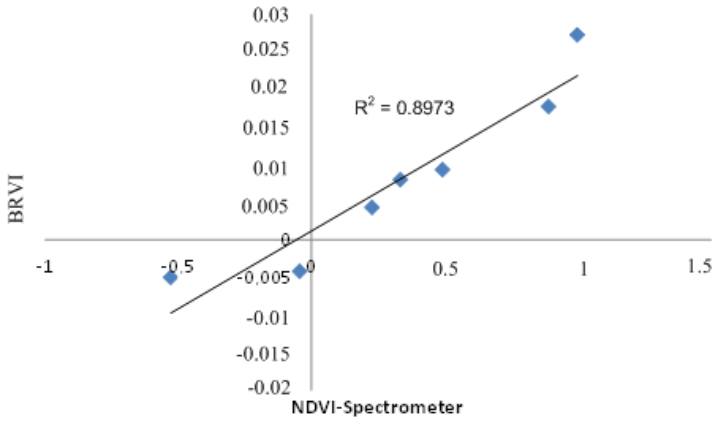

Fig. 4 - The result of camera sensor calibration

The estimation of Kcb using BRVI

The images of peanut plants were captured at different stages of plant growth, including the initial stage, development stage, and mid-season stage. Furthermore, the BRVI in the images was calculated using the QGis 3.10 software as shown in Figure 5.

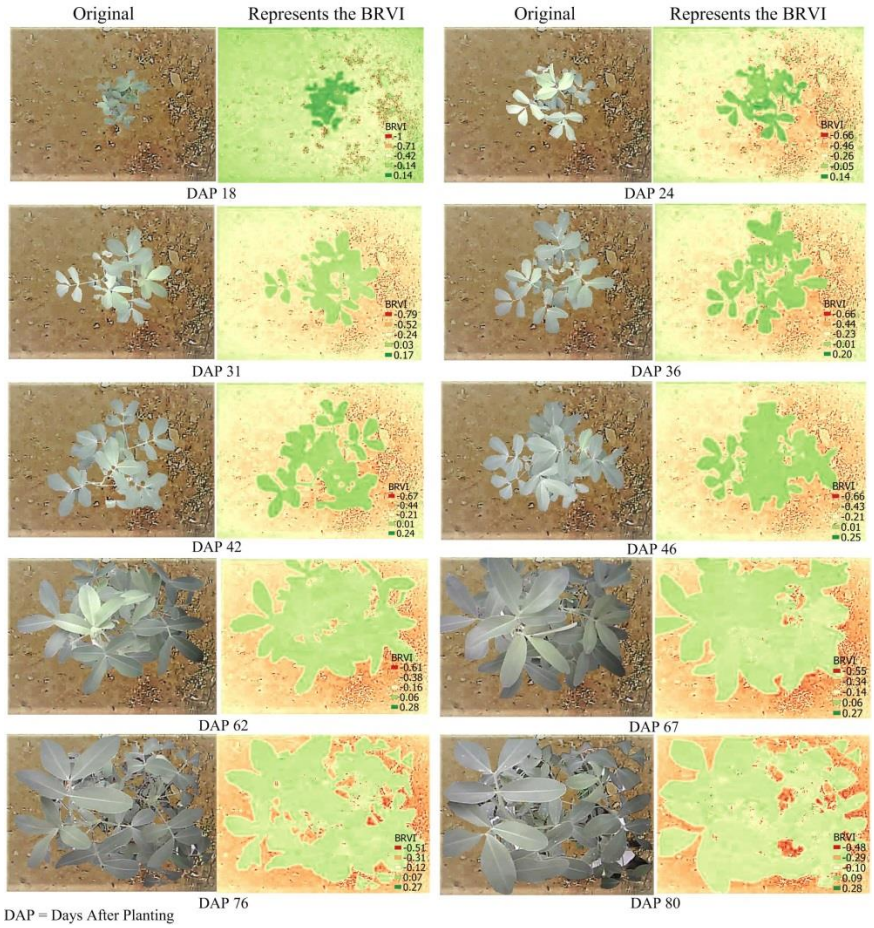

Fig. 5 - The calculation of the NDVI-RGB of peanut plant images from the initial stage to mid-season stage

The calculation results of the BRVI from the peanut plant images using a camera sensor indicated similar trend between the BRVI and Kcb-FAO. The trend was marked by constant value in the initial stage and an increase in the development stage, but constant value was restored in the mid-season stage. This shows a very strong correlation between BRVI and Kcb-FAO, as indicated by R^2 of 0.8748 (Figure 6). By implication, BRVI can be used to estimate the Kcb of peanut plants. This finding resonates with previous research reporting that the NDVI and Kcb of plants were positively correlated (*Niu et al., 2020*). In harmony, another study confirms that NDVI can be used to estimate Kc on the field in all plant phases *(Zhang et al., 2019*).

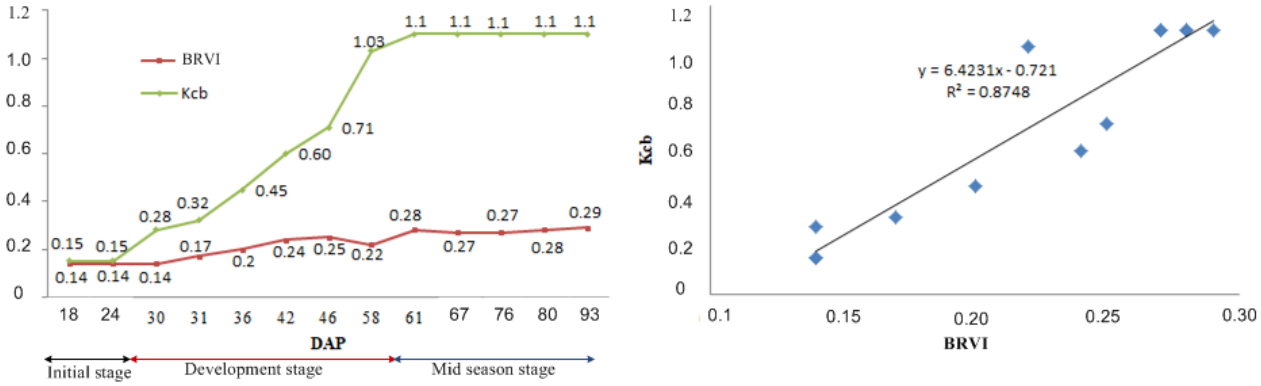

Fig. 6 - The trends of BRVI and Kcb-FAO in peanut

The estimation of ETo using minimum dataset requirements

ETo estimation based on DNN used a minimum requirement dataset in the form of Tmean, RHmean, and actual ETo recorded every 4 hours from January 8th, 2022 to January 15th, 2022. Input and target data are presented in Figure 7, while the ETo estimation results can be seen in Figures 8 and 9.

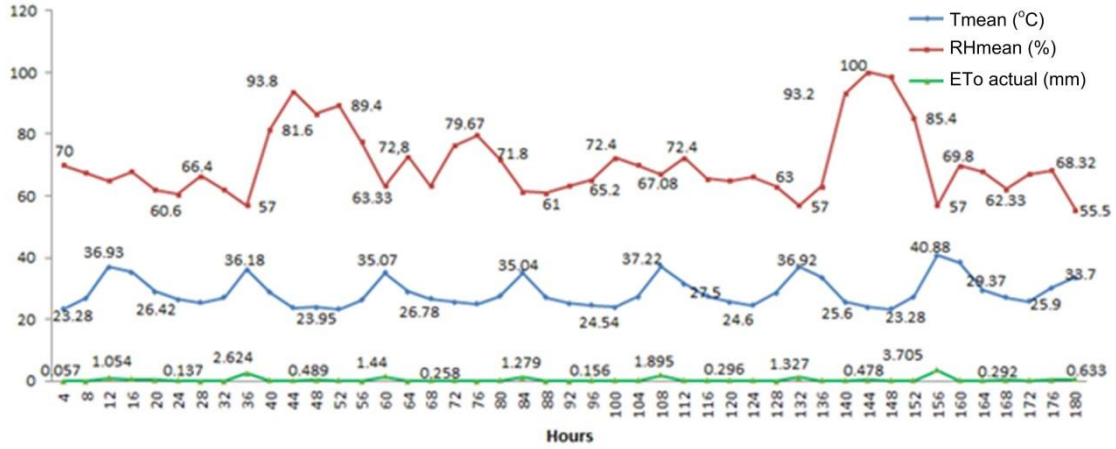

Fig. 7 - Input and target data for estimating ETo using DNN

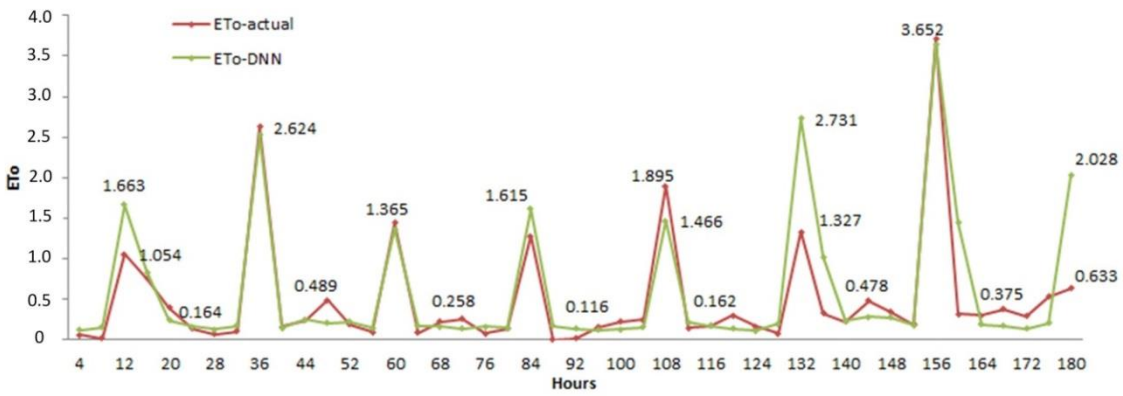

Fig. 8 - ETo estimation using DNN with minimum dataset requirements

Based on Figure 7, the trend of ETo is similar to that of Tmean but different from that of Rhmean. Tmean and ETo tend to increase simultaneously. On the other hand, when RHmean increases, ETo tends to decrease. This is coherent with a previous research which states that an increase in temperature increases ETo, but an increase in RH has the opposite effect *(Luo et al., 2021*). Figure 8 shows that ETo estimation using DNN with Tmean and RHmean as input data using 4 hidden layers (16-16-12-12) shows very good results. This is indicated by the trend associated with ETo-DNN, which is equal to the actual ETo. The ETo-DNN and actual ETo were relatively the same and coincided at 36, 60, and 156 hours respectively. The DNN using 4 hidden layers (16-16-12-12) with the *ReLU* activation function demonstrates a very good performance at epoch 1000 with a (mean absolute error) *MAE* of 0.1412 and R^2 of 0.7704 as shown in Figure 9.

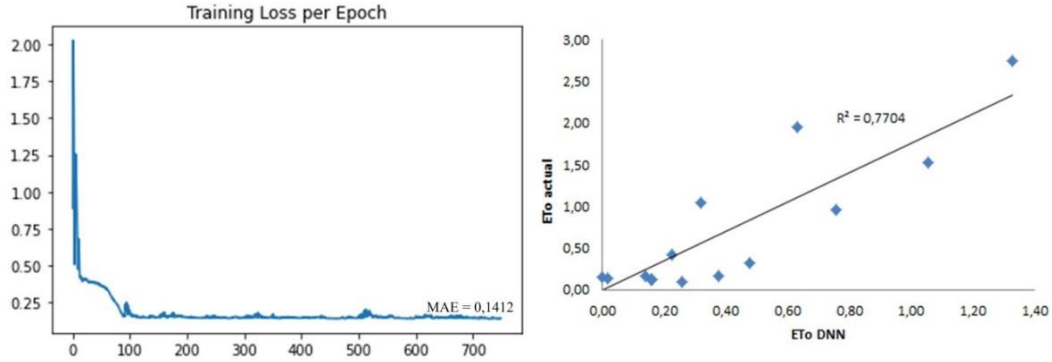

Fig. 9 - *MAE* and R^2 of ETo Estimation Using DNN with Minimum Dataset Requirement

The estimation of Kcb and Ke using DNN

From the initial stage to the late season stage, Tmean, RHmean, Kcb-FAO, and BRVI of peanut plants were recorded as input data to estimate Kcb and Ke. Kcb resulting from the BRVI transformation (Kcb-BRVI) and Ke-FAO calculated using equation 2 was used as a comparison against Kcb-DNN and Ke-DNN. The input and output data for the estimation of Kcb and Ke using DNN are presented in Figure 10 and Figure 11.

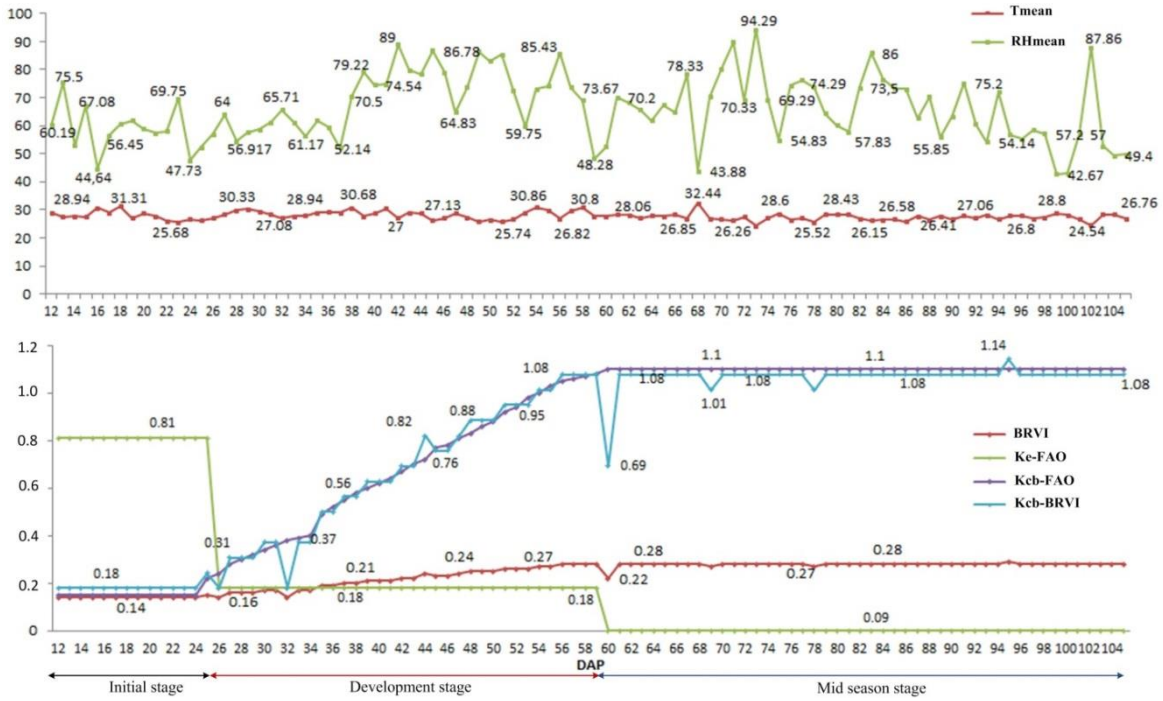

Fig. 10 - Dataset to estimate Kcb and Ke using DNN

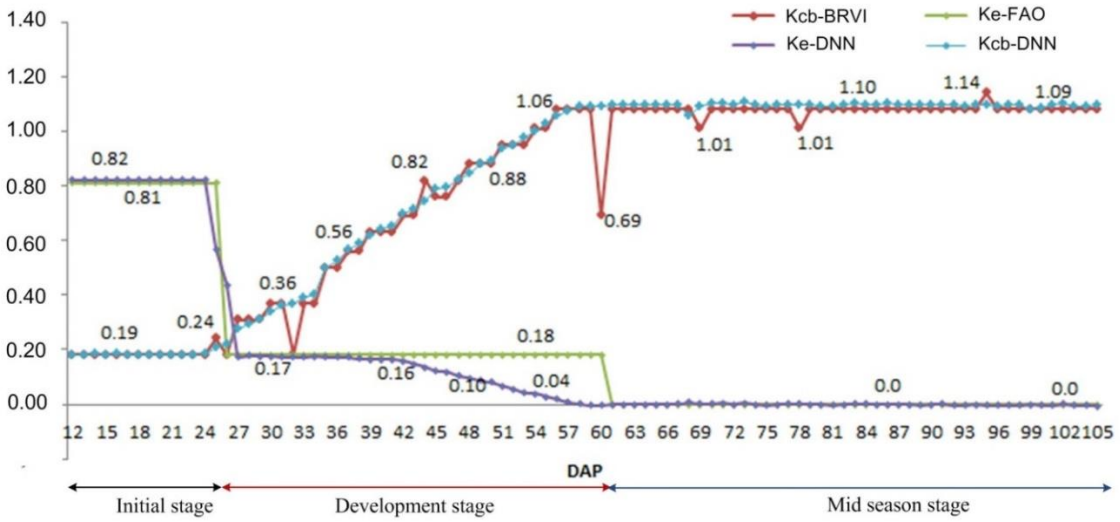

Fig. 11 - The trends of Kcb and Ke estimated using DNN

Figure 11 shows a very decent trend of Kcb and Ke as estimated using DNN with input data involving Tmean, RHmean, Kcb-FAO, and BRVI. Similar trends are identified between Kcb-DNN and Ke-DNN, and these trends coincide with those of Kcb-BRVI and Ke-FAO. Decent DNN performance was achieved at epoch 2500 with *MAE* of 0.021 as well as R^2 of 0.9496 and 0.999, respectively (Figure 12). Thus, the DNN model with 4 parameters in the input layer and 4 hidden layers (16-16-12-12) can be used to estimate Kcb and Ke.

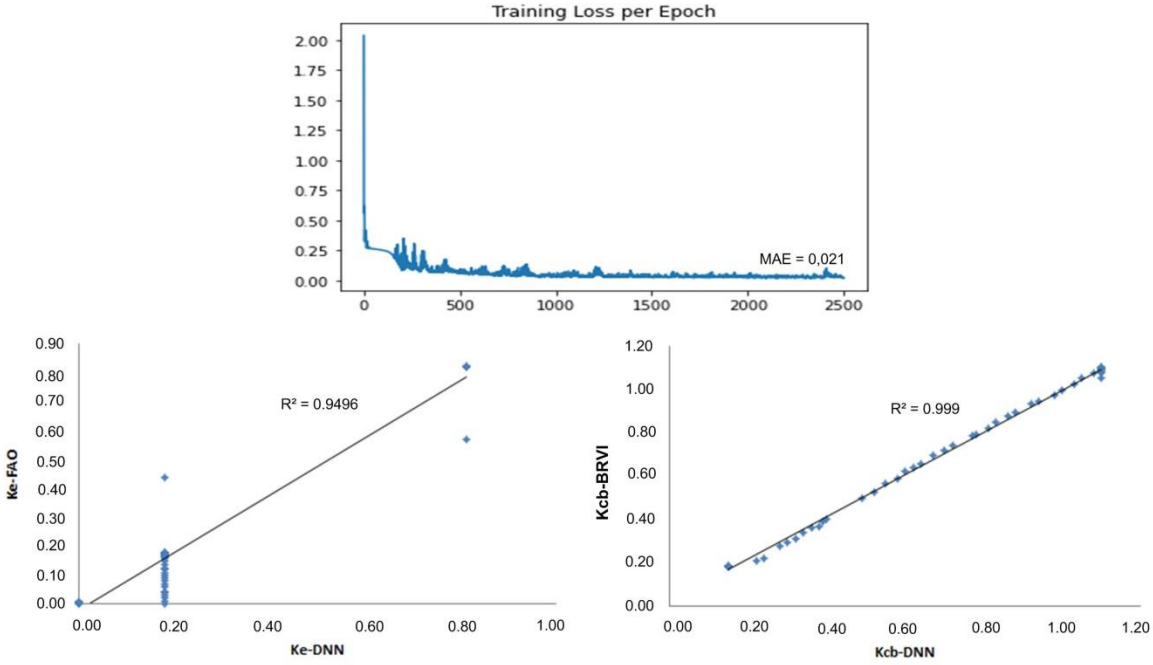

Fig. 12 - MAE and R^2 of Kcb and Ke estimation using DNN

CONCLUSIONS

The estimation of ETo using DNN with minimum dataset requirements can achieve highly accurate output. In this study, the minimum dataset requirements were Tmean and RHmean recorded from January 8th, 2022 to January 15th, 2022 (7 days) with 4 hours of data generation each day. This estimation has resulted in *MAE* of 0.1412 and R^2 of 0.7704. The findings demonstrate that ETo-DNN can be used as the basis for determining water requirements of crops in future studies. Likewise, the estimation of Ke and Kcb using DNN with datasets including Tmean, RHmean, Kcb-FAO, and BRVI report satisfactory accuracy rate, with *MAE* of 0.021 and R^2 of 0.9596 and 0.999 respectively. This confirms that Kcb-DNN and Ke-DNN can serve as a reference in calculating ETc in peanut plant.

ACKNOWLEDGEMENT

The author would like to thank mentors, especially families and all who have contributed to this research.

REFERENCES

[1] Allen, R. G., S.Pereira, L., Raes, D., & Smith, M. (1998). FAO Irrigation and Drainage Paper No. 56. In *Food and Agriculture Organization of the United Nations* (Vol.13, Issue 3). FAO - Food and Agriculture Organization of the United Nations. https://doi.org/10.1016/S0141-1187(05)80058-6

[2] Chen, J. M., & Liu, J. (2020). Evolution of evapotranspiration models using thermal and shortwave remote sensing data. *Remote Sensing of Environment*, *237* (December 2019), 111594. https://doi.org/10.1016/j.rse.2019.111594

[3] Delalieux, S., Hardy, T., Ferry, M., Gomez, S., Kooistra, L., Culman, M., & Tits, L. (2023). Red Palm Weevil Detection in Date Palm Using Temporal UAV Imagery. *Remote Sensing*, 15(5), 1–21. Retrieved from https://doi.org/10.3390/rs15051380

[4] de Oliveira, R. M., da Cunha, F. F., da Silva, G. H., Andrade, L. M., de Morais, C. V., Ferreira, P. M. O., Raimundi, F. P. G., de Jesus Freitas, A. R., de Souza, C. M., & de Oliveira, R. A. (2020). Evapotranspiration and crop coefficients of Italian zucchini cultivated with recycled paper as mulch. *PLoS ONE*, *15*(5), 1–16. https://doi.org/10.1371/journal.pone.0232554

[5] Dong, W., Li, C., Hu, Q., Pan, F., Bhandari, J., & Sun, Z. (2020). Potential Evapotranspiration Reduction and Its Influence on Crop Yield in the North China Plain in 1961-2014. *Hindawi Advances in Meteorology*, *2020*, 10. https://doi.org/10.1155/2020/3691421

[6] Elbeltagi, A., Deng, J., Wang, K., Malik, A., & Maroufpoor, S. (2020). Modeling long-term dynamics of crop evapotranspiration using deep learning in a semi-arid environment. *Agricultural Water Management*, *241*(March), 106334. https://doi.org/10.1016/j.agwat.2020.106334

[7] Feng, S., Zhou, H., & Dong, H. (2019). Using deep neural network with small dataset to predict material defects. *Materials and Design*, *162*, 300–310. https://doi.org/10.1016/j.matdes.2018.11.060

[8] Ferreira, L. B., da Cunha, F. F., de Oliveira, R. A., & Fernandes Filho, E. I. (2019). Estimation of reference evapotranspiration in Brazil with limited meteorological data using ANN and SVM – A new approach. *Journal of Hydrology*. https://doi.org/10.1016/j.jhydrol.2019.03.028

[9] Ferreira, L. B., & França, F. (2020). New approach to estimate daily reference evapotranspiration based on hourly temperature and relative humidity using machine learning and deep learning. *Agricultural Water Management*, *234*(February), 106113. https://doi.org/10.1016/j.agwat.2020.106113

[10] Fu, J., Gong, Y., Zheng, W., Zou, J., Zhang, M., Zhang, Z., Qin, J., Liu, J., & Quan, B. (2022). Spatial-temporal variations of terrestrial evapotranspiration across China from 2000 to 2019. *Science of the Total Environment*, *825*, 153951. https://doi.org/10.1016/j.scitotenv.2022.153951

[11] Huang, X., Gao, L., Crosbie, R. S., Zhang, N., Fu, G., & Doble, R. (2019). Groundwater recharge prediction using linear regression, multi-layer perception network, and deep learning. *Water (Switzerland)*, *11*(9), 19. https://doi.org/10.3390/w11091879

[12] Jiao, L., Lu, N., Fang, W., Li, Z., Wang, J., & Jin, Z. (2019). Determining the independent impact of soil water on forest transpiration: A case study of a black locust plantation in the Loess Plateau, China. *Journal of Hydrology*. https://doi.org/10.1016/j.jhydrol.2019.03.045

[13] Kiefer, M. T., Andresen, J. A., Doubler, D., & Pollyea, A. (2019). Development of a gridded reference evapotranspiration dataset for the Great Lakes region. *Journal of Hydrology: Regional Studies*. https://doi.org/10.1016/j.ejrh.2019.100606

[14] Liu, Y., Hatou, K., Aihara, T., Kurose, S., Akiyama, T., Kohno, Y., … Omasa, K. (2021). A Robust Vegetation Index Based on Different UAV RGB Images to Estimate SPAD Values of Naked Barley Leaves. *Remote Sensing*, 13(4), 1–21.

[15] Luo, Y., Gao, P., & Mu, X. (2021). Influence of meteorological factors on the potential evapotranspiration in Yanhe River Basin, China. *Water (Switzerland)*, *13*(9), 1–13. https://doi.org/10.3390/w13091222

[16] Niu, H., Wang, D., & Chen, Y. Q. (2020). Estimating Crop Coefficients Using Linear and Deep Stochastic Configuration Networks Models and UAV-Based Normalized Difference Vegetation Index (NDVI). *2020 International Conference on Unmanned Aircraft Systems, ICUAS 2020*, 1485–1490. https://doi.org/10.1109/ICUAS48674.2020.9213888

[17] Putra, B. T. W., & Soni, P. (2017). Evaluating NIR-Red and NIR-Red edge External Filters with Digital Cameras for Assessing Vegetation Indices Under Different Illumination. *Infrared Physics and Technology*, *81*, 148–156. https://doi.org/10.1016/j.infrared.2017.01.007

[18] Putra, B. T. W., Soni, P., Marhaenanto, B., Pujiyanto, Sisbudi Harsono, S., & Fountas, S. (2020). Using Information from Images for Plantation Monitoring: A Review of Solutions for Smallholders. *Information Processing in Agriculture*, *7*(1), 109–119. https://doi.org/10.1016/j.inpa.2019.04.005

[19] Reyes-gonzález, A., Kjaersgaard, J., Trooien, T., Hay, C., Ahiablame, L., Nacional, I., & Agr, D. I. (2018). Estimation of Crop Evapotranspiration Using Satellite Remote Sensing-Based Vegetation Index. *Advances in Meteorology*, *2018*(1).

[20] Saggi, M. K., & Jain, S. (2019). Reference evapotranspiration estimation and modeling of the Punjab Northern India using deep learning. *Computers and Electronics in Agriculture*, *156* (October 2018), 387–398. https://doi.org/10.1016/j.compag.2018.11.031

[21] Sánchez, J. M., Simón, L., González-piqueras, J., Montoya, F., & López-urrea, R. (2021). Monitoring Crop Evapotranspiration and Transpiration / Evaporation Partitioning in a Drip-Irrigated Young Almond Orchard Applying a Two-Source Surface Energy Balance Model. *Water MDPI*, *13*(73), 1–25.

[22] Schober, P., Boer, C., & Schwarte, L. A. (2018). Correlation Coefficients: Appropriate Use and Interpretation. *Anesthesia & Analgesia*, *126*(5), 1763–1768. https://doi.org/10.1213/ANE.0000000000002864

[23] Vulova, S., Meier, F., Duarte, A., Quanz, J., Nouri, H., & Kleinschmit, B. (2021). Modeling urban evapotranspiration using remote sensing, flux footprints, and artificial intelligence. *Science of the Total Environment*, *786*. https://doi.org/10.1016/j.scitotenv.2021.147293

[24] Wang, L., Duan, Y., Zhang, L., Rehman, T. U., Ma, D., & Jin, J. (2020). Precise estimation of NDVI with a simple NIR sensitive RGB camera and machine learning methods for corn plants. *Sensors (Switzerland)*, *20*(11), 1–15. https://doi.org/10.3390/s20113208

[25] Zhang, Y., Han, W., Niu, X., & Li, G. (2019). Maize crop coefficient estimated from UAV-measured multispectral vegetation indices. *Sensors (Switzerland)*, *19*(23), 1–17. https://doi.org/10.3390/s19235250

ONLINE DETECTION SYSTEM FOR CRUSHED RATE AND IMPURITY RATE OF MECHANIZED SOYBEAN BASED ON DEEPLABV3+
/
基于DeepLabV3+的大豆机械化收获破碎率和含杂率在线检测系统

Man CHEN *), Gong CHENG, Jinshan XU, Guangyue ZHANG, Chengqian JIN [1]
Nanjing Institute of Agricultural Mechanization, Ministry of Agriculture and Rural Affairs, Nanjing, Jiangsu / China
Tel: +8602584346113; E-mail: chm_world@163.com
Corresponding author: Man Chen
DOI: https://doi.org/10.35633/inmateh-70-48

Keywords: *soybean, machine-based harvesting quality, dynamic detection, image segmentation, DeepLabV3+*

ABSTRACT
In this study, an online detection system of soybean crushed rate and impurity rate based on DeepLabV3+model was constructed. Three feature extraction networks, namely the MobileNetV2, Xception-65, and ResNet-50 models, were adopted to obtain the best DeepLabV3+model through test analysis. Two well-established semantic segmentation networks, the improved U-Net and PSPNet, are used for mechanically harvested soybean image recognition and segmentation, and their performances are compared with the DeepLabV3+ model's performance. The results show that, of all the models, the improved U-Net has the best segmentation performance, achieving a mean intersection over union (F_{MIOU}) value of 0.8326. The segmentation performance of the DeepLabV3+ model using the MobileNetV2 is similar to that of the U-Net, achieving F_{MIOU} of 0.8180. The DeepLabV3+ model using the MobileNetV2 has a fast segmentation speed of 168.6 ms per image. Taking manual detection results as a benchmark, the maximum absolute and relative errors of the impurity rate of the detection system based on the DeepLabV3+ model with the MobileNetV2 of mechanized soybean harvesting operation are 0.06% and 8.11%, respectively. The maximum absolute and relative errors of the crushed rate of the same system are 0.34% and 9.53%, respectively.

摘要
为了实现大豆机械化收获破碎率和含杂在线检测，本研究构建了基于 DeepLabV3+的在线检测系统，并采用三种特征提取网络（MobileNetV2、Xcepton-65 和ResNet-50 模型）测试分析获得最佳的DeepLabV3+模型。引入改进的U-Net 和PSPNet 模型，评估DeepLabV3+模型的性能。结果表明，在所有模型中，改进的U-Net 具有最佳的分割性能，平均交并比值达到 0.8326。基于 MobileNetV2 的 DeepLabV3+模型的分割性能与改进的U-Net 相似，平均交并比值为0.8180。基于MobileNetV2 的DeepLabV3+模型分割大豆图像速度为168.6ms。以人工检测结果为基准，基于MobileNetV2 的DeepLabV3+模型检测大豆含杂率的最大绝对误差和相对误差分别为 0.06%和8.11%，破碎率的最大绝对误差和相对误差分别为 0.34%和9.53%。

INTRODUCTION
Soybean is one of the main crops grown in China and occupies an important position in food crops. At present, soybean harvesting in China is mainly conducted by a harvester for mechanized harvesting at the early stage of plant maturity. A mechanized soybean harvesting method is to use a rice–wheat combine harvester, configure a flexible header, and adjust the parameters of the threshing drum to harvest soybeans *(Chen et al., 2020)*. Different from cereal crops, soybean has agronomic characteristics of low pod setting and easy breakage. In the process of mechanized harvesting, using inappropriate harvesting machinery and selecting the harvesting period improperly can result in high impurity and crushed rates. At present, the intelligence level of soybean combine harvesters is low, and there is a lack of an online quality detection system for mechanized soybean harvesting.

[1] *Man Chen, Associate Prof. Ph.D. Eng.; Gong Cheng, Stud. Eng.; Jinshan Xu, Senior Eng.; Guangyue Zhang, Eng.; Chengqian Jin, Prof. Ph.D. Eng..*

Soybean harvester drivers cannot accurately determine the operation quality of a harvester, which can easily lead to high impurity rate and crushed rate of soybean mechanization, affecting the quality of harvested soybeans and reducing the economic benefits of soybean planting *(Kang et al., 2022)*. Therefore, an online inspection of the operation quality of mechanized soybean harvesting is urgently needed, which can provide a harvester driver with real-time information on harvesting quality crushed rate and impurity rate, helping the driver to determine the working status of the harvester in real time. This can effectively improve the quality of mechanized soybean harvesting.

Mechanically harvested soybeans typically contain crushed grains (e.g., skin-damaged grain and cotyledon split grain) due to mechanical damage and impurities (e.g., pods, plant stems, and leaves) in addition to intact grains. Mixed impurities differ obviously in color and in shape compared to intact grain. Namely, crushed grain does not change much in color but can vary in texture. Differences in color and texture between intact grains, crushed grains, and impurities enable the application of machine vision and image processing to the component classification of mechanically harvested soybean samples.

An online quality inspection system for mechanized soybean harvesting operation needs to segment intact grains, crushed grains, and impurities in soybean samples accurately. As a powerful technology in the field of artificial intelligence, deep learning has become a research hotspot in the field of agriculture *(Bhupendra et al., 2022)*. This technology has been applied in the fields of wheat variety classification and grain disease identification *(Laabassi et al., 2021)*, rice seed identification *(Zhang et al., 2021)*, and soybean plant leaf identification *(Wang et al., 2022)*.

Compared with traditional machine vision, deep learning is more robust and can learn more characteristics of soybean samples, such as the color and texture of impurities and crushed grains *(Jin et al., 2022)*. The DeepLabV3+ model is a semantic segmentation network, which has been proven to be effective and accurate in many studies *(Shoushtari et al., 2022)*.

In the field of agricultural production research, this technology has been applied to the classification of cucumber leaf disease severity *(Wang et al., 2021)*, wheat scab and lodging recognition *(Dai et al., 2021)*, lettuce abnormal leaf segmentation *(Wu et al., 2021)*, grape cultivation area recognition *(Sun et al., 2022)*, and rice lodging recognition *(Mu et al., 2022)*. The previous studies have demonstrated the promising application potential of the DeepLabV3+ model in semantic segmentation. The aforementioned studies have shown that semantic segmentation can be an effective method for grain recognition segmentation. Therefore, the application of semantic segmentation networks to identifying and segmenting mechanically harvested soybeans' intact grains, crushed grains, and impurities is promising.

On the basis of identifying and segmenting grain image components effectively using a reasonable scientific quantitative model, the online detection of grain mechanized harvesting quality can be realized. Chen et al. used an improved watershed algorithm to segment soybean images effectively and constructed an online detection system for mechanized soybean harvesting quality. The test results have shown that the designed system can accurately calculate the crushed and impurity rates and can also provide the visual monitoring and warning alarm of mechanized soybean harvesting quality *(Chen et al., 2020)*. Chen et al. segmented the images of rice grains harvested by a combine harvester using the U-Net model based on machine vision. The experimental results showed that the comprehensive evaluation index values of the rice grain segmentation, branch and stem segmentation, and stem segmentation were 99.42%, 88.56%, and 86.84%, respectively *(Chen et al., 2020)*. According to the results of recent related studies, an online inspection of mechanized soybean harvesting quality can be achieved by combining machine vision and deep learning technology.

This study aims to segment soybean sample composition (i.e., intact grain, crushed grain, and impurity) at the pixel level using the DeepLabV3+ model. In this study, the collected machine-harvested soybean sample images are labeled as "background," "intact grain," "crushed grain," and "impurity." Aiming to identify and segment image components of soybean samples accurately, this paper proposes a calculation model of the crushed and impurity rates of mechanized soybean harvesting operations based on the soybean image data. Three backbones, namely the MobileNetV2, ResNet-50, and Xception-65 models, are used to determine an optimal backbone for the DeepLabV3+ model. The improved U-Net model (*Jin et al., 2022*) and the PSPNet model (*Li et al., 2022*) are introduced to verify the performance of the DeepLabV3+ model. The field experiments are conducted to verify the performance of the proposed online quality inspection system for mechanized soybean harvesting based on the DeepLabV3+ model.

MATERIALS AND METHODS

Online quality inspection of mechanized soybean harvesting

This study developed an online detection device for the crushed and impurity rates of machine-harvested soybean quality and the corresponding test bench, as shown in Fig. 1.

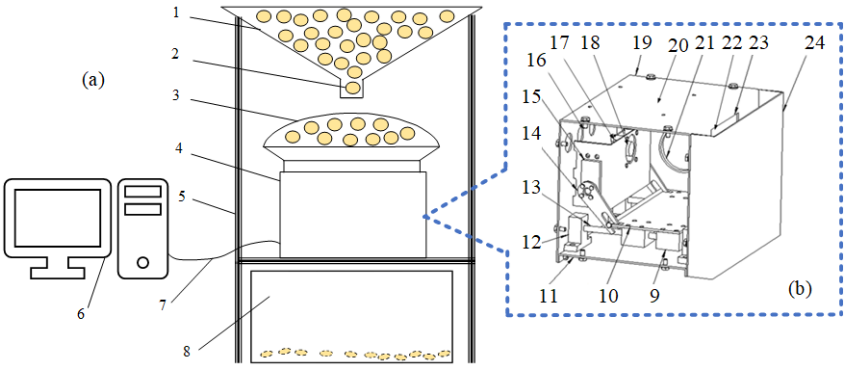

Fig. 1 – The online inspection system of the soybean harvesting machine operation quality. (a) The block diagram of the test bench for online detection of the soybean harvesting machine quality; (b) the structure of the online detection device of broken impurity content

1. storage bin for samples to be tested; 2. soybeans; 3. sampling funnel; 4. online detection device of crushed impurity content; 5. brackets, 6. image processing equipment; 7. data bus; 8. tested sample collection bin; 9. sliders; 10. telescopic plates; 11. bases; 12. guide rail seats; 13. guide rails; 14. levers; 15. direct-current steering gears; 16. data bus connectors; 17. industrial cameras; 18. industrial camera fixing bracket; 19. shell; 20. embedded data processing module; 21. light emitting diode visual light source; 22. transparent plexiglass; 23. photo window; 24. sampling chamber

The proposed online detection device for the crushed and impurity rates of machine-harvested soybean quality is composed of an image recognition part and a dynamic sample collection part. The image recognition part is used to collect and classify soybean samples in a photographing window, as well as to realize online recognition and segmentation of intact grains, crushed grains, and impurities in soybean samples. Meanwhile, the dynamic collection part is used to update soybean samples in a sampling bin dynamically. The online inspection system of the soybean harvesting machine operation quality controls the DC steering gear to rotate by 65° forward to drive the retractable plate to retract and release soybeans in the sampling bin. By reversing the DC steering gear by 65°, the system makes the telescopic plate extend, thus preventing the soybeans in the sampling bin from being discharged and achieving the goal of grain collection. The system realizes the dynamic update of soybean samples in the sampling bin by periodically controlling the forward and reverse rotation of the DC steering gear.

The image recognition part includes an industrial camera (LRCP10230, Huarui Vision Technology, Guangzhou, China), with a lens having a focal length of 12 mm and being 105 mm away from the transparent plexiglass, which is facing the photo window of the sampling bin. Under a LED visual light source, an RGB (red, green, blue) image captured by the industrial camera has a resolution of 1,280 × 1,024 pixels, and it is saved in the JPEG format. The image recognition part also includes an image processing device, which is mainly used for the recognition and classification of components of a soybean sample image. The image processing device is an Ubuntu18.04 host, which is Tsinghua Tongfang T45PRO laptop, with an Intel® Core® i7-6500U processor, 16-GB, 3,200-MHz DDR4 memory, and 6-GB Nvidia GeForce RTX3060 graphics card.

Data annotation and augmentation

A total of 300 images of machine-harvested soybean samples with a resolution of 1,280 × 1,024 were collected and saved as the original dataset. Generally, 50-70 soybeans were included in one image. The original image size was too large, which could cause the GPU memory to be exhausted, so the original images were downsampled. Image downscaling not only can save computational costs but can also serve as a basis for low-pixel-resolution vision sensor research. Therefore, each image was scaled to 512 × 512 pixels by bilinear interpolation. LabelMe 3.16.7, which is an Image Labeling Toolbox developed by the MIT Computer Science and Artificial Intelligence Laboratory, was used to label the images. The intact grains, crushed grains, and impurities of soybeans were marked by polygons first and then were given labels of “0” for background, “1” for crushed grains, “2” for intact grains, and “3” for impurities. Some of the RGB images and the corresponding label images are shown in Figs. 2(a) and 2(b), respectively. To avoid unbalanced performance evaluation on the test set, the data were randomly divided into a training set (240 images) and a test set (60 images) according to the division ratio of 4:1.

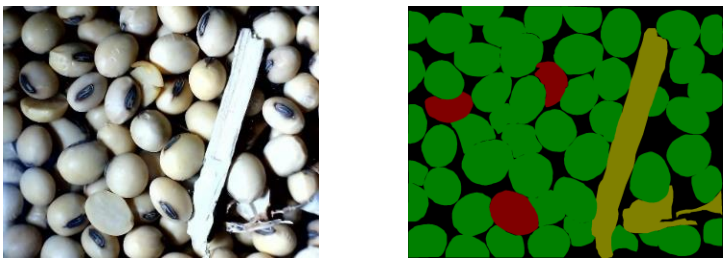

a) Original image *b) Labeled image*

Fig. 2 – An example of collected RGB images

Data augmentation plays a vital role in deep learning model training. A small number of training samples can cause overfitting or non-convergence of a deep learning-based model *(Deng et al., 2021)*. Data augmentation was performed on each image in the training set and the corresponding ground truth image *(Cotrim et al., 2020)*. The data augmentation methods used in this study included random image rotation (30–150°, 210–330°), random image scaling (0.5–0.8 times, 1.5–2.0 times), random image shearing (−30–30°), and horizontal mirroring; six augmented samples were generated for each training sample. Thereafter, the training set size was increased to 1,680 images by the above six methods. The training set images were randomly divided into a training set and a validation set according to the ratio of 9:1, so 1,512 images were used as a training set, and the remaining 168 images were used as a validation set. Based on the training set and validation set, the online identification and verification tests of different models for evaluating the soybean machine-based harvesting quality were conducted.

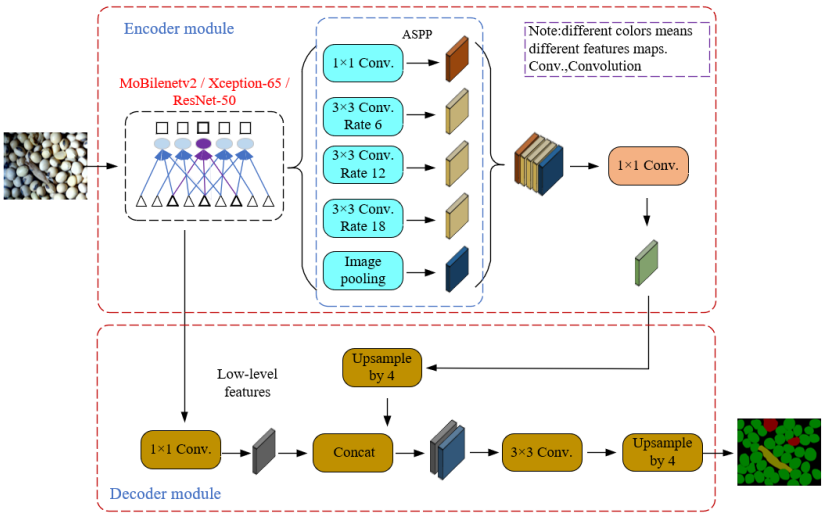

Fig. 3 – Block diagram of the DeepLabV3+ processing a machine-harvested soybean image

Deeplabv3+ architecture

The DeepLabV3+ model is a semantic segmentation network, which is based on the DeepLabV3 structure, where a simple and effective decoder has been added to refine segmentation results, especially the segmentation results along the boundary of a target object. The DeepLabV3+ uses a spatial pyramid pooling module or a two-in-one encoding-decoding structure for segmentation. As shown in Fig. 3, the DeepLabV3+ network consists of two main parts, encoder and decoder modules. It uses the Atrous Spatial Pyramid Pooling (ASPP) mechanism to detect convolutional features at multiple scales by applying atrous convolutions with different image-level feature rates. In the encoder module, the training set is input into the backbone to obtain the feature map, which is then input into the ASPP that consists of a 1 × 1 convolution, three 3 × 3 atrous convolutions (with the atrous rates of 6, 12, and 18), and an image pooling layer. The convolution layers extract features locally, while the image pooling layer extracts features globally, thus obtaining multi-scale features. All feature maps obtained by the ASPP are concatenated into combined feature maps. Then, a 1 × 1 convolutional layer is used to fuse the information in the combined feature map and reduce the number of channels of the feature map. The last feature map after the 1 × 1 convolution is used as an encoder output module. The encoder features are first bilinearly upsampled four times and then concatenated with the corresponding low-level features from the backbone with the same spatial resolution. Another 1 × 1 convolution is applied to the low-level features to reduce the number of channels. After concatenation, 3 × 3 convolutions are used to refine the features, followed by four simple bilinear upsampling.

Network training

The U-Net, PSPNet, and DeepLabV3+ models were trained and tested using Ubuntu20.04 host (Dell Precision 7920 Tower graphics workstation) with a GPU (Nvidia Quadro RTX5000 16 GB GPU), a 26-core CPU (Dual Intel® Xeon® Gold 6230R), 4.00 GHz), and a 128-GB, 3200-MHz DDR4 memory. The models were deployed using Python 3.6, torch 1.2.0, torchvision 0.4.0, scipy 1.2.1, numpy 1.17.0, matplotlib 3.1.2, opencv_python 4.1.2.30, tqdm 4.60.0, Pillow 8.2.0, and h5py 2.10.0 training environment, and the GPU and CPU dual devices were employed to train and test different networks. To train DeepLabV3+, improved U-Net and PSPNet models for soybean dataset in this study, weights of a pretrained model were used for initialization, which were fine-tuned with further training. These initial weights were obtained from pretrained model of the PASCAL VOC 2007 dataset *(Yin et al., 2021)*.

Field test design

The experimental site was the experimental soybean field in Houliu Village, Rencheng District, Jining City, Shandong Province. The soybean variety was also Qihuang 34; the moisture content was 12.1%; the thousand-kernel weight was 246.5 g. The test was conducted on October 18, 2021. The experimental harvesting machine was a 4LZ-6 intelligent soybean combine harvester. The field test was repeated test three times, with a single trip length of 200 m and an operating speed of 6 km/h. The test site is shown in Fig. 4.

Fig. 4 – Field validation experimental environment

The soybean sampling device was installed under the outlet of the grain conveying device of the 4LZ-6 intelligent soybean combine harvester, and the combine harvester was connected to the onboard power supply to debug the equipment. The combine harvester started harvesting, and the soybean crushed and impurity content detection device automatically and dynamically detected the operation effect online. After completing one field test, the machine was stopped, three samples were selected randomly from the grain tank, and the crushed rate and impurity rate were manually checked according to the NY/T738-2020 “Operation Quality of Soybean Combine Harvester” standard, which were used to verify the accuracy of the proposed system’s detection results. After the sampling was completed, the machine was started to perform the harvesting test; the field test was repeated two times; and the experimental data were used to verify the performance of the online detection system for monitoring soybean crushed rate and impurity rate.

Performance evaluation

In this study, precision rate P, recall rate R, comprehensive evaluation index F_1, intersection ratio F_{IOU}, average intersection ratio F_{MIOU}, and average processing speed I_{v} of a machine-harvested soybean sample image were used as evaluation indicators of the image recognition and classification results of different models, and they were respectively calculated as follows:

$$P = \frac{T_P}{(T_P+F_P)} \times 100\% \ \ [\%] \tag{1}$$

$$R = \frac{T_P}{(T_P+F_N)} \times 100\% \ \ [\%] \tag{2}$$

$$F_1 = \frac{2\times P\times R}{P+R} \times 100\% \ \ [\%] \tag{3}$$

$$F_{IOU} = \frac{T_P}{T_P+F_P+F_N} \tag{4}$$

$$F_{MIOU} = \sum_{i=1}^{n} \frac{F_{IOUi}}{n} \tag{5}$$

where: T_P is the number of correctly classified pixels predicted to be correctly classified;

F_{P} is the number of wrong classified pixels predicted to be correctly classified;

F_N is the number of correctly classified pixels predicted to be misclassified;

n is the number of categories of classification;

I_v is the average processing speed of a soybean sample image, [ms].

In the existing methods for quality detection of a soybean combine harvester, the impurity rate represents the percentage of the mass of grains and impurities in a sample; the crushed rate is the percentage of the mass of crushed and intact grains in a sample. According to the existing measurement methods, the pixel-based crushed and impurity rates were calculated as follows:

$$P_z = \frac{T_z}{(T_z + \partial T_w + \partial T_s)} \times 100\% \quad [\%] \tag{6}$$

$$P_s = \frac{T_s}{(T_w + T_s)} \times 100\% \quad [\%] \tag{7}$$

where: P_z is the impurity rate of soybean, [%];

P_s is the crushed rate of soybean, [%];

T_w is the number of pixels of intact grains in a predicted image;

T_s is the number of pixels of crushed grains in the predicted image;

T_z is the number of impurities pixels in the predicted image;

∂ is the ratio of the average mass of grains to the average mass of impurities for 1,000 pixel points. In laboratory conditions, *∂* was set to 8.66 by manual calibration.

The absolute and relative errors of the average value of the proposed system's detection results and manual detection results were used to evaluate the performance of the online DeepLabV3+-based monitoring system of soybean machine-based harvesting quality. The calculation formulae were as follows:

$$R_{az} = |\overline{P_{Sz}} - \overline{P_{Mz}}| \quad [\%] \tag{8}$$

$$R_{rz} = \frac{|\overline{P_{Sz}} - \overline{P_{Mz}}|}{\overline{P_{Mz}}} \times 100\% \quad [\%] \tag{9}$$

$$R_{as} = |\overline{P_{Ss}} - \overline{P_{Ms}}| \quad [\%] \tag{10}$$

$$R_{rs} = \frac{|\overline{P_{Ss}} - \overline{P_{Ms}}|}{\overline{P_{Ms}}} \times 100\% \quad [\%] \tag{11}$$

where: $\overline{P_{Sz}}$ is the average impurity rate of samples detected by the proposed system, [%];

$\overline{P_{Mz}}$represents the average impurity rate of manually detected samples, [%];

R_{az} represents the absolute error of the impurity rate, [%];

R_{rz} represents the relative error of the impurity rate, [%];

$\overline{P_{Ss}}$represents the average crushed rate of samples detected by the proposed system, [%];

$\overline{P_{Ms}}$ represents the average crushed rate of manually detected samples, [%];

R_{as} represents the absolute error of the crushed rate, [%];

R_{rs} represents the relative error of the crushed rate, [%].

RESULTS

Training performance

The recognition and classification performances of the improved U-Net, PSPNet, and DeepLabV3+ models for different backbone networks on the test set images are shown in Fig. 5. As shown in Fig. 5, compared to the other models, the improved U-Net achieved sample component profiles with better connectivity and smoother channel shapes.

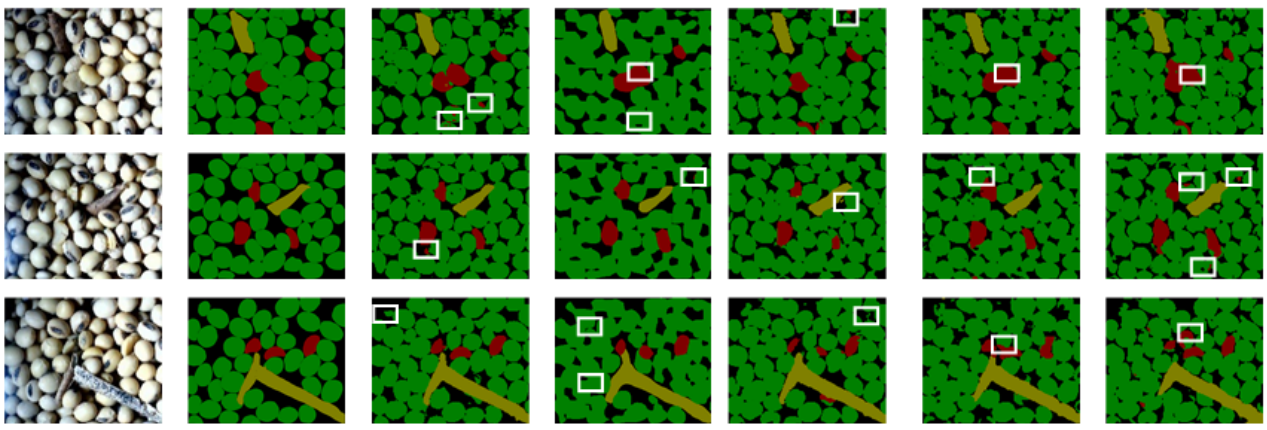

a) Original image b) Labeled image c) Improved U-Net d) PSPNet e) MobileNetV2 f) Xcepton-65 g) ResNet-50

Fig. 5– Classification results of different networks on the machine-harvested soybean images

The statistical results of different evaluation indicators of the recognition and classification effects of the improved U-Net, PSPNet, and DeepLabV3+ for different backbone networks on the test set are given in Table 1. This study focused on three metrics, namely F_1, F_{MIOU}, and I_{v}. Metric F_1 denotes the harmonic mean of precision and recall. The maximum F_1 indicates that a model has an optimal balance of recall and precision. Further, F_{MIOU} is a standard semantic segmentation metric, and it denotes the average value of the ratios of intersections and unions of all categories. The maximum F_{MIOU} indicates that a model achieves the optimal overall image recognition and segmentation performance. The proposed online detection method of machine-based soybean harvesting operation quality was applied to the mechanized soybean harvesting process to realize the online detection of a soybean harvester's operation quality. It should be noted that the processing time of a network directly defines the system's image recognition performance. A higher I_{v} indicates a faster image recognition speed of a model and demonstrates the actual needs of production are met better.

Table 1

Recognition and classification performances of different models on machine-harvested soybean images

Detection object	Parameter	Improved U-Net	PSPNet	DeepLabV3+		
		Vgg-16	MobileNetV2	MobileNetV2	Xception-65	ResNet-50
Intact grains	Precision rate [%]	89.04	86.19	87.63	88.54	85.45
	Recall rate [%]	95.07	90.66	95.61	93.62	94.43
	Comprehensive evaluation index [%]	91.75	88.18	91.25	90.90	89.51
	Intersection ratio [%]	0.8483	0.7891	0.8406	0.8346	0.8109
Crushed grains	Precision rate [%]	86.16	74.59	89.16	73.97	70.04
	Recall rate [%]	88.70	78.65	80.78	92.15	86.57
	Comprehensive evaluation index [%]	87.23	75.47	84.23	80.92	76.98
	Intersection ratio [%]	0.8043	0.618	0.7364	0.6916	0.6419
Impurities	Precision rate [%]	93.23	91.53	91.74	86.10	80.81
	Recall rate [%]	97.10	85.43	95.40	95.86	94.62
	Comprehensive evaluation index [%]	95.09	88.10	93.39	90.23	86.95
	Intersection ratio [%]	0.9068	0.7894	0.877	0.825	0.7702
Average intersection ratio [%]		0.8531	0.7322	0.8180	0.7837	0.741
Average processing speed of a soybean sample image [ms]		266.4	166.3	168.6	213.1	190.3

In terms of F_1, the improved U-Net model performed the best among all models, having the recognition accuracies of 91.75%, 87.23%, and 95.09% for the intact grains, crushed grains, and impurities, achieving improvements of 3.57%, 11.76%, and 6.99% compared with the PSPNet model, respectively. The recognition performance of the DeepLabV3+ model was similar to that of the improved U-Net. Among the DeepLabV3+ models, the DeepLabV3+ model based on MobileNetV2 had the best performance, with F_1 values of 91.25%, 84.23%, and 93.39% for the intact grains, crushed grains, and impurities, respectively. The F_{MIOU} value of the improved U-Net model was the highest among all models, reaching 0.8531. The PSPNet model had the lowest F_{MIOU} value, of only 0.7322. The F_{MIOU} value of the DeepLabV3+ was slightly lower than that of the improved U-Net model; particularly, the F_{MIOU} values of the DeepLabV3+ based on MobileNetV2, Xception-65, and ResNet-50 were 0.8180%, 0.7837%, and 0.741%, respectively. In terms of average image processing time, the U-Net model had the worst performance among all models, with an average image processing time of 266.4 ms. The image processing times of the DeepLabV3+ and PSPNet models based on the MobileNetV2 were the shortest, having values of 168.6 ms and 166.3 ms, respectively. Considering the image processing time and accuracy jointly, the DeepLabV3+ model based on the MobileNetV2 achieved best recognition and segmentation results with low time consumption among all models. According to the result, the DeepLabV3+ model based on MobileNetV2 was more suitable for online quality inspection of machine-based soybean harvesting than the other models.

Field test results analysis

During the test, the MobileNetV2-based DeepLabV3+ online quality inspection system for machine-harvested soybeans worked normally, realizing dynamic online detection of machine-harvested soybean samples. Table 2 provides statistical data of the bench and field experiments.

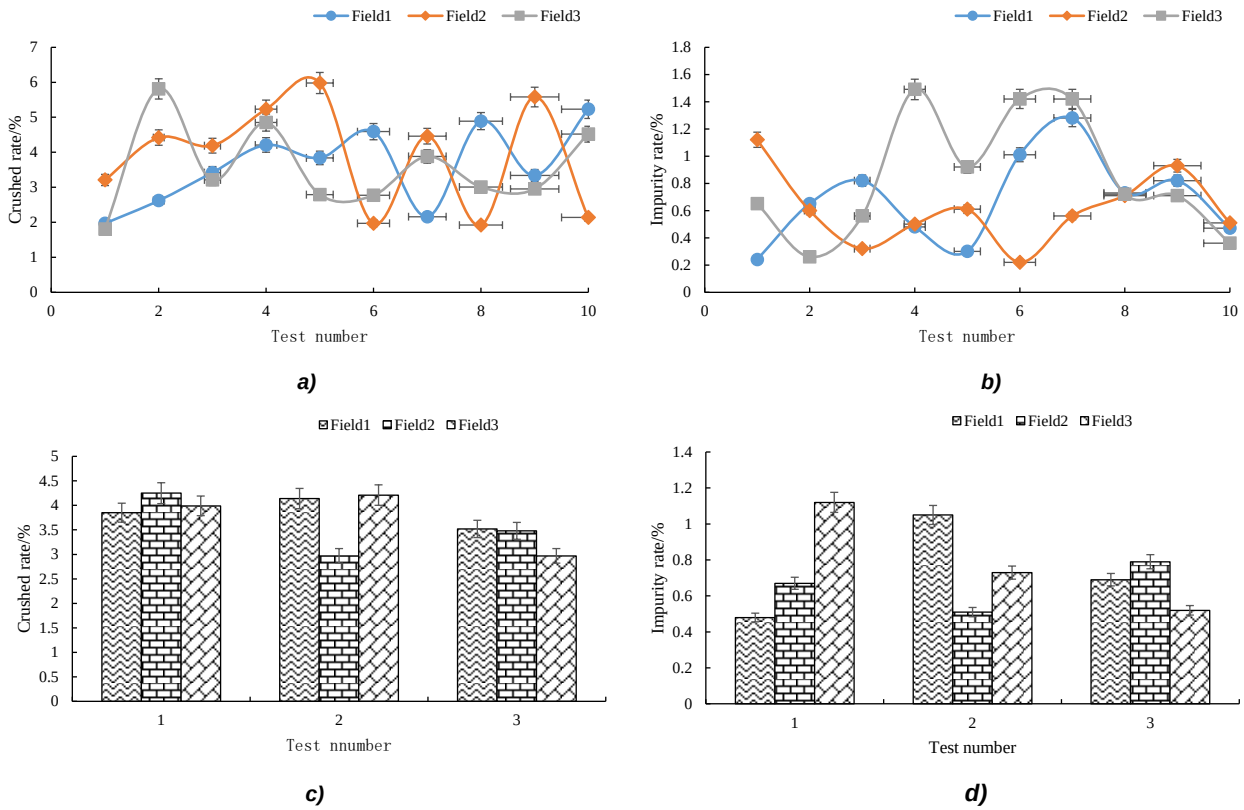

Fig. 6 – Field test results. System detection results of (a) crushed rate and (b) impurity rate. Manual detection results of (c) crushed rate and (d) impurity rate

The test results are shown in Fig. 6 and Table 2. In the online three-stroke mechanized soybean harvesting operation quality inspection test, the average impurity rates detected by the system and manual detection were 0.71% and 0.73%, respectively. Taking the manual detection results as a benchmark, the maximum absolute and relative errors of the system's impurity rate detection results were 0.06% and 8.11%, respectively. The average crushed rates detected by the system and manual detection were 3.70% and 3.71%, respectively. Taking the manual detection results as the standard values of impurity rate and crushed rate of soybean samples to be tested, the maximum absolute and relative errors of the system's crushed rate detection results were 0.34% and 9.53%, respectively. Therefore, there was a certain difference between the system's numerical results and the manual detection results. However, all detection results indicated that during the actual operation, the impurity rate of the soybean combine harvester was less than 3%, while the crushed rate was less than 5%. According to the NY/T738-2020 "Operation Quality of Soybean Combine Harvester" standard, the soybean harvester shall ensure that the impurity rate is less than 3% and the crushed rate is less than 5% during the soybean harvesting operation. It can be seen that both detection methods showed that the operational performance of the soybean combine harvester conformed to the national standard.

Table 2

Statistical results of the bench and field tests

Field test number	System monitoring results		Manual inspection results		Statistics			
	Average impurity rate of samples [%]	Average crushed rate of samples [%]	Average impurity rate of samples [%]	Average crushed rate of samples [%]	Absolute error of the impurity rate [%]	Relative error of the impurity rate [%]	Absolute error of the crushed rate [%]	Relative error of the crushed rate [%]
1	0.68	3.63	0.74	3.84	0.06	8.11	0.21	5.47
2	0.61	3.91	0.66	3.57	0.05	7.61	0.34	9.53
3	0.85	3.56	0.79	3.72	0.06	7.59	0.16	4.30

CONCLUSIONS

To realize online quality inspection of machine-harvested soybeans and ensure their quality, this paper proposes an online inspection system for machine-harvested soybeans based on deep learning. A machine-harvested soybean component detection model is constructed using three different backbones in the DeepLabV3+ model. The improved U-Net and PSPNet models are introduced to analyze the detection performance of the constructed detection models. Considering the real-time performance and accuracy jointly, an optimal detection model is determined, and the crushed and impurity rates of machine-harvested soybeans are calculated by the quantitative model. The results show that the improved U-Net model achieves the F_{MIOU} value of 0.8531 on intact grains, crushed grains, and impurities identification segmentation. The DeepLabV3+ model based on the MobileNetV2 has the F_{MIOU} value of 0.8180, while its F_1 values reach 91.25%, 84.23%, and 93.39% for the three soybean categories. In terms of speed, the MobileNetV2-based DeepLabV3+ model needs 168.6 ms to segment an image with a resolution of 512 × 512 pixels using an Nvidia Quadro RTX5000 16 GB GPU, while the improved U-Net model takes 266.4 ms for the same task. Based on the manual inspection results, in the field test, the maximum absolute and relative errors of the impurity rate of the DeepLabV3+ model using the MobileNetV2 are 0.06% and 8.11%, respectively, and those of the crushed rate are 0.34% and 9.53%, respectively. The quality detection results of the crushed and impurity rates obtained by the proposed system in the soybean machine-based harvesting test can meet the needs of actual production. In the future, we will continue to conduct relevant field trials to verify the reliability of the mechanized harvesting soybean quality inspection system, and promote the industrial application of the system.

ACKNOWLEDGEMENT

We greatly appreciate the careful and precise reviews by the anonymous reviewers and editors. This research was financially supported by the National Natural Science Foundation of China (No.32272004), and the National Key Research and Development Program of China (No. 2021YFD2000503), and the Natural Science Foundation of Jiangsu (No. BK20221188).

REFERENCES

[1] Bhupendra M. K., Miglani A. Kankar, P.K. (2022). Deep CNN-based damage classification of milled rice grains using a high-magnification image dataset. *Computers and Electronics in Agriculture*, Vol.195, pp.106811. United States. https://doi.org/10.1016/j.compag.2022.106811

[2] Chen J., Han M.N., Lian Y. et al (2020). Segmentation of impurity rice grain images based on U-Net model (基于 U-Net 模型的含杂水稻籽粒图像分割). *Transactions of the Chinese Society of Agricultural Engineering (Transactions of the CSAE)*. Vol.36, no.10, pp.174-180. Beijing / China. https://doi.org/10.11975/j.issn.1002-6819.2020.10.021

[3] Chen M., Ni Y.L., Jin C.Q. et al (2021). Online monitoring method of mechanized soybean harvest quality based on machine vision (基于机器视觉的大豆机械化收获质量在线监测方法). *Transactions of the Chinese Society for Agricultural Machinery*. Vol.52, no.1, pp.91-98. Beijing / China. https://doi.org/10.6041/j. issn.1000-1298.2021.01.010

[4] Chen Y.P., Kang Y., Wang T.E. et al (2020). Distribution regularities of the threshed mixtures in longitudinal axial flow flexible thresher of soybean harvester (大豆收获机纵轴流柔性脱粒装置脱出物分布规律). *Journal of China Agricultural University*. Vol.25, no.09, pp.104-111. Beijing / China. https://doi.org/10.11841/j.issn.1007-4333.2020.09.11

[5] Cotrim W. da S., Minim V.P.R., Felix L.B. et al (2020). Short convolutional neural networks applied to the recognition of the browning stages of bread crust. *J. Food Eng*. Vol.277, pp.109916. England. https://doi.org/10.1016/j.jfoodeng.2020.109916

[6] Dai Y.S., Zhong X.C., Sun C.M. et al (2021). Identification of fusarium head blight in wheat-based on image processing and Deeplabv3+ model (基于图像处理和 Deeplabv3+模型的小麦赤霉病识别). *Journal of Chinese Agricultural Mechanism*. Vol.42, no.9, pp.209-215. Jiangsu / China https://doi.org/10.13733/j.jcam.issn.2095-5553.2021.09.29

[7] Deng L., Li J. Han Z. (2021). Online defect detection and automatic grading of carrots using computer vision combined with deep learning methods. *LWT - Food Sci. Technol*. Vol.149, pp.111832. England. https://doi.org/10.1016/j.lwt.2021.111832

[8] Jin C.Q., Liu S.K. Chen M. (2022). Semantic segmentation-based mechanized harvesting soybean quality detection. *Science Progress*. Vol.105, no.2, pp.1-19. England. https://doi.org/10.1177/00368504221108518

[9] Jin C.Q., Liu S.K., Chen M. et al (2022). Online quality detection of machine-harvested soybean based on improved U-Net network (采用改进 U-Net 网络的机收大豆质量在线检测). *Transactions of the Chinese Society of Agricultural Engineering (Transactions of the CSAE)*. Vol.38, no.16, pp.70-80. Beijing/China. https://doi.org/10.11975/j.issn.1002-6819.2022.16.008

[10] Kang J.X, Wang X.S., Xie F.P. et al (2022). Design and experiment of symmetrical adjustable concave for soybean combine harvester (大豆联合收获机对称可调式凹板筛设计与试验). *Transactions of the Chinese Society of Agricultural Engineering (Transactions of the CSAE)*. Vol.38, no.2, pp.11-22. Beijing/China. https://doi.org/10.11975/j.issn.1002-6819.2022.02.002

[11] Laabassi K., Belarbi M.A., Mahmoudi S. et al (2021). Wheat varieties identification based on a deep learning approach. *Journal of the Saudi Society of Agricultural Sciences*. Vol.20, pp.281-289. Saudi Arabia. https://doi.org/10.1016/j.jssas.2021.02.008

[12] Li H.P., Li C.Y., Li G.B. et al (2022). Picking point positioning of multi variety table grapes based on deep learning (基于深度学习的多品种鲜食葡萄采摘点定位). *Journal of Chinese Agricultural Mechanization*. Vol.43, no.12, pp.155-161. Jiangsu/China. https://doi.org/10.13733/j.jcam.issn.20955553.2022.12.023

[13] Mu T.Y., Zhao W., Hu X.Y. et al (2022). Rice lodging recognition method based on UAV remote sensing combined with the improved DeepLabv3+ model (基于改进的 DeepLabV3+模型结合无人机遥感的水稻倒伏识别方法). *Journal of China Agricultural University*. Vol.27, no.2, pp.143-154. Beijing / China. https://doi.org/10.11841/j.issn.1007-4333.2022.02.14

[14] Shoushtari F.K., Sina S. Dehkordi A.N. (2022). Automatic segmentation of glioblastoma multiform brain tumor in MRI images: Using Deeplabv3+ with pre-trained Resnet18 weights. *Physica Medica*. Vol.100, pp.51-63. Italy. https://doi.org/10.1016/j.ejmp.2022.06.007

[15] Sun Z.T., Zhu S.N., Gao Z.J. et al (2022). Recognition of grape growing areas in multispectral images based on band enhanced DeepLabv3+ (基于波段增强的 DeepLabv3+多光谱影像葡萄种植区识别). *Transactions of the Chinese Society of Agricultural Engineering (Transactions of the CSAE)*. Vol.38, no.7, pp.229-236. Beijing/China. https://doi.org/10.11975/j.issn.1002-6819.2022.07.025

[16] Wang B., Li H., You J.W. et al (2022). Fusing deep learning features of triplet leaf image patterns to boost soybean cultivar identification. *Computers and Electronics in Agriculture*. Vol.197, pp.106914. United States. https://doi.org/10.1016/j.compag.2022.106914

[17] Wang C.S., Du P.F., Wu H.R. et al (2021). A cucumber leaf disease severity classification method based on the fusion of DeepLabV3+ and U-Net. *Computers and Electronics in Agriculture*. Vol.189, pp.106373. United States. https://doi.org/10.1016/j.compag.2021.106373

[18] Wu Z.C., Yung R.Z., Gao F.F. et al (2021). Segmentation of abnormal leaves of hydroponic lettuce based on DeepLabV3+ for robotic sorting. *Computers and Electronics in Agriculture*. Vol.190, pp.106443. United States. https://doi.org/10.1016/j.compag.2021.106443

[19] Yin Q.J., Yang W.Z., Ran M.G. et al (2021). FD-SSD: An improved SSD object detection algorithm based on feature fusion and dilated convolution. *Signal Processing: Image Communication*. Vol.98, pp.116402. Netherlands. https://doi.org/10.1016/j.image.2021.116402

[20] Zhang J., Qu M.Z., Gong Z.Y. et al (2022). Online double-sided identification and eliminating system of unclosed-glumes rice seed based on machine vision. *Measurement*. Vol.187, pp.110252. England. https://doi.org/10.1016/j.measurement.2021.110252

NUMERICAL ANALYSIS OF A NOVEL VERTICAL-AXIS WIND TURBINE LAYOUT
/
ANALIZA NUMERICĂ A UNEI NOI CONFIGURAŢII DE TURBINE EOLIENE CU AX VERTICAL

Dragos PREDA*[1)], Bogdan DURAN[1)], Adrian PANDELE[1)], Oana-Diana MANOLELI-PREDA[1)], Aneta IONESCU [1)]
[1)]Rolix Series Impex, 256 Basarabiei Blvd, District 3, Bucharest / Romania;
Tel: +4079-998642; E-mail: dragospreda@yahoo.com
DOI: https://doi.org/10.35633/inmateh-70-49

Keywords: *renewable energy, wind turbine, computational fluid dynamic, torque coefficient, vorticity magnitude*

ABSTRACT
Governmental incentives, technological progress, and lowering costs have made renewable energy more accessible and more affordable for residential areas. Switching to renewable energy sources not only reduces greenhouse gas emissions but also provides long-term financial gains, energy independence, and a cleaner environment for communities. In this study, a numerical analysis of a vertical-axis wind turbine layout that is easily adaptable to populated areas was conducted. Among the results are the variation of the torque coefficient during the course of a complete 360-degree rotation and the vorticity magnitude evolution at the nominal point. In order to validate the numerical results, a test campaign will be conducted inside the wind tunnel as part of further study. This campaign will be carried out using an experimental small-scale model.

REZUMAT
Stimulentele guvernamentale, progresele tehnologice și reducerea costurilor au făcut energia regenerabilă mai accesibilă și mai accesibilă pentru zonele rezidențiale. Trecerea la surse regenerabile de energie nu numai că reduce emisiile de gaze cu efect de seră, dar oferă și câștiguri financiare pe termen lung, independență energetică și un mediu mai curat pentru comunități. În acest studiu, a fost efectuată o analiză numerică a unei configurații de turbine eoliene cu ax vertical care poate fi, cu uşurinţă, adaptata la zonele populate. Printre rezultate se numără variația coeficientului de cuplu în cursul unei rotații complete de 360 de grade și evoluția vorticității la punctul nominal. Pentru validarea rezultatelor numerice, va fi efectuată o campanie de testare în interiorul tunelului de vânt, ca parte a studiilor viitoare. Această campanie se va desfășura folosind un model experimental la scară mică.

INTRODUCTION

Environmental concerns, technological advancement, governmental support, and market forces have all contributed to the emergence of renewable energy (*Deyu et al., 2020*). Despite the fact that there are still difficulties to be solved (*Ang et al., 2022*), the advancements made so far point to a bright future for renewable energy as a dependable and sustainable power source (*Sebestyén, 2021*). Over the past few decades, renewable energy has seen considerable change and growth and has continued to be essential to the world's energy transition (*Bhattarai et al., 2022*).

It's important to remember that wind energy is only one element in a varied mix of renewable energy sources that also includes solar, hydro, geothermal, and biomass (*Thellufsen et al., 2020*). A future energy system that is more resilient and sustainable can be built by combining these different energy sources.

Wind turbines are machinery that use the wind's energy to create electricity. Around the world, they are a well-liked and quickly expanding source of sustainable energy. A wind turbine is made up of numerous major parts (*Olabi et al., 2021*). The rotor, which frequently has three blades, absorbs the wind's kinetic energy. When the wind blows, a shaft that is attached to the blades spins (*Ramakrishnan et al., 2022*). A generator uses this spin to turn mechanical energy into electrical energy (*Drancă et al., 2019*). The turbine either uses the electricity it produces on-site or feeds it into the power grid.

There are several sizes of wind turbines, with capacities ranging from a few kilowatts to several megawatts (*Bilgili, et al., 2022*). The available wind resource, project economics, and the particular site needs are only a few examples of the variables that affect the turbine's size (*Neshat, et al., 2021*).

[1]*DragosPreda, researcher III degree; Bogdan Duran, researcher III degree; Adrian Pandele, engineer; Oana-Diana Manoleli-Preda, engineer; Aneta, Ionescu, engineer*

Despite the many benefits of wind energy, there are a few things to think about and difficulties to overcome. These include the wind's erratic behavior, the possibility of having an effect on the region's species and ecosystems (*Nazir et al., 2020*), the aesthetic impact, and public acceptability.

A wind turbine with a main rotor shaft that is vertically oriented is known as a vertical axis wind turbine (VAWT) (*Bucur, et al., 2021*). VAWTs feature blades that spin along a vertical axis as opposed to the horizontal axis as is the case with conventional horizontal-axis wind turbines (HAWTs). Without a yaw mechanism to spin the rotor into the wind, this design enables the turbine to catch wind from any direction (*Costea, et al., 2019*).

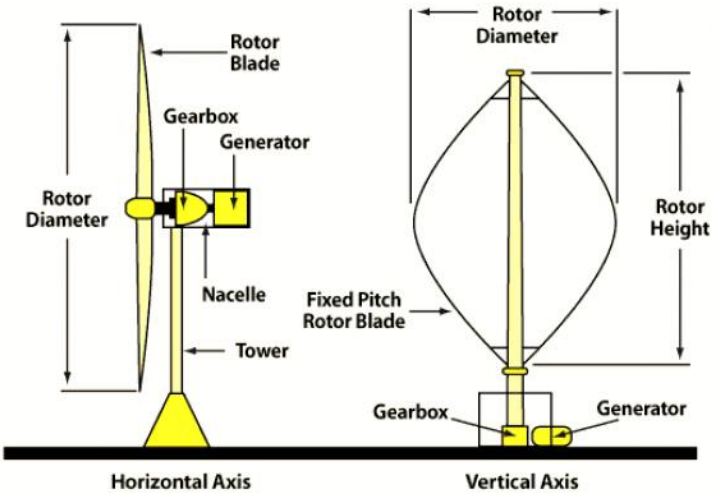

Fig.1 - VAWT vs. HAWT
(*Ahammed et al., 2021*)

Small VAWTs are often utilized in residential or small-scale applications when there is a lack of available space or where aesthetics play a significant role (*Malael, et al., 2021*). They have a smaller footprint than horizontal axis wind turbines, making them suited for locations with limited space. They may be put on roofs, in backyards, or in other urban or suburban settings (*Gall, et al., 2022*). Some compact VAWTs feature a sleek, contemporary style that is suited for applications where aesthetics are important and makes them visually appealing (*Condruz et al., 2019*).

Wind turbine integration in agriculture is an idea that blends renewable energy generation with agricultural land usage (*Skibko et al. 2021*). Wind turbines installed on fields allow farmers to create clean, sustainable power while still using the area for agriculture (*Calderon, et al., 2019*). Wind turbines can provide an extra revenue source for farmers by selling electricity to the grid or powering on-site enterprises. This diversification can aid in income stabilization during agricultural downturns (*Mostafaeipour et al., 2019*). Wind turbines have a low footprint, leaving the majority of the land open for agriculture. This allows farmers to make the most use of their land while potentially increasing their overall yield (*Bardi, et al., 2013*).

Figure 2 shows a movable platform with wind turbines and solar panels that was built as part of a research project and has a technological readiness level of 7 for producing electricity in agricultural fields in off-grid settings.

Fig. 2 - The mobile platform with wind turbines and solar panels for electric current production at agricultural farms in off-grid areas (*Preda et al., 2023*).

Energy requirements for irrigation, equipment, and other activities are frequently high for farmers (*Saputra et al., 2018*). On-site wind turbines can help offset these energy expenses, improving the profitability and sustainability of agriculture.

Farmers may reduce their reliance on unpredictable energy markets and outside energy sources by producing their own electricity (*Sampson al., 2020*). However, there are several difficulties and things to think about when incorporating wind turbines into agriculture. The main one is the high upfront cost, which some farmers may find to be prohibitive. Government assistance and financing sources can help with this issue (*Sutherland al., 2014*). A solution created for agricultural applications is shown in Figure 3. This platform is portable and may be placed in a field of crops. The energy it produces is then utilized to irrigate the crops.

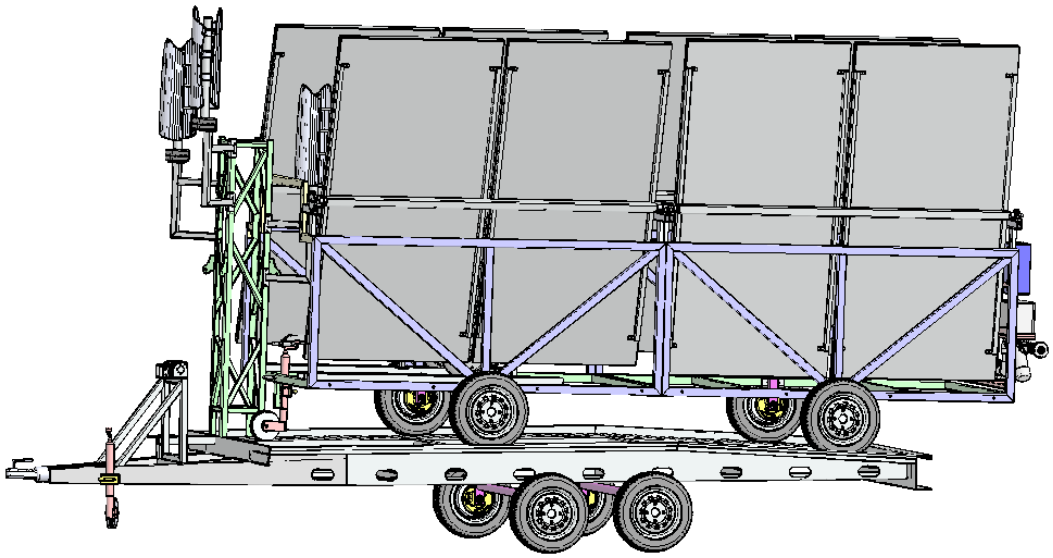

Fig. 3 - Mobile platform with wind turbines and solar panels for irrigating agricultural crops in off-grid areas (*Preda, et al., 2023*)

While wind turbines are a clean energy source, there are still environmental challenges to be addressed, such as the possibility of noise having an adverse effect on surrounding ecosystems or bird and bat collisions (*Njiri et al., 2016*).

A viable strategy for generating sustainable energy and diversifying agricultural operations is the integration of wind turbines into agriculture (*Chel et al., 2011*). However, to guarantee successful implementation and handle possible problems, thorough planning, consideration of local conditions, and stakeholder participation are essential.

Computational Fluid Dynamics is a method used to simulate and analyze fluid flows using numerical algorithms and computer calculations. CFD is a technology that may be used to analyze and improve the performance of VAWTs (*Mălăel et al., 2014*). Engineers may evaluate a variety of VAWT design elements, such as aerodynamic effectiveness (*Dumitrescu et al., 2019*), power production, and structural stresses, by using CFD models.

In order to evaluate the lift and drag forces operating on the turbine blades at various wind speeds and angles of attack, wind tunnel testing is used to measure the aerodynamic properties of VAWTs. This information is essential for refining the design and raising the turbine's overall effectiveness (*Sunny et al., 2016*).

Researchers can use methods like smoke or dye injection, particle image velocimetry (PIV), or flow visualization methods in wind tunnels (*Edwards, et al., 2015*) to see the airflow patterns around the VAWT model. These methods offer insightful information on the flow dynamics, turbulence, and wake effects connected to VAWTs.

MATERIALS AND METHODS

Two vertical-axis wind turbine layouts were examined in this study. Both arrangements consist of three Lenz-type (*Bucur et al., 2021*) wind turbines that are the same. The distinction between the two situations is that the second turbine in case 2 spins in the opposite direction. The analyses were performed with the same operational parameters and wind speed.

Using CFD methods, researchers may optimize their designs, boost productivity, and cut costs by gaining useful insights into the aerodynamic performance of VAWTs. To achieve accurate and trustworthy results, it's crucial to keep in mind that CFD is a complicated area that calls for knowledge of both fluid dynamics and numerical techniques. By replicating the airflow surrounding the turbine, CFD models may be utilized to analyze the aerodynamics and performance of VAWTs.

Computer-aided design (CAD) software or specialist CFD preprocessing tools are used to build the geometry of the VAWT, including the turbine blades, rotor, and surrounding structures. Figure 4 shows the 3D model of the Lenz-type vertical-axis wind turbine that was utilized in this study to assess the performance of a three-turbine array arrangement.

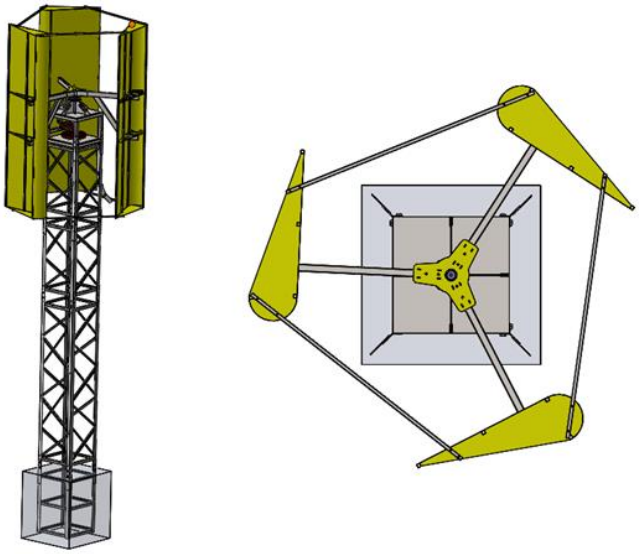

Fig. 4 - VAWT Lenz-type 3D CAD model
(*Bucur, et al., 2021*)

A computational mesh is generated around the VAWT geometry, dividing the domain into small cells or elements. The mesh should be fine enough to appropriately resolve the boundary layers and capture the key flow characteristics. The computational domain for our investigation was divided into four subdomains, with three representing the rotating domains (the turbines) and one representing the stationary domains (the environment). To achieve Yplus values less than one and apply the K-omega SST turbulence model, the initial element size was set-up at1e-03 mm with a ratio of 1.2. The number of elements and their types for each subdomain are shown in the below table.

Table 1

Mesh statistics

No.	Subdomain	No. of nodes	No. of elements	
			Tri3	***Quad4***
1.	Turbine 1	24211	87	23473
2.	Turbine 2	24038	93	23296
3.	Turbine 3	24259	101	23513
4.	Stator	27170	82	26247
5.	**TOTAL**	**99678**	**96894**	

Knowing the fluid parameters, such as air density and viscosity, is necessary for the simulation. It is also necessary to include boundary parameters, such as wind direction and speed, input and exit conditions, and wall characteristics. Figure 5 shows the input with blue and the outflow with red. Symmetry requirements for the domain's top and bottom were employed, and the interfaces (in yellow) between the rotors and the stator were specified.

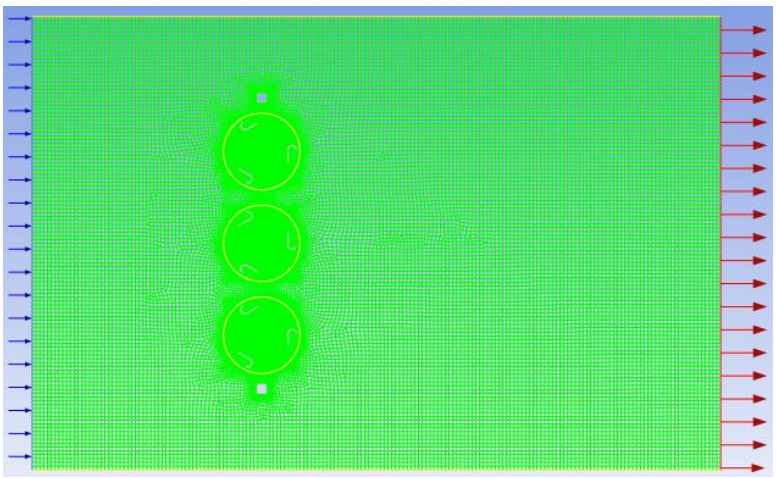

Fig. 5 - Boundary conditions

For CFD simulations, a variety of numerical techniques and solvers are available. Based on the specifics of the issue at hand and the level of precision required, the right solution is chosen. The governing equations for fluid flow are then solved by running the simulation. Table 2 lists the case parameters for the ANSYS Fluent solver.

Table 2

The ANSYS Fluent solver's case settings

Models	Solver	Pressure Based	Unsteady	2d
	Viscous Model	k-ω SST		
Materials	Air	Density, const		
Operating conditions	Pressure101325[Pa]			
Boundary Condition	Inlet	Velocity inlet; V_x=12m/s		
	Outlet	Pressure 0 [Pa]		
	Blades	wall		
	Interfaces	Interface rotors-stator		
	Rotors	Mesh motion	48[rad/s]	
	Stator	Stationary		
Solve	Controls	Solution	SIMPLE	Discretization 2nd order upwind
	Initialize	Inlet		
	Monitors	Residuals	10^{-6}	
		Force	Momentum coefficient	
	Iterate	3600 Steps	0.000364s time step size	
Report	Reference values	Inlet	Length=turbine's radius	

RESULTS

After the simulation is finished, post-processing is carried out to examine the outcomes. This might entail visualizing the flow patterns, computing aerodynamic forces, determining power output, or improving the design by changing the turbine shape or operating circumstances.

The connection between the aerodynamic forces acting on the turbine blades and the resulting torque generated by the rotor is described by the torque coefficient of a wind turbine, which is an important parameter. The torque coefficient (Ct) is defined as the ratio of the torque generated by the wind turbine to the dynamic wind pressure and the swept area of the rotor.

$$Ct = \frac{\text{Torque generated by the turbine}}{0.5 \times \rho \times A \times V^2} \quad (1)$$

where:

ρ is the air density [kg/m^3];

A is the swept area of the turbine rotor [m^2](swept area is the circular area covered by the rotating blades);

V is the wind speed [m/s] at the rotor plane.

The torque generated by the turbine can be expressed in terms of the rotor's rotational speed (ω) and the power coefficient (C_p):

$$\text{Torque}=0.5 \times \rho \times A \times V^2 \times Cp \times R \quad (2)$$

where:

Cp is the power coefficient, representing the efficiency of the turbine in converting the kinetic energy of the wind into mechanical power. It varies with the tip speed ratio (λ), which is the ratio of the blade tip speed to the wind speed. Cp is a dimensionless value between 0 and 1;

R is the radius of the rotor [m].

The power coefficient (Cp) is related to the torque coefficient (C_t) through the following equation:

$$Cp = Ct \times \lambda \quad (3)$$

where:

λ is efficiency factor in turbines (the efficiency factor is a measure of how efficiently a turbine converts the fluid's energy into power. It is defined as the ratio of the power output of the turbine to the kinetic energy of the fluid entering the turbine).

Due to different elements such blade twist, airfoil form, and aerodynamic properties, the torque coefficient is not constant over the length of the blade. The shape of the blades is tuned for wind turbines to perform at their best in a certain range of wind speeds. The torque coefficient tends to be smaller with lower wind speeds because there is less wind energy available. The torque coefficient rises with the wind speed until it reaches the peak torque coefficient, which is the highest value. The torque coefficient may begin to drop above the rated wind speed as the wind turbine starts to stall to protect itself from high loads.

Numerous design factors, such as the number of blades, airfoil profiles, and blade twist, have an impact on the torque coefficient distribution. In order to improve energy capture and overall efficiency, modern wind turbine designs strive to attain a high and smooth torque coefficient distribution.

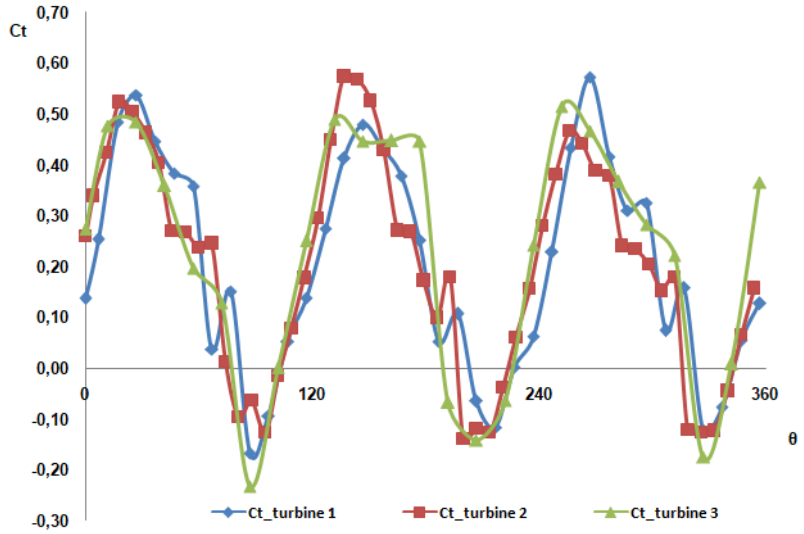

Fig. 6 - Torque coefficient case 1

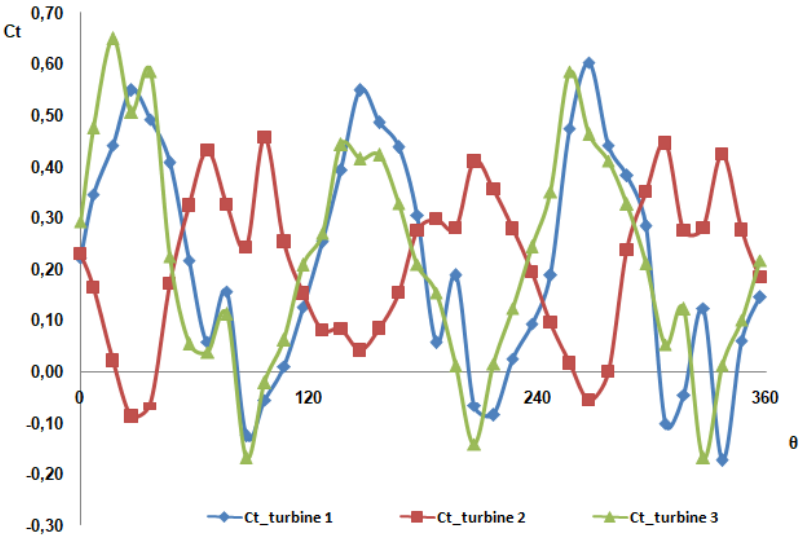

Fig. 7 - Torque coefficient case 2

The figures below depict the development of vorticity magnitude (figure 8) for the two cases that were examined. The streamlines were also shown in order to better see the interactions between the three turbines (figure 9).

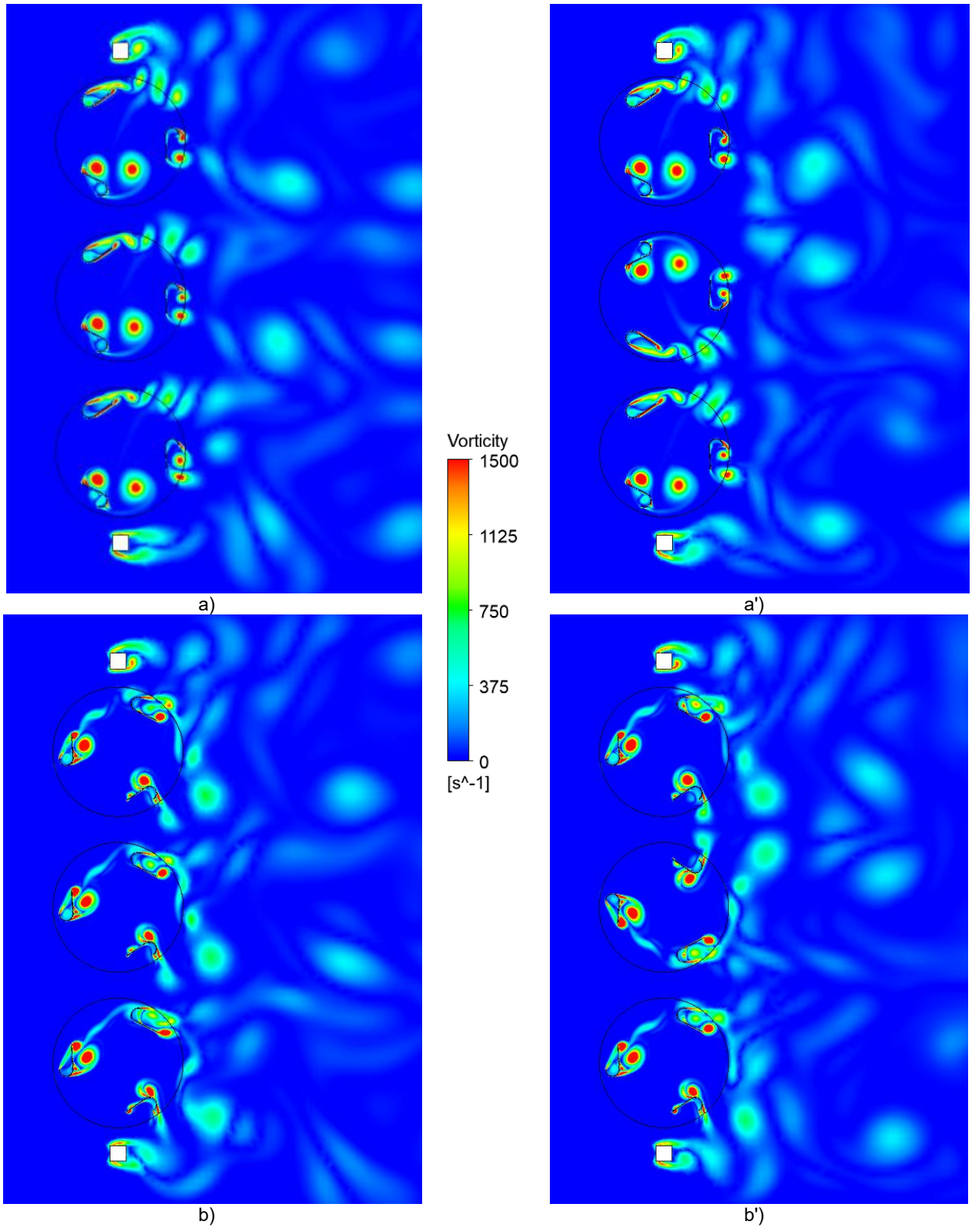

Fig. 8 - Vorticity magnitude
case 1: a) 0 degree; b) 60 degree;
case 2: a') 0 degree; b') 60 degree.

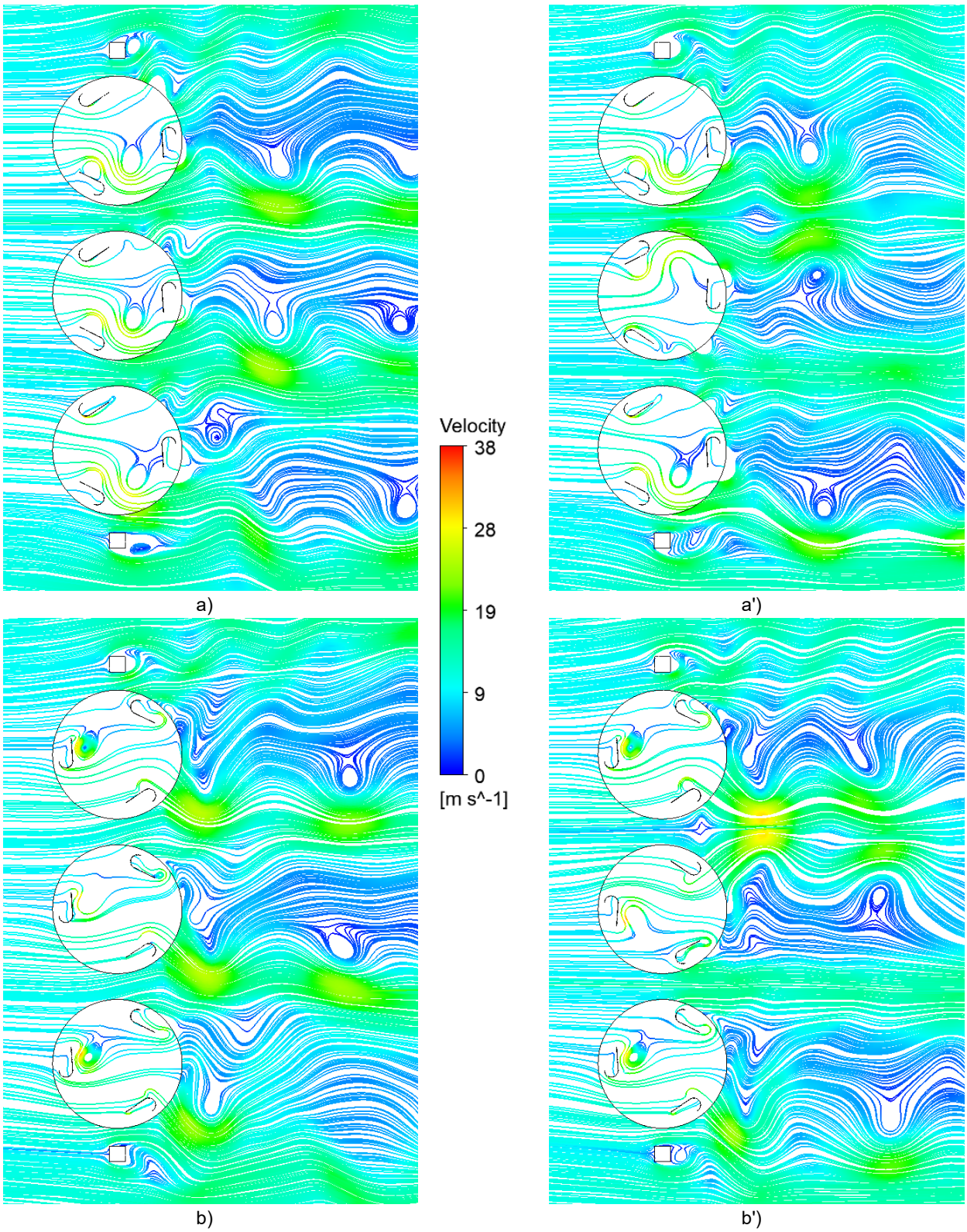

Fig. 9 - Velocity streamlines:
case 1: a) 0 degree; b) 60 degree;
case 2: a') 0 degree; b') 60 degree.

CONCLUSIONS

The main objective of this article was to quantitatively investigate a renewable energy solution that may be used in populated areas and also in agriculture. The numerical analysis was completed using CFD methods. The first example featured three wind turbines revolving in the same direction, and the second example involved the center turbine rotating in the opposite direction.

In order to investigate how the vortexes impact the operation of the wind turbines, the evolution of the vorticity magnitude and the streamlines were displayed at various locations of the blades. The arrangement from scenario 2 produced a higher power coefficient at the same rotational speed with a 1.5 percent gain in efficiency because of the high speed zones that are formed as a result of the middle turbine rotating in the opposite direction.

Future research will incorporate an experimental testing campaign in a wind tunnel where Particle Image Velocimetry technology may be used to observe the interactions between the turbines in order to verify the numerical findings.

ACKNOWLEDGEMENT

This work was carried out within Regional Operational Program 2014-2020, Priority Axis 1 - Promotion of technological transfer, Proof-of-Concept, supported by the Romanian Ministry of Development, Public Works and Administration, project SMIS 2014+code 156492, title "*Validation of the wind turbine concept developed for residential areas*"

REFERENCES

[1] Ahammed, Sajid and Utropolis, Glenmarie. (2021). Optimization of floating horizontal axis wind turbine blades for aerodynamic performance measurement. *Optimization* 8.6 (2021).

[2] Ang, Tze-Zhang et al. (2022). A comprehensive study of renewable energy sources: Classifications, challenges and suggestions. *Energy Strategy Reviews,* 43, 100939.

[3] Bardi, U., El Asmar, T., & Lavacchi, A. (2013). Turning electricity into food: the role of renewable energy in the future of agriculture. *Journal of cleaner production*, *53*, 224-231.

[4] Bilgili, Mehmet, and Hakan Alphan. (2022). Global growth in offshore wind turbine technology. *Clean Technologies and Environmental Policy.* 24.7: 2215-2227.

[5] Bhattarai, Utsav, Tek Maraseni, and Armando Apan. (2022). Assay of renewable energy transition: A systematic literature review. Science of the Total Environment 833: 155159.

[6] Bucur, Ioana Octavia, Ion Malael, and Mihai Predescu. (2021). Vertical Axis Wind Turbine Blade Manufacturing Using Composite Materials. *10th International Conference on ENERGY and ENVIRONMENT (CIEM).* IEEE, 2021.

[7] Bucur, I. O., et al. (2021). Drag Based Wind Turbine Lenz Type Manufacturing and Assembly. *IOP Conference Series: Materials Science and Engineering.* Vol. 1182. No. 1. IOP Publishing.

[8] Bucur, I. O., I. Malael, and D. Preda. (2021). Numerical investigation of a reduced scale Lenz wind turbine model for aerodynamic tunnel applications. *IOP Conference Series: Earth and Environmental Science*. Vol. 664. No. 1. IOP Publishing.

[9] Calderon, J., Cureg, J., Diaz, M., Guzman, J., Rudd, C., & Le, H. T. (2019). Smart Agriculture: An Off-Grid Renewable Energy System for Farms using Wind Power and Energy Storage. In *2019 IEEE Power & Energy Society Innovative Smart Grid Technologies Conference (ISGT).* pp. 1-5.

[10] Chel, A., & Kaushik, G. (2011). Renewable energy for sustainable agriculture. *Agronomy for sustainable development*, 31, 91-118.

[11] Condruz, Mihaela Raluca, et al. (2019). Manufacturing of advanced composite wind turbine blades for counter rotating vertical wind turbine. *Mater. Plast 57*: 45-56.

[12] Costea, Florina, and Ion Malael. (2019). Numerical efficiency evaluation of a vertical axis turbine equipped with 4 digits and 5 digits NACA airfoils. *E3S Web of Conferences*. Vol. 85. EDP Sciences.

[13] Drancă, Marius, Mihai Chirca, and Ştefan Breban, (2019), Comparative Design Analysis of Axial Flux Permanent Magnet Direct-Drive Wind Generators. *2019 11th International Symposium on Advanced Topics in Electrical Engineering (ATEE)*.

[14] Dumitrescu, Horia, et al. (2019). The standard and counter-rotating VAWT performances with LES. *Recent Advances in CFD for Wind and Tidal Offshore Turbines. Cham: Springer International Publishing*. 117-126.

[15] Edwards, Jonathan M., Louis Angelo Danao, and Robert J. Howell. (2015). PIV measurements and CFD simulation of the performance and flow physics and of a small-scale vertical axis wind turbine. *Wind Energy,* 18.2: 201-217

[16] Gall, Mihnea, Ion Mălăel, and Dragos Preda. (2022). Computational analysis of fence-type vertical axis wind turbines array suitable for urban architecture integration. *26th International Conference on Circuits, Systems, Communications and Computers (CSCC).* IEEE, 2022.

[17] Li, Deyu, Gaston Heimeriks, and Floor Alkemade. (2020). The emergence of renewable energy technologies at country level: relatedness, international knowledge spillovers and domestic energy markets. *Industry and Innovation* 27.9: 991-1013.
[18] Malael, Ion, and Ioana Octavia Bucur. (2021). Numerical Evaluation of the Flow around a New Vertical Axis Wind Turbine Concept. *Sustainability* 13.16: 9012.
[19] Mălăel, Ion, and Horia Dumitrescu. (2014). Numerical simulation of vawt flow using Fluent. *UPB Sci. Bull., Series D* 76.1.
[20] Mostafaeipour, A., Rezaei, M., Moftakharzadeh, A., Qolipour, M., & Salimi, M. (2019). Evaluation of hydrogen production by wind energy for agricultural and industrial sectors. *International Journal of Hydrogen Energy*, *44*(16), 7983-7995.
[21] Nazir, Muhammad Shahzad, et al. (2020). Potential environmental impacts of wind energy development: A global perspective. *Current Opinion in Environmental Science & Health* 13: 85-90.
[22] Neshat, Mehdi, et al. (2021). Wind turbine power output prediction using a new hybrid neuro-evolutionary method. *Energy 229*: 120617.
[23] Njiri, J. G., & Söffker, D. (2016). State-of-the-art in wind turbine control: Trends and challenges. *Renewable and Sustainable Energy Reviews*, *60*, 377-393.
[24] Olabi, Abdul Ghani, et al. (2021). A review on failure modes of wind turbine components. *Energies 14.17*: 5241.
[25] Preda Dragos et al. (2023). https://www.rolix.ro/proiecte_cercetare/pti_inma.htm
[26] Ramakrishnan, Agenya, and M. Siva Ramkumar. (2022). Review on Backup Storage System in Wind Energy Conversion System. *2022 International Conference on Sustainable Computing and Data Communication Systems (ICSCDS).*
[27] Sampson, G. S., Perry, E. D., & Tayler, M. R. (2020). The on-farm and near-farm effects of wind turbines on agricultural land values. *Journal of Agricultural and Resource Economics*, *45*(3), 410-427.
[28] Saputra, M., Syuhada, A., & Sary, R. (2018). Study of solar and wind energy using as water pump drive-land for agricultural irrigation. In *2018 4th International Conference on Science and Technology (ICST)* (pp. 1-4). IEEE.
[29] Sebestyén, Viktor. (2021). Renewable and Sustainable Energy Reviews: Environmental impact networks of renewable energy power plants. *Renewable and Sustainable Energy Reviews 151*: 111626.
[30] Skibko, Z., Tymińska, M., Romaniuk, W., & Borusiewicz, A. (2021). Impact of the Wind Turbine on the Parameters of the Electricity Supply to an Agricultural Farm. *Sustainability*, *13*(13), 7279.
[31] Sunny, Kalakanda Alfred, and Nallapaneni Manoj Kumar. (2016). Vertical axis wind turbine: Aerodynamic modelling and its testing in wind tunnel. *Procedia Computer Science 93*: 1017-1023.
[32] Sutherland, L.A., & Holstead, K.L. (2014). Future-proofing the farm: On-farm wind turbine development in farm business decision-making. *Land use policy*, *36*, 102-112.
[33] Thellufsen, Jakob Zinck, et al. (2020). Smart energy cities in a 100% renewable energy context. *Renewable and Sustainable Energy Reviews 129,* 109922.

EFFECTS OF LOW-FREQUENCY HIGH-VOLTAGE PULSED ELECTRIC FIELDS ON GERMINATION CHARACTERISTICS OF AGED RICE SEEDS

/

低频高压脉冲电场对陈年水稻种子萌发特性的影响

Tiangang HOU[1)], Zhenyu WANG[1)], Mingce ZHAO[1)], Cuihong LIU[1)], Mingjin XIN[1)], Liyan WU *[1)], Benhua ZHANG *[2)]

[1)]College of Engineering, Shenyang Agricultural University, Shenyang / China;

[2)]School of Mechanical and Electrical Engineering, Suqian College, Suqian / China

Tel: +86-139-4209-8712; E-mail: wly78528@syau.edu.cn

Corresponding author: Liyan Wu; Benhua Zhang

DOI: https://doi.org/10.35633/inmateh-70-50

Keywords: *LH-PEF, Rice seed, Germination characteristics, Physiological indices*

ABSTRACT

In this study, the effects of different electric field parameters on the germination characteristics of aged rice seeds were determined via low-frequency high-voltage pulsed electric field (LH-PEF) treatment. The Design-Expert software was used to design a rotating combination test, and response surface analysis was used to optimize five germination characteristics of rice seeds. The optimal treatment voltage was 13 kV and the optimal treatment time was 32.72 min. The results show that, under the optimal treatment conditions (P<0.01), the germination potential (GE), germination rate (GP), germination index (GI), vitality index (VI) and high vitality ratio (HVR) of the aged rice seeds increased by 23.7%, 17.7%, 43.2%, 59.7%, and 250%, respectively, compared to the control. The pulsed electric field's biological effect on the aged rice seeds was the most significant when the optimal treatment parameters were used. The results of this study provide a reliable reference for the parameter optimization of high-voltage electric field treatment of crop seeds.

摘要

本研究通过低频高压脉冲电场(LH-PEF)处理陈年水稻种子，研究不同电场参数对其萌发特性的影响，为提高陈年水稻种子活力提供了一种物理方法。本文利用 Design-expert 软件设计旋转组合试验，并利用响应面分析法，对水稻种子的 5 个萌发特性指标进行参数优化，得出最优处理电压为 13kV，最优处理时间为 32.72min。结果表明：陈年水稻种子在最优处理条件下，与对照相比，发芽势(GE)提高了 23.7%，发芽率(GP)提高了 17.7%，发芽指数(GI)提高了 43.2%，活力指数(VI)提高了 59.7%，高活力比(HVR)提高了 250%，各指标都达到极显著差异（P<0.01）。在最优参数的脉冲电场作用下，陈年水稻种子的电场生物学效应最明显，研究结果为后续作物种子高压电场处理的参数优化提供参考。

INTRODUCTION

Nearly half of the world's population consumes staple foods, such as rice (*Cheng et al, 2022*). Rice is a cereal crop that originated in China and is widely planted in the Yangtze and Pearl River Basins, Northeast China, India, Vietnam, Brazil, Japan, and other countries (*Fukushima et al, 2021; Wei et al, 2021*). Nearly half of the world's population consumes rice as staple foods. (*Cheng et al., 2022*). Rice seed quality significantly affects the yield (*Pang et al, 2018; Xu et al, 2018*). Seed vitality and vitality levels are key factors that determine seed quality and directly affect seed germination, seedling growth rate, and plant vitality (*Reed et al, 2022*). The vitality of rice seeds is the highest at harvest and gradually decreases with increasing seed age. Sowing low-vitality rice seeds causes significant economic losses to agricultural production (*Yan et al., 2018*). Therefore, enhancing the vitality of rice seeds is crucial for maximizing the yield of rice crops (*Kudratillaev, 2020*).

To obtain high-quality seeds, different physical, chemical, and biological methods have been recently used to process and pretreat crop seeds. Chemical treatment methods include seed coating, dressing, and soaking, as well as pretreatment with organic and inorganic solutions. Some studies have found that H_2O_2, as an important messenger molecule, can interact with ethylene and salicylic acid (SA) signaling molecules by inducing the expression of Arabidopsis thaliana (*AtNDPK2*) in cells, thereby activating antioxidant enzyme activity to regulate the physiological response of plants (*Barba-Espin et al, 2012*). Biological treatment methods include treating seeds with fungi, bacteria, plant products, or exogenous hormones.

Some studies have found that the mechanism of growth-promoting microorganisms primarily involves improving the ability of rhizosphere colonization to produce antibiotics and phytohormones; this promotes signal transduction, gene expression, chlorophyll synthesis, and rhizosphere growth, ultimately inducing plant resistance and promoting growth and yield (*Gutiérrez et al., 2015*). Compared to the possible harm that chemical treatment can inflict on the environment and the longer time periods required for biological treatment, physical treatment is more advantageous. Physical treatment methods can be classified into two types (*Wang et al., 2016; Shin et al, 2010*). Traditional physical treatment methods include mechanically damaging the seed husk, improving its permeability, removing the hard and dormant characteristics of the seeds, and ensuring suitable sand burial. By changing biological and non-biological conditions (e.g. microbial activity, effective radiation of ground photosynthesis, and temperature), the physiological process of seed germination and the survival of seedlings can be effectively promoted (*Yudaev et al, 2019*). Biophysical technologies such as electromagnetic fields, ultrasonic waves, and lasers have been widely used owing to their high efficiency. However, the use of emerging high-voltage electric field technology is becoming more widespread (*Patwardhan and Gandhare, 2016*). Studies have shown that a suitable high-voltage electrostatic field can improve the hydrophilicity of the surfaces of soybean seeds, thereby increasing the germination rate. Other studies have found that applying an appropriate pulsed electric field to barley seeds can improve their metabolic efficiency, thereby improving their emergence rate. Afrasiyab et al. found that chickpea seeds treated with a high-voltage electrostatic field exhibited improved germination activity. In addition, Jianzhong et al. found that appropriate high-voltage electric field treatment can promote the development of foxtail millet. Furthermore, Wang et al. conducted an experiment on the effective time over which electric fields influence seed germination and found that within the effective time, the electric field treatment of Caragana korshinskii seeds significantly improved the germination indices of the seeds and the nutrient content in the seedlings. The electric field treatment also improved the drought resistance of the plants. However, only a few studies have reported the use of low-frequency high-voltage pulsed electric fields (LH-PEFs) for the pretreatment of rice seeds (*Evrendilek et al., 2019; Tantamacharik et al, 2019*).

In this study, aged rice seeds were pretreated with LH-PEF. The Design-Expert software was used to design a rotation combination test, and response surface analysis was used to determine the optimal electric field parameters and to model and optimize five germination characteristics of rice seeds, including germination potential, germination rate, germination index, vitality index, and high vitality ratio. The biological effect of the pulsed electric field on the aged rice seeds was the most significant when the optimal parameters were employed. The results of this study provide a reliable reference for the parameter optimization of the high-voltage electric field treatment of crop seeds.

The rest of this paper is organized as follows. In Section 2, the materials and methods used in the experiment are described. Section 3 presents and analyzes the results, and Section 4 discusses their significance. Finally, Section 5 summarizes the findings of this study and draws the conclusions.

MATERIALS AND METHODS

Samples

Table 1

Physical characteristics of rice seeds.

Name	Hundred-grain mass (g)	Size (mm)		
		Length	Width	Thickness
DaoHuaxiang No. 2	29.95±0.35	9.87±0.36	5.65±0.31	4.12±0.33

The aged rice seeds used in the experiment were DaoHuaxiang No. 2, which were provided by the College of Engineering at Shenyang Agricultural University. The seed was harvested in October 2019 in Fushun City, Liaoning Province, with an initial moisture content of 12.3±0.3%, and was stored at 15 ℃ and a relative humidity of 60-65%. Aged rice seeds of the same size and appearance were selected for germination tests. The initial germination rate without electric field treatment was approximately 40%. The physical characteristics of the aged rice seeds are listed in Table 1.

Experimental equipment

A high-voltage electric field workbench was designed and constructed using a high-voltage power supply, copper mesh, copper plate, plastic insulating board, plastic insulated hollow tubes, and other materials, as shown in Figure 1.

The high-voltage power supply can be disassembled at any time to swap the DC, AC, and pulse power supplies. The output and grounding ends of the electric field generator were connected to the copper mesh and copper plate, which were separated by plastic insulated hollow tubes. The latter were available in a variety of lengths so that the distance between the upper and lower plates could be adjusted, which facilitated the execution of subsequent tests. The positive and negative plates were positioned at a distance of 0.05 m away from each other. After the high-voltage power supply was connected, a continuous and adjustable uniform high-voltage electric field was generated between the copper mesh and copper plate. A slide plate was placed halfway between the upper and lower copper electrode plates, and the test seed was placed at the center of the slide plate, as shown in Figure 1.

The test equipment included a pulsed electric field generator (*Dalian Zhongxing Electronic Technology Co., LTD.*), a Vp-5512a oscilloscope (*Japan Panasonic Corporation*), a Bsa124s-CW electronic balance (Germany Sartorius company, accuracy of 0.0001 g), an Rtop-268d intelligent artificial climate incubator (*Zhejiang Top Instrument Co., LTD*.; temperature control range: 0-50 ℃, temperature fluctuation: ±0.5 ℃, temperature uniformity: ±1 ℃, humidity control range: 50-95% RH, humidity fluctuation: ±5% RH), a copper plate, an acrylic insulation board and acrylic hollow tube (*Zhejiang Wenzhou Jumeng Technology Co., LTD*.), and vernier calipers with an electronic digital display and a precision of 0.01 mm. Additional items used in the experiment included a hygrometer, absorptive paper, distilled water, germinating box, germinating paper, stainless-steel tweezers, plastic partition, beaker, and burette.

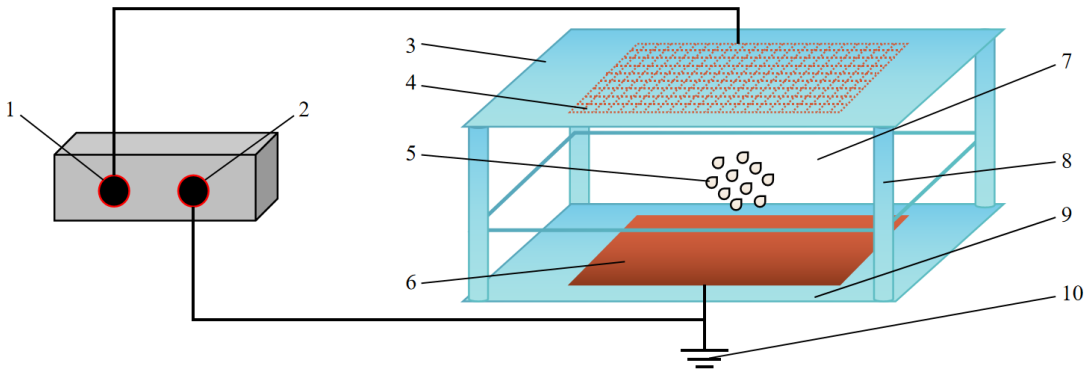

Fig. 1 - Schematic diagram of the workbench used for high-voltage electric field treatment
1) High-voltage power supply positive pole; 2) High-voltage power supply negative pole; 3) Positive plastic insulation board; 4) Copper mesh; 5) Rice seeds; 6) Copper plate; 7) Slide plate; 8) Plastic insulated hollow tubes; 9) Negative plastic insulation board; 10) Ground.

Methods and procedures

Experimental design of electric field treatment of rice seeds

Table 2

Experimental factors and coding values

Coding value	Electric field voltage (kV)	Treatment time (min)
-1.414	6	5
-1	8.05	13.05
0	13	32.5
1	17.95	51.95
1.414	20	60

Based on the results of the preliminary tests, the values of the low-frequency pulsed electric field parameters were as follows: the electric field voltage was 6-20 kV, the treatment time was 5-60 min, the direction of the field intensity was vertically downward, the electric field frequency was 10 Hz, and the electric field pulse width was 10 ms.

Using 13 kV and 32.5 min as the median values for the electric field voltage and treatment time, respectively, a secondary general rotation combination test was designed and analyzed using the Design-Expert software. Thirteen treatment groups and one control group were designed. The experimental factors and coding values are listed in Table 2.

Germination experiment of seeds

The experiment was conducted on June 14, 2021, at Laboratory 513, College of Information and Electrical Engineering, Shenyang Agricultural University, China. DaoHuaxiang No. 2 rice seeds with full grains of equal size were used. Fifty seeds were divided into several portions and numbered.

The seeds were treated according to the values listed in Table 2. Then they were soaked in 0.01% potassium chloride solution for 10 min, sterilized, and washed with distilled water three times before being placed in an incubator at a constant temperature for the germination test (*Wang et al., 2020*). The environment was established according to the following national standards: a constant temperature of 25℃, continuous light, and an equivalent humidity of 100%. For each electric field setting, four box tests were performed, and the average value of each quantity across the four tests was calculated.

During germination, rice seeds should be replenished regularly to ensure that a sufficient amount of water is available for seedling development. During this period, if mildew existed inside the sprouting box, it was treated immediately to prevent it from affecting the test results. To ensure the ventilation of the seed-growing environment, the box cover was removed in time to prevent the growth of seedlings. The number of germinations was recorded daily from day three until the seedlings were washed on day seven, and the relevant data were measured. Statistical criteria were defined according to the "Seed Examination," and all rice seedlings in each box were measured.

While the rice seeds were germinating, the germination potential, germination rate, and vitality index were used as germination indices. The germination potential (GE) is defined as:

$$GE = \frac{m_1}{M} \times 100\% \tag{1}$$

where m_1 is the number of germinated seeds on the third day, and M is the number of seeds used in the experiment. The germination rate (GP) is defined as:

$$GP = \frac{m_2}{M} \times 100\% \tag{2}$$

where m_2 is the number of seeds that grew into seedlings at the end of the experiment. The germination index (GI) is defined as:

$$GI = \sum (Gt / Dt) \tag{3}$$

where Dt is the number of germinating days and Gt is the number of germinating seeds per day corresponding to Dt. The vitality index (VI) is defined as:

$$VI = GI \times S \tag{4}$$

where S is the length (cm) or fresh weight (g) of a single normal seedling over a certain period.

The high vitality ratio (*HVR*) is defined as:

$$HVR = \frac{m_3}{M} \tag{5}$$

where m_3 is the number of seeds with a seedling height of at least 4 cm at the end of the experiment.

After the germination test, the seedlings were washed with clean water, and the surface was dried with absorbent paper. The lengths of the rice seedlings were measured using digital vernier calipers, and 100 plants were placed in each box. For each of the four tests using a given electric field, the average length of the seedlings in each box was calculated, and the average value for all four tests was taken as the seedling length for the given electric field and compared to the CK control group.

Data processing

The SPSS 23 and Design-Expert 8.0.5 data processing software programs were used to statistically analyze the data, and Origin and MATLAB were used to generate plots.

RESULTS

Effect of pulsed electric field on seed vitality of aged rice

Thirteen treatments for the rotary combination test and four repetitions at the median values were conducted. The test results are displayed in Table 3. As shown in the table, the germination potential, germination rate, germination index, vitality index, and high vitality ratio of the aged rice seeds after the LH-PEF treatment were significantly higher than those of the CK control group. When the electric field voltage was 13 kV and the treatment time was 32.5 min, all indices exhibited significant differences compared to the CK ($P < 0.01$) control group.

The Design Expert software was used to perform multiple regression fitting on the test data shown in Table 3, and a quadratic multinomial regression model was established for the germination potential, germination rate, germination index, vitality index, high vitality ratio, voltage, and treatment time of the rice seeds. A variance analysis for each item was conducted, and the results of the analysis are presented in Table 4.

Table 3

Design and results of rotary combination test

Test No.	Electric field voltage (kV)	Treatment time (min)	Germination potential (%)	Germination rate (%)	Germination index	Vitality index	High vitality ratio
CK	0	0	61.1	82.3	22.2	1.34	0.04
1	13	32.5	74.4**	97.1**	29.8**	2.2**	0.13**
2	8.05	51.95	68.1*	89.8**	26.1*	1.59*	0.05*
3	8.05	13.05	68.9*	90.2**	26.5**	1.71*	0.05*
4	13	5	70.3**	92.7**	27.4**	1.82*	0.08*
5	13	32.5	74.9**	97.7**	31**	2.27**	0.14**
6	13	32.5	74.7**	96.5**	30.8**	2.16**	0.13**
7	13	60	71.1*	92.1*	28.2**	1.84*	0.08*
8	6	32.5	65.5*	85.9*	24.1*	1.55*	0.07*
9	20	32.5	66.6*	85.7*	23.8*	1.48*	0.05*
10	17.95	13.05	69.1*	89.7**	27.1**	1.59**	0.06*
11	13	32.5	74.9**	96**	30.5**	2.22**	0.11**
12	13	32.5	75.1**	96.6**	31.6**	2.15**	0.12**
13	17.95	51.95	68.7*	88.7*	26.8*	1.69*	0.07*

Note: '*' represents significance ($P<0.05$); '**' represents extreme significance ($P<0.01$).

Table 4

Results of variance analysis for each index

Source of variation	Germination potential		Germination rate		Germination index		Vitality index		High vitality ratio	
	F value	*P* value	*F* value	*P* value	*F* value	*P* value	*F* value	*P* value	*F* value	*P* value
Model	161.22	0.0011**	123.99	0.0015**	29.38	0.0001**	118.52	0.0064**	13.63	0.0017**
V	3.91	0.0885	1.28	0.2951	0.183	0.6817	1.03	0.3431	0.002	0.9653
f	0.0033	0.9557	1.83	0.2187	0.0444	0.8391	0.005	0.9455	0.0689	0.8005
Vf	0.2254	0.6494	0.26	0.6258	0.0048	0.9469	7.07	0.0325*	0.1378	0.7214
V^2	722.82	0.0021**	578.49	0.0007**	136.59	0.0008**	495.99	0.0009**	50.05	0.0002**
f^2	151.96	0.0017**	85.7	0.001**	21.84	0.0023**	149.6	0.0003**	26.18	0.0014**
R^2	0.9914		0.9888		0.9545		0.9883		0.9069	
SNR	31.4637		27.6787		13.3595		25.6064		7.9298	

Note: '*' represents significance ($P<0.05$); '**' represents extreme significance ($P<0.01$); V is pulsed voltage in kV; *f* is treatment time in min.

Response surface analysis of the effect of pulsed electric field on germination potential of aged rice seeds

As shown in Table 3, the germination potential of the aged rice seeds after the LH-PEF treatment was significantly higher than that of the CK group ($P < 0.01$ or $P < 0.05$). Figure 2(a) shows a plot of the response surface analysis of the effect of pulsed electric field on the germination potential of the rice seeds. As shown in the figure, the germination potential of the rice seeds reached an optimal value with the increase in a certain combination of electric field voltage and treatment time.

A quadratic multinomial regression model for the relationship between the germination potential of the aged rice seeds and the electric field voltage and treatment time was established, and it was expressed as:

$$GE = 39.36 + 4.58V + 0.32f + 0.0001Vf - 0.18V^2 - 0.005f^2 \left(R^2 = 0.9914\right) \quad (6)$$

where:

GE is the germination potential of the rice seeds treated with a pulsed electric field (in %), V is the pulse voltage (in kV), and f represents the treatment time (in min).

Table 4 shows that the F value of the germination potential was 161.22 and the *P* value was 0.0011, indicating that the established expression between the germination potential, electric field voltage, and treatment time was extremely significant ($P < 0.01$). The signal-to-noise ratio of the relational model was 31.4637, indicating that the model was superior and the accuracy and reliability of the test were high. The data in Table 4 show that the squares of the electric field voltage and treatment time had a significant influence on the germination potential, but the electric field voltage, treatment time, and their interaction had no significant influence on the germination potential.

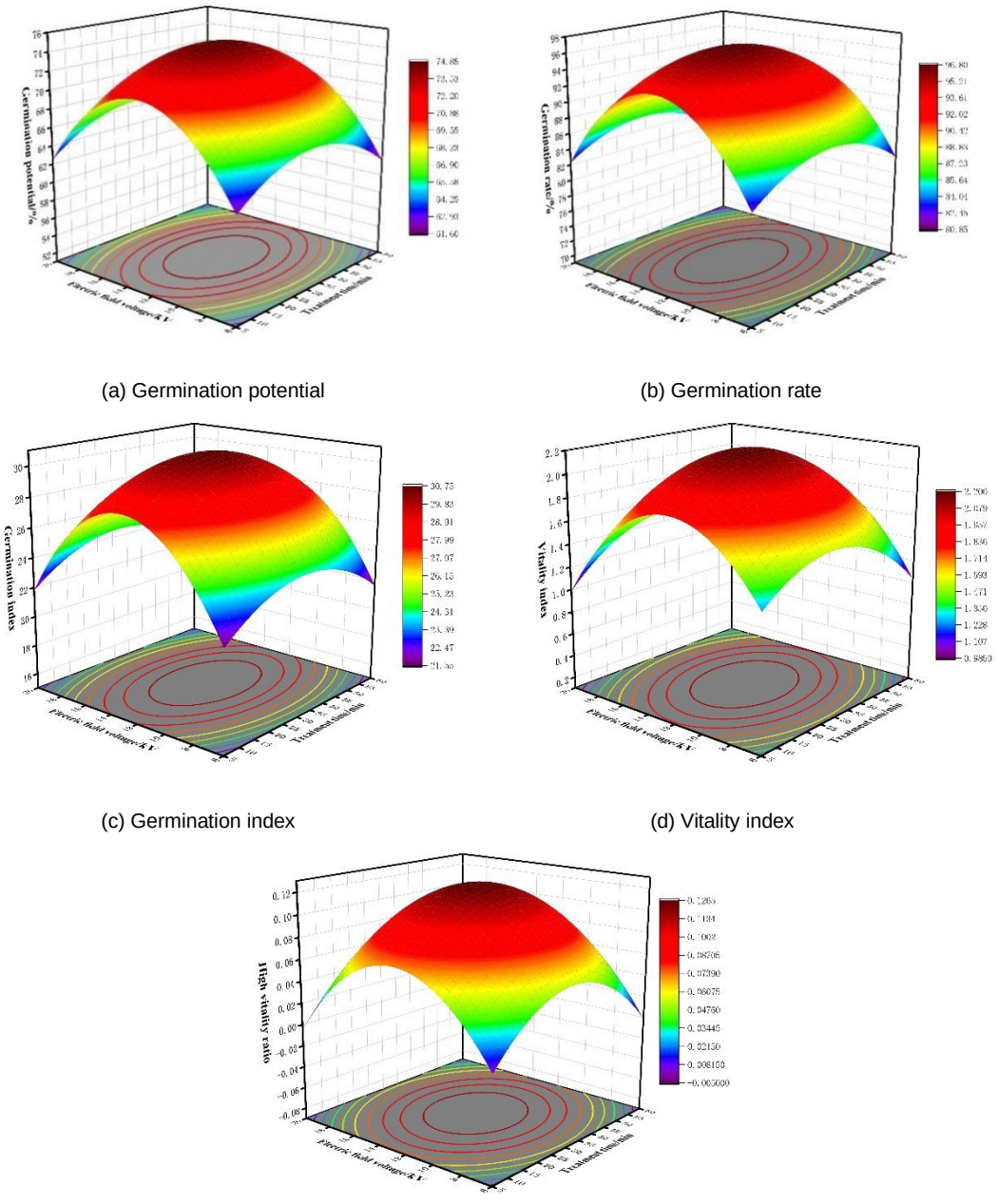

(a) Germination potential

(b) Germination rate

(c) Germination index

(d) Vitality index

(e) High vitality ratio

Fig. 2 - Response surface analysis of germination indices of rice seeds after pulsed electric field treatment

Response surface analysis of effect of pulsed electric field on germination rate of aged rice seeds

As shown in Table 3, the germination rate of aged rice seeds after the LH-PEF treatment was significantly higher than that of the CK group, and most of them showed extremely significant differences ($P < 0.01$). Significant differences were observed for the individual treatments ($P < 0.05$). Figure 2(b) shows a plot of the response surface analysis of the effect of the LH-PEF treatment on the germination rate of the rice seeds. As shown in Fig. 2(b), for different treatment times, the influence of the electric field voltage on the germination rate of the aged rice seeds was similar to that on the germination potential.

The effects of an extended treatment time on the germination rate of the aged rice seeds were similar for different electric field voltages. In summary, the germination rate of the rice seeds after the LH-PEF treatment reached an optimal value for a certain combination of electric field voltage and treatment time. A response surface analysis established a quadratic multinomial regression model for the relationship between the germination rate of the aged rice seeds and the electric field voltage and treatment time, and it was expressed as:

$$GP = 96.78 - 0.24V - 0.28f - 0.15Vf - 5.36V^2 - 2.07f^2 \quad \left(R^2 = 0.9888\right) \tag{7}$$

where: GP is the germination rate of the rice seeds treated with an LH-PEF (in %).

Table 4 shows that the F value of the germination rate was 123.99 and the *P* value was 0.0011, indicating that the established expression between the germination rate, electric field voltage, and treatment time was extremely significant (*P*< 0.01). The signal-to-noise ratio of the model was 27.6787, indicating that the model was superior and the accuracy and reliability of the test were high. The data in Table 4 indicate that the squares of the electric field voltage and treatment time had a significant influence on the germination rate, while the electric field voltage, treatment time, and their interaction had no significant influence on the germination rate.

Response surface analysis of effect of pulsed electric field on germination index of aged rice seeds

As shown in Table 3, the germination index of the aged rice seeds after the LH-PEF treatment was significantly higher than that of the CK group (*P* < 0.01 or *P* < 0.05). Figure 2(c) shows a plot of the response surface analysis of the effect of the LH-PEF on the rice seed germination index. As shown in Fig. 2(c), the rice seed germination index after the LH-PEF treatment reached an optimal value for a certain combination of electric field voltage and treatment time. A response surface analysis established a quadratic multinomial regression model for the relationship between the germination index of the aged rice seeds and the electric field voltage and treatment time, and it was expressed as:

$$GI = 30.74 + 0.1095V + 0.0539f + 0.025Vf - 3.21V^2 - 1.28f^2 \quad \left(R^2 = 0.9545\right) \tag{8}$$

where GI is the germination index of the rice seeds treated with an LH-PEF (in %).

Table 4 shows that the F value of the germination index was 29.38 and the *P* value was 0.0001, indicating that the established expression between the germination index, electric field voltage, and treatment time was extremely significant (*P* < 0.01). The signal-to-noise ratio of the relational model was 13.3595, indicating that the model was superior and the accuracy and reliability of the test were high. The data in Table 4 indicate that the squares of the electric field voltage and treatment time had a significant influence on the germination index, while the electric field voltage, treatment time, and their interaction had no significant influence on the germination index.

Response surface analysis of effect of pulsed electric field on vitality index of aged rice seeds

As shown in Table 3, the vitality index of the aged rice seeds after the LH-PEF treatment was significantly higher than that of the CK group, and most of the tests generated extremely significant differences (*P* < 0.01). Figure 2(d) shows a plot of the response surface analysis of the effect of the LH-PEF treatment on the vitality index of the rice seeds. As shown in Fig. 2(d), the vitality index after the LH-PEF treatment reached an optimal value for a certain combination of electric field voltage and treatment time. Moreover, the effect of treatment time on the vitality index was significant. A quadratic multinomial regression model was established for the relationship between the vitality index of the aged rice and the electric field voltage and treatment time, and it was expressed as:

$$VI = 2.20 - 0.0149V + 0.0010f + 0.0550Vf - 0.3494V^2 - 0.1919f^2 \quad \left(R^2 = 0.9983\right) \tag{9}$$

where VI is the vitality index of the rice seeds treated with an LH-PEF (in %).

Table 4 shows that *the* F value of the vitality index was 118.52 and the *P* value was 0.0064, indicating that the established relationship between the vitality index, electric field voltage, and treatment time was extremely significant (*P* < 0.01). The signal-to-noise ratio of the relational model was 25.6064, indicating that the model was superior, and the accuracy and reliability of the test were high. The data in Table 4 indicate that the squares of the electric field voltage and treatment time and the interaction between the electric field voltage and treatment time had a significant influence on the vitality index, but the electric field voltage and treatment time had no significant influence on the vitality index.

Response surface analysis of the effect of pulsed electric field on high vitality ratio of aged rice seeds

As shown in Table 3, the high vitality ratio of the aged rice seeds after the LH-PEF treatment was significantly higher than that of the CK group, and most of the tests generated extremely significant differences ($P < 0.01$). Figure 2(e) shows a plot of the response surface analysis of the effect of the LH-PEF treatment on the high vitality ratio of the rice seeds. As shown in Fig. 2(e), the high vitality ratio after the LH-PEF treatment reached an optimal value for a certain combination of electric field voltage and treatment time.

Moreover, the effect of treatment time on the high vitality ratio of the rice seeds was evident. A quadratic multinomial regression model was established for the relationship between the high vitality ratio of the aged rice and the electric field voltage and treatment time, and it was expressed as:

$$HVR = 0.1260 + 0.0002V + 0.0012f + 0.0025Vf - 0.0361V^2 - 0.0261f^2 \quad \left(R^2 = 0.9069\right) \quad (10)$$

where HVR is the high vitality ratio of the rice seeds treated with an LH-PEF (in %).

Table 4 shows that the F and P values of the high vitality ratio were 13.63 and 0.0017, respectively, indicating that the established relationship between the high vitality ratio, electric field voltage, and treatment time was extremely significant ($P < 0.01$). The signal-to-noise ratio of the model was 7.9298, indicating that the model was superior and the accuracy and reliability of the test were high. The data in Table 4 indicate that the squares of the electric field voltage and treatment time had a significant influence on the high vitality ratio, but the electric field voltage, treatment time, and their interaction had no significant influence on the high vitality ratio.

Parameter optimization

The maximum values of germination potential, germination rate, germination index, vitality index, and high vitality ratio of the aged rice seeds were used as the optimization objectives, and the weights of each of these five quantities were all 1. The binomial regression mathematical model, as expressed in Equations (6)–(10), was optimized using the response surface analysis method. The optimal combination of electric field voltage and treatment time for the LH-PEF treatment of the aged rice seeds was an electric field voltage of 13 kV and a treatment time of 32.72 min. Under the optimal conditions, the expected values of germination potential, germination rate, germination index, vitality index, and high vitality ratio of the aged rice seeds were 74.8%, 96.8%, 30.8, 2.20, and 0.13, respectively, which were significantly higher than those of the CK group ($P < 0.01$).

Validation test

Based on the results of the parameter optimization, the aged rice seeds were treated with a pulsed electric field voltage of 13 kV and a treatment time of 32.72 min. As shown in Figure 3 and Table 5, the comparison of rice seed germination between the treatment group and the control group.

Table 5

Comparison of parameters between treatment group (TG) and control group (CK)

Test No.	Electric field voltage (kV)	Treatment time (min)	Germination potential (%)	Germination rate (%)	Germination index	Vitality index	High vitality ratio
TG	13	32.72	75.6	96.4	31.8	2.14	0.14
CK	0	0	61.1	82.3	22.2	1.34	0.04

The germination potential, germination rate, germination index, vitality index, and high vitality ratio of aged rice seeds were 75.6%, 96.4%, 31.8, 2.14, and 0.14, respectively. Compared to the CK group, the germination potential increased by 23.7%, the germination rate increased by 17.7%, the germination index increased by 43.2%, the vitality index increased by 59.7%, the high vitality ratio increased by 250%, and all indices reached extremely significant differences ($P < 0.01$), consistent with the results of the parameter optimization.

Fig. 3 - Comparison between rice seed germination of treatment group (a) and control group (b). Scale bar, 1 cm

DISCUSSION

As a natural phenomenon, an electric field can affect the growth of organisms to various degrees (*Kovalyshyn., 2016*). The biological effects of LH-PEFs on organisms are the physical and chemical reactions that occur in them as a result of such an electric field, thus generating a comprehensive aftereffect (*Feng et al., 2020; Zhang et al., 2019*). In this study, electric field treatment with the appropriate parameters promoted rice seed germination. According to the test results, the germination potential, germination rate, germination index, vitality index, and high vitality ratio of the aged rice seeds reached an optimal value for a certain combination of electric field voltage and treatment time. When the electric field voltage was 13 kV, the plate spacing was 50 mm, the treatment time was 32.72 min, and the electric field frequency was 10 Hz, the germination indices of the aged rice seeds reached their maximum values.

According to the hypothesis of energy stimulation for seed germination, complex physical and chemical changes occurred in the interior of aged rice seeds after they were treated with an electric field with a voltage of 13 kV and a treatment time of 32.72 min, which provided appropriate energy stimulation for the germination of the aged rice seeds. As a result, the germination potential, germination rate, germination index, vitality index, and high vitality ratio of the aged rice seeds significantly improved. Since the test varieties used in this experiment are relatively simple, it is hoped that the wide applicability of this pretreatment method can be explored in the future.

CONCLUSIONS

1) Aged rice seeds were treated with LH-PEFs, and a rotating combination test was performed. The results showed that the germination potential, germination rate, germination index, vitality index, and high vitality ratio of the aged rice seeds reached an optimal value for a certain combination of electric field voltage and treatment time. Accordingly, the biological effect of the electric field on aged rice seeds depended on both the electric field voltage and treatment time.

2) When the electrode plate spacing was 50 mm and the electric field frequency was 10 Hz, the optimal LH-PEF treatment conditions were an electric field voltage of 13 kV and a treatment time of 32.72 min. After the aged rice seeds were treated with this electric field dose, all the germination indices were significantly different compared to the control group ($P < 0.01$). Specifically, the germination potential, germination rate, germination index, vitality index, and high vitality ratio were increased by 23.7%, 17.7%, 43.2%, 59.7%, and 250%, respectively, compared to the CK control group.

ACKNOWLEDGEMENT

This research was supported by the Basic Research Project of Liaoning Province (LSNJC201916, LSNJC201908).

REFERENCES

[1] Afrasiyab, A., Zafar, J., & Muhmmad, H., (2020), Effect of electric field on seed germination and growth parameters of chickpea Cicer arietinum L, *Ukrainian Journal of Ecology*, vol.10(4), pp.12-16;

[2] Barba-Espin, G., Nicolas, E., Almansa, M. S., Cantero-Navarro, E., Albacete, A., Hernández, J. A., & Díaz-Vivancos, P., (2012), Role of thioproline on seed germination: interaction ROS-ABA and effects on antioxidative metabolism, *Plant physiology and biochemistry: PPB*, vol.59, pp.30–36;

[3] Cheng E., Song P., Wang B., Hou T., Wu L., Zhang B., (2022), Determination of rice seed vigor by low-field nuclear magnetic resonance coupled with machine learning, *INMATEH Agricultural Engineering*, vol.67 (2), pp.533-542;

[4] Chen Licai, Huang Fang, Zhou Ming, Yang Weiguang, Shu Shifu, He Jie., (2016), Experimental study on biofield effect of uniform high voltage electrostatic field on rice seeds, *Acta Agriculturae-Jiangxi*, vol.28(05), pp.28-30 + 39;

[5] Evrendilek G.A., Karatas B., Uzuner S., Tanasov I., (2019), Design and effectiveness of pulsed electric fields towards seed disinfection, *Journal of the Science of Food and Agriculture*, vol.99(7), pp.3475-3480;

[6] Feng Longlong, Hou Tiangang, Wang Boxiao, Zhang Benhua., (2021), Assessment of rice seed vigour using selected frequencies of electrical impedance spectroscopy, *Biosystems engineering*, vol.209, ISSN 1537-5110, pp.53-63;

[7] Fukushima A, Uchino G, Akabane T, Aiseki A, Perera I, Hirotsu N., (2021), Phytic Acid in Brown Rice Can Be Reduced by Increasing Soaking Temperature, *Foods*, vol.10(1), pp.23;
[8] Gutiérrez H.F., Pensiero J.F., Zabala J.M., (2015), Effect of population combinations on the reproductive success and germination of seeds of Bromus auleticus (Poaceae), *Grass and Forage Science*, vol.70(1), pp.176-184;
[9] Hunt R.W., Zavalin A., Bhatnagar A., Chinnasamy S., Das K.C., (2009), Electromagnetic biostimulation of living cultures for biotechnology, biofuel and bioenergy applications, *International Journal of Molecular Sciences*, vol.10(10), pp.4515-4558;
[10] Kudratillaev A.S., (2020), Innovative technology to increase the yield of cotton, wheat and other agricultural crops to ensure the acceleration of their maturation, resistance to diseases and to ensure environmental cleanliness of the crop. *IOP Conference Series. Earth and Environmental Science*, vol.614(1);
[11] Kovalyshyn S., (2016), Study of structural changes in the cells of the stimulated seed sprouts, *International Agrophysics*, vol.30(4), pp.545-550;
[12] Pang J., Liu H., Zhang H., Liu A., He J., Liu Y., et al., (2018), Effect of corona treatment and dielectric separation on seed vigor of hybrid rice, *Agricultural Biotechnology*, vol.7(4), pp.48-54;
[13] Patwardhan, M.S., Gandhare W.Z., (2016), Improving germination of tomato seed by electric field treatment, *International Journal of Biosciences*, *Agriculture and Technology*, vol.7(1), pp.1-6;
[14] Reed R.C., Bradford K.J., Khanday I, (2022), Seed germination and vigor: ensuring crop sustainability in a changing climate. *Heredity*, vol.128, pp.450-459;
[15] Shin J., Lee S., Cho H., Pyun Y., Lee J., Chung M., (2010), Germination and subsequent inactivation of bacillus subtilis spores by pulsed electric field treatment, *Journal of Food Processing and Preservation*, vol.34, pp.43-54;
[16] Tantamacharik T., Leong S.Y., Leus M.J., Eyres G.T., (2019), Structural Changes Induced by Pulsed Electric Fields Increase the Concentration of Volatiles Released in Red Onion (Allium cepa L. var. Red Pearl) *Bulbs. Foods*, vol.8, pp.368;
[17] Wei L., Ma F., Du C., (2021), Application of FTIR-PAS in Rapid Assessment of Rice Quality under Climate Change Conditions, Foods, vol.10(1), pp.159;
[18] Wang H., Hu F., Wang C. et al., (2020), Effect of germination and high pressure treatments on brown rice flour rheological, pasting, textural, and structural properties. *J Food Process Preserv*, vol.44, pp.e14474;
[19] Xu Lx., Lin Yx., Wang Lh. et al., (2018), Dehiscence method: a seed-saving, quick and simple viability assessment in rice, *Plant Methods*, vol.14, pp. 68;
[20] Yudaev I., Ivushkin D., Belitskaya M., Gribust I., (2019), Pre-sowing treatment of ROBINIA PSEUDOACACIA L, seeds with electric field of high voltage, *IOP Conference Series*, *Earth and Environmental Science*, vol.403(1);
[21] Yan S.J., Huang W.J., Gao J.D., Fu H., Liu J., (2018), Comparative metabolomic analysis of seed metabolites associated with seed storability in rice (Oryza sativa L.) during natural aging, *Plant Physiology and Biochemistry*, vol.127, pp. 590-598;
[22] Zhang L., Li Chao-Qun, Jiang W., Mangang W., Sheng-Qi R., Jian-Ya Q., (2019), Pulsed electric field as a means to elevate activity and expression of α-amylase in barley malting, *Food and Bioprocess Technology*, vol.12(6), pp.1010-1020.

EFFECT OF TRANSPLANTER VIBRATION ON PARTICLE MOVEMENT VELOCITY OF SANDY LOAM SOIL BY USING DEM
/
移栽机振动对沙壤土颗粒运动速度的影响分析

Qiang SU[1)], Xuying LI[*1)], Fandi ZENG[1)], Hongbin BAI[1)], Junyue WANG[1,2)]
[1)] Inner Mongolia Agricultural University, College of Mechanical and Electrical Engineering, Hohhot/China;
[2)] China Academy of Agricultural Mechanization Science Co., Ltd. Hohhot Branch, National Grassland Animal Husbandry Equipment Engineering Technology Research Centre, Hohhot/China
Tel: +86-0471-4309215; E-mail: suqi5199@163.com
Corresponding author: Xuying Li
DOI: https://doi.org/10.35633/inmateh-70-51

Keywords: *hanging cup transplanter, soil bin test, vibration parameters, DEM, particle movement*

ABSTRACT
The sandy loam soil has complex movement characteristics during hole formation by hanging cup transplanters. In order to better investigate this point, the paper aims to investigate the disturbance pattern of transplanter vibration on sandy loam soil and the movement characteristics of soil particles by the discrete element method. The vibration characteristics of the transplanter operating on sandy loam soil were tested and analyzed, and the motion law of vibration parameters on sandy loam soil was investigated with the help of the discrete element method and soil bin test. The results showed that the vibration acceleration of the transplanter increased with the forward speed, the primary vibration frequency range was from 0 to 12 Hz, and the vibration amplitude increased linearly in the field of 1.21 to 9.19 mm. The Central Composite test resulted in the regression equations of vibration amplitude and vibration frequency on the average movement velocity of the particles. The response surface analysis showed that the effect of vibration amplitude on the average movement velocity of particles was greater than the effect of vibration frequency on the average movement velocity of particles. At the same time, the average movement velocity of the particles tends to increase significantly under the interaction of the two. This study provides data to support the design of planters for sandy loam soils, which is beneficial to promote seedling transplanting technology further.

摘要
吊杯式移栽机成穴过程中，砂壤土运动特性复杂。为更好地探究这一问题，本研究通过离散元法研究移栽振动对沙壤土的扰动规律和土壤颗粒的运动特性。对移栽机的振动特性进行了测试和分析，并借助于离散元仿真和土槽试验研究了振动参数对沙壤土颗粒速度的影响规律。结果表明，插秧机的振动加速度随前进速度的增加而增加，振动频率范围为 0 ~12Hz，振动振幅在 1.21 ~9.19mm 的范围内线性增加。中心组合试验得到振动振幅和振动频率对颗粒平均移动速度的回归方程，响应面分析表明，振动幅度对颗粒平均移动速度的影响大于振动频率对颗粒平均移动速度的影响。同时，在两者的相互作用下，颗粒的平均运动速度有明显增加的趋势。本研究为沙壤土移栽机的设计提供了数据支持，有利于进一步推广育苗移栽技术。

INTRODUCTION

In the past five years, the vegetable industry in China is developing steadily, and the use of transplanters can overcome labor shortages. It is worth mentioning that soil type is also a key factor in the performance of transplanters. However, scholars have not paid attention to the disturbance of transplanting machine on sandy loam soil. Part of the soil flows back into the hole, creating an uneven bottom and seriously affecting seedling growth and planting efficiency (*Frasconi et al., 2019; Mamun et al., 2020; Awuah et al., 2022*). In order to investigate the planting mechanism and optimize the structure of the planters, it is necessary not only to analyze the morphology of the holes formed by the planters but also to investigate the dynamic disturbance of the soil particles by the planters (*Bhambota et al., 2018*). In addition, vibrations caused by complex excitation in the field will accelerate the velocity of soil particle flow. None of the existing studies considered the effect pattern of soil disturbance by transplanter vibration caused by complex excitation in the field, and the field experiments failed to better reveal the disturbance pattern of soil particles by transplanter vibration.

Qiang Su, D. Eng; Xuying Li, Prof. Eng; Fandi Zeng, D. Eng; Hongbin Bai, M. S. Eng; Junyue Wang, D. Eng.

The discrete element method (DEM) is a numerical method that is suited to analyze the microscopic behavior of granular media. Tanaka used DEM to simulate the tillage process of a vibrating subsoiler. The soil profiles simulated by the deep vibrating subsoiler were compared with field tests. The areas of disturbance were very consistent, indicating that DEM can be used to study microscopic soil movement under the action of vibratory tools (*Tanaka et al., 2010*). The effect on operational performance in the case of agricultural machine vibration has been analyzed by related scholars using the discrete element method. Moreover, the interaction between the two was analyzed by considering the soil. For example, the working process of deep loosening machine vibration deep loosening and no vibration deep loosening was simulated (*Ma et al., 2020*), exploring the influence of a vibrating digging shovel on the range of soil disturbance (*Shi et al., 2021*). The cup-soil contact movement in the planting operation process can be simulated and the planter's complex kinematics characteristics under the action of the soil can be studied. Yang Qizhi analyzes the hole planting process of a hanging cup planter of a high speed hanging auto-transplanter to study the kinematic characteristics of the hanging cup planter under the more realistic action of soil and the interaction mechanism with the soil (*Yang et al., 2022*). Above studies provide ideas for this study.

Our research group conducted vibration tests on the transplanting machine in the early stage (*Su et al. 2022*), and conducted experimental research on hole parameters (*Zeng et al., 2023*). In summary, this study is based on theories such as vibration mechanics and discrete element method and combines vibration testing techniques, soil bin tests and discrete element simulation to analyze the effect law of transplanter vibration on sandy loam soil particles. The vibration test was carried out on the transplanter under complex excitation, and the collected vibration signals were analyzed. The vibration frequency and amplitude were introduced into the discrete element model of the contact action between the transplanter and soil to examine the influence law of the transplanter on the sandy loam soil under vibration.

MATERIALS AND METHODS

Hanging-cup transplanter structure and working principle

It consists of the seat, the three-point suspension, the ground wheel drive assembly, the transplanting assembly and the planting depth adjustment device, shown in Fig. 1a). The transplanting assembly mainly consists of a chain-row seedling feeder, a support plate, an eccentric disc, a cup transplanter, a single support frame and a mulching ballast wheel. The two transplanting units are fastened to the three-point suspension by U-bolts. The two ground wheel drive assemblies are fastened to the left and right sides of the three-point suspension, transmitting power to the chain feeder and the eccentric disc planting mechanism using a chain drive system. During operation, the tractor pulls the transplanter forward, and the ground wheel transmits the power to the seedling feeding mechanism and the planting mechanism, both of which work in a specific ratio; the seedlings are manually placed into the seedling feeding cup, and when the planting device rotates to a specific position above, it catches the seedlings falling from the seedling feeding cup and the planting device then drives the seedlings down. As the planter rotates into the soil, the planter opens up, and the seedlings fall into the expanded hole. Then the planter continues to rotate for the next planting. For the randomness of the complex excitation of the transplanter, the soil surface unevenness is regarded as the main source of transplanter vibration (*Su et al., 2022)*, as shown in Fig. 1b).

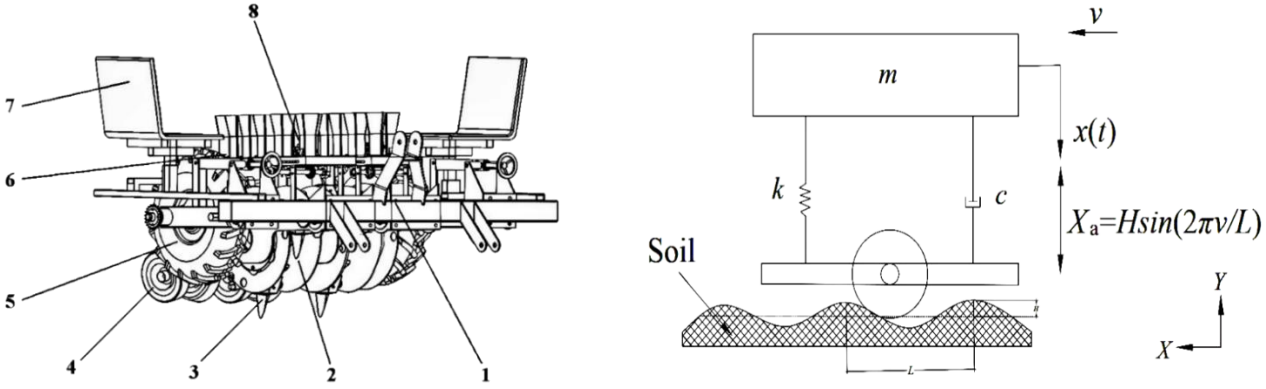

a) Structural of hanging cup transplanters *b) Vibration modeling of hanging cup transplanters*

Fig. 1 – Structural and vibration modeling of hanging cup transplanters

1 - Three-point hanging mechanism; 2 - Planting mechanism; 3 - Driving wheel; 6 - Planting depth adjustment mechanism; 7 - Seat; 8 - Chain feeding mechanism

Test conditions and test protocol

The test site was the soil bin laboratory at Inner Mongolia Agricultural University, equipped with an intelligent soil-machine-plant technology platform to carry out transplanting trials by the transplanting standard (JB-T 10291-2013 Dryland Planting Machinery) for tomato cavity tray seedlings.

The test machines and soil related physical parameters are shown in Table 1. The vibration signal acquisition equipment of the hanging cup transplanter is shown in Fig. 2.

Table 1

Main parameters of field trials

Item		Value
2ZP-2 type hanging-cup transplanter	Weight / [kg]	346
	Number of transplanted rows	2
	Row spacing / [mm]	500
	Spacing / [mm]	436
	Forward speed / [km/h]	0.8~2.4
Technology platform for intelligent soil-machine-plant systems	Rated speed / [km/h]	0.5~10
	Traction / [t]	1.5
	Power / [kW]	70
Soil parameters	Soil type	Sandy loam soil
	Moisture content / [%]	13.6
	Solidity / [MPa]	0.821
	Weight capacity / [g/cm^3]	1.26

This experiment uses the accelerometer installation position, as shown in Fig. 2, which can simultaneously test the vibration acceleration in three directions (*Wang et al., 2021*). The X-axis is defined as the transplanter forward direction, the Y-axis is defined as the transplanter lateral direction, and the Z-axis is defined as the direction of the transplanter perpendicular to the ground. The vibration characteristics of the transplanter were tested at 0.8, 1.2, 1.6, 2.0 and 2.4 km/h in a single factor test. The soil was rotated, levelled and suppressed before each test, and the planting depth was 60 mm. After the transplanter had stabilized, the vibration signals were collected for 8 s for each set of tests, and the average of three replicate tests was taken for analysis.

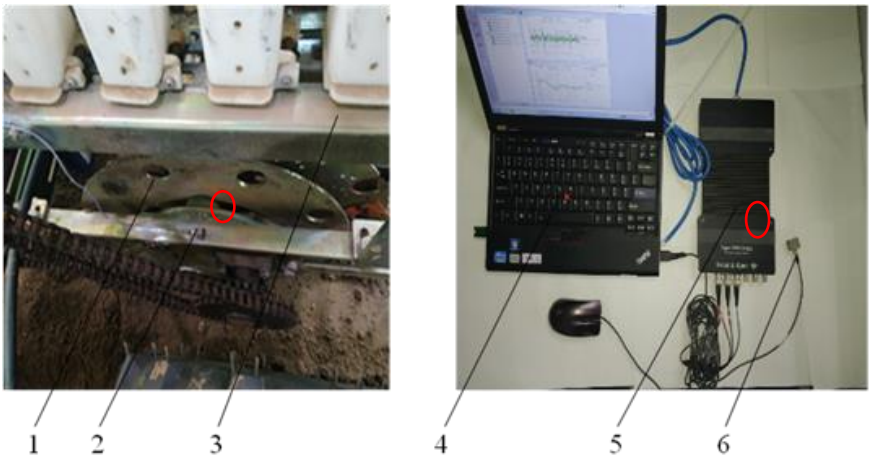

Fig. 2 - Vibration data acquisition diagram of transplanter

1 - planting mechanism; 2 - three-directional acceleration sensor attachment position; 3 - seedling feeding mechanism; 4 - computer with pulse software; 5 - data acquisition card; 6 - three-directional acceleration sensor.

Vibration test data analysis methods

The mean square value can describe the average energy or power of the vibration process. The positive square root of the mean square value is called the root mean square value of acceleration (RMS), or the practical value can better reflect the transplanter vibration, and the expression is:

$$\mathrm{RMS} = \left|\sqrt{\psi_x^2}\right| = \left|\frac{1}{N}\sum_{i=1}^{N} x_i^2\right| \quad (1)$$

where:

X_i is the vibration signal; ψ_x^2 is the mean square value of the acceleration; N is the average number of vibration signals.

Power Spectral Density (PSD) is a measure of the mean square value of a random variable that represents the variation of energy per unit frequency band of a signal with frequency.

The power spectral density is defined as follows:

$$G_{xx}(f) = \frac{1}{\Delta f} \lim_{f \to \infty} \frac{1}{T} \int_0^T x^2(t, f, \Delta f) dt \quad (2)$$

Soil bin validation tests

Validation trials were carried out in the soil bin laboratory at Inner Mongolia Agricultural University, equipped with an intelligent soil-machine-plant technology platform and contains less straw, weeds and other debris. The soil was a sandy loam, prepared according to the macroscopic properties such as moisture content and firmness that the soil model has in the EDEM simulation model, and pretreated by sprinkling, rototilling and ballasting. Considering the planting depth requirement of tomato seedlings in cavity trays, the planting depth was set at 60 mm and soil parameters were measured in the 0-60 mm soil layer in the test area. The average soil moisture content was controlled at around 13±2%, and the average soil firmness was 643.8 kPa.

At the end of the test, several sets of measurement points were selected at equal intervals in the test area. The hole depth and longitudinal length were obtained at once using a hole plotter, as shown in Fig. 3, which consisted of a grid coordinate paper, an acrylic rod and a base made of acrylic sheets. To measure, the top layer of soil is scraped off, the hole plotter is placed directly above the hole, the acrylic rod is inserted along the circular hole in the base until it touches the soil, and the position of the top point of the rod on the grid coordinate paper is marked in turn with a marker to read the coordinates of each marked point.

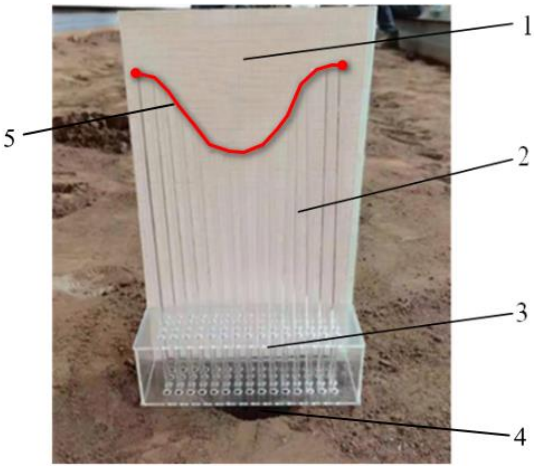

Fig. 3 - Hole plotter

1 - grid coordinate paper; 2 - acrylic rod; 3 - base made of acrylic sheet; 4 – hole; 5 - hole contour

Discrete element simulation analysis of transplanting process

In order to ensure that the simulated soil can accurately represent the actual soil conditions, the determination of relevant physical parameters and the calibration of simulation parameters have been completed for the sandy loam soil in Inner Mongolia (*Zeng et al., 2021*), as shown in Table 2. The simplification is carried out separately for the structural characteristics of sandy loam soils. Fig. 4 shows the different types of sandy loam particles, including spherical particles, nucleated particles, blocky triangular particles and columnar particles. Particle size is normally distributed.

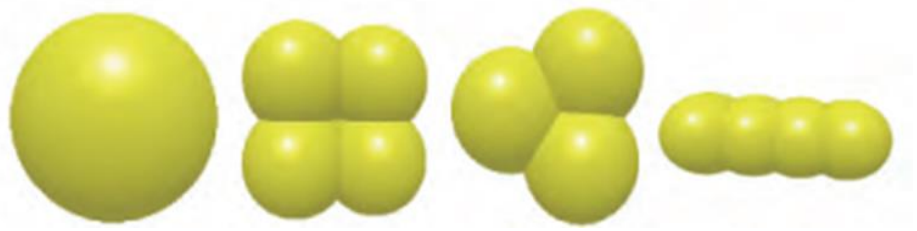

a) spherical particles *b) nucleated particles* *c) blocky triangular particles* *d) columnar particles*

Fig. 4 - Soil particle discrete element model

The mutual contact model between the planting device and the soil was set as Hertz–Mindlin (no slip) with a generation ratio of 1:1:1:1 (*Lv et al., 2021; Ma et al., 2021; Sun et al., 2018*). The particles were deposited by gravity after generation.

Table 2

Basic parameters of discrete element model

Simulation parameters	Value
Density of steel / [kg/m^3]	7850
Density of soil particles / [kg/m^3]	1452
Poisson's ratio of soil	0.42
Poisson's ratio of steel	0.3
Young's modulus of soil / [MPa]	10^6
Young's modulus of steel / [MPa]	7×10^{10}
Soil-soil restitution coefficient	0.45
Soil-steel restitution coefficient	0.35
Soil-soil static friction coefficient	0.4
Soil-steel static friction coefficient	0.85
Soil-soil rolling friction coefficient	0.3
Soil-steel rolling friction coefficient	0.13
Soil particle generation time / [s]	5
Simulation time / [s]	8
Time step	25%

A simulated soil trough of 1400 mm long, 500 mm wide and 300 mm high was used in the simulation, as shown in Fig. 5. In order to reduce the simulation time, only the individual planters were simulated, and the model of the planting mechanism was constructed using Pro/E and imported into the center of the working interface of the EDEM discrete element simulation software.

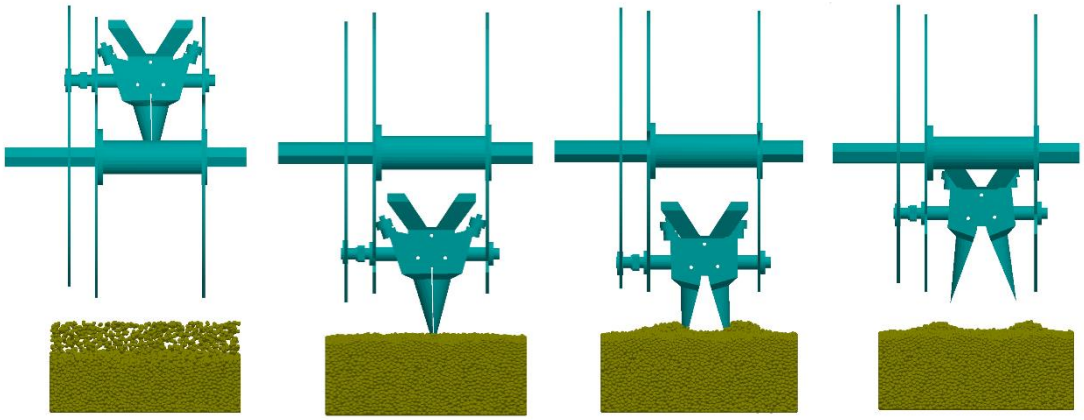

a) *b)* *c)* *d)*

Fig. 5 - Planter positions at different times

a) soil model generation; b) planter in contact with soil; c) generate pores; d) the planter leaves the soil

Based on the vibration data analyzed in the previous section, vibration frequencies of 0, 4, 8, 12 and 16 Hz and vibration amplitudes of 0, 3, 6, 9 and 12 mm were set for the transplanting simulation tests. Based on the agronomic requirements of transplanting and related research, the transplanter was set to a speed of 18.2 r/min (i.e. λ=1.22), a planting depth of 60 mm and a simulation time of 8 s.

Soil bin validation test

At the end of the simulation, the critical curve of the movement velocity of soil particles was plotted as the contour of the pitshaped cross section of soil disturbance, conditional on whether the soil has movement velocity, and the contour of soil accumulation on the surface was used as the contour of the monopoly-shaped cross section of soil disturbance. The holes were measured using a hole mapper, and the measured contour data points were curve fitted and compared with the simulation results, as shown in Fig.6.

In the soil bin test, the skidding of the transplanter tires caused the misalignment of the two fitted curves. The statistical analysis of the difference between the actual measurement points and the simulated points in the figure shows that the maximum misalignment value is 6 mm and the minimum is 0 mm, where the average value is 2.22 mm and the average difference is 1.35 mm.

The soil trough test fitted pore contours are consistent with the simulated pore contour crosssection in a V-shape. In order to further evaluate the consistency of the simulated and soil bin test values, the relevant parameters of the hole were compared.

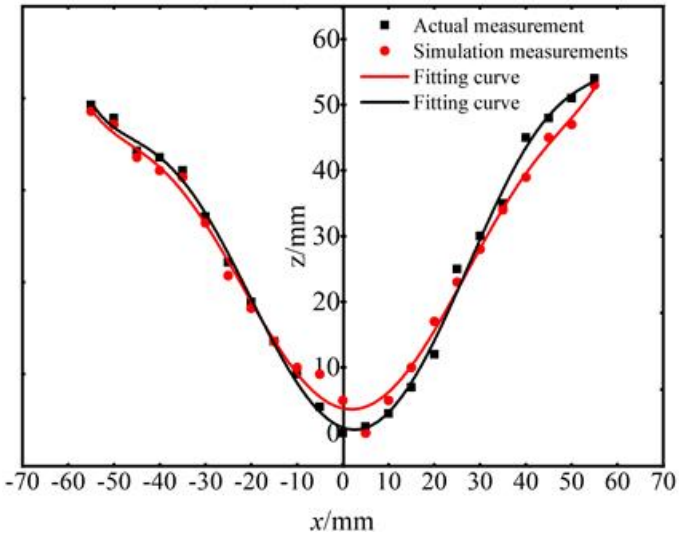

Fig. 6 - Measurement results of hole section

In order to further demonstrate the accuracy of the simulation experiment, the key parameters of the holes were analyzed. From Table 3, the experimental values of longitudinal length and width of the hole were larger than the simulated values, and the relative errors between the experimental and simulated results were within a reasonable range, which proved the reasonableness of the simulated data. The relative error of effective depth is 9.54%, which is probably due to the accumulation of errors in the measurement and software fitting process, and the relative error of hole width is 0.86%.

This also proves the reliability of using discrete element methods for research. In the future, the discrete element method will be further used for analysis.

Table 3

Comparison of the results of simulation and soil bin test

Indexes	Simulation values [mm]	Test values [mm]	Relative errors [%]
Longitudinal length of the hole / [mm]	102	104	1.92
Width of the hole / [mm]	57.6	58.1	0.86
Effective depth / [mm]	52.3	48.5	9.54

RESULTS

Analysis of vibration test results

Based on the time domain signal of the transplanter, the relationship between its forward speed and the Root Mean Square (*RMS*) value of acceleration can be solved, as shown in Fig. 7.

As can be seen from Fig. 6, the root mean square values of acceleration in the *X*, *Y* and *Z* directions increase as the forward speed increases, and when the forward speed of the transplanter is 0.8-2.4 km/h, the root-mean-square values of vibration acceleration in X-direction range from 0.06 to 0.31 m/s^2, in the Y-direction from 0.23 to 0.77 m/s^2, and in the *Z*-direction from 0.29 to 0.95 m/s^2.

The regression results show that there are linear correlation between the root mean square and forward speed.

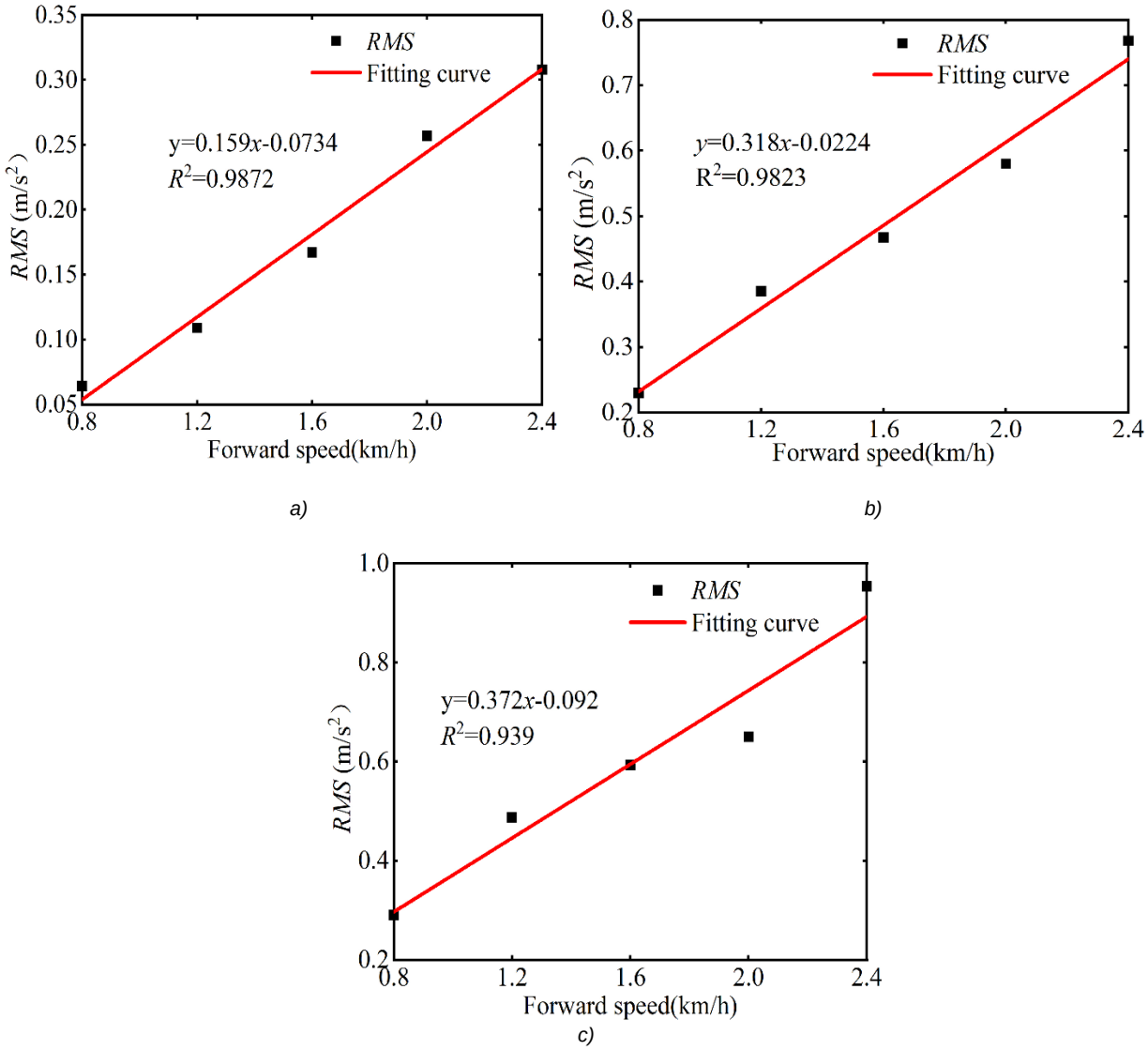

Fig. 7 – Distribution of root mean square acceleration of transplanter
a) X direction; b) Y direction; c) Z direction

The time domain signal of *Z*-direction vibration is shown in Fig. 8. The vibration is most intense in the direction perpendicular to the soil. This conclusion is consistent with the vibration test results in this article.

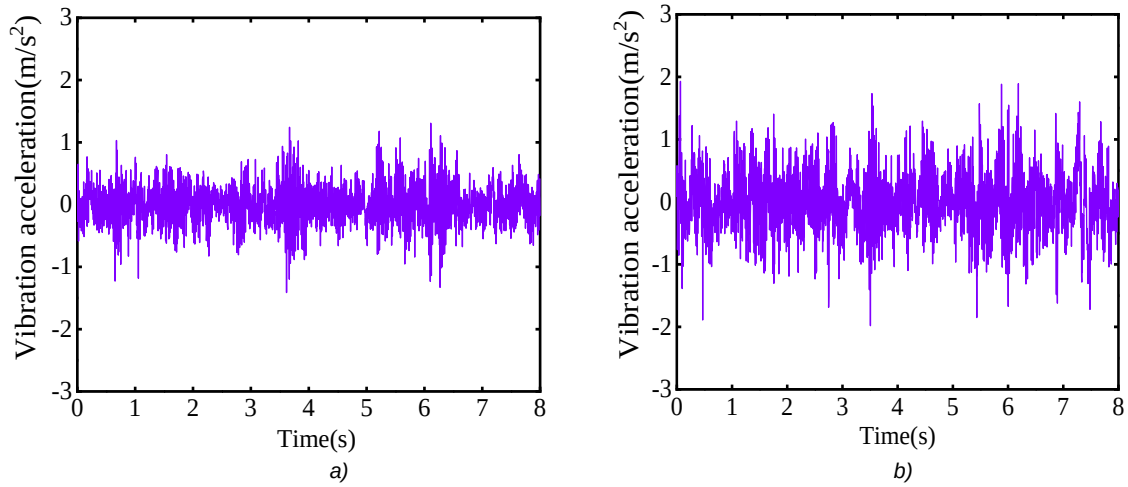

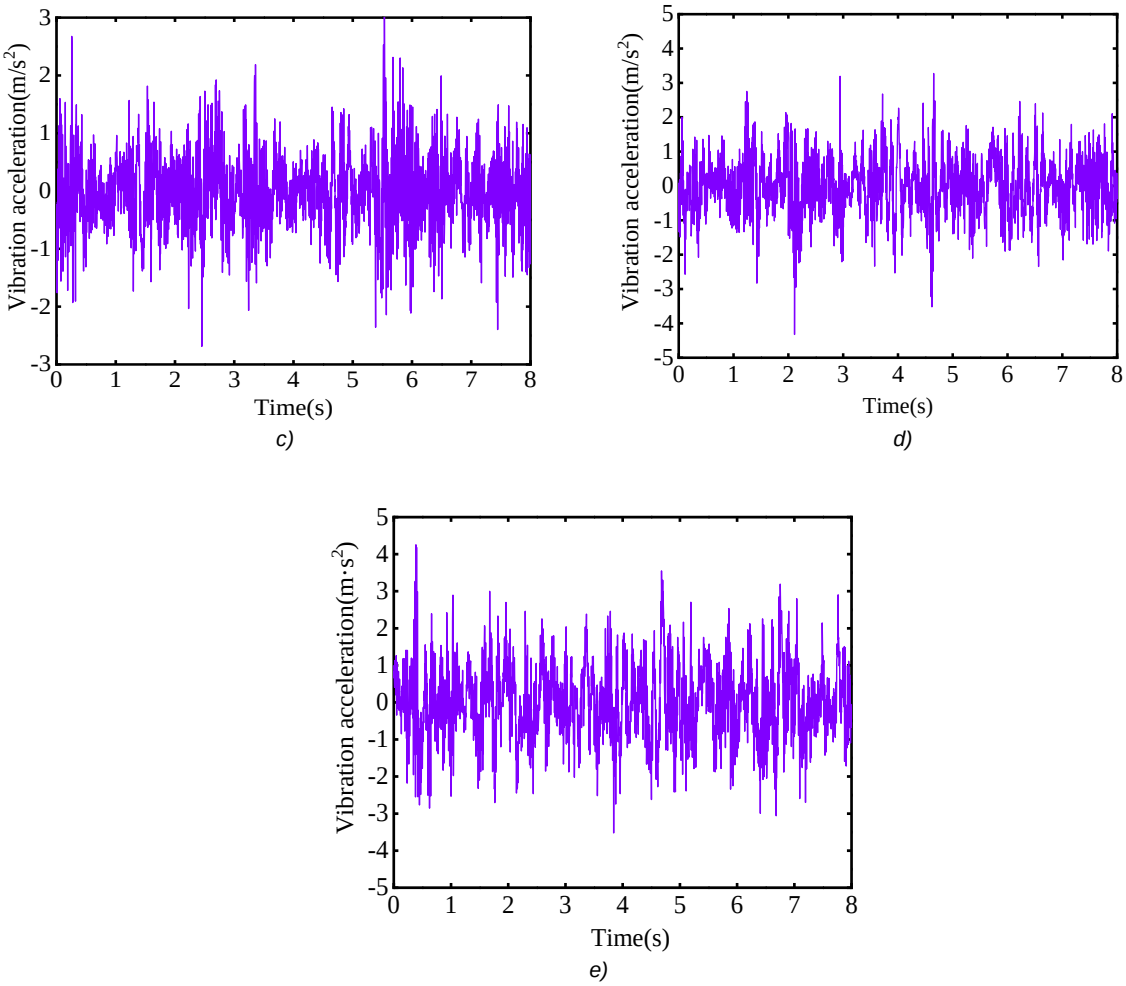

Fig. 8 - Time domain signals of vibration at different forward speeds of the transplanter
a) v=0.8 km/h; b) v=1.2 km/h; c) v=1.6 km/h; d) v=2.0 km/h; e) v=2.4 km/h

As shown in Table 4, with the increase of the forward speed, the maximum value, variance, standard deviation and effective value of the vibration acceleration tended to be increased. This shows a trend of positive correlation with forward speed.

Table 4

Time domain parameters statistics table

Forward Speed / [km/h]	Vibration data statistics/[m/s²]						
	Maximum Values	Minimum Values	Mean Value	Variance	Standard Deviation	Median	Valid Value
0.8	1.3070	-1.4116	-0.0016	0.1141	0.3379	-0.0013	0.2931
1.2	1.9276	-1.9807	-0.0068	0.2629	0.5128	-0.0226	0.4870
1.6	3.1437	-2.6875	-0.0085	0.4514	0.6719	-0.0063	0.5932
2.0	3.2731	-4.3245	-0.0093	0.7177	0.8472	-0.0086	0.6489
2.4	4.2535	-3.5225	0.0018	1.0504	1.0249	-0.0210	0.9526

The time-amplitude curve is obtained by quadratic integration of the time-domain signal, as shown in Fig.9a), where the maximum amplitude becomes more significant as the forward speed increases. The vibration amplitude increases significantly at a forward speed of 2 km/h. The power spectrum density curve was obtained by a fast Fourier transform of the time domain signal. According to the power spectrum density curve in Fig.9b), the vibration of the transplanter is primarily low-frequency vibration, and the frequency distribution of vibration energy is mainly concentrated in the frequency range of 1-12 Hz. The greater the forward speed, the more intense the vibration will be, but there will be no effect on the frequency distribution of the vibration energy range.

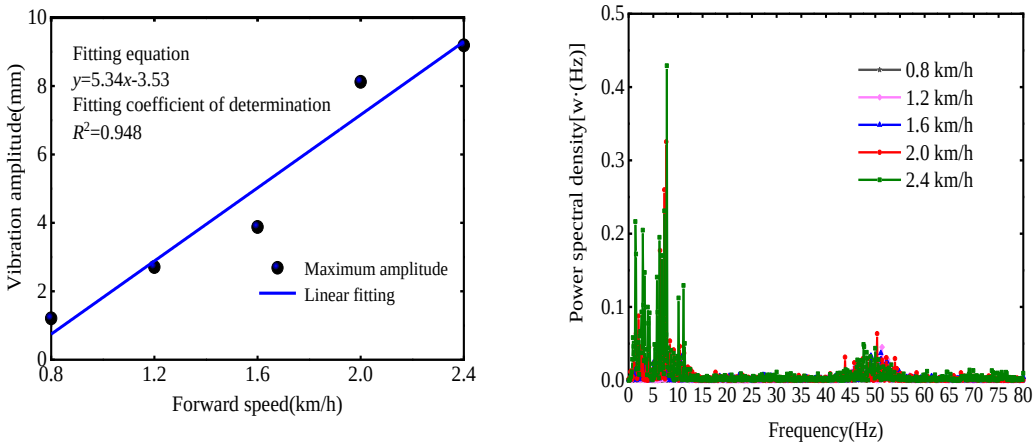

a) *b)*

Fig. 9 - Vibration test results

a) Fitting line between forward velocity and maximum amplitude; b) Power spectral density curves

Discrete element simulation results

Vibration increases the soil fragmentation effect and will accelerate the flow of soil particles (*Awuah et al., 2022*). When seedlings enter the soil, soil flow increases, and the planting depth of seedlings becomes shorter. The effect of machine vibrations on soil particles affects the quality of seedling planting. The simulated soil was divided into two layers and used to analyze the variation of soil movement velocity in the area where the transplanter operated. The average movement velocity variation curve of soil particles at a vibration frequency of 8 Hz and vibration amplitude of 6 mm were selected for analysis, as shown in Fig. 10. The movement trend of the two layers of soil is similar, but the movement speed is not the same. The movement speed of soil particles on the surface is significantly lower than that of the bottom particles.

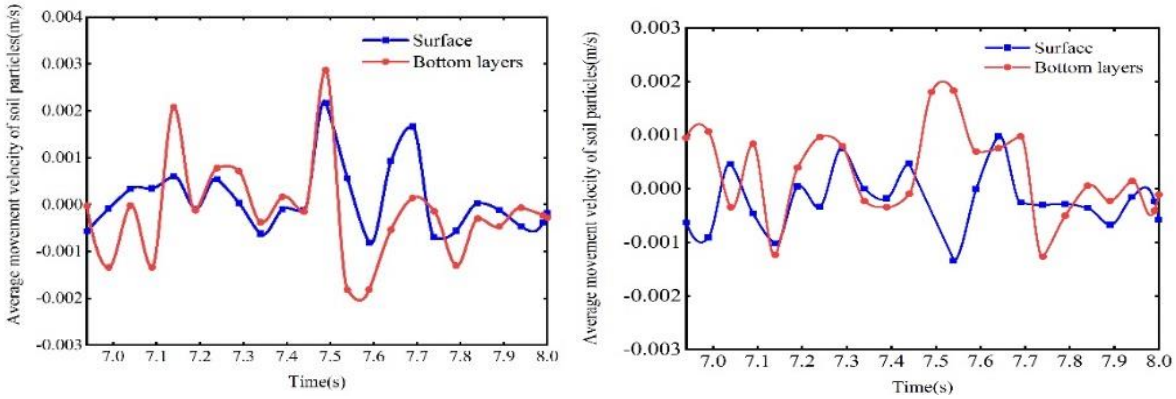

a) *b)*

Fig. 10 - Soil average movement velocity contrast graph

a) Vibration frequency is 8Hz; b) Vibration amplitude is 6 mm

Parametric regression orthogonal test

Central composite design

Combined with the design principle of orthogonal test, vibration frequency and vibration amplitude were selected as the test factors. The test factors are coded as shown in Table 5.

Table 5

Horizontal coding of test factors

Horizontal coding	Factors	
	A: Vibration amplitude	B: Vibration frequencies
	[mm]	[Hz]
-1.414	0	0
-1	3	4
0	6	8
1	9	12
1.414	12	16

According to the above analysis, the vibration parameters have the most significant effect on the average movement velocity of the particles in *Z*-direction. Therefore, the subsequent study will be conducted with the average movement velocity of the particles in *Z*-direction as the indices. An orthogonal test of two factors and five levels was designed using the Design Expert 11 software (STAT-EASE Inc., Minneapolis, USA). A total of 13 test combinations were conducted, and each combination was repeated several times, and the test results are shown in Table 6.

Table 6

Test design and results

No.	Test Factors and Levels		Target Value
	Vibration amplitude	Vibration frequencies	Average movement velocity of soil particles
	[mm]	[Hz]	[m/s]
1	1	1	0.0486
2	0	0	0.0183
3	0	0	0.0204
4	0	0	0.0189
5	-1	1	0.0321
6	1	-1	0.0289
7	0	-1.414	0.0170
8	0	0	0.0172
9	0	0	0.0212
10	-1.414	0	0.0295
11	1.414	0	0.0399
12	-1	-1	0.0253
13	0	1.414	0.0214

Establishment and significance analysis of regression model

Eq. 3 is a multiple regression fitting curve equation for the average movement velocity (*V*) of the particle with respect to the vibration amplitude (*A*) and vibration frequency (*B*).

$$V = 0.0152 + 0.0087A + 0.0036B + 0.0032AB + 0.0049A^2 + 0.0137B^2 \quad (3)$$

The Design Expert software was used to conduct the multiple regression fitting and variance analysis on the data from average movement velocity of soil particles, and the results are shown in Table 7.

Table 7 shows that the overall P-value of the model is less than 0.01, which indicates that the model is highly significant and R^2=0.9576 indicates a better fitting. The lack of fit term is non-significant (P=0.3296>0.05) indicating that the model can analyze and predict the change of average movement velocity of soil particles. The factors affecting the magnitude of average movement velocity of soil particles are vibration amplitude (*A*) and vibration frequency (*B*) in that order.

Table 7

Variance analysis of the regression model

Source	Sum of Squares	Freedom	Mean Square	F-value	p-value
Model	0.0021	5	0.0004	31.59	0.0001**
A	0.0006	1	0.0006	45.21	0.0003**
B	0.0001	1	0.0001	7.86	0.0264*
AB	0.0000	1	0.0000	3.08	0.1228
A^2	0.0002	1	0.0002	12.29	0.0099**
B^2	0.0013	1	0.0013	96.77	< 0.0001**
Residual	0.0001	7	0.0000		
Lack of Fit	0.0001	3	0.0000	1.56	0.3296
Pure Error	0.0000	4	0.0000		
Cor Total	0.0022	12			

*Note: * means significant (P < 0.05), and ** means extremely significant (P < 0.01).*

Fig. 11 shows the response surface of the influence of vibration amplitude and frequency on the average movement velocity of soil particles. When the vibration frequency is constant, the average motion speed of particles increases with the increase of vibration amplitude. When the vibration amplitude is constant, the average movement velocity of soil particles first decreases and then increases with the increase of vibration frequency. In the case of interaction between the two, there is a clear upward trend in the average motion speed of particles.

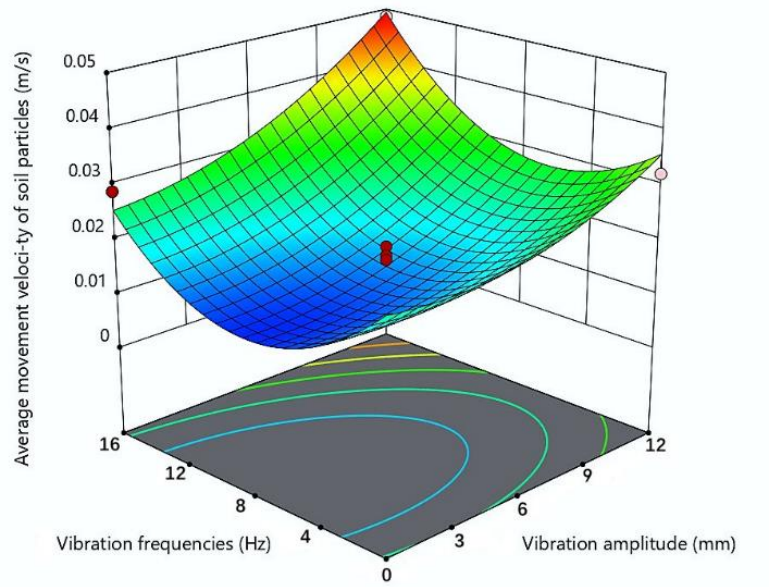

Fig. 11 - Response surface plots of interaction of two factors on average movement velocity of soil particles

CONCLUSIONS

This study used theoretical analysis, vibration testing experiments, discrete element simulation, and other methods to analyze the impact of transplanting machine vibration on the movement speed of soil particles in holes.

At an operating speed of 0.8-2.4 km/h, the vibration acceleration of the 2ZP-2 type hanging-cup transplanter increases with the forward speed, the frequency distribution of the vibration energy ranges from 1 to 12 Hz in the low-frequency band, and the vibration amplitude increases linearly in the range of 1.21-9.19 mm.

The Central Composite test resulted in the regression equations of vibration amplitude and vibration frequency on the average movement velocity of the particles. The response surface analysis showed that the effect of vibration amplitude on the average movement velocity of particles was greater than the effect of vibration frequency on the average movement velocity of particles. At the same time, the average movement velocity of the particles tends to increase significantly under the interaction of the two. In order to be more suitable for transplanting in sandy loam soil, the vibration amplitude of the transplanting machine should be as small as possible. And ensure the smoothness of the soil.

In addition, the use of transplanters to carry out the planting process has been known widely. Reviews related to productivity performance from these tools are closely related to topographic conditions, soil types, land area, plant species, community culture, the purpose of use, and the technology included as an added value to the tool. In the future studies, the plant species, water content and other factors deserve further experimental studies. Our test bench is already under development, and test methods for controlling variables are being proposed.

ACKNOWLEDGEMENT

This project was funded by the National Natural Science Foundation of China (32160423) and the Natural Science Foundation of the Inner Mongolia Autonomous Region of China (2019MS05031 and 2020MS05055).

REFERENCES

[1] Awuah E., Zhou J., Liang Z. et al, (2022). Parametric analysis and numerical optimisation of Jerusalem artichoke vibrating digging shovel using discrete element method. *Soil and Tillage Research*, 219, 105344. https://doi.org/10.1016/j.still.2022.105344Get rights and content

[2] Bhambota S., Dixit A.K., Manes G.S, Singh S.K, (2018). Development and evaluation of vertical cup with split base type metering mechanism cum dibbler for semi-automatic transplanter using cell feed type nursery. *International journal of current microbiology and applied sciences*, 7(6), 3600-3611. DOI:10.20546/ijcmas.2018.706.424

[3] Frasconi C., Martelloni L., Raffaelli M., Fontanelli M., Abou Chehade L., Peruzzi A., Antichi D, (2019). A field vegetable transplanter for use in both tilled and no-till soils. *Transactions of the ASABE*, 62(3), 593–602. DOI:10.13031/trans.12896

[4] Lv J., Liu Q., Li Z., Li J., Liu Z, (2021). Design and experiment of soil cultivating device of plowshare potato field cultivator (犁铧式马铃薯中耕机培土装置设计与试验). *Transactions of the Chinese Society for Agricultural Machinery*, 52(7), 71-82.

[5] Ma S., Niu C., Yan C., Tan H., Xu L. (2021). Discrete element method optimisation of a scraper to remove soil from ridges formed to cold-proof grapevines. *Biosystems Engineering*, 210, 156-170. https://doi.org/10.1016/j.biosystemseng.2021.08.014

[6] Mamun M.R.A., Islam A., Lucky A.K., Hossen M.A., (2020). Identification of puddling settling period of various soil textures for mechanical rice transplanting. *Agricultural Engineering International: CIGR Journal*, 22(4), 40-47.

[7] Ma X., Wang S., Wang H., (2020). Vibration soil crushing mechanism of self-excited vibration subsoiler in coastal area. *Journal of Coastal Research*, 103, 426-430. DOI:10.2112/SI103-087.1

[8] Shi Z., Chen T., Li S., Yang L., Yang M., (2021). Impact of vibration on tillage performance of subsoilers using the DEM. *INMATEH-Agricultural Engineering*, 64(02), 89-98. DOI:10.35633/inmateh-64-08

[9] Su Q., Li X., Zeng F., Wang J., Zhang Y., Bai H., Wu L., Wang Jie, (2022). Vibration characteristics test and analysis of hanging cup transplanter. *INMATEH-Agricultural Engineering*, 66(1), 279-288. DOI:10.35633/inmateh-66-28

[10] Sun J., Wang Y., Ma Y., Tong J., Zhang Z, (2018). DEM simulation of bionic subsoilers (tillage depth>40 cm) with drag reduction and lower soil disturbance characteristics. *Advances in Engineering Software*, 119, 30-37. https://doi.org/10.1016/j.advengsoft.2018.02.001

[11] Tanaka H., (2010). Simulation of soil loosening by a vibrating subsoiler by means of the distinct element method. *Journal of Agricultural and Food Chemistry*, 68, 13-17. DOI:10.11357/jsam1937.68.4_13

[12] Wang J., Xu C., Xu Y., Wang J., Zhou W., Wang Q., Tang H., (2021). Resonance analysis and vibration reduction optimization of agricultural machinery frame-taking vegetable precision seeder as an example. *Processes*, 9, 1979. https://doi.org/10.3390/pr9111979

[13] Yang Q., Zhang R., Jia C., (2022), Study of dynamic hole-forming performance of a cup-hanging planter on a high-speed seedling transplanter. *Frontiers of Mechanical Engineering*, 8, 896881. https://doi.org/10.3389/fmech.2022.896881

[14] Zeng F., Li X., Zhang Y., Zhao Z., Cheng C., (2021). Using the discrete element method to analyze and calibrate a model for the interaction between a planting device and soil particles. *INMATEH-Agricultural Engineering*, 63(01), 413-424. DOI:10.35633/inmateh-63-42

[15] Zeng F., Li X., Bai H., Cui J., Liu X., Zhang Y., (2023). Experimental research and analysis of soil disturbance behavior during the hole drilling process of a hanging-cup transplanter by DEM. *Processes* 11, 600. https://doi.org/10.3390/pr11020600

DESIGN AND FINITE ELEMENT ANALYSIS OF VARIABLE-DIAMETER THRESHING DRUM WITH MOVABLE RADIAL PLATES
/
幅盘移动式变直径脱粒滚筒的设计与有限元分析

Fazheng WANG[1,2], Yaoming LI[1,2*], Yanbin LIU [2], Kuizhou JI[1,2], Zeng LI [3], Xiangqian XU[3], Lei XU[3]

[1]School of Agricultural Engineering, Jiangsu University, Zhenjiang 212013 / China;
[2] Key Laboratory of Modern Agricultural Equipment and Technology (Jiangsu University), Ministry of Education, Zhenjiang 212013 / China
[3]Shandong Jindafeng Machinery Co., LTD., Jining 272114, China
Tel: 0511-88780048.; E-mail: ymli@ujs.edu.cn
Correspondence: Yaoming Li
DOI: https://doi.org/10.35633/inmateh-70-52

Keywords: *threshing drum, structural design, finite element analysis, modal analysis, wheat field test*

ABSTRACT
In view of the fact that the threshing gap of combine harvester can only be controlled by adjusting gravure screen and it is time-consuming and laboring, a kind of variable-diameter threshing drum with movable radial plates is developed by changing the diameter of threshing drum to adjust the threshing gap concentrically. All parts of the threshing drum were designed and checked by mechanical design principle, and the statics and modal analysis of the whole structure were carried out by ANSYS Workbench. The results show that the maximum deformation of the variable-diameter threshing drum with movable radial plates is 0.29 mm under boundary conditions. The maximum allowable deformation of the threshing drum in use is 3 mm, which meets the requirements of use. The equivalent stress of the threshing drum with variable diameter is up to 100 MPa, which is less than the yield strength of the material, and will not cause structural damage. According to the modal analysis, the natural frequency of the threshing drum does not cause resonance phenomenon. The field test of wheat was carried out after the processing of the variable-diameter threshing drum with movable radial plates was installed, and the working performance was compared with that of the ordinary drum. The results showed that the threshing performance was the best when the forward speed was 1 m/s, the grain entrainment loss rate was 0.53%, and the grain un-threshed rate was 0.065%. The grain breakage rate is 0.54%, and the performance is more than 50% higher than that of ordinary rollers. It lays a foundation for the adaptive adjustment of threshing gap in combine harvester.

摘要
针对目前联合收获机脱粒间隙只能调节凹版筛来控制且费时费力，研制了一种通过改变脱粒滚筒直径同心调节脱粒间隙的辐盘移动式变直径脱粒滚筒，同时对脱粒滚筒直径变化对脱粒性能的影响进行了分析。利用机械设计原理对脱粒滚筒进行了所有部件的设计校核，并利用 ANSYS Workbench 对整体结构进行了静力学和模态分析，结果表明，在边界条件下幅盘移动式变直径脱粒滚筒的最大变形量为 0.29 mm，小于脱粒滚筒在使用中允许最大变形量为 3 mm，符合使用要求，变直径脱粒滚筒等效应力最大为 100 MPa，小于材料的屈服强度，不会产生结构的损坏。根据模态分析，脱粒滚筒的固有频率不会造成共振现象，将加工好的辐盘移动式变直径脱粒滚筒安装后进行了小麦的田间试验，并与普通滚筒进行作业性能对比，结果证明，在前进速度为 1 m/s 时，脱粒性能最好。夹带损失率为 0.53%，未脱净率为 0.065%，破损率为 0.54%，性能较普通滚筒相比提升 50%以上。为联合收获机脱粒间隙自适应调节奠定了基础。

INTRODUCTION
In recent years, in order to improve the utilization rate of combine harvesters, combine harvesters that can be suitable for multiple crops by changing the relevant parts and parameters have appeared (*Kang J et al, 2023*) The adjustment of threshing device is an important part, and the threshing device is directly related to the threshing performance (*Deng X. et al, 2022*). Different varieties, different types and different characteristics of crops need different working parameters during harvest, threshing gap is a very important parameter, which affects the grain entrainment loss rate, grain un-threshed rate and crushing rate and other evaluation indicators (*Teng Y et al, 2020*). Therefore, a convenient device to adjust the threshing gap is needed.

For this reason, a platter mobile variable diameter threshing drum was designed, which can change the threshing gap by changing the diameter of the drum, so as to adapt to different kinds of crops in various complex working environments.

Due to the non-uniformity of materials and processing accuracy, the threshing drum is prone to unbalanced problems during operation. At the same time, the threshing drum with high-speed rotation generates excitation frequency in the periodic movement process. If the excitation frequency is similar to the natural frequency, resonance phenomenon will easily occur, which will lead to damage of the threshing drum components in the long run. The threshing performance of combine harvester is affected, so the corresponding analysis should be carried out in the design process of threshing drum to ensure its reliability.

The simulation analysis of mechanical parts in the design process has been widely used. Zhang Jian et al designed the buckwheat threshing device and carried out static and dynamic analysis with ANSYS (*Zhang J. et al, 2019*). Li Yongchun et al. designed a rice spiral drum and carried out modal analysis using ANSYS to avoid resonance (*Li Y et al, 2022*). He Ke et al designed a flexible corn threshing drum, and used ADAMS and Abaqus to carry out dynamic balance analysis, modal analysis and net stress analysis of the threshing drum (*He K. et al, 2018*).

In this paper, a variable-diameter threshing drum with movable radial plates is designed, and SolidWorks is used to model it. Statics and dynamics analysis are carried out by ANSYS Workbench to analyze and check the strength and stiffness of the threshing drum, and the natural frequency and vibration mode are obtained to prevent resonance. It provides a basis for the structural check of the variable diameter threshing drum and a reference for the design of drum components.

MATERIALS AND METHODS

Design of variable-diameter threshing drum with movable radial plates

Influence of cylinder diameter adjustment on threshing performance

The principle of threshing drum mainly includes impact, rubbing, brushing, vibration and rolling (*Kong D. et al, 2020; Liu P. et al, 2020; Ni G. et al, 2019*), through which the grain is removed from the stalk. This time, the variable diameter mobile threshing drum with movable radial plates adopts the nail tooth type, so the main threshing principle depends on the impact force, and the impact force of the threshing drum is mainly determined by the linear speed from the top of the drum.

The formula for the linear velocity of circular motion can be known as:

$$v = \frac{2\pi \cdot r}{T} \tag{1}$$

where:

v is the linear velocity, m/s; r is the radius of the threshing drum, m; T is the time required for the threshing cylinder to turn one circle, s.

It can be seen from the formula that when the speed remains unchanged, the larger the radius, the greater the linear speed, and the greater the impact force on the grain, and vice versa.

Drum structure design

Determination of spindle diameter

As for the spindle of the threshing drum, it is mainly used to transmit torque, and the longer the drum, the more torque it needs to transmit. The threshing drum designed in this paper is based on the Super Ruilong series of Wode Agricultural Machinery, and the length of the drum reaches 2.5 m. Therefore, the minimum diameter of the shaft is roughly estimated based on the torsion strength of the shaft. Therefore, it is necessary to design the spindle into a hollow shaft, and the design of a hollow shaft can save materials and reduce weight while meeting the strength. According to the torsional strength formula of the hollow shaft, the diameter of the main shaft can be obtained as:

$$D \geq A_0 \sqrt[3]{\frac{P}{n(1-\beta^4)}} \tag{2}$$

where:

$\beta = \frac{D_1}{D}$ that is, the ratio of the inner diameter D_1 of the hollow shaft to the outer diameter D, usually β=0.5~0.6

The engine power of the combined harvester is 103 kW, and the power consumption of the threshing drum during operation can account for about 20% to 30% of the engine, so the maximum power transmitted by the threshing drum is about 30.9 kW, and the rotational speed n of the drum is 800 r/min. A_0 is obtained by looking up the table. Bring all the data into equation (2) to obtain the outer diameter of the hollow shaft D≥35.1 mm. According to the mechanical design requirements, if there is a keyway on the same section, the shaft diameter should be increased by 5% to 7%.

However, the above calculation can only be used as a rough calculation, the spindle is not only subject to torque, but also the existence of bending moments during operation, so the bending moment and torque should be considered at the same time. The shaft diameter is calculated according to the bending moment and torque synthesis.

$$d \geq \sqrt[3]{\frac{M_e}{0.1[\sigma_{-1}]}} \quad (3)$$

where: $[\sigma_{-1}]$ is the allowable bending stress (MPa) of the shaft under symmetric cyclic variable stress, and M_e is the equivalent bending moment.

$$M_e = \sqrt{M^2 + (\alpha T)^2} \quad (4)$$

In the formula, $T = \frac{9550P}{n}$, M is the bending moment, and alpha is the conversion coefficient based on the properties of torque, P is the power of the drum, and n is the rotational speed of the drum.

In order to achieve good interchangeability of the combine and facilitate the replacement and disassembly of parts, the main shaft and the main shaft at the feeding end are splined and fastened by bolts to prevent axial movement. All the parts on the spindle can be easily removed, and the hydraulic cylinder is designed to be hollow and directly attached to the spindle. Finally, the total length of the spindle is determined to be 2713 mm. The outer diameter of the spindle is 65 mm and the inner diameter is 45 mm.

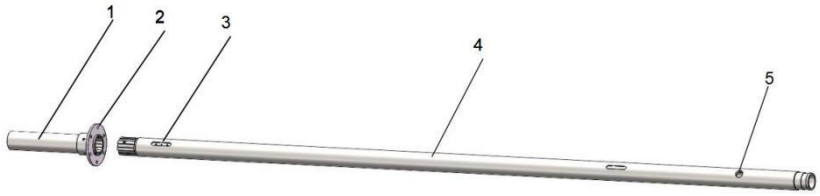

Fig. 1 - Principal axis

1. Spline shaft; 2. Spline shaft flange; 3. Parallel key; 4. Spindle body; 5. Tubing hole

Shaft sleeve design

The movable variable diameter threshing drum realizes the movement of the support plate by installing the support plate on the shaft sleeve. The support plate is welded on the shaft sleeve, the shaft sleeve is covered on the spindle, and the hydraulic cylinder is pushed to realize the forward and backward movement of the support plate, and then the diameter adjustment operation is completed with the mechanism.

The original bushing design is that the size of the inner diameter of the bushing is the same as the size of the outer diameter of the spindle, so that the bushing can be matched with the spindle, so the inner diameter of the bushing is 65 mm, and the outer diameter of the bushing is 71 mm in order to ensure a certain strength. At the same time, the parallel keyway is obtained on both sides, and the installation position of the flange is set aside on both sides to connect with the hydraulic cylinder and the guide rail pusher. According to the size relationship, the shaft sleeve is designed to be 1675 mm.

Later, considering the reasons of friction and processing conditions, the optimization design was further carried out. Because the length of the shaft sleeve design is too long, if the whole shaft sleeve is in contact with the spindle, the friction will be very large, resulting in the hydraulic cylinder thrust requirements being larger, which will lead to the weight of the hydraulic cylinder being increased. Affecting the use of the hydraulic cylinder may also be too large friction resistance, resulting in the hydraulic cylinder in the process of pushing and pulling will damage parts, resulting in the threshing cylinder not being able to be used normally. Another reason is that the shaft sleeve is too long, and the contact with the spindle requires the surface roughness of the inner surface of the shaft sleeve as small as possible, but if the shaft sleeve is too long, the existing tool

cannot bore out the internal hole that meets the requirements, so it was found a way to reduce the contact between the shaft sleeve and the spindle, but also to meet the coordination with the spindle. So, the spindle is designed in sections, divided into the front axle sleeve base, the middle axle sleeve, and the rear axle sleeve base.

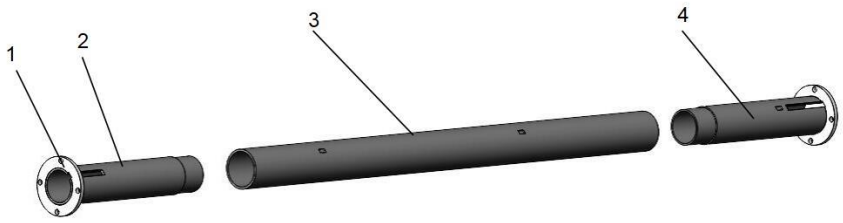

Fig. 2 - Shaft sleeve
1. Flange; 2. Front sleeve base; 3. Middle sleeve; 4. Rear sleeve base

The front and back bushings are still matched with the original scheme with the spindle, so the inner diameter of the front and back bushings is 65 mm, the outer diameter on the step is 72 mm, and the outer diameter under the step is 68 mm. With the sleeve base, the inner diameter of the middle sleeve is 68 mm, and the outer diameter is 76 mm. The convex parts of the front and rear bushing bases are inserted into the middle bushing and then welded to make it a whole. The flange of the front axle sleeve base is connected with the push plate of the guide rail by bolts, and the rear axle sleeve base is connected with the piston rod of the hydraulic cylinder by bolts. The small square hole on the shaft sleeve is the positioning hole for supporting the plate, which determines the welding installation position of the plate.

The overall structure after designing other structures is shown in Figure 3 below.

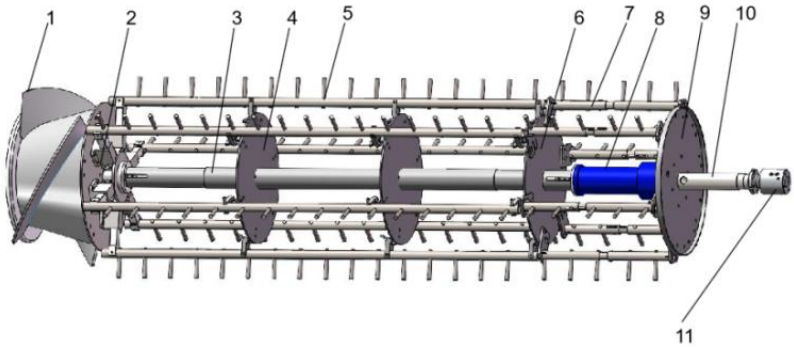

Fig. 3 - Structure diagram of Variable-diameter threshing drum with movable radial plates
1. Feeding wheel; 2. Side plate adjusting mechanism; 3. Shaft sleeve; 4. First middle plate adjusting mechanism; 5. Fixed gear rod; 6. Second intermediate plate adjusting mechanism; 7. Retractable gear rod; 8. Single piston rod hollow hydraulic cylinder; 9. Rear side plate; 10. Spindle; 11. Hydraulic rotary joint

Finite element simulation analysis

To check the rationality and safety of the variable diameter threshing drum designed with movable radial plates and to avoid accidents during use that may affect the harvest and even cause safety problems a simulation analysis has been provide. Therefore, the 3D model established in Solid Works was imported into ANSYS Workbench for statics and modal analysis. Through static analysis and research, the strength and stiffness of the movable variable diameter threshing drum are checked. The modal analysis is used to analyze whether there will be resonance phenomenon in the movable variable diameter threshing drum, which will destroy the structure.

Static analysis

After setting up a movable variable diameter threshing drum in solid works, the 3D model was output in Parasolid format with file suffix x-t after interference check on the model. The model was imported into ANSYS Workbench for static analysis. The operation process of static analysis is mainly divided into three stages: pre-processing, solving and post-processing. The pre-processing is the focus of its operation, which mainly includes the process of creating or importing geometric models, defining parameters, dividing grids, checking grid quality and setting boundary conditions.

Define the material and set the contact

When using ANSYS analysis, the first and important step is to define the properties of the material, only by defining the correct parameters, can you get the simulation results consistent with the actual situation (*Li H et al, 2012*). Material properties have been obtained by consulting relevant literature. In actual production, 45 steel and Q235A steel will be used, (*Yue F et al, 2018*), so the parameters of these two kinds of steel are set, and the details of parameters are shown in Table 1.

Table 1

Material attribute table

Materials	Density (kg/m^3)	Poisson's ratio	Modulus of elasticity	Yield strength (MPa)	Tensile strength (MPa)
45#	7.89 x 10^3	0.269	2.09 x 10^{11}	340	600
Q235A	7.86 x 10^3	0.288	2.12 x 10^{11}	235	390

After the material definition is completed, the Parasolid format model is imported into ANSYS Works2021, and corresponding materials are assigned to each part.

The imported model was divided into 248 geometries. Automatic contact was used and modified according to the actual situation. Binding contact and friction contact were set in total, and the friction coefficient was set at 0.15. A total of 315 connections are set.

Meshing

Grid division is the most important step in the pre-processing of finite element analysis, and the quality of grid division directly affects the accuracy of the simulation results. Because the structure of the movable variable diameter threshing drum is complex and its components are fine, automatic grid division is adopted, and only the size of the grid is set, and the size of the unit is set to 4.00 mm. The rest are default Settings, as shown in Figure 4 (a).

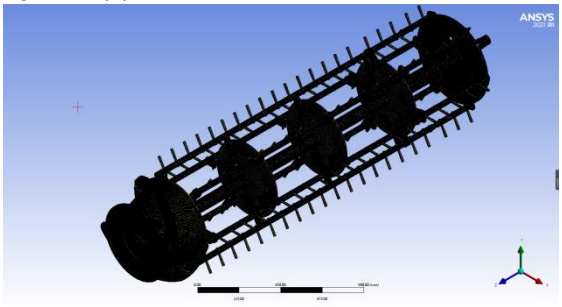

a Meshing situation

Quality	
Checking grid quality	Yes, wrong.
☐ Deflection of target	Default（0.90000）
☐ Target Jacobi ratio	Default（0.04000）
Grid metric	Cell mass
☐ Minimum	0.012003
☐ Maximum	1.
☐ Average	0.82797
☐ Standard deviation	0.10738

b Mesh quality

Fig. 4 - Grid of variable-diameter threshing drum with movable radial plates

The result of grid division is as follows: the number of nodes is 5904704 and the number of cells is 3004536. Open the grid metric as cell quality, and you can see that the minimum mass is 0.012003, the maximum mass is 1, the average mass is 0.82797, and the average mass is greater than 0.7, so the grid quality is good as shown in Figure 4 (b).

Setting of boundary conditions

The boundary conditions set in the finite element analysis are mainly load and constraint. This simulation is based on the idling condition of the threshing drum, and the air resistance and friction between bearings are ignored. Therefore, the boundary conditions of the drum are mainly derived from the limiting displacement of the bearing, the centrifugal force of the threshing tooth rod, the torque transmitted by the engine to the exiting drum and its own gravity (*Chen L. et al, 2023*).

The calculation formula of torque is:

$$T = \frac{9550P}{n} \tag{5}$$

where:

P is power, kW; n is the speed, r/min; T is the torque N/m.

The centrifugal force is calculated as follows:

$$F = ma = 4\pi^2 mn^2 r \tag{6}$$

where:

F is the centrifugal force and N; m is the mass of the tooth rod, kg; r indicates the distance between the center of mass of the tooth rod and the center of rotation of the drum.

According to the formula, the torque added to the drum is 246067 N.mm, the centrifugal force on the ordinary tooth rod is 10261.2 N, and the centrifugal force acting on the telescopic tooth rod is 3958.37 N. The boundary condition settings are shown in Figure 5. Centrifugal force is B, C, D, F, G, H, I, J.

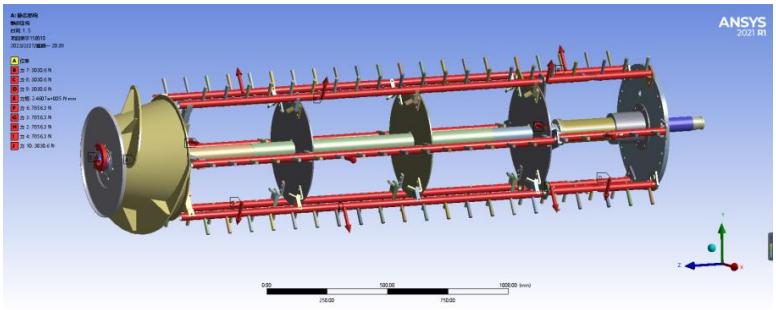

Fig. 5 - Boundary condition setting

Kinetic analysis

For the Variable-diameter threshing drum with movable radial plates, modal analysis is divided into two kinds, one is without prestress, that is, the drum is in a free state, not subject to any constraints and forces, and the actual situation is too big, the result is not of reference value, so choose the condition with prestress for simulation, that is, the application of boundary conditions. Under normal circumstances, the low-order frequency has a greater impact on the structure and is easy to destroy the structure. In order to make the simulation more realistic and better test the reliability of the design, under the above constraints, the lateral resistance of each tooth rod is increased to simulate the resistance of crops to the threshing tooth rod during the threshing process. Considering that the object has 6 degrees of freedom in the free state, the first 6 orders of the variable diameter threshing drum are mainly studied.

Field trial

After the preliminary design and finite element analysis, the Variable-diameter threshing drum with movable radial plates was processed and installed in the field test of the Wode Super Ryzen combine. At the same time, the working quality was compared with that of ordinary rollers. A field test of wheat was carried out in Danyang, Jiangsu Province, in June 2023. Before the test, oilcloth was bundled to the straw outlet of the combine to collect the outfall, and a 20-meter-long test area was marked with a marker. After the test, the grain entrainment loss rate and the Grain un-threshed rate were calculated by selecting the entrainment loss kernel and the unstripped kernel. The grain unloading in the grain box was weighed and the grain crushing rate was measured by random sampling. Each group of tests was repeated three times, and the performance indexes were averaged (*Yang L. et al, 2018; Li Y. et al, 2016*).

Fig. 6 - Wheat field trial

According to the national standard GB/T 5262-2008 "General Provisions for the Determination of Agricultural machinery test conditions" and GB/T 8097-2008 "Test Methods for Harvesting machinery Combine Harvester" relevant provisions for harvesting machinery test, the crop weight W(kg/m^2) per unit area was calculated in the field in a 1 m^2 square area according to the five-point sampling method before the test. Thus, the relationship between the traveling speed and the feeding amount is calculated:

$$q = B \cdot V_m \cdot W \tag{7}$$

where: q is the total feeding amount per unit time, kg/s; B is the working width of the combine harvester, m;

V_m is the working speed of the combine, m/s.

Therefore, in order to obtain different feeding amounts in the test, it can be achieved by changing the working speed of the combine. According to NY/T 995-2006 "Operation Quality of Grain (Wheat) Combined Harvesting Machinery", the evaluation indexes of threshing performance are grain entrainment loss rate, grain un-threshed rate and crushing rate. The test results of different harvesting speeds were obtained by weighing each group of samples through the test of the variable-diameter threshing drum with movable radial plates and the ordinary nail tooth drum.

RESULTS

Result of finite element analysis

Results of static analysis

The distribution of deformation, stress and strain is checked. As shown in Figure 7, the maximum deformation of the variable-diameter threshing drum with movable radial plates is 0.29 mm under the above boundary. According to the existing data, the maximum allowable deformation of the threshing drum in use is 3 mm, so this design is far less than 3 mm and meets the application requirements. The maximum equivalent stress of the variable diameter threshing drum is 100 MPa, which is less than the yield strength of the material, and will not cause structural damage.

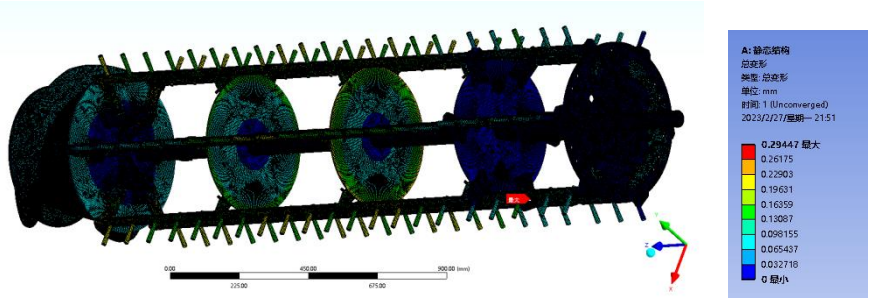

a Deformation

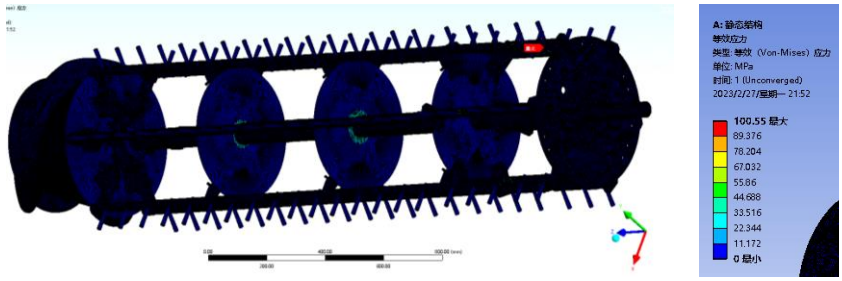

b Equivalent stress

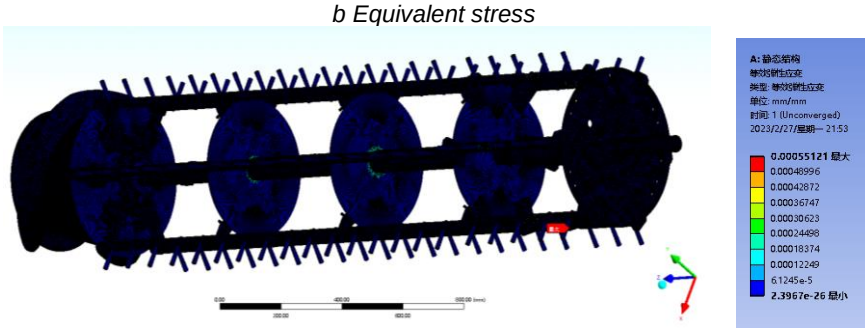

c Equivalent elastic strain

Fig. 7 - Static simulation results

Modal analysis results

The obtained natural frequencies and modes of the first six orders are shown in Table 2.

Table 2

The first six modal frequencies and modes of a variable-diameter threshing cylinder

Rank	Natural frequency	Maximum deformation	Mode description
1	41.131	8.6007 mm	The overall distortion of the drum, the bending of the threshing tooth rod in the -Y direction
2	89.876	7.1552 mm	The whole twist of the roller
3	101.46	4.4572 mm	The bend of the drum in the -Z direction, especially the plate
4	117	7.7289 mm	The bending twist of the drum in the +Y direction
5	123.21	9.6035 mm	The overall bend of the cylinder in the +Y direction

6	130.69	10.524 mm	The bending deformation of the whole cylinder along the +X direction

The modal analysis was carried out on the first six stages of the variable-diameter threshing drum with movable radial plates, and the deformation of each mode was briefly described. Figure 8 is the modal figure of the first six modes.

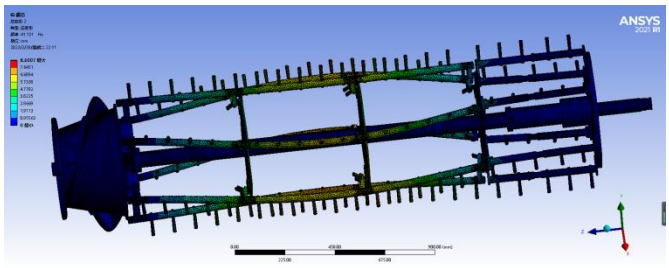

a) First mode pattern diagram

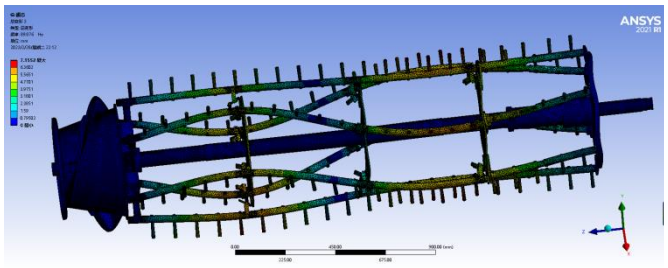

b) Second order mode pattern diagram

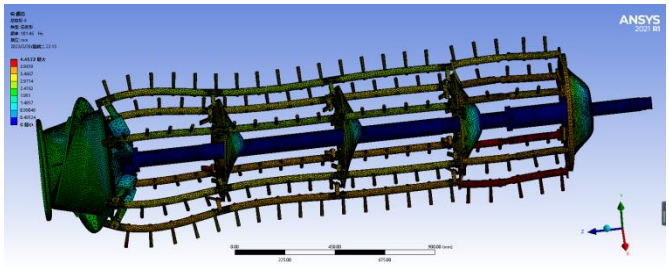

c) Third order mode pattern diagram

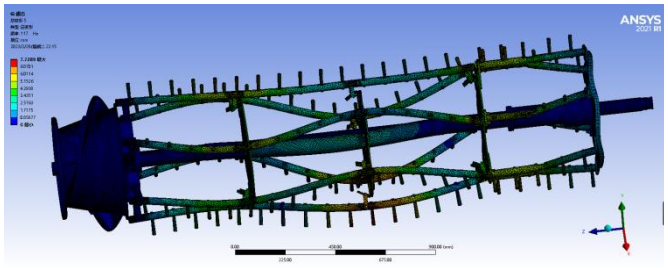

d) The fourth mode pattern diagram

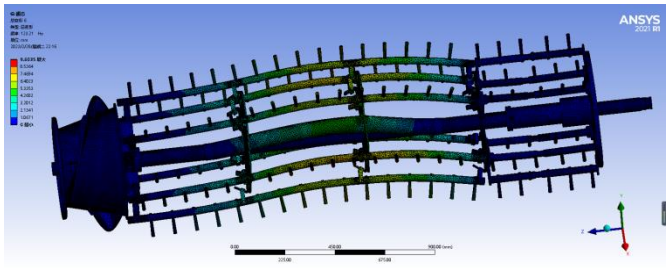

e) The fifth mode pattern diagram

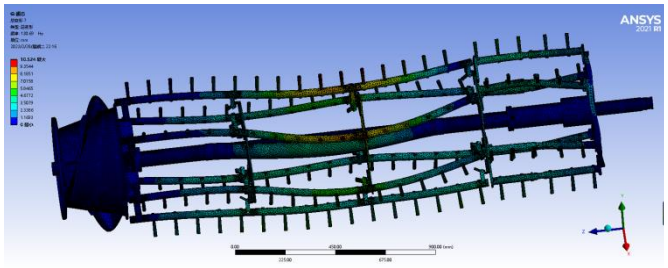

f) Sixth order mode pattern diagram

Fig. 8 - Figure of the first six modes

As can be seen from Table 2 and Figure 8, the first six deformations are mainly bending and twisting. Generally speaking, the first mode has the largest energy and is most likely to cause structural damage. The general conclusion is that the external excitation frequency should be less than 75% of the first-order natural frequency, otherwise it will be dangerous. The natural frequency of the first mode is 41.131, and 75% of it is 30.84825. Then it can be calculated according to the calculation formula of the external excitation frequency:

$$f = \frac{n}{60} \tag{8}$$

where: n is the rotational speed of the drum; f is the excitation frequency

The rotating speed of the roller in this design is 700~900 r/min, and the range of f obtained is 11.67~15, which is less than 75% of the natural frequency of the first order mode, so it meets the safety requirements, and the design avoids the structural damage caused by resonance.

Field test results

Field test results are shown in Table 3.

Table 3

Field test results

Rate of harvest (m/s)	Type of drum	Grain entrainment loss rate (%)	Grain un-threshed rate (%)	Percentage of breakage (%)
0.6	Variable-diameter threshing drum with movable radial plates	0.98	0.124	0.98
	Plain drum	2.16	0.45	2.13
0.8	Variable-diameter threshing drum with movable radial plates	0.76	0.108	0.67

Rate of harvest (m/s)	Type of drum	Grain entrainment loss rate (%)	Grain un-threshed rate (%)	Percentage of breakage (%)
	Plain drum	1.86	0.32	1.86
1.0	Variable-diameter threshing drum with movable radial plates	0.53	0.065	0.54
	Plain drum	1.56	0.24	1.54
1.2	Variable-diameter threshing drum with movable radial plates	0.87	0.098	0.76
	Plain drum	1.79	0.43	1.62
1.4	Variable-diameter threshing drum with movable radial plates	1.13	0.153	0.87
	Plain drum	2.31	0.67	1.93

After data processing of the test results in Table 3, line charts of the effects of two drum harvesting speeds on grain entrainment loss rate, grain un-threshed rate and crushing rate were drawn, as shown in Fig. 9-11.

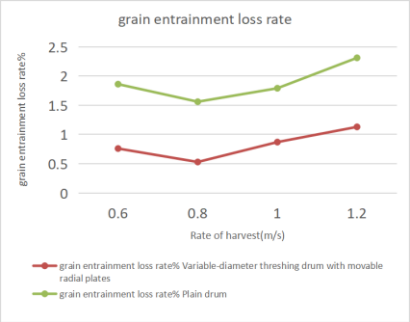

Fig. 9 - Effect of harvest speed on grain entrainment loss rate

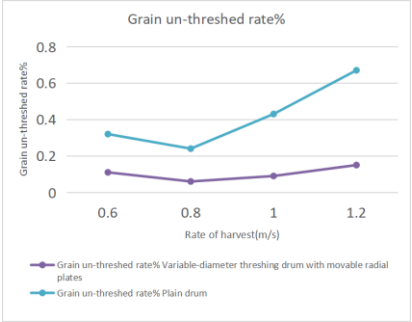

Fig. 10 - Effect of harvest speed on grain un-threshed rate

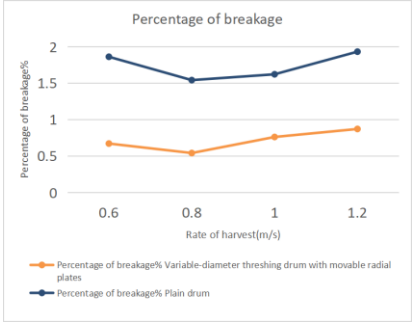

Fig. 11 - Effect of harvest speed on Grain breakage rate

As can be seen from Fig. 9, the loss rate of the variable diameter threshing drum decreases first and then increases, and the grain entrainment loss rate is in the range of 0.53% ~ 1.13% when the harvesting speed keeps increasing. Under the condition of increasing harvest speed, the grain entrainment loss rate decreases first and then increases, and the loss rate is in the range of 1.56% ~ 2.31%. From the broken line, the grain entrainment loss rate of the variable diameter threshing drum is smaller than that of the ordinary nail tooth drum.

As can be seen from Figures 10 and 11, the grain un-threshed rate and the grain breakage rate also decrease first and then increase with the increase of the advancing speed of the harvester, and the data of the variable-diameter threshing drum is better than that of the ordinary drum, which is in line with the national design standards.

To sum up, the threshing performance of the variable-diameter threshing drum with movable radial plates is generally better than that of the ordinary threshing drum. In the test process, the structure is reliable, there is no accident, and the reliability is high.

CONCLUSIONS

(1) The relationship between threshing performance and the diameter of the threshing drum was studied, and based on the principle of changing the diameter of the threshing drum, a variable-diameter threshing drum with movable radial plates was designed, which could realize the real-time adjustment of the threshing gap during the operation of the threshing drum to achieve the best threshing performance.

(2) Based on the variable-diameter threshing drum with movable radial plates, static and modal analysis were carried out by ANSYS Workbench to verify the strength and stiffness of the structure and ensure that the deformation under maximum stress meets the requirements. The maximum deformation is 0.29 mm, which meets the requirements of use. The first six natural frequencies were obtained through modal analysis to prevent resonance and ensure the reliability and safety of the design.

(3) The designed variable diameter threshing drum was processed and installed for wheat field test, and the operation effect was compared with that of ordinary threshing drum. The forward speed of the combine was taken as the influencing factor, when the forward speed is 1 m/s, the threshing performance is the best, the grain entrainment loss rate is 0.53%, the grain un-threshed rate is 0.065%, and the damage rate is 0.54%. The performance is more than 50% higher than that of the ordinary drum.

ACKNOWLEDGEMENT

I mainly completed the design of experiments and the writing of papers, Yaoming Li provided funding, and others provided trial assistance. The source of the project is the National Natural Science Foundation of China: "Research on Adaptive control Method of Variable diameter Roller and Threshing Device of Rice Combine Harvester" project No. 51975257.

REFERENCES

[1] Chen L., Li Y, Su Z., Liu Y., Yin Q. (2023). Design and test of a threshing cylinder with single motion and variable diameter of tooth bar (一种齿杆单动变直径脱粒滚筒的设计与试验) *Agricultural mechanization research* (05), 43-48. Doi: 10.13427 / j.carol carroll nki njyi. 2023.05.008.

[2] Deng X., Zhang T., Tang X., Pang Y., Ye F., Lin T., Luo S. (2022). Design and experiment of 4LZ-2.4S hand-held mung bean combine harvester (4LZ-2.4S 型手扶式绿豆联合收获机的设计与试验） Agricultural mechanization research (10), 43-51. Doi: 10.13427 / j.carol carroll nki njyi. 2022.10.010.

[3] He K., Wang Q., Geng D., Jin C., Zhu J., Zhang M. (2018). Simulation analysis of corn flexible threshing drum. Journal of Chinese agricultural mechanization （玉米柔性脱粒滚筒仿真分析）(07), 53-58. Doi: 10.13733 / j.j CAM. Issn 2095-5553.2018.07.011.

[4] Kong D.D., Lu H.C., Hu X. (2020). Development status and trend of semi-feeding rice combine harvester in China（我国半喂入式水稻联合收割机发展现状与趋势） *Times Agricultural Machinery*. (05), 19-21.

[5] Kang J., Wang X., Xie F., Luo Y, Li Q., Huang X. (2023). Performance test and analysis of differential threshing roller adapted to different maturity of soybean (适应不同成熟度大豆的差速脱粒滚筒性能试验与分析) *Chinese Journal of Agricultural Engineering.* (01), 38-49.

[6] Li.H. (2012). *Dynamic pillar type double spindle gantry CNC drilling machine design and finite element analysis* (动柱式双主轴龙门数控钻床设计及其有限元分析）(master's degree thesis, Nanjing Agricultural University).

[7] Li Y., Wang H., Wang Y., Yang M., Wang H., Liu X. (2022). Design and experiment of spiral drum for rice combine harvester（水稻联合收割机螺旋滚筒设计与试验） *Agricultural mechanization research* (09), 121-128. DOI: 10.13427 / j.carol carroll nki njyi. 2022.09.012.

[8] Li Y.M., Chen Y., Xu L.Z. & Li L. (2016). Optimization of structural parameters of threshing and separating device of inclined cut longitudinal combine （大豆机收清选筛田间性能试验与分析） *Chinese Journal of Agricultural Machinery* (09), 56-61.

[9] Liu P., Jin C., Ning X., Ni Y., Wang T., Yin X. (2020). Field performance test and analysis of soybean harvester cleaning screen（大豆机收清选筛田间性能试验与分析 ） *Chinese Journal of Agricultural Engineering.* (09), 36-43. https://kns.cnki.net/KCMS/detail/detail.aspx?dbname=CMFD201401&filena me=1013284993.nh

[10] Ministry of Agriculture of the People's Republic of China (2008). GB/T 5262-2008（农业机械试验条件测定方法的一般规定） *General Administration of Quality Supervision, Inspection and Quarantine of the People's Republic of China*; Standardization Administration of China.

[11] Ni G., Qin Y., Han K., Hou X., Zhang X. (2019). Ideas and technical ways to improve the profit of rice harvester operation. *Agricultural Equipment and Vehicle Engineering.* (S1), 71-73.

[12] Teng Y., Jin C., Chen Y., Liu P., Yin X., Wang T., Yu K. (2020). Design and optimization of segmented threshing device for rice and wheat combine（稻麦联合收获机分段式脱粒装置设计与优化） *Chinese Journal of Agricultural Engineering*. (12), 1-12.

[13] Yue F., Luo X., Ma F., Tang S., Jiang Y., Li H. (2018). Structure design and research of cylindrical backwashing filter for micro-irrigation（微灌用筒式反冲洗过滤器结构设计与研究） *Jiangsu Agricultural Sciences* (24), 248-251. doi:10.15889/j.issn.1002-1302.2018.24.068.

[14] Yang L., Wang W., Zhang H., Li L., Wang M., Hou M. (2018). Improved design and bench test of tangential flow - transverse axial flow corn threshing system（切流-横轴流玉米脱粒系统改进设计及台架试验） *Chinese Journal of Agricultural Engineering.* (01), 35-43.

[15] Zhang J., Gan P., Guan W.W. (2019). Design and finite element analysis of buckwheat threshing device（荞麦脱粒装置的设计及有限元分析） *Journal of Chinese agricultural mechanization* (07), 7 to 12. Doi: 10.13733 / j.j CAM. Issn 2095-5553.2019.07.02.

IMPROVING PERFORMANCE OF COLD ROOM REFRIGERATION SYSTEM BY DESUPERHEATING ENERGY RECOVERY USING PCMs
/
ÎMBUNĂTĂȚIREA PERFORMANȚEI UNUI SISTEM FRIGORIFIC (IFV) CE ECHIPEAZA O CAMERA FRIGORIFICA, PRIN RECUPERAREA ENERGIEI DIN PROCESUL DE DESUPRAINCALZIRE CU AJUTORUL PCM-urilor

Jamal AL DOURI[1,2)], Valentin APOSTOL[1)], Horatiu POP[1*)], Tudor PRISECARU[1)], Cornel Constantin PAVEL[1*)], Iulian UTA[1)], Claudia IONITA[1)]

[1)]Faculty of Mechanical Engineering and Mechatronics, National University of Science and Technology Politehnica of Bucharest / Romania

[2)]University of Technology / Iraq

Tel: +40744903488; E-mail: horatiu.pop@upb.ro

E-mail: cornel.pavel@stud.mec.upb.ro

Corresponding authors: Horaţiu POP; Cornel Constantin PAVEL

DOI: https://doi.org/10.35633/inmateh-70-53

Keywords: *vapour compression refrigeration, phase change material, evaporator, defrosting, thermal energy storage*

ABSTRACT

The paper aims to investigate how to improve the performance of a refrigeration system (Rs) that equips a cold room, by incorporating phase change materials (Phase Change Materials - PCMs) in these systems, a study that has not yet been extended experimentally. The study is carried out on a cold room within the National University of Science and Technology Politehnica Bucharest - Faculty of Mechanical and Mechatronics Engineering, Department of Thermodynamics, Engines, Thermal and Refrigeration Equipment.

This room is equipped with a refrigeration system with mechanical vapour compression (VCRs), which uses R404A as refrigerant. Mechanical vapour compression refrigeration system (VCRs) with an evaporation temperature below 0°C causes ice to form on the evaporator leading to reduced performance. Currently, the widely used methods for defrosting are the standard methods, the most used being the electric one, which of course consumes energy. This paper aims to evaluate the availability of heat that could be used in the defrosting process by means of PCMs. The study was made using the Engineering Equation Solver software, several types of PCMs and also different refrigerants (R600a, R600, R1234yf, R1234ze, R152a, R290, R32) and in this way it was intended to identify the right agent to be used for a particular type of PCM.

REZUMAT

Lucrarea investighează modul de îmbunătățire a performanței unei instalații frigorifice (IFV) ce echipează o camera frigorifica, prin încorporarea materialelor cu schimbare de fază (Phase Change Materials - PCM-uri) în aceste sisteme, studiu care nu a fost încă extins experimental. Studiul se realizează pe o cameră frigorifică din cadrul Universității Naționale de Știință și Tehnologie Politehnica București – Facultatea de Inginerie Mecanică si Mecatronica, Departamentul de Termotehnica, Motoare, Echipamente Termice și Frigorifice. Această camera este echipată cu o instalație frigorifică cu comprimare mecanică de vapori (IFV), ce folosește ca agent frigorific R404A. Sistemul frigorific cu comprimare mecanică de vapori (IFV), cu o temperatura de vaporizare mai mică de 0°C, determină depunerea de gheață la vaporizator care conduce la reducerea performanței acestuia. În prezent, metodele utilizate pe scară largă pentru degivrare sunt metodele standard, cea mai utilizata fiind cea electrica, care consuma bineînțeles energie. Lucrarea își propune să evalueze disponibilitatea de căldură ce ar putea fi utilizată în procesul de degivrare cu ajutorul PCM-urilor. Studiul s-a făcut cu ajutorul software-ului Engineering Equation Solver, folosind mai multe tipuri de PCM-uri și de asemenea diferiți agenți frigorifici (R600a, R600, R1234yf, R1234ze, R152a, R290, R32) și in acest mod se dorește a se identifica agentul potrivita fi utilizat pentru un anumit tip de PCM.

INTRODUCTION

In order to provide the consumer with quality products, food systems must use rapid cooling and cold storage technology. Over the past thirty years, the number of farms has increased, so energy efficient cold storage units have been needed. Cold storage is essential for vegetable farmers to preserve product quality.

Cold storage is an essential component in the food supply chain. Without rapid cooling and proper storage conditions, products deteriorate quickly. Nutritional losses and even damage to entire crops can occur. Initial rapid cooling to extract latent field heat extends shelf life and maintains product quality *(Kraemer et al., 2020)*.

Artificial cold is used in the food industry, for cooling and freezing food products, using temperatures up to -40°C, and for freeze-drying processes, drying products by freezing and sublimating ice in vacuum are carried out using temperatures from -40° C to -80°C.

There are several methods of cold processing of food products, among which the following were mentioned: refrigeration, i.e. rapid cooling to temperatures of 0...5°C, is a method aimed at rapid cooling of food products to final temperatures above the freezing point and freezing, i.e. cooling to the final temperature of -18... -25°C, with water hardening of the products in a proportion of over 95%; it is a method by which the food product is cooled to a final temperature well below the freezing point.

According to the above, there are two types of cold rooms, namely: refrigeration and freezing.

Refrigeration cold rooms are generally intended for the storage of medicines, wine, food, flowers, etc. The thickness of the panels used in their construction is between 60 mm and 100 mm. The temperature obtained inside will be maintained between +14°C and -25°C, depending on the customer's wishes.

Freezing cold rooms are intended, in general, for freezing products (meat, fish, etc.). This time, the thickness of the panels used will be greater, namely between 80 mm and 120 mm. The temperature obtained will be maintained between -25°C and will reach up to -40°C. The cooling and freezing time of the products can vary between 2 and 24 hours *(Horbaniuc B., 2006).*

If the refrigeration system () that equips the cold room operates at an evaporation temperature below 0ºC, ice is deposited on the evaporator and defrosting is required. Defrosting the evaporators is a necessary operation in the case of refrigeration systems used to freeze food products because the ice or snow that is deposited on the heat transfer surface of the batteries acts as a thermal insulator and thus reduces the free area for air circulation and reduces the performance of the system *(Qu et al., 2012)*.

Several classic defrosting procedures can be applied: *hot air defrosting* is used in rooms with positive temperatures or in the case of heat pump evaporators; *electric defrosting* process is used in rooms with negative temperatures; *reverse-cycle defrosting* can be used if the evaporator and the condenser are made up of pipes equipped with fins, by reversing the cycle, the evaporator becomes a condenser, and the condenser becomes an evaporator; *hot gas defrosting* – a process in which the evaporator is fed with hot vapours coming directly from the cooling system of the compressor while the rest of the installation works normally; *water defrosting* consists of spraying with water the evaporator loaded with ice *(Al Douri et al., 2021)*.

In current research, a new defrosting method using PCMs (Phase Change Materials) is noted. PCMs are materials that can absorb and release large amounts of energy when they change from one phase to another, such as from solid to liquid or vice versa. The PCMs have high thermal energy storage capacity and have the ability to release and absorb a large amount of energy at a constant temperature *(Regin et al., 2008).*

Also, there are several different ways to improve the efficiency of refrigeration system by using phase change materials like, advanced insulation, improve heat exchangers, and defrost mechanisms.

In 2018, researchers studied experimentally the effect of adding water as PCMs in the evaporator for the domestic refrigeration system, the experimental results showed that using three fins of PCM would reduce the energy consumption of the compressor by 17.4% per day *(Zarajabad at al., 2018).*

Other researchers investigated the effect of adding a slab with 5mm thickness eutectic aqueous solution as a PCM on the back between the evaporator and the insulation on the energy efficiency of the refrigerator, resulting in improved conduction heat transfer from the evaporator to the PCM and an increase in the coefficient of performance by 5-15%, and a decrease in the off and on number of the compressor which leads to the stability temperature in the room of the refrigerator *(Azzouz et al., 2008)*.

In another paper, the authors studied the enhance of a household refrigerator using PCMs with nanoparticle for increasing the thermal conductivity at the condenser, the results show that the consumption of energy was decreased by 13.06% and around 18% by using PCMs with nanoparticle *(Kumar et al.,2020).* Also, researchers investigated the effect of adding a slab of 5mm thickness from PCM to the evaporator and compared it to the evaporator without PCM. The results show an increase in the coefficient of performance of 10-30% compared to the evaporator without PCM *(Azzouz et al., 2009).*

The modern household refrigerator was studied by incorporating PCM into the structure of heat storage condensers, the results show a decrease in condensation temperature and a rise in evaporator temperature, resulting in a 12% increase in energy efficiency *(Cheng et al, 2011).*

Khan at al., (2015), investigated the effect of adding PCM behind the evaporator coil on the compressor on-off cycle for household refrigeration systems, and the results show that the number of compressor on-off cycles is about 3-5 times lower than that of the system without PCM, and the average compressor running time is reduced by 5-30% with PCM compared to without PCM.

Other researchers used four different types of PCM in the evaporator for two different refrigerator models to demonstrate the effect of adding PCM in the refrigeration system. The results show that for all PCMs, the temperature of the evaporator and condenser was increased by 2°C to 4°C, the off-on time of the compressor was improved, for refrigerator 1 using 1.8 kg of PCM resulted in an 8.8% energy savings, and for refrigerator 2 using 0.95 kg of PCM resulted in a 9.4% energy savings *(Yusufoglu et al., 2015)*.

Rahman et al., (2013), investigated the effect of adding PCM to the evaporator of a household refrigeration system and compared the systems with and without PCM. The results show that the system with PCM increases the COP (coefficient of performance) by 55-60% over the non-PCM and that in both cases, with and without PCM, the COP increases as the thermal load decreases and decreases as the thermal load increases.

The effect of adding PCM in the evaporator and paraffin as PCM in the condenser was then investigated for three types of household energy storage refrigeration systems: CSE refrigerator, DES refrigerator, and HSC refrigerator, and found that the DES refrigerator has the best economy energy, performance of up to 32%, which is higher than the total (28%) of the other two types of household refrigeration systems with energy storage *(Cheng et al., 2017)*.

In another article, it was studied the effect of adding a heat exchanger containing N-Octadecane as PCM before and after the condenser to compare the COP of the refrigerator with and without PCM, and the results show that using PCM in the household refrigeration cycle improves the convection process and results in a 9.58% increase in the household's performance coefficient *(Bakhshipour et al., 2017)*.

Other researchers analysed the experimental effect of adding a PCM heat exchanger in the evaporator to improve the efficiency of residential refrigeration systems; the results show that power consumption is decreased by 12% and COP is raised by 8% when compared to the refrigerator without PCM *(Elarem et al., 2017)*. Other authors investigated the effect of installing a PCM at three positions in the refrigeration system: before and after the compressor and after the condenser; the results show the efficiency improved by 6-8% *(Wang et al., 2007)*.

In another study, the researchers evaluated the performance of adding PCM to the frost-free household refrigeration system and compare it to the system without PCM; the results show that the energy consumption of the household refrigeration with PCM decreased by 18.6% and the compressor on-off time decreased by 13.6% compared with household refrigeration without PCM *(Liu et al., 2017)*.

In another paper, the authors studied experimentally the adding of PCM into the wall of a household refrigeration system; the experiments showed that the temperature of the air inside remained constant for 7h at –8◦C, resulting a decrease in the energy consumption by 30% to 54% *(Gin et al., 2011).*

In a new research paper, the effect of additional PCM in the condenser of the domestic refrigeration system was investigated experimentally, and the results showed that the energy consumption was reduced by 15%, and the COP of the refrigerator improved by 28% when compared to the system without PCM *(Dandotiya et al., 2017)*.

MATERIALS AND METHODS

System description

The cold room on which the study is carried out is a container mounted inside the CG 004 room, within the National University of Science and Technology Politehnica Bucharest - Faculty of Mechanical and Mechatronics Engineering, Department of Thermodynamics, Engines, Thermal and Refrigeration Equipment, this room having the role of keeping various food products at refrigeration or freezing temperatures.

The characteristics of the cold room are presented in Table 1. The cold room is complete and is made up of high-density heat-insulating panels and is equipped with a refrigerating unit with high energy efficiency, automation panel, door, and other accessories necessary for the proper functioning.

Table 1

Cold room characteristics

Dimensions	Length	Width	Height
External dimensions [m]	1.43	1.43	1.43
Internal dimensions [m]	1.2	1.2	1.2
Thickness of the walls and floor [m]		0.115	
Useful volume [m^3]		1.728	

Fig. 1 - Overview image of the experimental setup

The system (VCRs), in addition to the compressor, condenser, lamination valve and evaporator, also includes a heat exchanger (PCM-refrigerant discharged by the compressor), thermal energy storage through phase change. This thermal energy could be used externally for domestic water heating or within the scheme (inside) for evaporator defrosting. During defrosting, this thermal energy can be calculated (evaluated) because the equivalent of ice deposited on the evaporator (measured experimentally) that can be melted with this thermal energy is known. The installation works for 4 hours and during this time an amount of ice is collected, which is to be melted using an amount of PCM, then in 20 minutes the defrosting takes place. One of the major advantages of using PCMs in VCRs is their ability to reduce power consumption. Thus, energy consumption can be reduced if PCMs are used for defrosting. The potential use of PCMs in increasing the energy savings and COP of VCRs has also been highlighted in various scientific papers.

In the experiment there are five kinds of PCMs: RT 54 HC; SP 50; RT 44 HC; RT 35 HC and SP 31.

The properties of the PCMs used are presented in Table 2.

Table 2

PCMs properties

Property	SP 31	RT 35 HC	RT 44 HC	RT 54 HC	SP 50
Melting temperature [^oC]	31-33	34-36	41-44	53-54	50-51
Solidification temperature [^oC]	28-30	36-34	44-40	54-53	47-48
Heat storage capacity [kJ/kg]	210	240	250	200	220
Specific heat capacity [kJ/(kg·K)]	2	2	2	2	2
Density solid (at 20°C) [kg/m^3]	1.35	0.88	41-44	0.85	1.4
Density liquid (at 60°C) [kg/m^3]	1.3	0.77	44-40	0.8	1.3
Heat conductivity [W/(m·K)]	0.5	0.2	0.2	0.2	0.6

Sources: *https://www.rubitherm.eu/en/productcategory/organische-pcm-rt*
https://www.rubitherm.eu/en/productcategory/anorganische-pcm-sp

VCRS characteristics

The diagram and operating cycle of the refrigeration system are presented in Fig. 2 (a) and (b) respectively.

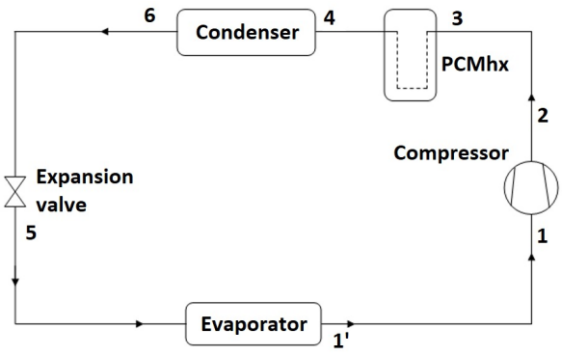

Fig. 2 - Schematic view of the refrigeration system with PCM

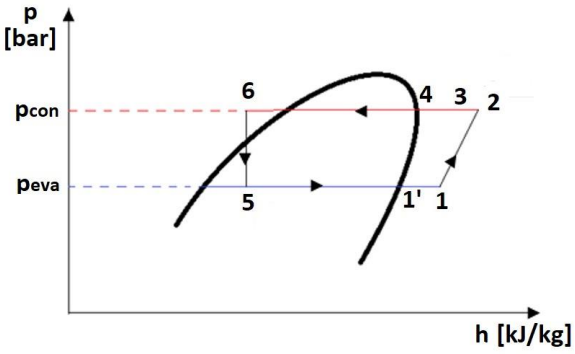

Fig. 3 - Thermodynamic cycle of the VCRS

Mathematical model

The evaporative pressure $p_{eva.}$ [bar], the condensing pressure $p_{con.}$[bar], overheating degree Δt_{sh} [°C] are determined experimentally. With these values, the following thermodynamic states of the refrigerant can be determined, in connection with Fig.3.

$$\begin{aligned}
&State\ 1' \rightarrow p_{eva.}\ \Pi\ x=1 \rightarrow t_{1'};\ h_{1'};\ v_{1'};\ s_{1'}\\
&State\ 1 \rightarrow p_{eva}\ \Pi\ (t_1=t_{1'}+\Delta t_{sh}) \rightarrow h_1;\ v_1;\ s_1\\
&State\ 2 \rightarrow p_{con}\ \Pi\ (s_1=s_2) \rightarrow t_2;\ h_2;\ v_2\\
&State\ 3 \rightarrow p_{con}\ \Pi\ (t_3=t_4+5) \rightarrow h_3;\ v_3;\ s_3\\
&State\ 4 \rightarrow p_{con}\ \Pi\ x=1 \rightarrow t_4;\ h_4;\ v_4;\ s_4\\
&State\ 6 \rightarrow p_{con}\ \Pi\ x=0 \rightarrow t_6;\ h_6;\ v_6;\ s_6\\
&State\ 5 \rightarrow p_{eva}\ \Pi\ (h_5=h_6) \rightarrow t_5;\ v_5;\ s_5
\end{aligned} \quad (1)$$

where:

p_{eva} is the evaporator pressure [bar]; x is the quality of refrigerant [-]; t is the temperature [°C]; h is the specific enthalpy [kJ/ kg]; s is the specific entropy [kJ/ (kg·K)]; v is the specific volume [m³/ kg].

The heat flux recovered with the PCM, $\dot{Q}_{recovery}$ is determined with the relation:

$$\dot{Q}_{recovery} = \dot{m} \cdot (h_2 - h_3) \quad (2)$$

where: $\dot{m}$ is the refrigerant flow rate [kg/s];

h_2 - the enthalpy of the refrigerant on state 2 [kJ/kg];

h_3 - the enthalpy of the refrigerant on state 3 [kJ/kg].

The heat required to melt the amount of PCM in four hours of operation, $\dot{Q}_{2-3}$ [W] is:

$$\dot{Q}_{2-3} = m_{PCM} \cdot \frac{\lambda_{PCM}}{\tau_{melting}} \quad (3)$$

where: m_{PCM} [kg] is the PCM mass required and results from an energy balance with the experimental measurement of the amount of ice deposited during the four hours of system operation, between two consecutive defrosts; λ_{PCM} [kJ/kg] the heat storage capacity, and $\tau_{melting}$ is the melting time [s].

In order to melt the respective PCM in 4 hours, the condition must be imposed that the heat flow recovered with the help of the PCM is equal to the heat flow required for melting the PCM, i.e. $\dot{Q}_{recovery} = \dot{Q}_{2-3}$. If $\dot{Q}_{recovery} > \dot{Q}_{2-3}$ the melting time of the PCM decreases.

Based on the mathematical model presented before, a program has been developed in Engineering Equation Solver software.

RESULTS

Following the numerical simulation for each type of PCM, but also for all refrigerants used, the results obtained are presented in Tables 3 and 4.

- For PCM type SP 31 the conditions that must be met and check are:
  1) The temperatures must be: t_3 > t_4 (condition met)
     Temperature t_3=t_4 + 5
     So, t_3=46.58 °C
  2) t_3 > $t_{melting}$ (condition met)
     $t_{melting}$ =33 °C for SP 31

The values for the melting temperature of the PCM, $t_{melting}$, are shown in Table 2, line 1.

Table 3

The parameters of the VCR system for PCM - SP 31

Den. no.	Property	t_2 [°C]	t_3 [°C]	t_4 [°C]	$\dot{m}$ [kg/s]	$\dot{Q}_{recovery}$ [kW]	m_{PCM} [kg]
1.	R 404 A	60.12	46,58	41.58	0.0087	0.1538	3.147
2.	R 600 a	49.63	46.58	41.58	0.00109	0.0065	3.147
3.	R600	50.94	46.58	41.58	0.00063	0.0054	3.147
4.	R1234yf	48.82	46.58	41.58	0.0047	0.01232	3.147
5.	R1234ze	50.73	46.58	41.58	0.00284	0.0126	3.147
6.	R 152 a	77.97	46.58	41.58	0.00207	0.08913	3.147
7.	R 290	61.91	46.58	41.58	0.00324	0.1105	3.147
8.	R 32	116.8	46.58	41.58	0.00629	0.5919	3.147
9.	R450a	56.38	46.58	41.58	0.03178	0.03315	3.147

- For PCM type RT 35 HC the conditions that must be met and check are:
  1) The temperatures must: t_3 > t_4 (condition met)
     Temperature t_3=t_4 + 5
     So, t_3=46.58 °C
  2) t_3 > $t_{melting}$ (condition met)
     $t_{melting}$ =36 °C for RT 35 HC

Table 4

The parameters of the VCRS system for PCM - RT 35 HC

Den. no.	Property	t_2 [°C]	t_3 [°C]	t_4 [°C]	$\dot{m}$ [kg/s]	$\dot{Q}_{recovery}$ [kW]	m_{PCM} [kg]
1	R 404 a	60.12	46.58	41.58	0.0087	0.1538	2.754
2	R 600 a	49.63	46.58	41.58	0.00109	0.0065	2.754
3	R600	50.94	46.58	41.58	0.00063	0.0054	2.754
4	R1234yf	48.82	46.58	41.58	0.0047	0.01232	2.754
5	R1234ze	50.73	46.58	41.58	0.00284	0.0126	2.754
6	R 152 a	77.97	46.58	41.58	0.00207	0.08913	2.754
7	R 290	61.91	46.58	41.58	0.00324	0.1105	2.754
8	R 32	116.8	46.58	41.58	0.00629	0.5919	2.754
9	R450a	56.38	46.58	41.58	0.03178	0.03315	2.754

- For PCM type RT 44 HC the conditions that must be met and check are:
  1) The temperatures must: t_3 > t_4 (condition met)
     Temperature t_3=t_4 + 5
     So, t_3=46.58°C
  2) t_3 >$t_{melting}$ (condition not met)
     $t_{melting}$ =44°C for RT 44 HC

It can be seen that the second condition is not met, being at the limit, so this PCM-type paraffin cannot be used in this case. Proceeding in the same way, it is observed that for the other two types of PCM: RT 54 HC and SP 50, the 2nd condition is not met. So, the types of PCM: RT 44 HC, RT 54 HC and SP 50 cannot be used in the PCM heat exchanger**.**

CONCLUSIONS

In this paper, the possibility of improving the performance of a cold room refrigeration system by desuperheating energy recovery using Phase Change Materials has been investigated. One of the most accessible and widely used methods of defrosting is electric defrosting. The performance of a refrigeration system can be improved if the electric defrosting process could be replaced with an PCM based defrosting system. In order to evaluate the heat required for melting the ice accumulated on the evaporator during operation, an experimental setup based on a vapor compression refrigeration operating system with R404A, and a cold room has been used. After evaluating the heat required for defrosting a thermodynamic study has been carried out for refrigerants R404A, R600a, R600, R1234yf, R1234ze, R152a, R290 and R32 considering the SP 31, RT 35 HC, RT 44 HC, RT 54 HC and SP 50 PCMs. The aim of the thermodynamic study is to evaluate if the heat available in the desuperheating process corresponding to each refrigerant can be used in the process of PCM melting. Not all studied PCMs are suitable for a PCM based defrosting system.

The main results point out that:

- for the refrigerant R404A, an amount of thermal energy from the desuperheating process of 0.1538 kW could be stored for a mass of 3.147 kg of PCM - SP 31 and for PCM - RT 35 HC, the same amount was stored for a significantly smaller mass of 2.754 kg of PCM.

- among the refrigerants analysed, for the same mass of PCM, the R32 refrigerant has the highest available thermal energy recovered from the desuperheating process.

- for the PCMs: RT 54 HC; SP 50 and RT 44 HC the analysed agents do not lead to temperature values in state 3 lower than the melting temperature of the PCM (t_3 > $t_{melting}$), the condition imposed for the required mass of PCM to melt, so they cannot be used in the present case studied.

- for the refrigerants R600, R600a, R1234yf, R1234ze, R450a, regardless of the type of PCM used, their use is not recommended in the analysed case, because the heat flow recovered with the help of the PCMs does not cover the heat flow necessary to melt the PCM.

Future work will involve experimental development of PCM based defrosting system that could improve the efficiency of vapor compression refrigeration systems.

ACKNOWLEDGEMENTS

This work has been funded by the European Social Fund from the Sectorial Operational Programme Human Capital 2014-2020, through the Financial Agreement with the title "Training of PhD students and postdoctoral researchers in order to acquire applied research skills - SMART". Contract no.13530/16.06.2022 - SMIS code:153734.

REFERENCES

[1] Azzouz K., Leducq D., Gobin D., (2008), Performance enhancement of a household refrigerator by addition of latent heat storage, *Int. J. Refrig.*, vol. 31, no. 5, pp. 892–901.

[2] Azzouz K., Leducq D., Gobin D. , (2009), Enhancing the performance of household refrigerators with latent heat storage: An experimental investigation, *Int. J. Refrig.*, vol. 32, no. 7, pp. 1634–1644.

[3] Al Douri, J., Hmood, K., Apostol, V., Pop, H., Alqaisy, S., Ibrean, B., (2021), Review regarding defrosting methods for refrigeration and heat pump systems, *TE-RE-RD*, Romania.

[4] Bakhshipour S., Valipour, M.S., Pahamli Y., (2017), Parametric analysis of domestic refrigerators using PCM heat exchanger, *Int. J. Refrig.*, vol. 83, pp. 1–13.

[5] Cheng, W. L., Mei, B. J., Liu, Y. N., Huang, Y. H., Yuan, X. D., (2011), A novel household refrigerator with shape-stabilized PCM (Phase Change Material) heat storage condensers: An experimental investigation, *Energy*, vol. 36, no. 10, pp. 5797–5804.

[6] Cheng, W. long, Ding, M., Yuan, X. Dong, Han, B. C., (2017), Analysis of energy saving performance for household refrigerator with thermal storage of condenser and evaporator, *Energy Convers. Manag.*, vol. 132, pp. 180–188.

[7] Dandotiya, D., Banker, N. D., (2017), Performance Enhancement of a Refrigerator Using Phase Change Material-Based Condenser: An Experimental Investigation, *Int. J. Air-Conditioning Refrig.*, vol. 25, no. 4, pp. 1–9.

[8] Elarem, R., Mellouli, S., Abhilash, E., Jemni, A., (2017), Performance analysis of a household refrigerator integrating a PCM heat exchanger, *Appl. Therm. Eng.*, vol. 125, pp. 1320–1333.

[9] Gin, B., Farid, M. M., Bansal, P., (2011), Modeling of phase change material implemented into cold storage application, *HVAC R Res.*, vol. 17, no. 3, pp. 257–267.

[10] Horbaniuc, B., (2006), *Refrigeration and air conditioning systems for the food industry, Cermi Publishing House (Instalații frigorifice și de climatizare pentru industria alimentară)*, Editura Cermi, Iași, Bucuresti.

[11] Kraemer R., Plouff A., Venn J., (2013), *Design of a small-scale Low-Cost Cold Storage System BE*. 487: Biosystems Design Project.

[12] Kumar, P., Elakkiyadasan, R., Sathishkumar, N., Prabhu, G., Balasubramanian, T., (2020), Performance enhancement of a domestic refrigerator with Nanoparticle Enhanced PCM over the condenser side, *FME Trans.*, vol. 48, no. 3, pp. 620–627.

[13] Khan, M., Afroz, H. M. M.,(2015), Effect of phase change material on compressor on-off cycling of a household refrigerator," *Sci. Technol. Built Environ.*, vol. 21, no. 4, pp. 462–468.

[14] Liu, Z., Zhao, D., Wang, Q., Chi, Y. , Zhang, L., (2017), Performance study on air-cooled household refrigerator with cold storage phase change materials, *Int. J. Refrig.*, vol. 79, pp. 130–142.

[15] Qu, M., Xia, L., Deng, S., Jiang, Y., (2012), *Appl. Energy,* 91, pp.122–129.

[16] Regin, A.F., Solanki, S.C., Saini, J.S., (2008), *Renew. Sustain. Energy Rev*. 12, 24382458.

[17] Rahman, R.,(2013), Performance Improvement of a Domestic Refrigerator Using Phase Change Material (PCM), *IOSR J. Mech. Civ. Eng.*, vol. 10, no. 4, pp. 08–16.

[18] Wang, F., Maidment, G., Missenden, J., Tozer, R. (2007), The novel use of phase change materials in refrigeration plant. Part 1: Experimental investigation, *Appl. Therm. Eng.*, vol. 27, no. 17–18, pp. 2893–2901.

[19] Yusufoglu, Y., Apaydin, T., Yilmaz, S., Paksoy, H.O. (2015), Improving performance of household refrigerators by incorporating phase change materials, *Int. J. Refrig.*, vol. 57, pp. 173–185.

[20] Zarajabad Ghahramani O., Ahmadi R., (2018), Employment of finned PCM container in a household refrigerator as a cold thermal energy storage system, *Therm. Sci. Eng. Prog.*, vol. 7, no. June, pp.115–124.

[21] *** *Engineering Equation Solver Academic Professional*, V.10.664-3D #4487, Faculty of Mechanical Engineering, University Politehnica of Bucharest, 2019.

[22] https://www.rubitherm.eu/en/productcategory/anorganische-pcm-sp

[23] https://www.rubitherm.eu/en/productcategory/organische-pcm-rt

RESEARCH ON THE SEEDING DEPTH ADJUSTMENT DEVICE BASED ON THE TIP OF FURROW OPENER FORCE MEASUREMENT

/

基于铲尖测力的播深调控装置的研究

Xianmin LIANG[1)], Xiangcai ZHANG[*1)], Xingcheng AN[1)], Meng Liu[1)], Xianliang WANG[1)], Zhongcai WEI[1)], Xiupei CHENG[1)] Hui LI[2)],

[1)]School of Agricultural and Food Science, Shandong University of Technology, Zibo (255000), China;
[2)]Shandong Academy of Agricultural Machinery Sciences, Jinan (250010), China
Tel: +86-15169235925; E-mail: zxcai0216@163.com
Corresponding author: Xiangcai Zhang
DOI: https://doi.org/10.35633/inmateh-70-54

Keywords: *furrow opener; depth of seeding; pressure sensor; automatic control*

ABSTRACT

An active-action seeding depth automatic control system was designed, with the purpose of effectively ensure the consistency and stability of the seeding depth when the seeder is operated in the field. Strain-gauge pressure sensor was used in the system, which can detect the force on the tip of the furrow opener in the soil in real time, proceed to the next step judge the change of the seeding depth in the soil according to the change of the pressure signal. In order to achieve consistency and stability of seeding depth, the control signal formation circuit will send a control signal when the pressure on the tip of furrow opener exceeds the appropriate pressure range, and the motor will be controlled to rotate clockwise or counterclockwise to drive the rack and pinion movement to realize the vertical lift of the furrow opener, so that the force on the tip of furrow opener in the soil remains within the appropriate range. The test results indicate that the seeding depth adjustment device based on the tip of furrow opener force measurement has stable and reliable control performance for controlling the seeding depth with an average seeding depth qualification rate of 94.56% and an average seeding depth variation coefficient of only 9.29%, which greatly ensures the consistency and stability of the seeding depth under the condition that the seeding depth is 30-70mm and the working speed is 3-7km/h.

摘要

为使播种机在田间作业时能有效保证播种深度的一致性和稳定性，设计了一种主动作用式播种深度自动控制系统。该系统采用应变式压力传感器实时探测开沟器铲尖在土壤中的受力情况，进而根据压力信号的变化判断开沟器在土壤中开沟深度的变化情况。为了实现播种深度的一致性与稳定性，控制信号形成电路会在铲尖受到的压力超出合适压力范围时发出控制信号，通过控制电机顺时针或逆时针旋转带动齿轮齿条运动进而实现开沟器的垂直升降，使开沟器铲尖在土壤中的受力保持在合适的范围内。试验结果表明，在开沟深度为 30-70mm,工作速度为 3-7km/h 情况下，基于铲尖测力的播深调节装置对控制播种深度具有稳定可靠的控制性能，平均播深合格率高达 94.56%，平均播深变异系数仅为 9.29%，极大保证了播深的一致性与稳定性。

INTRODUCTION

Seeding depth is one of the strict indicators required by agricultural technology *(Li et al. 2003)*, and in actual agricultural production, the germination, emergence, and growth of seeds are severely affected by seeding depth *(Gupta S C et al., 1988; Berti M T et al., 2008; Zhang et al., 2016)*. Inconsistent seeding depth can affect the uniformity of seedling emergence, leading to high and low seedling phenomena and ultimately affecting yield *(Wu et al., 2011)*. Therefore, conducting in-depth research on the control of the seeding depth of the seeder and controlling the seeding depth within a reasonable range is of great significance for creating a better environment for seed germination and emergence *(Karayel D et al., 2002; Poncet A M et al., 2018; Hakansson I et al., 2011; Knappenberger T et al., 2012; Fu et al., 2019)*.

Researchers have conducted extensive research on seeding profiling device, and in order to ensure the stability and consistency of seeding depth, passive adjustment methods were often used, including adjusting springs, parallel four-linked rods or manually adjusting the relative distance between the profiling assembly and the furrow opener in the vertical direction to achieve individual profiling *(Gao et al., 2019; Zhao et al., 1989)*.

However, due to the unstable performance of passive seeding depth control, researchers have gradually begun to focus on the research of active seeding depth control *(Bodhoff B V D et al., 1970; Jr J E M et al., 1988; Yuan et al., 2018; Mouazen A M et al., 2004; Anthonis Jet al., 2004)*. Among them, Li Yuhuan et al. *(Li et al. 2016)* designed a pneumatic corn seeding depth control system, which measures the pressure of the press wheel using a pressure sensor. According to the magnitude of the compaction pressure, an electric push rod was used to adjust the amount of soil covered by the soil covering device, thereby achieving the effect of controlling the seeding depth. Zhao Jinhui et al. *(Zhao et al. 2015)* designed a displacement sensor based control system for seeding and furrow depth, which achieves synchronous profiling and controllable seeding depth by controlling the hydraulic cylinder at the profiling mechanism. Cai Guohua et al. (*Cai et al. 2011*) and WEN et al. *(Wen l, et al. 2014)* used ultrasonic sensors to monitor the seeding depth in real-time and designed a control system to adjust the seeding depth through a hydraulic system. The development of active depth control technology in foreign countries was earlier, in which Amazon Company produced an electronic depth control device, which was an ultrasonic detector installed on a furrow opener. It not only can detect the depth of the seeding in real-time but it can also be adjusted through the hydraulic system when the depth of the seeding deviates from the specified value to achieve a consistent depth of seeding. E. T. Weatherly and C.G. Bowers Jr. *(Weatherly E T et al. 1977)* developed an active automatic control system for seeding depth of a seeder based on drying front sensors (DFS), which uses DFS to detect soil electric resistance to obtain soil moisture content, and then adjusts the disc furrow opener to the appropriate position through controllers, hydraulic systems, adjustment mechanisms, etc., that is, seeds are sown at a depth with appropriate soil moisture content. The above studies may achieve consistency in seeding depth by controlling seeding or by controlling soil cover thickness, but the machine structure is relatively complex and the response time of pneumatic, hydraulic and other transmission methods is long, resulting in significant adjustment errors. Therefore, further research is needed.

In this paper, for the problems of complicated structure and long adjustment time of existing seeding depth adjustment device, an active control adjustment device which can monitor the force of the furrow opener in the soil by pressure sensor and adjust the seeding depth in real time by the force on the tip of furrow opener is developed, which has fast response speed, short adjustment time and simple structure, and has important guiding significance to ensure the stability of seeding depth.

MATERIALS AND METHODS

Overall structure of seeding depth control device

The seeding depth control device mainly consists of three parts: the tip of furrow opener force measurement system, the motor lifting control system, and the human-computer interaction interface, as shown in Figure 1.

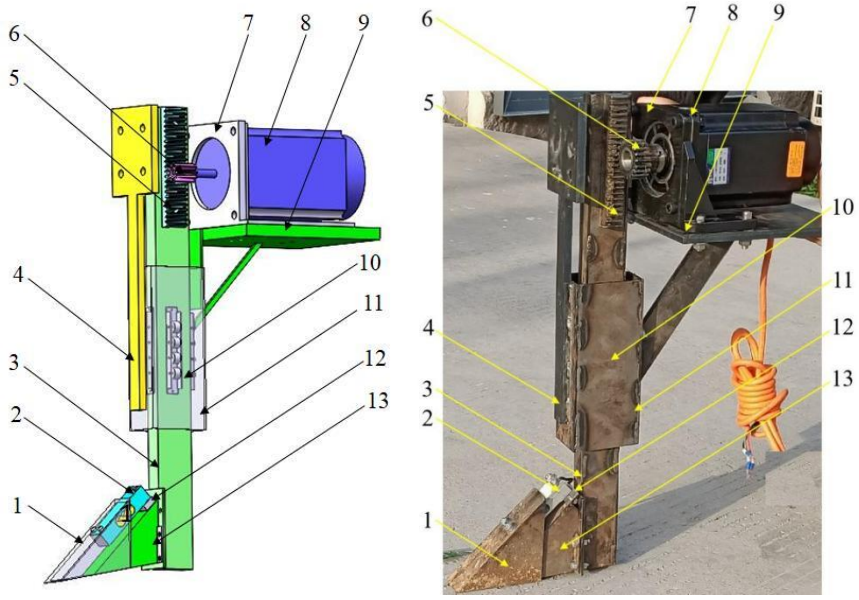

Fig. 1 – Overall structure of seeding depth control device

1 – Pressure sensor protective shell; 2 – Strain type pressure sensor; 3 – The shaft of furrow opener; 4 – Fixing frame; 5 – The straight gear; 6 – The straight rack; 7 – Motor base; 8 – Stepper motor; 9 – Motor fixed plate; 10 – Cylindrical guide; 11 – Guide shell; 12 – Pressure sensor gasket; 13 – The tip of furrow opener

The tip of furrow opener force measurement system consists of a shovel body and a Strain type pressure sensor, which is used to detect the force of the furrower tip in the soil in real time. The motor lifting control system consists of a stepper motor, a slide rail and a straight tooth gear rack, which is mainly used to adjust the lifting of the furrow opener and adjust the depth of the seeding in real-time. The human-computer interface consists of a serial screen and a control panel for the setting of seeding depth and the display of operating parameters. The main technical parameters of the whole machine are shown in Table 1.

Table 1

Main technical parameters of the machine

Parameters	Numerical value
Whole machine size (L×W×H) / (mm×mm×mm)	220×200×580
Whole machine quality / kg	20
Operating speed / (km/h)	3 - 7
Seeding depth adjustment range / mm	0 - 100
Power supply / V	220vAC

System working principle

Before the depth control system officially starts working, the tip of furrow opener force measurement system was used to measure the range of force exerted on the tip of the furrow opener under different seeding depth conditions in the soil. Then, the measured pressure range corresponding to the set seeding depth was inputted into the human-computer interaction interface. When the seeding depth control system officially starts to work, the tip of furrow opener force measurement system working in the soil monitors the situation of force exerted on the furrow opener in real time, and transmits the monitoring data to the microcontroller. After judgment and calculation, the microcontroller sends instructions to control the motor lifting to adjust the depth of the furrow opener entering the soil. The human-computer interaction interface can display the situation of force exerted on the tip of the furrow opener in the soil in real-time, and present the pressure data in the form of a curve. The system working principle is shown in Figure 2.

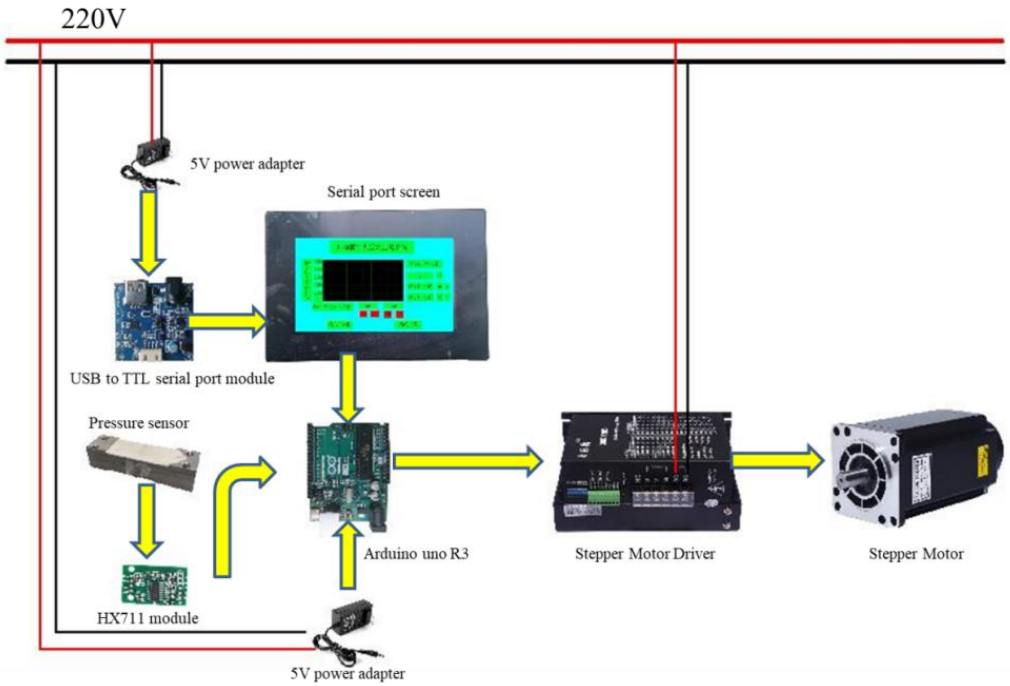

Fig. 2 – Working principle diagram

Design of shovel tip force measurement system

The tip of furrow opener force measurement system is mainly composed of a pressure sensor protective shell, a strain type pressure sensor, a pressure sensor gasket and the tip of furrow opener. The strain type pressure sensor was installed between the pressure sensor protective shell and the tip of furrow opener. When the furrow opener contacts the soil, the resistance of the soil to the pressure sensor protective shell causes the strain gauge of the pressure sensor to produce continuous deformation, and the generated pressure data will be displayed through the serial port screen, the specific connection method is shown in Fig. 3.

The pressure sensor used in this design was a strain gauge with a maximum range of 500 N produced by Sincere Electronics Technology, which was paired with the HX711 weighing module. In order to prevent damage to the pressure sensor caused by excessive deformation of the pressure sensor, a pressure sensor gasket was designed with a height equal to the maximum range deformation of the pressure sensor, so that when the deformation of the pressure sensor reaches its maximum value, the pressure sensor gasket will prevent further deformation of the pressure sensor, thus achieving the purpose of protecting the pressure sensor.

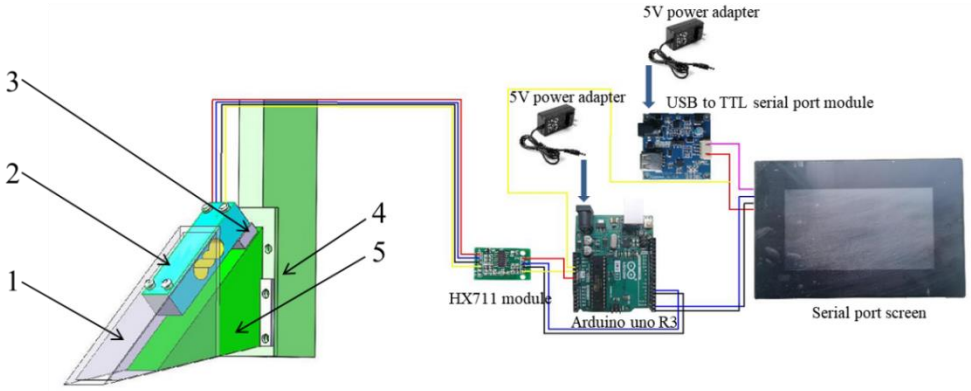

Fig. 3 – The structure diagram of furrow opener

1 – Pressure sensor protective shell; 2 – Strain type pressure sensor; 3 – Pressure sensor gasket; 4 – The shaft of furrow opener; 5 – The tip of furrow opener

Design of motor lift control system

As shown in Figure 4, the motor lifting control system is mainly composed of stepper motor, motor base, motor fixed plate, straight gear, straight rack, shovel shaft of furrow opener, cylindrical guide rail, guide rail shell, etc. Weld the straight gear rack onto the upper end of the shovel shaft of furrow opener, the straight gear is fixed on the motor shaft by key connection, the stepper motor is fixed on the guide rail shell through the base together with the motor fixed plate, and weld the four cylindrical guide rails to the same height in all four directions of the shovel shaft of furrow opener, use the guide rail shell as the track to form a sliding device for adjusting the lifting of the furrow opener. When the stepper motor receives instructions from the microcontroller to rotate, the straight gear will drive the straight rack to move up and down, thereby achieving the lifting and lowering about shovel shaft of furrow opener.

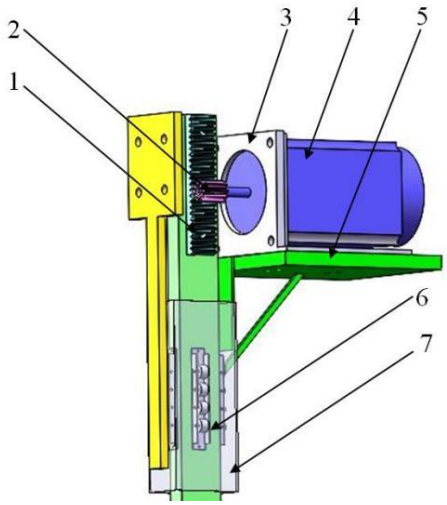

Fig. 4 – Motor lifting system

1 – The straight rack; 2 – The straight gear; 3 – Motor base; 4 – Stepper motor; 5 – Motor fixed plate; 6 – The cylindrical guide; 7 – The guide shell

To meet the lifting and lowering requirements of the furrow opener, a three-phase stepper motor with a torque of 50 N • M is selected, paired with a 3ND2283 driver, controlled by an Arduino Uno microcontroller. The physical connection is shown in Figure 5. The straight gear with an inner diameter of 19 mm and an outer diameter of 44 mm, with 2 modules and 20 teeth, and the straight rack with a length of 150 mm and a height and width of 20 mm, with 2 modules and 40 teeth, were used respectively.

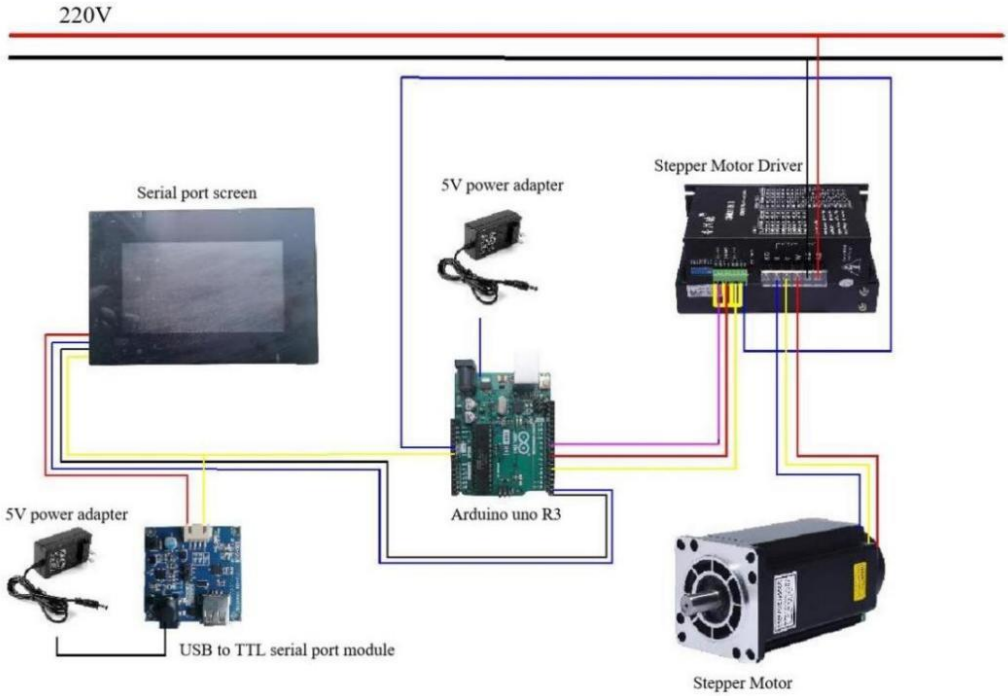

Fig. 5 – Motor lifting system physical connection diagram

Motor response time verification tests

The system used a three-phase stepper motor with a torque of 50 N•M. When the motor speed was below 200 r/min, the speed had no effect on the size of the torque output from the motor. To ensure the sensitivity during the adjustment process of the system, the torque of the stepper motor, and the accuracy of the furrow opener lifting, the maximum speed of the stepper motor was set to 60 r/min, and the acceleration and deceleration of the stepper motor adopted an S-shaped acceleration and deceleration curve. Due to the fact that the response time of the stepper motor from receiving the command to the start of the motor reaction was only a few milliseconds. Therefore, setting the response time of the stepper motor to increase its speed from 0 r/min to 60 r/min after the microcontroller sends instructions was called the response time of the stepper motor, the speed change during the process of the motor speed increasing from zero to the set speed after the microcontroller sent the command was recorded by an SD card, and the motor speed change curve is shown in Figure 6.

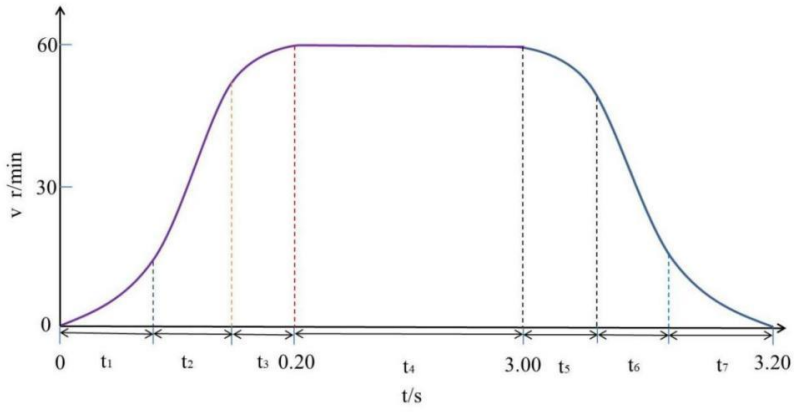

Fig. 6 – Motor response time curve

As can be seen from Figure 6, the motor acceleration process was divided into seven stages, accelerated motion phase t1 with increasing acceleration, uniform acceleration stage t2, accelerated motion phase t3 with decreasing acceleration, uniform speed stage t4, decelerating motion phase t5 with increasing acceleration, uniform deceleration stage t6, deceleration motion phase t7 with decreasing acceleration. In this process t1-t3 stage was called the response time of the stepper motor, that is, the response time of the stepper motor is 200 ms.

Since the prototype of the Sigmoid curve function can be represented by the following equation:

$$y = \frac{1}{1+e^{-t}} \quad (1)$$

Then the displacement Y of the stepper motor in 0.2 s can be expressed by the following equation:

$$Y = \int_0^{0.2} \frac{1}{1+e^{-t}} dt \quad (2)$$

Then the average speed of the stepper motor during the acceleration process can be expressed by the following equation:

$$v = \frac{Y}{t} \quad (3)$$

The speed of the stepper motor was 0.147 m/s at constant speed. In view of the fact that the adjustment speed of the furrow opener during the acceleration of the motor was much lower than the normal adjustment speed, which will delay the adjustment agility of the furrow opener, the furrow opener lifting response test was conducted to investigate its specific effect.

Design of human-computer interaction interface design

Figure 7 shows the human-computer interaction interface, which was designed by the HMI touch screen produced by Shenzhen Tao Jingchi Company. The display interface includes system switches, real-time display of the tip of furrow opener pressure curve, real-time display the tip of furrow opener Pressure data, appropriate pressure detection before operation, appropriate operation pressure data input, system settings, and other functions.

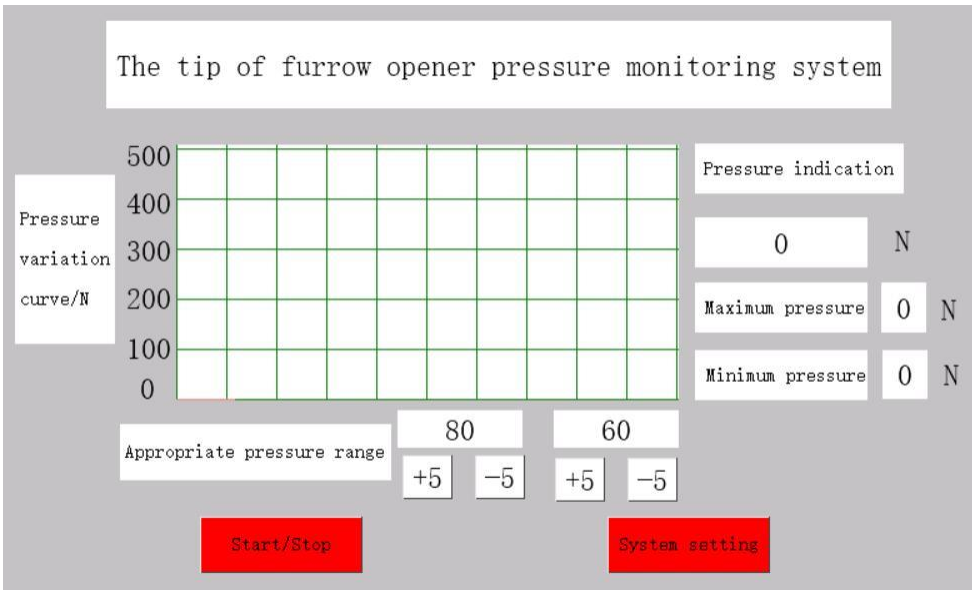

Fig. 7 – Human-computer interaction interface

Among them, the system switch button was responsible for the system start and the reset of the furrow opener after stopping work, the real-time display function of the tip of furrow opener pressure curve can display the force changes of the tip of furrow opener in real time and convert the pressure data into curve display, the tip of furrow opener real-time force display function can turn the pressure signal into a digital real-time display, the pre-operation suitable pressure detection function detects the maximum and minimum pressure for the plot to work at the right seeding depth before the official work, the suitable operating pressure input function can input the suitable pressure value obtained according to the suitable pressure detection function before the operation to change the working conditions of different plots, the system setting is mainly to adjust the brightness of the display screen.

Design of System circuit

The system mainly includes signal processing module, stepper motor driving module, Arduino control module, display screen and SD card recording module, which can realize the monitoring of real-time force of the tip of furrow opener in soil and real-time adjustment function of seeding depth. Through the design of each module and the selection of key components, the overall circuit of the seeding depth control system with the tip of furrow opener force measurement is shown in Figure 8.

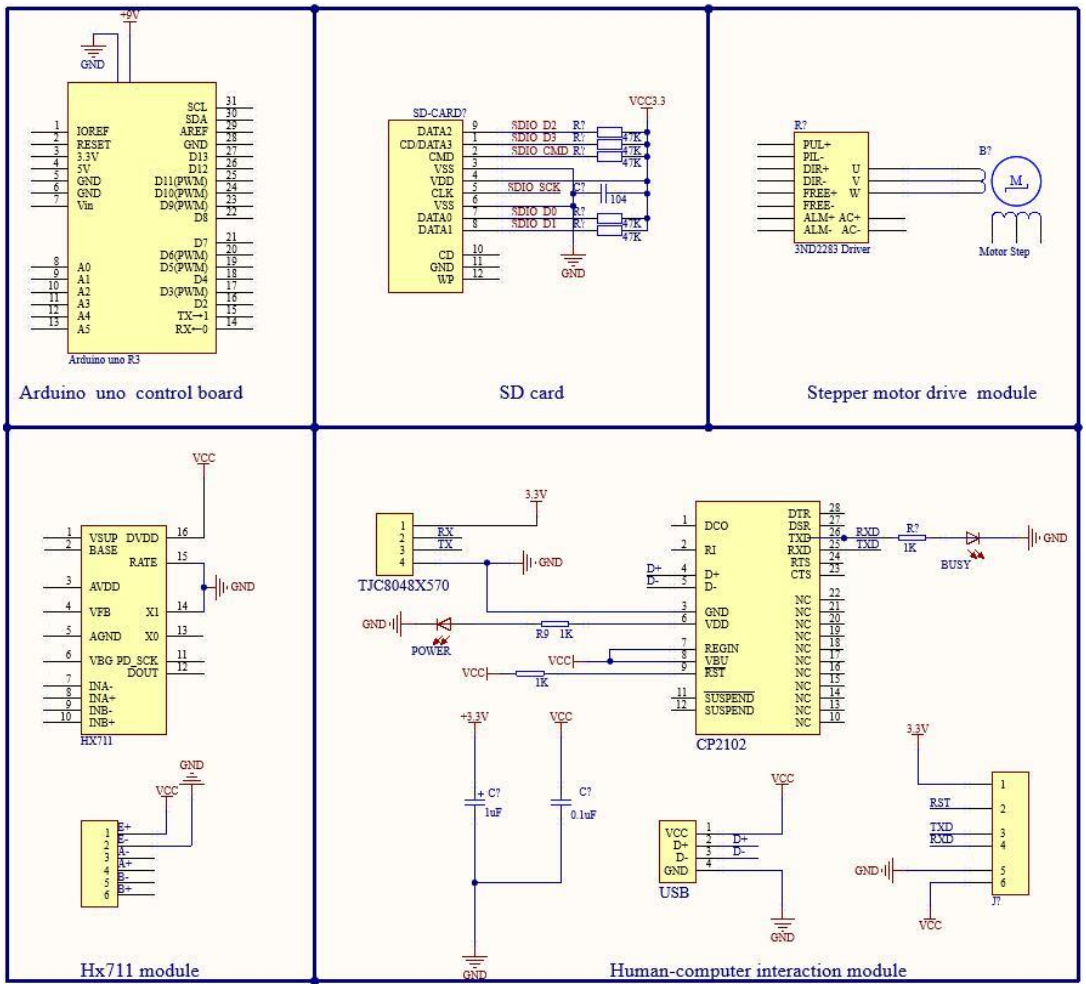

Fig. 8 – System circuit diagram

Design of system program

The system program control flow is shown in Figure 9, which mainly includes parameter setting, signal acquisition, data transmission, and system operation. At the beginning of the program, it was necessary to initialize the entire system, including a strain type pressure sensor, HX711 A/D conversion module, and the initialization of the corresponding I/O of the microcontroller. Set the program cycle to 50 ms, which means the sampling frequency was 200 HZ, after setting the tip of furrow opener force range and seeding depth, press the switch to start the official operation of the system.

When the pressure signal was generated, compare with the suitable pressure range N~M set in the microcontroller, if the force F on the tip of furrow opener was greater than N and less than M, the control circuit will not issue a signal, the motor will not rotate and the seeding depth will not change.

If the tip of furrow opener force F was less than N and greater than S (the value of the tip of furrow opener when it was nearly unstressed), the control circuit sends a low-level signal, at which time the motor counterclockwise rotation and the seeding depth begins to increase until the tip of furrow opener force was between N and M and the motor stops rotating.

If the tip of furrow opener force F was greater than M and less than B (the tip of furrow opener in the soil when encountering stones and other hard objects generated far beyond the pressure range of the value), the control circuit issued a high level signal, at which time the motor was clockwise rotation, seeding depth began to reduce, until the tip of furrow opener force between N to M motor stopped rotating.

If the force F on the tip of furrow opener was greater than B (when the tip of furrow opener encounters stones or higher hardness soil blocks in the soil) or less than S (when the tip of furrow opener encounters small pits in the soil causing suspension), the control circuit also does not issue a control signal and the seeding depth remains unchanged. At the same time, the operation information (real-time pressure value and pressure change curve of the tip of furrow opener) will be displayed on the human-computer interaction interface.

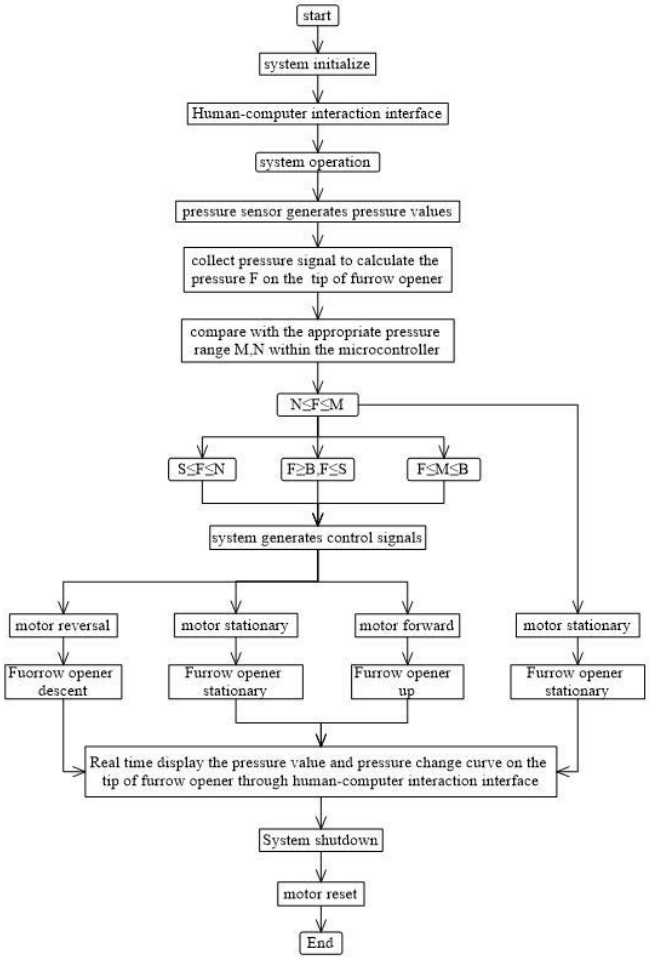

Fig. 9 – System workflow diagram

Soil trough test

To test the performance of the system in controlling seeding depth at different operating speeds and depths, a test was conducted in a soil bin at the Agricultural Machinery Equipment Laboratory of Shandong University of Technology in March 2023. The selected soil trough was 40 meters long and 2.5 meters wide, with a hauling vehicle as the traction power source. The test setup is shown in Figure 10.

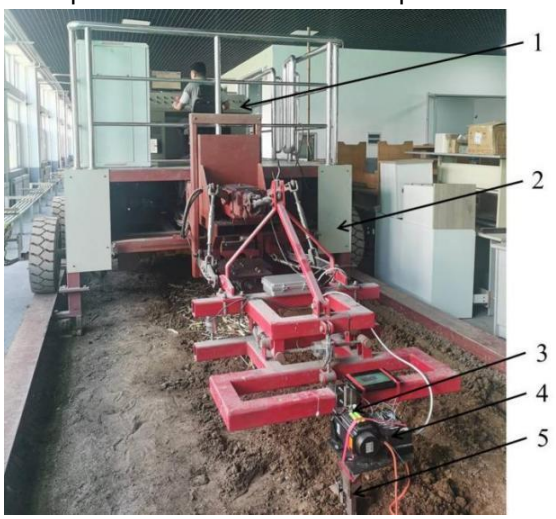

Fig. 10 – Seeding depth stability test

1 – Tractor control console; 2 – The hauling vehicle; 3 – Stepper motor; 4 – Motor driver; 5 – furrow opener

The working object of the furrow opener is field soil, but due to the complex working conditions in the field, the soil conditions are difficult to control, and the difficulty of the experiment is high. Therefore, an indoor soil bin was selected for the experiment. The soil bin was sprinkled with water five days before the test, and the soil was tested for water content, soil firmness, and the percentage of 5 mm particles on the test day.

A number of 50 uniformly distributed measurement points within 25 m of the middle of the soil bin test bench were selected, J-K750-I soil compactness meter of Beijing Jinkelida Electronic Technology Co., Ltd. and JK-500 high-frequency moisture detector of Jiangsu Youke Instrument Co., Ltd. were selected for measurement, and the average soil density and soil moisture content obtained from the measurement are shown in Table 2.

Table 2

Soil mechanical and physical parameter

Soil depth mm	Soil density kPa%	Soil moisture content %	Proportion of soil particles/%(≥ 5 mm)
30	60.16	9.13	12.57
50	61.58	10.52	10.13
70	61.74	12.61	9.76

According to the operating depth of the seeder and the seeding depth requirements of different crops *(Yao et al., 2007; Yao et al., 2007; Zhang et al., 2010; Chen et al., 2009)*, the selected seeding depths were 30, 50, and 70 mm, respectively, and the tests were conducted under the conditions of 3, 5, and 7 km/h of the forward speed of the hauling vehicle. In order to simplify the test, no seeding operation was carried out to evaluate the seeding depth control effect by furrow depth etc. In order to reduce the measurement error caused by the difference in height of the ground surface on both sides of the seeding furrow, the height from the center of the seeding furrow to the ground surface was selected as the seeding depth measurement method as shown in Figure 11. In the whole test process, first of all, calibration tests should be carried out, and the seeding depths of 30, 50 and 70 mm should be selected respectively, and the working speeds of 3, 5 and 7 km/h. Without the participation of the motor lifting control system, the force of the tip of the furrow opener in the plot should be determined by the tip of furrow opener force measurement system, and then the suitable force range of the tip of furrow opener in the plot under different seeding depth conditions should be determined, and the test data should be recorded by SD card. Subsequently, in the seeding depth control test of the furrow opener, in order to avoid the influence of the acceleration and deceleration process of the hauling vehicle on the seeding depth, points were selected in the middle 25m area of the soil trough test stand, and one measurement point was selected every two theoretical seed distances, and a total of 100 measurement points were selected. According to the judgment standard of qualified seeding depth (H±10) mm in the agricultural industry standard NY/T 1768-2009 "Technical specification for quality evaluation of no-till seeders", the qualified seeding depths were 20-40 mm, 40-60 mm, and 60-80 mm under the target seeding depths of 30, 50, and 70 mm, respectively *(Fu et al., 2018; Gao et al., 2019).*

The calculation formula for each parameter is as follows:

$$\begin{cases} \eta = \frac{n}{N} \times 100\% \\ h_p = \frac{\sum h_i}{N} \\ S_h = \sqrt{\frac{\sum (h_i - h_p)^2}{N}} \\ V_h = \frac{S_h}{h_p} \times 100\% \end{cases} \quad (4)$$

In the formula: η is the seeding depth qualification rate, the unit is %; n is the number of qualified seeding depth; N is the total number of measuring points for seeding depth; h_p is the average seeding depth, the unit is mm; h_i is measurement of seeding depth, the unit is mm; S_h is the Standard deviation of seeding depth, the unit is mm; V_h is the coefficient of variation of seeding depth, the unit is %.

Fig. 11 – Measurement methods for seeding depth

RESULTS

Without the participation of the motor lifting control system, the force acting on the tip of furrow opener was measured using the tip of furrow opener force measurement system at depths of 30, 50, and 70 mm, and at speeds of 3, 5, and 7 km/h. The test results are shown in Table 3. The selection criteria for the appropriate pressure range of the tip of furrow opener when the seeding depth is 30, 50, or 70 mm are as follows.

$$\begin{cases} F_3 = \frac{F_{max}+F_{min}}{2} \pm 10 \\ F_5 = \frac{F_{max}+F_{min}}{2} \pm 20 \\ F_7 = \frac{F_{max}+F_{min}}{2} \pm 30 \end{cases} \quad (5)$$

Table 3

Calibration test results

Speed(km/h)	Seeding depth/mm	Minimum pressure/N	Maximum pressure/N	Suitable pressure range/N
3	30	97	135	110—130
3	50	219	283	230—270
3	70	368	442	375—435
5	30	117	143	120—140
5	50	238	312	255—295
5	70	391	467	400—460
7	30	103	152	115—135
7	50	251	331	270—310
7	70	407	493	420—480

By summarizing the seeding depth data of measurement points, the variation curve of seeding depth is obtained as shown in Figure 12. (a), (b), (c), (d), (e), (f), (g), (h), and (I) are the variation curves of seeding depth under the conditions of target seeding depth of 30 mm, 50 mm, 70 mm, and working speed of 3, 5, and 7 km/h.

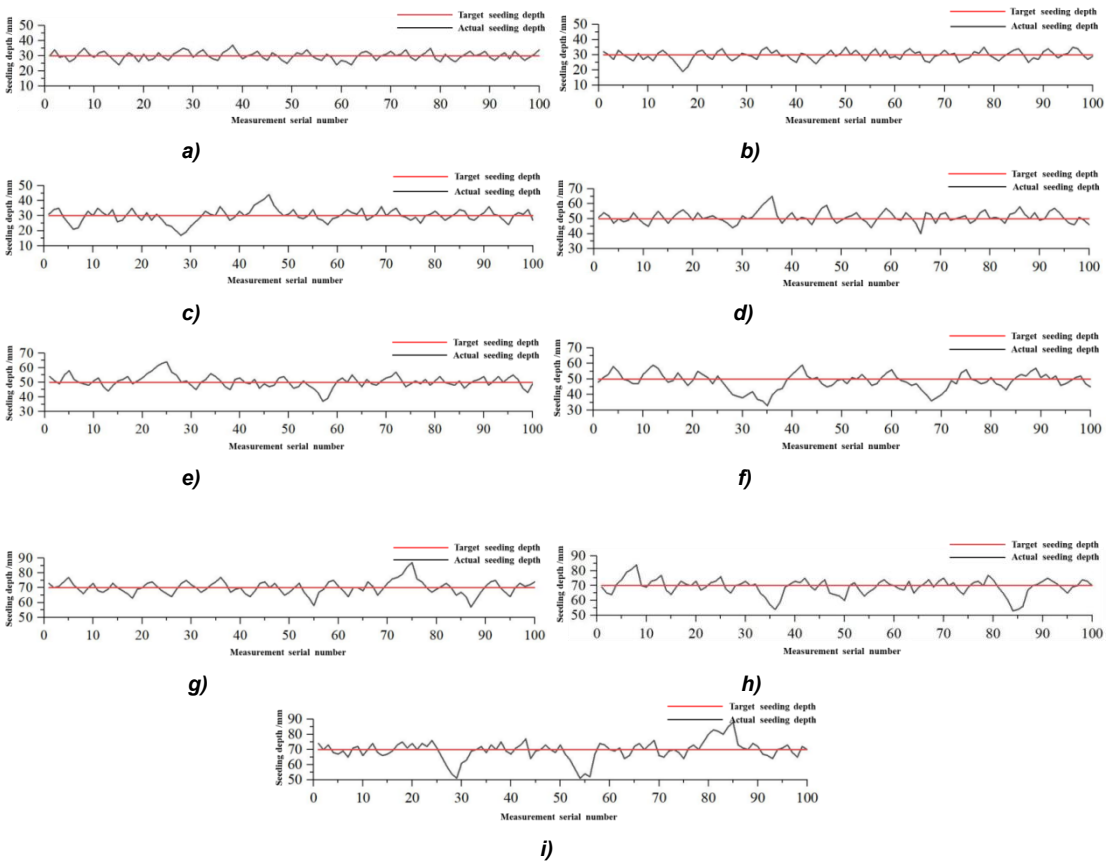

Fig. 12 – Variation curve of seeding depth

Figure 12 shows the measurement data of seeding depth under three different seeding speeds and

three different set seeding depths. From the variation curve of seeding depth, it can be seen that the seeding depth under the active adjustment method fluctuates in a small range at the set value, with a few discontinuous and unqualified seeding depth data. This demonstrates the advantage of fast motor adjustment response.

Table 4

Test results of soil tank test

Speed (km/h)	Set broadcast depth / mm	Average seeding depth / mm	Seeding depth qualification rate / %	Standard deviation of seeding depth	Coefficient of variation of seeding depth / %
3	30	30.03	100	2.71	8.94
3	50	50.12	98	3.82	7.47
3	70	70.15	96	4.53	6.46
5	30	29.63	97	3.04	10.26
5	50	50.63	95	4.20	8.29
5	70	69.24	92	5.36	7.74
7	30	30.11	95	4.36	14.48
7	50	48.53	91	5.34	11.01
7	70	69.57	87	6.26	9.00

The results of the analysis by extracting the data in the graph are shown in Table 4. The analysis of the average value of the seeding depth shows that the maximum error of the average value of the seeding depth was 1.12 mm under this active adjustment method, and the maximum error of the seeding depth value was 9 mm when the depth of the furrow was 70 mm at the working speed of 7 km/h, and the overall seeding depth value was slightly less than the set seeding depth value. Through the analysis of the seeding depth qualification rate, it can be seen that different seeding depths and different seeding speeds had a certain degree of influence on the active adjustment method, with the same working speed, as the seeding depth increases, the soil conditions become more complex, and the seeding depth qualification rate was gradually decreasing.

With increasing seeding speed at the same seeding depth, the seeding depth qualification rate also shows a gradually decreasing trend, the highest seeding depth qualification rate reaches 100% when the working speed was 3 km/h and the seeding depth was 30 mm, and the lowest seeding depth qualification rate was only 87% when the working speed was 7 km/h and the seeding depth was 70 mm. Through the analysis of the standard deviation and coefficient of variation of seeding depth, it can be seen that the variation of seeding depth standard deviation was relatively small whether it was the case of gradually increasing seeding depth at the same working speed or the case of gradually increasing working speed at the same seeding depth. However, the coefficient of variation of seeding depth shows a gradual increasing trend in both cases, that is, the consistency of seeding depth decreases with the increase of seeding depth and working speed. In the data obtained from the soil trough test, it can be seen that the maximum seeding depth qualification rate was 100%, the minimum was 87%, and the average value was 94.56%, and the maximum coefficient of variation of seeding depth was 14.48%, the minimum was 6.46%, and the average value was 9.29%. From the above data, it can be seen that the seeding depth adjustment device based on the tip of furrow opener force measurement can fully meet the operational requirements.

CONCLUSIONS

From the perspective of monitoring the force on the tip of furrow opener, a seeding depth control device based on the force measurement of the tip of furrow opener was designed. By monitoring the signal of the change in force on the tip of furrow opener, the Arduino microcontroller was used to control the stepper motor to rotate and drive the handle of furrow opener to vertical movement, thereby achieving the goal of adjusting the depth of seeding. Realizing closed-loop control of seeding depth and the tip of furrow opener force provides a new approach for the design and research of automatic control devices for seeding depth.

The seeding depth adjustment device based on the tip of furrow opener force measurement has the characteristics of short response time, high sensitivity and accurate control. The average speed of the acceleration stage was 55 mm/s and the working speed of the stepper motor was 60 r/min (147 mm/s), which greatly ensures the sensitivity of the device and realizes the accurate control of seeding depth.

The soil trough test shows that the seeding depth adjustment device based on the tip of furrow opener force measurement has stable and reliable control performance when the depth of seeding was 30-70 mm and the working speed was 3-7 km/h. The qualified seeding depth was as high as 94.56%. Although the coefficient

of variation of seeding depth increases with the increase of seeding depth and working speed, the average remains at 9.29%, and the consistency of seeding depth was relatively stable.

ACKNOWLEDGEMENTS

This work was financially supported by the National Natural Science Foundation of China (Grant No. 51805300).

REFERENCES

[1] Anthonis J., Mouazen A.M., Saeys W. et al. (2004). An automatic depth control system for online measurement of spatial variation in soil compaction, Part 3: Design of depth control system [J]. *Biosystems Engineering, 89*(1): 59-67.

[2] Berti M.T., Johnson B.L., Henson R.A. (2008). Seeding depth and soil packing affect pure live seed emergence of cuphea [J]. Industrial Crops& Products, 27(3): 272-278.

[3] Boshoff B.V.D. (1970). Automatic depth control for seed planter based on soil conductance sensing [D]. *Raleigh: North Carolina State University*.

[4] Cai G., Li H., Li H. et al. (2011). Design of test-bed for automatic depth of furrow opening control system based on ATmega128 single chip microcomputer（基于 ATmega128 单片机的播深自控系统试验台的设计）[J]. *Transactions of the CSAE, 27*(10): 11-16.

[5] Chen H., Huang H., Yang Y. et al. (2009). Design of row-followed no-till wheat and maize planter under controlled traffic farming system（固定道对行小麦/玉米通用免耕播种机设计）[J]. *Transactions of the Chinese Society for Agricultural Machinery, 40*(3): 72-76.

[6] Fu W. (2019). Study on key technology of quality control for maize no-tillage drilling machinery（玉米免耕精密播种质量控制关键技术研究）[D]. *Beijing: China Agricultural University.*

[7] Fu W., Dong J., Mei H. et al. (2018). Design and test of pneumatic downforce control system for planting（玉米播种单体下压力控制系统设计与试验）[J]. *Transactions of the Chinese Society for Agricultural Machinery, 49*(6): 68-77.

[8] Gupta S.C., Swanjb, Schneider E.C. (1988). Planting depth and tillage interactions on corn emergence [J]. *Soil Science Society of America Journal, 52*(4): 1122-1127.

[9] Gao Y., Wang X., Yang S. et al. (2019). Development of CAN-based sowing depth monitoring and evaluation system（基于 CAN 总线的播种深度监测评价系统研究）[J]. *Transactions of the Chinese Society for Agricultural Machinery, 50*(12): 23-32.

[10] Gao Y., Wang X., Yang S. et al. (2019). Design and test of pneumatic downforce control system for planting（播种机气动式下压力控制系统的设计与试验）[J]. *Transactions of the Chinese Society for Agricultural Machinery, 50*(7): 19-29, 83.

[11] Hakansson I., Arvidsson J., Keller T. et al. (2011). Effects of seedbed properties on crop emergence: 1. Temporal effects of temperature and sowing depth in seedbeds with favourable properties [J]. *Acta Agriculturae Scandinavica, Section B-Plant Soil. Science, 61*(5): 458-468.

[12] Jr J.E.M. (1988). Interactive planter depth control and pneumatic downpressure system [J]. *Transactions of the ASAE, 31*(1): 14-18.

[13] Karayel D., Ozmerzi A. (2002). Effect of tillage methods on sowing uniformity of maize [J]. *Canadian Biosystems Engineering, 44: 2-23.*

[14] Knappenberger T., Koller K. (2012). Spatial assessment of the correlation of seeding depth with emergence and yield of corn [J]. *Precision Agriculture, 13*: 163-180.

[15] Li B. (2003). Agricultural Mechanics（农业机械学）[M]. *Beijing: China Agricultural press*, 48-71.

[16] Li Y., Meng P., Geng D. et al. (2016). Intelligent system for adjusting and controlling corn seeding depth（玉米播深智能控制系统研究）[J]. *Transactions of the Chinese Society for Agricultural Machinery, 49*(Supp.): 62-68.

[17] Mouazen A.M., Anthonis J., Saeys W. et al. (2004). An automatic depth control system for online measurement of spatial variation in soil compaction, Part 1: Sensor design for measurement of frame height variation from soil surface [J]. *Biosystems Engineering, 89*(2): 139-150.

[18] Poncet A.M., Fulton J.P., Mcdonald T. P., et al. (2018). Effect of heterogeneous field conditions on corn seeding depth accuracy and uniformity [J]. *Applied Engineering in Agriculture, 34*(5): 819-830.

[19] Wu H., Cui Y., Sun C. (2011). Study on relations of sowing depth and seeding emergence of different types of maize seeds （不同类型玉米杂交种播深与出苗相关性研究）[J]. *Journal of Maize Sciences, 19*(2): 109-113.
[20] Wen L., Fan X., Liu Z., et al. (2014). The design and development of the precision planter sowing depth control system [J]. *Sensors & Transducers, 162* (1): 53-58.
[21] Weatherly E. T., Bowers Jr C. G. (1997). Automatic depth control of a seed planter based on soil drying front sensing [J]. *Transactions of ASAE, 40*(2): 295-305.
[22] Yuan Y., Bai H., Fang X., et al. (2018). Research progress on maize seeding and its measurement and control technology（玉米播种与测控技术研究进展）[J/OL]. *Transactions of the Chinese Society for Agricultural Machinery, 49*(9): 1-18.
[23] Yao Z., Wang X., Gao H., et al. (2007). Improvement on the device for separate application of fertilizer and seed for no-till wheat drill（小麦免耕播种机种肥分施机构的改进与应用效果）[J]. Transactions of the Chinese Society of Agricultural Engineering (Transactions of the CSAE), 23(1): 120-124.
[24] Yao Z., Li H., Gao H. et al. (2007). Design and experiment of a no-tillage wheat seeding equipment, on field covered with corn, in double crop culture per year（一年两熟区玉米覆盖地小麦免耕播种机设计与试验）[J]. *Transactions of the Chinese Society of Agricultural Machinery, 38*(8): 57-61.
[25] Zhang R. (2016). Study on precision depth-control mechanism of corn no-till planter in double-cropping area（一年两熟地区麦茬地玉米免耕播种播深控制机构的研究）[D]. Beijing: China Agricultural University.
[26] Zhao H. (1989). An ultrasonic sensor attached to the opener（装在开沟器上的超声波探测器）[J]. *Machinery for Cereals, Oil and Food Processing* (1): 43.
[27] Zhao J., Liu L., Yang X., et al. (2015). Design and laboratory test of control system for depth of furrow opening（播种机开沟深度控制系统的设计与室内试验）[J]. *Transactions of the Chinese Society of Agricultural Machinery, 31*(6): 35-41.
[28] Zhang X.H, Li H., et al. (2010). Design and experiment on no-till planter in horizontal residue-throwing finger-wheel type for maize（水平拨草轮式玉米免耕播种机设计与试验）[J]. *Transactions of the Chinese Society for Agricultural Machinery, 41*(12): 39-43.

OPTIMUM DESIGN FOR BREAKING DEVICE WITH DOUBLE ROLLER BASED EDEM
/
基于 EDEM 的双滚轮破碎装置优化设计

Ruili WANG [1], Deshuai LI [1]; Peiyuan LI [1], Xueyin BAI [1], Tiejun WANG [1], Wei WANG*[1], Yingbo ZHAO[2]
[1]College of Engineering, Shenyang Agricultural University, Shenyang / China
[2]Heishan Chuanqi Agricultural Machinery Equipment Co, Ltd, Jinzhou / China
Tel:18804045818; E-mail: syww@syau.edu.cn
DOI: https://doi.org/10.35633/inmateh-70-55

Keywords: *round bale corn stalks, roller structure, crushing device, numerical simulation*

ABSTRACT

Straw found in the field can be conveniently stored and transported through mechanical packaging, and it undergoes crushing during its utilization. The effectiveness of the crushing process directly impacts the efficiency of material utilization. However, current crushing devices available in the market lack specialized mechanisms suitable for the unique characteristics of round corn stalks. To address this issue, the necessary simulation parameters were determined, and an experiment was conducted using the ternary quadratic combination test method. The test factors considered were the center height difference of the knife roller, lower roller speed, and cutter thickness. The response value of the experiment was the material crushing rate. By analyzing the results, the optimal structural parameters were identified. These included a center height difference of 390 mm for the knife roller, a lower roller speed of 14 r/min, and a cutter thickness of 110 mm. With these parameters, the crushing rate of the round straw crushing device reached 93.77%, and the particle passing ratio was 98.52%. To validate the research findings, a test device was constructed and used to confirm the reliability of the obtained results.

摘要

田间秸秆主要通过机械打包方便进行存储运输,在其使用时进行破碎处理,破碎效果直接影响物料利用效率. 目前,市面上的破碎装置缺乏适用于圆包玉米秸秆物料特性的专用破包装置. 测定必要仿真参数,并基于三元二次组合试验方法进行试验. 确定了以刀辊中心高度差, 下置辊转速和刀具厚度为测试因子,以物料破碎率为测试响应的响应值,得出了最优结构参数,即刀辊中心高度差 390 mm,下置辊转速 14r/min,刀具厚度为 110 mm,此时圆包秸秆破碎装置的破碎率为 93.77%,颗粒通过比例为 98.52%,并据此搭建试验装置验证研究结果可靠.

INTRODUCTION

The utilization of straw bale breaking devices has experienced significant growth, garnering global interest in recent decades. This can be attributed to several factors, including the technique's minimal impact on device structure and the excellent heat production capabilities of straw. The combustion of corn stalks yields a high calorific value, generating heat energy equivalent to 0.5 kg to 0.7 kg of standard coal per 1 kg of dry corn stalk. As a result, straw bale breaking serves as an environmentally friendly, clean, and renewable energy source.

Numerous studies have addressed the mechanical behavior of straw bales at various scales, as documented in the literature *(Bou Ali, 1993; Carrick et al., 1998; King, 2003; Rakowski, 2010; Walker et al., 2004)*. Presently, there are several types of breaking devices in China. However, many of them draw reference from foreign machines, resulting in a considerable disparity between domestic and international situations. Foreign machines are not suitable for our country's circumstances and are costly *(Wen et al., 2020; Yu et al., 2014; Choi et al., 2016; Karayel, D., 2023; Porteus, Sc., 1988; Kornecki, TS., 2022)*. Discrete element simulation technology has been widely employed by scholars both domestically and internationally in the field of agricultural machinery *(Wang et al., 2022; Zhang et al., 2022; Yan et al., 2022; Yu et al., 2020; Liu et al., 2022; Zhou et al., 2022; Feng et al., 2016)*, effectively reducing research and development costs.

This study aims to investigate the mechanical properties and breaking characteristics of round-packed corn stalks using physical experiments and numerical simulations. The structure of the breaking and tearing roller is analyzed to explore the breaking and tearing mechanism of round-packed corn stalks. The findings offer a numerical and theoretical foundation for optimizing the design of mechanical structure parameters, supporting the practical production and processing of round-packed corn stalks.

MATERIALS AND METHODS

Determination of simulation parameters

The focus of this research is the round corn stalks that are collected and packed using the 404Pro type Wittmann round straw baler. Based on the formation principle of round-baled corn stalks, the components of these round-baled stalks consist of intact corn stalks, a significant amount of soil, short stalks, leaves, stalk nodes, and a mixture of soil and silk stalks. The average density of the round corn stalks was measured at 196.08 $\mathrm{kg/m^3}$, with an average moisture content of 16% using the drying method. Due to the irregular nature of conventional physical property measuring equipment and the characteristics of round baled straw materials, it is necessary to conduct scale model tests. The preparation of model materials is one of the main aspects of these tests. Samples were extracted from the original bales of corn stalks and compressed to obtain samples with the same density for testing using the WDW-200 microcomputer-controlled electronic universal testing machine. The test device is mainly PL2-C40C high-speed camera, test plane and lens spacing of 880 mm, the use of high-speed camera on the specimen free fall and rebound process for filming, with a marker pen to mark the bottom edge of the specimen center, to facilitate high-speed camera trajectory to capture and data statistics. In order to ensure the performance effect of recording the falling process, the optimal falling height of the specimen is 370 mm and the distance between the horizontal reference points is 180 mm after several tests.

Determining the collision recovery coefficient between the plate and the device is essential. This coefficient represents an object's ability to deform and return to its original state after a collision. Its value is defined as the ratio of the normal velocity of the object after collision to the normal velocity before collision. It serves as a crucial contact parameter for the simulation test of stacking angles using discrete element simulation software. The test setup, as depicted in Fig. 1, primarily includes the PL2-C40C high-speed camera positioned at a distance of 880 mm from the test plane. The high-speed camera captures the free fall and rebound process of the sample, with a marker pen used to mark the center of the sample's bottom edge. This marking facilitates trajectory capture and data analysis by the high-speed camera. After conducting multiple tests, an optimal falling height of 370 mm and a distance of 180 mm between horizontal reference points were determined to ensure effective recording of the falling process.

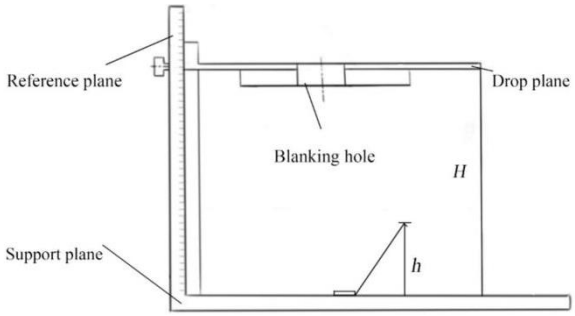

Fig. 1 - Test principle for determination of collision recovery coefficient

Assuming that the sample is only affected by gravity during the falling process, the normal velocity v_1 before the collision and the normal velocity v_2 after the collision are obtained according to the kinetic energy theorem.

$$v_1 = \sqrt{2gh} \tag{1}$$

$$v_2 = \sqrt{2gH} \tag{2}$$

The coefficient of collision recovery

$$\mathrm{e} = \frac{|v_2|}{|v_1|} = \sqrt{\frac{h}{H}} \tag{3}$$

where:

v_1 is the normal velocity before collision, mm·s^{-1}; v_2 is the normal velocity after collision separation, mm·s^{-1}; h is the falling height before collision, mm; H is the maximum height of bounce after collision separation, mm.

The displacement-time curve of the sample's falling and collision rebound process was obtained by utilizing the tracking function of the PLEXLOGplusII high-speed camera analysis software and the drawing function of Origin software. This curve, depicted in Fig. 2, was then applied to equation (3) to determine the collision recovery coefficient between round bundles of corn stalks and between round bundles of straws and

steel plates, based on the selected material of the contact bottom plate. The test process was conducted 10 times to ensure accuracy, resulting in the determination of the collision recovery coefficient between round bundle straw samples and between round bundle straw samples and steel plates. The collision recovery coefficient between round bundle straw samples ranged from 0.3 to 0.4, while that between round bundle straw samples and steel plates ranged from 0.2 to 0.35.

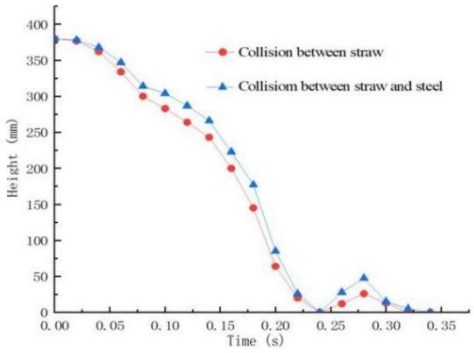

Fig. 2 - Motion displacement-time curve of a corn stalk in round bales colliding with a measured object.

Establishment of discrete element simulation model of corn stalk round bale

The initial step involves establishing the geometric model of the corn stalk round bale. This is accomplished by using Solid-Works to model the bale, which is then saved in x_t format and imported into EDEM. EDEM, developed by DEM-Solutions, Edinburgh, UK, is a CAE software based on the discrete cell method, which is widely used to simulate and study the mechanical properties of particles and the action on particles. (*Luo Shuai et al., 2018*). The Poisson's ratio, shear modulus, and density of the corn stalk round bale are specified, taking into consideration relevant literature, and the static friction coefficient, rolling friction coefficient, and collision recovery coefficient between the geometry and particles are also set. To conduct the discrete element simulation of the breaking process, it is necessary to create models for the particles constituting the round bale. Fig. 3 illustrates the sequence of the physical map of the round bale, the 3D diagram, and the particle bonding diagram, presented from left to right.

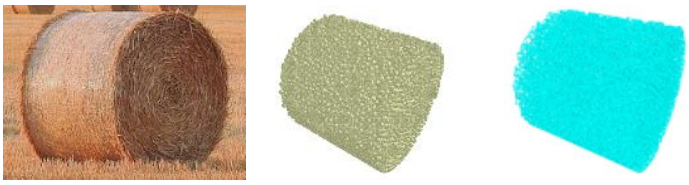

Fig. 3 - Corn stalk round bale

Table 1

Simulation parameters

Material parameters	Numerical value	Geometric parameters	Numerical value
Density [kg/m^3]	189.7	**Density [kg/m^3]**	8864
Poisson's ratio	0.35	**Poisson's ratio**	0.35
Shear modulus	2.01	**Shear modulus**	7.9x10^4
Recovery coefficient between materials	0.37	**Material and geometry recovery coefficient**	0.275
Static friction coefficient between materials	1.22	**Static friction coefficient between material and geometry**	0.465
Rolling friction coefficient between materials	0.54	**Rolling friction coefficient between material and geometry**	0.25

Analysis of influencing factors

By altering the structural and operating parameters of the machine, the working performance of the round straw shredder can be enhanced. Hence, the test variables selected include the center height difference of the counter roller, cutter thickness, number of teeth on a single cutter, rotation speed of the upper roller, and rotation speed of the lower roller. A single-factor simulation test is conducted, with the material crushing rate serving as the evaluation index.

Through the analysis of variance, it becomes possible to explore the contribution of variations from different sources to the overall variation and further determine the influence of experimental factors on the evaluation index.

The test levels are determined based on theoretical calculations and a thorough review of relevant literature, as presented in Table 2.

Table 2

Factors and levels of single factor test

Experimental factors	Levels						
Counter roller height difference [mm]	0	195	390	585	780	975	1170
Single tool tooth number	5	6	7	8	9		
Tool thickness [mm]	70	80	90	100	110		
Top roller speed [rpm]	10	12	14	16	18		
Lower roller speed [rpm]	10	12	14	16	18		

Based on the relevant literature and the actual characteristics of broken round corn stalks, the unnecessary materials for composite crushing were carefully weighed. As a result, the average crushing rate achieved by the round corn stalk crusher was found to be 85%, aligning with the findings of previous research conducted by the enterprise.

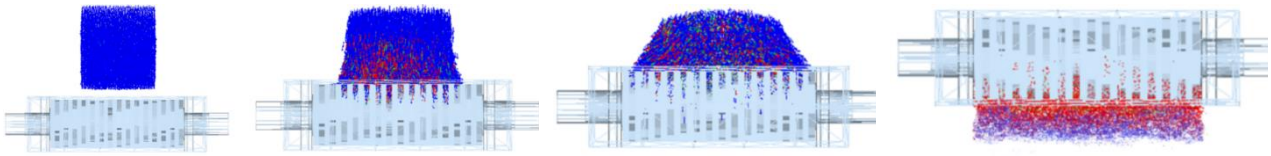

Fig. 4 - Simulation process of round corn stalk crushing

Influence of the number of cutter teeth on the broken rate of straw

The optimal conclusions drawn from the one-way test in Table 2 are described below. The upper roller operates at a rotation speed of 16 r/min, while the lower roller rotates at 14 r/min. The center height difference is set to 585 mm, the cutter thickness is 80 mm, and the number of teeth varies between 5, 6, 7, 8, and 9. A total of five groups of simulation tests are conducted, and the results are depicted in Fig. 5. The experimental findings indicate that the number of cutter teeth has a significant influence on the straw crushing rate ($P > 0.05$). However, it does not have a significant impact on the material crushing rate. Notably, when the experimental factors consist of eight teeth, the material crushing rate of the material block is higher, and the trend of the crushing rate remains relatively consistent throughout the simulation time. On the other hand, when the number of teeth is five, the crushing rate is the lowest, resulting in the poorest crushing effect. Furthermore, the change in material crushing rate is similar between 2 to 3 s when the number of teeth is six. However, there is a significant reduction in material crushing rate during the intervals of 0 to 2 s and 3 to 4.2 s. Although the number of cutter teeth exhibits an increasing trend in material breakage rate, the rate of increase is not substantial. Consequently, the number of cutter teeth is not considered as an investigated factor in the subsequent multi-factor test.

The verification test was conducted following the test method outlined in relevant references (*Yang Tao et al., 2017*), using the material crushing rate as the test index. Crushing rate refers to the percentage of the mass of the material required for composite crushing to the total mass of the original material after crushing treatment, and the ratio of bond breaking is used as the evaluation index of the crushing rate in the simulation test, which is determined by Formula 4.

$$p_p = \frac{n}{N} \times 100\% \quad (4)$$

where:

P_p is material crushing rate, %; n is number of bond breaks; N is total number of bonding keys.

The productivity was calculated using Formula 5.

$$E_0 = \frac{m}{T \cdot p_1} \times 60 \quad (5)$$

where:

E_0 is productivity, kg/(kW·h); P_1 is the total mass of materials, kg; T is Time, min; m is quality, kg.

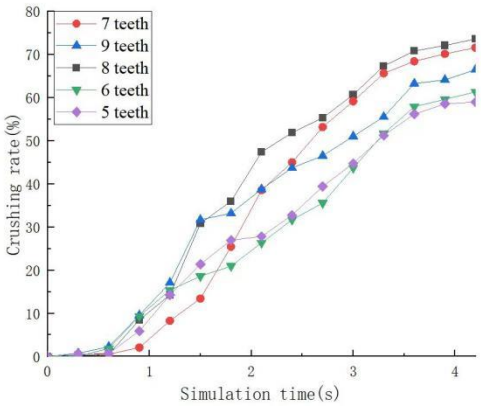

Fig. 5 - Variation curve of particle crushing rate with different cutter teeth

The influence of cut thickness on straw crushing rate

The parameters for the round straw shredder are determined as follows: the rotation speed of the upper roller is 16 r/min, the lower roller is 14 r/min, the center height difference is 585 mm, the number of teeth is 7, and the thickness ranges from 70 to 110 mm with intervals of 10 mm. Five sets of simulation tests are conducted, and the results are presented in Fig. 6. The experimental findings reveal that the thickness of the cutter has a significant impact on the straw crushing rate ($P < 0.05$) as well as the material crushing rate. With the rotation speeds of the upper and lower cutter rolls and the center height difference of the cutter roll kept constant, it is observed that variations in the inner blade thickness between 70 and 80 mm do not significantly affect the test results. However, when the thickness reaches 90 mm, the crushing rate is lower within the 1 to 3-s range compared to other thickness ranges. As the simulation time increases to 3 to 4.2 s, the crushing rate tends to peak at different tool thicknesses. Consequently, the tool thickness can be considered as an investigated factor in the subsequent multi-factor test.

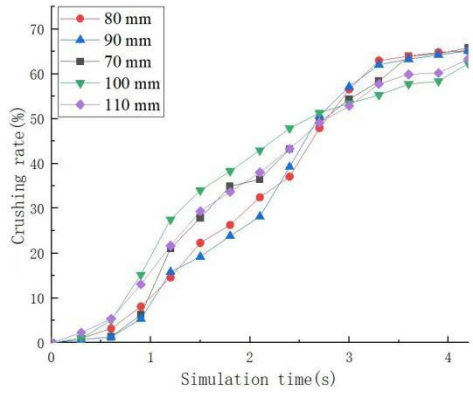

Fig. 6 - Variation curve of particle crushing rate with varying tool thicknesses.

The influence of rotation speed of lower roll on straw crushing rate

A series of simulation tests are conducted with different parameters: the rotation speed of the upper roller is set at 16 r/min, the number of cutter teeth is 7, the center height difference is 585 mm, the cutter thickness is 80 mm, and the rotation speed of the lower roller varies between 10, 12, 14, 16, and 18 r/min. The results of these tests are depicted in Fig. 7. The experimental findings demonstrate that the lower roller speed has a significant influence on the straw crushing rate ($P < 0.05$) and also affects the material crushing rate. When the rotation speed of the lower roller is set at 12, 14, and 16 r/min, the material crushing rate remains relatively stable, outperforming the rates obtained at other rotation speeds. Notably, the highest material crushing rate is achieved at 14 r/min, reaching 82.85%. In contrast, when the rotation speed is 10 r/min, the material crushing rate is significantly lower at 66.86% compared to the rates obtained at other rotation speeds, indicating a relatively poor crushing effect. It is evident that the rotation speed of the lower roller exerts a substantial influence on the material crushing rate, and the rate notably increases within the 1 to 3-s interval as the rotation speed of the lower roller increases. Therefore, the rotation speed of the lower roller will be investigated further as a factor in subsequent multi-factor tests.

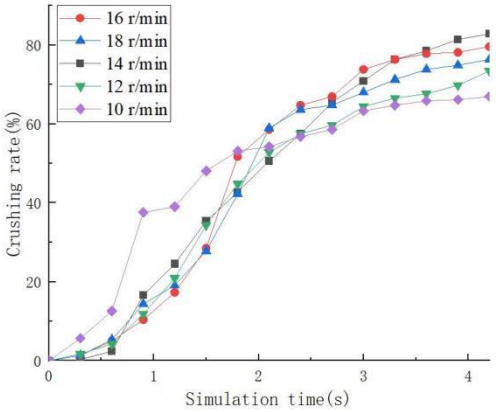

Fig. 7 - Variation curve of particle crushing rate with varying lower roller speeds.

The influence of rotation speed of the top roller on straw crushing rate

It has been established that the rotation speed of the lower roller is 14 r/min, the number of teeth is 7, the center height difference is 585 mm, the tool thickness is 80 mm, and the rotation speed of the upper roller varies between 10, 12, 14, 16, and 18 r/min. Five sets of simulation tests are conducted, and the results are displayed in Fig. 8. The experimental findings indicate that the top roller speed has a significant influence on the straw crushing rate ($P > 0.05$) but does not significantly affect the material crushing rate. Higher rotation speeds of the upper roller, such as 16 and 18 r/min, result in higher material crushing rates, with a trend that aligns with the simulation time. Conversely, a rotation speed of 10 r/min yields the lowest material crushing rate, indicating poor material crushing effectiveness. The change in material crushing rate between 2 and 3 s is comparable to that at 14 r/min; however, the crushing effect is worse than other rotation speeds during the intervals of 0–2 s and 3–4.2 s. Consequently, it is observed that the material crushing rate increases with an increase in the speed of the upper roller, but the impact is not significant. As a result, the rotation speed of the upper roller is not considered an investigated factor in the subsequent multi-factor test.

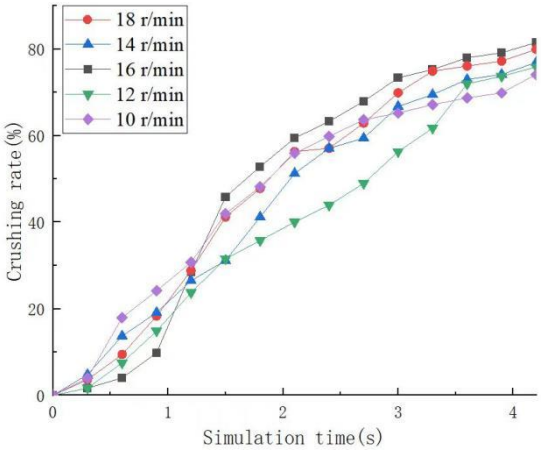

Fig. 8 - Variation curve of particle crushing rate with different rotating speeds of the upper roller

The influence of height difference of knife roll center on straw crushing rate

It is established that the rotation speed of the upper roller is 16 r/min, the lower roller is 14 r/min, the number of teeth is 7, the cutter thickness is 80 mm, and the height difference between the centers of the two cutter shafts varies between 0, 195, 390, 585, and 780 mm. Five sets of simulation tests are conducted, and the results are illustrated in Fig. 9. The experimental findings reveal that the difference in center height of the knife roller has a significant impact on the straw crushing rate ($P < 0.05$) and also influences the material crushing rate. When the height difference between the centers of the two rollers is 390 mm, the material crushing rate reaches its highest value at 82.0%. When the height difference is 195 mm and 585 mm, the change in crushing rate shows no significant variation, and the rates are recorded as 73.4% and 76.3%, respectively. When the center height difference is 0 mm, the material crushing rate is notably lower compared to the rate at 390 mm, and the lowest peak value of the material crushing rate is observed at 780 mm, with a rate of only 66.9%.

Furthermore, when the center height difference is 0, 195, 390, 585, and 780 mm, the material crushing rate exhibits a trend of initially increasing and then decreasing, with the best effect observed when the center height difference ranges from 195 to 585 mm. Consequently, the center height difference of the knife roller is considered an investigated factor in the subsequent multi-factor test.

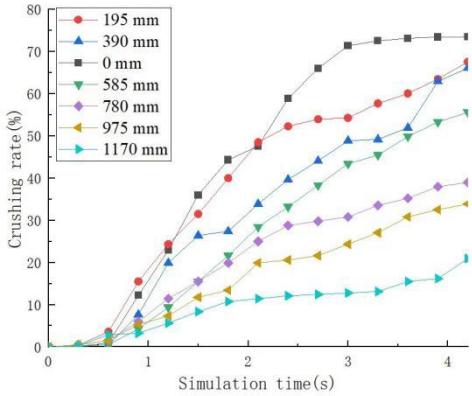

Fig. 9 - Variation curve of particle crushing rate with different center height.

The aforementioned test results demonstrate the significant influence of the center height difference, cutter thickness, and lower roller speed on the material crushing rate ($P < 0.05$). These factors can be considered as important variables for subsequent multi-factor tests.

Scheme design and result analysis of combined test

Test Purpose

(1) To assess the rationality of the structure of the double-roller differential round-baled corn stalk shredder used in this research, and evaluate if the key components meet the specified requirements.

(2) To verify if the crushing efficiency of the shredding device meets the design criteria and desired efficiency.

(3) To determine the optimal structural parameters for the shredding device of the double-roller differential round-baled corn stalk shredder.

Test method and evaluation index

(1) Material crushing rate: This term pertains to the proportion of the required material mass for composite crushing within a single workflow in relation to the total material mass.

(2) Particle passing ratio: This concept indicates the percentage of particles passing through the discharge port within a single workflow relative to the total number of particles in the entire model. Its calculation formula is represented by Formula 6.

$$p_t = \frac{s}{S} \times 100\% \quad (6)$$

where:

P_t is particle passing ratio; s refers to the number of particles passing through a single operation, one; S is total number of particles.

Particle Passing Ratio: is the percentage of the number of particles passing through the outlet in a single workflow compared to the number of particles in the entire model.

Test model

The traditional shredding device exhibits inadequate crushing effectiveness on round straw, with issues such as uneven distribution of cutter utilization benefits and significant loss of certain cutters. To address these concerns, a differential crushing method utilizing two rollers is proposed. This method involves crushing round straw through the relative rotation of the crushing cutter roller, while simultaneously enabling automatic transportation due to the substantial mass of the straw itself, thereby enhancing work efficiency. The differential-roller-type bale breaking device is employed to break and preliminarily crush round-packed corn stalks, facilitating subsequent processing. Optimizing the design of the round-packed straw shredding device is instrumental in improving the effective utilization rate of round-packed corn stalks. To achieve this, the following design requirements are presented for the shredding device:

(1) The straw material should be effectively and preliminarily broken, ensuring a successful bag-breaking outcome.

(2) The bag-breaking device should be equipped with a motor capable of meeting production requirements through the designed rotation speed.

(3) The occurrence of blockages should be avoided.

(4) The preliminarily crushed material should meet the processing and application requirements, such as achieving a crushing rate of 60% for incineration power generation.

(5) The cutter chamber of the device should possess a simple structure, exhibit high working efficiency and reliability, and maintain optimal working conditions continuously.

The frame is connected to the bottom of the motor and the bottom of the reducer through connecting plates on both sides, while the top of the steel structure in the middle of the frame is fixedly connected to the bottom of the cutter chamber main body using connecting plates. One end of the motor's output shaft is firmly connected to one end of the reducer's input shaft through a coupling, and the other end of the reducer's output shaft is fixedly connected to the cutter shaft via a coupling. The cutter shaft extends from the reducer through the machine body and is rotatably connected to one side of the inner wall of the cutter chamber body using a bearing. The outlet is axially secured with an end cover. On the inner surface of the cutter shaft within the main body of the chassis, the cutter and spacer are firmly attached. A second cutter shaft, positioned symmetrically with the first cutter shaft along the centerline, is mounted between the two sides of the inner wall of the chassis and on one side of the cutter shaft. The two shafts extend through the machine body to one side of the chassis. There is no noticeable difference between the top and bottom of the chassis body. Typically, the top surface is used as the inlet, and the bottom as the outlet. The distance between the center lines of the cutter shafts measures 420 mm, as depicted in Fig. 10, when compared to the actual equipment.

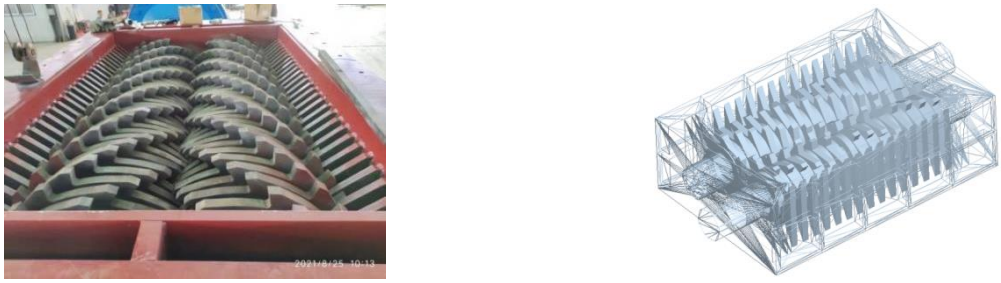

Fig. 10 - Shredding device comparison diagram

After analyzing the results of the single-factor tests and reviewing relevant literature, three significant factors were identified for further investigation: the height difference of the cutter roller center, the cutter thickness, and the rotating speed of the lower roller. The evaluation indexes used were the crushing rate of the round-packed corn straw material model and the particle passing ratio in a single operation. Taking into account the device design and the results of the single-factor tests, and considering real-world working conditions, the levels of the various factors were determined as outlined in Table 3.

Table 3

Test factor level table

level	parameter		
	Center height difference[mm]	Tool thickness[mm]	Lower roller speed[rpm]
-1	195	90	12
0	390	100	14
1	585	110	16

RESULTS

Test scheme and results

Based on the findings from previous single-factor simulation tests and relevant research on differential roller equipment both domestically and internationally, and considering the practical production requirements, the following parameters have been determined: the rotational speed of the upper cutter roller is set at 16 r/min, while the lower cutter roller's speed ranges from 10 to 16 r/min.

The cutter thickness is set between 70 mm and 110 mm to align with operational needs, and the number of cutter teeth is fixed at 7. Additionally, considering the material's structural characteristics and test results, the optimal range for the height difference between the centers of the two rollers is established as 70 mm to 90 mm.

By assessing the significance of each index and establishing the relationships among the factors, the optimal parameter combination for the roller differential speed package breaking equipment has been determined. The test factors are represented by the codes shown in Table 4, and the corresponding test results are presented in Table 5. X_1, X_2, and X_3 denote the coded values of the factors.

Table 4

Test scheme and results

No.	Center height difference / [mm]	Tool thickness / [mm]	Lower roller speed / [rpm]	Material crushing rate / [%]	Particle passing ratio / [%]
1	-1	-1	0	86.24	96.07
2	-1	1	1	88.99	95.44
3	1	0	1	89.46	97.3
4	-1	0	-1	90.77	95.73
5	0	1	-1	89.34	97.52
6	1	0	-1	87.84	95.14
7	0	0	0	88.99	96.47
8	1	0	-1	84.54	95.46
9	0	0	0	91.1	96.74
10	0	0	0	90.24	97.46
11	0	0	0	93.31	98.02
12	0	-1	1	92.17	97.1
13	0	0	0	92.21	96.67
14	-1	1	0	88.01	94.76
15	1	-1	0	90.31	96.64
16	0	0	0	90.12	98.01
17	0	1	1	93.48	98.62

Table 5

Significance test results of regression relationship of material crushing rate

Source of variation	Sum of square	Degree of freedom	Mean square	F value	P value	Significance
Model	66.31	9	7.37	5.63	0.0164	*
X_1	8.29	1	8.29	6.34	0.0399	*
X_2	1.35	1	1.35	1.03	0.3429	
X_3	4.82	1	4.82	3.69	0.0963	
X_1X_2	4.49	1	4.49	3.44	0.1062	
X_1X_3	11.22	1	11.22	8.58	0.0220	*
X_2X_3	2.71	1	2.71	2.07	0.1935	
X_1^2	24.81	1	24.81	18.97	0.0033	**
X_2^2	3.66	1	3.66	2.08	0.1382	
$X_1X_2^2$	11.66	1	11.66	8.92	0.0203	*
Residual	9.15	7	1.31			
Lack of Fit	1.76	3	0.59	0.32	0.8113	
Pure Error	7.38	4	1.84			
Sum	75.46	16				

Establishment of Regression Model and Analysis of Variance

As shown in Tables 5 and 6, the regression coefficient test results reveal significant effects of the primary term X_1 and the quadratic terms X_1X_3 and $X_1X_2^2$ on crushing rate X ($P < 0.05$). Additionally, the quadratic term X_1^2 exhibits an extremely significant effect on crushing rate X ($P < 0.01$). Furthermore, the quadratic term $X_1^2X_2$ has a significant effect on the particle passing ratio Y ($P < 0.05$), and the quadratic term X_1^2 significantly affects the particle passing ratio Y ($P < 0.01$). From Tables 4–4 and 4–5, it can be observed that the model's p-value for crushing rate X is 0.0164, and the p-value for the particle passing ratio Y is 0.0174. Both values are less than 0.05, indicating the significance of the model. On the other hand, the missing items have p-values of 0.8113 and 0.9201, respectively, which exceed 0.05, suggesting their lack of significance.

The difference between the determination coefficient R^2 and the adjusted R-squared (R_{Adj}^2) is less than 0.2, confirming the reliability of the model. Consequently, the regression model can effectively analyze and predict the data related to the test target.

Table 6

Results of significance test of regression relationship of particle passing ratio

Source of variation	Sum of square	Degree of freedom	Mean square	F value	P value	Significance
Model	13.66	9	1.52	5.51	0.0174	*
X_1	0.99	1	0.99	3.61	0.0994	
X_2	0.44	1	0.44	1.58	0.2490	
X_3	0.38	1	0.38	1.39	0.2771	
X_1X_2	0.01	1	0.01	0.03	0.8615	
X_1X_3	0.86	1	0.86	3.10	0.1215	
X_2X_3	0.15	1	0.15	0.55	0.4818	
X_1^2	8.17	1	8.17	29.66	0.0010	**
X_2^2	0.46	1	0.46	1.66	0.2389	
$X_1^2X_2$	2.13	1	2.13	7.73	0.0273	*
Residual	1.93	7	0.28			
Lack of Fit	0.20	3	0.068	0.16	0.9201	
Pure Error	1.73	4	0.43			
Sum	15.61	16				

Influence of interaction of test factors on response index

To provide a more visual representation of the interaction among the test factors, response surface analysis of the regression model was conducted using Design Expert software. The resulting response surface charts, shown in Fig. 11 and 12, illustrate the impact of the interaction between the center height difference of the cutter roller, the cutter thickness, and the rotation speed of the lower roller on both crushing rate and the particle passing ratio. By setting one of the factors to zero and analyzing the influence of the other two factors on crushing rate and particle passing ratio, the response surface analysis reveals the trend and effect of each factor on the test results.

The influence of various factors on crushing rate is shown in Fig. 11.

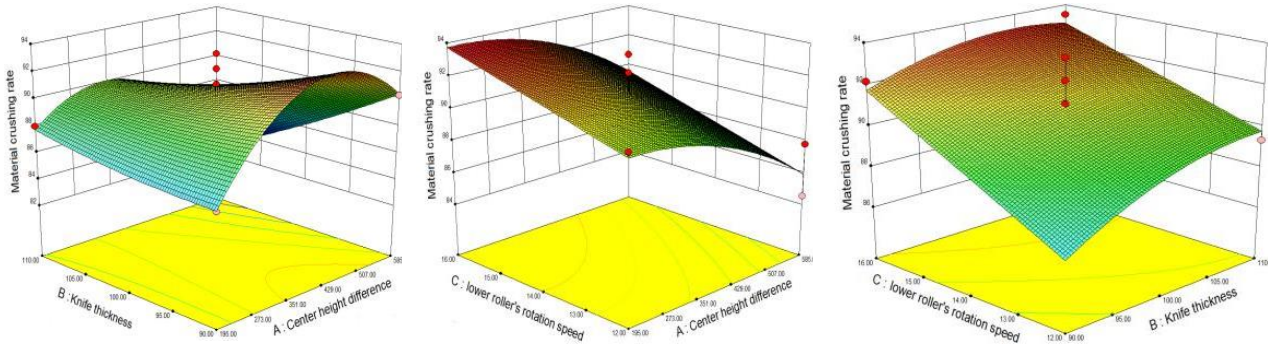

Fig. 11 - Effect of interaction of factors on bond fracture rate

Fig. 11 illustrates the impact of the interaction between the center height difference of the cutter roller and the cutter thickness on the bonding fracture rate, with the rotation speed of the lower roller set at the central value. As the center height difference increases and the cutter thickness decreases, the bonding fracture rate initially increases and then decreases. Similarly, the interaction between the center height difference of the cutter roller and the rotation speed of the lower roller influences the bonding fracture rate, with an increasing trend observed as the difference in center height and rotation speed increases. Likewise, when considering the interaction between the cutter thickness and the rotation speed of the lower roller, a higher bonding fracture rate is observed as the cutter thickness and rotation speed decrease.

The response surface depicting the influence of each factor on the particle passing ratio is displayed in Fig. 12.

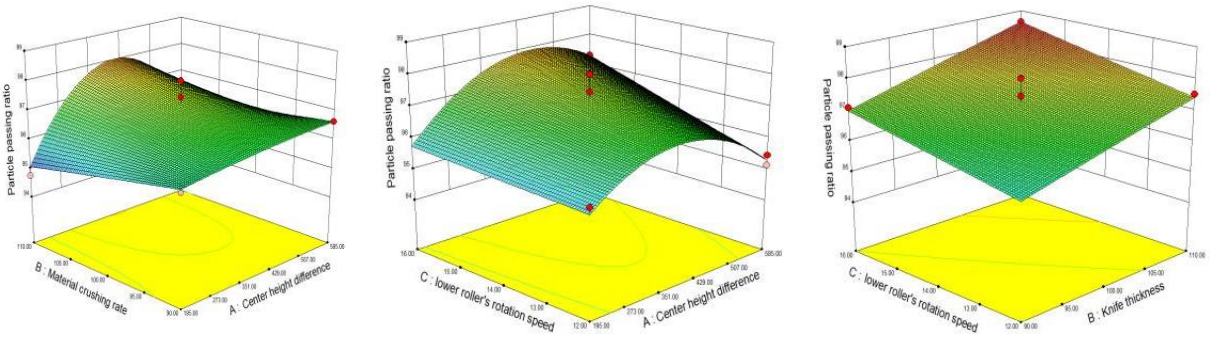

Fig. 12 - Effect of interaction between factors on particle passing ratio.

Fig. 12 illustrates the impact of the interaction between the center height difference of the knife roller and the knife thickness on the particle passing ratio when rotation speed of the lower roller is at the center position. As the height difference between the center of the cutter roller increases and the cutter thickness decreases, the particle passing ratio initially increases and then decreases. Similarly, the interaction between the height difference of the cutter roller center and the rotation speed of the lower roller influences the particle passing ratio, showing an increasing trend as the height difference and rotation speed increase. Furthermore, the interaction between the cutter thickness and the rotation speed of the lower roller affects the particle passing ratio, with a decreasing cutter thickness and an increasing rotation speed leading to an upward trend in the particle passing ratio.

Parameter optimization and verification

By considering the height difference between the center of the cutter roller (X_1), the thickness of the cutter head (X_2), and the rotation speed of the lower roller (X_3) as constraints, and the number of bond breaks (X) and the particle passing ratio (Y) as objectives, a structural optimization parameter model for the round corn stalk breaking device is established. The calculation method for the model is presented in Formula7.

$$\begin{cases} maxX \\ maxY \\ 195 \le X_1 \le 585 \\ 70 \le X_2 \le 110 \\ 12 \le X_3 \le 16 \end{cases} \quad (7)$$

After optimizing the regression equation, the optimal combination of parameters for the round corn stalk breaking device is determined as follows: a height difference of 390 mm between the center of the cutter roller, a cutter head thickness of 110 mm, and a rotation speed of the lower roller at 14 r/min.

Based on the optimized parameter combination, a crushing test is conducted on the straw round bale. Through analysis of the test results, the Design-Expert software is utilized to further optimize the three test factors within their respective ranges. The optimal process parameters are determined as follows: a center height difference of 390 mm, a cutter thickness of 110 mm, and a lower roller speed of 14 r/min.

Under these optimal conditions, the shredder achieves the best crushing effect, with a bond crushing rate of 93.48% and a particle passing rate of 98.62%. The details of the test scheme can be found in Table 7.

Table 7

Results of significance test of regression relationship of particle passing ratio

Name	value
Center height difference of knife roller [mm]	390
Cutter head thickness [mm]	110
Lower roller speed [rpm]	14

The experiment was conducted three times using the optimal parameter combination, and the crushing rate and working efficiency rate of the material were measured. The average values were calculated, resulting in a crushing rate of 93.77% and a working efficiency of 98.52%. The prediction deviation between the experiment and the model described above is within 5%, indicating the reliability of the regression model.

Then with crushing five round-packed corn stalks, the following conclusions were drawn:

Five rounds of bench tests were conducted to crush round-packed corn stalks, and the figure illustrates the comparison between the crushed materials and the simulation results.

The material crushing rates were 94.63%, 93.95%, 95.12%, 92.16%, and 94.01%, respectively, with an average of 93.97%. Using the simulation test results as a benchmark, the results were subjected to a T-test in Origin software, yielding a P-value of 0.705 (>0.05), confirming the reliability of the test results. The productivity values were 5125.7 kg/h, 5336.2 kg/h, 5203.1 kg/h, 5107.4 kg/h, and 5259.6 kg/h, respectively, with an average of 5206.4 kg/h. Compared to the traditional double-roller structure, the double-roller differential corn stalk round bale breaking device proposed in this study demonstrates improvements in material crushing rate and productivity.

CONCLUSIONS

In this study, a breaking device based on double-roller structure was designed considering the unique external surface profiles and interior tissue of straw bale, combined with knowledge of agricultural mechanics, agricultural engineering, materials science, and other fields.

Straw bale was broken during the bale-breaking period, and the bale breaking model was established in stages. The accuracy and scientific nature of the model were verified by comparing the breaking rate collected from conventional breaking with experimental data.

(1) Compared with the existing breaking device, the breaking device with double-roller studied in this paper has the following advantages. A ternary quadratic combination experiment was conducted to determine the best structural parameters of the shredding device for the roller differential round corn stalk shredder. The regression equation was derived, along with an assessment of its impact on the results. The optimal parameters, including a center height difference of 390 mm, tool thickness of 110 mm, and lower roller speed of 14 r/min, were determined and validated through bench testing. Simultaneously, various control groups were established and applied in the subsequent simulation tests to verify the superiority of this structure.

(2) The model parameters of the straw bundle were determined by the factor test. The optimal parameters, including a center height difference of 390 mm, tool thickness of 110 mm, and lower roller speed of 14 r/min, were determined and validated through bench testing. The more the deviation from the above data, the less accurate the results will be. Therefore, a ternary secondary combination experiment was conducted. By defining a reasonable calculation domain in the EDEM calculation could reduce the calculation time without affecting the whole.

(3) This design method can be applied to the design of other breaking parts of agricultural machinery. This approach is not limited to straw bales and has strong generality to solve the problem of efficient utilization of straw. In order to make better use of agricultural mechanics to solve the problem of straw utilization, a database matching a variety of straw organisms with the actual production conditions of more agricultural machinery will be established in the future, so as to provide more inspirations for the design of agricultural machinery from the perspective of agricultural mechanization. This method ignores the anisotropy of components in straw bale because only breaking rate of straw bale was analyzed in this study. Therefore, to make our model closer to the actual soil environment, the next steps will be to add the characteristic parameters of the straw breaking force caused by interior components and to perform further exploration by coupling the ANSYS and EDEM methods.

ACKNOWLEDGEMENT

This study was supported by the Liaoning Provincial Science and Technology Plan Project, (2022JH1/10400017).

REFERENCES

[1] Bou Ali, G. (1993). *Straw bales and straw bale wall systems* (Master's thesis). Tucson, AZ, United States, The University of Arizona.

[2] Carrick, J., & Glassford, J. (1998). Vertical loading, creep, transverse loading, and racking loading on plastered straw-Bale walls, Sydney, Australia, *University of New South Wales*.

[3] Choi, Young, Lee, Chai-Sig, Lee, Jae-Sun. (2012). Comparison of Labor-Saving and Economical Efficiency on Mechanical Transplants of Ginseng Seeding. *The Journal of the Korean Society of International Agriculture*, Vol. 24, pp. 203–206, South Korea.

[4] Feng, T.X. et al. (2016) Optimization design and test research of plug seedings end-effector in greenhouse（温室末端执行器插拔播种的优化设计与试验研究）. *Beijing University of technology*, Beijing/China.

[5] Karayel, D., Canakci. M., Topakci. M., Aktas. A. (2023). Technical evaluation of transplanters' performance for potted seedlings. *Turkish Journal of Agriculture and Forestry*, Vol. 47, pp. 116–123, Turkey.
[6] King, B. (2003). Load-bearing straw bale construction. *Ecological Building Network*.
[7] Kornecki, TS., Kichler, C. (2022). Development of a No-Till Transplanter for Walk-Behind Tractors. *Applied Engineering in Agricultur*e. Vol. 38, pp. 865–872, United States of America.
[8] Luo, S. et al. (2018) Parameter calibration of discrete elemental method for vermicompost substrate based on JKR bonding model. (基于 JKR 粘结模型的蚯蚓粪基质离散元法参数标定). Journal of Agricultural Machinery.
[9] Liu, R. et al. (2022). Numerical Simulation of Seed-Movement Characteristics in New Maize Delivery Device. *Agriculture*, Vol.12, Issue 1944, Switzerland.
[10] Porteus, Sc., Parish, Rl., Wright, Me. (1988). A Mechanical Transplanter for Coastal Marsh Stabilization. *Louisiana Agriculture*, Vol. 31, pp. 12, United States of America.
[11] Rakowski, M. R. (2010). *Structural behaviour of plastered straw bale panels under non-uniform loading* (Doctoral thesis). Kingston.
[12] Walker, P., & Ay, B. (2004). Compression load testing straw bale walls. Bath, UK, *University of Bath*.
[13] Wang, Y. et al. (2022). Design of and Experiment on Reciprocating Inter-Row Weeding Machine for Strip-Seeded Rice. *Agriculture*, Vol.12, Issue 1956, Switzerland.
[14] Wen, Y.S. et al. (2020). Development of insertion and ejection type seedling taking device for vegetable plug seedlings（蔬菜穴盘苗插入顶出式取苗装置研制）. *Transactions of the Chinese Society of Agricultural Engineering*, Vol.36, Issue 22, pp. 96–104, Beijing/China.
[15] Yang, T, et al. (2017) Research on straw crushing technology and equipment（秸秆粉碎技术及设备的研究）. Sichuan Agriculture and Agricultural Machinery.
[16] Yan, D. et al. (2022). Soil Particle Modeling and Parameter Calibration Based on Discrete Element Method. *Agriculture*, Vol.12, Issue 1421, Switzerland.
[17] Yu, W.J. et al. (2020). Parameter Calibration of Pig Manure with Discrete Element Method Based on JKR Contact Model. *AgriEngineering*, Issue 2, pp. 367–377, Switzerland.
[18] Yu, X. et al. (2014) Current Situation and Prospect of Transplanter.（播秧机的未来与展望） *Transactions of the Chinese Society for Agricultural Machinery*, Issue 45, pp. 45–53, Beijing/China.
[19] Zhang, X., et al. (2022). The Design and Experiment of Vertical Variable Cavity Base Fertilizer Fertilizing Apparatus. *Agriculture*, Vol.12, Issue 1793, Switzerland.
[20] Zhou, L. et al. (2022). Analysis and Design of Operating Parameters of Floor-Standing Jujube Pickup Device Based on Discrete Element Method. *Agriculture*, Vol.12, Issue 1904, Switzerland.

TRIBOLOGICAL RESEARCH OF THE CHROME- GRAY CAST IRON COUPLING WITH LUBRICATION IN DIFFERENT ENVIRONMENTS

/

CERCETĂRI TRIBOLOGICE ALE CUPLEI CROM-FONTA CENUȘIE CU LUBRIFIERE ÎN DIFERITE MEDII

Valerian CEREMPEI[1)], Eduard BANARI*[1)], Gheorghe POȘTARU[1)], Lucreţia POPA[2)]

[1)] Technical University of Moldova, Chisinau/ Republic of Moldova;

[2)] National Institute of Research – Development for Machines and Installations Designed for Agriculture and Food Industry – INMA Bucharest

Tel: (+373) 787 81 968 E-mail: edu.banari@gmail.com

DOI: https://doi.org/10.35633/inmateh-70-56

Keywords: *tribological coupling, lubrication, biodiesel, mixed biofuel, coefficient of friction, wear.*

ABSTRACT

In the given article, the results of the tribological research of the chrome-gray cast iron coupling are presented, the friction conditions between the cylinder liner and the compression segment being lubricated in various environments are modeled: diesel (control), pure biodiesel B100 and biodiesel-diesel B20 mixture. It was established that the average values of the coefficient of friction in the chrome-gray cast iron coupling, in the case of using biofuels B20, B100 as the lubricating material, are higher in relation to diesel fuel: by 15.6% for B20 and, respectively, by 23.3% for B100. The values of the total wear of the tribological coupling decreased, in relation to diesel, by 36.8% in the case of lubrication with B20 and by 39.5% - with B100.

REZUMAT

În articolul dat sunt prezentate rezultatele cercetărilor tribologice ale cuplei crom-fonta cenușie, fiind modelate condițiile de frecare dintre cămașa cilindrului și segmentul de compresiune cu lubrifiere în variate medii: motorină (martor), biodiesel pur B100 și amestec biodiesel-motorină B20. S-a stabilit că, valorile medii ale coeficientului de frecare în cupla crom-fonta cenușie, în cazul utilizării biocombustibililor B20, B100 în calitate de materialul lubrifiant, sunt mai înalte în raport cu motorina: cu 15,6% pentru B20 și, respectiv, cu 23,3% pentru B100. Valorile uzurii totale ale cuplei tribologice s-au micșorat, în raport cu motorină, cu 36,8% în cazul lubrifierii cu B20 și cu 39,5% - cu B100.

INTRODUCTION

At present, human society is faced with a variety of problems, the solution of which is imperative. According to the studies of established specialists (*FAO, 2016; Neupane D., et al., 2022; Bojariu R., et al., 2021; Tayari S., et al., 2020; Sun S., and Li K., 2020; Cerempei V., 2016; Schumacher L. G., 1996*), solving these problems requires a series of stringent measures:

- Ensuring food and energy security in the conditions of increased population growth in global society, degradation of soil fertility and depletion of deposits of fossil energy resources;
- Improving the ecological situation that bears the increasing negative impact of global warming caused by the increase in the concentration of greenhouse gases (GHG) in the Earth's atmosphere.

In connection with the exacerbation of the energy and climate crisis, it has become imperative for scientists and manufacturers to resort to the search and assimilation of new types of alternative fuels from renewable energy sources. To this category of fuels belongs the biofuel obtained from vegetable oils and from the residues of the food industry, called biodiesel, which ensures the conservation of GHG greenhouse gases and meets the economic requirements (hourly G_h consumption and specific g_e of fuel in small quantities), ecological and the exploitation techniques of compression ignition engines (CI engines). Biodiesel, or fatty acid methyl ester (FAME), is a liquid biofuel composed of mono-alkyl esters derived from animal or vegetable fats, which is obtained through the transesterification reaction. At the same time, biodiesel possesses the physico-chemical and exploitation properties, which are similar to those of diesel fuel, which allows it to be used in its pure state or mixed with diesel fuel in the combustion chamber, without essential changes in compression ignition engines (*Atabani A. E., et al., 2012; Knothe G., 2017*).

Due to its properties, biodiesel is produced and used to fuel motor vehicles at a constantly increasing rate (*Priya Deora P. S., et al., 2022; Vasiliev I. P., 2009; Dugin G. S., 2010*), being considered as a real alternative for petroleum fuels in different regions of the world – in Europe, on the American continent, in the countries of Southeast Asia (*Benea B. C., 2014; Cheremisinov P. N., 2019; Peterson C. L., et al., 1995*).

The advantages and prospects of biofuel production, as well as evidence of compliance with environmental protection requirements have been demonstrated by the results of multi-year use of biodiesel in different countries of the world (*Esmaeili H. A, 2022; Okoye P. U., et al., 2020; Sun S., and Li K., 2020; Smolinicov M. V., 2020; Geambașu S., 2018; Benea B. C., 2014; Corkwell K. C., et al., 2003; Hăbășescu I. et al., 2009*). According to the estimates of specialists in the field of compression ignition engines (*Jeswani H. K., 2020; Corsini A., et al., 2015; Burnete N., Naghiu A., Marișiu F., et al., 2008*), alcohol esters from vegetable oils appear to be the most promising alternative to fossil fuels.

The analysis of the situation in the field of biodiesel uses for fueling compression ignition engines demonstrates that the existing sources of information (*Hăbășescu I., Cerempei V., et al., 2008; Beșleagă I., 2011; Geambașu S., 2018; Benea B. C., 2014; Markov V. A., et al., 2015; Grekhov L. V., et al., 2015*) contain data on the physico-chemical and exploitation properties of esters (density, kinematic viscosity, cetane number, ignition temperatures, cloudiness, freezing, lower calorific value), the values of which are suitable for combustion in CI engines. Also in the above-mentioned sources, based on production tests, the general information is specified regarding the fact that fueling the engine with biodiesel ensures the reliability of its assemblies at the same level in relation to diesel.

Australian researchers (*Kalam Azad et al., 2019*) studied the tribological characteristics (coefficient of friction *COF*, wear and lubrication stability) on a four-ball tribotester using the ASTM D4172 standard in the environment of ultra-low sulfur diesel and of mixed eco-fuel B20 (20% biodiesel - 80% diesel). Each type of fuel/lubricant was studied for 3600 seconds (1 hour) after break-in and transition periods, the values of the friction coefficient at the end of the steady state friction period were with the lubrication in the diesel medium *COF*=0.09, and in the medium B20- *COF*=0.04. It is necessary to specify that the tribometer with four balls is used to study highly stressed couplings with risks of seizure, the resistance of the lubricant to high pressure being appreciated. In the tribometer with four balls, class I friction torques are used, their interaction occurs, theoretically, at a point with the following parameters: rotation speed - V=0.2-0.5 m/s, load - F≤8 kN, hardness surfaces - 62 HRC.

In internal combustion engines, including CI engines, the chrome-gray cast iron coupling in the compression segment piston-cylinder liner joint largely determines the reliability and durability of their operation. The mentioned coupling belongs to class III, the interaction of the elements occurring at the level of curved, cylindrical surfaces, with alternating movements. Therefore, the friction conditions in the four-ball tribotester do not effectively model the operation of the coupling in the piston ring-cylinder liner joint.

It should be noted that the fuels used in internal combustion engines, including in compression ignition (CI) engines, must have the ability to lubricate the contact surfaces of the movable joints of the parts of the engine equipment. This capacity is important, because it allows the reduction of frictional forces and reduces the wear of the joint surfaces of the tribological couplings: piston segment-cylinder liner, plunger-cylinder, injector-injector. It is known that diesel is obtained from crude oil by refining/distillation, being a mixture of C_nH_m aromatic, naphthenic and paraffinic hydrocarbons, containing from 12 to 20 carbon atoms in the molecules (*Kartashevich A. N., et al., 2014*). Diesel loses its lubricating capacity when sulfur compounds are removed from it (*Glushchenko A. A., 2019*). At the same time, biodiesel is a liquid synthetic fuel that is obtained through the chemical reactions of esterification and transesterification from natural triglycerides (vegetable oils, animal fats), the final product being a methyl ester of fatty acids. The results of previous research demonstrate that biodiesel, unlike diesel, does not require the use of active chemical additives for the proper functioning of the engine, which serve to reduce the probability of calamine deposition on the joined surfaces, of seizure of these surfaces, etc.

Diesel and biodiesel, having different origins and chemical compositions, respectively, demonstrate heterogeneous physicochemical properties (density, viscosity, surface tension of a drop of liquid, etc.). In these circumstances, it is of scientific and practical interest to research the behavior of an important tribological coupling from the CI engines endowment in the environment of diesel (control) and experimental biofuels: pure biodiesel B100, biodiesel-diesel mixtures. From the above-mentioned joints, in our view, the most complex and significant is the one formed by the compression segment and the cylinder liner, because they work at high temperatures (up to 600°C), with alternating loads and being subjected to the corrosive action of the products of burning. Therefore, *the purpose of our research* is to ensure the high values of the reliability and durability of the operation of the CI engine fueled with biofuel by determining the tribological characteristics of the compression segment-cylinder liner joint when they operate in the environment of diesel, biodiesel-diesel mixture, biodiesel.

MATERIALS AND METHODS

Based on the formulated goal, the following **specific objective** of the research was put forward: measuring the values of the coefficient of friction ***f*** between the chromed surface of the body and that of the gray cast iron GCI counterbody, as well as the wear ***U*** of these surfaces with lubrication in the diesel environment (control) and of biofuels (experiment): pure biodiesel B100, mixture B20 (20% vol. biodiesel-80% vol. diesel).

Tribological research was carried out in the specialized laboratory of the Technical University of Moldova on the MVPD-1KPI installation (Fig. 1) according to the method proposed by recognized specialists in the field of tribology (*Azhder V.V. et al., 1988; Croitoru D.M. et al., 1992*). The modeling of the actual operating conditions of the cylinder liner-piston segments coupling was obtained on a reciprocating friction machine with the frequency of n=3 double strokes/sec (180 double strokes/min) according to the scheme represented in figure 2, a. The body investigated (Fig. 2, b) was made in the form of a rectangular parallelepiped from steel 20 GOST 1050-2013 (2C22, EN 10083-2:2006), and the counterbody - from gray cast iron GCI 21 GOST 1412-85; (220, BS 1452:1990) (Fig. 2, c). The width of the side of the counter body, which was in contact with the chrome surface of the body, was 2 mm, while the area of the contact surface in the friction clutch was 20 mm^2.

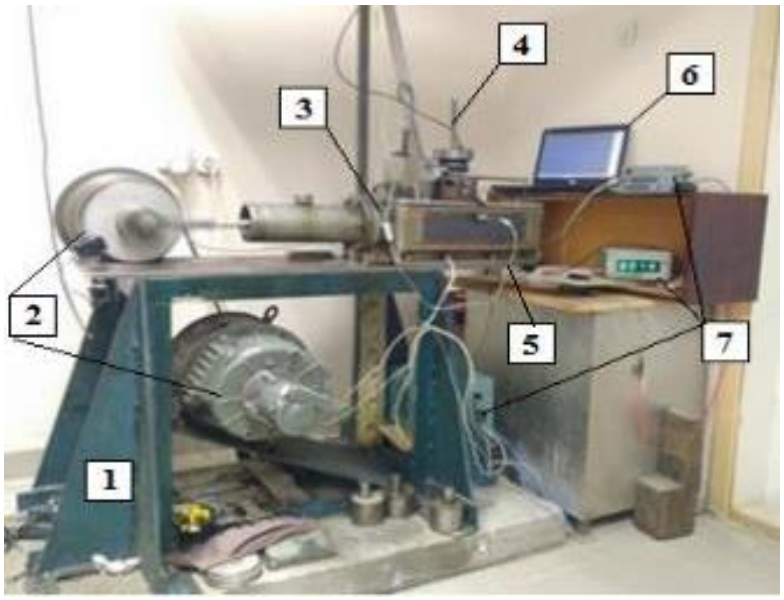

Fig. 1 - Tribological coupling research facility:
1 - frame; 2 - drive unit; 3 - tribological coupling test device with alternative movement; 4 - load loading device; 5 – fuel dosing device; 6 - computer; 7 - block of the electronic software complex

The working surface of the body was covered by the galvanic method with a layer of chrome, having a thickness of 0.1 mm. The contacted surfaces of the body and counterbody had after grinding the roughness R_a=0.20±0.02μm, which is indicated for the working surfaces of the cylinder liner and piston rings. Compliance with the above-mentioned conditions allowed the effective modeling of the operating conditions in the CI engines of the compression segment-cylinder liner coupling to be carried out within the tribological research. The choice of the compression segment for tribological research is argued by the fact that it supports thermo-dynamic loads with the highest values of the entire set of segments.

A drive assembly 2 (Fig. 1) is mounted on the frame 1 of the tribological coupling research facility, which includes the electric motor, the belt drive and the connecting rod-crank mechanism. From the above-mentioned mechanism, the reciprocating movement is transmitted to a tribological coupling testing device 3, where the coupling elements are installed: body and counterbody. Device 4 performs the constant load loading of the tribological coupling elements. The lubricant (researched fuel) is dosed by the device 5. The body with the chrome surface, which imitates the operation of the piston ring, was caught in a special device and performed the reciprocating movements, being driven by an electric motor.

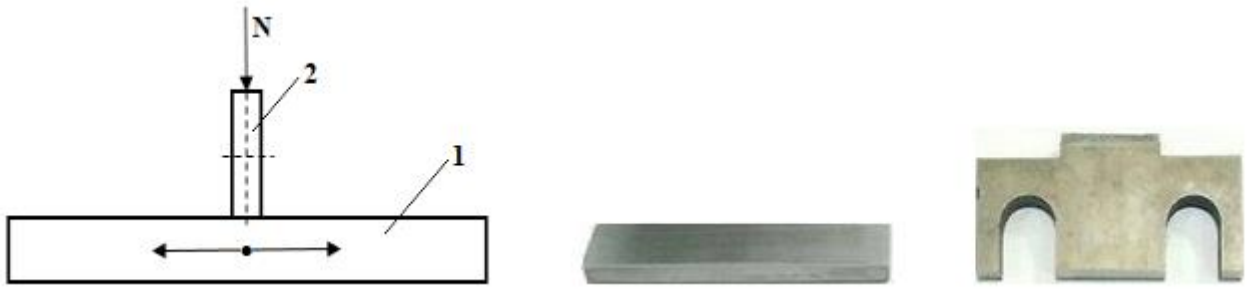

a) b) c)

Fig. 2 - The tribological coupling elements researched

a) tribological coupling research scheme: 1- body, chromed surface; 2- counterbody, GCI
b) body with chrome surface; c) counterbody - gray cast iron

In the entire research process of the tribological coupling in the friction area, the fuel with which the CI engines were fed was dosed in regulated quantities: at stage one - pure diesel; at the second stage - B20 and at the third stage - B100. The load applied to the friction coupling had a value of 20 N. The supplied dose of fuel on the friction surface was one drop every 6 seconds, being provided with the help of a dropper. The duration of each research stage was 400.000 double runs (cycles), with the values of the tribological parameters (number of cycles, temperature in the friction zone, friction force) being recorded with the help of an electronic command and control system (ECCS) equipped with the friction machine. Body and counterbody mass check was done after every 50.000 double runs. The component parts of the ECCS are the respective sensors and transducers, an electronic block 7 (Fig.1), monitored by the corresponding software, with the processor at the base of the laptop 6, Dell Inspiron model. The tribological study was carried out at the ambient temperature t=20±2°C.

Before and after each research cycle of the tribological coupling, the tested samples (Fig. 2 b, c) were weighed using the VLA-200 analytical balance to determine their mass loss (wear). Preventively, before weighing, the body and counterbody were degreased with solutions of Nefras-C50/170 (GOST 8505-80) and sanitary alcohol C_2H_5OH (GOST 5962-2013). The measurement of the microhardness of the chrome surface was carried out according to GOST 9450-76 with the help of a PMT-3 device, the diagonal of the pyramid imprint in the researched material being measured, the applied force having the value of 1N. A diamond pyramid with a square base, having an angle between two opposite side faces of 136°, was used as the indenter. The microhardness value of the chrome surface was determined as the arithmetic mean of 9 measurements and was H_μ=13.44±1.28 GPa (1344±128 kgf/mm^2). The measurement of the surface roughness of the samples was carried out with the help of a profilograph-profilometer, SURTRONIC-25 model (manufacturer - Taylor Hobson, USA).

In order to verify the results obtained in the tribological research, bench research and tests were carried out under the exploitation conditions of compression ignition engines of the DC4 11.0/12.5 type (compression ratio ε=16), fueled with biofuel. It should be noted that agricultural tractors (Belarus brand) are equipped with DC4 11.0/12.5 engines, models D-240, D-241, D-243, which occupy about 52% of their total in agriculture in the Republic of Moldova. During the stand research, the D-241 engine was fueled with diesel (control) and experimental fuels: pure biodiesel B100 and small biofuels B20, B50. In the process of production tests, four D-243 engines were divided into two groups: a) control group (2 units), fueled with diesel fuel; b) the experimental group (2 units), fueled with B20 biofuel. Engine tests were carried out at the "Chetrosu" Didactic Experimental Station, Anenii Noi district, various agricultural works being carried out: preparing the soil before sowing, agricultural crops sowing, care operations for field and perennial crops (protection from diseases and pests, tillage between rows, administration of fertilizers, etc.), various transport works. The volume of work performed by each tractor varied between 647-724 engine-hours, which coincides with the average annual load of a Belarus 82.1 type tractor in the Republic of Moldova.

The assessment of the reliability and durability of the researched and tested engines was carried out based on the measurement of the values of the functional parameters that characterize the technical condition of the engines (engine oil pressure, gas flow rate in the engine crankcase, compression pressure, engine oil consumption during combustion, fuel injection pressure) and the properties of the engine oil in action. The pressures at the end of the compression in the cylinders of the D-241L engines were measured using a compressor (compressometer G-324D), and the oil pressure in the engine lubrication system - with the on-board equipment of the tractors.

Oil consumption during combustion was determined by measuring the volumetric amount of the portion of oil periodically added to the crankcase bath up to the level regulated by the engine manufacturing plant. The operational reliability of the tested engines was determined according to the recommendations of the interstate standard GOST 54783-2011.

The obtained values of the results of the experiments were processed with the application of the facilities of the STATGRAPHICS, MATLAB and Microsoft Office Excel programs.

RESULTS

The obtained values of the friction coefficient in the chrome-gray cast iron tribological coupling confirm the influence of the chemical composition of the lubricating material on the interaction process in the movable joint (Fig. 3). The average values of the coefficient of friction ***f***, in the case of using biofuels B20, B100 as the lubricating material, are higher in relation to diesel (***f***=0.03584): by 15.6% (***f***=0.04244) for B20 and by 23.3% (***f***=0.04675) for B100, respectively. The increase in the friction coefficient in the case of lubrication with the investigated biofuels probably occurred due to their higher viscosity values: B20 has viscosity $\boldsymbol{\mu}$ = 4.43 mm^2/s (9.4% higher), B100 - $\boldsymbol{\mu}$ = 8 mm^2/s (1.98 times higher), than that of diesel fuel - $\boldsymbol{\mu}$ = 4.05 mm^2/s.

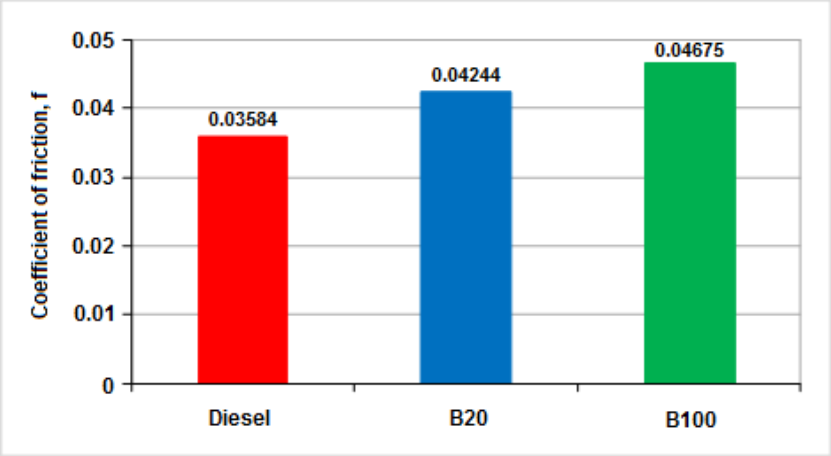

Fig. 3 - The average values of the friction coefficient of the tribological coupling depending on the lubricant used

It is important that at the temperature of the laboratory environment of 20±2°C, with the transition from diesel to B20 mixture and pure B100 biodiesel, the gradient of the increase of the friction coefficient ***f*** is lower than that of the volume fraction (% vol.) of biodiesel in the fuel mixture:

$$\frac{f_d - f_B}{f_d} < \frac{B}{100} \quad (1)$$

where:

f_B, f_d – values of friction coefficients in the biofuel and diesel environment, respectively;

B, %vol – volume fraction of biodiesel mixed with diesel.

As mentioned above, the researchers (*Kalam Azad, et al., 2019*) obtained the following values of the friction coefficient in the studies on a four-ball tribotester: in the diesel environment *COF* = 0.09, and in the B20- environment *COF*=0.04. The values obtained in our research on the car with alternating movements and with the same lubricants are lower for diesel (*COF*=0.036) and equal for B20 (*COF*=0.042). The difference in COF values can be explained by the differences in friction conditions and chemical composition, physico-chemical and exploitation properties of the investigated lubricants.

Our results regarding the values of the kinematic viscosity of diesel and biofuels at 20^{0}C coincide with the results of measurements at the same temperature, presented in the report of the Technical University of Cluj Napoca, 2010. In this report it is demonstrated that increasing the temperature has the effect of decreasing the viscosity of the studied fuels: at the temperature of 70°C the viscosity of diesel and B20M75E5 mixture (20% biodiesel, 75% diesel, 5% ethanol) was $\boldsymbol{\mu}$=1.7 mm^2/s, and that of pure biodiesel B100 decreased to 3.1 mm^2/s. The presented data allow us to assume that the further increase of the temperature in the tribological coupling up to 300-400°C, which happens in the combustion chamber of the engine, will have the consequence of equalizing the viscosities of the studied fuels: diesel, B20 mixture, pure B100 biodiesel. Under these conditions, the friction coefficient in the piston segment-cylinder liner joint can have equal values for the mentioned fuels.

The results of research on the dynamics of wear ***U*** for the elements of the tribological coupling (body - chromed surface and counterbody - cast iron GCI) with the variation of lubricants (diesel, biofuels B20, B100) demonstrate that the dependence of ***U*** values according to the number of cycles ***n*** (research duration ***τ***) obviously carries a rectilinear character (Fig.4). This finding is very important, because it indicates that the wear process in the performed experiments proceeded normally, without mechanical seizure. From the graph it can be seen that, after completing 400 thousand cycles, which is equivalent to 16 km, the wear values of the body – chrome surface, in the B20 biofuel mixture environment, increased by 0.1 mg (by 14.3%) in relation to diesel. At the same time, with the increase in biodiesel concentration up to 100% (B100), a decrease in ***U*** wear by 14.3% (by 0.1 mg) compared to B20 and equal to diesel wear is highlighted. Taking into account the fact that the tribological experiments are carried out under complex conditions and have a multifactorial character, wear being dependent on the physical-mechanical properties of the joined surfaces, the physical-chemical properties of the lubricating materials, the state of the environment, it can be found that, in cases of the use of different lubricants (diesel, B20, B100) the differences identified in the values of body wear with the chrome surface (Δ=±0.1mg) throughout the duration of the research are not large.

The wear values of the tribological coupling element, counterbody, from gray cast iron GCI, demonstrate that, after achieving 400 thousand friction cycles with the use of biofuels B20 and B100 as lubricants, the total wear of the counterbody (*U*≈1.7 mg) in both cases has lower values compared to wear in the diesel environment (*U*=3.1 mg) (Fig.4). The results of concrete measurements indicate that, in the case of using biofuels B20 and B100 for surface lubrication, the wear value *U* of the GCI counterbody decreased by 48.4% and 45.2%, respectively, in relation to the wear value of the diesel-lubricated counterbody.

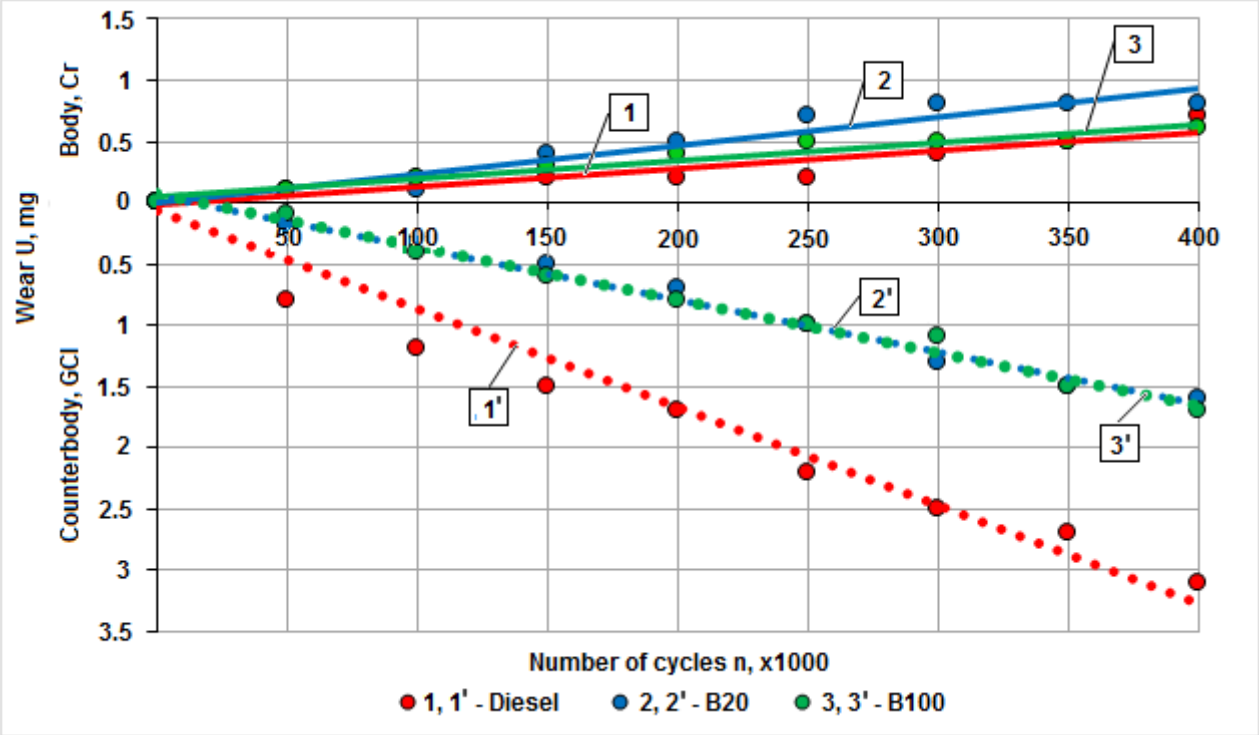

Fig. 4 - Dynamics of wear of tribological coupling elements with the use of different lubricants (diesel, biofuels B20, B100)

The character of the dynamics of the total wear U_t of the tribological coupling depending on the number of cycles ***n*** demonstrates that the exploitation of the tribological coupling with the use of biofuels B20 and B100 as lubricant ensures the lower values of the total wear U_t in relation to the case of lubrication in the diesel environment (Fig. 5). For example, in the friction process of the tribological coupling with the use of biofuels for lubrication, the total wear values U_t of the body - chrome surface and the counterbody - gray cast iron GCI, for the entire duration of the research, decreased by 36.8% for the B20 case (U_t *=2.4 mg*) and, respectively - by 39.5% for the case of B100 (U_t*=2.3 mg*) in relation to lubrication in the diesel medium (U_t*=3.8 mg*). The substantial decrease in total wear of the tribological coupling in the case of lubrication with B20, B100 biofuels is probably due to the chemical composition as well as the higher viscosity of the biodiesel, which overall improves the lubrication properties of the pure B100 biodiesel and the biodiesel-blend diesel B20.

It is important that mixing biodiesel with diesel in a ratio of 20:80 has a synergistic effect, because the value of total wear U_t of the tribological coupling elements with the use of B20 blend and pure B100 biodiesel as a lubricant does not differ much and is equal to U_t=*2.4 mg* and with U_t=*2.3 mg*, respectively.

So, the tribological research carried out demonstrated the veracity of our hypothesis regarding the positive impact of the lubricating material from biofuels (pure biodiesel B100 and biodiesel-diesel mixture B20) on the friction process in the tribological coupling chrome surface - gray cast iron. The given hypothesis was based on the results of studies of the physical-chemical and operational properties of the above-mentioned fuels.

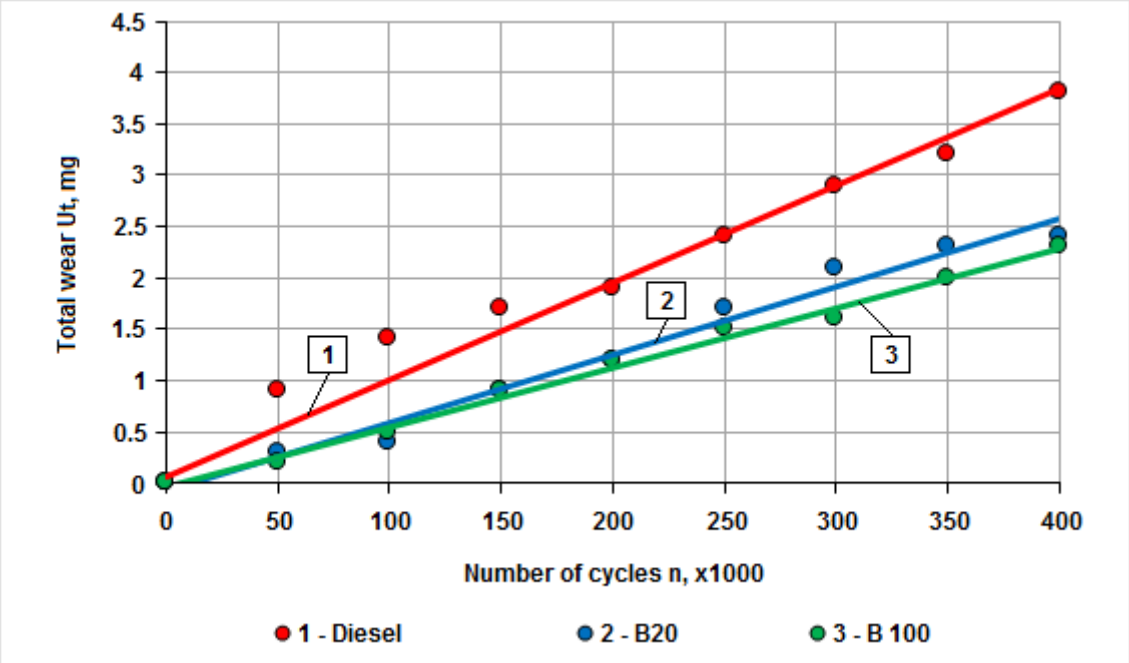

Fig. 5 - Dynamics of the total wear of the tribological coupling with the use of different lubricants (diesel, biofuels B20, B100)

The results of bench research of the D-241 engine and production trials of the D-243 engines confirm the positive impact of biofuels on the parameters of operational reliability and durability. The values of the functional parameters of the D-243 engines, subjected to tests under the conditions of agricultural production, being fed with diesel fuel and B20 mixture, indicate that the technical condition of the engines was stable and in accordance with the operating rules, submitted by the manufacturing plant in Minsk. The functional parameters that characterize the technical condition of the tested engines had the following values: coolant temperature - ≤85-90ºC, oil temperature in the engine crankcase bath - ≤ 75-82 ºC, engine oil pressure – 0.30-0.32 MPa, gas flow rate in the engine crankcase - 79-81 l/min, compression pressure – 19.5-21.3 MPa, engine oil consumption during combustion - 112...137 g/h, fuel injection pressure – 17.5-18.0 MPa. The physico-chemical and exploitation properties of the engine oil in action (kinematic viscosity, alkalinity, sulfated ash content) changed in the process of production trials equally in engines fueled with diesel and mixed biofuel B20.

CONCLUSIONS

1. It was established based on tribological research that the average values of the coefficient of friction in the chrome-gray cast iron coupling, in the case of using biofuels B20, B100 as the lubricating material, are higher in relation to diesel: by 15.6% for B20 and by 23.3% for B100, respectively.

The increase in the coefficient of friction in the environment of the investigated biofuels probably occurred due to the higher values of their viscosity.

2. The values of the total wear U_t of the tribological coupling for the entire duration of the research decreased, in relation to the lubrication in the diesel medium, by 36.8% for the B20 case and by 39.5% for the B100 case. The substantial decrease in total wear of the tribological coupling in the case of lubrication with B20, B100 biofuels is probably due to their chemical composition, as well as their higher viscosity, which overall improves the lubrication properties of B100, B20 biofuels.

3. The results of bench research and production trials confirm the positive impact of biofuels B20, B100 on the parameters of reliability and durability of operation of compression ignition engines.

REFERENCES

[1] Atabani, A. E., et al. (2012). A comprehensive review on biodiesel as an alternative energy resource and its characteristics. *Renewable and Sustainable Energy Reviews.* Vol.16, № 4, pp. 2070-2093. https://doi.org/10.1016/j.rser.2012.01.003.

[2] Azhder, V.V., Drozdov, Iu N., Komendant, et al., (1988). The main laws of friction, lubrication and seizing during accelerated and decelerated cyclic sliding. (Основные закономерности трения, смазки и заедания при ускоренном и замедленном циклическом скольжении). *Friction and wear*, № 4, v.9, (*Трение и износ)*, № 4, v.9, pp. 581-591) (*in Russian)*

[3] Benea, B.C. (2014). Research on the use of biofuels for motor vehicle engines. (*Cercetări privind utilizarea biocarburanților pentru motoarele de autovehicule).* [Doctoral dissertation, University of Brașov]. 92 p. *(in Romanian)*

[4] Beșleagă; Ig. (2011). *The energetic and ecological performances of compression ignition engines fueled with various types of fuels*. (*Performanţele energetice şi ecologice ale motoarelor cu aprindere prin comprimare alimentate cu diverse tipuri de combustibili*). [Doctoral dissertation, State Agrarian University of Moldova, Chișinău. 130 p. *(in Romanian)*

[5] Bojariu, Roxana, Boincian, B., et al.; coordonator: Hurmuzachi, Iurie. (2021). *Best practice guide to adapting to climate change and implementing climate change mitigation measures in the agricultural sector (Ghid de bune practici întru adaptarea la schimbările climatice și implementarea măsurilor de atenuare a schimbărilor climatice în sectorul agricol)* / UCIP IFAD. Ed. Print-Caro, Chișinău, 2021- 120p. ISBN 978-9975-56856-2 *(in Romanian).* *http://dspace.uasm.md/bitstream/handle/123456789/6570/Ghid_agricultura_web.pdf?sequence=1&isAllowed=y*

[6] Burnete, N., Naghiu, A., Marișiu, F., Cecilia, R., Deac, T., et al. (2008). *Diesel and biofuel engines for urban transport*. (*Motoare diesel și biocombustibili pentru transportul urban).* Mediamira Publishing House, Cluj-Napoca, 1058 p. ISBN 978-973-713-217-8. *(in Romanian)*

[7] Cerempei, V. (2016). *Technology and technical means of production and use of biofuels based on monoatomic alcohols*: (*Tehnologia și mijloacele tehnice de producere și utilizare a biocombustibililor în baza alcoolilor monoatomici)* [Doctoral dissertation. ITA Mecagro-UASM, Chisinau] [Tz. de doct. habilitat în tehnică. ITA Mecagro-UASM, Chișinău]. 239 p. http://www.cnaa.md/files/theses/2016/50722/valerian_cerempei_thesis.pdf. *(in Romanian)*

[8] Cheremisinov, P. N. (2019). *Increasing the applicability limit of alternative fuels with rapeseed oil additives in automotive diesel engines* (Увеличение предела применяемости альтернативных топлив с добавками рапсового масла в автотракторных дизелях). [Doctoral dissertation, University of Nizhnii Novgorod], 133 p. https://www.dissercat.com/content/uvelichenie-predela-primenyaemosti-alternativnykh-topliv-s-dobavkami-rapsovogo-masla-v-avtot *(in Russian)*

[9] Corkwell, K. C., et al. (2003). Review of Exhaust Emissions of Compression ignition Engines Operating on E Diesel Fuel Blends. *SAE Technical Paper 2003-01-3283*. ISSN: 0148-7191, p. 1-16. DOI: https://doi.org/10.4271/2003-01-3283.

[10] Corsini, A., Marchegiani, A., Rispoli, F., Sciulli, F., Venturini, P. (2015). Vegetable Oils as Fuels in Diesel Engine. Engine Performance and Emissions*. Energy Procedia.* vol. 81, pp. 942-949. https://doi.org/10.1016/j.egypro.2015.12.151.

[11] Dugin, G. S. (2010). The use of bioethanol fuel in vehicles (Применение биоэтанольного топлива на автотранспорте). *Alternative fuel transport* (*Транспорт на альтернативном топливе*), № 5 (17), pp. 48-51. https://cyberleninka.ru/article/n/primenenie-bioetanolnogo-topliva-na-avtotransporte.pdf

[12] Esmaeili, H. A (2022). Critical review on the economic aspects and life cycle assessment of biodiesel production using heterogeneous nanocatalysts. *Fuel Processing Technology.* Vol. 230, https://doi.org/10.1016/j.fuproc.2022.107224.

[13] Geambașu, S. (2018). *Research on the influence of biofuels on the ecological and energetic behavior of compression ignition engines* (*Cercetări privind influența biocombustibililor asupra comportamentului ecologic și energetic al motoarelor cu aprindere prin comprimare).* [Doctoral dissertation, University of Brașov] 108 p. https://www.unitbv.ro/documente/cercetare/doctorat-postdoctorat/sustinere-teza/2018/sanda-geambasu/02_REZUMAT_TEZA.pdf *(in Romanian)*

[14] Glushchenko, A. A. (2019). *Study of the quality of fuels and lubricants and the use of alternative fuels (Исследование качества топливо-смазочных материалов и применение альтернативных видов топлив)* / A.A. Glushchenko – Ulianovsk: UlGU, 318 p. *(in Russian)*

[15] Grekhov, L. V., Markov, V. A., Devianin, S. N., Bykovskaia, L. I. (2015). Research on the fuel supply process of a diesel engine operating on mixtures of diesel fuel and rapeseed oil methyl ester (Исследования процесса топливоподачи дизеля, работающего на смесях дизельного топлива и метилового эфира рапсового масла). *AutoGas Filling Complex + Alternative Fuel. NGV fuel АвтоГазоЗаправочный Комплекс + Альтернативное Топливо. Газомоторное топливо*), № 7, ISSN 2073-8323, p. 21-30. https://www.mashin.ru/files/2015/agzk7_15_min.pdf *(in Russian)*

[16] Hăbășescu, I., Cerempei, V., et al. (2009). *Biomass energy: Technologies and technical means. (Energie din biomasă: Tehnologii și mijloace tehnice)*. Bons Offices, Chișinău, 368 p. ISBN 978-9975-80-301-4. *(in Romanian)*

[17] Jeswani, H. K., Chilvers, A., Azapagic, A. (2020). Environmental sustainability of biofuels: A review. *Proceedings of the Royal Society. A.* Vol. *476*, https://doi.org/10.1098/rspa.2020.0351.

[18] Kalam Azad, M.G. Rasul, M.M.K. Khan, Subhash C. Sharma (2019). Ecofuel and its compatibility with different automotive metals to assess diesel engine durability. *Advances in Eco-Fuels for a Sustainable Environment*, pages 337-351. ISBN 978-0-08-102728-8. https://doi.org/10.1016/B978-0-08-102728-8.00012-7.

[19] Kartashevich, A. N. Tovstyka, V. S. Gordeenko, A. V. (2014). *Fuel, lubricants and technical fluids (Топливо, смазочные материалы и технические жидкости)* Minsk: Novoe znanie; M.: INFRA-M, 421 s. https://www.polessu.by/sites/default/files/sites/default/files/02per/03document/014.pdf

[20] Knothe, G. Biodiesel fuels (2017). *Progress in Energy and Combustion Science.* Vol. *58,* 2017, p. 36-59. https://doi.org/10.1016/j.pecs.2016.08.001.

[21] Croitoru, D. M., Gurianov, V, V., Azhder, V. V., Cheban, V. F., Poshtaru, G. I. (1992). Tribological properties of iron-carborundum composite galvanic coatings. (Трибологические свойства композиционных гальванических покрытий железо-карборунд.) *Bulletin of the Academy of Sciences of the Republic of Moldova. Physics and Engineering,* (*Buletinul Academiei de Științe a Republicii Moldova. Fizica și tehnica), nr. 3,* p. 89-95. *(in Russian)*

[22] Markov, V. A., Stremiacov, A. V., Devianin, S. N., Neverova, V. V. (2015). *Indicators of toxicity of exhaust gases of a diesel engine running on multicomponent mixed biofuels. Security in the technosphere* (Показатели токсичности отработавших газов дизельного двигателя, работающего на многокомпонентных смесевых биотопливах). Безопасность в техносфере, №*5*. pp. 1-13 https://vestnik.astu.org/temp/4e06af8c3f7150d2e6e8eec79b34c48d.pdf *(in Russian)*

[23] Neupane, D., Adhikari, P., et al. (2022). Does Climate Change Affect the Yield of the Top Three Cereals and Food Security in the World? *Earth. Vol. 3,* p. 45-71. https://doi.org/10.3390/earth3010004.

[24] Okoye, P. U., Longoria, A., Sebastian, P. J., Wang, S., Li, S., Hameed, B. H. (2020). A review on recent trends in reactor systems and azeotrope separation strategies for catalytic conversion of biodiesel-derived glycerol. *Science of the Total Environment.* Vol. 719, https://doi.org/10.1016/j.scitotenv.2019.134595.

[25] Peterson, C. L., Reece, D. L., Hammond, B. et al. (1995). Commercialization of Idaho Biodiesel (HySEE) from Ethanol and Waste Vegetable Oil. *ASAE Paper.* № 956738. pp. 1-6.

[26] Priya, Deora, P. S., Verma, Y., Muhal, R. A., Goswami, C., Singh, T. (2022). Biofuels: An alternative to conventional fuel and energy source. *Mater. Today Proc.* Vol. 48, pp. 1178-1184. https://doi.org/10.1016/j.matpr.2021.08.227.

[27] Schumacher, L. G., Borgelt, S. C., Fosseen, D., Goetz, W., Hires, W. (1996). Heavy-duty engine exhaust emission tests using methyl ester soybean oil/diesel fuel blends. *Bioresource. Technology.* Vol*.* 57, pp. 31-36. https://doi.org/10.1016/0960-8524(96)00043-0.

[28] Smolnikov, M. V. (2020). *Improving the applicability of alternative fuels with ethanol additives in automotive diesel engines*. (Улучшение показателей применяемости альтернативных топлив с добавками этанола в автотракторных дизелях). [Doctoral dissertation, University of Kirov] 173 p. https://www.dissercat.com/content/uluchshenie-pokazatelei-primenyaemosti-alternativnykh-topliv-s-dobavkami-etanola-v-avtotrakt *(in Russian)*

[29] Sun, S., LI, K. (2020). Biodiesel production from phoenix tree seed oil catalyzed by liquid lipozyme TL100L. *Renewable Energy.* Vol. 151, pp. 152-160. https://doi.org/10.1016/j.renene.2019.11.006

[30] Tayari, S., Abedi, R., Rahi, A. (2020). Comparative assessment of engine performance and emissions fueled with three different biodiesel generations. *Renewable Energy.* Vol. 147, pp. 1058-1069. https://doi.org/10.1016/j.renene.2019.09.068.

[31] Vasilev, I. P. (2009). *The influence of vegetable origin fuels on the environmental and economic performance of a diesel engine. (Васильев, И. П. Влияние топлив растительного происхождения на экологические и экономические показатели дизеля, Восточноукраинский национальный университет имени Владимира Даля*. *East Ukrainian National University - Lugansk*, 2009. 240p.). ISBN 978-966-590-726-8. *(in Russian)* https://www.studmed.ru/vasilev-i-p-vliyanie-topliv-rastitelnogo-proishozhdeniya-na-ekologicheskie-i-ekonomicheskie-pokazateli-dizelya_450d2701923.html

[32] ***Organization of the United Nations (FAO) (2016). *The State of Food and Agriculture: Climate change, Agriculture and Food security Food and Agriculture*., Rome, 194 p. ISBN 978-92-5-109374-0, ISSN 0081-4539, http://www.fao.org/3/a-i6030e.pdf.

[33] *** Technical University of Cluj-Napoca. (2010) Program: IDEAS; Project type: Projects of Exploratory research. Project code: ID_1098 (Universitatea Tehnică din Cluj-Napoca. (2010). (Programul: IDEI; Tipul proiectului: Proiecte de cercetare exploratorie. Cod proiect: ID_1098; Nr. Contract: 88/01.10.2007) http://users.utcluj.ro/~ibarabas/idei1098/pdf/1098_2008.pdf *(in Romanian)*

ANALYSIS OF THE DEPENDENCE OF TRACTION RESISTANCE FORCE ON FORWARD SPEED FOR TRACTOR-CULTIVATOR AGGREGATES
/
ANALIZA DEPENDENȚEI FORȚEI DE REZISTENȚĂ LA TRACȚIUNE DE VITEZA DE AVANS PENTRU AGREGATELE TRACTOR-CULTIVATOR

Petru CÂRDEI, Nicolae CONSTANTIN, Cătălin PERSU, Vergil MURARU, Raluca SFIRU, Mihaela NIȚU*)
National Institute of Research – Development for Machines and Installations Designed for Agriculture and Food Industry – INMA Bucharest / Romania
E-mail: rosumihaelan@yahoo.com
DOI: https://doi.org/10.35633/inmateh-70-57

Keywords: *force, parameters, statistic, correlation, dependence, exponent*

ABSTRACT
The article presents results generated by research on the influence of forward speed on the traction resistance force for soil processing machines. Statistical estimators are proposed to highlight the intensity of the connection between the traction resistance force and the forward speed and an optimal evaluation method of an exponent of the work speed to explain as well as possible the behaviour of the traction resistance force. It is found that the variance and the standard deviation are the statistical estimators that highlight the most intensively the connection between the traction resistance force and the forward speed.

REZUMAT
Articolul prezintă rezultatele obținute în urma cercetărilor privind influența vitezei de înaintare asupra forței de rezistență la tracțiune pentru mașinile de prelucrat solul. Se propun estimatori statistici pentru a evidenția intensitatea legăturii dintre forța de rezistență la tracțiune și viteza de înaintare şi o metodă optimă de evaluare a unui exponent al vitezei de lucru pentru a explica cât mai bine comportamentul forței de rezistență la tracțiune. Se constată că varianța și abaterea standard sunt estimatorii statistici care evidențiază cel mai intens legătura dintre forța de rezistență la tracțiune și viteza de înaintare.

1. INTRODUCTION

In the last decades, numerous kinds of research in the field of working processes of agricultural machines intended for work have been methodically directed in the last decades towards experimental or theoretical-empirical research (*Moeenifar et al., 2014; Ranjbar et al., 2013; Naderloo et al., 2009; Singh et al., 2018; Al-Shamiry et al., 2020; Elsheikha et al., 2021; Kushwaka et al., 1996; Al-Suhaibani et al., 2010)*. The classical literature until then was dominated by theoretical calculation supplemented by experiments for the calculation of model constants and validation *(Cârdei et al., 2023; Krasnicenko et al., 1964; McKyes E., 1985; Sandru et al., 1982; Sandru et al., 1983; Scripnic et al., 1979; Tecusan & Ionescu, 1982; Toma et al., 1978).*

However, there have been attempts at statistical modelling since the middle of the 20th century, *(Harrison & Reed, 1962)*. In particular, the experimental search for the dependence of the tillage draft force on the speed of advance of agricultural aggregates intended for soil processing began a few decades ago. Until then, the estimates of the traction force contained the contribution of the forward speed to the traction resistance force in simpler or more complicated analytical formulas, *(Cârdei et al., 2023; Damanauskas & Janulevicis, 2022; Cardei et al., 2020; Cardei et al., 2019; Krasnicenko et al., 1964; McKyes E., 1985; Sandru et al., 1982; Sandru et al., 1983; Scripnic et al., 1979; Tecusan & Ionescu, 1982; Toma et al., 1978),* purely theoretical or theoretical-empirical, (*American Society of Agricultural Engineers, 2023; Moeenifar et al., 2014)*, sometimes with complex theoretical relationships including the geometry of the machine and working parts, *(Al-Neama & Hertzilius, 2017)*.

The theoretical or theoretical-empirical formulas contain a number of "constants" or "coefficients", which also vary primarily with the parameters neglected in the model (soil moisture, soil cohesion and adhesion, the temperature in the soil layer in which work is being done, type of processed soil, etc.), but also with parameters contained in the model, but unknown variations. The experimental estimates of these "constants" or "coefficients" are few, and then engineering intuition is used in the design calculations. Although appreciable, this intuition also has its limits, especially in the context where experiments are increasingly limited in terms of time and activities. On the other hand, all theoretical formulas must be validated experimentally.

Therefore, the theoretical formulas are doubly conditioned by the experiment by finding the "constants" of the model and by validating them.

In the conditions in which the experimental research took a large scale, statistics was more and more involved in the process of extracting the essences from the experimental data, the authors emphasize, *Da Silva et al., (2020)* or *Gomez & Gomez, (1976)*, referring to modern agriculture. Intending to rationalize fuel consumption, *Mamkagh A.M., (2018)* reviews the main influencing factors: forward speed, tractor weight, and tire pressure. Finally, *Sadek et al., (2021),* determine a linear regression equation based on experimental data, in which, in addition to the forward speed, the gang angle, the inclination angle, the working depth and the disk diameter also appear. *Ahmed & Al-Sayed, (2022),* give results regarding the influence of working speed and soil type on the performance of the Massey Ferguson tractor (model 290). Statistical modelling has become a frequently used tool for formulating some predictions of tensile strength, having speed and working depth as predictors as well as others *(Afify et al., 2020; Kim et al., 2020; Rashidi et al., 2013; Rashidi et al., 2013; Saleh et al., 2021)*. Artificial neural networks began to be used in the last decade to predict physical quantities of interest in the field of agricultural soil processing *(Shafei et al., 2018; Çarman et al., 2021; El Wahed & Aboukarima, 2007; Al-Dosary et al., 2020; Çarman et al., 2019; Askari & Abbaspour-Gilandeh, 2020)*. Non-linear regression formulas for the problem of predicting the tensile strength are given or used, in the case of a disk plough *(Almaliki et al., 2019; Shafaei et al., 2018)*.

The relationship between tillage draft force and the forward speed has been investigated by many researchers, *(Moeenifar et al., 2014; Ranjbar et al., 2013; Naderloo et al., 2009; Singh et al., 2017; Al-Shamiry et al., 2020; Damanauskas & Janulevicis, 2022; Cardei et al., 2020; Cardei et al., 2019; Elsheikha et al., 2021; Kushwaka & Linke, 1996; Gatea A.A., 2013; Oprescu et al., 2021; Odero A.J., 2019; Salahloo et al., 2021; Afify et al., 2020; Kim et al., 2020; Rashidi et al., 2013; Rashidi et al., 2013; Saleh et al., 2021; Al-Neama & Hertzilius, 2017; Okoko & Ajav, 2020; Askari et al., 2017)* for example. Some of the authors note the efficiency with which the variance of the traction resistance force highlights the influence of the forward speed *(Naderloo et al., 2009)*. In general, in low working speed ranges, all authors agree that the traction resistance force increases with increasing feed speed. However, the statistical analysis of linear regression also leads to inverse dependencies between the traction resistance force and the forward speed *(Abbaspour-Gilandeh et al., 2020)*.

The problem of the dependence of the tillage draft force on the forward speed has been raised for a very long time. It was hoped that optimal values of the working speed would be found that would minimize the traction resistance force. The implications are very important: the reduction of energy consumption, the emission of polluting gases, and the possible increase in productivity. Even if theoretically and experimentally, the existence of these optimal points was not demonstrated, optimal points were obtained by putting additional conditions, among which, for example, the achievement of a desired productivity *(Cardei et al., 2019)*. Experimentally, it has been observed that the optimal values determined in this way, or critical values of the advance speed, are impossible to reach by the aggregates used or, if they can be reached, they negatively affect the quality of the work performed (it is lost from the programmed working depth, or there is inappropriate granulation, for example) *(Cardei et al., 2019; Kushwaka & Linke, 1996)*.

In some cases, reaching high forward speed values negatively affects the resistance structures of the agricultural machine *(Cardei et al., 2012)*. The attempt of *Zhang & Kushwaha, (1999),* to investigate the influence of the forward speed on the wave propagation length in front of the working body is interesting. The influence of the forward speed on the traction power transfer indices for agricultural tractors, to make energy consumption more efficient during soil processing and cultivation, was studied by the authors *Md-Tahir et al., (2021)*. An important study mainly addresses the influence of humidity together with that of the advanced speed on soil processing *(Okyere et al., 2018)*. Few works address the subject of the quality of soil processing works in relation to the speed of agricultural machinery *(Latypov & Kalimullin, 2020; Wang et al., 2021)*.

In the framework of the above research, those carried out by the authors of this article in the last five-six years are included. The obtained results are partially described in a series of works of which this article is the last *(Cârdei et al., 2023a; Cârdei et al., 2023b; Cârdei et al., 2021a; Cârdei et al., 2021b)*. The MCLS complex cultivator was conceived and designed to carry out a large number of research activities: the investigation of the parameters of the work regime on the output parameters of the system, those that give the quality of the work (from an agrotechnical and economic point of view); investigating the behaviour of different types of working bodies (it is possible to mount at least 8-10 types of working bodies on the structure); the research of soil processing in three variants of working width, being able to use traction capacities with different powers (the structure is modulated and can work in three variants, see fig. 1). Initially, a large experimental plan was designed. Later it was found that the designed experimental plan was much oversized for our

capacities and financing possibilities. For this reason, many aspects remain to be researched with the structure itself, but also relative to the extremely diverse and complex problem of soil processing with agricultural machines intended for soil works that can be carried out with MCLS (complex machine for soil works).

2. MATERIALS AND METHODS

The subject of the research whose results are described in this article consists of the experimental recordings made with the MCLS complex tractor-cultivator aggregate, the version with a working width of 1m. One of the seven experiments has already been analysed in some works (*Cârdei et al., 2023a; Cârdei et al., 2023)*. The experiments carried out with the 1 m working width variant of the MCLS complex cultivator were described in *Cârdei et al., (2023)* and in more detail in *Cârdei et al., (2023)*. Digital recordings were made for each of the seven experiments. In fig. 1-4 the four basic configurations of MCLS can be seen: the folded form (for transport) and the working variants with widths of 4, 2 and 1 m, in fig. 2, 3 and 4.

Fig. 1 – Tractor unit 80 HP - MCLS, in the folded state

Fig. 2 – Variant with 4 m working width of MCLS with 80 HP tractor

Fig. 3 – The 2 m working width version of the MCLS with an 80 HP tractor

Fig. 1 - The 2 m working width version of the MCLS with a 45 HP tractor

Additional details about how the experiments were carried out can be found in *Cârdei et al., (2023a)* and *Cârdei et al., (2023b)*.

The recording of each experiment consisted of a file containing a matrix with variable dimensions from experiment to experiment: a variable number of rows and a fixed number of 13 columns. The first column corresponds to the time recording (equidistant steps in time, corresponding to the recording frequency of 100 Hz). The next twelve columns correspond to the recording of the signals from the deformation sensors mounted on each of the twelve supports of the working parts of the cultivator. As a result, the file (data structure) of an experiment will be symbolized with:

$$A_{j,k}^{i}, i = 1, \dots, 7, j = 1, \dots, n_i, k = 1, \dots, 13 \quad (1)$$

where the upper index $i = 1, .., 7$ corresponds to the experiment, in the order in which the seven experiments are listed in table 1 by their codes, $j = 1, \dots, n_i$ is the index of the rows of the data matrix and varies from 1 to n_i, the number of rows corresponding to the selection of the stable work sequence from each experiment, and k is the column index, for 1 the column of times is indicated, and from 2 to 13, are the columns that contain the records corresponding to the twelve supports of the working parts.

The forward speed is denoted by v, which is a vector with seven components, representing each forward speed considered constant in the respective experiment, on the stable work portion:

$$v_i, i = 1, \dots, 7. \quad (2)$$

With these notations, the vector of average values of the tillage draft force on the working body will be given by the formula:

$$F_i = \frac{\sum_{j=1}^{n_i} \sum_{k=2}^{13} A_{j,k}^{i}}{12 n_i}, i = 1, \dots, 7. \quad (3)$$

For the values of the average resistance forces on the entire cultivator, it is proposed to multiply the average force per working body, (3), by the number of parts of the structure (neglecting the friction of the working depth adjustment wheels with the soil):

$$R_i = 12F_i, i = 1, \dots, 7. \quad (4)$$

The study of the dependence of the deformation resistance forces on the forward speed includes the RMS (root mean square) calculation. The calculation formula is the following:

$$RMS_i = \sqrt{\frac{\sum_{j=1}^{n_i} \sum_{k=2}^{13} \left(A_{j,k}^i\right)^2}{12n_i}}, i = 1, \dots, 7. \quad (5)$$

The next stage of the study of the dependence of tillage traction forces on forward speed will use the variance of the data, that is, the RMS calculated with the recorded force values from which the average value per cultivator is subtracted, (3).

$$Var_i = \sqrt{\frac{\sum_{j=1}^{n_i} \sum_{k=2}^{13} \left(A_{j,k}^i - F_i\right)^2}{12n_i}}, i = 1, \dots, 7. \quad (6)$$

In the third stage of investigating the influence of the forward speed on the tensile strength exerted by the cultivator, records of equal size will be selected from the records (1) corresponding to the seven experiments. Obviously, for each of the seven selections that have been worked on so far, the number of lines will be reduced to the number corresponding to the smallest selection. The equalization of the dimensions of the records entered into the calculation is done to be able to calculate the correlations between the data of the seven experiments (records) and to estimate the influence of the speed of advance on the value of the correlation coefficients. In this way, the necessary tools for regression analysis are also prepared.

3. RESULTS

The results presented below include descriptive statistical estimators of the experimental data described in “Material and Methods”, obtained on the version of the initial selection of the stable sequence corresponding to each experiment and on the version of data files limited to the condition of the same recording length. For the last version, the correlations between the data files are also given, relative to all the twelve recording channels corresponding to all the supports of the working bodies of the MCLS with the working width version of 1 m. Results of inferential statistical analysis such as regression analysis to find the relationship between tensile strength and work speed are also presented in this chapter. Results are also given regarding the study of quartiles and experimental points designated as outliers, all investigated for a possible connection with the speed of advance. A final result presented is a method to establish a variant of determining the optimal exponent for the forward speed in the representation of the variance of the traction resistance force.

3.1. The average values of traction forces per working part, per experience

The statistical estimators defined in “Material and Methods” are calculated for the seven selections from field recordings. They contain electrical signals that are converted into strain values and which, in turn, are converted into stress values, accepting the hypothesis that the material of the supports behaves linearly elastic throughout the experiments.

The experiences are ordered in ascending order according to the forward speeds that characterize them as in Tables 1 and 2. The selected sequences were extracted from the total recordings based on the identification of a stable operating regime (no big shocks, or intense oscillations).

Table 1

The dimensions of the matrices that store the maximum data sequences selected from the total records

Experiment code	Rows	Cols	Forward speed, m/s
T2_R2_1500rpmtxt	4001	13	0.781
T1_R2_2400rpmtxt	4001	13	0.789
T1_R3_1500rpmtxt	2501	13	1.095
T2_R2_2700rpmtxt	1501	13	1.613

Experiment code	Rows	Cols	Forward speed, m/s
T2_R3_1500rpmtxt	2501	13	1.613
T3_R2_1500rpmtxt	2201	13	2.158
T2_R3_2000rpmtxt	1701	13	2.256

Some of the statistical estimators exposed in “Material and Methods” are listed in Table 2: the average value of the traction resistance force per working part, the average total tillage draft force corresponding to the entire cultivator, the average value of the RMS per working part, and the average variance on the working body. The last column of Table 2 identifies the experiment by its code. It must be specified that, in this article, when it is written forward speed, average resistance force on the working part or the entire cultivator, or RMS, it is meant the vectors containing the values of these quantities for each of the seven experiments.

It is found that, in this case, the RMS does not reflect new aspects compared to the average value. The Pearson correlation coefficient between the average tillage draft force on the working part and the RMS has a very high value, 0.954. The Pearson correlation coefficient between the average tillage draft force on the working body and the forward speed has an important but negative value, -0.684. The Pearson correlation coefficient between forward speed and RMS has a negative value, of -0.467.

Table 2

The average values of the tillage draft force per working body and cultivator, for the version with a working width of 1 m, working at a working depth of 10 cm. Entire selections of data files have been processed

The tillage draft force on the working body, N	Total tillage draft force, N	Average RMS per working body, N	The variance of tillage draft forces, N	experiment code
478.413	5740.954	509.552	175.398	T2_R2_1500rpmtxt
518.448	6221.375	541.368	155.857	T1_R2_2400rpmtxt
491.532	5898.387	518.961	166.483	T1_R3_1500rpmtxt
508.530	6102.357	544.803	195.469	T2_R2_2700rpmtxt
495.540	5946.479	526.732	178.569	T2_R3_1500rpmtxt
448.719	5384.632	500.626	221.985	T3_R2_1500rpmtxt
452.695	5432.344	500.985	214.600	T2_R3_2000rpmtxt

The Pearson correlation coefficient between the average value of the tillage draft force per working body and the variance has a large negative value, -0.801. A particularly important value is the Pearson correlation coefficient between forward speed and variance, 0.92.

3.2. Results obtained on data sequences of equal sizes

To facilitate the calculation of the correlation between the records corresponding to the seven experiments, the data files are all cut at a number of rows equal to that of the minimum length record. Results similar to those in Table 2, for data files of equal size, are given in Table 3. Between the results included in Tables 2 and 3, the differences are small, compared to the average values.

Table 3

The average values of the tillage draft force per working body and cultivator, for the version with a working width of 1 m, working at a working depth of 10 cm, for records of equal dimensions

The tillage draft force on the working body, N	Total tillage draft force, N	Average RMS per working body, N	The variance of tillage draft forces, N	Experiment cod
489.587	5875.039	518.864	171.828	T2_R2_1500rpmtxt
513.947	6167.359	536.168	152.758	T1_R2_2400rpmtxt
482.382	5788.590	508.670	161.407	T1_R3_1500rpmtxt
508.530	6102.357	544.803	195.469	T2_R2_2700rpmtxt
491.364	5896.373	520.502	171.708	T2_R3_1500rpmtxt
434.721	5216.651	488.809	223.500	T3_R2_1500rpmtxt
454.788	5457.452	501.457	211.253	T2_R3_2000rpmtxt

The Pearson correlation coefficients between the data matrices (except the time column), in the version with equal dimensions, are given in Table 4. It is found that the maximum value of the Pearson correlation

coefficient (except the correlations of the matrices with themselves) is 0.384, in the case experiments T2_R2_1500rpmtxt and T2_R3_1500rpmtxt, which correspond to working speeds of 0.781 m/s and 1.613 m/s. The value of the correlation coefficient between experiments T2_R2_2700rpmtxt and T2_R3_1500rpmtxt, 0.127, which is one-third of the maximum value in table 4, although the two experiments were carried out with equal work speeds, brings a new argument to the randomness of the work process of the cultivator. This finding confirms the statements made in (*Cârdei et al., 2023a)* and (*Cârdei et al., 2023b)*.

In the case of processing data from files of equal size, the Pearson correlation coefficient between the average traction resistance forces on the working body and the forward speed has a negative value, of -0.734. And in this case, the average tensile strength of the working body and the RMS is highly correlated (0.951). The Pearson correlation coefficient between the forward speed and RMS is negative, -0.542. The correlation between the average value per working part of the traction resistance force and RMS is high, but negative, which implies inverse dependence. The correlation coefficient of variance with RMS is high, 0.897.

Table 4

Pearson correlation coefficients between the experimental data of the seven experiments

	T2_R2_ 1500rpmtxt	T1_R2_ 2400rpmtxt	T1_R3_ 1500rpmtxt	T2_R2_ 2700rpmtxt	T2_R3_ 1500rpmtxt	T3_R2_ 1500rpmtxt	T2_R3_ 2000rpmtxt
T2_R2_1500rpmtxt	1.000	0.264	0.268	0.163	0.384	0.180	0.144
T1_R2_2400rpmtxt	0.264	1.000	0.23	0.123	0.274	0.151	0.038
T1_R3_1500rpmtxt	0.268	0.230	1.000	0.168	0.165	0.136	0.013
T2_R2_2700rpmtxt	0.163	0.123	0.168	1.000	0.127	0.096	0.115
T2_R3_1500rpmtxt	0.384	0.274	0.165	0.127	1.000	0.238	0.043
T3_R2_1500rpmtxt	0.180	0.151	0.136	0.096	0.238	1.000	0.015
T2_R3_2000rpmtxt	0.144	0.038	0.013	0.115	0.043	0.015	1.000

3.3. Regression analyses

For the case where the data files with the original dimensions are analysed (after separating the work sequences with a stable regime), the main results appear in Table 2. The importance of the forward speed parameter using regression approximation of the other parameters will be tested. The multilinear regression calculator, free online, (*www.statskingdom.com*) is used as a calculation tool. For additional explanations regarding the regression analysis, you can consult the literature (*Clocotici V.; Anghel et al., 2020)*.

For the dependence of the average tillage draft force on the working body on the forward speed, the regression is obtained:

$$F = 528.893602 - 29.925106v \quad (7)$$

with the coefficient of determination R^2 =0.468179, which shows that the work speed explains 46.8% of the variation of the average tillage draft force on the working part. The adjusted determination coefficient has a value of 0.361814, and the multiple correlation coefficient is 0.684236. The rejection probabilities of the regression coefficients (6) are, for the free term 0.00000258053 less than 0.05 and 0.08998, greater than 0.05. As a result, the linear regression (7) is weaker than the model that does not contain the independent variable v.

For the RMS dependence on the forward speed, the regression is obtained:

$$RMS = 540.895831 - 13.900419v \quad (8)$$

with the coefficient of determination R^2=0.217649, which shows that the work speed explains 21.88% of the RMS of the average tillage draft force on the working part. The adjusted determination coefficient has a value of 0.0611788, and the multiple correlation coefficient is 0.919695. The rejection probabilities of the regression coefficients (6) are, for the free term 0.00000089 less than 0.05 and 0.21294, greater than 0.05. As a result, the linear regression (8) is weaker than the model that does not contain the independent variable v.

For the dependence of the variance of the average tillage draft force on the tensile strength of the working body on the forward speed, the regression is obtained:

$$Var = 131.870213 + 37.386658v \quad (9)$$

with the coefficient of determination R^2=0.845839, which shows that the forward speed explains 84.58% of the variance of the average resistance force on the working part. In relation (8), by Var, it was noted the variance of the average traction resistance force on the working body. The adjusted determination coefficient has a value of 0.815007, and the multiple correlation coefficient is 0.919695.

The rejection probabilities of the regression coefficients (6) are, for the free term 0.00000793687 less than 0.05 and 0.00336019, also less than 0.05. As a result, the linear regression (9) is better than the model that does not contain the independent variable v.

For the case where data files with equal sizes are analysed (after reducing the work sequences with the stable regime to the number of rows of the smallest data file), the main results appear in Table 3. The tests are similar to those made for the results obtained in the case of the original data files, using the same processing tool (*www.statskingdom.com/410multi_linear_regression.html*).

For the dependence of the average tillage draft resistance force on the working body on the forward speed, the regression is obtained:

$$F = 532.730864 - 34.332562v \quad (10)$$

with the coefficient of determination R^2 =0.537891, which shows that the forward speed explains 53.8% of the variation of the average tillage draft force on the working body. The adjusted determination coefficient has a value of 0.445469, and the multiple correlation coefficient is 0.733411.

The rejection probabilities of the regression coefficients (6) are, for the free term 0.00000246185 less than 0.05 and 0.0606795, greater than 0.05. As a result, the linear regression (10) is weaker than the model that does not contain the independent variable v.

For the RMS dependence, the regression is obtained:

$$RMS = 542.572238 - 17.344266v \quad (11)$$

with the coefficient of determination R^2=0.294075, which shows that the forward speed explains 29.4% of the variance of the average tillage draft force on the working body. The adjusted determination coefficient has a value of 0.15289, and the multiple correlation coefficient is 0.542287. The rejection probabilities of the regression coefficients (6) are, for the free term 0.00000097 less than 0.05 and 0.208549, greater than 0.05.

As a result, the linear regression (11) is weaker than the model that does not contain the independent variable v.

For the dependence of the variance of the average tillage draft force on the working body on the work speed, the regression is obtained:

$$Var = 126.322016 + 39.172138v \quad (12)$$

with the coefficient of determination R^2=0.803943, which shows that the forward speed explains 80.39% of the variance of the average tillage draft force on the working body. The adjusted determination coefficient has a value of 0.764732, and the multiple correlation coefficient is 0.896629.

The rejection probabilities of the regression coefficients (11) are, for the free term 0.000246048 less than 0.05 and 0.00623692 also less than 0.05.

As a result, the linear regression (12) is better than the model that does not contain the independent variable v.

3.4. The intensity of the correlation between the variance of the tillage draft force and the forward speed

Starting from the relationship found between the variance of the average resistance force on the working body and the forward speed, the problem arises of the existence of an exponent of the working speed that maximizes the intensity of this relationship. By the optimal value of the speed exponent, it is understood the value of the power of the forward speed, which maximizes the coefficient of determination of the vectors of the forward speed (raised to the respective power) and the average resistance force on the working body. A regression study for values of the speed exponent between 1 and 4.5, performed both for the initial data and for the dimensionally equalized data, followed by an ordinary polynomial interpolation, leads to the curves in fig. 5. The curves in fig. 5 are the dependences of the determination coefficient R^2 to the forward speed exponent. You can graphically observe the existence of a maximum point of the coefficient of determination, both for the initial data and for those of equal size. In the case of the curve corresponding to the initial data (of different sizes), the coordinates of the optimal point are α_{opt}=2.368, R^2_{opt}=0.878, and in the case of data of equal sizes, α_{opt}=2.454, R^2_{opt}=0.839.

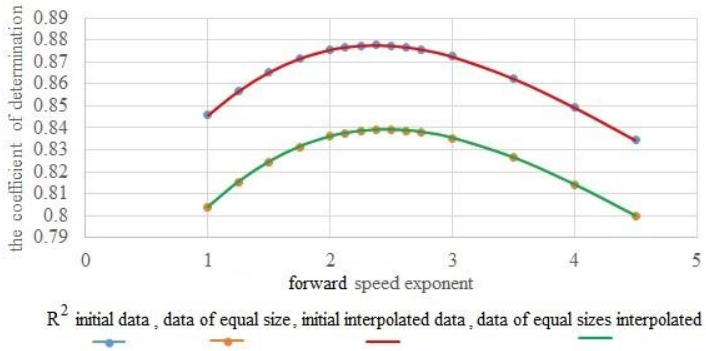

Fig. 5 - Interpolation data and interpolation curves used to calculate the optimal work speed, exponent

The speed exponents, determined in this way, cannot be entered into the formula for calculating the tensile strength because, from a dimensional point of view, the speed at a power that is not an integer has no dimensional meaning. For this reason, the use of the above result is conditioned by the reconsideration of the calculation formula by introducing the speed as a dimensionless factor (speed divided by an important speed in the work process, for example, a critical speed of propagation of waves in soil).

3.5. The analysis of the Quartiles, boxplot graphical representations

According to *Clocotici V. and https://en.wikipedia.org/wiki/Box_plot*, in descriptive statistics, a boxplot or boxplot is a method for graphically demonstrating the local properties of data distribution, spread groups and asymmetry of numerical data through their quartiles. In this sub-chapter, the possible connection between the distribution of the quartiles of the experiments and their other characteristics is studied, in comparison with the speed of progress of each experiment. This analysis was done to find new estimators significantly related to the aggregate advance speed. Finding such estimators contributes to the widening of the range of statistical tools for investigating the involvement of the speed of advance in the quantities of energetic and economic nature of the work process, but also to the creation of new directions in the modelling, of the soil processing phenomenon. Finding such estimators contributes to the widening of the range of statistical tools for investigating the influence of the working speed in the quantities of energetic and economic nature of the work process, but also to the creation of new directions in the statistical modelling, of the soil processing phenomenon. The box plot graphic representation is given in fig. 6.

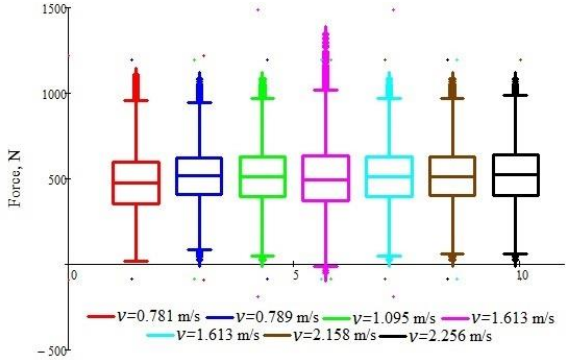

Fig. 6 - Boxplot graphical representations for each of the seven experiments performed for the aggregate consisting of the 45 HP tractor and the 1 m wide version of the MCLS

Table 5

Important statistical estimators involved in the investigation of the relationships between the parameters of the MCLS work process and the aggregate advance speed

Experiment code	Average of outliers per experiment, N	Number of outliers	The variance of outliers	Average of the original data, N	The standard deviation of the original data, N	The variance of the original data
T2_R2_1500rpmtxt	1012.533	148	0.558	478.413	175.400	30764.988
T1_R2_2400rpmtxt	818.985	211	6.377	518.448	155.859	24291.887
T1_R3_1500rpmtxt	930.699	99	2.85	491.532	166.486	27717.492
T2_R2_2700rpmtxt	1086.370	197	2.30	508.530	195.475	38210.409
T2_R3_1500rpmtxt	930.699	99	2.85	495.540	178.572	31887.955
T3_R2_1500rpmtxt	930.699	103	3.361	448.719	221.989	49279.026
T2_R3_2000rpmtxt	883.709	71	3.267	452.695	214.605	46055.503

The Pearson correlation coefficient between the three characteristics of the box-plot analysis, which are given in table 5, are listed in table 6. In addition, the correlation is also made with the velocity vector of the seven experiments. It was also introduced in the table the Pearson correlation coefficients and the main statistical characteristics calculated using the data files with the original selection: the average value, the standard deviation and the variance. It is found that the standard deviation and the variance of the original data are highly correlated with the forward speed.

As a result, it can be concluded that with the increase in the working speed, the parasitic vibration energy of the entire MCLS structure will also increase, with all the negative consequences, including affecting the quality of soil processing. The variance of the original data is strongly and positively related to the speed of advance (correlation coefficient 0.919). The linear regression study shows that the forward speed explains 84.42% of the behaviour of the variance of the traction resistance force. Even more intense and positive is the connection between the standard deviation of the original data and the speed of advancement (correlation coefficient 0.92). The variation of the forward speed, according to the linear regression analysis, explains 84.58% of the behaviour of the standard deviation of the original data.

Table 6

Pearson correlation coefficients between the main estimators from the study of quartiles and box plot diagrams, together with other estimators of descriptive statistics

	Average of outliers per experiment	Number of outliers	The variance of outliers	Average of the original data	The standard deviation of the original data, N	The variance of the original data	Forward speed
Average of outliers per experiment	1	0.194	-0.784	0.067	0.200	0.163	0.015
Number of outliers	0.194	1	0.294	0.759	-0.481	-0.477	-0.589
The variance of outliers	-0.784	0.294	1	0.320	-0.227	-0.191	-0.036
Average of the original data	0.067	0.759	0.320	1	-0.801	-0.808	-0.684
The standard deviation of the original data, N	0.200	-0.481	-0.227	-0.801	1	0.999	0.92
The variance of the original data	0.163	-0.477	-0.191	-0.808	0.999	1	0.919
Forward speed	0.015	-0.589	-0.036	-0.684	0.92	0.919	1

4. Comments

After calculating the average value of the tillage draft force on the active body, the linear regression analysis between the vector of these average values and the vector of forward speeds (the first column in Table 2 and the last in Table 1), leads to a coefficient of determination R^2=0.468, the Pearson correlation coefficient between the two vectors being -0.684. Therefore, the working speed can explain at most 46.8% of the behaviour of the average value of the traction resistance force on the working body. In addition, these vectors are highly (according to (*www.umfcv.ro*) for example) correlated but vary inversely or are negatively correlated. The statistical analysis of the regression gives the values of the probabilities of rejection of the regression relationship coefficients, approximately 0.0 for the constant term and 0.057 for the term of the first degree. The last value being greater than 0.05, the hypothesis of the correctness of the linear regression is rejected. Therefore, this type of connection is unlikely between the two vectors.

The results in table 7 show that the most significant estimator for the dependence of tillage draft force on the forward speed is the variance. The same result is obtained by the linear regression study carried out in subchapter 3.3. Variance is the statistical estimator of tillage draft force most strongly related to forward speed.

The intensity of the link between the variant of the average tillage draft force on the working part and the speed of advancement is also of interest for the suggestion that the coefficient of determination (taken as an objective function) can be optimized, in this case, maximized. More interesting is that the exponent of the speed that achieves the maximization is quite close to 2, as it was shown in chapter 3.4. It should be mentioned that the value of 2 of the forward speed exponents is very common in the calculation formulas proposed for the tillage draft force generated by agricultural machines intended for soil processing (*Letosnev M.N., 1959; American Society of Agricultural Engineers, 2003; Ranjbar et al., 2013; Singh et al., 2018*). In *Moeenifar et al., (2014*), a formula with an exponent, generally non-integer, is used for the forward speed. Significant effects of the working speed of some agricultural machines intended for soil processing were also found experimentally using the variance of the tillage draft force, by the authors *Naderloo et al., (2009*) for example. From the study

in subchapter 3.4, it can also be found, which was to be expected, that using longer experimental sequences, the intensity of the found link increases.

Table 7

Correlations between the main parameters of the work process. The hatched cells correspond to the processing of the original data, and the non-hatched cells correspond to data files of equal size

	The average tillage draft force on the working body	Variance	Forward speed	RMS
The average tillage draft force on the working body	1	-0.801	-0.684	0.954
Variance	-0.801	1	0.92	-0.587
Forward speed	-0.684	0.92	1	-0.467
RMS	0.954	-0.587	-0.467	1
The average tillage draft force on the working body	1	-0.778	-0.733	0.951
Variance	-0.778	1	0.897	-0.548
Forward speed	-0.733	0.897	1	-0.542
RMS	0.951	-0.548	-0.542	1

Almost linear and increasing dependences of tensile strength on feed rate, over narrow speed ranges, have been found by numerous researchers (*Elsheikha et al., 2021; Al-Suhaibani & Ghaly, 2010*), and our article confirms this finding. The authors *Kushwaka & Linke, (1996*) conclude that the working speed influences the resistance force of an agricultural aggregate for processing the soil. The study ok *Kushwaka & Linke, (1996*) reaches interesting conclusions related to the existence of a critical value of the forward speed (specificity of each soil), above which the energy consumption of the tractor becomes lower. Some of these conclusions were also reached in *Cardei et al., (2019*) starting from the theoretical formula of tensile strength proposed by Goriacikin *(Letosnev M.N., 1959*). The conclusions in the present paper confirm most of the results found in *Cardei et al., (2019*) or *Letosnev M.N., (1959*) but do not disprove any of them.

The use of quartile analysis and boxplot graphic representation was tried in this article to find some statistical estimators strongly related to the speed of advance. The results were weak, in the sense that in subchapter 3.5 insignificant correlations were found between the forward speed and the main estimators chosen from the quartile analysis (the number of outliers, the average and the variance of the resistance forces per working part). A single couple attracts attention, having a correlation coefficient of -0.784, a value recorded between the variance of the outliers and the average value of the tillage draft force per experiment. As for our purpose, first of all, the maxima of correlation with the speed of advance were interesting, it can be stated that the analysis of quartiles and box plot diagrams does not bring new elements to the study.

The experimenters have found, not only in the experiments analysed in this article but also in other experiments, that, at least apparently, there are situations in which the increase in the forward speed of the aggregate leads to a decrease in the tillage draft force. This aspect can be related to a hypothetical critical speed (specificity of soil type, humidity and other environmental conditions) described in *Kushwaka & Linke, (1996*) or in *Cardei et al., (2019*), but, often, as shown in *Gatea A.A., (2013*), the phenomenon happens due to the decrease of the working depth, practically the partial exit of the active body from the furrow.

In subchapter 3.5 it was showed that the standard deviation and the variance of the tillage draft force are well or even very well correlated. Other authors have also found such results. For example, *Odero A.J., (2019*) (table 4.2), for the disc plough, makes a number nine experiments for three forward speeds and three working depths. The correlation coefficient of tensile strength with working depth has a value of 0.597, and with speed, 0.773. The bilinear regression analysis gives for the predictors working depth and forward speed the coefficient of determination R^2=0.95 with the adjusted value 0.94. Therefore, the two predictors together explain 95% of the behaviour of the dependent variable, tillage draft force. In the same conditions, for a tiller plough, the correlations of force with depth and forward speed have values of 0.439 and 0.884, respectively. The regression analysis provides R^2=0.97 with an adjusted value of 0.97. Both for the disc plough and for the plough with the tiller, both predictors (depth and forward speed) are considered to be very significant collective predictors. Obviously, to complete the remaining 5% or 3% of the behaviour of the traction resistance force, the frictional forces can be studied. In the case of the tiller plough, if instead of the speed it is considered the square of it, it reaches R^2=0.98 with the adjusted value 0.97, and for the disk plough, at R^2=0.96 with the adjusted value 0.94. This is just a suggestion for the dependence on the square of the speed. However, it is possible to follow the path of numerical optimization introduced in subchapter 3.4.

5. CONCLUSIONS

The results presented in this article, compared to the results of other researchers who have investigated in a similar way the problem of the influence of the speed of advance of agricultural machines intended for soil processing on the tensile strength, allow us to express some useful conclusions for those who try to highlight this connection in experimental data.

C1) The forward speed influences the intensity of the tillage draft force on the entire machine and the working part. The influence becomes clearer if the variance and standard deviation of the tillage draft force are used.

C2) It cannot be certain that conclusion C1) is valid for all soils and different humidity levels of the same soil. Therefore, conclusion C1) must also be studied to other environmental conditions, working depths, etc.

C3) Evidence of the intensity of the connection (correlation) between the tillage draft force and the forward speed is made difficult by two phenomena: the first consists in the fact that the component of the traction resistance force given by the forward speed is usually small in the usual range of speeds advancement, and its increase must be done with caution because it negatively affects the quality of the work; the second reason consists in the fact that with the increase in the speed of advance, there are also losses of the working depth which can lead to the erroneous conclusion that the increase in the working speed leads (perhaps starting from certain values) to the decrease of the tillage draft force or the growth rate of the same force.

C4) It is possible that starting from certain forward speeds, the increasing speed of the tillage draft force decreases (so the derivative of the tillage draft force to the working speed) and not the traction force itself.

C5) The use of non-linear regression analysis allows finding indicative powers for the dependence of the variance of the tillage draft force, powers that can then be used in theoretical or theoretical-empirical modelling of the tillage draft force.

C6) Although the analysis of quartiles and outliers did not indicate significant links between forward speed and tillage draft force or its statistical estimators, the subject is not considered closed and can be further addressed for cultivators but also for other agricultural machines to be processed on the ground.

C7) Continuation of research aimed at agricultural machines of the type of working variants of the MCLS, are conditioned by: direct measurements of the tillage draft force, accelerometry measurements, control measurements or monitoring of the working depth, measurements of the working width and monitoring, estimation productivity, consumption and work qualities (working depth, granulation or granulation ratio). These are just a few directions to continue, but next to them there are others equally important: the introduction of soil qualities into the soil, namely moisture, cohesion, adhesion, degree levelling, density, compactness, resistance to penetration, other mechanical properties, etc. Time and money will solve them all, in a positive or negative sense.

ACKNOWLEDGEMENT

This work was supported by a grant of the Romanian Research and Innovation Ministry, through Programme 1 - Development of the national research-development system, sub-programme 1.2. Institutional performance - Projects for financing excellence in RDI, contract no. 1 PFE/2021.

REFERENCES

[1] Abbaspour-Gilandeh Y., Fazeli M., Roshanianfard A., Hernandez-Henandez M., Gallardo Bernal I., Hernandez-Henandez J.L., (2020). *Prediction of Draft Force of a Chisel Cultivator Using Artificial Neural Networks and Its Comparison with Regression Model*. Agronomy, Vol. 10, No. 4, pp. 1-14.

[2] Afify M.T., El-Haddad Z.A., Lamia A.A.D., (2020). *Modeling the Effect of Soil-Tool Interaction on Draft Force Using Visual Basic*. Annals of Agricultural Sciences, Moshtohor, Vol. 58, No. 3, pp. 223-232.

[3] Al-Dosary N.M.N., Al-Hamed S.A., Aboukarima A.M., (2020). *Application of adaptive neuro-fuzzy inference system to predict draft and energy requirements of a disk plow*. International Journal of Agriculture and Biological Engineering, Vol. 13, No. 2, pp. 198-207.

[4] Almaliki S., Himoud M.S., Muhsin S.J., (2019). *A Stepwise Algorithm for Prognostication Draft Requirements of Disk Plough*. Journal of Engineering and Applied Sciences, Vol. 14, No. 8, pp. 10335-10340.

[5] Al-Neama A.K.A, Hertzilius T., (2017). *Draft forces prediction model for standard single tines by using principles of soil mechanics and soil profle evaluation*. Landtechnik, Vol. 72, No. 3, pp. 157–164.

[6] Ahmed M.A.AbE., Al-Sayed A.B., (2022). *Effect of Forward Speed and Soil Type in Massey Ferguson Tractor (Model 290) Performance*. Diyala Agricultural Sciences Journal, Vol. 14, No. 2, pp. 33-42.

[7] Al-Shamiry F.M.S., Al-Qarni A.M., Munassar A.S., (2020). *Effect of Tillage Depth and Tractor Forward Speed on Some Technical Indicators of the Moldboard Plow*. International Journal of Progressive Sciences and Technologies, Special Issue October, pp. 28-37.

[8] Al-Suhaibani S.A., Ghaly A.E., (2010). *Effect of Plowing Depth of Tillage and Forward Speed on the Performance of a Medium Size Chisel Plow Operating in a Sandy Soil.* American Journal of Agricultural and Biological Sciences, Vol. 5, No. 3, pp. 247-255.

[9] American Society of Agricultural Engineers [ASAE]. D497.4(2003). *Agricultural machinery management data*. In: ASAE. ASAE standards 2003. ASAE, St. Joseph, MI, USA, pp. 373-380.

[10] Anghel M.G., Grigorescu D.L., Dumbrava S.G., (2020). *Theoretical aspects regarding the use of linear regression in the study of economic correlations*, Romanian Journal of Statistics - Supplement 7.

[11] Askari M., Shahgholi G., Abbaspour-Gilandeh Y., (2017). *The effect of tine, wing, operating depth and speed on the draft requirement of subsoil tillage tines*. Researches in Agriculture Engineering, Vol. 63, No. 4, pp. 160-167.

[12] Askari M., Abbaspour-Gilandeh Y., (2020). *Predicting the Imposed Forces on the Tines and Tractor Fuel Consumption during Subsoiling Operation Using Adaptive Neuro-Fuzzy Inference System (ANFIS)*. Agricultural Mechanization and System Research, Vol. 21, No. 47, pp. 47-66.

[13] Çarman K., Çitil E., Taner A., (2019). *Artificial Neural Network Model for Predicting Specific Draft Force and Fuel Consumption Requirement of a Mouldboard Plough*. Selcuk Journal of Agriculture and Food Sciences, Vol. 33, No. 3, pp. 241-247.

[14] Çarman K., Marakoğlu T., Taner A., Çıtıl E., (2021). *Prediction of Draft Force and Disturbed Soil Area of a Chisel Tine in Soil Bin Conditions Using Draft Force and Its Comparison with Regression Model*, Selcuk Journal of Agriculture and Food Sciences, Vol. 35, No. 1, pp. 56-64.

[15] Cardei P., Constantin N, Muraru V., Persu C., Sfiru R., (2023a). *Estimation of the random intensity of the soil tillage draft forces in the supports of the working bodies of a cultivator*. Preprint RG. DOI:10.13140/RG.2.2.34201.49760

[16] Cardei P., Constantin N, Muraru V., Persu C., Sfiru R., (2023b). The random vibrations of the active body of the cultivators, preprint RG, DOI: 10.13140/RG.2.2.12391.11684.

[17] Cardei P., Condruz P., Sfiru R., Muraru C., (2020). T*ests for Physical Laws of Draft Force Generated in Tillage Operations*, ERDEW. Journal of Scientific Conference Proceedings, Jelgava. DOI: 10.22616/ERDev2020.19.TF309

[18] Cardei P., Muraru S.L., Sfiru R., Muraru V., (2019). *General structure of tillage draft force. Consequences in experimental and applicative researches*. INMATEH Agricultural Engineering, Vol. 59, No. 3, pp. 253-262.

[19] Cardei P., Constantin N., Gradinaru V., Marin E., Manea D., Matache M., Muraru V., Muraru C., Pirna I., Sfiru R., Sorica C., Stanciu L., Vladut V., (2012). *Structural analysis and new materials focused on mechanics, mechatronics, maintenance and operation of technical equipment for agriculture and the food industry (Analiza structurală şi materiale noi focalizate pe mecanică, mecatronică, mentenanţă şi exploatarea echipamentelor tehnice pentru agricultură şi industrie alimentară)* Terra Nostra Publishing House, Iasi.

[20] Cardei P., Constantin N., Sfiru R., Muraru V., Condruz P., (2021a). *Modular load-bearing structures for the study of interactions between the soil and working parts of agricultural machines*. Journal of Physics Conference Series, Vol. 1781, No. 1, pp. 1-10, 012063.

[21] Cardei P., Nicolae C., Sfiru R., Muraru V., Muraru S.L., (2021b). *Structural analysis of a modulated load-bearing structure designed to investigate the interaction between soil and the working parts of agricultural machines.* Journal of Physics Conference Series, Vol. 1781, No. 1, pp. 1-15, 012064.

[22] Clocotici V., Explanatory dictionary of statistics (Dictionar explicativ de statistica), https://profs.info.uaic.ro/~val/statistica/StatGloss.htm

[23] Damanauskas V., Janulevicis A., (2022*). Effect of tillage implement (spring tine cultivator, disc harrow), soil texture, forward speed, and tillage depth on fuel consumption and tillage quality.* Journal of Agricultural Engineering, Vol. 53. doi.org/10.4081/jae.2022.1371

[24] Da Silva R.P., dos Santos A. F., de Oliveira B.R., Souza J. B. C., de Oliveira D.T., Carneiro F.M., (2020). *Potential of using statistical quality control in agriculture 4.0*. Ciência Agronômica Journal, Vol. 51, pp. 1-15.

[25] El Wahed A., Aboukarima M., (2007). *Draft models of chisel plow based on simulation using artificial neural networks.* Misr Journal of Agricultural Engineering, Vol. 24, No. 1, pp. 42-61.
[26] Elsheikha, A.M., Al-Rajhi, M.A., El-Shabasy T.M., (2021). *Effect of Coating Plow Shares with Some Materials on Draft Force Requirement*. Journal of Soil Sciences and Agricultural Engineering, Vol. 12, No. 9, pp. 611-614.
[27] Fechete-Tutunaru L.V., Gaspar F., Gyorgy Z., (2019). *Soil-tool interaction of a simple tillage tool in sand*. E3S Web of Conferences 85, 08007.
[28] Gatea A.A., (2013). *Influence of tillage pattern and forward speed of the tractor in the efficiency tillage*. International Journal of Agricultural Science and Research, Vol. 3, No. 4, pp. 109-120.
[29] Gomez K.A., Gomez A.A., (1984). *Statistical procedures for agricultural research.* Second edition, John Wiley & Sons, (first edition, 1976).
[30] Harrison, H. P., and W. B. Reed. (1962). *An analysis of draft, depth and speed of tillage equipment*. Canadian Agricultural Engineering, Vol. 4, No. 1, pp. 20–23.
[31] Kim Y.S., Kim T.J., Kim Y.J., Lee S.D., Park S.U., Kim W.S., (2020). *Development of a Real-Time Tillage Depth Measurement System for Agricultural Tractors: Application to the Effect Analysis of Tillage Depth on Draft Force during Plow Tillage*. Sensors (Basel), Vol. 20, No. 3, 912.
[32] Krasnicenko A. V., (1964). *Farm Machinery Builder Manual (Manualul constructorului de masini agricole)*. Technical Publishing House Bucharest/ Romania.
[33] Kushwaka R.L., Linke C., (1996). *Draft-speed relationship of simple tillage tools at high operating speeds*. Soil and Tillage Research, Vol. 39, No. 1-2, pp. 61-73.
[34] Latypov R., Kalimullin M., (2020). *The dependence of the quality of soil treatment on the parameters and operating modes of the working bodies of the cutter, ERSME, IOP*. Conferences Series: Materials Science and Engineering.
[35] Letosnev M.N., (1959). *Agricultural Machinery (Masini Agricole)*, Ministry of Agriculture and Forestry, State Agro-Forest Publishing House, Bucharest.
[36] Mamkagh A.M., (2018). *Effect of Tillage Speed, Depth, Ballast Weight and Tire Inflation Pressure on the Fuel Consumption of the Agricultural Tractor - A Review*. Journal of Engineering Research and Reports, Vol. 3, No. 2, pp. 1-7.
[37] McKyes E., (1985). *Soil Cutting and Tillage*, vol. 7, Elsevier Science, eBook ISBN: 9780444601049.
[38] Md-Tahir H., Zhang J., Xia J., Zhou Y., Zhou H., Dun J., Sultan M., Mamona H., (2021). *Experimental Investigation of Traction Power Transfer Indices of Farm-Tractors for Efficient Energy Utilization in Soil Tillage and Cultivation Operations*. Agronomy, Vol. 11, No. 168, pp. 2-16.
[39] Moeenifar A., Mousavi-Seyedi S., R., Kalantari D., (2014). *Influence of tillage depth, penetration angle and forward speed on the soil/thin-blade interaction force.* Agric Eng Int: CIGR Journal, vol. 16, no.1, p. 69-74.
[40] Naderloo L., Alimadani R., Akram A., Javadikia P., Khanghah H.Z., (2009). *Tillage depth and forward speed effects on draft of three primary tillage implement in clay loam soil*. Journal of Food, Agriculture & Environment, vol. 7, No. 3&4, pp: 382-385.
[41] Nkakini S.O., Ekemube R. A., (2020). *Evaluation of the Effects of Tractor Forward Speed and Tillage Depthon Fuel Consumption during Ploughing Operation*. Journal of Newviews in Engineering and Technology, Vol. 2, No. 2, pp. 60-69.
[42] Odero A.J., (2019). *Effects of tillage depth and speed on drawbar power and performance of disc and mouldboard ploughs in silt loam soil*. Thesis, Egerton University.
[43] Okyere F.G., Moon B.E., Qasim W., Basak J.K., Kahn F., Kang D.S., Yoon Y.C., Kim H.T., (2018). *Tillage Operational Analysis Based on Soil Moisture Content, Machine Speed, and Disc Space of Compact Disc Harrow*. Journal of Biosystems Engineering, Vol. 43, No. 3, pp. 161-172.
[44] Okoko P., Ajav E.A., (2020). *Determination of Draft Force for a 3-bottom Disc Plough under Sandy Loam Soil Conditions.* American Journal of Agricultural and Biological Sciences, Vo. 15, pp. 60-67.
[45] Oprescu M., Biris S.S., Cardei P., Muraru V., (2021). *Experimental Research on quality and energetic indices of equipment for opening and compartmentalizing watering furrows*. Conference: 20th International Scientific Conference Engineering for Rural Development, Jelgava. DOI: 10.22616/ERDev.2021.20.TF204
[46] Ranjbar I., Rashidi M., Najjarzadeh I., Niazkhani A., Niyazadeh M., (2013). *Modeling of Moldboard Plow Draft ForceBased on Tillage Depth and Operation Speed*. Middle-East Journal of Scientific Research 17 (7): 891-897.

[47] Rashidi M., Lehmali H.F., Akbari H., Jaberinasab B., (2013). *Effect of Soil Moisture Content, Tillage Depth and Forward Speed on Draft Force of Double Action Disc Harrow*. American-Eurasian Journal of Agricultural & Environmental Sciences, Vol. 11, No. 8, pp. 1124-1128.
[48] Rashidi M., Lehmali H.F., Beni M.S., Malekshahi M., Namin S.T., (2013). *Prediction of Disc Harrow Draft Force Based on Soil Moisture Content, Tillage Depth and Forward Speed*. Middle-East Journal of Scientific Research, Vol. 15, No. 2, pp. 260-265.
[49] Sadek M.A., Chen Y., Zeng Z., (2021). *Draft force prediction for a high-speed disc implement using discrete element modelling*. Biosystem Engineering, 202, pp. 133-141.
[50] Salahloo M., Alasti B.M., Mardani A., Abbasgholipour M., (2021). *Effect of Forward Speed, Working Depth and Overlay Parameters of Cultivator Tillage on Power Consumption and Draft Force*. Iranian Journal of Biosystem Engineering, Vol. 51, No. 4, pp. 749-756.
[51] Saleh A., Sani M.T., Suleiman M.L., (2021). *Effects of Speed on Draft for Selected Tractor-Driven Tillage Implements in Samaru Soil, Zaria, Nigeria.* Journal of Applied Sciences and Environmental Management, Vol. 25, No. 5, pp. 751-757.
[52] Sandru A., Popescu S., Cristea I., Neculaiasa V., (1983). *Agricultural machinery exploitation.* Didactic and Pedagogical Publishing House, Bucharest/ Romania.
[53] Sandru A., Badescu M., Sandru L., (1982). *Reduce energy consumption by rational use of agricultural aggregates (Reducerea consumului de energie prin folosirea rationala a agregatelor agricole)*, Romanian Writing Publishing House (Editura Scrisul Romanesc), Craiova/ Romania.
[54] Scripnic V., Babiciu P., (1979), *Agricultural machines (Masini agricole)*, Ceres Publishing House, Bucharest/ Romania.
[55] Shafei S.M., Loghavi M., Kamgar S., (2018). *A comparative study between mathematical models and the ANN data mining technique in draft force prediction of disk plow implement in clay loam soil*. Agricultural Engineering International: CIGR Journal, Vol.20, No. 2, pp. 71–79.
[56] Shafaei S.M., Loghavi M., Kamgar S., Raoufat M.H., (2018). *Potential assessment of neuro-fuzzy strategy in prognostication of draft parameters of primary tillage implement*. Annals of Agrarian Science, Vol. 16, pp. 257-266.
[57] Singh J., Chatha S.S., Sidhu B.S., (2018). *Influence of Tillage Depth and Plough Speed on Performance of Primary Tillage Tools.* Asian Journal of Engineering and Applied Technology, Vol. 7, No. S2, pp: 138-142.
[58] Tecusan N., Ionescu E., (1982). *Tractors and automobiles (Tractoare si automobile)*, Didactic and Pedagogical Publishing House, Bucharest/ Romania.
[59] Toma D., Neagu T., Florescu I., Lepsi S., (1978). *Agricultural tractors (Tractoare agricole)*, Didactic and Pedagogical Publishing House, Bucharest/ Romania.
[60] Wang M., Fu Zuoli, Zheng Z., Huang Y., Wei W, (2021). *Effect of Performance of Soil Cultivator with Different Surface Textures of Shovel Wing*. Agriculture, Vol. 11, No. 11, pp. 1-11.
[61] Zhang Z.X., Kushwaha R.L., (1999). *Operating speed effect on the advancing soil failure zone in tillage operation*. Canadian Agricultural Engineering, Vol. 41, No. 2, pp. 87-92.
[62] *** https://www.umfcv.ro/files/b/i/Biostatistica%20MG%20-%20Cursul%205%20-%20Corelatii.pdf
[63] *** https://www.statskingdom.com/410multi_linear_regression.html
[64] *** https://en.wikipedia.org/wiki/Box_plot

WRITING INSTRUCTIONS

Article Types

Three types of manuscripts may be submitted:

1. **Regular articles:** These should describe new and carefully confirmed findings, and experimental procedures should be given in sufficient detail for others to verify the work. The length of a full paper should be the minimum required to describe and interpret the work clearly (max.10 pages, even number);
2. **Reviews:** Submissions of reviews and perspectives covering topics of current interest are welcome and encouraged (max.12 pages, even number).

Manuscripts should be written in English (American or British usage is accepted, but not a mixture of these) and submitted **electronically** at the following e-mail addresses: ***inmatehjournal@gmail.com***
Please be sure to include your full affiliation and e-mail address (see Sample manuscript)
The authors are responsible for the accuracy of the whole paper and references.
There are allowed 2 papers by each first author.
The text layout should be in single-column format. To avoid unnecessary errors it is strongly advised to use the "spell-check" and "grammar check" functions of your word processor.

Review Process

All manuscripts are reviewed by 2 members of the Scientifically Review Office. Decisions will be made as rapidly as possible and the journal strives to return reviewers' comments to authors in approx.3 weeks.
The editorial board will re-review manuscripts that are accepted pending revision.

NOTE:

Submission of a manuscript implies: that the work described has not been published before (excepting as an abstract or as part of a published lecture or thesis) that it is not under consideration for publication elsewhere.

1. REGULAR ARTICLES

- Manuscripts should be concise, in ***1.15 line spacing***, and should have 2 cm all over margins. The font should be ***Arial 10 pt.*** Ensure that each new paragraph is clearly indicated, using **TAB at 1 cm**.
- Title will be ***Arial 12 pt***. and explicit figures will be ***Arial 9 pt***.
- Text will be written in English.
- Chapters' titles are written by ***Arial 10 pt, Bold, Uppercase*** (e.g. **INTRODUCTION, MATERIALS AND METHODS**), between chapters is left a space for 10 pt. At the beginning of each paragraph, TAB of 1 cm.
- The paper body will be written in ***Arial 10 pt., Justify alignment***.

TITLE ***Arial 12 pt., Uppercase, Bold, Center*** *(in English language)* and ***Bold Italic*** *(in native language).*
Should be a brief phrase describing the contents of the paper. Avoid long titles; a running title of no more than 100 characters is encouraged (without spaces).
AUTHORS ***ARIAL 9, Bold, Centre alignment***
Under the paper's title, after a space (enter) 9 pt., write ***authors' names*** and ***affiliations (Arial 8 pt.-Regular)***
When the paper has more than one author, their name will be followed by a mark (Arabic numeral) as superscript if their affiliation is different. Less than 6 authors.
Corresponding author's name (next row), ***(Arial 8 pt.)***. Should be added also: phone, fax and e-mail information, for the paper corresponding author (***font: 8 pt., Italic***).
KEYWORDS ***(In English)*** about 4 to 7 words that will provide indexing references should be listed (title: ***Arial 10pt, bold italic,*** text ***Arial 10 pt., italic***).
A list of non-standard *Abbreviations* should be added. In general, non-standard abbreviations should be used only when the full term is very long and used often. Each abbreviation should be spelled out and introduced in parentheses the first time it is used in the text. Standard abbreviations (such as ATP and DNA) need not to be defined.
ABSTRACT ***(in English and Native language, Arial 10 pt.)***, the title *bold*; the text of abstract: *italic*) should be informative and completely self-explanatory, briefly present the topic, state the scope of the experiments, indicate significant data, and point out major findings and conclusions. The Abstract should be max.250 words. Complete sentences, active verbs, and the third person should be used, and the abstract should be written in the past tense. Standard nomenclature should be used and abbreviations should be avoided. No literature should be cited.
INTRODUCTION (***Arial 10 pt.)*** should provide a clear statement of the problem, the relevant literature on the subject, and the proposed approach or solution. It should be understandable to colleagues from a broad range of scientific subjects. We should refer to the current stage of researches performed in the field of the paper to be published, by quoting up-to-date specialty studies, preferably published after 2006, excepting certain referential specialty books/studies, especially papers issued in magazines/journals/conferences/ISI quoted symposia or in other international data bases, which are well known and available.

MATERIALS AND METHODS (***Arial 10 pt.***) should be complete enough to allow experiments to be reproduced. However, only truly new procedures should be described in detail; previously published procedures should be cited, and important modifications of published procedures should be mentioned briefly. Methods in general use need not be described in detail.

RESULTS (***Arial 10 pt.***) should be clarity presented. The results should be written in the past tense when describing findings in the authors' experiments. Results should be explained, but largely, without referring to the literature. Discussion, speculation and detailed interpretation of data should not be included in the Results, but should be put into the Conclusions section.

CONCLUSIONS (***Arial 10 pt.***) The main conclusions drawn from results should be presented in a short Conclusions section. Do not include citations in this section.

Formulae, symbols and abbreviations: Formulae will be typeset in Italics (preferable with the Equation Editor of Microsoft Office 2003) and should be written or marked as such in the manuscript, unless they require a different styling. They should be referred to in the text as Equation (4) or e.g. (4). The formulae should be numbered on the right side, between brackets ***(Arial 10 pt.)***:

$$P = F \cdot v \quad (1)$$

Terms of the equation and the unit measure should be explained, e.g.

P is the power, [W];
F – force, [N];
v – speed, [m/s]

SI units must be used throughout.

Tables should be self-explanatory without reference to the text. The details of the methods used in the experiments should preferably be described in the legend instead of in the text. The same data should not be presented both in table and graph form or repeated in the text.
Table's title will be typed ***Arial 9 pt, Bold, Centered***
In the table, each row will be written Arial 9 pt, single-spaced throughout, including headings and footnotes.
The table should be numbered on the right side, ***Arial 10 pt.***

Figures ***(Arial 9 pt., Bold, Center)*** should be typed in numerical order (Arabic numerals). Graphics should be high resolution (e.g.JPEG). Figure number is followed by what represent the figure or graph e.g.:

Fig. 1 – Test stand

Legend: ***Arial 8 pt, Italic, Center,*** e.g.:
1 - plansifter compartments; 2- break rolls; 3 – semolina machines; 4 – reduction rolls; 5 – flour

ACKNOWLEDGMENTS (***Arial 10 pt.***) of people, grants, funds etc should be brief (*if necessarily*).

REFERENCES (***Arial 10 pt.***)
(In alphabetical order, in English and in the original publication language).
Minimum 10 references, last 10 years, minimum 3 references from the last 2 years

It can be used "*References*" tool from the *Word Editor*. **APA Style (American Psychological Association)**
https://apastyle.apa.org/style-grammar-guidelines/references/examples

All references must be provided in English
Authors are fully responsible for the accuracy of the references.

References should be **alphabetically**, with complete details, as follows:

Examples:
Books: https://apastyle.apa.org/style-grammar-guidelines/references/examples/book-references

Jackson, L. M. (2019). *The psychology of prejudice: From attitudes to social action* (2nd ed.). American Psychological Association. https://doi.org/10.1037/0000168-000

Kesharwani, P. (2020). *Nanotechnology based approaches for tuberculosis treatment*. Academic Press.

Sapolsky, R. M. (2017). *Behave: The biology of humans at our best and worst*. Penguin Books.

Torino, G. C., Rivera, D. P., Capodilupo, C. M., Nadal, K. L., & Sue, D. W. (2019). *Microaggression theory: Influence and implications*. John Wiley & Sons. https://doi.org/10.1002/9781119466642

In text:

- ***Parenthetical citations***: (Jackson, 2019; Sapolsky, 2017)
- ***Narrative citations***: Jackson (2019) and Sapolsky (2017)

Journal Article:
https://apastyle.apa.org/style-grammar-guidelines/references/examples/journal-article-references

Grady, J. S., Her, M., Moreno, G., Perez, C., & Yelinek, J. (2019). Emotions in storybooks: A comparison of storybooks that represent ethnic and racial groups in the United States. *Psychology of Popular Media Culture*, *8*(3), 207–217. https://doi.org/10.1037/ppm0000185

In text:

- ***Parenthetical citation***: (Grady et al., 2019)
- ***Narrative citation***: Grady et al. (2019)

Conference or Symposium:
https://apastyle.apa.org/style-grammar-guidelines/references/examples/conference-proceeding-references

Duckworth, A. L., Quirk, A., Gallop, R., Hoyle, R. H., Kelly, D. R., & Matthews, M. D. (2019). Cognitive and noncognitive predictors of success. *Proceedings of the National Academy of Sciences*, *USA*, *116*(47), 23499–23504. https://doi.org/10.1073/pnas.1910510116

In text:

- ***Parenthetical citation***: (Duckworth et al., 2019)
- ***Narrative citation***: Duckworth et al. (2019)

Dissertation / Thesis:
https://apastyle.apa.org/style-grammar-guidelines/references/examples/published-dissertation-references

Zambrano-Vazquez, L. (2016). *The interaction of state and trait worry on response monitoring in those with worry and obsessive-compulsive symptoms* [Doctoral dissertation, University of Arizona]. UA Campus Repository. https://repository.arizona.edu/handle/10150/620615

In text:

- ***Parenthetical citations***: (Kabir, 2016; Miranda, 2019; Zambrano-Vazquez, 2016)
- ***Narrative citations***: Kabir (2016), Miranda (2019), and Zambrano-Vazquez (2016)

https://apastyle.apa.org/style-grammar-guidelines/references/examples/unpublished-dissertation-references

Harris, L. (2014). *Instructional leadership perceptions and practices of elementary school leaders* [Unpublished doctoral dissertation]. University of Virginia.

In text:

- ***Parenthetical citation***: (Harris, 2014)
- ***Narrative citation***: Harris (2014)

Patents: Names and initials of authors, year (between brackets), patent title (Italic), patent number,country:
Grant, P. (1989). *Device for Elementary Analyses*. Patent. No.123456. USA.

Legal regulations and laws, organizations:
https://apastyle.apa.org/style-grammar-guidelines/references/examples/iso-standard-references

International Organization for Standardization. (2018). *Occupational health and safety management systems—Requirements with guidance for use* (ISO Standard No. 45001:2018). https://www.iso.org/standard/63787.html

Occupational Safety and Health Administration. (1970). *Occupational safety and health standards: Occupational health and environmental control: Occupational noise exposure* (OSHA Standard No. 1910.95). United States Department of Labor. https://www.osha.gov/laws-regs/regulations/standardnumber/1910/1910.95

In text:

- ***Parenthetical citations***: (International Organization for Standardization, 2018; Occupational Safety and Health Administration, 1970)
- ***Narrative citations***: International Organization for Standardization (2018) and Occupational Safety and Health Administration (1970)

Web references: The full URL should be given in text as a citation, if no other data are known. If the authors, year, and title of the documents are known and the reference is taken from a website, the URL address has to be mentioned after these data.

Citation in text

Please ensure that every reference cited in the text is also present in the reference list (and vice versa).

Do not cite references in the Abstract and Conclusions !.

Unpublished results, personal communications as well as URL addresses are not recommended in the references list.

Making personal quotations (one, at most) should not be allowed, unless the paper proposed to be published is a sequel of the cited paper. Articles in preparation or articles submitted for publication, unpublished, personal communications etc. should not be included in the references list.

Citations style

***Text**:* All citations in the text may be made directly (or parenthetically) as bellow.

- ***single author**:* the author's name (without initials, unless there is ambiguity) and the year of publication:
  "as previously demonstrated *(Brown, 2010)*".
- ***two authors**:* both authors' names and the year of publication: *(Adam and Brown, 2008; Smith and Hansel, 2006; Stern and Lars, 2009)*
- ***three or more authors**:* first author's name followed by "et al." and the year of publication: "As has recently been shown *(Werner et al., 2005; Kramer et al., 2000)* have recently shown ...."

Citations of groups of references should be listed first alphabetically, then chronologically.

Units, Abbreviations, Acronyms

- Units should be metric, generally SI, and expressed in standard abbreviated form.
- Acronyms may be acceptable, but must be defined at first usage.

2. REVIEWS

Summaries, reviews and perspectives covering topics of current interest in the field, are encouraged and accepted for publication. Reviews do not have the requirements for regular articles. However, should include: (*) an introductory chapter, (**) a careful and critical presentation of the relevant aspects of the topic approached and (***) emphasis of the aspects that aren't known and require further research to progress.

Edited by: INMA Bucharest
6, Ion Ionescu de la Brad Blvd., sect. 1, Bucharest, ROMANIA
Tel: +4021.269.32.60; Fax: +4021.269.32.73
https:// inmateh.eu
e-mail: ***inmatehjournal@gmail.com***